Bimetallic Nanostructures

Bimetallic Nanostructures

Shape-Controlled Synthesis for Catalysis, Plasmonics, and Sensing Applications

Edited by

Ya-Wen Zhang

College of Chemistry and Molecular Engineering
Peking University
Beijing
China

WILEY

This edition first published 2018
© 2018 John Wiley & Sons Ltd

All rights reserved. No part of this publication may be reproduced, stored in a retrieval system, or transmitted, in any form or by any means, electronic, mechanical, photocopying, recording or otherwise, except as permitted by law. Advice on how to obtain permission to reuse material from this title is available at http://www.wiley.com/go/permissions.

The right of Ya-Wen Zhang to be identified as the author of the editorial material in this work has been asserted in accordance with law.

Registered Office
John Wiley & Sons, Inc., 111 River Street, Hoboken, NJ 07030, USA
John Wiley & Sons Ltd, The Atrium, Southern Gate, Chichester, West Sussex, PO19 8SQ, UK

Editorial Office
The Atrium, Southern Gate, Chichester, West Sussex, PO19 8SQ, UK

For details of our global editorial offices, customer services, and more information about Wiley products visit us at www.wiley.com.

Wiley also publishes its books in a variety of electronic formats and by print-on-demand. Some content that appears in standard print versions of this book may not be available in other formats.

Limit of Liability/Disclaimer of Warranty
In view of ongoing research, equipment modifications, changes in governmental regulations, and the constant flow of information relating to the use of experimental reagents, equipment, and devices, the reader is urged to review and evaluate the information provided in the package insert or instructions for each chemical, piece of equipment, reagent, or device for, among other things, any changes in the instructions or indication of usage and for added warnings and precautions. While the publisher and authors have used their best efforts in preparing this work, they make no representations or warranties with respect to the accuracy or completeness of the contents of this work and specifically disclaim all warranties, including without limitation any implied warranties of merchantability or fitness for a particular purpose. No warranty may be created or extended by sales representatives, written sales materials or promotional statements for this work. The fact that an organization, website, or product is referred to in this work as a citation and/or potential source of further information does not mean that the publisher and authors endorse the information or services the organization, website, or product may provide or recommendations it may make. This work is sold with the understanding that the publisher is not engaged in rendering professional services. The advice and strategies contained herein may not be suitable for your situation. You should consult with a specialist where appropriate. Further, readers should be aware that websites listed in this work may have changed or disappeared between when this work was written and when it is read. Neither the publisher nor authors shall be liable for any loss of profit or any other commercial damages, including but not limited to special, incidental, consequential, or other damages.

Library of Congress Cataloging-in-Publication Data

Names: Zhang, Ya-Wen, 1965– editor.
Title: Bimetallic nanostructures : shape-controlled synthesis for catalysis, plasmonics, and sensing applications / edited by Professor Ya-Wen Zhang.
Description: Hoboken, NJ : John Wiley & Sons, 2018. | Includes bibliographical references and index. |
Identifiers: LCCN 2018010417 (print) | LCCN 2018017086 (ebook) | ISBN 9781119214632 (pdf) | ISBN 9781119214625 (epub) | ISBN 9781119214649 (cloth)
Subjects: LCSH: Metal catalysts. | Nanostructured materials.
Classification: LCC QD505 (ebook) | LCC QD505 .B556 2018 (print) | DDC 541/.395–dc23
LC record available at https://lccn.loc.gov/2018010417

Cover design by Wiley
Cover image: Courtesy of Ya-Wen Zhang

Set in 10/12pt Warnock by SPi Global, Pondicherry, India

10 9 8 7 6 5 4 3 2 1

Contents

List of Contributors *xiii*

Part I Fundamentals and Structural Characterization of Shape-Controlled Bimetallic Nanostructures *1*

1 Introduction of Bimetallic Nanostructures *3*
Zhi-Ping Zhang and Ya-Wen Zhang
1.1 Metallic Nanoparticles *3*
1.2 Bimetallic Nanoparticles *6*
1.2.1 Electronic Effect *7*
1.2.2 Lattice Stress *8*
1.2.3 Bifunctional Effect *9*
1.2.4 Ensemble Effect *9*
1.3 Bimetallic Nanostructures *10*
1.3.1 Alloyed Structure *10*
1.3.2 Core–Shell *11*
1.3.3 Heterostructure *11*
1.3.4 Factors Affecting the Mixing Patterns *12*
1.4 Bimetallic Nanostructure-Dependent Performance *12*
1.4.1 Elemental Composition and Distribution-Property Correlation *13*
1.4.2 Size–Property Correlation *14*
1.4.3 Geometric Structure-Property Correlation *15*
1.4.4 Phase Structure-Property Correlation *16*
1.5 Controlled Synthesis *17*
1.6 Outline of This Book *18*
1.7 References *19*

2 Theoretical Models for Bimetallic Surfaces and Nanoalloys *23*
Hong Jiang
2.1 Introduction *23*
2.2 Theoretical Approaches to Inter-Atomic Interactions *24*
2.2.1 First-Principles Approaches *24*
2.2.2 Empirical Inter-Atomic Potentials for Metallic Systems *29*
2.2.3 Lattice Models *31*
2.3 Global Optimization Methods *33*

2.3.1 Basin-Hopping Algorithm *33*
2.3.2 Genetic Algorithm *35*
2.4 Statistical Approaches *35*
2.4.1 Molecular Dynamics Simulation *36*
2.4.2 Monte Carlo Simulation *38*
2.4.3 Superposition Approach to Thermodynamic Properties of Nanoparticles *39*
2.5 Electronic Properties and Catalytic Activity of Bimetallic Systems *41*
2.5.1 The d-Band Model for Chemical Adsorption at Transition Metal Surfaces *41*
2.5.2 Tuning the Reactivity of Bimetallic Surfaces: Strain, Ligand, and Ensemble Effects *43*
2.5.2.1 Strain Effect *43*
2.5.2.2 Ligand Effect *44*
2.5.2.3 Ensemble Effect *44*
2.6 Computational Design of Bimetallic Heterogeneous Catalysts *44*
2.6.1 Transition State and Adsorption Energy-Scaling Relations *45*
2.6.2 The Sabatier Principle and the Volcano Plot *47*
2.6.3 High-Throughput Screening of Bimetallic Catalysts *49*
2.7 Concluding Remarks *50*
2.8 Acknowledgments *51*
2.9 References *51*

3 In situ Characterization Techniques of Bimetallics *61*
Rui Si
3.1 Introduction *61*
3.2 Electron Microscopy *62*
3.3 Infrared Spectroscopy *72*
3.4 X-Ray Absorption Fine Structure *79*
3.5 Conclusions and Outlook *91*
3.6 References *92*

Part II Synthesis, Characterization, and Properties of Shape-Controlled Bimetallic Nanostructures *97*

4 Bimetallic Nanopolyhedrons and Nanospheres *99*
Lin-Xiu Dai and Ya-Wen Zhang
4.1 Introduction *99*
4.2 Architecture of Bimetallic Nanospheres and Nanopolyhedrons *100*
4.2.1 Solid Solution *101*
4.2.2 Intermetallic Compounds *101*
4.2.3 Core–Shell Nanocrystals *102*
4.3 General Principles of Shape Evolution *103*
4.3.1 Equilibrium Shape: Wulff Polyhedron *103*
4.3.2 Nucleation Mechanism of Metal Nanocrystals *104*
4.3.3 Growth of Metal Nanocrystals *105*
4.4 Key Factors for Shape Evolution in Colloidal Synthesis *108*

4.4.1 Redox Potentials *108*
4.4.2 Reduction Rate *108*
4.4.3 Lattice Mismatch *110*
4.4.4 Facet-Specific Capping Agents *111*
4.5 Synthetic Approaches to Bimetallic Nanospheres and Nanopolyhedrons *113*
4.5.1 Continuous Growth *113*
4.5.1.1 Coreduction *113*
4.5.1.2 Thermal Decomposition *114*
4.5.1.3 Combination of Thermal Decomposition and Reduction *115*
4.5.2 Seed-Mediated Growth *116*
4.5.3 Combination of Underpotential Deposition and Galvanic Replacement Reaction *117*
4.6 Catalytic Properties of Bimetallic Nanospheres and Nanopolyhedrons *118*
4.6.1 Effects of Adsorption Energy and Facet Type in Bimetallics *119*
4.6.2 Shape-Dependent Catalytic Reactions *123*
4.6.2.1 Pt–Ni Nanocrystals for Oxygen Reduction Reaction *123*
4.6.2.2 Pt–Pd Nanocrystals for Methanol Electrooxidation *123*
4.6.2.3 Au–Pd Nanocrystals for Suzuki Coupling Reaction *124*
4.7 Conclusions and Outlook *124*
4.8 References *125*

5 Bimetallic Convex and Concave Nanostructures *133*
Shaojie Jiang, Yiliang Luan, Xiaokun Fan, Zewei Quan, and Jiye Fang
5.1 Introduction *133*
5.2 Synthetic Methods *134*
5.2.1 Synthesis of Bimetallic Concave Structures *135*
5.2.1.1 Galvanic Replacement *136*
5.2.1.2 Coreduction with a Control of Capping Ligand(s) *140*
5.2.1.3 Selective Etching (or Site-Specific Etching) *142*
5.2.1.4 Seed-Mediated Growth *145*
5.2.2 Synthesis of Bimetallic Convex Structure *146*
5.3 Structural Characterization *149*
5.3.1 Crystal Facets *149*
5.3.2 Case Studies *150*
5.3.2.1 {hk0} Facets *150*
5.3.2.2 {hkl} Facets *152*
5.4 Selected Properties *152*
5.4.1 SERS Characteristics *154*
5.4.1.1 Case of Ag Convex NCs *154*
5.4.1.2 Case of Ag Concave NCs *154*
5.4.1.3 Cases of Bimetallic Noble Metals *155*
5.4.2 Electrocatalytic Performance *156*
5.4.2.1 Cases of Pt–Cu Nanostructures *158*
5.4.2.2 Cases of Pt-Pd Concave NCs and Others *160*
5.4.3 Chemically Catalytic Behaviors *161*
5.4.3.1 Cases of Hydrogenation *161*
5.4.3.2 Cases of 4-Nitrophenol Reduction *163*

5.4.3.3 Cases of Other Reactions *163*
5.5 Conclusions *166*
5.6 References *166*

6 Bimetallic Nanoframes and Nanoporous Structures *172*
Hongliang Li, An Zhang, Zhicheng Fang, and Jie Zeng
6.1 Introduction *172*
6.2 Principles for the Formation of Bimetallic Nanoframes and Nanoporous Structures *173*
6.2.1 Top-Down Approach *174*
6.2.2 Bottom-Up Approach *176*
6.3 Synthetic Methods *178*
6.3.1 Template-Assisted Method *178*
6.3.1.1 Hard Template *178*
6.3.1.2 Soft Template *181*
6.3.1.3 Sacrificial Template *188*
6.3.2 Oxidative Etching *195*
6.3.3 Galvanic Replacement Reaction *199*
6.3.4 Kirkendall Effect *207*
6.3.5 Electrochemical Dealloying *210*
6.3.6 Assembly *213*
6.3.7 Other Methods of Interest *219*
6.4 Summary and Outlook *223*
6.5 References *225*

7 Bimetallic Dendritic Nanostructures *247*
Kun Yuan and Ya-Wen Zhang
7.1 Introduction *247*
7.2 Synthesis of Bimetallic Dendritic Nanostructures *248*
7.2.1 Coreduction *249*
7.2.2 Galvanic Replacement Reaction *251*
7.2.3 Seed-Mediated Growth *253*
7.2.4 Other Methods *257*
7.3 Properties and Applications of Bimetallic Dendritic Nanostructures *258*
7.3.1 Plasmonics *258*
7.3.2 Catalysis *261*
7.4 Conclusion and Outlook *265*
7.5 References *265*

8 Bimetallic Ultrathin Nanowires *271*
Junrui Li, Zheng Xi, and Shouheng Sun
8.1 Introduction *271*
8.2 Chemical Synthesis of Ultrathin Bimetallic Nanowires *273*
8.2.1 Synthetic Fundamentals *273*
8.2.2 Anisotropic Growth into Ultrathin Nanowires *274*
8.3 Chemical Synthesis of Ultrathin Bimetallic Nanowires *276*
8.3.1 Bimetallic Alloy Nanowires *277*
8.3.2 Bimetallic Core–Shell Nanowires *280*

8.3.3 Bimetallic Nanowires Formed by Directional Aggregation of Nanoparticles *282*
8.4 Concluding Remarks *284*
8.5 References *286*

9 Bimetallic Nanoplates and Nanosheets *293*
Bing Dong, Ziyu Yang, and Yanglong Hou
9.1 Introduction *293*
9.2 Synthesis of Bimetallic Nanoplates and Nanosheets *294*
9.2.1 Seeded Epitaxial Growth Process *294*
9.2.2 Coreduction Process *297*
9.2.3 Solvothermal Reaction *299*
9.2.4 Galvanic Replacement Reaction *300*
9.2.5 Electrodeposition Process *301*
9.2.6 Other Processes *302*
9.3 Properties and Applications of Bimetallic Nanoplates and Nanosheets *304*
9.3.1 Magnetic Properties *304*
9.3.2 Catalytic Applications *304*
9.3.3 Optical and Biomedical Applications *306*
9.4 Conclusions and Perspectives *307*
9.5 References *309*

Part III Applications of Shape-Controlled Bimetallic Nanostructures *315*

10 Electrocatalysis *317*
Jiwhan Kim, Juhyuk Choi, Jinkyu Lim, and Hyunjoo Lee
10.1 Introduction *317*
10.2 Effect of Bimetallic Nanostructures *318*
10.2.1 Electronic Effect *318*
10.2.2 Bifunctional Effect *318*
10.2.3 Ensemble Effect *319*
10.2.4 Morphology Effect *321*
10.3 Characterization Techniques *322*
10.3.1 Electron Microscopy *322*
10.3.2 X-ray Diffraction Pattern (XRD) *323*
10.3.3 X-ray Photoelectron Spectroscopy (XPS) and X-ray Absorption Spectroscopy (XAS) *324*
10.3.4 Electrochemical Measurements *326*
10.4 Electrocatalytic Reactions Using Bimetallic Nanostructures *327*
10.4.1 Oxygen Reduction Reaction (ORR) *327*
10.4.1.1 ORR Using Pt–M Alloy Structures *327*
10.4.1.2 ORR Using Pt–M Intermetallic Structures *329*
10.4.1.3 Model Surface *330*
10.4.1.4 Shape-Controlled Pt_3Ni Nanoparticles with (111) Facets *331*
10.4.1.5 Durability of the Bimetallic Nanoparticle Catalysts *333*
10.4.2 Fuel Oxidation *334*

10.4.2.1 Hydrogen Oxidation *335*
10.4.2.2 Methanol Oxidation *336*
10.4.2.3 Formic Acid Oxidation *337*
10.4.2.4 Oxidation of Other Small Organics *338*
10.4.3 Oxygen Evolution Reaction *339*
10.4.3.1 Alloy with Another Precious Metals *339*
10.4.3.2 Alloy with 3d Metals *340*
10.5 Perspective *340*
10.6 Conclusion *342*
10.7 Acknowledgments *343*
10.8 References *343*

11 Heterogeneous Catalysis *360*
Yuchen Pei and Wenyu Huang
11.1 Introduction *360*
11.2 Oxidation *361*
11.2.1 CO Oxidation *361*
11.2.1.1 Monometallic NPs *362*
11.2.1.2 Compositional and Structural Effect in Bimetallic NPs *362*
11.2.2 Preferential CO Oxidation in H_2-Rich Feeds (PROX) *368*
11.2.2.1 Spherical Core–Shell NPs *368*
11.2.2.2 Hollow Cubic NPs *370*
11.2.3 Selective Oxidation of Alcohols and Amines *370*
11.3 Hydrogenation/Dehydrogenation *376*
11.3.1 Selective Hydrogenation of Nitroarenes *376*
11.3.1.1 Spherical and Random-Shaped NPs *377*
11.3.1.2 Dendrite NPs *379*
11.3.1.3 Cubic/Octahedral NPs *381*
11.3.1.4 Hollow NPs *385*
11.3.2 Hydrogenation of Alkenes and Alkynes *389*
11.3.2.1 The Alkene Hydrogenation on Pt NPs *389*
11.3.2.2 Alkene Hydrogenation on Shaped Bimetallic NPs *390*
11.3.2.3 Semi-Hydrogenation of Alkynes on Shaped Bimetallic NPs *392*
11.3.3 Selective Hydrogenation of α,β-Unsaturated Aldehydes *395*
11.3.3.1 The Synergy of Bimetallic Combinations *396*
11.3.3.2 Capping Agent Effect *398*
11.4 H_2 Evolution Reaction *399*
11.5 Coupling Reactions *403*
11.5.1 Spherical NPs *403*
11.5.2 Polyhedral NPs *404*
11.5.2.1 Promotion of Activity Arising from High Index Facets and Larger Surface Area *404*
11.5.2.2 The Facet-Activity Relationship *408*
11.6 Conclusion *410*
11.7 Acknowledgments *410*
11.8 References *410*

12 Plasmonics *425*
Liang Zhou, Tian Zhao, Xiao-Yong Wang, Ling-Dong Sun, and Chun-Hua Yan
12.1 Introduction to Plasmonics *425*
12.2 Preparation of Gold Nanoparticles *428*
12.3 Assembly of Gold Nanoparticles *431*
12.3.1 Assembly of Gold Nanoparticles *431*
12.3.2 Reversible Assembly of Gold Nanoparticles *432*
12.3.3 Assembly of Gold Nanoparticles on Substrate *433*
12.4 Plasmonics of Bimetallic Nanocrystals *434*
12.4.1 Au–Ag Nanostructure *434*
12.4.2 Au–Pd Nanostructure *439*
12.4.3 Other Bimetallic Plasmonic Nanostructures *443*
12.5 Application of Plasmonic Nanostructures *444*
12.5.1 Bio-Imaging Application *445*
12.5.2 Photothermal Application *445*
12.5.3 Biodetection Based on SPR *446*
12.6 Concluding Remarks *447*
12.7 References *448*

13 Sensing *459*
Haijuan Li and Yongdong Jin
13.1 Plasmonic Sensors *460*
13.1.1 Bimetallic SPR Sensors *460*
13.1.2 Sensors Based on LSPR Peak Shift *461*
13.1.2.1 LSPR Shift Induced by Binding of the Analytes with the Sensor *461*
13.1.2.2 LSPR Sensors Based on Selective Etching of a Metallic Component from the Preformed Bimetallic Nanoparticles *462*
13.1.2.3 LSPR Sensors Based on Enzyme-Guided Metallic Crystal Growth *467*
13.2 Bimetallic Sensors Based on Surface-Enhanced Raman Spectroscopy *470*
13.3 Electrochemical Sensors Based on Bimetallic Nanoparticles *473*
13.3.1 Detection of Heavy Metal Ions *473*
13.3.2 Detection of Uric Acid *475*
13.3.3 Nonenzymatic Detection of Hydrogen Peroxide *475*
13.3.4 Detection of Glucose *477*
13.3.5 Electrochemical Immunosensors *478*
13.3.6 Detection of other Electroactive Molecules *481*
13.4 Sensors Based on the Enzyme-Mimicking Properties of Bimetallic NPs *482*
13.5 Sensors Based on Luminescent Bimetallic Nanoclusters *484*
13.5.1 Detection of Heavy Metal Ions *484*
13.5.2 Detection of Sulfide Anion *485*
13.5.3 Detection of Other Small Molecules *485*
13.6 Conclusions *489*
13.7 Acknowledgments *489*
13.8 References *489*

Index *499*

List of Contributors

Juhyuk Choi
Department of Chemical and Biomolecular Engineering, Korea Advanced Institute of Science and Technology, Daejeon, South Korea

Lin-Xiu Dai
College of Chemistry and Molecular Engineering, Peking University, Beijing, China

Bing Dong
Beijing Key Laboratory for Magnetoeletric Materials and Devices (BKL-MEMD), College of Engineering, Peking University, Beijing, China

Xiaokun Fan
Department of Chemistry, Southern University of Science and Technology, Shenzhen, Guangdong, P. R. China

Jiye Fang
Department of Chemistry, State University of New York at Binghamton, New York, USA

Zhicheng Fang
Hefei National Laboratory for Physical Sciences at the Microscale, Department of Chemical Physics, University of Science and Technology of China, Hefei, Anhui, P. R. China

Yanglong Hou
Beijing Key Laboratory for Magnetoeletric Materials and Devices (BKL-MEMD), and
Beijing Innovation Center for Engineering Science and Advanced Technology (BIC-ESAT), College of Engineering, Peking University, Beijing, China

Wenyu Huang
Department of Chemistry, Iowa State University, Ames, IA,USA
Ames Laboratory, U.S. Department of Energy, Ames, IA, USA

Hong Jiang
Beijing National Laboratory for Molecular Sciences, College of Chemistry and Molecular Engineering, Peking University, Beijing, China

Shaojie Jiang
Department of Chemistry, State University of New York at Binghamton, New York, USA

Yongdong Jin
State Key Laboratory of Electroanalytical Chemistry, Changchun Institute of Applied Chemistry, Chinese Academy of Sciences

Jiwhan Kim
Department of Chemical and Biomolecular Engineering, Korea Advanced Institute of Science and Technology, Daejeon, South Korea

Hyunjoo Lee
Department of Chemical and Biomolecular Engineering, Korea Advanced Institute of Science and Technology, Daejeon, South Korea

Haijuan Li
State Key Laboratory of Electroanalytical Chemistry, Changchun Institute of Applied Chemistry, Chinese Academy of Sciences

Hongliang Li
Hefei National Laboratory for Physical Sciences at the Microscale, Department of Chemical Physics, University of Science and Technology of China, Hefei, Anhui, P. R. China

Junrui Li
Department of Chemistry, Brown University, Providence, Rhode Island, USA

Jinkyu Lim
Department of Chemical and Biomolecular Engineering, Korea Advanced Institute of Science and Technology, Daejeon, South Korea

Yiliang Luan
Department of Chemistry, State University of New York at Binghamton, New York, USA

Yuchen Pei
Department of Chemistry, Iowa State University, Ames, IA, USA

Zewei Quan
Department of Chemistry, Southern University of Science and Technology, Shenzhen, Guangdong, P. R. China

Rui Si
Shanghai Synchrotron Radiation Facility, Shanghai Institute of Applied Physics, Chinese Academy Sciences, Shanghai, China

Ling-Dong Sun
College of Chemistry and Molecular Engineering, Peking University, Beijing, China

Shouheng Sun
Department of Chemistry, Brown University, Providence, Rhode Island, USA

Xiao-Yong Wang
College of Chemistry and Molecular Engineering, Peking University, Beijing, China

Zheng Xi
Department of Chemistry, Brown University, Providence, Rhode Island, USA

Chun-Hua Yan
College of Chemistry and Molecular Engineering, Peking University, Beijing, China

Ziyu Yang
Beijing Key Laboratory for Magnetoeletric Materials and Devices (BKL-MEMD), College of Engineering, Peking University, Beijing, China

Kun Yuan
College of Chemistry and Molecular Engineering, Peking University, Beijing, China

Jie Zeng
Hefei National Laboratory for Physical Sciences at the Microscale, Department of Chemical Physics, University of Science and Technology of China, Hefei, Anhui, P. R. China

An Zhang
Hefei National Laboratory for Physical Sciences at the Microscale, Department of Chemical Physics, University of Science and Technology of China, Hefei, Anhui, P. R. China

Ya-Wen Zhang
College of Chemistry and Molecular Engineering, Peking University, Beijing, China

Zhi-Ping Zhang
College of Chemistry and Molecular Engineering, Peking University, Beijing, China

Tian Zhao
College of Chemistry and Molecular Engineering, Peking University, Beijing, China

Liang Zhou
College of Chemistry and Molecular Engineering, Peking University, Beijing, China

Part I

Fundamentals and Structural Characterization of Shape-Controlled Bimetallic Nanostructures

1

Introduction of Bimetallic Nanostructures

Zhi-Ping Zhang and Ya-Wen Zhang

College of Chemistry and Molecular Engineering, Peking University, Beijing, China

1.1 Metallic Nanoparticles

Nanostructured particles are materials with at least one dimension at the nanoscale level (between 0.1 nm and 100 nm). Their scales are at the transition area between atomic clusters and bulk materials, and their optical, electrical, mechanical, magnetic, and catalytic properties are significantly different from those of bulk materials due to their quantum size effect, small size effect, surface effect, quantum tunneling effect, and dielectric confinement effect. There is no doubt that it is an exciting subject focusing on promising application of nanomaterials in various fields such as functional materials, sophisticated equipment, environmental remediation, and renewable energy processing.

In the elemental periodic table, more than two-thirds of the elements are metals. Metals are a class of glossy materials with good thermal and electrical conductivity, and are widely applied in architecture, electronic devices, information science, biomedical technology, and catalysis. For example, steel (iron) is often used for building; tungsten wire is applied in photoelectric instrument; ytterbium is applied in laser materials; and germanium is a valuable semiconductor material. Metal is fundamental to industry and life. In 1875, Pt/V_2O_5 catalysts were applied in the large-scale production of sulfuric acid. Around 1913, $Fe/Al_2O_3/K_2O$ catalysts were used for ammonia synthesis, which was a significant reaction for the production of chemical fertilizer[1]. In the 1970s and 1980s, Pt, Pd, and Rh were developed for automobile emission control, including CO and HC oxidations and NO reduction[1].

In order to improve their material properties and enhance their atomic utilization efficiency, metallic materials were also manufactured in nanoscales. The preparation of metallic nanoparticles dates from 1850s. In 1857, Faraday synthesized his famous Au colloids through the reduction of Au(III) ions with phosphorous in water[2]. In 1941, Rampino and Nord prepared colloidal dispersion of Pd by reduction with hydrogen[3].

Attributed to the two main factors, unique surface effect and quantum size effect, metallic nanomaterials have exhibited different properties from the corresponding bulk

Bimetallic Nanostructures: Shape-Controlled Synthesis for Catalysis, Plasmonics, and Sensing Applications, First Edition. Edited by Ya-Wen Zhang.
© 2018 John Wiley & Sons Ltd. Published 2018 by John Wiley & Sons Ltd.

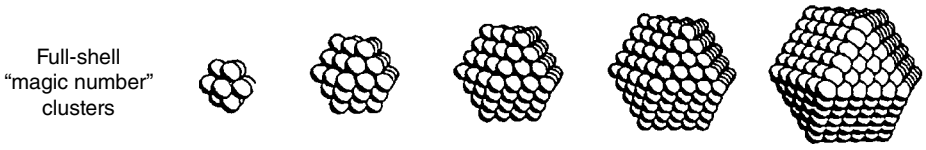

Number of shells	1	2	3	4	5
Number of atoms in cluster	13	55	147	309	561
Percentage of surface atoms	92	76	63	52	45

Figure 1.1 The percentage of surface atoms with the change of the size of nanoparticles. Modified with permission from ref. [4], copyright 2009 Wiley-VCH.

materials and have attracted increasing attention due to their potential application in catalysis, plasmonic, sensing, magnetic recording and other fields. For example, Pt nanoparticles (NPs) are good catalysts for energy storage, Au NPs are candidates for photothermal therapy, Fe NPs are magnetic materials for spintronic devices. The first main factor, surface effect, results in the large surface-to-volume ratios of metallic nanoparticles (NPs). As shown in Figure 1.1, the percentage of surface atoms increases dramatically with the decreased size of nanoparticles[4]. So when the sizes of nanoparticles are decreasing, the distributions of low-coordinated or coordinatively unsaturated atoms, including corner, edge, kink and step sites, on the surface of small particles will be increasing. Unsaturated coordination environment gives rise to the strong trend of active surface atoms to capture other atoms or migrate, and leads to the change of electronic energy band, spin conformation of surface atoms. One example is the large difference of the melting points between bulk gold and 1.5 nm gold nanoparticles[5]. The former is 1064 °C, while the latter is reduced to ca. 500 °C. The lowered melting point of 1.5 nm gold nanoparticles is because the low-coordinated surface atoms dominate about 80% of the total atoms and are easily mobilized under thermal perturbation.

The second main factor, the quantum size effect, leads to the shifting electronic energy bands and the change of band gap between the highest occupied molecular orbital (HOMO) and the lowest unoccupied molecular orbital (LUMO). As shown in Figure 1.2, in one bulk metallic material, the effectively continuous energy band is the combination of an infinite number of very similar orbitals; and in individual atom, the energy band turns into discrete atomic orbitals; while the energy bands of a nanoparticle fall somewhere between continuous and discrete energy bands. Thus, it gives rise to the interesting phenomenon that the properties of nanoparticles are distinct from those of bulk materials, such as size-induced metal-insulator transition[6]. That is, most of bulk metals are conductors, but the electroconductivity of the corresponding metal NPs becomes weaker with the decreasing size, and these particles turn into insulators when their sizes are small enough. It depends on the magnitude between HOMO-LUMO gap (somewhere called the *Kubo gap*, δ) and thermal energy. Another famous example is the property change of gold (Au) with its size. Bulk Au material is a yellow metal with noble and nonmagnetic feature, but its corresponding 10 nm nanoparticles are red, its 2–3 nm nanoparticles are superior catalysts with magnetism, and its smaller clusters become insulators[6].

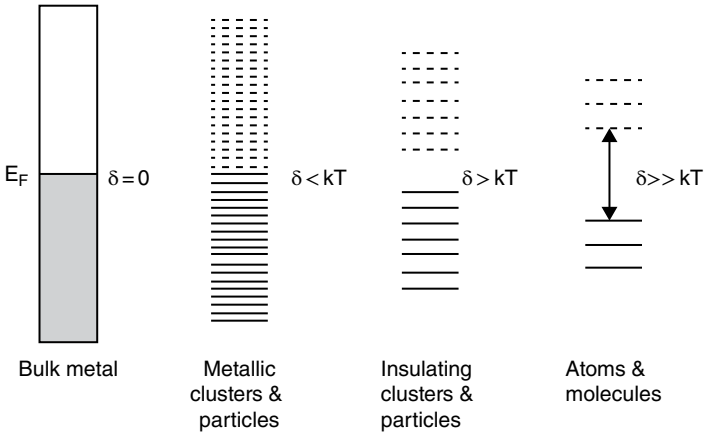

Figure 1.2 The energy band and the density of states as the decreasing size of metallic materials. δ is called the *Kubo gap*. Modified with permission from ref. [6], copyright 2006 Royal Society of Chemistry.

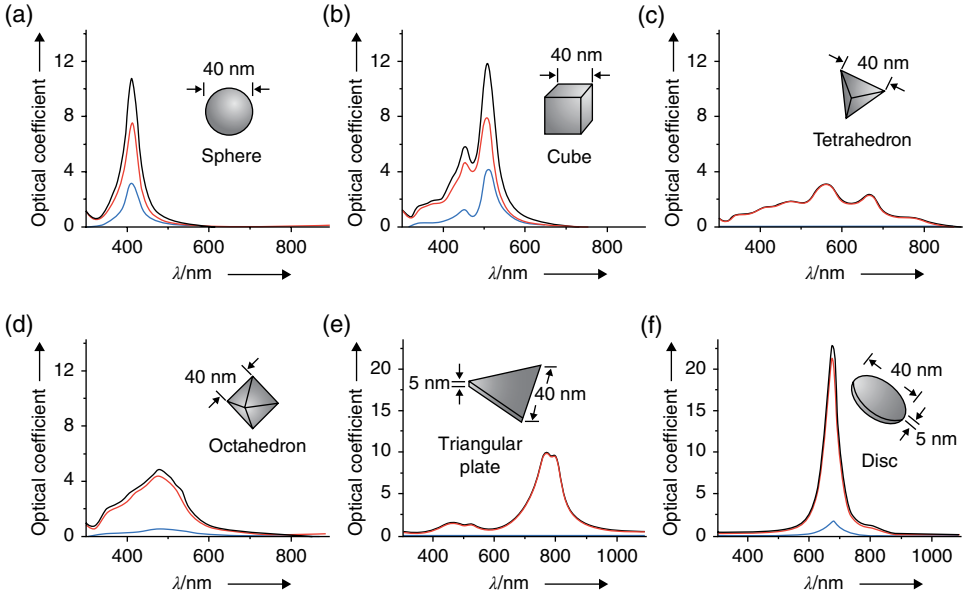

Figure 1.3 Simulated UV-Visible spectra of Ag nanoparticles with different shapes but the same size of 40 nm. The top, middle and bottom curves in every panel represent extinction, absorption and scattering spectra, respectively. Reprinted with permission from ref. [4], copyright 2009 Wiley-VCH.

In addition to the size of metallic nanomaterials, their structure and shape also influence their intrinsic physical and chemical properties and their potential applications. One notable example is the different simulated UV-Visible spectra of Ag nanoparticles with different shapes but the same size of 40 nm, as illustrated in Figure 1.3. The number, intensity, and position of localized surface plasmon resonance (LSPR) peaks can be fine-tuned by shape control. They are dependent on the following three points [4]: (1) the number of LSPR peaks is determined by the number of ways in which the electron

density of a nanoparticle can be polarized; (2) the position of LSPR peaks can be tuned by altering corner sharpness and/or shape anisotropy; and (3) the intensity of LSPR peaks is affected by shape symmetry.

For Ag nanosphere, a strong dipole resonance at 410 nm and a weak quadrupole resonance at 370 nm are observed (Figure 1.3a). Recent calculations indicate that surface charges are mainly accumulated at sharp corners. This enhanced charge separation results in the reduced restoring force for electron oscillation and the red-shifted LSPR peak when all other parameters are comparable. Therefore, compared to the nanosphere, the most intense peaks of nanocube, nanotetrahedron, and nanooctahedron are red-shifted, and the largest red-shift exists on the nanotetrahedron due to its largest corner sharpness (Figure 1.3b–1.3d). Besides, the weakest intensity of LSPR peak also occurs on the nanotetrahedron due to its T_d symmetry. As shown in Figures 1.3e and 1.3f, compared with the triangular nanoplate, the intensity of LSPR peak of the nanodisc is much greater because the circular symmetry of the nanodisc can provide a greater effective dipole moment. The above example demonstrates that the properties of metallic nanoparticles are highly related to their shapes. Therefore, the precise control of their size, shape, distribution, and monodispersion is crucial for the property optimization of metallic nanoparticles. Within the past decades, many solution-phase methods have been developed to prepare the shape-controlled metallic nanoparticles through the manipulation of their nucleation and growth process.

1.2 Bimetallic Nanoparticles

Since the Bronze Age, humans have formed alloys simply by mixing or melting two metals. The hybrid bimetallic material could have more excellent properties (e.g., hardness, ductility, and malleability) than either one of the metals involved. For example, when alloying iron with copper and chromium, steel would exhibit enhanced mechanical properties in hardness, ductility and malleability, and improved resistance to corrosion.

In general, bulk alloyed materials must be melted at high temperatures, and most of the two kinds of metals in the bulk state are even immiscible. At the nanoscale level, however, the two metals may become miscible, and their melting point could decline substantially with the decease of their size. This is because the formation of both enthalpy and Gibbs free energy of bimetallic materials decreases with particle size. Taking Cu–Ni as an example: although Cu-Ni has a positive formation enthalpy of the bulk immiscible system, Cu–Ni has a negative formation enthalpy when the particles are smaller than a critical size[7]. In this case, the alloying process first takes place in the dilute solute regions, then broadens to the dense solute regions, and finally forms the alloyed structure in the whole particle. It is apparent that bimetallic nanoparticles, composed of two distinct metal elements, are a new class of nanomaterials. On one hand, they exhibit different properties than their bulk bimetallic materials; on the other hand, they exhibit unique properties that differ from those of the corresponding pure monometallic counterparts and their physical mixings.

Modern interest in the synthesis and optical property of bimetallic nanoparticles dates from 1960s. In 1964, Morriss and Collins synthesized colloidal Au@Ag core-shell nanoparticles using 5.9 nm of Au nuclei, and compared their experimental optical

properties with the calculated results in different wavelength ranges[8]. In 1975, Papavassiliou discovered that the position of the absorption spectra of Au-Ag alloy solution depended on the composition of the alloy[9]. Commercial interest in bimetallic catalysts also dates from the 1960s due to their different activities toward hydrocarbon reforming from their parent metals[10]. The unexpected properties of bimetallic nanoparticles have inspired numerous further investigations on their syntheses, characterizations, properties, and applications.

Although bimetallic nanoparticles are more complicated than monometallic nanoparticles in many aspects, including synthesis control and structure characterization, they are superior in many ways. First, the incorporation of late transition elements, such as Fe, Co, and Ni, into the noble metallic nanoparticles can reduce the cost of materials, such as Pt–Ni alloy. Second, the electrical, physical, and chemical properties of bimetallic nanoparticles are not only associated with the two different metals but also can be modified easily by changing their composition, size, and shape. Furthermore, optimum components or an optimal structure of bimetallic nanoparticles can achieve a maximized atomic utilization rate and an excellent material property. The property modulation of bimetallic nanoparticles is mainly dependent on synergetic effects between two distinct elements, including electronic effect, lattice stress, bifunctional effect, and ensemble effect.

1.2.1 Electronic Effect

Electron transfer and charge redistribution occurs between two dissimilar atoms through d-state hybridization, and it gives rise to a change in density of state and d-band center of metal atoms. If the electronegativity of A is larger than that of B or B has a higher Fermi level, the electron will transfer from B to A, making the d-band center of A deeper and the d-band center of B shift up.

The adsorption energy of reaction species (reactant, intermediate, and product) on the metallic surface is related with the d-band center of the surface atoms, and further affects the catalytic activity. One example is Pt–M alloy nanocatalysts toward oxygen reduction reaction (ORR) (early-transition metals, M, include Y, Zr, Ti, Ni, and Co) investigated by Yoo et al.[11]. As shown in Figure 1.4, because early transition metals possess smaller eletronegativity than Pt, the electrons flowed from M to Pt, which made the d-band center of Pt in the Pt–M NPs deeper and reduced the binding energy of the oxygen-containing species. Due to the volcano curve trend between the activity of ORR and the binding energy of the oxygen-containing species, Pt–M NPs exhibited the same volcano curve trend between the activity for ORR and the shifting d-band centers of Pt caused by the electronic perturbation of alloys. The d-band center of Pt and the binding energy of the oxygen-containing species in the Pt_3Y NPs was the most appropriate, so that Pt_3Y NPs exhibited the highest transition rate for adsorbed OH to water and further displayed the best activity toward ORR.

The electronic effect of multimetallic nanomaterials not only affects their catalytic property but also affects their optical property. Taking Au@Pd as an example, the LSPR peak of Au spheres was located at 524 nm. When the thickness of the Pd shell was 0.7 nm, the peak position was blue-shifted to 495 nm, attributed to the electron transfer from Pd to Au[12].

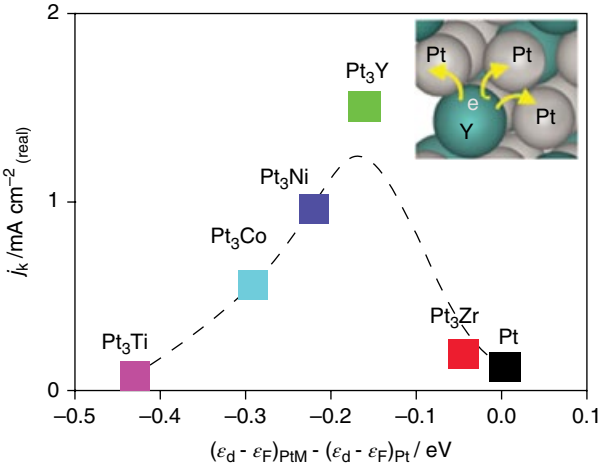

Figure 1.4 Kinetic current density for ORR on Pt_3M nanocatalysts and pure Pt nanocatalyst electrodes as a function of the d-band centers. Modified with permission from ref. [11], copyright 2012 American Chemical Society.

1.2.2 Lattice Stress

Lattice strain (compression or expansion) in core-shell or twin crystal caused by the different spatial arrangement of surface atoms results in a shift of d-band centers of metal or a change of d-band width; thus, it modulates the performance of bimetallic nanoparticles. A compressive strain causes a deeper d-band center of surface atom, and an expansive strain gives rise to a shallower d-band center of surface atom, as shown in Figure 1.5. As in the case of PtCu@Pt nanoparticles studied by Strasser and co-workers, the d-band centers of Pt in the Pt shell were modified by the compressive strain caused by the lattice mismatch between the Pt-rich shell and the PtCu core. Thus, it led to the weakened chemisorption of oxygenated species on the Pt shell, further giving rise to an enhanced catalytic reactivity toward ORR[13]. Predicted by density functional theory calculations, if the Pt–O binding energy (E_o) on the surface of Pt-based nanoparticles is

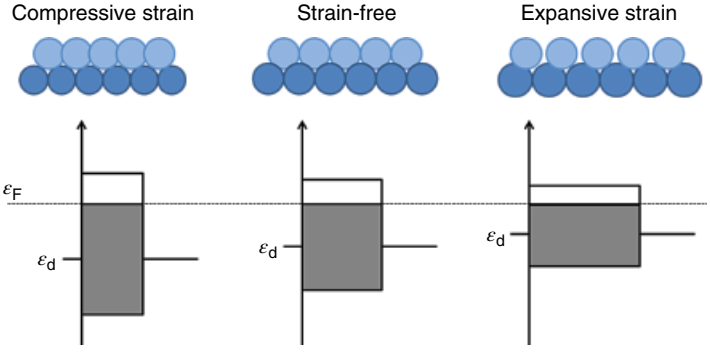

Figure 1.5 The shift of d-band centers of metal attributed to the lattice strains.

0.2 eV higher than the value on the Pt (111) surface, the Pt-based nanoparticles will display the maximum ORR activity. So fct-FePt/Pt nanoparticles (fct, face-centered tetragonal) with the ΔE_o of 0.23 eV exhibited higher activity than fcc-FePt/Pt nanoparticles (fcc, face-centered cubic) with the ΔE_o of 0.26 eV toward ORR due to their smaller, overcompressed Pt strain[14].

1.2.3 Bifunctional Effect

The surfaces of bimetallic nanoparticles can offer multiple catalytic sites, which adsorb different reactant molecules or intermediates respectively. The adsorption of different reactant species on different sites can avoid the poison risk for active sites caused by competitive adsorption of different species on the same site. Besides, when each metallic component can catalyze different elementary reaction steps, the co-adsorption can be helpful for the transformation of reaction intermediates. For instance, for Pt monometallic eletrocatalyst toward methanol oxidation reaction (MOR), CO is a poisoning species to Pt because of the strong bond energy of Pt–CO and the difficulty in the formation of the Pt–OH; while in the system of the Pt–Pd bimetallic catalysts, surface Pt sites catalyze the dehydrogenation of methanol to form Pt–CO, and surface Pd sites catalyze the dissociation of water to form Pd–OH, then Pt–CO reacts with Pd–OH to generate CO_2, which regains Pt sites and enhances the reaction activity[15].

Furthermore, in the hybridization system of highly catalytic metals (e.g., Pt, Pd, or Rh) with plasmonic metals (e.g., Au, Ag, or Cu), the surfaces of bimetallic nanoparticles can offer multifunctional sites[16]. For example, Majima et al. demonstrated the plasmon-enhanced production of H_2 from water and methanol on Pt-tipped Au nanorods[17]. As illustrated in Figures 1.6a and 1.6b, upon irradiation with visible and near-IR light, the Au nanorod had the excellent capability to absorb light, then photoelectrons were transferred to the Pt-tips, and finally, the Pt-tips generated highly active catalytic activity to reduce H_2O for the production of H_2, while methanol was oxidized at the electron-deficient Au nanorod.

1.2.4 Ensemble Effect

In some cases of catalysis, specific groupings of surface atoms take on distinct mechanistic functionalities. For example, Magnussen et al. studied electrocatalysis in Pd/Au(111) electrodes. Pd monomer on Au(111) is the smallest ensemble for the adsorption and oxidation of CO, while H adsorption requires Pd dimers or larger ensembles[18]. Another example is the synthesis of vinyl acetate by coupling of ethylene and acetate on Pd–Au bimetallic catalysts prepared by deposition of Pd on Au surface investigated by Goodman et al.[19]. As shown in Figure 1.6c, ethylene and acetate were adsorbed on different Pd monomers, and the optimized distance is 3.3 Å, so the Pd–Au(100) with the distance between two neighboring Pd monomers of 4.08 Å exhibited higher activity than Pd–Au(111) surface with the distance of 4.99 Å (Figure 1.6d). The high activity of a Pd monomer for vinyl acetate formation is due to an ensemble effect—that is, Pd monomers isolated by Au could prevent the formation of byproducts.

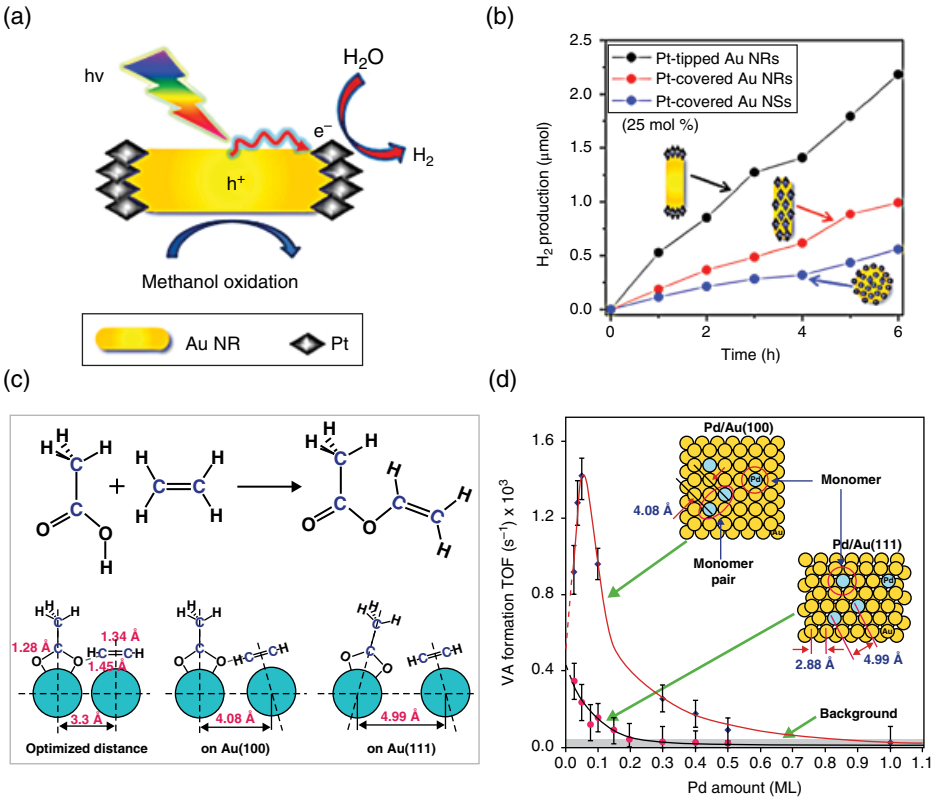

Figure 1.6 (a) Reaction mechanism for H_2 production on Pt-tipped Au nanorods. (b) Time course of H_2 production on Pt-tipped Au nanoparticles under visible-light irradiation. Modified with permission from ref. [17], copyright 2014 American Chemical Society. (c) Schematic for vinyl acetate (VA) synthesis; (d) VA formation rates (TOFs) as a function of Pd coverage on Au(100) and Au(111). Modified with permission from ref. [19], copyright 2005 American Association for the Advancement of Science.

1.3 Bimetallic Nanostructures

The property and function application of bimetallic nanoparticles is heavily related with their structures. Bimetallic nanostructures are complicated and can be classified into three main types: alloyed structure (intermetallic or solid solution), core–shell, and heterostructure according to the mixing patterns of two different metals (A and B), as illustrated in Figure 1.7.

1.3.1 Alloyed Structure

Both of the two alloyed structures have homogeneous distribution of atom A and atom B, whether on the surface or inside the particle. The distributions of atom A and atom B in the intermetallic structure have long-range order (Figure 1.7a), while a solid-solution nanoparticle has a structure with a random distribution of atom A and atom B in the particle (Figure 1.7b). The atomic ordering in the intermetallic structure, such as Au_3Cu, gives rise to a lattice structure distinct from the individual metals, and takes on

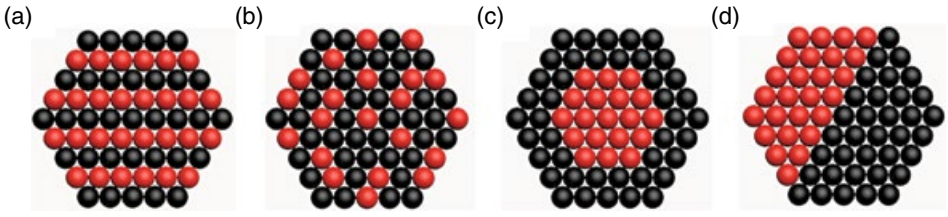

Figure 1.7 Bimetallic nanostructures with different atomic arrangements: (a) intermetallic structure; (b) solid solution; (c) core–shell structure; (d) heterostructure.

a well-defined stoichiometry, rather than random mixing[16]. The solid-solution structure exhibits a single and new crystal phase, and the value of the lattice parameter is between that of A and that of B. For example, in $PtCu_3$ nanocage, its X-ray diffraction (XRD) pattern demonstrated the pure intermetallic $PtCu_3$ phase, and no obvious peaks of Pt or Cu were observed[20]. During the formation process of the alloyed structure, two metallic precursors are often reduced or decomposed simultaneously to form a single kind of crystal nucleus. Then two corresponding metallic atoms grow surrounding the nucleus. Another case is that one kind of metallic atoms (A) firstly forms a nanocrystal, then the other kind of metallic atoms (B) replaces part of A by galvanic replacement; or B diffuses into core A and A diffuses out to B shell, finally resulting in a homogeneous distribution of two distinct atoms.

1.3.2 Core–Shell

Core–shell nanoparticles have a boundary between the core and the shell, with one metal segregation (A or B) as the core and the other metal collection (B or A) as the shell, as illustrated in Figure 1.7c. One kind of metal precursor is reduced first, and it gives rise to the generation of an inner core. Then the other kind of metal precursor is decomposed into metallic atoms and grows on the surface of the core. Finally, a core–shell forms. The surface of the core–shell only exposes atom B or atom A. Generally speaking, the core–shell structure displays the phase of A and the phase of B simultaneously. The core–shell structure may be helpful for crystal phase structure of shell B to inherit that of core A, which is thermodynamically stable or even metastable for B. For example, the thermodynamic stable phase of Ru is hexagonal-close-packed (hcp), but in Pt@Ru (core–shell) nanotetrahedrons, shell Ru had the same phase (fcc) with core Pt due to the layered growth of Ru on the surface of fcc core Pt[21]. One reverse phenomenon may occur in the core-shell structure; that is, the phase transformation of core occurs simultaneously during the formation of core-shell. One example is the synthesis of fcc Au@Pt rhombic nanoplates through the epitaxial growth of Pt on hcp Au sheets [22]. Because the hcp phase was not a thermodynamic stable phase for core Au, the growth of shell Pt gave rise to the transformation of core A from the hcp phase to the fcc phase.

1.3.3 Heterostructure

The common types of heterostructures include dendritic structures, dimers, multipods, dumbbells, and Janus particles. In heterostructures, section A and section B share one or a few mixing interfaces, as shown in Figure 1.7d. The heterostructure displays the

phase of A and the phase of B simultaneously. In this kind of structure, atom A and atom B appear on different surfaces, respectively. If a secondary metal B is attached on one side of collection A by island growth instead of conformal overgrowth, heterostructure forms. For example, using the cubic Pt as seeds, Au was grown into a rod, adopting the anisotropic overgrowth on the Pt seed induced by large lattice mismatch (4.08% mismatch between Au and Pt). Finally, the Pt seed and the Au rod were both exposed in the heterostructure[23]. Liz-Marzán et al. demonstrated the synthesis of Ag–Au–Ag segmented nanorods through the deposition of Ag at both ends of Au nanorods using penta-twinned Au nanorods as seeds[24]. The length of bimetallic nanorods could be controllably grown to several micrometers and the thickness was increased only slightly, so their longitudinal resonant mode was greatly red-shifted. In another case, if individual nucleation and growth of A and B appear on a shared mixing interface and the deposition is nonepitaxial, heterostructure also forms.

1.3.4 Factors Affecting the Mixing Patterns

The mixing patterns of two different metals (A and B) not only are related with precise control over nucleation and growth processes but also depend on several factors[25]:

1) *Bond energy.* If the bond energy of A–B is stronger than that of A–A and that of B–B, one of the following two cases probably occurs. When the precursor of A and the precursor B are reduced or the atom A and the atom B deposit simultaneously, it tends to form the alloyed structure; and when the nanoparticles of A form preferentially, the atoms B will attach on the interface of A to form core–shell by layered growth. Otherwise, it tends to form a heterostructure.
2) *Surface energy.* The composition with lower surface energy tends to segregate on the surface of NPs. However, if the surface is decorated by surfactant or facet-specific capping agent, the surface will expose specific composition or specific facet.
3) *Atomic radius.* If the atomic radii of A and B are equal, it tends to form the alloyed structure or form core–shell by epitaxial growth. Otherwise, it tends to form a heterostructure by island growth.
4) *Charge transfer.* The electron transference between A and B favors the formation of A–B bond, which is helpful for mixing.
5) *Size of bimetallic nanoparticles.* Phase separation in bimetallic clusters is dependent on the size of nanoparticles, predicted by Monte Carlo simulation[26]. That is, the alloying effect in a nanoparticle of radius r is the result of the competition between the enthalpy of a demixing phase transformation and the interfacial energy required to create a new surface on demixing[27]. The enthalpy of demixing is proportional to r^3 and the interfacial energy is proportional to r^2. So when the size of nanoparticles is small, the interfacial energy dominates, and it is less than enthalpy of demixing, the nanoparticles will stay as alloyed structure. Therefore, many of the two kinds of metals are immiscible in the bulk solid state but are miscible in the nanocluster state, such as Au and Pt.

1.4 Bimetallic Nanostructure-Dependent Performance

Different elemental composition ratios and various shapes of bimetallic materials have influences on their atomic arrangements, interactions between adjacent atoms, stacking patterns, and spatial atomic coordination environments. Since many physical and

chemical properties of bimetallic nanostructures are highly shape-dependent, surface-sensitive, and structure-sensitive, their promising functions can be optimized through the adjustment of various structure-dependent factors, including their composition, elemental distribution, size, geometric structure, and phase structure.

1.4.1 Elemental Composition and Distribution-Property Correlation

The properties of bimetallic nanoparticles are intensively dependent on the intrinsic nature of the elemental compositions of the whole nanoparticles and the surface elemental distributions. For example, the catalytic activities of Fe_xPt_{100-x} alloy nanoparticles with the average size of about 2.5 nm in the electro-oxidation of formic acid followed the order of $Fe_{42}Pt_{58} > Fe_{54}Pt_{46} \approx Fe_{58}Pt_{42} > Fe_{15}Pt_{85} > Fe_{10}Pt_{90} > Fe_{63}Pt_{37}$. The $Fe_{42}Pt_{58}$ nanoparticles displayed the highest activity, the best stability, and the strongest tolerance to CO poisoning[28]. For alloyed structure of two plasmonic metals, the plasmon resonances of alloys can be interpolated between those of corresponding monometallic nanoparticle. An example is the tunable surface plasmon resonance (SPR) frequency of Au_xAg_{100-x}. The SPR peak for $Au_{0.82}Ag_{0.18}$, $Au_{0.60}Ag_{0.40}$, $Au_{0.52}Ag_{0.48}$, $Au_{0.39}Ag_{0.61}$ nanoparticles of about 8 nm in sizes were 515 nm, 476 nm, 451 nm, 430 nm, respectively[29]. As illustrated in Figure 1.8, for the oxidation of toluene, the activity order of catalysts

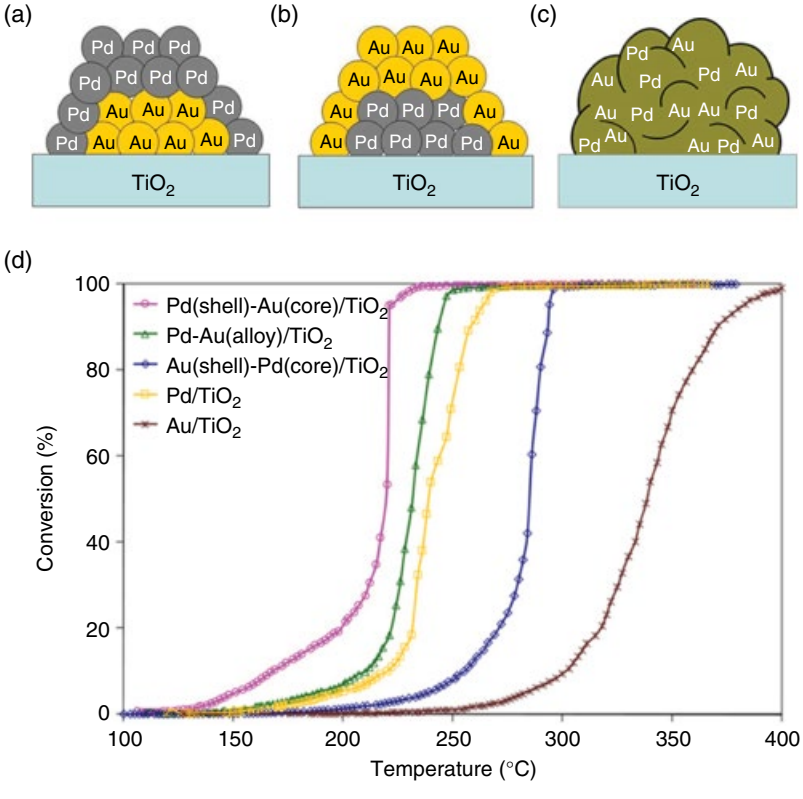

Figure 1.8 Models proposed for: (a) Pd(shell)-Au(core)/TiO_2; (b) Au(shell)-Pd(core)/TiO_2; (c) Pd-Au(alloy)/TiO_2; and (d) conversion of toluene on different catalysts. Modified with permission from ref. [30], copyright 2012 Elsevier.

followed Pd(shell)–Au(core)/TiO_2 > Pd–Au alloy/TiO_2 > Pd/TiO_2 > Au(shell)–Pd(core)/TiO_2 > Au/TiO_2[30]. The reaction activity was dependent on the preferential adsorption of oxygen molecules on the surfaces of catalysts. Pd exhibited the higher affinity for oxygen than Au, so the catalytic activity of Pd/TiO_2 is higher than that of Au(shell)–Pd(core)/TiO_2 and Au/TiO_2. The activity order of Pd(shell)–Au(core)/TiO_2 > Pd–Au alloy/TiO_2 > Pd/TiO_2 was due to the electronic promotion effect of Au for Pd.

1.4.2 Size–Property Correlation

The properties of bimetallic nanoparticles are also dependent on their sizes. First, the miscibility and ordering of bimetallic structures are related with the size of nanoparticle. When the size is sufficiently small, the interface energy will overcome the enthalpy of demixing. Thus, it results in the formation of alloyed structure. For example, Au and Pt in the bulk state are immiscible, but form a random solid solution in nanoparticles with the radii less than 3 nm; 2–3 nm of CoPt NPs can transform from the disordered structure to the ordered structure at 773 – 923 K, while the transition point of the bulk CoPt is at 1023 K.

Besides, the size of bimetallic nanoparticle strongly affects its catalytic performance. With its decreasing size, bimetallic nanoparticle possesses an increased surface-to-volume ratio, a higher proportion of surface atoms, and a higher density of active sites such as atomic steps, edges, corners, and kinks. These sites exhibit abundant unsaturated coordination environments and dangling bonds, which make the adsorption of reactants easy and make the energy barriers lower. So the catalytic activity of small nanoparticles is often higher than that of large nanoparticles. However, sometimes the catalytic activity is not linearly dependent on the size. For example, as illustrated in Figure 1.9, Pd

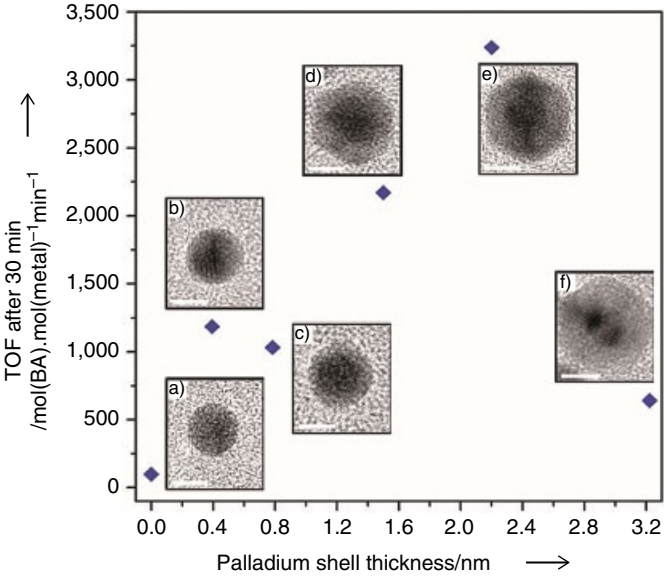

Figure 1.9 Catalytic properties of icosahedral Au@Pd core@shell nanocrystals versus palladium shell thicknesses for the solvent-free oxidation of benzyl alcohol (BA). Modified with permission from ref. [31], copyright 2013 Wiley-VCH.

grew on the surface of Au core of 7.1 nm in size layer by layer, and this precise control of nucleation and growth rates enabled the synthesis of icosahedral Au@Pd with the tunable shell size ranging from 0.4 to 3.2 nm; when the Pd shell thickness was 2.2 nm, isosahedral Au@Pd had the maximum catalytic activity towards the oxidation of benzyl alcohol because of the optimized synergy between Au and Pd; while thinner or thicker shells resulted in lower activities[31].

Furthermore, the absorption wavelengths of plasmonic bimetallic nanoparticles display variation with their adjustable sizes. For example, when Ag shell on the Au nanorod thickened with the increased size of Au@Ag NP, Au@Ag NP exhibited a continuous blue-shift of extinction spectra and the color of corresponding solution changed from red to orange due to the alterant composition and aspect ratio of NP attributed to preferential side deposition rather than end deposition of Ag on the Au rod[32].

1.4.3 Geometric Structure-Property Correlation

The geometric structures of bimetallic nanoparticles can be classified into zero-dimensional (nanosphere, nanopolyhedron, nanoframe, convex, and concave), one-dimensional (nanowire, nanotube, nanorod), and two-dimensional structures (nanosheet, nanoplate, nanoribbon) according to the dimensionality of nanoparticles. The bimetallic nanoparticles with different morphologies expose different facets, exhibit different surface atomic arrangements, and possess distinct electronic distributions, which further lead to the tunable physical and chemical properties.

Zero-dimensional nanoparticles with fcc structure often possess low-index facets of {111}[1] and {100} as a result of the driving force of minimum total energy, and different polyhedrons exhibit different performances. For example, as shown in Figure 1.10a, Pt–Pd nanocubes with the exposed {100} facets displayed a higher activity than Pt–Pd nanotetrahedron with the exposed {111} facets toward MOR did[33].

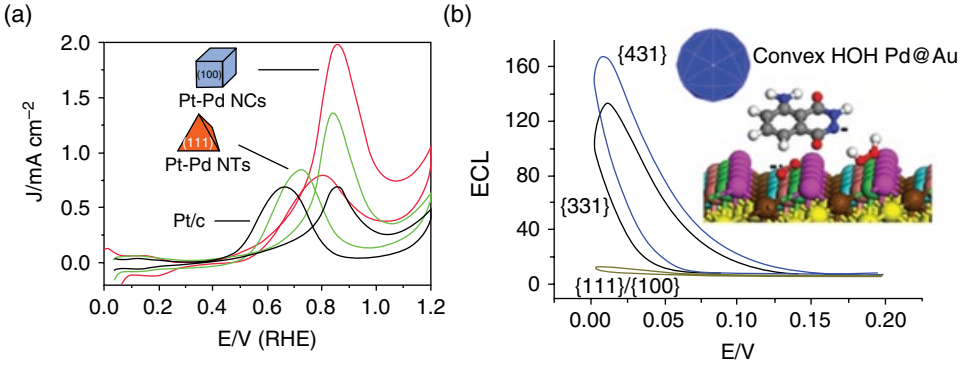

Figure 1.10 (a) The activities of Pt-Pd nanocubes (NCs), Pt-Pd nanotetrahedrons (NTs) and Pt/C toward methanol oxidation reaction. Modified with permission from ref. [33], copyright 2011 American Chemical Society. (b) Electrochemiluminescence (ECL) potential curves of luminol/H_2O_2 system on convex hexoctahedral (HOH), concave trisoctahedral, and truncated octahedral Pd@Au nanocrystal. Modified with permission from ref. [35], copyright 2014 American Chemical Society.

According to recent research, the coordination number of the surface atoms on a high-index facet is low due to the existence of abundant kinked, cornered, edged, and stepped atoms. These atoms are high-energy active sites. So sometimes synthesis methods could be optimized to obtain nanopolyhedrons with high-index facets. For example, hexoctahedral Au–Pd alloy NPs with {hkl} high-index facets were prepared through the assistance of Cu^{2+} ion by etching effect, and the NPs displayed excellent catalytic activity for formic acid oxidation and good tolerance to methanol[34]. Convex hexoctahedral Pd@Au NPs with {431} high-index facets were synthesized when combining fast-growth kinetics with capping effect, and they exhibited enhanced catalytic performances toward electrochemiluminescence compared to concave trisoctahedral Pd@Au NPs with {331} high-index facets and truncated octahedral Pd@Au NPs with {111} and {100} facets (Figure 1.10b) because of the abundant kink and step sites on {431} facets[35]. Highly branched concave Au/Pd NPs showed an improvement of surface-enhanced Raman spectra (SERS) due to their many intra- and interparticle gaps, tips, edges and hot spots[36].

Besides, porous nanoparticles and nanoframes often expose lots of highly unsaturated coordination sites (high-energy active sites), which lead to the enhanced catalytic activities[37]. For example, Pt_3Ni nanoframes achieved 36-fold increase in mass activities toward ORR when compared with Pt/C[38].

The dimensionality of nanomaterials plays an important role in their catalytic properties (activity, selectivity, and stability). The ultrathin features of one-dimensional or two-dimensional nanomaterials guarantee more accessible sites and unsaturated coordination sites, as well as accelerate reaction rates. For example, ultrathin Pt–Cu nanosheets displayed nine times higher activity than Pt/C for ethanol oxidation reaction[39]. Generally speaking, zero-dimensional NPs show lower stability with time due to their tendency to agglomerate and form larger particles in order to reduce surface area and surface energy; while one-dimensional NPs display higher stability due to the less agglomeration. Furthermore, the dimensionality change of nanomaterials can adjust their anisotropic property. Tunable aspect ratio of anisotropic plasmonic metallic particles gives rise to the change of surface plasmon resonance, including the resonance wavelengths and the resonance intensities. For example, Au/Ag nanorods show a much greater enhancement in local field and SERS activity than Au/Ag nanospheres do.

1.4.4 Phase Structure-Property Correlation

A_xB_y nanoparticles with diverse phase structures exhibit different properties due to their different bond distances of A–A, A–B, B–B, and different coordination environments. Different phase structures determine electronic energy level of metals and spatial distribution of constituent elements. For example, the FePt NPs with fcc structure (Figure 1.11a) were weakly superparamagnetic, while the FePt NPs with fct structure (Figure 1.11b) were ferromagnetic, and the latter displayed the better activity and durability than the former toward ORR (Figure 1.11c) because of their stable intermetallic stack of Fe and Pt[40]. The crystal phase of fcc Co@Pt nanocrystals could be transformed to homogeneous fct structure by annealing at 700 K. The former displayed zero coercivity, while the latter were ferromagnetic with a coercivity value of 5.3 kOe at room temperature[41].

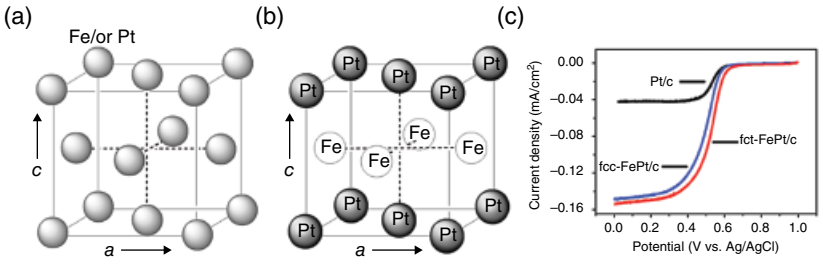

Figure 1.11 Schematic illustration: (a) fcc-FePt; and (b) fct-FePt. ORR current densities from the commercial Pt/C, fcc-FePt/C, and fct-FePt/C catalysts. Modified with permission from ref. [40], copyright 2014 American Chemical Society.

1.5 Controlled Synthesis

The controlled synthesis of bimetallic nanostructures has attracted enormous interest because the property of bimetallic nanostructures is not only related with elemental nature, but also heavily dependent on the synthetic methods. Different methods affect the elemental distribution, size, geometric structure, and phase structure of bimetallic nanoparticles, further determining the performance of bimetallic nanoparticles. Precise control of the elemental distribution, size, geometric structure, and phase structure plays a valuable role in optimizing their functionality and application performance. Therefore, it is necessary to well understand the recent progress in the controlled synthesis of bimetallic nanostructures.

In the last few decades, several strategies have been achieved to prepare bimetallic nanostructures, including microwave, ultrasonic, sol-gel, microemulsion, and chemical precipitation. However, the controlled synthesis of bimetallic nanostructures still remain a challenge due to its complexity, such as its difficulty in ensuring synchronous nucleation and growth of different metals due to their distinct kinetic and thermodynamic properties.

The synthesis methods can be categorized into three kinds: solid-state method, gaseous-state method, and solution-state method[42]. The solid-state method needs long-time high-temperature heating and annealing, such as two kinds of bulk metals melting into alloys using metallurgy. The gaseous-state method requires complicated apparatus, such as mixed metallic vapors condense and form clusters or nanoparticles using chemical vapor deposition. The solution-state method is the most simple and powerful approach—for example, two metallic precursors being reduced and forming alloys simultaneously using thermal decomposition.

The solution-based approach can be classified into four types: continuous growth, crystallites coalescence, seeded-growth, and galvanic replacement[43], as shown in Figure 1.12. Several key factors, such as redox potentials of distinct metal precursors, surface tension and interface energy, surfactant and facet-specific capping agent, reducing agent, and experimental condition (concentration of reactants, mole ratio between precursors, temperature, time, atmosphere, pressure), should be controlled accurately in order to obtain monodisperse nanoparticles. By adjusting kinetic and thermodynamic factors, reduction rate or decomposition rate of metallic precursors can be optimized to trigger proper atomic packing styles and nucleation patterns. This further

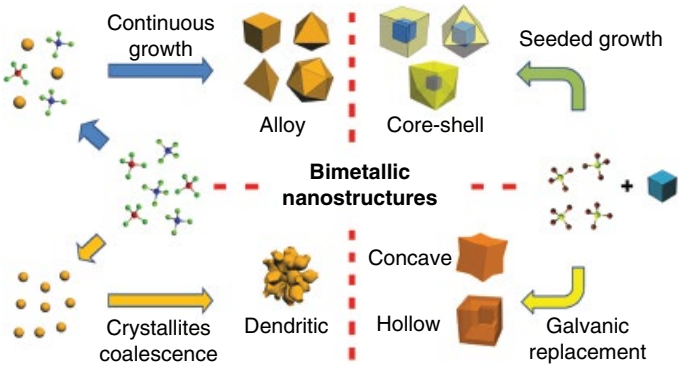

Figure 1.12 Four solution-state-controlled synthesis routes of bimetallic nanostructure. Modified with permission from ref. [43], copyright 2012 Royal Society of Chemistry.

leads to expected growth process and finally determines the preparation output of well-defined bimetallic nanoparticles.

1.6 Outline of This Book

The main subject of this book is shape-controlled synthesis of bimetallic nanostructures for catalysis, plasmonics, and sensing application. The book is divided into three sections: the first one primarily introduces some basic chemical and physical knowledges of bimetallic structures, including fundamentals, computational models, and *in situ* characterization techniques; the second provides a brief summary of the recent development of synthetic methods, characterization methods, and properties of bimetallic structures from the perspective of morphology effect, including zero-dimensional nanomaterials, one-dimensional nanomaterials, and two-dimensional nanomaterials; and the last one illustrates applications of current interest derived from their properties.

A well-defined nanostructure provides a simple but clear physical model for the interpretation of structure-property relationship. The construction of calculation model and quantum computation for bimetallic nanostructures is helpful for the study of growth process and the mechanism of property. In Chapter 2 of Part One, we will address computational models of bimetallic nanostructure.

A variety of experimental characterization techniques, including electron microscopy, mass spectrometry, X-ray spectroscopy, and ultraviolet-visible spectroscopy, have been used to study structures and properties of bimetallic nanoparticles. Recently, the development of *in-situ* surface characterization makes it possible to track the growth process of bimetallic nanoparticles from atoms to nanostructures. Since the observation of the change on the surface of shape-controlled bimetallic nanoparticles in real time using *in situ* characterization is helpful to understand the nature of nanoparticles, we will focus on the *in situ* characterization techniques in Chapter 3 of Part One.

The chemical and physical properties of bimetallic nanoparticles are closely related to their structures, so shape control (including the atomic distributions on the surface and in the whole particle, size, geometric structure, and phase structure) of the bimetallic nanostructures is critical for the improvement and optimization of their tunable

physical and chemical properties. In Part Two, we will introduce the synthesis, characterization, and properties of shape-controlled bimetallic nanostructures, including zero-dimensional (Chapter 4 to Chapter 6), hierarchical and one-dimensional (Chapter 7 and Chapter 8), and two-dimensional (Chapter 9) structures.

Bimetallic nanostructures exhibit many interesting and unique properties, and their attractive properties make them applicable in different fields. In Part Three, we will describe some applications of shape-controlled bimetallic nanostructures, including electrocatalysis in Chapter 10, heterogeneous catalysis in Chapter 11, plasmonics in Chapter 12, and sensing in Chapter 13.

The book is addressed to a wide circle of academic researchers in nanoscience, nanochemistry, and nanomaterial, and to those working in the areas of industry including nanotechnology, catalysis, and optoelectronics. A systematic summary of controlled synthesis, characterization, properties, and applications of well-defined bimetallic nanostructures in this book is helpful for establishing a comprehensive grasp of fundamental knowledge and recent development of bimetallic nanoparticles.

1.7 References

1 Bartholomew, C. H., and Farrauto, R. J. (2006). Fundamentals of Industrial Catalytic Processes. *Fundamentals of Industrial Catalytic Processes*, 2nd ed. Hoboken, NJ: John Wiley & Sons, Inc.

2 Faraday, M. (1857). *Philos. Trans. R. Soc. London*, 147.

3 Rampio, L. D., and Nord, F. F. (1941). Applicability of palladium synthetic high polymer catalysts. *Journal of the American Chemical Society*, 63 (12), 3268–3268.

4 Xia, Y., Xiong, Y., Lim, B. and Skrabalak, S. E. (2009). Shape-controlled synthesis of metal nanocrystals: simple chemistry meets complex physics? *Angewandte Chemie-International Edition*, 48 (1), pp. 60–103.

5 Corain, B., Schmid, G. and Toshima, N. (2008). metal nanoclusters in catalysis and materials science: the issue of size control. Amsterdam: Elsevier.

6 Roduner, E. (2006). Size matters: why nanomaterials are different. *Chemical Society Reviews*, 35 (7),. 583–592.

7 Qi, W. (2016). Nanoscopic thermodynamics, *Accounts of Chemical Research*, 49 (9), 1587–1595.

8 Morriss, R. H., and Collins, L. F. (1964). Optical properties of multilayer colloids. *Journal of Chemical Physics*, 41 (11), 3357–3363.

9 Papavassiliou, G. C. (1976). Surface-plasmons in small Au–Ag alloy particles. *Journal of Physics F-Metal Physics*, 6 (4), L103–L105.

10 Sinfelt, J. H. (1977). Catalysis by alloys and bimetallic clusters, *Accounts of Chemical Research*, 10 (1), 15–20.

11 Hwang, S. J., Kim, S. K., Lee, J. G., Lee, S. C., Jang, J. H., Kim, P., Lim, T. H., Sung, Y. E. and Yoo, S. J. (2012). Role of electronic perturbation in stability and activity of Pt-based alloy nanocatalysts for oxygen reduction, *Journal of the American Chemical Society*, 134 (48), 19508–19511.

12 Zhang, L., Xie, Z. X., and Gong, J. L. (2016). Shape-controlled synthesis of Au-Pd bimetallic nanocrystals for catalytic applications, *Chemical Society Reviews*, 45 (14), 3916–3934.

13 Strasser, P., Koh, S., Anniyev, T., Greeley, J., More, K., Yu, C., Liu, Z., Kaya, S., Nordlund, D., Ogasawara, H., Toney, M. F. and Nilsson, A. (2010). Lattice-strain control of the activity in dealloyed core-shell fuel cell catalysts, *Nature Chemistry*, 2 (6), 454–460.

14 Zhang, S., Zhang, X., Jiang, G. M., Zhu, H. Y., Guo, S. J., Su, D., Lu, G. and Sun, S. H. (2014). Tuning nanoparticle structure and surface strain for catalysis optimization, *Journal of the American Chemical Society*, 136 (21), 7734–7739.

15 Liu, Y., Chi, M., Mazumder, V., More, K. L., Soled, S., Henao, J. D. and Sun, S. (2011). Composition-controlled synthesis of bimetallic PdPt nanoparticles and their electro-oxidation of methanol, *Chemistry of Materials*, 23 (18), 4199–4203.

16 Gilroy, K. D., Ruditskiy, A., Peng, H. C., Qin, D. and Xia, Y. (2016). Bimetallic nanocrystals: syntheses, properties, and applications, *Chemical Reviews*, 116 (18), 10414–10472.

17 Zheng, Z. K., Tachikawa, T. and Majima, T. (2014). Single-particle study of Pt-modified Au nanorods for plasmon-enhanced hydrogen generation in visible to near-infrared region, *Journal of the American Chemical Society*, 136 (19), 6870–6873.

18 Maroun, F., Ozanam, F., Magnussen, O. M. and Behm, R. J. (2001). The role of atomic ensembles in the reactivity of bimetallic electrocatalysts, *Science*, 293 (5536), 1811–1814.

19 Chen, M. S., Kumar, D., Yi, C. W. and Goodman, D. W. (2005). The promotional effect of gold in catalysis by palladium-gold, *Science*, 310 (5746), 291–293.

20 Xia, B. Y., Wu, H. B., Wang, X. and Lou, X. W. (2012). One-pot synthesis of cubic $PtCu_3$ nanocages with enhanced electrocatalytic activity for the methanol oxidation reaction, *Journal of the American Chemical Society*, 134 (34), 13934–13937.

21 Gu, J., Guo, Y., Jiang, Y. Y., Zhu, W., Xu, Y. S., Zhao, Z. Q., Liu, J. X., Li, W. X., Jin, C. H., Yan, C. H. and Zhang, Y. W. (2015). Robust phase control through hetero-seeded epitaxial growth for face-centered cubic Pt@Ru nanotetrahedrons with superior hydrogen electro-oxidation activity, *Journal of Physical Chemistry C*, 119 (31), 17697–17706.

22 Fan, Z., Zhu, Y., Huang, X., Han, Y., Wang, Q., Liu, Q., Huang, Y., Gan, C. L. and Zhang, H. (2015). Synthesis of ultrathin face-centered-cubic Au@Pt and Au@Pd core-shell nanoplates from hexagonal-close-packed au square sheets, *Angewandte Chemie-International Edition*, 54 (19), 5672–5676.

23 Habas, S. E., Lee, H., Radmilovic, V., Somorjai, G. A. and Yang, P. (2007). Shaping binary metal nanocrystals through epitaxial seeded growth, *Nature Materials*, 6 (9), 692–697.

24 Mayer, M., Scarabelli, L., March, K., Altantzis, T., Tebbe, M., Kociak, M., Bals, S., de Abajo, F. J. G., Fery, A. and Liz-Marzan, L. M. (2015). Controlled living nanowire growth: precise control over the morphology and optical properties of AgAuAg bimetallic nanowires, *Nano Letters*, 15 (8), 5427–5437.

25 Ferrando, R., Jellinek, J. and Johnston, R. L. (2008). Nanoalloys: from theory to applications of alloy clusters and nanoparticles, *Chemical Reviews*, 108 (3), 845–910.

26 Christensen, A., Stoltze, P. and Norskov, J. K. (1995). Size dependence of phase-separation in small bimetallic clusters, *Journal of Physics-Condensed Matter*, 7 (6), 1047–1057.

27 Cortie, M. B. and McDonagh, A. M. (2011). Synthesis and optical properties of hybrid and alloy plasmonic nanoparticles, *Chemical Reviews*, 111 (6), 3713–3735.

28 Chen, W., Kim, J. M., Sun, S. H. and Chen, S. W. (2007). Composition effects of fept alloy nanoparticles on the electro-oxidation of formic acid, *Langmuir*, 23 (22), 11303–11310.

29 Wang, C., Yin, H., Chan, R., Peng, S., Dai, S. and Sun, S. (2009). One-pot synthesis of oleylamine coated AuAg alloy NPs and their catalysis for CO oxidation, *Chemistry of Materials*, 21 (3), 433–435.

30 Hosseini, M., Barakat, T., Cousin, R., Aboukais, A., Su, B. L., De Weireld, G. and Siffert, S. (2012). Catalytic performance of core-shell and alloy Pd–Au nanoparticles for total oxidation of VOC: The Effect of Metal Deposition, *Applied Catalysis B-Environmental*, 111 pp. 218–224.

31 Henning, A. M., Watt, J., Miedziak, P. J., Cheong, S., Santonastaso, M., Song, M., Takeda, Y., Kirkland, A. I., Taylor, S. H. and Tilley, R. D. (2013). Gold-palladium core-shell nanocrystals with size and shape control optimized for catalytic performance, *Angewandte Chemie-International Edition*, 52 (5), 1477–1480.

32 Zhang, C., Yin, A. X., Jiang, R., Rong, J., Dong, L., Zhao, T., Sun, L. D., Wang, J., Chen, X. and Yan, C. H. (2013). Time-temperature indicator for perishable products based on kinetically programmable Ag overgrowth on Au nanorods, *ACS Nano*, 7 (5), 4561–4568.

33 Yin, A. X., Min, X. Q., Zhang, Y. W. and Yan, C. H. (2011). Shape-selective synthesis and facet-dependent enhanced electrocatalytic activity and durability of monodisperse Sub-10 nm Pt-Pd tetrahedrons and cubes, *Journal of the American Chemical Society*, 133 (11), 3816–3819.

34 Zhang, L., Zhang, J., Kuang, Q., Xie, S., Jiang, Z., Xie, Z. and Zheng, L. (2011). Cu^{2+}-assisted synthesis of hexoctahedral Au-Pd alloy nanocrystals with high-index facets, *Journal of the American Chemical Society*, 133 (43), 17114–17117.

35 Zhang, L., Niu, W., Gao, W., Qi, L., Lai, J., Zhao, J. and Xu, G. (2014). Synthesis of convex hexoctahedral palladium@gold core-shell nanocrystals with {431} high-index facets with remarkable electrochemiluminescence activities, *Acs Nano*, 8 (6), 5953–5958.

36 Zhang, L. F., Zhong, S. L. and Xu, A. W. (2013). Highly branched concave Au/Pd bimetallic nanocrystals with superior electrocatalytic activity and highly efficient SERS enhancement, *Angewandte Chemie-International Edition*, 52 (2), 645–649.

37 Zhang, Z. P., Zhu, W., Yan, C. H. and Zhang, Y. W. (2015). Selective synthesis of rhodium-based nanoframe catalysts by chemical etching of 3d metals, *Chemical Communications*, 51 (19), 3997–4000.

38 Chen, C., Kang, Y., Huo, Z., Zhu, Z., Huang, W., Xin, H. L., Snyder, J. D., Li, D., Herron, J. A., Mavrikakis, M., Chi, M., More, K. L., Li, Y., Markovic, N. M., Somorjai, G. A., Yang, P. and Stamenkovic, V. R. (2014). Highly crystalline multimetallic nanoframes with three-dimensional electrocatalytic surfaces, *Science*, 343 (6177), 1339–1343.

39 Saleem, F., Zhang, Z., Xu, B., Xu, X., He, P. and Wang, X. (2013). Ultrathin Pt-Cu nanosheets and nanocones, *Journal of the American Chemical Society*, 135 (49), 18304–18307.

40 Kim, J., Lee, Y. and Sun, S. H. (2010). Structurally ordered FePt nanoparticles and their enhanced catalysis for oxygen reduction reaction, *Journal of the American Chemical Society*, 132 (14), 4996–4997.

41 Park, J. I., Kim, M. G., Jun, Y. W., Lee, J. S., Lee, W. R. and Cheon, J. (2004). Characterization of superpararnagnetic "core-shell" nanoparticles and monitoring their anisotropic phase transition to ferromagnetic "solid solution" nanoalloyse, *Journal of the American Chemical Society*, 126 (29), 9072–9078.

42 Wang, D. and Li, Y. (2011). Bimetallic nanocrystals: liquid-phase synthesis and catalytic applications, *Advanced Materials*, 23 (9), 1044–1060.

43 Gu, J., Zhang, Y. W. and Tao, F. (2012). Shape control of bimetallic nanocatalysts through well-designed colloidal chemistry approaches, *Chemical Society Reviews*, 41 (24), 8050–8065.

2

Theoretical Models for Bimetallic Surfaces and Nanoalloys

Hong Jiang

Beijing National Laboratory for Molecular Sciences, College of Chemistry and Molecular Engineering, Peking University, Beijing, China

2.1 Introduction

Bimetallic clusters, nanoparticles and surfaces have attracted tremendous interest in the past decades due to their intriguing physical and chemical properties, and their promising applications in many fields of materials science including catalysis, nanomagnetism, optics, and nanomedicines, to name a few only[1–6]. Theoretical simulation has played an important role in interpreting experimental findings on versatile properties of bimetallic systems[5, 6]. This is partly due to the fact that experimental characterization of bimetallic nanoparticles, in spite of recent impressive developments[7], is still quite limited in terms of structural resolution, and the interpretation of experimental findings relies heavily on theoretical modeling. Most nanoparticles of fundamental or practical interest fall in the nonscaling regime in the sense that their properties can not be inferred by extrapolation of the properties of their bulk counterparts. From the theoretical perspective, metal nanoparticles provide ideal testbeds for the development of novel theoretical concepts and techniques, and present a series of questions of fundamental interest. For example, the need to predict the most stable structures of metal clusters with tens or even hundreds of atoms has driven the flourishing development of various global optimization techniques[8, 9]. The study of the stability of multi-component metal nanoparticles as a function of the size, structural motifs, and composition at finite temperature has pushed the development of thermodynamics in the nanoscale[10].

A hierarchical set of computational methods have been applied to theoretical study of bimetallic systems that address different aspects of their properties[6]:

1) Theoretical approaches for the description of inter-atomic potentials, or potential energy surface (PES). These approaches are needed to obtain structural, energetic (zero temperature), mechanical, and thermodynamic properties of target materials[11].
2) Global optimization methods to obtain the most stable structures of nanoparticles for given composition and size[6, 12].

Bimetallic Nanostructures: Shape-Controlled Synthesis for Catalysis, Plasmonics, and Sensing Applications, First Edition. Edited by Ya-Wen Zhang.
© 2018 John Wiley & Sons Ltd. Published 2018 by John Wiley & Sons Ltd.

3) Statistical approaches to the study of structural stability and thermodynamical properties of nanoalloys at finite temperature[13–15], and to the simulation of kinetic processes such as growth and melting[16].
4) Theoretical approaches for the characterization of the chemical and physical properties of bimetallic systems that are closely related to their target applications. For example, for the application of bimetallic nanoparticles in heterogeneous catalysis, it is important to characterize their electronic properties and chemical activity[17, 18].

In this chapter, we will give an overview of various theoretical approaches that have been used in the study of bimetallic systems.

2.2 Theoretical Approaches to Inter-Atomic Interactions

2.2.1 First-Principles Approaches

The central theme of electronic structure theory is to solve the Schrödinger equation for a many-electron system with fixed nuclear coordinates $\{\mathbf{R}_I\}$ (i.e., with a given geometric structure of the system),

$$\widehat{H}_{\mathrm{el}}\,\Psi\left(\{\mathbf{r}_i\};\{\mathbf{R}_I\}\right)=E_{\mathrm{el}}\left(\{\mathbf{R}_I\}\right)\Psi\left(\{\mathbf{r}_i\};\{\mathbf{R}_I\}\right) \tag{2.1}$$

with $\widehat{H}_{\mathrm{el}}$ being the electronic Hamiltonian operator (atomic units are used through the paper),

$$\widehat{H}_{\mathrm{el}}\equiv\sum_i\left[-\frac{1}{2}\nabla_i^2-\sum_I\frac{Z}{|\mathbf{r}_i-\mathbf{R}_I|}\right]+\frac{1}{2}\sum_{i\neq j}\frac{1}{|\mathbf{r}_i-\mathbf{r}_j|}\equiv\widehat{T}+\widehat{V}_{\mathrm{ne}}+\widehat{V}_{\mathrm{ee}}, \tag{2.2}$$

where we have introduced the operators corresponding to the kinetic energy, the nuclei–electron interaction, and electron–electron interaction, respectively. The ground-state solution of the Schrödinger equation gives the potential energy surface (PES) as a function of nuclear coordinates

$$U\left(\{\mathbf{R}_I\}\right)=E_{\mathrm{el}}\left(\{\mathbf{R}_I\}\right)+\frac{1}{2}\sum_{I\neq J}\frac{Z_IZ_J}{|\mathbf{R}_I-\mathbf{R}_J|}. \tag{2.3}$$

Various theoretical methods have been developed to solve the N-electron Schrödinger equation, and they can be roughly divided into two categories based on the target variational quantity: the wave-function theory (WFT) approaches and density-functional theory (DFT)[19]. The starting point of various WFT approaches is the Hartree-Fock approximation, in which the ground-state N-electron wavefunction is approximated as a single Slater determinant wavefunction $\Phi(\{\mathbf{r}_i\})$ in terms of a set of one-electron wavefunctions (commonly termed as orbitals) $\{\psi_n(\mathbf{r})\}$, and applying the variational principle for the ground state total energy leads to the Hartree-Fock equations, which have to be solved in a self-consistent-field (SCF) manner. For most of the chemical and physical problems of interest, the HF theory is not adequate. In the WFT framework, a variety of post-HF *ab initio* methods have been developed,

including configuration interaction (CI), coupled cluster (CC) and Møller-Plesset (MP) perturbation theory[20]. The main advantage of WFT methods, especially compared to DFT methods, is that the accuracy of WFT methods can be systematically improved, which, however, is inevitably accompanied by rapidly increasing computational cost[19]. WFT methods have been mainly developed for molecular systems. In principles, they can also be applied to material systems (crystals and surfaces) without fundamental difficulty. In practice, the situations are much more complicated. A lot of efforts have been invested in the development of WFT methods for solids with promising progress[21–23]. However, those methods are still not used commonly in routine theoretical materials research because of their demanding computational cost for complicated materials.

DFT methods[19, 24] have become the workhorse for first-principles modeling of various materials in recent decades since they provide a good compromise between the accuracy and efficiency[25]. Nowadays, with the development of a handful of efficient DFT-based computational software packages, including WIEN2k[26], VASP[27], abinit[28], FHI-AIMS[29] and Quantum ESPRESSO[30], to name a few most widely used ones only, and the widespread availability of high-performance computational facility, material systems with hundreds or even thousands of atoms can be readily modeled with feasible computational cost[31]. In the following, we give a brief overview of DFT and its major approximations involved.

The foundation of DFT is the Hohenberg-Kohn (HK) theorems[32]. The first HK theorem states that for a given form of electron–electron interaction $v_{ee}(r_{12})$, physically Coulomb interaction $v_{ee}\left(r_{12}\right) \equiv \frac{1}{r_{12}}$, there is a one-to-one correspondence between the ground-state electron density $\rho(\mathbf{r})$ and the local external potential $v(\mathbf{r})$ up to an additive constant. The second HK theorem states that the ground-state total energy for a given system defined by the external potential $v(\mathbf{r})$ can be uniquely represented as a functional of $\rho(\mathbf{r})$, $E_v[\rho(\mathbf{r})]$, which satisfies the variational principle and gives the exact ground-state total energy by taking the minimum of the functional with respect to all physically allowed electron density $\rho(\mathbf{r})$. Based on the assumption that the ground-state electron density $\rho(\mathbf{r})$ of the interacting system is also that of a fictitious N-electron noninteracting system, Kohn and Sham (KS) [33] proposed the following ansatz for the ground state total energy:

$$E\left[\rho\left(\mathbf{r}\right)\right] = \sum_{n}^{N}\left\langle\psi_{n}\right|-\frac{1}{2}\nabla^{2}\left|\psi_{n}\right\rangle + \int \mathrm{d}^{3}r\, v\left(\mathbf{r}\right)\rho\left(\mathbf{r}\right) + \frac{1}{2}\int \mathrm{d}^{3}r\mathrm{d}^{3}r' \frac{\rho\left(\mathbf{r}\right)\rho\left(\mathbf{r}'\right)}{\left|\mathbf{r}-\mathbf{r}'\right|} + E_{\mathrm{XC}}\left[\rho\left(\mathbf{r}\right)\right] \tag{2.4}$$

$\psi_n(\mathbf{r})$ are eigen-solutions of the following single-particle Kohn-Sham equation:

$$\left[-\frac{1}{2}\nabla^{2} + v\left(\mathbf{r}\right) + v_{\mathrm{H}}\left(\mathbf{r}\right) + v_{\mathrm{XC}}\left(\mathbf{r}\right)\right]\psi_{n}\left(\mathbf{r}\right) = \epsilon_{n}\,\psi_{n}\left(\mathbf{r}\right) \tag{2.5}$$

where $v_{\mathrm{H}}(\mathbf{r})$ is the Hartree potential and $v_{\mathrm{XC}}\left(\mathbf{r}\right) \equiv \delta E_{\mathrm{XC}}/\delta\rho\left(\mathbf{r}\right)$ is the exchange-correlation potential. The Kohn-Sham equation is derived by requiring the

electron density of the original interacting system can be calculated from the N's lowest eigen-orbitals

$$\rho(\mathbf{r}) = \sum_n f_n \left|\psi_n(\mathbf{r})\right|^2, \tag{2.6}$$

in which f_n denotes the occupation number of the n-th orbital, equal to 1 for N-lowest energy orbitals, and 0 otherwise. In Eq. (2.4) the first term denotes the kinetic energy of the Kohn-Sham noninteracting system, the second term is the interaction energy between electrons and nuclei, the third term is the classical Coulomb interaction between electrons, also termed as the Hartree energy, and the last term is the exchange-correlation energy, which is the only one whose exact form is unknown. Physically, it consists of two major contributions,

$$E_{\mathrm{XC}}\left[\rho(\mathbf{r})\right] = \left[\left\langle \Psi_\rho \middle| \hat{T} \middle| \Psi_\rho \right\rangle - \left\langle \Phi_\rho \middle| \hat{T} \middle| \Phi_\rho \right\rangle\right] + \left[\left\langle \Psi_\rho \middle| V_{\mathrm{ee}} \middle| \Psi_\rho \right\rangle - \frac{1}{2}\int \mathrm{d}^3 r \mathrm{d}^3 r' \frac{\rho(\mathbf{r})\rho(\mathbf{r}')}{|\mathbf{r}-\mathbf{r}'|}\right], \tag{2.7}$$

where the first bracketed term represents the difference between the kinetic energy of the interacting system and the noninteracting Kohn-Sham system, and the second bracketed term is the difference between the full electron–electron Coulomb interaction energy and its classical counterpart (i.e., the Hartree energy).

The Hohenberg-Kohn-Sham density-functional theory provides an in-principle-exact theoretical framework to obtain the ground-state total energy of many-electron interacting systems by solving a set of single-electron Schrödinger equations. Compared to the WFT approaches, which uses the N-electron many-body wavefunction, a function of $3N$ spatial coordinates of all electrons, as the basic variation quantity, DFT uses the electron density $\rho(\mathbf{r})$, a function of three-dimensional spatial coordinates, as the basic variational quantity, and is therefore formally a dramatic simplification[19]. However, the complexity of solving the many-body problem of N-electron interacting systems is transformed into the construction of the exchange-correlation functional E_{XC}, and unfortunately the fundamental principles underlying DFT have not provided any straightforward guidelines regarding how to build approximations to E_{XC} in practice. Fortunately, partly because E_{XC} accounts for only a fraction of the total energy, even some kind of crude approximation to E_{XC} can already deliver rather reasonable results.

In the past decades, a great deal of efforts have been invested in the development of approximate exchange-correlation functionals[34–36], and tens of approximate functionals are currently available, although the number of the most popularly used ones is much smaller. The functionals developed so far can be categorized in terms of Jacob's ladder proposed by Perdew[37]. Starting from the Hartree approximation, which neglects the exchange-correlation term completely, and therefore represents the earth world of electronic structure theory, the first rung in Jacob's ladder is the local density approximation (LDA), in which E_{XC} is a local functional of electron density with a functional form taken from the simplest many-electron interacting system, the homogeneous electron gas (HEG),

$$E_{\mathrm{XC}}^{\mathrm{LDA}}\left[\rho(\mathbf{r})\right] = \int \epsilon_{\mathrm{XC}}^{\mathrm{HEG}}\left(\rho(\mathbf{r})\right)\rho(\mathbf{r})\mathrm{d}^3 r \tag{2.8}$$

where $\in_{\mathrm{XC}}^{\mathrm{HEG}}(\rho)$ is the exchange-correlation energy per electron for the HEG model system. Although apparently being a very crude approximation, the LDA is surprisingly successful in theoretical description of many inhomogeneous electron systems, including, in particular, elemental metals[34], which can be partially attributed to the fact that E_{XC} in the LDA satisfies several exact relations that can be derived for the exact E_{XC}.

The second rung of Jacob's ladder refers to approximate functionals falling into the category of generalized gradient approximation (GGA), which can be formally written as

$$E_{\mathrm{XC}}^{\mathrm{GGA}}\left[\rho(\mathbf{r})\right]=\int \in_{\mathrm{XC}}^{\mathrm{HEG}}\left(\rho(\mathbf{r})\right)\rho(\mathbf{r})f\left(\rho(\mathbf{r}),\nabla\rho(\mathbf{r})\right)\mathrm{d}^3r \tag{2.9}$$

Among the most widely used GGA functionals are the B88 exchange[38], the LYP correlation[39], PW91[40] and the PBE exchange-correlation[41] functionals.

The approximate functionals in the third rung are termed as meta-GGA(mGGA),

$$E_{\mathrm{XC}}^{\mathrm{mGGA}}\left[\rho(\mathbf{r})\right]=\int \in_{\mathrm{XC}}^{\mathrm{HEG}}\left(\rho(\mathbf{r})\right)\rho(\mathbf{r})f\left(\rho(\mathbf{r}),\nabla\rho(\mathbf{r}),\tau(\mathbf{r})\right)\mathrm{d}^3r, \tag{2.10}$$

where $\tau(\mathbf{r})\equiv\sum_{n}^{N}\frac{1}{2}\left|\nabla\psi_n(\mathbf{r})\right|^2$ is the Kohn-Sham kinetic energy density. The functionals up to the second and third rung are often called semilocal approximations in the literature [34], and they are computationally very efficient and therefore widely used in first-principles materials research. On the other hand, semilocal functionals suffer from several intrinsic difficulties. For example, semilocal approximations generally underestimate the band gaps of insulating systems systematically[42, 43], and they often give qualitatively wrong description of many strongly correlated materials[44]. Approximate functionals in the fourth and fifth rungs are fully nonlocal functionals of electron density. The functionals in the fourth rung are called hyper-GGA, or more commonly known as hybrid functionals, and are usually obtained by mixing the Hartree-Fock exchange (also named exact exchange) with LDA, GGA, or mGGA[45, 46]. For material systems, the most widely used hybrid functionals are PBE0[46]

$$E_{\mathrm{XC}}^{\mathrm{PBE0}}=0.25\left(E_{\mathrm{X}}^{\mathrm{HF}}-E_{\mathrm{X}}^{\mathrm{PBE}}\right)+E_{\mathrm{XC}}^{\mathrm{PBE}} \tag{2.11}$$

and HSE06[47], which is similar to PBE0, but using the screened Coulomb interaction in the exact exchange part, $v_{\mathrm{ee}}(r;\mu)=\mathrm{erfc}(\mu r)/r$,

$$E_{\mathrm{XC}}^{\mathrm{HSE06}}=0.25\left(E_{\mathrm{X}}^{\mathrm{HF},\mu}-E_{\mathrm{X}}^{\mathrm{PBE},\mu}\right)+E_{\mathrm{XC}}^{\mathrm{PBE}} \tag{2.12}$$

While the fourth-rung functionals depend on occupied orbitals via the exact exchange, the fifth-rung functionals are more sophisticated, and depend on both occupied and unoccupied states. A variety of fifth-rung functionals have been proposed, including, in particular, the correlation energy from the random phase approximation (RPA) in the adiabatic connection fluctuation dissipation theorem (ACFDT) framework[49, 50], and the doubly hybrid functionals[51]. While the fifth-rung functionals can provide significantly improved accuracy for many properties[49, 51, 52], they are also computationally very expensive, and therefore their application is currently limited to relatively simple

molecules and solids. It should also be mentioned that there have been continuing efforts to develop more accurate and efficient treatments of van der Waals type weak interactions in the DFT framework[53, 54].

When applied to metallic systems, Kohn-Sham DFT often takes the finite temperature DFT formalism [55] in which the occupation numbers of Kohn-Sham orbitals are determined by the Fermi-Dirac distribution,

$$f_n = f^{\mathrm{FD}}\left(\frac{\in_n - \mu}{\sigma}\right) = \frac{1}{1+\exp\left(\in_n - \mu\right)/\sigma}, \tag{2.13}$$

where μ is the chemical potential determined by the total number of electrons, and $\sigma \equiv k_{\mathrm{B}}T$ with k_{B} being the Boltzmann constant, and T the electronic temperature. When using the finite-temperature formalism, the target quantity that is optimized during the SCF procedure becomes the Helmholtz free energy,

$$A = E\left[\rho;T\right] - TS\left(\left\{f_n\right\}\right) \tag{2.14}$$

where

$$S\left(\left\{f_n\right\}\right) = -k_{\mathrm{B}}\sum_n \left[f_n \ln\left(f_n\right) + \left(1-f_n\right)\ln\left(1-f_n\right)\right] \tag{2.15}$$

is the electronic entropy. It is important to note that in most cases the electronic temperature used in DFT calculations of metallic systems is of fictitious nature. The real target is still the ground state energy, and the main goal of introducing the finite temperature, often termed as the smearing approach, is to smooth the discontinuity at the Fermi energy, by which the accuracy of numerical integration over the Brillouin zone for a given set of k-points can be significantly improved[56]. Using the finite temperature is also beneficial to accelerate the convergence of SCF iterations, which is often more difficult for metallic systems than for insulating systems. As a smearing technique, using the Fermi-Dirac function is not most efficient, and several alternatives have proposed. In particular, Methfessel and Paxton (MP)[57] proposed a series of smearing functions by expanding the step function in a complete orthonormal set of functions,

$$S_0\left(x\right) = \frac{1-\mathrm{erf}\left(x\right)}{2} \tag{2.16}$$

$$S_N\left(x\right) = S_0\left(x\right) + \sum_{n=0}^{N} A_n H_{2n-1}\left(x\right)\mathrm{e}^{-x^2} \tag{2.17}$$

where $H_n(x)$ is the n-th order Hermite polynomial, and A_n is the expansion coefficient whose explicit formula can be found in [57]. When using the N-th order MP smearing, the free energy, which is the variational quantity and determines the forces used in structural optimization, deviates from the ground state energy, the physical quantity of interest, by the order of $N+2$ in σ, and the ground state energy can be obtained by the following analytic extrapolation,

$$E_{\sigma=0} \approx \frac{1}{N+2}\left[\left(N+1\right)F\left(\sigma\right) + E\left(\sigma\right)\right]. \tag{2.18}$$

Another important issue concerns the accuracy of current DFT methods for transition metal systems. In spite of active developments of various density functional approximations summarized above, semilocal density functional approximations remain to be the workhorse for first-principles studies of transition metal systems including bulk, surfaces and nanoparticles, and in general they can deliver satisfactory accuracy. One of notable failures of semilocal approximations is about the formation energies of Cu-Au inter-metallic compounds. It is found that both LDA and GGA (in the PBE scheme) underestimate the formation energies of Cu_3Au, CuAu, and $CuAu_3$ by about 50%, and in addition, they predict a stable structure, $CuAu_2$-β_2 [58], which is experimentally unobserved. Both of the two problems can be solved by using the screened hybrid functional HSE[59]. We can expect that similar problems may exist in theoretical prediction of the relative stability of bimetallic nanoparticles in different structures, but a systematic assessment of the issue is yet to be undertaken.

2.2.2 Empirical Inter-Atomic Potentials for Metallic Systems

Because of the complexity of the structure of bimetallic systems and demanding computational cost of first-principles approaches outlined above for large systems, empirical inter-atomic potentials (also termed as force fields) are also widely used in theoretical study of bimetallic systems[60–63].

Inter-atomic potentials can be generally written as [60]

$$U\left(\{\mathbf{R}_i\}\right)=\sum_i \phi_2\left(\mathbf{R}_i,\mathbf{R}_j\right)+\sum_{i<j<k}\phi_3\left(\mathbf{R}_i,\mathbf{R}_j,\mathbf{R}_k\right)+\ldots+\sum_{i<j<\ldots<n}\phi_n\left(\mathbf{R}_i,\mathbf{R}_j,\ldots,\mathbf{R}_n\right) \quad (2.19)$$

where ϕ_2, ϕ_3, ϕ_n denotes two-body, three-body, and n-body terms of interatomic potentials. The inter-atomic potentials with only the first (two-body) term are called *pair potentials,* and those with additional terms are called many-body potentials. The pair potentials, as the simplest inter-atomic potentials, are intrinsically limited for metallic systems[64]. They always suffer from the so-called the dilemma of the cohesive energy and vacancy formation energy: however, optimized, only one of the two quantities can be accurately described. All pair potentials result in the so-called Cauchy discrepancy: one can derive analytically that elastic constants of the systems described by the pair potentials follow exactly the so-called Cauchy relations, e.g., $C_{12}=C_{44}$ for cubic systems and $C_{13}=C_{44}$ and $C_{11}=3C_{12}$ for hexagonal systems, which are, however, rarely valid for most metallic systems in reality. Pair potentials also have intrinsic difficulty in predicting the inward relaxation of metallic surfaces commonly observed in many transition metal surfaces, and often overestimate the melting temperature by up to 20%[64].

Compared to popular classical force fields for molecular and biological systems, inter-atomic potentials for metallic materials are usually more complicated, and their construction is theoretically more demanding. The challenges can be mainly attributed to two factors[65]: (1) the inter-atomic interactions for metallic systems have strong many-body characters, such that simplistic force fields based on pair (two-body) interactions usually perform very poorly for metallic systems; and (2) while typical molecular systems have roughly fixed connectivity among atoms, as long as no bond breaking and formation processes are involved, the chemical bonding in metallic systems is more

versatile. For example, the coordination number of a transition metal atom can vary dramatically in different chemical environments, which affects its bonding with surrounding atoms. A lot of different empirical many-body inter-atomic potentials have been developed for transition and noble metals[60, 65–68], and among the most widely used ones are those based on the embedded atom model (EAM) [69–71] and the second-moment approximation to the tight-binding model (SMTB)[72–74]. There are plenty of other models, which, in spite of having different names and theoretical origins, share similar features as the EAM or SMTB methods[67]. Therefore we only give a brief introduction to EAM and SMTB methods. More details regarding inter-atomic potentials for binary transition metal systems can be found in several recent reviews[60, 64, 65], and the monograph by Finnis[74].

In the EAM method[65, 67, 69–71], the total atomistic potential energy as a function of all atomic coordinates can be written as the sum of two contributions:

$$U\left(\{\mathbf{R}_i\}\right)=\frac{1}{2}\sum_{i\neq j}\Phi_{s_i,s_j}\left(R_{ij}\right)+\sum_i F_{s_i}\left(\bar{\rho}_i\right) \tag{2.20}$$

In Eq. (2.20), s_i denotes the chemical species of the i-th atom, $\Phi_{s,s'}$ is the pair interaction between the s and s'-type atom, and F_s is the embedding energy of the s-type atom, which is a function of the electron density at the position $\mathbf{R}_i$ contributed by surrounding atoms, with $\bar{\rho}_i \equiv \sum_{j\neq i}\rho_{s_j}(R_{ij})$. The first term in the EAM potential represents the pairwise inter-atomic repulsion, and the second term describes the energy gain when embedding an atom into a background electron density, which is mainly motivated by the DFT description of inter-atomic interaction in metals. For the construction and use of the EAM interatomic potentials, it is important to note that the partitioning of the total interatomic potential energy into the pair interaction and the embedding energy is not unique. In fact, one can easily show that the following transform[65],

$$\begin{aligned} &F_{s_i}\left(\bar{\rho}_i\right)\rightarrow F_{s_i}\left(\bar{\rho}_i\right)+g_{s_i}\bar{\rho}_i \\ &\Phi_{s_i,s_j}\left(R_{ij}\right)\rightarrow \Phi_{s_i,s_j}\left(R_{ij}\right)-g_{s_i}\bar{\rho}_{s_j}\left(R_{ij}\right)-g_{s_j}\bar{\rho}_{s_i}\left(R_{ij}\right) \end{aligned} \tag{2.21}$$

where g_s is a species-dependent constant, would give the same total potential energy, although with different pair-interaction and embedding terms. The standard EAM potentials have a central-force character, are suitable mainly to simple and noble metals in the bulk phase, and they are usually not adequate for transition metals and metal nanoparticles for which a proper consideration of angular dependence in the inter-atomic potentials is crucial. Several EAM schemes with angular dependence have been proposed, including the modified EAM (MEAM)[75, 76], the embedded defect method (EDM)[77], and angular dependent potential (ADP)[78], which can significantly improve the accuracy of EAM potentials.

In the SMTB approach, the inter-atomic potential is also represented as a sum of an attractive many-body term and a repulsive pair term, which is very similar to that of EAM but is inspired in the tight-binding framework[74]. There are several variants of SMTB potentials. A typical one, sometimes termed as the Gupta potential, reads as follows [72, 73]:

$$U\left(\{\mathbf{R}_i\}\right)=-\sum_i\sqrt{\sum_j\xi_{s_is_j}^2\exp\left[-q_{s_is_j}\left(\frac{R_{ij}}{R_{s_is_j}^0}-1\right)\right]}+\sum_i\sum_{j\neq i}A_{s_is_j}\exp\left[-p_{s_is_j}\left(\frac{R_{ij}}{R_{s_is_j}^0}-1\right)\right] \tag{2.22}$$

where $p_{ss'}$, $q_{ss'}$, $A_{ss'}$, $R_{ss'}^0$ and $\xi_{ss'}$ are species dependent fitting parameters. In practice, the sum in Eq. (2.22) is often taken only within a certain cutoff interaction distance $R_{s_is_j}^c$, which is usually taken as the second or third neighbor distances in the bulk material.

2.2.3 Lattice Models

The structure of compositionally disordered systems, including both bulk alloys and multi-component nanoparticles with given structural motifs, can be characterized by the configurational arrangement of component species over given lattice sites that exhibit slight deviation from some ideal lattice. In many cases, the chemical ordering is the only property of interest, and therefore structural details regarding the deviation of each atom from ideal lattice sites can be coarse-grained, which leads to an effective Hamiltonian that depends only on the occupation configuration, characterized by a vector of site variables, $\sigma\equiv\{\sigma_1,\sigma_2,\ldots,\sigma_N\}$, in which $\sigma_i=1$ or -1 if the i-th site is occupied by A or B, respectively, for a binary system $A_{1-x}B_x$.

The simplest lattice model is the Ising model, which is a classic phenomenological model Hamiltonian in statistical mechanics widely used for the illustration of fundamental principles of phase transition[79]. The Ising model can be derived in the tight-binding (TB) approximation[80], and therefore is often termed as TB Ising model (TBIM). When considering only pair interactions, the total energy for a multicomponent alloy system can be written as [80]

$$E=\frac{1}{2}\sum_{i,j}\sum_{a,b}p_i^a\,p_j^b\in_{ij}^{ab} \tag{2.23}$$

where i and j denote site indices, a and b denote the chemical species, $\{p_i^a\}$ are occupation numbers, $p_i^a=1$ if the site i is occupied by the species a, and $\in_{ij}^{ab}$ denotes the pair interaction between an atom of type a at the site i and the other atom of type b at the site j. Obviously, there is the relation $\sum_a p_i^a=1$ for any site i. For a binary system $A_{1-x}B_x$ with $a=$ A or B, defining $p_i^A=p_i$ and $p_i^B=1-p_i$, and considering only the nearest neighboring pair interactions, Eq. (2.23) can be simplified as

$$\begin{aligned}E&=\frac{1}{2}\sum_{i,j}p_ip_j\in_{AA}+p_i\left(1-p_j\right)\in_{AB}+\left(1-p_i\right)p_j\in_{AB}+\left(1-p_i\right)\left(1-p_j\right)\in_{AA}\\&=\frac{1}{2}\sum_{i,j}\in_{BB}+\sum_{i,j}\left(\in_{AB}-\in_{BB}\right)p_i+\sum_{i,j}\frac{\in_{AA}+\in_{BB}-2\in_{AB}}{2}p_ip_j\\&=V_0+\left(\tau-V\right)\sum_i z_ip_i+V\sum_{i,j}p_ip_j\end{aligned} \tag{2.24}$$

where we have defined $V_0\equiv N_p\in_{BB}$ with N_p denoting the total number of pairs, $\tau\equiv\frac{1}{2}\left(\in_{AA}-\in_{BB}\right)$, $V\equiv\frac{1}{2}\left(\in_{AA}+\in_{BB}-2\in_{AB}\right)$ and z_i is the coordination number of the

i-th site. The latter is a constant for bulk systems, but is site-dependent for surfaces and nanoparticles. Eq. (2.24) can be transformed into the more familiar expression based on the spin variable by using the relation $S_i = 2p_i - 1$,

$$E = E_0 + \frac{\tau}{2}\sum_i z_i S_i + \frac{V}{4}\sum_{\langle i,j\rangle} S_i S_j. \tag{2.25}$$

To simulate nanoalloys more accurately, the TB Ising model can be generalized in several ways. First of all, it is straightforward to include the interactions between more distant pairs than the nearest neighboring ones, which leads to [80]

$$E = E_0 + \sum_i J_i^{(1)} S_i + \sum_{i,j} J_{ij}^{(2)} S_i S_j \tag{2.26}$$

where the effective one-site and two-site interactions are given by

$$J_i^{(1)} = \frac{1}{4}\sum_j \left(\in_{ij}^{AB} - \in_{ij}^{BB}\right) \tag{2.27}$$

and

$$J_{ij}^{(2)} = \frac{1}{8}\left(\in_{ij}^{AA} + \in_{ij}^{BB} - 2\in_{ij}^{AB}\right) \tag{2.28}$$

It is also possible to take into account the size mismatch effects between different species by considering an additional contribution in the coefficients of the linear term that can be evaluated from a many-body interaction potential[81]. Eqs. (27) and (28) provide the relations between the cluster expansion coefficients and the inter-atomic interaction energies ($\in_{ij}^{AA}$, $\in_{ij}^{BB}$, and $\in_{ij}^{AB}$), and the latter have more transparent physical meanings and can be even derived directly from the tight-binding model. The generalized TB Ising model has been widely used in theoretical study of surface segregation and phase transition in alloy surfaces and nanoparticles[6, 80–82].

The lattice models can be formally derived in a systematic way by the so-called cluster expansion formalism[83, 84]. Starting from the microscopic states of an alloy system characterized in terms of site variables σ, the vibration index ν that indicates the deviation from the equilibrium positions, the electronic index e that denotes possible electronic excitations for a given structure, we can define the free energy corresponding to a given configuration as follows:

$$F(\sigma, T) = -k_B T \sum_{\nu\in\sigma}\sum_{e\in\nu} \exp\left[-\beta E(\sigma, \nu, e)\right] \tag{2.29}$$

In practice, the main interest is often just the ground-state total energy as a function of the configuration, $E(\sigma)$, which can be regarded as the $T \to 0$ limit of $F(\sigma, T)$. It can be proven [84] that any function of the configuration σ can be exactly represented by the following cluster expansion formalism[85]:

$$E(\sigma) = J_0 + \sum_i J_i S_i(\sigma) + \sum_{i<j} J_{ij} S_i(\sigma) S_j(\sigma) + \sum_{i<j<k} J_{ijk} S_i(\sigma) S_j(\sigma) S_k(\sigma) + \ldots \tag{2.30}$$

where the coefficients J_0, J_i, J_{ij},⋯ are termed as effective cluster interactions (ECIs). Since the values of ECIs depend only on the topology structure of the corresponding clusters, Eq. (2.30) can be written more concisely as [85]

$$E(\sigma) = J_0 + \sum_{\alpha} m_\alpha J_\alpha \bar{\Pi}_\alpha(\sigma) \tag{2.31}$$

where α denotes the clusters that are symmetrically distinct, m_α is the multiplicity of the α cluster, and $\bar{\Pi}_\alpha(\sigma)$ is the correlation function defined as

$$\bar{\Pi}_\alpha(\sigma) = \frac{1}{m_\alpha} \sum_{(i_1<i_2<\ldots<i_g)\in\alpha} S_{i_1}(\sigma) S_{i_2}(\sigma) \ldots S_{i_g}(\sigma) \tag{2.32}$$

In practice, it is found that for many properties, including the total energy, the summation considered in the cluster expansion can be effectively truncated, and only a finite number of clusters, including a few short-range pairs and triplets (and sometimes quadruplets), are adequate to provide an accurate representation. In most cases, the CEI parameters can be determined by fitting the ground-state total energies of tens of representative configurations in their relaxed geometric structures calculated by first-principles approaches[85, 86].

2.3 Global Optimization Methods

Any theoretical study of a particular system starts with some initial structure. Compared to bulk crystal materials, the structures of bimetallic nanoparticles are very difficult to determine experimentally[6]. Even a reasonable initial guess of the structure can be difficult to obtain since nanoparticles are very different from bulk materials in terms of chemical bonding. It is therefore highly desirable to determine the structure based on theoretical calculations. Structure prediction is a grand challenge for bulk crystal materials[87], and even more so for nanoparticles with multiple components[88, 89].

For small bimetallic nanoparticles with a few tens of atoms, it is often important to know the global minimum (GM) structure. Finding the GM structure is highly challenging from a theoretical point of view since the number of local minimum structures increases exponentially with the number of atoms. Various global optimization (GO) algorithms have been used for theoretical prediction of the structure of nanoparticles. Here we will give an overview of two most popular approaches for nanoparticle structure optimization. More detailed discussion of various global optimization techniques can be found in recent published monographs [6, 8, 9] and reviews[88–90].

2.3.1 Basin-Hopping Algorithm

The basin-hopping (BH) algorithm [8, 9, 91], also termed as Monte Carlo plus energy minimization [92], is one of the most widely used global optimization approaches for cluster structures. The practical algorithm for the BH method is very simple:

1) Start with an initial structure, denoted as $\mathbf{x}_k$, and run a local energy minimization to the nearest local minimum structure, denoted as $\mathbf{x}_k^*$, using a standard local minimization technique.
2) Make a random move from $\mathbf{x}_k^*$ to create a tentative new structure, denoted as $\mathbf{x}_{k+1}$, and perform an energy minimization to reach $\mathbf{x}_{k+1}^*$.
3) Accept or reject the new local minimum structure using the standard Metropolis criterion, i.e., if $E(\mathbf{x}_{k+1}^*) < E(\mathbf{x}_k^*)$, the new structure is accepted; otherwise, the new structure is accepted only if $\exp(-[E(\mathbf{x}_{k+1}^*) - E(\mathbf{x}_k^*)]/k_B T)$ is greater than a random number generated in the range of [0, 1].
4) Repeat the preceding two steps until a certain convergence criterion is met.

Obviously, what is the crucial for the efficiency of the BH method is how to make the move from a local minimum structure. A simple and generally effective scheme[9], sometimes called a shake move[6, 91], is to perturb the Cartesian coordinates of all atoms randomly in terms of a uniform distribution in the range of $[-d_{max}, d_{max}]$, where the parameter d_{max} specifies the maximally allowed displacement. It is often necessary to consider other move schemes that take into account the specificity of target systems. For nanoparticles, the following schemes for the MC move are often used[6]: (a) Brownian move, in which the atoms are displaced by following a short time (typically a few hundred steps) Brownian molecular dynamics (MD) at high temperature; (b) twist move[89], in which a set of atoms, selected by randomly choosing a cutting plane, is rotated around the axis normal to the cutting plane by a randomly chosen angle; and (c) exchange move, in which two unlike atoms exchange their positions. The exchange move is the most important elementary move for the optimization of chemical ordering. In general, the pair of the atoms to be swapped are selected randomly, but the random exchange can become inefficient for large nanoparticles with intermediate compositions[6], resulting in a very high rejection rate. For the optimization of nanoparticles with known general characters, such as the tendency to form core-shell or intermixed structures, it is often significantly more efficient by using some tailored exchange schemes[6, 93].

Besides the parameters used in defining elementary moves, the main computational parameter in the BH algorithm is the temperature that determines the acceptance ratio for a MC move, and its value has significant influences on the efficiency of the BH approach. It has been found that the optimal temperature for different types of elementary moves is usually different. The shake move often requires a high temperature (around 2000 K), but the optimal temperature for the exchange move is around several hundred Kelvin, and can also depend on the composition of nanoparticles. For example, in a systematic investigation of the BH optimization of Au–Rh, Cu–Ni and Ag–Pd nanoparticles with the composition of $A_{989}B_{300}$[6], it is found that for Au–Rh nanoparticles, the optimal temperature is between 500 and 900 K, while that for Cu–Ni and Ag–Pd nanoparticles is 100 K. For the BH optimization with different elementary moves, it is often advantageous to use different MC temperatures for different moves.

The BH algorithm has been widely used in global optimization of various mono- and multi-component nanoparticles[6, 94]. There are several new developments that try to further improve efficiency of the basin-hopping algorithm, including the parallel excitable walker (PEW)[95] and the HISTO algorithm, which can be regarded as a BH-with-memory approach[94]. The efficiency of the BH approach can also be further

improved by exploiting more versatile MC schema. In a recent work by Rondina and Da Silva[96], eleven local and nonlocal MC move operators that are tailored for global optimization of nanoparticles, including one that is motivated by the mating (or crossover) operation in the genetic algorithm, have been explored and allow an efficient exploration of the potential energy surface.

2.3.2 Genetic Algorithm

The genetic algorithm (GA) is a global optimization technique inspired the principles of natural evolution, and belongs to a large class of evolution algorithms[89, 97]. The genetic algorithm has been widely used for global structural optimization of nanoparticles[89, 98–102].

The GA global optimization scheme usually consists in the following procedures [89, 103]:

1) *Initialization.* A set of initial structures is generated, usually by sampling the target configuration space randomly, and all structures are relaxed to their corresponding local minimum structures, and form the initial pool (preselection pool) from which a population is selected.
2) *Natural selection.* The population is generated using the relaxed structures based on the principle of the survival of the fittest from the preselection pool. The fitness of each individual structure is measured by its total energy.
3) *Crossover (or mating).* New candidate individuals are generated by performing the crossover operation, often in the cut and splice scheme[104], to pairs of parents selected from the current generation, and then locally optimizing them. The main technical challenge for the crossover operation is that when putting the two parts taken from their respective parent structures, the new structure may not have correct size (and composition, for multiple-component systems), or it may have atoms that are too close to each other, and therefore a careful design of the algorithm is needed[103].
4) *Mutation.* New structures are introduced to the preselection pool by the random variation of the structures selected from the current population, with the similar schema as used in the basin-hopping approach.
5) *Iteration.* Steps (1) to (4) are repeated until a certain convergence criterion has been satisfied.

2.4 Statistical Approaches

While the global optimization aims at finding the most stable ground-state structure, it is often important to investigate thermodynamical properties at finite temperature[13–15,105], and in some cases even kinetic processes such as phase transition, growth, and melting [16] are the main interest. For the simulation of those properties and processes, it is often important to combine energetic calculations, either by first-principles approaches or from empirical potentials, with some statistical approaches. This section present an overview of major statistical approaches used in theoretical study of nanoalloys.

2.4.1 Molecular Dynamics Simulation

In molecular dynamics simulations, the motion of all atoms in the system of interest is assumed to follow Newtonian classical dynamics, with the forces on each atom determined by the gradient of the inter-atomic potential function,

$$M_i \frac{\mathrm{d}^2 \mathbf{R}_i(t)}{\mathrm{d}t^2} = -\frac{\partial}{\partial \mathbf{R}_i} U\left(\{\mathbf{R}_j\}\right) \tag{2.33}$$

Starting from some initial structure and randomly assigned velocities, the Newtonian equation can be solved numerically in the time domain with well-established algorithms[106]. MD simulations can be undertaken in different statistical ensembles. The simplest ensemble is the micro-canonical (constant-*NVE*) ensemble, which is a natural time evolution of the system without any constraint. For MD simulations in other ensembles like the constant *NVT* (canonical) ensemble or constant *NTP* ensemble, certain thermostat schemes have to be used[106]. A typical MD simulation is usually divided into two stages termed as equilibration and sampling (or measurement), respectively. In the equilibration stage, the system is propagated for a certain period, and the velocities of all atoms are adjusted once in a while such that the instantaneous temperature as defined in terms of the average kinetic energy is equal to the desired temperature, and the thermodynamic properties of the system does not change with time. In the sampling (or measurement) stage, a thermodynamic property of intererest A can be calculated by a time averaging of the corresponding microscopic quantity, which is a function of the coordinates and momentums of all particles $A(\{\mathbf{R}_i, \mathbf{P}_i\})$ in general, over a period of Ts,

$$\langle A \rangle = \frac{1}{T_s} \int_0^{T_s} A\left(\{\mathbf{R}_i(t), \mathbf{P}_i(t)\}\right) \mathrm{d}t. \tag{2.34}$$

Compared to other statistical approaches, the MD method has the advantage that the evolution of the system follows a physical trajectory, and therefore it can be used to simulate in a physically transparent way kinetic processes like melting and growth[12, 107–109]. The melting behavior of nanoparticles at high temperatures is important for their practical use[10]. Starting either from the global minimization structure or structures with high-symmetry, the melting behavior of nanoparticles can be modeled by performing a series of constant-temperature MD simulation with gradually increasing temperature. For example, using MD simulations, Mottet et al.[107] studied the variation of the melting temperature of Ag icosahedral clusters as a result of incorporating a single impurity atom (M=Ni, Cu, Pd, and Au) in the center, and they found that melting temperature increases significantly if the impurity atom has a smaller size than the Ag atom due to the strain relaxation.

In terms of the adequacy of sampling, standard MD approaches can be limited by the time scale accessible by a typical MD simulation, which is mainly determined by the computational cost for the calculation of inter-atomic potentials. Even when using analytic empirical potentials, the typical time for MD simulations of nanoparticles usually does not exceed a few 10 ms[6], which can be inadequate for systems in which configuration spaces are separated by high activation barriers.

A lot of enhanced sampling techniques, including accelerated MD[110], metadynamics[111], integrated tempering sampling (ITS)[112], to name a few only, have been developed. Most of them have been developed for molecular simulations of biological and solution systems, and their applications for inorganic nanostructured materials are still rare. Here we present briefly the main idea of the ITS approach as an example.

The basic idea of the ITS method, developed by Gao et al.[112–114], is to sample the configuration space characterized by the potential function $U(\mathbf{x})$, with $\mathbf{x} \equiv \{\mathbf{R}_I\}$, using a generalized non-Boltzmann distribution that is obtained from a sum of normal Boltzmann distributions in a range of temperatures,

$$W\left(U\left(\mathbf{x}\right)\right) = \sum_k n_k \mathrm{e}^{-\beta_k U(\mathbf{x})} \tag{2.35}$$

In Eq. (2.35), $\beta_k \equiv 1/k_\mathrm{B}T_k$ denote a series of temperatures that cover both the low and high temperatures around the target simulation temperature β_0, and n_k denotes the statistical weight of the Boltzmann distribution at the temperature β_k. In practice, the non-Boltzmann distribution $W(U)$ as shown in Eq. (2.35) is realized by conducting the standard MD simulation in terms of the effective potential function

$$U_\mathrm{eff}\left(\mathbf{x}\right) \equiv -\frac{1}{\beta_0}\ln W\left(U\left(\mathbf{x}\right)\right) = -\frac{1}{\beta_0}\ln \sum_k n_k \mathrm{e}^{-\beta_k U(\mathbf{x})} \tag{2.36}$$

In particular, the force on the I-th atom used in the MD simulation is calculated by [113]

$$\mathbf{F}_{\mathrm{eff},I} = -\frac{\partial U_\mathrm{eff}}{\partial \mathbf{R}_I} = \frac{\sum_k n_k \beta_k \mathrm{e}^{-\beta_k U}}{\beta_0 \sum_k n_k \mathrm{e}^{-\beta_k U}}\mathbf{F}_I \tag{2.37}$$

where $\mathbf{F}_I$ is the physical force calculated from the real potential function U. A proper choice of the weighting factors (n_k) is important to achieve optimal sampling efficiency and can be determined in an iterative way[115]. One of the remarkable features of the ITS method is that although the simulation is conducted at a particular temperature (β_0) with a nonphysical effective potential, the ensemble average of a physical quantity A at any particular temperature β falling in the range covered by $\{\beta_k\}$, denoted as A_β, can be extracted from the ITS simulation trajectories by a proper re-weighting scheme [116, 117]

$$\left\langle A_\beta \right\rangle \equiv \frac{\int A\left(\mathbf{x}\right)\mathrm{e}^{-\beta U(\mathbf{x})}\mathrm{d}\mathbf{x}^N}{\int \mathrm{e}^{-\beta U(\mathbf{x})}\mathrm{d}\mathbf{x}^N} = \frac{\left\langle A\left(\mathrm{x}\right)\mathrm{e}^{-\beta U(\mathbf{x})+\beta_0 U_\mathrm{eff}(\mathbf{x})}\right\rangle_W}{\left\langle \mathrm{e}^{-\beta U(\mathbf{x})+\beta_0 U_\mathrm{eff}(\mathbf{x})}\right\rangle_W} \tag{2.38}$$

where $\left\langle \ldots \right\rangle_W$ denotes the ensemble average in the generalized non-Boltzmann distribution W, formally defined as

$$\left\langle \ldots \right\rangle_W \equiv \frac{\int \ldots \mathrm{e}^{-\beta_0 U_\mathrm{eff}(\mathbf{x})}\mathrm{d}\mathbf{x}^N}{\int \mathrm{e}^{-\beta_0 U_\mathrm{eff}(\mathbf{x})}\mathrm{d}\mathbf{x}^N} \tag{2.39}$$

2.4.2 Monte Carlo Simulation

From a mathematical perspective, the Monte Carlo (MC) method can be regarded as a general technique to carry out numerical integration in high-dimensional space based on random sampling[118]. In the context of statistical physics, MC is a powerful approach to calculate equilibrium thermodynamic properties by sampling the configuration space in a Markov random process[106]. In equilibrium statistical mechanics, a macroscopic property can often be calculated in terms of a weighted integration of the corresponding microscopic quantity in the configuration space,

$$\langle A \rangle = \frac{1}{Z} \int \exp\left[-\beta U(\mathbf{x})\right] A(\mathbf{x}) \mathrm{d}\mathbf{x}^N \tag{2.40}$$

where $Z \equiv \int \exp[-\beta U(\mathbf{x})] \mathrm{d}\mathbf{x}^N$ is the configurational partition function. In the Metropolis MC approach, Eq. (2.40) is implemented numerically by starting from an initial structure in the configuration space, and repeating the following steps for a lot of times until certain convergence criteria are satisfied: (1) make a change (move) to the current structure; (2) calculate the change of the potential energy due to the move, $\Delta U = U(\mathbf{x}_{\text{new}}) - U(\mathbf{x}_{\text{old}})$; (3) accept the move with the probability:

$$P_{\text{acc}} = \min\left[1, \exp\left(-\beta \Delta U\right)\right] \tag{2.41}$$

which means that the move is always accepted for $\Delta U < 0$, and in the case of $\Delta U > 0$, the move is accepted if $\exp(-\beta \Delta U)$ is larger than a random number uniformly generated in the interval (0,1). In principle, all move schemes used in global optimization techniques like the basin-hopping method just discussed can be also used in Monte Carlo simulations. For bimetallic alloy systems, however, the most widely move schemes are displacement (shake) and exchange moves[6, 14].

Standard Metropolis MC as described above can be used to sample the configuration space in the canonical (constant *NVT*) ensemble efficiently. In statistical modeling of nanoparticles, it is often desirable to simulate the system in grand canonical ensemble, in which the chemical potential μ, volume V and temperature T are constant, and therefore both the number of particles and the internal energy can fluctuate. The partition function for the grand canonical ensemble can be written as [106]

$$Q(\mu, V, T) = \sum_{N=0}^{\infty} \frac{\exp(\beta \mu N)}{\Lambda^{3N} N!} \int \mathrm{d}\mathbf{x}^N \exp\left(-\beta U\left(\mathbf{x}^N\right)\right) \tag{2.42}$$

where $\Lambda \equiv \sqrt{h^2/(2\pi m k_{\mathrm{B}} T)}$ is the thermal de Broglie wavelength, and the corresponding probability density for the system having N particles in the configuration $\mathbf{x}^N$ reads,

$$P_{\mu VT}\left(\mathbf{x}^N; N\right) = \frac{\exp\left[\beta\left(U\left(\mathbf{x}^N\right) - N\mu\right)\right]}{Q(\mu, V, T) \Lambda^{3N} N!} \tag{2.43}$$

In the grandcanonical MC simulation (GMC), besides standard trial moves in the configuration space, there are also trial moves related to the change of the particle number by either inserting a particle at a random position or removing a randomly selected particle with the acceptance probability given by

$$P_{\text{acc}}\left(N \to N+1\right) = \min\left(1, \frac{\exp\left\{\beta\left[\mu - U\left(\mathbf{x}^{N+1}\right) + U\left(\mathbf{x}^{N}\right)\right]\right\}}{\Lambda^3\left(N+1\right)}\right)$$
$$P_{\text{acc}}\left(N \to N-1\right) = \min\left(1, \Lambda^3 N \exp\left\{-\beta\left[\mu + U\left(\mathbf{x}^{N-1}\right) - U\left(\mathbf{x}^{N}\right)\right]\right\}\right) \tag{2.44}$$

In statistical simulation of alloyed surfaces and nanoparticles, especially for the study of surface segregation, a semi-grandcanonical Monte Carlo (SGMC) scheme is often used[71, 119], in which the total number of atoms $N = N_A + N_B$ (using the bimetallic systems A_xB_{1-x} as an example), temperature T, and the chemical potential difference $\Delta\mu = \mu_A - \mu_B$ are fixed. Besides normal MC steps involving the change of configuration coordinates, a change of chemical identity of a randomly chosen atom, termed as *transmutation* in the some literature, is introduced with the acceptance probability given by

$$P_{\text{acc}} = \min\left(1, \frac{P_{\text{new}}}{P_{\text{old}}}\right) \tag{2.45}$$

with

$$P\left(\mathbf{x}^N; N_A, N_B\right) = \left(N_A! N_B!\right)^{-1} \exp\left[\frac{U\left(\mathbf{x}^N\right) - N_A\mu_A - N_B\mu_B}{k_{\text{B}}T}\right] \tag{2.46}$$

For the simulation of surface segregation in bimetallic surfaces and nanoalloys, the SGMC scheme has the advantage of greatly increasing the convergence speed compared to the standard GMC scheme since the segregating species can reach the favorable region without having to diffuse to there[71].

2.4.3 Superposition Approach to Thermodynamic Properties of Nanoparticles

As far as equilibrium thermodynamic properties are concerned, both MD and MC techniques can have the difficulties of sampling the configurational space in a statistically converged way. In both cases, there are risks of getting trapped in local regions in the configuration space such that the ergodic principle is violated, and the problem can become more severe at lower temperatures. The superposition approach, also known as the inherent structure approach[120], can serve as a complement to standard MD or MC techniques to calculate thermodynamic properties for nanoparticles with a small or intermediate size by taking advantage of the information obtained from global optimization calculations[121].

Most global optimization techniques, when successfully applied, can give not only the global minimum structure but also a large number of local minimum (LM) structures. One can take advantage of those LM structures and calculate the partition function at given temperature by simply summing up the contributions from all available LM structures. Neglecting the contributions from translation and rotation, which can be regarded

as nearly constant for different structural types, the partition function at the given temperature can be calculated

$$Z(\beta) = \sum_{\alpha} n_{\alpha} q_{\alpha}^{\text{vib}} \exp(-\beta \Delta E_{\alpha}) \tag{2.47}$$

where α is the index denoting LM structures, q_{α}^{vib} is the vibration partition function for α-th LM structure calculated by taking the corresponding energy minimum as the energy zero, and n_{α} is the multiplicity of the LM structure. In the harmonic approximation, q_{α}^{vib} can be calculated simply as

$$q_{\alpha}^{\text{vib}} = \prod_{i} \frac{2}{\sinh(\beta \hbar \omega_{\alpha,i}/2)} \tag{2.48}$$

which, in the classical limit, can be further simplified as

$$q_{\alpha}^{\text{vib}} = \prod_{i} \frac{1}{\beta \hbar \omega_{\alpha,i}} \tag{2.49}$$

One important application of the superposition approach is to study the relative stability of nanoparticles in different structural motifs at finite temperature. For nanoparticles that are smaller than some critical size, noncrystalline structural motifs such as icosahedral or decahedral structures can become more stable than crystalline motifs. The relative stability of different structural motifs depends on the size, composition, and temperature. The superposition method provides a straightforward approach to take into account entropic effects once a global optimization study has provided adequate information of representative local minimum structures. The importance of entropic effects in relative stability of nanoparticles has been addressed by several studies[122, 123]. Many nanoparticles can exhibit solid-solid transitions at some temperature in which the most stable structure changes from one geometric motif to another one.

Compared to conventional MD or MC techniques, the superposition approach has several advantages[6]. First, the method is intrinsically ergodic as long as the local minimum structures considered are complete or statistically representative. Second, the method calculates directly the partition function, from which any thermal equilibrium properties can be derived. In contrast, conventional MD or MC techniques have great difficulty in calculating the partition function itself, and any thermodynamical properties that are directly related to the partition function such as the entropy and the free energy. The latter have to be calculated indirectly by, for example, the free energy perturbation theory[124]. Third, the superposition approach is most accurate in the low-temperature regime, which is exactly the one that is most challenging for standard MD or MC, and it is therefore highly complementary to the conventional statistical techniques. The last but not the least point is that the superposition approach can capture quantum mechanical effects such as zero-point energies straightforwardly, which is again highly challenging to be accounted for in the MD or MC approaches.

2.5 Electronic Properties and Catalytic Activity of Bimetallic Systems

In this section we focus on electronic properties of bimetallic systems and their influences on catalytic activity from a theoretical perspective[17, 18].

2.5.1 The d-Band Model for Chemical Adsorption at Transition Metal Surfaces

The d-band model developed by Hammer and Nørskov[126–128] has played an important role in understanding chemical adsorption on transition metal (TM) surfaces at the molecular level. In TM solids, the electronic states arising from s and p orbitals of transition metal atoms are spatially highly delocalized, and form wide energy bands in the energy domain due to strong inter-atomic overlap of neighboring atomic orbitals. In contrast, the overlap of neighboring TM d orbitals is much weaker, and therefore leads to narrow energy bands. As a result of different characters of sp and d states, the chemical adsorption of a molecule on the TM surface can be decomposed into two steps, as illustrated in Figure 2.1. In the first step, the frontier orbitals of the adsorbate interact with the wide sp band of the TM surface, and as a result, the originally discrete molecule levels become the renormalized resonance peaks. They are shifted toward lower energy, and their widths are determined by the interaction strength. In the second step, the renormalized molecular states interact with the narrow d-band of the TM surface, and split into bonding and anti-bonding states. The adsorption energy can therefore be decomposed as

$$\Delta E_{\mathrm{ad}} = \Delta E_{\mathrm{ad,sp}} + \Delta E_{\mathrm{ad,d}} \tag{2.50}$$

The first term, corresponding to the contribution due to the interaction of the adsorbate with the TM sp states, can well be approximated to be the same for different transition metals or the same transition metal with different local structures, and therefore the variation of ΔE_{ad} can be mainly attributed to that of the second term. Based on extensive theoretical studies[127, 128], it has been well established that the magnitude

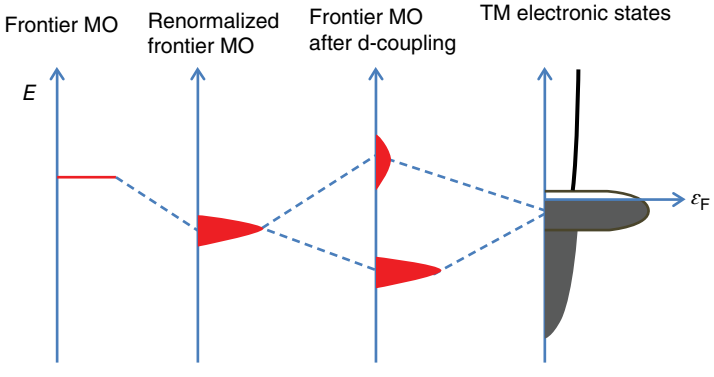

Figure 2.1 Illustration of the d-band model, adapted from ref. [125].

of $\Delta E_{ad,d}$ is strongly correlated to the d-band center with respect to the Fermi level (ε_F), which can be calculated by

$$\varepsilon_d = \frac{\int_{-\infty}^{+\infty} \rho_d(\varepsilon)(\varepsilon - \varepsilon_F)\mathrm{d}\varepsilon}{\int_{-\infty}^{+\infty} \rho_d(\varepsilon)\mathrm{d}\varepsilon} \tag{2.51}$$

where $\rho_d(\varepsilon)$ is the projected density of states (PDOS) corresponding to the d orbitals of surface TM atoms. In general, the higher d-band center in energy leads to stronger adsorption if the adsorption geometry is similar, and there is a very good linear correlation between the adsorption energy and ε_d[127, 128]. The d-band model can be derived in a semi-quantitative way [125, 129] from the Anderson-Newns model[130]. It has been found to be widely valid for many systems, and the few exceptional cases can often be explained by further considering the contribution of the Pauli repulsion due to orbital orthogonalization[131].

The d-band model provides a direct connection between the intrinsic electronic properties of transition metal surfaces and their catalytic activity of transition metals. The variation of the d-band center can often be rationalized or even predicted based on some simple theoretical arguments, which can then be used to further understand the variation of catalytic activity in different situations. A lot of insights can be obtained by using a highly simplified rectangular band model[128, 132] in which the PDOS on the surface atom to which the adsorbate is directly bond is approximated to be constant within a certain energy range, as illustrated in Figure 2.2. In this rectangular d-DOS model, the d-band center can be calculated as

$$\varepsilon_d = \left(\frac{1}{2} - \frac{n_d}{10}\right) W_d \tag{2.52}$$

where n_d is the number of d-electrons and W_d is the d-band width. Due to the strong intra-atomic repulsion among d-electrons (the Hubbard U), n_d for a given transition metal can be regarded as constant in different chemical bonding environments, which

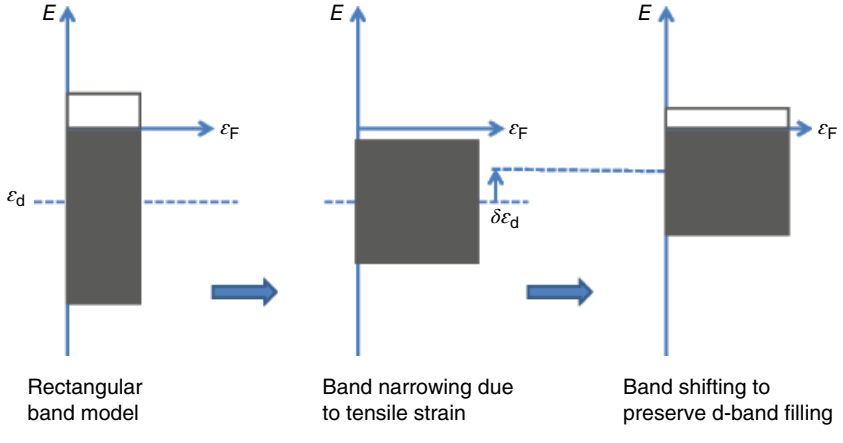

Figure 2.2 Illustration of the rectangular band model, adapted from ref. [128].

is confirmed by theoretical calculations[133, 134], and therefore ε_d is proportional to the d-band width to a good approximation[133, 134]. It is straightforward to show that the band width is mainly determined by the coordinate numbers (z), and the strength of the inter-atomic orbital overlap between nearest neighboring atoms. Eq. (2.52), together with the d-band model, gives a simple explanation to the well-known phenomenon that the adsorption is stronger at lower-coordinated sites (such as kinks and steps) than that at higher coordinated sites (facets)[135]. It can also be used to understand the variation of the catalytic activity when the transition metal is strained or compressed[128]. When the transition metal is subject to tensile strain, the d-band is narrowed as a result of reduced inter-atomic overlap, which would reduce the number of d-electrons, and therefore the d-band has to shift toward higher energy to maintain a constant n_d. An opposite process occurs if the transition metal surface is compressed. The d-band model can also be used to rationalize the fact that the binding of a molecule to transition metal nanoparticles is usually significantly stronger than that to transition metal surfaces, since nanoparticles contain more low coordinated surface atoms.

2.5.2 Tuning the Reactivity of Bimetallic Surfaces: Strain, Ligand, and Ensemble Effects

Electronic and catalytic properties of bimetallic systems have been systematically investigated theoretically by mainly considering so-called monolayer bimetallic surfaces (MBS) (as illustrated in Figure 2.3)[132, 136–138], which are especially useful to illuminate basic mechanisms underlying the tuning of electronic and chemical properties of bimetallic systems. There are three main mechanisms for the tuning of reactivity of transition metal surfaces as a result of introducing the second (guest) metal[125, 132–134, 139].

2.5.2.1 Strain Effect

When introducing the guest metal as an adlayer to the host metal, the guest metal has to take the lattice structure of the substrate, forming a pseudomorphic overlayer, and

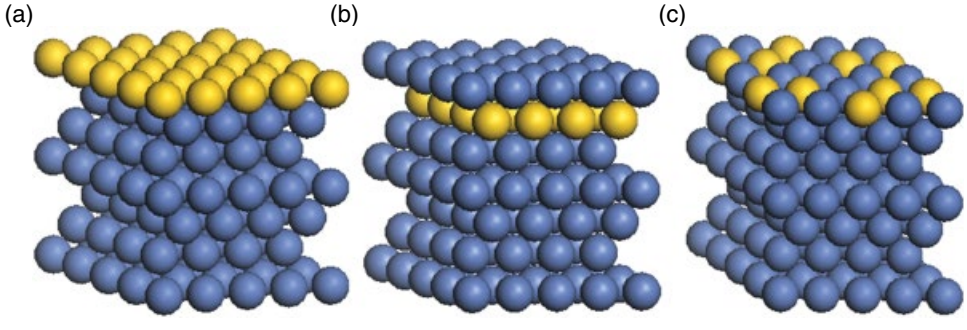

Figure 2.3 Illustration of monolayer bimetallic surfaces that are widely used to investigate electronic and catalytic properties of bimetallic systems: (a) the overlayer structure in which a mono-layer of the guest metal on top of the host metal; (b) the subsurface monolayer structure in which the second layer of the host metal is replaced by the guest metal; and (c) the alloyed (intermixed) surface with a pure metal substrate.

therefore may experience a compressive or tensile strain due to the difference in the effective atomic size of of guest and host metals, which can change the d-band width, and therefore shift the d-band center upward or downward, depending on whether the strain is tensile or compressive.

2.5.2.2 Ligand Effect

The second mechanism refers to the modification of the electronic properties due to the fact that the two metals in general have different capability of accepting or donating electrons, i.e., electronegativity, and therefore they can form heteronuclear bonds that are significantly different from those in pure metals. The latter effect is often termed as the *ligand effect* and is especially important for the tuning of surface electronic properties[136]. In most cases, the strain and the ligand effects are intertwined, and it is often difficult to tell which one is dominant. One way to look into the ligand effect without being interfered by the strain effect is to consider the subsurface structured bimetallic surfaces in which the subsurface layer of the host metal is replaced by the guest metal (Figure 2.3(b)). In this case, the host metal atoms at the top layer are not affected by the strain effect, and the modification of their electronic and chemical properties is purely caused by the different chemical environments induced by the presence of the subsurface guest metal. Kitchin et al.[134] investigated the variation of Pt surfaces due to the presence of 3d-transition metals in the subsurface layer, and they found that the d-band center of surface Pt atoms is shifted toward lower energy as a result of the presence of subsurface 3d metals, leading to significant weakening of dissociative adsorption of hydrogen and oxygen molecules.

2.5.2.3 Ensemble Effect

This, also known as the geometric effect, refers to the effect related to particular geometric arrangements of transition metal atoms on bimetallic surfaces[139]. Adsorbate molecules can interact simultaneously with an ensemble of different transition metal atoms, and the adsorption energy depends sensitively on the ensemble configuration. For example, Andersson et al.[140] found that the oxygen-binding energies on a series of surface alloys, denoted as A_xB_{1-x}/B, can be well approximated by a simple interpolation scheme,

$$\Delta E\left(A_xB_{1-x}/B\right) = x\Delta E\left(A/B\right) + \left(1-x\right)\Delta E\left(B/B\right) \tag{2.53}$$

An even more intriguing aspect of the ensemble effect is that bimetallic surfaces can exhibit some peculiar catalytic activity due to the presence of some special ensembles of transition metal atoms [141–143].

2.6 Computational Design of Bimetallic Heterogeneous Catalysts

The most attractive aspect of bimetallic systems, in particular for their applications in heterogeneous catalysis, is the possibility of tuning catalytic properties by changing their composition, which makes them especially attractive in the era when computational design of new materials via high-throughput computation becomes increasingly a new paradigm of materials research[31, 144–146]. On the other hand, heterogeneous

catalysis is very challenging from the theoretical point of view since a brute-force computation of catalytic properties that can be directly measured experimentally is often very expensive in practice, if not impossible. Indeed, thanks to recent tremendous developments in theoretical methodologies and high-performance computational facilities, a direct and sophisticated modeling of complicated catalytic systems becomes possible by combining first-principles electronic structure calculations, reaction kinetic theory and statistical modeling. A notable example is the theoretical modeling of ammonia synthesis on Ru-based catalysts by Nøskov et al.[147], in which reaction rates of ammonia synthesis over a ruthenium nanoparticle catalyst have been directly evaluated by combining density functional theory calculations of elementary reactions with a kinetic approach that accounts for the full complexity of the catalytic system under experimental conditions. Although such first-principles-based kinetic treatment of the overall catalytic systems becomes increasingly possible, it is nevertheless not feasible to use such approaches for high-throughput screening of thousands of candidate systems. The latter requires additional theoretical approximations. In this section we will discuss several important concepts that are crucial for high-throughput computational design of solid catalysts.

2.6.1 Transition State and Adsorption Energy-Scaling Relations

First-principles approaches are now routinely used to calculate activation barriers of elementary surface reactions using efficient techniques such as climb image nudged edge band (CI-NEB)[149] or related techniques. However, such calculations are very expensive, and it is still not feasible to carry out such calculations for all elementary processes in complex reaction networks on each candidate system that is considered in high-throughput screening of solid state catalysts. A crucial simplification in such studies is the establishment of the linear scaling relations between activation energies and the reaction energies or adsorption energies, which were originally discovered by Brønsted[150] and Evans and Polanyi[151], during the early years of modern catalysis, therefore named as BEP relations[125]. With similar active site structure, the activation energies and the reaction energies for a lot of elementary surface reactions on different transition metal surfaces follow very well a linear relation[148, 152, 153]. Even more remarkably, the same scaling relation can be valid for a set of reactions belonging to the same class[148, 153, 154], as illustrated in Figure 2.4, which clearly shows that the calculated activation energies and reaction energies for the chemisorption of N_2, CO, NO, and O_2 on the same type of transition metal surfaces follow a universal linear relation.

Besides the BEP scaling relation between the activation barriers and the reaction energies, several other important scaling relationships among adsorption energies of various species have also been established based on extensive theoretical investigations[155–159]. Based on systematic theoretical calculations of the adsorption energies of hydrogen-containing molecules AH_x, including CH_x ($x = 0, 1, 2, 3$), NH_x ($x = 0, 1, 2$), OH_x($x = 0, 1$), and SH_x ($x = 0, 1$) on a range of close-packed and stepped transition metal surfaces, Abild-Pedersen et al.[155] discovered that the adsorption energy of the molecule AH_x on a transition metal surface with the composition denoted by M in the geometric structure denoted by s, is linearly correlated to that of the atom A on the same surface

$$\Delta E^{s}_{AH_x}(M) = \gamma_{AH_x} \Delta E^{s}_{A}(M) + \zeta^{s}_{AH_x} \tag{2.54}$$

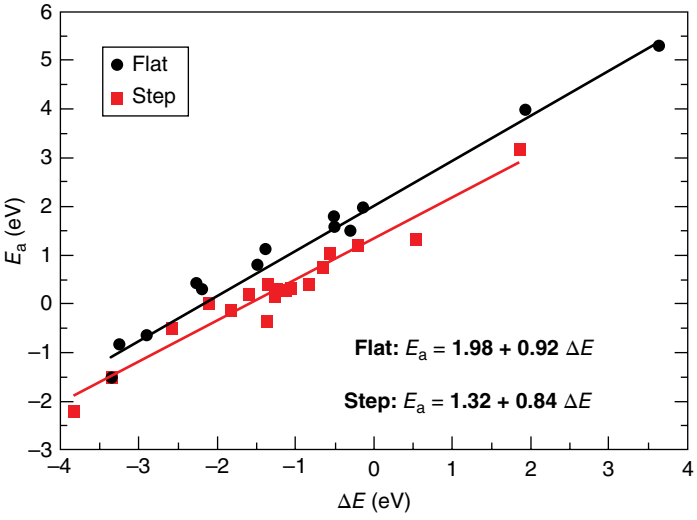

Figure 2.4 The BEP relation between the transition state energies and the chemisorption energy of N_2, CO, NO and O_2 molecules on typical transition metal surfaces, using the data from ref. [148].

Eq. (2.54) explicitly indicates that the slope γ depends only on the molecule, but the intercept ζ depends on both the molecule, and the surface geometric structure, which means that the value of ζ is different for closely packed surfaces and the stepped surfaces, and depends on the adsorption sites (atop, bridge, or hollow sites). More remarkably, the value of γ corresponding to AH_x can be evaluated to a good approximation in terms of the valence of AH_x,

$$\gamma_{AH_x} = \frac{x^A_{\max} - x}{x^A_{\max}} \tag{2.55}$$

where $x^A_{\max}$= 4, 3, 2, and 2 for A = C, N, O, and S, respectively, is the maximum number of hydrogen atoms that can bond to A. In other words, the slope of the scaling relation is related to the coordination unsaturatedness of the central atom A in the adsorbate molecule. The scaling relations can be generalized to the adsorption energies of any pair of adsorbates that bond to the transition metal surface in a similar way, e.g., between the adsorption energies of different oxygenates (O, OH, OOH, OCH_3, etc.)[157], and between the adsorption energies of adsorbates with the anchor atoms belonging to the same group (e.g., O and S, N, and P, etc.)[160], or with similar highest occupied molecular orbital (HOMO) energies[161]. The generalized scaling relation between species 1 and 2 can be written as

$$\Delta E^S_2(M) = \gamma_{1,2}\Delta E^s_1(M) + \zeta^s_{1,2}. \tag{2.56}$$

The adsorption scaling relations can be generalized in several importance cases[159]. For a molecule that bonds to transition metal surfaces by several unsaturated atoms, denoted by j, the linear scaling relation also holds with the slope that can be well approximated by [162]

$$\gamma = \sum_j \left(1 - \frac{x_j}{x_{\max}^{A_j}} \right) \tag{2.57}$$

The scaling relations, including the transition state scaling (BEP) relations and the adsorption energy scaling relations, have played very important roles in establishing a molecular-level understanding of heterogeneous catalysis on transition metal surfaces, and their importance can be viewed from the following three perspectives[156, 159]. First of all, the scaling relations provide an extremely efficient way to evaluate adsorption energies of a large number of reactants and intermediate species that are usually present in most of important catalytic systems, based on the adsorption energies of a few simple species, such as O, C, and H, which can dramatically reduce computationally cost of theoretical catalysis research[147]. Second, the scaling relations can be used to build highly simplified, and in many cases, analytic models for originally complicated reaction networks, which can be used to provide much more in-depth understanding of reaction mechanisms, and reveal dominant factors in a much more transparent way. Finally, the scaling relations can be used to obtain insights into the fundamental nature of the adsorbate-transition metal interactions. For example, the intercept parameters in the scaling relations differ for different surface types (e.g., closed packed vs stepped) and different adsorption sites[156], which provide a quantitative characterization of the structure sensitivity of the reaction concerned.

2.6.2 The Sabatier Principle and the Volcano Plot

Using the scaling relations discussed above in combination with kinetic models of the reaction networks of any particular catalytic systems naturally leads to the so-called Sabatier principle, which is the guiding rule underlying many works on rational design of new catalysts[163]. Established originally based on empirical observations, the Sabatier principle states that to achieve optimal overall catalytic activity, the interactions between molecular species involved in the catalytic cycle and the catalyst should be neither too weak nor too strong, which indicates that the catalytic activity as a function of the adsorption strength forms a volcano-type curve, and the main goal of catalyst design is to find the catalysts that correspond to the the peak of the volcano curve. The basic physical picture underlying the Sabatier principle is quite simple. The main role of the catalyst is to attract the reactant molecules to their proximity of each other, and weaken the intramolecular bonds in the reactants to facilitate forming new chemical bonds. Once the final product molecule is formed, it has to leave the catalyst to make the catalytic site available for the next round of reactions to occur. If the interaction between molecules and the catalyst is too weak, the reactant molecule could not be activated adequately; on the other hand, if the adsorption is too strong, then reaction intermediates would strongly bond to the catalytic site, which would essentially stop the catalytic cycle and leads to a low overall catalytic activity. Because of the presence of scaling relations between adsorption energies of different species involved in catalytic reactions, it is possible to correlate the overall catalytic activity to the adsorption energies of one or a few species, usually with simple structure, that can be calculated in a relatively easy way. The latter are often termed as the activity descriptor of the

concerned catalytic system, the identification of which is crucial for high-throughput computation-based design of new catalysts[145].

The volcano plot can be built by correlating experimentally measured catalytic activity data with the calculated values of the descriptor[140, 164, 166]. However, in recent studies, it becomes increasingly common to use the first-principles-based kinetic modeling[167] to establish the volcano relations[165, 168, 169]. Considering the importance of the volcano plot in theoretical design of new catalysts, we consider two examples to illustrate the necessary procedures to set up such relations. Figure 2.5 illustrates the volcano plots for two important catalytic reactions that have attracted intensive interest recently—the elecrochemical oxygen reduction reaction (ORR) and carbon dioxide hydrogenation to methanol. The efficiency and cost of the electro-catalyst for the ORR, $O_2(g) + 4H^+ + 4e^- \rightarrow 2H_2O(l)$, is currently the main bottleneck for the large-scale application for the H_2-based fuel-cell technology, and huge efforts have been invested on understanding reaction mechanisms and searching for more efficient and low-cost catalysts[170]. The ORR involves at least four electron transfer steps, and therefore, the reaction mechanism can be quite complicated. A detailed theoretical modeling of the reaction is very challenging, especially if the electrode-solution interface has to be considered in the modeling. Based on in-depth first-principles based theoretical analysis in combination with experimentally measured catalytic activity of typical catalysts, it has been now well established that the performance of an ORR catalyst correlates well with the binding energy of oxygen atom on the catalyst, which can be well characterized by a volcano plot, as shown in Figure 2.5(left)[164, 171]. As a second example, we consider carbon dioxide hydrogenation to methanol, which has been regarded as a promising route for CO_2 activation. Based on comprehensive computational investigations of different possible reaction paths, Grabow and Mavrikakis [172] suggest that the most likely reaction path is one composed of eight elementary reactions (see ref. [172] for more details). Studt et al.[165] then used the scaling relations between the oxygen adsorption energy ΔE_O and the adsorption energies and transition-state energies of all

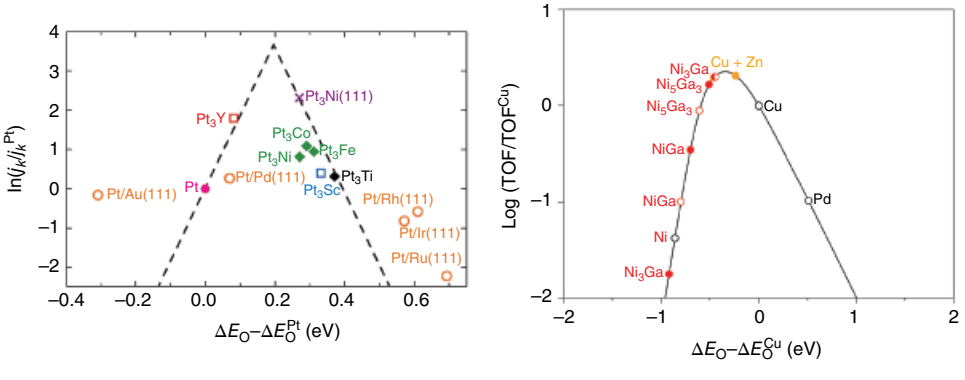

Figure 2.5 **Left**: The volcano plot for the oxygen reduction reaction (ORR) as represented by the measured current density as a function of the calculated oxygen-binding energy, both referenced to platinum. Reproduced from ref. [164] with permission from Macmillan Publ. Ltd., Nat. Chem. ©2009. **Right**: The activity volcano plot for CO_2 hydrogenation to methanol represented by the calculated turnover frequency (TOF) as a function of the binding energy of the oxygen atom ΔE_O referenced to Cu(211). Reproduced from ref. [165] with permission from Macmillan Publ. Ltd., Nat. Chem. ©2014.

intermediates involved in CO_2 hydrogenation and a simple mean-field kinetic model to obtain the theoretically calculated turnover frequency (TOF) as a function of ΔE_O, which exhibits a well-defined volcano behavior, as shown in Figure 2.5 (right).

2.6.3 High-Throughput Screening of Bimetallic Catalysts

Based on the models that have been discussed thus far, high-throughput computation has been widely used for theoretical design of new bimetallic catalysts for particular purposes[140, 146, 165, 166, 168, 169, 173–175]. In general, the common procedures[140] for rational design of solid catalysts are as follows:

1) *Identification of the descriptor.* Because of the approximate nature of the scaling relationships, the choice of the descriptor depends on the particular catalytic system that is concerned. Extensive first-principles calculations are often needed to identify the most suitable species whose adsorption energy gives optimal linear correlations with the reaction energies and activation energies of all important elementary steps involved in the catalytic cycles.
2) *Establishment of the volcano curve that predicts the optimal value of the descriptor.*
3) *High-throughput screening of a large number of candidates.* For bimetallic systems, it is relatively straightforward to build a candidate database containing hundreds or even thousands of candidate bimetallic systems. In practice, however, additional constraints need to be considered because of the high-dimensionality of the chemical space corresponding to bimetallic systems. Often, only the simplest configurations are considered, and in some cases, the adsorption energies on alloyed surface are simply estimated by using the adsorption energies on pure metal surfaces based on linear scaling relations[140]. It is also important to bear in mind that searching for optimal solid catalysts is a multiobjective optimization problem[140]. Therefore, the activity as characterized by the descriptor is not the only factor that needs be concerned, and other factors such as the stability and the price of the predicted catalysts also need to be taken into account.
4) *Theoretical scrutiny of the most promising candidates based on more sophisticated theoretical investigations.* Once a small set of promising solid catalysts have been identified, they can be further investigated theoretically based on more accurate approaches, both in terms of their chemical stability and their activity.
5) *Experimental verification.* Finally, theoretically predicted solid catalysts can be prepared experimentally to verify their catalytic activity.

We illustrate the state of the art in the high-throughput computation design of bimetallic solid catalysts using two recent examples.

One of the earliest examples of high-throughput computational study of bimetallic catalysts was undertaken by Greeley et al.[166]. It has been well established that the free energy of hydrogen adsorption ΔG_H can well be used as the descriptor to characterize the hydrogen evolution reaction (HER) catalytic activity[176]. Using the periodic DFT method, the authors calculated the value of ΔG_H on more than 700 different transition-metal surface alloys that are formed by considering 16 metals (Fe, Co, Ni, Cu, As, Ru, Rh, Pd, Ag, Cd, Sb, Re, Ir, Pt, Au, and Bi) in a simple configuration composed of a pure metal substrate with the second metal (solute) alloyed into the surface layer in an ordered way. In addition, the authors also considered the stability of each alloy surface

against surface segregation, intrasurface transformation such as island formation and de-alloying, and the oxygen adsorption. Based on such high-throughput computational screening, several surface alloys that are both active and stable are predicted. For one of the predicted surface alloy, BiPt, the authors carried out further calculations to verify its activity and stability. Finally the results of computational screening were validated by experiment, and it was found that indeed the HER activity of BiPt surface alloy is comparable to that of pure Pt.

As a second example, Hansgen et al. [168] used first-principles-based approaches to predict new bimetallic catalysts for the ammonia decomposition reaction. The authors first investigated the coverage-dependent binding energies of nitrogen and hydrogen atom on a series of pure transition metal surfaces. The latter are fitted by linear relations, $Q_A(\theta_A) = Q_{A(0)} + IP\theta_A$, where θ_A is the coverage of the adsorbate A, and IP denotes the interaction parameter that characterizes the inter-atomic interaction strength. Using these coverage-dependent atomic binding energies, molecular heats of chemisorption (Q_{NH_x}) and the activation barriers of the elementary steps involved in the ammonia decomposition reaction are also estimated by using the bond-order conservation model[177]. The ammonia conversion at 850 K for various transition metal surfaces is then calculated by micro-kinetic modeling, which, when plotted against the nitrogen-binding energy ($Q_{N(0)}$), shows a clear volcano-type behavior, indicating that $Q_{N(0)}$ can be chosen as the descriptor for this reaction. Based on the volcano plot obtained in this way, the authors performed a DFT search to identify bimetallic surfaces with the nitrogen-binding energy close to the optimal value of 134 kcal/mol. In particular, they considered Pt-based monolayer bimetallic surfaces with the ad-layer (M–Pt–Pt(111)) and the subsurface (Pt–M–Pt(111)) configurations (M = Ti, V, Cr, Mn, Fe, Co, and Ni), and they found that Ni–Pt–Pt(111) has a nitrogen-binding energy of 130.7 kcal/mol, and is therefore predicted to be catalytically active for ammonia decomposition. The latter was experimentally verified, which clearly demonstrates the efficacy of the first-principles-based framework for solid catalyst discovery.

2.7 Concluding Remarks

We have given an overview on various theoretical models that are used for understanding structural, energetic, thermodynamic, and catalytic properties of bimetallic systems. In spite of great efforts that have been invested in this field, three grand challenges still call for substantial breakthroughs in methodological developments:

1) Linearly scaling (O(N)) first-principles approaches that can treat metallic nanoparticles with hundreds and even thousands of atoms efficiently and accurately are greatly desirable, but are also highly challenging from a theoretical perspective. As a result of the vanishing HOMO-LUMO gap, linear scaling approaches for metallic systems is notoriously challenging. Recent developments in the field are promising[178], but more efforts are still needed to make such methods routinely applicable to transition metal nanoparticles.
2) Kinetic processes such as growth, mixing and coalescence of bimetallic nanoparticles have been computationally simulated by molecular dynamics techniques based on empirical inter-atomic potentials[16]. Most of the studies published so far

consider gas phase processes. Obviously a more realistic modeling of such kinetic processes should take into account real growth conditions, which differ in different preparation techniques[179]. To perform such studies requires first and foremost the availability of inter-atomic potentials that can treat metallic, covalent, and ionic bondings on the same footing. The development of such comprehensively applicable inter-atomic potentials is still in its burgeoning stage.

3) Theoretical study of catalytic properties of bimetallic systems is currently limited to either small clusters or bimetallic surface with highly simplified configurations. There are still huge gaps between model systems that are feasible for theoretical treatments and real bimetallic catalyst nanoparticles that are used experimentally. What is equally or even more challenging is to take into account reactive conditions (finite temperature, supports, surface defects, the presence of promoter or poisonous species) in theoretical evaluation of catalytic activity of bimetallic catalysts.

2.8 Acknowledgments

This work is supported by the National Key Research and Development Program of China (Grant 2016YFB0701100). The author thanks Dr. Yuechao Wang for the help during the preparation of the manuscript.

2.9 References

1 Ferrando, R., J., J., and Johnston, R.L. (2008). Nanoalloys: From theory to applications of alloy clusters and nanoparticles. *Chem. Rev.*, 108, 845–910.
2 Calvo, F. (ed.) (2013) *Nanoalloys: From Fundamentals to Emergent Applications*, Elsevier.
3 Johnston, R.L., and Wilcoxon, J.P. (eds) (2012). *Metal Nanoparticles and Nanoalloys*, Elsevier.
4 Alloyeau, D., Mottet, C., and Ricolleau, C. (eds) (2012). *Nanoalloys: Synthesis, Structure and Properties*. London: Springer.
5 Mariscal, M.M., Oviedo, O.A., and Leiva, E.P.M. (eds.) (2013). *Metal Clusters and Nanoalloys: From Modeling to Applications*. New York: Springer.
6 Ferrando, R. (2016). *Structure and Properties of Nanoalloys*. Amsterdam: Elsevier.
7 Mejia-Rosales, S., Ponce, A., and Jose-Yacaman, M. (2013). Experimental techniques for structural characterization, in *Nanoalloys: From Fundamentals to Emergence Applications*, Elsevier.
8 Wales, D.J. (2003). *Energy Landscapes*, Cambridge University Press.
9 Oganov, A.R. (ed.) (2011). *Modern Methods of Crystal Structure Prediction*. Hoboken, NJ: Wiley-VCH.
10 Calvo, F. (2015). Thermodynamics of nanoalloys. *Phys. Chem. Chem. Phys.*, 17, 27 922–27 939.
11 Fortunelli, A. and Barcaro, G. (2013). Density-functional theory of free and supported metal nanoclusters and nanoalloys. In *Metal Clusters and Nanoalloys: From Modeling to Applications* (eds M.M. Mariscal, O.A. Oviedo, and E.P.M. Leiva). New York: Springer, chap. 2, pp. 29–80.

12 Ferrando, R. (2013). Global optimization of free and supported clusters, in *Metal Clusters and Nanoalloys: From Modeling to Applications* (eds Mariscal, O.A. Oviedo, and E.P.M. Leiva), Springer, New York, chap. 6, pp. 195–214.

13 Kaszkur, Z. (2013). Thermodynamical properties of nanoalloys, in *Nanoalloys: From Fundamentals to Emergent Applications*. Amsterdam: Elsevier.

14 Mottet, C. (2013). Structure and chemical ordering in nanoalloys: Toward nanoalloy phase diagrams. In *Metal Clusters and Nanoalloys: From Modeling to Applications* (eds. M.M. Mariscal, O.A. Oviedo, and E.P.M. Leiva). New York: Springer, chap. 7, pp. 215–242.

15 Oviedo, O.A. and Leiva, E.P.M. (2013). Metal Clusters and Nanoalloys: From Modeling to Applications, *Springer, chap.* 10, pp. 215–242.

16 Ferrando, R. (2013). Kinetic aspects: nucleation, mixing and coalescence, in *Nanoalloys: From Fundamentals to Emergent Applications*. Amsterdam: Elsevier.

17 Bazin, D., Fechete, I., Garin, F., Barcaro, G., Negreiros, F.R., Sementa, L., and Fortunelli, A. (2013). Reactivity and catalysis by nanoalloys, in *Nanoalloys From Fundamentals to Emergent Applications* (ed. F. Calvo). Amsterdam: Elsevier.

18 Piccolo, L. (2012). Surface studies of catalysis by metals: Nanosize and alloying effects. In *Nanoalloys: Synthesis, Structure and Properties* (eds D. Alloyeau, C. Mottet, and C. Ricolleau). London: Springer, pp. 369–404.

19 Kohn, W. (1999). Nobel lecture: Electronic structure of matter? wave functions and density functionals. *Rev. Mod. Phys.*, 71, 1253–1266.

20 Helgaker, T., Jorgensen, P., and Olsen, J. (2000). *Molecular Electronic-Structure Theory*. New York: John Wiley & Sons.

21 Evarestov, R.A. (2007). *Quantum Chemistry of Solids: The LCAO First-Principles Treatments of Crystals*. Berlin, Heidelberg: Springer-Verlag.

22 Booth, G.H., Grüneis, A., Kresse, G., and Alavi, A. (2013). Towards an exact description of electronic wavefunctions in real solids. *Nature*, 493, 365–370.

23 Fulde, P. (2016). Wavefunction-based electronic-structure calculations for solids. *Nature Phys.*, 12, 106–107.

24 Parr, R.G. and Yang, W. (1989). *Density-Functional Theory of Atoms and Molecules*. New York: Oxford University Press.

25 Martin, R.M. (2004). *Electronic Structure: Basic Theory and Practical Methods*. Cambridge, UK: Cambridge University Press.

26 Blaha, P., Schwarz, K., Madsen, G.K.H., Kvasnicka, D., and Luitz, J. (2001). *WIEN2k, An Augmented Plane Wave + Local Orbitals Program for Calculating Crystal Properties*. Austria: Karlheinz Schwarz, Techn. Universität Wien.

27 Kresse, G. and Furthmüller, J. (1996). Efficient iterative schemes for *ab initio* total-energy calculations using a plane-wave basis set. *Phys. Rev. B*, 54 (16), 11 169.

28 Gonze, X., Amadon, B., Anglade, P., Beuken, J.M., Bottin, F., Boulanger, P., Bruneval, F., Caliste, D., Caracas, R., Cote, M., Deutsch, T., Genovese, L., Ghosez, P., Giantomassi, M., Goedecker, S., Hamann, D., Hermet, P., Jollet, F., Jomard, G., Leroux, S., Mancini, M., Mazevet, S., Oliveira, M., Onida, G., Pouillon, Y., Rangel, T., Rignanese, G.M., Sangalli, D., Shaltaf, R., Torrent, M., Verstraete, M.J., Zérah, G., and Zwanziger, J.W. (2009). Abinit: first-principles approach to material and nanosystem properties. *Comput. Phys. Commun.*, 180, 2582–2615.

29 Blum, V., Gehrke, R., Hanke, F., Havu, P., Havu, V., Ren, X., Reuter, K., and Scheffler, M. (2009). Ab initio molecular simulations with numeric atom-centered orbitals. *Comput. Phys. Commun.*, 180, 2175–2196.

30 Giannozzi et al., P. (2009). QUANTUM ESPRESSO: a modular and open-source software project for quantum simulations of materials. *J.Phys.:Condens.Matter*, 21, 395 502.

31 Jain, A., Shin, Y., and Persson, K.A. (2016). Computational predictions of energy materials using density functional theory. *Nature Rev. Mater.*, 1, 15 004.

32 Hohenberg, P. and Kohn, W. (1964). *Inhomogeneous Electron Gas.* 136, 864.

33 Kohn, W. and Sham, L.J. (1965). *Self-Consistent Equations including Exchange and Correlation Effetcs.* 140, 1133.

34 Perdew, J.P. and Kurth, S. (2003). in *A Primer in Density Functional Theory* (eds C. Fiohais, F. Nogueira, and M. Marques). Berlin, Heidelberg: Springer, Verlag, chap. 1, pp. 1–55.

35 Burke, K. (2012). Perspective on density functional theory. *J. Chem. Phy.*, 136, 150 901.

36 Cohen, A.J., Mori-Sanchez, P., and Yang, W. (2012). Challenges for density functional theory. *Chem. Rev.*, 112, 289–320.

37 Perdew, J.P. and Schmidt, K. (2001). Jacob's ladder of density functional approximations for the exchange-correlation energy. *AIP Conf. Proc.*, 577, 1.

38 Becke, A.D. (1988). Density-fnnctional exchange-energy approximation with correct asymptotic behavior. *J. Chem. Phys.*, 88, 2547.

39 Lee, C., Yang, W., and Parr, R.G. (1988). *Phys. Rev. B*, 37, 785.

40 Perdew, J.P. (1991). in *Electronic Structure of Solids 1991* (eds P. Ziesche and H. Eschrig), Akademie Verlag, Berlin, p. 11.

41 Perdew, J. P., Burke, K., and Ernzerhof, M. (1996). Generalized gradient approximation made simple. *Phys. Rev. Lett.,* 77, 3865.

42 Aryasetiawan, F. and Gunnarsson, O. (1998). The *GW* method. *Rep. Prog. Phys.*, 61, 237.

43 Jiang, H. (2010). The *GW* method: basic principles, latest developments and its applications for d- and f-electron systems. *Acta. Phys. -Chim. Sin.*, 26, 1017.

44 Jiang, H. (2015). First-principles approaches for strongly correlated materials: a theoretical chemistry perspective. *Int. J. Quantum Chem.*, 115, 722–730.

45 Becke, A.D. (1993). A new mixing of Hartree–Fock and local density-functional theories. *J. Chem. Phys.,* 98, 1372.

46 Perdew, J.P., Ernzerhof, M., and Burke, K. (1996). Generalized Gradient Approximation Made Simple. *J. Chem. Phys.*, 105, 9982.

47 Heyd, J., Scuseria, G.E., and Ernzerhof, M. (2003). *Hybrid functionals based on a screened Coulomb potential.* 118, 8207.

48 Heyd, J., Scuseria, G.E., and Ernzerhof, M. (2006). Erratum: "hybrid functionals based on a screened coulomb potential" [*J. Chem. Phys.*118, 8207 (2003)]. *J. Chem. Phys.*, 124, 219 906.

49 Ren, X., Rinke, P., Joas, C., and Scheffler, M. (2012). Random-phase approximation and its applications in computational chemistry and materials science. *J. Mater. Sci.*, 47, 7447–7471.

50 Jiang, H. and Engel, E. (2007). Random-phase-approximation-based correlation energy functionals: Benchmark results for atoms. 127, 184 108.

51 Zhang, I.Y. and Xu, X. (2011). Doubly hybrid density functional for accurate description of thermochemistry, thermochemical kinetics and nonbonded interactions. *Int. Rev. Phys. Chem.*, 30, 115–160.

52 Cui, Z.H., Wu, F., and Jiang, H. (2016). First-principles study of relative stability of rutile and anatase TiO_2 using the random phase approximation. *Phys. Chem. Chem. Phys.*, 18, 29 914–29 922.

53 Klimes, J. and Michaelides, A. (2012). Perspective: Advances and challenges in treating van der waals dispersion forces in density functional theory. *J. Chem. Phys.*, 137, 120 901.

54 Hermann, J., DiStasio, Jr., R.A., and Tkatchenko, A. (2017). First-principles models for van der waals interactions in molecules and materials: Concepts, theory, and applications. *Chem. Rev.*, 117, 4714–4758.

55 Mermin, N.D. (1965). Thermal properties of the inhomogeneous electron gas. *Phys. Rev.*, 137, A1441.

56 Kresse, G. and Furthmuller, J. (1996). Efficiency of ab-initio total energy calculations for metals and semiconductors using a plane-wave basis set. *Comput. Mater. Sci.*, 6, 15–50.

57 Methfessel, M. and Paxton, A.T. (1989). High-precision sampling for brillouin-zone integration in metals. *Phys. Rev. B*, 40, 3616–3621.

58 Ozolins, V., Wolverton, C., and Zunger, A. (1998). Cu-Au, Ag-Au, Cu-Ag, and Ni-Au intermetallics: First-principles study of temperature-composition phase diagrams and structures. *Phys. Rev. B*, 57, 6427.

59 Zhang, Y., Kresse, G., and Wolverton, C. (2014). Nonlocal first-principles calculations in cu-au and other intermetallic alloys. *Phys. Rev. Lett.*, 112, 075 502.

60 Li, J.H., Dai, X.D., Liang, S.H., Tai, K.P., Kong, Y., and Liu, B.X. (2008). Interatomic potentials of the binary transition metal systems and some applications in materials physics. *Phys. Rep.*, 455, 1–134.

61 Shan, B., Wang, L., Yang, S., Hyun, J., Kapur, N., Zhan, Y., Nicholas, J.B., and Cho, K. (2009). First-principles-based embedded atom method for PdAu nanoparticles. *Phys. Rev. B*, 80, 035 404.

62 Atanasov, I., Ferrando, R., and Johnston, R.L. (2014). Structure and solid solution properties of Cu-Ag nanoalloys. *J. Phys.: Condens. Matter*, 26, 275 301.

63 Gould, A.L., Rossi, K., Catlow, C.R.A., Baletto, F., and Logsdail, A.J. (2016). Controlling structural transitions in auag nanoparticles through precise compositional design. *J. Phys. Chem. Lett.*, 7, 4414–4419.

64 Rafii-Tabar, H. and Mansoori, G.A. (2004). Interatomic potential models for nanostructures, in *Encyclopedia of Nanoscience and Nanotechnology*, vol. 4, American Scientific Publishers, pp. 231–247.

65 Mishin, Y. (2005). Interatomic potentials for metals, in *Handbook of Materials Modeling*, Springer, pp. 459–478.

66 Raeker, T.J. and DePristo, A.E. (1991). Theory of chemical bonding based on the atom-homogeneous electron gas system. *Int. Rev. Phys. Chem.*, 10, 1–54.

67 Foiles, S.M. and Baskes, M.I. (2012). Contributions of the embedded-atom method to materials science and engineering. *MRS Bulletin*, 37, 485–492.

68 Handley, C.M. and Behler, J. (2014). Next generation interatomic potentials for condensed systems. *Eur. Phys. J. B*, 87, 152.

69 Daw, M.S. and Baskes, M.I. (1983). Semiempirical, quantum mechanical calculation of hydrogen embrittlement in metals. *Phys. Rev. Lett.*, 50, 1285.

70 Daw, M.S. and Baskes, M.I. (1984). Embedded-atom method: Derivation and application to impurities, surfaces, and other defects in metals. *Phys. Rev. B*, 29, 6443–6453.

71 Foiles, S.M. (1985). Application of the embedded-atom method to liquid transition metals. *Phys. Rev. B*, 32, 3409 – 3415.

72 Gupta, R.P. (1981). Lattice relaxation at a metal surface. *Phys. Rev. B*, 23, 6265–6270.

73 Cleri, F. and Rosato, V. (1993). Tight-binding potentials for transition metals and alloys. *Phys. Rev. B*, 48, 22–33.

74 Finnis, M. (2003). *Interatomic Forces in Condensed Matter*, Oxford University Press.

75 Baskes, M.I. (1987). Application of the embedded-atom method to covalent materials: A semiempirical potential for silicon. *Phys. Rev. Lett.*, 59, 2666–2669.

76 Baskes, M.I. (1992). Modified embedded-atom potentials for cubic materials and impurities. *Phys. Rev. B*, 46, 2727–2742.

77 Pasianot, R., Farkas, D., and Savino, E.J. (1991). Empirical many-body interatomic potential for bcc transition metals. *Phys. Rev. B*, 43, 6592–6561.

78 Mishin, Y., Mehl, M.J., and Papaconstantopoulos, D.A. (2005). Phase stability in the Fe–Ni system: Investigation by first-principles calculations and atomistic simulations. *Acta Materialia*, 53, 4029–4041.

79 Chandler, D. (1987). *Introduction to Modern Statistical Mechanics*, Oxford University Press, New York.

80 Treglia, G., Legrand, B., Ducastelle, F., Saul, A., Gallis, C., Meunier, I., Mottet, C., and Senhaji, A. (1999). Alloy surfaces: segregation, reconstruction andalloys transitions. *Comput. Mater. Sci.*, 15, 196–235.

81 Lopes, A., Treglia, G., Mottet, C., and Legrand, B. (2015). Ordering and surface segregation in $Co_{1-c}Pt_c$ nanoparticles: A theoretical study from surface alloys to nanoalloys. *Phys. Rev. B*, 91, 035 407.

82 Müller, M. and Albe, K. (2005). Lattice monte carlo simulations of FePt nanoparticles: Influence of size, composition, and surface segregation on order-disorder phenomena. *Phys. Rev. B*, 72, 094 203.

83 Sanchez, J.M., Ducastelle, F., and Gratias, D. (1984). Generalized cluster description of multi-component systems. *Physica*, 128A, 334–350.

84 de Fontaine, D. (1994). Cluster approach to order-disorder transformations in alloys. *Solid State Phys.*, 47, 33–176.

85 Zunger, A. (1994). First-principles statistical mechanics of semiconductor alloys and intermetallic compounds, in *Statics and Dynamics of Alloy Phase Transformations* (eds P.E.A. Turchi and A. Gonis), Plenum Press.

86 van de Walle, A. (2009). Multicomponent multisublattice alloys, nonconfigurational entropy and other additions to the alloy theoretic automated toolkit. *CALPHAD*, 33, 266–278.

87 Woodley, S.M. and Catlow, R. (2008). Crystal structure prediction from first principles. *Nat. Mater.*, 7, 937–946.

88 Heiles, S. and Johnston, R.J. (2013). Global optimization of clusters using electronic structure methods. *Int. J. Quantum Chem.*, 113, 2091–2109.

89 Johnston, R.L. (2003). Evolving better nanoparticles: Genetic algorithms for optimising cluster geometries. *Dalton Trans.*, pp. 4193–4207.

90 Wales, D.J. and Scheraga, H.A. (1999). Global optimization of clusters, crystals, and biomolecules. *Science*, 285, 1368.

91 Wales, D.J. and Doye, J.P.K. (1997). Global optimization by basin-hopping and the lowest energy structures of lennard-jones clusters containing up to 110 atoms. *J. Phys. Chem. A*, 101, 5111.

92 Li, Z. and Scheraga, H.A. (1987). Monte carlo-minimization approach to the multiple-minima problem in protein folding. *Proc. Natl. Acad. Sci. USA*, 84, 6611–6615.

93 Laasonen, K., Panizon, E., Bochicchio, D., and Ferrando, R. (2013). Competition between icosahedral motifs in AgCu, AgNi, and AgCo nanoalloys: A combined atomistic and DFT study. *J. Phys. Chem. C*, 117, 26 405–26 413.

94 Rossi, G. and Ferrando, R. (2009). Searching for low-energy structures of nanoparticles: a comparison of different methods and algorithms. *J. Phys.: Condens. Matter*, 9, 084 208.

95 Rossi, G. and Ferrando, R. (2006). Global optimization by excitable walkers. *Chem. Phys. Lett.*, 423, 17–22.

96 Rodina, G.G. and Da Silva, J.L.F. (2013). Revised basin-hopping monte carlo algorithm for structure optimization of clusters and nanoparticles. *J. Chem. Inf. Model.*, 53, 2282–2298.

97 Lyakhov, A.O., Oganov, A.R., and Valle, M. (2011). Crystal structure prediction using evolutionary approach, in *Modern Methods of Crystal Structure Prediction*, Wiley-VCH.

98 Nunez, S. and Johnston, R.L. (2010). Structures and chemical ordering of small cu-ag clusters. *J. Phys. Chem. C*, 114, 13 255–13 266.

99 Oh, J.S., Nam, H.S., Choi, J.H., and Lee, S.C. (2013). Prediction of atomic structure of Pt-based bimetallic nanoalloys by using genetic algorithm. *Met. Mater. Int.*, 19, 513–518.

100 Lysgaard, S., Myrdal, J.S.G., Hansen, H. A., and Vegge, T. (2015). A DFT-based genetic algorithm search for AuCu nanoalloy electrocatalysts for CO_2 reduction. *Phys. Chem. Chem. Phys.*, 17, 28 270–28 276.

101 Shayeghi, A., Götz, D., Davis, J.B., Schäfer, R., and Johnston, R.L. (2015). Pool-BCGA: a parallelised generation-free genetic algorithm for the *ab initio* global optimisation of nanoalloy clusters. *Phys. Chem. Chem. Phys.*, 17, 2104–2118.

102 Aslan, M., Davis, J.B.A., and Johnston, R.L. (2016). Global optimization of small bimetallic Pd-Co binary nanoalloy clusters: a genetic algorithm approach at the DFT level. *Phys. Chem. Chem. Phys.*, 18, 6676–6682.

103 Vilhelmsen, L.B. and Hammer, B. (2014). A genetic algorithm for first principles global structure optimization of supported nano structures. *J. Chem. Phy.*, 141, 044 711.

104 Deaven, D.M. and Ho, K.M. (1995). Molecular geometry optimization with a genetic algorithm. *Phys. Rev. Lett.*, 75, 288.

105 Ducastelle, F. (2012). Chemical order and disorder in alloys, in *Nanoalloys: Synthesis, Structure and Properties*, Springer.

106 Frenkel, D. and Smit, B. (2002) *Understanding Molecular Simulation: From Algorithm to Applications* (2nd ed.). Singapore: Elsevier.

107 Mottet, C., Rossi, G., Baletto, F., and Ferrando, R. (2005). Single impurity effect on the melting of nanoclusters. *Phys. Rev. Lett.*, 95, 035 501.

108 Baletto, F., Mottet, C., and Ferrando, R. (2003). Growth of three-shell onionlike bimetallic anoparticles. *Phys. Rev. Lett.*, 90, 135 504.

109 Parsina, I. and Baletto, F. (2010). Tailoring the structural motif of AgCo nanoalloys: Core/shell versus janus-like. *J. Phys. Chem. C*, 114, 1504–1511.

110 Voter, A.F., Montalenti, F., and Germann, T.C. (2002). Extending the time scale in atomistic simulation of materials. *Annu. Rev. Mater. Res.*, 32, 321–346.

111 Laio, A. and Gervasio, G.L. (2008). Metadynamics: a method to simnanoalloys events and reconstruct the free energy in biophysics, chemistry and material science. *Rep. Prog. Phys.*, 71, 126 601.

112 Yang, L., Liu, C.W., Shao, Q., Zhang, J., and Gao, Y.Q. (2015). From thermodynamics to kinetics: Enhanced sampling of rare events. *Acc. Chem. Res.*, 48, 947–955.

113 Gao, Y.Q. (2008). An integrate-over-temperature approach for enhanced sampling. *J. Chem. Phys.*, 128, 064 105.

114 Sun, G. and Jiang, H. (2015). *Ab initio* molecular dynamics with enhanced sampling for surface reaction kinetics at finite temperatures: $CH_2 <=> CH + H$ on Ni(111) as a case study. *J. Chem. Phys.*, 143, 234 706.

115 Gao, Y.Q. (2008). Self-adaptive enhanced sampling in the energy and trajectory spaces: Accelerated thermodynamics and kinetic calculations. *J. Chem. Phys.*, 128, 134 111.

116 Gao, Y.Q. and Yang, L. (2006). On the enhanced sampling over energy barriers in molecular dynamics simulations. *J. Chem. Phy.*, 125, 114 103.

117 Zhao, P., Yang, L.J., Gao, Y.Q., and Lu, Z.Y. (2013). Facile implementation of integrated tempering sampling method to enhance the sampling over a broad range of temperatures. *Chem. Phys.*, 415, 98–105.

118 Press, W.H., Flannery, B.P., Teukolsky, S.A., and Vetterlin, W.T. (1989). *Numerical Recipes: The Art of Scientific Computing*, Cambridge University, Cambridge, England.

119 Atanasov, I. and Hou, M. (2009). Equilibrium ordering properties of Au-Pd alloys and nanoalloys. *Surf. Sci.*, 603, 2639–2651.

120 Calvo, F., Doye, J.P.K., and Wales, D.J. (2002). Equilibrium properties of clusters in the harmonic superposition approximation. *Chem. Phys. Lett.*, 366, 176–183.

121 Wales, D.J. (2015). Perspective: Insight into reaction coordinates and dynamics from the potential energy landscape. *J. Chem. Phy.*, 142, 130 901.

122 Doye, J.P.K. and Calvo, F. (2001). Entropic effects on the size dependence of cluster structure. *Phys. Rev. Lett.*, 86, 3570–3573.

123 Panizon, E. and Ferrando, R. (2015). Solid-solid transitions in Pd-Pt nanoalloys. *Phys. Rev. B*, 92, 205 417.

124 Zwanzig, R.W. (1954). High-temperature equation of state by a perturbation method. I. nonpolar gases. *J. Chem. Phys.*, 22, 1420.

125 Nørskov, J.K., Studt, F., Abild-Pedersen, F., and Bligaard, T. (2014). *Fundamental Concepts in Heterogeneous Catalysis*, John Wiley & Sons.

126 Hammer, B. and Nørskov, J.K. (1995). Electronic factors determining the reactivity of metal surfaces. *Surf. Sci.*, 343, 211–220.

127 Hammer, B., Morikawa, Y., and Nørskov, J.K. (1996). Co chemisorption at metal surfaces and overlayers. *Phys. Rev. Lett.*, 76, 2141.

128 Hammer, B., Nørskov, J.K. (2000). Theoretical surface science and catalysis: calculations and concepts. *Adv. in Catalysis*, 45, 71–129.

129 Bligaard, T. and Nörskov, J.K. (2008). Heterogeneous catalysis, in *Chemical Bonding at Surfaces and Interfaces* (eds A. Nilsson, L.G.M. Pettersson, and J.K. Nøskov), Elsevier.

130 Newns, D.M. (1969). Self-consistent model of hydrogen chemisorption. *Phys. Rev.*, 178, 1123–1135.

131 Xin, H. and Linic, S. (2010). Communications: Exceptions to the d-band model of chemisorption on metal surfaces: The dominant role of repulsion between adsorbate states and metal d-states. *J. Chem. Phy.*, 132, 221 101.

132 Ruban, A., Hammer, B., Stoltze, P., Skriver, H., and Nørskov, J. (1997). Surface electronic structure and reactivity of transition and noble metals. *J. Mol. Catal. A: Chem.*, 115, 421–429.

133 Kitchin, J.R., Nørskov, J.K., Barteau, M.A., and Chen, J.G. (2004). Role of strain and ligand effects in the modification of the electronic and chemical properties of bimetallic surfaces. *Phys. Rev. Lett.*, 93, 156 801.

134 Kitchin, J.R., Nørskov, J.K., Barteau, M.A., and Chen, J.G. (2004). Modification of the surface electronic and chemical properties of Pt(111) by subsurface 3 d transition metals. *J. Chem. Phy.*, 120, 10 240–10 246.

135 Kolasinski, K.W. (2008). *Surface Science: Foundations of Catalysis and Nanoscience*, Wiley, 2nd edn.

136 Rodriguez, J.A. and Goodman, D.W. (1992). The nature of the metal-metal bond in beimetallic surfaces. *Science*, 257, 897–903.

137 Chen, J.G., Menning, C.A., and Zellner, M.B. (2008). Monolayer bimetallic surfaces: Experimental and theoretical studies of trends in electronic and chemical properties. *Surf. Sci. Rep.*, 63, 201–254.

138 Yu, W., Porosoff, M.D., and Chen, J.G. (2012). Review of Pt-based bimetallic catalysis: From model surfaces to supported catalysts. *Chem. Rev.*, 112, 5780–5817.

139 Ponec, V. (2001). Alloy catalysts: the concepts. *Appl. Catal. A: General*, 222, 31–45.

140 Andersson, M.P., Bligaard, T., Kustov, A., Larsen, K.E., Greeley, J., Johannessen, T., Christensen, C.H., and Nørskov, J.K. (2006). Toward computational screening in heterogeneous catalysis: Pareto-optimal methanation catalysts. *J. Catal.*, 239, 501–506.

141 Maroun, F., Ozanam, F., Magnussen, O.M., and Behm, R.J. (2001). The role of atomic ensembles in the reactivity of bimetallic electrocatalysts. *Science*, 293, 1811–1814.

142 Vang, R.T., Honkala, K., Dahl, S., Vestergaard, E.K., Schnadt, J., Laegsgaard, E., Clausen, B.S., Nørskov, J.K., and Besenbacher, F. (2005). Controlling the catalytic bond-breaking selectivity of Ni surfaces by step blocking. *Nature Materials*, 4, 160–162.

143 Chen, M., Kumar, D., Yi, C.W., and Goodman, D.W. (2005). The promotional effect of gold in catalysis by palladium-gold. *Science*, 310, 291–294.

144 Hautier, G., Jain, A., and Ong, S.P. (2012). From the computer to the laboratory: materials discovery and design using first-principles calculations. *J. Mater. Sci.*, 47, 7317–7340.

145 Curtarolo, S., Hart, G.L.W., Nardelli, M.B., Mingo, N., Sanvito, S., and Levy, O. (2013). The high-throughput highway to computational materials design. *Nature Materials*, 12, 191–201.

146 Nørskov, J.K. and Bligaard, T. (2013). The catalyst genome. *Angew. Chem. Int. Ed.*, 52, 776–777.

147 Honkala, K., Hellman, A., Remediakis, I.N., Logadottir, A., Carlsson, A. Dahl, S., Christensen, C.H., and Nørskov, J.K. (2005). Ammonia synthesis from first-principles calculations. *Science*, 307, 555–558.

148 Nørskov, J.K., Bligaard, T., Logadottir, A., Bahn, S., Hansen, L.B., Bollinger, M., Bengaard, H., Hammer, B., Sljivancanin, Z., Mavrikakis, M., Xu, Y., Dahl, S., and Jacobsen, C.J.H. (2002). Universality in heterogeneous catalysis. *J. Catal.*, 209, 275–278.

149 Henkelman, G., Uberuaga, B.P., and Jónsson, H. (2000). A climbing image nudged elastic band method for finding saddle points and minimum energy paths. *J. Chem. Phys.*, 113, 9901.

150 Brønsted, J.N. (1928). Acid and basic catalysis. *Chem. Rev.*, 5, 231–338.

151 Evans, M.G. and Polanyi, N.P. (1936). Further considerations of the thermodynamics of chemical equilibria and reaction rates. *Trans. Faraday Soc.*, 32, 1333–1360.

152 Liu, Z.P. and Hu, P. (2001). General trends in CO dissociation on transition metal surfaces. *J. Chem. Phy.*, 114, 8244.

153 Michaelides, A., Liu, Z.P., Zhang, C.J., Alavia, A., King, D., and Hu, P. (2003). Identification of general linear relationships between activation energies and enthalpy changes for reactions at surfaces. *J. Am. Chem. Soc.*, 125, 3704–3705.

154 Bligaard, T., Nørskov, J.K., Dahl, S., Matthiesen, J., Christensen, C.H., and Sehested, H. (2004). The Brønsted-Evans-Polanyi relation and the volcano curve in heterogeneous catalysis. *J. Catal.*, 224, 206–217.

155 Abild-Pedersen, F., Greeley, J., Studt, F., Rossmeisl, J., Munter, T.R., Moses, P.G., Skúlason, E., Bligaard, T., and Nørskov, J.K. (2007). Scaling properties of adsorption energies for hydrogen-containing molecules on transition-metal surfaces. *Phys. Rev. Lett.*, 99, 016 105.

156 Montemore, M.M. and Medlin, J.W. (2014). Scaling relations between adsorption energies for computational screening and design of catalysts. *Catal. Sci. Tech.*, 4, 3748 – 3761.

157 Calle-Vallejo, F., Loffreda, D., Koper, M.T.M., and Sautet, P. (2015) Introducing structural sensitivity into adsorption-energy scaling relations by means of coordination numbers. *Nature Chem.*, 7, 403–410.

158 Abild-Pedersen, F. (2016). Computational catalyst screening: Scaling, bond-order and catalysis. *Catal. Today*, 272, 6–13.

159 Greeley, J. (2016). Theoretical heterogeneous catalysis: Scaling relationships and computational catalyst design. *Annu. Rev. Chem. Biomol. Eng.*, 7, 605–635.

160 Calle-Vallejo, F., Martinez, J.I., Garcia-Lastra, J.M., Rossmeisl, J., and Koper, M.T.M. (2012). Physical and chemical nature of the scaling relations between adsorption energies of atoms on metal surfaces. *Phys. Rev. Lett.*, 108, 116 103.

161 Montemore, M.M. and Medlin, J.W. (2014). A unified picture of adsorption on transition metals through different atoms. *J. Am. Chem. Soc.*, 136, 9272–9275.

162 Jones, G., Studt, F., Abild-Pedersen, F., Nørskov, J.K., and Bligaard, T. (2011). Scaling relationships for adsorption energies of C_2 hydrocarbons on transition metal surfaces. *Chem. Eng. Sci.*, 66, 6318.

163 Nørskov, J.K., Bligaard, T., J., R., and Christensen, C.H. (2009). towards the computational design of solid catalysts. *Nature Chem.*, 1, 37–46.

164 Greeley, J., Stephens, I.E.L., Bondarenko, A.S., Johansson, T.P., Hansen, H.A., Jaramillo, T.F., Rossmeisl, J., Chorkendorff, I., and Nørskov, J.K. (2009). Alloys of platinum and early transition metals as oxygen reduction electrocatalysts. *Nat. Chem.*, 1, 552–556.

165 Studt, F., Sharafutdinov, I., Abild-Pedersen, F., Elkjaer, C.F., Hummelshøj, J.S., Dahl, S., Chorkendorff, I., and Nørskov, J.K. (2014). Discovery of a Ni-Ga catalyst for carbon dioxide reduction to methanol. *Nat. Chem.*, 6, 320–324.

166 Greeley, J., Jaramillo, T., Bonde, J., Chorkendorff, I., and Nørskov, J.K.(2006). Combinatorial high-throughput screening of electrocatalytic materials for hydrogen evolution. *Nat. Mater.*, 5, 909–913.

167 Medford, A.J., Shi, C., Hoffmann, M.J., Lausche, A.C., Fitzgibbon, S.R., Bligaard, T., and Nørskov, J.K. (2015). CATmap: A software package for descriptor-based microkinetic mapping of catalytic trends. *Catal. Lett.*, 145, 794–807.

168 Hansgen, D.A., Vlachos, D.G., and Chen, J.G. (2010). Using first principles to predict bimetallic catalysts for the ammonia decomposition reaction. *Nature Chem.*, 6, 484 00 489.

169 Tsai *et al.*, C. (2016). Direct water decomposition on transition metal surfaces: Structural dependence and catalytic screening. *Catal. Lett.*, 146, 718–724.

170 Shao, M., Chang, Q., Dodelet, J.P., and Chenitz, R. (2016). Recent advances in electrocatalysts for oxygen reduction reaction. *Chem. Rev.*, 116, 3594–3657.

171 Nørskov, J.K., J., R., Logadottir, A., Lindqvist, L., and Kitchin, J.R. (2004). Origin of the overpotential for oxygen reduction at a fuel-cell cathode. *J. Phys. Chem. B*, 108, 17 886–17 892.

172 Grabow, L.C. and Mavrikakis, M. (2011). Mechanism of methanol synthesis on Cu through CO_2 and CO hydrogenation. *ACS Catal.*, 1, 365–384.

173 Greeley, J. and Mavrikakis, M. (2004). Alloy catalysts designed from first principles. *Nat. Mater.*, 3, 810–815.

174 Alayoglu, S., Nilekar, A.U., Mavrikakis, M., and Eichhorn, B. (2008). Ru-Pt core-shell nanoparticles for preferential oxidation of carbon monoxide in hydrogen. *Nat. Mater.*, 7, 333–338.

175 Studt, F., Abild-Pedersen, F., Bligaard, T., Sørensen, R.Z., Christensen, C.H., and Nørskov, J.K. (2008). Identification of non-precious metal alloy catalysts for selective hydrogenation of acetylene. *Science*, 320, 1320–1322.

176 Nørskov, J.K., Bligaard, T., Logadottir, A., Kitchin, J.R., Chen, J.G., Pandelov, S., and Stimming, U. (2005). Trends in the exchange current for hydrogen evolution. *J. Electrochem. Soc.*, 152, J23–J26.

177 Shustorovich, E. and Sellers, H. (1998). The ubi-qep method: a practical theoretical approach to understanding chemistry on transition metal surfaces. *Surf. Sci. Rep.*, 31, 1–119.

178 Aarons, J., Sarwar, M., Thompsett, D., and Skylaris, C.K. (2016). Perspective: Methods for large-scale density functional calculations on metallic systems. *J. Chem. Phy.*, 145, 220 901.

179 Petit, C. and Repain, V. (2012). Nucleation and growth of bimetallic nanoparticles, in *Nanoalloys: Synthesis, Structure and Properties*. Berlin: Springer.

3

In situ Characterization Techniques of Bimetallics

Rui Si

Shanghai Synchrotron Radiation Facility, Shanghai Institute of Applied Physics, Chinese Academy Sciences, Shanghai, China

3.1 Introduction

Multiple techniques are required to detect both structural properties (electronic structure, short-range and long-range periodic structures, surface structure, etc.) and textural properties (morphology, shape and size, defects) of either single metal or bimetals. Specifically, X-ray photoelectron spectroscopy (XPS) for valence and electron transfer of investigated metal on surface; X-ray absorption spectroscopy (XAS) for local coordination structure around metal center; X-ray diffraction (XRD) for long-range ordering structure of crystal phase; infrared (IR) spectroscopy for surface adsorbents and intermediate of surface metal interacting with surrounding circumstances; electron microscopy including transmission electron microscope (TEM); and scanning electron microscope (SEM) for morphology or assembly of studied samples, as well as their crystal shape and size; and Raman spectroscopy for surface defects (e.g., oxygen vacancies, etc.) of measured nanostructures.

However, among these advanced experimental tools, only a few can provide extra structural and/or textural information on bimetallic nanostructures, especially the correlation between investigated two metals, while others are generally effective for both single metal and bimetals. For instance, TEM gives direct observations on shape and size of studied nanostructures, which is usual to single metal. On the other hand, with the help of energy dispersive spectroscopy (EDS), TEM can also obtain the elemental dispersion across the 1D or 2D profile on tested nanomaterials. Another example is IR spectroscopy, which normally provides information of surface adsorbents, as well as the intermediates during catalytic reaction. If suitable probing molecules (e.g., CO, N_2O, etc.) are applied, the relationship between two metals, or the doping effect of secondary component, can also be hypothesized. More importantly, XAS, particularly X-ray absorption fine structure (XAFS), is elementally sensitive technique and can solve the short-range (<6–8 Å) coordination structure (distance, coordination number, degree of ordering, etc.) around each studied metal, which should be appropriate to characterize bimetallic nanostructures.

Bimetallic Nanostructures: Shape-Controlled Synthesis for Catalysis, Plasmonics, and Sensing Applications, First Edition. Edited by Ya-Wen Zhang.
© 2018 John Wiley & Sons Ltd. Published 2018 by John Wiley & Sons Ltd.

Recently, *in situ* characterization techniques are more attractive than those ex-situ ones, probably because of the more reliable "structure–function" relationship can be obtained in the former conditions. Here, the "*in situ*" is a wide concept that could be during the synthetic procedure, pretreatment/posttreatment circumstances or reaction-containing conditions; could be in the gas, liquid, or solution media with adjustable temperature and pressure; could weakly or strongly interact with probing molecules (CO, N_2O, etc.) or means (electron or X-ray beam). As for bimetallic nanostructures, the appropriate approaches to *in situ* are actually very limited. For example, XPS normally acts under high vacuum condition and different from the realistic preparation or treatment circumstances. Although ambient pressure XPS has been recently developed to bridge the *pressure gap*, the up limit for gas concentration is still very low (usually several Pa). However, due to the rapid improvement on sample holder skills, environmental TEM (ETEM) can reach several mmHg of pressure easily, which can be certainly regarded as possible *in situ* technique. On the other hand, IR and hard X-ray XAS (XAFS) measurements generally do not affect the structural or textural detections in the wide range of working temperatures (from liquid He to above 1000°C) and/or pressures (from ultra-high vacuum to high pressure of over 100 GPa). Furthermore, IR source is almost transparent to common solid or liquid samples, and the damage of X-ray photons to nanomaterials can be effectively bypassed if extra operations such as defocusing or use of filter, are conducted in experiments.

Therefore, in this chapter, three typical *in situ* characterization techniques—electron microscopy, IR spectroscopy, and XAFS—will be introduced in detail, and several findings related to practical applications will be examined.

3.2 Electron Microscopy

As already discussed, electron microscopy, especially TEM and high-resolution TEM (HRTEM), can provide direct observations on morphology / shape and size of nanostructure for metals or their compounds. More assisted functions, such as scanning transmission electron microscopy (STEM), EDS, or selected area electron diffraction (SAED), can provide extra information on dispersion of different metals, crystal phase of investigated materials in microdomains, which is actually specific to bimetallic nanostructures. So, in this section, more examples will be described and analyzed to explain the application of electron microscopy to characterize bimetallic nanostructures, particularly corresponding to the studied structure–function relationship.

Kuwano et al. studied the thermoequilibrium state of short-range order (SRO) and the ordering process to the long-range order (LRO) phase in Cu_3Pt by the *in situ* TEM technique[1]. They confirmed that the SRO state is stable at a high temperature, while the degree of order fluctuates temporally as well as spatially at high temperatures[1]. On the other hand, some microdomains can become seeds of the LRO phase, and the transformation to LRO proceeds almost continuously without a process of nucleation[1].

Ramirez et al. prepared the NiTi films and determined the key parameters for processing Ni–Ti thin film crystals using *in situ* TEM heating methods with the Johnson–Mehl–Avrami–Kolmogorov theory[2]. During heating, they found a correlation between the average grain size and temperature[2]. However, crystallization and phase

transformation processes are sensitive to stoichiometry—that is, a Ti-rich sample that underwent the same heating and cooling conditions did not crystallize polymorphically, but in a manner encumbered by precipitation[2]. Furthermore, with cooling, Johnson et al. directly observed the conversion of the high temperature phase (austenite) to its low temperature phases (*R*-phase and martensite)[2].

Li et al. prepared the Ru–Co/Al_2O_3 catalyst and conducted a detailed investigation of the initial stages of the formation of metal nanoparticles during the incipient wetness synthesis process for both Co on γ-Al_2O_3 and Ru-promoted Co on γ-Al_2O_3 catalysts[3]. The synthesis was performed in the reaction cell of an environmental TEM so that the processes could be followed using *in situ* atomic resolution imaging, *z*-contrast imaging, and nanospectroscopy[3]. They discovered that metal precursors were found to have a highly nonuniform distribution on the alumina support, leading to a nonuniform distribution of metal particles in the final catalysts[3]. Moreover, after initial reduction, many nanoparticles nucleate on multiple sites of the γ-Al_2O_3 grains, giving a nonuniform dispersion of 1–3 nm particles[3]. On the other hand, in the Ru-promoted Co/γ-alumina sample under the same reducing conditions, the large particles contain a strong Co oxide component while smaller particles are mostly pure Ru, CoO, and bimetallic CoRu particles[3]. *In situ* electron energy loss spectroscopy (EELS) nano-analysis shows that Co exists in metallic form only in the small 1–3 nm bimetallic CoRu particles[3]. Their experimental results directly show that the addition of Ru promotes the formation of individual CoRu bimetallic nanoparticles and enhances the reducibility of small Co particles in the Co(Ru)/ γ-Al_2O_3 systems with ETEM[3].

Kröger et al. investigated the formation of stress-induced martensite in a pseudo-elastic Ni–Ti shape memory alloy with the focused ion beam technique, by *in situ* TEM[4]. A miniature tensile specimen for *in situ* straining was produced using spark-erosion, while the formation of stress induced martensite was observed in the environment of a rectangular hole that was sputtered into the thin part of the miniature tensile specimen using the focused ion beam technique[4]. Experiments showed that the formation of martensite started at specific locations, and the sharp corner of the rectangular hole probably acted as a stress raiser[4]. Furthermore, it was also observed at the intersection of a grain boundary with the rim of the rectangular hole[4]. Microstructural evidence for the role of a grain boundary during the growth of martensite was provided, and it was found that it can represent an obstacle for the propagation of a martensite/austenite interface and that it can also promote nucleation of martensite[4].

Li et al. investigated the microstructure evolution of Ni-25 at% Al thin films prepared by magnetron co-sputtering by using *in-situ* TEM study from room temperature to 750 °C[5]. The diffraction rings of both Ni and Al are present in the SAED of as deposited films, and then the diffraction ring of Al disappears when the films are heated up to 300 °C[5]. At 500 °C and 700 °C, the diffraction rings and spots of $L1_2$ intermetallic Ni_3Al phase are found, respectively, which means that the formation of ordered Ni_3Al phase starts from 500 °C[5]. Moreover, it is found that the grain growth is relatively slow due to grain boundary pinning when the temperature is lower than 300 °C while all of normal grain growth, abnormal grain growth, and annealing twinning occur at higher temperatures[5].

In et al. observed the effect of thermal stress on phase transitions in the constrained Ag_2Te nanowire, covered with platinum cladding layers, by *in situ* HRTEM[6]. The *in situ* SAED patterns in Figure 3.1 show that nanowire is single crystalline at room

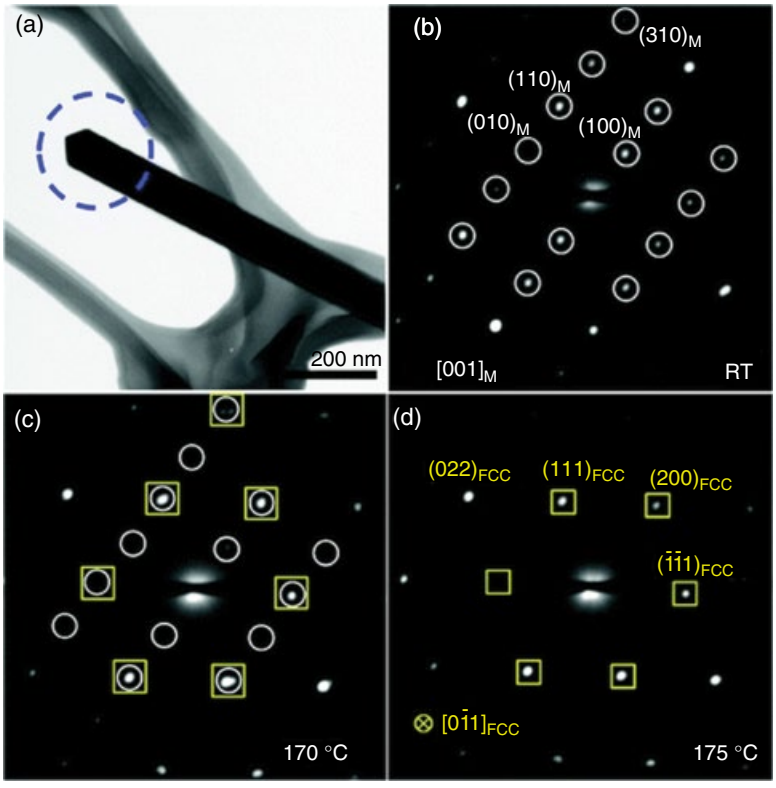

Figure 3.1 *In situ* SAED patterns of a freestanding Ag_2Te nanowire obtained from the circle in (a) the bright-field TEM image on a heating-cooling cycle; (b–d) SAED patterns obtained during heating at temperatures of (b) RT; (c) 170 °C; (d) 175 °C (M, monoclinic; circle, monoclinic spot; square, *fcc* spot). Reprinted with permission from ref. [6]. Copyright (2010), American Chemical Society.

temperature with a growth direction of [010] monoclinic[6]. The diffraction pattern is indexed to the [100] monoclinic zone pattern of monoclinic Ag_2Te from 170 °C upon indicating the beginning of a phase transition to the *fcc* phase[6]. At 175 °C, all spots that originated from the monoclinic structure disappeared, while some high index diffraction spots remained split[6]. The SAED was indexed to the $[011]_{fcc}$ zone axis pattern. They also found that transition to the *fcc* structure was completed at 180 °C[6]. To alleviate the stress acting on the nanowire, phase transition from monoclinic to the *bcc* took place near the interfaces at 150 °C, followed by gradually phase change to the *fcc* phase inside the nanowire[6]. Furthermore, they observed in real time that a *bcc* layer grows within the *fcc* layer to alleviate the thermal stress at 200 °C[6]. The *in situ* HRTEM observation of the constrained phase transition of Ag_2Te nanowires illustrates unique phase transition dynamics under compression in atomic detail and also provides direct insight into how nanomaterials would behave when constrained by overlayers in a device[6].

Khan et al. prepared nano-sized bimetallic dispersoids consisting of (Pb) and β-(Sn) phases of eutectic composition ($Pb_{26.1}Sn_{73.9}$) embedded in aluminum and Al–Cu–Fe quasicrystalline matrices by rapid solidification processing[7]. *In situ* TEM heating

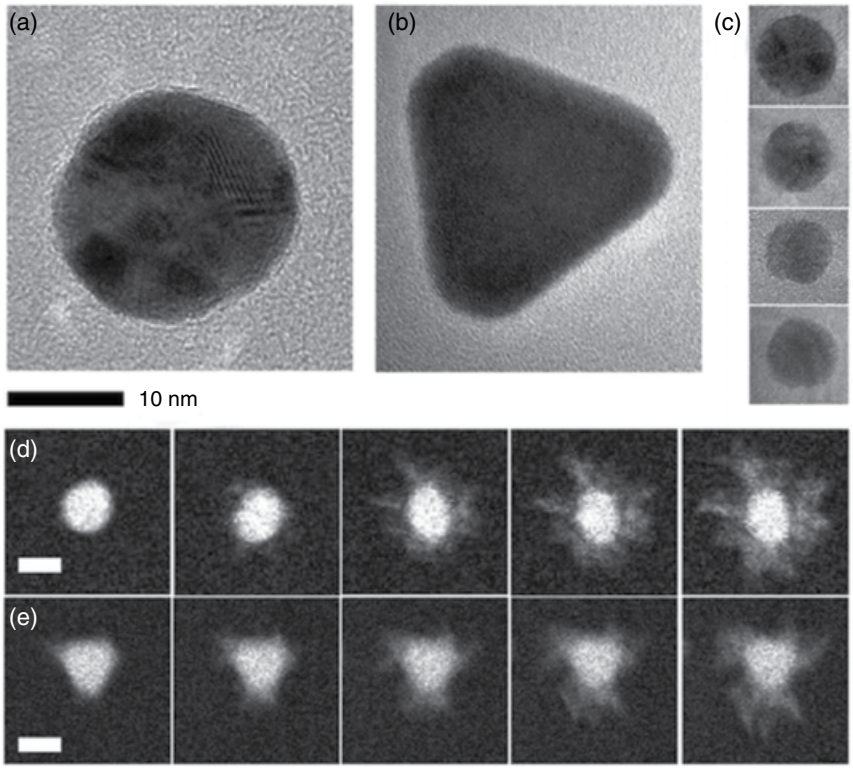

Figure 3.2 HRTEM images of (a, b) 15 nm; and (c) 5 nm Au particles; (d, e) time lapse series following the growth of Pd on 15 nm Au seeds with different morphology; (d, e) time lapse series following the growth of Pd on 15 nm Au seeds with different morphology; (d) icosahedral and (e) triangular over 92.4 s (scale bar: 10 nm). Reprinted with permission from ref. [9]. Copyright (2013), American Chemical Society.

stage experiment has been carried out for the alloy particles to study the melting and the solidification behavior indicating formation of a single-phase metastable *fcc* (Pb) in the nanoparticles prior to the melting during heating[7]. Solidification of these particles begins with nucleation of *fcc* (Pb), which phase separates into *fcc* (Pb) and *b*-(Sn) lamellae in the solid state[7].

Biswas et al. described an innovative approach in which bimetallic alloy seeds of Au_xAg_{1-x} are used to enhance the growth kinetics of Ge nanowires, via a vapor – liquid – solid (VLS) growth technique and found that Au_xAg_{1-x} alloy seeds reduce the critical diameter of the Ge nanowires in this liquid-seeded growth approach[8]. They established the correlation between the growth kinetics and equilibrium eutectic compositions in the ternary growth systems by *in situ* TEM heating experiments[8].

Jungjohann et al. investigated Pd growth in dilute aqueous Pd salt solutions containing Au nanoparticle seeds using *in situ* liquid cell TEM[9]. Au–Pd core–shell nanostructures are formed via deposition of Pd^0, generated by the reduction of chloropalladate complexes by radicals (see Figure 3.2)[9]. On the other hand, the size and shape of the Au seeds determine the morphology of the Pd shells, via preferential Pd incorporation

in low-coordination sites and avoidance of extended facets[9]. They have shown the evolution of the growth initiated by reduction of the Pd precursor by the electron beam on 5 nm and 15 nm Au nanoparticles, respectively[9]. When the Au nanoparticles are about 5 nm, Pd is deposited on the Au particles and grown from 5 – 6 to 22.8 nm diameter, corresponding to the formation of an obvious Pd shell with ~ 8 nm thickness[9]. The Au nanoparticle, clearly distinguished with its brighter *Z*-contrast at the center of the darker Pd shell, plays the role of a seed particle templating the growth of Pd, which transforms it into a Au – Pd core – shell nanostructure[9]. When the Au nanoparticles increased to large size (15 nm, 30 nm), they found accelerated growth at corners and asperities, while deposition in facets is suppressed[9]. This nonuniform growth causes a strongly varying thickness of the Pd shell, and the slower depletion of Pd ions in the solution promotes competing growth processes, such as the homogeneous nucleation of small Pd clusters in solution and incorporation into the Au seeds[9]. Their real-time observations rationalize the pathways toward different morphologies of Au – Pd core – shell nanoparticles: complete epitaxial Pd shells, partial Pd coverage, flower-like Pd morphologies, and growth of dendritic chains[9].

Tang et al. reported a new solid – liquid – solid (SLS) growth mechanism of a silicide phase in Si NWs using *in situ* TEM[10]. The new SLS mechanism is analogous to the VLS in relying on a liquid-mediating growth seed. In SLS growth of Ni disilicide, the Ni atoms are supplied from remote Ni particles by interstitial diffusion through a Si nanowire to the preexisting Au–Si liquid alloy drop at the tip of the nanowire[10]. Upon supersaturation of both Ni and Si in Au, an octahedral nucleus of Ni disilicide ($NiSi_2$) forms at the center of the Au liquid alloy, which thereafter sweeps through the Si NW and transforms Si into $NiSi_2$[10]. The dissolution of Si by the Au alloy liquid mediating layer proceeds with contact angle oscillation at the triple point where Si, oxide of Si, and the Au alloy meet, whereas $NiSi_2$ is grown from the liquid mediating layer in an atomic stepwise manner[10].

Li et al. investigated the effect of sample thickness on the martensitic transformation of NiTi *in situ* TEM study[11]. They found that the transformation temperature gradually decreased with decreasing sample thickness[11]. No transformation was observed when the thickness was below a critical value (~22 nm and ~50 nm) for *R* phase and martensitic, respectively, for the Ti-50.8 at% Ni alloy studied[11]. They observed the martensitic transformation at 20 °C, –60 °C, and –140 °C[11]. Furthermore, as the thickness decreased to 50 nm, only one stage of transformation ($B_2 \rightarrow R$) was observed. In the thinnest regions (20 nm thick), the B_2 structure remained unchanged even when the temperature was lowered to –140 °C, indicating suppression of the martensitic transformation[11]. In their view, this apparent "size effect" was attributed to the depletion of Ti in the matrix caused by surface oxidation, as confirmed by oxygen content measurements[11]. These findings demonstrate that natural oxidation and its influence on the transformation temperature must be taken into consideration in the fabrication of micro-electro-mechanical devices using NiTi[11].

Gontard et al. described a tomographic heating holder for TEM that can be used to study supported catalysts at temperatures of up to ~1,500 °C and used the holder to illustrate the evolution of the active phases of Pt nanoparticles on carbon black and PtPd nanoparticles on γ-alumina with temperature[12]. They found that particle size distributions and changes in active surface area are quantified from tilt series of images acquired after subjecting the specimens to increasing temperatures[12]. The porosity of

the alumina support and the sintering mechanisms of the catalysts are shown to depend on distance from the heating filament[12].

Xin et al. studied Pt–Co bimetallic nanoparticles during oxidation in O_2 and reduction in H_2 atmospheres using an aberration corrected environmental TEM[13]. During oxidation at 250 °C in 0.1 mbar O_2 gas environment, Co migrates to the nanoparticle surface forming a strained epitaxial CoO film which is confirmed to be CoO via lattice spacing measurement (see Figure 3.3 for details)[13]. The formation of CoO can be characterized as a two-stage process: (I) conformal coating and (II) island growth.

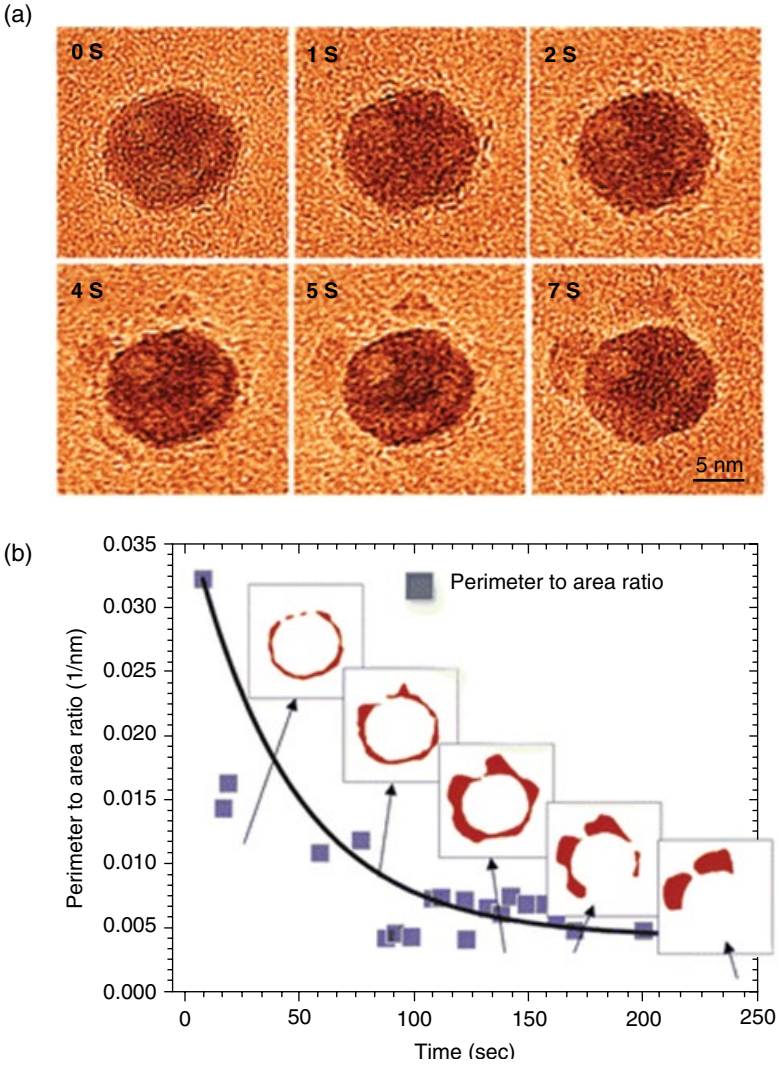

Figure 3.3 Atomic-scale reaction dynamics of a single $Pt_{0.5}Co_{0.5}$ nanoparticle in an oxidizing environment (0.1 mbar O_2, 250 °C): (a) Sequential images of the particles during oxidation; (b) The quantification of the perimeter-to-area ratio of the segregated CoO phase as a function of time. The initial time in the label of panel *a* is arbitrary. The sample was heated at 250 °C for 15 minutes before the images were taken to allow for sample stabilization. Reprinted with permission from ref. [13]. Copyright (2014), American Chemical Society.

Initially, Co atoms migrate to the surface of the Pt – Co nanoparticle and form CoO, which is cubic with an epitaxial relationship with the host Pt – Co cubic lattice. It subsequently forms islands via strain relaxation[13]. They have captured the atomic restructuring by aberration-corrected environmental TEM as a function of time[13]. When putting Pt–Co nanoparticles that have been oxidized at 400 °C in 0.14 mbar of O_2 into the reduction atmosphere, they found Co segregation process is reversible by low-angle annular dark-field scanning TEM (LAADF-STEM) images of the *in situ* reduction[13]. Prior to reduction (0 s), the cobalt oxide formed patches surrounding the Pt-rich particles[13]. As hydrogen reacts with the cobalt oxide, the cobalt oxide patches (see Figure 3.1.3) decrease. Formation of new particles was observed during reduction, which were identified to be metallic Co (Figure 3.1.3, 241 – 503 s)[13]. These particles first grew larger and then shrunk and disappeared, a process that was accompanied by complementary changes of the Pt-rich particles[13]. A high-resolution ADF-STEM image shows the structure near the surface of the particles in the {111} orientation[13]. Interestingly, the outermost atomic layer appears brighter than the layer underneath. Because the contrast in ADF-STEM images approximately scales with $Z^{1.7}$, this image strongly suggests that the {111} surface is Pt rich and the underlayer is Co rich[13]. Thus, after reduction, cobalt migrates back to the bulk, leaving a monolayer of platinum on the surface[13].

Wang et al. examined the oxidation of high-purity Ni doped with 4.1 at% Al by *in situ* TEM[14]. Experiments were performed on nanoposts fabricated from solution-annealed bulk material[14]. They found that the initial oxidation is observed to occur by multisite oxide nucleation, formation of an oxide shell followed by cavity nucleation, and growth at the metal/oxide interface[14]. Furthermore, one of the most interesting *in situ* TEM observations was the formation of a cavity that leads to the faceting of the metal and subsequent oxidation occurring by an atomic ledge migration mechanism on the faceted metal surface[14].

Wu et al. revealed a growth mode by an *in situ* TEM study of nucleation and growth of Au on Pt icosahedral nanoparticles[15]. Quantitative analysis of growth kinetics was carried out based on real-time TEM data (Figure 3.4), which shows the process involves: (1) deposition of Au on corner sites of Pt icosahedral nanoparticles; (2) diffusion of Au from corners to terraces and edges; and (3) subsequent layer-by-layer growth of Au on Au surfaces to form Pt@Au core – shell nanoparticles[15]. Deposition of Au was monitored by *in situ* TEM through analyzing the surface changes of isolated Pt icosahedrons along the [111] viewing axis of a tetrahedron subunit[15]. Distances along the six labeled directions were used to quantitatively analyze the growth of Au on the Pt icosahedrons. These six distances are categorized into two groups: three distances between the two opposite corners (Dc) and three distances between the two parallel opposite sides (Ds). In this sequence, recording started 5 min after the moment the stock solution was introduced into the liquid cell [15]. The *in situ* TEM data show conformal coating of Au on all corners and edges, followed by a characteristic oscillation in Dc with continuous growth on the sides. Both Dc and Ds began to increase around 600 s after the fluid flow was introduced. Dc grew by 2 nm within the first 1000 s, followed by a drop in thickness by about 1 nm between 1000 and 1200 s. During the same time period, all three Ds values increased continuously. After the initial stage, Dc oscillated up to 2 nm on all corners. This growth pattern was observed for the deposition of Au on other isolated icosahedra as well, indicating the growth of Au on corners and edges follows a

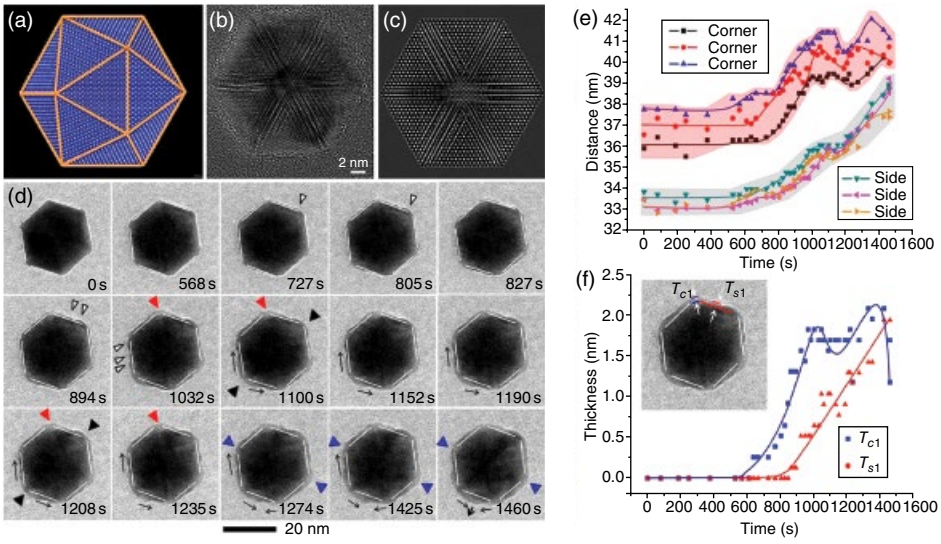

Figure 3.4 Pt icosahedral crystals and Au growth on a Pt icosahedron: (a) 3D model of a Pt icosahedron used as a seed in this growth study; (b) aberration-corrected TEM micrograph showing the atomic structures of a Pt icosahedron; (c) simulated TEM image of b; (d) sequential images show the growth of Au on the isolated Pt icosahedral nanoparticle. The triangles indicate the surface change on the corner of Pt icosahedron; (e) measured distances between corners or sides as a function of time; and (f) measured thickness of a representative corner and side of Pt icosahedron as a function of growth time. The inset indicates how the thickness of the corner and side was measured Reprinted with permission from ref. [15]. Copyright (2015), American Chemical Society.

characteristic oscillation in D[15]. The *in situ* TEM results indicate diffusion of Au from corner islands to terraces and edges is a kinetically controlled growth, as evidenced by a measurement of diffusion coefficients for these growth processes, which involve a hybrid process with nucleation-initial island growth, surface diffusion, and subsequent layer growth[15]. This hybrid model does not fall under any of the three existing growth models—namely, layer-by-layer growth, island growth, and island-on-wetting layer growth[15].

Luo et al. reported the early-stage oxidation of Ni (001) thin films alloyed with 10 or 20 at% Cr at 700 °C has been directly visualized using *in-situ* TEM[16]. Independent of Cr concentration, the oxidation initiates via nucleation of surface NiO islands and subsurface Cr_2O_3 (see Figure 3.5 for details)[16]. The NiO grows and transits into a continuous film, followed by the nucleation and growth of $NiCr_2O_4$ islands[16]. NiO whiskers are observed to preferentially nucleate/grow from the $NiCr_2O_4$ islands through a short-circuit diffusion of Ni along the $NiCr_2O_4$ interfaces in Ni–10 at% Cr[16]. During the *in suit* TEM, oxidation atmosphere leads to the formation of small oxide islands (5–10 nm), and continued oxidation leads to the formation of large oxide islands about a few hundred nanometers, which consist of both NiO and Cr_2O_3 oxide phases[16]. Spatially, the secondary oxide sprouts from the primary oxide. Morphologically, the primary oxide is large and compact, while the secondary oxide is whisker-like. EDS compositional mapping and SAD analysis identified the primary oxide as $NiCr_2O_4$, while the whisker-like secondary oxide is NiO[16]. A similar structural and morphological evolution also

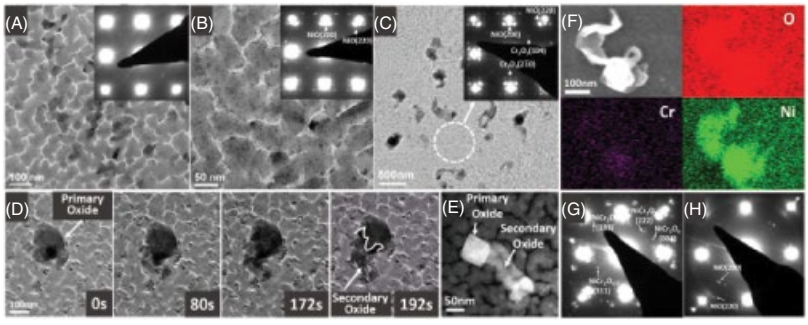

Figure 3.5 (A–E) Bright-field TEM and high angle annular dark filed (HAADF) STEM images showing the typical morphologies of oxides formed at different stages during the *in situ* oxidation of Ni–10 at% Cr and (F–H). Detailed SAD and chemical mapping analysis reveal the structure of the primary and secondary oxides. Reprinted with permission from ref. [16]. Copyright (2015), American Chemical Society.

occurs for the Ni–20 at% Cr alloy[16]. However, growth of a whisker-like secondary NiO phase from the primary $NiCr_2O_4$ did not occur. Instead, the $NiCr_2O_4$ islands continue to grow on the alloy surface with further oxidation[16]. The edges of the $NiCr_2O_4$ oxide islands expand primarily on <100> directions with more limited growth in other directions. Adjacent $NiCr_2O_4$ islands merge together without kinetic hindrance to form a single $NiCr_2O_4$ island[16].

Anton et al. prepared Ni–Fe alloy particles with vapor deposit on thin films of amorphous carbon (α-C) inside a specially equipped TEM, and reactions with the substrate were observed at elevated temperatures[17]. They found that alloy particles with composition Ni80:Fe20 (permalloy) graphitized *a*-C is in the same way as pure Ni, without any phase separation[17]. Annealing of a mixed phase of finely dispersed Ni–Fe oxide or deposition of Ni–Fe under oxygen at above 300 °C resulted in nucleation of three-dimensional crystallites of virtually pure Ni, which graphitized the carbon, while the remaining phase of small particles was converted to inactive Ni-ferrite, $NiFe_2O_4$[17].

Pan et al. studied dynamics of thermally induced composition redistribution of sandwich-like Pt–Ni octahedral electrocatalysts by *in situ* variable-temperature ETEM[18]. Dislocations were observed and on heating treatment moved toward the surface over time, resulting in an alloy nanoparticle with significant increase of Ni content on the surface[18]. The contrast inside *in situ* TEM nanoparticles varied, reflecting the change in composition and structure, especially those features related to lattice strain[18]. On annealing, boundaries of the 2 nm thick outer shell became less distinguishable over time, accompanied with rounding off of the facets of octahedral nanoparticles[18]. The heterogeneity in composition created strong driving force for atoms to move within the as-made Pt–Ni octahedral nanoparticles at elevated temperatures, resulting in redistribution of both Pt and Ni elements[18].

Jiang et al. reported a dynamic morphological evolution of palladium-copper (PdCu) nanocrystal within a nano-reactor, with atmospheric pressure hydrogen at the atomic scale[19]. *In situ* TEM videos (Figure 3.6) reveal that spherical PdCu particles transform

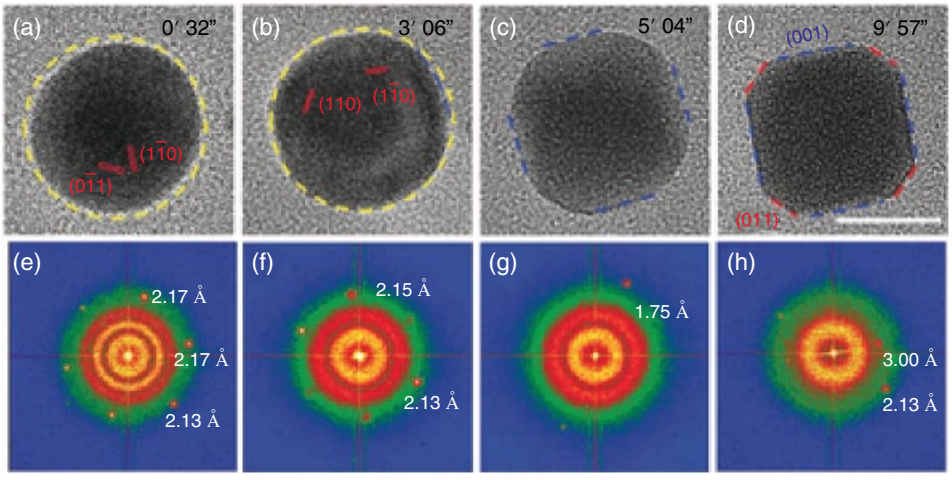

Figure 3.6 Lattice-resolved TEM images and the corresponding FFT patterns show the morphological evolution of the PdCu nanocrystal when exposed to H_2 at 1 bar and with heating at 600 K. Scale bar: 10 nm Reprinted with permission from ref. [19]. Copyright (2016), John Wiley and Sons.

into truncated cubes at high hydrogen pressure[19]. First principles calculations demonstrate that the surface energies decline with hydrogen pressure, with a new order of $\gamma_{H\text{-}001} < \gamma_{H\text{-}110} < \gamma_{H\text{-}111}$ at 1 bar. A comprehensive Wulff construction based on the corrected surface energies is perfectly consistent with the experiments[19].

Anumol et al. synthesized intermetallic Bi–Pt by sequential reduction of Pt and Bi salts in ethylene glycol under microwave irradiation[20]. During *in situ* TEM, at 550 °C, most particles transform to hollow particles with a single hollow[20]. On further heating, the densification of the particle by mass transport from the exterior to the interior resulted in the decrease in void size (from ~40 nm to ~20 nm) with a corresponding increase in shell thickness, as evident from the TEM image recorded at 600 °C[20]. They also found that once the shell is formed, the mass transport from the interior to the shell driven by curvature effect results in rapid diffusion from the core to the shell and the formation of hollow structure[20]. This observation can be rationalized based on the large driving force for mass transport from a nanoporous aggregate toward the concave region in a sintered shell[20]. Coupled with the favorable interdiffusion due to the negative heat of mixing, this mass transport leads to the direct formation of a hollow intermetallic of PtBi[20].

In summary, the experimental parameters including metal components (Cu–Pt, Ni–Al, Au–Ag, Bi–Pt, etc.), synthetic approaches (incipient wetness impregnation, vapor deposition, wet chemical methods, magnetron sputtering, etc.), *in situ* techniques for electron microscopy (TEM, HRTEM, EDS, EELS, etc.), temperature range (from RT to 1200°C), and atmospheres (inert gases, H_2, O_2, vacuum, liquid, etc.), have been listed in Table 3.1. It can be clearly seen that *in situ* electron microscopy is a powerful tool to characterize bimetallic nanostructures and can provide unique information on morphology, shape and size, and elemental dispersion for studied samples.

Table 3.1 Summary of *in-situ* electron microscopy characterization on bimetallic nanomaterials.

		In-situ conditions			
Metal	**Synthesis**	***T* (°C)**	**Atmosphere**	**Technique**	**Ref.**
Cu–Pt	arc furnace/Ar	677–727	Ar	TEM	1
Ni–Ti	magnetron/Ar sputtering chamber	465–515 20 to –140	Ar	TEM, SEM	2, 4 11
Co–Ru	incipient wetness impregnation	400	H_2/N_2	TEM, EELS	3
Ni–Al	magnetron co-sputtering	300–700	Ar O_2	TEM, SAED	5 14
Ag–Te	vapor transport	150–200	Ar	HRTEM, TEM, SAED	6
Pb–Sn	melting	25–182	Ar	TEM, EDS	7
Au–Ag	vapor-liquid-solid growth	455	H_2/Ar	TEM, SEM	8
Au–Pd	deposition and reduction	25	liquid	TEM, EELS, EDS	9 15
Au–Ni	solid-liquid-solid growth	20	liquid	TEM	10
Pd–Pt	deposition	500–975	N_2	TEM	12
Pt–Co	colloidal deposition	250	O_2 and H_2	TEM, EELS	13
Ni–Cr	melting	700	O_2	HRTEM, TEM, SAED	16
Fe–Ni	vapor deposition	400–800	Ar	TEM, EDS	17
Pt–Ni	incipient wetness impregnation	200	vacuum	TEM, EDS	18
Pd–Cu	modified chemical method	327	H_2	HRTEM, TEM, SAED, EDS	19
Bi–Pt	microwave-assisted reduction	400–1200	liquid	TEM, EDS	20

3.3 Infrared Spectroscopy

Infrared spectroscopy, mainly in the form of Fourier transform infrared spectroscopy (FTIR) or diffuse reflectance infrared Fourier transform spectroscopy (DRIFTS), is sensitive to surface structure, i.e., surface adsorbents with different gases (CO, NO, etc.) and intermediates during synthesis or reaction. Those results are largely dependent on the characteristics of investigated metals, and can be distinguished between bimetallic materials. This section analyzes more examples to explain the application of infrared spectroscopy to characterize bimetallic nanostructures, particularly corresponding to the inside synthetic mechanism or reaction pathways.

Cimino et al. prepared Pt–Rh/La–Al_2O_3 via incipient wetness impregnation method and investigated the effect of H_2S during the catalytic partial oxidation of methane under self-sustained high-temperature conditions[21]. They employed the *in situ* DRIFTS of CO adsorbed at room temperature on the reduced, sulphur-poisoned and hydrogen-reactivated Rh–Pt/La–Al_2O_3 catalyst[21]. The band dominated at 2095 and 2025 cm^{-1} is due to a rhodium gem-dicarbonyl species following sample reduction at 800 °C, and the band at 2060 cm^{-1} can be assigned to CO adsorption on Pt clusters, which also includes to a lesser extent the contribution of CO bonded to metallic Rh particles[21]. Then CO adsorbed at room temperature following exposure to H_2S is employed. Once again, the linearly adsorbed CO band becomes the only distinct band in the CO spectrum following sulphation accompanied by a shift to higher wavenumbers, from 2060 cm^{-1} for a freshly reduced sample to 2075 cm^{-1} following sulphation[21]. Following hydrogen treatment, the bands in the spectrum of the hydrogen-reactivated sample are less intense compared to the freshly reduced sample. The profile of the spectra are very similar, suggesting that the bimetallic Rh–Pt catalyst can also be reactivated following sulphur poisoning[21]. The *in situ* DRIFT experiments indicate that sulphur acts as a selective poison by preferentially adsorbing on smaller well-dispersed Rh crystallites while larger metallic Rh sites are mostly unaffected; the presence of Pt does not directly influence the way S adsorbs on highly dispersed Rh sites[21].

Li et al. prepared bimetallic Pd–Ir/TiO_2 by coinstantaneous chemical reduction processes and investigated the surface species formed during H_2–SCR reaction by *in situ* FTIR spectroscopy[22]. Under H_2–SCR reaction conditions, predominant various N_xO_y species are formed on Pd/TiO_2 and Ir/TiO_2, as indicated by the appearance of multiple bands at below 1640 cm^{-1}[22]. Specifically, the band at 1605 cm^{-1} is assigned to bridging bidentate nitrate species, while the bands at 1580 and 1300 cm^{-1} are assigned to chelating bidentate nitrate species on TiO_2[22]. For bimetallic Pd–Ir/TiO_2 under H_2-SCR conditions, similar N_xO_y species are formed on the surface of TiO_2. In addition, mononitrosyl on Ir_0 particles (band at 1880 cm^{-1}) and well-defined Ir^0 nitrosyl complexes (band at 1820 cm^{-1}) are observed, indicating that Ir species exist in metallic form in bimetallic Pd–Ir/TiO_2 in the temperature range studied[22]. They found that the addition of Pd species to Ir/TiO_2 greatly suppresses the oxidation of Ir species during reaction and confirmed the adsorption and activation of NO occur on Ir sites by observations from *in situ* FTIR spectra[22].

Sandoval et al. prepared Au–Ag/TiO_2 by sequential deposition-precipitation focused on the evolution of the Au and Ag species during the activation of the catalysts leading to the formation of bimetallic particles[23]. The evolution of the gold and silver species present at the surface of the metal particles studied by *in situ* CO-DRIFTS reveals an increasing proportion of silver atoms in the bimetallic particles during activation under hydrogen, while chemical analysis indicates a gradual elimination of the chlorides with temperature[23]. They concluded that the optimum temperature of activation of 550 °C for the reaction of CO oxidation is the result of a competition between these positive and negative effects[23].

Auvray et al. prepared Pt–Pd/Al_2O_3 catalysts by co-impregnation and sequential impregnation of the metals and used the catalysts on NO oxidation activity with the effect of propene, water[24]. They found the addition of palladium to Pt/Al_2O_3 efficiently oxidized propene and therefore significantly limited the inhibition of NO oxidation by propene[24]. So they proposed a mechanism to explain the NO oxidation

promotion lying behind the addition of Pd by *in situ* DRIFT[24]. The *in situ* DRIFT measurements and flow reactor experiments showed that propene was less stable and able to react with surface nitrates on Pd–Pt/Al_2O_3 catalyst at low temperature (175 °C)[24]. On Pt/Al_2O_3, however, the propene consumption proceeded initially through selective catalytic reduction of NO, which took place at a higher temperature (240 °C). So, propene combustion and consequently NO oxidation occurred at lower temperature on bimetallic Pd–Pt/Al_2O_3 catalysts[24].

Whiting et al. synthesized bimetallic 1 wt% Au – Pd/TiO_2 catalysts that achieve high activity for the oxidation of methanol to methyl formate at low temperature[25]. Using *in situ* DRIFTS, they demonstrate that *in situ* activation during methanol oxidation enhances the catalytic activity at low temperature[25]. When increasing reaction temperature, the bands visible at 2920 and 2823 cm^{-1} are assigned to methoxy species, ($\nu_s(CH_3)$ and $2\delta_2(CH_3)$, respectively), and this provides evidence that intermediate species exist on the catalyst surface during the reaction[25]. On the other hand, during the DRIFTS spectra of 1 wt% Au – Pd/TiO_2 catalyst under a flowing N_2 atmosphere for 1, 5, and 16 h (with H_2O present), they also found a rise in intensity of bands at 1360, 1380 (ν_s(OCO), and 1580 cm^{-1} (ν_{as}(OCO)) assigned to adsorbed (unidentate) formate ions[25]. It is entirely plausible that methyl formate undergoes hydrolysis to form formic acid, which, when adsorbed on the surface, produces unidentate formate species[25]. So they thought surface adsorbates, particularly formate species, build up on the catalyst surface during the reaction and are proven vital to enhancing the catalytic effect[25].

Sun et al. prepared bimetallic Pd-Au/Al_2O_3 using incipient wetness as well as the ion exchange method[26]. During the *in situ* DRIFT experiment, two strong peaks at 2070 and 1960 cm^{-1} were assigned to linear and twofold bridging CO species. A shoulder at 2105 cm^{-1} was assigned to linearly adsorbed CO atop Au atoms; its intensity increased with Au content. A band at ~ 1970 cm^{-1} was assigned to CO on contiguous Pd sites created by CO-induced segregation of Pd atoms to the surface[26].

On the other hand, the thermal desorption behavior of the PdAu/SiO_2 catalysts is different in several aspects. The atop and twofold bridging CO peak positions do not shift appreciably during thermal desorption, and the fractional surface coverage by bridging CO after thermal desorption at 260 °C is less than that for the monometallic samples[26]. Moreover, alloying with Au weakens the interaction between CO and surface Pd atoms, consistent with electron transfer from Au to the Pd d-band[26]. So Sun et al. postulated that the DRIFTS thermal desorption experiments demonstrated that alloying with Au reduced the CO adsorption energy on surface Pd sites[26].

Najafishirtari et al. applied colloidal preparation methods to synthesize AuCu nanocrystals in the ordered tetragonal phase with an atomic composition close to 50:50 and deposited the nanocrystals on Al_2O_3[27]. The combined analyses by EDX-STEM, SAED, and *in situ* DRIFTS highlighted a phase segregation between gold and copper upon the high-temperature (350 °C) oxidizing treatment[27]. While gold remained localized in nanocrystal entities, copper was finely dispersed on Al_2O_3, likely in the form of oxide clusters[27]. The presence of Cu^{2+} (e.g., CuO) was supported by combined CO and NO adsorption DRIFTS studies[27]. Furthermore, they found that the composition of the NCs and consequently the CO oxidation reaction rate were also affected by the CO/O_2 reacting atmosphere: regardless of the pretreatment, the same catalytic activity was approached over time on stream at temperatures as low as 100 °C as probed by CO adsorption monitored by DRIFTS[27].

Moscu et al. synthesized the bimetallic Pt–Sn/Al_2O_3 via impregnation of the support with colloidal nanoparticles[28]. During *in situ* DRIFT experiment, a rather symmetric band centered at 2050 cm^{-1} assigned to CO adsorbed linearly on platinum atoms in a Pt–Sn alloy phase and all the carbonyl bands observed were related to surface Pt atoms, suggesting that most of the surface Pt was present as part of the Pt–Sn alloy phase[28]. After introduction of molecular oxygen in the feed at 225 °C, a large shift toward higher wavenumbers led to the formation of a doublet at ca. 2077 and 2067 cm^{-1} typical of CO adsorbed on pure Pt particles[28]. They also found that surface Pt of the alloy phase (band at 2050 cm^{-1}) was not the main surface Pt species under $CO/H_2/Ar$ at 150 °C[28]. Furthermore, *in situ* DRIFTS analysis showed that Pt and Sn segregated after exposure of the Pt–Sn sample to O_2 under CO PROX reaction conditions both at 150 °C and 225 °C, forming well-dispersed platinum sites and presumably a SnO_x phase[28].

Gibson et al. prepared supported AuPd bimetallic nanoparticles with a standard sol-immobilization method with temperature control[29]. They demonstrated the restructuring of AuPd nanoparticles under CO oxidation conditions using a combined XAFS/DRIFTS approach (see Figure 3.7 for details)[29]. The DRIFTS spectra confirm the reduction of PdO to Pd by 150 °C, with the loss of the bands observed at 2157 and 2137 cm^{-1}, which can be assigned to CO adsorbed on Pd^{2+} and Pd^{+} of PdO[29]. As the bands due to PdO decrease, a shoulder at 2115 cm^{-1} becomes visible, which can be

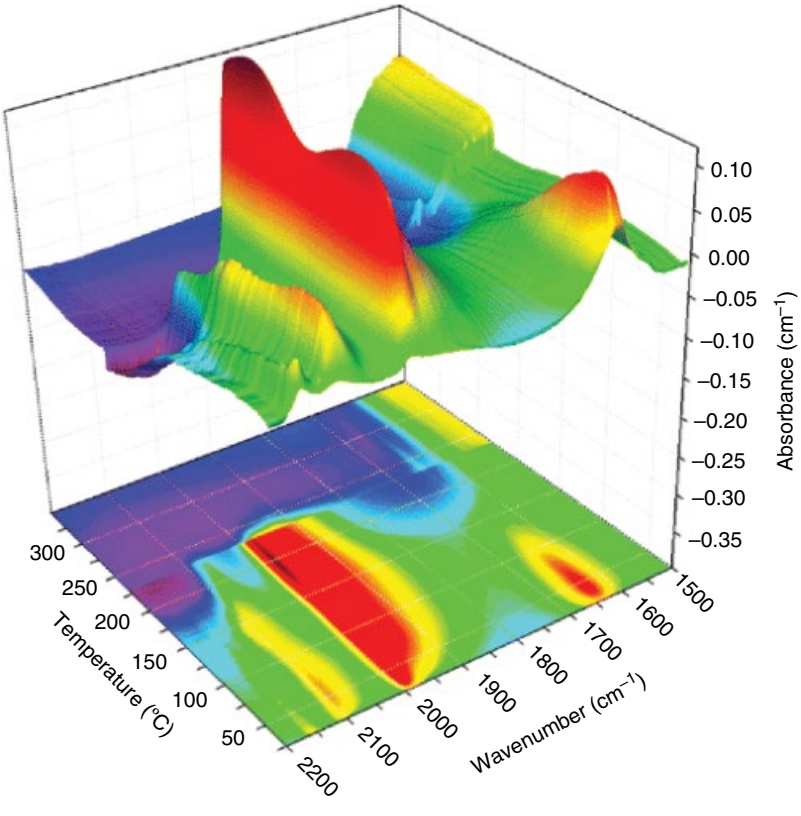

Figure 3.7 DRIFTS spectra taken during the ramp to 350 °C (open access). Ref.[29].

tentatively assigned to CO adsorbed on Au^0. This band becomes visible at 101 °C and disappears by 175 – 200 °C[29]. Infrared bands consistent with linear adsorbed CO on Pd, bridge-bonded CO on Pd and CO on Pd threefold sites were observed at 2090, 1990, and 1930 cm^{-1}[29]. At 125 – 150 °C as the PdO is reduced, the linear and bridged CO adsorbed on Pd increase in intensity. After light-off, at approximately 240 °C, no further surface adsorbates can be observed in the DRIFTS spectra. On cooling to 325 °C surface adsorbed species, namely CO adsorbed on Pd, could again be observed. During this cooling stage, no CO adsorbed on Pd^{2+} or Pd^{+} was observed, in agreement with the XAFS results that showed that no reoxidation of the catalyst occurred. On cooling and under O_2 at RT there is no evidence of Au at the surface; the band for CO adsorbed on Au at 2110 cm^{-1} is not observed[29]. So the DRIFTS spectra showed that although Au was present on the surface during the initial stages of reaction the surface rearranged just before light-off, and contained only Pd atoms thereafter[29].

Singh et al. synthesized bimetallic Pt and Ru substituted TiO_2 catalysts using the sonochemical method, which was found to be highly active for dry reforming reaction[30]. The bimetallic catalyst 2% Pt 2% Ru/TiO_2 sintered under time on stream condition and also resulted in the formation of amorphous carbon on to the surface of catalysts, which made them an inactive catalyst for reforming process[30]. Furthermore, they found the surface intermediates during these reactions by *in situ* FTIR at different temperatures for reforming processes[30]. The peaks corresponding to CO_2 adsorption were not observed in case of 4% Ru/TiO_2 and 2% Pt 2% Ru/TiO_2 for dry reforming and this indicates the Eley-Rideal mechanism on both catalysts[30].

Ang et al. synthesized monometallic (Ni and Cu) and bimetallic (Ni–Cu) with highly dispersed Ni–Cu nanoparticles supported on SiO_2 via an *in situ* self-assembly core–shell precursor route for the water-gas shift reaction[31]. They found that oleic acid can promote the dispersion of both monometallic and bimetallic particles, anchoring small metal particles to the support via enhanced metal-support interactions[31]. The DRIFTS results in Figure 3.8 suggest that CO is adsorbed on the Cu sites in the Ni–Cu alloy thereby suppressing methanation[31]. Additionally, stronger CO adsorption on the 5Ni5Cu/SiO_2 (OA) catalyst activates the surface terminal hydroxyl groups on silica for enhanced CO conversion[31]. The *in situ* DRIFT spectra of the reduced 5Ni5Cu/SiO_2 (OA) catalyst showed that the carbonyl formation on the Ni–Cu alloy occurs at a lower temperature of 150 °C and at a lower wavenumber of 2012 cm^{-1}[31]. Moreover, there was a gradual consumption of the terminal OH groups at 3747 cm^{-1} together with the decrease in the intensity of the carbonyl band as the temperature was increased[31]. They also found that the stronger CO adsorption was observed with 5Ni5Cu/SiO_2 (OA); enabling the activation of terminal OH groups on the SiO_2 surface for the reaction[31]. In contrast, depletion of the terminal OH groups on the SiO_2 surface was not observed in 5Ni5Cu/SiO_2 due to weaker CO adsorption[31].

Aguirre et al. synthesized bimetallic gold-iridium on ceria catalysts by deposition-precipitation with urea[32]. *In situ* DRIFTS was used to investigate the reactivity of the active sites[32]. They found that CO chemisorbed onto iridium sites (2096, 2060, and 2012 cm^{-1}) was found inactive, whereas carbon monoxide on metallic gold sites (Au^0–CO, 2110 cm^{-1}) exhibited reactivity for CO oxidation[32]. Furthermore, in the bimetallic catalyst, new active sites ($Au^{\delta-}$–CO, 2095 and 2026 cm^{-1}) together with Au^0-CO species were observed, most likely produced by the isolation and stabilization of gold atoms by iridium[32].

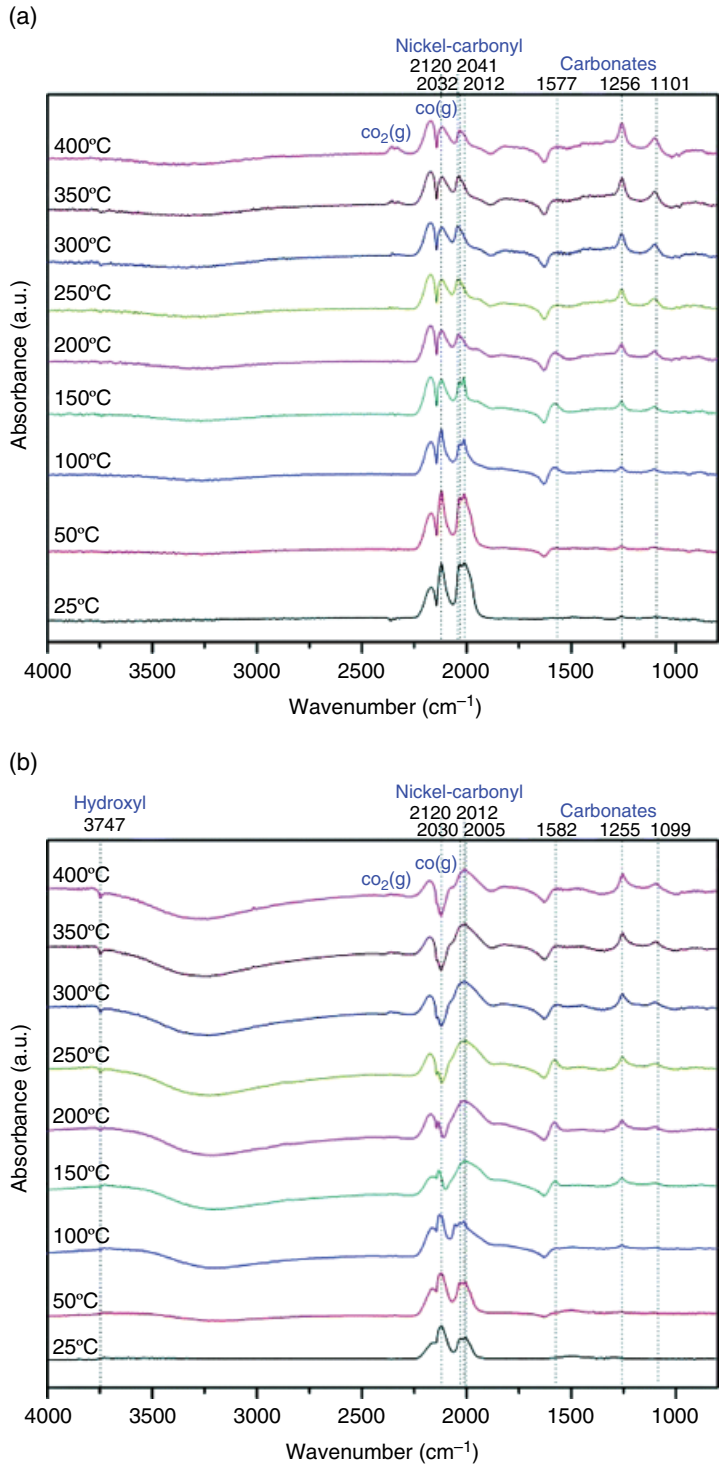

Figure 3.8 FTIR spectra of the (a) 5Ni5Cu/SiO_2; (b) 5Ni5Cu/SiO_2 (OA) catalysts under continuous flow of CO and H_2 at temperature increments of 50 °C. Reprinted with permission from ref. [31]. Copyright (2016), Royal Society of Chemistry.

Su et al. prepared monometallic and bimetallic Co–Cu catalysts by the wetness co-impregnation method applying to alcohols synthesis directly from syngas[33]. *In situ* CO-DRIFTS was employed to determine the surface structure of $CoCu/SiO_2$ using CO as a probe molecule. Two peaks at 2060 (noted as "I") and 2018 (noted as "II") cm^{-1} could be assigned to linearly adsorbed CO on metallic Co[33]. In addition, the peak I gradually disappears after switching off gaseous CO while the peak II doesn't change. Therefore, the peak I should be attributed by CO adsorbed on the metallic Co plane facet with a large number of contiguous Co atoms[33]. The peak II, which is independent of CO coverage, resulted from the CO adsorbed on step or corner sites of Co particle[33]. Two peaks in the region of 2130–2160 cm^{-1} were observed for $5Cu/SiO_2$ after the removal of CO, being allocated to CO adsorbed on Cu sites[33]. A single peak of CO adsorption on Co sites at 2018 cm^{-1} was detected for $5Co2.5Cu/SiO_2$ in CO. After switching off gaseous CO, the peak for CO adsorption on Cu sites was also observed[33]. The absence of the peak I for $5Co2.5Cu/SiO_2$ implied that the flat Co plane on the surface in pure Co particles is different with that for CoCu[33]. Likely, the surface of CoCu bimetallic particles was largely covered by Cu atoms, while the Co sites with low coordination were exposed[33]. So they thought Cu atoms prefer to agglomerate on the surface of CoCu bimetallic particles and constrain Co ensemble size[33].

A summary of this section and the experimental parameters, including metal components (Pt–Rh, Co–Cu, Au–Cu, Au–Ag, Pt–Sn, etc.), synthetic approaches (incipient wetness impregnation, vapor deposition, solvent extraction, dip coating, etc.), *in situ* techniques for IR spectroscopy (FTIR, DRIFTS, etc.), temperature range (from RT to 800°C) and gases (inert, CO, NO, C_3H_6, etc.), have been listed in Table 3.2.

Table 3.2 Summary of *in-situ* IR characterization on bimetallic nanomaterials.

		***In-situ* conditions**			
Metal	**Synthesis**	***T* (°C)**	**Gas**	**Technique**	**Ref.**
Pt–Rh	dip-coating	800	CO	DRIFTS	21
Pd–Ir	chemical reduction	100–200	NO, H_2, O_2, He	FTIR	22
Au–Ag	sequential deposition	25	CO, He	DRIFTS	23
Pt–Pd	wetness impregnation	150, 250	NO, C_3H_6, O_2	DRIFTS	24
Au–Pd	solvent extraction wetness impregnation	30 25–260	CO	DRIFTS, FTIR	25, 26, 29
Au–Cu	colloidal method	25	CO, NO	DRIFTS	27
Pt–Sn	colloidal method	150	CO	DRIFTS	28
Pt–Ru	sonochemical synthesis	500	CO	DRIFTS	30
Cu–Ni	incipient wetness impregnation	50–400	CO	DRIFTS	31
Au–Ir	deposition-precipitation	35–200	CO	DRIFTS, FTIR	32
Co–Cu	incipient wetness co-impregnation	25	CO	DRIFTS	33

Obviously, *in situ* infrared spectroscopy is good to characterize bimetallic nanostructures and can provide useful messages regarding reaction mechanisms and intermediates during catalytic studies.

3.4 X-Ray Absorption Fine Structure

X-ray absorption fine structure (XAFS), including X-ray absorption near edge spectroscopy (XANES) and extended X-ray absorption fine structure (EXAFS), effectively detects both electronic structure (valence, electron transfer, etc.) and local coordination structure (distance, coordination number, Debye-Waller factors, etc.) of tested metal centers. The related data-analysis approaches such as linear combination fit on XANES spectra and profile fitting on EXAFS spectra, can provide further quantitative results on the investigated samples. Owing to its elementally sensitive feature, XAFS is probably the best characterization technique to bimetallic nanostructures. Additionally, hard X-ray is pretty penetrative to general solids, which makes itself suitable for the *in situ* measurements. So, in this section, more examples will be described and analyzed to explain the application of XAFS to characterize bimetallic nanostructures, especially focusing on the structural evolutions during synthesis, pretreatment/posttreatment and catalytic reaction.

Bensaddil et al. applied NH_4ReO_4 and H_2PtCl_6 to synthesize PtRe bimetallic samples, which were dispersed on γ-alumina by incipient wetness impregnation, and the corresponding XAFS experiments at Pt-L_{III} and Re-L_{III} edges were done at LURE synchrotron facility in Orsay[34]. With the help of data-analysis, they claimed that the sulfur bond to rhenium shows a much greater stability than that to platinum[34]. Furthermore, the chlorine plays no direct role in the structural stabilization of the metal particles[34].

Cimini et al. prepared the PtRh/NaY bimetallic sample by the ion-exchange method, and the QEXAFS spectra were measured at the Synchrotron Radiation Source (SRS) in Daresbury[35]. Here, the QEXAFS technique proved to be a very powerful tool for investigating the formation and growth of metal particles supported on a zeolite (Figure 3.9), and they proved the existence of monometallic Rh as well as bimetallic RhPt clusters.

Nashner et al. applied the molecular cluster precursor, $PtRu_5C(CO)_{16}$, to synthesize PtRu bimetallic samples, which were dispersed on carbon black by incipient wetness impregnation from a THF solution[36]. The corresponding XAFS experiments were done at National Synchrotron Light Source (NSLS), located at the Brookhaven National Laboratory (BNL). With the help of data-analysis, they claimed that the *fcc* structure of the [PtRu5]/C nanoparticles can be obtained via thermodynamic control[36]. Moreover, the coalescence of Ru centers on a Pt-rich core generates a transient structure which undergoes a further reconstruction to give the final 1.5-nm nanoparticles[36].

Reifsnyder et al. prepared $PdAu/SiO_2$ samples via a deposition-precipitation method, by using$[Pd(NH_3)_4][NO_3]_2$ and$[Au(en)_2]Cl_3$ as metal salts[37]. They collected the XAFS data on Au L_3 and Pd K edges at NSLS of BNL and observed that a series of Pd-Au alloy films exhibit a similar negative feature near 3 eV resulting from loss of white line intensity, indicating a decrease in the density of unoccupied Au 5d states relative to bulk

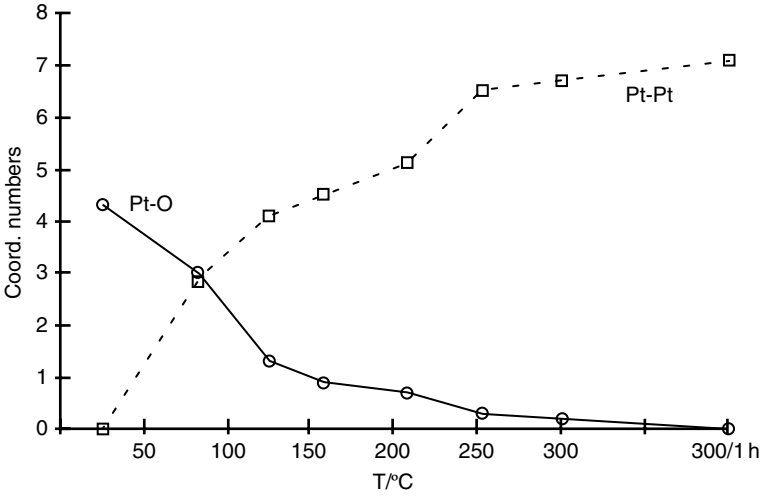

Figure 3.9 Evolution of the coordination numbers of sample during reduction. Reprinted with permission from ref. [35]. Copyright (1997), American Chemical Society.

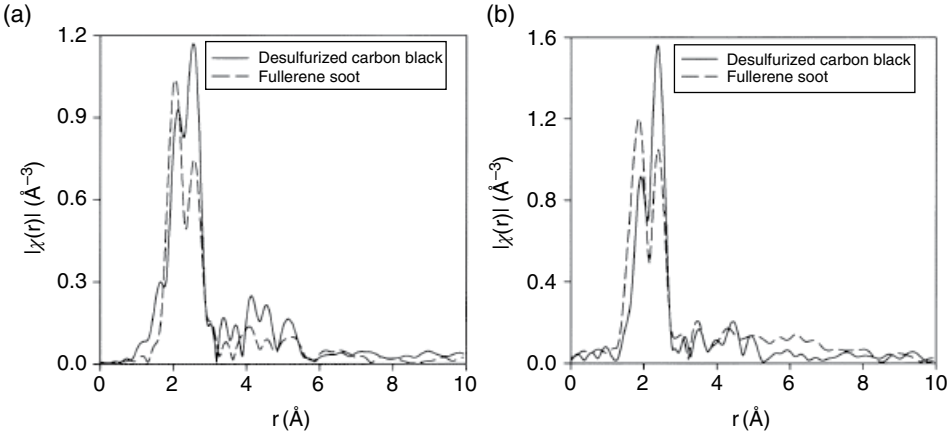

Figure 3.10 Fourier-transformed EXAFS data measured at 190 K from the carbon-supported [$PtRu_5$]/C nanoparticles after activation at 673 K under H_2: (a) Pt L_3; and (b) Ru K edges. Reprinted with permission from ref. [38]. Copyright (1999), American Chemical Society.

Au[37]. They also verified that the Pd surface enrichment in some of their catalysts may be originated from sequential reduction of Au and Pd ions during the catalyst synthesis[37].

Hills et al. utilized $PtRu_5C(CO)_{16}$ and $Pt_2Ru_4(CO)_{18}$ to disperse 1–2 wt% Pt and/or Ru on different carbon supports by incipient wetness from a THF solution[38]. The EXAFS data collected at NSLS of BNL (see Figure 3.10 for details) indicated that differences in the coordination environments of the two metals reflect the preferential occupation of surface sites by the Pt centers[38]. The compositional distribution, which was found to be 1:5 for [$PtRu_5$] and 2:4 for [Pt_2Ru_4], suggests a uniform coalescence of precursor

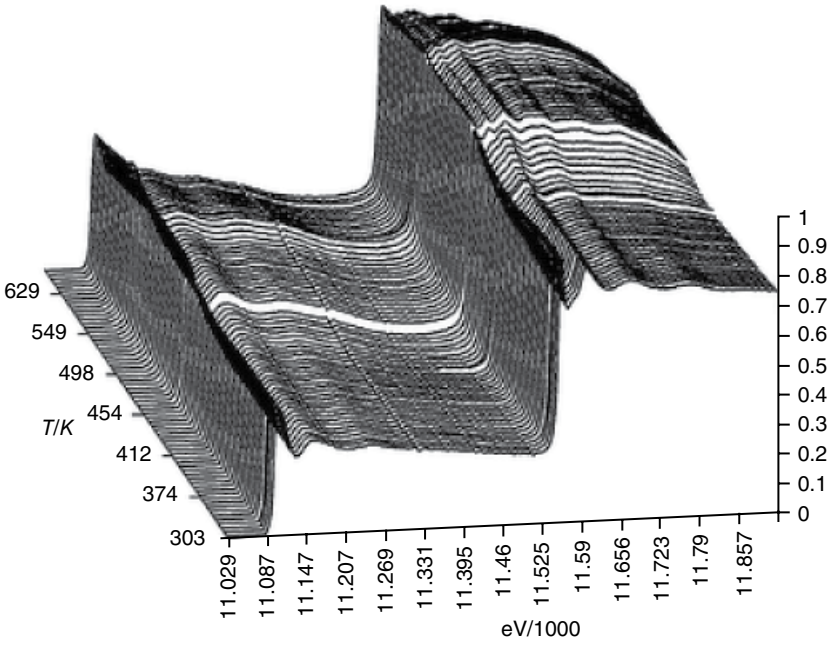

Figure 3.11 ED-EXAFS spectra for the Pt L and Ge K edges in the temperature range 298–670 K. Each spectra represents a total acquisition time of 8 s (1000 acquisitions @ 8 ms each). Reprinted with permission from ref. [40]. Copyright (2001), Royal Society of Chemistry.

clusters during activation[38]. The nanoparticle interaction with the fullerene soot suggests formation of a Ru carbide phase at the support-nanoparticle boundary[38].

Ronning et al. prepared $CoRe/Al_2O_3$ samples via an incipient wetness co-impregnation method, by using $Co(NO_3)_2 \cdot 6H_2O$ and $HReO_4$ as metal salts[39]. They collected the XAFS data on Rh L_3 edges at European Synchrotron Radiation Facility (ESRF). With the help of data-analysis, they claimed that the reduction of rhenium is not catalyzed by cobalt[39]. Further reduction of the bimetallic catalyst (12 h) leads to the complete reduction of rhenium, except for the rhenium phase that interacts strongly with the support[39].

Fiddy et al. prepared $Pt(acac)_2/H_ISiO_2$ sample by impregnation and $GeBu_4$ was incorporated by injection under vacuum to the pre-prepared it[40]. The XAFS measurements were made at the SRS. This work shows that considerable structure/phase information may be derived from explicit analysis of the EXAFS from two edges interrogated simultaneously[40]. This methodology related to energy-dispersive (ED) EXAFS (see Figure 3.11 for details) could be used for the simultaneous interrogation of a number of systems containing elements showing K or L_{III} edges in the correct energetic proximity[40].

Hungria et al. obtained the bimetallic $Pd–Cu/CeZrO_x/Al_2O_3$ and $Pd–Cu/CeZrO_x$ samples via a co-impregnation method, and the XANES experiments at the Ce L_{III} and Pd K-edges were performed at LURE[41]. Evidenced by *in situ* XANES (Figure 3.12), copper-promoting effects for CO oxidation (with either O_2 or O_2–NO mixtures) are attributed to the formation of a Pd–Cu alloy in contact with the Ce–Zr mixed oxide component[41]. The achievement of optimum properties for the Pd–Cu alloy is

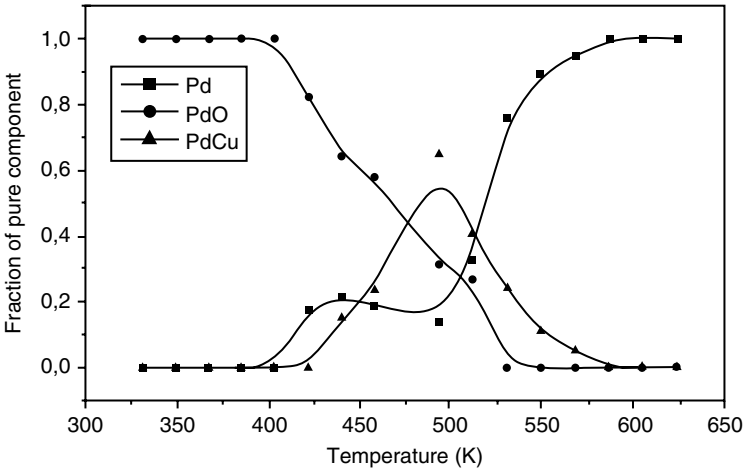

Figure 3.12 Evolution of individual components as a function of the reaction temperature in the *in situ* XANES spectra at the Pd K-edge of $PdCu_{33}$/CZA. Reprinted with permission from ref. [41]. Copyright (2002), Elsevier B.V.

proposed to be favored by a preferential interaction between copper and alumina, probably leading to a decrease in the copper concentration of the alloy phase[41]. The destruction of the alloy under reaction conditions at high temperatures required for NO activation is proposed as the main cause for the absence of copper-promoting effects for NO reduction in these systems[41].

Guczi et al. prepared $PtCo/Al_2O_3$ and PtCo/NaY samples via an incipient wetness method, by using $Co(NO_3)_2 \cdot 6H_2O$ and$[Pd(NH_3)_4][NO_3]_2$ as metal salts[42]. The corresponding XAFS experiments at Co K and Pt L_3 edge were done at LURE. They verified that the reduction of Co^{2+} ions is facilitated and monometallic Co clusters and bimetallic Pt–Co nanosized particles are formed on addition of Pt to Co. EXAFS gives evidence of the size of particles[42].

Bazin et al. prepared Ru–Co/NaY samples via ion exchange of NaY zeolite, by using $Co(NO_3)_2 \cdot 6H_2O$ and $Ru(NH_3)_6Cl_3$ as metal salts[43]. They collected the XAFS data on Co K and Ru K edges at LURE. With the help of data-analysis, they claimed that some cobalt nanoparticles are in intimate contact with ruthenium[43]. Furthermore, comparison of the freshly reduced and spent catalysts revealed that the size of cobalt particles increased only slightly while ruthenium interacted with light atoms.[43].

Keresszegi et al. reported the preparation of bimetallic catalyst 0.75wt%Bi-5wt%Pd/Al_2O_3 via a preferential deposition of promoter metal adatoms onto the surface of Pd particles[44]. The XAFS measurements were carried out at Deutsches Elektronensynchrotron (DESY). XANES/EXAFS spectroscopy in Figure 3.13 revealed that both the promoter metal (Bi) and the active noble metal component (Pd) were in a reduced state in the presence of oxygen when the reaction ran with a high rate and 100% selectivity to acetophenone[44]. This observation conforms with the classical dehydrogenation mechanism of alcohol oxidation on Pt-group metals, namely that the reaction proceeds via dehydrogenation and the coproduct hydrogen is oxidized to water[44]. The reduced state of the noble metal is due to the presence of surface hydrogen and the alcohol/carbonyl compound redox couple[44].

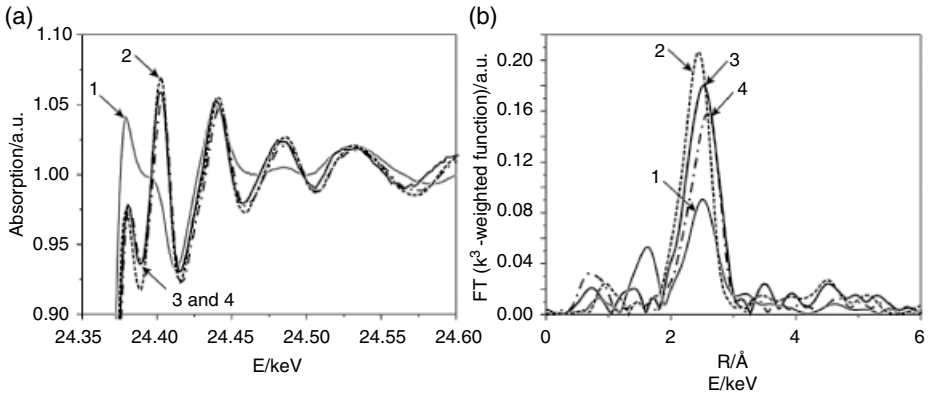

Figure 3.13 Selected X-ray absorption spectra of Bi–Pd/Al_2O_3 at the Pd *K*-edge during the reaction series shown: (a) normalized XANES spectra; and (b) Fourier-transformed k^3-weighted EXAFS functions. The spectra were taken in He-saturated toluene at 46 °C (1), in He-saturated solution of 1-phenylethanol at 62 °C; (2), in O_2-saturated toluene at 27 °C; (3), and in H_2-saturated toluene at 82 °C; (4). Reprinted with permission from ref. [44]. Copyright (2004), Elsevier B.V.

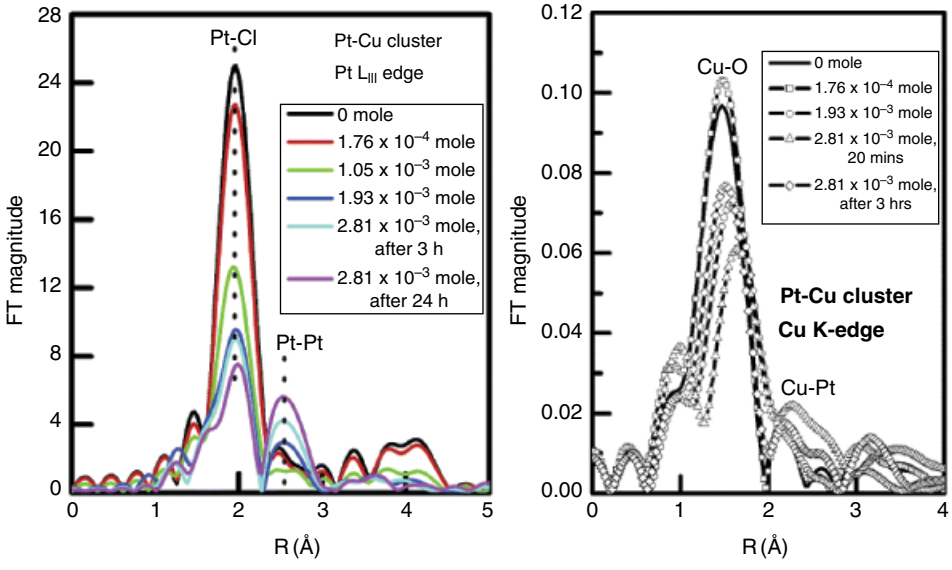

Figure 3.14 FT of EXAFS data, uncorrected for phase shift. Reprinted with permission from ref. [45]. Copyright 2004, American Chemical Society.

Hwang et al. synthesized the bimetallic Pt–Cu clusters in microemulsions containing *n*-heptane as the continuous oil phase, and the XAFS spectra (Figure 3.14) were recorded at the National Synchrotron Radiation Research Center (NSRRC)[45]. *In situ* XAFS results at the Pt L_{III}-edge revealed that the Pt^{4+} ions of the H_2PtCl_6 solution were reduced to Pt^{2+} first and then to Pt^0 to form Pt clusters in reverse microemulsions[45]. The Cu K-edge XAFS results indicated the reduction of Cu^{2+} to Cu^0[45]. It appears that the Cu clusters formed in the microemulsion were adsorbed onto the surface of the Pt, as

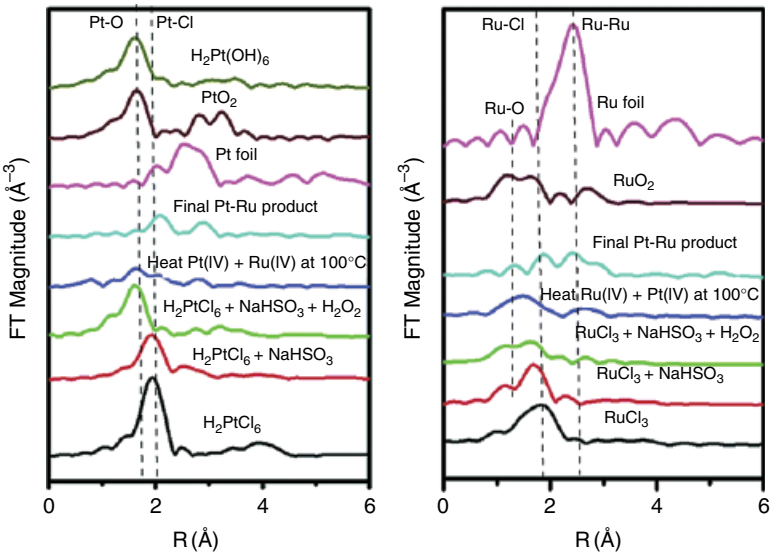

Figure 3.15 FT-EXAFS spectra at the Pt L_{III}-edge (Left) and Ru K-edge (Right) of various reaction steps during the formation of Pt-Ru bimetallic NPs. Reprinted with permission from ref. [46]. Copyright 2006, American Chemical Society.

evidenced from the lower Cu–Pt coordination and absence of the Pt–Cu coordination[45]. The stability of Pt–Cu can be further improved if the synthesis would be carried out in the presence of air. Possible structural models were proposed to account for the XAFS observations on the formation of Pt–Cu clusters in a microemulsion system at the early stages during the addition of various amounts of the reducing agent[45].

Hwang et al. prepared the carbon-supported Pt–Ru bimetallic nanoparticles by using a slight modification of the colloidal reduction method[46]. The XAFS spectra were recorded at the SPring-8, which suggests the presence of both Pt and Ru metallic and ionic contributions in the colloidal product[46]. On the basis of the XAFS structural parameters determined by Figure 3.15, they found that atomic-scale distribution of Ru is much better than that of Pt[46].

Sarma et al. prepared Pt–Ru nanoparticles by adding H_2PtCl_6 and $RuCl_3$ into EG solution[47]. The corresponding XAFS experiments at Ru K- and Pt L_{III}-edge were done at the SPring-8 and NSRRC. They verified that well-defined Pt–Ru nanoparticles were formed at 160 °C reflux for 0.5 h of the reaction mixture[47]. Moreover, they found that the atomic-scale distribution of Pt and Ru is better in the final Pt-Ru nanoparticles compared to the Pt-Ru nanoparticles prepared by a modified Watanabe process[47].

Mukainakano et al. prepared $PdNi/Al_2O_3$ samples via an incipient wetness method, by using $Ni(NO_3)_2 \cdot 6H_2O$ and $PdCl_2$ as metal salts[48]. They collected the QXAFS data on Pd K-edge at the SPring-8. They verified that the interaction between Pd and Ni was observed at a lower reduction temperature, and that as a result, the bimetallic particles with a well mixture of Pd and Ni are formed[48]. Therefore, the preparation method can influence the surface composition and the sequential impregnation enhanced the surface composition of Pd.[48].

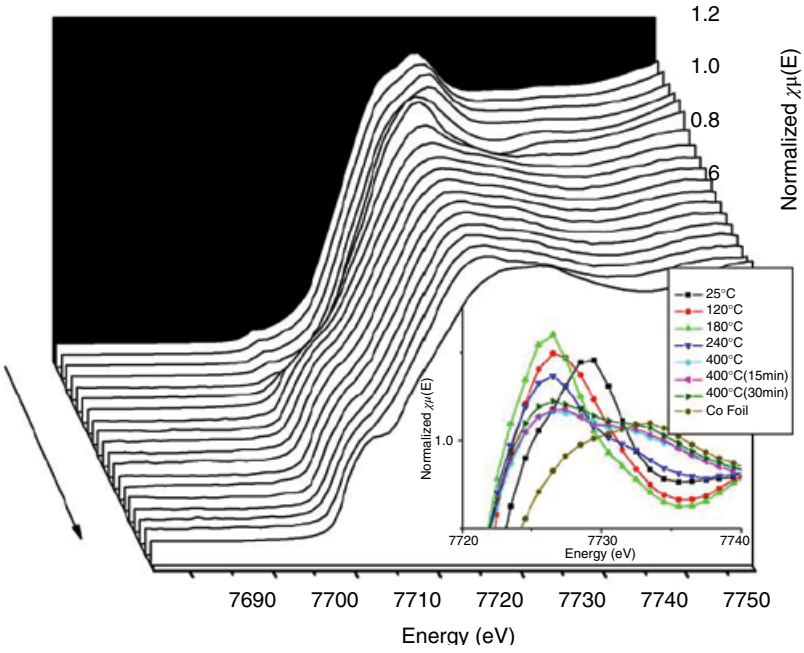

Figure 3.16 Time-resolved Co K-edge XANES spectra of Pt-Co/cSWNT during hydrogen pre-reduction. The cobalt foil was included as the gray dotted curve. Inset: detailed white lines of selected XANES spectra. Reprinted with permission from ref. [49]. Copyright 2009, Elsevier B.V.

Wang et al. reported the synthesis of Pt–Co bimetallic catalyst by a sequential impregnation method[49]. The XAFS experiments were carried out at NSLS of BNL, which indicates that a core–shell structure with Co as the core and a Pt–Co alloy phase as the shell, where Pt was atomically dispersed (see Figure 3.16 for details)[49]. However, the Co may not be fully covered by Pt, and thus Co may also affect the activity and selectivity[49].

Tupy et al. prepared $NiPt/Al_2O_3$ and NiPt/C samples via a wet impregnation method[50]. The XAFS were performed at NSLS of BNL. They verified that the surface of the NiPt catalysts is mainly Pt-terminated in a H_2 environment[50]. Moreover, *in situ* experiments also show that upon reduction of the "spent" catalyst, the Ni segregation can be reversed, resulting in a Pt-enriched surface[50].

Alayoglu et al. reported the synthesis of a bimetallic Co–Cu nanomaterials via thermolysis method, and the *in-situ* XAFS measurements were carried out in Advanced Light Source (ALS) of Argonne National Laboratory (ANL)[51]. In O_2 both metals are significantly oxidized and Cu segregates to the surface in the Cu^+ state. In H_2 this segregation is reversed, with Co coming to the surface; the majority of Co atoms being probed are reduced and Cu is fully reduced[51]. The reduction of Co in the Co–Cu nanoparticles in H_2 notably also occurs at much lower temperatures than were previously identified to be necessary for pure Co nanoparticles[51]. The extent of this reduction may also be dependent on the pressure of H_2, as is shown in the case for pure Co nanoparticles[51]. Accordingly, *in situ* X-ray spectroscopy studies of these Co–Cu nanoparticles in Figure 3.17 were also carried out under reaction conditions for the CO_2/H_2 reaction, which showed that both

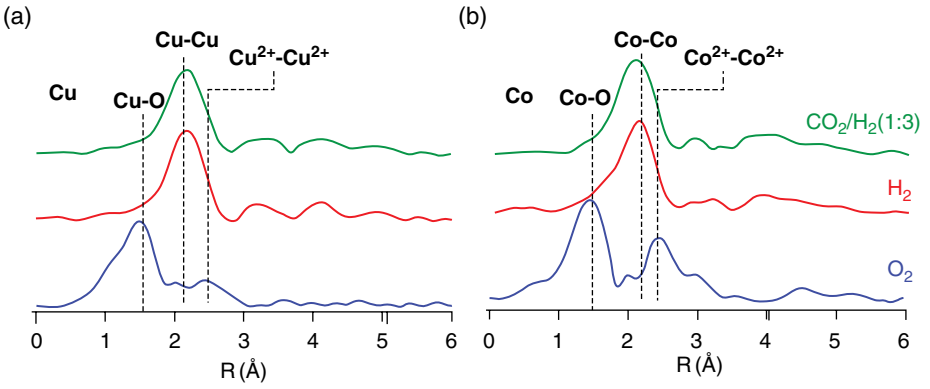

Figure 3.17 k^3-weighted EXAFS oscillations for (a) Co and (b) Cu at 350 °C and under various conditions: 0.02 bar O_2, 0.02 bar H_2, and 1 bar CO_2/H_2 (1:3). Vertical dashed lines indicate Co(Cu) – O, $Co^0(Cu^0)$ – $Co^0(Cu^0)$, and $Co^{2+}(Cu^{2+})$ – $Co^{2+}(Cu^{2+})$ near neighbor shells/distances, respectively. Reprinted with permission from ref. [51]. Copyright 2013, American Chemical Society.

Co and Cu are maintained in a fully reduced oxidation state during the reaction, despite the potential for oxidation by water produced during reaction[51].

Asanova et al. prepared Pd–Ir bimetallic nanoparticles by adding a $Pd[(NH_3)_4](NO_3)_2$ solution into a $K_2[IrCl_6]$ solution[52]. The *in situ* XAFS data on Pd K- and Ir L_{III}-edge were carried out at Pohang Accelerator Laboratory (PAL). The XAFS results verified that the formed Pd- and Ir-rich bimetallic nanoparticles were solid solutions different in shape and composition[52].

Kitla et al. prepared Cu/Ni-CeO_2/ZrO_2 samples via an impregnation method[53]. They collected the XAFS data on Ni K- and Cu K-edges at the Swiss Light Source (SLS). They verified that an alloy between Cu and Ni forms under these conditions and Cu causes a decrease of the reduction temperature of Ni[53]. Furthermore, their research revealed a lower reduction temperature of NiO and CuO in bimetallic alloyed samples as compared to monometallic catalysts[53].

Maclennan et al. first synthesized monometallic nanoparticles by using sodium borohydride as a reducing agent, and the sequential reduction of Pd "shell" onto Au "core" by using ascorbic acid[55]. Pd K- edge and Au L_{III}-edge XAFS measurements (see Figure 3.18 for details) were conducted at APS of ANL. The reduction of Pd(II) occurs quickly for about 4 min, then begins to plateau, and after 8 min the Pd is fully reduced[54]. Kinetic treatment of the data indicates that the reduction of Pd(II) onto the Au surface is a first-order reaction with a rate constant of 0.0468 min^{-1}[54]. It was found that, when using Au(0) nanoparticles in the presence of Pd(II) as the reaction catalyst, the Pd(II) becomes reduced to Pd(0) upon exposure to the crotyl alcohol[54]. In addition, the products from this reaction (*in situ* formed AuPd NPs) were treated with O_2 for up to 3 h, and no significant changes in the spectra or coordination numbers were seen[54].

Ishiguro et al. purchased Pt_3Co/C and Pt_3Ni/C as cathode catalysts, and carried out *in situ* Co/Ni K-edge QXAFS at the SPring-8[55]. They verified that Pt-based bimetallic catalysts had Pt rich surfaces and Pt – Co/Ni bimetallic cores, and the redox reactions during the voltage cycling process took place on the Pt-rich catalyst surfaces for all three catalysts.[55].

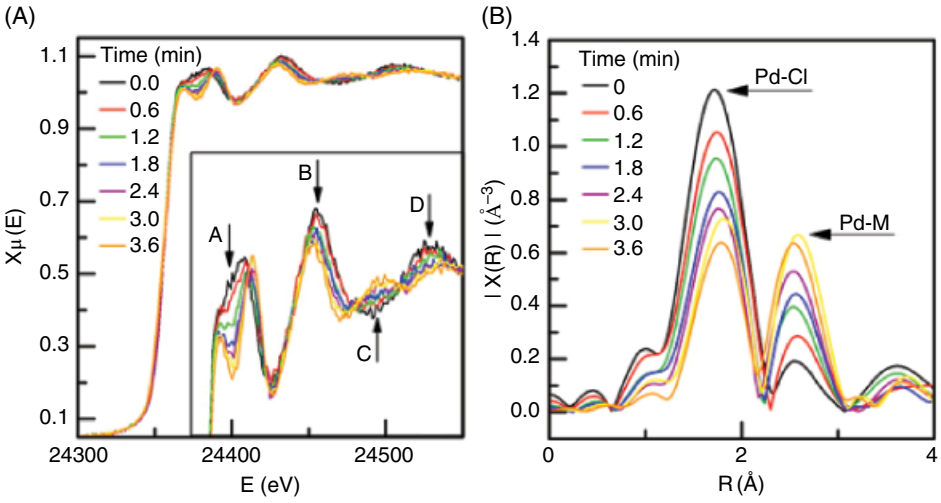

Figure 3.18 Time-resolved Pd K-edge XAFS in (A) E-space with inset of enlarged postedge image and (B) R-space for the nanoparticles formed *in situ* during the oxidation of crotyl alcohol in water. Au:Pd = 1:1, Pd:Substrate = 1:1/2. Reprinted with permission from ref. [54]. Copyright 2013, American Chemical Society.

Sharafudinov et al. prepared $NiGa/SiO_2$ sample via impregnation, and the XAFS measurements were taken at the ESRF[56]. It was demonstrated that supported nanocrystalline intermetallic Ni–Ga particles of the desired phase and composition can be produced by direct reduction of the corresponding nitrates in a flow of hydrogen, which are active and selective toward hydrogenation of CO_2 to methanol[56]. Upon decomposition of nitrates, highly dispersed Ni(II) nanocrystallites serve as centers for further reduction of the nickel and gallium oxides and metallic gallium is incorporated into the nickel crystal lattice to form an intermetallic phase formation of the stoichiometric Ni–Ga compound always proceeds through one or more Ni-rich Ni–Ga phases (see Figure 3.19 for details)[56].

Voronov et al. prepared $Co–Re/Al_2O_3$ via a co-impregnation method[57]. They collected the XAFS data on Re K- and Co K-edges at the ESRF. They verified a local distortion of the Co environment in intimate contact with the Re, which may contribute to the observed increase in catalytic activity for the Re-promoted catalysts compared to the unpromoted Co catalyst[57]. Furthermore, a minor fraction of Re (approx. 15%) remains unreduced in lower oxidation states after a typical reduction procedure for FT synthesis catalysts[57].

Jia et al. prepared $PtCo_3$/HSC and PtCo/HSC via an impregnation method[58]. They carried out the XAFS experiment on Pt L_{III}- and Co K-edges at NSLS of BNL, and verified that their bulk morphologies are retained under the electrochemical acidic environment during reactions[58]. Moreover, these two catalysts possess similar Pt–Pt and Pt–Co bond distances and Pt coordination numbers albeit their dissimilar morphologies, and the similar activity is thus ascribed to the comparable strain, ligand, and particle size effects[58].

Jia et al. purchased Pt_xCo/C and Pt/C catalysts to collect the XAFS data on Pt L_{III}- and Co K-edges at NSLS at BNL[59]. With the help of data-analysis, they claimed that the

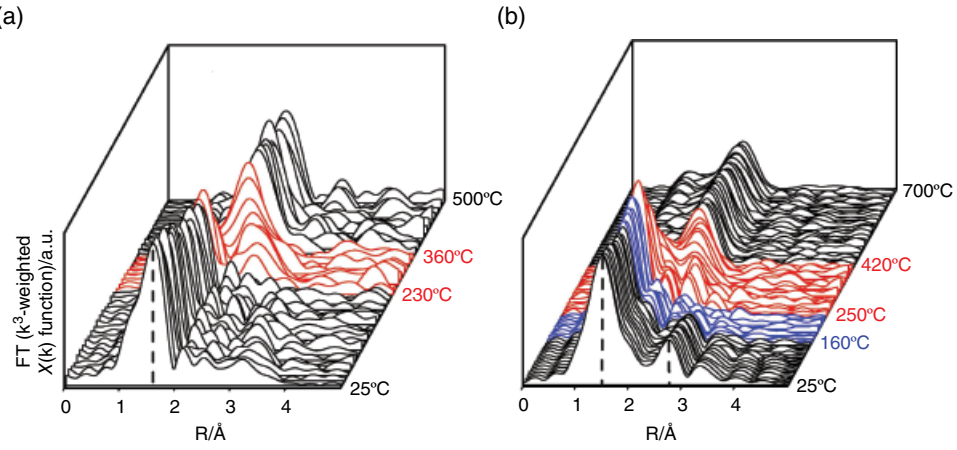

Figure 3.19 Fourier-transformed EXAFS profiles at the (a) Ni K-edge and (b) Ga K-edge during temperature-programmed reduction of metal nitrates to form Ni_5Ga_3/SiO_2. Reprinted with permission from ref. [56]. Copyright (2014), Elsevier B.V.

distance of Pt–Pt contracts linearly with an increase in *in situ* Co/Pt atomic ratio, as expected from Vegard's law[59]. Furthermore, the ORR activity of the Pt_xCo/C and Pt/C nanoparticles is linearly related to their bulk average Pt–Pt bond length[59].

Hong et al. obtained $Co–Ru/SiO_2$ catalysts via an incipient wetness impregnation method, and the Ru K- and Co-K edges QXAFS at the SOLEIL[60]. Time-resolved QXAFS, performed under *in situ* conditions throughout the preparation of co-impregnated $Co–Ru/SiO_2$ systems, give access to the speciation and evolution of ruthenium, used at a low loading as a reduction promoter of supported cobalt nanoparticles (Figure 3.20)[60]. Cobalt reduction is promoted even at a low level of ruthenium doping. Introducing organic additives such as sorbitol in the impregnation solution is shown to be a cheap and convenient way to prevent ruthenium loss in the gas phase, which would be particularly crucial if a very low loading of reduction promoter were used[60].

Wei et al. prepared Pt–Re/C via an impregnation method[61]. They collected the XAFS data on Pt $L_{II,III}$- and Re L_{III}-edges at NSLS of BNL, and verified that the Pt–Re/C catalyst consists of Re/ReO_x-rich surface that slightly modifies the electronic properties of Pt, leading to stronger CO adsorption on the bimetallic catalyst[61].

Simson et al. prepared $PdAu/SiO_2$ samples via an incipient wetness impregnation method[62]. The XAFS data were carried out on Pd K- and Au L_{III}-edges at the DESY. With the help of data-analysis, they claimed that thermal treatment in H_2 – He atmosphere showed a pronounced phase separation toward Pd- and Au-rich phases above 160 °C[62]. Moreover, slow cooling in an inert atmosphere led to the (re)formation of three bimetallic phases—namely, Pd_3Au_1, Pd_1Au_1, and Pd_1Au_3[62].

Scott et al. prepared $Rh–Pd/CeO_2$ via an incipient wetness technique[63]. They collected the XAFS data on Rh K- and Pd K-edges at the SPring-8. They verified that with heating in a CO atmosphere at 100–400 °C, the ceria support and surface noble metal species are strongly reduced, yielding CeO_{2-x} ($x = 0.2–0.3$), Rh^0, and Pd^0[63]. Moreover, surface PdO species are more rapidly reduced with heating at 200–400 °C in CO than surface Rh_2O_3 species[63].

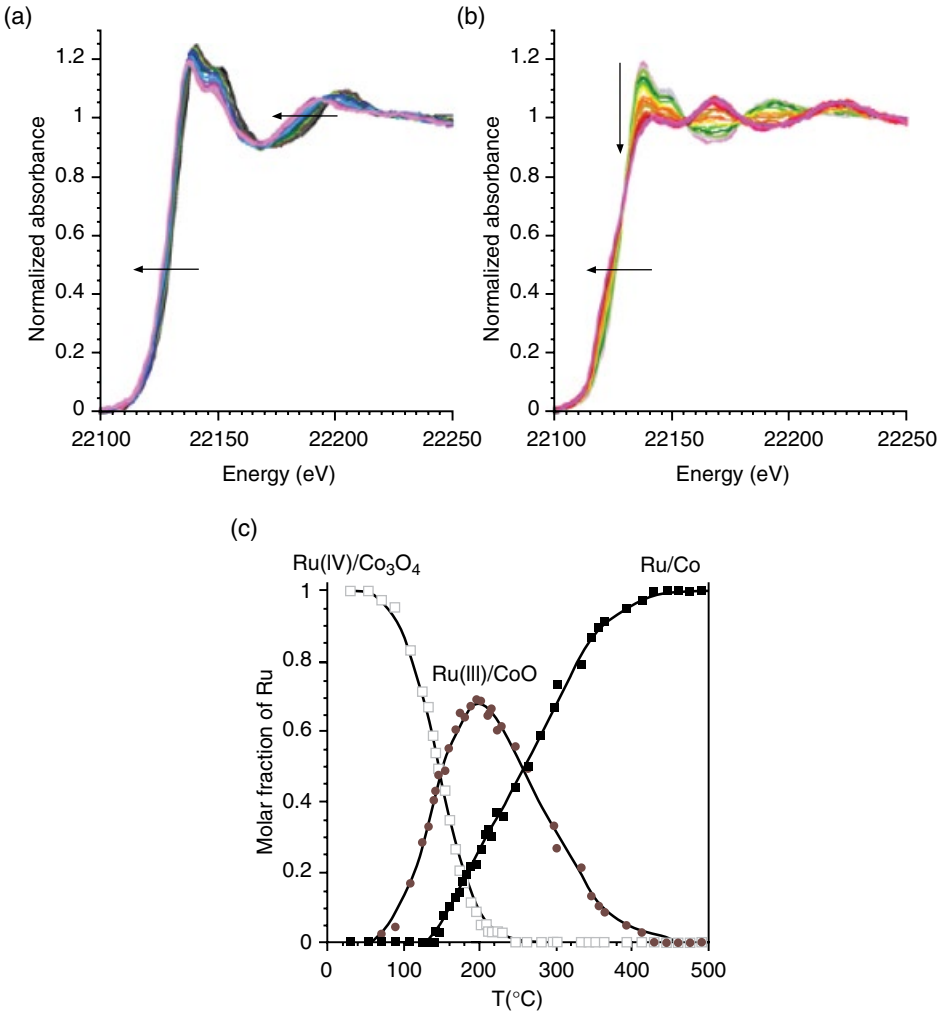

Figure 3.20 Reduction of ruthenium monitored on CoRu-sorb/SiO_2 by in situ Ru K XANES-TPR measurements: (a) between 29 °C and 200 °C; (b) between 200 °C and 500 °C; (c) speciation of the Ru phases as a function of temperature during reduction determined by MCR-ALS analysis. Reprinted with permission from ref. [60]. Copyright (2015), American Chemical Society.

Moraes et al. prepared $NiPt/CeO_2$ samples via a co-impregnation of the support, using aqueous solution of $Ni(NO_3)_2 \cdot 6H_2O$ and H_2PtCl_6[64]. They collected the XAFS data on Ni K- and Pt L_{III}-edges at the Brazilian Synchrotron Light Source (BSLS). The decrease of the intensity of the white line in XANES spectra indicated the progressive reduction of NiO under 5% H_2/He mixture, as temperature was increased to 773 K[64]. Furthermore, Pt segregated toward the surface of the Ni particles and promoted the hydrogenation of highly active carbon species adsorbed at the surface at a higher rate than carbon diffusion into bulk nickel.[64].

Table 3.3 lists the characteristics of the experimental results just described. The key parameters include metal components (Pt–Cu, Pd–Bi, Co–Re, Rh–Pd, etc.), synthetic

Table 3.3 Summary of *in-situ* XAFS characterization on bimetallic nanomaterials.

		***In-situ* conditions**			
Metal	**Synthesis**	***T* (°C)**	**Gas**	**Technique**	**Ref.**
Pt–Rh	ion exchange	300	H_2	EXAFS	35
Pt–Ge	impregnation	25–397	10%H_2/He	XANES, EXAFS	40
Cu–Pd	coprecipitation	RT–380	CO/NO/O_2	XANES, EXAFS	41
Pd–Bi	deposition	62–81	O_2/toluene H_2/ toluene	XANES, EXAFS	44
Pt–Cu	colloidal reduction	RT	N_2H_4	XANES, EXAFS	45
Pt–Ru	impregnation	-123–500	H_2	XANES, EXAFS	36
	impregnation	-83, 400	H_2	EXAFS	38
	colloidal reduction	RT–300	5%H_2/He	XANES, EXAFS	46
	coprecipitation	160	EG solution	XANES, EXAFS	47
Ni–Pd	co-impregnation sequential impregnation	40–490	5%H_2/Ar	EXAFS	48
Cu–Co	coprecipitation	350	O_2 H_2 CO_2/H_2	EXAFS	51
Pd–Ir	coprecipitation	RT–180	N_2	EXAFS	52
Cu–Ni	impregnation	27–387	5%H_2/He	XANES, EXAFS	53
Ni–Ga	impregnation	25–700	90%H_2/He	EXAFS	56
Co–Re	co-impregnation	RT–450	5%H_2/He	EXAFS	39
	co-impregnation	400	100%H_2	EXAFS	57
Co–Ru	ion exchange	300,400	H_2, He	XANES, EXAFS	43
	impregnation	29–200 200–500	5%H_2/He	XANES, EXAFS	60
Co–Pt	impregnation	RT,400	Air,N_2,H_2	XANES, EXAFS	42
	impregnation	400	100%H_2	XANES	49
	from company	RT	N_2	XANES, EXAFS	59
	impregnation	RT	N_2	XANES, EXAFS	58
	from company	80	N_2	XANES, EXAFS	55
Pt–Re	impregnation	450,530	H_2	EXAFS	34
	impregnation	225	100%H_2 3%H_2O/He 3%CO/He	XANES, EXAFS	61
Au–Pd	deposition precipitation	-173	H_2	XANES, EXAFS	37
	impregnation	315	He	XANES, EXAFS	62
	reduction	21	20%O_2/He	XANES, EXAFS	54
Rh–Pd	impregnation	100–400	CO	XANES, EXAFS	63
Ni–Pt	impregnation	225	EG solution	XANES, EXAFS	50
	co-impregnation	300–500	5%H_2/He	XANES, EXAFS	64
	from company	80	N_2	XANES, EXAFS	55

approaches (incipient wetness impregnation, coprecipitation, colloidal reduction, ion exchange, etc.), *in situ* techniques of XANES and/or EXAFS, temperature range (from liquid nitrogen to ca. 500°C), and gases (CO, NO, H_2, O_2, etc.). It could be the most broad application to characterize bimetallic nanostructures, and can provide specific information on electronic structure and short-range coordination structure of studied metals.

3.5 Conclusions and Outlook

The *in situ* characterization of bimetallic nanocrystals, especially from the view of structural evolution, has been rapidly improved recently. Besides the regular approaches (e.g., XRD and XPS), the elementally sensitive techniques have significantly contributed to distinguishing the effects of two different metals during the investigation of bimetallic nanocrystals. Among them, electron microscopy, infrared spectroscopy, and X-ray absorption fine structure have specific characteristics to detect microscopic/macroscopic, bulk/surface and electronic/geometric structures of each component in measured samples.

Electron microscopy, with the help of aberration-corrected technique, provided direct observations on morphology, shape and size of bimetallic nanocrystals at the atomic scale. On the other hand, aberration-corrected STEM with EDS detected the elemental distribution of each metal inside a nanostructure. Furthermore, images with SAED skills determined the crystal phase of bimetallic nanocrystals. More importantly, the above characterization approaches have been successfully applied to multiple environmental status such as high/low temperatures and various gas compositions. This development allows us to monitor the changes of structure (crystal shape and size, internal structure within one nanoparticle, etc.) under working or semi-operando conditions and further correlate the performance of bimetallic nanocrystals to their structural evolutions on the basis of *in situ* experimental data.

Infrared spectroscopy, including FTIR and DRIFTS, detected the interaction between surface of bimetallic nanocrystals and the surrounding circumstances. Since it has nearly zero damage on the investigated samples during measurements, *in situ* infrared techniques were attractive to a number of researchers. Evolutions on surface structure such as adsorbents, intermediates, chemical bond between metal and gases molecules, were finely monitored during synthesis or catalytic tests. Meanwhile, *in situ* FTIR/DRIFTS really distinguished specific structure of each metal in bimetallic nanocrystals. Therefore, *in situ* infrared techniques can help us to deeply understand the formation mechanisms and reaction pathways under different atmospheres.

Probably, the most useful characterization for bimetallic nanocrystals is XAFS, which belongs to elementally sensitive technique and showed ability of identifying both electronic structure (XANES) and local coordination structure (EXAFS) of each metal in the studied samples. With the help of appropriate data-analysis and profile simulation, researchers obtained crucial parameters, including distance and coordination number between two metals, Debye-Waller factor for each type of atoms, and valence or oxidation state of different elements for bimetallic nanocrystals. More importantly, hard X-ray is pretty penetrative to metallic solids and suitable for carrying out *in situ* measurements, if irradiation damage can be minimized. Thus, the application of *in situ* XAFS technique dramatically expanded our scope to study the "structure–function" relationship for bimetallic nanomaterials.

Although the big step has been made for *in situ* characterization, more wide ranges for various circumstances (e.g., temperature, pressure, and atmosphere) should be built to probe the nature of structural evolutions on bimetallic nanocrystals in catalysis and other fields. Examples could include rapid heating to high temperature (>1500°C) with minutes or even seconds, or a high-pressure (>10 MPa) reaction with high concentrations of combustion or toxic gases (H_2, CO, etc.). To realize these targets, advanced synchrotron radiation facility, which can provide X-ray with extremely high flux ($\times 10^6$ better than lab-based instrument) and time-resolve ability (seconds to milliseconds), is quite promising. With synchrotron radiation, infrared skills have been also well developed and more new techniques have appeared recently. Last but not least, ETEM, a brand-new concept, will continue to expand our detection limits in the near future.

3.6 References

1 Kuwano, N., Chiwata, N., Oki, K. (1999). *In situ* TEM Observation of long range ordering via short range order in Cu_3Pt. *Bulletin of Materials Science*, 22(3), 697–700.

2 Ramirez, A. G., Ni, H., Lee, H.-J. (2006). Crystallization of amorphous sputtered NiTi thin films. *Materials Science and Engineering A*, 438–440, 703–709.

3 Li, P., Liu, J., Nag, N., Crozier, P. A. (2006). *In situ* synthesis and characterization of Ru promoted Co/Al_2O_3 Fischer–Tropsch catalysts, *Applied Catalysis A*, 307, 212–221.

4 Kröger, A., Wernhardt, R., Somsen, C., Eggeler, G., Wieck, A. (2006). *In situ* transmission electron microscopy-investigations on the strain-induced B19'-phase in NiTi shape memory alloys structured by focused ion beam. *Materials Science and Engineering A*, 438–440, 513–516.

5 Li, P.-Y., Lu, H.-M., Tang, S.-C., Meng, X.-K. (2009). An *in-situ* TEM investigation on microstructure evolution of Ni-25 at.% Al thin films. *Journal Alloys and Compounds*, 478, 240–245.

6 In, J., Yoo, Y., Kim, J., Seo, K., Kim, H., Ihee, H., Oh, S. H., Kim, B. (2010). *In Situ* TEM observation of heterogeneous phase transition of a constrained single-crystalline Ag_2Te nanowire. *Nano Letters,* 10, 4501–4504.

7 Khan, P. Y., Bhattacharya, V., Biswas, K., Chattopadhyay, K. (2013). Melting and solidification behavior of Pb–Sn embedded alloy nano-particles. *Journal Nanoparticle Research*, 15, 2049.

8 Biswas, S., O'Regan, C., Petkov, N., Morris, M. A., Holmes, J. D. (2013). Manipulating the growth kinetics of vapor – liquid – solid propagated Ge nanowires. *Nano Letters,* 13, 4044–4052.

9 Jungjohann, K. L., Bliznakov, S., Sutter, P. W., Stach, E. A., Sutter, E. A. (2013). *In situ* liquid cell electron microscopy of the solution growth of Au – Pd core – shell nanostructures. *Nano Letters,* 13, 2964–2970.

10 Tang, W., Picraux, S. T., Huang, J. Y., Liu, X. H., Tu, K. N., Dayeh, S. A. (2013). Gold catalyzed nickel disilicide formation: a new solid – liquid – solid phase growth mechanism. *Nano Letters,* 13, 6009–6015.

11 Li, H. X., Maoa, S. C., Zang, K. T., Liu, Y., Guo, Z. X., Wang, S. B., Zhang, Y. F., Yin, X. Q. (2014). An *in situ* TEM study of the size effect on the thermally induced martensitic transformation in nanoscale NiTi shape memory alloy. *Journal Alloys and Compounds,* 588, 337–342.

12 Gontard, L. C., Dunin-Borkowski, R. E., Fernández, A., Ozkaya, D., Tomographic, T. K. (2014). Heating holder for *in situ* TEM: study of Pt/C and $PtPd/Al_2O_3$ catalysts as a function of temperature. *Microscopy and Microanalysis*, 20, 982–990.

13 Xin, H. L., Alayoglu, S., Tao, R., Genc, A., Wang, C.-M., Kovarik, L., Stach, E. A., Wang, L.-W., Salmeron, M., Somorjai, G. A., Zheng, H. M. (2014). Revealing the atomic restructuring of Pt – Co nanoparticles. *Nano Letters,* 14, 3203–3207.

14 Wang, C.-M., Schreiber, D. K., Olszta, M. J., Baer, D. R., Bruemmer, S. M. (2015). Direct *In situ* TEM observation of modification of oxidation by the injected vacancies for Ni–4Al alloy using a microfabricated nanopost. *ACS Applied Material & Interfaces*, 7, 17272–17277.

15 Wu, J. B., Gao, W. P., Wen, J. G., Miller, D. J., Lu, P., Zuo, J.-M., Yang, H. (2015). Growth of Au on Pt icosahedral nanoparticles revealed by low-dose *in situ* TEM. *Nano Letters,* 15, 2711–2715.

16 Luo, L. L., Zou, L. F., Schreiber, D. K., Baer, D. R., Bruemmer, S. M., Zhou, G. W., Wang, C.-M. (2016). *In-situ* transmission electron microscopy study of surface oxidation for Ni–10Cr and Ni–20Cr alloys. *Scripta Materialia,* 114, 129–132.

17 Anton, R. (2009). *In Situ* TEM investigations of reactions of Ni, Fe and Fe–Ni alloy particles and their oxides with amorphous carbon. *Carbon*, 47, 856–865.

18 Pan, Y.-T., Wu, J. B., Yin, X., Yang, H. (2016). *In Situ* ETEM study of composition redistribution in Pt-Ni octahedral catalysts for electrochemical reduction of oxygen. *AIChE Journal*, 62(2), 399–407.

19 Jiang, Y., Li, H. B., Wu, Z. M., Ye, W. Y., Zhang, H., Wang, Y., Sun, C. H., Zhang, Z. (2016). *In situ* observation of hydrogen-induced surface faceting for palladium–copper nanocrystals at atmospheric pressure. *Angewandte Chemie*, 128, 12615–12618.

20 Anumol, E. A., Nethravathi, C., Ravishankar, N. (2013). Mechanistic insights into a non-classical diffusion pathway for the formation of hollow intermetallics: a route to multicomponent hollow structures. *Particle & Particle Systems Characterization*, 30, 590–598.

21 Cimino, S., Lisi, L., Russo, G., Torbati, R. (2010). Effect of partial substitution of Rh catalysts with Pt or Pd during the partial oxidation of methane in the presence of sulphur. *Catalysis Today*, 154, 283–292.

22 Li, J., Wu, G. J., Guan, N. J., Li, L. D. (2012). NO selective reduction by hydrogen over bimetallic Pd–Ir/TiO_2 catalyst. *Catalysis Communications*, 24, 38–43.

23 Sandoval, A., Delannoy, L., Méthivier, C., Louis, C., Zanella, R. (2015). Synergetic effect in bimetallic Au–Ag/TiO_2 catalysts for CO oxidation: new insights from *in situ* characterization. *Applied Catalysis A*, 504, 287–294.

24 Auvray, X., Olsson, L. (2015). Stability and activity of Pd-, Pt- and Pd-Pt catalysts supported on alumina for NO oxidation. *Applied Catalysis B*, 168, 342–352.

25 Whiting, G. T., Kondrat, S. A., Hammond, C., Dimitratos, N., He, Q., Morgan, D. J., Dummer, N. F., Bartley, J. K., Kiely, C. J., Taylor, S. H., Hutchings, G. J. (2015). Methyl formate formation from methanol oxidation using supported gold – palladium nanoparticles. *ACS Catalysis*, 5, 637–644.

26 Sun, K. Y., Wilson, A. R., Thompson, S. T., Lamb, H. H. (2015). Catalytic deoxygenation of octanoic acid over supported palladium: effects of particle size and alloying with gold. *ACS Catalysis*, 5, 1939–1948.

27 Najafishirtari, S., Brescia, R., Guardia, P., Marras, S., Manna, L., Colombo, M. (2015). Nanoscale transformations of alumina-supported AuCu ordered phase nanocrystals and their activity in CO oxidation. *ACS Catalysis*, 5, 2154–2163.

28 Moscu, A., Veyre, L., Thieuleux, C., Meunier, F., Schuurman, Y. (2015). CO PROX over Pt–Sn/Al_2O_3: a combined kinetic and *in situ* DRIFTS study. *Catalysis Today*, 258, 241–246.

29 Gibson, E. K., Beale, A. M., Catlow, C. R. A., Chutia, A., Gianolio, D., Gould, A., Kroner, A., Mohammed, K. M. H., Perdjon, M., Rogers, S. M., Wells, P. P. (2015). Restructuring of AuPd nanoparticles studied by a combined XAFS/DRIFTS approach. *Chemistry of Materials*, 27, 3714–3720.

30 Singh, S. A., Madras, G. (2016). Sonochemical synthesis of Pt, Ru doped TiO_2 for methane reforming. *Applied Catalysis A*, 518, 102–114.

31 Ang, M. L., Miller, J. T., Cui, Y., Mo, L., Kawi, S. (2016). Bimetallic Ni–Cu alloy nanoparticles supported on silica for the water-gas shift reaction: activating surface hydroxyls via enhanced CO adsorption. *Catalysis Science & Technology*, 6, 3394–3409.

32 Aguirre, A., Barrios, C. E., Aguilar-Tapia, A., Zanella, R., Baltanás, M. A., Collins, S. E. (2016). *In-situ* DRIFT study of Au–Ir/Ceria catalysts: activity and stability for CO oxidation. *Topics in Catalysis*, 59, 347–356.

33 Su, J. J., Zhang, Z. P., Fu, D. L., Liu, D., Xu, X.-C., Shi, B. F., Wang, X., Si, R., Jiang, Z., Xu, J., Han, Y.-F. (2016). Higher alcohols synthesis from syngas over CoCu/SiO_2 catalysts: dynamic structure and the role of Cu. *Journal of Catalysis*, 336, 94–106.

34 Bensaddik, A., Caballero, A., Bazin, D., Dexpert, H., Didillon, B., Lynch, J. (1997). *In situ* study by XAS of the sulfidation of industrial catalysts: the Pt and PtRe/Al_2O_3 systems. *Applied Catalysis A*, 162, 171–180.

35 Cimini, F., Prins, R. (1997). QEXAFS investigation of the particle growth of PtRh cluster supported on NaY. *Journal of Physical Chemistry B*, 101, 5277–5284.

36 Nashner, M. S., Frenkel, A. I., Somerville, D., Hills, C. W., Shapley, J. R., Nuzzo, R. G. (1998). Core shell inversion during nucleation and growth of bimetallic Pt/Ru nanoparticles. *Journal of American Chemistry Society*, 120, 8093–8101.

37 Reifsnyder, S. N., Lamb, H. H. (1999). Characterization of silica-supported Pd-Au clusters by X-ray absorption spectroscopy. *Journal of Physical Chemistry B*, 103, 321–329.

38 Hills, C. W., Nashner, M. S., Frenkel, A. I., Shapley, J. R., Nuzzo, R. G. (1999). Carbon support effects on bimetallic Pt-Ru nanoparticles formed from molecular precursors. *Langmuir*, 15, 690–700.

39 Ronning, M., Nicholson, D. G., Holmen, A. (2001). *In situ* EXAFS study of the bimetallic interaction in a rhenium-promoted alumina-supported cobalt ficher-tropsch catalyst. *Catalysis Letters*, 72(3–4), 141–146.

40 Fiddy, S. G., Newton, M. A., Campbell, T., Corker, J. M., Dent, A. J., Harvey, I., Salvini, G., Turin, S., Evans, J. (2001). *In situ*, time resolved, and simultaneous multi-edge determination of local order change during reduction of supported bimetallic (Pt-Ge). Catalyst precursors using energy dispersive EXAFS. *Chemical Communications*, 445–446.

41 Hungria, A. B., Iglesias-Juez, A., Martinez-Arias, A., Fernandez-Garcia, M., Anderson, J. A., Conesa, J. C., Soria, J. (2002). Effects of cobalt on the catalytic properties of bimetallic Pd-Cu/(Ce,Zr)O_x/Al_2O_3 and Pd-Cu/(Ce,Zr)O_x catalysts for CO and NO elimination. *Journal of Catalysis*, 206, 281–294.

42 Guczi, L., Bazin, D., Kovacs, I., Borko, L., Schay, Z., Lynch, J., Parent, P., Lafon, C., Stefler, G., Koppany, Z., Sajo, I. (2002). Structure of Pt-Co/Al_2O_3 and Pt-Co/NaY bimetallic catalysts: characterization by in situ EXAFS, TPR, XPS and by activity in Co (carbon monoxide). hydrogenation. *Topics in Catalysis*, 20, 129–139.

43 Bazin, D., Kovacs, I., Lynch, J., Guczi, L. (2003). Ru-Co/NaY Bimetallic Catalysts: *In situ* EXAFS study at Co K and Ru K absorption edges. *Applied Catalysis A*, 242, 179–186.

44 Keresszegi, C., Grunwaldt, J. D., Mallat, T., Baiker, A. (2004). *In situ* EXAFS Study on the oxidation state of Pd/Al_2O_3 and $Bi\text{-}Pd/Al_2O_3$ during the liquid-phase oxidation of 1-phenylethanol. *Journal of Catalysis*, 222, 268–280.

45 Hwang, B. J., Tsai, Y. W., Sarma, L. S., Tseng, Y. L., Liu, D. G., Lee, J. F. (2004). Genesis of bimetallic Pt-Cu cluster in reverse micelles investigated by *in situ* X-ray absorption spectroscopy. *Journal of Physical Chemistry B*, 108, 20427–20434.

46 Hwang, B. J., Chen, C. H., Sarma, L. S., Chen, J. M., Wang, G. R., Tang, M. T., Liu, D. G., Lee, J. F. (2006). Probing the formation mechanism and chemical states of carbon-supported Pt-Ru nanoparticles by *in situ* X-ray absorption spectroscopy. *Journal of Physical Chemistry B*, 110, 6475–6482.

47 Sarma, L. S., Chen, C. H., Kumar, S. M. S., Wang, G. R., Yen, S. C., Liu, D. G., Sheu, H. S., Yu, K. L., Tang, M. T., Lee, J. F., Bock, C., Chen, K. H., Hwang, B. J. (2007). Formation of Pt-Ru nanoparticles in ethylene glycol solution: an *in situ* X-ray absorption spectroscopy study. *Langmuir*, 23, 5802–5809.

48 Mukainakano, Y., Yoshida, K., Okumura, K., Kunimori, K., Tomishige, K. (2008). Catalytic performance and QXAFS analysis of Ni catalysts modified with Pd for oxidative steam reforming of methane. *Catalysis Today*, 132, 101–108.

49 Wang, X. M., Li, N., Pfefferle, L. D., Haller, G. L. (2009). Pt-Co bimetallic ctalyst supported on single walled carbon nanotube: XAS and aqueous phase reforming activity studies. *Catalysis Today*, 146, 160–165.

50 Tupy, S. A., Karim, A. M., Bagia, C., Deng, W., Huang, Y. L., Vlachos, D. G., Chen, J. G. (2012). Correlating ethylene glycol reforming activity with *in situ* EXAFS detection of Ni segregation in supported NiPt bimetallic catalysts. *ACS Catalysis*, 2, 2290–2296.

51 Alayoglu, S., Beaumont, S. K., Melaet, G., Lindeman, A. E., Musselwhite, N., Brools, C. J., Marcus, M. A., Guo, J., Liu, Z., Kruse, N., Somorjai, G. A. (2013). Surface, composition changes of redox stabilized bimetallic CoCu nanoparticles supported on silica under H_2 and O_2 atmospheres and during reaction between CO_2 and H_2: *in situ* X-ray spectroscopy characterization. *Journal of Physical Chemistry C*, 117, 21803–21809.

52 Asanova, T. I., Asanov, I. P., Kim, M. G., Gerasimov, E. Y., Zadesenets, A. V., Plyusnin, P. E., Korenev, S. V. (2013). On formation mechanism of Pd-Ir bimetallic nanoparticles through thermal decomposition of $[Pd(NH_3)_4][IrCl_6]$. *Journal of Nanoparticle Research*, 15, 1994–2009.

53 Kitla, A., O. Safonova, V., Fottinger, K. (2013). Infrared studies on bimetallic copper/nickel catalysts supported on zirconia and ceria/zirconia. *Catalysis Letters*, 143, 517–530.

54 Maclennan, A., Banerjee, A., Hu, Y. F., Miller, J. T., Scott, R. W. J. (2013). *In Situ* X-ray absorption spectroscopic analysis of gold-palladium bimetallic nanoparticle catalysts. *ACS Catalysis*, 3, 1411–1419.

55 Ishiguro, N., Kityakarn, S., Sekizawa, O., Uruga, T., Sasabe, T., Nagasawa, K., Yokoyama, T., Tada, M. (2014). Rate enhancements in structural transformations of Pt-Co and Pt-Ni bimetallic cathode catalysts in polymer electrolyte fuel cells studied by *in situ* time-resolved X-ray absorption fine structure. *Journal of Physical Chemistry C*, 118, 15874–15883.

56 Sharafudinov, I., Elkjaer, C. F., Carvalho, H. W. P. D., Gardini, D., Chiarello, G. L., Damsgaard, C. D., Wagner, J. B., Grunwaldt, J. D., Dahl, S., Chorkendorff, I. (2014). Intermetallic compounds of Ni and Ga as catalysts for the synthesis of methanol. *Journal of Catalysis*, 320, 77–88.

57 Voronov, A., Tsakoumis, N. E., Hammer, N., Beek, W. V., Emerich, H., Ronning, M. (2014). The state and location of Re in Co-Re/Al_2O_3 catalysts during Ficcher-Tropsch synthesis: exploring high-energy XAFS for *in situ* catalysts characterisation. *Catalysis Today*, 229, 23–33.

58 Jia, Q. Y., Caldwell, K., Strickland, K., Ziegelbauer, J. M., Yu, Z. Q., Ramaker, D. E., Mukerjee, S. (2015). Improved oxygen reduction activity and durability of dealloyed $PtCo_x$ catalysts for proton exchange membrane fuel cells: strain, ligand, and particle size effects. *ACS Catalysis*, 5, 176–186.

59 Jia, Q. Y., Liang, W. T., Bates, M. K., Mani, P., Lee, W., Mukerjee, S. (2015). Activity descriptor identification for oxygen reduction on platinum-based bimetallic nanoparticles: *in situ* observation of the linear composition-strain-activity. *ACS Nano*, 9(1), 387–400.

60 Hong, J. P., Marceau, E., Khodakov, A. Y., Gaberova, L., Griboval-Constant, A., Girardon, J. S., Fontaine, C. L., Briois, V. (2015). Speciation of ruthenium as a reduction promoter of silica-supported Co catalysts: a time-resolved *in situ* AXS investigation. *ACS Catalysis*, 5, 1273–1282.

61 Wei, Z. H., Karim, A. M., Li, Y., King, D. L., Wang, Y. (2015). Elucidation of the roles of Re in steam reforming of glycerol over Pt-Re/C catalysts. *Journal of Catalysis*, 322, 49–59.

62 Simson, S., Jentys, A., Lercher, J. A. (2015). Dynamic phase separation in supported Pd-Au catalysts. *Journal of Physical Chemistry C*, 119, 2471–2482.

63 Scott, M. S., Waterhouse, G. I. N., Kato, K., Chang, S. L. Y., Idriss, H., Sohnel, T. (2015). Structural analysis of Rh-Pd/CeO_2 catalysts under reductive conditions: an X-ray investigation. *Topics in Catalysis*, 58, 123–133.

64 Moraes, T. S., Neto, R. C. R., Ribeiro, M. C., Mattos, L. V., Kourtelesis, M., Ladas, S., Verykios, X., Noronha, F. B. (2016). Ethanol conversion at low temperature over CeO_2-supported Ni-based catalysts effect of Pt addition to Ni catalyst. *Applied Catalysis B*, 181, 754–768.

Part II

Synthesis, Characterization, and Properties of Shape-Controlled Bimetallic Nanostructures

4

Bimetallic Nanopolyhedrons and Nanospheres

Lin-Xiu Dai and Ya-Wen Zhang

College of Chemistry and Molecular Engineering, Peking University, Beijing, China

4.1 Introduction

Bimetallic nanocrystals have been attracting tremendous attention in recent years, and are widely investigated in heterogeneous catalysis, low-temperature fuel cells and other technological applications[1–15]. Compared with monometallic nanocrystals, bimetallic nanocrystals are more economic, efficient, and adjustable. In particular, minimizing the usage of noble metals in bimetallic nanocrystals is very critical to their scale-up industrial utilization. Generally, there are a lot of possibilities to improve the catalytic performance of bimetallic nanocrystals by tuning the shape, composition, crystalline phase, lattice strain, and surface element distribution of two distinct metals. In addition, two or more metals are often required to simultaneously or sequentially handle different elementary reaction steps in a heterogeneous catalytic reaction. The overall physicochemical properties of bimetallic nanocrystals often surpass the simple overlapping of individual character of two distinct metals under optimized atomic arrangement and surface structure. Hence, shape-controlled synthesis of bimetallic nanocrystals is significant for their enhanced catalytic performances and corresponding technological applications.

In principle, the size of a nanocrystal determines the surface-to-bulk atomic ratio and the proportion of atom types (e.g., vertex, terrace, and step), while the shape governs the types of facets on its surface and thus the arrangement of surface atoms[16–20]. Metal nanocrystals with different shapes expose corresponding facets {*hkl*}, which typically have certain atomic arrangements on their surface layers. For example, metal nanocrystals in cube shape expose {100} facet, while octahedral nanocrystals present {111} facet. Varying the facets of the nanocrystals can generate abundant geometrical and electronic structures, which tend to show significant differences in catalytic activity and selectivity[21, 22]. Therefore, shape-controlled synthesis of bimetallic nanocrystals has more potential to improve the performance of metal nanocrystals for practical

Bimetallic Nanostructures: Shape-Controlled Synthesis for Catalysis, Plasmonics, and Sensing Applications, First Edition. Edited by Ya-Wen Zhang.
© 2018 John Wiley & Sons Ltd. Published 2018 by John Wiley & Sons Ltd.

applications, although it is very difficult to transform monometallic to bimetallic nanocrystals by controlling their composition and the shape.

The mixing of two metals (M and N) is related to several factors, including lattice parameters, bonding energy, and surface energy. In addition, kinetic factors should be considered in conjunction with thermodynamics to define the atomic arrangements and the shape of the bimetallic nanocrystals. Coreduction, thermal decomposition, seed-mediated growth, and galvanic replacement are common colloidal synthetic approaches for controlled synthesis of metal nanocrystals. In this chapter, we firstly describe the classification of the architecture of bimetallic nanospheres and nanopolydrons, and then elaborate the general nucleation and growth mechanism of metal nanocrystals. Next, we will discuss four key factors that govern the synthesis of bimetallic nanocrystals with polyhedral and spherical shapes in above four synthetic routes: (1) redox potentials; (2) reduction rates; (3) lattice mismatch; and (4) facet-specific capping agent effects. Finally, we will review real synthetic cases to demonstrate how to construct different bimetallic nanoployhedrons with such architectures. Moreover, polyhedral-shape-correlated structure sensitivity in some important catalytic reactions will be illustrated. The objective of this chapter is to summarize the key factors and synthetic strategies in preparing nanopolyhedrons and nanospheres of bimetallic nanocrystals, which contributes to realizing the designed synthesis of bimetallic nanocrystals with target shape and facets exposed.

4.2 Architecture of Bimetallic Nanospheres and Nanopolyhedrons

Generally, the architecture of bimetallic nanospheres and nanopolydrons can be classified into two main categories namely alloy and core–shell structures, the alloy structure includes intermetallic compound and solid solution according to the distributions of two component elements and atomic ordering (Figure 4.1). An intermetallic compound consists of well-defined stoichiometry with strictly ordered atomic arrangement. In contrast, solid solution allows random mix of two metals in the lattices. Core–shell structures can be disparate atomic arrangements on the sides of interface corresponding to different metals. Even though these three kinds of architectures have the same composition and atomic ratio, their performance may greatly differ. In the following,

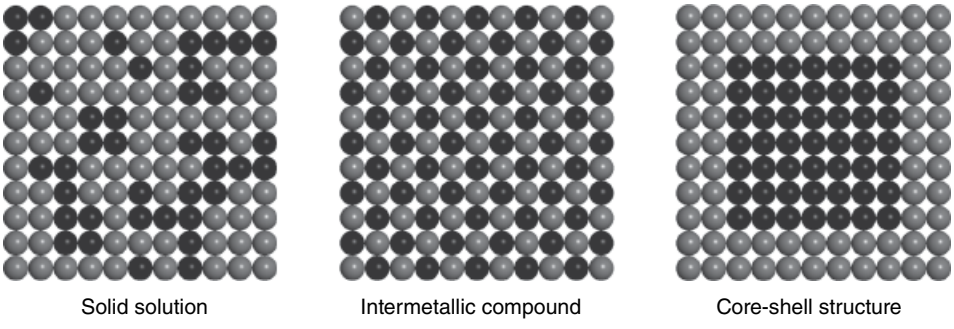

Figure 4.1 Classification of bimetallic nanocrystals according to their element distributions.

some cases about the synthesis of intermetallic compounds, solid solution, and core–shell nanocrystals of bimetallics in spherical and polyhedral shapes will be shown on how to make use of the intrinsic nature of two metals and extrinsic environments that we can control during the synthetic protocols.

4.2.1 Solid Solution

Solid solution is one of the most common bimetallic nanostructures with disordered atomic arrangements. The formation of solid solution requires stronger bonding between two metals (M and N) than that of M–M and N–N, similar lattice parameters and surface energy in thermodynamics. However, some kinetic factors such as reduction rate and diffusion rate can break down the above general rules and induce the formation of the nonequilibrium phase. Now, coreduction and thermal decomposition are the most commonly used methods to synthesize M–N nanocrystals of solid solutions (see section 4.5). Both routes work effectively on adjusting the ratio of M to N in the bimetallic nanocrystals, but it is difficult to control the M/N ratio of the bimetallic nanocrystals in specific shape.

4.2.2 Intermetallic Compounds

For some bimetallics, two metals tend to form a new crystalline structure with well-defined stoichiometry, in which constituent atoms are strictly arranged such as PtFe (face-centered tetragonal, P4/mmm), Pt_3Ti, PtPb, PtBi, and $PtCu_3$[23–26]. Thermodynamically, the change in Gibbs free energy upon mixing (ΔG_{mix}) under a given set of experimental conditions will determine the final atom positions and order in a bimetallic system. The more negative the ΔG_{mix} is, the more miscible the two metal atoms are. However, most cases show the difficulties to obtain intermetallic compounds by one-step method, which are likely to produce alloys with disordered atomic ordering. Therefore, further post-treatment in high temperature together with inert atmosphere is needed to transform alloys to intermetallic compound[27]. The advantages of intermetallic compounds over alloys are the improved catalytic and magnetic properties, which depend on the more precise control of composition and surface structure. Kang et al. first reported the synthesis of highly monodisperse Pt_3Zn nanocrystals toward methanol oxidation (MOR)[28]. Pt–Zn nanospheres and nanocubes were synthesized, the latter appear in the presence of benzyl ether. Reaction temperature is the key to the incorporation of Zn into Pt, even in the absence of a strong reducing agent. The Pt–Zn alloy phase can be transformed into the Pt_3Zn intermetallic phase through post-annealing. The intermetallic Pt_3Zn shows better MOR performance and poisoning tolerance than the alloy phase. Vicente et al. investigated the structure-dependent catalytic properties of the Pd–Sn system for selective citral hydrogenation[29]. Pd shows little selectivity for such a reaction, but the addition of Sn significantly increases the selectivity toward unsaturated alcohols. The improved selectivity is attributed to the formation of the Pd_3Sn intermetallic phase, which modifies both the geometric and the electronic properties of the Pd sites, favoring the formation of new sites for the selective citral hydrogenation. In terms of magnetism, intermetallic compounds composed of one 3d metal (e.g., Fe, Co, Ni) and other 4d or 5d metal (e.g., Pd, Pt) have been identified as good magnetic nanomaterials for future information storage. Some Sn-based

intermetallic nanocrystals (e.g., Fe–Sn, Co–Sn, and Fe–Co–Sn) with low 3d metal concentration also possess enhanced capacity as an anode in Li ion batteries[30, 31].

4.2.3 Core–Shell Nanocrystals

The synthesis of core–shell nanocrystals has drawn tremendous attention because of their enhanced performances through electronic coupling and strain effect, good physicochemical stability as well as serving as transition state for the formation of other nanostructures. A core–shell nanocrystal is comprised of inner core (metal M) and a shell made of another metal (N), typically denoted by M@N. The seed-mediated approach is commonly used to prepare core–shell nanocrystals. Metal M is often preferentially reduced to act as seeds or templates, metal N will take it as the heterogeneous nucleation sites to grow through chemical reduction, thermal decomposition or transmetalation process[32–37] Multilayered core–shell nanostructures like onions can be also obtained[38]. This method can take advantage of the synthetic knowledge of shape-controlled monometallic nanocrystals to construct target lattice orientation and facet exposed for the epitaxial growth of the second metal. The synthesis of bimetallic core–shell nanocrystals has been successfully realized with shell thickness controllable down to one atomic layer, which is relative to practically physicochemical properties. When we design noble metal-based catalysts with core–shell structure for heterogeneous catalysis, a non-noble metal core encapsulated by active noble-metal with a single layer is an ideal bimetallic structure, which owns the highest atom utilization efficiency and the lowest cost of noble metals (e.g., Pt, Pd, Rh) as well as the strongest strain effect on catalytic behaviors. There are three common methods to grow one monolayer of one metal on the surface of another metal. The first is seed-mediated growth through adjusting the stoichiometric ratio of two metal precursors to deposit several atomic layers of the shell metal on the seed[39–41] Another method is the combination of underpotential deposition (UPD) and galvanic replacement, in which a sacrificial monolayer is first deposited by UPD, and then another metal with higher redox potentials replaces the layer to form M@N nanostructure[42–44]. Post-treatment is one of the most simple routes to obtain core–shell nanocrystals, in which alloy or intermetallic nanocrystals are annealed, induced, or dealloyed to thermodynamically stable atom distribution by elemental segregation, and it can also be applied to the synthesis of intermetallic nanocrystals from alloy precursors[26, 45–47]. As shown in Figure 4.2, Oezaslan et al. concluded general synthetic strategies toward Pt-based core – shell nanocrystals[48].

Strain effect and electronic coupling can still exist in a core–shell nanocrystal with less six shell layers. There are a number of research cases on shell thickness-dependent catalytic performances for the bimetallic nanocrystals. Wang et al. reported such a volcano-shaped relationship between the thickness of Pt shell in Pd@Pt icosahedrons and the mass activity of oxygen reduction reaction. Pd icosahedrons serving as seeds, whose twin boundaries and vertical relaxation led the platinum overlayers to a corrugated structure under compressive strain. The core–shell nanocrystals with an average of 2.7 platinum overlayers showed eight- and sevenfold enhanced specific activities and mass activities toward ORR, respectively, relative to a commercial Pt/C catalyst[49].

Although core–shell nanostructures with more than six atomic layers have lost the ability to modulate their catalytic properties, there are many advantages for other applications to prepare multilayer core–shell nanocrystals, including tuning the optical

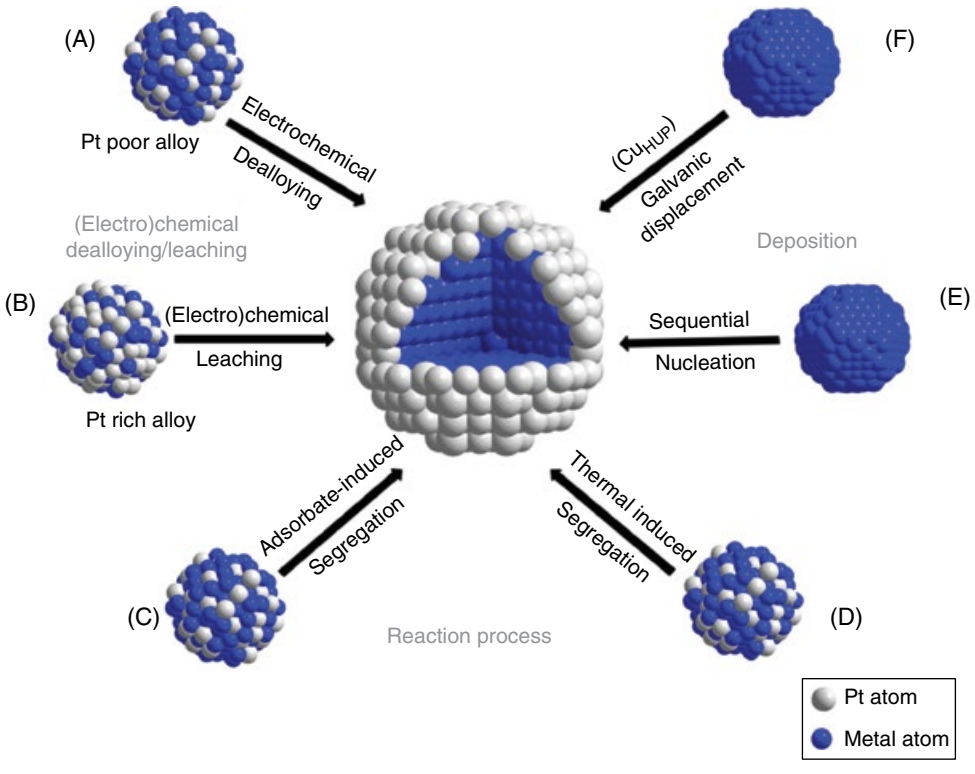

Figure 4.2 Illustration of basic synthesis approaches for the preparation of Pt-based core–shell nanoparticle catalysts. Electrochemical (acid) dealloying/leaching results in (A) dealloyed Pt-based bimetallic core–shell nanoparticles and (B) Pt-skeleton core–shell nanoparticles, respectively. Reaction process routes generate segregated Pt skin core–shell nanoparticles induced either by (C) strong binding to adsorbates or (D) thermal annealing. The preparation of (E) heterogeneous colloidal core–shell nanoparticles and (F) Pt monolayer core–shell nanoparticles is via heterogeneous nucleation and UPD followed by galvanic replacement, respectively. Reprinted with permission from ref. [48]. Copyright (2013) American Chemical Society.

properties over a broad range, enhancing the thermal and chemical stabilities, and improving magnetic properties. For example, the position and intensity of localized surface plasmon resonance (LSPR) of the core–shell nanocrystals are extremely sensitive to shell thickness until the thickness reaches a critical value, and thus the LSPR responsive properties will be dominated by the shell metal of core–shell nanocrystals with excessive thickness[50].

4.3 General Principles of Shape Evolution

4.3.1 Equilibrium Shape: Wulff Polyhedron

Under constant temperature and volume conditions, the growth of the crystals tends to equilibrium with the lowest surface energy in an ideal situation, which is the Gibbs-Wulff theorem. A metal nanocrystal with a thermodynamically stable morphology,

looks like a nearly spherical polyhedron, which is called the Wulff polyhedron. The structural criteria of Wulff polyhedron possess several conditions[51]. If a surface can be described by the Miller index (*hkl*) and its surface area (*S*), the surface tension (γ_{hkl}) and the distance from surface to the center of the polyhedron (R_{hkl}) follow the relation:

$$\frac{\gamma_{hkl}}{R_{hkl}} = \text{const.} \tag{4.1}$$

If it is isotropic, which meets the water droplet model:

$$\gamma_{hkl} S_{hkl} = \gamma S \tag{4.2}$$

Then,

$$\frac{\gamma}{R} = \text{const.} \tag{4.3}$$

Equation (4.3) represents an ideal spherical nanocrystal, because *R* must be constant. However, it is more complex for the actual metal nanocrystals. For example, the face-centered cubic (*fcc*) structure with the coordination number of 12 (CN = 12), has two polyhedral structures: the Wigner–Seitz polyhedron (unit cell in the direct space) and its dual (Wigner–Seitz unit cell in the reciprocal space), known as the first Brillouin zone. The latter is a cubo-octahedron with six square faces (100) and eight hexagonal faces (111). Their coordination numbers are 8 and 9, respectively. As the Wulff criteria is applied for (111) and (100) facets, Eq. (4.4) is obtained:

$$\frac{\gamma_{111}}{\gamma_{100}} = \frac{R_{111}}{R_{100}} = \frac{\sqrt{3}}{2} \tag{4.4}$$

If the surface energy does not have much difference, the Wulff polyhedron will not be deviated from the cubo-octahedron shape. Except for the single crystal structure, some nanocrystals may also have multiply twinned structures, such as decahedrons and icosahedrons. The lattice strain produced by the twinned defects will increase the total energy of the nanocrystals. If the increased energy is less than the decreased surface energy of the system, the twinned structure should be more stable and favored.

4.3.2 Nucleation Mechanism of Metal Nanocrystals

It is generally stated that the formation of metal nanocrystals undergoes nucleation and growth stages. The nucleation modes can be divided into homogeneous nucleation and heterogeneous nucleation. LaMer model was widely used to describe the homogeneous nucleation and growth, which inspires us that it is necessary to make all nuclei formed simultaneously and rapidly in order to obtain monodisperse metallic nanocrystals with controlled morphology[52, 53]. As shown in Figure 4.3, metal precursors are firstly reduced or decomposed into nuclei, and then these nuclei grow up to seeds under the control of the thermodynamics and kinetics, and finally surfactants and facet-specific capping agents induce the formation of shape-controlled nanocrystals

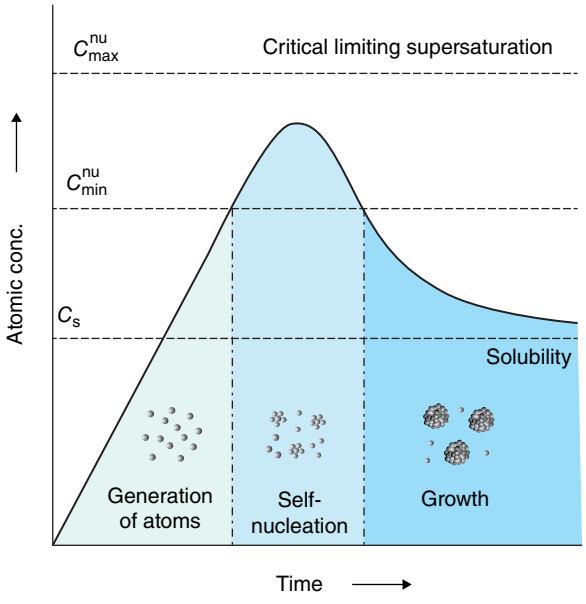

Figure 4.3 LaMer model for homogeneous nucleation and growth. Reproduced with permission from ref. [52]. Copyright (1950), American Chemical Society.

For heterogeneous nucleation, the activation energy on the given crystal nuclei must be lower than that of the spontaneous nucleation. If ignoring the replacement reaction between two metals, the continuous growth of heterogeneous nucleation also conforms to the LaMer model.

4.3.3 Growth of Metal Nanocrystals

Nanocrystals can be regarded as the slice of the bulk materials along specific facets. The total energy (free energy) of nanocrystals consists of the surface and bulk free energy. The surface energy can be described by the following equation:

$$\gamma = \frac{1}{2} N_b \varepsilon \rho_a \tag{4.5}$$

N_b is the number of broken bonds, ε is the bond strength, ρ_a is surface atom density. In the case of *fcc* metal nanocrystals, the surface energy exhibits an order of $\{111\} < \{100\} < \{110\}$. When surrounded by the same volume, the surface area of the octahedron and the tetrahedron is significantly larger than that of the cube. So large nanocrystals tend to develop into Wulff polyhedrons with the lowest surface energy and total energy. For small nanocrystals, a multiple twined nanostructure with only {111} facet exposed is more favored and stable, as long as the increased lattice energy is less than the reduced surface energy reduction (Figure 4.4)[54]. Generally, the strain energy caused by twin defects increases as the particle size increases. Both the single-crystal nanostructure and twinned nanostructure depend on the reduction rate of metal precursors. Decreasing the reduction rate of metal precursors to near equilibrium is pivotal

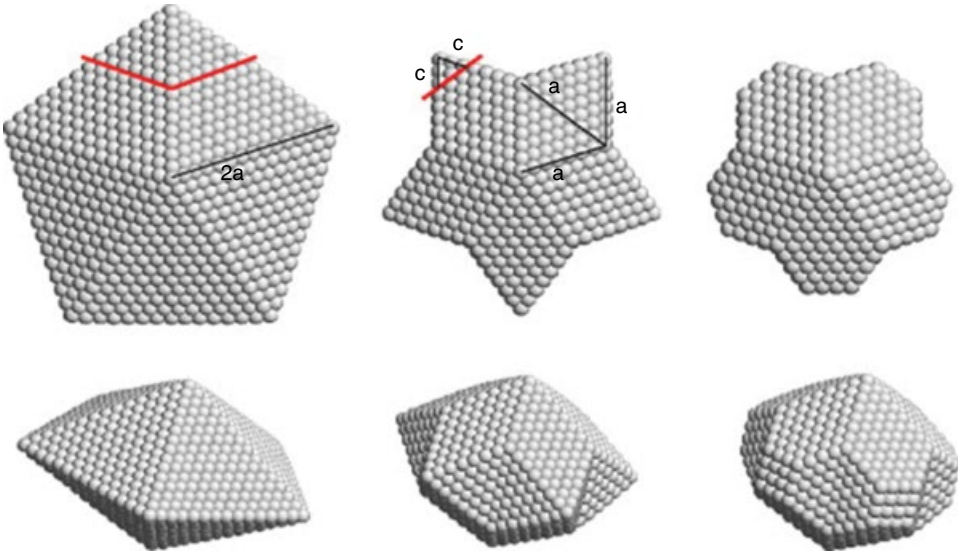

Figure 4.4 Multiply twinned nanocrystals. Modified with permission from ref. [54]. Copyright (2007), Acta Materialia Inc.

to form twined nuclei. While the potential barrier from the twined nuclei into the single-crystal nuclei is so high that thermodynamically stable twined structure is finally formed. When accelerating the reduction rate of the metal precursors makes the nucleation and growth of nanocrystals controlled by kinetics, the single-crystal structures will be finally obtained.

The kinetic control of growth process is reflected in the particle size distribution and shape evolution. Peng et al. first proposed the focusing of size distributions that stated small particles grow faster than large particles for the uniform size distribution at fixed nanoparticle concentration[55]. At a fixed monomer concentration, assuming that diffusion is the rate-limiting step, the size-dependent growth rate can be obtained according to the Gibbs-Thomson equation:

$$S_{\mathrm{r}} = S_{\infty} \exp\left(\frac{2\sigma V_{\mathrm{m}}}{rRT}\right) \tag{4.6}$$

S_{r} and S_{∞} are the solubility of the nanocrystal and the bulk solid; σ is specific surface energy, V_{m} is the molar volume of the materials, r is the radius of the nanocrystal, R is the gas constant; and T is the absolute temperature.

If $2\sigma V_m/rRT << 1$, the diffusion-controlled growth rate of the nanocrystal with size r is

$$\frac{dr}{dt} = K\left(\frac{1}{r} + \frac{1}{\delta}\right)\left(\frac{1}{r^*} - \frac{1}{r}\right) \tag{4.7}$$

K is a constant proportional to the diffusion constant of the monomer, δ is the thickness of the diffusion layer. At a fixed concentration, r^* is the critical radius for which the solubility of the nanocrystal is exactly the concentration of the monomers in solution.

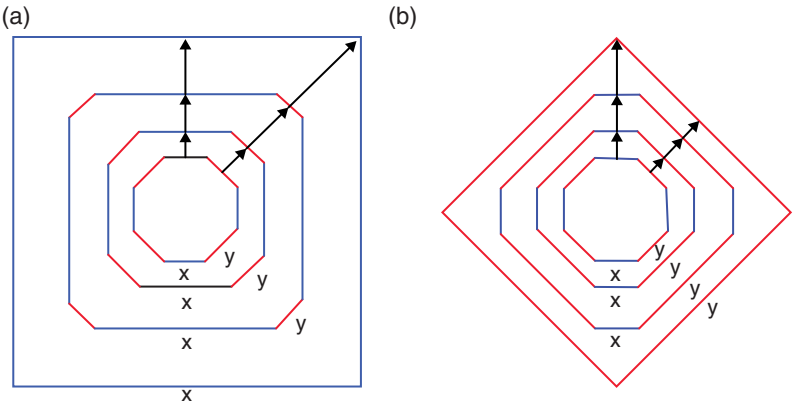

Figure 4.5 Morphological changes in a hypothetical 2D crystal during continuous growth: (a) faster growth in the *y* direction; (b) faster growth in the *x* direction. Reproduced with permission from ref. [53]. Copyright (2009), Wiley-VCH Verlag GmbH & Co. KGaA, Weinheim.

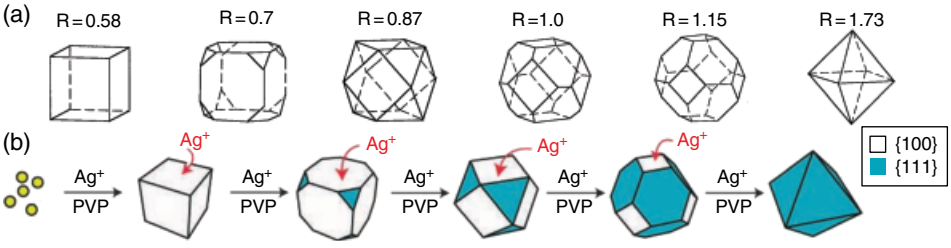

Figure 4.6 (a) Cubo-octahedral shapes as a function of the ratio, *R*, of the growth rate in the <100> to that of the <111>. Reproduced with permission from ref. [58]. Copyright (2000), American Chemical Society. (b) The effect of selective adsorption of Ag^+ on {100} facet on the morphology of nanocrystals. Reproduced with permission from ref. [60]. Copyright (2006), Wiley-VCH Verlag GmbH & Co. KGaA, Weinheim.

For a given-sized nanocrystal, it dissolves (grows) to produce divergent size distribution if the monomer concentration in solution is lower (higher) than its solubility, which is called size self-focusing of the nanocrystal, also known as Ostwald ripening[56].

Shape evolution of nanocrystals is also controlled by the growth kinetics[57]. Taking two-dimensional (2D) octagonal nanocrystal as an example, as shown in Figure 4.5. Suppose there are two growth directions (*x* and *y*) corresponding to two sets of facets with different surface energy, when the growth rate of the *y* direction is greater than that of the *x* direction, the facet perpendicular to the *y* direction would completely disappear, and square nanocrystal would be obtained (Figure 4.5a). Conversely, only facets perpendicular to the *y* direction would expose (Figure 4.5b)[53]. The growth principle of 2D nanocrystals can be applied to a 3D nanostructure. Figure 4.6a shows a group of cubooctahedral shapes as a function of the ratio, *R*, of the growth rate in the <100> to that of the <111>. If $R \le 0.58$, a cube forms; $0.58 < R < 0.87$, a truncated cube forms; $0.87 \le R < 1.73$, a truncated octahedron forms. And $R \ge 1.73$, the particle exhibits octahedral shape[58]. Under the combined control of kinetics and thermodynamics, shape evolution process can be observed in the

synthesis of the nanocrystal[59]. As shown in Figure 4.6b, when introducing polyvinylpyrrolidone (PVP) and silver nitrate solution into presynthesized Ag nanocubes, Ag^+ ions were consequently deposited on the {100} facet of Ag nanocubes, which led to the morphology evolution from cube to truncated octahedron, and finally to octahedron[60]. PVP, as the facet-specific capping reagent, were selectively adsorbed on the {111} facet to slow down the growth rate of the {111} facet, thus octahedral structure was formed.

4.4 Key Factors for Shape Evolution in Colloidal Synthesis

4.4.1 Redox Potentials

Standard reduction potential can not only quantify the difficulty in reducing one metal precursor in aqueous solution, but also provide a general trend of reducibility of different metal precursors in nonaqueous solution. Metal ions intrinsically differ in reduction potential. The difference of redox potentials of different metal precursors can be narrowed and expanded by changing the coordination environment of metal ions. According to Marcus theory, ligands strongly coordinating with metal ions will lower the redox potential to a different degree based on the identity and concentration of ligands. As shown in Figure 4.7, ligands such as $C_2O_4^{2-}$, halides, oleylamine (OAm), and metal carbonyls are often used to coordinate with Pt^{2+} or Pd^{2+} to decrease their redox potentials to that value of non-noble metals in preparing Pt-based or Pd-based nanoalloys with tunable polyhedral shapes[61–65]. The coordination between metal ions and ligands will not only influence the overall reduction kinetics by slowing down the reduction rate of metal precursors but also bind preferentially with specific facets of the nanocrystals to influence the ultimate facet exposure[66, 67]. $C_2O_4^{2-}$ ions were found to selectively adsorb on {111} facet of noble metals to induce the formation of polyhedral nanocrystals[61, 62]. Pd^{2+} and halides (Cl^-, Br^-, or I^-) form Pd-halide complexes, whose stability constants follow the order of $[PdI_4]^{2-} > [PdBr_4]^{2-} > [PdCl_4]^{2-}$. When $PdCl_4^{2-}$ ions were wrapped by cetyltrimethylammonium bromide (CTAB), the reduction rate of Pd^{2+} cations was adjusted to an appropriate value that ensured a kinetic-controlled growth for Pd nanorods[68]. Zhou et al. found that $PdCl_4^{2-}$ and $PtCl_4^{2-}$ served as metal precursors to form Pd@Pt octahedra with a core–shell structure due to higher reduction potential of $PdCl_4^{2-}$. When KBr was added to produce $PtBr_4^{2-}$ and $PdBr_4^{2-}$ with close reduction potentials, the initial reduction rates decreased to form Pd-Pt alloy nanocrystals[69].

Choosing different metals precursors and introducing new complexing agents are alternatives to tune the redox potentials of metal ions. The higher the standard reduction potential is, the faster the reduction rate of metal precursor is. Besides, the difference of redox potential can be skillfully exploited by underpotential deposition[70–72]. Hence, different types of metal precursors, coordinating agents, and UPD can be rationally utilized to decrease the difference of redox potentials between two metals in the synthesis of bimetallic nanocrystals with controlled shape.

4.4.2 Reduction Rate

Generally speaking, a rapid reduction rate will lead to single-crystalline nuclei, which can serve as the seeds of cubes, octahedrons with O_h symmetry and tetrahedrons with T_d symmetry. However, a slow reduction rate favors the formation of fivefold twinned

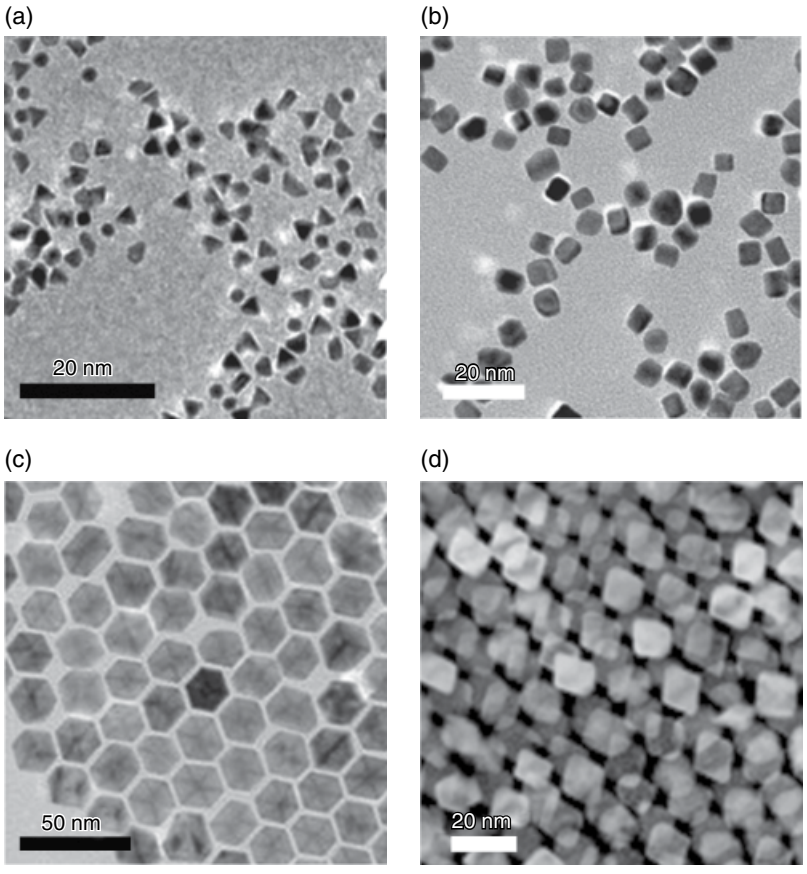

Figure 4.7 TEM images of (a) Pt-Pd nanotetrahedrons in the presence of $C_2O_4^{2-}$; (b) Pt–Pd nanocubes in the presence of Br^- and I^-. Reprinted with permission from ref. [61]. Copyright (2011), American Chemical Society. (c) Pt–Ni rhombic dodecahedrons in the presence of OAm. Reprinted with permission from ref. [63]. Copyright (2014), American Association for the Advancement of Science. (d) Pt–Ni nanoctahedrons in the presence of $W(CO)_6$. Reprinted with permission from ref. [64]. Copyright (2010), American Chemical Society.

nuclei with I_h symmetry in the nucleation stage, such as icosahedrons and dodecahedrons. When the reduction rate is slow, the nucleation and growth processes will be under near-equilibrium conditions. Thus, the metal precursor with higher redox potential will be reduced prior to the other precursor. This growth behavior is typically epitaxial growth route, which tends to form core–shell nanocrystals[73]. Reduction rate is determined by the redox potentials of metal precursors and reaction conditions (temperature, time, and reductant, etc.). High temperatures can compensate for the effect of weak reductants on reduction rate and make bimetallic nanocrystals reach thermodynamically stable state. The reaction time depends on the growth stages of bimetallic nanocrystals. The formation of metallic nanocrystals involves nucleation stage and growth stage. As reaction time prolongs, bimetallic nanocrystals gradually expose regular shape or experience shape reconstruction. Ascorbic acid (AA), HCHO, amine, polyol, and poly(vinylpyrrolidone) (PVP) are prevalent reductants, and some

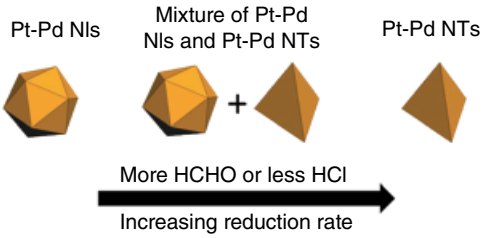

Figure 4.8 Schemes of Pt–Pd bimetallic nanocrystals obtained under addition of different amounts of HCHO and HCl.

reductants like PVP can serve as capping agents. Strong reductants (e.g., $NaBH_4$ and hydrazine) result in a too-fast reduction rate to well control the shape of the final products. To increase or decrease the concentration of reductants can modulate their reducibility[74] In aqueous system, the reducibility of reductants can be tuned by changing the pH value of solution. For example, AA will show stronger reducibility in base environment than that in acidic and neutral conditions based on Le Chatelier's principle. Yin et al. demonstrated the shape-controlled synthesis of Pt–Pd nanocrystals, including single-crystalline nanotetrahedrons (NTs), and multiple twined nanoicosahedrons, which are both enclosed by {111}-facets[62]. K_2PtCl_4 and Na_2PdCl_4 were reduced by HCHO solution in the presence of sodium oxalate ($Na_2C_2O_4$) as {111}-facet capping agent. The HCHO oxidation half-reaction is shown as:

$$HCHO + H_2O \rightarrow 4H^+ + CO_2 \uparrow + 4e^-$$

Therefore, the reducing capacity of HCHO will be remarkably restrained along with decreasing the pH value. High concentration of H^+ in solution would slow down the reduction rate of metal precursors. As indicated in Figure 4.8, a proper amount of HCl solution was needed for the preparation of multiple twinned Pt–Pd NIs. Without HCl or with more HCHO added, no multiple twinned NIs but single-crystalline Pt–Pd NTs would be obtained. This typical case indicates the influence of reduction rates on the nucleation stage of bimetallic nanocrystals and the ultimate shape of products. Considering that the shape evolution of bimetallic nanocrystals is deeply dependent on the kinetic behaviors, the nucleation and growth step should be carefully controlled by using proper reductants and optimized reaction conditions.

4.4.3 Lattice Mismatch

The difference of lattice parameters can affect the structures of bimetallic nanocrystals, such as solid solution, intermetallic compounds, and core–shell nanocrystals with different shell thickness[75]. High lattice mismatch generates large lattice strain and raises the interfacial energy, thus resulting in disordered atomic arrangement[76]. General rules that less than 5% lattice mismatch facilitates the epitaxial growth of core–shell nanocrystals are followed by most experimental results. Pt and Pd, Au and Ag with low lattice mismatch (0.85% and 0.17%) are miscible couples, and are easy to form alloy or core–shell nanocrystals[77, 78]. However, there are unexpected combinations of two metals breaking down the rules. As shown in Figure 4.9, Au@Pd, Pd@Cu, Au@Cu and Au@Ni core–shell nanocrystals with lattice mismatch of 4.88%, 7.1%, 11.4%, and 13.6%, respectively, were successfully synthesized[79–82]. Au@Ni core–shell nanocrystals with 13.6%

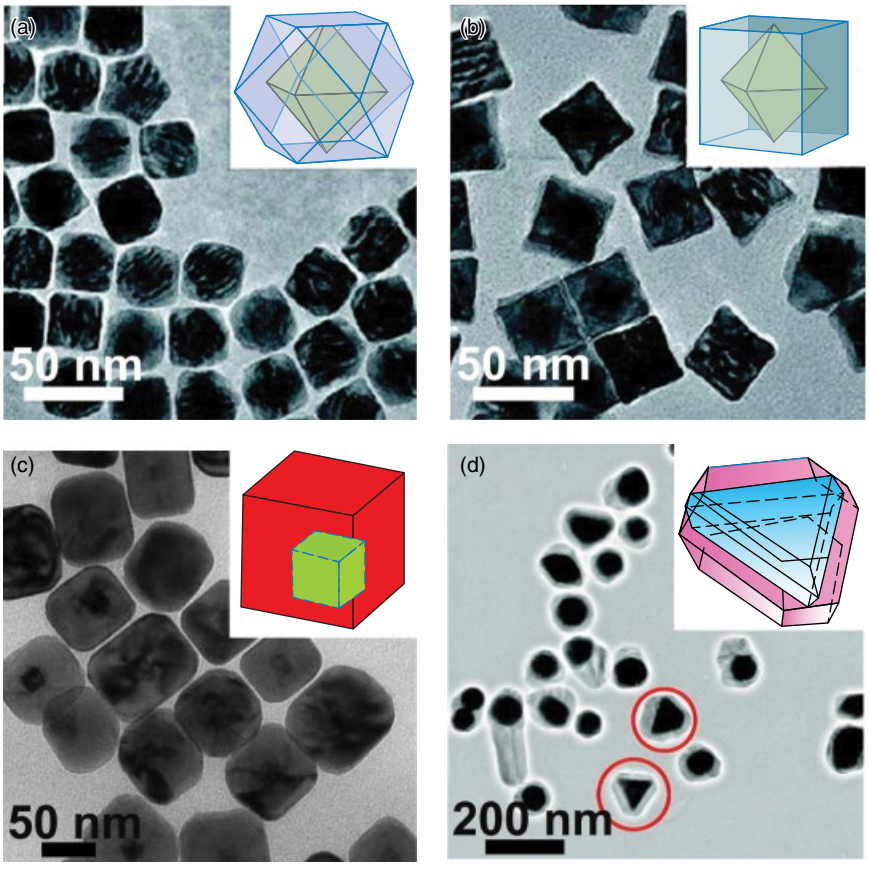

Figure 4.9 TEM images of (a) Au@Pd truncated nanocubes, (b) Au@Pd nanocubes. Rreprinted with permission from ref. 79. Copyright (2008), American Chemical Society. (c) Pd@Cu nanocubes. Reprinted with permission from ref. 80. Copyright (2012), American Chemical Society. (d) Au@Cu nanocrystals. Reprinted with permission from ref. 81. Copyright (2010), American Chemical Society.

lattice mismatch were prepared by the seed-mediated method, which may result from the lower electronegativity of Ni (1.91) than that of Au (2.54) and smaller bond energy of Ni–Ni ($203\,kJ\cdot mol^{-1}$) than that of Au–Au ($247\,kJ\cdot mol^{-1}$)[82]. In addition, Fan et al. pointed out that the shell metal with smaller atom radius is easier to epitaxially grow on the core, as they could uniformly release the lattice strain resulting from the lattice mismatch[79]. It seems that epitaxial growth is a good way to inherit the lattice orientation of monometallic seed to form similar shape in preparing bimetallic nanocrystals. While the bond strength of two hetero metal atoms should be stronger than the homo metal atoms, which determines the difficulties in the formation of bimetallic nanocrystals.

4.4.4 Facet-Specific Capping Agents

Facet-specific capping agents that mainly regulate the growth rate of specific facet by strong surface adsorption, are widely used in shape-controlled synthesis of metal nanocrystals. The growth of capped facet by some facet-specific capping agent will be

hindered; thus, specific facet will be retained on the surface of nanocrystals. The facet-specific capping ligands, which are effective for the shape-controlled synthesis of monometallic nanocrystals, have been demonstrated during past decades. However, the effectiveness of this synthetic strategy for bimetallic system may vary with concrete situations. There are various kinds of facet-specific capping agents, including inorganic ions, small organic molecules, gases, and polymers. The role of these agents is deeply affected by real reaction system, and results in different influences in the growth stage of the nanocrystals. On one hand, these facet-specific capping agents bind with certain facet to lower the surface energy by thermodynamic control. The relative surface energy of different facets is the decisive factor for the final shape of bimetallic nanocrystals. On the other hand, the growth of capped facets is limited by kinetic control to retain the target facet[83]. Hence, {*hkl*}-facet capping agents are used to synthesize bimetallic nanocrystals with {*hkl*} facet exposed. For example, $C_2O_4^{2-}$ ions serving as {111}-facet capping agents contribute to the formation of tetrahedrons, octahedrons and icosahedrons. Carbon monoxide and Br^- are typical {100}-facet capping agents for the preparation of bimetallic nanocubes. Wu et al. synthesized Pt_xNi_{1-x} $(0 < x < 1)$ nanocrystals with shapes ranging from octahedral, truncated octahedral, and cubic by using different facet-specific capping agents, as shown in Figure 4.10[84] They found that $Pt(acac)_2$ and $Ni(acac)_2$ could be reduced to form Pt–Ni octahedrons in the presence of PVP and benzoic acid in benzylalcohol. By simply replacing the benzoic acid with aniline under the same conditions, the formation of Pt–Ni truncated octahedrons became favorable. The addition of aniline was believed to act as a coreductant and a growth inhibition agent of {100}

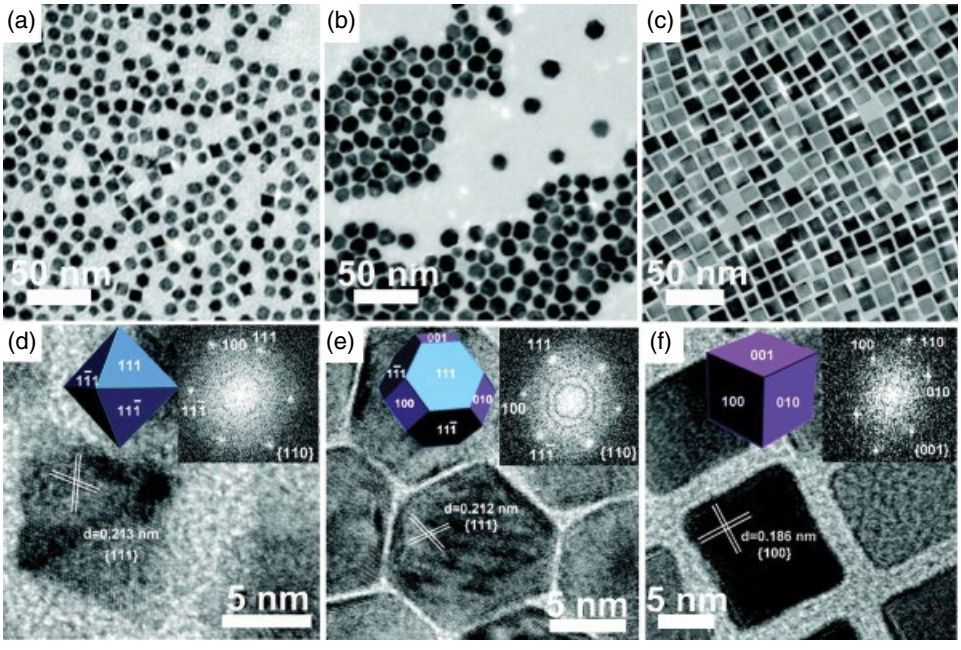

Figure 4.10 TEM images and HRTEM images of $PtNi_2$ octahedrons (a, d), $PtNi_2$ truncated octahedrons (b, e), and $PtNi_2$ cubes (c, f). Reprinted with permission from ref. [84]. Copyright (2012), American Chemical Society.

facet to affect the reaction kinetics. When CO and KBr serve as the {100}-facet capping agent, well-defined Pt–Ni nanocubes are the prevalent products. This case shows the great importance of facet-specific capping agents for the shape-controlled synthesis of bimetallic nanocrystals. It is worth noticing that the growth stage should be finely tuned together with the nucleation process. Wang et al. realized the synthesis of Pd–Rh truncated nano-octahedrons and NIs by controlling the selective nucleation of twinned seeds or single crystal seeds, and their relative growth rates along different facets (e.g., (111) and (100) facets), through finely adjusting the Pd–Rh ratio and the amount of facet-specific capping agent-KBr[85]. In all, a facet-specific capping agent can play a vital role in modulating the shapes of bimetallic nanocrystals when thermodynamic parameters and kinetical conditions are synchronously satisfied in one reaction system during the synthesis.

4.5 Synthetic Approaches to Bimetallic Nanospheres and Nanopolyhedrons

Many studies deal with the synthesis of bimetallic nanocrystals with well-defined shape, in which the synthetic protocols are capable of generating similar products as long as some key factors mentioned in section 4.3 are rationally employed and precisely controlled. In this section, we focus on the controllable synthesis approaches toward bimetallic nanospheres and nanopolyhedrons, including continuous growth, seed-mediated growth, and the combination of UPD and galvanic replacement. Among the periodic table of the elements for the bimetallics, the metals in bimetallic nanocrystals involve catalytic platinum group ones (e.g., Pt, Pd, Rh, Ru, and Ir), magnetic ones (e.g., Fe, Co, Ni), plasmonic ones (e.g., Au, Ag), and other metals (e.g., Cu and Sn). By varying the combinations of these metals, bimetallic nanocrystals can be generated in a broad range of compositions and are extensively used in many fields.

4.5.1 Continuous Growth

Continuous growth refers that metal atoms or clusters reduced or decomposed from precursors are continuously added to nuclei, and then the nuclei grow up into uniform alloy nanocrystals. This route can be divided into three main methods: coreduction, thermal decomposition, and combination of thermal decomposition and reduction in practical synthesis.

4.5.1.1 Coreduction

Coreduction is the most common method for preparing M–N nanocrystals, which is simultaneous reduction of two metal precursors to metallic state, requiring their nucleation together to generate bimetallic nanocrystals with highly alloying degree. While the nucleation and growth of nanocrystals depend critically on the reduction rates of two metal precursors, facet-specific capping agents are also indispensable to modulate the surface energy and growth rate of different facets for target bimetallic shapes. Therefore, experimental parameters such as reduction potential of metal precursor, reaction temperature, ligand and reducing capacity of reductant can be rationally tailored to obtain desired atom arrangements. Generally, metal ions with similar

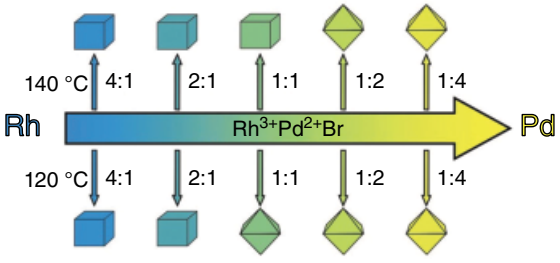

Figure 4.11 Scheme of the shape evolution of Rh–Pd alloy with the Rh/Pd ratio. Reprinted with permission from ref. [88]. Copyright (2014), Royal Society of Chemistry.

reduction potentials should be selected for alloyed nanocrystals via coreduction. Huang et al. reported the synthesis of single-crystalline Pt–Pd nanocrystals with controllable shapes and tunable compositions[86]. Different halides were selected to act as the facet-specific capping agents, the addition of I^- ions induced the formation of Pt–Pd nanocubes enclosed by {100} facet, and the addition of Cl^- ions contributed to the formation of Pt–Pd nanooctahedrons/nanotetrahedrons bounded by {111} facets under the same conditions. When I^- ions and Cl^- ions coexisted in this system, Pt–Pd nanocubes were main products, which are consistent with the suggested chemisorption capability of halides to metal surface in the order of $I^- > Br^- > Cl^-$. The high coverage of I^- on metal surface suppressed the adsorption of Cl^-, only exhibiting the shape-directed effect of I^-. Interestingly, when NaI or NaCl was substituted with another halide NaBr, the reactions yielded mixed nanocrystals (mainly containing nanobars, cubes, and cuboctahedra) with no selectivity to a specific shape. Lim et al. first demonstrated that Pd–Pt star-shaped decahedrons with well-defined twinned structures can be synthesized by coreduction of Na_2PdCl_4 and K_2PtCl_4 in aqueous solution because of that PVP with weak reducing capability slowed down the reduction rate to kinetically control the nucleation and growth of the Pt-Pd nanocrystals[87]. Yan et al. successfully synthesized Rh–Pd nanocubes and nanoctahedrons under precise control of sluggish reaction kinetics by ultra-slow injection of metal salts[88]. Pd preferred to overgrow along the <100> direction, whereas the growth behavior of Rh was dominant along the <111> direction. As shown in Figure 4.11, varying the feed ratio of two metal precursors can achieve the shape transition between the cube and the octahedron. Furthermore, decreasing the reaction temperature under the same feed ratio of Pd and Rh would retard the reduction of $PdBr_4^{2-}$ to form Rh-rich seeds, leading to displaying the growth behavior of Pd in final products. Zhang et al. prepared high-quality (100)-terminated Pt_3M nanocubes (M = Pt or 3d-transition metals Co, Fe, and Ni) through coreduction of $Pt(acac)_2$ and M-salt[89]. It was identified that the addition of $W(CO)_6$ was served as reductant and buffer to slow down the nucleation process, when the metal precursors were reduced, Pt clusters can be steadily and continuously provided for the growth stage, which favored the evolution of Pt_3M nanocrystals. Meanwhile, an optimized ratio of oleylamine to oleic acid is the key factor to enable the lowest total surface energy on {100} facets in order to develop cubic nanocrystals.

4.5.1.2 Thermal Decomposition

Thermal decomposition is another powerful route to synthesize bimetallic nanocrystals, which refers to the simultaneous decomposition of two metal precursors under certain temperature to form M–N nanocrystals. Traditionally, thermal decomposition

has been a favored method when working with metal precursors with relatively low reduction potentials, such as Fe, Co, and Ni. In this method, metal precursors include the carbonyls ($M_x(CO)_y$) and acetylacetonates ($M(acac)_n$), which could immediately decompose into M^{n+} and M^0, respectively, under moderate conditions. Thus, it is not uncommon to see the combination of thermal decomposition and reduction. Similar to coreduction, reaction temperature, precursor type, feed ratio, facet-specific capping agent, ligand, solvent, and reaction time are all crucial parameters to the synthesis of bimetallic nanocrystals with well-defined shape. The decomposition temperature is the intrinsic nature of metal precursor, so how to narrow the difference of the decomposition or reduction rate between two metal precursors is worth considering. Also, like coreduction, the matched decomposition or reduction rate can be obtained by tuning the relative precursor concentration, introducing some ligands or certain catalysts assisting in precursor decomposition. For instance, Bönnemann et al. prepared Fe–Co nanocrystals through the concurrent thermal decomposition of $Fe(CO)_5$ and $Co_2(CO)_8$ in tetrahydronaphthalene[90]. The difference of decomposition temperature between $Fe(CO)_5$ at 200 °C and $C_{O2}(CO)_8$ at 150 °C resulted only in Co nanoparticles with a small amount of Fe particles, which were not alloyed in the region of 180–200 °C. Whereas the decomposition of $Fe(CO)_5$ can be finished at 150 °C under catalysis by aluminum trialkyl. This decrease in the decomposition temperature enabled the preparation of Fe–Co alloyed nanospheres. Lanza et al. presented the preparation of Pd–Sn alloy and intermetallic nanocrystals[91]. Complexes of Pd (II) and Sn (IV) precursors were thermally decomposed in oleylamine, which served as solvent, coordination agent, and reducing agent, leading to the formation of monodispersed nanoparticles with varied crystallographic structures. However, the difference in decomposition temperature provides the opportunity to prepare core–shell nanocrystals. When the reaction temperature is slightly lower than the decomposition temperature of a less stable metal precursor, monometallic nanocrystals will first appear and serve as the nucleation sites or seeds for further decomposition of another metal precursor through increasing reaction temperature or prolonging reaction time. For example, Son et al. synthesized Pd@Ni core–shell nanocrystals using sequential thermal decomposition of metal-surfactant complexes due to the difference of decomposition temperature between Pd-TOP and Ni-TOP[92]. Robinson et al. achieved the syntheses of a series of alloyed nanoparticles by the thermal decomposition of neutral bimetallic carbonyl clusters and molecular bimetallic carbonyl cluster anions, such as $[FeCo_3(CO)_{12}]^-$, $[Fe_3Pt_3(CO)_{15}]^{2-}$, $[FeNi_5(CO)_{13}]^{2-}$, and $[Fe_4Pt(CO)_{16}]^{2-}$. This method is very effective in composition control of bimetallic NCs without phase separation[93].

4.5.1.3 Combination of Thermal Decomposition and Reduction

The combination of thermal decomposition and reduction is favored for the synthesis of bimetallic nanocrystals when different types of metal precursors are chosen to simultaneous decomposition and reduction. Chen et al. realized the controlled synthesis of FePt nanocubes through concurrent decomposition of $Fe(CO)_5$ and reduction of $Pt(acac)_2$ at relatively low temperature[94]. Synthetic studies revealed that by controlling the addition sequence of the stabilizers (oleic acid and oleylamine), FePt nanocubes could be prepared. The amine reacts with Pt to form a stable Pt–NH_2– complex, while the –COOH group of oleic acid molecule does not have a strong tendency to bind to Pt. Adding oleic acid first and following aging stage at 120 °C during the initial stage of the

reaction, conduced to the generation of cubic Pt-rich nuclei. In a kinetic-growth process, the Fe-rich species prefer to deposit on the (100) plane, leading to the formation of cubic shape. If oleylamine was added first, sphere-like Fe–Pt nanoparticles were separated. This indicates that the control of nucleation and growth are critical to producing uniform Fe–Pt nanocubes with Pt-rich core and Fe-rich shell.

4.5.2 Seed-Mediated Growth

Seed-mediated growth is an effective route to prepare core–shell nanocrystals. Well-defined metal seeds serve as heterogeneous nucleation sites for the other metal atoms reduced or decomposed from metal precursors. The deposition of atoms on the surface of a seed is governed by both thermodynamics and kinetics. Atoms generally preferentially deposit at surface sites with high surface energy. The rate of atom deposition relative to the surface diffusion rate for the adatoms determines the final configuration. In general, there are three recognized growth modes: Frank-van der Merwe, layered growth; Volmer-Weber (VW), island growth; and Stranski – Krastanov (SK), first layered growth and later island growth[95]. Fan et al. reported that the epitaxial growth of Pt, Pd, and Ag on Au octahedron seeds exhibited different growth modes[79]. Pd and Ag adopted layered growth mode to form Au@Pd and Au@Ag core–shell nanocubes, while Pt led to island growth mode to form rough Au@Pt core–shell nanospheres, even though Pt and Au have a smaller lattice mismatch than that of Pd and Au. The difference of growth mode between Pt and other two metals is attributed to higher Pt–Pt bond energy.

Compared with homogeneous nucleation, heterogeneous nucleation can be realized with the lower atom concentration and higher energy barrier. Kinetically controlling deposition rate and diffusion rate of shell metal by changing reaction temperature can modulate the growth mode of shell metal. For example, Xia et al. found that deposition of Pt on Pd seeds at different temperatures showed different deposition positions of shell atoms[96]. When the temperature is below 180 °C, kinetic-controlled discrete Pt atoms formed on the surface of Pd seeds. Increasing temperature to 180 °C or 200 °C would result in Pd@Pt core–shell concave nanocubes and Pd@Pt core–shell nanocubes, in which thermodynamic control is dominant. Of course, reaction temperature determines deposition rate and diffusion rate; their difference would make great influence on the shape of bimetallic nanocrystals.

Overgrowth of a different material on well-faceted seeds allows the use of the defined seed morphology to control nucleation and growth of the secondary structure. Habas et al. used highly faceted cubic Pt seeds to direct the epitaxial overgrowth of lattice-matched Pd to produce shape-controlled core–shell nanocrystals[97]. The shape of Pt@Pd core–shell nanocrystals can be further tuned by adding facet-specific capping agent-NO_2 to alter the growth rate along the <111> and <100> directions, such as Pt@Pd nanocubes, nanocubooctahedrons, and nanooctahedrons, as shown in Figure 4.12. When they extended it to lattice-mismatched Au, anisotropic growth formed Au nanorods with a single partially embedded Pt cube at the perimeter. This conformal growth is also applied to Au@Ag and Au@Pt core–shell nanodecahedrons[98, 99]. In all, template-directed epitaxial deposition is quite useful to retain the same facet exposure in synthesizing bimetallic nanocrystals. For example, Au tetrahexahedrons (THHs), trisoctahedrons (TOHs), and icosahedrons are employed as the core supports to direct

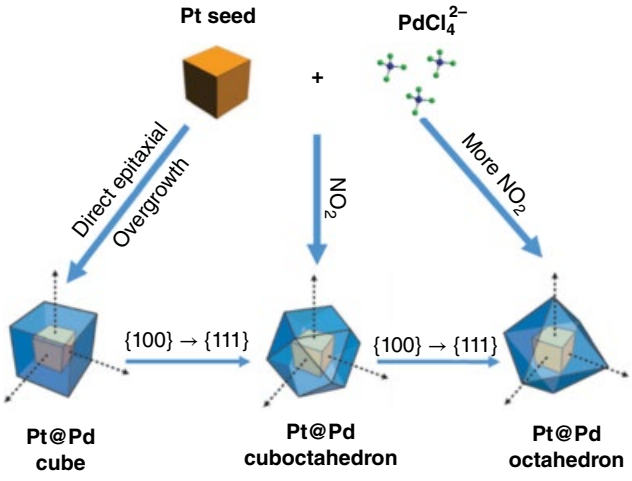

Figure 4.12 Scheme of the shape evolution of Pt@Pd alloy with NO_2 addition to tune the growth rates along the <100> and <111> directions. Modified with permission from ref. [97]. Copyright (2007), Nature Publishing Group.

the growth of the Pd or Ag shells to prepare respective Au@Pd THHs, Au@Pd TOHs and Au@Ag icosahedrons[100, 101]. In addition, seeds with different facet exposure can result in the same shell structure. For example, Au nanocube seeds can also be used to synthesize Au@Pd core–shell THHs, which is rationalized by large lattice mismatch between Pd and Au[102].

4.5.3 Combination of Underpotential Deposition and Galvanic Replacement Reaction

With underpotential deposition (UPD), a non-noble metal can form a monolayer on the surface of noble metal at a potential much higher than the equilibrium potential[103]. When the weighted average electronegativity of two metals is higher than a critical value, such as 1.93 in catadecylamine, a number of combinations of two metals can be used to synthesize well-defined bimetallic nanocrystals[104]. A galvanic replacement reaction involves the oxidation of one metal (named as a sacrificial template) by another kind of metal ions having a more positive reduction potential, which is favored in the synthesis of hollow bimetallic nanocrystals. Thus, the combination of UPD and galvanic replacement contains two consecutive processes: (1) a sacrificial-monolayer deposits onto the surface of one metal nanocrystal at underpotential; (2) another kind of metal ions galvanically replace the UPD layer. Cu^{2+} ions are usually used as the sacrificial mediators. Precise control over the number of deposited atomic layers is very difficult only through seed-mediated growth. The coupling of UPD and galvanic replacement reaction is an effective way to prepare the monolayer deposition of noble metal atoms or additional layers by repeating the process sequentially, in which non-noble metal ions serve as sacrificial mediators for the reduction of noble metal precursors. In addition, this method can assist the synthesis of bimetallic nanocrystals when two metals have large differences in redox potential. For example,

Zhang et al. employed UPD of Cu on Au as a bridge to prepare Au–Pd nanohexoctahedrons enclosed by 48 high-index facets with a uniform size, while phase separation would occur in the absence of Cu^{2+} due to a large reduction potential gap between $AuCl_4^-$/Au and Pd^{2+}/Pd[105]. When $AuCl_4^-$, Pd^{2+}, and Cu^{2+} were added together, Au nuclei formed first, and then a Cu monolayer was deposited on Au nuclei, and finally Cu and Pd^{2+} or $AuCl_4^-$ went through the galvanic replacement process. Sasaki et al. realized a series of controllable monolayer deposition of noble metals based on the combination of UPD and galvanic replacement reaction. They first employed UPD to deposit Cu monolayer on Pd nanocrystals, followed by galvanic replacement reaction between Pt^{2+} and Cu to form Pd@Pt monolayer core–shell nanocrystals[106]. In addition to the synthesis of bimetallic nanocrystals with single shell, the methodology can be extended to core–shell structures with double shells through repeated UPD and galvanic replacement processes. For Pd@Au@Pt nanocrystals, an outermost Pt monolayer and a Pd–Au sublayer were coated on the Pd core[107]. At first, Cu UPD occurred on Pd core, followed by galvanic replacement reaction between $AuCl_4^-$ and Cu to form Pd-Au core–shell nanocrystals with Pd–Au alloy shell. The second Cu UPD occurred on a preformed Pd–Au alloy shell, and then Pt^{2+} replaced the Cu monolayer to form Pd@Au@Pt nanocrystals with Pt shell and Pd–Au subshell. Yu et al. demonstrated UPD-coupled galvanic replacement reaction on polyhedral nanocrystals to form shape-controlled bimetallic nanocrystals, which is closely related to the selective deposition of satellite atoms on specific site of the central nanocrystals based on the geometry-dependent heterogeneous electron distribution[108]. This site-selective deposition approach is applicable to central nanocrystals in various polyhedral shapes, and the satellite atoms can further develop their own shape and size through crystal growth kinetics control[109]. Octahedrons, truncated octahedrons with different truncation degrees, and cubes with different exposed crystallographic facets were used as the central nanocrystals. The satellite atoms were deposited only on the corners or along the edges, as shown in Figure 4.13. The corners and edges with higher curvatures than the facets of any polyhedron are regions of electron accumulation, favoring the reduction of satellite metal precursors. In addition, changing the size of central seeds or deposition metals and tuning the selective placement of satellite nanocrystals on the corners, edges, and facets of the primary nanocrystals can effectively realize controlled synthesis of bimetallic nanocrystals in shape, size, and element distribution.

4.6 Catalytic Properties of Bimetallic Nanospheres and Nanopolyhedrons

The catalytic properties of bimetallic nanocrystals, including their activity, selectivity, and durability, can be improved through the rational design of the composition, size, shape, and structure of bimetallic nanocrystals. With the rapid development of the characterization techniques, the catalytic mechanism understanding for certain catalytic reaction on the specific catalyst has been deepened into the levels of atoms and molecules. In this section, we focus on the dependent relationship between shape and catalytic properties of bimetallic nanopolyhedrons, and describe some typical heterogeneous catalytic reactions on well-defined bimetallic catalysts.

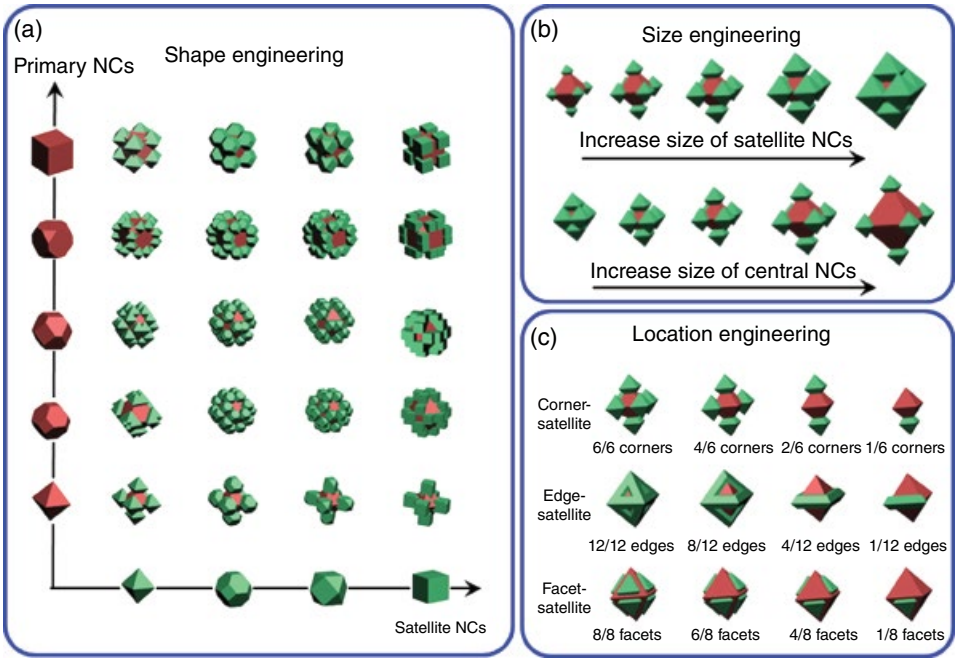

Figure 4.13 Illustration of the architectural diversity of heterogeneous metal nanocrystals through shape, size, and location engineering using binary heterogeneous metal nanocrystals as examples. Reprinted with permission from ref. [109]. Copyright (2014), American Chemical Society.

4.6.1 Effects of Adsorption Energy and Facet Type in Bimetallics

Heterogeneous catalytic reaction generally involves the adsorption of reactants onto the surface of a catalyst, the reaction among the adsorbed species, and the desorption of products away from the surface. The two thermodynamic parameters, i.e., the adsorption energy of reactants and the desorption energy of products, are decisive factors for actual catalytic process. Two distinguished volcano-shaped principles describing the relationship between adsorption energy or adsorption heat and catalytic reaction rate or activity were consecutively proposed by Sabatier and Balandin[110, 111]. Sabatier's principle states that too strong or too weak adsorption energy of the reactants on catalytic surface is inferior to optimal value to achieve superior catalytic performance. Balandin plotted the catalytic performance as a function of the adsorption heat, and revealed that the volcano plot reached the maximum value when the binding energy was moderate. The adsorption energy is mainly affected by geometry structure and electronic structure on the surface of bimetallic nanocrystals.

Generally, geometry structure, i.e., atomic arrangement, depends on the exposed facet type. Different facets display different atom-packing modes. For example, depositing Pd atoms on the Au(100) showed better catalytic activity for acetoxylation of ethylene to vinyl acetate than that on the Au(111) surface[112]. Two neighboring Pd monomers with a distance of 4.08 Å on the Pd–Au(100) surface are closer than those with a spacing of 4.99 Å on the Pd–Au(111) to couple the adsorbed surface species, yielding a much higher rate of vinyl acetate formation. Thus, the atomic arrangement,

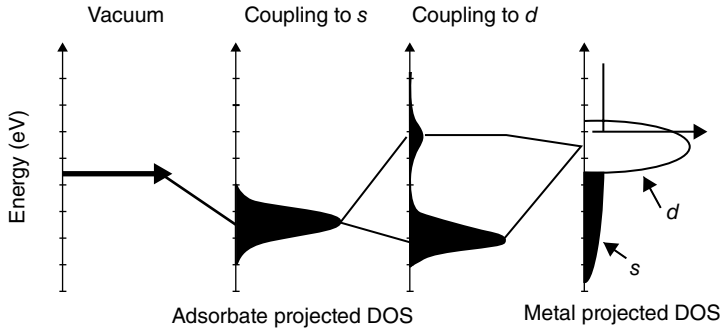

Figure 4.14 Schematic illustration of the formation of a chemical bond between an adsorbate valence level and the s and d states of a transition metal surface. Reprinted with permission from ref. [114]. Copyright (2005), Springer Science + Business Media, Inc.

which well matches the geometry of adsorbed molecules, facilitates the rapid reaction of adsorbed species to obtain desired products.

With the assistance of theoretical study such as density functional theory (DFT) simulations on the electronic effect of bimetallic nanocrystals through d-state hybridization, the adsorption energy was found to be linearly increased or decreased with the d-band center position of surface atoms. Later, the Brønsted-Evans-Polanyi (BEP) relation emerged to correlate the catalytic activity with the position and width of the d-band of metal nanocrystals, which also exhibited a volcano plot.

The well-known d-band theory was proposed by Nørskov and cowokers[113, 114]. As shown in Figure 4.14, the valence states of the transition metal surface atoms can be divided into two parts: the free-electron-like *s* electron states and the more localized *d* electron states. When the adsorption reaction occurs, the valence band of the adsorbed molecules is coupled with the metal *s* states first and then switches on the coupling to the metal *d* states later. The coupling to the broad *s* band leads to a broadening and shift of the adsorbate states. Nearly all transition metals have a wide and semi-filled *s* band, such that the difference between metals is mainly reflected in the more localized d band rather than *s* band. The interaction of the adsorbate states with *d* band gives rise to the formation of separate bonding and anti-bonding orbits, and the strength of the bond depends on the relative occupancy of these orbits. The more the bonding orbit is filled, the stronger the bond is. For the transition metal surface, the occupancy of anti-bond orbit only depends on the energy of these states relative to the Fermi level. The d-band center is used to measure the relative position between the metal d band and Fermi level. When the d-band center for transition metals is below the Fermi level, the interaction between the adsorbates and the metal surfaces is strong. Otherwise, the interaction is weak.

In general, the d-band center shifts upward in the transition metal region from right to left or from the bottom up, resulting in a stronger bond. The position of d-band center is determined by its width and its filling. The filling of *d* band is directly correlated with the occupancy of the *d* orbits, and the width of *d* band is a function of the coordination number, the atomic spacing, and the d-orbital spatial distribution. It is difficult to change the d-band filling for a single transition metal, but alloying with another element is effective to do so. As shown in Figure 4.15, the alloying effect on the d-band center includes the following types: (1) electron transfer from or to the d-states

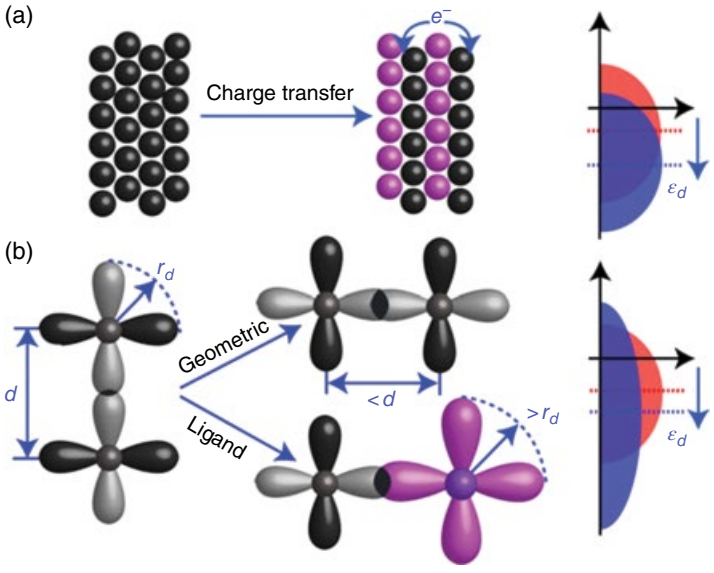

Figure 4.15 Mechanisms about the center change of the local d-band via two routes, including (a) charge transfer from one element to another (i.e., change in d-band filling); and (b) a change in the overlap between d-states and the valence orbitals of neighboring atoms leading to a change in the d-band width. Reprinted with permission from ref. [115]. Copyright (2012), Springer Science + Business Media, Inc.

localized on the atom without a change in the width or shape of d-band (Figure 4.15a); (2) mixing the local d-orbit and the valence band of adjacent atom changes the width of *d* band without a significant change in the filling of the d-band (Figure 4.15b); (3) a combination of the charge transfer and the width change of the d-band[115].

As shown in Figure 4.16a, when Pt alloys with early transition metals or more active transition metals, electrons will migrate from other transition metals to Pt atoms. Thus, the occupancy of d-band of Pt atoms will increase and the adsorption will decrease due to the downshift of d-band center[116]. The d-band center position is also influenced by the facet type-dependent coordination number of surface atoms. The higher coordination number leads to deeper d-band center and lower adsorption energy. Surface atoms in the {111}-facets, the {100}-facets, and {110}-facets have coordination numbers of 9, 8, and 7, respectively. By contrast, the atoms on the nanosized defects, such as steps or kinks, can have a coordination number of 6. Thus, {111}-facets have the highest stability among all facets. For monometallic Pt, the d-band center positions of Pt(111), Pt(100) and Pt(110) are –2.76 eV, –2.90 eV, –2.54 eV, respectively.

When introducing Ni into Pt, the d-band center position will shift down to different degree according to the shape of parent metal. Stamenkovic et al. found that the shift of d-band center from Pt(111) to $Pt_3Ni(111)$ is larger than that on the other two facets. Thus, $Pt_3Ni(111)$ also exhibited the highest catalytic activities toward oxygen reduction reaction (ORR) (Figure 4.16b)[117]. Furthermore, strain can induce the shift of d-band center. In general case, if the lattice is compressed, d-band center will shift down. In contrast, expanded lattice results in the upshifted d-band center. For example, the lattice strain of Pt deposition on Ru(0001), Pd(111), and Au(111) surface should be compression, small compression, and expansion, respectively[118].

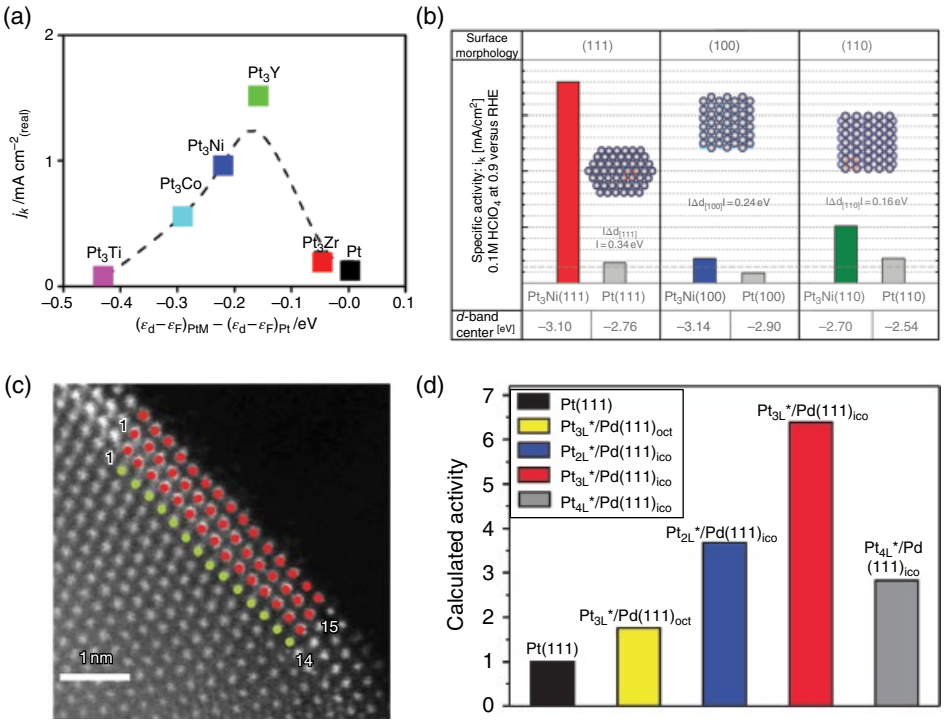

Figure 4.16 (a) Kinetic current density at 0.9V for ORR on Pt_3M alloy nanocatalysts and pure Pt nanocatalyst as a function of the measured d-band centers. Reprinted with permission from ref. [116]. Copyright (2012), American Chemical Society. (b) ORR activity of Pt_3Ni and Pt measured at 0.9V versus RHE with different facet exposed. Values of d-band center position for Pt_3Ni *(hkl)* and Pt *(hkl)* surfaces obtained from UPS spectra are listed to compare their electronic effect on ORR activity. Reprinted with permission from ref. [117]. Copyright (2007), American Association for the Advancement of Science. (c) Atomic-resolution HAADF-STEM images of Pd@Pt 2.7 L icosahedra about the detailed arrangements of Pd and Pt atoms (14 dots: Pd atoms; 15 dots: Pt atoms). Scale bar, 1 nm. (d) Analysis of the ORR activity of Pt_{nL}*/Pd(111) icosahedra slab models using DFT calculations. Specific activities (versus the pure Pt (111) surface) of Pd@Pt_{nL} icosahedra using the Pt_{nL}^*/Pd(111) icosahedral slab models, denoted as Pt_{nL}*/Pd(111) icosahedra, at a tensile strain of 2.4% for the Pd surface. The result for Pt_{3L}*/Pd(111) octahedra is included for comparison, relative to the pure Pt(111) surface. Images in (c, d) were reprinted with permission from ref. [49]. Copyright (2015), Nature Publishing Group.

In addition, bimetallic nanocrystals with core–shell structure can serve as a model system to study the strain effect by tuning the shell thickness. The thinner the shell layers are, the stronger the strain effect is. Wang et al. prepared Pd@Pt core–shell nanocrystals with the shell thickness from 0.7 to 4.3 overlayers (Figure 4.16c,d)[49]. Interestingly, the core–shell nanocrystals with an average of 2.7 platinum overlayers, showed the highest ORR activity. DFT calculations indicate that the activity enhancement can be attributed to the weakened binding of hydroxyl to the compressed platinum surface supported on Pd. As the d-band center gets closer to the Fermi level of shell metals, the adsorption energy of formic acid on the metal surface will increase, leading to the high decomposition rate of formic acid. Therefore, volcano plots provide significant guidance to design bimetallic catalysts, whose d-band center locates just right on the maxima of catalytic activity. More endeavors should be centered on selecting the optimal combination of

metals, and engineering them to some theoretically prescribed composition, size, shape, and structure to optimize their catalytic performances.

4.6.2 Shape-Dependent Catalytic Reactions

The controlled synthesis of bimetallic nanocrystals not only significantly enhances the catalytic properties compared with that of monometallic nanocrystals but also is advantageous to the research of catalytic mechanism. Understanding the promotion effect of shape, size, composition, or bimetallic structure on catalytic behaviors, and constructing a volcano plot between catalytic activity and some adjustable parameters of bimetallic nanocrystals are crucial to the design of application-oriented robust catalysts. With the development of synthetic chemistry and the deep insight into catalytic mechanisms, bimetallic nanocrystals show great potentials in various industrially relevant applications. In this section, some typical bimetallic nanocrystals will be presented to elaborate the importance of controlled synthesis in some shape-dependent catalytic reactions.

4.6.2.1 Pt–Ni Nanocrystals for Oxygen Reduction Reaction

There have been many studies on optimizing Pt-based bimetallic nanocrystals for oxygen reduction reaction (ORR). Pure Pt catalyst has some disadvantages toward ORR, including high overpotential, atomic leaching, and low activity. Among Pt-based catalysts, Pt–Ni system with high ORR performance has been most widely investigated. For ORR, the barrier of the rate-determining step derives from the weak adsorption of oxygen and strong adsorption of OH species. Both the adsorption of O_2 and the desorption of OH are structure sensitive; thus, specific facets exposed with the optimized d-band center position are required. The Pt_3Ni alloy shows remarkably higher ORR activity than Pt, and the specific activities on its low-index facets exhibit an order of $Pt_3Ni\{100\} < Pt_3Ni\{111\}$[64]. Furthermore, Pt–Ni nanooctahedrons with the Pt-skin surface are typically high-efficiency catalysts[117]. In 2015, Huang et al. made a breakthrough on the specific activity and mass activity toward ORR by surface-doping on Pt–Ni nanoctahedrons[119]. A series of transition metals such as Cr, Mn, Fe, Co, Mo, W, and Re were introduced to form M-doped Pt_3Ni nanooctahedrons. Ultimately, Mo-doped Pt_3Ni nanooctahedrons exhibited 81-fold and 73-fold enhancement in specific activity and mass activity for ORR against a commercial Pt/C catalyst, respectively.

4.6.2.2 Pt–Pd Nanocrystals for Methanol Electrooxidation

The reaction routes of methanol electrooxidation (MOR) involve a direct path and an indirect path according to the absence or the existence of CO* as an intermediate, respectively. The surface of noble metals will be strongly adsorbed by CO, leading to a decreasing catalytic performance until complete deactivation, especially for the {100} facets. According to BEP relation, optimal adsorption strength of CO* species or transforming CO* to other species requires optimized d-band center position. For instance, twinned defects in multitwinned structure nanocrystals induce lattice strain to disturb the electronic structure of surface atoms, thus influencing the catalytic activity of bimetallic nanocrystals. Both Pt–Pd alloy nanoicosahedra (NIs) and nanotetrahedra (NTs) are enclosed by {111} facets, while the high density of twin-plane defects and high lattice strains contribute to higher MOR performance of Pt–Pd NIs than that of single-crystalline Pt–Pd NTs, as well as commercial Pt catalysts (Pt black and Pt/C)[62].

4.6.2.3 Au–Pd Nanocrystals for Suzuki Coupling Reaction

Suzuki coupling reaction refers to the cross-coupling of aryl halides with arylboronic acids to synthesize unsymmetrical biaryls, which have been extensively used in the synthesis of natural products, nucleoside analogues, and pharmaceuticals. Recently, Suzuki coupling reaction has been widely served as a model reaction to test the catalytic performance of Pd-based nanocrystals with various shapes. For example, Wang et al. designed and prepared two types of Pd nanoshells enclosed by high-index {730} and {221} facets through heteroepitaxial growth on high-index-faceted Au nanocrystals[100]. The turnover numbers per surface atom of the high-index faceted Pd shells have been found to be three to seven times higher than those of Pd and Au–Pd core–shell nanocubes that possess only {100} facets for the Suzuki coupling catalytic reaction. Yang et al. reported octahedral gold nanocrystal-directed overgrowth of Au@Pd core–shell heterostructures with fine control of particle shapes from octahedral to truncated octahedral, cubooctahedral, truncated cubic, and concave cubic structures[120]. Octahedrons and concave cubes were chosen to compare their catalytic activities. Both catalysts can serve as highly efficient and recyclable catalysts for the Suzuki coupling reaction. Concave cubes were found to be superior catalysts attributed to their exposed high index {730} facets.

4.7 Conclusions and Outlook

The controlled synthesis, characterization, and application of bimetallic nanocrystals have been dramatically developed toward maturity in recent years, which enhances their existing properties and endows them with novel properties. Continuous growth, seed-mediated growth, and UPD-coupled galvanic replacement reaction are typical routes in colloidal synthesis to prepare bimetallic NCs with well-defined shape, especially for nanospheres and nanopolyhedrons. Thermodynamics and kinetic factors, including reduction potential of metal precursors, lattice parameter, reduction rate, facet-specific capping agents, temperature, and reaction time, have a striking influence on the nucleation and growth of bimetallic nanocrystals. The resulting morphologies directly determine their physical and chemical properties. Building volcano-shape relationship between structure and properties facilitates application-oriented synthesis of bimetallic nanocrystals, which is one of the most fundamental motivations to develop the controlled synthesis of bimetallic nanocrystals. A vast set of bimetallic nanocrystals are well-suited for a broad range of applications. Understanding these syntheses and properties at a molecular level requires reliable experiments in harmony with theoretical simulation, and advanced characterization techniques.

The controlled synthesis of bimetallic nanocrystals in small reactors with limited volumes hardly meets the demand of industrial applications. Thus, there is no doubt that scaling up the production of the nanocrystals for industrial applications, together with keeping the original structures of bimetallic nanocrystals, will encounter unpredictable challenges. Another shortcoming of some bimetallic structures is their chemical and thermal instability during storage and catalytic reaction. Pt–M (M = non-noble metals) bimetallic nanocrystals are prone to compositional changes due to leaching and corrosion during the catalytic process.

The shape-controlled synthesis of Pt- and Pd-based nanocrystals has been deeply investigated, while the molecular-level understanding of the interactions between the functional

groups of capping agents and a specific facet should be coupled with DFT calculations. Atom resolution *in situ* characterization instruments is imperative to directly observe the shape evolution and facet reconstruction, as well as to explore surface chemistry and structure of bimetallic nanocrystals under synthetic conditions or catalytic process.

4.8 References

1 Gilroy, K. D., Ruditskiy, A., Peng, H.-C., Qin, D., Xia, Y. (2016). Bimetallic nanocrystals: syntheses, properties, and applications. *Chemical Reviews,* 116 (18), 10414–10472.

2 Zheng, J.-N., He, L.-L., Chen, F.-Y., Wang, A.-J., Xue, M.-W., Feng, J.-J. (2014). Simple one-pot synthesis of platinum-palladium nanoflowers with enhanced catalytic activity and methanol-tolerance for oxygen reduction in acid media. *Electrochimica Acta,* 137 431–438.

3 Liu, Y., Chi, M., Mazumder, V., More, K. L., Soled, S., Henao, J. D., Sun, S. (2011). Composition-controlled synthesis of bimetallic PdPt nanoparticles and their electro-oxidation of methanol. *Chemistry of Materials,* 23 (18), 4199–4203.

4 Cui, C., Gan, L., Li, H.-H., Yu, S.-H., Heggen, M., Strasser, P. (2012). Octahedral PtNi nanoparticle catalysts: exceptional oxygen reduction activity by tuning the alloy particle surface composition. *Nano Letters,* 12 (11), 5885–5889.

5 Jeyabharathi, C., Venkateshkumar, P., Mathiyarasu, J., Phani, K. L. N. (2008). Platinum–tin bimetallic nanoparticles for methanol tolerant oxygen-reduction activity. *Electrochimica Acta,* 54 (2), 448–454.

6 Wang, C., Chi, M., Li, D., van der Vliet, D., Wang, G., Lin, Q., F. Mitchell, J., More, K. L., Markovic, N. M., Stamenkovic, V. R. (2011). Synthesis of homogeneous Pt–bimetallic nanoparticles as highly efficient electrocatalysts. *ACS Catalysis,* 1 (10), 1355–1359.

7 Wu, H., Li, H., Zhai, Y., Xu, X., Jin, Y. (2012). Facile synthesis of free-standing Pd-based nanomembranes with enhanced catalytic performance for methanol/ethanol oxidation. *Advanced Materials,* 24 (12), 1594–1597.

8 Fu, S., Zhu, C., Du, D., Lin, Y. (2015). Facile one-step synthesis of three-dimensional Pd–Ag bimetallic alloy networks and their electrocatalytic activity toward ethanol oxidation. *ACS Applied Materials & Interfaces,* 7 (25), 13842–13848.

9 Wang, Q.-L., Fang, R., He, L.-L., Feng, J.-J., Yuan, J., Wang, A.-J. (2016). Bimetallic PdAu alloyed nanowires: rapid synthesis via oriented attachment growth and their high electrocatalytic activity for methanol oxidation reaction. *Journal of Alloys and Compounds,* 684, 379–388.

10 Dutta, S., Ray, C., Sarkar, S., Roy, A., Sahoo, R., Pal, T. (2015). Facile Synthesis of Bimetallic Au–Pt, Pd–Pt, and Au–Pd nanostructures: enhanced catalytic performance of Pd–Pt analogue towards fuel cell application and electrochemical sensing. *Electrochimica Acta,* 180 1075–1084.

11 Serna, P., Concepción, P., Corma, A. (2009). Design of highly active and chemoselective bimetallic gold–platinum hydrogenation catalysts through kinetic and isotopic studies. *Journal of Catalysis,* 265 (1), 19–25.

12 Cai, S., Duan, H., Rong, H., Wang, D., Li, L., He, W., Li, Y. (2013). Highly active and selective catalysis of bimetallic Rh3Ni1 nanoparticles in the hydrogenation of nitroarenes. *ACS Catalysis,* 3 (4), 608–612.

13 Guczi, L., Boskovic, G., Kiss, E. (2010). Bimetallic cobalt based catalysts. *Catalysis Reviews—Science and Engineering,* 52 (2), 133–203.

14 Zhang, L., Xie, Z., Gong, J. (2016). Shape-controlled synthesis of Au–Pd bimetallic nanocrystals for catalytic applications, *Chemical Society Reviews,* 45 (14), 3916–3934.

15 Major, K. J., De, C., Obare, S. O. (2009). Recent advances in the synthesis of plasmonic bimetallic nanoparticles. *Plasmonics,* 4 (1), 61–78.

16 Deng, Y.-J., Wiberg, G. K. H., Zana, A., Sun, S.-G., Arenz, M. (2017). Tetrahexahedral Pt nanoparticles: comparing the oxygen reduction reaction under transient vs steady-state conditions. *ACS Catalysis,* 7 (1), 1–6.

17 Sugimura, F., Nakamura, M., Hoshi, N. (2017). The oxygen reduction reaction on kinked stepped surfaces of Pt. *Electrocatalysis,* 8 (1), 46–50.

18 Zhang, L., Chen, D., Jiang, Z., Zhang, J., Xie, S., Kuang, Q., Xie, Z., Zheng, L. (2012). Facile syntheses and enhanced electrocatalytic activities of Pt nanocrystals with {hkk} high-index surfaces. *Nano Research,* 5 (3), 181–189.

19 Yu, N.-F., Tian, N., Zhou, Z.-Y., Huang, L., Xiao, J., Wen, Y.-H., Sun, S.-G. (2014). Electrochemical Synthesis of Tetrahexahedral Rhodium Nanocrystals with Extraordinarily High Surface Energy and High Electrocatalytic Activity. *Angewandte Chemie International Edition,* 53 (20), 5097–5101.

20 Lee, H.-E., Yang, K. D., Yoon, S. M., Ahn, H.-Y., Lee, Y. Y., Chang, H., Jeong, D. H., Lee, Y.-S., Kim, M. Y., Nam, K. T. (2015). Concave rhombic dodecahedral Au nanocatalyst with multiple high-index facets for CO_2 reduction. *ACS Nano,* 9 (8), 8384–8393.

21 Huang, M. H., Rej, S., Hsu, S.-C. (2014). Facet-dependent properties of polyhedral nanocrystals. *Chemical Communications,* 50 (14), 1634–1644.

22 Huang, M. H., Lin, P.-H. (2012). Shape-controlled synthesis of polyhedral nanocrystals and their facet-dependent properties. *Advanced Functional Materials,* 22 (1), 14–24.

23 Casado-Rivera, E., Volpe, D. J., Alden, L., Lind, C., Downie, C., Vázquez-Alvarez, T., Angelo, A. C. D., DiSalvo, F. J., Abruña, H. D. (2004). Electrocatalytic activity of ordered intermetallic phases for fuel cell applications. *Journal of the American Chemical Society,* 126 (12), 4043–4049.

24 Chung, D. Y., Jun, S. W., Yoon, G., Kwon, S. G., Shin, D. Y., Seo, P., Yoo, J. M., Shin, H., Chung, Y.-H., Kim, H., Mun, B. S., Lee, K.-S., Lee, N.-S., Yoo, S. J., Lim, D.-H., Kang, K., Sung, Y.-E., Hyeon, T. (2015). Highly durable and active PtFe nanocatalyst for electrochemical oxygen reduction reaction. *Journal of the American Chemical Society,* 137 (49), 15478–15485.

25 Abe, H., Matsumoto, F., Alden, L. R., Warren, S. C., Abruña, H. D., DiSalvo, F. J. (2008). Electrocatalytic performance of fuel oxidation by Pt3Ti nanoparticles. *Journal of the American Chemical Society,* 130 (16), 5452–5458.

26 Wang, C., Chi, M., Li, D., Strmcnik, D., van der Vliet, D., Wang, G., Komanicky, V., Chang, K.-C., Paulikas, A. P., Tripkovic, D., Pearson, J., More, K. L., Markovic, N. M., Stamenkovic, V. R. (2011). Design and synthesis of bimetallic electrocatalyst with multilayered Pt-skin surfaces. *Journal of the American Chemical Society,* 133 (36), 14396–14403.

27 Yan, Y., Du, J. S., Gilroy, K. D., Yang, D., Xia, Y., Zhang, H. (2017). Intermetallic nanocrystals: syntheses and catalytic applications. *Advanced Materials,* 1605997-n/a.

28 Kang, Y. J., Pyo, J. B., Ye, X. C., Gordon, T. R., Murray, C. B. (2012). Synthesis, shape control, and methanol electro-oxidation properties of Pt–Zn alloy and Pt_3Zn intermetallic nanocrystals. *ACS Nano,* 6 (6), 5642–5647.

29 Vicente, A., Lafaye, G., Especel, C., Marécot, P., Williams, C. T. (2011). The relationship between the structural properties of bimetallic Pd–Sn/SiO_2 catalysts and their performance for selective citral hydrogenation. *Journal of Catalysis,* 283 (2), 133–142.

30 Wang, X.-L., Feygenson, M., Chen, H., Lin, C.-H., Ku, W., Bai, J., Aronson, M. C., Tyson, T. A., Han, W.-Q. (2011). Nanospheres of a new intermetallic FeSn5 phase: synthesis, magnetic properties and anode performance in li-ion batteries. *Journal of the American Chemical Society,* 133 (29), 11213–11219.

31 Xin, F., Wang, X., Bai, J., Wen, W., Tian, H., Wang, C., Han, W. (2015). A lithiation/delithiation mechanism of monodispersed MSn_5 (M = Fe, Co and FeCo) nanospheres. *Journal of Materials Chemistry A,* 3 (13), 7170–7178.

32 Hou, S., Hu, X., Wen, T., Liu, W., Wu, X. (2013). Core–shell noble metal nanostructures templated by gold nanorods. *Advanced Materials,* 25 (28), 3857–3862.

33 Zhang, Y., Bu, L., Jiang, K., Guo, S., Huang, X. (2016). Concave Pd–Pt core–shell nanocrystals with ultrathin Pt shell feature and enhanced catalytic performance. *Small,* 12 (6), 706–712.

34 Park, J.-I., Cheon, J. (2001). Synthesis of "solid solution" and "core–shell" type cobalt – platinum magnetic nanoparticles via transmetalation reactions. *Journal of the American Chemical Society,* 123 (24), 5743–5746.

35 Alayoglu, S., Nilekar, A. U., Mavrikakis, M., Eichhorn, B. (2008). Ru–Pt core–shell nanoparticles for preferential oxidation of carbon monoxide in hydrogen. *Nature Materials,* 7 (4), 333–338.

36 Zhou, S., Varughese, B., Eichhorn, B., Jackson, G., McIlwrath, K. (2005). Pt–Cu core–shell and alloy nanoparticles for heterogeneous NO_x reduction: anomalous stability and reactivity of a core–shell nanostructure. *Angewandte Chemie International Edition,* 44 (29), 4539–4543.

37 Alayoglu, S., Eichhorn, B. (2008). Rh – Pt bimetallic catalysts: synthesis, characterization, and catalysis of core – shell, alloy, and monometallic nanoparticles. *Journal of the American Chemical Society,* 130 (51), 17479–17486.

38 Bhattarai, N., Casillas, G., Khanal, S., Salazar, J. J. V., Ponce, A., Jose-Yacaman, M. (2013). Origin and shape evolution of core–shell nanoparticles in Au–Pd: from few atoms to high Miller index facets. *Journal of Nanoparticle Research,* 15 (6), 1660.

39 Park, J., Zhang, L., Choi, S.-I., Roling, L. T., Lu, N., Herron, J. A., Xie, S., Wang, J., Kim, M. J., Mavrikakis, M., Xia, Y. (2015). Atomic layer-by-layer deposition of platinum on palladium octahedra for enhanced catalysts toward the oxygen reduction reaction. *ACS Nano,* 9 (3), 2635–2647.

40 Kristian, N., Wang, X. (2008). Pt shell–Au core/C electrocatalyst with a controlled shell thickness and improved Pt utilization for fuel cell reactions, *Electrochemistry Communications,* 10 (1), 12–15.

41 Yan, S., Zhang, S. (2012). Methanol electrooxidation on carbon supported Au core–Pt shell nanoparticles synthesized by an epitaxial growth method, *International Journal of Hydrogen Energy,* 37 (12), 9636–9644.

42 Higuchi, E., Hayashi, K., Chiku, M., Inoue, H. (2012). Simple Preparation of Au Nanoparticles and THEIR APPLICATION to Au core/Pt shell catalysts for oxygen reduction reaction. *Electrocatalysis,* 3 (3), 274–283.

43 Zhai, J., Huang, M., Dong, S. (2007). Electrochemical designing of Au/Pt core shell nanoparticles as nanostructured catalyst with tunable activity for oxygen reduction. *Electroanalysis,* 19 (4), 506–509.

44 Kuai, L., Geng, B., Wang, S., Sang, Y. (2012). A general and high-yield galvanic displacement approach to Au–M (M = Au, Pd, and Pt) core–shell nanostructures with porous shells and enhanced electrocatalytic performances. *Chemistry–A European Journal,* 18 (30), 9423–9429.

45 Liu, Z., Jackson, G. S., Eichhorn, B. W. (2010). PtSn intermetallic, core–shell, and alloy nanoparticles as CO-tolerant electrocatalysts for H_2 oxidation. *Angewandte Chemie International Edition,* 49 (18), 3173–3176.

46 Heggen, M., Oezaslan, M., Houben, L., Strasser, P. (2012). Formation and analysis of core–shell fine structures in Pt bimetallic nanoparticle fuel cell electrocatalysts. *The Journal of Physical Chemistry C,* 116 (36), 19073–19083.

47 Gan, L., Heggen, M., Rudi, S., Strasser, P. (2012). Core–shell compositional fine structures of dealloyed Pt_xNi_{1-x} nanoparticles and their impact on oxygen reduction catalysis. *Nano Letters,* 12 (10), 5423–5430.

48 Oezaslan, M., Hasché, F., Strasser, P. (2013). Pt-based core–shell catalyst architectures for oxygen fuel cell electrodes. *The Journal of Physical Chemistry Letters,* 4 (19), 3273–3291.

49 Wang, X., Choi, S.-I., Roling, L. T., Luo, M., Ma, C., Zhang, L., Chi, M., Liu, J., Xie, Z., Herron, J. A., Mavrikakis, M., Xia, Y. (2015). Palladium–platinum core–shell icosahedra with substantially enhanced activity and durability towards oxygen reduction. *Nature Communications,* 6 7594.

50 Ma, Y., Li, W., Cho, E. C., Li, Z., Yu, T., Zeng, J., Xie, Z., Xia, Y. (2010). Au@Ag core – shell nanocubes with finely tuned and well-controlled sizes, shell thicknesses, and optical properties. *ACS Nano,* 4 (11), 6725–6734.

51 Dupas, C., Houdy, P., Lahmani, M. (2007). Nanoscience: nanotechnologies and nanophysics. Berlin: Springer-Verlag.

52 LaMer, V. K., Dinegar, R. H. (1950). Theory, production and mechanism of formation of monodispersed hydrosols. *Journal of the American Chemical Society,* 72 (11), 4847–4854.

53 Xia, Y., Xiong, Y., Lim, B., Skrabalak, S. E. (2009). Shape-controlled synthesis of metal nanocrystals: simple chemistry meets complex physics? *Angewandte Chemie International Edition,* 48 (1), 60–103.

54 Müller, M., Albe, K. (2007). Structural stability of multiply twinned FePt nanoparticles. *Acta Materialia,* 55 (19), 6617–6626.

55 Peng, X., Wickham, J., Alivisatos, A. P. (1998). Kinetics of II-VI and III-V colloidal semiconductor nanocrystal growth: "focusing" of size distributions. *Journal of the American Chemical Society,* 120 (21), 5343–5344.

56 Thessing, J., Qian, J., Chen, H., Pradhan, N., Peng, X. (2007). Interparticle influence on size/size distribution evolution of nanocrystals. *Journal of the American Chemical Society,* 129 (10), 2736–2737.

57 Langille, M. R., Personick, M. L., Zhang, J., Mirkin, C. A. (2012). Defining rules for the shape evolution of gold nanoparticles. *Journal of the American Chemical Society,* 134 (35), 14542–14554.

58 Wang, Z. L. (2000). Transmission electron microscopy of shape-controlled nanocrystals and their assemblies. *The Journal of Physical Chemistry B,* 104 (6), 1153–1175.

59 Zhang, Q., Han, L., Jing, H., Blom, D. A., Lin, Y., Xin, H. L., Wang, H. (2016). Facet control of gold nanorods. *ACS Nano,* 10 (2), 2960–2974.

60 Tao, A., Sinsermsuksakul, P., Yang, P. (2006). Polyhedral silver nanocrystals with distinct scattering signatures. *Angewandte Chemie International Edition,* 45 (28), 4597–4601.

61 Yin, A.-X., Min, X.-Q., Zhang, Y.-W., Yan, C.-H. (2011). Shape-selective synthesis and facet-dependent enhanced electrocatalytic activity and durability of monodisperse Sub-10 nm Pt – Pd tetrahedrons and cubes. *Journal of the American Chemical Society,* 133 (11), 3816–3819.

62 Yin, A.-X., Min, X.-Q., Zhu, W., Wu, H.-S., Zhang, Y.-W., Yan, C.-H. (2012). Multiply twinned Pt–Pd nanoicosahedrons as highly active electrocatalysts for methanol oxidation. *Chemical Communications,* 48 (4), 543–545.

63 Chen, C., Kang, Y., Huo, Z., Zhu, Z., Huang, W., Xin, H. L., Snyder, J. D., Li, D., Herron, J. A., Mavrikakis, M., Chi, M., More, K. L., Li, Y., Markovic, N. M., Somorjai, G. A., Yang, P., Stamenkovic, V. R. (2014). Highly crystalline multimetallic nanoframes with three-dimensional electrocatalytic surfaces. *Science,* 343 (6177), 1339.

64 Zhang, J., Yang, H., Fang, J., Zou, S. (2010). Synthesis and oxygen reduction activity of shape-controlled Pt_3Ni nanopolyhedra. Nano *Letters,* 10 (2), 638–644.

65 Mourdikoudis, S., Liz-Marzán, L. M. (2013). Oleylamine in nanoparticle synthesis. *Chemistry of Materials,* 25 (9), 1465–1476.

66 Li, L., Hu, F., Xu, D., Shen, S., Wang, Q. (2012). Metal ion redox potential plays an important role in high-yield synthesis of monodisperse silver nanoparticles. *Chemical Communications,* 48 (39), 4728–4730.

67 Lohse, S. E., Burrows, N. D., Scarabelli, L., Liz-Marzán, L. M., Murphy, C. J. (2014). Anisotropic noble metal nanocrystal growth: the role of halides. *Chemistry of Materials,* 26 (1), 34–43.

68 Berhault, G., Bausach, M., Bisson, L., Becerra, L., Thomazeau, C., Uzio, D. (2007). Seed-mediated synthesis of Pd nanocrystals: Factors influencing a kinetic- or thermodynamic-controlled growth regime. *The Journal of Physical Chemistry C,* 111 (16), 5915–5925.

69 Zhou, M., Wang, H., Vara, M., Hood, Z. D., Luo, M., Yang, T.-H., Bao, S., Chi, M., Xiao, P., Zhang, Y., Xia, Y. (2016). Quantitative analysis of the reduction kinetics responsible for the one-pot synthesis of Pd–Pt bimetallic nanocrystals with different structures. *Journal of the American Chemical Society,* 138 (37), 12263–12270.

70 Obradović, M. D., Grgur, B. N., Gojković, S. L., Vračar, L. M. (2007). Enhancement of the electrochemical reduction of oxygen at platinum by nickel underpotential deposition. *Journal of Solid State Electrochemistry,* 11 (1), 77–83.

71 Bakos, I., Szabó, S., Pajkossy, T. (2011). Deposition of platinum monolayers on gold. *Journal of Solid State Electrochemistry,* 15 (11), 2453–2459.

72 Yu, Y., Hu, Y., Liu, X., Deng, W., Wang, X. (2009). The study of Pt@Au electrocatalyst based on Cu underpotential deposition and Pt redox replacement. *Electrochimica Acta,* 54 (11), 3092–3097.

73 Lee, Y. W., Kim, M., Kim, Z. H., Han, S. W. (2009). One-step synthesis of Au@Pd core – shell nanooctahedron. *Journal of the American Chemical Society,* 131 (47), 17036–17037.

74 Hong, J. W., Kim, D., Lee, Y. W., Kim, M., Kang, S. W., Han, S. W. (2011). Atomic-distribution-dependent electrocatalytic activity of Au–Pd bimetallic nanocrystals. *Angewandte Chemie International Edition,* 50 (38), 8876–8880.

75 Yao, Y., He, D. S., Lin, Y., Feng, X., Wang, X., Yin, P., Hong, X., Zhou, G., Wu, Y., Li, Y. (2016). Modulating fcc and hcp ruthenium on the surface of palladium–copper alloy through tunable lattice mismatch. *Angewandte Chemie International Edition,* 55 (18), 5501–5505.

76 Tabatabaei, S., Sadrnezhaad, S. K. (2014). Facile synthesis of monodisperse thermally immiscible Ag–Ni alloy nanoparticles at room temperature. *Bulletin of Materials Science,* 37 (6), 1447–1452.

77 Long, N. V., Duy Hien, T., Asaka, T., Ohtaki, M., Nogami, M. (2011). Synthesis and characterization of Pt–Pd alloy and core–shell bimetallic nanoparticles for direct methanol fuel cells (DMFCs): enhanced electrocatalytic properties of well-shaped core–shell morphologies and nanostructures, *International Journal of Hydrogen Energy,* 36 (14), 8478–8491.

78 Xu, W., Niu, J., Shang, H., Shen, H., Ma, L., Li, L. S. (2013). Facile synthesis of AgAu alloy and core/shell nanocrystals by using Ag nanocrystals as seeds. *Gold Bulletin,* 46 (1), 19–23.

79 Fan, F.-R., Liu, D.-Y., Wu, Y.-F., Duan, S., Xie, Z.-X., Jiang, Z.-Y., Tian, Z.-Q. (2008). Epitaxial growth of heterogeneous metal nanocrystals: from gold nano-octahedra to palladium and silver nanocubes. *Journal of the American Chemical Society,* 130 (22), 6949–6951.

80 Jin, M., Zhang, H., Wang, J., Zhong, X., Lu, N., Li, Z., Xie, Z., Kim, M. J., Xia, Y. (2012). Copper can still be epitaxially deposited on palladium nanocrystals to generate core–shell nanocubes despite their large lattice mismatch. *ACS Nano,* 6 (3), 2566–2573.

81 Tsuji, M., Yamaguchi, D., Matsunaga, M., Alam, M. J. (2010). Epitaxial growth of Au@ Cu core – shell nanocrystals prepared using the PVP-assisted polyol reduction method. *Crystal Growth & Design,* 10 (12), 5129–5135.

82 Tsuji, M., Yamaguchi, D., Matsunaga, M., Ikedo, K. (2011). Epitaxial growth of Au@Ni core – shell nanocrystals prepared using a two-step reduction method. *Crystal Growth & Design,* 11 (5), 1995–2005.

83 Satyavolu, N. S. R., Tan, L. H., Lu, Y. (2016). DNA-mediated morphological control of Pd–Au bimetallic nanoparticles. *Journal of the American Chemical Society,* 138 (50), 16542–16548.

84 Wu, Y., Cai, S., Wang, D., He, W., Li, Y. (2012). Syntheses of water-soluble octahedral, truncated octahedral, and cubic Pt–Ni nanocrystals and their structure–activity study in model hydrogenation reactions. *Journal of the American Chemical Society,* 134 (21), 8975–8981.

85 Wang, S.-B., Zhu, W., Ke, J., Lin, M., Zhang, Y.-W. (2014). Pd–Rh nanocrystals with tunable morphologies and compositions as efficient catalysts toward Suzuki cross-coupling reactions. *ACS Catalysis,* 4 (7), 2298–2306.

86 Huang, X., Li, Y., Li, Y., Zhou, H., Duan, X., Huang, Y. (2012). Synthesis of PtPd bimetal nanocrystals with controllable shape, composition, and their tunable catalytic properties. Nano *Letters,* 12 (8), 4265–4270.

87 Lim, B., Wang, J., Camargo, P. H. C., Cobley, C. M., Kim, M. J., Xia, Y. (2009). Twin-induced growth of palladium-platinum alloy nanocrystals. *Angewandte Chemie International Edition,* 48 (34), 6304–6308.

88 Yan, Y., Zhan, F., Du, J., Jiang, Y., Jin, C., Fu, M., Zhang, H., Yang, D. (2015). Kinetically-controlled growth of cubic and octahedral Rh–Pd alloy oxygen reduction electrocatalysts with high activity and durability. *Nanoscale,* 7 (1), 301–307.

89 Zhang, J., Fang, J. (2009). A general strategy for preparation of Pt 3d-transition metal (Co, Fe, Ni). *Nanocubes. Journal of the American Chemical Society,* 131 (51), 18543–18547.

90 Bönnemann, H., Brand, R. A., Brijoux, W., Hofstadt, H. W., Frerichs, M., Kempter, V., Maus-Friedrichs, W., Matoussevitch, N., Nagabhushana, K. S., Voigts, F., Caps, V. (2005). Air stable Fe and Fe–Co magnetic fluids—synthesis and characterization. *Applied Organometallic Chemistry,* 19 (6), 790–796.

91 Lanza, R., Bersani, M., Conte, L., Martucci, A., Canu, P., Guglielmi, M., Mattei, G., Bello, V., Centazzo, M., Rosei, R. (2014). Effect of crystalline phase and composition on the catalytic properties of PdSn bimetallic nanoparticles in the PROX reaction. *The Journal of Physical Chemistry C,* 118 (44), 25392–25402.

92 Son, S. U., Jang, Y., Park, J., Na, H. B., Park, H. M., Yun, H. J., Lee, J., Hyeon, T. (2004). Designed synthesis of atom-economical Pd/Ni bimetallic nanoparticle-based catalysts for sonogashira coupling reactions. *Journal of the American Chemical Society,* 126 (16), 5026–5027.

93 Robinson, I., Zacchini, S., Tung, L. D., Maenosono, S., Thanh, N. T. K. (2009). Synthesis and characterization of magnetic nanoalloys from bimetallic carbonyl clusters. *Chemistry of Materials,* 21 (13), 3021–3026.

94 Chen, M., Kim, J., Liu, J. P., Fan, H., Sun, S. (2006). Synthesis of FePt nanocubes and their oriented self-assembly. *Journal of the American Chemical Society,* 128 (22), 7132–7133.

95 Zhang, Z., Lagally, M. G. (1997). Atomistic processes in the early stages of thin-film growth. *Science,* 276 (5311), 377.

96 Xia, X., Xie, S., Liu, M., Peng, H. C., Lu, N., Wang, J., Kim, M. J., Xia, Y. (2013). On the role of surface diffusion in determining the shape or morphology of noble-metal nanocrystals. *Proceedings of the National Academy of Sciences,* 110 (17), 6669–6673.

97 Habas, S. E., Lee, H., Radmilovic, V., Somorjai, G. A., Yang, P. (2007). Shaping binary metal nanocrystals through epitaxial seeded growth. *Nature Materials,* 6 (9), 692–697.

98 Tsuji, M., Nakamura, N., Ogino, M., Ikedo, K., Matsunaga, M. (2012). Crystal structures and growth mechanisms of octahedral and decahedral Au@Ag core–shell nanocrystals prepared by a two-step reduction method. *Crystengcomm,* 14 (22), 7639.

99 Bian, T., Zhang, H., Jiang, Y., Jin, C., Wu, J., Yang, H., Yang, D. (2015). Epitaxial growth of twinned Au–Pt core–shell star-shaped decahedra as highly durable electrocatalysts. *Nano Letters,* 15 (12), 7808–7815.

100 Wang, F., Li, C., Sun, L.-D., Wu, H., Ming, T., Wang, J., Yu, J. C., Yan, C.-H. (2011). Heteroepitaxial growth of high-index-faceted palladium nanoshells and their catalytic performance. *Journal of the American Chemical Society,* 133 (4), 1106–1111.

101 Tsuji, M., Ogino, M., Matsunaga, M., Miyamae, N., Matsuo, R., Nishio, M., Alam, M. J. (2010). Crystal structures and growth mechanisms of icosahedral Au@Ag core–shell and Au/Ag twin nanocrystals prepared by PVP-assisted N,N-dimethylformamide reduction. *Crystal Growth & Design,* 10 (9), 4085–4090.

102 Lu, C.-L., Prasad, K. S., Wu, H.-L., Ho, J.-a. A., Huang, M. H. (2010). Au nanocube-directed fabrication of Au – Pd core – shell nanocrystals with tetrahexahedral, concave octahedral, and octahedral structures and their electrocatalytic activity. *Journal of the American Chemical Society,* 132 (41), 14546–14553.

103 Herrero, E., Buller, L. J., Abruña, H. D. (2001). Underpotential deposition at single crystal surfaces of Au, Pt, Ag and other materials. *Chemical Reviews,* 101 (7), 1897–1930.

104 Wang, D., Peng, Q., Li, Y. (2010). Nanocrystalline intermetallics and alloys. *Nano Research,* 3 (8), 574–580.

105 Zhang, L., Zhang, J., Kuang, Q., Xie, S., Jiang, Z., Xie, Z., Zheng, L. (2011). Cu2 + - assisted synthesis of hexoctahedral Au–Pd alloy nanocrystals with high-index facets. *Journal of the American Chemical Society,* 133 (43), 17114–17117.

106 Sasaki, K., Naohara, H., Cai, Y., Choi, Y. M., Liu, P., Vukmirovic, M. B., Wang, J. X., Adzic, R. R. (2010). Core-protected platinum monolayer shell high-stability electrocatalysts for fuel-cell cathodes. *Angewandte Chemie International Edition,* 49 (46), 8602–8607.

107 Xing, Y., Cai, Y., Vukmirovic, M. B., Zhou, W.-P., Karan, H., Wang, J. X., Adzic, R. R. (2010). Enhancing oxygen reduction reaction activity via Pd – Au alloy sublayer mediation of Pt monolayer electrocatalysts. *The Journal of Physical Chemistry Letters,* 1 (21), 3238–3242.

108 Yu, Y., Zhang, Q., Yao, Q., Xie, J., Lee, J. Y. (2013). Guiding principles in the galvanic replacement reaction of an underpotentially deposited metal layer for site-selective deposition and shape and size control of satellite nanocrystals. *Chemistry of Materials,* 25 (23), 4746–4756.

109 Yu, Y., Zhang, Q., Yao, Q., Xie, J., Lee, J. Y. (2014). Architectural design of heterogeneous metallic nanocrystals—principles and processes. *Accounts of Chemical Research,* 47 (12), 3530–3540.

110 Sabatier, P. (1911). Hydrogénations et déshydrogénations par catalyse, *Berichte der deutschen chemischen Gesellschaft,* 44 (3), 1984–2001.

111 Balandin, A. A. (1969). Modern state of the multiplet theor of heterogeneous catalysis. *Advances in Catalysis,* 19, 1–210.

112 Chen, M., Kumar, D., Yi, C.-W., Goodman, D. W. (2005). The promotional effect of gold in catalysis by palladium-gold. *Science,* 310 (5746), 291.

113 Hammer, B., Nörskov, J. K. (1995). Why gold is the noblest of all the metals. *Nature,* 376 (6537), 238–240.

114 Nilsson, A., Pettersson, L. G. M., Hammer, B., Bligaard, T., Christensen, C. H., Nörskov, J. K. (2005). The electronic structure effect in heterogeneous catalysis. *Catalysis Letters,* 100 (3–4), 111–114.

115 Xin, H., Holewinski, A., Schweitzer, N., Nikolla, E., Linic, S. (2012). Electronic structure engineering in heterogeneous catalysis: identifying novel alloy catalysts based on rapid screening for materials with desired electronic properties. *Topics in Catalysis,* 55 (5–6), 376–390.

116 Hwang, S. J., Kim, S.-K., Lee, J.-G., Lee, S.-C., Jang, J. H., Kim, P., Lim, T.-H., Sung, Y.-E., Yoo, S. J. (2012). Role of electronic perturbation in stability and activity of Pt-based alloy nanocatalysts for oxygen reduction. *Journal of the American Chemical Society,* 134 (48), 19508–19511.

117 Stamenkovic, V. R., Fowler, B., Mun, B. S., Wang, G., Ross, P. N., Lucas, C. A., Marković, N. M. (2007). Improved oxygen reduction activity on $Pt_3Ni(111)$ via increased surface site availability. *Science,* 315 (5811), 493–497.

118 Adzic, R. R., Zhang, J., Sasaki, K., Vukmirovic, M. B., Shao, M., Wang, J. X., Nilekar, A. U., Mavrikakis, M., Valerio, J. A., Uribe, F. (2007). Platinum monolayer fuel cell electrocatalysts. *Topics in Catalysis,* 46 (3–4), 249–262.

119 Huang, X., Zhao, Z., Cao, L., Chen, Y., Zhu, E., Lin, Z., Li, M., Yan, A., Zettl, A., Wang, Y. M., Duan, X., Mueller, T., Huang, Y. (2015). High-performance transition metal–doped Pt_3Ni octahedra for oxygen reduction reaction. *Science,* 348 (6240), 1230.

120 Yang, C.-W., Chanda, K., Lin, P.-H., Wang, Y.-N., Liao, C.-W., Huang, M. H. (2011). Fabrication of Au–Pd core–shell heterostructures with systematic shape evolution using octahedral nanocrystal cores and their catalytic activity. *Journal of the American Chemical Society,* 133 (49), 19993–20000.

5

Bimetallic Convex and Concave Nanostructures

Shaojie Jiang[1], Yiliang Luan[1], Xiaokun Fan[2], Zewei Quan[2], and Jiye Fang[1]

[1] *Department of Chemistry, State University of New York at Binghamton, New York, USA*
[2] *Department of Chemistry, Southern University of Science and Technology, Shenzhen, Guangdong, P. R. China*

5.1 Introduction

Noble metal is a generic term of some peculiar metal elements, including but not limited to palladium (Pd), silver (Ag), gold (Au), and platinum (Pt). For their unique physical and/or chemical characteristics, noble metal nanocrystals (NCs) have been used in many fields, such as catalysis, electronics, photonics, energy conversion, sensing, and biomedicine. For examples, through the localized surface plasmon resonance (LSPR), changing the shape of Au or Ag NCs could modify the collective oscillation of free electrons in the NCs in response to the oscillating electric field of the incident light; Pt and Pt-based alloys are significant catalysts, particularly in the oxygen reduction reaction (ORR) and direct oxidation of small fuel molecules in proton-exchange membrane fuel cells (PEMFCs), and in fine organic syntheses; Pd is also the primary catalyst in many industrial applications, such as the reduction of automobile emission and many organic reactions.

Although these metals have enormous advantages, as precious resources, especially Pt, they are scarce, imposing serious limitations to many industry-scale applications. The abundance of noble metals in earth's crust is extremely low. With the increasing demand for applications, their prices are raised quickly as well. To tackle this issue, various strategies have been proposed to reduce the usage of these precious metals, including a full replacement and partial replacement of them. In recent years, it was also realized that bimetallic NCs that are generated by alloying a less expensive transition metal into a noble metal NC could not only reduce the use of noble metal but also improve their catalytic[1–4] and electrocatalytic[5–7] performance due to the modified surface electronic structure[8,9]. Therefore, control of the composition (especially the surface composition) of alloy NCs becomes an important strategy to tune their physical and chemical behaviors in a number of applications including catalytic, electrocatalytic and Surface-Enhanced Raman Scattering (SERS) performance.

Optimization of shape and size of metallic NCs is another strategy to maximize their utilization efficiency. Since the ratio of surface atoms to total atoms in an NC increases as NC size decreases, reducing the size of NCs will increase the fraction of surface

Bimetallic Nanostructures: Shape-Controlled Synthesis for Catalysis, Plasmonics, and Sensing Applications, First Edition. Edited by Ya-Wen Zhang.
© 2018 John Wiley & Sons Ltd. Published 2018 by John Wiley & Sons Ltd.

(as well as sub-surface) atoms as reactive sites to improve reactive activity. However, a continuous decrease of the size of an NC is not feasible. For instance, in the case of catalysis, extremely minimizing the catalyst size to hundreds of atoms or less (typically, < 1 nm in diameter) will result in a loss of certain properties associated with catalyst's crystallinity. In addition, catalysts in ultra-small sizes will raise a new problem during its regeneration and recovery, significantly decreasing its usable lifetime. To balance the size limitation, manipulation of particle shape is an alternative route to improve the atomic arrangement on surfaces. High-index facets {*hkl*}, in which at least one index is greater than unity contain a high density of low-coordinated atoms that could be acted as catalytically active sites and exist in the forms of steps, edges, corners, and kinks. Metallic convex or concave NCs usually provide a high fraction of high-index cryptographic facets.

Practically, these composition-, size-, and shape-controlled bimetallic NCs are very promising over a spectrum of applications. For example, alloyed Pt–M (M is a 3d-transition metal) NCs have demonstrated dramatic activity enhancement in electrocatalysis and organic catalytic reactions. Such a superb performance can be attributed to a surface electronic structure modification from the bimetallic synergetic effect (composition control) and surface atomic arrangement improvement (shape control), which is associated with the selected crystallographic facets exposed on the particle surface and possible lattice strain effect. In the aspect of composition control the charge transfer between the surface Pt and sublayer **M** atoms could downshift the d-band center of Pt[10,11], resulting in weaker bonding strength between Pt and oxygenated species; whereas in the shape control a selected lattice plane with certain atomic density possesses a specific surface energy, which could reach the work function required for catalytic adsorption/desorption. Meanwhile, Pt atoms on a bimetallic NC surface could be "compressed" due to the smaller atomic radius of **M**. Such a local distortion, that is *lattice strain,* results in a local lattice change, leading to an alternation of surface function as well[12,13].

It has been reported that high-indexed metallic NCs possess a high density of low-coordinated atoms, steps, edges, tips, corners, and kinks, and can serve as hot spots where the electromagnetic field is focused and also as more active catalytic sites. Convex and concave NCs are generally the most common morphologies that provide high-index facets. This chapter starts with a brief review of the recent progress of bimetallic concave and convex NC syntheses, in which several synthetic approaches such as galvanic replacement, coreduction, and seed-mediated growth are outlined. Then, classification and characterization of these metallic convex and concave NCs with some typical case studies are described. In the last section, some relevant properties such as optical, electrocatalytic, and chemical catalytic behavior are selected, and the relationship between their unique property and associated lattice plane is discussed as well.

5.2 Synthetic Methods

The preparation of bimetallic convex and concave NCs can follow the similar strategies that are used for the synthesis of other polyhedral with a precise shape control. As outlined by Tao et al., the synthesis of shape-controlled bimetallic NCs can be summarized in four routes, including continuous growth, crystallites coalescence, seeded growth,

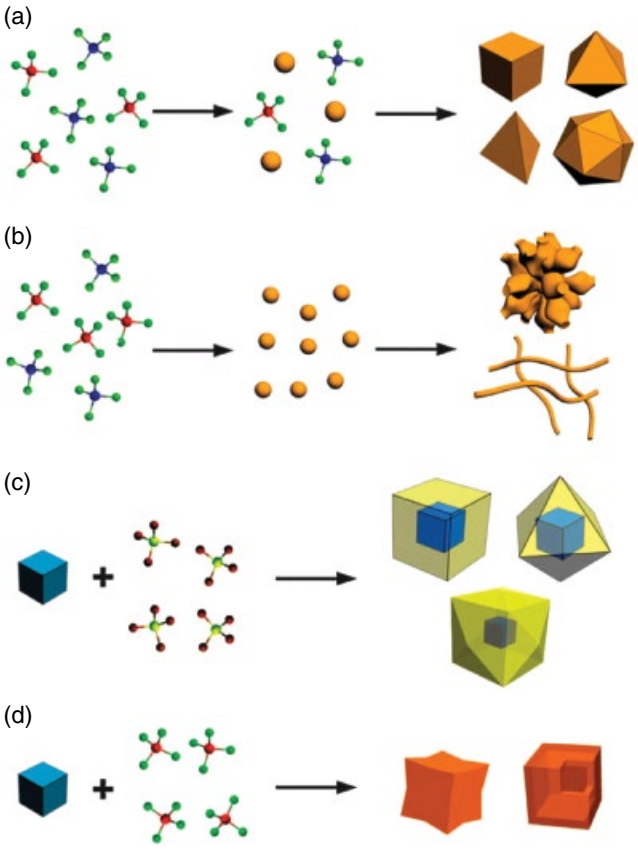

Figure 5.1 Four routes toward shape-controlled bimetallic nanocrystals: (a), continuous growth; (b), crystallites coalescence; (c), seeded growth; and (d), galvanic replacement reaction. Adapted with permission from ref. [14]. Copyright (2012), Royal Society of Chemistry.

and galvanic replacement reaction (Figure 5.1)[14]. To achieve a desired concave or convex structure, some kinetic and thermodynamic conditions (e.g., temperature, reagent ratio, capping ligands) have to be satisfied in order to tune the nucleation and successive growth processes in addition to performance of a traditional synthetic reaction, such as galvanic replacement, coreduction, selective etching, and seed-mediated growth. Thanks to the great exploration from many research groups, there is an extensive collection of literature in describing the synthetic protocols for generating bimetallic convex and concave nano-architectures with specific properties. In this section, we only focus on the most commonly practiced synthetic approaches.

5.2.1 Synthesis of Bimetallic Concave Structures

Usually, a bimetallic concave NC is enclosed by high-index facets that possess a high surface energy. It was determined that the concave structures are kinetically favorable products. As a fundamental starting point, H. Zhang et al. have discussed such a structure of noble metals in evolution processes of both dissolution, and overgrowth[15].

Table 5.1 presents some possible dissolution directions to generate concave NCs of noble metals from different template polyhedra, such as cubes, octahedra, and tetrahedra. These possible dissolution directions include <100>, <111>, and their "combined" directions <100> + <110> and <110> + <111>. Experimentally, it was observed that only these dissolution directions could lead to a formation of concave NCs, depending on their dissolution rate competition. Dissolution on facets such as {110}, {100} + {111}, and {100} + {110} + {111} is not a favorable way to achieve concave surfaces[15]. The other way to achieve concave NCs is an overgrowth process. Generally speaking, all the concave NCs generated through dissolution can be reversely produced using an overgrowth strategy by tuning the growth rate in each crystallographic direction as shown in Table 5.2. It is worth mentioning that a dissolution process normally generates concave structures with rounded vertices, whereas an overgrowth-based method usually results in faceted, concave structures[15]. Both types of products could possess the same symmetry but different shape profiles. The evolution of bimetallic concave NCs is quite similar to those already discussed, except for an introduction of composition factor. This means that the element-dependent kinetic rate difference in a dissolution or overgrowth process could be an additional influence on the NC development of its final morphology.

This section discusses four methods used for bimetallic concave NC preparation, using some specific examples. The four approaches include galvanic replacement, coreduction with a control of capping ligand(s), selective etching (or site-specific etching), and seed-mediated growth. It should be pointed out that some of these methods are capable of producing bimetallic NCs with very similar geometric profiles. Sometimes, it is versatile to derive more complicated structures of bimetallic NCs from a solution system using a combination of two or more different synthetic techniques.

5.2.1.1 Galvanic Replacement

Galvanic replacement represents a class of remarkable synthetic routes for the preparation of bimetallic NCs with hollow interiors and/or concave surfaces. The precursors of the second metal, a less reactive metal $\mathbf{M}_2$, can be reduced by the "seed" metal, $\mathbf{M}_1$, as a core template. As one of the conditions for such a process, the reduction potential of the $\mathbf{M}_2$ should be sufficiently higher than that of the "seed" metal, $\mathbf{M}_1$. Consequently, predisposed seeds of the $\mathbf{M}_1$ as the templates are usually essential in a typical galvanic process. $\mathbf{M}_2$ cations are then introduced into the solution system and adsorbed on the seed surfaces ($\mathbf{M}_1$). The $\mathbf{M}_2$ cations get electrons from the $\mathbf{M}_1$ seeds while the positive charges are transferred to the $\mathbf{M}_1$ seed atoms and move from the deposition sites to the solution as $\mathbf{M}_1$ cations[14]. Such a process can be alternatively described as an oxidation and dissolution of the templated metal from the seed surfaces accompanied by a site-preferential deposition of more noble metal $\mathbf{M}_2$ through its corresponding reduction. To successfully build concave structures, the lattice mismatch between $\mathbf{M}_1$ and $\mathbf{M}_2$ as well as the desired anisotropy of the redox reactivity on different sites of the particle surfaces should be insightfully considered[15]. The size and morphology of the resultant concave NCs can be tuned by varying the size and shape of the sacrificial templates and by controlling the extent of the replacement reaction.

One of the typical examples is the synthesis of Pt–Cu concave nanocubes using a hydrothermal process[16]. As shown in Figure 5.2(a–e), it was observed that the morphology of evolved Pt–Cu NCs changed from sphere-like NCs to cube-like NCs and

Table 5.1 Possible concave nanocrystals that could be synthesized by site-specific dissolution of cubes, octahedra, and tetrahedra (all of them have slight truncation at corners). Adapted with permission from ref. [15]. Copyright (2012), Wiley.

Dissolution sites	Cubes	Octahedra	Tetrahedra
	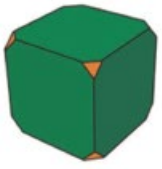		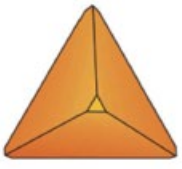
(100)	Concave cubes 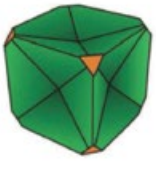	Concave truncated octahedron	
(111)	Concave cuboctahedron	Concave octahedron	Concave tetrahedron 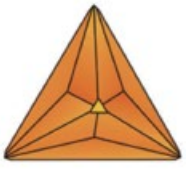
(100) + (110)	Octapod	Octapod	Tetrapod 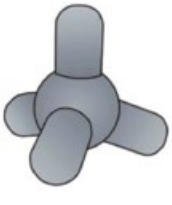
(110) + (111)	hexapod 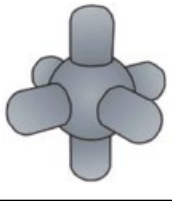	hexapod	

Table 5.2 Possible concave nanocrystals that could be produced by seed-overgrowth along preferential directions on different shapes of seeds: cubes, octahedra, and tetrahedra (all of them have slight truncation at corners). Adapted with permission from ref. [15]. Copyright (2012), Wiley.

Overgrowth directions	Cubes	Octahedra	Tetrahedra
			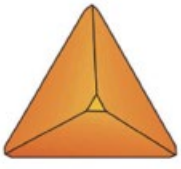
(100)	Hexapod	Hexapod	
(111)	Octapod	Trisoctahedron	Tetrapod 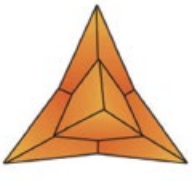
(100) + (110)	Concave cuboctahedron	Concave octahedron	Concave tetrahedron
(110) + (111)	Concave cube 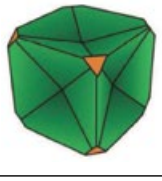	Concave truncated octahedron	

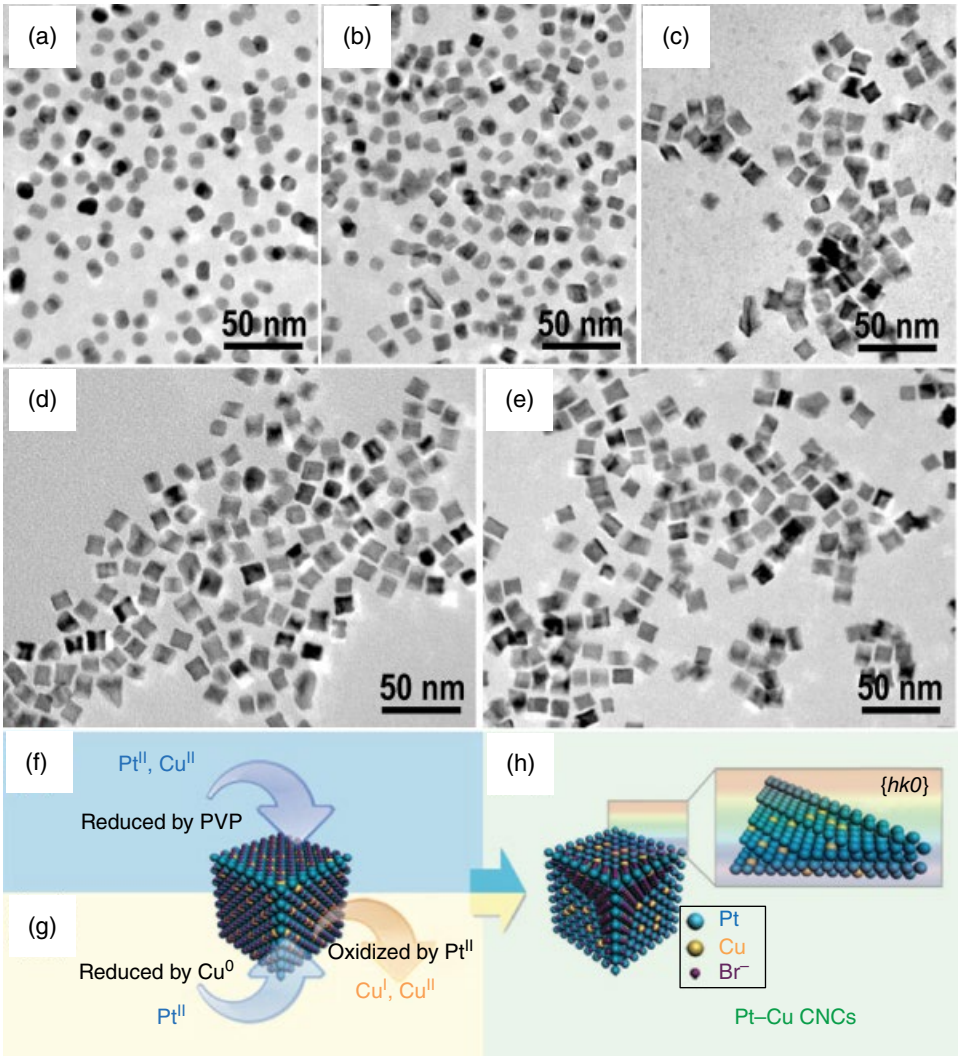

Figure 5.2 Growth time-dependent TEM images of the Pt–Cu concave nanocubes prepared at 160°C (a–e) and proposed growth mechanisms (f–h). (a) 1 h; (b) 2 h; (c) 3 h; (d) 4 h; (e) 6 h; (f) Pt^{2+}; and Cu^{2+} species are reduced to bimetallic seeds by PVP and further evolve to large nanopolyhedra; (g) Cu atoms from selected {100} are further oxidized by Pt^{2+} species through a galvanic replacement and dissolved into the solution, meanwhile the reduced Pt atoms are deposited at the corners or edges of the NCs; (h) high-index facet-terminated Pt–Cu concave nanocubes are finally developed. Adapted with permission from ref. [16]. Copyright (2012), Wiley.

then to concave cubic NCs, and the shape development is time-dependent. Based on this observation, the growth mechanisms were proposed as the following three steps: (1) Pt^{2+} and Cu^{2+} species are reduced to bimetallic Pt–Cu seeds by poly(vinylpyrrolidone) (PVP) and the seeds subsequently grow into large nanopolyhedra; (2) due to the relatively higher concentration of the $[PtBr_4]^{2-}$ species around the {100} facets of the generated Pt–Cu NCs as it was determined that Br^- from $[PtBr_4]^{2-}$ species can be selectively

adsorbed on the {100} facets, the reduced Cu atoms from the {100} facets can be further oxidized by Pt^{2+} species through a galvanic replacement and dissolved into the solution, while the reduced Pt atoms are deposited at the corners or edges of the NCs; (3) such a process leads to a formation of Pt–Cu concave nanocubes terminated with high-index facets as illustrated in Figure 5.2(f–h)[16].

Similarly, Pt–Pd concave nanocubes can be prepared using a polyol approach[17]. Small Pt–Pd cubic seeds can be generated through a coreduction of $[PtCl_6]^{2-}$ and $[PdCl_4]^{2-}$ by ascorbic acid in the presence of Br^- ions in the initial stage. It was determined that a preferential chemisorption of Br^- ions on {100} of Pt–Pd cubic seeds results in metallic atoms being deposited on edges and corners during the growth process, leading to concave structures. It was proposed that the reaction rate of Br^--induced galvanic replacement between $[PtCl_6]^{2-}$ and Pd atoms was critical to determining the final products, whereas the overgrowth at corners and edges of the nanocubes through coreductions benefits the seed-overgrowth of the cubic structures into high-indexed concave nanocubes.

5.2.1.2 Coreduction with a Control of Capping Ligand(s)

In an *fcc* noble metal-based NC system, high-index facets possess higher surface energies and are unable. During a growth of NCs, it is an energetically favorable direction for these high-index facets to vanish rapidly. However, in a solution-based process, binding of organic species such as surfactants and/or inorganic ions could significantly alter the total surface energy order among each facet on an NC. In this case, a high-surface-energy high-index facet could become a low-total-surface-energy plane with a selective capping of certain ligand(s). Such a tentative stable surface would be reserved during the crystal growth, leading to a formation of high-index facet-terminated concave nanostructures. One of the examples is the preparation of Pt_3Co concave nanocubes[4]. In a high-temperature solution containing oleylamine and oleic acid, Pt_3Co concave nanocubes were yielded through a coreduction of platinum (II) acetylacetonate $[Pt(acac)_2]$ and cobalt(II) acetate tetrahydrate $[Co(ac)_2]$ in the presence of tungsten hexacarbonyl $[W(CO)_6]$. It was proposed that the Pt^{2+} and Co^{2+} released from their precursors at high temperature might be initially reduced by the organic species, resulting in Pt–Co seeds. As shown in Figure 5.3a, the reduction of Pt^{2+} could also be promoted by tungsten (W) freshly yielded from the decomposition of $W(CO)_6$ through a "Pt^{2+}-W buffering interaction" to quickly form a Pt-skeleton during the nucleation process and to sustainably provide Pt atoms during the further crystallographic growth process. The reduced Co could simultaneously be incorporated into the Pt-skeleton, forming alloy NCs. The shape evolution of the Pt–Co NCs is dependent on a competition of selective binding from different ligands. On the one hand, carbon monoxide (CO), decomposed from $W(CO)_6$, has a preferential binding feature on Pt(100)[18]. On the other hand, it was determined that oleylamine and oleic acid have different binding abilities on diverse facets and a relatively high ratio between oleylamine and oleic acid could suppress the crystallographic growth along <100> when additional metal atoms/clusters continuously deposit on the NCs. Thus, high-index facet-bounded concave structures of Pt_3Co could eventually be produced through such an anisotropic overgrowth. The similar synthetic approach was also applied to a preparation of Pt_3Fe concave nanocubes using $Pt(acac)_2$ and iron(III)

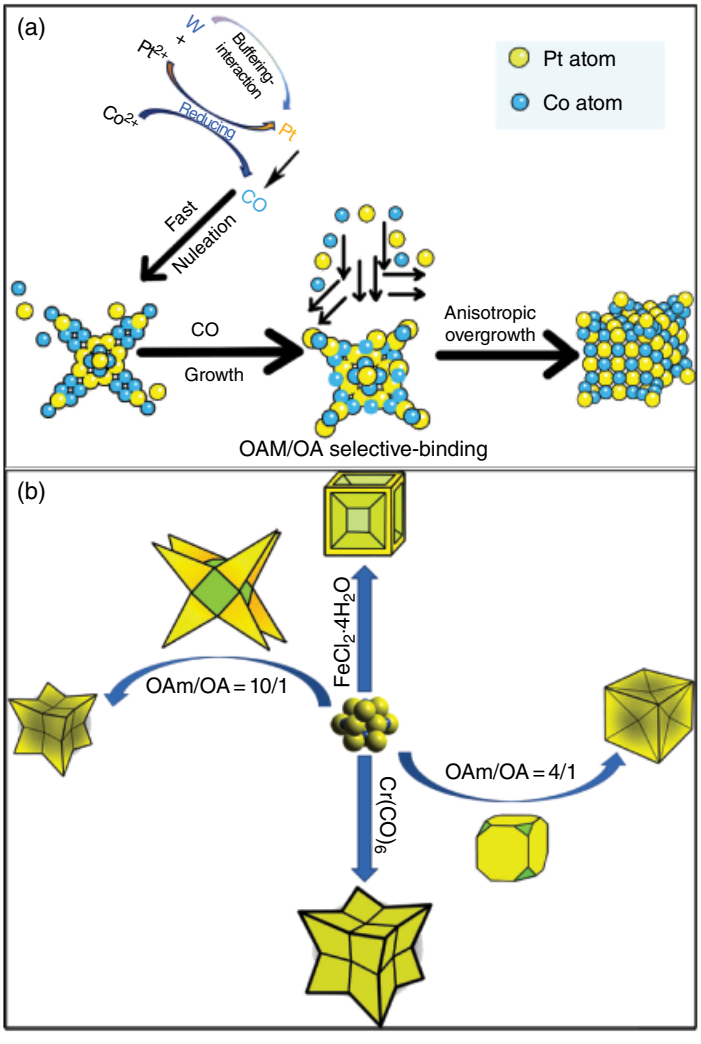

Figure 5.3 Proposed growth mechanisms: (a) formation mechanism of Pt_3Co concave nanocubes (OAM: oleylamine; OA: oleic acid); (b) selective binding mechanism with various influences in the formation of Pt_3Fe concave nanocubes. (OAm: oleylamine; OA: oleic acid). Adapted with permission from ref. [3,4] and modified. Copyright (2014 and 2015), Wiley.

acetylacetonate [$Fe(acac)_3$] as the precursors[3]. As illustrated in Figure 5.3b, it indicated that the concavity of high-indexed Pt_3Fe NCs can be enhanced by the following factors besides the aforementioned selective binding mechanism: (1) high ratio between oleylamine and oleic acid; (2) use of $Pt(acac)_2$ and $Fe(acac)_3$ precursors instead of $PtCl_4$ and $FeCl_2$; and (3) appropriate Pt/Fe ratio. In addition, a replacement of $W(CO)_6$ by $Cr(CO)_6$ could accelerate the nucleation and subsequent growth processes, leading to large NCs.

It has also been proved that amine groups can control the surface structure of Pt-based NCs[19,20]. This type of ligand function can be depicted using the excavation of rhombic dodecahedral (RD) $PtCu_3$ NCs as an example[19]. It was found that the amine groups from *n*-butylamine are vital and can preferentially absorb on {110} facets of bimetallic $PtCu_3$ NCs, leading to a shape evolution of octahedral NCs to edge-concave octahedral NCs and finally excavated RD NCs exclusively enclosed by {110} facets, as shown in Figure 5.4. It is also versatile for tuning the $PtCu_3$ morphology by controlling the amount of *n*-butylamine.

5.2.1.3 Selective Etching (or Site-Specific Etching)

Since the reaction activity of each element in a bimetallic NC is different, it is possible to "extract" the less-noble metal from the alloy through some reactions through a preferential direction, rearranging the remaining metal atoms and leading to a new nanostructure. The preparation Pt–Ni concave nano-octahedra is one of the best examples where the selective etching method was used [2]. In a typical procedure, Pt–Ni nano-octahedra were presynthesized via a hydrothermal process in the presence of benzyl alcohol and PVP. The Pt–Ni concave nano-octahedra were generated by dispersing the resultant Pt–Ni nano-octahedra in water and dimethylglyoxime-ethanol solution with a 12 h stirring before diluting acetic acid was added. Such a site-specific etching process can be described using the following reaction equations:

$$Ni^{o} \rightleftarrows Ni^{2+} + 2e^{-} \tag{5.1}$$

$$\frac{1}{2}O_2 + H_2O + 2e^{-} \rightleftarrows 2OH^{-} \tag{5.2}$$

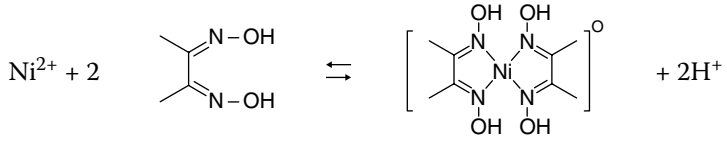

(5.3)

Ni atoms on the surface of Pt-Ni nano-octahedra can be selectively oxidized to Ni^{2+} by the oxygen in the air (equations 5.1 and 5.2). The generated Ni^{2+} then coordinates dimethylglyoxime to form a red precipitation under a neutral condition, leading to the dissolution of Ni from the Pt–Ni surfaces (equation 5.3). Pt wouldn't be oxidized, and Pt-dimethylglyoxime complex wasn't determined in the solution, either. Eventually, the red dimethylglyoxime nickel precipitate could be dissolved in acetic acid and removed, resulting in Pt–Ni concave nano-octahedra in which only element Ni was etched[2]. It was also reported that such an etching process starts at the corners of the octahedral along <100> directions. Once new {100} facets form as round corners, the etching directions shift to <110> and <111>[2]. This etching mechanism has been supported by density functional theory (DFT) calculations and is illustrated in Figure 5.5. Figure 5.6 demonstrates some TEM and high-resolution transmission electron microscopic (HRTEM) images of Pt–Ni concave octahedral NCs prepared using high Ni-fraction ($PtNi_3$ and $PtNi_{10}$) octahedral precursors. It is interesting to learn that the Ni

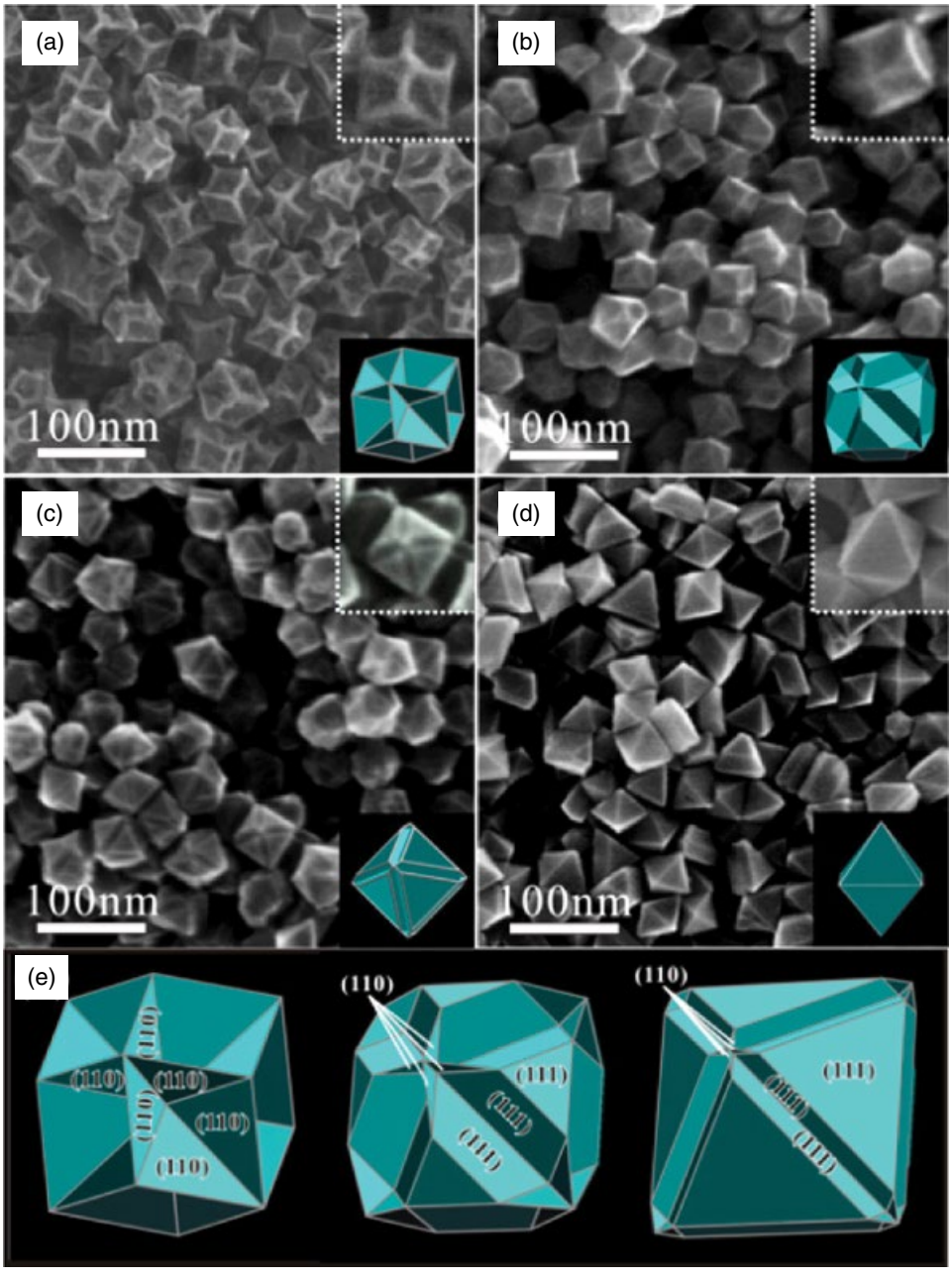

Figure 5.4 SEM images and models of various bimetallic $PtCu_3$ NCs prepared using different amounts of *n*-butylamine: (a) 1.50 mL; (b) 0.50 mL; (c) 0.30 mL; (d) 0.05 mL; and (e) schematic models of excavated RD and edge-concave octahedral shapes, showing the morphology evolution from excavated RD to octahedron. Adapted with permission from ref. [19]. Copyright (2014), Royal Society of Chemistry, and Copyright (2011), American Chemical Society.

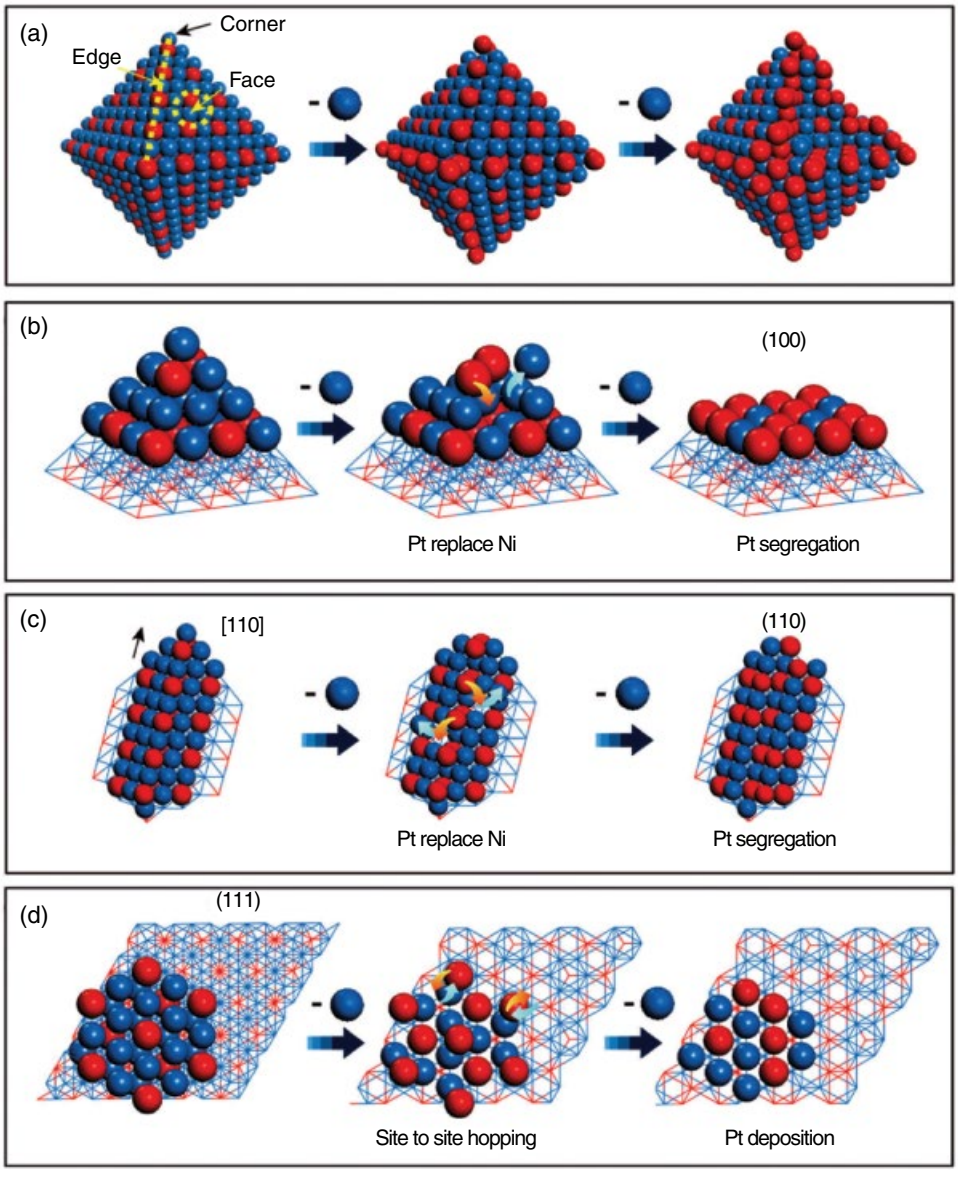

Figure 5.5 Etching mechanism of a Pt–Ni octahedral NC proposed by structural dynamics analysis and DFT calculation, showing the evolution from (a) whole NC; (b) a Ni corner; (c) a (110) edge; and (d) a (100) face, respectively. Deposition of Pt atoms and removal of Ni atoms are indicated by arrows. Adapted with permission from ref. [2]. Copyright (2012), Wiley.

component from Ni-rich Pt–Ni octahedral NCs cannot be unlimitedly extracted, although high Ni-fraction Pt–Ni octahedral precursors can result in the concave octahedral NCs with high concavity. It was further determined that etching of Ni in the dimethylglyoxime system ceases once the Ni/Pt molar ratio reduces to 1:3, due to the high stability of Pt_3Ni phase[2].

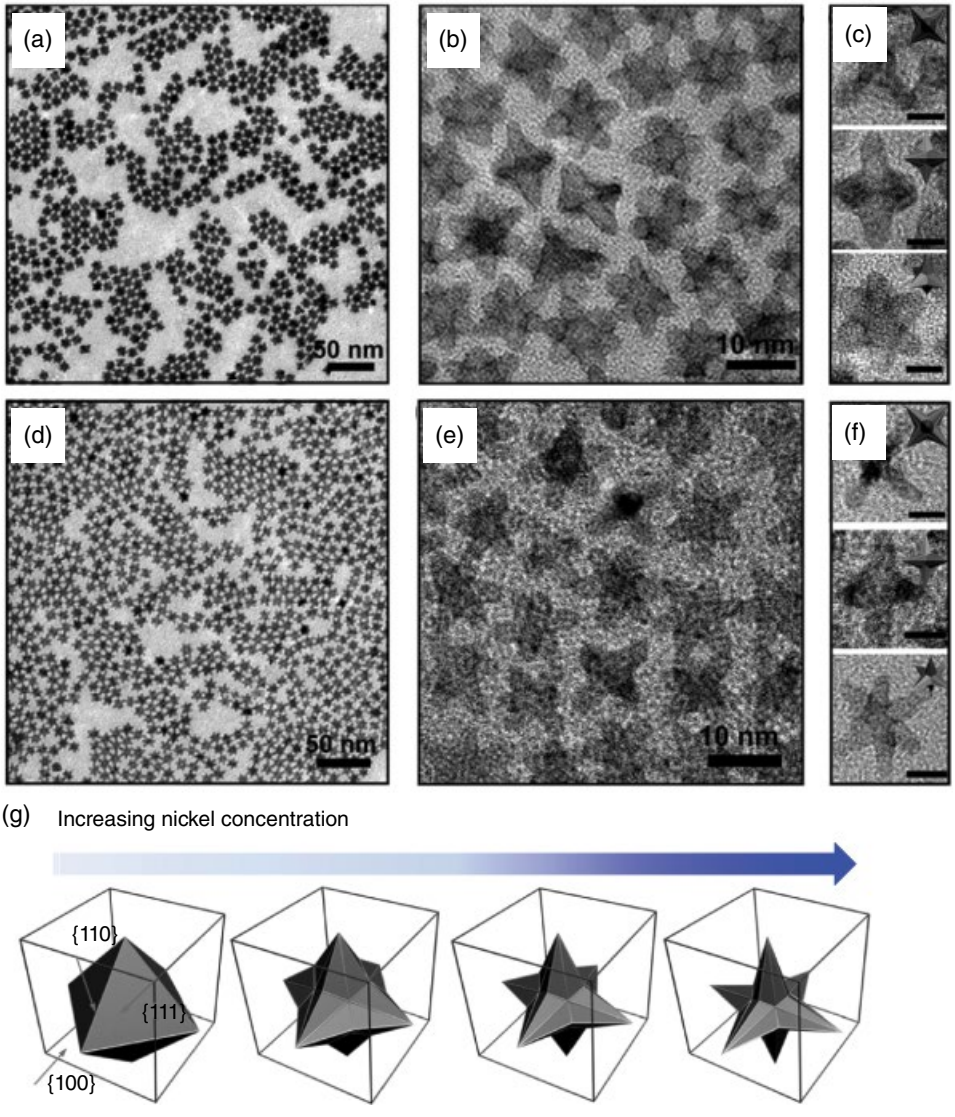

Figure 5.6 TEM images and model of the resultant Pt–Ni concave octahedral NCs. (a)–(c), concave structures corroded from $PtNi_3$ octahedra; (d)–(f) concave structures corroded from $PtNi_{10}$ octahedra; (c) and (f), HRTEM images, and corresponding models orientated along <100> (top panel), <110> (middle panel), and <111> (bottom panel) directions, respectively (all scale bars are 5 nm); (g) models, showing the concave shape evolution as a function of Ni/Pt molar ratio in the octahedral precursors. Adapted with permission from ref. [2]. Copyright (2012), Wiley.

5.2.1.4 Seed-Mediated Growth

In this approach, once metal seeds are introduced, an epitaxial growth on the seeds could occur with the assistance of surfactant(s) in the solution. A good example is the preparation of highly branched Au–Pd concave nanostructures with high-index facets using core–shell Au–Pd as the seeds[21]. In this study, aqueous solutions of $HAuCl_4$, Na_2PdCl_4,

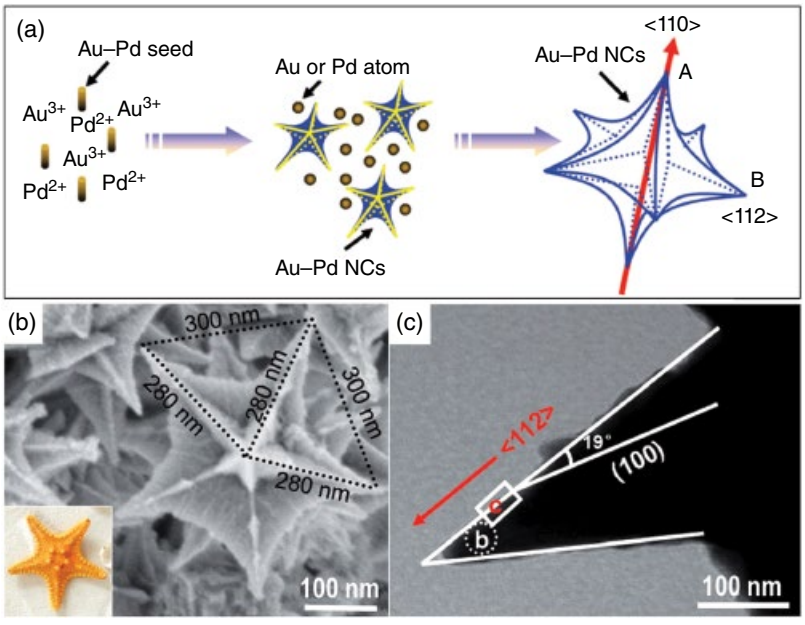

Figure 5.7 Schematic view and EM images of the Au–Pd concave branched core–shell fivefold symmetric NCs: (a) Schematic illustration of the branched NCs formed from multi-twin units. A and B represent the growth directions along <110> and <112>, respectively; (b) SEM image of branched NCs. The inset shows the photograph of a starfish; (c) TEM image of one branch of an Au–Pd core–shell NC. Adapted with permission from ref. [21] and modified. Copyright (2013), Wiley.

$AgNO_3$, HCl, and ascorbic acid were sequentially added to a binary surfactant solution containing cetyltrimethylammonium chloride (CTAC) and didodecyldimethylammonium bromide (DDAB) in a molar ratio of 4, followed by addition of Au–Pd core–shell nanorods as the seeds that were pre-prepared from a surfactant solution[21]. The system was kept at room temperature overnight to allow an epitaxial growth on the Pd shells. As indicated in Figure 5.7a, the branches grew in parallel with {111} twin boundaries along the <112> direction. It was observed that each of the resultant nanostars exhibited highly branched structure like a starfish (Figure 5.7b.c). With an assumption that perfect fivefold twinned NCs were formed, the epitaxial growth should proceed along A and B, two types of growth directions with different growth rates. Using Pd nanocubes as the seeds, the seed-mediated approach was also applied to a $HAuCl_4$-ascorbic acid-CTAC aqueous solution system to yield Au–Pd concave core–shell trisoctahedra (TOH) that are enclosed by {331} high-index facets[22]. Alternatively, Au–Pd concave core–shell TOH was also generated in a counter seed-mediated system in which Pd cubic seeds were replaced by Au TOH seeds and the $HAuCl_4$ solution was replaced by the K_2PdCl_4 solution[23].

5.2.2 Synthesis of Bimetallic Convex Structure

The preparation of convex structured bimetallic NCs including regular nanorods, nanocubes, nano-octahedra, and nanotetrahedra has been reviewed recently[24]. Various versatile synthetic routes such as coreduction, thermal decomposition, galvanic replacement, and seed-mediated growth were also discussed[24–26] and they are therefore skipped in this chapter.

It worth pointing out that some convex nanopolyhedra bound by high-index facets (*vide infra*) can also be prepared using the electrochemical square-wave-potential (SWP) method[27,28] that is not discussed in this chapter, using solution-based approaches as discussed in the concave section, and using a capping ligand-controlled coreduction approach in a high-temperature organic solution system[29,30]. Interestingly, it has become a powerful approach to evolve bimetallic convex nanopolyhedra using the seed-mediated heteroepitaxial growth. For example, it was reported that {431} high-index facet-terminated convex hexoctahedral (HOH) Pd–Au core–shell NCs were prepared by growing the Au-shell on pre-prepared Pd nanocubes in an aqueous solution in the presence of $HAuCl_4$, ascorbic acid (AA), and cetylpyridinium chloride (CPC) through a seed-mediated growth process[31]. The similar approach also yielded Au–Pd convex core–shell nano-polyhedra enclosed by high-index facets from an aqueous solution containing $HAuCl_4$, K_2PdCl_4, lascorbic acid, and pre-prepared octahedral Au seeds[32]. In the case of octahedral Au seeds, the morphology of the generated Au–Pd NCs can vary from rhombic dodecahedra to HOH by further tuning the growth time via a kinetic control (*vide infra*) as shown in Figure 5.8. When the

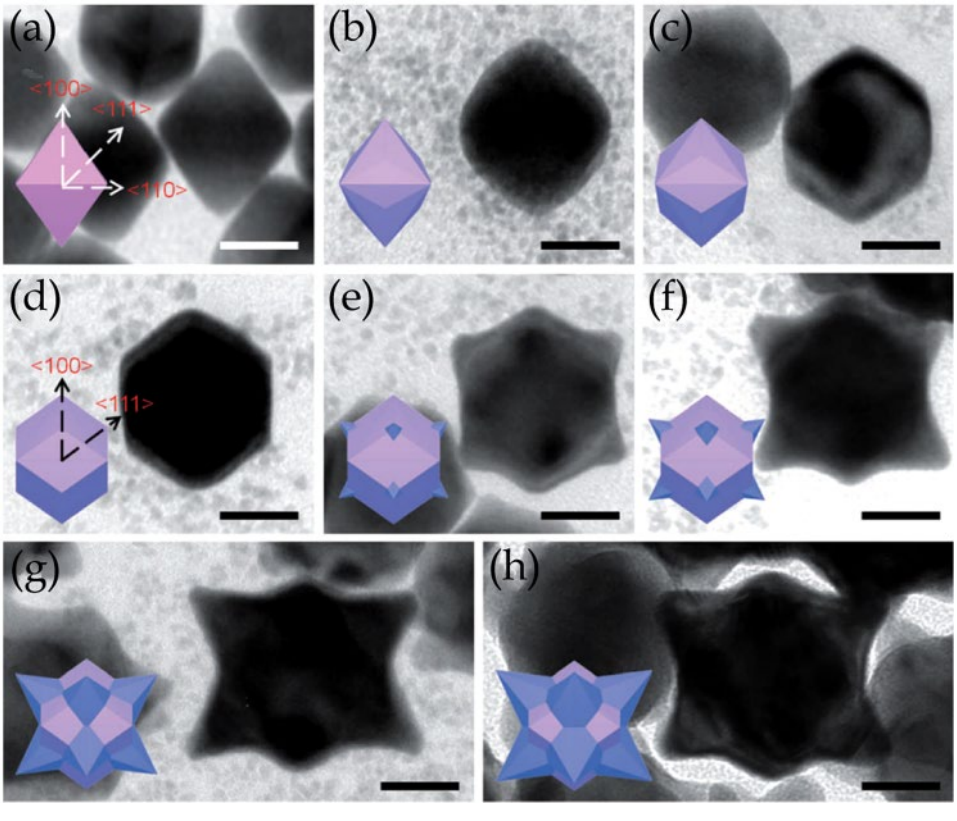

Figure 5.8 TEM images and corresponding geometric models of Au–Pd convex core–shell nanopolyhedra prepared via a combination of octahedral Au seeds-mediated process and dynamic growth with different core–shell growth times: (a) 0 min; (b) 0.5 min; (c) 1 min; (d) 2 min; (e) 3 min; (f) 5 min; (g) 10 min; and (h) 20 min. The scale bars are 20 nm. Adapted with permission from ref. [32] and modified. Copyright (2012), Wiley.

octahedral Au seeds were replaced by TOH Au seeds, it was demonstrated that a similar seed-mediated aqueous system (K_2PdCl_4, ascorbic acid, and Au seeds without $HAuCl_4$) could generate convex HOH and tetrahexahedra (THH) by varying the concentration of each component (for THH, NaBr was also introduced)[23].

In addition, it has been demonstrated that high-indexed convex NCs can be achieved through fast-growth kinetics[33]. A driving force of such a fast growth process may grow out of the supersaturation of metal atoms in a solution due to fast reaction rates[34]. As shown in Figure 5.9a, the producing rate of Au atoms from a reduction of $HAuCl_4$ in a surfactant-containing solution steers the final morphology of the resultant Pd–Au core–shell convex NCs when presynthesized cubic Pd NCs are used as the seeds[31], whereas the growth time of Pd shell-formation in a similar surfactant-containing solution can also determine the final morphology of the harvested Au–Pd core–shell convex NCs when pre-prepared octahedral Au NCs are utilized as the seeds (Figure 5.8 and Figure 5.9b)[32].

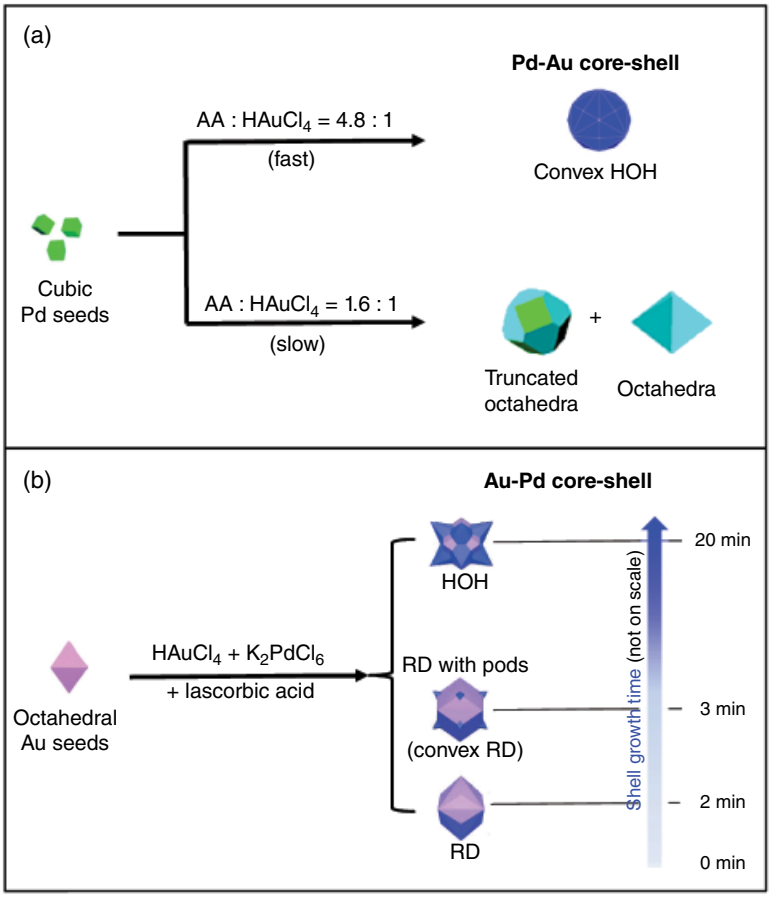

Figure 5.9 Preparation approaches of bimetallic convex core–shell formation. Modified from ref. [31,32].

5.3 Structural Characterization

5.3.1 Crystal Facets

As previously discussed, metallic NCs can be classified into convex and concave polyhedra from the geometric point of view. One way to distinguish a convex polyhedron from a concave one is to check its interior face angles. A polyhedron whose each interior angle is less than 180° is known as a convex polyhedron, whereas a polyhedron with at least one interior angle greater than 180° is referred to as a concave polyhedron. Most metals from groups 9 to 11 possess an *fcc* structure at room temperature. For a polyhedron of an *fcc* metal such as Pt or Pd, a triangular diagram as shown in Figure 5.10 can be used to illustrate the relationship between polyhedral profile and surface facets[23,35]. Each polyhedron located at the vertices in Figure 5.10 is terminated with one of the following three plane families of low Miller indices, {110}, {111}, and {100}, generating rhombic dodecahedron, octahedron, and cube geometries, respectively. By picking different combinations of two vertices or three vertices, we can obtain high-index planes along a sideline or inside the triangle. On a high-index plane (*hkl*), at least one index is greater than 1. For example, a THH is bounded by 24 high-index facets {*hkl*} ($h > k > l = 0$); a trapezohedron (TPH) by 24 high-index facets {*hkl*} ($h > k = l > 0$); a TOH by 24 high-index facets {*hkl*} ($h = k > l > 0$); and an HOH by 48 high-index facets {*hkl*} ($h > k > l > 0$). By following the order of THH → TPH → TOH → HOH, there is a tendency of "increase" in facet indices, that is, {*hk0*} → {*hkk*} → {*hhl*} → {*hkl*} ($h > k > l > 0$), suggesting that more edge and corner sites (or more rough surfaces) are involved in the latter polyhedra[35]. Since the facet-dependent surface energies follow the order of $\gamma_{\{111\}} < \gamma_{\{100\}} < \gamma_{\{110\}} < \gamma_{\{hkl\}}$ in an *fcc* crystal[36], the high-index facets should be unstable during a crystallization evolution and are preferentially annihilable in a thermodynamic equilibrium[35].

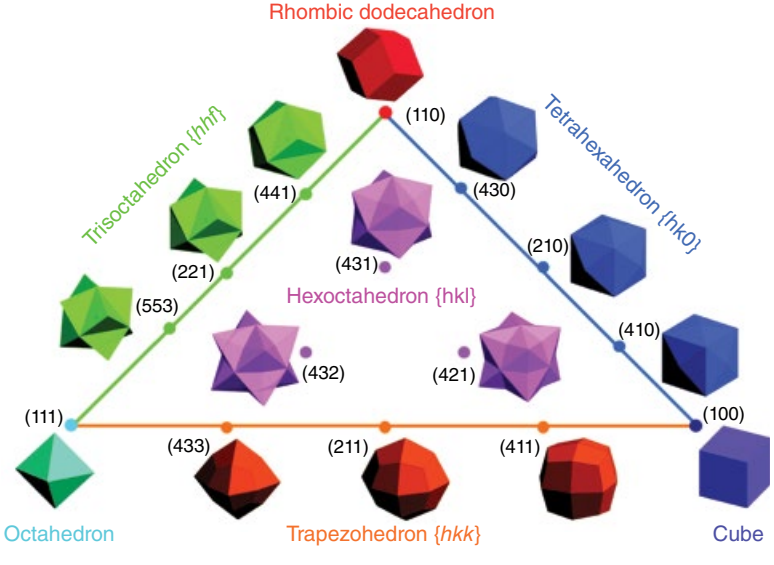

Figure 5.10 Triangular diagram of *fcc* polyhedral nanocrystals enclosed by different crystallographic facets. Adapted with permission from ref. [23]. Copyright (2010), American Chemical Society.

The structures of atomic arrangement on high-index facets are rough with stepped atoms. Lang et al. introduced the step notation to describe high-index surface in the general form: $(hkl) = n(h_t k_t l_t) \times (h_s k_s l_s)$, where $(h_t k_t l_t)$ and $(h_s k_s l_s)$ represents terrace planes and step planes, respectively, while n is the number of atoms in the width of the terrace[37]. For example, surface (755) of an *fcc* TPH is designated in the step notation as (755) = 6(111) × (100), indicating that the (755) facet is composed of (111) oriented terrace planes in width of six atoms and (100) oriented step planes. In addition, if a stepped surface has the steps that also are high-index planes, then it is called a kinked surface. Table 5.3 lists general step notation information for THH, TOH and TPH shown on the three sidelines of the triangle in Figure 5.10 in crystallographic zones of [001], [01$\bar{1}$]. and [1$\bar{1}$0], respectively[35]. In addition to the step notation, a microfacet notation developed by Van Hove and Somorjai defines that any high-index surface can be decomposed into three linearly independent low-index microfacets $(h_1 k_1 l_1)$, $(h_2 k_2 l_2)$ and $(h_3 k_3 l_3)$: $(hkl) = a_\lambda^1(h_1 k_1 l_1) + a_\mu^2(h_2 k_2 l_2) + a_\nu^3(h_3 k_3 l_3)$, where the factors a^1, a^2, and a^3 are the vector decomposition coefficients and the subscripts λ, μ and ν are the relative sizes of the three-component microfacets in terms of the number of two-dimension unit cells on each facet [38]. The previous (755) surface in the TPH can therefore be designated in microfacet notation as (755) = 5_5(111) + 2_1(100).

Technically, it is still a challenge to accurately identify high-index surfaces on a polyhedron. One approach to the Miller indices determination on a high-index surface is to resolve the surface atomic arrangement as well as the microfacets illustrations using HRTEM images. The right panel in Table 5.3 shows the projection angles that can be utilized for a fast indexation of high-index facets on a polyhedron when the projection direction is parallel to [001] or [110] crystallographic zone axis[35]. For THH and TPH NCs, [001] is the optimal projection axis to generate fourfold symmetric convex octagons; for TOH and HOH NCs, [110] is the optimal direction to generate twofold symmetric concave octagons. With a measurement of the projection angles of the appropriate octagonal projection and calculation using proper equations listed in Table 5.3, the type of the polyhedron and Miller indices of its surfaces could be quickly determined.

5.3.2 Case Studies

5.3.2.1 {hk0} Facets

Figure 5.11a is a high-angle annular dark-field scanning transmission electron microscopic (HAADF-STEM) image, showing ~22 nm THH $PtNi_4$ NCs prepared through a high-temperature solution approach[29]. An HRTEM image of a single THH NC that was observed along the [001] zone axis is presented in Figure 5.11b. As labeled in Figure 5.11b, the average values of the projection angles, α and β, were determined as 133.6(5)° and 136.3(5)°, respectively. According to the projection angle formula depicted in Table 5.3, $\alpha = 2arctan\left(\frac{h}{k}\right)$, the average value of h/k can be calculated as 2.3360 ± 0.0135 ≈ 7/3. The Miller indices of the $PtNi_4$ THH facets were consequently assigned as {730}[29]. By considering the nature of bimetallic $PtNi_4$, in which both Pt and Ni have *fcc* structures in their single crystals, it is reasonably believed that the $PtNi_4$ THH NCs should similarly possess high-indexed facets that Pt THH NCs have[28]. The exposed

Table 5.3 Information of four-type high-indexed *fcc* nanopolyhedra and project method in their Miller Index determination. Adapted with permission from ref. 35 and modified. Copyright (2013), American Chemical Society.

High-indexed polyhedron	Zone	Surface facets	Miller index (n≥2)	Step notation	Projection direction	Projection image	Projection angel / degree
Tetrahexahedron (THH)	[001]	$\{hk0\}_{24}$ (h>k>0)	(n,n−1,0) (n,1,0)	n(110)×(100) n(100)×(110)	[001]	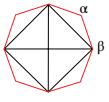	$\alpha = 2\arctan\left(\frac{h}{k}\right)$ $\beta = 270 - \alpha$
Trapezohedron (TPH)	$[01\bar{1}]$	$\{hkk\}_{24}$ (h>k>0)	(n+1,n−1,n−1) (2n−1,1,1)	n(111)×(100) n(100)×(111)	[001]	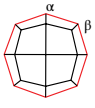	$\alpha = 2\arctan\left(\frac{h}{k}\right)$ $\beta = 270 - \alpha$
Trisoctahedron (TOH)	$[1\bar{1}0]$	$\{hhl\}_{24}$ (h>l>0)	(n+1,n+1,n−1) (2n−1,2n−1,1)	n(111)×(110) n(110)×(111)	[110]	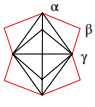	$\alpha = 2\arctan\left(\frac{\sqrt{2}h}{h-l}\right)$ $\beta = 90 - (\alpha/2) + (\gamma/2)$ $\gamma = 2\arctan\left(\frac{\sqrt{2}h}{l}\right)$
Hexoctahedron (HOH)		$\{hkl\}_{48}$ (h>k>l>0)			[110]	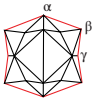	$\alpha = 2\arctan\left(\frac{\sqrt{2}h}{k-l}\right)$ $\beta = 90 - (\alpha/2) + (\gamma/2)$ $\gamma = 2\arctan\left(\frac{k+h}{\sqrt{2}l}\right)$

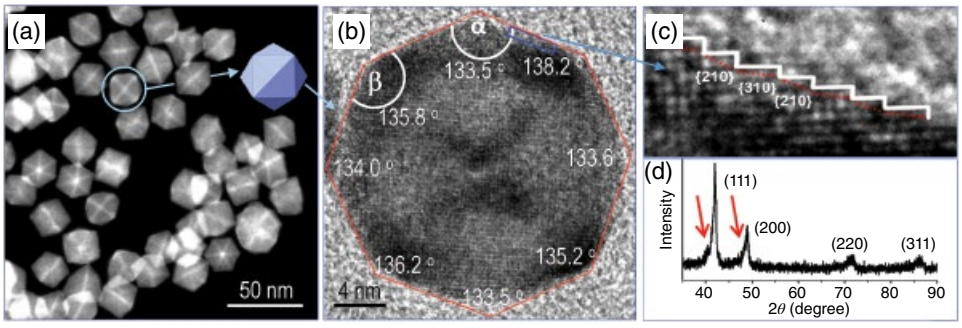

Figure 5.11 EM images and XRD pattern of $PtNi_4$ tetrahexahedral nanocrystals: (a) HAADF-STEM image; (b) HRTEM of a single nanocrystal recorded along the [001] zone axis with the measured projection angles between surfaces; (c) HRTEM image zoomed from the boxed area in (b), displaying the surface atomic steps marked as {210} and {310}; and (d) XRD pattern of the nanocrystals, showing the *fcc* structure and Pt–Ni composition segregation. Adapted with permission from ref. [35] and modified. Copyright (2010), American Chemical Society.

surface indexation of the $PtNi_4$ THH NCs can be corroborated from the atomic arrangement in which {310} and {210} subfacets periodically stack up, as delineated in Figure 5.11c. In this case, it is also worth noting that the composition of Pt and Ni atoms is not uniformly distributed from the edges to the center in the THH NCs, as indicated by the X-ray diffraction (XRD) pattern (Figure 5.11d). The aslant XRD peak shoulders marked with the arrows in Figure 5.11d suggest an underlying segregation of two components. Such a nonuniform compositional distribution can also be observed from the different Z-contrast between the edges and interior region in Figure 5.11a.

5.3.2.2 {hkl} Facets

An HOH can be perceived as a TOH with its <111> edges bending outward from edge centers or a THH with its <100> edges contracting inward from edge centers. As a result, each facet of a TOH or a THH splits into two facets, resulting in an HOH bounded by 48 high-index facets. Lee et al. synthesized Au–Pd concave core–shell HOH NCs with Pd/Au atomic ratio of 0.5 (Figure 5.12a–c)[14]. The fringes of the HOH NCs in the TEM image (Figure 5.12d) indicate the existence of Pd shells that overgrew on the Au templates. The projection angles observed along the [110] zone axis (Figure 5.12e) suggest that the HOH NCs are bounded by {432} facets. The {432} planes can be designated in the step notation as 2(111) × (210), which shows {432} facets are kinked facets due to high-index step planes, (210).

5.4 Selected Properties

Some unique properties of the bimetallic convex and concave NCs have been identified and reported. These behaviors grow out of not only the bimetallic synergetic effect but also the high-indexed facets exposed on these nanopolyhedra. This section outlines several kinds of dominant properties of these convex and concave NCs from the recent progress of the study using some typical examples, including optical, electrocatalytic, and chemical catalytic performance. It should be emphasized that shape- and composition-dependent

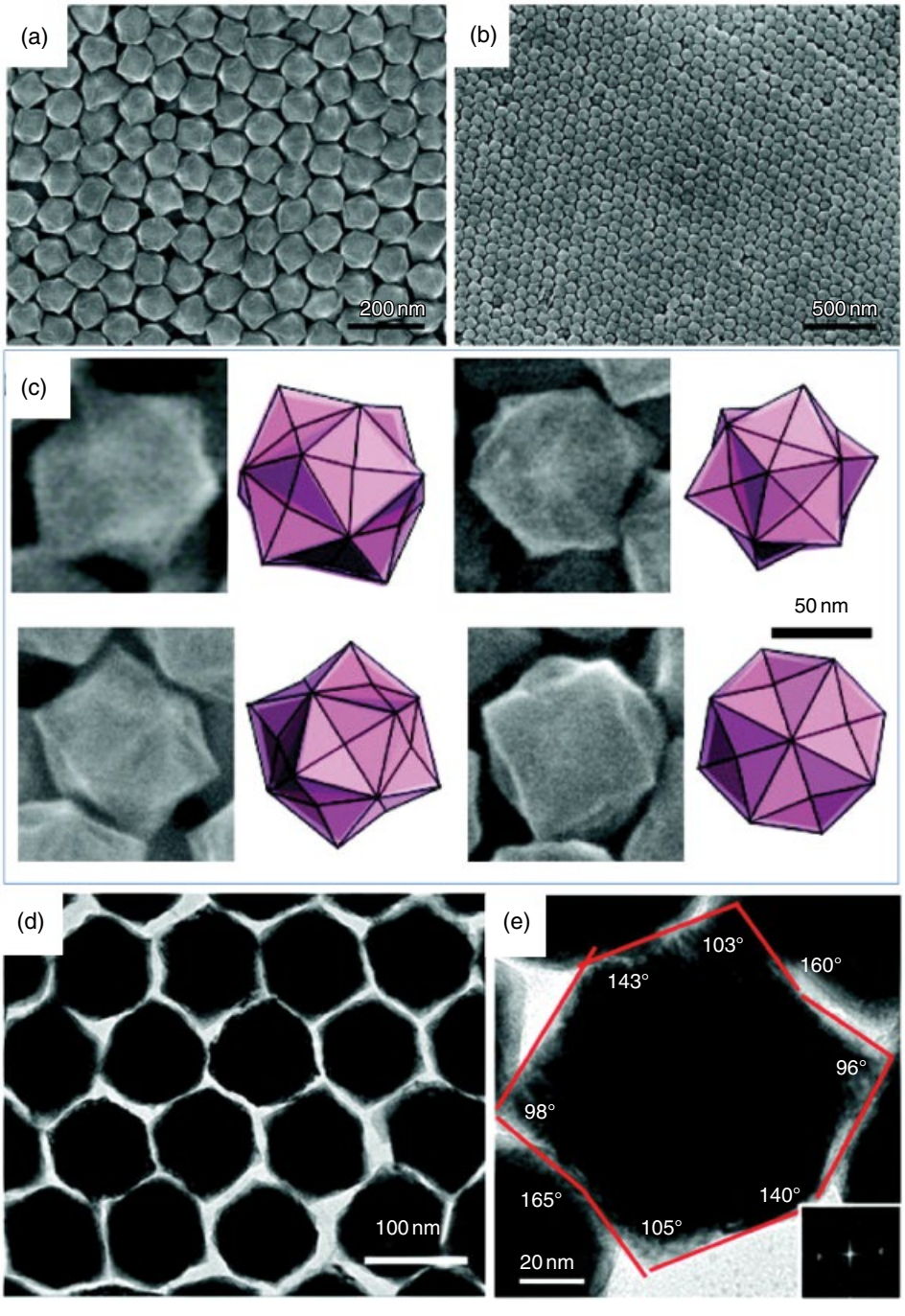

Figure 5.12 EM images and models of Au–Pd core–shell hexoctahedron nanocrystals: (a) and (b) SEM images; (c) SEM images of an individual nanocrystal in different orientations with the corresponding geometrical models; (d) TEM image of overall morphology; (e) TEM images of an individual nanocrystal recorded along the [110] zone axis with the corresponding FFT pattern (inset). Adapted with permission from ref. [14] and modified. Copyright (2010), American Chemical Society.

magnetism [39,40], entropic force-induced superstructures[41], and magnetic force-induced superstructures[42] of these bimetallic convex and concave NCs are of significant properties as well. Limited to the length scale of this chapter, however, these aspects are not included in this section.

5.4.1 SERS Characteristics

It is believed that some sites on metallic concave NCs such as their sharp corners and edges could focus the electromagnetic field, leading to enormous SERS signals[43,44]. In the SERS point of view, concave (or even plate-like[45]) NCs of some noble metals, such as Ag and Pd, are more interesting than their convex counterparts. As one of the unique features provided by these metallic concave NCs, SERS is significant for optical labeling and sensing applications[46]. Although this chapter is concentrated on bimetallic systems, we must review the studies on a single metal such as Ag, the most efficient SERS substance, as the starting point for the binary discussion. This section attempts to articulate such an advantage using several examples.

5.4.1.1 Case of Ag Convex NCs

Using a solution-based anisotropic etching approach, the surface structure of Ag octahedral NCs that were prepared from hot 1,5-pentanediol in the presence of PVP [47] and stored in ethanol can be etched in a PVP-aqueous solution by introducing a mixed etching agent, concentrated ammonium hydroxide and 30% hydrogen peroxide (9:1)[44]. Since such an etching is more preferential in <100> when the concentration of the etching agent is increased, Ag NCs with different geometries could result from different etching stages starting from the octahedron-shaped NCs through the tuning of the etching conditions. Figure 5.13 illustrates a comparison of single-particle-based SERS intensities from three classes of typical NCs[44], octahedron, gapped octahedron and octapod, showing the alteration of their plasmonic characteristics as a function of their surface structure modification during the etching process. Compared to the octahedral NC with flat faces, Figure 5.13 indicates that the existence of hot spots presented in the gaps, tips, and edges favors the SERS signal, especially for the longer wavelength of the excitation.

5.4.1.2 Case of Ag Concave NCs

Xia et al. prepared Ag concave TOHs, concave octahedral and conventional octahedral NCs using an improved solution approach[43], and further compared SERS spectra of 1,4-benzenedithiol (1,4-BDT) adsorbed on the surfaces of these NCs from aqueous suspensions with roughly the same particle concentration. Since the Ag concave TOH consists of the most intraparticle gaps, tips, and edges among the three classes of NCs, it should generate locally enhanced or amplified electromagnetic fields on the particle surface, exhibiting the highest SERS enhancement factor (EF) under the same observation conditions. As shown in Figure 5.14, this was validated by the fact that the SERS signals from the Ag concave TOHs and Ag concave octahedra are approximately 12 and 4 times stronger, respectively, than that from the conventional Ag octahedra with flat faces[43].

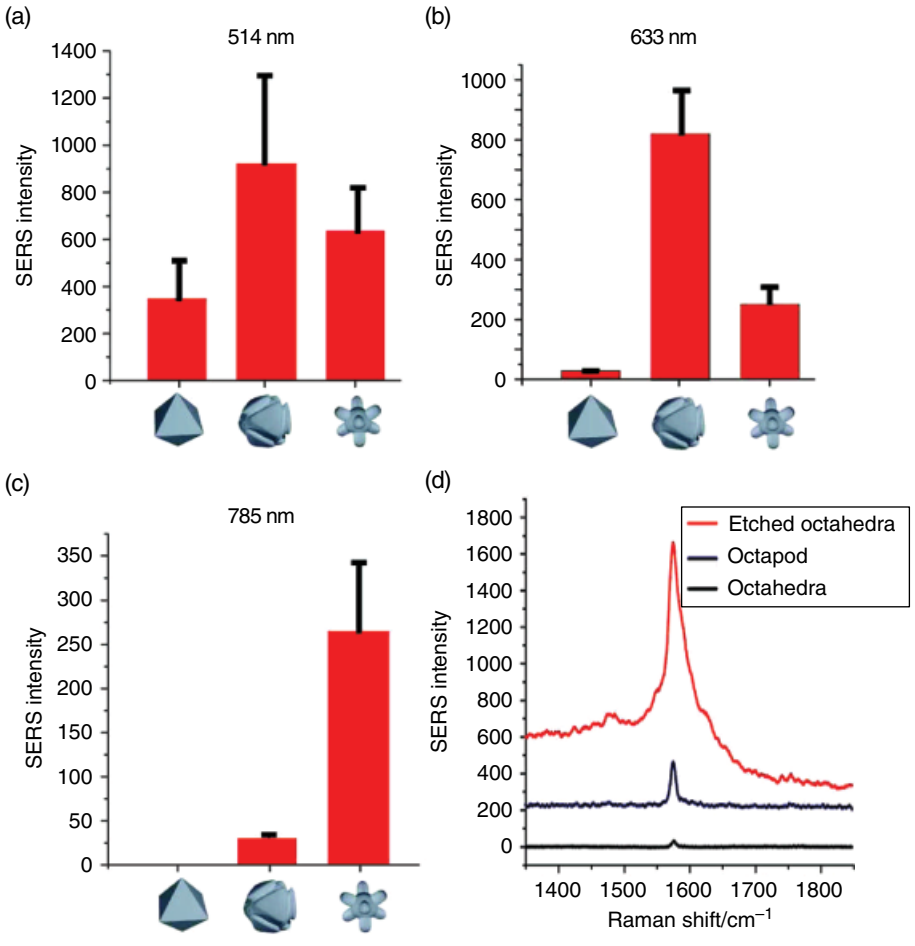

Figure 5.13 Single-particle Raman scattering of benzenethiol at 1584 cm^{-1}: (a), (b), and (c), average SERS intensities for three types of particles using excitation wavelengths of 514, 633, and 785 nm, respectively. Error bars represent standard deviation; (d) representative SERS spectra for three types of particles obtained during 1 s integration using an excitation wavelength of 633 nm. Adapted with permission from ref. [44] and modified. Copyright (2010), American Chemical Society.

5.4.1.3 Cases of Bimetallic Noble Metals

It was reported that noble metals such as Au[48] and Pd[45] as well as their bimetallic composite structures such as Au–Ag[49] and Au–PtZn[50] with "hot spots" generally resulted from sharpened corners/edges embrace unique SERS characteristic. A combination of such a SERS function and catalytic feature from a Ag–Au core–shell system has been demonstrated in a recent report[49]. By titrating aqueous $HAuCl_4$ into an aqueous suspension of Ag cuboctahedra in the presence of ascorbic acid, NaOH and PVP, core–shell structured Ag–Au cuboctahedra and Ag–Au concave cuboctahedra could be generated through a galvanic replacement reaction[49]. The composition, as well as the morphology of Ag–Au cuboctahedra, can be controlled by tuning the volumes of $HAuCl_4$. Figure 5.15a illustrates the SERS spectra collected from 1,4-BDT

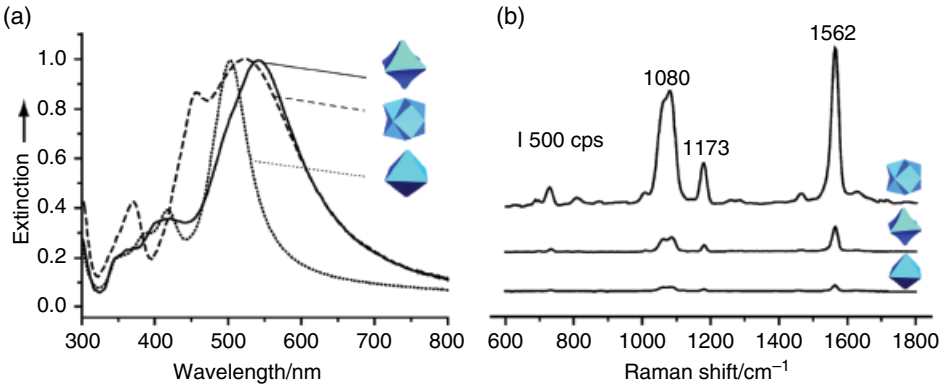

Figure 5.14 UV/Vis and SERS spectra of 75 nm Ag nanocrystals. (a), UV/Vis spectra of Ag nanocrystals with different shapes: solid curve—concave octahedra, dash curve—concave TOHs, and dot curve—conventional octahedra; (b), aqueous solution-based SERS spectra of 1,4-BDT adsorbed on the concave TOHs, concave octahedra, and conventional octahedra (from top to bottom) recorded with λ_{ex} = 514 nm. Adapted with permission from ref. [43] and modified. Copyright (2011), Wiley.

adsorbed on the Ag cuboctahedra, Ag–Au cuboctahedra and Ag-Au concave cuboctahedra, among which the EF of Ag–Au concave cuboctahedra ranks the best, showing SERS signal of a ~74-fold increase compared to that of the original Ag cuboctahedra at an excitation wavelength of 785 nm. Besides the advantage that the concave structure embraces excellent SERS activity, it was believed that the stronger bond between Au and thiolate could make an additional contribution to such an enhancement of the SERS signal[51]. It was also reported that the Au atoms are preferentially deposited onto the Au{100} facets through a galvanic replacement reaction, resulting in a formation of Ag–Au concave cuboctahedron at the sites of {111} facets. By combining the superb SERS performance with the catalytic feature of the surface Au atoms in the resultant Ag–Au concave cuboctahedra, Figure 5.15b–c presents time-dependent SERS spectra during a reduction of 4-nitrothiophenol (4-NTP) to 4-aminothiophenol (4-ATP) by $NaBH_4$ through a 4,4'-dimercaptoazobenzene (trans-DMAB) intermediate and a subsequent oxidation of 4-ATP back to trans-DMAB upon the introduction of H_2O_2, respectively, demonstrating that the Ag–Au core–shell concave cuboctahedra could be a unique SERS probe for monitoring these reactions. In addition, with a protection of those Au "shells," the Ag–Au concave cuboctahedra are remarkably stable in these reactions.

5.4.2 Electrocatalytic Performance

Bimetallic (mainly, Pt-based) NCs as a major class of catalysts are significant for electrochemical reactions such as small organic molecule electro-oxidations and ORR used in PEMFCs as well as hydrogen-evolving reactions (HERs) used in water-alkali electrolyzers. A number of strategies have been utilized to balance the size issue and to maximize the use of precious Pt resources. This includes the composition tuning such as an incorporation of a second metal (such as Cu, Ni, Co, Fe) into Pt for an electro-oxidation[9,52–54], construction of core–shell structures[55,56], and manipulation of catalyst morphology[57–59]. The study of facet-controlled electrochemical catalysts

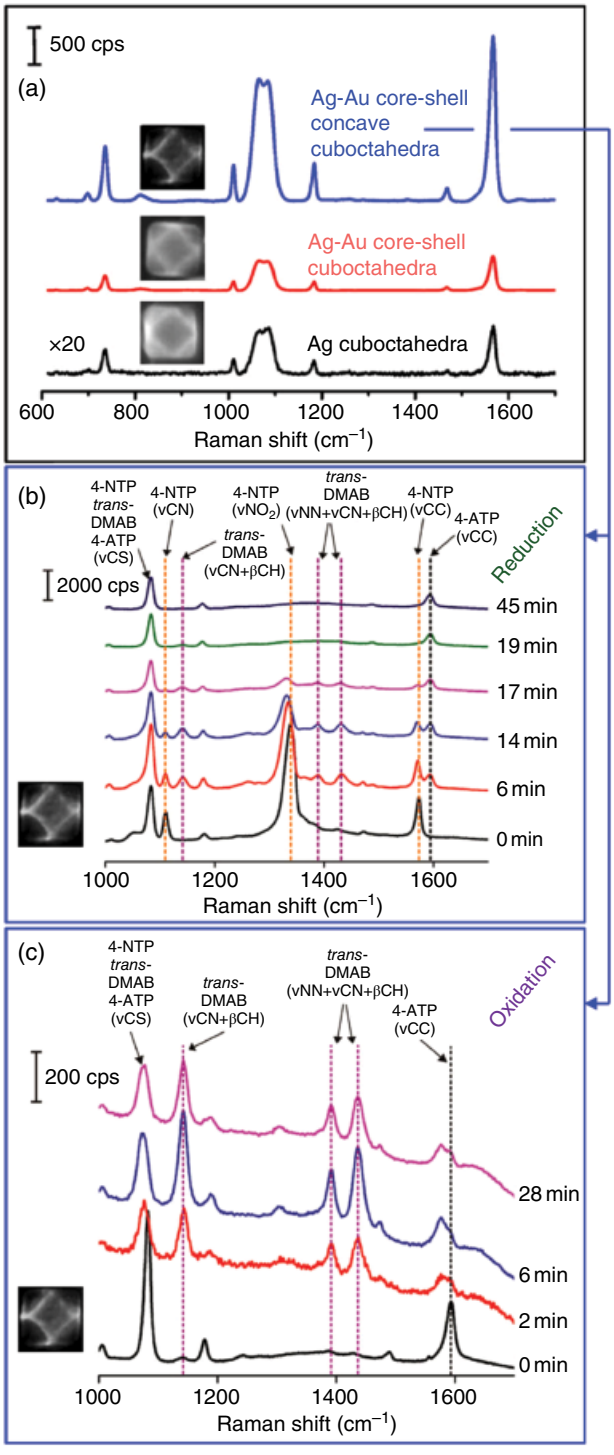

Figure 5.15 SERS spectra at an excitation wavelength of 785 nm: (a) spectra were collected from 1,4-BDT adsorbed on substrates of Ag cuboctahedra, Ag–Au core–shell cuboctahedra, and Ag–Au concave cuboctahedra, respectively; (b) spectra were recorded during the reduction of 4-NTP to 4-ATP reduced by $NaBH_4$ and catalyzed by Ag-Au concave cuboctahedra; and (c) spectra were recorded during the oxidation of 4-ATP oxidized by H_2O_2 and catalyzed by Ag–Au concave cuboctahedra. Adapted with permission from ref. [49] and modified. Copyright (2010), American Chemical Society.

has attracted an increasing attention in recent years due to the fact that a certain type of surface with a unique structure of the atomic arrangement on a metallic catalyst could promote a specific electrochemical reaction. For example, high-index planes of Pt, which are abundant on step sites, such as sharp corners and edges of a NC with low-coordinated atoms, are generally deemed as the most promising catalytic promoters for cleaving C-H and C-O bonds[28,60,61] in formic acid oxidation reaction (FOR) and methanol oxidation reaction (MOR), whereas Pt–Ni {111} facets are believed as the best catalytic planes for ORR[8,9,62]. Both the convex and concave polyhedral NCs can present high-indexed facets[25,35], which is intriguing for small molecule electro-oxidations. In the followings, several case studies in this aspect are provided.

5.4.2.1 Cases of Pt–Cu Nanostructures

In recent years, it has been realized that Pt–Cu concave NCs possess a superior electrocatalytic activity towards small molecule electro-oxidation[52,53]. As shown in Figure 5.16a–d, Pt–Cu concave particles in size of 50–70 nm with various compositions were produced through a KNO_3–$LiNO_3$ molten salt system[63]. Analysis suggests that these bimetallic Pt–Cu concave structures have an *fcc* polycrystal structure and can be considered as alloys. As indicated in Figure 5.16e–h, both composition-dependent MOR and FOR activities of these carbon-loaded Pt–Cu concave structures were investigated in 0.1 M $HClO_4$ solution using cyclic voltammetry (CV) and chronoamperometric methods. The area current densities of all the carbon-supported concave structures are higher than the values of state-of-the-art commercial Pt/C in both MOR (at 0.85 V vs. RHE) and FOR (at 0.45 V vs. RHE) measurements. It was further identified that the concave structure with a composition of Pt_3Cu exhibits the best electrocatalytic behaviors in both MOR and FOR, suggesting that the Pt_3Cu concave structure could be an emarkable anode catalysts in the fuel cell industry.

Y. Qi et al.[64] conducted the MOR study of carbon-supported $Pt_{59}Cu_{41}$ (~Pt_3Cu_2) concave nanocubes (edge length: ~15 nm), and carbon-supported $Pt_{2.8}Cu$ spherical particles (2–5 nm in size) and commercial Pt/C catalyst (Vulcan XC-72) in 0.1M $HClO_4$. It showed that a forward current density of the Pt_3Cu_2 concave nanocubes is as high as 4.7 $mAcm^{-2}$, which is 3.0-fold and 4.7-fold higher than those of the spherical $Pt_{2.8}Cu$/C and Pt/C, respectively. The high electrocatalytic activity of Pt_3Cu_2 toward MOR was mainly attributed to the {511} high-indexed facets as well as the composition effect. Both specific and mass activities for MOR on shape- and composition-dependent Pt–Cu were also systematically studied by Yin et al.[16]. The MOR catalytic activities of Pt–Cu concave nanocubes were evaluated compared to that of the state-of-the-art Pt/C, conventional Pt–Cu nanocubes (terminated with {100}), as well as their trimetallic counterparts. As shown in Figure 5.17, it turns out that the high-indexed facet-bounded alloy concave nanocubes (such as Pt–Cu and Pt–Pd–Cu) demonstrate a promising performance toward MOR[16]. The superior performance of Pt–Cu concave catalysts bounded with high-index facets was not only identified from cubic structures but also other morphologies such as hexapod concave nanostructures[65].

In addition, it was recently reported that Pt–Cu convex NCs with a hexapod morphology and various compositions, as a counterpart of the concave class, show enhanced electrocatalytic performance toward ORR[66]. For example, a specific activity of 3.7 mA/cm^2_{Pt} and mass activity of 2.4 A/mg_{Pt} were obtained at 0.9V from carbon black-supported hexapod $PtCu_2$. Although the pods are enclosed by high-index facets as characterized in such a type of convex architectures, it is believed that {111} facets exposed on the seeds should result in the high ORR activity in the given potential range.

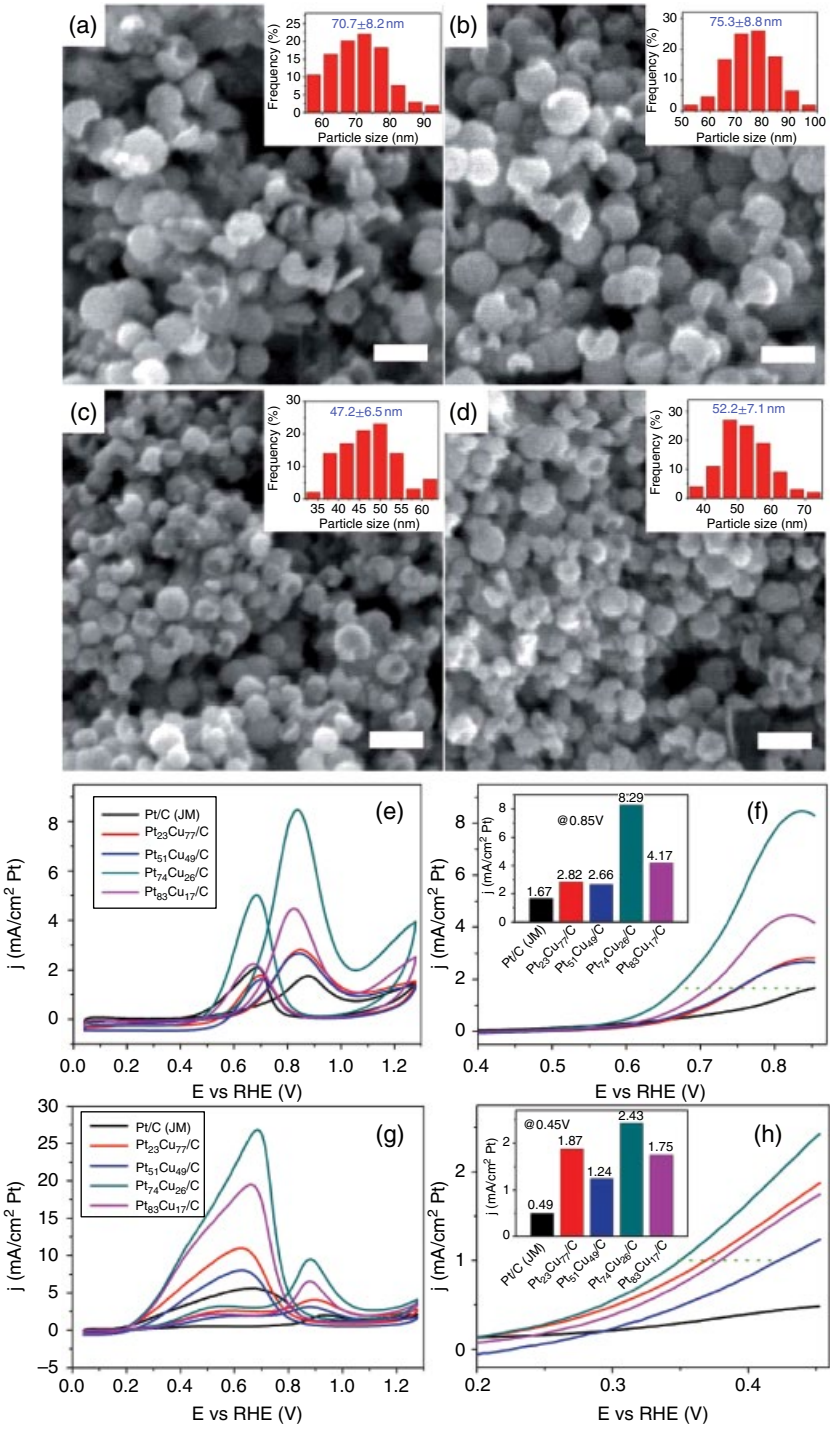

Figure 5.16 SEM images, particle sizes and size distributions, MOR and FOR performance of various Pt–Cu concave nanoparticles: (a)–(d), SEM images and particle size distribution histograms (insets) of $Pt_{23}Cu_{77}$, $Pt_{51}Cu_{49}$, $Pt_{74}Cu_{26}$, and $Pt_{83}Cu_{17,}$ respectively (scale bars: 100 nm); (e) and (f) CVs and linear sweep voltammetry of Pt/C and carbon-supported bimetallic concave catalysts (Pt–Cu/C) with different Pt/Cu molar ratios in 0.1 M $HClO_4$ + 1 M MeOH (scan rate: 50 mV s^{-1}); the inset shows area current density at 0.85 V (*vs.* RHE) for each catalyst; (g) and (h) CVs and linear sweep voltammetry of Pt/C and carbon-supported bimetallic concave catalysts (Pt–Cu/C) with different Pt/Cu molar ratios in 0.1 M $HClO_4$ + 0.5 M HCOOH (scan rate: 100 mV s^{-1}); the inset shows area current density at 0.45 V (*vs.* RHE) for each catalyst. Adapted with permission from ref. [63]. Copyright (2012), Royal Society of Chemistry.

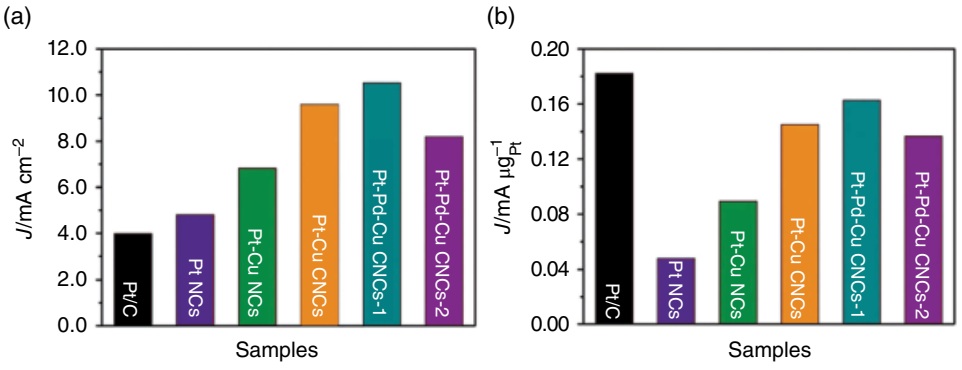

Figure 5.17 MOR performance comparison of different types of catalysts: (a), specific activity; (b) Pt-based mass activity. Sample codes: Pt–Pd–Cu CNCs, trimetallic concave nanocubes; Pt–Cu CNCs, bimetallic concave nanocubes; Pt–Cu NCs, bimetallic conventional nanocubes; Pt NCs, commercial Pt/C catalysts (20 wt% of <3.5 nm Pt nanoparticles supported on activated carbons, Johnson Matthey). Adapted with permission from ref. [16]. Copyright 2012 Wiley.

5.4.2.2 Cases of Pt-Pd Concave NCs and Others

Similar to the Pt–Cu system, Pt–Pd concave nanocubes terminated on high-index facets with synergetic effects between Pt and Pd exhibit composition-dependent electrocatalytic activity toward MOR, in which the Pt_3Pd_2-based catalyst shows the highest activity of MOR (Figure 5.18a) and the best-improved tolerance toward CO poisoning[17]. The ORR performance of Pt–Pd concave nanocubes as a function of the composition has been explored as well[67]. As illustrated in Figure 5.18b, among a commercial Pt/C and 18 nm Pt–Pd concave nanocubes with different contents of Pt from 3.4 wt% to 34.3 wt%, the Pt–Pd catalysts with 3.4 wt% of Pt exhibited the highest mass activity measured at 0.9 V versus RHE[67]. It was also reported that FeNi concave nanostructures with high-index facets can be used for detecting electro-oxidation of 4-aminophenol (4-AP), a significant "indicator compound" that can be used for *Escherichia coli* (*E. coli*) detection.

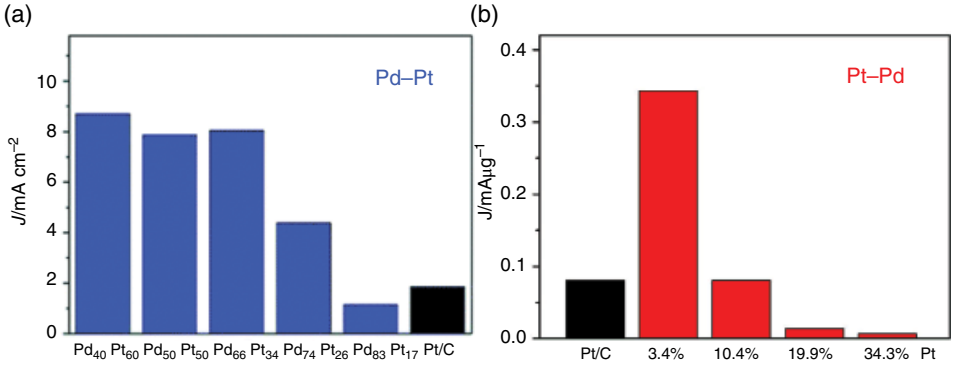

Figure 5.18 MOR and ORR activities of composition-dependent Pt–Pd concave nanocubes and commercial Pt/C catalyst. (a), MOR specific activity obtained in a N_2-purged 0.5 M H_2SO_4 + 1.0 M CH_3OH aqueous solution at a sweep rate of 50 mV s^{-1}; (b), ORR mass activity at 0.9 V versus RHE obtained in an O_2-saturated 0.1 M $HClO_4$ solution at a sweep rate of 10 mV s^{-1} and a rotation rate of 1600 rpm at room temperature. Adapted with permission from ref. [17] and ref. [67] and modified. Copyright (2014), Royal Society of Chemistry, and Copyright (2011), American Chemical Society.

It is also an intermediate or degradation product in drug synthesis. An electrochemical determination of 4-AP is, therefore, important for sensing biotoxins in water remediation and for monitoring pharmaceutical wastes. According to the authors of the report[68], such FeNi concave nanocubes and nanocages exhibit more than 10- and 100-fold enhancement of electroactivities for the detection of 4-AP compared to FeNi cuboctahedra, respectively.

5.4.3 Chemically Catalytic Behaviors

Since a heterogeneous catalytic reaction is closely linked with the surface structure of the catalyst, the catalytic performance could be therefore improved by altering the crystallographic facets on the surface of a catalyst through tailoring its particle shape. Investigations have been shown that each type of crystallographic facet on a catalyst has its own peculiarities for catalytic activity. For example, high-indexed Au facets favor the breaking of C=C bonds[69]. As a prototype of high-index faceted NCs, bimetallic convex and concave nanostructures should be a class of promising catalysts for promoting certain organic reactions in addition to the electrochemical performance, as described above. In this section, we choose several typical examples from recent literature to emphasize these properties.

5.4.3.1 Cases of Hydrogenation

The hydrogenation of olefins, that is, the addition of hydrogen to double (or even triple) bonds in hydrocarbons, is a typical reaction and is widely used in petrochemical, pharmaceutical, and fine agricultural chemical industries. Recent investigations indicate that high-index bimetallic catalysts should be one of the best promoters for such type of reaction. Wang et al. prepared Pt_3Co concave nanocubes and applied them in a hydrogenation of styrene as a model reaction. Evaluation indicates that the metallic catalysts are indispensable for facilitating this conversion of styrene under the reported experimental conditions. As shown in Figure 5.19a, this study further demonstrated that the *turnover frequency* (TOF), defined as the substrate (styrene) in number of moles that is converted by one mole of active catalyst within a fixed span of time, of the high-indexed Pt_3Co concave nanocubes is ~1.25-fold and ~2-fold of that for the {100}-terminated Pt_3Co nanocubes and for the Pt nanocubes, respectively[4], showing that the turnover rate closely connects to the dissociative adsorption of H_2 and activation of unsaturated bond. It was further identified that the hydrogenation of styrene can also be promoted by high-index facet-bounded Pt_3Fe concave nanocubes[3]. Such bimetallic concave catalysts possess a high fraction of low-coordinated atoms on their surfaces with a unique reactivity of H-H cleavage and C=C bond activation, demonstrating high TOF, which is ~1.2-fold of that for the {100}-surrounded Pt_3Fe nanocubes in a similar particle size (Figure 5.19b). On the other hand, Wu et al. reported the performance of Pt–Ni convex nanostructures in hydrogenations of C=C and N=C bonds, such as benzalacetone, styrene, and nitrobenzene[1]. They determined that the rate of hydrogenation is dependent on not only the composition but also the crystallographic index (shape) of the catalysts. In particular, the Pt–Ni bimetallic nanocatalysts are more active than their monometallic counterparts, possibly due to synergistic effects between Pt and Ni. The catalytic activity is also positively associated with the fraction of the exposed {111} facets. Figure 5.19c articulates a catalytic performance of 11–12 nm $PtNi_2$ octahedra,

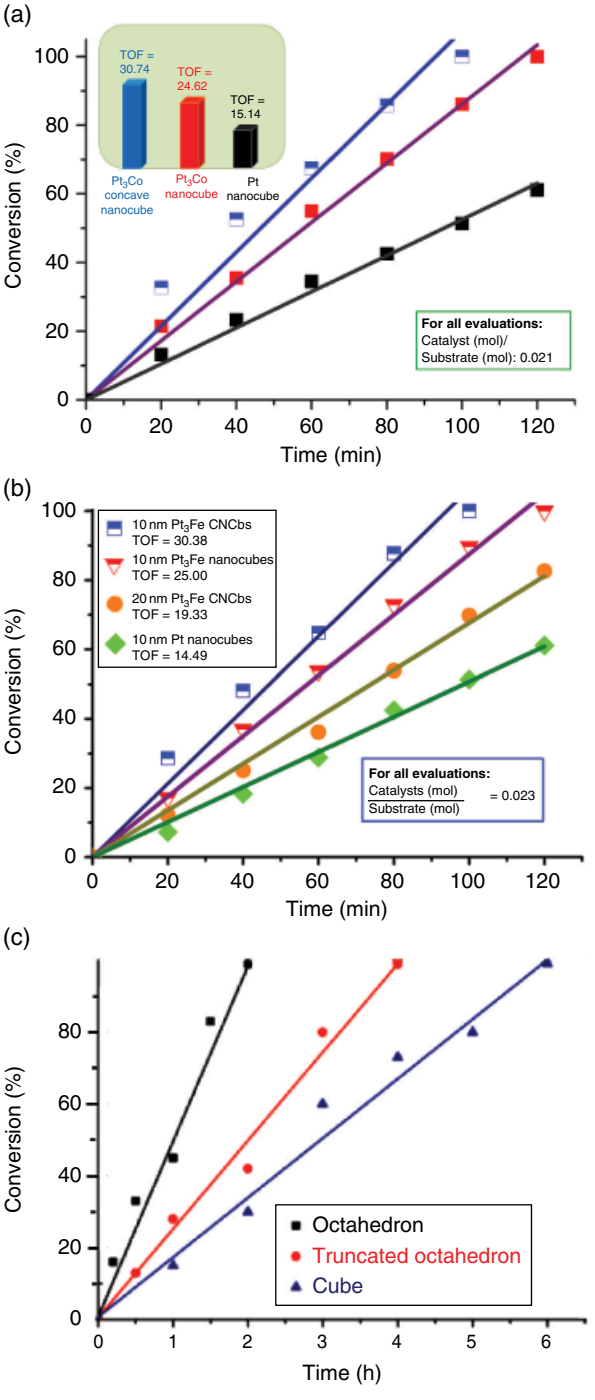

Figure 5.19 Conversion percentage of hydrogenation with different bimetallic convex and concave catalysts and Pt catalysts as a function of reaction time (TOF unit: [mol converted styrene]/[mol catalyst × h]): (a) hydrogenation of styrene on Pt_3Co concave nanocubes, Pt_3Co nanocubes and Pt nanocubes (all sizes are ~15 nm); (b) hydrogenation of styrene on 10 nm and 20 nm Pt_3Fe concave nanocubes, 10 nm Pt_3Fe nanocubes and 10 nm Pt nanocubes; (c) hydrogenation of benzalacetone on 11.8 nm $PtNi_2$ octahedra, 12.5 nm $PtNi_2$ truncated octahedral, and 11.2 nm $PtNi_2$ cubes. Adapted with permission from refs. [1,3,4] and modified. Copyright (2014, 2015), Wiley, and Copyright (2012), American Chemical Society.

truncated octahedra and cubes in the hydrogenation of benzalacetone. It was concluded that the ratio of TOF among the three classes of convex nanocatalysts, $PtNi_2$ octahedra, truncated octahedra and cubes, is 139 : 114 : 95 = 1.46 : 1.20 : 1, respectively[1].

Zhang et al. demonstrated catalytic behaviors of carbon-supported Pd–Cu bimetallic catalysts with a shape-control in the hydrogenation of 3-nitrostyrene (3-NT) in comparison with that of commercial Pd/C catalysts, showing the catalytic influence of both composition and surface structure on the reaction[70]. It was determined that incorporation of Cu component into the Pd catalyst (4–11 at% Cu) could dramatically select 3-ethylnitrobenzene instead of 3-ethylaniline as the product although the general the 3-NT conversation percentage was decrease compared to the pure Pd catalyst. This indicates that the bimetallic Pd–Cu catalysts possess much higher chemoselectivity (>99.9%) to C=C than to $-NO_2$ in this hydrogenation reaction. Further analysis in their time-dependent selectivity (Figure 5.20) interestingly indicates that the 48 nm $Pd_{95}Cu_5$ concave tetrahedra (CTH) exhibit a higher activity toward the conversion of the selected 3-ethylnitrobenzene product in comparison with the 50 nm convex rhombohedral tetrapod (RTP) $Pd_{93}Cu_7$ (the composition effect is ignored at this point). Reducing the size of CTH to 10 nm does not greatly influence the variation of the activity. The Pd–Cu CTHs are bounded with {111} and {110} facets, whereas RTPs are terminated with {111} planes only. It might, therefore, be inferred that the {110} facets of Pd–Cu catalysts possess the highest selectivity and activity to the C=C hydrogenation in this reaction.

5.4.3.2 Cases of 4-Nitrophenol Reduction

As a model reaction, it is meaningful to convert more toxic 4-nitrophenol (4-NP) to 4-AP that is also a useful intermediate in many drug syntheses. As indicated in Figure 5.21, Pt_3Fe concave nanocubes terminated with high-index facets show excellent catalytic characteristic toward the reduction of 4-NP by $NaBH_4$ at room temperature[3]. The similar catalytic behavior in 4-NP reduction can also be determined on Au–Pt concave core–shell nanocubes prepared through a galvanic replacement process[71], possibly owing to the exposedness of high-indexed Pt facets.

5.4.3.3 Cases of Other Reactions

It was reported that Pt–Pd nanocages with hollow interiors and porous walls feature enhanced activity and selectivity toward CO oxidation in the presence of hydrogen[72]. As shown in Figure 5.22a–b, the CO conversion temperature is dependent on the Pt–Pd size. With sizes of 8 and 12 nm, the maximum conversion temperatures were determined at 150°C. It seems that a small size favors the conversion at a low temperature. However, the large size of Pt–Pd nanocages (20 nm) provides a stable selectivity of CO oxidation against a dropping down when the temperature increases[72]. After a trace-deposition of Au on Pt–Ni octahedra, as another example, the Pt_3Ni-$Au_{0.5}$ core–shell concave nanooctahedra exhibit exceptional catalytic activities in both Suzuki-Miyaura reaction and reduction of nitrobenzene from formic acid[73] in comparison with other counterparts as shown in Figure 5.22c–d. These superior catalytic properties are attributed to a synergetic effect between the geometrical unique (atoms located on high-index facets such as steps) and electronic contribution from the trimetallic structure in which electrons are believed to transferred from the Au domains to Pt[73,74]. In addition, $Pt_3Ni–Ag_{0.5}$ concave nanooctahedra also show the best catalytic performance in selective oxidation of benzyl alcohol to benzaldehyde among its analogues, $Pt_3Ni–M_{0.5}$ (M = Rh, Au, Cu) and $Pt_3Ni–Ag_x$ (x = 2 and 8), which possess the similar shape but different shells (electronic effect)[73].

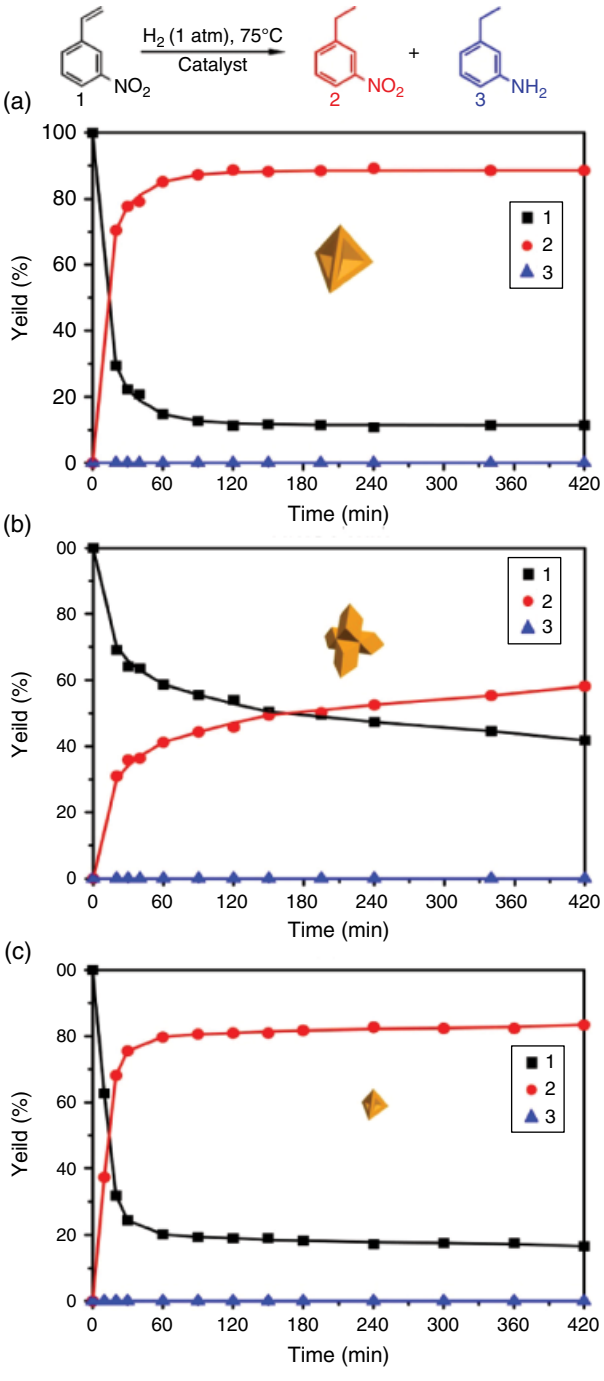

Figure 5.20 Time-dependent hydrogenation yield of 3-NT with H_2 using on Pd-Cu bimetallic catalysts: (a) 48 nm $Pr_{95}Cu_5$ concave tetrahedra (CTHs); (b) 50 nm $Pr_{93}Cu_7$ convex rhombohedral tetrapod (RTPs); and (c) 10 nm $Pr_{89}Cu_{11}$ concave tetrahedra (CTHs). Contrasts of the curves correspond to the compounds presented on the top of the figure. Adapted with permission from ref. [70]. Copyright (2015), Tsinghua University Press and Springer-Verlag Berlin Heidelberg.

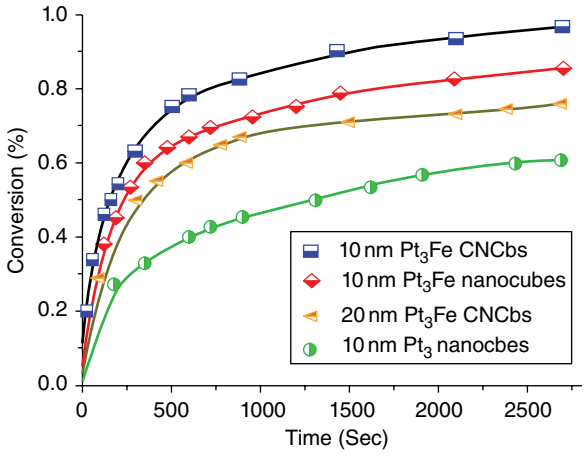

Figure 5.21 Conversion percentage of 4-NT by $NaBH_4$ on various Pt_3Fe convex and concave catalysts and Pt catalysts as a function of reduction time (CNCb: concave nanocube). Adapted with permission from ref. [3]. Copyright (2015), Wiley.

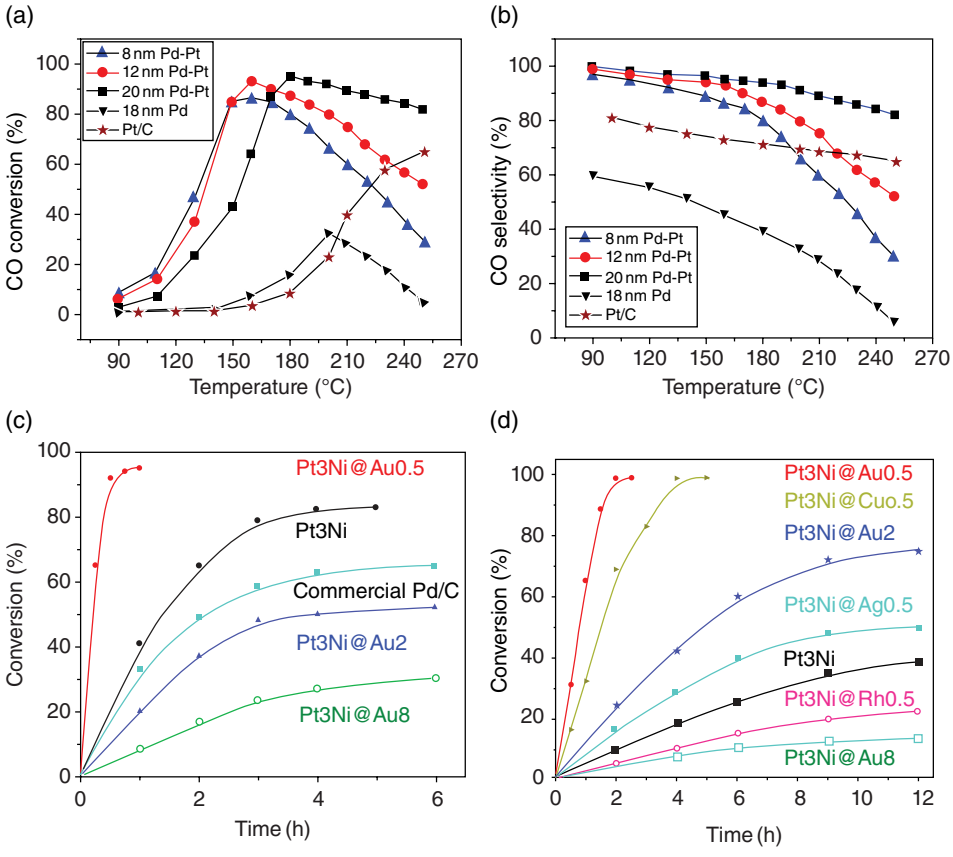

Figure 5.22 Performance of bi- and trimetallic concave catalysts. (a) and (b) activity and selectivity as a function of reaction temperature for CO preferential oxidation in the presence of H_2 on various Pt–Pd nanocages and Pt/C, respectively; (c) and (d) conversion percentage as a function of reaction time in Suzuki-Miyaura reaction and in nitrobenzene reduction in the presence of various catalysts, respectively. Metal M (M = Au, Cu, Ag, and Rh) was coated on $PtNi_3$ concave octahedra. Adapted with permission from refs. [72,73] and modified. Copyright (2011 and 2013), American Chemical Society.

5.5 Conclusions

Bimetallic convex and concave NCs terminated with high-index facets have been intensively studied due to their unique surface structure-dependent behaviors. These nanostructures can be developed using either a site-specific dissolution or seed-overgrowth strategy from a hot solution or hydrothermal system. In terms of the reaction approaches, a galvanic replacement, or coreduction with a control of capping ligand(s), or seed-mediated growth could be utilized and preparation examples for each are included as a case study in the first part of this chapter. The generated bimetallic convex and concave NCs are generally enclosed with low-coordinated atoms. Identification of their surface structure and morphology is essential. The relevant discussion is provided in the second part of this chapter. The last part of this chapter deals with various properties. Ag- and Pd-based NCs with these polyhedral morphologies (especially the concave shape) can act as very promising substrates to enhance SERS signals. The hot spots presented in the gaps, tips, and edges in these nanostructures can focus the electromagnetic field and favor the "amplification" of SERS signal especially for the long wavelength of the excitation. On the other hand, these bimetallic convex and concave NCs possess high-indexed facets that are originated from steps, edges, tips, corners, and kinks, and are very promising catalytic promoters for cleaving C-H and C-O bonds. By taking the advantage of composition control (surface electronic structure modification in a bimetallic system) and shape control (*selective use* of the crystallographic planes with lattice strain effect), these high-index bimetallic NCs exhibit high performance in small molecule electro-oxidation and many chemical catalysis as presented in this chapter. These research outcomes discussed in this chapter open an array of possibilities for a further study on these bimetallic nanostructures.

5.6 References

1 Wu, Y., Cai, S., Wang, D., He, W. and Li, Y. (2012). Syntheses of water-soluble octahedral, truncated octahedral, and cubic Pt–Ni nanocrystals and their structure–activity study in model hydrogenation reactions. *Journal of the American Chemical Society*, 134, 8975–8981.

2 Wu, Y., Wang, D., Niu, Z., Chen, P., Zhou, G. and Li, Y. (2012). A strategy for designing a concave Pt-Ni alloy through controllable chemical etching. *Angewandte Chemie International Edition*, 51 (50), 12524–12528.

3 Wang, C., Lin, C., Zhao, B., Zhang, L., Kumbhar, A., Fan, G., Sun, K., Zhang, J., Chen, S. and Fang, J. (2015). High-indexed Pt_3Fe nanocatalysts and their enhanced catalytic performance in dual organic reactions. *ChemNanoMat*, 1 (5), 331–337.

4 Wang, C., Lin, C., Zhang, L., Quan, Z., Sun, K., Zhao, B., Wang, F., Porter, N., Wang, Y. and Fang, J. (2014). Pt_3Co concave nanocubes: synthesis, formation understanding, and enhanced catalytic activity toward hydrogenation of styrene. *Chemistry—A European Journal*, 20 (6), 1753–1759.

5 Wu, J., Gross, A. and Yang, H. (2011). Shape and composition-controlled platinum alloy nanocrystals using carbon monoxide as reducing agent. *Nano Letters*, 11 (2), 798–802.

6 Cui, C., Gan, L., Li, H.-H., Yu, S.-H., Heggen, M. and Strasser, P. (2012). Octahedral PtNi nanoparticle catalysts: exceptional oxygen reduction activity by tuning the alloy particle surface composition. *Nano Letters*, 12 (11), 5885–5889.

7 Taylor, E., Chen, S., Tao, J., Wu, L., Zhu, Y. and Chen, J. (2013). Synthesis of Pt–Cu nanodendrites through controlled reduction kinetics for enhanced methanol electro-oxidation. *ChenSusChem*, 6 (10), 1863–1867.

8 Stamenkovic, V. R., Fowler, B., Mun, B. S., Wang, G., Ross, P. N., Lucas, C. A. and Marković, N. M. (2007). Improved oxygen reduction activity on $Pt_3Ni(111)$ via increased surface site availability. *Science*, 315 pp. 493–497.

9 Zhang, J., Yang, H., Fang, J. and Zou, S. (2010). synthesis and oxygen reduction activity of shape-controlled Pt_3Ni nanopolyhedra. *Nano Letters*, 10 (2), 638–644.

10 Nørskov, J. K., Bligaard, T., Rossmeisl, J. and Christensen, C. H. (2009). Towards the computational design of solid catalysts. *Nature Chemistry*, 1 pp. 37–46.

11 Wu, J., Li, P., Pan, Y.-T. F., Warren, S., Yin, X. and Yang, H. (2012). Surface lattice-engineered bimetallic nanoparticles and their catalytic properties. *Chemical Society Review*, 41 pp. 8066–8074.

12 Srivastava, R., Mani, P., Hahn, N. and Strasser, P. (2007). Efficient oxygen reduction fuel cell electrocatalysis on voltammetrically dealloyed Pt–Cu–Co nanoparticles. *Angewandte Chemie International Edition*, 46 (47), 8988–8991.

13 Strasser, P., Koh, S., Anniyev, T., Greeley, J., More, K., Yu, C., Liu, Z., Kaya, S., Nordlund, D., Ogasawara, H., Toney, M. F. and Nilsson, A. (2010). Lattice-strain control of the activity in dealloyed core–shell fuel cell catalysts. *Nature Chemistry*, 2, 454–460.

14 Gu, J., Zhang, Y.-W. and Tao, F. (2012). Shape control of bimetallic nanocatalysts through well-designed colloidal chemistry approaches. *Chemical Society Reviews*, 41 (24), 8050–8065.

15 Zhang, H., Jin, M. and Xia, Y. (2012). Noble-metal nanocrystals with concave surfaces: synthesis and applications. *Angewandte Chemie International Edition*, 51 (31), 7656–7673.

16 Yin, A.-X., Min, X.-Q., Zhu, W., Liu, W.-C., Zhang, Y.-W. and Yan, C.-H. (2012). Pt-Cu and Pt-Pd-Cu Concave nanocubes with high-index facets and superior electrocatalytic activity. *Chemistry—A European Journal*, 18 (3), 777–782.

17 Zhan, F., Bian, T., Zhao, W., Zhang, H., Jin, M. and Yang, D. (2014). Facile Synthesis of Pd-Pt Alloy Concave nanocubes with high-index facets as electrocatalysts for methanol oxidation. *CrystEngComm*, 16 (12), 2411–2416.

18 Kang, Y., Ye, X. and Murray, C. B. (2010). Size- and shape-selective synthesis of metal nanocrystals and nanowires using co as a reducing agent. *Angewandte Chemie International Edition*, 49, 6156–6159.

19 Jia, Y., Jiang, Y., Zhang, J., Zhang, L., Chen, Q., Xie, Z. and Zheng, L. (2014). Unique excavated rhombic dodecahedral $ptcu_3$ alloy nanocrystals constructed with ultrathin nanosheets of high-energy {110} facets. *Journal of the American Chemical Society*, 136 (10), 3748–3751.

20 Huang, X., Zhao, Z., Fan, J., Tan, Y. and Zheng, N. (2011). Amine-assisted synthesis of concave polyhedral platinum nanocrystals having {411} high-index facets. *Journal of the American Chemical Society*, 133 (13), 4718–4721.

21 Zhang, L.-F., Zhong, S.-L. and Xu, A.-W. (2013). Highly branched concave Au/Pd bimetallic nanocrystals with superior electrocatalytic activity and highly efficient sers enhancement. *Angewandte Chemie International Edition*, 52 (2), 645–649.

22 Zhang, L., Niu, W., Li, Z. and Xu, G. (2011). Facile synthesis and electrochemiluminescence application of concave trisoctahedral Pd@Au core–shell nanocrystals bound by {331} high-index facets. *Chemical Communications*, 47 (37), 10353–10355.

23 Yu, Y., Zhang, Q., Liu, B. and Lee, J. Y. (2010). Synthesis of nanocrystals with variable high-index Pd facets through the controlled heteroepitaxial growth of trisoctahedral Au templates. *Journal of the American Chemical Society*, 132 (51), 18258–18265.

24 Gilroy, K. D., Ruditskiy, A., Peng, H.-C., Qin, D. and Xia, Y. (2016). Bimetallic nanocrystals: syntheses, properties, and applications. *Chemical Reviews*, 116 (18), 10414–10472.

25 Gan, L., Cui, C., Heggen, M., Dionigi, F., Rudi, S. and Strasser, P. (2014). Element-specific anisotropic growth of shaped platinum alloy nanocrystals. *Science*, 346 (6216), 1502–1506.

26 Chen, S., Jenkins, S. V., Tao, J., Zhu, Y. and Chen, J. (2013). Anisotropic seeded growth of Cu–M (M = Au, Pt, or Pd) bimetallic nanorods with tunable optical and catalytic properties. *The Journal of Physical Chemistry C*, 117, 8924–8932.

27 Xiao, J., Liu, S., Tian, N., Zhou, Z.-Y., Liu, H.-X., Xu, B.-B. and Sun, S.-G. (2013). Synthesis of convex hexoctahedral Pt micro/nanocrystals with high-index facets and electrochemistry-mediated shape evolution. *Journal of the American Chemical Society*, 135 (50), 18754–18757.

28 Tian, N., Zhou, Z.-Y., Sun, S.-G., Ding, Y. and Wang, Z. L. (2007). Synthesis of tetrahexahedral platinum nanocrystals with high-index facets and high electro-oxidation activity. *Science*, 316 (5825), 732–735.

29 Wang, C., Zhang, L., Yang, H., Pan, J., Liu, J., Dotse, C., Luan, Y., Gao, R., Lin, C., Zhang, J., Kilcrease, J. P., Wen, X., Zou, S. and Fang, J. (2017). High-indexed Pt_3Ni alloy tetrahexahedral nanoframes evolved through preferential Co etching. *Nano Letters*, 17 (4), 2204–2210.

30 Ding, J., Bu, L., Guo, S., Zhao, Z., Zhu, E., Huang, Y. and Huang, X. (2016). Morphology and phase controlled construction of Pt–Ni nanostructures for efficient electrocatalysis. *Nano Letters*, 16 (4), 2762–2767.

31 Zhang, L., Niu, W., Gao, W., Qi, L., Lai, J., Zhao, J. and Xu, G. (2014). Synthesis of convex hexoctahedral palladium@gold core–shell nanocrystals with {431} high-index facets with remarkable electrochemiluminescence activities. *ACS Nano*, 8 (6), 5953–5958.

32 Kim, D., Lee, Y. W., Lee, S. B. and Han, S. W. (2012). Convex polyhedral Au@Pd core–shell nanocrystals with high-index facets. *Angewandte Chemie International Edition*, 51 (1), 159–163.

33 Personick, M. L. and Mirkin, C. A. (2013). Making sense of the mayhem behind shape control in the synthesis of gold nanoparticles. *Journal of the American Chemical Society*, 135 (49), 18238–18247.

34 Lin, H.-X., Lei, Z.-C., Jiang, Z.-Y., Hou, C.-P., Liu, D.-Y., Xu, M.-M., Tian, Z.-Q. and Xie, Z.-X. (2013). Supersaturation-dependent surface structure evolution: from ionic, molecular to metallic micro/nanocrystals. *Journal of the American Chemical Society*, 135 (25), 9311–9314.

35 Quan, Z., Wang, Y. and Fang, J. (2013). High-index faceted noble metal nanocrystals. *Accounts of Chemical Research*, 46 (2), 191–202.

36 Zhou, Z.-Y., Tian, N., Li, J.-T., Broadwell, I. and Sun, S.-G. (2011). Nanomaterials of high surface energy with exceptional properties in catalysis and energy storage. *Chemical Society Reviews*, 40, 4167–4185.

37 Liang, B., Joyner, R. W. and Somorjai, G. A. (1972). Low energy electron diffraction studies of chemisorbed gases on stepped surfaces of platinum. *Surface Science*, 30 (2), 454–474.

38 Hove, M. A. V. and Somorjai, G. A. (1980). A new microfacet notation for high-miller-index surfaces of cubic materials with terrace, step and kink structures. *Surface Science*, 92 (2-3), 489–518.

39 Moghimi, N., Rahsepar, F. R., Srivastava, S., Heinig, N. and Leung, K. T. (2014). Shape-dependent magnetism of bimetallic FeNi nanosystems. *Journal of Materials Chemistry C*, 2,6370–6375.

40 Sun, S., Murray, C. B., Weller, D., Folks, L. and Moser, A. (2000). Monodisperse FePt nanoparticles and ferromagnetic FePt nanocrystal superlattices. *Science*, 287 (5460), 1989–1992.

41 Li, R., Zhang, J., Tan, R., Gerdes, F., Luo, Z., Xu, H., Hollingsworth, J. A., Klinke, C., Chen, O. and Wang, Z. (2016). Competing interactions between various entropic forces toward assembly of Pt_3Ni octahedra into a body-centered cubic superlattice. *Nano Letters*, 16, 2792–2799.

42 Yang, Z., Wei, J., Bonville, P. and Pileni, M.-P. (2015). Beyond entropy: magnetic forces induce formation of quasicrystalline structure in binary nanocrystal superlattices. *Journal of the American Chemical Society*, 137 (13), 4487–4493.

43 Xia, X., Jie Zeng, McDearmon, B., Zheng, Y., Li, Q. and Xia, Y. (2011). Silver nanocrystals with concave surfaces and their optical and surface-enhanced raman scattering properties. *Angewandte Chemie International Edition*, 50 (52), 12542–12546.

44 Mulvihill, M. J., Ling, X. Y., Henzie, J. and Yang, P. (2010). Anisotropic etching of silver nanoparticles for plasmonic structures capable of single-particle SERS. *Journal of the American Chemical Society*, 132 (1), 268–274.

45 Xiong, Y., McLellan, J. M., Chen, J., Yin, Y., Li, Z.-Y. and Xia, Y. (2005). Kinetically controlled synthesis of triangular and hexagonal nanoplates of palladium and their SPR/SERS properties. *Journal of the American Chemical Society*, 127 (48), 17118–17127.

46 Wiley, B. J., Im, S. H., Li, Z.-Y., McLellan, J., Siekkinen, A. and Xia, Y. (2006). Maneuvering the surface plasmon resonance of silver nanostructures through shape-controlled synthesis. *Journal of Physical Chemistry B*, 110 (32), 15666–15675.

47 Tao, A., Sinsermsuksakul, P. and Yang, P. (2006). Polyhedral silver nanocrystals with distinct scattering signatures. *Angewandte Chemie International Edition*, 45, 4597–4601.

48 Rycenga, M., Langille, M. R., Personick, M. L., Ozel, T. and Mirkin, C. A. (2012). Chemically isolating hot spots on concave nanocubes. *Nano Letters*, 12 (12), 6218–6222.

49 Zhang, J., Winget, S. A., Wu, Y., Su, D., Sun, X., Xie, Z.-X. and Qin, D. (2016). Ag@Au concave cuboctahedra: a unique probe for monitoring Au-catalyzed reduction and oxidation reactions by surface-enhanced Raman spectroscopy. *ACS Nano*, 10 (2), 2607–2616.

50 Lee, K. W., An, H., Haam, S., Baik, H. and Lee, K. (2015). Regiospecific growth of Au on a concave PtZn nanocube forming an Au-PtZn surface mosaic nanocube and an Au-PtZn octapod. *CrystEngComm*, 17 (36), 6838–6842.

51 Wu, D.-Y., Liu, X.-M., Duan, S., Xu, X., Ren, B., Lin, S.-H. and Tian, Z.-Q. (2008). Chemical enhancement effects in SERS spectra: a quantum chemical study of pyridine interacting with copper, silver, gold and platinum metals. *Journal of Physical Chemistry C*, 112 (11), 4195–4204.

52 Xu, D., Bliznakov, S., Liu, Z., Fang, J. and Dimitrov, N. (2010). Composition-dependent electrocatalytic activity of Pt-Cu nanocube catalysts for formic acid oxidation. *Angewandte Chemie International Edition*, 49 (7), 1282–1285.

53 Xu, D., Liu, Z., Yang, H., Liu, Q., Zhang, J., Fang, J., Zou, S. and Sun, K. (2009). Solution-based evolution and enhanced methanol oxidation activity of monodisperse platinum-copper nanocubes. *Angewandte Chemie International Edition*, 48 (23), 4217–4221.

54 Yang, H., Zhang, J., Sun, K., Zou, S. and Fang, J. (2010). Enhancing by weakening: electrooxidation of methanol on Pt_3Co and Pt nanocubes. *Angewandte Chemie International Edition*, 49 (38), 6848–6851.

55 Alayoglu, S., Nilekar, A. U., Mavrikakis, M. and Eichhorn, B. (2008). Ru–Pt core–shell nanoparticles for preferential oxidation of carbon monoxide in hydrogen. *Nature Materials*, 7, 333–338.

56 Kristian, N., Yu, Y., Gunawan, P., Xu, R., Deng, W., Liu, X. and Wang, X. (2009). Controlled synthesis of Pt-decorated Au nanostructure and its promoted activity toward formic acid electro-oxidation. *Electrochimica Acta*, 54 (21), 4916–4924.

57 Solla-Gullón, J., Vidal-Iglesias, F. J., López-Cudero, A., Garnier, E., Feliu, J. M. and Aldaza, A. (2008). Shape-dependent electrocatalysis: methanol and formic acid electrooxidation on preferentially oriented Pt nanoparticles. *Phys. Chem. Chem. Phys.*, 10, 3689–3698.

58 Lebedeva, N. P., Koper, M. T. M., Feliu, J. M. and Santen, R. A. V. (2002). Role of Crystalline Defects in Electrocatalysis: Mechanism and kinetics of Co adlayer oxidation on stepped platinum electrodes. *Journal of Physical Chemistry B*, 106 (50), 12938–12947.

59 Lee, S. W., Chen, S., Sheng, W., Yabuuchi, N., Kim, Y.-T., Mitani, T., Vescovo, E. and Shao-Horn, Y. (2009). Roles of surface steps on Pt nanoparticles in electro-oxidation of carbon monoxide and methanol. *Journal of the American Chemical Society*, 131 (43), 15669–15677.

60 Tian, N., Zhou, Z.-Y. and Sun, S.-G. (2008). Platinum metal catalysts of high-index surfaces: from single-crystal planes to electrochemically shape-controlled nanoparticles. *Journal of Physical Chemistry C*, 112 (50), 19801–19817.

61 Adzic, R. R., Triokovic, A. V. and Ogrady, W. E. (1982). Structural effects in electrocatalysis. *Nature*, 296, 137–138.

62 Choi, S.-I., Xie, S., Shao, M., Odell, J. H., Lu, N., Peng, H.-C., Protsailo, L., Guerrero, S., Park, J., Xia, X., Wang, J., Kim, M. J. and Xia, Y. (2013). Synthesis and characterization of 9 nm Pt–Ni octahedra with a record high activity of 3.3 a/Mgpt for the oxygen reduction reaction. *Nano Letters*, 13 (7), 3420–3425.

63 Zhao, H., Yu, C., You, H., Yang, S., Guo, Y., Ding, B. and Song, X. (2012). A green chemical approach for preparation of Pt_xCu_y nanoparticles with a concave surface in molten salt for methanol and formic acid oxidation reactions. *Journal of Materials Chemistry*, 22 (11), 4780–4789.

64 Qi, Y., Bian, T., Choi, S.-I., Jiang, Y., Jin, C., Fu, M., Zhang, H. and Yang, D. (2014). Kinetically controlled synthesis of Pt-Cu alloy concave nanocubes with high-index facets for methanol electro-oxidation. *Chemical Communications*, 50 (5), 560–562.

65 Liu, X., Wang, W., Li, H., Li, L., Zhou, G., Yu, R., Wang, D. and Li, Y. (2014). One-pot protocol for bimetallic Pt/Cu hexapod concave nanocrystals with enhanced electrocatalytic activity. *Scientific Reports*, 3, 1404.

66 Li, Y., Quan, F., Zhu, E., Chen, L., Huang, Y. and Chen, C. (2015). PtxCuy nanocrystals with hexa-pod morphology and their electrocatalytic performances towards oxygen reduction reaction. *Nano Research*, 8 (10), 3342–3352.

67 Zhang, H., Jin, M., Wang, J., Li, W., Camargo, P. H. C., Kim, M. J., Yang, D., Xie, Z. and Xia, Y. (2011). Synthesis of Pd-Pt bimetallic nanocrystals with a concave structure through a bromide-induced galvanic replacement reaction. *Journal of the American Chemical Society*, 133 (15), 6078–6089.

68 Moghimi, N., Abdellah, M., Thomas, J. P., Mohapatra, M. and Leung, K. T. (2013). Bimetallic feni concave nanocubes and nanocages. *Journal of the American Chemical Society*, 135 (30), 10958–10961.

69 Schimpf, S., Lucas, M., Mohr, C., Rodemerck, U., Brückner, A., Radnik, J., Hofmeister, H. and Claus, P. (2002). Supported gold nanoparticles: in-depth catalyst characterization and application in hydrogenation and oxidation reactions. *Catalysis Today*, 72 (1–2), 63–78.

70 Zhang, L., Su, H., Sun, M., Wang, Y., Wu, W., Yu, T. and Zeng, J. (2015). Concave Cu-Pd bimetallic nanocrystals: ligand-based co-reduction and mechanistic study. *Nano Research*, 8 (7), 2415–2430.

71 Li, H., Wu, H., Zhai, Y., Xu, X. and Jin, Y. (2013). Synthesis of monodisperse plasmonic Au core-Pt shell concave nanocubes with superior catalytic and electrocatalytic activity. *ACS Catalysis*, 3 (9), 2045–2051.

72 Zhang, H., Jin, M., Liu, H., Wang, J., Kim, M. J., Yang, D., Xie, Z., Liu, J. and Xia, Y. (2011). Facile synthesis of Pd-Pt alloy nanocages and their enhanced performance for preferential oxidation of CO in excess hydrogen. *ACS Nano*, 5 (10), 8212–8222.

73 Wu, Y., Wang, D., Chen, X., Zhou, G., Yu, R. and Li, Y. (2013). Defect-dominated shape recovery of nanocrystals: a new strategy for trimetallic catalysts. *Journal of the American Chemical Society*, 135 (33), 12220–12223.

74 Yang, J., and Ying, J. Y. (2011). Nanocomposites of Ag_2s and noble metals. *Angewandte Chemie International Edition*, 50 (20), 4637–4643.

6

Bimetallic Nanoframes and Nanoporous Structures

Hongliang Li, An Zhang, Zhicheng Fang, and Jie Zeng

Hefei National Laboratory for Physical Sciences at the Microscale, Department of Chemical Physics, University of Science and Technology of China, Hefei, Anhui, P. R. China

6.1 Introduction

Surface atoms situate themselves in an anisotropic local environment compared with the interior ones in three-dimensional periodicity. The special coordination environment endows these surface atoms with unsaturated coordination, high free energy, atomic migration, rearrangement of crystal structures, and other properties[1]. These distinct features significantly influence the physical and chemical processes. To maximize the contributions made by surface atoms, one of the most promising methods is to prepare nanoporous materials with an open spatial structure[2]. Over the past few decades, growing attention has been paid on these nanoporous materials owing to their superior performance in a number of applications, including catalysis[3–5], separation[6,7], biomedicine[8–10], sensing[11–13], energy storage[14–16], environmental remediation[17–19], and so forth. Exemplified with the application in catalysis, the enormous interest of nanoporous nanomaterials in catalysis stems from a series of key advantages[20]. The open structure of nanoporous materials enables the accelerated mass and electron transfer during the reaction. Besides, these nanoporous materials contain abundant low coordination sites that are catalytically active. As a bonus, the porous structure also improves the selectivity by molecular sieving or large differences of diffusitivity in nanopores[21–23]. Moreover, nanoporous materials can effectively isolate catalytic species and stabilize particles against sintering, leading to superior durability. In photocatalysis, porous nanomaterials are assumed to improve scattering and thus the absorption of light[24]. In addition, there are several other advantages of nanoporous materials in catalysis, such as high utilization efficiency of catalysts and functionality in the pores.

Porous materials can be branched out into various categories from different perspectives. For example, on the basis of pore sizes, those in the range of 2 nm and below are called micropores; those in the range of 2 and 50 nm are denoted as mesopores; those above 50 nm are macropores. Notably, the uniformity of size and shape of the voids in

Bimetallic Nanostructures: Shape-Controlled Synthesis for Catalysis, Plasmonics, and Sensing Applications, First Edition. Edited by Ya-Wen Zhang.
© 2018 John Wiley & Sons Ltd. Published 2018 by John Wiley & Sons Ltd.

porous nanostructures plays a prominent and important role in controlling the performance in a specific application[25]. A typical example is that a zeolite with uniform pores can separate molecules by selectively absorbing a small molecule from a mixture containing molecules too large to enter its pores. In addition, considering the different compositions in the porous nanostructures, they can be divided into organic and inorganic porous nanostructures, or more specifically into polymer, ceramic, metal, semiconductor, carbon, and composite porous structures. Here, we mainly cover significant issues in bimetallic nanoframes and nanoporous structures with pore sizes below 100 nm. In this work, *nanoframes* refer to those nanocrystals composed of only ridges without side faces or nanocages with large cavity on side faces. Three-dimensional bimetallic nanocrystals consisting of multiple branches with high accessibility are overviewed in this chapter as well.

Bimetallic nanoframes and nanoporous structures integrate the advantages of bimetallic materials (e.g., ligand effect and ensemble effect) and nanoporous structures as discussed above. Correspondingly, synthesis of bimetallic nanoframes and nanoporous structures seems fairly complicated, as both compositional and structural issues need to be taken into consideration. In recent years, a vast variety of methods have been developed for fabricating nanoframes and nanoporous structures made from metals such as Au, Ag, Pd, Pt, Rh, Fe, and Ni[26–29]. These methods can be divided into two complementary categories: top-down and bottom-up strategies. The top-down strategy is mainly established on dissolution in a site- and/or element-specific fashion. When such selective dissolution occurs, the region and/or element experiencing faster dissolution will be etched away to yield bimetallic nanoframes and nanoporous structures. As for the bottom-up strategy, it is likely to generate bimetallic nanoframes and nanoporous structures through directionally controlled overgrowth.

In this chapter, we will begin with a detailed discussion on the synthetic principles that can be utilized to guide the preparation of bimetallic nanoframes and nanoporous structures from top-down and bottom-up perspectives. Then we examine representative progress in the experimental implementation of these synthetic approaches, with a focus on the following methods: templating, oxidative etching, galvanic replacement, Kirkendall effect, electrochemical dealloying, and assembly. Moreover, some other methods of interest, including atomic migration, underpotential deposition (UPD), and Ostwald ripening, have also been presented. Several characterization analyses and properties of these bimetallic nanoframes and nanoporous structures can be also discovered in this section. Finally, we conclude this chapter with a summary and outlook highlighting future perspectives on the development in this field.

6.2 Principles for the Formation of Bimetallic Nanoframes and Nanoporous Structures

In general, the diversified synthetic protocols for nanoframes and nanoporous structures can be summarized in two complementary types, including top-down and bottom-up approaches (Figure 6.1)[26,30–32]. The top-down synthesis, also known as conventional manufacturing, starts from large solid materials, parts of which are then broken down to generate porous structures. The bottom-up approach, also known as molecular manufacturing, refers to that small individual building blocks are linked

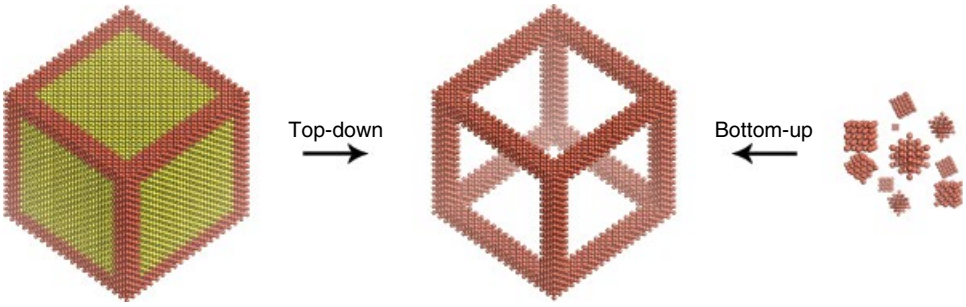

Figure 6.1 Schematic illustration showing the top-down and bottom-up strategies for the preparation of nanoframes.

together to generate large hierarchical structures, finally resulting in nanoframes or nanoporous structures.

6.2.1 Top-Down Approach

In nanoscale synthesis, various protocols follow the top-down mode[33–37]. The original large solid materials are typically sourced from diverse categories, such as carbons, silicas, metals, as well as metal oxides, sulfides, selenides, tellurides, nitrides, phosphines. Specifically, while comprising only two elements, bimetallic nanocrystals can take multiple architectures from nonordered alloys to intermetallic compounds, core–shell structures, and heterostructures according to the spatial distribution of their constituent elements[38]. The key to the top-down approach relies on how to drive the structural dissolution of the raw materials. Conventional strategies to disintegrate the materials are based on factors such as erosion, focused ion beams, manufacture of microprocessing, and atomic force microscopy tips as a writing device[30]. However, most of the products obtained from the conventional methods are still relatively large in geometry far beyond the nanoscale. In chemical synthetic processes, the driving forces for the disintegration are commonly classified into two types: kinetic and thermodynamic driving forces. The kinetic driving forces typically derive from the difference between the redox potentials, concentration gradient, and other kinetic factors. A typical thermodynamic driving force is originated from the reduction of Gibbs free energy.

The reduction of aqueous metallic oxidized species, $M^{z+}{}_{(aq)}$, leads to neutral metallic atoms and these constitute the construction blocks of clusters and metallic nucleus. This process is the result of consecutive redox reactions in which the electrons of a reducing agent, Red^{u}, are transferred to the metal according to the following electrochemical equations:

$$mM^{z^+}_{(aq)} + (mz)e^- \rightarrow M^0_m \tag{6.1}$$

$$Red^{u} \rightarrow O^{u+1}_x + e^{-1} \tag{6.2}$$

$$mM^{z^+}_{(aq)} + (mz)Red^{u} \rightarrow (mz)O^{u+1}_x + M^0_m \tag{6.3}$$

where O_x^{u+1} is the oxidized species. The driving force of the process is the difference between the redox potentials, ΔE, between Eqs. (6.1) and (6.2). The magnitude of ΔE determines the value of the equilibrium constant, K, of Eq. (6.3) according to:

$$\ln K = \frac{zF}{RT}\Delta E \tag{6.4}$$

The reduction reaction of $mM_{(aq)}^{z^+}$ is thermodynamically possible only if ΔE is positive, which implies that the redox potential of the reducing agent must have a more negative value than that of the metallic species. Generally, the involvement of any redox reaction during the synthesis of bimetallic nanoframes and nanoporous structures is related to the existence of ΔE. For instance, galvanic replacement is driven by the difference between the redox potentials of different metallic species[28]. The driving force of oxidative etching originates from the disparate potentials between oxidizers and metallic species. In addition, in the electrochemical dealloying, the electrons directly provided by the electrochemical system can be directly regarded as the driven force.

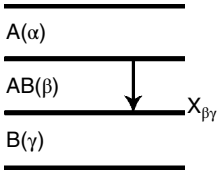

Figure 6.2 Schematic diagram of the cross section of a planar layered structure depicting the diffusion of A atoms from A to B through the AB interface.

Diffusion is a process of mass transport across a concentration gradient. For simplicity, a planar layered model is given to illustrate the diffusion kinetics, as shown in Figure 6.2. In this case, the influence of the variation in interfacial area during the growth can be avoided. Firstly, the diffusion of A atoms from A to B through the AB interface is taken as example to demonstrate the diffusion kinetics. According to the Fick's first law of diffusion, the velocity of the interface between AB and B is given as:

$$\frac{dx_{\beta\gamma}}{dt} = -\frac{D_\beta}{\left(C_{\beta\gamma}^{eq} - C_{\gamma\beta}^{eq}\right)}\frac{dC_\beta}{dx} \tag{6.5}$$

where $dx\beta\gamma/dt$ is the velocity of the interface between AB and B; $D\beta$ is the diffusion coefficient of A in AB; $Ceq\beta\gamma$ and $Ceq\gamma\beta$ are equilibrium concentrations of A species in AB and in B near the AB-B interface, respectively; $dC\beta/dx$ is the concentration gradient of A at the AB-B interface. This mechanism could also be applied to the diffusion of B atoms from B to A[39,40]. If the diffusion coefficient of A in AB is different from that of B in AB, pores will appear, which is generally termed as Kirkendall effect. For example, if A diffuse into B faster than that of B into A, accompanied with the diffusion of voids, the excess vacancies will be condensed in A, resulting in the formation of voids.

When dealing with spherical cases, we should consider the effect of Gibbs-Thomson potential on the growth rate. Similarly, we firstly consider the diffusion of A atoms from A to B through AB interface. The velocity of the spherical interface at r_2 can be approximately described by the following equation:

$$\frac{dr_2}{dt} \approx \frac{D_\beta}{kT}\left(-\frac{\Delta\mu_\beta}{\Delta r}\right) \tag{6.6}$$

where

$$\Delta\mu_\beta = \Delta G_{silicide} + \left(\frac{2\gamma_2\Omega}{r_2} - \frac{2\gamma_1\Omega}{-r_1}\right) = \Delta G_{silicide} + 2\Omega\left(\frac{\gamma_2}{r_2} + \frac{\gamma_1}{r_1}\right) \tag{6.7}$$

r_2 and r_1 are the radius of the outer and inner surface, respectively; γ_2 and γ_1 are the interfacial energy per atom of the AB-A and AB-B interfaces, respectively; Ω is the atomic volume; ΔG_{AB} is the formation energy of AB per atom. If ΔG_{AB} is negative with the positive second term, the curvature induces a lower flux of B. As such, the Gibbs-Thomson effect prevents the out-diffusion flux.

6.2.2 Bottom-Up Approach

Another underlying basic tool of nanotechnology is the bottom-up approach, where the system develops from smaller building blocks to bigger and more complex structures[41–44]. Template-free methods may use directed self-assembly of nanoparticles and the interaction between specific kinds of molecules, which act as links in order to build more complex structures. The key to the bottom-up approach in generating nanoframes and nanoporous structures is to link the individual building blocks. Common methods for the linkage include ripening, gelation, and cross-linking, as shown in Figure 6.3.

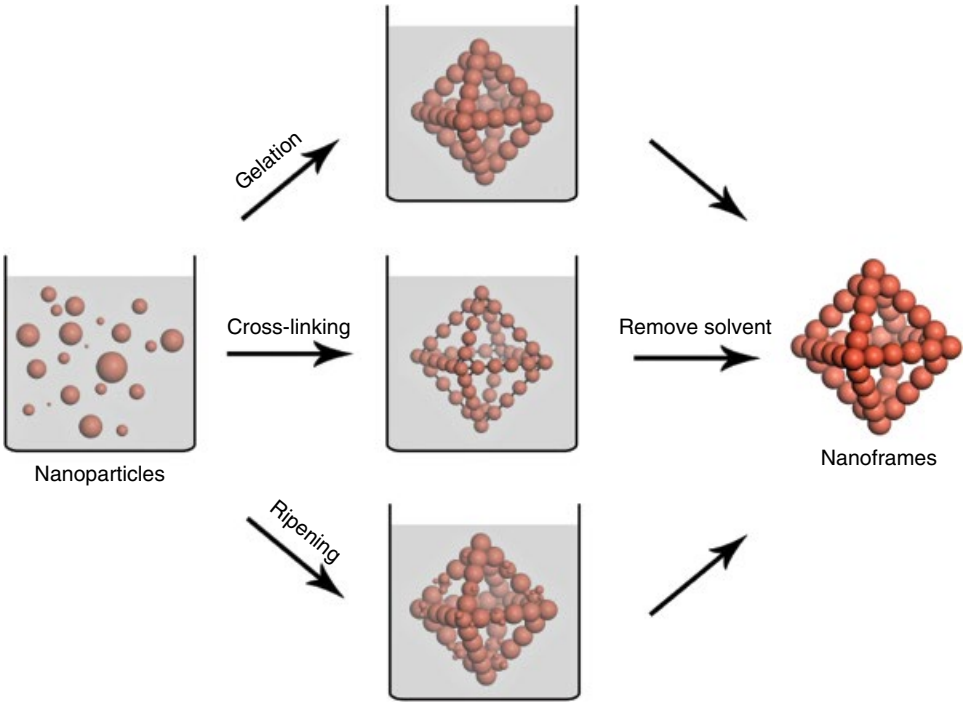

Figure 6.3 Schematic diagram illustrating three methods based on the bottom-up approach.

A typical bottom-up approach to the synthesis of nanoframes and nanoporous structures is based on ripening, where large particles form at the expense of the dissolution of smaller one. Theoretically, this process can be described by the well-known Gibbs-Thomson relation:

$$C_r = C_e \exp\left[\frac{2\gamma\Omega}{R_B T}\cdot\frac{1}{r}\right] \approx C_e\left[1+\frac{2\gamma\Omega}{R_B T}\cdot\frac{1}{r}\right] \tag{6.8}$$

where C_e is the solute concentration at a plane interface in the matrix in equilibrium with particle of infinite radius; C_r is the solubility at the surface of a spherical particle with radius r; γ is the specific interfacial energy of the matrix-precipitate particle boundary; Ω is the mean atomic (or molar) volume of the particle; R_B is the universal gas constant; and T is the absolute temperature. As such, the diffusion of atoms from smaller to larger particles is driven by the difference between C_r and C_e. Therefore, the average particle radius increases with the decrease of the total number of particles and the total free surface enthalpy of the system. The ripening kinetics generally follows three equations:

$$\nabla^2 C = 0\left(\text{kinetic equation}\right) \tag{6.9}$$

$$\frac{\partial f}{\partial t} + \frac{\partial\left(f dR/dt\right)}{\partial R} = 0\left(\text{continuity equation}\right) \tag{6.10}$$

$$Q = G\int_0^\infty R^3 f\left(R,t\right)dR\left(\text{mass conservation equation}\right) \tag{6.11}$$

where dR/dt is the growth or shrinkage rate of a particle as given by the kinetic equation; Q is the mole fraction of the second phase particle; and G is a geometrical factor that depends on the particle morphology. As Ostwald ripening involves the mass transfer process, it can serve as a means to generate interior space for the crystallite aggregates. In this regard, the cavity is expected to be generated in a location where crystallites are smaller and/or less compact when the Ostwald ripening proceeds[45].

Sol-gel approach is generally regarded as an efficient strategy in the formation of multimetallic porous three-dimensional networks[46–48]. Started from individual spherical metal particles, a network of interconnected nanowires would be formed in the final product. Nanochains are formed by the controlled coalescence of metal particles, and their interconnection accompanying with interpenetration leads to the formation of a self-supporting network. The resulting hydrogel is transferred into a solid porous aerogel by supercritical drying. During the process, sol particles are either dispersed in aqueous media or formed by chemical reaction from dissolved precursors. Subsequent condensation reactions lead to the formation of an irregular three-dimensional branched network. Notably, supercritical drying is applied to prevent the direct phase transition of the solvent from the liquid to the gas phase. As such, the collapse of the fragile pores inside the structure is minimized, and the porosity of the network is mainly retained during the removal of the solvent.

Another method to glue building blocks is to use organic ligands as linkers[49–52]. In this case, individual metal particles first self-assemble into deformable spherical aggregates *supraspheres* and are then linked to form extended structures. These assembled

suprasphères are plastic and moldable against arbitrarily shaped masters and can be thermally hardened and structurally evolved into porous, polycrystalline metal monoliths. Final conversion is achieved by heating, which removes organic molecules, stabilizing the particles and allowing for fusion. Heating of suprasphères solutions leads to nanoporous metals of overall macroscopic dimensions, and localized radiation using collimated electron beam is used to prepare metallized surface micropatterns.

6.3 Synthetic Methods

The past decades have witnessed development of many methods for preparing bimetallic nanoframes and nanoporous structures with different compositions and morphologies. Despite the diversity of involved synthetic protocols, they can be summarized in two complementary types, i.e., bottom-up and top-down approaches, as discussed in section 6.2. On one hand, the top-down approach includes various methods ranging from templating, oxidative etching, galvanic replacement, Kirkendall effect, and electrochemical dealloying. On the other hand, assembly represents a classical method that is part of the bottom-up category. In the following discussion, we elaborate on these methods so to highlight the principles outlined in section 6.2.

6.3.1 Template-Assisted Method

Template-assisted synthesis represents an effective technique toward achieving a high degree of morphological control for nanomaterials[27,53–57]. Using a preexisting template with desired structural features as a guide, such template-assisted method is capable of producing nanomaterials with diverse morphologies[58–62], especially open nanoframes and nanoporous structures[63–65]. As defined in the Merriam-Webster's Dictionary, a *template* is generally referred to a "gauge, pattern or mold used as a guide to the form of a piece being made," which reveals the directing nature of templates[66]. Typically, an intact process based on template-assisted synthesis involves the following three steps:

1) Preparation of a template with desired structural features
2) Creation of a hybrid composite composed of the starting template and the target product
3) Removal of the original template, just leaving behind the target product

During the entire synthesis, the removal step is essential to induce the formation of nanoframes and nanoporous structures. It should be noted that the original template must be stable enough to retain its original structure away from detrimental changes. Moreover, the template should be easily removed without destroying the desired structure in the removal step. Based on their nature, the templates utilized in the fabrication of bimetallic nanoframes and nanoporous structures can be categorized into three main types: namely, hard, soft, and sacrificial templates.

6.3.1.1 Hard Template

The hard-templating synthesis represents a straightforward method toward the preparation of mesoporous materials of carbons[67,68], metals[69–72], and metal

oxides[73–75]. Typically, alternatives for hard templates used in the synthesis are multifarious, including assembled colloidal crystals, mesoporous silica, zeolites, and alumina membranes[27]. Among these, colloidal silica is of high scientific value due to a series of advantages such as facile synthesis, tunable structures, and ease of removal[76–83]. Figure 6.4 illustrates three pathways for preparing periodically porous structures with colloidal silica as the hard template:

1) A preformed colloidal silica is infiltrated with precursor materials to form a three-dimensionally porous structure after removal of the template.
2) Templates and small particles are co-deposited to form a three-dimensionally porous structure after removal of the template.
3) Core–shell structures are assembled into periodic arrays to form a close-packed hollow array after removal of the template[84].

In some cases, an additional step is required in which the surface of the template needs to be modified to adjust its chemical compatibility with the precursors prior to deposition of the latter. Eychmüller et al. have demonstrated a facile synthesis of two sets of porous AuPt nanostructures, i.e., a macroporous nanostructure and a nanostructure consisting of hollow spheres, using silica spheres modified with 3-aminopropyltrimethoxysilane as the hard template (Figure 6.5)[85]. After the template was immersed in an aqueous solution containing Au particles, the small Au particles flew freely to and were then deposited in the interstices of the colloidal template. Then, the

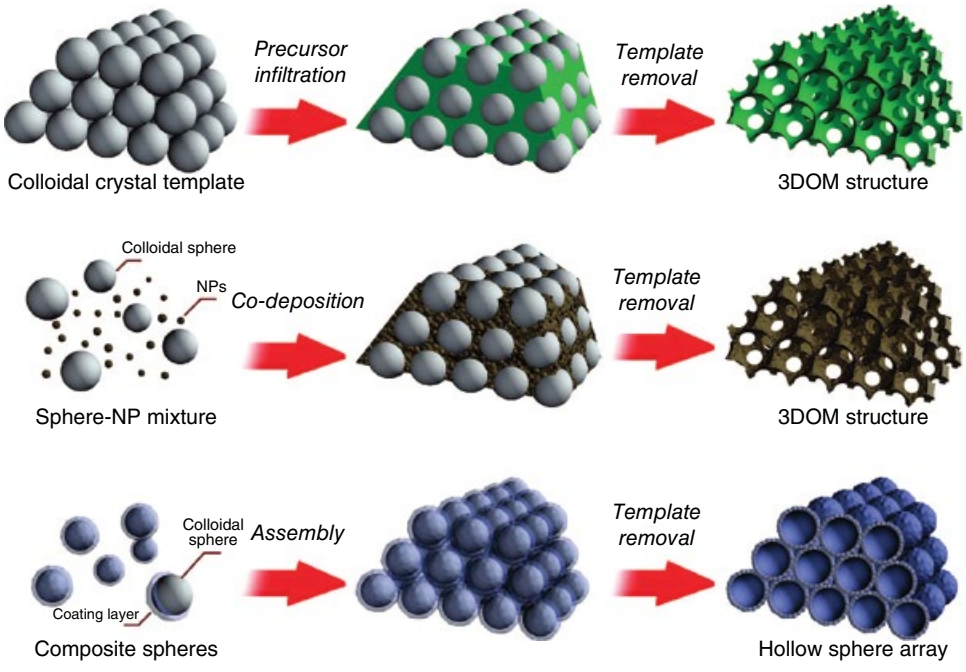

Figure 6.4 Schematic illustration showing three pathways of preparing periodically porous nanostructures based on silica as the template. Reproduced with permission ref. [84]. Copyright (2008), American Chemical Society.

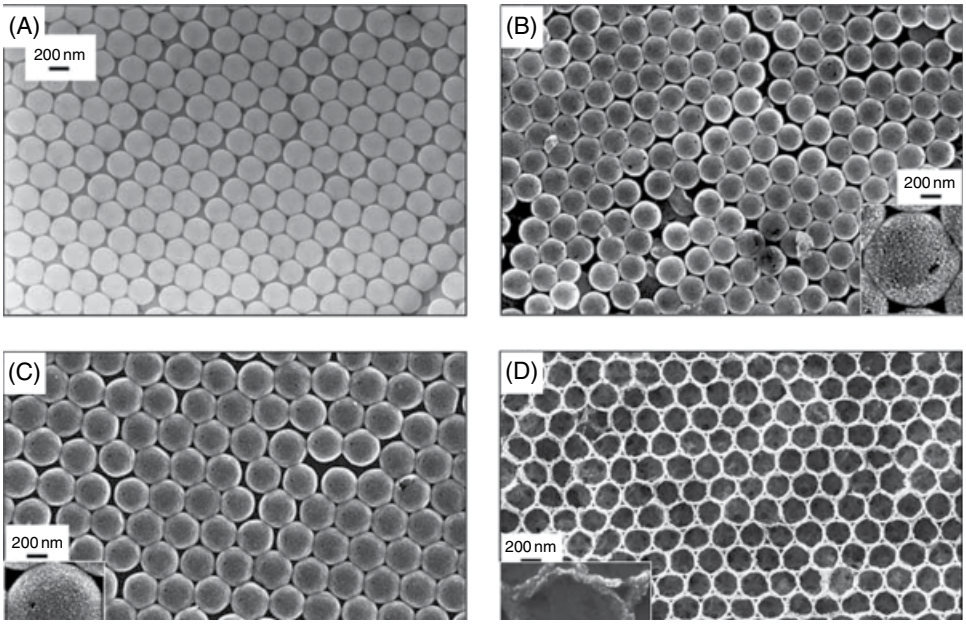

Figure 6.5 (A) SEM image of a template consisting of 267-nm silica particles. (B,C) SEM images of ordered hollow AuPt particles obtained using (B) 267- and (C) 300-nm silica as the template. (D) SEM images of ordered AuPt structures with larger pores. Reproduced with permission ref. [85]. Copyright (2005), Wiley-VCH.

template embedded with Au particles was dipped into a plating solution in order to coat it with Pt atoms. During the plating process, the predeposited small Au particles can serve as seeds to accelerate the reduction of $PtCl_6^{2-}$ ions by ascorbic acid. Finally, removing the silica template with hydrofluoric acid produced ordered Au–Pt nanostructures with hierarchical porosity. As shown in Figure 6.5, B and C, the resulting product exhibited a tunable hollow volume as the starting template with different sizes was used in the synthesis. By contrast, by increasing the concentration of Au particles and extending the immersion time, Au–Pt structures with relatively large pores were obtained in the final product (Figure 6.5D). In addition, mesoporous Pt–Ru alloy nanostructures with different compositions and uniform sizes have also been successfully synthesized by using SBA–15 and KIT–6 as hard templates[78]. Despite great achievements toward construction of porous structures on the basis of hard templates, the morphologies of obtained products have been largely restricted to limited structures, including spheres, powders with irregular shapes, and films on conductive substrates. Exemplified with mesoporous Pt particles, Yamauchi et al. have demonstrated shape- and size-controlled synthesis of porous nanostructures in hard templates[86]. By using KIT–6 and SBA–15 as the starting template, polyhedral and olive-shaped mesoporous Pt nanostructures with uniform sizes have been successfully synthesized, respectively. Such a method provides a generic platform for the preparation of mesoporous metallic nanostructures with other compositions.

Apart from colloidal silica, porous anodic aluminium oxide (AAO) membranes with vertically aligned porous structures also represent a kind of commonly used hard

template for the fabrication of well-defined nanoporous structures[87–94]. Typically, the AAO templates consist of a dense array of cylindrical nanopores arranged in well-ordered domains, allowing the access and deposition of precursors/target products. Masuda and coworkers first developed a two-step anodization process to generate well-ordered porous AAO templates[95,96]. By adjusting the synthetic parameters, the structure of pores in AAO templates can be exquisitely controlled, providing an excellent platform to tailor the morphology of resulting replicas from the AAO templates[94].

Gösele et al. have utilized porous AAO membranes as a hard template to fabricate nanoporous PtCo alloy nanowires, as illustrated in Figure 6.6A[97]. Initially, concentrated PtCo precursors were continuously electrodeposited into a porous AAO template at a constant potential that favors the reduction of Co^{2+} ions in the electrolyte, so that only a small amount of Pt (1% or even less) was incorporated into the nanowires. The as-deposited Pt_1Co_{99} nanowires then underwent dealloying treatment in H_3PO_4, during which most Co atoms were selectively dissolved accompanying the evolution of porosity in the nanowires. Depending on the dealloying time, the AAO membrane could be partly or completely removed. It should be noted that the presence of AAO membranes is of great significance to the formation of these nanoporous nanowires, since no solid interconnected structures were left when PtCo nanowires were first released from AAO membranes and subsequently subjected to the same dealloying treatment. On the one hand, the initial reaction between H_3PO_4 and external AAO is believed to consume abundant H^+ ions, leading to slow dissolution of Co atoms so that Pt atoms have more time to diffuse to and then passivate the surface of nanowires. On the other hand, the nanochannels of AAO can largely limit the mass transport of H_3PO_4 from the bulk solution to the dissolution front to guarantee a relatively slow dealloying process. Generally, upon the formation of Pt-rich surface on porous nanowires resistant to the etching, the acid was believed to be mainly consumed for dissolving the porous AAO template.

In addition to common hard templates such as colloidal silica and AAO membranes, some other templates have also been utilized to guide the preparation of diverse bimetallic nanoporous structures[98–100]. He et al. have utilized resin nanospheres as a hard template to create hollow interiors inside the mesoporous silica microspheres and as carriers to transport pregrown Au–Pt alloy clusters into the microspheres[101]. As demonstrated in Figure 6.7A, AuPt@resin nanospheres with a uniform size were obtained by a one-step hydrothermal method. Then, the nanospheres were used as ideal templates to transport the pregrown Au–Pt nanocrystals into the mesoporous silica microspheres *via* a general aerosol process. In particular, a unique Au–Pt yolk@shell nanostructure was obtained in the silica microspheres (Figure 6.7, B and C).

6.3.1.2 Soft Template

It is widely accepted that the hard-templating method is effective in generating diverse porous and hollow nanostructures. However, this method still suffers from several intrinsic disadvantages, including a complex multistep process involving preparation and removal of desirable templates, fragility of the hollow structures during removal of the template, and a relatively low yield of the resultant product. To overcome this problem, synthesis based on soft (liquid or gaseous) templates has attracted growing attention in producing different kinds of nanoporous structures[102–104]. In this section,

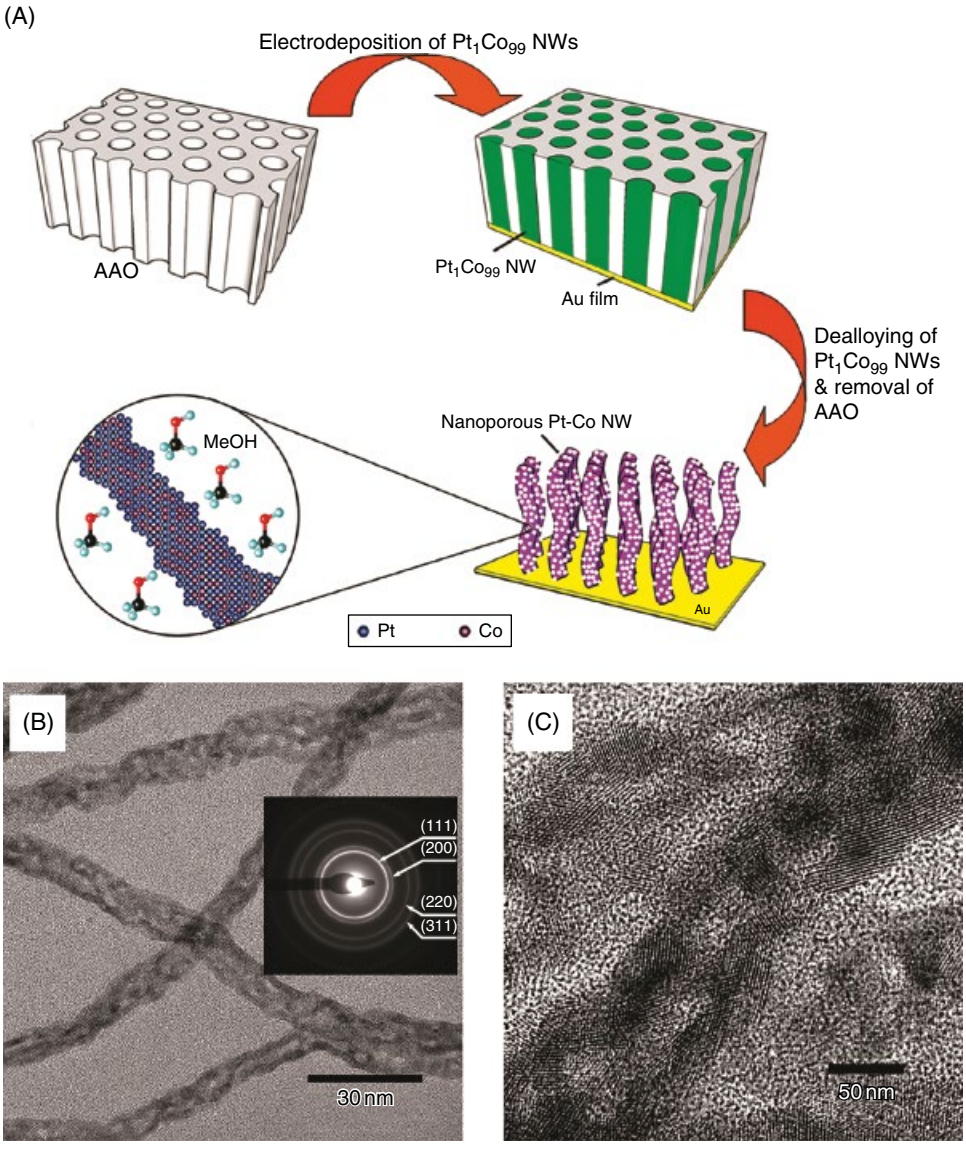

Figure 6.6 (A) Schematic illustration showing the formation process of porous PtCo alloy nanowires. (B) TEM and (C) HR-TEM images of porous PtCo alloy nanowires obtained with dealloying time of 15 h. The inset in (B) shows the SAED pattern of as-prepared porous PtCo alloy nanowires. Reproduced with permission ref. [97]. Copyright (2009), American Chemical Society.

we discuss the directing roles of some representative soft templates, including emulsion droplets, supramolecular micelles, polymer aggregates/vesicles, and gas bubbles, in fabrication of nanoporous structures.

Lyotropic liquid crystals (LLCs), which are formed by the self-assembly of surfactant micelles, can be directly utilized as a structure-directing agent for the fabrication of porous nanostructures[105–111]. Typically, a highly concentrated solution of

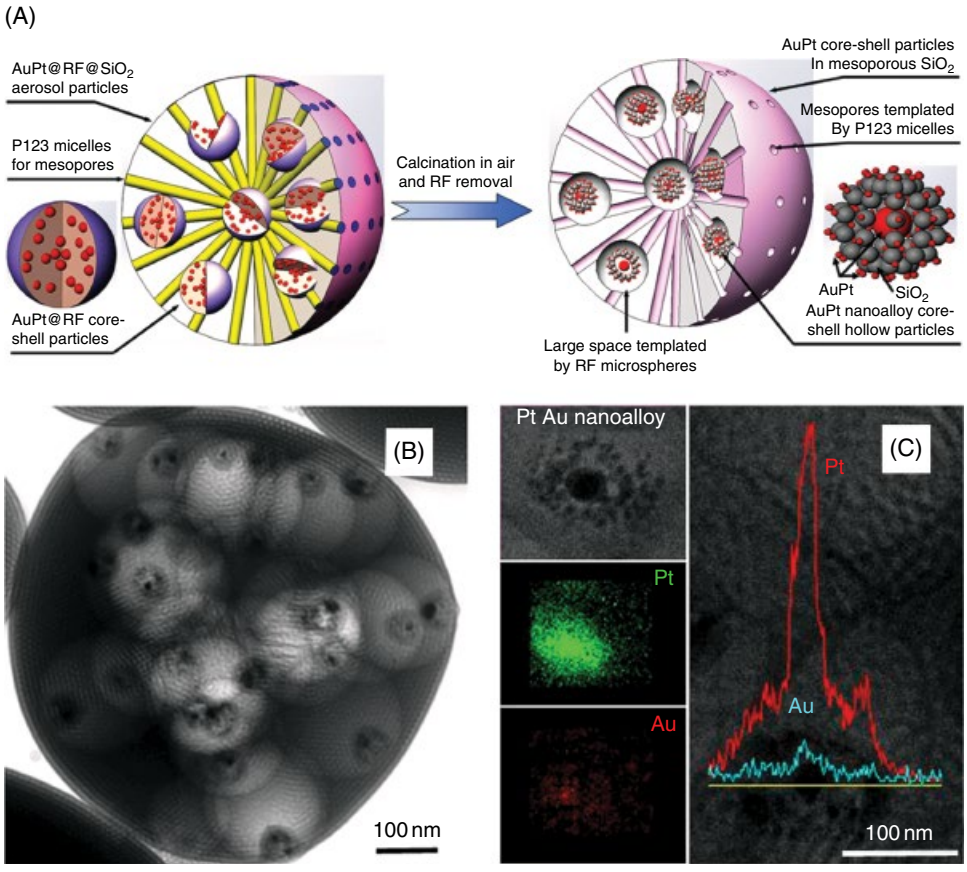

Figure 6.7 (A) Schematic illustration showing the formation process of yolk-shell AuPt@SiO_2 particles. (B) TEM image of as-prepared AuPt@SiO_2 particles. (C) Compositional analysis of as-prepared AuPt@SiO_2 particles. Reproduced with permission ref. [101]. Copyright (2016), American Chemical Society.

surfactants around 30 wt% or more is necessary in order to synthesize LLCs. By using different concentrations of a certain surfactant, the micellar structure of LLCs can be varied, allowing facile manipulation over structures of the resultant products. As shown in Figure 6.8A, Yamauchi et al. have successfully prepared mesoporous PtAu nanostructures by utilizing LLC films that were spontaneously formed from a diluted surfactant solution through solvent evaporation[112]. In the first step, hexagonally ordered LLC templates were prepared on conductive substrates from a diluted surfactant solution containing $PtCl_6^{2-}$ and $AuCl_4^-$ ions. Electrochemical reduction of the involved metal precursors followed by the deposition of metal atoms was then carried out with Pt and Ag/AgCl electrodes as the counter and reference electrodes, respectively. The resultant mesoporous PtAu films were obtained after removal of surfactants and undeposited species. It should be noted that the concentration of $PtCl_6^{2-}$ and $AuCl_4^-$ ions in LLCs exports an inevitable impact on the final composition in the product. It was found that a Au-rich content was observed in the product over the entire range of LLC compositions, as the Au species were preferentially reduced derived from the higher reduction

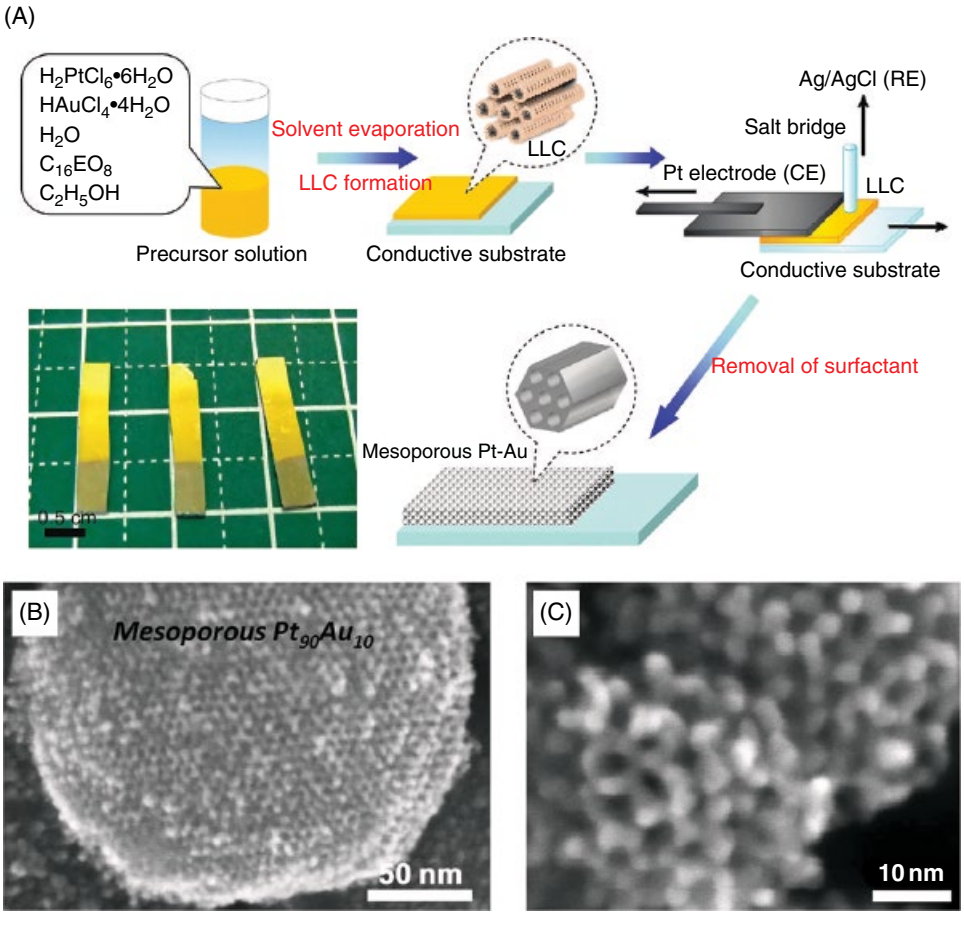

Figure 6.8 (A) Schematic illustration showing the formation process of mesoporous PtAu alloy films using electrochemical deposition. (B,C) SEM images of mesoporous $Pt_{90}Au_{10}$ alloy films with different magnifications. Reproduced with permission ref. [112]. Copyright (2012), American Chemical Society.

potential of $AuCl_4^-$/Au (+1.00 V vs. SHE) compared with that of $PtCl_4^{2-}$/Pt (+0.76 V vs. SHE). By contrast, the variation trend toward the composition in the product is different as a function of the original composition in the LLCs. In detail, when the original composition in LLCs changed in the range of $Au^{3+}/(Pt^{4+}+Au^{3+}) = 0.0–0.4$, the Au content in the product increased remarkably. For comparison, the Au content in the product did not change so greatly when the LLC composition was above $Au^{3+}/(Pt^{4+}+Au^{3+}) = 0.7$.

In other research, Chen et al. investigated the detailed formation process of mesoporous Pt–Ru nanostructures with the assistance of a LLC template on the basis of *in-situ* small-angel X-ray scattering, *in-situ* X-ray diffraction, and X-ray absorption near-edge structure spectra[113]. The results are provided in Figure 6.9, indicating that metallic precursors were quickly reduced in the early stage of electrochemical reduction into metallic atoms for aggregation. The size of metal particles saturated to ~4.5 nm as confined by the geometry of LLCs, together with an optimized ordering domain size

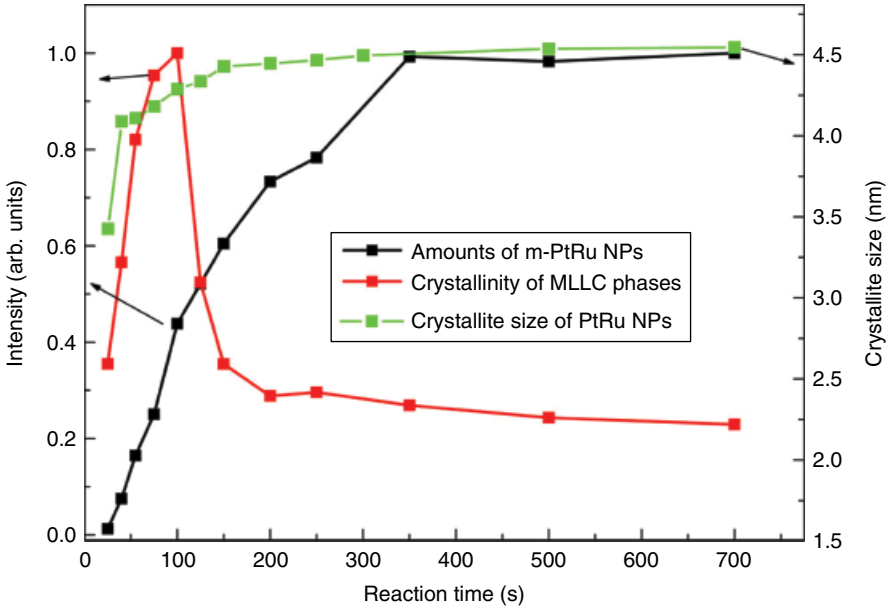

Figure 6.9 Crystallinity of the MLLC-Pt–Ru complex, the amounts of m-PtRu particles, and average crystallite size of Pt–Ru particles as a function of electroreduction time. Reproduced with permission ref. [113]. Copyright (2012), American Chemical Society.

up to ~180 nm. In the following process, inconspicuous growth in the size of metal particles was observed. Hence, the continuous increase in the phase volume at this stage could be interpreted as a rapid growth in the number density of particles at a constant size. Meanwhile, the crystallinity of the LLC phase was considerably deteriorated with the reaction time during this period. In the last stage, highly populated Pt–Ru nanoparticles agglomerated into an inverted mesostructure of the hexagonally packed LLC template.

Bimetallic nanoporous structures can also be prepared utilizing polymers as the template[114–120]. As such, the as-obtained product can take different architectures, since polymers typically possess flexible structures, which can aggregate into spherical, cylindrical, hollow micelles, or lamellar phases depending on the concentration of solvents. Russell et al. have successfully constructed bimetallic Pt–Au nanorings and hollow cylindrical nanostructures on the basis of a polystyrene-*block*-poly(2-vinylpyridine)-*block*-poly(ethylene oxide) (PS-*b*-P2VP-*b*-PEO) triblock copolymer as the template[121]. First, dispersion of an aqueous solution containing H_2PtCl_6 into a trifluorotoluene solution of PS-*b*-P2VP-*b*-PEO produced an emulsion-induced hollow micelle (EIHM), comprising a water nanodroplet stabilized by PEO, H_2PtCl_6/P2VP, and PS, sequentially. Then the addition of an aqueous solution containing $LiAuCl_4$ into the dispersion led to the formation of a complex between $LiAuCl_4$ and PEO. The resulting spherical EIHM structure was transformed to a hollow cylindrical micelle by the fusion of spherical EIHM with the addition of methanol. This structural transition was reversible by the alternative addition of methanol and trifluorotoluene. In the last step, oxygen plasma was used to generate hollow Pt–Au concentric spheres and cylindrical

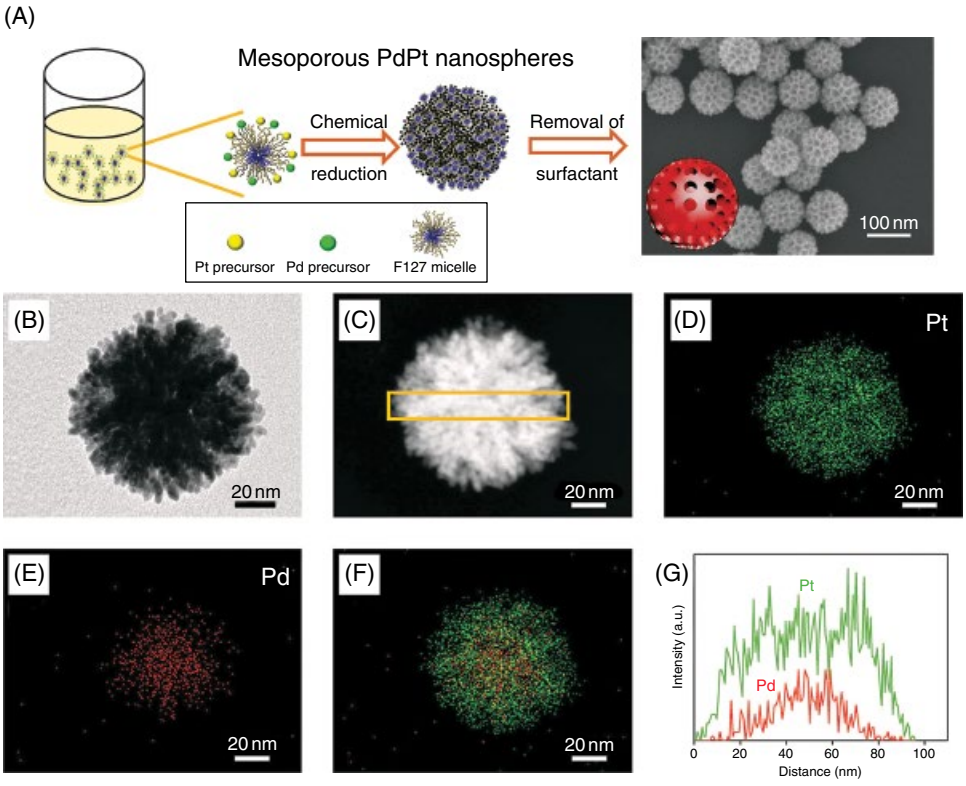

Figure 6.10 (A) Schematic illustration showing the formation process of mesoporous PdPt nanospheres. (B) TEM image of mesoporous Pd–Pt nanospheres. (C) HAADF-STEM image of mesoporous Pd–Pt nanospheres. (D-F) STEM-EDX elemental mapping of (D) Pt, (E) Pd, and (F) merged images in an individual mesoporous Pd–Pt nanosphere. (G) Elemental line-scanning profiles in the region marked by a box in (C). Reproduced with permission ref. [122]. Copyright (2015), American Association for the Advancement of Science.

nanostructures. In another example, Wiesner et al. backfilled the open pores of degraded block copolymers with Au and Cu metal particles, followed by removal of the involved polymers to generate three-dimensionally networked structures[119].

Based on a surfactant-directing method, Jiang et al. have successfully synthesized bimetallic PdPt spheres with large pores, as shown in Figure 6.10[122]. It should be noted that during such synthesis the concentration of surfactant (F127) and reduction kinetics of metal precursors are critical to formation of mesoporous structures. As evidenced by the formation of nonporous aggregations in the absence of F127, F127 is believed to serve as the pore-inducing agent as well as the protecting agent for preventing the aggregations and/or suppressing the random growth of mesoporous metals. In addition, a relatively slow reduction rate of metallic precursors is of necessity to decrease the number of nuclei formed at the early stage. These nuclei serve as seeds and undergo continuous growth to afford the final products with a relatively large particle size. For extension, the as-presented method is effective in fabricating mesoporous multimetallic nanostructures with other compositions, such as PdPtCu spheres and core–shell Au@PdPt spheres. The types of soft templates are diverse, especially those in a liquid

phase[123–132]. Xu et al. once took advantage of interfacial nanodroplets as a structural guider to fabricate hierarchically porous Au-based particles[133]. The interfacial nanodroplets, which were formed through direct adsorption of emulsions onto the surface of particles, served as soft templates in a galvanic replacement reaction to guide the formation of porous Au, Au–Pt, and Au–Pd structures. The schematic illustration showing the synthetic steps, together with the scanning electron microscopy (SEM) images of representative porous Au–Pt particles, is shown in Figure 6.11. In another instance, Yamauchi et al. have successfully prepared multilayered mesoporous bimetallic Pt–Pd alternating films using layer-by-layer electrochemical deposition[125]. The mesoporous Pt and Pd layers were alternatively electrodeposited from two kinds of metallic precursors with the assistance of micelle assembly in a dilute electrolyte, namely, a K_2PtCl_4 aqueous solution with a Brij 58 surfactant and a Na_2PdCl_4 aqueous solution with a P123 surfactant. It should be noted that in this synthetic system a series of multilayered mesoporous Pt–Pd films with different layer thicknesses could be prepared simply by changing the deposition time.

In addition to the liquid form, the soft templates can also adopt the gaseous form[134–137]. Utilizing the hydrogen bubble as a soft template, Li et al. have successfully prepared Au–Pt foam films by cathodic co-deposition[138]. Specifically, the *in-situ* generated hydrogen bubble during the electrochemical reduction of $HAuCl_4$ and H_2PtCl_6 was hard to diffuse outward initially and expected to serve as a pore-directing agent to guide the formation of Au–Pt alloy films with three-dimensionally hierarchical pores consisting of interconnected dendrite walls. During the entire evolution, the coalescence of hydrogen bubbles occurred, leading to some relatively large pores. Moreover, by simply varying the molar ratio of $HAuCl_4/H_2PtCl_6$ in the feeding solutions, Au–Pt films with different compositions were obtained in the final product (Figure 6.12).

In some cases, integration of both hard and soft templates is typically utilized to produce different nanoporous structures[138–140]. Lu et al. have demonstrated a general synthetic route to three-dimensionally hierarchical networks composing of nanowire-like elements using a dual template based on liquid crystals and silica[141]. The synthetic process is schematically illustrated in Figure 6.13. First, a film of mesoporous silica is coated onto a conductive substrate through the co-assembly of the silicate and surfactant molecules followed by removal of the surfactant. Then, the pore channels are filled with metal particles through electrodeposition. In the last step, the silica template is removed to create a replicated mesoporous nanowire network. Besides the excellent control over the composition, this approach enables precise structural tuning by replication of the complicated but well-studied silicate/liquid-crystalline mesophases. For example, the diameter of resultant nanowires can be tuned from 2 to 20 nm depending on the pore sizes of the template, and the sizes of pores in the nanowire networks can be tuned from 1 to 4 nm depending on the thickness of the pore walls of the templates. In another example, Lin et al. have proposed a facile method to preparation of one-dimensionally hierarchical mesoporous PtCu nanostructures with mesopores using Te nanowires and Pluronic F–127 surfactant as a dual template[140]. Under the typical synthetic condition, Te nanowires serve as a hard template, enabling the evolution of one-dimensional nanostructures. Meanwhile, kinetically controlled reduction of metal precursors in the presence of F–127 as the soft template is critical to inducing the formation of hierarchically porous PtCu nanostructures. It is worth noting that the atomic percentages of Pt in final products are higher than those in the precursors due to the higher standard reduction potential of $PtCl_6^{2-}/Pt$ compared with that of Cu^{2+}/Cu.

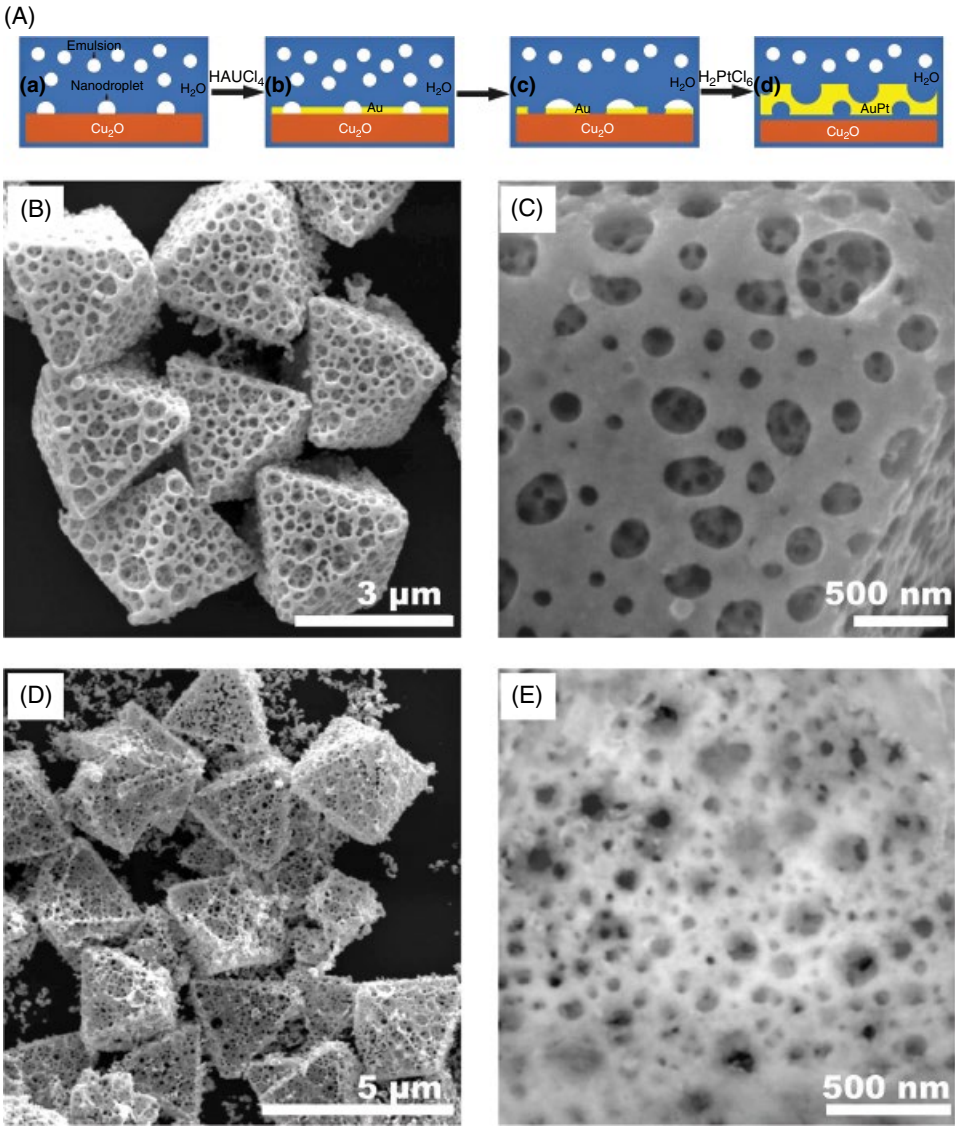

Figure 6.11 (A) Schematic illustration showing the formation process of porous Au–Pt particles. (B,C) SEM images of porous Au–Pt particles with different magnifications. (C,D) SEM images of porous Au–Pt particles synthesized *via* galvanic reaction in the presence of interfacial nanodroplets with different magnifications. Reproduced with permission ref. [133]. Copyright (2014), Nature Publishing Group.

6.3.1.3 Sacrificial Template

Classically, the aforementioned strategies based on hard and soft templates are effective in generating porous and hollow structures, whereas both methods suffer from poor control over the structure of the resultant products. The obtained samples generally have a relatively large size up to hundreds of nanometers with nonuniform porosity. As

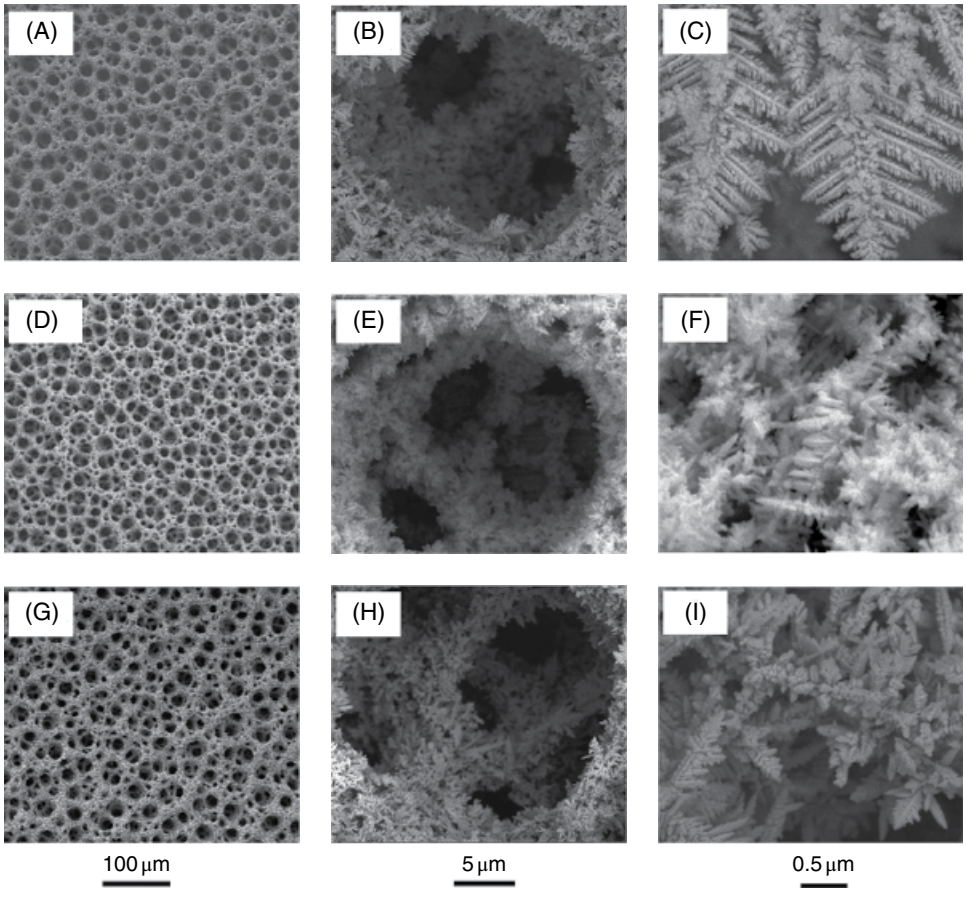

Figure 6.12 SEM images with different magnifications of (A-C) $Au_{100}Pt_1$, (D-F) $Au_{100}Pt_6$, and (G-I) $Au_{100}Pt_8$ alloy foams. Reproduced with permission ref. [138]. Copyright (2009), American Chemical Society.

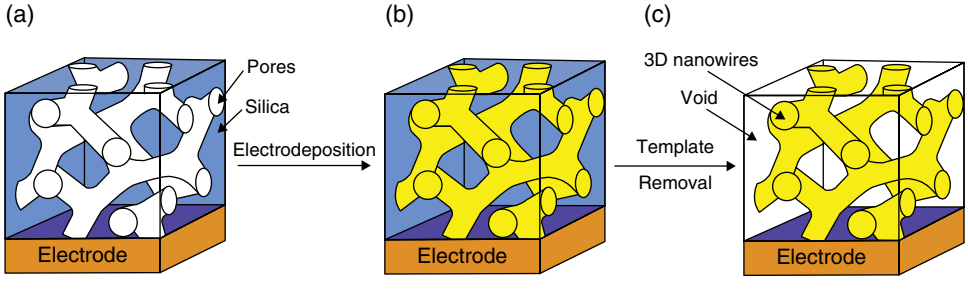

Figure 6.13 Schematic illustration showing the formation process of three-dimensional nanowire networks with a dual template. Reproduced with permission ref. [141]. Copyright (2004), Wiley-VCH.

supplementary, there is another kind of template called sacrificial templates that sacrifice themselves at the same time of the formation of the target product[142–145]. Such a method based on the sacrificial template could achieve, to some extent, precise mastery of the morphology of resultant hollow and porous nanostructures. Han et al. have developed a general synthetic route of high amenability for the production of uniform multicomponent nanotubes, including Pt–Pd, Pt–Ag, and Pd–Ag bimetallic alloys, using ZnO nanowires as a sacrificial template (Figure 6.14)[146]. In such synthesis, ZnO nanowires are believed to provide heterogeneous nucleation sites for metal atoms, which could facilitate the reduction of metal precursors by lowering the activation

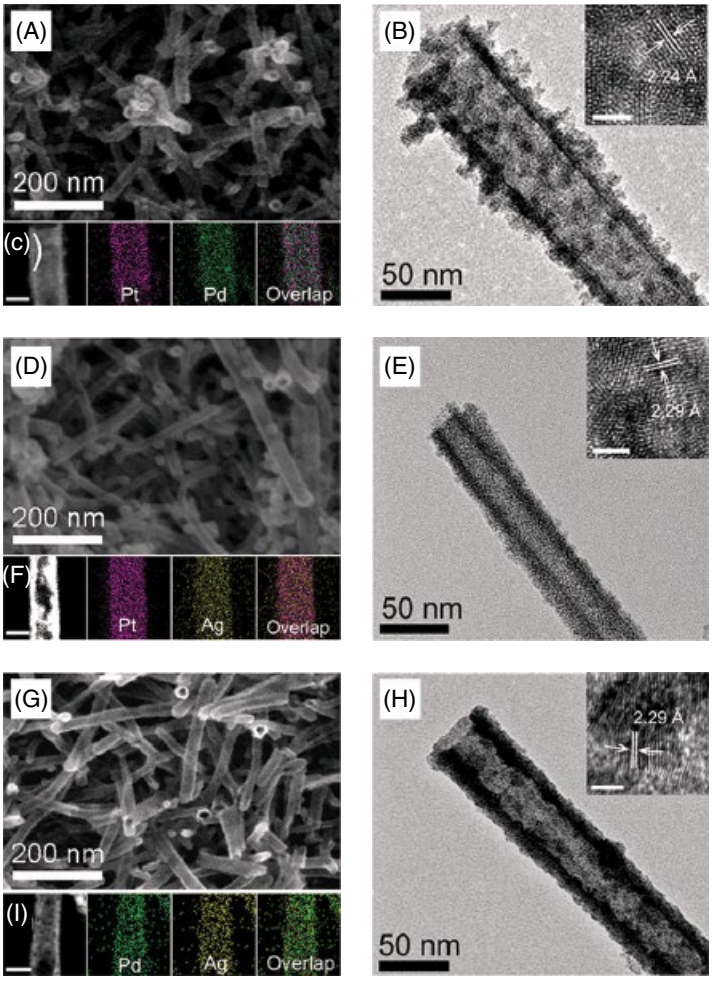

Figure 6.14 (A-C) SEM, TEM, and STEM-EDX mapping images of Pt–Pd nanotubes, respectively. The inset in B shows the HRTEM image of Pt–Pd nanotubes. (D-F) SEM, TEM, and STEM-EDX mapping images of Pt–Ag nanotubes, respectively. The inset in E shows the HRTEM image of Pt–Ag nanotubes. (G-I) SEM, TEM, and STEM-EDX mapping images of Pd–Ag nanotubes, respectively. The inset in H shows the HRTEM image of Pd–Ag nanotubes. The scale bars in the insets of B, E, and H indicate 2 nm. The scale bars in C, F, and I indicate 50 nm. Reproduced with permission ref. [146]. Copyright (2012), American Chemical Society.

energy for nucleation on the surface. Moreover, controlled reduction kinetics through a complementary effect between metal precursors and nucleation sites on the surface is essential to the formation of multimetallic alloy nanotubes. As for the synthesis of Pt–Ag and Pd–Ag alloy nanotubes, it is posited that $PtCl_4^{2-}$ and $PdCl_4^{2-}$ ions retarded the reduction kinetics of Ag^+ ions and thus prevented homogeneous nucleation of Ag atoms, resulting in the formation of bimetallic alloy nanotubes. Similarly, Cu_2O crystals with controllable structures have been used as the sacrificial template for synthesis of hollow metal and bimetallic nanocages[147]. Typically, three steps are involved in such synthesis: growth of Cu_2O crystals with different morphologies, formation of core–shell Cu_2O@MCu (M = Pt and Pd) structures in a H_2PtCl_6 or H_2PdCl_4 aqueous solution, and then dissolution of the inner Cu_2O cores in an ammonia solution.

A remarkable advantage of the method based on sacrificial templates is that it can be utilized to generate nanoframes with well-defined geometric shapes[148,149]. A typical example involves the synthesis of cubic AgPd nanoframes using Ag nanocubes as a sacrificial template[150]. As shown in Figure 6.15A, the fabrication process involves the co-titration of aqueous $AgNO_3$ and Na_2PdCl_4 solutions into an aqueous suspension containing Ag nanocubes in the presence of ascorbic acid and poly(vinyl pyrrolidone). Then newly formed Ag and Pd atoms derived from the reduction by ascorbic acid would preferentially nucleate on the surface of the Ag template. For face-centered cubic Ag nanocubes on which the surface was passivated by poly(vinyl pyrrolidone), the surface free energies of various facets on a Ag nanocube would undertake a new order of $\gamma_{(110)} > \gamma_{(111)} > \gamma_{(100)}$. As such, the Ag and Pd atoms would preferentially nucleate on the edges enclosed by {110} facets in the initial stage because of the highest free energy there. As the reaction proceeds with increase in the co-titration volume for both precursors, some of the Ag and Pd atoms newly deposited on the edges could migrate to the corners covered by {111} facets through surface diffusion. By controlling the amounts of $AgNO_3$ and Na_2PdCl_4, two types of core-frame Ag@AgPd nanocubes with Ag and Pd atoms deposited at the edges only or at both edge and corner sites could be obtained. In the last step, both core-frame Ag@AgPd nanocubes were converted into cubic AgPd nanoframes (Figure 6.15, B and C) by selectively removing the Ag template in the core with H_2O_2. In another instance, McEachran et al. reported the synthesis of decahedral Au–Ag nanoframes through surfactant-free templating of pentagonal Ag nanocrystals[151]. In this approach, they carried out selective deposition of Au atoms on the decahedral Ag templates, followed by preferential dissolution of Ag from the Au-coated decahedra with H_2O_2. The schematic illustration showing the morphological evolution and transmission electron microscopy (TEM) images of samples at different stages were shown in Figure 6.16. It should be noted that different products were obtained when Au-coated decahedra with different amounts of Au were employed. Specifically, Au-based nanocages with some Au retained at both facets and edges were generated after reacting H_2O_2 with Au-coated decahedra whose amount of deposited Au was more than ca. $15\%_{Au/Ag}$ (where $X\%_{Au/Ag}$ represents X mol % Au relative to Ag present in the template). However, for the decahedra whose amount of deposited Au was less than *ca.* $15\%_{Au/Ag}$, Au remained predominantly as the frame after treatment with H_2O_2. Dissolution and redeposition of Ag took place to form Au–Ag alloy nanoframes using H_2O_2 with a lower concentration (*ca.* 0.05 M). When using Ag templates with pentagonal twinning and {111} facets, such as icosahedra and pentagonal faceted rods, corresponding nanoframes could be synthesized based on this procedure as well.

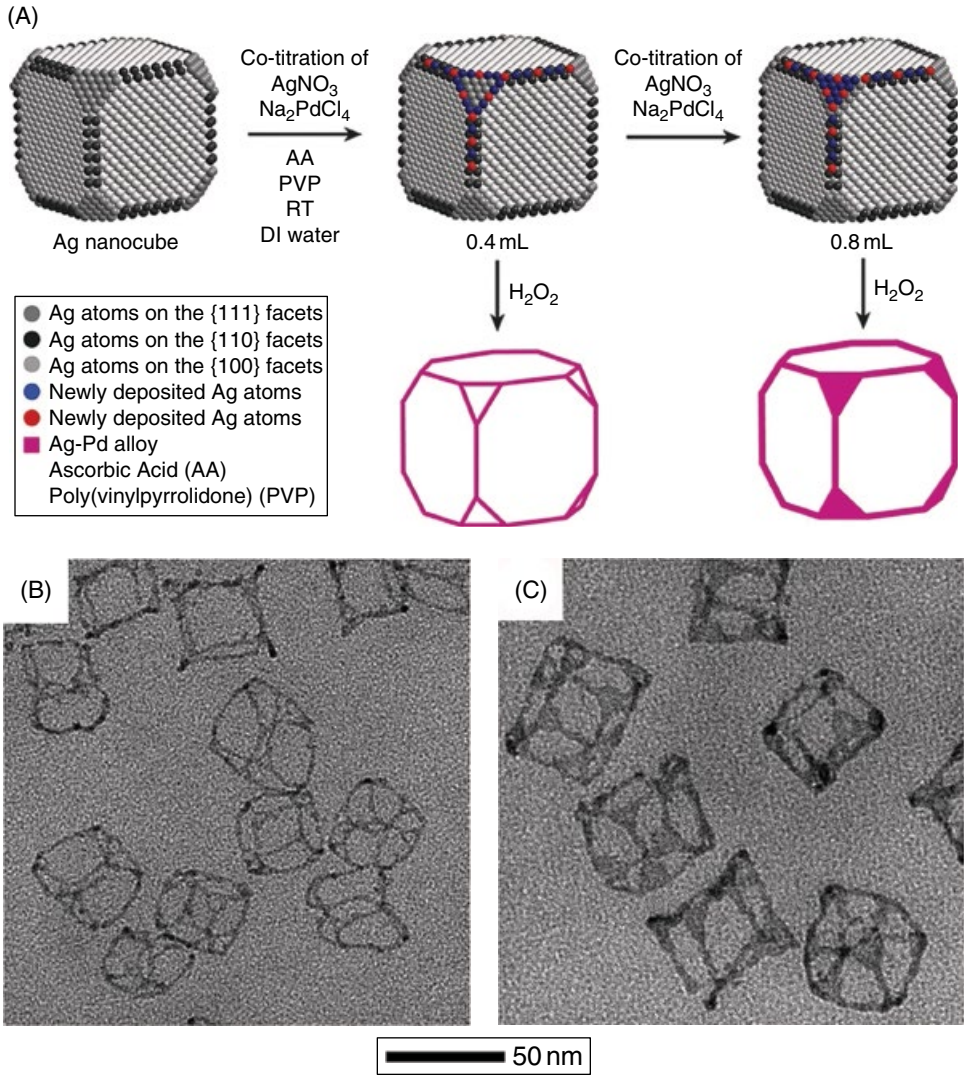

Figure 6.15 (A) Schematic illustration showing the formation process of two different types of Ag–Pd nanoframes prepared by templating with a Ag nanocube. (B,C) TEM images of two types of Ag–Pd nanoframes obtained by selectively removing the Ag template in the core-frame Ag@AgPd nanocubes. Reproduced with permission ref. [150]. Copyright (2016), Wiley-VCH.

The driving force directing the elimination of sacrificial templates is diverse. Yang et al. have demonstrated a smart method for the preparation of hollow nanocrystals and cage-bell nanostructures (typically referring to a movable core enclosed by a shell with nanochannels) through the inside-out diffusion of multiply twinned Ag seeds[152]. In detail, after the initial formation of core–shell Ag–M (M = Ru, Rh, Pd, Pt, Os, Ir, Pt–Ru, Pt–Rh, Pt–Os, Pt–Ru–OS, or Pt–Rh–Os) and M_A–Ag–M_B (M_A = Au or Pt; M_B = Ru, Os, Ir, Pt, or Pt–Rh) particles, Ag is then extracted from the core or the inner shell by bis(*p*-sulfonatophenyl)phenylphosphane (BSPP), leaving behind an organosol of hollow and

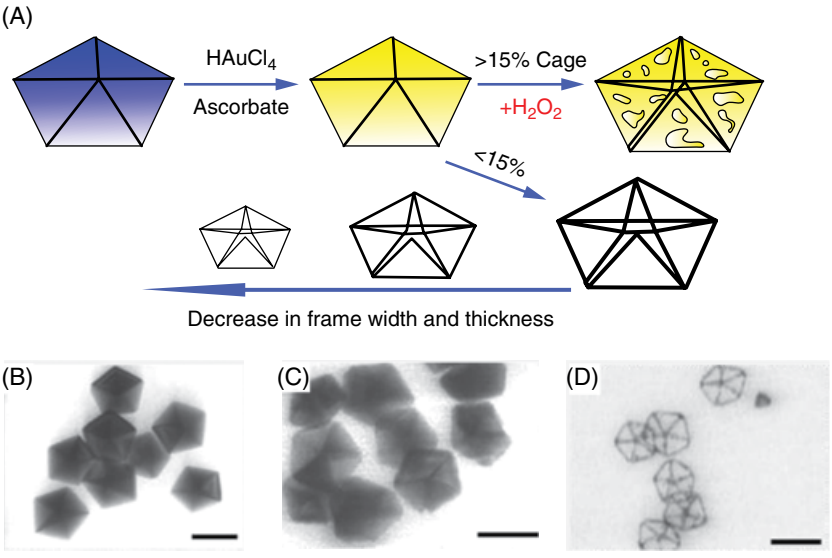

Figure 6.16 (A) Schematic illustration showing the formation process of Au–Ag nanoframes and nanocages with Ag decahedra as the sacrificial template. (B) TEM image of Ag decahedra. (C) TEM image of Ag decahedra after the deposition of Au. (D) TEM image of the frameworks after the dissolution of Ag with hydrogen peroxide. All scale bars are 50 nm. Reproduced with permission ref. [151]. Copyright (2011), American Chemical Society.

cage-bell nanostructures, respectively (Figure 6.17A). Under normal circumstances without the assistance of BSPP, it could take months to complete the inside-out diffusion of Ag seeds. By contrast, BSPP can bind strongly with Ag as soluble AgI-BSPP complexes to drive the outward diffusion of Ag in the core–shell particles, enabling the completion of the inside-out diffusion of Ag in a much shorter time within 24–28 h. This method, based on the preferential dissolution of Ag, has been widely employed by many research groups to prepare bimetallic nanoframes and nanoporous structures. Yang et al. have presented the synthesis of bimetallic heterodimers consisting of Ag and hollow Pt particles through a structural transformation at an elevated temperature[153]. In this strategy, core–shell Ag@Pt particles were first prepared and, subsequently, converted into bimetallic Ag–Pt heterodimers via the inside-out migration of Ag in the core–shell Ag@Pt particles. Elevated temperatures were employed to accelerate the inside-out diffusion of Ag from the core region. Jin et al. have prepared porous Au–Ag nanoshells through selectively etching Ag from the preformed Au–Ag nanoshells using H_2O_2, which is from the surface-confined enzymatic oxidation of glucose in the presence of oxygen.

Bimetallic nanoframes and nanoporous architectures taking a core–shell structure can also be prepared based on the sacrificial templateing. Park et al. have successfully synthesized Au nanorings coated with Pt framework (Pt@Au nanorings) using Au nanoplates as the sacrificial template[154]. It is believed that the rim-preferential growth of Pt was caused by electronic shuttling through thin Ag layers on the Au nanoplates. As shown in Figure 6.18A, the bound Ag^+ ions were first reduced to Ag atoms by ascorbic acid. When Pt^{4+} ions were added to this solution, galvanic replacement

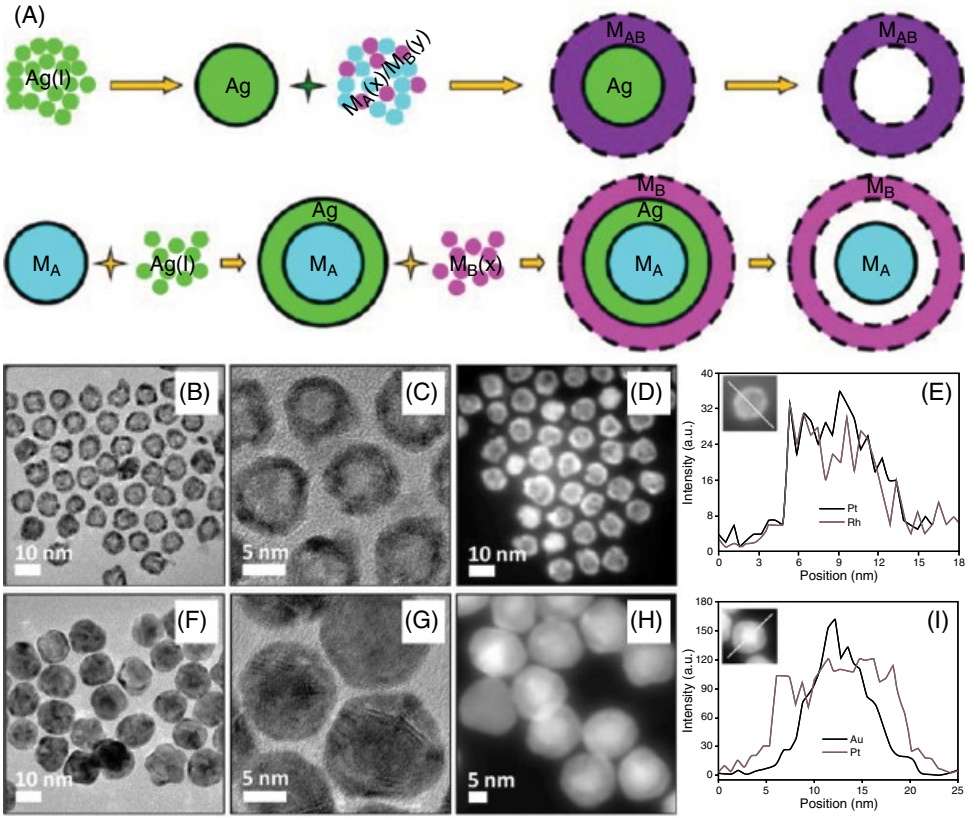

Figure 6.17 (A) Schematic illustration showing the formation process of hollow and cage-bell bimetallic nanocrystals. (B-E) TEM image, HRTEM image, HAADF-STEM image, and EDX line-scanning profiles of hollow Pt–Rh nanocrystals. (F-I) TEM image, HRTEM image, HAADF-STEM image, and EDX line-scanning profiles of cage-bell Au–Pt nanocrystals. Reproduced with permission ref. [152]. Copyright (2012), American Chemical Society.

reaction between Ag and Pt^{4+} ions exclusively took place at the periphery due to the higher surface energy of the edge and vertex as compared to the terrace. The oxidized Ag^{+} ions in the solution were then reduced to Ag atoms on the Au {111} facets (i.e., the flat top and bottom terraces) by ascorbic acid. Therefore, Ag^{+} ions played the role of electron shuttle in such synthesis for Pt^{4+} reduction at the edges and vertices. Next, the central Au nanodisks coated with Ag were selectively etched away by the addition of Au^{3+} ions, leaving only the Pt framework. In the last step, addition of ascorbic acid to the reaction solution triggered the reduction of Au^{+} ions and regrowth of the obtained Au atoms on the surface of Pt skeletons. In a similar instance, their group has demonstrated the preparation of one-dimensional core–shell Pt@Au nanoframes[155]. Pentagonal Au nanorods served as the sacrificial template, on the edge of which Au was preferentially deposited to generate core–shell Au@Pt nanorods. After etching the core Au nanorods, elongated Pt nanoframes were prepared, followed by coating of Au around Pt ridges to result in the formation of Pt@Au metal nanoframes.

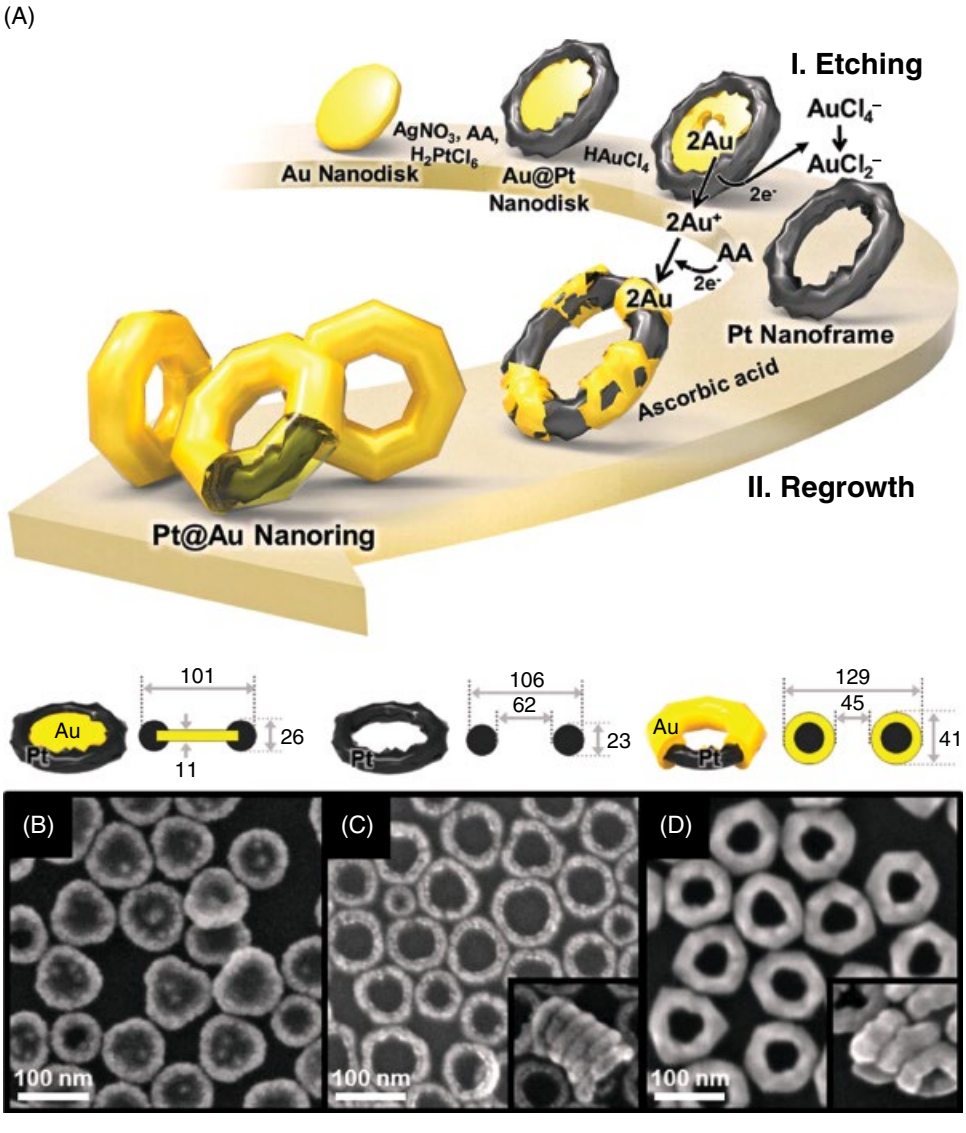

Figure 6.18 (A) Schematic illustration showing the formation process of core–shell Pt@Au nanorings. (B-C) SEM images of (B) rim-preferentially Pt-coated Au nanodisks (Au@Pt nanodisks), (C) Pt nanoframes, and (D) Pt@Au nanorings. The morphology and size information (all scales in nm) are described on the upper side of each image. The insets in B and C represent the corresponding side view of the samples. Reproduced with permission ref. [154]. Copyright (2014), American Chemical Society.

6.3.2 Oxidative Etching

Oxidative etching, which is part of the top-down approach, represents a powerful approach for the dissolution of certain facets and/or active component from the multi-metallic system[156–159]. By selecting an appropriate oxidant, usually air, acid or basic

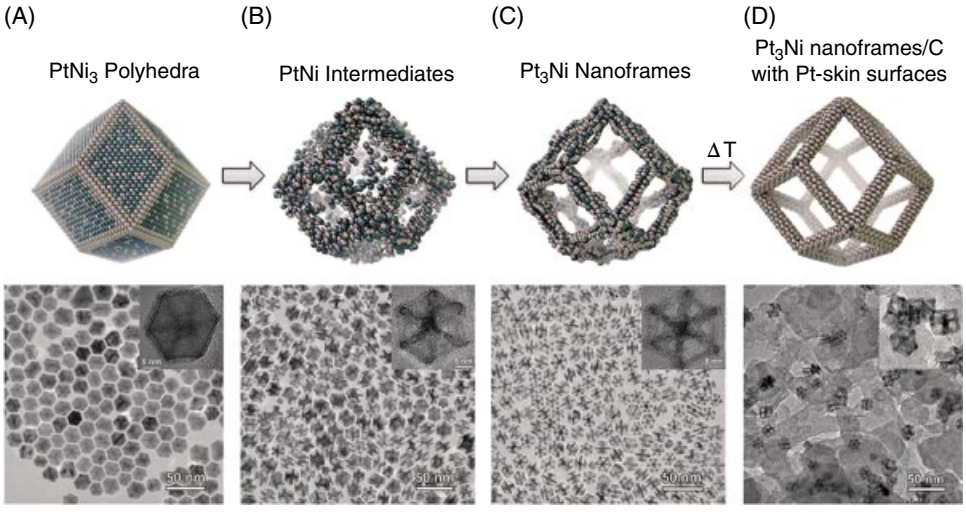

Figure 6.19 Schematic illustrations and corresponding TEM images of the samples obtained at four representative stages during the evolution process. (A) Initial solid $PtNi_3$ polyhedra. (B) PtNi intermediates. (C) Final hollow Pt_3Ni nanoframes. (D) Annealed Pt_3Ni nanoframes with Pt(111)-skin–like surfaces dispersed on high–surface area carbon. Reproduced with permission ref. [164]. Copyright (2014), American Association for the Advancement of Science.

solutions, such oxidative etching can be triggered to generate shaped nanoporous structures[160–163]. The key of oxidative etching derives from the difference of reduction potentials, with the redox potential of the oxidant negative compared with that of the metallic species. In a classical example, Chen et al. reported the transformation from solid $PtNi_3$ rhombic dodecahedra to Pt_3Ni nanoframes through spontaneous corrosion in air[164]. The schematic illustrations and corresponding TEM images of the samples at representative stages are presented in Figure 6.19. It is important to point out that the compositional variation from $PtNi_3$ to Pt_3Ni was ascribed to the inhomogeneous distribution of both elements in the initial rhombic dodecahedra and the high dissolution rate of Ni. In the original solid $PtNi_3$ polyhedra, Ni exhibited a relatively homogeneous distribution inside the particles, whereas Pt was relatively concentrated at the edges. Such elemental distribution resulted from preferential etching of low-coordinated Ni along the edges under the presence of trace oxygen in the solution during the initial synthesis. During the following transformation to nanoframes, both Pt and Ni species were removed from the interior, leaving the stable Pt_3Ni composition on the edges. In the ensuing research, this group additionally presented the evolutionary trajectory of phase segregation in PtNi rhombic dodecahedra[165]. The anisotropic growth of a Pt-rich phase along the <111> and <200> directions at the initial growth stage results in Pt segregation to the 14 axes in a rhombic dodecahedron, forming a highly branched, Pt-rich tetradecapod embedded in a Ni-rich shell. With longer growth time, the Pt-rich phase selectively migrates outward through the 14 axes to the 24 edges so that the rhombic dodecahedron becomes a Pt-rich frame enclosing a Ni-rich interior.

In a following research, Li et al. have reported a novel two-phase approach toward the corrosion from $PtNi_{10}$ octahedra to Pt_4Ni nanoframes[166]. In this strategy, the active component of Ni in oil-soluble $PtNi_{10}$ octahedra, which resided in the upper toluene

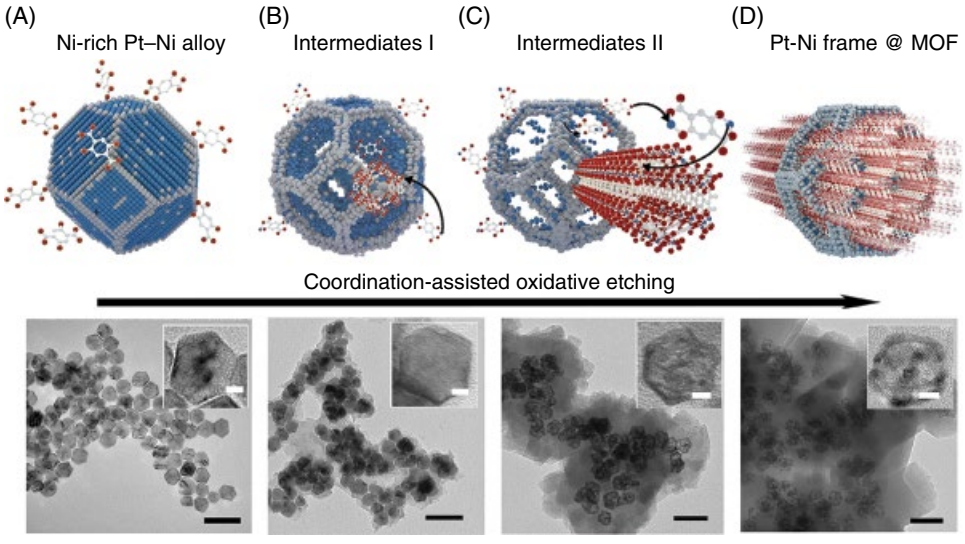

Figure 6.20 Schematic illustrations and corresponding TEM images of the samples obtained at four representative stages during the coordination-assisted oxidative etching process. (A) Initial solid PtNi polyhedra. (B) PtNi frame@MOF intermediates I. (C) PtNi frame@MOF intermediates II. (D) Final PtNi frame@MOF. The scale bars are 50 nm. Insets are the magnified TEM images, and the scale bars, 5 nm. Reproduced with permission ref. [169]. Copyright (2015), Nature Publishing Group.

phase, suffered from etching and was then transferred into a lower aqueous phase with coordination by ethylenediaminetetraacetate (EDTA). Due to the existence of the phase-transfer interface promoted by EDTA, the corrosion reaction proceeded at an accelerated rate under the mild conditions. Specifically, the resultant products of octahedral Pt_4Ni nanoframes were successfully fabricated for the first time, and porous $PtNi_4$ octahedra could be obtained when a common chelating agent EDTA disodium salt was reduced. After a systematic study of this two-phase system, a *synergetic corrosion* mechanism is proposed to account for the formation of octahedral Pt4Ni nanoframes, involving contributions from many species (i.e., O_2, H_2O, H^+, oleyamine, and $EDTA^{4-}$).

Nanoframes of different composites can be incorporated together to construct a hybrid structure with free accessibility and multifunctional properties[167–169]. Li et al. presented a unique *in-situ* etching and coordination for exploiting bimetallic Pt–Ni nanoframes incorporating with a functionalized metal-organic framework (MOF), thereby forming a frame within frame structure[169]. The schematic illustrations and corresponding TEM images of the samples at representative stages are presented in Figure 6.20. Starting with the truncated Pt-rich Pt–Ni octahedra, the O_2 in the air would generate a shell with lower contrast on the surface. Successive etching under the presence of O_2 would produce Pt–Ni nanoframes maintaining the original symmetry. Meanwhile, the abandoned Ni^{2+} ions during the etching process were captured by organic linkers, i.e., 2,5-dioxidoterephthalate, to produce a well-defined MOF of Ni_2dobdc on the surface of Pt–Ni nanoframes. The inherent process was related to the following equations:

$$1/2\,O_2 + H_2O + 2e^- \rightleftarrows 2OH^- \tag{6.12}$$

$$\mathrm{Ni}(0) - 2\,\mathrm{e}^- \rightleftarrows \mathrm{Ni}^{2+} \tag{6.13}$$

$$2\mathrm{Ni}^{2+} + \mathrm{dobdc}^{4-} \rightleftarrows \mathrm{Ni}_2\mathrm{bodbc} \tag{6.14}$$

Especially, once the precipitation of Ni_2dobdc in Eq. (6.14) occurred, the equilibrium of oxidative etching reactions would be broken and shifted toward the generation of Ni2+ (Eq. 6.13), thus largely accelerating the etching rate to promote the formation of Pt–Ni nanoframes.

In addition to Pt–Ni nanoframes, bimetallic nanoframes in delicate structures with other compositions have also been investigated[170–172]. Yang et al. have successfully fabricated cubic Pd–Rh nanoframes and nanoboxes through controllable growth of Pd–Rh nanocubes and then selective removal of Pd[173]. As shown in Figure 6.21A, CH_2O in the solution exports a decisive impact on the structure of the final product. In the initial stage, Pd nanocubes were first synthesized considering a higher redox potential of Pd^{2+}/Pd (0.915 V vs. SHE) than that of Rh^{3+}/Rh (0.76 V vs. SHE). Then Pd and Rh underwent co-growth into larger nanocubes. In the absence of CH_2O, the slow reduction rate indicates fewer nuclei in the solution for the growth. As such, Pd and Rh atoms were allowed to cover the whole surface after the initial occupation of the highly active site, resulting in the formation of nanoboxes after removal of the Pd core. By contrast, the presence of CH_2O would accelerate the reduction of precursors and then increase the nucleation rate. In this case, the formed metal atoms would preferentially grow on the highly active sites that are usually located at the vertices and edges of the nanocubes, generating core-frame Pd@PdRh nanocubes. As a result, after the removal of the Pd core, Pd–Rh nanoframes are obtained. In another instance, Yamauchi et al. reported a facile strategy for synthesis of dendritic Pt–Pd nanocages with hollow interiors and porous dendritic shells through selective etching of Pd cores from the preformed Pt-on-Pd particles using an excess amount of concentrated nitric acid[174]. It is noted that use of concentrated nitric acid (14 M) and long etching time (5 days) are both necessary for the current etching process. After all, the Pd cores are protected by the Pt shells exhibiting a good chemical stability. In addition to these three-dimensional nanoframes with well-defined structures, other porous bimetallic nanocrystals in one- and two-dimensional structures have also been demonstrated. For example, Zhang et al. have synthesized ultrathin two-dimensional Pd–Pt nanorings by selective epitaxial growth of Pt atoms on the periphery of preformed Pd nanosheets in combination with subsequent oxidative etching using Br-/O_2 pairs[175]. As demonstrated by Yang et al., one-dimensional Au nanorods enclosed by a porous shell composed of Au–Ag were synthesized *via* the dealloying treatment of core–shell Au@AuAg nanorods with the assistance of $Fe(NO_3)_3$[176].

The formation of nanoporous structures during the dealloying process requires elaborate design with many parameters into consideration[177–180]. For instance, previous studies show that the nanoporisity is formed spontaneously if and only if the size of particles exceeds a critical value due to the competition between the leaching of transition metals and surface diffusion of residual component[180,181]. As demonstrated by Snyder et al., a minimum particle size of ca. 15 nm is necessary for $PtNi_3$ particles in order to evolve fully formed porosity[181]. Strasser et al. studied the effect of atmosphere in controlling the formation of nanoporosity under free acid leaching (Figure 6.22)[180]. While leaching in the presence of O_2 enabled nanoporous particles

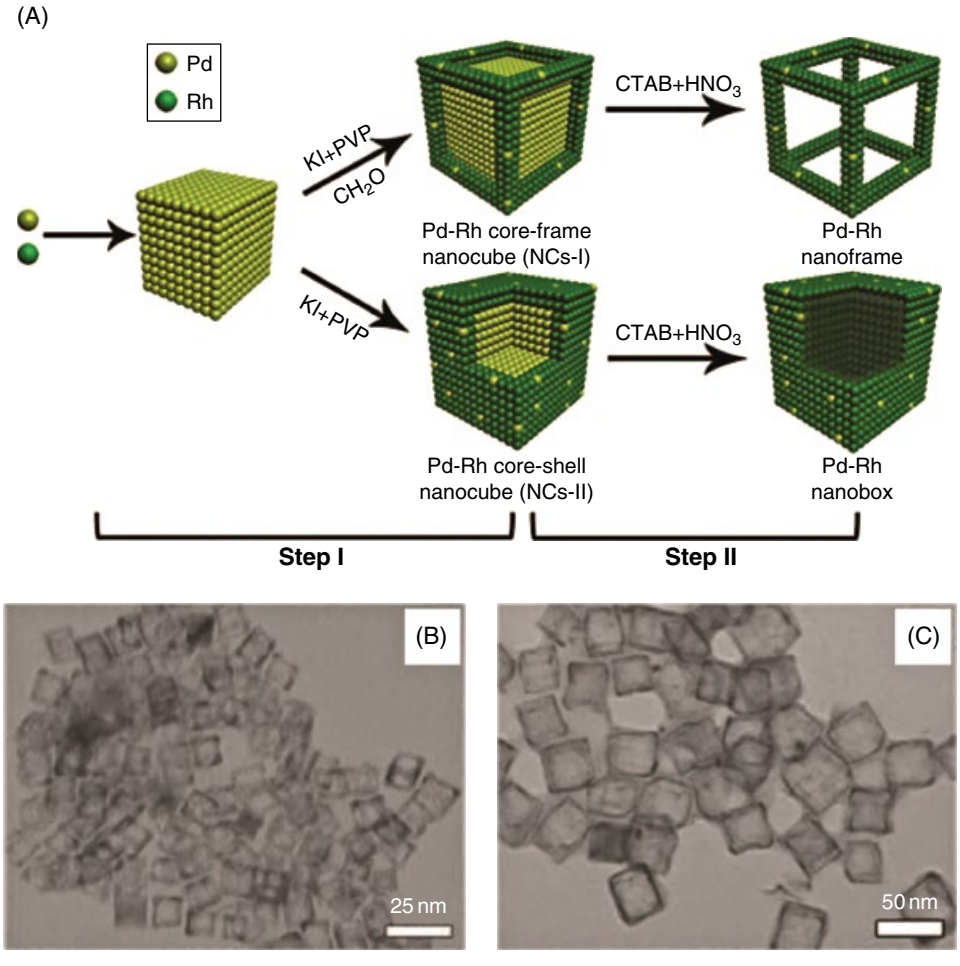

Figure 6.21 (A) Schematic illustration showing the formation process of cubic PdRh nanoframes and nanoboxes. Step I: Hydrothermal synthesis of core-frame and core–shell nanocubes. Step II: Selective etching of Pd cores to generate nanoframes and nanoboxes. (B, C) TEM images of (B) cubic PdRh nanoframes and (C) cubic PdRh nanoboxes. Reproduced with permission ref. [173]. Copyright (2015), Royal Society of Chemistry.

at larger sizes (>13 nm), O_2-free leaching effectively avoided the formation of nanoporosity even in large particles and kept them in a solid architecture. The O_2-induced nanoporosity was intrinsically associated with a drastic loss of Ni while generating thick Pt shells. Under O_2-free leaching, the formation of nanoporosity was effectively delayed, showing more solid core–shell particles with a Pt-rich shell and a higher Ni content retained at the core.

6.3.3 Galvanic Replacement Reaction

Galvanic replacement is a redox process, in which a metal is oxidized by the ions of a second metal with a higher reduction potential when both species are in contact in a solution phase[182–188]. In general, a galvanic replacement reaction can be broken

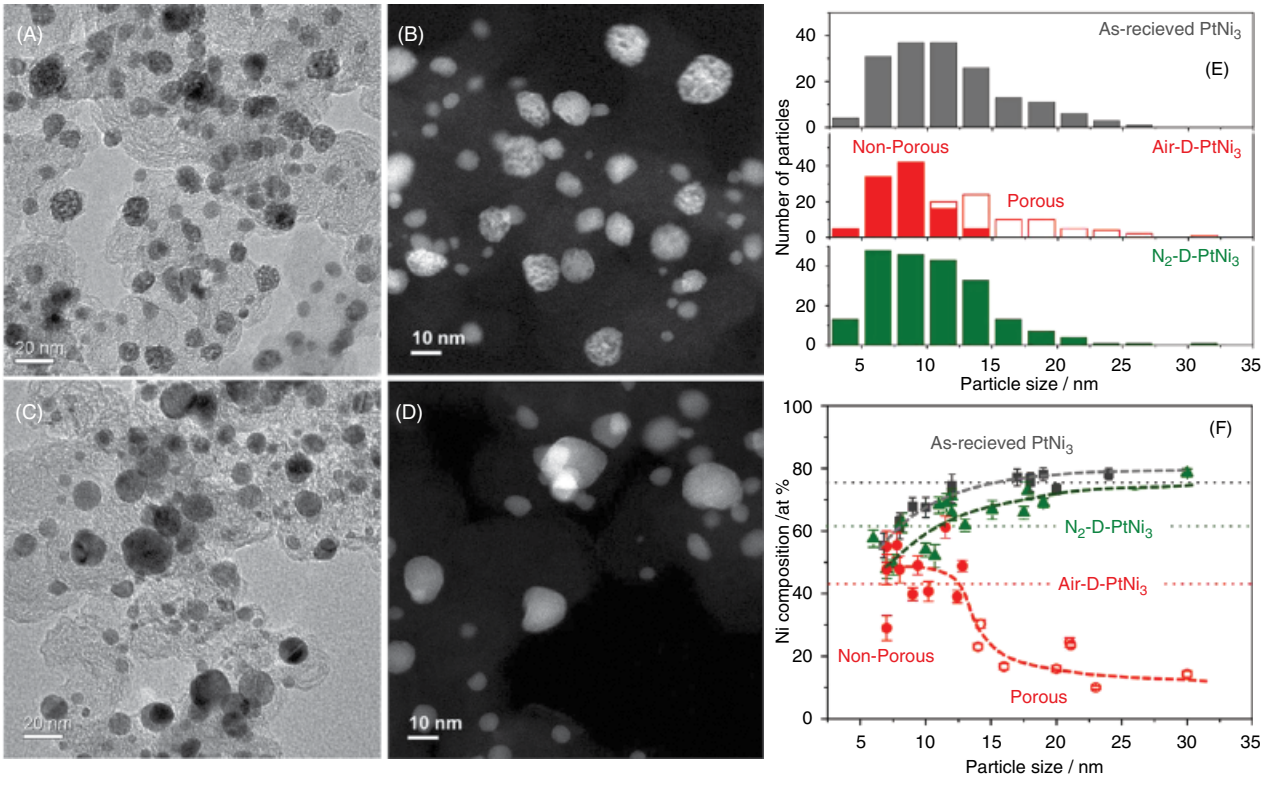

Figure 6.22 (A) TEM and (B) HAADF-STEM images of Air-D-$PtNi_3$ samples with nanoporous structures that were chemically dealloyed in air. (C) TEM and (D) HAADF-STEM images of N_2-D-$PtNi_3$ samples with nonporous structures that were chemically dealloyed in N_2. (E) Size distributions of as-received $PtNi_3$, Air-D – $PtNi_3$ and N_2-D-$PtNi_3$ samples. (F) Correlations between the size, composition, and porosity in the three samples, where the horizontal dot lines represent the average compositions. Only the particles well focused in the TEM images were used for the analysis in (E) and (F). Reproduced with permission ref. [180]. Copyright (2013), American Chemical Society.

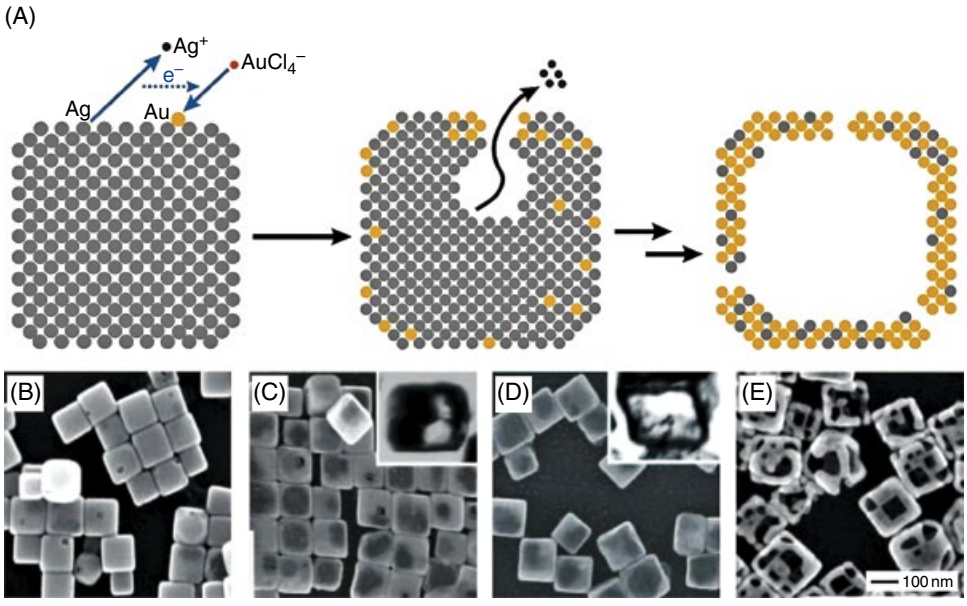

Figure 6.23 (A) Schematic illustration showing the key steps involved during the galvanic replacement reaction between Ag nanocubes and $HAuCl_4$. (B-D) SEM images of samples obtained at different stages of the reaction process. The insets in (C) and (D) show TEM images of individual structures to reveal the hollow interior. Reproduced with permission ref. [201]. Copyright (2008), Springer.

down into two half reactions: the oxidation of the first metal at the anode accompanying with the loss of electrons and the reduction of the second metal ions together with the deposition of the resulting second metal atoms at the cathode. The driving force of a galvanic replacement reaction is the difference of reduction potentials of two metal species involved, with the potential of the second metal necessarily being higher than that of the first one[28]. Typically, the final structure derived from a galvanic replacement reaction is featured with a porous shell, since the oxidation and dissolution of atoms tend to occur from specific sites of the template associated with the difference in chemical reactivity and/or the shielding of certain regions by a layer of the second metal deposited during the reaction[189–194]. Such a method allows facile manipulation over the porosity through varying the amount of precursors added into the reaction solution. In addition, elemental compositions of the final products can be tuned by reacting the template with different salt precursors[195–200]. Overall, galvanic replacement offers a facile and versatile route to a variety of advanced multifunctional nanostructures often characterized by tightly controlled sizes and shapes, hollow interiors, and porous walls, together with tunable elemental compositions.

Figure 6.23 shows a classical example involving the galvanic replacement reaction between Ag nanocubes and $HAuCl_4$[201]. The standard reduction potential of $AuCl_4^-$/Au pair (0.99 V vs. SHE) is higher than that of AgCl/Ag (0.22 V vs. SHE), so the Ag nanocubes can be oxidized in accordance with the following equation:

$$Ag(s) + AuCl_4^-(aq) \rightarrow AgCl(s) + Au(s) + 3Cl^-(aq) \tag{6.15}$$

When $HAuCl_4$ was added, Ag atoms at defect sites on the surface of nanocubes were selectively oxidized and dissolved, together with the deposition of generated Au atoms. Necessarily, a small pit was formed on the surface, from which continuous dissolution of Ag from the interior occurred to empty the rest of the structure. By contrast, the added $AuCl_4^-$ was continuously reduced and deposited in the form of Au atoms on the exterior. After sufficient $HAuCl_4$ was added to the reaction, partially hollowed-out Ag nanocube was observed, leading to the generation of cubic Au–Ag nanoframes in the product. Continuous addition of excess $HAuCl_4$ decreased the thickness of ridges due to dealloying of Ag atoms from the nanoframes. At a certain point, the ridges became so fragile that the nanoframes evolved into fragments as a result. In addition to $HAuCl_4$, $HAuCl_2$ can also be selected as an oxidative agent to react with Ag nanocubes according to the following equation:

$$\mathrm{Ag(s)} + \mathrm{AuCl_2^-(aq)} \rightarrow \mathrm{AgCl(s)} + \mathrm{Au(s)} + \mathrm{Cl^-(aq)} \tag{6.16}$$

It should be noted that the fragments were not observed in the final product even when excess $HAuCl_2$ was added. The different products can be ascribed to the amount of Au(0) being deposited per each Ag(0) dissolved[202]. On one hand, $AuCl_2^-$ generates one Au(0) atom per Ag(0) atom. The as-prepared nanocages have much thicker edges, and they are robust enough to form nanoframes during the dealloying process. On the other hand, $AuCl_4^-$ generates one Au(0) atom per every three Ag(0) atoms. Thus, the edges of nanocages are extremely thin, and these nanocages would easily evolve into discrete fragments during the dealloying process. To compare the effect of porosity on the catalytic performance, Zeng et al. have evaluated the catalytic properties of Au-based nanostructures with different porosity using a model reaction based on the reduction of *p*-nitrophenol by $NaBH_4$[203]. By titrating Ag nanocubes with $HAuCl_4$ in an aqueous solution under refluxing, they were able to prepare three different types of Au-based hollow nanostructures, including nanocages, nanoboxes, and partially hollow nanoboxes, as shown in Figure 6.24, A–C. The kinetic data shown in Figure 6.24, E-H, indicate the catalytic activity will increase as the particle is more open and the wall thins. The good intrinsic electrical connection across the entire surface of a Au nanocage makes it a much better catalyst than small Au solid nanoparticles for a redox reaction. In addition, a typical compensation effect was observed in this catalytic system, which can be explained by the assumption of kinetic regime switching.

Generally, galvanic replacement reaction offers a facile method to generate nanostructures with controlled shapes, as the product typically exhibits a shape closely resembling that of the original template. In addition to cubic nanoframes, nanoframes with other shapes can also be obtained[204–210]. Li et al. reported the synthesis of octahedral Au–Ag nanoframes by a modified galvanic replacement reaction[211]. Upon sequent addition of $AgNO_3$, CuCl, and $HAuCl_4$ into a solution of octadecylamine, truncated Ag polyhedra were formed first and then gradually evolved into octahedral Au–Ag nanoframes, as shown in Figure 6.25. It is believed that selective deposition of Au atoms, which were derived from the galvanic replacement reaction between Ag and $HAuCl_4$, on the high-energy {110} facets took responsibility for the morphological evolution from truncated Ag polyhedra to hollow Au–Ag octahedra. The appearance of nanoframes was attributed to the fact that Ag in the stable {111} facets was easier to be etched by $AuCl_4^-$, while etching of Ag in the sides of octahedra was more difficult due

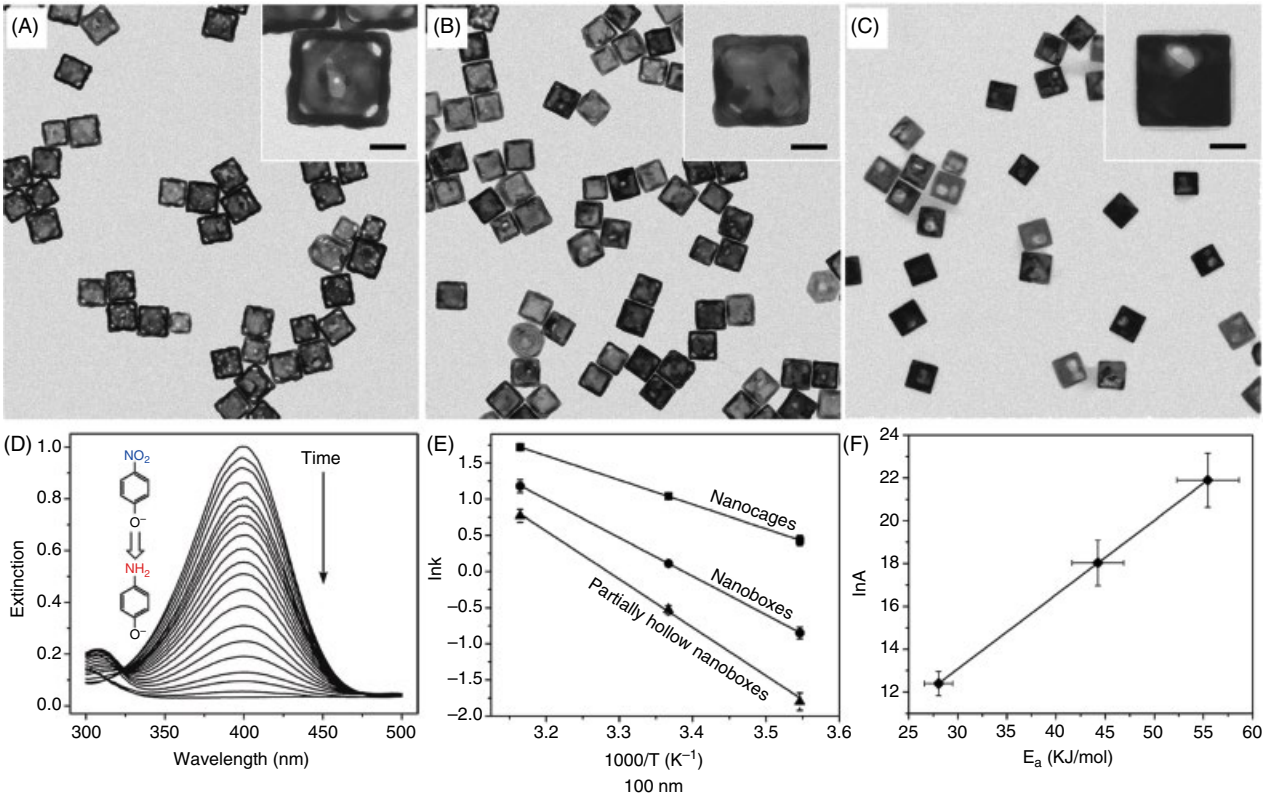

Figure 6.24 (A-C) TEM images of (A) Au–Ag nanocages, (B) Au–Ag nanoboxes, and (C) partially hollow Au–Ag nanoboxes. (D) The extinction spectra at different reaction times, indicating the disappearance of the peak for p-nitrophenol due to the reduction of $-NO_2$ group into $-NH_2$ group. (E) Arrhenius plots for reactions catalyzed by nanocages, nanoboxes, and partially hollow nanoboxes. The activation energy (E_a) can be calculated from the slope of the linear fitting in each case. (F) Plot of pre-exponential factors (ln *A*) versus E_a of the Arrhenius equation, demonstrating the compensation effect for catalysts based on nanocages or nanoboxes. Reproduced with permission ref. [203]. Copyright (2010), American Chemical Society.

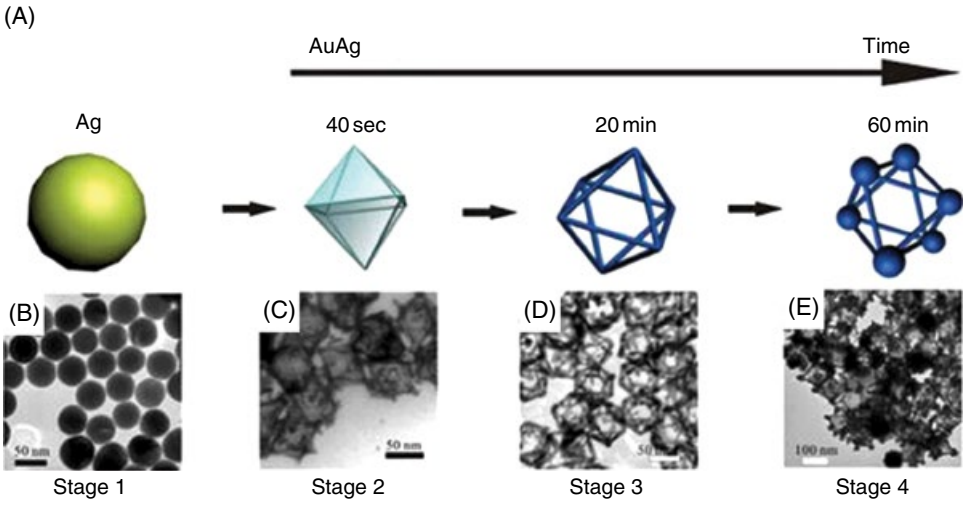

Figure 6.25 (A) Schematic illustration showing the formation process of Au–Ag octahedral nanoframes. (B) TEM image of Ag particles. (C – E) TEM images of the samples with different reaction times after $HAuCl_4$ was added: (C) 40 s, (D) 20 min, and (E) 60 min. Reproduced with permission ref. [211]. Copyright (2012), American Chemical Society.

to the covering of Ag with Au. When the reaction time was further added, $AuCl_4^-$ and Ag^+ ions in the solution were co-reduced by octadecylamine and resultant Au and Ag atoms selectively deposited on the corners of the octahedral nanoframes. In another example, Neretina et al. have adapted galvanic replacement reaction to obtain a fundamentally altered product in which an immobilized core is confined in nanoshells, nanocages, and nanoframes (Figure 6.26)[212]. In the devised route, a Wulff-shaped template (i.e., a truncated octahedron enclosed by six square {100} facets and eight hexagonal {111} facets) of Au, Pt, or Pd, was formed after dewetting of the deposited ultrathin films. Subsequently, through the reduction of Ag^+ ions with the presence of ascorbic acid, neutral Ag atoms were readily deposited on the surface of the template to yield a conformal core–shell structure. By varying the reductant to citrate, the product is a Wulff-shaped Au core enclosed within a Ag nanocube. A galvanic replacement reaction is then carried out on the Ag shell by exposing these structures to $HAuCl_4$, leading to the formation of a porous shell with a framework encapsulating the original template.

Typically, such method involves sequential processes associated with the preparation of the first metal with a desired structure and the addition of the second metal ions to trigger the galvanic replacement reaction[213–215]. By contrast, some research groups have also demonstrated one-pot synthesis involving *in situ* galvanic replacement reaction to prepare bimetallic nanoframes and nanoporous structures[216]. For example, Lou et al. have demonstrated an efficient synthesis of intermetallic $PtCu_3$ nanocages through reduction of H_2PtCl_6 and $Cu(acaca)_2$ by oleylamine in the presence of cetyltrimethylammonium bromide (CTAB)[217]. In such synthesis, CTAB would probably affect the reduction rates of Pt and Cu species, resulting in the preferential formation of Cu nanocrystals in the initial stage although the standard reduction potential for Cu^{2+}/Cu (0.34 V vs. SHE) is more negative than that of the Pt^{2+}/Pt pair (1.18 V vs. SHE). The following galvanic replacement of Cu nanocrystals with Pt^{2+} ions in the solution finally

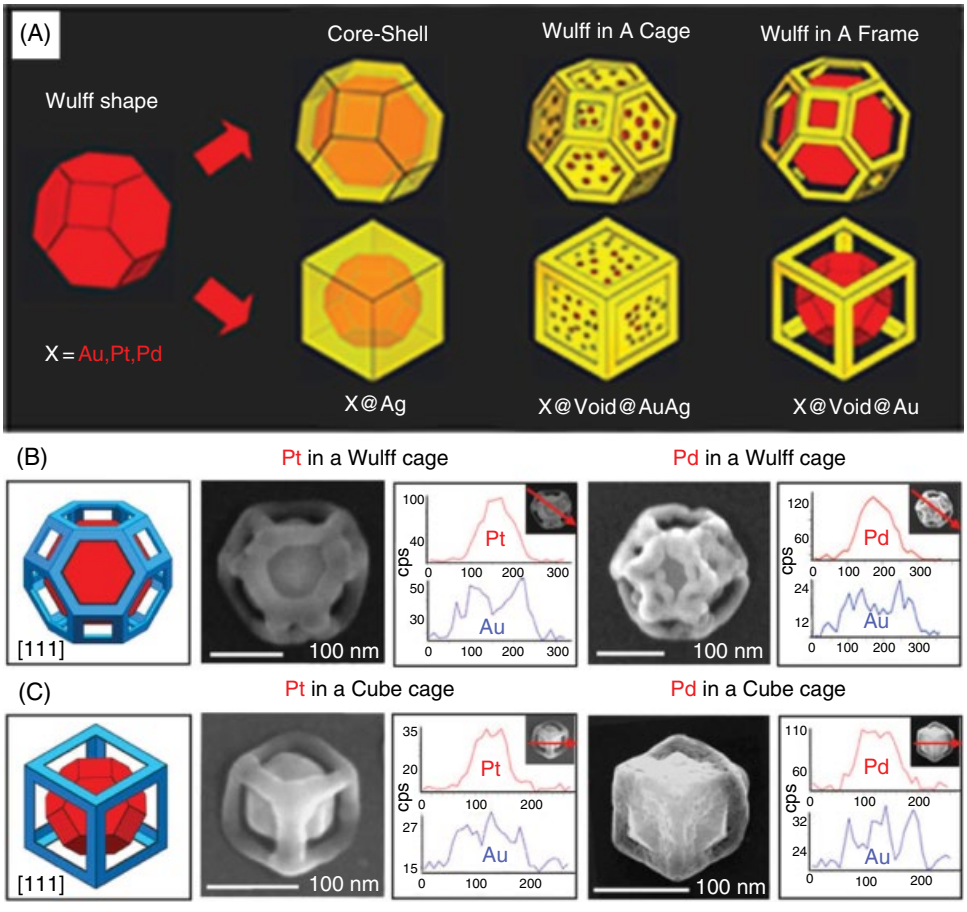

Figure 6.26 (A) Schematic illustration showing the formation of different porous bimetallic nanocrystals derived from Wulff-shaped Au nanocrystals. (B) Geometrical model, SEM images, and elemental line scans of Pt@Ag and Pd@Ag nanocrystals with a truncated octahedral geometry. (C) Geometrical model, SEM images, and elemental line scans of Pt@Ag and Pd@Ag nanocrystals with a cubic geometry. Reproduced with permission ref. [212]. Copyright (2016), American Chemical Society.

leads to the formation of $PtCu_3$ hollow nanocages. Likewise, Li et al. have achieved successful one-pot synthesis of uniform IrCu nanoframes through *in-situ* galvanic replacemenrt reaction between $IrCl_3$ and afore-formed Cu nanocrystals[218]. In another example, Wang et al. have developed a one-pot synthetic strategy to prepare uniform PtCu nanocrystals with systematic shape evolution from dendritic to yolk-cage and box nanostructures[219]. The use of glycine was demonstrated to alter the reduction kinetics of metal precursors. The dominating complexation-formation of Pt^{4+} with glycine in an aqueous solution makes the reduction of Cu^{2+} ions to Cu atoms more favorable than Pt species. Then Pt^{4+} ions react with Cu nanocrystals in the solution, and finally yolk-cage or box Pt–Cu nanocrystals were formed as the *in-situ* galvanic replacement reaction continued.

The galvanic replacement reaction can be coupled with coreduction by introducing a reductant into a galvanic replacement reaction. A typical synthesis was conducted in a mixture containing Pd nanocubes and K_2PtCl_4 in the presence of KBr as a capping agent together with citric acid as a reducing agent (Figure 6.27)[220]. An interplay of two

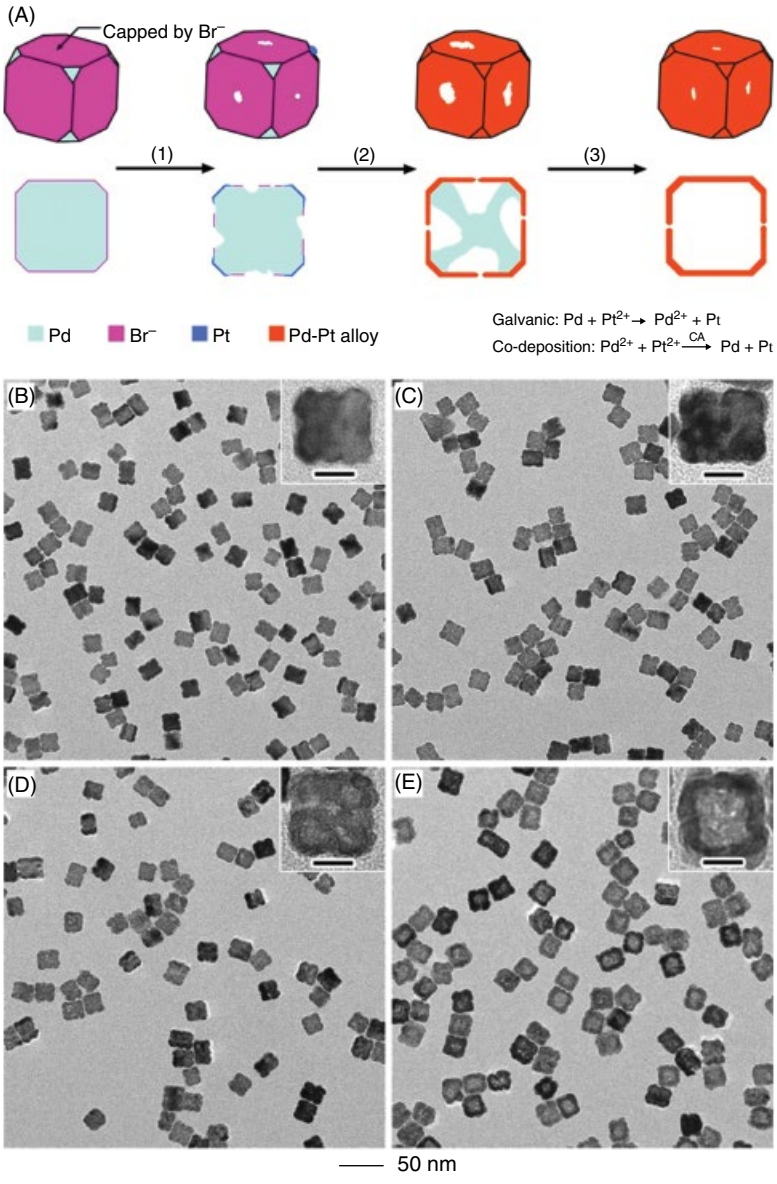

Figure 6.27 (A) Schematic illustration showing the formation process of Pd–Pt nanocages obtained through coupling of coreduction with galvanic replacement reaction. (B-C) TEM images of Pd–Pt alloy nanostructures obtained at different periods of time: (A) 0.5, (B) 2, (C) 6, and (D) 15 h. The insets show TEM images of individual nanocrystals at a higher magnification. The scale bars in the insets are 10 nm. Reproduced with permission ref. [220]. Copyright (2011), American Chemical Society.

different processes determined the success of this synthesis: (1) the galvanic replacement between Pd nanocubes and $PtCl_4^{2-}$ ions and (2) the coreduction of $PdCl_4^{2-}$ derived from the galvanic replacement and $PtCl_4^{2-}$ added into the system. In the initial stage, Pd atoms were preferentially oxidized and dissolved from the {100} facets of Pd nanocubes by reacting with $PtBr_4^{2-}$ via a galvanic replacement mechanism. As the galvanic reaction proceeded, the Pd nanocube gradually disappeared, accompanied by the formation of a Pd–Pt concave nanocube. Meanwhile, the $PdCl_4^{2-}$ ions derived from the galvanic replacement, together with the $PtCl_4^{2-}$ ions remaining in the solution, were coreduced into atoms by citric acid and then deposited on the side faces of the concave nanocube. The newly formed Pd atoms in the walls were less vulnerable to galvanic replacement than the pure Pd in the original nanocube owing to the formation of a Pd–Pt alloy. As such, a cubic Pd–Pt alloy nanocage was formed via a combination of Pd dissolution (due to galvanic replacement) and Pd–Pt overgrowth (due to coreduction).

6.3.4 Kirkendall Effect

As part of the top-down approach, the Kirkendall effect normally refers to a classical phenomenon in metallurgy with a nonreciprocal mutual diffusion process at the interface of coupled materials[221–225]. Typically, the Kirkendall effect is derived from mass transport across a concentration gradient. A major consequence of the Kirkendall effect is the creation of voids, i.e., Kirkendall voids, close to the interface driven by the differences in diffusion rates of distinct species[226]. These Kirkendall voids generally deteriorate the properties at the interface on the macroscopic and micrometer scale. By contrast, in the nanoworld the Kirkendall effect has received scientific attention in the positive contributions to the fabrication of different hollow and porous nanostructures[227–240]. The formation of hollow nanocrystals based on the nanoscale Kirkendall effect is schematically illustrated in Figure 6.28[225]. Solid nanocrystals containing at least one of the elements of the final shell (A) are initially synthesized, followed by reaction with a second element (B) to yield an AB compound. As such, an originally formed AB layer would cover the surface of solid core nanocrystals (A), hindering the subsequent conversion of A to AB. Subsequently, the diffusion through the interface will dominate the following reaction. Meanwhile, if the outward diffusion of A is much faster than the inward diffusion of B, an inward flux of vacancies would accompany the outward flux of A to balance the diffusivity difference. Continuous coalescence

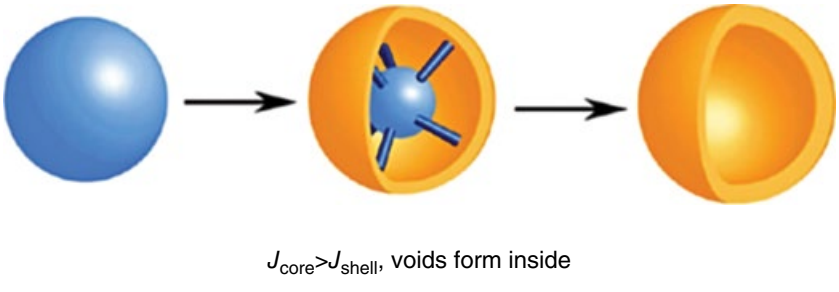

Figure 6.28 Schematic illustration of the Kirkendall effect for the formation of hollow nanocrystals. Reproduced with permission ref. [225]. Copyright (2013), American Chemical Society.

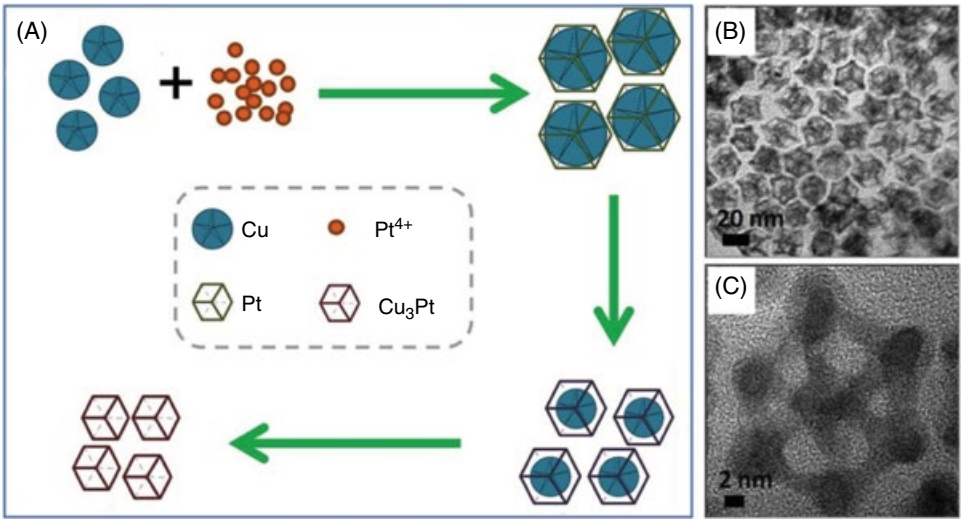

Figure 6.29 (A) Schematic illustration showing the formation process of Cu_3Pt alloy nanoframes. (B,C) TEM images of Cu_3Pt alloy nanoframes. Reproduced with permission ref. [242]. Copyright (2014), Nature Publishing Group.

of such vacancies will finally lead to the formation of Kirkendall voids. Conventional treatment of the Kirkendall treatment only considers the bulk diffusion of growth species and vacancies. Later, Fan et al. proposed a conceptual extension that the development of the hollow interior undergoes two stages[241]. The initial stage is the generation of small Kirkendall voids intersecting the compound interface via a bulk diffusion process, whereas the second stage is dominated by surface diffusion of the core material (i.e., the fast-diffusing species) along the pore surface. Methods based on the nanoscale Kirkendall effect can give rise to highly crystalline hollow nanocrystals with a high yield even in the quantum regime.

Yang et al. demonstrated the preparation of Cu_3Pt nanoframes based on the Kirkendall effect, as shown in Figure 6.29[242]. Upon the anisotropic growth of Pt on multiple twinned Cu seeds, core–shell Cu@Pt particles were first prepared, followed by transformation into Cu_3Pt nanoframes. Specifically, the diffusion of Cu atoms in the Pt shell is faster than that of Pt atoms in the Cu core due to the smaller size of Cu atoms (the atomic radii of Cu and Pt are 145 and 177 pm, respectively). As such, the difference between fluxes of Cu and Pt would generate a net flux of metal atoms from the center to the surface, leading to the formation of a hollow interior until the stable Cu_3Pt alloy phase is formed. Meanwhile, the anisotropic growth of Pt on the surface of twinned Cu seeds caused the preferred distribution of Pt on the edges in the core–shell Cu@Pt particles, which takes responsibility for the formation of nanoframes instead of polyhedra with continuous Pt surface and hollow interiors.

It is believed that the Kirkendall effect can be utilized together with other methods in effectively promoting the generation of hollow and porous nanocrystals[243,244]. Combining sequential galvanic replacement reaction and the Kirkendall effect, Puntes et al. reported a universal strategy to the preparation of a series of concentric double-walled nanoboxes (Figure 6.30)[245]. Upon the addition of Au precursors, the Ag

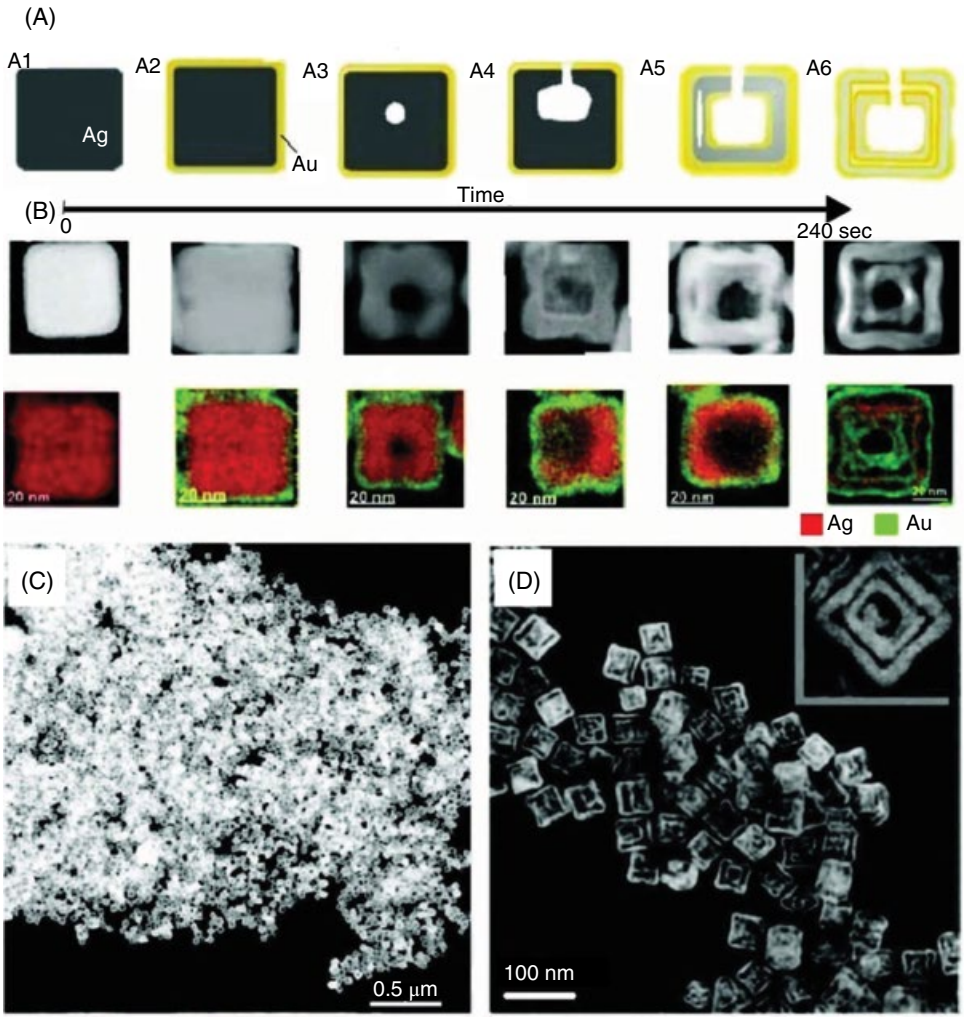

Figure 6.30 (A) Schematic illustration showing the formation process of Au–Ag double-walled nanoboxes. (B) HAADF-STEM images and EDX maps of the samples obtained at different stages of evolution indicated in (A). (C,D) TEM images of Au–Ag double-walled nanoboxes. Reproduced with permission ref. [245]. Copyright (2011), American Association for the Advancement of Science.

nanocubes underwent galvanic replacement reaction with Au precursors, leading to the deposition of a thin Au shell on the surface of Ag nanocubes. Continuous galvanic replacement reaction leads to the formation of small pinholes in the walls, from which the Ag cube is emptied. As the reaction ensues, the wall can be modeled as a diffusion intermetallic couple composed of a thin Ag film sandwiched between two Au layers, allowing the formation of Kirkendall cavities beneath the surface. Since the diffusion of Ag into Au is faster than that of Au into Ag, these voids grow and coalesce, resulting in the formation of Au–Ag double-walled nanoboxes. In addition, Schaak's group deposited Fe onto Sn particles, and the faster diffusion of Sn into Fe could generate hollow intermetallic M–Sn (M = Fe, Co, Ni, and Pd) nanocrystals[246].

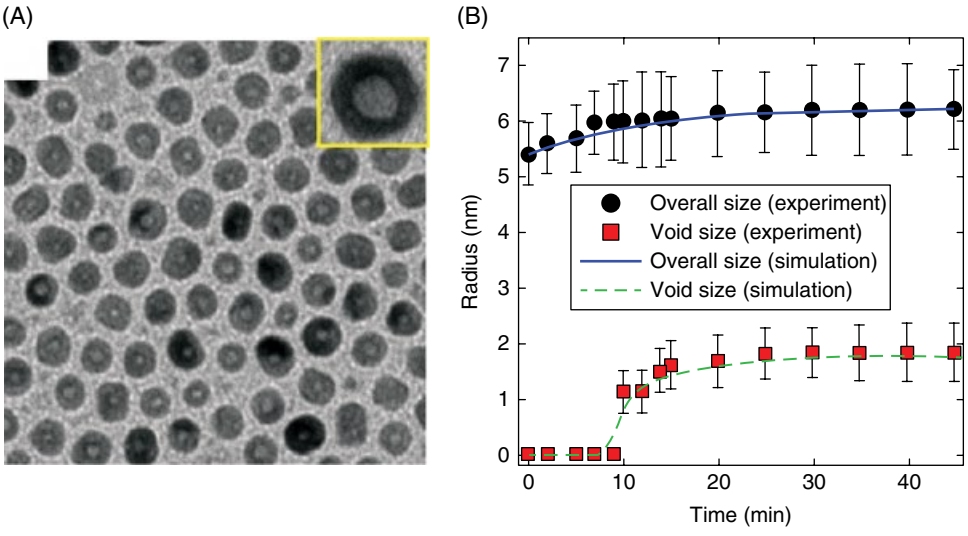

Figure 6.31 (A) TEM image of hollow intermetallic NiZn particles. (B) The correlation between the overall size and void size from experiment and simulation. The error bar represents the standard deviation of the radius. Reproduced with permission ref. [247]. Copyright (2013), American Chemical Society.

Rioux et al. demonstrated an effective synthesis of hollow NiZn intermetallic particles by the thermolysis of metal precursors[247]. After the injection of a diethylzinc solution, preformed Ni particles progressively transformed to a hollow Ni–Zn intermetallic structure owing to the nanoscale Kirkendall effect associated with unequal diffusion rates of Ni and Zn (Figure 6.31A). Moreover, they have developed an isotropic diffusion model utilizing Fick's law of diffusion to describe the formation of voids owing to vacancy coalescence. By fitting the experimental data obtained during the evolution of voids, the effective diffusivities of metals and vacancies were evaluated numerically on the order of 10–20 and 10–19 m2/s, respectively. In addition, the model captures the phenomenon that the void appeared 10 min after the injection of diethylzinc. In the subsequent process, the size of voids increased rapidly and then leveled out after 30 min (Figure 6.31B).

6.3.5 Electrochemical Dealloying

To date, one of the most effective approaches toward the fabrication of bimetallic nanoporous structures is selective dealloying using bi- and multi-metallic raw materials[248–250]. The forms of driving forces behind the dealloying are diverse, among which an electrochemical etching procedure is widely recognized toward achieving effective removal of certain facets and/or less stable elements from alloys. This electrochemical dealloying is conceptually similar to the oxidative etching, both of which involve a redox reaction in order to realize the removal of a substantial portion of the starting materials to create porosity. The present method established on electrochemical dealloying involves directly providing electrons in order to trigger the occurrence of only oxidation reaction related to the dissolution metal atoms with no need for the reduction reaction of oxidative agents.

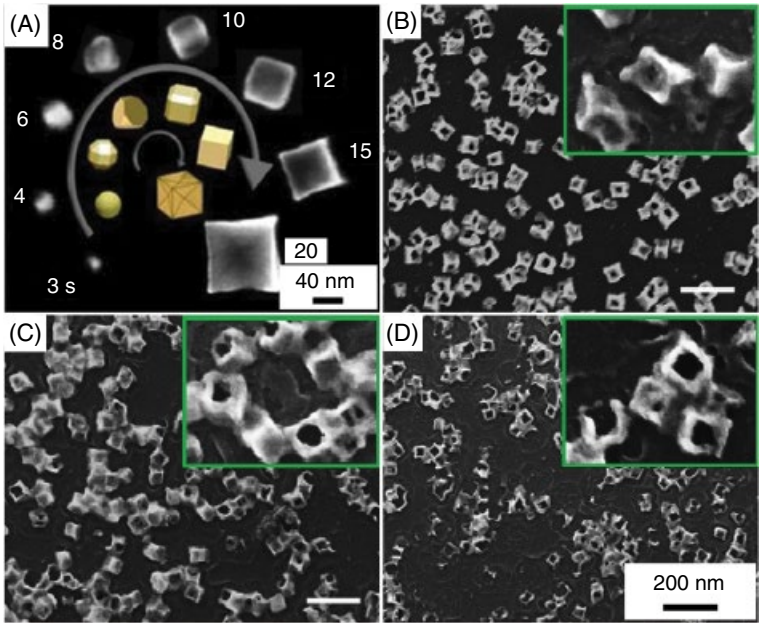

Figure 6.32 (A) SEM image of typical Fe–Ni nanocubes with increasing deposition time from 3 to 20 s. (B-D) SEM images of Fe–Ni nanocages obtained after one, two, and three CV cycles in a 10 mM PBS solution at pH = 3 and a scan rate of 50 mV s^{-1}, respectively. Reproduced with permission ref. [251]. Copyright (2013), American Chemical Society.

In a classical example, Moghimi et al. have demonstrated a novel, surfactant-free approach for synthesizing concave alloy nanocages through an electrochemical process[251]. Exemplified with monodispersed concave FeNi nanocages, electrodeposition of solid FeNi alloy particles was first carried out from an electrolyte containing $NiCl_2$ and $FeCl_2$, followed by the process of electroleaching. By increasing the deposition time from 3 to 20 s, the morphological evolution of FeNi alloy nanostructures was observed from spherical particles to truncated cubes, cubes with sharp corners, and finally concave cubes, as depicted in Figure 6.32 A. It is believed that the presence of Cl^- and Ni^{2+} ions in the solution would increase the reduction rate of Fe^{2+} ions, leading to kinetically controlled formation of concave nanocubes with exposed high-index facets. Later on, concave FeNi nanocages were obtained by a controlled electroleaching process, hollowing out the interiors of the concave nanocubes. Since the point of highest surface energy is located at the center of the concave face, leaching and dissolution started at this site and continued to the edges until the center was completely hollowed out. SEM images of the concave nanoframes obtained after one, two, and three cyclic voltammetry cycles are shown in Figure 6.32, B–D, respectively. It should be noted that since the etching is driven by the high reactivity of the high-index planes located at the cavity, the present method of producing nanocages is material-independent and can be extended to any concave nanostructures.

Compared with chemical dealloying that has been demonstrated as an important strategy to obtain bimetallic particles, electrochemical dealloying has a lot of issues that need to be further identified. In this regard, Wang et al. have presented a comprehensive

study using electrochemical dealloying methods to control the morphology of ordered Cu_3Pt intermetallic particles[252]. As schematically illustrated in Figure 6.33, CuPt nanocrystals with different porous structures were obtained under distinct conditions. In such synthesis, spherical, cubic, polyhedral Cu–Pt particles with different porosity were obtained by varying the electrochemical conditions, such as scan rate, upper

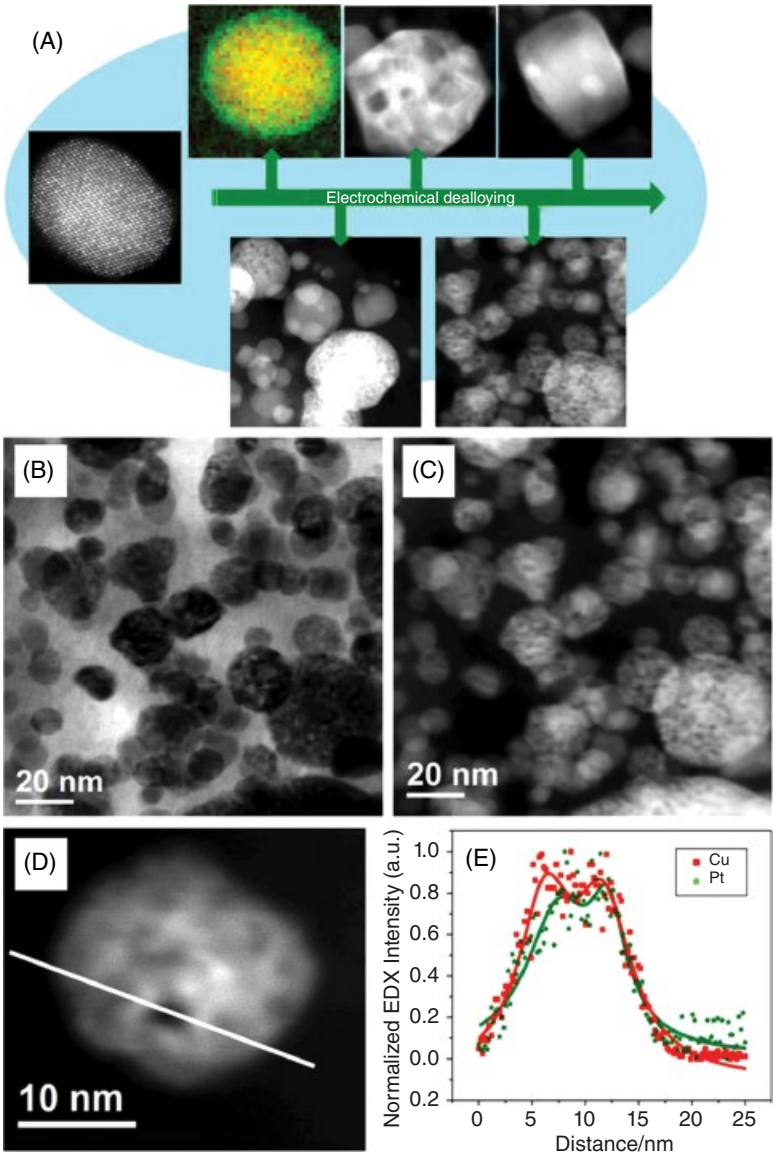

Figure 6.33 (A) Schematic illustration showing the formation of different Cu–Pt nanostructures obtained under distinct conditions. (B) BF and (C) HAADF-STEM images of Cu_3Pt/C intermetallic particles after holding the potential at +1.0 V for 3 h. (C) HAADF-STEM image of an individual Cu–Pt particle. (D) Elemental line-scanning profiles along the direction marked by a white line in (C). Reproduced with permission ref. [252]. Copyright (2015), American Chemical Society.

potential limit, scan time, and the number of cycles. In details, as the dissolved Pt ions would diffuse to the bulk solution, spherical Cu_3Pt/C nanoparticles were formed with a Pt-rich shell on the surface at a slow scan rate. By contrast, during the fast-scan potential cycling, the dissolved Pt ions on the surface had no time to diffuse outside and then redeposited on the electrode surface in the form of Pt atoms, forming Pt (100) facets dominated as a cubic structure. Notably, compared with the potential at +0.8 V, only when the potential was held at +1.0 V did the majority of the particles form nanoporous structures with internal voids within the particle. In addition, nanoporous structure gradually coarsened and formed larger pores after 1000 potential cycles, and Pt diffused and redeposited on the surface to form a Pt-rich shell.

In general, electrochemical dealloying represents a powerful approach for tuning the surface structure and morphology of nanocrystals[253–257]. To shed light on the structural evolution and possible morphological manipulation based on the electrochemical dealloying, Strasser et al. have investigated the atomic process related to how the morphology and intraparticle composition depend on the size of PtCo and PtCu alloy particles during the electrochemical dealloying[258]. The evolution in size-dependent morphology and composition of dealloyed PtCu and PtCo particles is schematically illustrated in Figure 6.34A. Both types of dealloyed PtCo and PtCu particles indicate the existence of three different size regimes associated with characteristic structural morphologies and compositions. Single core–shell particles are exclusively evolved by dealloying particles below a typical diameter of 10–15 nm. Multiple core–shell particles with irregular shaped multiple Co/Cu rich cores dominate when the sizes of particles are between 15 and 30 nm. Above the second critical diameter of about 30 nm, surface pits and nanopores next to multiple Co/Cu rich cores are presented in the dealloyed PtCo and PtCu particles, as shown in Figure 6.34, B and C.

To decipher the different powers provided by chemical and electrochemical leaching, Wang et al. have examined both dealloying methods exemplified with ordered Cu_3Pt intermetallic nanoparticles[259]. Figure 6.35 shows structural and compositional characterizations of an individual Cu_3Pt particle prepared by electrochemical and chemical dealloying methods. It is found that the electrochemical dealloying method led to the formation of a thin Pt shell of around 1 nm in thickness with an ordered Cu_3Pt core structure, while chemical leaching gave rise to a "spongy" structure with no ordered structure being preserved. In addition, it is worth noting that the intermetallic core structure was preserved after electrochemical dealloying treatment, which is quite different from the nanoporosity of nanoparticles in the chemical dealloying process.

6.3.6 Assembly

Self-assembly has been identified within the field of nanotechnology as an important process where small building blocks spontaneously organize into ordered structures by thermodynamic and dynamic constraints[260–272]. Typically, self-assembly is related to thermodynamic equilibrium with the organized structures being characterized by the minimum in the total free energy of the system[273]. In this section, we mainly focus on self-assembly of bimetallic nanomaterials in different forms varying from three-dimensionally dendritic structures to aerogel framework. In particular, metallic aerogels combine the advantages of metals and aerogels, such as the metallic backbone enabling rapid electronic transfer, large surface area providing more reactive sites, high

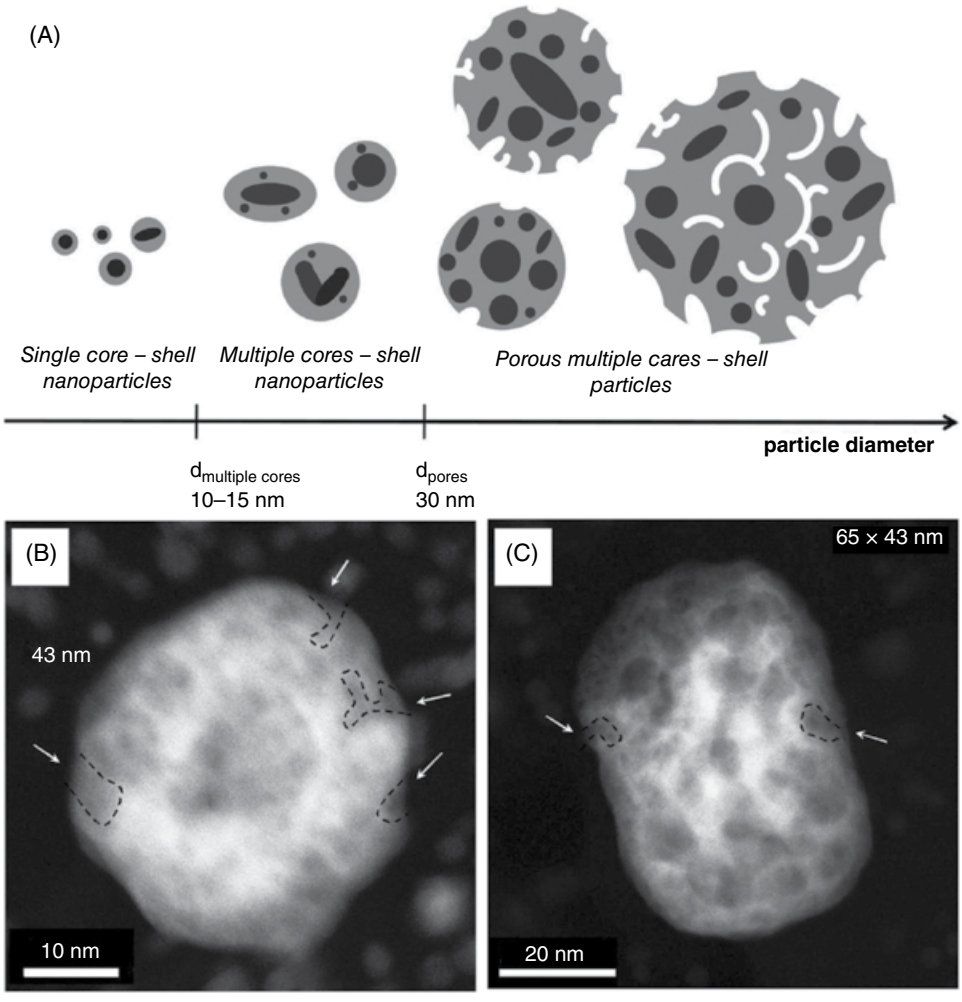

Figure 6.34 (A) Schematic illustration showing the evolution in size-dependent morphology and composition of dealloyed Pt–Cu and Pt–Co particles. (B,C) HAADF images of dealloyed (B) Pt–Cu and (C) Pt–Co particles with diameters larger than 40 nm. As a guide to the eye, the white arrows and black dashed lines denote the pores on the surface. Reproduced with permission ref. [258]. Copyright (2012), American Chemical Society.

porosity accelerating mass transfer, and self-supportability eliminating support corrosion[274–285]. Compared with the strategies mentioned above, such self-assembly exhibits simply operation and high efficiency without suffering from time-consuming multistep procedures, such as the addition of extra harsh reagents to remove the templates.

In a typical example, Pt–Fe alloy nanocrystals with highly porous features and three-dimensional channels were successfully fabricated through continuous assembly of small Pt–Fe particles[286]. The TEM images of samples obtained at representative stages, together with the schematic illustration showing the structural evolution, were shown in Figure 6.36. In the initial stage, abundant small Pt–Fe particles emerged when

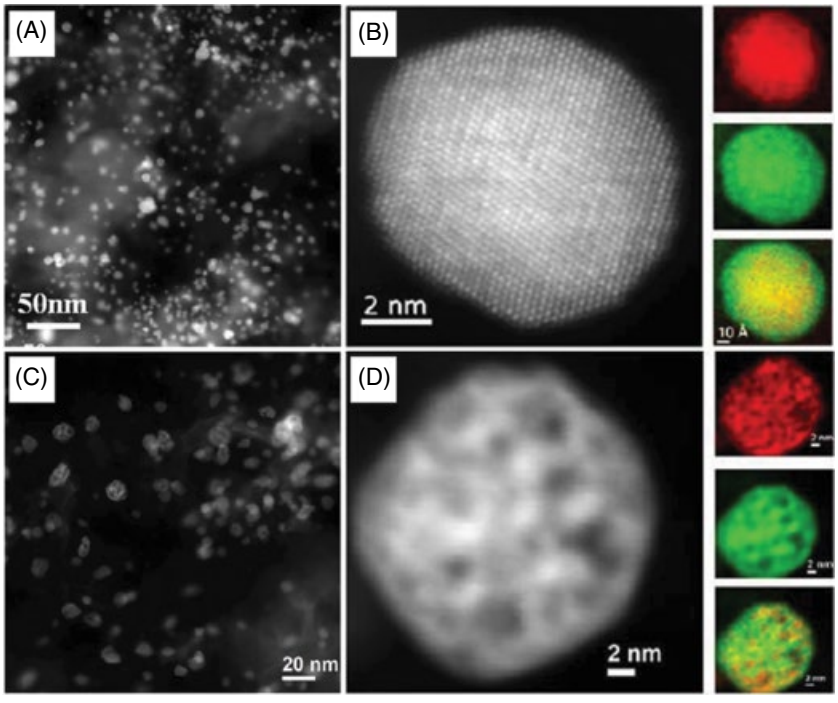

Figure 6.35 (A) HAADF-STEM image of Cu_3Pt/C intermetallic particles after electrochemical dealloying. (B) HAADF-STEM and STEM-EDX elemental mapping images of an individual Cu_3Pt particle. (C) HAADF-STEM image of Cu_3Pt/C intermetallic particles after chemical dealloying. (D) HAADF-STEM and STEM-EDX elemental mapping images of an individual Cu_3Pt particle. Reproduced with permission ref. [259]. Copyright (2012), American Chemical Society.

a critical concentration of nuclei was reached. The force, which originates from a high ratio of volume to surface area of small particles, drives the small particles to coalesce to generate some larger particles. Continuous reaction would evanish the isolated small particles, resulting in the formation of porous nanostructures finally. The growth process of this unique porous structure is accord with the oriented attachment mechanism except for the polycrystalline nature of initial Pt–Fe nanocrystals. However, it should be noted the explosive generation of a high concentration of small particles in the initial stage generated some minor misorientation at the interface, resulting in imperfect oriented attachment rather than adopting the thermodynamically most stable mode.

Over the past few decades, the sol-gel approach has been emerged as a powerful method for the formation of porous nanostructures[287–290]. During the process, sol particles are either dispersed in the solution or formed by chemical reaction from dissolved precursors, followed by subsequent condensation reactions that would lead to the formation of an irregular three-dimensional branched network. Since this process normally takes place in aqueous media and the created pores are filled with water, this state of condensation is denoted as hydrogels. In the next step, supercritical drying should be applied in order to obtain a solid material. This drying technique stands out due to the prevention of a direct phase transition of the solvent from the liquid to the gas phase. Hence, the forces leading to the collapse of the fragile pores inside the

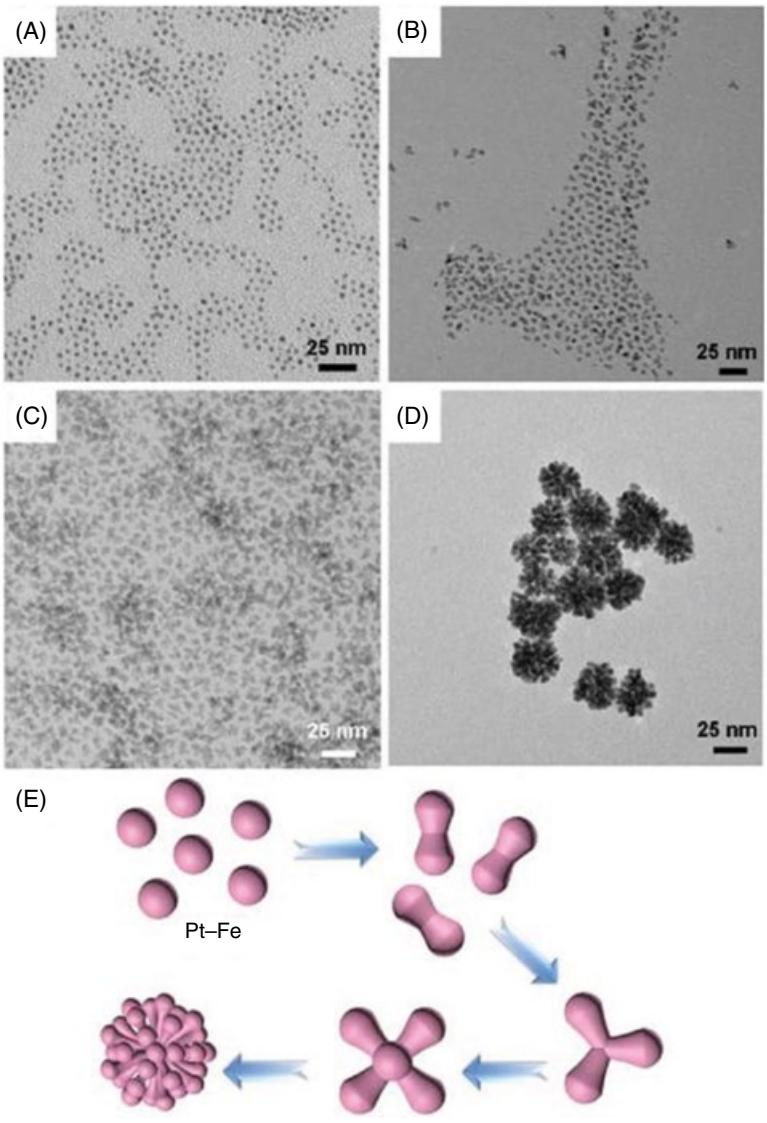

Figure 6.36 (A–D) TEM images of the sample collected at different reaction time: (a) 3, (b) 5, (c) 7, and (d) 10 min. (E) Scheme illustration showing the formation process of porous PtFe nanodendrities. Reproduced with permission ref. [286]. Copyright (2015), Springer.

structure are minimized, and the porosity of the network is mainly retained during removal of the solvent. The resulting porous monoliths are named aerogels. Eychmüller et al. presented a general method of high amenability to prepare porous three-dimensional aerogels with different compositions, as shown in Figure 6.37[291]. Starting from individual metal particles, gelation generates a network of interconnected nanowires. Then the resulting hydrogels transferred into a solid and porous aerogel by supercritical drying. Several multimetallic structures containing Au, Ag, Pt, and Pd can be facilely

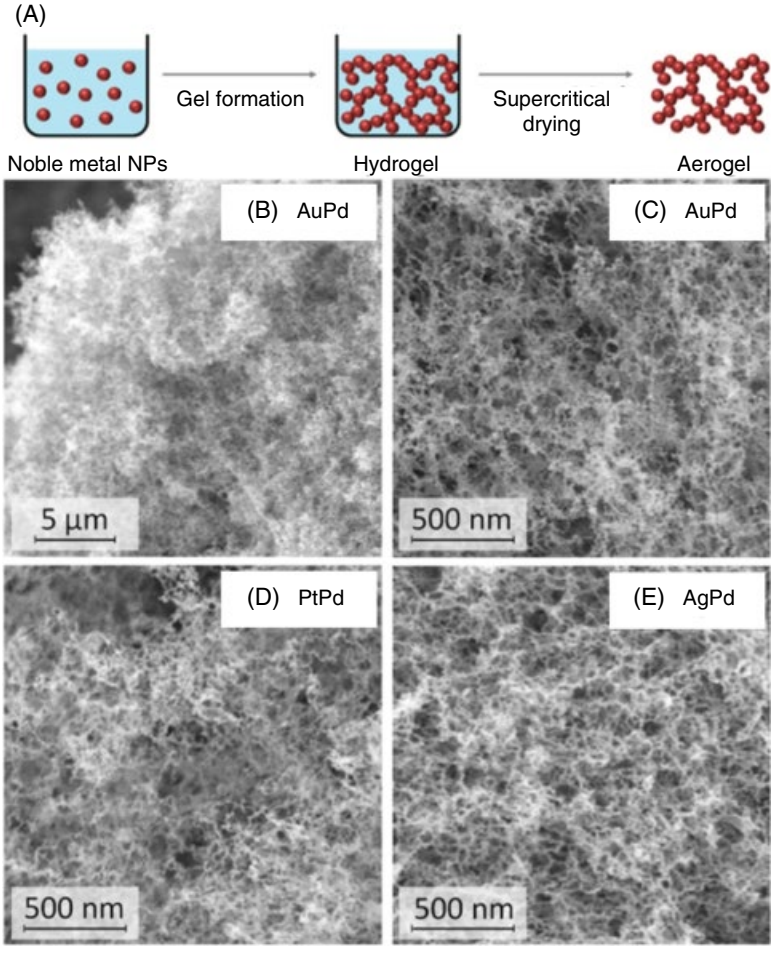

Figure 6.37 (A) Schematic illustration showing the formation of aerogels from individual particles. (B–D) SEM images of (B,C) Au–Pd, (D) Pt–Pd, and (E) Ag–Pd aerogels with porous networks. Reproduced with permission ref. [291]. Copyright (2014), American Chemical Society.

prepared based on this template-free self-assembly method. It should be noted that the involved gelation is initiated under a concentrated solution of metal particles about 50 times higher than the initial one. In addition, an elevated temperature during the gelation process leads to controllable acceleration of gelation and simultaneous strong improvement of reproducibility.

In general, such a sol-gel method is quite facile without complicated steps. Nevertheless, the creation of such nanostructures has been largely limited to irregular solid building blocks, leaving behind opportunities to design novel architectures displaying unique morphologies and physical characteristics. In a representative instance, Arachchige et al. have reported a facile yet powerful strategy for the self-assembly of Au–Ag, Pd–Ag, and Pt–Ag alloy nanoshells into large self-supported monolithic gel structures by engineering the *in-situ* ionic strength of the precursor colloids with the intentional addition of NaCl[292]. Moreover, they have also demonstrated the direct

cross-linking of Au–Ag alloy particles into mesoporous Au–Ag aerogels *via* chemical oxidation of the surface ligands. The introduction of $C(NO_2)_4$ to Au–Ag sols facilitated the oxidation of surface thiolate, creating low coordinated active sites on the surface. The formed active sites are highly reactive, allowing direct interfacial linkages resulting in the formation of hydrogels. Unlike the solid gels prepared by oxidative assembly, these novel nanostructures exhibit mesoporosity that can be altered by changing the hollow diameter of the precursor nanoshells and the accessibility of molecules to the inner surface of the hollows.

One plausible approach to endowing aerogels with specific properties while preserving their other attributes is to tune the structure of building blocks. For instance, Cai et al. demonstrated a facile bottom-up method to prepare bimetallic aerogels composed entirely of hollow PdNi nanospheres with controllable chemical composition and shell thickness (Figure 6.38)[281]. Serving as the building blocks, the hollow PdNi

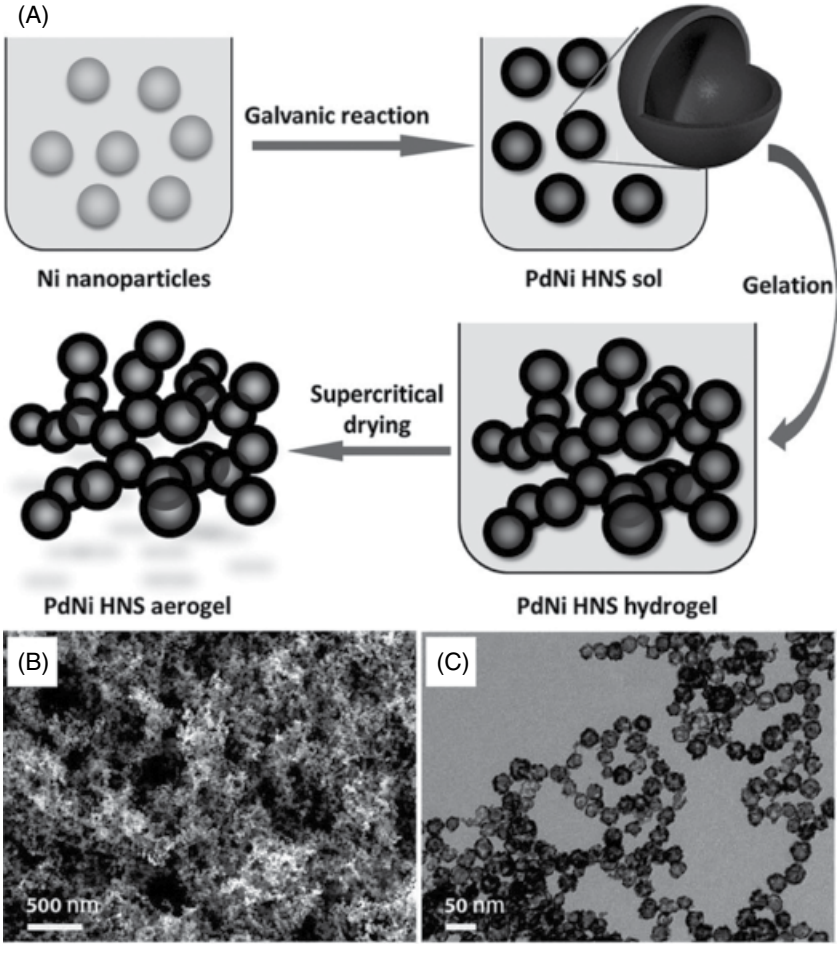

Figure 6.38 (A) Schematic illustration showing the formation process of hollow PdNi aerogels through combination of galvanic replacement reaction and self-assembly. (B) SEM and (C) TEM images of PdNi aerogels. Reproduced with permission ref. [281]. Copyright (2015), Wiley-VCH.

nanospheres were synthesized *via* a galvanic replacement reaction between sacrificial Ni particles and K_2PdCl_4. After concentrating the sols and eliminating parts of the stabilizers to reach a *metastable state*, the gelation process was achieved by heating the concentrated sols at an elevated temperature. In the last step, self-supported aerogels were obtained after supercritical drying. By adding different amounts of Pd precursors, the composition in the resulting Pd–Ni aerogels could be facilely varied with the Ni content ranging from 3% to 19%, as the molar ratio of the Ni/Pd precursors varies from 1:2 to 4:1. In another example, Arachchige et al. successfully prepared bimetallic alloy aerogels (Au–Ag, Pd–Ag, Pt–Ag) based on a novel approach that involves the salt-mediated self-assembly of metal nanoshells followed by supercritical drying[293]. The initial alloy nanoshells were prepared by employing a galvanic replacement reaction of sacrificial Ag nanotriangles with corresponding metal precursors.

6.3.7 Other Methods of Interest

Compared with the synthesis of monometallic nanocrystals, precise control over the structure of bimetallic nanocrystals is typically more complicated, because the compositional and geometrical arrangements of different metal atoms must be considered. Nanoscale phase segregation, resulting from the rearrangement of atoms in alloy particles, can be utilized to construct bi- and multi-metallic nanocrystals with precise atomic compositions in a three-dimensional fashion[294–300]. To this end, one needs to control directionality of the phase segregation to create nanostructures with atoms located in the desired positions, such as the facet center, edge, or vertex location of facet-controlled particles. Typically, the involved atomic migration is generally induced by the fundamental differences in metal-metal bonding, metal surface free energy, and heats of formation of the corresponding surface metal oxide[301–303]. This would then yield compositional heterogeneity on the surface of alloy particles, potentially with anisotropic physicochemical properties[304–307]. For example, Tsung et al. have utilized metal migration at the atomic scale in a core–shell particle to synthesize cubic Pd–Rh nanoboxes and Rh nanoframeworks[308]. The TEM images of samples obtained at different stages, together with the schematic illustration showing the synthetic process, are provided in Figure 6.39. Starting with Pd nanocubes, Pd–Rh core–island–shell nanocubes were first synthesized through epitaxial growth. Next, the core–island–shell nanocubes underwent transformation to either Pd–Rh nanoboxes through alternate pathways involving migration and oxidative etching of the Pd cubic core. Under migration treatment by moving the original core–island–shell reaction solution to a pressure vessel at a raised temperature, Pd atoms relocated from the core to the gaps between surfaces of the Rh framework, resulting in the formation of Pd–Rh nanoboxes. In the case of Rh nanoframeworks, Pd was selectively etched away by dilute hydrochloric acid or metal ions from the alloyed nanoboxes. During the whole process, the Rh islands provide a framework matrix for the migration of Pd atoms, and can be finally observed intact as a nanoframework after etching of nanoboxes. This is owing to the higher chemical stability of Rh in terms of higher Rh–Rh bond energy and slower kinetics of halide complexation for Rh, compared with the case of Pd. In another example, Lee et al. have demonstrated the feasibility of three-dimensionally compositional control within a faceted nanocrystal by utilizing the energy gradients induced by surface-bound moieties[309]. By using core–shell Pt@Ni octahedra, they show that the nanoscale

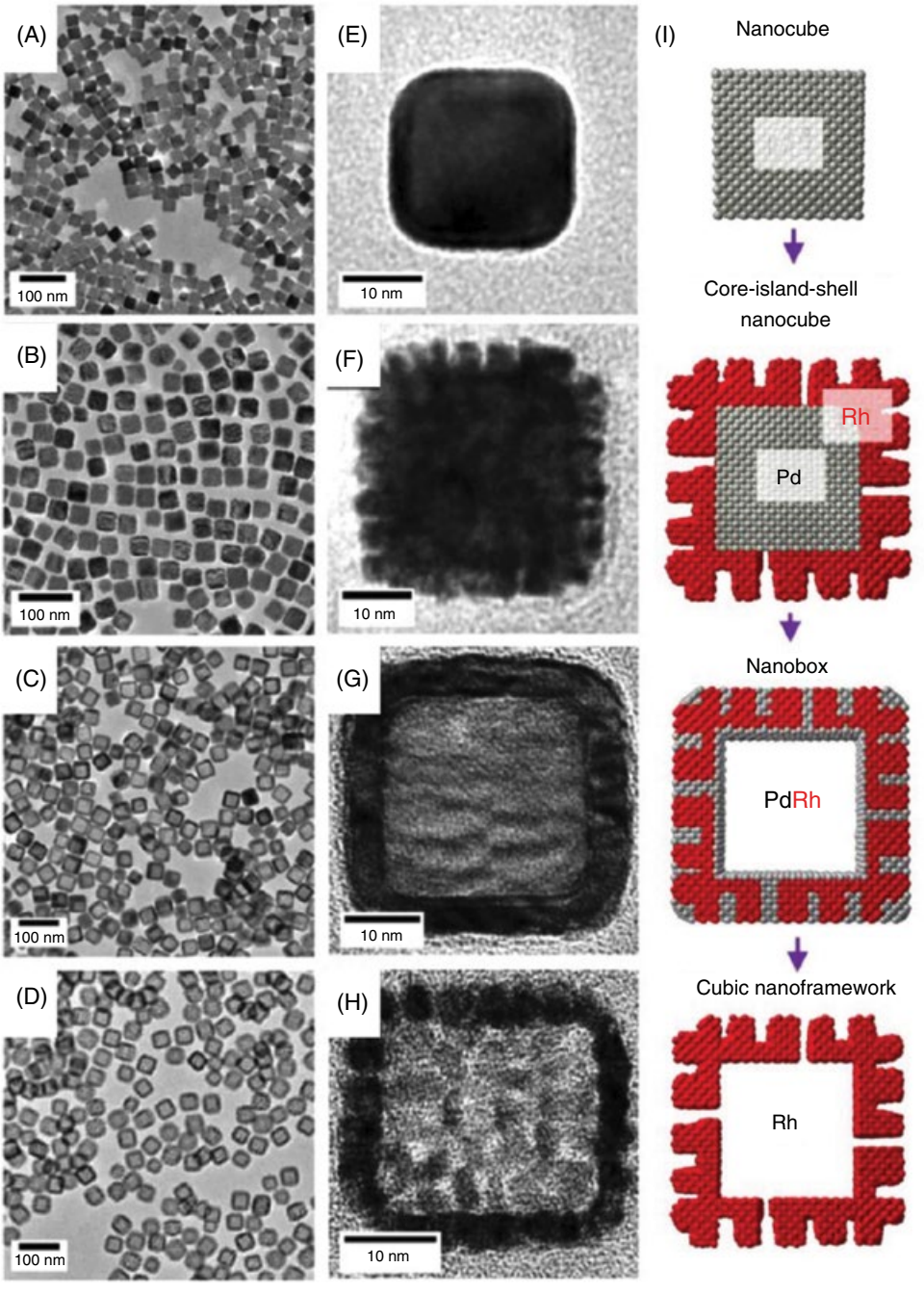

Figure 6.39 (A–H) TEM images of (A, E) Pd nanocubes, (B, F) Pd–Rh core–island–shell nanocubes, (C, G) Pd – Rh nanoboxes, and (D, H) cubic Rh nanoframes. (I) Schematic illustration showing the structural evolution from Pd nanocubes to cubic Rh nanoframes. Reproduced with permission ref. [308]. Copyright (2013), American Chemical Society.

phase segregation can have directionality and be geometrically controlled to produce a Ni octahedron that is penetrated by Pt atoms along three orthogonal Cartesian axes and is coated by Pt atoms along its edges. This peculiar anisotropic diffusion of Pt core atoms along the <100> vertex, and then toward the <110> edges, is explained via the minimum strain energy for Ni–Ni pair interactions. The selective removal of the Ni-rich phase by etching then results in structurally fortified Pt-rich skeletal Pt–Ni alloy framework nanostructures.

UPD refers to the deposition of a small amount of metal atoms on a foreign metal substrate at a potential more positive than that, predicted by Nernst equation, on the same metal surface[310]. The UPD process has been widely used to direct the growth of different types of nanostructures like Au octahedra, Au nanorods, Au–Pd alloy hexoctahedra, and Pd concave nanostructures[311–314]. In the case of hollow nanostructures, a vast variety of procedures have been reported based on the top-down methodology, where a sacrificial material is removed to generate the hollow interiors. By contrast, the UPD process offers a bottom-up approach to fabricate hollow nanocrystals. Based on this concept, our group prepared novel Pt–Cu hierarchical trigonal bipyramid nanoframes (HTBNFs) with controllable sizes[315]. As shown in Figure 6.40, the obtained nanocrystal took the shape of a pyramid, but with ordered hierarchical frame units. Three main branches were first observed in each HTBNF, and the

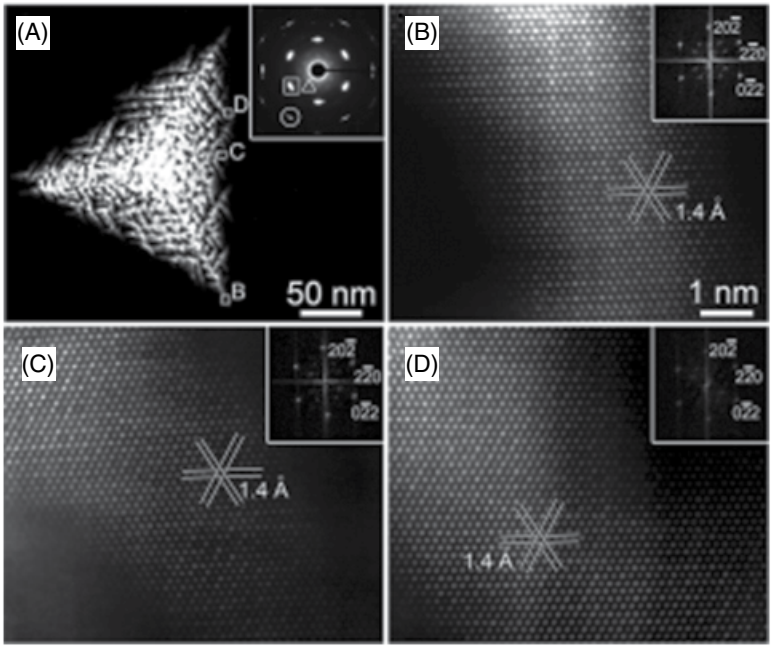

Figure 6.40 (A) HAADF-STEM image of an individual Pt–Cu HTBNFs. The inset of (A) shows the SAED pattern taken from this particle. The spots (marked by circle, square, and triangle) could be indexed to the allowed {422} reflection, the allowed {220} reflection, and the formally forbidden 1/3{422} reflection, respectively. (B-D) HAADF-HRTEM images recorded from B–D marked with white boxes in (A), respectively. Insets show corresponding FFT patterns. The scale bar in (B) also applies to (C) and (D). Reproduced with permission ref. [315]. Copyright (2015), Wiley-VCH.

secondary, tertiary, and higher-order branches stretched outward. In the formation of HTBNFs, Cu^{2+} was found to play a pivotal role by facilitating the generation of plate-like seeds at the initial stage. The UPD of Cu occurred in this system and prevented the deposition of atoms on certain surface. Accordingly, the plate-like seeds grew at the corners, and thus protruded three arms along <211 > directions, leading to the formation of tripods. Afterward, the similar UPD process worked during the growth of secondary, tertiary, and high-order branches along specific crystallographic directions. In another example, Li et al. have presented the preparation of a novel nanostructure, namely, porous Pd octahedra covered with monolayer Ru atoms nanocrystals[316]. Taking advantage of UPD and thermodynamic control, octahedral Pd nanocrystals with six hollow cavities were generated from the Pd concave nanocubes. Stack faults near the surface of nanocrystals were observed, and the monolayer of Ru atoms always occupied the hexagonal close-packed sites.

Ostwald ripening represents another bottom-up approach to the synthesis of nanostructures with well-defined structures[317]. When a two-phase mixture is formed *via* a first-order phase transformation process, the mixture will not initially be in the thermodynamic equilibrium because of the large surface area. The increase of the size of the second phase can decrease the total interfacial area, and thus the total energy of the two-phase system[318]. The dissolution of smaller particles and the redeposition of the dissolved species onto larger particles are termed as Ostwald ripening[319]. Yu et al. demonstrated the fabrication of highly porous Ni–Sn microcages composed of tiny nanoparticles *via* Ostwald ripening[320]. In the first step, Ni–Sn particles initially self-aggregated into solid microspheres, followed by the transformation into yolk-shell structured particles (Figure 6.41). Then, the Ostwald ripening occurs in the formation of hollow microcages consisting of particles larger than the aggregates. In general, Ostwald ripening is regarded as a physical process for matter relocation. Nevertheless, in the solution system, complex chemical processes may also be involved in this process.

In addition to the aforementioned strategies based on a series of chemical and electrochemical methods, biosynthesis based on the reducing capacity of electrochemically active bacteria can be used in the reduction of metal ions into nanoparticles as an eco-friendly way to recycle metal resources. Liu et al. reported the preparation of Pd–Au porous nanostructures using of an electrochemically active bacterium *via* a hydrothermal reaction, in the absence of harsh additives such as chemical reducing agents, toxic surfactants, and stabilizers[321]. In this case, the bacterium not only served as a reducing agent, but also functioned as a supporting material and doping heteroatom sources. The green-synthesized heteroatom-doped bio-Pd–Au alloys broke through the limitation of applying bionanoparticles directly in electrocatalysis, and showed superior activity and durability toward alkaline and acidic electrooxidation. Moreover, another widely used method in the fabrication of nanomaterials is microwave dielectric heating, which exhibits a series of advantages compared with conventional heating, such as fast, uniform and deep heating, low cost, and high energy efficient. In a typical example, microwave irradiation was employed in the shape-controlled synthesis of bimetallic alloy nanocrystals and a unique single-crystalline Pd–Pt alloy hypercubic nanostructure, a four-dimensional analogue, with both special concave surfaces and a hollow interior was synthesized by one-pot strategy under microwave irradiation in an extremely short time without using any sacrificial template and any post-treatment[322].

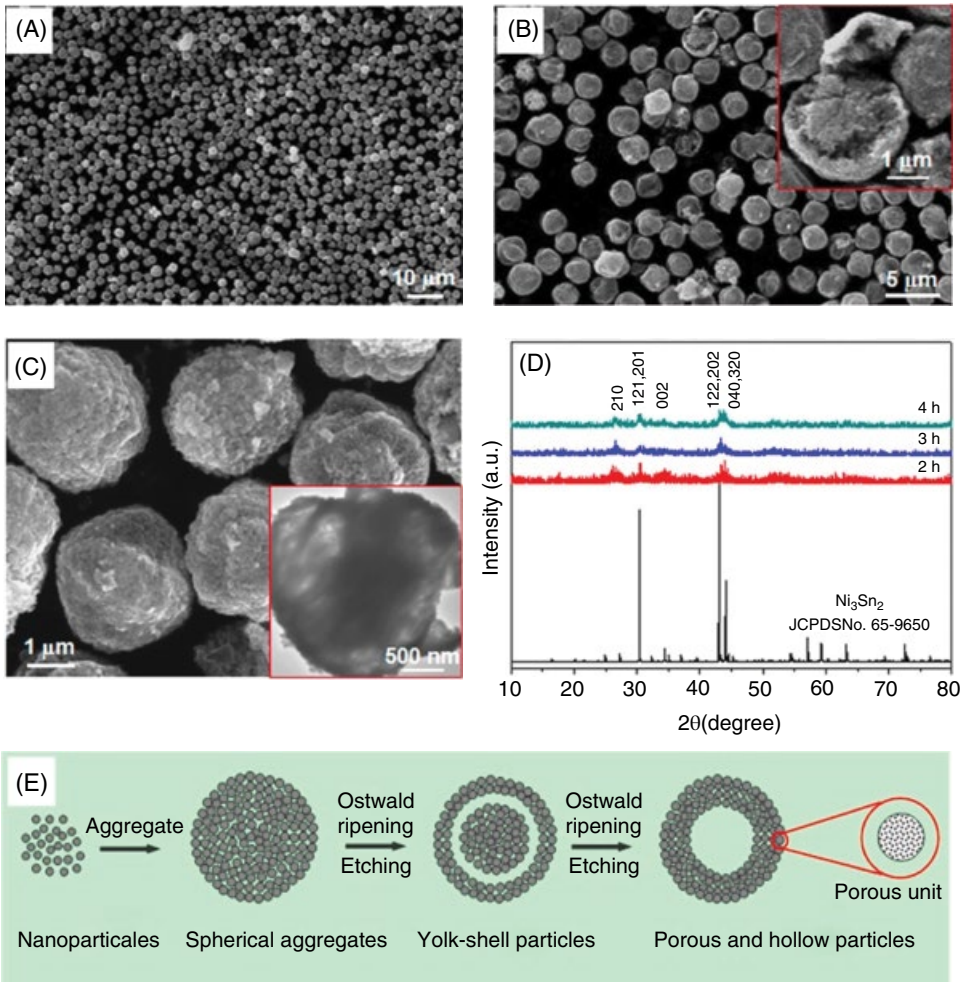

Figure 6.41 (A–C) SEM images of yolk-shell Ni–Sn intermetallic particles obtained at 4 h. The insets of panels B and C show SEM and TEM images of a typical yolk-shell particle, indicating that hollowing is ascribed to inward Ostwald ripening. (D) XRD patterns of the intermediates obtained at different crystallization times (2, 3, and 4 h). (E) Schematic illustration showing the formation process of hollow Ni_3Sn_2 porous cages based on Ostwald ripening and etching. Reproduced with permission ref. [320]. Copyright (2014), American Chemical Society.

6.4 Summary and Outlook

Achieving exquisite mastery over the structure of bimetallic nanocrystals has emerged as one of the foremost scientific endeavors due to the dependence of the overall physicochemical properties on the structure of nanomaterials. Recent years have witnessed the rapid and significant progress with regard to morphological control of solid bimetallic polyhedra under both thermodynamically and kinetically controlled conditions[323]. Unfortunately, precisely controlled synthesis of bimetallic nanoframes and nanoporous structures is still at the infancy stage. This chapter focused on rational

design and structural control of bimetallic nanoframes and nanoporous structures. First, synthetic principles were discussed in detail from two complementary perspectives: top-down and bottom-up strategies. Several common driving forces during the synthesis of such open structures were accessed based on the concentration gradient, difference of reduction potentials, and minimum of surface energy. Specifically, we divided the strategies for the synthesis of branched metal nanocrystals into the following categories: templating-assisted growth, oxidative etching, galvanic replacement, Kirkendall effect, electrochemical dealloying, assembly, and other methods. Despite these significant advances in the synthesis of bimetallic nanoframes and nanoporous structures, there still exist many challenges ahead. Several important issues that need to be addressed are listed as following:

1) From the synthetic part, it is still difficult to prepare bimetallic nanoframes and nanoporous structures with desired combinations of structural and compositional issues. It is widely acknowledged that almost all the physicochemical properties of these nanomaterials are largely dependent on the size, shape, composition, and porous structure. The aforementioned methods established on hard and soft templates are of great difficulty toward achieving precise control over the structure of bimetallic nanoframes and nanoporous structures. As such, the as-obtained morphologies derived from both methods are essentially limited to only powers with irregular shapes or films on conductive substrates. In contrast, despite some progress in generating bimetallic nanoframes and nanoporous structures with well-defined shapes through solution-phase synthesis, challenges are still present toward the precisely controlled synthesis for tuning the degree of hollowing, thickness of ridges, elemental composition, and elemental distribution.
2) It still remains as a grand challenge to attain reproducible synthesis of bimetallic nanoframes and nanoporous structures at a relatively large scale in order to meet the requirement for industrial applications. The present development to some extent stays in an empirical science obtaining different nanostructures based on experimental observations, still far away from the establishment based on quantitative theory and solid understanding. On one hand, the preparation process is extremely sensitive to the experimental conditions. In many cases, the unexpected effects of impurities existing in essentially all chemical regents can be greatly amplified owing to the autocatalytic nature of nanocrystal growth, resulting in irreproducible results associated with the synthetic process. On the other hand, almost all of the syntheses are currently carried out in the laboratory for fundamental research with a production scale at milligram to gram scale. By contrast, the practical applications require kilograms or tons of such materials. Simply enlarging the synthetic scale will perhaps alter the growth kinetics to a point where the products are no longer expected.
3) Moreover, structural instability of some bimetallic nanoframes and nanoporous materials is another shortcoming during storage or when used in a specific application. It is generally accepted that metastable nanocrystals can undergo detrimental changes in terms of composition and morphology over time, which exporting an undesirable impact on the overall performance[324]. Considering the high surface energy possessed by nanoporous materials, they are more susceptible to the ambient conditions, possibly resulting in the transition to an architecture that is more thermodynamically favorable. In addition, elemental stability should also be taken into consideration in the synthesis of bimetallic nanocrystals. On one hand, the more

reactive element in bimetallic nanocrystals tends to dissolve or leach into the solution over time, which can vary the elemental content. On the other hand, the elemental distribution could also be varied through atomic migration and rearrangement occurring in some bimetallic nanoframes and nanoporous structure.

4) To date, there is still a lack powerful *in situ* tools capable of directly visualizing the nucleation and growth process. As such, fundamental understanding of the growth mechanisms of bimetallic nanoframes and nanoporous structures is yet to be developed, which has largely limited the selectivity in carving the three-dimensional morphology. Parallel to this advancement, theoretical studies for simulation of the nanostructure evolution during the synthesis, which to a large extent are still missing, would also be important for gaining insight into the process of nanoframes formation, and providing guidance for the future studies.

6.5 References

1 Wu, B. H., Zheng, N. F. (2013). Surface and interface control of noble metal nanocrystals for catalytic and electrocatalytic applications. *Nano Today*, 8 (2), 168–197.

2 Valtchev, V., Tosheva, L. (2013). Porous nanosized particles: preparation, properties, and applications. *Chemical Reviews*, 113 (8), 6734–6760.

3 Xu, X. B., Zhang, Z. C., Wang, X. (2015). Well-defined metal-organic-framework hollow nanostructures for catalytic reactions involving gases. *Advanced Materials*, 27 (36), 5365–5371.

4 Zhang, L., Roling, L. T., Wang, X., Vara, M., Chi, M. F., Liu, J. Y., Choi, S. I., Park, J., Herron, J. A., Xie, Z. X., Mavrikakis, M., Xia, Y. N. (2015). Platinum-based nanocages with subnanometer-thick walls and well-defined, controllable facets. *Science*, 349 (6246), 412–416.

5 Snyder, J., Fujita, T., Chen, M. W., Erlebacher, J. (2010). Oxygen reduction in nanoporous metal-ionic liquid composite electrocatalysts. *Nature Materials*, 9 (11), 904–907.

6 Deng, Y., Qi, D., Deng, C., Zhang, X., Zhao, D. (2008). Superparamagnetic high-magnetization microspheres with an Fe_3O_4@SiO_2 core and perpendicularly aligned mesoporous SiO_2 shell for removal of microcystins. *Journal of the American Chemical Society*, 130 (1), 28–29.

7 Yamaguchi, A., Uejo, F., Yoda, T., Uchida, T., Tanamura, Y., Yamashita, T., Teramae, N. (2004). Self-assembly of a silica-surfactant nanocomposite in a porous alumina membrane. *Nature Materials*, 3 (5), 337–341.

8 Chen, Y., Xu, P. F., Wu, M. Y., Meng, Q. S., Chen, H. R., Shu, Z., Wang, J., Zhang, L. X., Li, Y. P., Shi, J. L. (2014). Colloidal RBC-shaped, hydrophilic, and hollow mesoporous carbon nanocapsules for highly efficient biomedical engineering. *Advanced Materials*, 26 (25), 4294–4301.

9 Zhang, Y., Hsu, B. Y. W., Ren, C. L., Li, X., Wang, J. (2015). Silica-based nanocapsules: synthesis, structure control and biomedical applications. *Chemical Society Reviews*, 44 (1), 315–335.

10 Piao, Y., Kim, J., Na, H. B., Kim, D., Baek, J. S., Ko, M. K., Lee, J. H., Shokouhimehr, M., Hyeon, T. (2008). Wrap-bake-peel process for nanostructural transformation from β-FeOOH nanorods to biocompatible iron oxide nanocapsules. *Nature Materials*, 7 (3), 242–247.

11 Huan, T. N., Ganesh, T., Kim, K. S., Kim, S., Han, S. H., Chung, H. (2011). A three-dimensional gold nanodendrite network porous structure and its application for an electrochemical sensing. *Biosensors and Bioelectronics*, 27 (1), 183–186.

12 Liu, L. F., Scholz, R., Pippel, E., Gosele, U. (2010). Microstructure, electrocatalytic and sensing properties of nanoporous $pt_{46}ni_{54}$ alloy nanowires fabricated by mild dealloying. *Journal of Materials Chemistry*, 20 (27), 5621–5627.

13 Zhai, D. Y., Liu, B. R., Shi, Y., Pan, L. J., Wang, Y. Q., Li, W. B., Zhang, R., Yu, G. H. (2013). Highly sensitive glucose sensor based on Pt nanoparticle/polyaniline hydrogel heterostructures. *ACS Nano*, 7 (4), 3540–3546.

14 Liu, H., Li, W., Shen, D. K., Zhao, D. Y., Wang, G. X. (2015). Graphitic carbon conformal coating of mesoporous TiO_2 hollow spheres for high-performance lithium ion battery anodes. *Journal of the American Chemical Society*, 137 (40), 13161–13166.

15 Zuo, X. X., Chang, K., Zhao, J., Xie, Z. Z., Tang, H. W., Li, B., Chang, Z. R. (2016). Bubble-template-assisted synthesis of hollow fullerene-like MoS_2 nanocages as a lithium ion battery anode material. *Journal of Materials Chemistry A*, 4 (1), 51–58.

16 Moon, G. D., Joo, J. B., Dahl, M., Jung, H., Yin, Y. D. (2014). Nitridation and layered assembly of hollow TiO_2 shells for electrochemical energy storage. *Advanced Functional Materials*, 24 (6), 848–856.

17 Pan, J. H., Zhang, X. W., Du, A. J., Sun, D. D., Leckie, J. O. (2008). Self-etching reconstruction of hierarchically mesoporous F-TiO_2 hollow microspherical photocatalyst for concurrent membrane water purifications. *Journal of the American Chemical Society*, 130 (34), 11256–11257.

18 Zhang, Y. X., Xu, S. C., Luo, Y. Y., Pan, S. S., Ding, H. L., Li, G. H. (2011). Synthesis of mesoporous carbon capsules encapsulated with magnetite nanoparticles and their application in wastewater treatment. *Journal of Materials Chemistry*, 21 (11), 3664–3671.

19 Zhang, Y. K., He, Z. J., Wang, H. C., Qi, L., Liu, G. H., Zhang, X. J. (2015). Applications of hollow nanomaterials in environmental remediation and monitoring: a review. *Frontiers of Environmental Science & Engineering*, 9 (5), 770–783.

20 Prieto, G., Tüysüz, H., Duyckaerts, N., Knossalla, J., Wang, G.-H., Schüth, F. (2016). Hollow nano- and microstructures as catalysts. *Chemical Reviews*, 116 (22), 14056–14119.

21 Chen, Z., Cui, Z. M., Li, P., Cao, C. Y., Hong, Y. L., Wu, Z. Y., Song, W. G. (2012). Diffusion induced reactant shape selectivity inside mesoporous pores of Pd@Meso-SiO_2 nanoreactor in suzuki coupling reactions. *Journal of Physical Chemistry C*, 116 (28), 14986–14991.

22 Kuo, C. H., Tang, Y., Chou, L. Y., Sneed, B. T., Brodsky, C. N., Zhao, Z. P., Tsung, C. K. (2012). Yolk-shell nanocrystal@ZIF-8 Nanostructures for gas-phase heterogeneous catalysis with selectivity control. *Journal of the American Chemical Society*, 134 (35), 14345–14348.

23 Zhang, W. N., Lu, G., Cui, C. L., Liu, Y. Y., Li, S. Z., Yan, W. J., Xing, C., Chi, Y. R., Yang, Y. H., Huo, F. W. (2014). A family of metal-organic frameworks exhibiting size-selective catalysis with encapsulated noble-metal nanoparticles. *Advanced Materials*, 26 (24), 4056–4060.

24 Nguyen, C. C., Vu, N. N., Do, T. O. (2015). Recent advances in the development of sunlight-driven hollow structure photocatalysts and their applications. *Journal of Materials Chemistry A*, 3 (36), 18345–18359.

25 Davis, M. E. (2002). Ordered porous materials for emerging applications. *Nature*, 417 (6891), 813–821.

26 Fang, Z. C., Wang, Y. C., Liu, C. X., Chen, S., Sang, W., Wang, C., Zeng, J. (2015). Rational design of metal nanoframes for catalysis and plasmonics. *Small*, 11 (22), 2593–2605.

27 Liu, Y. D., Goebl, J., Yin, Y. D. (2013). Templated synthesis of nanostructured materials. *Chemical Society Reviews*, 42 (7), 2610–2653.

28 Xia, X. H., Wang, Y., Ruditskiy, A., Xia, Y. N. (2013). 25th anniversary article: galvanic replacement: a simple and versatile route to hollow nanostructures with tunable and well-controlled properties. *Advanced Materials*, 25 (44), 6313–6333.

29 Xu, Y., Zhang, B. (2014). Recent advances in porous Pt-based nanostructures: synthesis and electrochemical applications. *Chemical Society Reviews*, 43 (8), 2439–2450.

30 Biswas, A., Bayer, I. S., Biris, A. S., Wang, T., Dervishi, E., Faupel, F. (2012). Advances in top-down and bottom-up surface nanofabrication: techniques, applications & future prospects. *Advances in Colloid and Interface Science*, 170 (1–2), 2–27.

31 Lim, B., Xia, Y. N. (2011). Metal nanocrystals with highly branched morphologies. *Angewandte Chemie-International Edition*, 50 (1), 76–85.

32 Perez-Ramirez, J., Christensen, C. H., Egeblad, K., Christensen, C. H., Groen, J. C. (2008). Hierarchical zeolites: enhanced utilisation of microporous crystals in catalysis by advances in materials design. *Chemical Society Reviews*, 37 (11), 2530–2542.

33 An, Q. Y., Zhang, P. F., Wei, Q. L., He, L., Xiong, F. Y., Sheng, J. Z., Wang, Q. Q., Mai, L. Q. (2014). Top-down fabrication of three-dimensional porous V_2O_5 hierarchical microplates with tunable porosity for improved lithium battery performance. *Journal of Materials Chemistry A*, 2 (10), 3297–3302.

34 Canelas, D. A., Herlihy, K. P., DeSimone, J. M. (2009). Top-down particle fabrication: control of size and shape for diagnostic imaging and drug delivery. *Wiley Interdisciplinary Reviews-Nanomedicine and Nanobiotechnology*, 1 (4), 391–404.

35 Chen, J. S., Zhu, T., Yang, X. H., Yang, H. G., Lou, X. W. (2010). Top-down fabrication of α-Fe_2O_3 single-crystal nanodiscs and microparticles with tunable porosity for largely improved lithium storage properties. *Journal of the American Chemical Society*, 132 (38), 13162–13164.

36 Li, C. L., Yin, C. L., Mu, X. K., Maier, J. (2013). Top-down synthesis of open framework fluoride for lithium and sodium batteries. *Chemistry of Materials*, 25 (6), 962–969.

37 Wang, D. Y., Mohwald, H. (2004). Template-directed colloidal self-assembly—the route to 'top-down' nanochemical engineering. *Journal of Materials Chemistry*, 14 (4), 459–468.

38 Gilroy, K. D., Ruditskiy, A., Peng, H. C., Qin, D., Xia, Y. N. (2016). Bimetallic nanocrystals: syntheses, properties, and applications. *Chemical Reviews*, 116 (18), 10414–10472.

39 Tyrrell, H. J. V. (1964). The origin and present status of Fick's diffusion law. *Journal of Chemical Education*, 41 (7), 397–400.

40 Tu, K. N., Gosele, U. (2005). Hollow nanostructures based on the Kirkendall effect: design and stability considerations. *Applied Physics Letters*, 86 (9), 093111.

41 Chen, Q., Bae, S. C., Granick, S. (2011). Directed self-assembly of a colloidal Kagome lattice. *Nature*, 469 (7330), 381–384.

42 Glotzer, S. C., Solomon, M. J. (2007). Anisotropy of building blocks and their assembly into complex structures. *Nature Materials*, 6 (8), 557–562.

43 Li, F., Josephson, D. P., Stein, A. (2011). Colloidal assembly: the road from particles to colloidal molecules and crystals. *Angewandte Chemie-International Edition*, 50 (2), 360–388.

44 Peng, Z. B., Liu, H. T. (2016). Bottom-up nanofabrication using DNA nanostructures. *Chemistry of Materials*, 28 (4), 1012–1021.

45 Baldan, A. (2002). Review progress in Ostwald ripening theories and their applications to nickel-base superalloys part i: Ostwald ripening theories. *Journal of Materials Science*, 37 (11), 2171–2202.

46 Antonietti, M., Fechler, N., Fellinger, T. P. (2014). Carbon aerogels and monoliths: control of porosity and nanoarchitecture via sol-gel routes. *Chemistry of Materials*, 26 (1), 196–210.

47 Ciriminna, R., Fidalgo, A., Pandarus, V., Beland, F., Ilharco, L. M., Pagliaro, M. (2013). The sol-gel route to advanced silica-based materials and recent applications. *Chemical Reviews*, 113 (8), 6592–6620.

48 Mann, S., Burkett, S. L., Davis, S. A., Fowler, C. E., Mendelson, N. H., Sims, S. D., Walsh, D., Whilton, N. T. (1997). Sol-gel synthesis of organized matter. *Chemistry of Materials*, 9 (11), 2300–2310.

49 Dey, P., Blakey, I., Thurecht, K. J., Fredericks, P. M. (2013). Self-assembled hyperbranched polymer-gold nanoparticle hybrids: understanding the effect of polymer coverage on assembly size and SERS performance. *Langmuir*, 29 (2), 525–533.

50 Maye, M. M., Luo, J., Lim, I. I. S., Han, L., Kariuki, N. N., Rabinovich, D., Liu, T. B., Zhong, C. J. (2003). Size-controlled assembly of gold nanoparticles induced by a tridentate thioether ligand. *Journal of the American Chemical Society*, 125 (33), 9906–9907.

51 Merican, Z., Schiller, T. L., Hawker, C. J., Fredericks, P. M., Blakey, I. (2007). Self-assembly and encoding of polymer-stabilized gold nanoparticles with surface-enhanced raman reporter molecules. *Langmuir*, 23 (21), 10539–10545.

52 Alivisatos, A. P., Johnsson, K. P., Peng, X. G., Wilson, T. E., Loweth, C. J., Bruchez, M. P., Schultz, P. G. (1996). Organization of 'nanocrystal molecules' using DNA. *Nature*, 382 (6592), 609–611.

53 Suzuki, K., Sato, S., Fujita, M. (2010). Template synthesis of precisely monodisperse silica nanoparticles within self-assembled organometallic spheres. *Nature Chemistry*, 2 (1), 25–29.

54 Wang, X., Choi, S. I., Roling, L. T., Luo, M., Ma, C., Zhang, L., Chi, M. F., Liu, J. Y., Xie, Z. X., Herron, J. A., Mavrikakis, M., Xia, Y. N. (2015). Palladium-platinum core-shell icosahedra with substantially enhanced activity and durability towards oxygen reduction. *Nature Communications*, 6 pp. 7594.

55 Zhao, X., Chen, S., Fang, Z. C., Ding, J., Sang, W., Wang, Y. C., Zhao, J., Peng, Z. M., Zeng, J. (2015). Octahedral Pd@$Pt_{1.8}$Ni Core-shell nanocrystals with ultrathin ptni alloy shells as active catalysts for oxygen reduction reaction. *Journal of the American Chemical Society*, 137 (8), 2804–2807.

56 Meng, M., Fang, Z. C., Zhang, C., Su, H. Y., He, R., Zhang, R. P., Li, H. L., Li, Z. Y., Wu, X. J., Ma, C., Zeng, J. (2016). Integration of kinetic control and lattice mismatch to synthesize Pd@AuCu core-shell planar tetrapods with size-dependent optical properties. *Nano Letters*, 16 (5), 3036–3041.

57 Kim, K., Lee, T., Kwon, Y., Seo, Y., Song, J., Park, J. K., Lee, H., Park, J. Y., Ihee, H., Cho, S. J., Ryoo, R. (2016). Lanthanum-catalysed synthesis of microporous 3d graphene-like carbons in a zeolite template. *Nature*, 535 (7610), 131–135.

58 Liang, S., Liu, X. L., Yang, Y. Z., Wang, Y. L., Wang, J. H., Yang, Z. J., Wang, L. B., Jia, S. F., Yu, X. F., Zhou, L., Wang, J. B., Zeng, J., Wang, Q. Q., Zhang, Z. Y. (2012). Symmetric and asymmetric Au-AgCdSe hybrid nanorods. *Nano Letters*, 12 (10), 5281–5286.

59 Wang, L. B., Wang, Y. C., Guo, H. Y., Huang, J. L., Zhao, Y. L., Liu, Q. Y., Wu, X., Zeng, J. (2015). Au-Pd alloy octapods with high electrocatalytic activity for the oxidation of formic acid. *Particle & Particle Systems Characterization*, 32 (3), 295–300.

60 Xia, X. H., Zeng, J., McDearmon, B., Zheng, Y. Q., Li, Q. G., Xia, Y. N. (2011). Silver nanocrystals with concave surfaces and their optical and surface-enhanced raman scattering properties. *Angewandte Chemie-International Edition*, 50 (52), 12542–12546.

61 Xia, X. H., Zeng, J., Oetjen, L. K., Li, Q. G., Xia, Y. N. (2012). Quantitative analysis of the role played by poly(vinylpyrrolidone) in seed-mediated growth of Ag nanocrystals. *Journal of the American Chemical Society*, 134 (3), 1793–1801.

62 Zeng, J., Zhu, C., Tao, J., Jin, M. S., Zhang, H., Li, Z. Y., Zhu, Y. M., Xia, Y. N. (2012). Controlling the nucleation and growth of silver on palladium nanocubes by manipulating the reaction kinetics. *Angewandte Chemie-International Edition*, 51 (10), 2354–2358.

63 Jang, H. J., Hong, S., Park, S. (2012). Shape-controlled synthesis of Pt nanoframes. *Journal of Materials Chemistry*, 22 (37), 19792–19797.

64 Shahjamali, M. M., Bosman, M., Cao, S. W., Huang, X., Cao, X. H., Zhang, H., Pramana, S. S., Xue, C. (2013). Surfactant-free sub–2 nm ultrathin triangular gold nanoframes. *Small*, 9 (17), 2880–2886.

65 Xie, S. F., Lu, N., Xie, Z. X., Wang, J. G., Kim, M. J., Xia, Y. N. (2012). Synthesis of Pd-Rh core-frame concave nanocubes and their conversion to Rh cubic nanoframes by selective etching of the Pd cores. *Angewandte Chemie-International Edition*, 51 (41), 10266–10270.

66 Merriam-Webster.com, http://www.merriam-webster.com.

67 Hoffmann, C., Thieme, S., Bruckner, J., Oschatz, M., Biemelt, T., Mondin, G., Althues, H., Kaskel, S. (2014). Nanocasting hierarchical carbide-derived carbons in nanostructured opal assemblies for high-performance cathodes in lithium-sulfur batteries. *ACS Nano*, 8 (12), 12130–12140.

68 Ryoo, R., Joo, S. H., Jun, S. (1999). Synthesis of highly ordered carbon molecular sieves via template-mediated structural transformation. *Journal of Physical Chemistry B*, 103 (37), 7743–7746.

69 Lu, L. H., Eychmuller, A., Kobayashi, A., Hirano, Y., Yoshida, K., Kikkawa, Y., Tawa, K., Ozaki, Y. (2006). Designed fabrication of ordered porous Au/Ag nanostructured films for surface-enhanced raman scattering substrates. *Langmuir*, 22 (6), 2605–2609.

70 Shin, H. J., Ko, C. H., Ryoo, R. (2001). Synthesis of platinum networks with nanoscopic periodicity using mesoporous silica as template. *Journal of Materials Chemistry*, 11 (2), 260–261.

71 Lu, L., Eychmüller, A. (2008). Ordered macroporous bimetallic nanostructures: design, characterization, and applications. *Accounts of Chemical Research*, 41 (2), 244–253.

72 Jiang, P., Cizeron, J., Bertone, J. F., Colvin, V. L. (1999). Preparation of macroporous metal films from colloidal crystals. *Journal of the American Chemical Society*, 121 (34), 7957–7958.

73 Jiao, F., Jumas, J. C., Womes, M., Chadwick, A. V., Harrison, A., Bruce, P. G. (2006). Synthesis of ordered mesoporous Fe_3O_4 and γ-Fe_2O_3 with crystalline walls using post-template reduction/oxidation. *Journal of the American Chemical Society*, 128 (39), 12905–12909.

74 Lai, X. Y., Li, X. T., Geng, W. C., Tu, J. C., Li, J. X., Qiu, S. L. (2007). Ordered mesoporous copper oxide with crystalline walls. *Angewandte Chemie-International Edition*, 46 (5), 738–741.

75 Velev, O. D., Kaler, E. W. (2000). Structured porous materials via colloidal crystal templating: from inorganic oxides to metals. *Advanced Materials*, 12 (7), 531–534.

76 Wang, D. H., Zhou, W. L., McCaughy, B. F., Hampsey, J. E., Ji, X. L., Jiang, Y. B., Xu, H. F., Tang, J. K., Schmehl, R. H., O'Connor, C., Brinker, C. J., Lu, Y. F. (2003). Electrodeposition of metallic nanowire thin films using mesoporous silica templates. *Advanced Materials*, 15 (2), 130–133.

77 Jiang, J. H., Kucernak, A. (2009). Synthesis of highly active nanostructured ptru electrocatalyst with three-dimensional mesoporous silica template. *Electrochemistry Communications*, 11 (3), 623–626.

78 Karthika, P., Ataee-Esfahani, H., Wang, H. J., Francis, M. A., Abe, H., Rajalakshmi, N., Dhathathreyan, K. S., Arivuoli, D., Yamauchi, Y. (2013). Synthesis of mesoporous Pt-Ru alloy particles with uniform sizes by sophisticated hard-templating method. *Chemistry—An Asian Journal*, 8 (5), 902–907.

79 Ye, L., Wang, Y., Chen, X. Y., Yue, B., Tsang, S. C., He, H. Y. (2011). Three-dimensionally ordered mesoporous pd networks templated by a silica super crystal and their application in formic acid electrooxidation. *Chemical Communications*, 47 (26), 7389–7391.

80 Doi, Y., Takai, A., Sakamoto, Y., Terasaki, O., Yamauchi, Y., Kuroda, K. (2010). Tailored synthesis of mesoporous platinum replicas using double gyroid mesoporous silica (KIT–6) with different pore diameters via vapor infiltration of a reducing agent. *Chemical Communications*, 46 (34), 6365–6367.

81 Shin, H. J., Ryoo, R., Liu, Z., Terasaki, O. (2001). Template synthesis of asymmetrically mesostructured platinum networks. *Journal of the American Chemical Society*, 123 (6), 1246–1247.

82 Kibsgaard, J., Gorlin, Y., Chen, Z. B., Jaramillo, T. F. (2012). Meso-structured platinum thin films: active and stable electrocatalysts for the oxygen reduction reaction. *Journal of the American Chemical Society*, 134 (18), 7758–7765.

83 Chen, P. K., Lai, N. C., Ho, C. H., Hu, Y. W., Lee, J. F., Yang, C. M. (2013). New synthesis of MCM–48 nanospheres and facile replication to mesoporous platinum nanospheres as highly active electrocatalysts for the oxygen reduction reaction. *Chemistry of Materials*, 25 (21), 4269–4277.

84 Stein, A., Li, F., Denny, N. R. (2008). Morphological control in colloidal crystal templating of inverse opals, hierarchical structures, and shaped particles. *Chemistry of Materials*, 20 (3), 649–666.

85 Lu, L. H., Capek, R., Kornowski, A., Gaponik, N., Eychmuller, A. (2005). Selective fabrication of ordered bimetallic nanostructures with hierarchical porosity. *Angewandte Chemie-International Edition*, 44 (37), 5997–6001.

86 Wang, H. J., Jeong, H. Y., Imura, M., Wang, L., Radhakrishnan, L., Fujita, N., Castle, T., Terasaki, O., Yamauchi, Y. (2011). Shape- and size-controlled synthesis in hard templates: sophisticated chemical reduction for mesoporous monocrystalline platinum nanoparticles. *Journal of the American Chemical Society*, 133 (37), 14526–14529.

87 Qin, Y., Pan, A. L., Liu, L. F., Moutanabbir, O., Bin Yang, R., Knez, M. (2011). Atomic layer deposition assisted template approach for electrochemical synthesis of Au crescent-shaped half-nanotubes. *ACS Nano*, 5 (2), 788–794.

88 Wang, Q., Sun, X., Luo, S. J., Sun, L. N., Wu, X. L., Cao, M. H., Hu, C. W. (2007). Controllable synthesis of PbO nano/microstructures using a porous alumina template. *Crystal Growth & Design*, 7 (12), 2665–2669.

89 Sulka, G. D., Brzozka, A., Liu, L. F. (2011). Fabrication of diameter-modulated and ultrathin porous nanowires in anodic aluminum oxide templates. *Electrochimica Acta*, 56 (14), 4972–4979.

90 Gu, G. H., Suh, J. S. (2010). Hexagonally patterned silver nanoparticles electrodeposited on an aluminum surface-enhanced raman scattering. *Journal of Physical Chemistry C*, 114 (16), 7258–7262.

91 Cui, C. H., Li, H. H., Yu, S. H. (2011). Large scale restructuring of porous Pt-Ni nanoparticle tubes for methanol oxidation: a highly reactive, stable, and restorable fuel cell catalyst. *Chemical Science*, 2 (8), 1611–1614.

92 Du, C. Y., Chen, M., Wang, W. G., Yin, G. P. (2011). Nanoporous PdNi alloy nanowires as highly active catalysts for the electro-oxidation of formic acid. *ACS Applied Materials & Interfaces*, 3 (2), 105–109.

93 Sanz, B., Blaszczyk-Lezak, I., Mijangos, C., Palacios, J. K., Muller, A. J. (2016). New double-infiltration methodology to prepare PCL-PS core-shell nanocylinders inside anodic aluminum oxide templates. *Langmuir*, 32 (31), 7860–7865.

94 Lee, W., Park, S. J. (2014). Porous Anodic Aluminum Oxide: Anodization and Templated Synthesis of Functional Nanostructures. *Chemical Reviews*, 114 (15), 7487–7556.

95 Masuda, H., Fukuda, K. (1995). Ordered metal nanohole arrays made by a 2-step replication of honeycomb structures of anodic alumina. *Science*, 268 (5216), 1466–1468.

96 Masuda, H., Yada, K., Osaka, A. (1998). Self-ordering of cell configuration of anodic porous alumina with large-size pores in phosphoric acid solution. *Japanese Journal of Applied Physics*, 37 (11a), L1340–L1342.

97 Liu, L. F., Pippel, E., Scholz, R., Gosele, U. (2009). Nanoporous Pt-Co alloy nanowires: fabrication, characterization, and electrocatalytic properties. *Nano Letters*, 9 (12), 4352–4358.

98 Peterson, A. K., Morgan, D. G., Skrabalak, S. E. (2010). Aerosol synthesis of porous particles using simple salts as a pore template. *Langmuir*, 26 (11), 8804–8809.

99 Kinkead, B., van Drunen, J., Paul, M. T. Y., Dowling, K., Jerkiewicz, G., Gates, B. D. (2013). Platinum ordered porous electrodes: developing a platform for fundamental electrochemical characterization. *Electrocatalysis*, 4 (3), 179–186.

100 Liu, R., Qu, F. L., Guo, Y. L., Yao, N., Priestley, R. D. (2014). Au@Carbon yolk-shell nanostructures via one-step core-shell-shell template. *Chemical Communications*, 50 (4), 478–480.

101 Li, X. C., Zheng, W. J., Chen, B., Wang, L., He, G. H. (2016). Rapidly constructing multiple AuPt nanoalloy yolk@shell hollow particles in ordered mesoporous silica microspheres for highly efficient catalysis. *ACS Sustainable Chemistry & Engineering*, 4 (5), 2780–2788.

102 Yamauchi, Y., Kuroda, K. (2008). Rational design of mesoporous metals and related nanomaterials by a soft-template approach. *Chemistry—An Asian Journal*, 3 (4), 664–676.

103 Yamauchi, Y., Komatsu, M., Fuziwara, M., Nemoto, Y., Sato, K., Yokoshima, T., Sukegawa, H., Inomata, K., Kuroda, K. (2009). Ferromagnetic mesostructured alloys: design of ordered mesostructured alloys with multicomponent metals from lyotropic liquid crystals. *Angewandte Chemie-International Edition*, 48 (42), 7792–7797.

104 Takai, A., Yamauchi, Y., Kuroda, K. (2010). Tailored electrochemical synthesis of 2d-hexagonal, lamellar, and cage-type mesostructured Pt thin films with extralarge periodicity. *Journal of the American Chemical Society*, 132 (1), 208–214.

105 Yamauchi, Y., Sugiyama, A., Morimoto, R., Takai, A., Kuroda, K. (2008). Mesoporous platinum with giant mesocages templated from lyotropic liquid crystals consisting of diblock copolymers. *Angewandte Chemie-International Edition*, 47 (29), 5371–5373.

106 Luo, K., Walker, C. T., Edler, K. J. (2007). Mesoporous silver films from dilute mixed-surfactant solutions by using dip-coating. *Advanced Materials*, 19 (11), 1506–1509.

107 Attard, G. S., Bartlett, P. N., Coleman, N. R. B., Elliott, J. M., Owen, J. R., Wang, J. H. (1997). Mesoporous platinum films from lyotropic liquid crystalline phases. *Science*, 278 (5339), 838–840.

108 Attard, G. S., Goltner, C. G., Corker, J. M., Henke, S., Templer, R. H. (1997). Liquid-crystal templates for nanostructured metals. *Angewandte Chemie-International Edition*, 36 (12), 1315–1317.

109 Bartlett, P. N., Pletcher, D., Esterle, T. F., Low, C. T. J. (2013). The deposition of mesoporous ni/co alloy using cetyltrimethylammonium bromide as the surfactant in the lyotropic liquid crystalline phase bath. *Journal of Electroanalytical Chemistry*, 688 pp. 232–236.

110 Bender, F., Mankelow, R. K., Hibbert, D. B., Gooding, J. J. (2006). Lyotropic liquid crystal templating of groups 11 and 12 metal films. *Electroanalysis*, 18 (16), 1558–1563.

111 Yamauchi, Y., Momma, T., Fuziwara, M., Nair, S. S., Ohsuna, T., Terasaki, O., Osaka, T., Kuroda, K. (2005). Unique Microstructure of Mesoporous Pt (H_I-Pt) Prepared via direct physical casting in lyotropic liquid crystalline media. *Chemistry of Materials*, 17 (25), 6342–6348.

112 Yamauchi, Y., Tonegawa, A., Komatsu, M., Wang, H. J., Wang, L., Nemoto, Y., Suzuki, N., Kuroda, K. (2012). Electrochemical synthesis of mesoporous Pt-Au binary alloys with tunable compositions for enhancement of electrochemical performance. *Journal of the American Chemical Society*, 134 (11), 5100–5109.

113 Liang, Y. C., Juan, Y. W., Lu, K. T., Jeng, U. S., Chen, S. A., Chuang, W. T., Su, C. J., Liu, C. L., Pao, C. W., Lee, J. F., Sheu, H. S., Chen, J. M. (2012). Formation process of mesostructured PtRu nanoparticles electrodeposited on a microemulsion lyotropic liquid crystalline template as revealed by in situ XRD, SAXS, and XANES. *Journal of Physical Chemistry C*, 116 (50), 26649–26655.

114 Hsueh, H. Y., Chen, H. Y., Hung, Y. C., Ling, Y. C., Gwo, S., Ho, R. M. (2013). Well-defined multibranched gold with surface plasmon resonance in near-infrared region from seeding growth approach using gyroid block copolymer template. *Advanced Materials*, 25 (12), 1780–1786.

115 Vukovic, I., ten Brinke, G., Loos, K. (2013). Block Copolymer Template-Directed Synthesis of well-ordered metallic nanostructures. *Polymer*, 54 (11), 2591–2605.

116 Vukovic, I., Punzhin, S., Vukovic, Z., Onck, P., De Hosson, J. T. M., ten Brinke, G., Loos, K. (2011). Supramolecular route to well-ordered metal nanofoams. *ACS Nano*, 5 (8), 6339–6348.

117 Hsueh, H. Y., Chen, H. Y., She, M. S., Chen, C. K., Ho, R. M., Gwo, S., Hasegawa, H., Thomas, E. L. (2010). Inorganic gyroid with exceptionally low refractive index from block copolymer templating. *Nano Letters*, 10 (12), 4994–5000.

118 Hsueh, H. Y., Huang, Y. C., Ho, R. M., Lai, C. H., Makida, T., Hasegawa, H. (2011). Nanoporous gyroid nickel from block copolymer templates via electroless plating. *Advanced Materials*, 23 (27), 3041–3046.

119 Cowman, C. D., Padgett, E., Tan, K. W., Hovden, R., Gu, Y. B., Andrejevic, N., Muller, D., Coates, G. W., Wiesner, U. (2015). Multicomponent nanomaterials with complex networked architectures from orthogonal degradation and binary metal backfilling in ABC triblock terpolymers. *Journal of the American Chemical Society*, 137 (18), 6026–6033.

120 Li, C. L., Sato, T., Yamauchi, Y. (2013). Electrochemical synthesis of one-dimensional mesoporous Pt nanorods using the assembly of surfactant micelles in confined space. *Angewandte Chemie-International Edition*, 52 (31), 8050–8053.

121 Koh, H. D., Park, S., Russell, T. P. (2010). Fabrication of Pt/Au concentric spheres from triblock copolymer. *ACS Nano*, 4 (2), 1124–1130.

122 Jiang, B., Li, C. L., Imura, M., Tang, J., Yamauchi, Y. (2015). Multimetallic mesoporous spheres through surfactant-directed synthesis. *Advanced Science*, 2 (8), 1500112.

123 Wang, L., Nemoto, Y., Yamauchi, Y. (2011). Direct synthesis of spatially-controlled Pt-on-Pd bimetallic nanodendrites with superior electrocatalytic activity. *Journal of the American Chemical Society*, 133 (25), 9674–9677.

124 Ataee-Esfahani, H., Imura, M., Yamauchi, Y. (2013). All-metal mesoporous nanocolloids: solution-phase synthesis of core-shell Pd@Pt nanoparticles with a designed concave surface. *Angewandte Chemie-International Edition*, 52 (51), 13611–13615.

125 Wang, H. J., Ishihara, S., Ariga, K., Yamauchi, Y. (2012). All-metal layer-by-layer films: bimetallic alternate layers with accessible mesopores for enhanced electrocatalysis. *Journal of the American Chemical Society*, 134 (26), 10819–10821.

126 Li, C. L., Imura, M., Yamauchi, Y. (2014). Displacement plating of a mesoporous Pt skin onto Co nanochains in a low-concentration surfactant solution. *Chemistry-A European Journal*, 20 (12), 3277–3282.

127 Liu, J. H., Zhang, X. L., Zhang, J. D., Li, S. M., Yu, M. (2012). Synthesis and characterization of Ag-Ni nanorings based on plasmid DNA templates. *Materials Letters*, 67 (1), 277–279.

128 Zhang, X. J., Li, D. (2006). Metal-compound-induced vesicles as efficient directors for rapid synthesis of hollow alloy spheres. *Angewandte Chemie-International Edition*, 45 (36), 5971–5974.

129 Xu, Y., Yuan, Y. Q., Ma, A. J., Wu, X., Liu, Y., Zhang, B. (2012). Composition-tunable Pt-Co alloy nanoparticle networks: facile room-temperature synthesis and supportless electrocatalytic applications. *ChemPhysChem*, 13 (10), 2601–2609.

130 Thepkaew, J., Therdthianwong, S., Kucernak, A., Therdthianwong, A. (2012). Electrocatalytic activity of mesoporous binary/ternary PtSn-based catalysts for ethanol oxidation. *Journal of Electroanalytical Chemistry*, 685 pp. 41–46.

131 Wang, H. J., Wang, L., Sato, T., Sakamoto, Y., Tominaka, S., Miyasaka, K., Miyamoto, N., Nemoto, Y., Terasaki, O., Yamauchi, Y. (2012). Synthesis of mesoporous Pt films with tunable pore sizes from aqueous surfactant solutions. *Chemistry of Materials*, 24 (9), 1591–1598.

132 Jiang, J. H., Kucernak, A. (2004). Mesoporous microspheres composed of PtRu alloy. *Chemistry of Materials*, 16 (7), 1362–1367.

133 Ma, A. J., Xu, J., Zhang, X. H., Zhang, B., Wang, D. Y., Xu, H. L. (2014). Interfacial nanodroplets guided construction of hierarchical Au, Au-Pt, and Au-Pd particles as excellent catalysts. *Scientific Reports*, 4 pp. 4849.

134 Shin, H. C., Liu, M. L. (2005). Three-dimensional porous copper-tin alloy electrodes for rechargeable lithium batteries. *Advanced Functional Materials*, 15 (4), 582–586.

135 Shin, H. C., Liu, M. L. (2004). Copper foam structures with highly porous nanostructured walls. *Chemistry of Materials*, 16 (25), 5460–5464.

136 Shin, H. C., Dong, J., Liu, M. L. (2003). Nanoporous structures prepared by an electrochemical deposition process. *Advanced Materials*, 15 (19), 1610–1614.

137 Plowman, B. J., O'Mullane, A. P., Selvakannan, P. R., Bhargava, S. K. (2010). Honeycomb nanogold networks with highly active sites. *Chemical Communications*, 46 (48), 9182–9184.

138 Takai, A., Saida, T., Sugimoto, W., Wang, L., Yamauchi, Y., Kuroda, K. (2009). Preparation of mesoporous Pt-Ru alloy fibers with tunable compositions via evaporation-mediated direct templating (EDIT) method utilizing porous anodic alumina membranes. *Chemistry of Materials*, 21 (14), 3414–3423.

139 Kuroda, Y., Yamauchi, Y., Kuroda, K. (2010). Integrated structural control of cage-type mesoporous platinum possessing both tunable large mesopores and variable surface structures by block copolymer-assisted Pt deposition in a hard-template. *Chemical Communications*, 46 (11), 1827–1829.

140 Fu, S., Zhu, C., Song, J., Engelhard, M. H., Xia, H., Du, D., Lin, Y. (2016). Kinetically controlled synthesis of Pt-based one-dimensional hierarchically porous nanostructures with large mesopores as highly efficient orr catalysts. *ACS Applied Materials & Interfaces* 8 (51), 35213–35218.

141 Wang, D. H., Luo, H. M., Kou, R., Gil, M. P., Xiao, S. G., Golub, V. O., Yang, Z. Z., Brinker, C. J., Lu, Y. F. (2004). A general route to macroscopic hierarchical 3d nanowire networks. *Angewandte Chemie-International Edition*, 43 (45), 6169–6173.

142 Zhang, H., Wang, H., Xu, Y., Zhuo, S. F., Yu, Y. F., Zhang, B. (2012). Conversion of Sb_2Te_3 hexagonal nanoplates into three-dimensional porous single-crystal-like network-structured Te plates using oxygen and tartaric acid. *Angewandte Chemie-International Edition*, 51 (6), 1459–1463.

143 Li, Z. Q., Li, W. Y., Camargo, P. H. C., Xia, Y. N. (2008). Facile synthesis of branched an nanostructures by templating against a self-destructive lattice of magnetic Fe nanoparticles. *Angewandte Chemie-International Edition*, 47 (50), 9653–9656.

144 Zhang, G. X., Sun, S. H., Cai, M., Zhang, Y., Li, R. Y., Sun, X. L. (2013). Porous dendritic platinum nanotubes with extremely high activity and stability for oxygen reduction reaction. *Scientific Reports*, 3 pp. 1526.

145 Ding, L. X., Wang, A. L., Li, G. R., Liu, Z. Q., Zhao, W. X., Su, C. Y., Tong, Y. X. (2012). Porous Pt-Ni-P composite nanotube arrays: highly electroactive and durable catalysts for methanol electrooxidation. *Journal of the American Chemical Society*, 134 (13), 5730–5733.

146 Choi, B. S., Lee, Y. W., Kang, S. W., Hong, J. W., Kim, J., Park, I., Han, S. W. (2012). Multimetallic alloy nanotubes with nanoporous framework. *ACS Nano*, 6 (6), 5659–5667.

147 Hong, F., Sun, S. D., You, H. J., Yang, S. C., Fang, J. X., Guo, S. W., Yang, Z. M., Ding, B. J., Song, X. P. (2011). Cu_2O Template strategy for the synthesis of structure-definable noble metal alloy mesocages. *Crystal Growth & Design*, 11 (9), 3694–3697.

148 Xia, B. Y., Wu, H. B., Wang, X., Lou, X. W. (2013). Highly concave platinum nanoframes with high-index facets and enhanced electrocatalytic properties. *Angewandte Chemie-International Edition*, 52 (47), 12337–12340.

149 Ham, S., Jang, H. J., Song, Y., Shuford, K. L., Park, S. (2015). Octahedral and cubic gold nanoframes with platinum framework. *Angewandte Chemie-International Edition*, 54 (31), 9025–9028.

150 Li, J. M., Sun, X. J., Qin, D. (2016). Ag-enriched Ag-Pd bimetallic nanoframes and their catalytic properties. *ChemNanoMat*, 2 (6), 494–499.

151 McEachran, M., Keogh, D., Pietrobon, B., Cathcart, N., Gourevich, I., Coombs, N., Kitaev, V. (2011). Ultrathin gold nanoframes through surfactant-free templating of faceted pentagonal silver nanoparticles. *Journal of the American Chemical Society*, 133 (21), 8066–8069.

152 Liu, H., Qu, J. L., Chen, Y. F., Li, J. Q., Ye, F., Lee, J. Y., Yang, J. (2012). Hollow and cage-bell structured nanomaterials of noble metals. *Journal of the American Chemical Society*, 134 (28), 11602–11610.

153 Liu, H., Yang, J. (2014). Bimetallic Ag-hollow Pt heterodimers via inside-out migration of Ag in core-shell Ag-Pt nanoparticles at elevated temperature. *Journal of Materials Chemistry A*, 2 (19), 7075–7081.

154 Jang, H. J., Ham, S., Acapulco, J. A. I., Song, Y., Hong, S., Shuford, K. L., Park, S. (2014). Fabrication of 2d Au nanorings with Pt framework. *Journal of the American Chemical Society*, 136 (50), 17674–17680.

155 Lee, S., Jang, H. J., Jang, H. Y., Hong, S., Moh, S. H., Park, S. (2016). Synthesis and optical property characterization of elongated AuPt and Pt@Au metal nanoframes. *Nanoscale*, 8 (8), 4491–4494.

156 Pugh, D. V., Dursun, A., Corcoran, S. G. (2003). Formation of nanoporous platinum by selective dissolution of Cu from $Cu_{0.75}Pt_{0.25}$. *Journal of Materials Research*, 18 (1), 216–221.

157 Wang, D. S., Zhao, P., Li, Y. D. (2011). General preparation for Pt-based alloy nanoporous nanoparticles as potential nanocatalysts. *Scientific Reports*, 1 pp. 37.

158 Liu, K., Bai, Y. C., Zhang, L., Yang, Z. B., Fan, Q. K., Zheng, H. Q., Yin, Y. D., Gao, C. B. (2016). Porous Au-Ag nanospheres with high-density and highly accessible hotspots for SERS analysis. *Nano Letters*, 16 (6), 3675–3681.

159 Wu, Y. E., Wang, D. S., Niu, Z. Q., Chen, P. C., Zhou, G., Li, Y. D. (2012). A strategy for designing a concave Pt-Ni alloy through controllable chemical etching. *Angewandte Chemie-International Edition*, 51 (50), 12524–12528.

160 Zheng, Y. Q., Zeng, J., Ruditskiy, A., Liu, M. C., Xia, Y. N. (2014). Oxidative etching and its role in manipulating the nucleation and growth of noble-metal nanocrystals. *Chemistry of Materials*, 26 (1), 22–33.

161 Wang, F., Li, C. H., Sun, L. D., Xu, C. H., Wang, J. F., Yu, J. C., Yan, C. H. (2012). Porous single-crystalline palladium nanoparticles with high catalytic activities. *Angewandte Chemie-International Edition*, 51 (20), 4872–4876.

162 Wang, R. Y., Xu, C. X., Bi, X. X., Ding, Y. (2012). Nanoporous surface alloys as highly active and durable oxygen reduction reaction electrocatalysts. *Energy & Environmental Science*, 5 (1), 5281–5286.

163 Lyu, L. M., Huang, M. H. (2011). Investigation of relative stability of different facets of Ag_2O nanocrystals through face-selective etching. *Journal of Physical Chemistry C*, 115 (36), 17768–17773.

164 Chen, C., Kang, Y. J., Huo, Z. Y., Zhu, Z. W., Huang, W. Y., Xin, H. L. L., Snyder, J. D., Li, D. G., Herron, J. A., Mavrikakis, M., Chi, M. F., More, K. L., Li, Y. D., Markovic, N. M., Somorjai, G. A., Yang, P. D., Stamenkovic, V. R. (2014). Highly crystalline multimetallic nanoframes with three-dimensional electrocatalytic surfaces. *Science*, 343 (6177), 1339–1343.

165 Niu, Z. Q., Becknell, N., Yu, Y., Kim, D., Chen, C., Kornienko, N., Somorjai, G. A., Yang, P. D. (2016). Anisotropic phase segregation and migration of Pt in nanocrystals en route to nanoframe catalysts. *Nature Materials*, 15 (11), 1188–1194.

166 Wang, Y., Chen, Y. G., Nan, C. Y., Li, L. L., Wang, D. S., Peng, Q., Li, Y. D. (2015). Phase-transfer interface promoted corrosion from $PtNi_{10}$ nanoctahedra to Pt_4Ni nanoframes. *Nano Research*, 8 (1), 140–155.

167 Lang, L. M., Shi, Y., Wang, J., Wang, F. B., Xia, X. H. (2015). Hollow core-shell structured Ni-Sn@C nanoparticles: a novel electrocatalyst for the hydrogen evolution reaction. *ACS Applied Materials & Interfaces*, 7 (17), 9098–9102.

168 Wu, Y. E., Wang, D. S., Zhou, G., Yu, R., Chen, C., Li, Y. D. (2014). Sophisticated construction of Au islands on Pt-Ni: an ideal trimetallic nanoframe catalyst. *Journal of the American Chemical Society*, 136 (33), 11594–11597.

169 Li, Z., Yu, R., Huang, J. L., Shi, Y. S., Zhang, D. Y., Zhong, X. Y., Wang, D. S., Wu, Y. E., Li, Y. D. (2015). Platinum-nickel frame within metal-organic framework fabricated in situ for hydrogen enrichment and molecular sieving. *Nature Communications*, 6 pp. 8248.

170 Sui, Y. M., Fu, W. Y., Zeng, Y., Yang, H. B., Zhang, Y. Y., Chen, H., Li, Y. X., Li, M. H., Zou, G. T. (2010). Synthesis of Cu_2O nanoframes and nanocages by selective oxidative etching at room temperature. *Angewandte Chemie-International Edition*, 49 (25), 4282–4285.

171 Zhang, Q., Cobley, C. M., Zeng, J., Wen, L. P., Chen, J. Y., Xia, Y. N. (2010). Dissolving Ag from Au-Ag alloy nanoboxes with H_2O_2: a method for both tailoring the optical properties and measuring the H_2O_2 concentration. *Journal of Physical Chemistry C*, 114 (14), 6396–6400.

172 Shui, J. I., Chen, C., Li, J. C. M. (2011). Evolution of nanoporous Pt-Fe alloy nanowires by dealloying and their catalytic property for oxygen reduction reaction. *Advanced Functional Materials*, 21 (17), 3357–3362.

173 Ye, W., Kou, S. F., Guo, X., Xie, F., Sun, H. Y., Lu, H. T., Yang, J. (2015). Controlled synthesis of bimetallic Pd-Rh nanoframes and nanoboxes with high catalytic performances. *Nanoscale*, 7 (21), 9558–9562.

174 Wang, L., Yamauchi, Y. (2013). Metallic nanocages: synthesis of bimetallic Pt-Pd hollow nanoparticles with dendritic shells by selective chemical etching. *Journal of the American Chemical Society*, 135 (45), 16762–16765.

175 Li, Y., Wang, W. X., Xia, K. Y., Zhang, W. J., Jiang, Y. Y., Zeng, Y. W., Zhang, H., Jin, C. H., Zhang, Z., Yang, D. R. (2015). Ultrathin two-dimensional Pd-based nanorings as catalysts for hydrogenation with high activity and stability. *Small*, 11 (36), 4745–4752.

176 Guo, X., Ye, W., Sun, H. Y., Zhanga, Q., Yang, J. (2013). A dealloying process of core-shell Au@AuAg nanorods for porous nanorods with enhanced catalytic activity. *Nanoscale*, 5 (24), 12582–12588.

177 Huang, C. C., Hwu, J. R., Su, W. C., Shieh, D. B., Tzeng, Y., Yeh, C. S. (2006). Surfactant-assisted hollowing of Cu nanoparticles involving halide-induced corrosion-oxidation processes. *Chemistry-A European Journal*, 12 (14), 3805–3810.

178 Gong, M. X., Fu, G. T., Chen, Y., Tang, Y. W., Lu, T. H. (2014). Autocatalysis and selective oxidative etching induced synthesis of platinum-copper bimetallic alloy nanodendrites electrocatalysts. *ACS Applied Materials & Interfaces*, 6 (10), 7301–7308.

179 Soejima, T., Kimizuka, N. (2009). One-pot room-temperature synthesis of single-crystalline gold nanocorolla in water. *Journal of the American Chemical Society*, 131 (40), 14407–14412.

180 Gan, L., Heggen, M., O'Malley, R., Theobald, B., Strasser, P. (2013). Understanding and controlling nanoporosity formation for improving the stability of bimetallic fuel cell catalysts. *Nano Letters*, 13 (3), 1131–1138.

181 Snyder, J., McCue, I., Livi, K., Erlebacher, J. (2012). Structure/processing/properties relationships in nanoporous nanoparticles as applied to catalysis of the cathodic oxygen reduction reaction. *Journal of the American Chemical Society*, 134 (20), 8633–8645.

182 Sun, Y. G., Mayers, B. T., Xia, Y. N. (2002). Template-engaged replacement reaction: a one-step approach to the large-scale synthesis of metal nanostructures with hollow interiors. *Nano Letters*, 2 (5), 481–485.

183 Lu, X. M., Tuan, H. Y., Chen, J. Y., Li, Z. Y., Korgel, B. A., Xia, Y. N. (2007). Mechanistic studies on the galvanic replacement reaction between multiply twinned particles of Ag and $HAuCl_4$ in an organic medium. *Journal of the American Chemical Society*, 129 (6), 1733–1742.

184 Seo, D., Song, H. (2009). Asymmetric hollow nanorod formation through a partial galvanic replacement reaction. *Journal of the American Chemical Society*, 131 (51), 18210–18211.

185 Kim, M. H., Lu, X. M., Wiley, B., Lee, E. P., Xia, Y. N. (2008). Morphological evolution of single-crystal Ag nanospheres during the galvanic replacement reaction with $HAuCl_4$. *Journal of Physical Chemistry C*, 112 (21), 7872–7876.

186 Bansal, V., Jani, H., Du Plessis, J., Coloe, P. J., Bhargava, S. K. (2008). Galvanic replacement reaction on metal films: a one-step approach to create nanoporous surfaces for catalysis. *Advanced Materials*, 20 (4), 717–723.

187 Cobley, C. M., Xia, Y. N. (2010). Engineering the Properties of Metal Nanostructures Via Galvanic Replacement Reactions. *Materials Science and Engineering: R: Reports*, 70 (3–6), 44–62.

188 Goris, B., Polavarapu, L., Bals, S., Van Tendeloo, G., Liz-Marzan, L. M. (2014). Monitoring galvanic replacement through three-dimensional morphological and chemical mapping. *Nano Letters*, 14 (6), 3220–3226.

189 Londono-Calderon, A., Bahena, D., Yacaman, M. J. (2016). Controlled synthesis of Au@AgAu yolk-shell cuboctahedra with well-defined facets. *Langmuir*, 32 (30), 7572–7581.

190 Gong, X. Z., Yang, Y., Huang, S. M. (2010). A novel side-selective galvanic reaction and synthesis of hollow nanoparticles with an alloy core. *Journal of Physical Chemistry C*, 114 (42), 18073–18080.

191 Song, H. M., Anjum, D. H., Sougrat, R., Hedhili, M. N., Khashab, N. M. (2012). Hollow Au@Pd and Au@Pt core-shell nanoparticles as electrocatalysts for ethanol oxidation reactions. *Journal of Materials Chemistry*, 22 (48), 25003–25010.

192 Mohl, M., Dobo, D., Kukovecz, A., Konya, Z., Kordas, K., Wei, J. Q., Vajtai, R., Ajayan, P. M. (2011). Formation of CuPd and CuPt Bimetallic Nanotubes by Galvanic Replacement Reaction. *Journal of Physical Chemistry C*, 115 (19), 9403–9409.

193 Liang, H. P., Zhang, H. M., Hu, J. S., Guo, Y. G., Wan, L. J., Bai, C. L. (2004). Pt hollow nanospheres: facile synthesis and enhanced electrocatalysts. *Angewandte Chemie-International Edition*, 43 (12), 1540–1543.

194 Vasquez, Y., Sra, A. K., Schaak, R. E. (2005). One-pot synthesis of hollow superparamagnetic CoPt nanospheres. *Journal of the American Chemical Society*, 127 (36), 12504–12505.

195 Liu, R., Sen, A. (2012). Unified synthetic approach to silver nanostructures by galvanic displacement reaction on copper: from nanobelts to nanoshells. *Chemistry of Materials*, 24 (1), 48–54.

196 Lee, D. G., Kim, S. M., Jeong, H., Kim, J., Lee, I. S. (2014). Surface-specific deposition of catalytic metal nanocrystals on hollow carbon nanospheres via galvanic replacement reactions of carbon-encapsulated MnO nanoparticles. *ACS Nano*, 8 (5), 4510–4521.

197 Sutter, E., Jungjohann, K., Bliznakov, S., Courty, A., Maisonhaute, E., Tenney, S., Sutter, P. (2014). In situ liquid-cell electron microscopy of silver-palladium galvanic replacement reactions on silver nanoparticles. *Nature Communications*, 5 pp. 4946.

198 Zhang, W. Q., Yang, J. Z., Lu, X. M. (2012). Tailoring galvanic replacement reaction for the preparation of Pt/Ag bimetallic hollow nanostructures with controlled number of voids. *ACS Nano*, 6 (8), 7397–7405.

199 Yang, X., Roling, L. T., Vara, M., Elnabawy, A. O., Zhao, M., Hood, Z. D., Bao, S. X., Mavrikakis, M., Xia, Y. A. (2016). Synthesis and characterization of Pt-Ag alloy nanocages with enhanced activity and durability toward oxygen reduction. *Nano Letters*, 16 (10), 6644–6649.

200 Jiang, T. T., Song, J. L. Q., Zhang, W. T., Wang, H., Li, X. D., Xia, R. X., Zhu, L. X., Xu, X. L. (2015). Au-Ag@Au hollow nanostructure with enhanced chemical stability and improved photothermal transduction efficiency for cancer treatment. *ACS Applied Materials & Interfaces*, 7 (39), 21985–21994.

201 Au, L., Chen, Y. C., Zhou, F., Camargo, P. H. C., Lim, B., Li, Z. Y., Ginger, D. S., Xia, Y. N. (2008). Synthesis and optical properties of cubic gold nanoframes. *Nano Research*, 1 (6), 441–449.

202 Au, L., Lu, X. M., Xia, Y. N. (2008). A comparative study of galvanic replacement reactions involving Ag nanocubes and $AuCl_2$- or $AuCl_4$-. *Advanced Materials*, 20 (13), 2517–2522.

203 Zeng, J., Zhang, Q., Chen, J. Y., Xia, Y. N. (2010). A comparison study of the catalytic properties of Au-based nanocages, nanoboxes, and nanoparticles. *Nano Letters*, 10 (1), 30–35.

204 Metraux, G. S., Cao, Y. C., Jin, R. C., Mirkin, C. A. (2003). Triangular nanofrarnes made of gold and silver. *Nano Letters*, 3 (4), 519–522.

205 Zhang, J. T., Qiu, C. C., Ma, H. Y., Liu, X. Y. (2008). Facile fabrication and unexpected electrocatalytic activity of palladium thin films with hierarchical architectures. *Journal of Physical Chemistry C*, 112 (36), 13970–13975.

206 Chen, C., Loo, J., Deng, M., Kox, R., Huys, R., Bartic, C., Maes, G., Borghs, G. (2009). Hollow platinum nanoshell tube arrays: fabrication and characterization. *Journal of Physical Chemistry C*, 113 (14), 5472–5477.

207 Hong, J. W., Kang, S. W., Choi, B. S., Kim, D., Lee, S. B., Han, S. W. (2012). Controlled synthesis of Pd-Pt alloy hollow nanostructures with enhanced catalytic activities for oxygen reduction. *ACS Nano*, 6 (3), 2410–2419.

208 Guo, S. J., Dong, S. J., Wang, E. (2008). A general method for the rapid synthesis of hollow metallic or bimetallic nanoelectrocatalysts with urchinlike morphology. *Chemistry—A European Journal*, 14 (15), 4689–4695.

209 Sieb, N. R., Wu, N. C., Majidi, E., Kukreja, R., Branda, N. R., Gates, B. D. (2009). Hollow metal nanorods with tunable dimensions, porosity, and photonic properties. *ACS Nano*, 3 (6), 1365–1372.

210 Polavarapu, L., Zanaga, D., Altantzis, T., Rodal-Cedeira, S., Pastoriza-Santos, I., Pérez-Juste, J., Bals, S., Liz-Marzán, L. M. (2016). Galvanic replacement coupled to seeded growth as a route for shape-controlled synthesis of plasmonic nanorattles. *Journal of the American Chemical Society*, 138 (36), 11453–11456.

211 Hong, X., Wang, D. S., Cai, S. F., Rong, H. P., Li, Y. D. (2012). Single-crystalline octahedral Au-Ag nanoframes. *Journal of the American Chemical Society*, 134 (44), 18165–18168.

212 Hajfathalian, M., Gilroy, K. D., Golze, S. D., Yaghoubzade, A., Menumerov, E., Hughes, R. A., Neretina, S. (2016). A Wulff in a cage: the confinement of substrate-based structures in plasmonic nanoshells, nanocages, and nanoframes using galvanic replacement. *ACS Nano*, 10 (6), 6354–6362.

213 Yu, Y., Zhang, Q. B., Xie, J. P., Lee, J. Y. (2013). Engineering the architectural diversity of heterogeneous metallic nanocrystals. *Nature Communications*, 4 pp. 1454.

214 Xie, S. F., Jin, M. S., Tao, J., Wang, Y. C., Xie, Z. X., Zhu, Y. M., Xia, Y. N. (2012). Synthesis and characterization of Pd@M_xCu_{1-X} (M = Au, Pd, and Pt) nanocages with porous walls and a yolk-shell structure through galvanic replacement reactions. *Chemistry—A European Journal*, 18 (47), 14974–14980.

215 Chen, J. Y., McLellan, J. M., Siekkinen, A., Xiong, Y. J., Li, Z. Y., Xia, Y. N. (2006). Facile synthesis of gold-silver nanocages with controllable pores on the surface. *Journal of the American Chemical Society*, 128 (46), 14776–14777.

216 Dhavale, V. M., Kurungot, S. (2015). Cu-Pt nanocage with 3-D electrocatalytic surface as an efficient oxygen reduction electrocatalyst for a primary Zn-air battery. *ACS Catalysis*, 5 (3), 1445–1452.

217 Xia, B. Y., Wu, H. B., Wang, X., Lou, X. W. (2012). One-pot synthesis of cubic $PtCu_3$ nanocages with enhanced electrocatalytic activity for the methanol oxidation reaction. *Journal of the American Chemical Society*, 134 (34), 13934–13937.

218 Pei, J. J., Mao, J. J., Liang, X., Chen, C., Peng, Q., Wang, D. S., Li, Y. D. (2016). Ir-Cu nanoframes: one-pot synthesis and efficient electrocatalysts for oxygen evolution reaction. *Chemical Communications*, 52 (19), 3793–3796.

219 Zhang, Z. C., Yang, Y., Nosheen, F., Wang, P. P., Zhang, J. C., Zhuang, J., Wang, X. (2013). Fine tuning of the structure of Pt-Cu alloy nanocrystals by glycine-mediated sequential reduction kinetics. *Small*, 9 (18), 3063–3069.

220 Zhang, H., Jin, M. S., Liu, H. Y., Wang, J. G., Kim, M. J., Yang, D. R., Xie, Z. X., Liu, J. Y., Xia, Y. N. (2011). Facile synthesis of Pd-Pt alloy nanocages and their enhanced performance for preferential oxidation of Co in excess hydrogen. *ACS Nano*, 5 (10), 8212–8222.

221 Wang, J. X., Ma, C., Choi, Y. M., Su, D., Zhu, Y. M., Liu, P., Si, R., Vukmirovic, M. B., Zhang, Y., Adzic, R. R. (2011). Kirkendall effect and lattice contraction in nanocatalysts: a new strategy to enhance sustainable activity. *Journal of the American Chemical Society*, 133 (34), 13551–13557.

222 Smigelskas, A. D., Kirkendall, E. O. (1947). Zinc diffusion in alpha brass. *Transactions of the American Institute of Mining and Metallurgical Engineers*, 171 pp. 130–142.

223 Fan, H. J., Gosele, U., Zacharias, M. (2007). Formation of nanotubes and hollow nanoparticles based on kirkendall and diffusion processes: a review. *Small*, 3 (10), 1660–1671.

224 Yin, Y. D., Rioux, R. M., Erdonmez, C. K., Hughes, S., Somorjai, G. A., Alivisatos, A. P. (2004). Formation of hollow nanocrystals through the nanoscale Kirkendall effect. *Science*, 304 (5671), 711–714.

225 Wang, W. S., Dahl, M., Yin, Y. D. (2013). Hollow nanocrystals through the nanoscale Kirkendall effect. *Chemistry of Materials*, 25 (8), 1179–1189.

226 Yang, Y., Guder, F., Zacharias, M. (2010). Diffusion-induced void evolution in core-shell nanowires: elaborated view on the nanoscale Kirkendall effect. *Israel Journal of Chemistry*, 50 (4), 439–448.

227 Chen, X. Y., Zhang, Z. J., Qiu, Z. G., Shi, C. W., Li, X. L. (2007). Hydrothermal fabrication and characterization of polycrystalline linneite (Co_3S_4) nanotubes based on the Kirkendall effect. *Journal of Colloid and Interface Science*, 308 (1), 271–275.

228 Zhang, L. Z., Yu, J. C., Zheng, Z., Leung, C. W. (2005). Fabrication of hierarchical porous iron oxide films utilizing the Kirkendall effect. *Chemical Communications*, (21), 2683–2685.

229 Tian, L., Yang, X. F., Lu, P., Williams, I. D., Wang, C. H., Ou, S. Y., Liang, C. L., Wu, M. M. (2008). Hollow single-crystal spinel nanocubes: the case of zinc cobalt oxide grown by a unique Kirkendall effect. *Inorganic Chemistry*, 47 (13), 5522–5524.

230 Yin, Y. D., Erdonmez, C. K., Cabot, A., Hughes, S., Alivisatos, A. P. (2006). Colloidal synthesis of hollow cobalt sulfide nanocrystals. *Advanced Functional Materials*, 16 (11), 1389–1399.

231 Fan, H. J., Knez, M., Scholz, R., Nielsch, K., Pippel, E., Hesse, D., Zacharias, M., Gosele, U. (2006). Monocrystalline spinel nanotube fabrication based on the Kirkendall effect. *Nature Materials*, 5 (8), 627–631.

232 Liu, B., Zeng, H. C. (2004). Fabrication of ZnO "dandelions" via a modified Kirkendall process. *Journal of the American Chemical Society*, 126 (51), 16744–16746.

233 Radi, Z., Barna, P. B., Labar, J. (1996). Kirkendall voids and the formation of amorphous phase in the Al-Pt thin-film system prepared by high-temperature successive deposition. *Journal of Applied Physics*, 79 (8), 4096–4100.

234 Ye, L. N., Wu, C. Z., Guo, W., Xie, Y. (2006). MoS_2 Hierarchical hollow cubic cages assembled by bilayers: one-step synthesis and their electrochemical hydrogen storage properties. *Chemical Communications* (45), 4738–4740.

235 Zhang, G. Q., Wang, W., Yu, Q. X., Li, X. G. (2009). Facile one-pot synthesis of PbSe and $NiSe_2$ hollow spheres: Kirkendall-effect-induced growth and related properties. *Chemistry of Materials*, 21 (5), 969–974.

236 Liang, X., Wang, X., Zhuang, Y., Xu, B., Kuang, S. M., Li, Y. D. (2008). Formation of CeO_2-ZrO_2 solid solution nanocages with controllable structures via Kirkendall effect. *Journal of the American Chemical Society*, 130 (9), 2736–2737.

237 Chiang, R. K., Chiang, R. T. (2007). Formation of hollow Ni_2P nanoparticles based on the nanoscale Kirkendall effect. *Inorganic Chemistry*, 46 (2), 369–371.

238 Zhang, G. Q., Yu, Q. X., Yao, Z., Li, X. G. (2009). Large scale highly crystalline Bi_2Te_3 nanotubes through solution phase nanoscale Kirkendall effect fabrication. *Chemical Communications* (17), 2317–2319.

239 Railsback, J. G., Johnston-Peck, A. C., Wang, J. W., Tracy, J. B. (2010). Size-dependent nanoscale Kirkendall effect during the oxidation of nickel nanoparticles. *ACS Nano*, 4 (4), 1913–1920.

240 Gao, J. H., Liang, G. L., Zhang, B., Kuang, Y., Zhang, X. X., Xu, B. (2007). FePt@CoS_2 yolk-shell nanocrystals as a potent agent to kill HeLa cells. *Journal of the American Chemical Society*, 129 (5), 1428–1433.

241 Fan, H. J., Knez, M., Scholz, R., Hesse, D., Nielsch, K., Zacharias, M., Gosele, U. (2007). Influence of Surface Diffusion on the Formation of Hollow Nanostructures Induced by the Kirkendall Effect: The Basic Concept. *Nano Letters*, 7 (4), 993–997.

242 Han, L., Liu, H., Cui, P. L., Peng, Z. J., Zhang, S. J., Yang, J. (2014). Alloy Cu_3Pt nanoframes through the structure evolution in Cu-Pt nanoparticles with a core-shell construction. *Scientific Reports*, 4 pp. 6414.

243 Wang, Y. L., Cai, L., Xia, Y. N. (2005). Monodisperse spherical colloids of Pb and their use as chemical templates to produce hollow particles. *Advanced Materials*, 17 (4), 473–477.

244 Xie, W., Herrmann, C., Kompe, K., Haase, M., Schlucker, S. (2011). Synthesis of bifunctional Au/Pt/Au core/shell nanoraspberries for in situ SERS monitoring of platinum-catalyzed reactions. *Journal of the American Chemical Society*, 133 (48), 19302–19305.

245 Gonzalez, E., Arbiol, J., Puntes, V. F. (2011). Carving at the nanoscale: sequential galvanic exchange and Kirkendall growth at room temperature. *Science*, 334 (6061), 1377–1380.

246 Chou, N. H., Schaak, R. E. (2007). Shape-controlled conversion of β-Sn nanocrystals into intermetallic M-Sn (M = Fe, Co, Ni, Pd) nanocrystals. *Journal of the American Chemical Society*, 129 (23), 7339–7345.

247 Jana, S., Chang, J. W., Rioux, R. M. (2013). Synthesis and modeling of hollow intermetallic Ni-Zn nanoparticles formed by the Kirkendall effect. *Nano Letters*, 13 (8), 3618–3625.

248 Newman, R. C., Sieradzki, K. (1994). Metallic corrosion. *Science*, 263 (5154), 1708–1709.

249 Renner, F. U., Stierle, A., Dosch, H., Kolb, D. M., Lee, T. L., Zegenhagen, J. (2006). Initial corrosion observed on the atomic scale. *Nature*, 439 (7077), 707–710.

250 Pareek, A., Borodin, S., Bashir, A., Ankah, G. N., Keil, P., Eckstein, G. A., Rohwerder, M., Stratmann, M., Grunder, Y., Renner, F. U. (2011). Initiation and inhibition of dealloying of single crystalline Cu_3Au (111) Surfaces. *Journal of the American Chemical Society*, 133 (45), 18264–18271.

251 Moghimi, N., Abdellah, M., Thomas, J. P., Mohapatra, M., Leung, K. T. (2013). Bimetallic FeNi concave nanocubes and nanocages. *Journal of the American Chemical Society*, 135 (30), 10958–10961.

252 Wang, D. L., Yu, Y. C., Zhu, J., Liu, S. F., Muller, D. A., Abruna, H. D. (2015). Morphology and activity tuning of Cu_3Pt/C ordered intermetallic nanoparticles by selective electrochemical dealloying. *Nano Letters*, 15 (2), 1343–1348.

253 Koh, S., Strasser, P. (2007). Electrocatalysis on bimetallic surfaces: modifying catalytic reactivity for oxygen reduction by voltammetric surface dealloying. *Journal of the American Chemical Society*, 129 (42), 12624–12625.

254 Wang, D. L., Xin, H. L. L., Hovden, R., Wang, H. S., Yu, Y. C., Muller, D. A., DiSalvo, F. J., Abruna, H. D. (2013). Structurally ordered intermetallic platinum-cobalt core-shell

nanoparticles with enhanced activity and stability as oxygen reduction electrocatalysts. *Nature Materials*, 12 (1), 81–87.

255 Chen, S., Gasteiger, H. A., Hayakawa, K., Tada, T., Shao-Horn, Y. (2010). Platinum-alloy cathode catalyst degradation in proton exchange membrane fuel cells: nanometer-scale compositional and morphological changes. *Journal of the Electrochemical Society*, 157 (1), A82–A97.

256 Chen, L. Y., Guo, H., Fujita, T., Hirata, A., Zhang, W., Inoue, A., Chen, M. W. (2011). Nanoporous PdNi bimetallic catalyst with enhanced electrocatalytic performances for electro-oxidation and oxygen reduction reactions. *Advanced Functional Materials*, 21 (22), 4364–4370.

257 Vineesh, T. V., Mubarak, S., Hahm, M. G., Prabu, V., Alwarappan, S., Narayanan, T. N. (2016). Controllably alloyed, low density, free-standing Ni-Co and Ni-graphene sponges for electrocatalytic water splitting. *Scientific Reports*, 6 pp. 31202.

258 Oezaslan, M., Heggen, M., Strasser, P. (2012). Size-dependent morphology of dealloyed bimetallic catalysts: linking the nano to the macro scale. *Journal of the American Chemical Society*, 134 (1), 514–524.

259 Wang, D. L., Yu, Y. C., Xin, H. L. L., Hovden, R., Ercius, P., Mundy, J. A., Chen, H., Richard, J. H., Muller, D. A., DiSalvo, F. J., Abruna, H. D. (2012). Tuning oxygen reduction reaction activity via controllable dealloying: a model study of ordered Cu_3Pt/C intermetallic nanocatalysts. *Nano Letters*, 12 (10), 5230–5238.

260 Zhou, Y. F., Yan, D. Y. (2009). Supramolecular self-assembly of amphiphilic hyperbranched polymers at all scales and dimensions: progress, characteristics and perspectives. *Chemical Communications* (10), 1172–1188.

261 Vogel, N., Retsch, M., Fustin, C.-A., del Campo, A., Jonas, U. (2015). Advances in colloidal assembly: the design of structure and hierarchy in two and three dimensions. *Chemical Reviews*, 115 (13), 6265–6311.

262 Papadas, I. T., Vamvasakis, I., Tamiolakis, I., Armatas, G. S. (2016). Templated self-assembly of colloidal nanocrystals into three-dimensional mesoscopic structures: a perspective on synthesis and catalytic prospects. *Chemistry of Materials*, 28 (9), 2886–2896.

263 Liu, K., Zhao, N. N., Kumacheva, E. (2011). Self-assembly of inorganic nanorods. *Chemical Society Reviews*, 40 (2), 656–671.

264 Liu, J. W., Liang, H. W., Yu, S. H. (2012). Macroscopic-scale assembled nanowire thin films and their functionalities. *Chemical Reviews*, 112 (8), 4770–4799.

265 Boles, M. A., Engel, M., Talapin, D. V. (2016). Self-assembly of colloidal nanocrystals: from intricate structures to functional materials. *Chemical Reviews*, 116 (18), 11220–11289.

266 Hu, L., Zhang, R. R., Chen, Q. W. (2014). Synthesis and assembly of nanomaterials under magnetic fields. *Nanoscale*, 6 (23), 14064–14105.

267 Abecassis, B. (2016). Three-dimensional self assembly of semiconducting colloidal nanocrystals: from fundamental forces to collective optical properties. *ChemPhysChem*, 17 (5), 618–631.

268 Lunn, D. J., Finnegan, J. R., Manners, I. (2015). Self-assembly of "patchy" nanoparticles: a versatile approach to functional hierarchical materials. *Chemical Science*, 6 (7), 3663–3673.

269 Grzybowski, B. A., Wilmer, C. E., Kim, J., Browne, K. P., Bishop, K. J. M. (2009). Self-assembly: from crystals to cells. *Soft Matter*, 5 (6), 1110–1128.

270 De Volder, M., Hart, A. J. (2013). Engineering hierarchical nanostructures by elastocapillary self-assembly. *Angewandte Chemie-International Edition*, 52 (9), 2412–2425.

271 Zhang, S. Y., Regulacio, M. D., Han, M. Y. (2014). Self-assembly of colloidal one-dimensional nanocrystals. *Chemical Society Reviews*, 43 (7), 2301–2323.

272 Grzelczak, M., Vermant, J., Furst, E. M., Liz-Marzan, L. M. (2010). Directed self-assembly of nanoparticles. *ACS Nano*, 4 (7), 3591–3605.

273 Whitesides, G. M., Grzybowski, B. (2002). Self-assembly at all scales. *Science*, 295 (5564), 2418–2421.

274 Bigall, N. C., Herrmann, A. K., Vogel, M., Rose, M., Simon, P., Carrillo-Cabrera, W., Dorfs, D., Kaskel, S., Gaponik, N., Eychmuller, A. (2009). Hydrogels and aerogels from noble metal nanoparticles. *Angewandte Chemie-International Edition*, 48 (51), 9731–9734.

275 Liu, W., Herrmann, A. K., Bigall, N. C., Rodriguez, P., Wen, D., Oezaslan, M., Schmidt, T. J., Gaponik, N., Eychmüller, A. (2015). Noble metal aerogels-synthesis, characterization, and application as electrocatalysts. *Accounts of Chemical Research*, 48 (2), 154–162.

276 Liu, W., Herrmann, A. K., Geiger, D., Borchardt, L., Simon, F., Kaskel, S., Gaponik, N., Eychmüller, A. (2012). High-performance electrocatalysis on palladium aerogels. *Angewandte Chemie-International Edition*, 51 (23), 5743–5747.

277 Wen, D., Liu, W., Haubold, D., Zhu, C., Oschatz, M., Holzschuh, M., Wolf, A., Simon, F., Kaskel, S., Eychmuller, A. (2016). Gold aerogels: three-dimensional assembly of nanoparticles and their use as electrocatalytic interfaces. *ACS Nano*, 10 (2), 2559–2567.

278 Gao, X. N., Esteves, R. J., Luong, T. T. H., Jaini, R., Arachchige, I. U. (2014). Oxidation-induced self-assembly of Ag nanoshells into transparent and opaque Ag hydrogels and aerogels. *Journal of the American Chemical Society*, 136 (22), 7993–8002.

279 Liu, W., Rodriguez, P., Borchardt, L., Foelske, A., Yuan, J. P., Herrmann, A. K., Geiger, D., Zheng, Z. K., Kaskel, S., Gaponik, N., Kotz, R., Schmidt, T. J., Eychmuller, A. (2013). Bimetallic aerogels: high-performance electrocatalysts for the oxygen reduction reaction. *Angewandte Chemie-International Edition*, 52 (37), 9849–9852.

280 Zhu, C. Z., Shi, Q. R., Fu, S. F., Song, J. H., Xia, H. B., Du, D., Lin, Y. H. (2016). Efficient synthesis of MCu (M = Pd, Pt, and Au) aerogels with accelerated gelation kinetics and their high electrocatalytic activity. *Advanced Materials*, 28 (39), 8779–8783.

281 Cai, B., Wen, D., Liu, W., Herrmann, A. K., Benad, A., Eychmuller, A. (2015). Function-led design of aerogels: self-assembly of alloyed PdNi hollow nanospheres for efficient electrocatalysis. *Angewandte Chemie-International Edition*, 54 (44), 13101–13105.

282 Shi, Q. R., Zhu, C. Z., Li, Y. J., Xia, H. B., Engelhard, M. H., Fu, S. F., Du, D., Lin, Y. H. (2016). A facile method for synthesizing dendritic core-shell structured ternary metallic aerogels and their enhanced electrochemical performances. *Chemistry of Materials*, 28 (21), 7928–7934.

283 Armor, J. N., Carlson, E. J., Carrasquillo, G. (1986). Metallic aerogels: a novel synthesis of very fine copper powder. *Materials Letters*, 4 (8–9), 373–376.

284 Xu, W. W., Du, A., Xiong, J., Zhang, Z. H., Shen, J., Zhou, B. (2016). Freestanding titanium metallic aerogel. *Materials & Design*, 97 pp. 93–97.

285 Freytag, A., Sanchez-Paradinas, S., Naskar, S., Wendt, N., Colombo, M., Pugliese, G., Poppe, J., Demirci, C., Kretschmer, I., Bahnemann, D. W., Behrens, P., Bigall, N. C. (2016). Versatile aerogel fabrication by freezing and subsequent freeze-drying of colloidal nanoparticle solutions. *Angewandte Chemie-International Edition*, 55 (3), 1200–1203.

286 Ji, Y. J., Wu, Y. E., Zhao, G. F., Wang, D. S., Liu, L., He, W., Li, Y. D. (2015). Porous bimetallic Pt-Fe nanocatalysts for highly efficient hydrogenation of acetone. *Nano Research*, 8 (8), 2706–2713.

287 Arachchige, I. U., Brock, S. L. (2007). Sol-gel methods for the assembly of metal chalcogenide quantum dots. *Accounts of Chemical Research*, 40 (9), 801–809.

288 Arachchige, I. U., Brock, S. L. (2006). Sol-gel assembly of CdSe nanoparticles to form porous aerogel networks. *Journal of the American Chemical Society*, 128 (24), 7964–7971.

289 Arachchige, I. U., Mohanan, J. L., Brock, S. L. (2005). Sol-gel processing of semiconducting metal chalcogenide xerogels: influence of dimensionality on quantum confinement effects in a nanoparticle network. *Chemistry of Materials*, 17 (26), 6644–6650.

290 Mohanan, J. L., Arachchige, I. U., Brock, S. L. (2005). Porous semiconductor chalcogenide aerogels. *Science*, 307 (5708), 397–400.

291 Herrmann, A. K., Formanek, P., Borchardt, L., Klose, M., Giebeler, L., Eckert, J., Kaskel, S., Gaponik, N., Eychmüller, A. (2014). Multimetallic aerogels by template-free self-assembly of Au, Ag, Pt, and Pd nanoparticles. *Chemistry of Materials*, 26 (2), 1074–1083.

292 Ranmohotti, K. G. S., Gao, X. N., Arachchige, I. U. (2013). Salt-mediated self-assembly of metal nanoshells into monolithic aerogel frameworks. *Chemistry of Materials*, 25 (17), 3528–3534.

293 Gao, X. N., Esteves, R. J. A., Nahar, L., Nowaczyk, J., Arachchige, I. U. (2016). Direct cross-linking of Au/Ag alloy nanoparticles into monolithic aerogels for application in surface-enhanced raman scattering. *ACS Applied Materials & Interfaces*, 8 (20), 13076–13085.

294 Cui, C. H., Gan, L., Heggen, M., Rudi, S., Strasser, P. (2013). Compositional segregation in shaped Pt alloy nanoparticles and their structural behaviour during electrocatalysis. *Nature Materials*, 12 (8), 765–771.

295 Gauthier, Y., Joly, Y., Baudoing, R., Rundgren, J. (1985). Surface-sandwich segregation on nondilute bimetallic alloys: $Pt_{50}Ni_{50}$ and $Pt_{78}Ni_{22}$ probed by low-energy electron diffraction. *Physical Review B*, 31 (10), 6216–6218.

296 Gan, L., Cui, C. H., Heggen, M., Dionigi, F., Rudi, S., Strasser, P. (2014). Element-specific anisotropic growth of shaped platinum alloy nanocrystals. *Science*, 346 (6216), 1502–1506.

297 Becknell, N., Zheng, C. D., Chen, C., Yang, P. D. (2016). Synthesis of $PtCo_3$ Polyhedral nanoparticles and evolution to Pt_3Co nanoframes. *Surface Science*, 648 pp. 328–332.

298 Wang, G. F., Van Hove, M. A., Ross, P. N., Baskes, M. I. (2005). Quantitative prediction of surface segregation in bimetallic Pt-M alloy nanoparticles (M = Ni, Re, Mo). *Progress in Surface Science*, 79 (1), 28–45.

299 Ahmadi, M., Behafarid, F., Cui, C. H., Strasser, P., Cuenya, B. R. (2013). Long-range segregation phenomena in shape-selected bimetallic nanoparticles: chemical state effects. *ACS Nano*, 7 (10), 9195–9204.

300 Arán-Ais, R. M., Dionigi, F., Merzdorf, T., Gocyla, M., Heggen, M., Dunin-Borkowski, R. E., Gliech, M., Solla-Gullón, J., Herrero, E., Feliu, J. M., Strasser, P. (2015). Elemental anisotropic growth and atomic-scale structure of shape-controlled octahedral Pt-Ni-Co alloy nanocatalysts. *Nano Letters*, 15 (11), 7473–7480.

301 Tao, F., Grass, M. E., Zhang, Y. W., Butcher, D. R., Renzas, J. R., Liu, Z., Chung, J. Y., Mun, B. S., Salmeron, M., Somorjai, G. A. (2008). Reaction-driven restructuring of Rh-Pd and Pt-Pd core-shell nanoparticles. *Science*, 322 (5903), 932–934.

302 Wang, L. L., Johnson, D. D. (2009). Predicted trends of core-shell preferences for 132 late transition-metal binary-alloy nanoparticles. *Journal of the American Chemical Society*, 131 (39), 14023–14029.

303 Ruban, A. V., Skriver, H. L., Norskov, J. K. (1999). Surface segregation energies in transition-metal alloys. *Physical Review B*, 59 (24), 15990–16000.

304 Zhang, Z. C., Luo, Z. M., Chen, B., Wei, C., Zhao, L., Chen, J. Z., Zhang, X., Lai, Z. C., Fan, Z. X., Tan, C. L., Zhao, M. T., Lu, Q. P., Li, B., Zong, Y., Yan, C. C., Wang, G. X., Xu, Z. J. C., Zhang, H. (2016). One-pot synthesis of highly anisotropic five-fold-twinned PtCu nanoframes used as a bifunctional electrocatalyst for oxygen reduction and methanol oxidation. *Advanced Materials*, 28 (39), 8712–8717.

305 Kim, H. Y., Cho, S., Sa, Y. J., Hwang, S. M., Park, G. G., Shin, T. J., Jeong, H. Y., Yim, S. D., Joo, S. H. (2016). Self-supported mesostructured Pt-based bimetallic nanospheres containing an intermetallic phase as ultrastable oxygen reduction electrocatalysts. *Small*, 12 (38), 5347–5353.

306 Hu, G. Z., Nitze, F., Gracia-Espino, E., Ma, J. Y., Barzegar, H. R., Sharifi, T., Jia, X. E., Shchukarev, A., Lu, L., Ma, C. S., Yang, G., Wagberg, T. (2014). Small palladium islands embedded in palladium-tungsten bimetallic nanoparticles form catalytic hotspots for oxygen reduction. *Nature Communications*, 5 pp. 5253.

307 Ding, J. B., Bu, L. Z., Guo, S. J., Zhao, Z. P., Zhu, E. B., Huang, Y., Huang, X. Q. (2016). Morphology and phase controlled construction of Pt-Ni nanostructures for efficient electrocatalysis. *Nano Letters*, 16 (4), 2762–2767.

308 Sneed, B. T., Brodsky, C. N., Kuo, C. H., Lamontagne, L. K., Jiang, Y., Wang, Y., Tao, F., Huang, W. X., Tsung, C. K. (2013). Nanoscale-phase-separated Pd-Rh boxes synthesized via metal migration: an archetype for studying lattice strain and composition effects in electrocatalysis. *Journal of the American Chemical Society*, 135 (39), 14691–14700.

309 Oh, A., Baik, H., Choi, D. S., Cheon, J. Y., Kim, B., Kim, H., Kwon, S. J., Joo, S. H., Jung, Y., Lee, K. (2015). Skeletal octahedral nanoframe with cartesian coordinates via geometrically precise nanoscale phase segregation in a Pt@Ni core-shell nanocrystal. *ACS Nano*, 9 (3), 2856–2867.

310 Herrero, E., Buller, L. J., Abruna, H. D. (2001). Underpotential deposition at single crystal surfaces of Au, Pt, Ag and other materials. *Chemical Reviews*, 101 (7), 1897–1930.

311 Jackson, S. R., McBride, J. R., Rosenthal, S. J., Wright, D. W. (2014). Where's the silver? imaging trace silver coverage on the surface of gold nanorods. *Journal of the American Chemical Society*, 136 (14), 5261–5263.

312 Niu, W. X., Zhang, W. Q., Firdoz, S., Lu, X. M. (2014). Controlled synthesis of palladium concave nanocubes with sub–10-nanometer edges and corners for tunable plasmonic property. *Chemistry of Materials*, 26 (6), 2180–2186.

313 Personick, M. L., Langille, M. R., Zhang, J., Mirkin, C. A. (2011). Shape control of gold nanoparticles by silver underpotential deposition. *Nano Letters*, 11 (8), 3394–3398.
314 Zhang, L., Zhang, J. W., Kuang, Q., Xie, S. F., Jiang, Z. Y., Xie, Z. X., Zheng, L. S. (2011). Cu2 + -assisted synthesis of hexoctahedral Au-Pd alloy nanocrystals with high-index facets. *Journal of the American Chemical Society*, 133 (43), 17114–17117.
315 Chen, S., Su, H. Y., Wang, Y. C., Wu, W. L., Zeng, J. (2015). Size-controlled synthesis of platinum-copper hierarchical trigonal bipyramid nanoframes. *Angewandte Chemie-International Edition*, 54 (1), 108–113.
316 Ge, J., He, D., Bai, L., You, R., Lu, H., Lin, Y., Tan, C., Kang, Y., Xiao, B., Wu, Y., Deng, Z., Huang, W., Zhang, H., Hong, X., Li, Y. (2015). Ordered porous Pd octahedra covered with monolayer Ru atoms. *Journal of the American Chemical Society*, 137 (46), 14566–14569.
317 Liu, B., Zeng, H. C. (2005). Symmetric and asymmetric ostwald ripening in the fabrication of homogeneous core-shell semiconductors. *Small*, 1 (5), 566–571.
318 Wang, F. D., Richards, V. N., Shields, S. P., Buhro, W. E. (2014). Kinetics and mechanisms of aggregative nanocrystal growth. *Chemistry of Materials*, 26 (1), 5–21.
319 Voorhees, P. W. (1985). The theory of Ostwald ripening. *Journal of Statistical Physics*, 38 (1–2), 231–252.
320 Liu, J., Wen, Y. R., van Aken, P. A., Maier, J., Yu, Y. (2014). Facile synthesis of highly porous Ni-Sn intermetallic microcages with excellent electrochemical performance for lithium and sodium storage. *Nano Letters*, 14 (11), 6387–6392.
321 Liu, J., Zheng, Y., Hong, Z., Cai, K., Zhao, F., Han, H. (2016). Microbial synthesis of highly dispersed PdAu alloy for enhanced electrocatalysis. *Science Advances*, 2 pp. e1600858.
322 Dai, L., Zhao, Y. X., Chi, Q., Huang, T., Liu, H. F. (2014). Controlled synthesis of Pd-Pt alloy nanohypercubes under microwave irradiation. *CrystEngComm*, 16 (24), 5206–5211.
323 Xia, Y. N., Xiong, Y. J., Lim, B., Skrabalak, S. E. (2009). Shape-controlled synthesis of metal nanocrystals: simple chemistry meets complex physics? *Angewandte Chemie-International Edition*, 48 (1), 60–103.
324 Hansen, T. W., Delariva, A. T., Challa, S. R., Datye, A. K. (2013). Sintering of catalytic nanoparticles: particle migration or ostwald ripening? *Accounts of Chemical Research*, 46 (8), 1720–1730.

7

Bimetallic Dendritic Nanostructures

Kun Yuan and Ya-Wen Zhang

College of Chemistry and Molecular Engineering, Peking University, Beijing, China

7.1 Introduction

Metal materials have been widely used by humankind in agriculture, construction and war since the Bronze Age. Nowadays, metal nanocrystals have drawn great interests of researchers in applications like catalysis, photonics, electronics and biology due to their versatile physical and chemical properties[1–12]. These properties can be easily tuned by modulating the size, shape, and composition of the metal nanomaterials via different kinds of synthesis methods. It is well known that the surface area of an inorganic nanoparticle depends on its size while the surface structure is up to its shape[13–15]. However, for a metal nanoparticle one can implement more changes on shape than on size in many cases by various synthetic approaches. Up to now, researchers have synthesized a vast variety of metal nanostructures including zero-dimensional nanostructures like nanocubes and nanooctahedras, one-dimensional nanowires and nanotubes, two-dimensional nanoplates and nanosheets and three-dimensional nanodendrites[3–5, 7–10, 12]. Metal nanomaterials with different morphologies usually have distinguishable properties and promising applications because of their diverse surface structures and chemical states.

In recent years, the dendritic nanostructures have been intensively investigated both on fundamental researches and applications owing to their unique structures and material properties[16–20]. Such a dendritic nanostructure decorated with many branches usually has a relatively large surface area, and promises a vast amount of surface atoms, especially the high percentage of edge, corner, and stepped atoms that benefit many catalytic reactions. So far, the dendritic nanostructures of Au, Ag, Cu, Zn have been obtained via some preparation methods such as electronic and electroless deposition, galvanic replacement reaction and aqueous phase reduction[19–22]. These nanodendrites of Au, Ag, and Cu have a great potential on optical applications like surface-enhanced Raman spectroscopy (SERS) and sensing[19, 23, 24]. For example, the Cu nanodendrites synthesized by Kang et al. via an electrochemical method exhibited a good performance on electroreduction of H_2O_2 and NO_3^- detection[18]

Compared with the monometallic nanodendrites, bimetallic dendritic nanostructures can be readily modified in compositions except for the size and shape since they

Bimetallic Nanostructures: Shape-Controlled Synthesis for Catalysis, Plasmonics, and Sensing Applications, First Edition. Edited by Ya-Wen Zhang.
© 2018 John Wiley & Sons Ltd. Published 2018 by John Wiley & Sons Ltd.

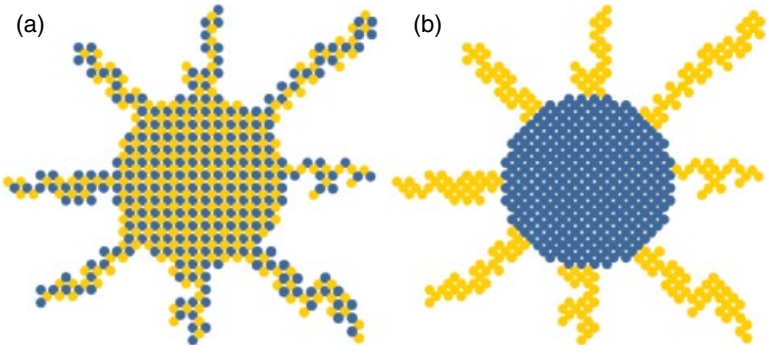

Figure 7.1 Two kinds of bimetallic dendritic nanostructures: (a) alloyed; (b) heterostructure.

consist of two different metals[25–30]. Therefore, they have synergetic effects on material properties arising from both geometric effects and electronic effects that the monometallic ones do not have. However, the synthesis of the bimetallic nanodendrites is more challenging due to the distinct properties of the two metals. As shown in Figure 7.1a and b, there are two kinds of bimetallic nanodendrites, which are different in structure—that is, alloyed and heterostructured ones. The bimetallic nanodendrites obtained by coreduction often have an alloyed structure, while the ones obtained by seed-mediated growth are usually heterostructures[25, 27, 30, 31]. In addition, the galvanic replacement reaction is widely used to synthesize bimetallic nanodendrites and can produce both alloy structure and heterostructure[28, 32]. The alloyed ones have relatively uniform distributions of two metals in the whole structure. In contrast, the heterostructures are core–shell-like A-on-B structures with metal B acting as a core and metal A acting as branches. Both of the two structures have been exploited for applications like catalysis. For instance, alloyed Pt–Ag tubular dendritic nano-forests (tDNFs) obtained by Tseng et al. via galvanic replacement reaction performed an enhanced activity in light-enhanced methanol oxidation reaction (MOR)[28]. Xia et al. obtained Pt-on-Pd heterogeneous nanodendrites by seed-mediated growth, which showed a much higher activity than pure Pt aggregates toward the oxidation of formic acid[31].

In this chapter, we will first introduce several general strategies on the synthesis of bimetallic dendritic nanostructures including coreduction, galvanic replacement reaction, seed-mediated growth, and other methods. Then we will discuss their useful properties and applications on optics and catalysis.

7.2 Synthesis of Bimetallic Dendritic Nanostructures

So far, researchers have developed plenty of liquid-phase methods for synthesizing various bimetallic nanostructures with tunable dimensionality. By regulating the experiment parameters such as metal precursors, coordination ligands, capping agents, and reaction temperature, the bimetallic nanocrystals with different sizes and shapes can be obtained. However, it seems somewhat difficult to synthesize dendritic metal nanocrystals due to their high anisotropy in crystal structures. In general, three routes have been

developed for synthesizing the bimetallic nanodendrites: (1) anisotropic overgrowth caused by defects such as twins and dislocations on the crystal seeds; (2) aggregation-based growth through well-known oriented attachment mechanism; and (3) branched growth induced by the direction of capping ligands. Under the driving force from the minimization of total Gibbs free energy, these routes are attained by modulating the growth rates and defect sites of different crystal faces with amendable surface free energies during the growth of dendritic nanostructures.

In this section, we are going to summarize several common methods to synthesize the bimetallic dendritic nanostructures containing coreduction, galvanic replacement reaction and seed-mediated growth. In addition, we will discuss the growth mechanism and key factors involved in preparing the bimetallic nanodendrites in every method, assisted by illustrating some typical synthetic examples.

7.2.1 Coreduction

It is a common and simple strategy to synthesize bimetallic nanostructures by the coreduction of two metal precursors in solutions[33–36]. The final morphology of the product can be adjusted by tuning appropriate experiment conditions, such as metal precursor, reaction temperature, and reductant and capping agent[33, 35, 37, 38]. Thus, coreduction is conveniently applied to synthesize the metallic dendritic nanostructures by many researchers[25, 30, 39, 40].

The synthesis principles of the coreduction method can be simply divided into two categories: aggregation-based growth and ligand-directed branching. In the former one, two metal precursors are reduced simultaneously into small alloyed nanoparticles in solution, by choosing appropriate metal precursors and reductants. Under the high concentration of the small nanoparticles, the adjacent particles aggregate to reduce the total surface energy through the oriented attachment, since the small particles have a high surface energy as well as high mobility. Further, twin defects and/or dislocations are easily formed during the attachment of these small nanoparticles, which are beneficial to the produce the dendritic nanostructures. As for the ligand-directed branching approach, a specific capping ligand is introduced to selectively bind to the specific facets of the nanoparticles and thus reduces the growth rate of the selected facets. In addition, the capping ligands coordinated with the nanoparticles may serve as a confined framework that may facilitate and even guide the formation of the nanodendrites. Therefore, the bimetallic dendritic nanostructures can be synthesized with the assistance of appropriate capping ligands.

However, a difficulty in controlling the processes of nucleation and growth of bimetallic nanodendrites should be eased before carrying out the synthesis. This difficulty is mainly caused by the difference of the reduction potentials between the two metal ions in solutions. Thus, a key factor that must be precisely manipulated is keeping the close reduction rates of the two metal precursors so as to avoid discrete nucleation and growth of two different metals during the synthesis of nanodendrites. Some groups have solved this problem via different strategies, such as selecting a suitable reductant, surfactant, or coordination ligand[25, 30, 40]. For instance, Zhao et al. have reported a facile coreduction method for synthesizing Pt–Cu bimetallic nanocrystals with a dendritic structure[30]. In this one-step process, the metal precursors (K_2PtCl_4 and $CuCl_2$) were reduced by formic acid, with Pluronic F127 serving as a stabilizing agent.

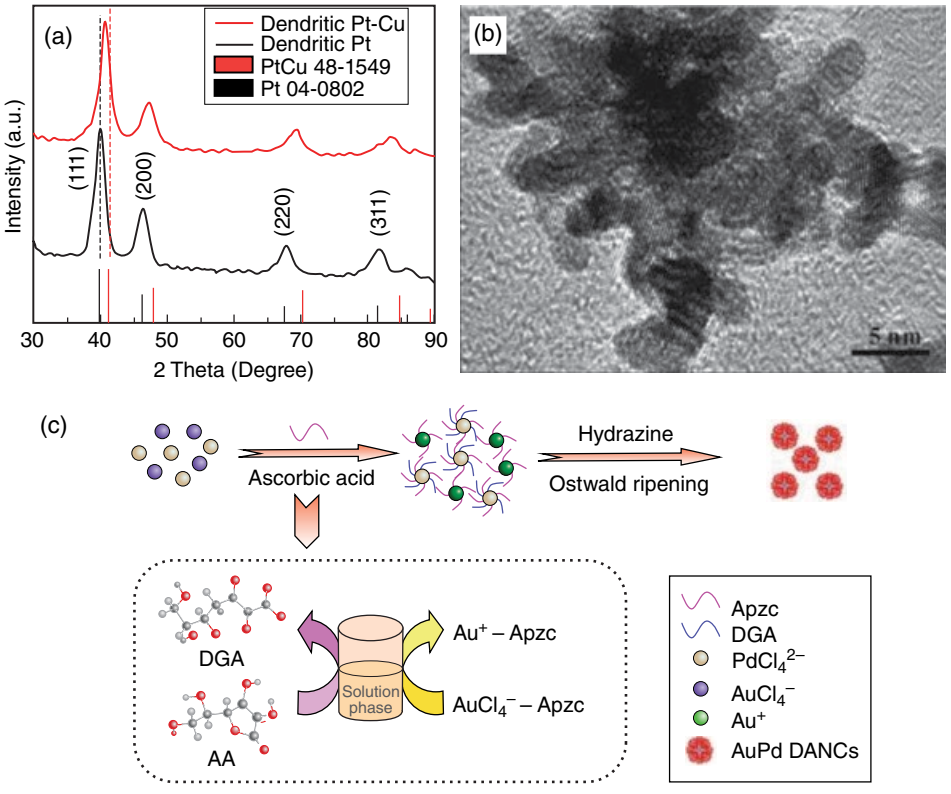

Figure 7.2 (a) XRD patterns of dendritic Pt–Cu and Pt nanostructures synthesized by the same reduction method. (b) HRTEM images of dendritic Pt–Cu nanostructures. Images in (a, b) were reprinted with permission from ref. [30]. Copyright 2011, Elsevier Ltd. (c) Schematic diagram of the formation mechanism of Au–Pd nanodendrites. Reprinted with permission from ref. [25]. Copyright 2015, Elsevier Ltd.

The X-ray diffraction (XRD) result (Figure 7.2a) shows that the as-prepared nanodendrites are Pt–Cu alloy, and the high resolution transmission electron microscope (HRTEM) image (Figure 7.2b) suggests the formation of the dendritic nanostructures based on the aggregation of elongated Pt–Cu nanoparticles. Additionally, the Au–Pd dendritic alloyed nanocrystals were synthesized via a one-pot coreduction method, using $HAuCl_4$ and H_2PdCl_4 as the metal precursors, 3-aminopyrazine-2-carboxylic acid (Apzc) as the capping agent, and ascorbic acid (AA) plus hydrazine as the reducing agent[25]. The as-prepared Au–Pd nanodendrites have a polycrystalline structure and expose (111) planes of fcc Au–Pd mainly. Controlled experiments indicated that the formation of Au–Pd nanodendrites contained two steps (Figure 7.2c): first of all, the Apzc-$AuCl_4^-$ species were reduced by AA accompanied by the conversion of AA to 2,3- diketo-1-gulonic acid (DGA); then were further reduced by hydrazine with the assistance of Pd-DGA species to generate the Au–Pd nanodendrites.

The surfactants and dispersion agents are usually used in a reduction method to avoid aggregation of the nanoparticles as well as to modulate the structure of the product[41–43]. However, the catalysts synthesized in the existence of the surfactants perform

a declined activity because the surfactants, which are difficult to remove, usually occupy partial of the active sites. In consideration of this, Cai et al. developed a one-step surfactant-free coreduction method using K_2PtCl_4 and $CuSO_4$ as the metal precursors and ascorbic acid (AA) as the reducing agent[40]. Structural analyses show that the as-prepared Pt–Cu dendritic spherical nanocrystals with an average size of 52.4 nm have an alloyed structure with a good crystallinity, which show extraordinary electro-catalytic activity for MOR.

7.2.2 Galvanic Replacement Reaction

The galvanic replacement reaction is a process that uses a more active metal (compared with another metal) as a sacrifice template to react with the ions of the inactive metal with a higher reduction potential[13]. The synthesis principle of the bimetallic dendritic nanostructures obtained by galvanic replacement reaction is based on selective etching. In such a reaction for synthesizing the bimetallic nanodendrites, the ions of the inactive metal are reduced by the other metal, and thus a primary battery is formed. Then both of the two metal ions will move into the cathode. Along with the increase of the concentration of the ions of the sacrifice metal, they can also get electrons and be reduced to regenerate the sacrifice metal on the surface of the inactive metal. During the deposition of the metal atoms, defects such as twins and dislocations can be formed and lead to branches evolved from the defective facets. Finally, the bimetallic nanodendrites are obtained under the continuous reaction.

In addition, sometimes the sacrifice metal is pre-prepared to have a dendritic structure. Then it will serve as a template to carry out the galvanic replacement reaction and finally form the bimetallic nanodendrites. Before the reaction is proceeded, the reduction potentials of the two metals should be taken into account. For example, the reduction potential of Ag^+/Ag is 0.80 V, and that of Cu^{2+}/Cu is 0.34 V[13]. Since Cu has a more negative reduction potential than Ag, Ag–Cu dendritic nanostructures were synthesized via Cu substrate reacting with $AgNO_3$ in a galvanic replacement reaction[41–43]. Though these Ag–Cu dendrites have similar morphologies, they have a few differences on details about the synthetic methods. In the work of Yu et al., the reaction took place on a porous Cu foam substrate and a heterogeneous structure with a trace amount of Cu uniformly covered the surface was obtained[41]. The growth mechanism (Figure 7.3a and b) was proposed as a Cu–Ag primary battery, in which Cu reacts with Ag^+ to form Cu^{2+} ions and Ag. Further, with more and more Cu^{2+} migrating to the cathode, some Cu^{2+} ions receive electrons to form Cu which will deposit on the surface of the dendrites. This mechanism was not unique since Chen et al. obtained the Ag–Cu dendritic nanocrystals via the same process, but they used an electrodeposition method to gain Cu nanostructures for further reacting with $AgNO_3$, which was different from the former[42]. Interestingly, Motevalli et al. used a zinc foil to react with different copper salts to gain Cu substrate, and they found that only when $CuCl_2$ was chosen as the copper source could they obtain Cu dendrites, and finally Ag–Cu dendrites[43].

As for bimetallic dendritic nanostructures of noble metals, Ag–Pd dendrites were obtained by Yi et al. via a multi-stage galvanic replacement reaction (MGRR)[29]. The Cu foil was used as a sacrifice to react with $AgNO_3$ to gain Ag dendrites for the MGRR followed by reacting with Na_2PdCl_4. The SEM images (Figure 7.4a) show no obvious

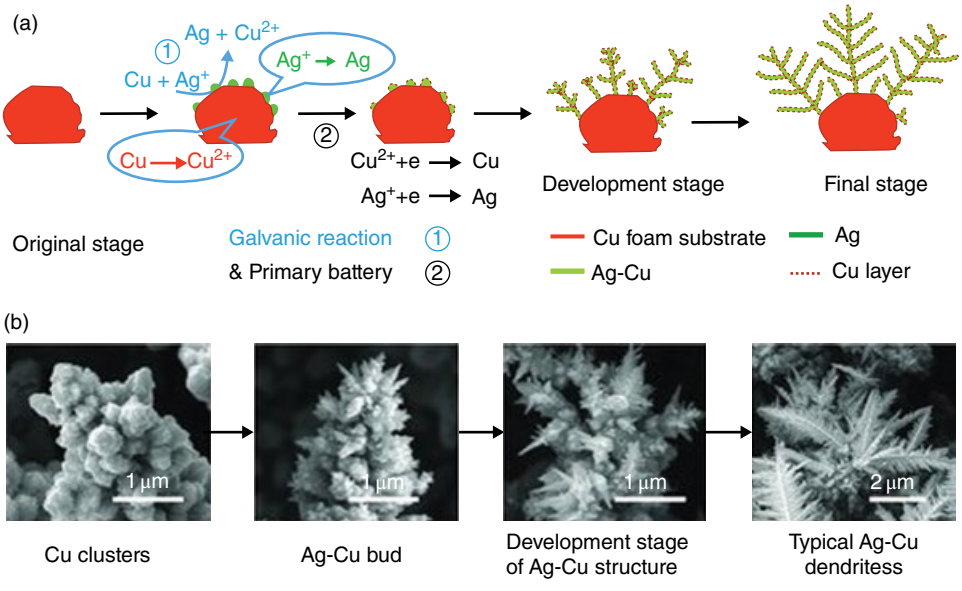

Figure 7.3 Schematic diagram of the formation mechanism of Ag-Cu dendrites. (a) Detailed formation process of nanocrystals with different morphologies in different stages. (b) Scanning electron microscopy (SEM) images of the Ag–Cu nanocrystals in different growth stages. Reprinted with permission from ref. [41]. Copyright (2011), Wiley-VCH Verlag GmbH & Co. KGaA, Weinheim.

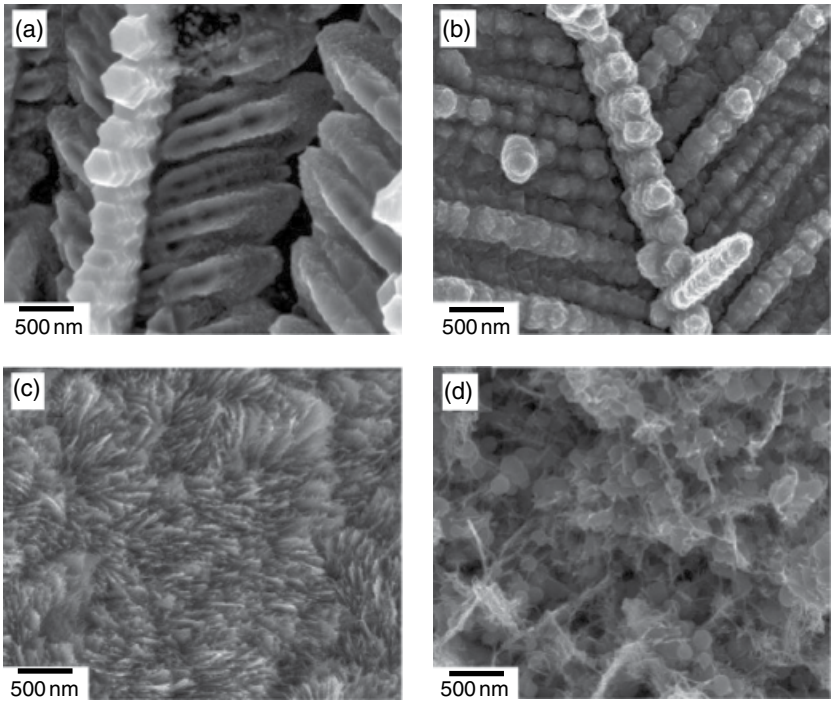

Figure 7.4 SEM images of Ag–Pd dendritic structures after different cycles of MGRR: (a) 1 cycle, (b) 3 cycles, (c) 5 cycles, (d) 7 cycles. Reprinted with permission from ref. [29]. Copyright (2012), Elsevier B.V.

change of the Ag dendrites after the first reaction cycle. However, there were some Ag–Pd flakes emerging at the surface of the Ag dendrites after three reaction cycles (Figure 7.4b). When the Ag dendrites went through five reaction cycles, they were fully covered by the Ag–Pd flakes with a uniform thickness (Figure 7.4c). As shown in Figure 7.4d, after seven reaction stages, the Ag–Pd flakes were almost replaced by a lot of cavities, which can also be seen in Figure 7.4c. The atomic ratio of Pd in the sample increased along with the cycle numbers of the MGRR. It is suggested that the MGRR does better in controlling the morphologies and compositions of the bimetallic nanostructures than one-stage galvanic replacement reaction. Similarly, Tang et al. changed Na_2PdCl_4 to $HAuCl_4$ and successfully synthesized Ag–Au dendrites via the MGRR, thanks to the advantages of MGRR on modality and composition control[44]

Although the galvanic replacement reaction is very effective on synthesizing the bimetallic nanodendrites, especially when other methods like coreduction and seed-mediated growth method are unattainable, it should be carried out carefully in case of overreaction[13]. In order to form a dendritic structure, the quantities of both the sacrifice metal and the ions of the other metal must be controlled. In addition, experiment conditions like reaction temperature and reaction time should be precisely considered. Notably, the MGRR is a powerful tool to regulate the morphology and composition of the bimetallic nanocrystals since it can easily manipulate the extent of the reaction[45, 46].

7.2.3 Seed-Mediated Growth

The seed-mediated growth method can be regarded as the most important strategy to synthesize bimetallic heterostructures[13, 47–50]. It usually contains the preparation of the seed and heterogeneous nucleation and growth on the seed. Since it divides the nucleation and growth into two parts, it is easier to control the size and shape of the metal nanocrystals. To obtain nanostructures with specific morphologies, the seeds need to be prepared precisely to have well-defined characteristics. Then the other metal atoms deposit on the surface of the seeds and further grow into different kinds of morphologies via a heterogeneous nucleation, usually. Using seeds with twinned structures and appropriate capping ligands, the facets with high surface free energy will grow faster than low-energy facets, and thus, dendritic nanostructures will form. And after the introduction of the seeds, the bimetallic nanodendrites can be obtained via not only the epitaxial overgrowth but also the oriented attachment. The two processes correspond to different nucleation cases, which will be further discussed later in the chapter.

Works of synthesizing the bimetallic nanodendrites by the seed-mediated growth method using different kinds of seeds have been reported[27, 31, 51–54]. Noble metals such as Pt and Pd show excellent electrocatalytic activity in many electrochemical reactions[55–59]. Pt and Pd have the same fcc structure and small lattice mismatch, and they can easily achieve the epitaxial growth[52]. Therefore, many researchers choose Pt and Pd to synthesize bimetallic dendritic nanostructures via seed-mediated growth method[27, 31, 51–53]. For instance, Xia et al. synthesized Pt–Pd nanodendrites by reducing K_2PtCl_4 using L-ascorbic acid, with Pd nanocrystals as seeds obtained from the reduction of Na_2PdCl_4 by L-ascorbic acid[51]. The HRTEM image (Figure 7.5a) of a single Pt–Pd dendritic nanostructure shows that the lattice fringe from the core of Pd to the branch of Pt is continuous, which indicates that the dendritic growth mechanism is based on epitaxial growth of Pt on the Pd seed. It is suggested that the nucleation of

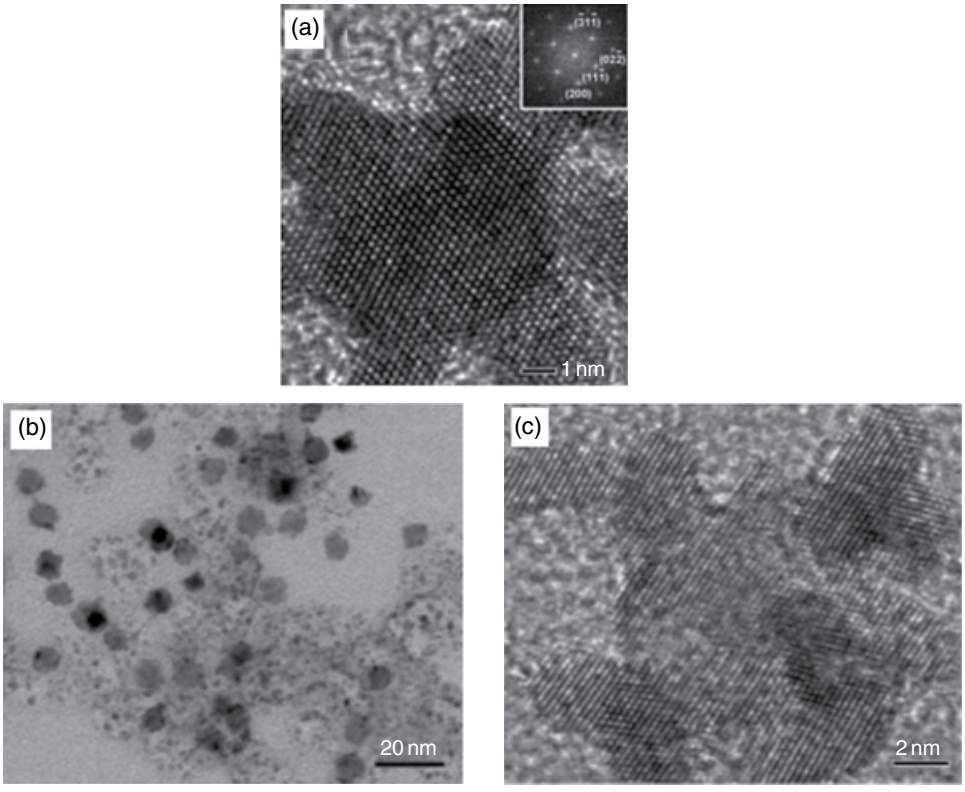

Figure 7.5 (a) HRTEM image of the Pt–Pd nanostructure, the identical FT patterns shown in the inset suggest that the Pt branches have the same lattice orientation as the Pd core. Reprinted with permission from ref. [51]. Copyright 2009, American Association for the Advancement of Science. (b) TEM image of Pt–Pd nanodendrites synthesized in the presence of Pd seeds. The reaction time was 1 min. (c) HRTEM image of a single Pt–Pd nanodendrite. Images in (b, c) were reprinted with permission from ref. [31]. Copyright (2010), Tsinghua University Press and Springer-Verlag Belin Heidelberg.

Pt is heterogeneous rather than homogeneous in this synthesis. It might be a self-catalyzing process in which the Pt nuclei on the Pd seeds become the active site for further atom addition. Therefore, the Pt atoms prefer to deposit on the existing Pt nuclei attached on the Pd seeds and develop into branches. Another work from Xia et al. proposed a different kind of growth mechanism of Pt–Pd nanodendrites[31]. The TEM image (Figure 7.5b) of 1 min reaction after the addition of L-ascorbic acid to the mixture of Pd seeds and K_2PtCl_4 reveals that many Pt particles exist except for the Pt-on-Pd particles. It indicates that both heterogeneous and homogeneous nucleation are coexistent at the initial stage of the growth process. And the HRTEM image (Figure 7.5c) suggests that the small Pt particles obtained from the homogeneous nucleation should compose the Pt branches formed through the oriented attachment. In addition, Yang et al. synthesized the Pt–Pd nanodendrites using $Pd(acac)_2$ and $Pt(acac)_2$ as the metal precursors in oleylamine. And the as-prepared dendritic Pt–Pd sample shows both good electrocatalytic activity and stability in the oxygen-reduction reaction.

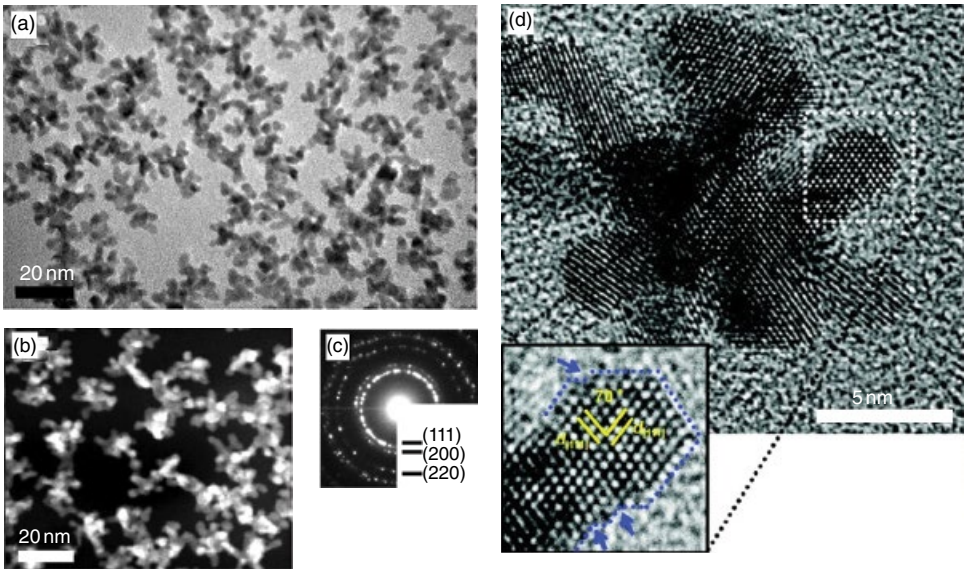

Figure 7.6 (a) Bright-field TEM image; (b) HAADF-STEM image; (c) corresponding SAED pattern of the Pt–Pd nanodendrites; and (d) highly magnified TEM image. The arrows in the inset of (d) exhibit several atomic steps on the Pt branch surface. Reprinted with permission from ref. [53]. Copyright (2011), American Chemical Society.

It has been established that the seed-mediated growth method usually consists of two steps. However, Yamauch et al. have proposed a direct synthesis of Pt–Pd bimetallic dendritic nanostructures whose interior is Pd and exterior is dendritic Pt[53]. Unlike the traditional seed-mediated growth method, they suggested a one-pot route, using K_2PtCl_4 and Na_2PdCl_4 as the metal precursors, Pluronic P123 as the capping agent, and ascorbic acid (AA) as the reducing agent. Due to the different redox potentials, the Pd precursor was preferentially reduced by AA before Pt. Then Pt was deposited on the formed Pd seeds to form the Pt-on-Pd nanodendrites.

Figure 7.6a shows the TEM image of the Pt–Pd nanodendrites whose sizes are 8–15 nm. The high-angle annular dark-field scanning TEM (HAADF-STEM) image is shown in Figure 7.6b, which provides a better view. The selected-area electron diffraction (SAED) result (Figure 7.6c) indicates an fcc structure of the Pt–Pd nanodendrites. The HRTEM image (Figure 7.6d) of a Pt–Pd nanodentrite shows that it has 3-nm-wide Pt branches extending in various directions. And the space between the adjacent fringes (0.23 nm) indicates that each Pt nanoarm is single-crystalline.

Uniquely, Raj et al. obtained the Pt–Pd nanodendrites (Figure 7.7a) using H_2PtCl_6 and K_2PdCl_4 as the metal precursors, AA as the reducing agent, and multiwall carbon nanotubes (MWCNTs) as the support but without any surfactant[27]. Similarly, the growth mechanism of the Pt–Pd dendritic nanostructures is based on the difference of reduction potentials among the $PtCl_6^{2-}$, $PtCl_4^{2-}$, and $PdCl_4^{2-}$ species. But there is something unique in the mechanism since it is a surfactant-free method. As shown in Figure 7.7b, first, $PtCl_6^{2-}$ and $PdCl_4^{2-}$ experienced a coreduction process after the addition of AA along with the formation of $PtCl_4^{2-}$ and Pd nanoparticles on the surface of MWCNTs.

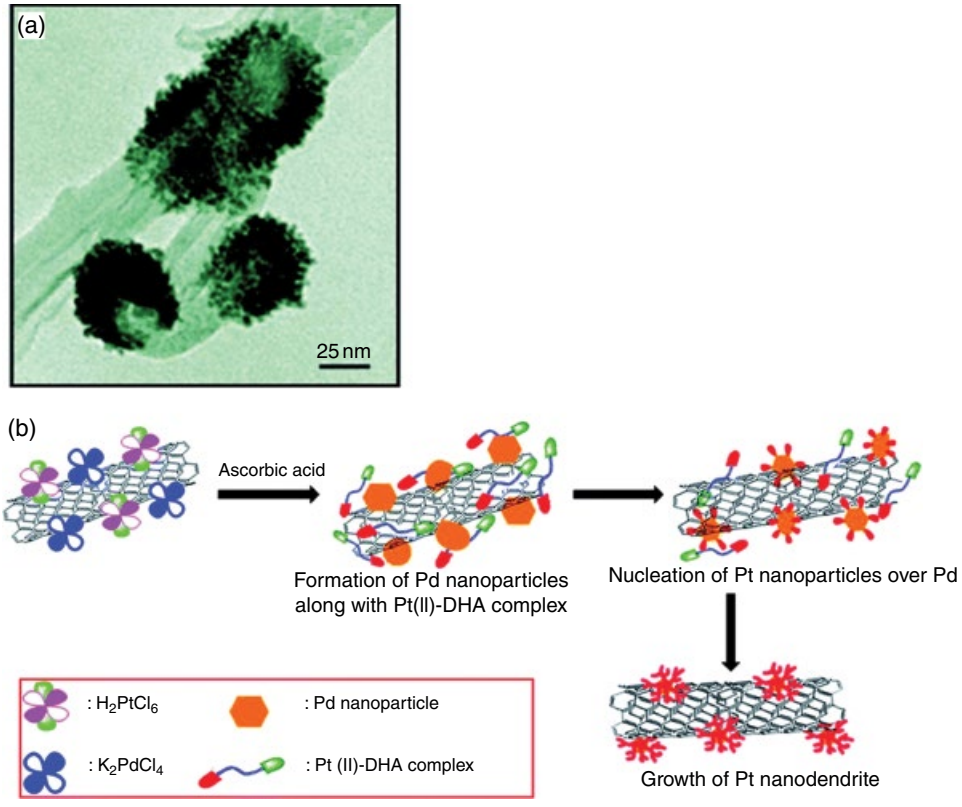

Figure 7.7 (a) TEM image of MWCNT-supported $Pt_{64}Pd_{36}$ nanocatalyst. (b) Schematic diagram of the formation of Pt–Pd nanodendrites over MWCNTs. Reprinted with permission from ref. [27]. Copyright 2013, Royal Society of Chemistry.

Then the Pt (II) ions combined with the dehydroascorbic acid (DHA) coming from the oxidation of AA and formed $PtCl_4^{2-}$-DHA species. Finally, the $PtCl_4^{2-}$-DHA species were reduced by the excess AA and nucleated, followed by growing to dendritic nanostructures on the surface of Pd nanoparticles which served as seeds *in situ*.

The Pt–Au dendritic nanostructures were obtained via seed-mediated growth method using Au particles as seeds by Eichhorn et al[54]. The Au seeds were prepared via the reduction of $HAuCl_4$ in the mixture of decahydronaphthalene and oleylamine. And $Pt(acac)_2$ was added to the as-prepared solution to obtain the final product. Structure characterizations show that the core of the dendrites is nearly pure Au with a size of 6–18 nm, and the diameter of Pt branch is about 7 nm. It is suggested that the growth mechanism of Pt branches is a template-growth process. Such a Pt–Au heterogeneous dendritic nanostructure has a better CO tolerance for hydrogen activation.

Actually, the seed-mediated growth method is similar to the galvanic replacement reaction, since both of them need to prepare a "template" at first. Nevertheless, the "template" in a galvanic replacement reaction is going to be sacrificed while the seed-mediated growth method just uses the "template" as a seed to grow other nanostructures. Sometimes when the reduction potential of the seed is lower than another metal

that is going to deposit on it, the galvanic replacement reaction must be inhibited[60–62]. To solve this problem, one can enhance the reduction rate by using a powerful reductant. For instance, the reductants in the works of synthesizing Pt–Pd nanodendrites using Pd as seeds that we have previously discussed are all AA agents. Therefore, the galvanic replacement reaction can be controlled in an acceptable range. Another way to avoid the galvanic replacement reaction is to use suitable ligands to coordinate with the metal ions to change their reduction potentials. In the work of Raj et al., the formation of $PtCl_4^{2-}$-DHA prevented Pt(II) from reacting with Pd seed[27].

7.2.4 Other Methods

In addition to the strategies we have already discussed, there are other methods for synthesizing the bimetallic dendritic nanostructures. Kang et al. have reported an electrochemical method to obtain Cu–Ni dendrites[63]. The electrodeposition was performed in a three-electrode cell using a Cu foil as the substrate and an aqueous solution containing $CuCl_2$, $NiSO_4$, and Na_2SO_4 as the electrolyte. Three potentials, –0.8, –1.0, and –1.2 V were applied in the chronoamperometry technique to complete the deposition of Cu–Ni. SEM images (Figure 7.8a and b) show that the Cu–Ni dendrites obtained from different potentials have similar morphologies. It indicates that the tip-splitting structure is of great significance in the growth process of the dendrites. Other Cu–Ni dendritic nanostructures were gained by Song et al. in the same way, in which they only changed $CuCl_2$ to $CuSO_4$, $NiSO_4$ to $NiCl_2$, and Cu foil substrate to titanate film[64]. And the composition of the Cu–Ni dendrites could be controlled by tuning the applied potential during the electrodeposition.

Uniquely, heterogeneously branched Pt–Au nanostructures were synthesized via a post-synthesis modification method by Yang et al[65]. First of all, Au nanoparticles were obtained via a reduction method using $HAuCl_4$ as the metal precursors and $NaBH_4$ as the reducing agent. Then the as-prepared Au nanoparticles were used together with $Pt(acac)_2$ to form Pt-on-Au branched nanoparticles. Finally, the as-prepared Pt-on-Au branched nanoparticles were supported on carbon black, followed by thermally treatment at 300 °C in air for an hour and then at 400 °C in 5%H_2/Ar for two hours.

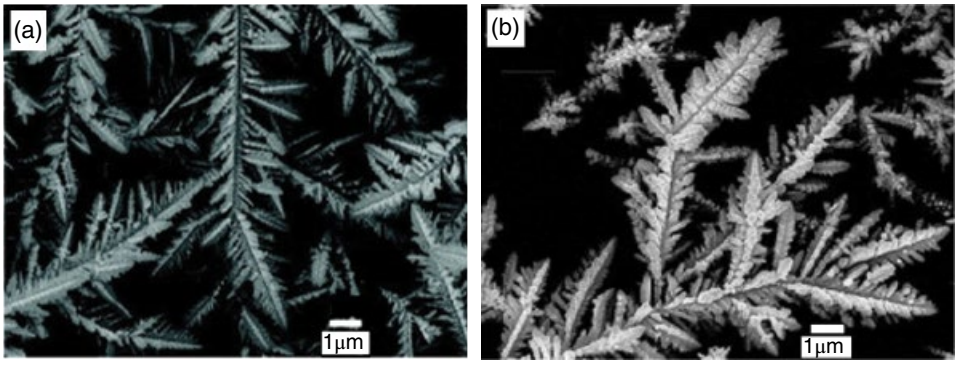

Figure 7.8 SEM images of the morphologies of the Cu–Ni dendritic structures obtained at a potential of (a) –0.8 V; and (b) –1.2 V with an electrolysis time of 3600 s. Reprinted with permission from ref. [63]. Copyright 2007, American Chemical Society.

The Pt–Au branched nanostructure obtained after the thermally treatment became much smoother and had much fewer branches than before; nevertheless, it displayed a much better electrocatalytic activity than commercial Pt/C in the oxidation of formic acid.

7.3 Properties and Applications of Bimetallic Dendritic Nanostructures

The unique structure of bimetallic dendritic nanocrystals with large surface area as well as high percentage of edge, corner, and stepped atoms endows them with excellent properties toward many important applications. In this section, we mainly focus on the optical and catalytic properties as well as applications of the bimetallic dendritic nanostructures.

7.3.1 Plasmonics

Metals like Cu, Ag, Au, Pd, Ru, Rh, and Pt have drawn considerable interest because of their unique optical properties, which are known as the localized surface plasmon resonance (LSPR), emanating from the interaction of the electromagnetic wave under the resonant condition and the free electrons in metals[66–70]. Many applications have been developed using the LSPR phenomenon of metals, such as SERS, sensors, photocatalysis, and photothermal therapy[66–70]. And the LSPR of a given metal nanostructure is strongly influenced by its morphology and composition.

Bimetallic dendritic nanostructures made by these metals can exhibit enhanced photocatalytic activities and SERS properties than monometallic nanodendrites or bimetallic nanostructures with different morphologies or compositions[28, 29, 32, 39, 41, 44]. For example, Tseng et al. have reported a Pt–Ag tDNFs synthesized via galvanic replacement reaction, exhibited a good performance toward the light-enhanced MOR[28]. Its dendritic morphology is shown in the TEM image of Figure 7.9a. The HRTEM image and EDS result (Figure 7.9b) verified a hollow structure in tubular nature for the Pt–Ag tDNFs. It is well known that Pt has a relative high activity toward MOR, but least photocatalytic activity for light-enhanced MOR. However, with the introduction of Ag into Pt, an enhancement of 6.4% on activity for MOR under the light is obtained for the Pt–Ag tDNFs, as indicated in Figure 7.9c. The open-circuit potential (OCP) measurement under the same condition as Figure 7.9c is shown in Figure 7.9d, which displays a negative shift of 0.9% in OCP, coinciding with the results in Figure 7.9c. Since Ag has a strong LSPR effect, it is no wonder that the enhancement of photocatalytic activity is attributed to the LSPR effect of the dendritic nanostructure in the catalytic process. Nevertheless, it is a complicated process consisting of plasmonic heating, electron injection, and magnification of local electromagnetic field, etc. In brief, the LSPR will result in a strong electric field that helps to take away the electrons from the methanol molecules and enhances the activity of Pt. Although more investigations are still needed to carry out to make clear the catalytic mechanism, such a bimetallic dendritic nanostructure has great potentials for photocatalytic fuel cells.

Another example is the heterogeneous Ag–Cu dendrites synthesized via the galvanic replacement reaction by Yu et al. as described in section 7.2.2, which exhibited a notably enhanced SERS property[41]. Compared with the Ag particles, pure Ag dendrites and Ag particles/dendrites (nanostructures consist of both of them), the SERS spectrum of

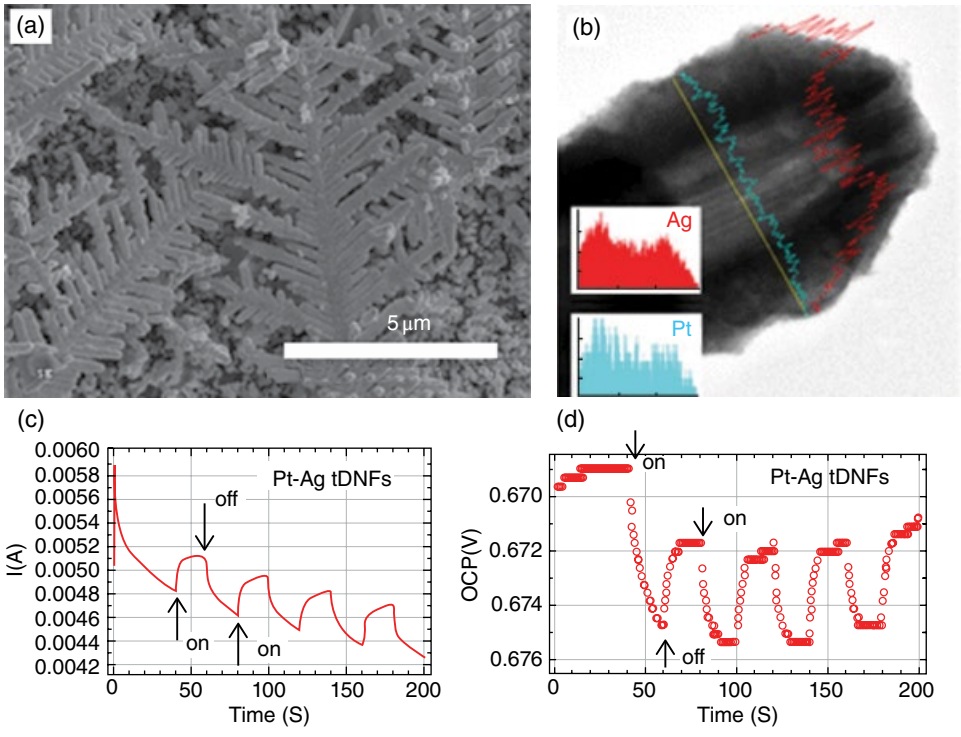

Figure 7.9 (a) SEM image of Pt–Ag tDNFs. (b) HRTEM image and EDS linear result of one branch. (c) The chronoamperometric (CA) on-off test for Pt–Ag tDNFs. The polarization potential is −0.3 V_{SCE}. Reference electrode: saturated calomel electrode (SCE); counter electrode: Pt-coated Ti mesh. The illumination was conducted under a solar simulator (SADHUDESIGN; 400–1000 nm; class B; 1000 $W \cdot m^{-2}$). (d) The OCP measurement during the on-off test under illumination for Pt–Ag tDNFs. Reprinted with permission from ref. [28] (open access).

10^{-6} M rhodamine 6G (R6G) using the Ag–Cu dendrites as substrates in Figure 7.10a shows the highest intensities. In addition, the SERS signal intensities of samples using the pure Ag particles and dendrites as substrates are similar, indicating that the morphology is not the key factor for determining the SERS properties. It is the trace amount of Cu coated on the surface of the Ag dendrites that is of great significance for the enhancement of the SERS signal intensities. Some researchers suggested that the better properties of the bimetallic nanostructures were due to the pinholes existing in the structures, which can enhance the electromagnetic field as the hot spots. However, the exact explanation of the enhancement still needs further investigation. Similarly, the superiority of the bimetallic nanostructures on SERS, in contrast to the monometallic samples, have been reported by Cheng et al[32]. They synthesized an Au–Ag dendritic nanostructure via the galvanic replacement reaction and found that its SERS activity obtained using the crystal violet as a probe increased with the immersion time of the galvanic replacement reaction.

The morphologies and compositions of the bimetallic dendritic nanostructures also have a remarkable effect on their SERS properties. Liu et al. synthesized a series of dendritic and porous Ag–Pd nanostructures with different compositions[39]. Using

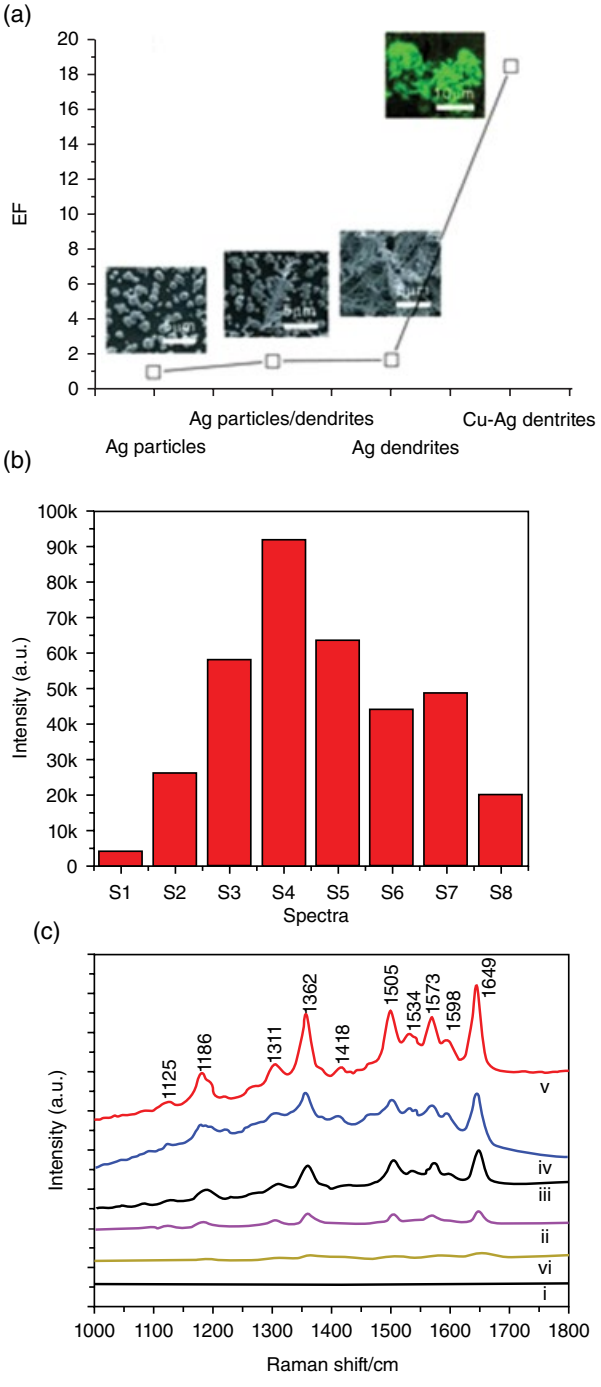

Figure 7.10 (a) Relative enhancement factors (REFs) of the samples prepared using the 532 nm excitation laser lines. The band located at around 1363.5 cm^{-1}, with the largest relative SERS effect, was chosen for estimation of the REFs. Reprinted with permission from ref. [41]. Copyright 2011, Wiley-VCH Verlag GmbH & Co. KGaA, Weinheim. (b) The average peak intensity of the 1510 cm^{-1} line for 40 SERS spectra of 10 nM R6G on Ag, Pd, and Ag–Pd alloy nanostructures: (S1) dendritic Pd; (S2) dendritic $Ag_{24}Pd_{76}$; (S3) dendritic $Ag_{59}Pd_{41}$; (S4) dendritic $Ag_{79}Pd_{21}$; (S5) sphere-like Ag; (S6) sphere-like $Ag_{83}Pd_{17}$; (S7) porous $Ag_{65}Pd_{35}$; and (S8) porous $Ag_{11}Pd_{89}$. Reprinted with permission from ref. [39]. Copyright (2011), Elsevier Inc. (c) Raman spectra of 10^{-6} M R6G on (i) Pd nanocrystals on the Cu foil; (ii) Ag dendrites; or (iii–vi) Ag-Pd samples obtained after different stages of MGRR: (iii) 1 cycle; (iv) 3 cycles; (v) 5 cycles; (vi) 7 cycles. Reprinted with permission from ref. [29]. Copyright (2012), Elsevier B.V.

R6G as probe molecule, the average intensities of the 1510 cm^{-1} line for SERS on the as-prepared samples are showed in Figure 7.10b, and the background signal has been removed. As can be seen, with a similar composition, the dendritic Ag–Pd nanostructures show higher SERS intensities than that of the sphere-like and porous ones. Additionally, the SERS intensities of the samples with similar morphologies increase with decreasing the Pd content, since the SERS activity of Pd is much lower than that of Ag. What's more, the morphologies of the Ag–Pd nanodendrites changed along with the Pd content. The Ag–Pd nanodendrites with higher Pd content have fewer and irregular branches. It is well accepted that the gaps in the bimetallic nanostructures are beneficial to the enhancement of the SERS property. Thus, the Ag–Pd nanodendrites with higher Pd content have fewer gaps, and end up with a lower SERS enhancement. Notably, the porous $Ag_{65}Pd_{35}$ and dendritic $Ag_{59}Pd_{41}$ both exhibit a higher SERS intensity than sphere-like $Ag_{65}Pd_{35,}$ which can be attributed to the presence of the pinholes in the structures served as the hot spots.

Interestingly, the work of Yi et al. showed different results from the former[29]. The Pd content in the Ag–Pd dendrites increased with the reaction stages proceed during MGRR. Figure 7.10c shows SERS of 10^{-6} M R6G on the as-obtained Ag–Pd dendrites with different compositions via the MGRR method. As can be seen with expectation, Ag dendrites showed higher intensities than pure Pd and Ag–Pd nanostructures with a relatively high Pd content prepared after seven cycles of the MGRR, since Ag has a much better intrinsic activity than Pd. Nevertheless, the Ag–Pd nanodendrites obtained after one, three, and five cycles of MGRR all exhibited enhanced SERS activities in contrast with the pure Ag dendrites. The sample gained after five cycles had the highest SERS activity among all of the samples. It is believed that the bimetal effect may facilitate the SERS activity enhancement. More importantly, it can be attributed to the changes of the corresponding morphologies. The MGRR left holes after Ag was replaced, and the Ag–Pd nanodendrites obtained after five cycles had a lot of flakes with needles, which could largely enhance the adsorption of the sensing molecules. All of these characteristics result in more hot spots and higher SERS activity. Similarly, Tang et al. found the enhancement of the SERS property on Au–Ag nanodendrites[25].

7.3.2 Catalysis

The generation, storage, and conversion of energy source are of great significance for addressing current energy crisis, which is increasingly serious. Proton-exchange membrane fuel cell (PEMFC) is a process that converts chemical energy to electrical energy and generats power onsite for the applications like vehicles and other electronic devices. It has attracted great research interests since it is a clean energy and also a substitute to the fossil fuel[71–73]. There are two electrode reactions in a fuel cell: anode reaction of the oxidation of the fuel and cathode reaction of the reduction of the oxygen. The bimetallic dendritic nanostructures exhibit excellent electrocatalytic activities toward both of the anode and cathode reaction of the fuel cells due to their enhanced specific surface area and high percentage of stepped, edge, and corner sites[13–15]. And as bimetallic nanostructures, they are superior to the monometallic nanostructures because of the synergetic effects of the bimetals deriving from their geometric effect and electronic effect.

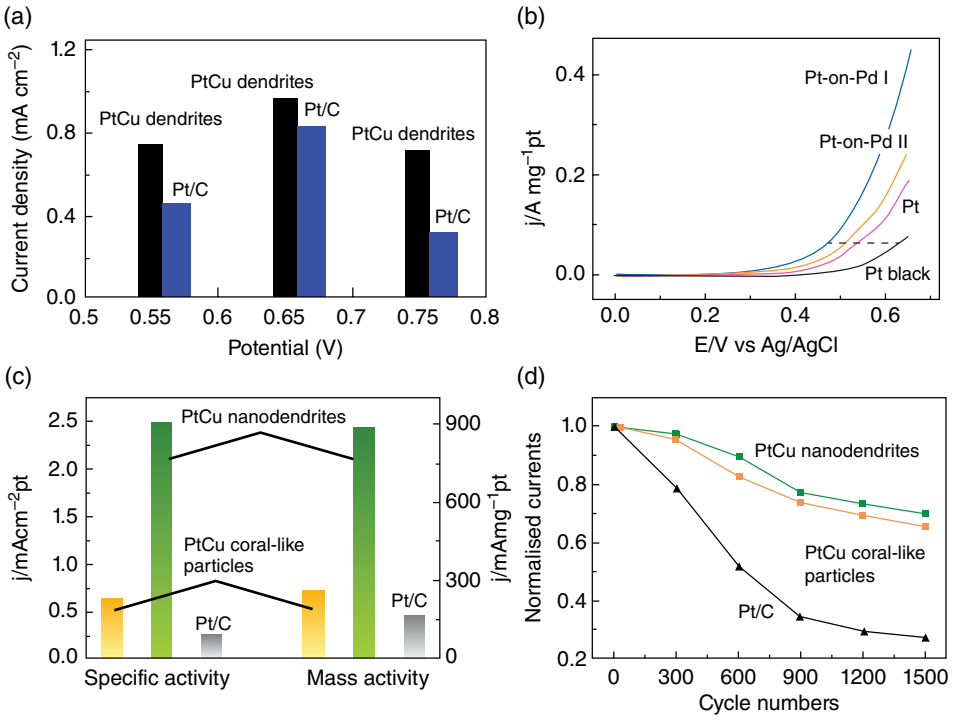

Figure 7.11 (a) The specific activity in positive scan for Pt–Cu nanodendrites and Pt/C at 0.55, 0.65, and 0.75 V, respectively. Reprinted with permission from ref. [30]. Copyright 2011, Elsevier Ltd. (b) Linear-sweep voltammograms of commercially Pt black, Pt-on-Pd I, Pt-on-Pd II, and Pt nanodendrites without Pd cores in an aqueous solution containing 0.5 M H_2SO_4 and 1 M methanol. Reprinted with permission from ref. [53]. Copyright (2011), American Chemical Society. (c) The bar graph of specific activities and mass activities (at −0.2 vs. Ag/AgCl) of PtCu coral-like nanoparticles, PtCu dendritic nanostructures and commercial Pt/C in alkaline conditions. (d) The stability test of normalized current during 1,500 cycles. Images in (c, d) were reprinted with permission from ref. [40] (open access).

MOR is a very important reaction for both fundamental research and application of fuel cells[74–76]. Pt–Cu nanodendrites obtained by Zhao et al. showed an enhanced activity toward the MOR in contrast to the commercial Pt/C[30]. Figure 7.11a shows 1.6, 1.2, and 2.2 times activities of the as-prepared Pt–Cu nanodendrites as commercial Pt/C at 0.55, 0.65, and 0.75 V in an acidic solution, respectively.

Several factors may give rise to the enhancement of the activity. First, the dendritic structure shows a large surface area that will provide more active sites for the adsorption of the reactant and intermediate molecules. Second, the dendrites with a good connectivity facilitate the electron conductivity and promote the reaction kinetics. Third, the introduction of Cu increases the tolerance of CO of the catalysts as revealed by Knudsen et al[77]. Last but not least, the Pt–Cu alloy will experience a rearrangement of the surface structure because of the dealloying of Cu when it catalyzes the MOR, and the new structure of Pt may have more active crystal faces for the MOR. Therefore, the reasons for the enhancement in the catalytic activity of the Pt–Cu nanodendrites are attributable to the dendritic structure and the alloying effect of Pt–Cu alloy. Besides, the Pt-on-Pd nanaodendrites with two different Pt/Pd ratios synthesized

by Yamauchi et al. showed higher activities for MOR than the pure Pt nanodendrites and commercial Pt black[53].

Figure 7.11b shows that the activity of Pt-on-Pd nanaodendrites with Pt/Pd ratios of 6.1/1 is about 2.8 times as that of Pt/Pd ratios of 1/1, 3.3 times as that of pure Pt nanodendrites and 5.5 times as that of the commercial Pt black. The Pd core plays an important role in the enhancement of the activity as a result of the formation of the pseudo Pt–Pd alloying heterointerface facilitated by the high miscibility of Pt and Pd. And this unique structure is beneficial to the C–H cleavage reaction due to the reduction of the electronic binding energy of Pt. Another Pt–Cu nanodendrites prepared by Cai et al. exhibited a high electrocatalytic activity for MOR, too[40].

As can be seen in Figure 7.11c, the specific activity of the Pt–Cu spherical nanodendrites is three times higher than that of the Pt–Cu coral-like nanostructures and nine times higher than that of the commercial Pt/C at –0.2 V (vs. Ag/AgCl) in an alkaline solution. As for the mass activity, the Pt–Cu spherical nanodendrites are also the best one among the three catalysts. Additionally, the Pt–Cu spherical nanodendrites showed a better performance in the investigation of stability than the other two catalysts (Figure 7.11d). The factors that making the Pt–Cu spherical nanodendrites good electrocatalysts for MOR are similar to the former, just because that the dendritic structures could provide more stepped and edged sites on the bimetallic surfaces, and possess the alloying effect together with the lattice strain effects. Furthermore, the Pt–Cu spherical nanodendrites had a higher activity than the Pt–Cu coral-like nanostructures as a result of the absence of any surfactants in the synthesis of nanodendrites, which resulted in a better electron conductivity and fewer occupations of the active sites caused by the adsorption of the surfactant molecules.

As the cathode reaction of a fuel cell, oxygen reduction reaction (ORR) is very significant and is intensely investigated by researchers[78–80]. However, its slow kinetics limits its commercial application. For instance, Xia et al. synthesized Pt–Pd nanodendrites via the seed-mediated growth method and investigated their catalytic properties toward ORR[51]. Figure 7.12a shows that the ORR mass activities at 0.80–0.95 V (vs. RHE) of the as-prepared Pt–Pd nanodendrites are three times higher than that of the Pt aggregates obtained without the Pd seed. It is well known that ORR is structure-sensitive on the surface of Pt. And the activity order of the low-index Pt facets toward ORR carried out in a nonadsorbing electrolyte (e.g., perchloric acid) is (110) > (111) ≫ (100). The as-prepared Pt–Pd nanodendrites mainly expose Pt(111) along with a few Pt(110) while the facets of Pt aggregates are indefinite. Therefore, the superior of the Pt–Pd nanodendrites to the Pt aggregates is accessible. Another Pt–Pd nanodendrites prepared by Xia et al. with a similar method also exhibited excellent activities toward ORR[31]. As shown in Figure 7.12b, the ORR mass activities at 0.9 V (vs. RHE) of the Pt–Pd nanodendrites are 3.1 and 5.3 times that of the commercial Pt black and Pt/C (and 3.5 and 6.0 times if only considering the Pt mass). Besides the facet effects of the as-prepared Pt–Pd nanodendrites, the large surface area also facilitates the enhancement of the activity. Figure 7.12c shows the ORR specific activities of the Pt–Pd dendritic nanostructures and Pt nanoparticles prepared by Yang et al[52]. And the Pt–Pd nanodendrites show around double activities in contrast with the Pt nanoparticles. The introduction of Pd into Pt reduces the adsorption of OH_{ad} on the surface of Pt and enhances the activities because a low coverage of OH_{ad} on the Pt sites is beneficial to the reaction kinetics. The three works above carried out the ORR in solution of $HClO_4$, in

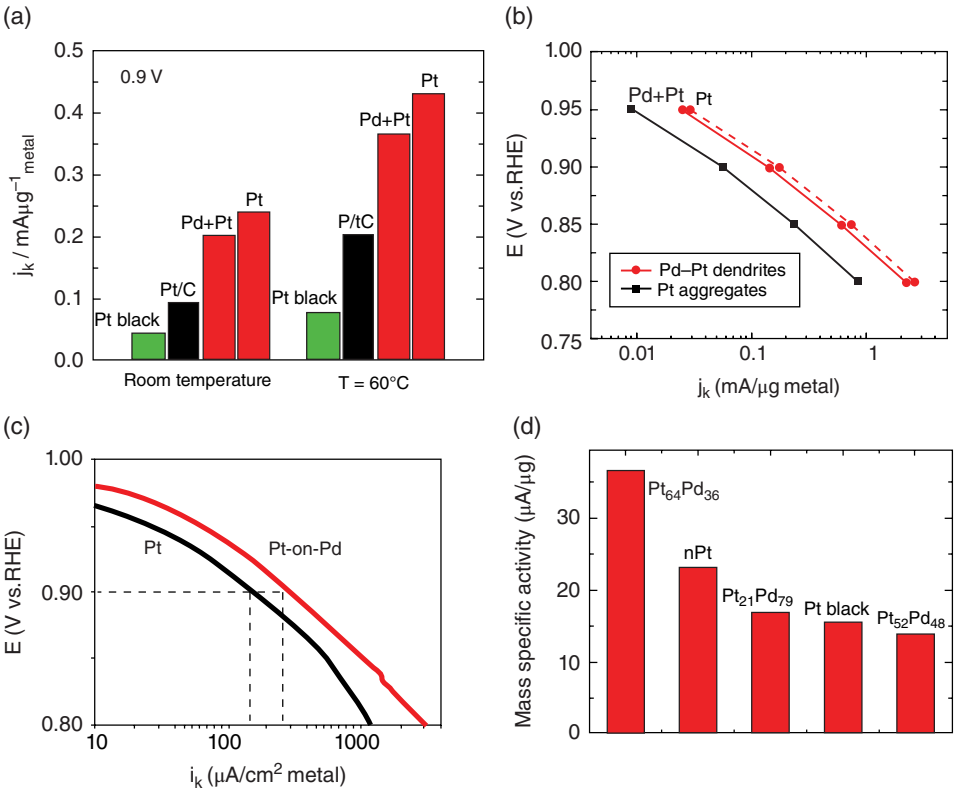

Figure 7.12 (a) Mass activity (at 0.9 V vs. RHE) for Pt–Pd nanodendrites, Pt/C and Pt black, given as kinetic current densities (j_k) normalized in reference to the loading amount. Reprinted with permission from ref. [51]. Copyright 2009, American Association for the Advancement of Science. (b) Mass activities of the Pt–Pd nanodendrites and Pt aggregates, given as kinetic current densities (j_k) normalized against the loading amount of metal (break line is the activity based on the mass of Pt). Reprinted with permission from ref. [31]. Copyright (2010), Tsinghua University Press and Springer-Verlag Belin Heidelberg. (c) Specific kinetic current densities (i_k) for carbon-supported Pt-Pd and Pt samples. Reprinted with permission from ref. [52]. Copyright 2009, American Chemical Society. (d) Plot of the mass activity of the Pt and Pt–Pd samples. Rotation rate: 1600 rpm. Ring potential: 0.85 V. Scan rate: 5 mV s^{-1}. Reprinted with permission from ref. [27]. Copyright (2013), Royal Society of Chemistry.

which the activity of Pt(111) was superior to Pt(100). However, when carrying out ORR in H_2SO_4, Pt(100) is more active than Pt(111). Raj et al. synthesized Pt–Pd nanodendrites with different compositions and investigated their properties toward ORR[27]. Figure 7.12d shows a mass activity order of $Pt_{64}Pd_{36}$ > Pt nanoparticles > $Pt_{21}Pd_{79}$ > Pt black > $Pt_{52}Pd_{48}$ obtained at 0.9 V in a H_2SO_4 solution. The $Pt_{64}Pd_{36}$ nanodendrites showed a higher activity than pure Pt nanoparticles, which is attributed to the downshift of the d-band center of the sample arising from the Pt@Pd core–shell nanostructure. And it can reduce the adsorption of OH_{ad} on Pt, too. Furthermore, the $Pt_{64}Pd_{36}$ sample exposed more Pt(100) than the $Pt_{21}Pd_{79}$ and $Pt_{52}Pd_{48}$ with more Pt(111). The $Pt_{21}Pd_{79}$ sample was superior to the $Pt_{52}Pd_{48}$ one, which might be due to the fewer formation of Pt-OH_{ad} and the maximum utilization of Pt.

7.4 Conclusion and Outlook

In recent years, many kinds of bimetallic nanocrystals with well-defined shape and surface structure have been synthesized due to the progress of shape-controlled synthetic chemistry and techniques. However, the investigations of the bimetallic dendritic nanostructures are still in a primary stage in contrast to the conventional morphologies like nanopolyhedrons and nanospheres. In this chapter, we have introduced some common synthesis methods, properties, and applications of the bimetallic dendritic nanostructures in brief. As classical synthesis strategies for the bimetallic nanocrystals, coreduction, galvanic replacement reaction as well as seed-mediated growth methods and their corresponding synthetic examples were introduced here. Then we discussed the properties and applications of the bimetallic dendritic nanostructures on optics and catalysis. In general, they have great potentials on SERS and electrocatalysis including MOR and ORR.

Though various synthetic strategies have been successfully created in the past years, efficient methods to obtain the bimetallic dendritic nanostructures in a large scale still need to be developed. And there are still some questions unsolved about both on the growth mechanism and catalytic properties of the bimetallic nanodendrites. On the one hand, different synthesis methods have different growth mechanisms, and these mechanisms are not always clear. For instance, is the nucleation heterogeneous or homogeneous, or both of them existing? Are the nanostructures obtained through continuous growth or oriented attachment? And in a galvanic replacement reaction, why do these nanodendrites rather than other nanostructures come into being? On the other hand, the structure-activity relationship of the bimetallic nanodendrites is still unclear in applications such as SERS and catalysis. Researchers ascribe the enhanced SERS activities of the bimetallic nanodendrites to the enhanced electromagnetic field originated from the pinholes existing in the dendritic nanostructures, but there is no direct evidence to confirm that. Therefore, more delicate characterizations such as *in situ* or *operando* techniques are required for a deeper insight into the growth mechanism and the structure-activity relationship between the enhancement of the activity and the highly branched structure. Furthermore, these fascinating nanostructures are supposed to be expanded to more bimetallic systems other than Au, Ag, Cu, Pt, Pd, and more applications besides SERS, MOR, and ORR. For example, Rh and Ir are two of the most expensive metals due to their rarity, while they are relatively useful in many applications, such as ethanol oxidation reaction (EOR) and oxygen evolution reaction (OER). It is expected that Rh- and Ir-based bimetallic dendritic nanostructures will result in an enhanced activity, with reducing the limitation of their applications caused by their high prices.

7.5 References

1 Baghbani-Arani, F., Movagharnia, R., Sharifian, A., Salehi, S., Shandiz, S. A. S. (2017). Photo-catalytic, anti-bacterial, and anti-cancer properties of phyto-mediated synthesis of silver nanoparticles from Artemisia tournefortiana Rchb extract. *Journal of Photochemistry and Photobiology B: Biology*, 173, 640–649.

2 Benkato, K., O'Brien, B., Bui, M. N., Jasinski, D. L., Guo, P., Khisamutdinov, E. F. (2017). Evaluation of thermal stability of RNA nanoparticles by temperature gradient gel electrophoresis (TGGE) in native condition, 123–133.

3 Blaber, M. G., Arnold, M. D., Ford, M. J. (2010). A review of the optical properties of alloys and intermetallics for plasmonics. *Journal of Physics: Condensed Matter*, 22(14), 143201.

4 Cortie, M. B., McDonagh, A. M. (2011). Synthesis and optical properties of hybrid and alloy plasmonic nanoparticles. *Chemical Reviews*, 111(6), 3713–3735.

5 Ferrando, R., Jellinek, J., Johnston, R. L. (2008). Nanoalloys: from theory to applications of alloy clusters and nanoparticles. *Chemical Reviews*, 108(3), 845–910.

6 Kakati, N., Maiti, J., Lee, S. H., Jee, S. H., Viswanathan, B., Yoon, Y. S. (2014). Anode catalysts for direct methanol fuel cells in acidic media: do we have any alternative for Pt or Pt–Ru? *Chemical Reviews*, 114(24), 12397–12429.

7 Kwizera, E. A., Chaffin, E., Wang, Y., Huang, X. (2017). Synthesis and properties of magnetic-optical core-shell nanoparticles. *RSC Advances*, 7(28), 17137–17153.

8 Li, G., Feng, L., Chang, J., Wickman, B., Grönbeck, H., Liu, C., Xing, W. (2014). Activity of platinum/carbon and palladium/carbon catalysts promoted by Ni2P in direct ethanol fuel cells. *ChemSusChem*, 7(12), 3374–3381.

9 Motl, N. E., Smith, A. F., DeSantis, C. J., Skrabalak, S. E. (2014). Engineering plasmonic metal colloids through composition and structural design. *Chemical Society Reviews*, 43(11), 3823–3834.

10 Schuller, J. A., Barnard, E. S., Cai, W., Jun, Y. C., White, J. S., Brongersma, M. L. (2010). Plasmonics for extreme light concentration and manipulation. *Nat Materials*, 9(3), 193–204.

11 Sebastián, D., Serov, A., Artyushkova, K., Gordon, J., Atanassov, P., Aricò, A. S., Baglio, V. (2016). High performance and cost-effective direct methanol fuel cells: Fe-N-C methanol-tolerant oxygen reduction reaction catalysts. *ChemSusChem*, 9(15), 1986–1995.

12 Yu, Y., Zhang, Q., Yao, Q., Xie, J., Lee, J. Y. (2014). Architectural design of heterogeneous metallic nanocrystals—principles and processes. *Accounts of Chemical Research*, 47(12), 3530–3540.

13 Gilroy, K. D., Ruditskiy, A., Peng, H.-C., Qin, D., Xia, Y. (2016). Bimetallic nanocrystals: syntheses, properties, and applications. *Chemical Reviews*, 116(18), 10414–10472.

14 Lim, B., Xia, Y. (2011). Metal nanocrystals with highly branched morphologies. *Angewandte Chemie International Edition*, 50(1), 76–85.

15 Ye, E., Regulacio, M. D., Zhang, S.-Y., Loh, X. J., Han, M.-Y. (2015). Anisotropically branched metal nanostructures. *Chemical Society Reviews*, 44(17), 6001–6017.

16 Bolocan, A., Mihaiescu, D. E., Meşterca, A. R., Spirescu, V. A., Tote, E. M., Mogoantă, L., Mogoşanu, G. D., Grumezescu, A. M. (2015). In vitro and in vivo applications of 3D dendritic gold nanostructures. *Romanian journal of morphology and embryology = Revue roumaine de morphologie et embryologie*, 56(3), 915–924.

17 Fang, J., You, H., Kong, P., Yi, Y., Song, X., Ding, B. (2007). Dendritic silver nanostructure growth and evolution in replacement reaction. *Crystal Growth & Design*, 7(5), 864–867.

18 Qiu, R., Cha, H. G., Noh, H. B., Shim, Y. B., Zhang, X. L., Qiao, R., Zhang, D., Kim, Y. I., Pal, U., Kang, Y. S. (2009). Preparation of dendritic copper nanostructures and their characterization for electroreduction. *The Journal of Physical Chemistry C*, 113(36), 15891–15896.

19 Wang, Y., Camargo, P. H. C., Skrabalak, S. E., Gu, H., Xia, Y. (2008). A facile, water-based synthesis of highly branched nanostructures of silver. *Langmuir*, 24(20), 12042–12046.

20 Weiner, R. G., DeSantis, C. J., Cardoso, M. B. T., Skrabalak, S. E. (2014). Diffusion and seed shape: intertwined parameters in the synthesis of branched metal nanostructures. *ACS Nano*, 8(8), 8625–8635.

21 López, C. M., Choi, K.-S. (2006). Electrochemical synthesis of dendritic zinc films composed of systematically varying motif crystals. *Langmuir*, 22(25), 10625–10629.

22 Yan, C., Xue, D. (2008). A modified electroless deposition route to dendritic Cu metal nanostructures. *Crystal Growth & Design*, 8(6), 1849–1854.

23 Pradhan, M., Maji, S., Sinha, A. K., Dutta, S., Pal, T. (2015). Sensing trace arsenate by surface enhanced Raman scattering using a FeOOH doped dendritic Ag nanostructure. *Journal of Materials Chemistry A*, 3(19), 10254–10257.

24 Wen, X., Xie, Y.-T., Mak, W. C., Cheung, K. Y., Li, X.-Y., Renneberg, R., Yang, S. (2006). Dendritic nanostructures of silver: facile synthesis, structural characterizations, and sensing applications. *Langmuir*, 22(10), 4836–4842.

25 Chen, L.-X., Jiang, L.-Y., Wang, A.-J., Chen, Q.-Y., Feng, J.-J. (2016). Simple synthesis of bimetallic AuPd dendritic alloyed nanocrystals with enhanced electrocatalytic performance for hydrazine oxidation reaction. *Electrochimica Acta*, 190, 872–878.

26 Cheng, L.-C., Huang, J.-H., Chen, H. M., Lai, T.-C., Yang, K.-Y., Liu, R.-S., Hsiao, M., Chen, C.-H., Her, L.-J., Tsai, D. P. (2012). Seedless, silver-induced synthesis of star-shaped gold/silver bimetallic nanoparticles as high efficiency photothermal therapy reagent. *Journal of Materials Chemistry*, 22(5), 2244–2253.

27 Ghosh, S., Mondal, S., Retna Raj, C. (2014). Carbon nanotube-supported dendritic Pt-on-Pd nanostructures: growth mechanism and electrocatalytic activity towards oxygen reduction reaction. *Journal of Materials Chemistry A*, 2(7), 2233–2239.

28 Lin, C.-T., Shiao, M.-H., Chang, M.-N., Chu, N., Chen, Y.-W., Peng, Y.-H., Liao, B.-H., Huang, H. J., Hsiao, C.-N., Tseng, F.-G. (2015). A facile approach to prepare silicon-based Pt-Ag tubular dendritic nano-forests (tDNFs) for solar-light-enhanced methanol oxidation reaction. *Nanoscale Research Letters*, 10(1), 74.

29 Yi, Z., Tan, X., Niu, G., Xu, X., Li, X., Ye, X., Luo, J., Luo, B., Wu, W., Tang, Y., Yi, Y. (2012). Facile preparation of dendritic Ag–Pd bimetallic nanostructures on the surface of Cu foil for application as a SERS-substrate. *Applied Surface Science*, 258(14), 5429–5437.

30 Zhang, J., Ma, J., Wan, Y., Jiang, J., Zhao, X. S. (2012). Dendritic Pt–Cu bimetallic nanocrystals with a high electrocatalytic activity toward methanol oxidation. *Materials Chemistry and Physics*, 132(2), 244–247.

31 Lim, B., Jiang, M., Yu, T., Camargo, P. H. C., Xia, Y. (2010). Nucleation and growth mechanisms for Pd-Pt bimetallic nanodendrites and their electrocatalytic properties. *Nano Research*, 3(2), 69–80.

32 Wang, C., Fang, J., Jin, Y., Cheng, M. (2011). Fabrication and surface-enhanced Raman scattering (SERS) of Ag/Au bimetallic films on Si substrates. *Applied Surface Science*, 258(3), 1144–1148.

33 Chen, L., Chabu, J. M., Liu, Y. (2013). Bimetallic AgM (M = Pt, Pd, Au) nanostructures: synthesis and applications for surface-enhanced Raman scattering. *RSC Advances*, 3(13), 4391–4399.

34 Li, W., Kuai, L., Qin, Q., Geng, B. (2013). Ag–Au bimetallic nanostructures: co-reduction synthesis and their component-dependent performance for enzyme-free H2O2 sensing. *Journal of Materials Chemistry A*, 1(24), 7111–7117.

35 Sun, L., Zhang, Q., Li, G. G., Villarreal, E., Fu, X., Wang, H. (2017). Multifaceted gold–palladium bimetallic nanorods and their geometric, compositional, and catalytic tunabilities. *ACS Nano*, 11(3), 3213–3228.

36 Zhang, B., Guo, R., Liu, X. (2008). Synthesis and characterization of nanostructured bimetallic films on α-Al2O3 substrates using electroless deposition. *Applied Surface Science*, 254(17), 5394–5398.

37 Lohse, S. E., Burrows, N. D., Scarabelli, L., Liz-Marzán, L. M., Murphy, C. J. (2014). Anisotropic noble metal nanocrystal growth: the role of halides. *Chemistry of Materials*, 26(1), 34–43.

38 Zhang, L., Zhang, J., Kuang, Q., Xie, S., Jiang, Z., Xie, Z., Zheng, L. (2011). Cu^{2+}-assisted synthesis of hexoctahedral Au–Pd alloy nanocrystals with high-index facets. *Journal of the American Chemical Society*, 133(43), 17114–17117.

39 Chen, L., Liu, Y. (2011). Synthesis and characterization of dendritic and porous Ag–Pd alloy nanostructures. *Journal of Colloid and Interface Science*, 364(1), 100–106.

40 Kang, S., Gao, G., Xie, X., Shibayama, T., Lei, Y., Wang, Y., Cai, L. (2016). Synthesis of surfactant-free Cu–Pt dendritic heterostructures with highly electrocatalytic performance for methanol oxidation reaction. *Materials Research Letters*, 4(4), 212–218.

41 Chen, X., Cui, C.-H., Guo, Z., Liu, J.-H., Huang, X.-J., Yu, S.-H. (2011). Unique heterogeneous silver–copper dendrites with a trace amount of uniformly distributed elemental Cu and their enhanced SERS properties. *Small*, 7(7), 858–863.

42 Kang, Y., Chen, F. (2013). Preparation of Ag–Cu bimetallic dendritic nanostructures and their hydrogen peroxide electroreduction property. *Journal of Applied Electrochemistry*, 43(7), 667–677.

43 Rahmatolahzadeh, R., Ebadi, M., Motevalli, K. (2017). Preparation and characterization of Cu clusters and Cu–Ag alloy via galvanic replacement method for azo dyes degradation. *Journal of Materials Science: Materials in Electronics*, 28(8), 6056–6063.

44 Yi, Z., Chen, S., Chen, Y., Luo, J., Wu, W., Yi, Y., Tang, Y. (2012). Preparation of dendritic Ag/Au bimetallic nanostructures and their application in surface-enhanced Raman scattering. *Thin Solid Films*, 520(7), 2701–2707.

45 Dong, J., Ye, Y., Zhang, W., Ren, Z., Huo, Y., Zheng, H. (2015). Preparation of Ag/Au bimetallic nanostructures and their application in surface-enhanced fluorescence. *Luminescence*, 30(7), 1090–1093.

46 Yi, Z., Zhang, J.-B., Chen, Y., Chen, S.-J., Luo, J.-S., Tang, Y.-J., Wu, W.-D., Yi, Y.-G. (2011). Triangular Au–Ag framework nanostructures prepared by multi-stage replacement and their spectral properties. *Transactions of Nonferrous Metals Society of China*, 21(9), 2049–2055.

47 Hu, Y., Zhang, A.-Q., Li, H.-J., Qian, D.-J., Chen, M. (2016). Synthesis, study, and discrete dipole approximation simulation of Ag–Au bimetallic nanostructures. *Nanoscale Research Letters*, 11(1), 209.

48 Li, Q., Jiang, R., Ming, T., Fang, C., Wang, J. (2012). Crystalline structure-dependent growth of bimetallic nanostructures. *Nanoscale*, 4(22), 7070–7077.

49 Rong, Y., Dandapat, A., Huang, Y., Sasson, Y., Zhang, L., Dai, L., Zhang, J., Guo, Z., Chen, T. (2016). Spatially-controlled growth of platinum on gold nanorods with tailoring plasmonic and catalytic properties. *RSC Advances*, 6(13), 10713–10718.

50 Satija, J., Tharion, J., Mukherji, S. (2015). Facile synthesis of size and wavelength tunable hollow gold nanostructures for the development of a LSPR based label-free fiber-optic biosensor. *RSC Advances*, 5(86), 69970–69979.

51 Lim, B., Jiang, M., Camargo, P. H. C., Cho, E. C., Tao, J., Lu, X., Zhu, Y., Xia, Y. (2009). Pd–Pt Bimetallic nanodendrites with high activity for oxygen reduction. *Science*, 324(5932), 1302–1305.

52 Peng, Z., Yang, H. (2009). Synthesis and oxygen reduction electrocatalytic property of Pt-on-Pd bimetallic heteronanostructures. *Journal of the American Chemical Society*, 131(22), 7542–7543.

53 Wang, L., Nemoto, Y., Yamauchi, Y. (2011). Direct synthesis of spatially-controlled Pt-on-Pd bimetallic nanodendrites with superior electrocatalytic activity. *Journal of the American Chemical Society*, 133(25), 9674–9677.

54 Zhou, S., McIlwrath, K., Jackson, G., Eichhorn, B. (2006). Enhanced CO tolerance for hydrogen activation in Au – Pt dendritic heteroaggregate nanostructures. *Journal of the American Chemical Society*, 128(6), 1780–1781.

55 Allendorf, M. D. (2016). Oxygen reduction reaction: a framework for success. *Nature Energy*, 1(5), 16058.

56 Liu, J., Jiao, M., Lu, L., Barkholtz, H. M., Li, Y., Wang, Y., Jiang, L., Wu, Z., Liu, D.-J., Zhuang, L., Ma, C., Zeng, J., Zhang, B., Su, D., Song, P., Xing, W., Xu, W., Wang, Y., Jiang, Z., Sun, G. (2017). High performance platinum single atom electrocatalyst for oxygen reduction reaction. *Nature Communications*, 8, 15938.

57 Shao, M., Chang, Q., Dodelet, J.-P., Chenitz, R. (2016). Recent advances in electrocatalysts for oxygen reduction reaction. *Chemical Reviews*, 116(6), 3594–3657.

58 Zhang, Y., Hsieh, Y.-C., Volkov, V., Su, D., An, W., Si, R., Zhu, Y., Liu, P., Wang, J. X., Adzic, R. R. (2014). High performance Pt monolayer catalysts produced via core-catalyzed coating in ethanol. *ACS Catalysis*, 4(3), 738–742.

59 Zhuang, L., Wang, W., Hong, F., Yang, S., You, H., Fang, J., Ding, B. (2012). Porous platinum mesoflowers with enhanced activity for methanol oxidation reaction. *Journal of Solid State Chemistry*, 191, 239–245.

60 Gao , C., Lu , Z., Liu , Y., Zhang, Q., Chi, M., Cheng, Q., Yin, Y. (2012). Highly stable silver nanoplates for surface plasmon resonance biosensing. *Angewandte Chemie International Edition*, 51(23), 5629–5633.

61 Sanedrin, R. G., Georganopoulou, D. G., Park, S., Mirkin, C. A. (2005). Seed-mediated growth of bimetallic prisms. *Advanced Materials*, 17(8), 1027–1031.

62 Yang, Y., Liu, J., Fu, Z.-W., Qin, D. (2014). Galvanic replacement-free deposition of Au on Ag for core–shell nanocubes with enhanced chemical stability and SERS activity. *Journal of the American Chemical Society*, 136(23), 8153–8156.

63 Qiu, R., Zhang, X. L., Qiao, R., Li, Y., Kim, Y. I., Kang, Y. S. (2007). CuNi dendritic material: synthesis, mechanism discussion, and application as glucose sensor. *Chemistry of Materials*, 19(17), 4174–4180.

64 Tong, S., Xu, Y., Zhang, Z., Song, W. (2010). Dendritic bimetallic nanostructures supported on self-assembled titanate films for sensor application. *The Journal of Physical Chemistry C*, 114(49), 20925–20931.

65 Peng, Z., Yang, H. (2009). PtAu bimetallic heteronanostructures made by post-synthesis modification of Pt-on-Au nanoparticles. *Nano Research*, 2(5), 406–415.

66 Hutter, E., Fendler, J. H. (2004). Exploitation of localized surface plasmon resonance. *Advanced Materials*, 16(19), 1685–1706.

67 Liu, Z., Aydin, K. (2016). Localized surface plasmons in nanostructured monolayer black phosphorus. *Nano Letters*, 16(6), 3457–3462.

68 Luther, J. M., Jain, P. K., Ewers, T., Alivisatos, A. P. (2011). Localized surface plasmon resonances arising from free carriers in doped quantum dots. *Nat Mater*, 10(5), 361–366.

69 Nishi, H., Hiroya, S., Tatsuma, T. (2015). Potential-scanning localized surface plasmon resonance sensor. *ACS Nano*, 9(6), 6214–6221.

70 Willets, K. A., Van Duyne, R. P. (2007). Localized surface plasmon resonance spectroscopy and sensing. *Annual Review of Physical Chemistry*, 58(1), 267–297.

71 Hu, Y., Li, X., Yan, L., Yue, B. (2017). Improving the overall characteristics of proton exchange membranes via nanophase separation technologies: a progress review. *Fuel Cells*, 17(1), 3–17.

72 Huo, W., Ye, L., Lv, W., Niu, Y., Fei, J., Waqas, M., He, W. (2016). Reduced electrochemical performances of proton exchange membrane fuel cells due to gaseous diffusion in electrolytes. *RSC Advances*, 6(99), 97194–97198.

73 Ke, C., Li, J., Li, X., Shao, Z., Yi, B. (2012). Protic ionic liquids: an alternative proton-conducting electrolyte for high temperature proton exchange membrane fuel cells. *RSC Advances*, 2(24), 8953–8956.

74 Li, P., Mi, W., Su, Q., Luo, C. (2014). Catalytic oxidation of methanol by aqueous POM on Al_2O_3 supported catalysts and electrochemical performance of POM. *Fuel Cells*, 14(1), 56–63.

75 Li, X., Hodson, H., Batchelor-McAuley, C., Shao, L., Compton, R. G. (2016). Improving formate and methanol fuels: catalytic activity of single Pd coated carbon nanotubes. *ACS Catalysis*, 6(10), 7118–7124.

76 Wang, C.-H., Hsu, H.-C., Chang, S.-T., Du, H.-Y., Chen, C.-P., Wu, J. C.-S., Shih, H.-C., Chen, L.-C., Chen, K.-H. (2010). Platinum nanoparticles embedded in pyrolyzed nitrogen-containing cobalt complexes for high methanol-tolerant oxygen reduction activity. *Journal of Materials Chemistry*, 20(35), 7551–7557.

77 Knudsen, J., Nilekar, A. U., Vang, R. T., Schnadt, J., Kunkes, E. L., Dumesic, J. A., Mavrikakis, M., Besenbacher, F. (2007). A Cu/Pt near-surface alloy for water – gas shift catalysis. *Journal of the American Chemical Society*, 129(20), 6485–6490.

78 Guo, C., Zheng, Y., Ran, J., Xie, F., Jaroniec, M., Qiao, S.-Z. (2017). Engineering high-energy interfacial structures for high-performance oxygen-involving electrocatalysis. *Angewandte Chemie International Edition*, 56(29), 8539–8543.

79 Kamai, R., Kamiya, K., Hashimoto, K., Nakanishi, S. (2016). Oxygen-tolerant electrodes with platinum-loaded covalent triazine frameworks for the hydrogen oxidation reaction. *Angewandte Chemie International Edition*, 55(42), 13184–13188.

80 Liu, Y., Mustain, W. E. (2013). High stability, high activity Pt/ITO oxygen reduction electrocatalysts. *Journal of the American Chemical Society*, 135(2), 530–533.

8

Bimetallic Ultrathin Nanowires

Junrui Li, Zheng Xi, and Shouheng Sun

Department of Chemistry, Brown University, Providence, Rhode Island, USA

8.1 Introduction

Controlling nanomaterial sizes, shapes, and crystal structures is essential to tune their optical, electronic, magnetic and catalytic properties[1]. This requires first developing reliable synthetic processes that can lead to the formation of nanomaterials with both inside and surface structures controlled at the atomic precision. Recent research progress has made it possible to synthesize monodisperse nanomaterials with tunable/enhanced functionalities[2]. Depending on the process involved in each synthesis, we may categorize these methods as top-down method[3], hard-template method[4], sol-gel process[5,6], micelle-mediated process[7,8], precipitation method[9], hydrothermal synthesis[10], and microwave-assisted synthesis[11,12], which have all been well-summarized in literature. In addition, the high-temperature solution-phase synthesis takes advantage of homogeneous solution-phase reaction in the presence of a capping agent or a combination of capping agents to control nanoparticle nucleation and growth, and has become a popular choice for producing ultrafine nanomaterials with near-atomic precision controls on nanomaterial dimensions, compositions, and structures[13–16].

Ultrathin nanowires represent a new class of nanomaterials with their components confined and structure extended only in one dimension. In previous publications, the dimension range of ultrathin nanowires is not explicitly specified. Summarizing from various reports, in this chapter, we define the ultrathin nanowires as those with wire diameter less than 10 nm and aspect ratio > 5. Traditionally, nanowires are made via chemical reactions in porous alumina[17], polycarbonate membrane, and carbon nanotubes[18]. However, this hard template-assisted synthesis does have its limit in incorporating multicomponent metals into the wire structure and in controlling the ultrafine wire dimensions. More and more efforts are now being made toward finding homogeneous solution phase reactions for the preparation of ultrathin nanowires in which the reaction condition can be carefully monitored to inhibit the growth of thermodynamically more stable polyhedral nanoparticles[19]. In these syntheses, the growth of

Bimetallic Nanostructures: Shape-Controlled Synthesis for Catalysis, Plasmonics, and Sensing Applications, First Edition. Edited by Ya-Wen Zhang.
© 2018 John Wiley & Sons Ltd. Published 2018 by John Wiley & Sons Ltd.

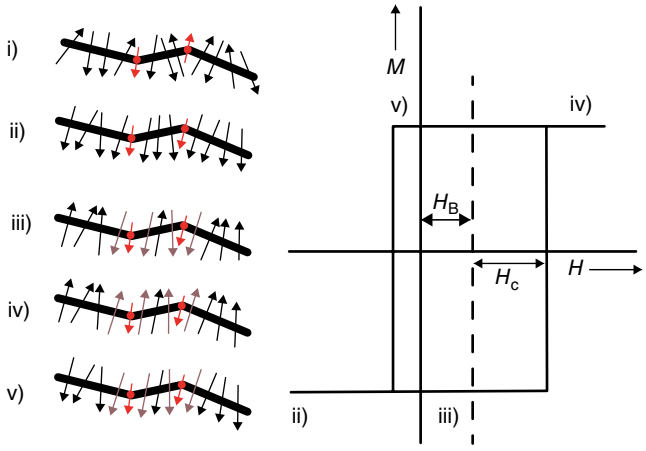

Figure 8.1 Moment configuration of ultrathin Pt or Pd nanowires at different stages in a shifted hysteresis loop. (i) Random regular moments and "localized" moments seen at "vulnerable" lattice structures in the nanowire without a magnetic field, (ii) all moments are aligned after cooling to a certain temperature in the presence of a field; (iii) the regular moments rotate in the opposite direction and the localized moments remain "locked" when the field is reversed. Some moments align preferentially in the direction of adjacent "locked" moments due to interfacial interactions. In other words, "locked" moments exert a microscopic torque on the adjacent moments; (iv) an extra field (H_B) is needed to overcome the microscopic torque and completely reverse the moments; (v) when the field returns to its original direction, the aligned moments are reversed in the smaller field (H_C—H_B) because the "localized" moments exert a torque in the same direction as the field. Reproduced with permission from ref. [21]. Copyright (2008), Wiley-VCH Verlag GmbH & Co. KGaA, Weinheim.

ultrathin nanowires is often realized by differentiating the small binding difference between a capping agent and different crystal facets, or by channeling the reaction in an ultrathin one-dimensional micelle or reverse-micelle template[11]. Once properly prepared, ultrathin metallic nanowires can show some very interesting quantized/ballistic conduction[20], ferromagnetism[21], and highly efficient catalysis[22,23], which are tunable by their anisotropic/multifunctional structures. For example, Pt or Pd ultrathin nanowires become ferromagnetic while their bulk or nanoparticle counterparts are paramagnetic or superparamagnetic[21]. The ferromagnetism was believed to arise from magneto-elastic coupling along the radial direction of the wires, as shown in Figure 8.1. The "defects" in the nanowire structure (e.g., twin boundaries, stacking faults, and bending of nanowires) were proposed to contribute to the random magnetic moment, and they are aligned when an external magnetic field is applied. Conductive metallic nanowires can also be assembled into a network[24], that shows promises for future flexible electronics[25], or as free-standing catalysts to simplify chemical reaction processes[26]. For instance, ultrathin Ag nanowires assembled into a three-dimensional array show interesting quantum transport along the one-dimensional structure. Such coherently oriented array of ultrathin metallic nanowires may function as nanoconnectors required to build nanoscale electronic circuits. Furthermore, the ultrathin nature of these nanowires facilitates their colloidal stability and their surface modifications in solutions, especially in biological solutions, making it possible to

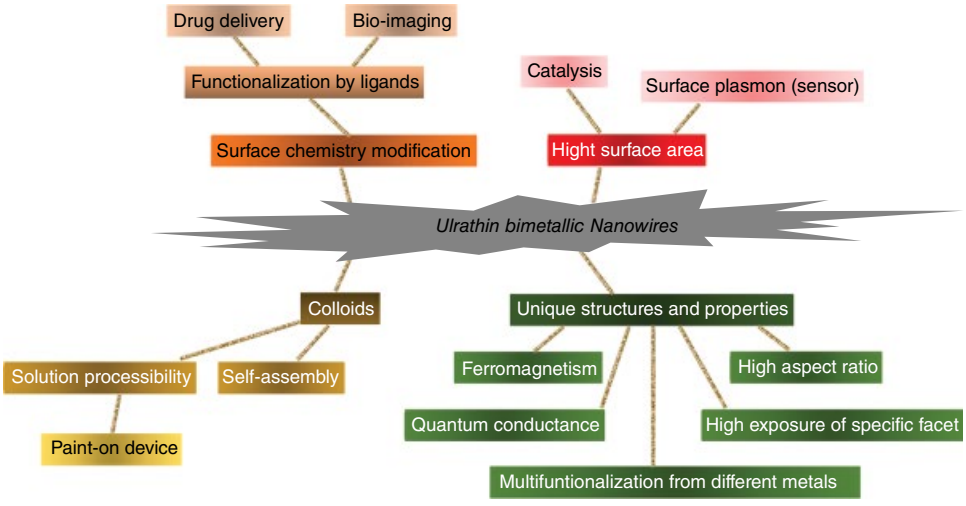

Figure 8.2 Potentials of ultrathin bimetallic nanowires in various areas of research interests and applications.

develop nanowire-based devices for sensing[27] and biodetection[28]. These properties and application potentials (Figure 8.2) can be further tuned by nanowire compositions, making the studies of bimetallic (or multimetallic) ultrathin nanowires especially attractive[29].

8.2 Chemical Synthesis of Ultrathin Bimetallic Nanowires

8.2.1 Synthetic Fundamentals

Chemical synthesis of nanomaterials can follow different mechanisms, but it generally involves the nucleation and growth processes when the growing materials (solutes) reach supersaturation in a specific solvent. This supersaturation condition can be created by dissolving a proper amount of solutes in the solvent[1]. Once the concentration of the solutes drops below the supersaturation threshold, the growth of nanoparticles dominates the reaction process and the growth is accomplished by adding monomers to the existing nuclei or by Ostwarld ripening. This procedure has been well-described in the classical LaMer model as illustrated in Figure 8.3. LaMer and Dinegar proposed that the processes leading to the formation of monodisperse nanoparticles involve three main stages: (I) concentration of the monomers present in the solution reaches the nucleation threshold and supersaturation is created; (II) a rapid self-nucleation occurs to form a large number of nuclei and the monomers are consumed in the meantime, which results in the decrease of monomer concentration below the supersaturation threshold, preventing any possible new nucleation process from occurring; (III) total free energy of the system drives the addition of monomers to the existing nuclei and promotes Ostwald ripening, forming larger particles by consuming the smaller ones.

Capable of controlling the reaction condition at each of these three stages is essential to produce nanoparticles with narrow size (less than 10% standard deviation in

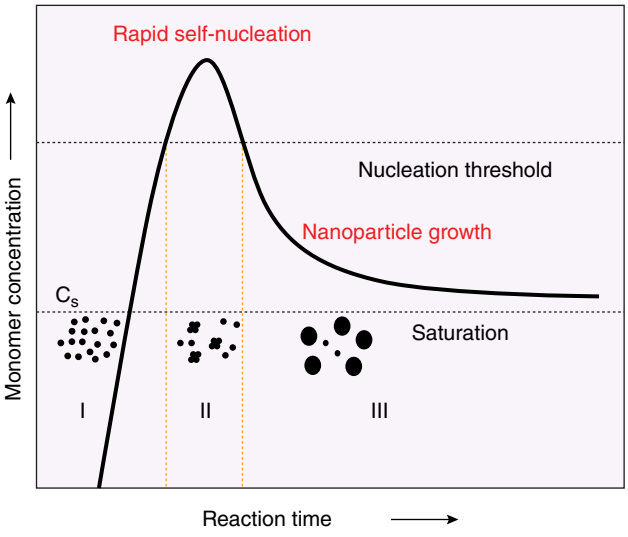

Figure 8.3 LaMer model of the nucleation and growth process to monodisperse nanoparticles. Reproduced from ref. [30] with permission. Copyright (1950), American Chemical Society.

diameter) and shape distributions. In principle, a short nucleation stage offers a foundation for the formation of monodisperse nanoparticles. Whether the nuclei grow or dissolve is determined by the critical size (r^*) of these nuclei and the concentration of the monomers present in the reaction solution[31]. With the monomers being consumed and their concentration being dropped, Ostwald ripening may proceed by dissolving thermodynamically unstable smaller particles and by growing the dissolved monomers onto the larger particles. At this stage, the reaction time needs to be extended to consume the smaller particles and to obtain nanoparticle product with a narrow size distribution. Care must be taken here to avoid the overgrowth of the particles. Alternatively, the synthesis may proceed via the Finke-Watzky two-step mechanism in which slow continuous nucleation is followed by rapid particle growth[32]. In this mechanism, continuous and slow nucleation occurs in a solution that is far from supersaturated and the growth is completed by an autocatalytic process that facilitates surface atom depositions.

8.2.2 Anisotropic Growth into Ultrathin Nanowires

The growth of nanoparticles often favors the deposition and migration of adatoms on different crystal facets to minimize the nanoparticle surface energy. An anisotropic growth of nanoparticles is a kinetically controlled process in which adatoms are deposited onto a specific crystal facet or along a certain crystal direction. In the solution-phase-based synthesis, this anisotropic growth is often controlled by differential interactions of a capping agent with different crystal facets. In general, a strong binding of the capping agent to a specific facet would block the access of adatoms to this facet, leading to the preferential growth of the nanoparticles on the facet that is weakly bound by the capping agent. Various synthetic strategies have been developed to explore this capping agent induced anisotropic growth into nanowires, including micelle-mediated

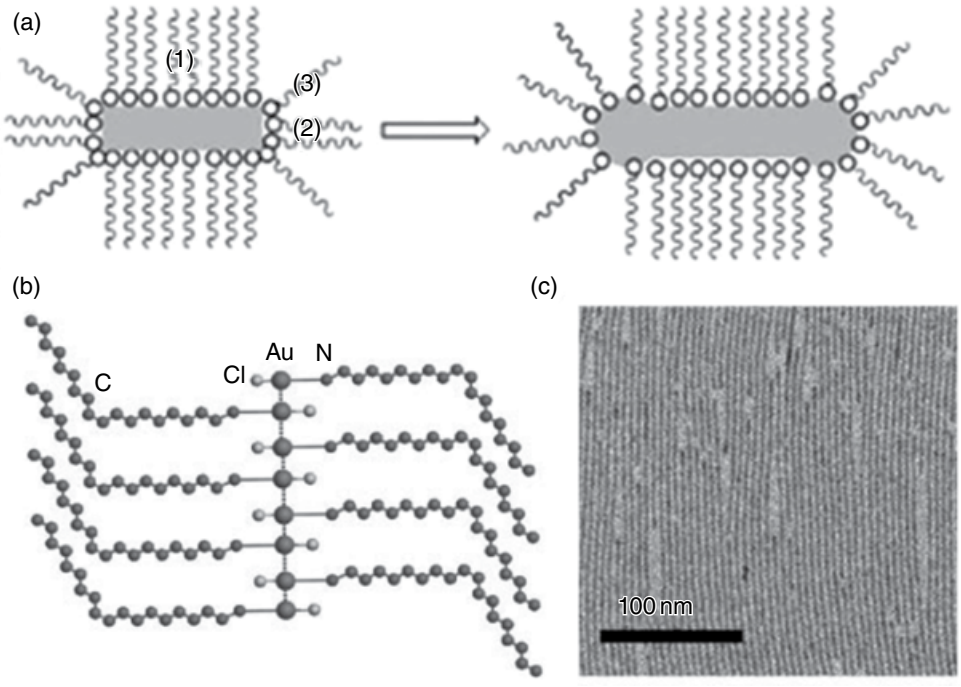

Figure 8.4 (a) Schematic illustration of the micellar-mediated growth of ultrathin nanowires templated by alkylamines. Reproduced with permission from ref. [34]. Copyright (2007), Wiley-VCH Verlag GmbH & Co. KGaA, Weinheim. (b) Schematic illustration of linear chain formed by [(oleylamine) $AuCl]_n$ inorganic polymers, which lead to the formation of gold ultrathin nanowires. Reproduced with permission from ref. [38]. Copyright (2008), American Chemical Society. (c) TEM images of Au nanowires with 500 nm in length and 2 nm in diameter via the seed-mediated synthesis method. Reproduced with permission from ref. [39]. Copyright (2014), American Chemical Society.

growth[33,34], seed-mediated growth[33], kinetically controlled growth[35], oxidative etching[36], and aggregation-directed growth[37].

The micelle-mediated growth method is to guide the growth of nanowires in a micelle or reverse-micelle structure formed by amphiphilic molecules via a self-assembly process. Long-chain alkylamines, such as oleylamine, are commonly used for the synthesis as they serve both as a "soft-template" and as a reducing agent to slowly reduce metal cations into metal atoms. The amine group at the end of the long-chain structure can also bond to the surface of the nanostructures to efficiently stabilize the structure against uncontrolled aggregation in the reaction medium. Due to the shape effect of the "soft-template" curvature, the alkylamines can only pack loosely at the tip of the curvature, which favors the deposition of adatoms onto the tip end, forming the nanowire structure. As illustrated in Figure 8.4a, area (1) is densely packed due to the self-assembly of the lipid molecules into the ordered organic structure, creating a hydrophobic barrier that prevents adatoms from easy deposition; area (2) is less densely packed due to the limited area exposed to the molecules, making it more easily for adatoms to deposit in this area; area (3) is most accessible to the adatoms. Overall, the easy deposition in area (2) and (3) plus the added heating leads to the formation of the

one-dimensional structure[34]. Alternatively, the ultrathin nanowires may be formed via a linear polymeric precursor as demonstrated in the synthesis of Au ultrathin nanowires. In this synthesis process, the Au salt precursor reacts with oleylamine, forming an [(oleylamine)AuCl] inorganic polymer (Figure 8.4b). The growth of nanowires proceeds via the reduction and coalescence of these polymers. The one-dimensional structure is stabilized by Au–Au bonds via aurophilic interaction together with the interaction between the long-chain oleylamine[38].

Seed-mediated synthesis of ultrathin nanowires involves a two-step process in which "seeding nanoparticles" are first synthesized, followed by an anisotropic growth process. The size of "seeding nanoparticles" can determine the diameter of the nanowires obtained[39,40], and the length of the nanowires is controlled by varying the ratio of the seeding nanoparticles to the metal salt precursor. Cetyltrimethylammonium bromide (CTAB)[33], poly-(vinylpyrrolidone) (PVP), alkylamines[39], or even halide ions[11] are often used as capping agents to guide the growth of nanowires. With careful control on the reaction condition, this seed-mediated growth method can yield very uniform ultrathin nanowires, as shown in the synthesis of ultrathin Au nanowires (Figure 8.4c).

The kinetically controlled growth of nanowires takes advantage of the surface energy differentiation created by surfactants attached to the surface of the existing nanostructures. The growth of nanowires depends on the competitive deposition rates of adatoms onto the different low-index crystal facets in the presence of surfactants. For example, in the synthesis of Au or Ag nanowires, deposition onto the (100) facet is inhibited by CTAB, and nanowires are formed via faster growth along the [111] direction[33,41]. In addition to CTAB-like surfactants, some peptides are also studied as facet-specific capping agent to control the growth of nanowires[42].

In the oxidative etching process, oxygen, metal ions, and halide ions are used to control the anisotropic growth. Trace amount of $FeCl_3$ or $FeCl_2$ can be added to slow the reduction rate of H_2PtCl_4 by oxidizing Pt back to Pt (II), which facilitates Pt deposition preferentially onto the (111) facet[43]. The presence of Fe-containing salts may also accelerate the reduction of Ag-salt for the formation of Ag nanowires[44]. The combination of halide ion and O_2 is commonly used as an effective etching oxidant to control the nucleation and growth of single crystal nanowires[45]. It is believed that the halide/O_2 combination tends to "smoothen" the defects or twin-boundaries formed during the nanowire growth stage. Such combination may also be used to reshape the nanowires.

Aggregation-directed growth utilizes the directional aggregation of the pre-formed nanoparticles into one-dimensional structures. Under certain conditions, self-organized nanoparticles can fuse together according to the diffusion-limited aggregation growth[46]. However, this method tends to yield nanowires without the desired nanowire structure control[47,48]. High temperatures and extended reaction time are generally needed to allow the nanoparticles fusion into nanowires.

8.3 Chemical Synthesis of Ultrathin Bimetallic Nanowires

The interests in synthesizing ultrathin metallic nanowires arise from the expected anisotropic properties confined uniquely in the one dimension of a few nanometer across. The first reports of ultrathin metallic nanowires via chemical synthesis method were Au and Ag nanowires synthesized in the existence of hexadecyltrimethylammonium

bromide, CTAB, or oleylamine[40,49–51]. In these syntheses, Au and Ag nanoparticles were first synthesized as seeds to mediate the growth of ultrathin nanowires with the wire diameters dependent on the size of the seeding nanoparticles. Direct reduction of metal precursors in PVP and CTAB usually led to the formation of nanowires with large diameters that are out of the ultrathin range defined in this chapter[52,53]. The ultrafine features obtained from these syntheses have inspired the extensive efforts on using similar chemical methods to prepare ultrathin nanowires containing more than one metal. Based on the morphology and structure features, in this chapter, we divide these nanowires in the following categories: (1) bimetallic alloy nanowires; (2) bimetallic core–shell nanowires; and (3) bimetallic tortuous nanowires. Multimetallic nanowires containing more than two metal components can be made in the same way as described for the synthesis of bimetallic nanowires.

8.3.1 Bimetallic Alloy Nanowires

The direct approach to bimetallic alloy nanowires is the coreduction of two different metal precursors in one reaction condition and the formation of solid solution structure along one dimension. Alternatively, the alloy nanowires can be made by seed-mediated growth into a core–shell nanowire followed by the controlled core–shell metal diffusion into the solid solution structure[54]. The successful production of monodisperse bimetallic nanowires should allow deep understanding of alloy electronic and geometric effects on one-dimensional optical, electronic, magnetic, and catalytic properties.

Pt-based bimetallic nanowires are most extensively studied due to their potential applications in catalysis, biosensors, energy conversion, and magnetic storage[55,56]. One of the earlier work was the Pt–Fe nanowires prepared in a micelle-mediated growth with oleylamine serving as solvent, reducing agent and structure-directing agent[34]. In this synthesis, iron pentacarbonyl ($Fe(CO)_5$) was paired with $Pt(acac)_2$ (acac = acetylacetonate) for the alloy formation. $Fe(CO)_5$ was decomposed and $Pt(acac)_2$ was reduced at 160 °C in the cylinder-like micellar structure formed by oleylamine, leading to the growth of Pt–Fe alloy into nanowires. The process only required 30 min to finish and Pt–Fe nanowires were formed only at 2–3 nm across. The length of the nanowires was tuned by the volume ratio of oleylamine to 1-octadecene. For example, the volume ratio of 1:1 gave shorter (20 nm) nanowires, 3:1 yielded 100 nm long nanowires, and only oleylamine led to the formation of 200 nm long nanowires, as shown in Figure 8.5a. These nanowires have a very close Fe:Pt ratio (~1:1) and have a face center cubic type structure (commonly known as A1 structure). When annealed at 750 °C for 1 h, the fcc-structure was converted into the chemically ordered face-centered tetragonal (fct) structure (commonly known as $L1_0$ structure) that is strongly ferromagnetic (Figure 8.5b). Pt–Fe nanowires (~2.5 nm in diameter) could also be prepared by similar reactions at a lower temperature (115 °C) in the micellar structure formed by sodium oleate and oleylamine in 1-octadecene[57] and used as seeds to grow thicker nanowires via the same reaction in the presence of oleylamine and oleic acid as surfactants. The synthetic procedure could be easily extended to the synthesis of Pt–Co nanowires by replacing $Fe(CO)_5$ with dicobalt octacarbonyl ($Co_2(CO)_8$). These Pt–Co nanowires have an average diameter of 2.5 nm and length of 50–500 nm, as shown in Figure 8.5c.

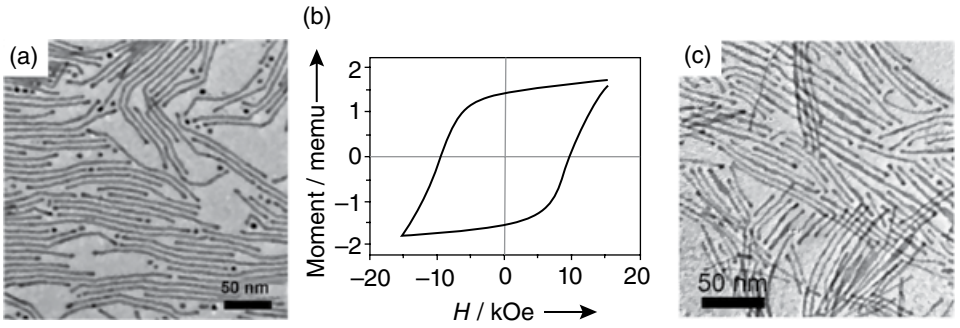

Figure 8.5 (a) TEM image of 200 nm $Fe_{55}Pt_{45}$ nanowires. (b) Magnetic hysteresis loop of the 200-nm $Fe_{55}Pt_{45}$ nanowires annealed in Ar at 750 °C for 1 h. (a) and (b) were reproduced from ref. [60] with permission. Copyright (2007) Wiley-VCH Verlag GmbH & Co. KGaA, Weinheim. (c) TEM images of 2.5 nm wide $Pt_{37}Co_{63}$ nanowires, reproduced from ref. [57] with permission. Copyright (2013), Wiley-VCH Verlag GmbH & Co. KGaA, Weinheim.

Oleylamine-mediated synthesis was used to prepare CuPt nanorods (20.3 ± 2.7 nm × 2.3 ± 0.2 nm) (Figure 8.6a) via 1,2-hexadecanediol reduction of $Cu(acac)_2$ and $Pt(acac)_2$ at 225 °C in 1-octadecene[58]. Likely due to the fact that Pt-based nanoparticles were formed when oleylamine and oleic acid were co-present in the reaction solution[59], the Cu–Pt nanorod product was contaminated by Cu–Pt nanoparticles and a size selection procedure had to be applied to separate the nanorods from nanoparticles. Oleylamine was thought to be a key component in the synthesis of nanorods due to its stronger binding to the (100) facets. Increasing the amount of oleylamine gave longer nanorods (Figure 8.6b). Replacing 1-octadecene with dibenzyl ether or diphenyl ether further increased the length of the nanorods up to 37.1 ± 10.1 nm (Figure 8.6c) or 55.5 ± 7.8 nm (Figure 8.6d). The growth of the nanowires seems to be very temperature dependent, as reaction temperatures lower than 225 °C yield only polyhedral nanoparticles. Increasing the amount of 1,2-hexadecanediol led to the formation of Cu–Pt nanocubes (Figure 8.6e).

A more general process leading to the synthesis of ~2.3 nm wide PtM (M = Pd, Ru, Au, Fe) nanowires was to coreduce H_2PtCl_6 and another metal chloride in the CTAB soft-template formed in a two-phase water-chloroform system[61].A strong reducing agent sodium borohydride was used to initiate the coreduction for the alloy nanowire formation at room temperature (Figure 8.7a). Compared to the nanowires formed in the oleylamine template, these nanowires have a worm-like morphology, indicating that CTAB could not form smooth channels in the two-phase solution system.

The alloy nanowires obtained from the solution phase syntheses outlined above often have a solid solution structure, not the chemically ordered alloy structure. However, a recent synthesis demonstration showed that Pt–Pb nanowires with an ordered intermetallic structure could be prepared by reducing $Pt(acac)_2$ and $Pb(acac)_2$ with *tert*-butylamine-borane (TBAB) complex at 180 °C in diphenyl ether with the combination of adamantanecarboxylic acid (ACA), hexadecanethiol (HDT) and hexadecylamine (HDA) as the capping agent[62]. Increasing the capping agent twice as much in the reaction solution led to the formation of nanoparticles. The PtPb nanowires have a hexagonal structure and the addition of the adatoms is favored along [001] direction, as

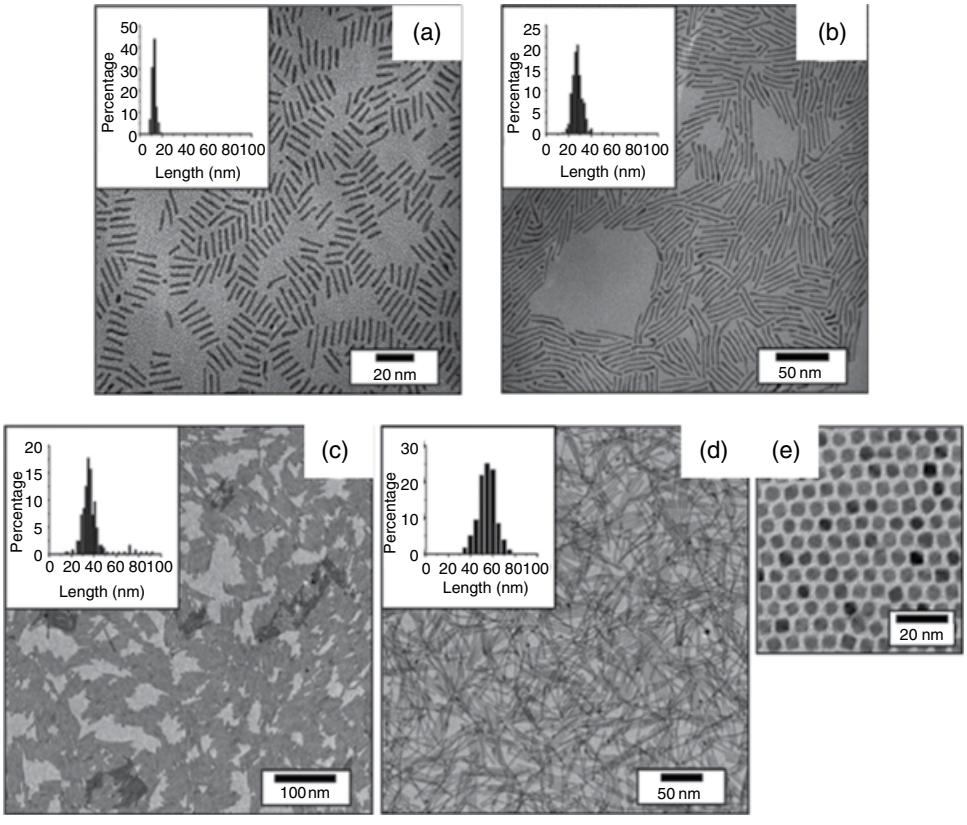

Figure 8.6 TEM images of Cu–Pt nanorods with average lengths of (c) 12.6 ± 1.9 nm, (d) 27.8 ± 4.4, (d) 37.1 ± 10.1, and (f) 55.5 ± 7.8 nm (histograms of lengths are shown in the corresponding insets) and of (g) Cu–Pt cubes. (c)–(g) were reproduced from ref. [58] with permission. Copyright (2009), American Chemistry Society.

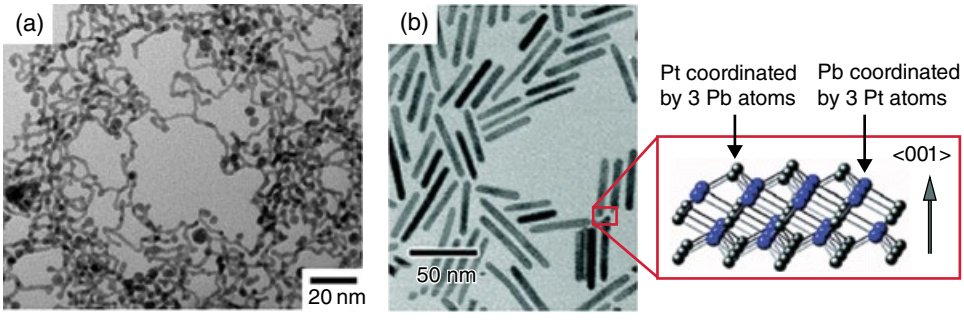

Figure 8.7 (a) TEM images of the alloy PtM nanowires with worm-like structure and porous nanonetwork on a TEM grid (M = Au). Reproduced from ref. [61] with permission. Copyright (2010), American Chemical Society. (b) Intermetallic Pt–Pb nanowires with preferential deposition of adatoms along <001 > direction. Reproduced from ref. [62] with permission. Copyright (2007), American Chemical Society.

shown in Figure 8.7b. It is noteworthy that the formation of intermetallic structures usually requires high temperature annealing treatment after the solution phase synthesis[63]. Alloying Pt with Pb promotes the intermetallic structure formation along the [001] direction at the synthetic temperature. This makes it possible to prepare intermetallic Pt–Pb–M nanowires or other shaped nanoparticles for property studies. Pt–Pb nanowires have been demonstrated to show much enhanced activity toward the electrooxidation of methanol.

A galvanic replacement method was used as a general method to prepare Pd–M alloy nanowires (M = Pt, Au) by employing Te nanowires as a sacrificial template[64]. The Te nanowires were synthesized from a hydrothermal procedure with PVP serving as a structure-directing agent. Then these nanowires were mixed with H_2PdCl_4, H_2PtCl_6, or $HAuCl_4$ in ethylene glycol to react at 50 °C for more than 13 h to consume Te nanowires and to produce Pd–M nanowires. The Pd–M nanowires replicate the morphology of the Te nanowires and have a diameter of ~10.8 nm. Pd and other metal components were alloyed throughout the nanowires. Changing the starting ratio of metal precursors could tune the final composition of the Pd–M nanowires. In the synthesis, the Pd-precursor was reduced preferentially by the Te nanowires to form a backbone structure for the nanowire growth. Without the presence of the Pd precursor, only nanoparticles were obtained. Through more carefully controlled etching at room temperature, Pd–Te nanowires were synthesized[65].

8.3.2 Bimetallic Core–Shell Nanowires

Bimetallic core–shell nanowires expose one metal component on their surface, allowing the study of interfacial interactions between the core and the shell in one dimension, and their effects on surface properties, such as electrocatalytic activity toward the ORR demonstrated in the PtNi/Pt nanowire systems[66]. These PtNi/Pt core–shell nanowires were prepared from the reduction of Pt/NiO nanowires. In this synthesis, the Pt/NiO nanowires were prepared by coreduction of $Pt(acac)_2$ and $Ni(acac)_2$ in the 1-octadecene solution of $W(CO)_6$, glucose, oleylamine, and PVP at 140 °C. $W(CO)_6$ was believed to release CO that can help to reduce the Pt salt and to "poison" the Pt (100) facets, facilitating the Pt nanowire formation[67,68]. NiO shell was then deposited on the formed Pt nanowires, giving Pt/NiO nanowires. These Pt/NiO nanowires were further heat-treated in the $Ar + H_2$ (3%) atmosphere to form Pt–Ni nanowires. Subject to the further cyclic voltammetry treatment in 0.1 M $HClO_4$ solution, surface/subsurface Ni was etched away, leading to the formation of PtNi/Pt nanowires with a "jagged" Pt surface and a shrunken nanowire diameter from ~5.0 nm to ~2.2 nm. This jagged Pt surface was proven to show extremely high activity toward ORR.

To have a better shell morphology and to minimize the Pt use in the core–shell nanowire structure, Pd–Pt core–shell nanowires were designed and prepared[23]. These core–shell nanowires were made by seed-mediated growth in which 2 nm wide Pd nanowires were presynthesized by reducing $Pd(NO_3)_2$ with $NaBH_4$ in the toluene solution of octadecylamine and dodecyltrimethylammonium bromide. These Pd nanowires were anchored on the common carbon support and were coated with Cu. A Pt monolayer could then be deposited around each nanowire via the Cu underpotential deposition (UPD) in which Cu was galvanically displaced by Pt[69].The Pd/Pt core–shell nanowires could also be prepared by growing a thin Pt shell directly over Pd

nanowires by adding H_2PtCl_6 dropwise to the aqueous solution of Pd nanowires and KBr[65]. The core–shell structure was formed via a galvanic replacement reaction initiated by Br^- that was used to control Pd replacement by Pt, forming a smooth Pt shell. Pt shell thickness was tuned by the amount of H_2PtCl_6 added. The addition of Br^- was crucial to the Pt shell deposition. With the existence of Br^-, Cl^- in the Pt precursor was replaced and $PtBr_6^{2-}$ was formed due to its relatively higher stability compared to $PtCl_6^{2-}$. This led to a slow Pt deposition kinetics and the formation of a smooth and thin Pt shell (Figure 8.8). Additionally, Br^- acted as a capping agent to help better disperse the Pd nanowires in the solution. Adding more Br^- in the solution led to the decrease of Pt deposition, giving thinner Pt shell around the nanowire structure. The thin (<1 nm) Pt shell showed much enhanced activity toward ORR due to the ligand effect of Pd, while the Pd core became irrelevant to the Pt catalysis if the Pt shell was > 1 nm thick.

In general, the seed-mediated growth method is a popular choice for the synthesis of core–shell nanowires. In addition to Pd–Pt nanowires mentioned above, other bimetallic core–shell nanowires can be prepared. For example, Au–Pt nanowires were synthesized by slowly depositing Pt onto Au nanowires that were pre-made by reducing $HAuCl_4$ with KBH_4 in the presence of Triton X-114 (TX-114) at 0 °C[70]. The deposition of Pt over Au was made possible by adding the ice-cold aqueous solution of H_2PtCl_6 dropwise to the Au nanowire dispersion. The presence of TX-114 prevented separate nucleation of Pt via its strong π-d interaction with Pt[71], weakening the Pt–Pt bond and promoting the deposition of Pt onto Au surface. More complicated core–shell Pd_xAu_{1-x}/Pt ($x = 0 - 0.75$) nanowires could also be prepared by growing Pt over PdAu nanowires[72]. 30 × 2 nm PdAu nanowires were first prepared by $NaBH_4$ reduction of

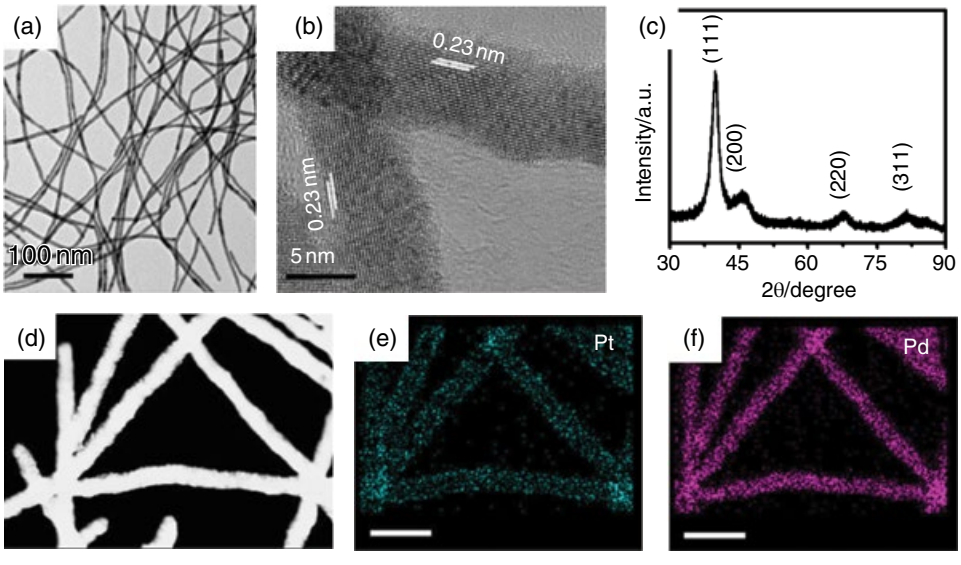

Figure 8.8 TEM image (a), HRTEM image (b), and XRD pattern (c) of the Pd/Pt nanowires (21.2 at% Pt) nanowires prepared by the Br^--mediated growth method. HAADF/STEM image (d) and EDS mapping analysis showing the elements Pt (e) and Pd (f). Scale bar = 20 nm. Reproduced from ref. [65] with permission. Copyright (2015), American Chemical Society.

$Pd(NO_3)_2$ and $HAuCl_4 \cdot xH_2O$ in toluene solution of octadecylamine (ODA) and dodecyltrimethylammonium bromide (DTAB). The Pt monolayer was coated onto PdAu nanowires via a Cu UPD/galvanic replacement procedure[73].

8.3.3 Bimetallic Nanowires Formed by Directional Aggregation of Nanoparticles

In addition to the formation of the "uniform" alloy or core–shell structures, nanowires can also be formed by directional aggregation of nanoparticles, giving a new type of one-dimensional structure with segregated metal components. It seems that anisotropic growth of noble metals is much more easily controlled than the non-noble metals[74].

The fused nanowires of Pt–Rh with an average diameter of 5 nm were obtained by reacting K_2PtCl_6 and the pre-synthesized 3.3 nm Rh nanocubes in an aqueous PVP solution at 200 °C (in an autoclave)[75]. In the process, K_2PtCl_6 was reduced on the surface of Rh nanocubes via galvanic replacement, forming the nanowire structure with Pt and Rh coexisting in their discreet cubic structure and the particles showing the oblong shape (Figure 8.9a). From the TEM analysis (inset in Figure 8.9a), the lattice mismatch between Pt and Rh (~3.2%) seems to play an important role in the anisotropic growth of Pt over Rh. Notably, long reaction time (12 h) was required in this synthesis to allow the fusion of nanoparticles into nanowires. Short reaction time (6 h, for example) gave only nanoparticles. Rh seeds needed to be present in the right amount to form nearly 100% Pt–Rh nanowires.

Beads-like PtM (M = Fe, Ni, or Co) nanowires were prepared by coreduction of $Pt(acac)_2$ and $M(acac)_x$, ($Fe(acac)_3$, $Ni(acac)_2$ or $Co(acac)_2$) at around 200 °C with oleylamine as both solvent and surfactant, cetyltrimethylammonium chloride (CTAC) as a structural template and glucose as a reducing agent[76]. 5 h of reaction produced

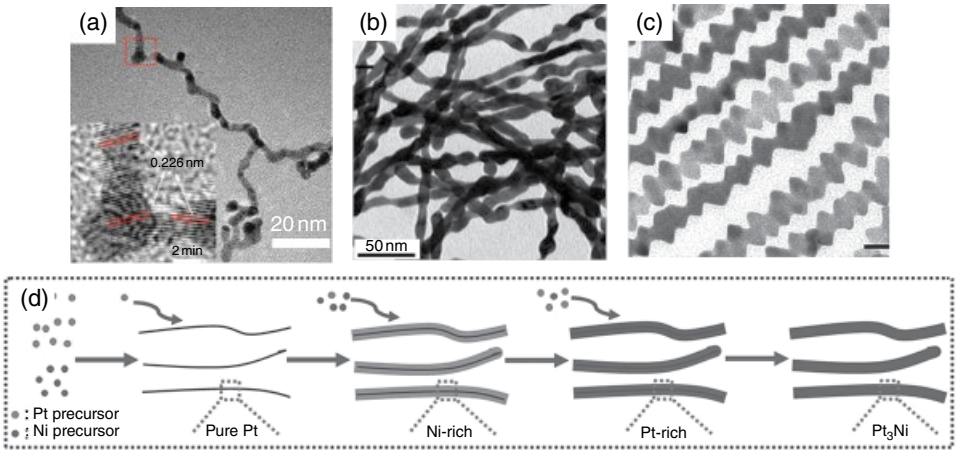

Figure 8.9 (a) HRTEM image of PtRh nanowires, the inlet image showed lattice spacing of Pt(111) facet. Reproduced from ref. [75] with permission. Copyright (2010), American Chemical Society. (b) TEM image of Pt_3Ni nanowires with beads-like structure. (c) Schematic illustration of the growth mechanism of the Pt_3Ni nanowires. (b) and (d) are reproduced from ref. [79] with permission. Copyright (2015), Wiley-VCH Verlag GmbH & Co. KGaA, Weinheim.

100 nm × 9 nm nanowires with beads-like chain structure (Figure 8.9b) that was formed by seed-mediated growth of M (Ni for example) on the Pt seeding wires followed by Pt–Ni alloying in different segment along the wire direction, as illustrated in Figure 8.9c. The addition of base metals to Pt could create a compressive strain at Pt surface and therefore tune the electronic structure via the alloy effect to favor the Pt electrocatalysis towards ORR[77]. By changing the reaction temperature to 160 °C and using the same reactants, hierarchical Pt_3Co nanowires with uneven diameters and high-density [310] facets were obtained[78]

Reducing H_2PtCl_6 with ascorbic acid in the presence of Pd nanocubes, PVP, sodium lauryl sulfate (SLS), and NaBr at 180 °C led to the formation of worm-like branched PdPt nanowires (200 nm × 3 nm) (Figure 8.10a)[80]. The nanowires contain the

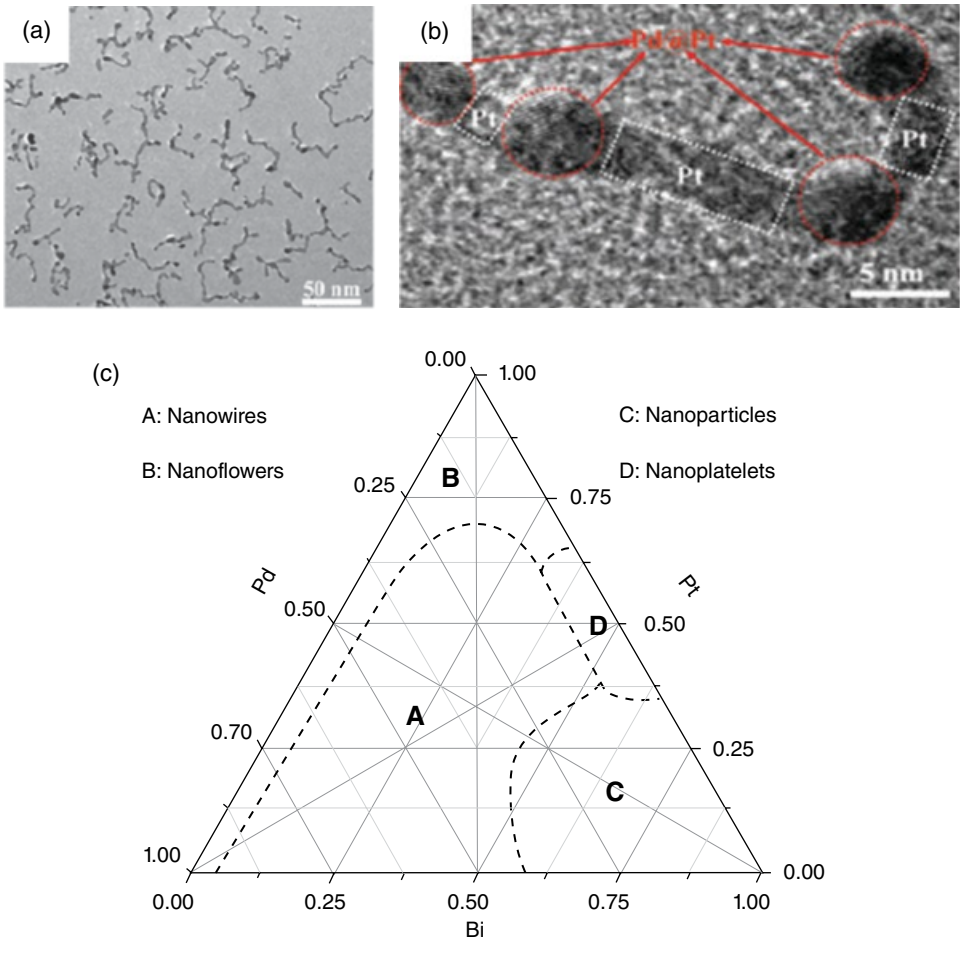

Figure 8.10 TEM (a) and HRTEM (b) images of Pd–Pt heterostructured nanowires (circles and rectangles marked the locations of Pd and Pt, respectively). Reproduced from ref. [80] with permission. Copyright (2009), Royal Society of Chemistry. (c) Schematic Illustration of shape evolution mediated by Bi, Pt, and Pd Elements. Reproduced from ref. [82] with permission. Copyright (2013), American Chemical Society.

segregated phase of Pt and Pd (Figure 8.10b) that was formed via the aggregation growth mechanism. The seeding Pd nanocubes were preserved in the wire structure during the epitaxial growth of Pt onto the surface of Pd (the lattice mismatch between Pd and Pt is 0.77%). This aggregation growth method was extended to prepare worm-like PdAg nanowires (200 nm × 5–8 nm) by coreduction of $AgNO_3$ and $Pd(NO_3)_2$ in ethylene glycol with PVP as the surfactant[81]

Structurally more complicated Pt-on-$Pd_{0.85}Bi_{0.15}$ nanowires were prepared by mixing $Pt(acac)_2$, $Pd(acac)_2$ and bismuth neodecanoate $Bi(NE)_3$ in the oleylamine solution of NH_4Br[82,83]. Pd and Bi first grew into nanowires[83], followed by deposition of Pt islands onto these nanowires to form a grape-like structure. In the synthesis, the morphology of the nanowires was controlled by the Bi-precursor amount. Increasing the mass of $Bi(NE)_3$ by 10 times could lead to the formation of porous nanoparticles, not nanowires. Detailed studies on precursor-composition dependent formation of nanoparticles/nanowires yielded a phase diagram (Figure 8.10c) from which we can see that pure Pd–Bi nanowires can be synthesized without adding $Pt(acac)_2$ and when Pt is present, Pt can be deposited on Pd–Bi nanowire surface, forming nanowires with a rugged surface.

Directional aggregation approach can be applied to make other types of bimetallic nanowires. AuAg bimetallic nanowires with atomic ratio of Au:Ag = 2:1 were synthesized via the combined seed-mediated growth and oriented attachment[85]. In the synthesis, $HAuCl_4 \cdot xH_2O$ and $AgNO_3$ were dissolved in octadecylamine (ODA) at 90 °C and kept the solution at this temperature for 4 h without mechanical stirring to produce 2–3 nm ultrathin Au–Ag nanowires.

Figure 8.11a illustrates the growth mechanism of Au–Ag nanowires. In the first 10 min of reaction period, 2–3 nm Au nanoparticles were formed. The preformed Au nanoparticles induced the nucleation of Ag according to the noble-metal-induced-reduction strategy[86]. Au and Ag were deposited onto the nanoparticles anisotropically to yield the nanowires (Figure 8.11b and c). The nanowires were formed via the seed-mediated and fusion growth mechanism. Similarly, thicker Au–Ag nanowires could be obtained by growing Ag and Au alternatively on the surface of Au particle seeds[87]. Increasing the reaction temperature to 100 °C and keeping the Ag:Au molar ratio at 1:2 led to the formation of ultrathin AgAu nanowires with Ag:Au 3:1 and the nanowires in helical packing[88]. STEM-HAADF studies indicate that the nanowire actually contains the mixture of icosahedral and decahedral packing of Ag–Au alloy nanoparticles, as shown in Figure 8.12a and b. Helical packing was also observed from the multimetallic nanowires of the Pd-modified Ag–Au nanowires due to the self-winding behavior of the nanowires in the presence of a tertiary metal[89]. The deposition of tertiary metal is key to initializing the winding of preformed bimetallic nanowires. In this demonstration, the Ag–Au nanowires were mixed with ascorbic acid and H_2PdCl_4 in DMF/water mixture followed by static incubation at room temperature for 10 days. It was observed that the deposition of Pd and the twisting of the seeding Ag–Au nanowires occurred almost simultaneously, forming double helixes, as shown in Figure 8.12c.

8.4 Concluding Remarks

This chapter outlines the chemical synthesis of ultrafine metallic nanowires, especially bimetallic nanowires with their diameter in sub-10 nm and aspect ratio >5. In this chemical synthetic process, the classical LaMer model is applicable to describe the

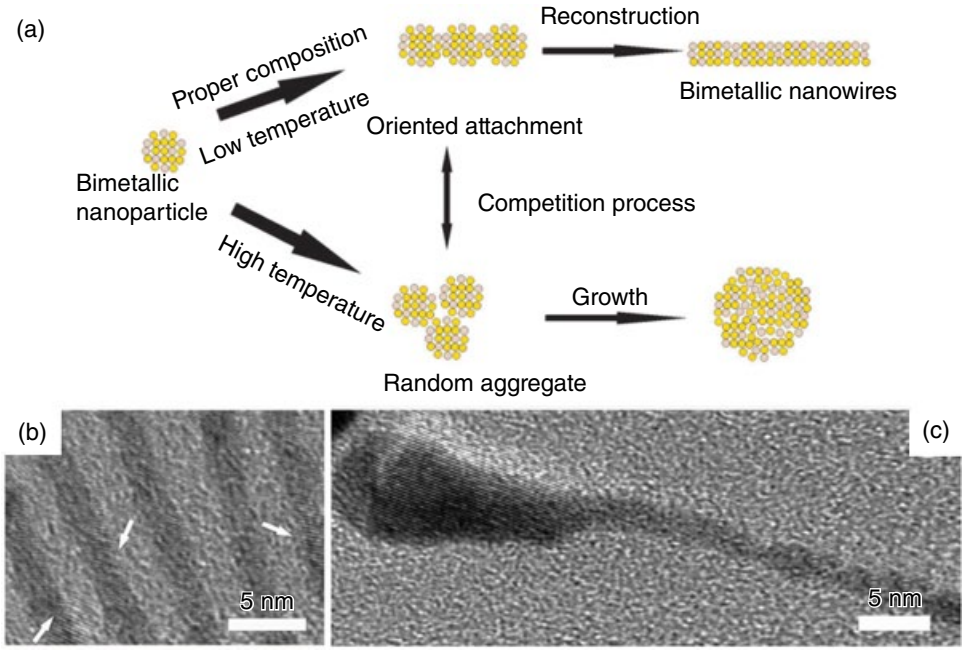

Figure 8.11 (a) Schematic illustration of the growth mechanism of AuAg bimetallic nanowires. TEM (b) and HR-TEM (c) images of AuAg nanowires obtained at 1 h reaction time. Reproduced from ref. [85] with permission. Copyright (2011), Royal Society of Chemistry.

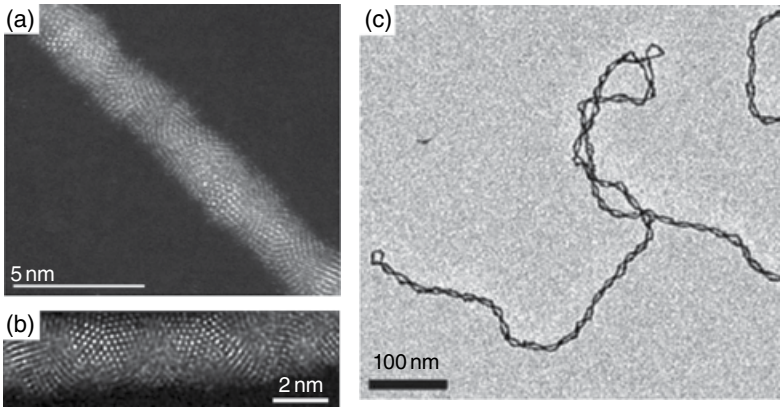

Figure 8.12 (a) Aberration-corrected STEM-HAADF images of the Ag–Au nanowires with the helical icosahedral structure; (b) aberration-corrected STEM-HAADF image of the helical array of decahedral nanowire. Reproduced with permission from ref. [88]. Copyright (2011), American Chemical Society. (c) TEM image of a typical AgAu/Pd double helix, reproduced with permission from ref. [89]. Copyright (2011), American Chemical Society.

nucleation and the growth of initial structure of the nanowires but the key to the successful synthesis lies in controlling anisotropic growth of nanostructures in one-dimension. This can be realized by exploring the binding difference between surfactant molecules and different crystal facets. More commonly, the nanostructure growth

process is limited in a soft-template formed by the self-assembly of lipid molecules in a proper solvent. Depending on the reaction condition, the nanowires can be formed in an alloy or a core–shell form, and the seed-mediated growth process is commonly applied to prepare these nanowires. The nanowires can also be prepared by controlled fusion of two different nanoparticles along one direction. The methods developed for the syntheses of bimetallic nanowires can be extended easily to multicomponent nanowires, as demonstrated in the reports of multimetallic alloy nanowires of PtPdFe[90], PtNiFe[22], and PtCuFe[60], as well as core–shell nanowires of PtFe/Au or PtFe/Pd[91].

Despite the great success demonstrated in the synthesis of ultrathin metallic nanowires, the current methods seem to be extremely well suited for preparing Pt- or Au-based multimetallic nanowires, but not for producing ultrathin nanowires of Pd- or Ag-based alloys[76]. It is even more challenging to prepare nanowires of the first-row transition metals and their alloys. It seems that the solution-phase methods developed thus far cannot offer the desired anisotropic growth of early transition metals into ultrathin nanowires, and as a result, thermodynamically more stable morphologies or nanowires of larger diameters (>10 nm) are usually obtained. More research is needed to develop new soft-template and surfactant-directed growth methods to prepare ultrathin nanowires of these earlier transition metals.

The precise controls of dimension, composition, and structure of ultrathin multimetallic nanowires should allow the preparation of a class of new low-dimensional nanomaterials or devices with tunable physical and chemical properties for optical, electronic, magnetic, and catalytic applications.

8.5 References

1 Burda, C., Chen, X., Narayanan, R., El-Sayed, M. A. (2005). Chemistry and properties of nanocrystals of different shapes. *Chemical Reviews*, 105 (4), 1025–1102.

2 Wu, L., Mendoza-Garcia, A., Li, Q., Sun, S. (2016). Organic Phase Syntheses of Magnetic Nanoparticles and Their Applications. *Chemical Reviews*, 116 (18), 10473–10512.

3 Merkel, T. J., Herlihy, K. P., Nunes, J., Orgel, R. M., Rolland, J. P., DeSimone, J. M. (2009). Scalable, shape-specific, top-down fabrication methods for the synthesis of engineered colloidal particles. *Langmuir*, 26 (16), 13086–13096.

4 Hurst, S. J., Payne, E. K., Qin, L., Mirkin, C. A. (2006). Multisegmented one-dimensional nanorods prepared by hard-template synthetic methods. *Angewandte Chemie International Edition*, 45 (17), 2672–2692.

5 Trewyn, B. G., Slowing, I. I., Giri, S., Chen, H.-T., Lin, V. S.-Y. (2007). Synthesis and functionalization of a mesoporous silica nanoparticle based on the sol–gel process and applications in controlled release. *Accounts of chemical research*, 40 (9), 846–853.

6 Chen, D.-H., He, X.-R. (2001). Synthesis of nickel ferrite nanoparticles by sol-gel method. *Materials Research Bulletin*, 36 (7), 1369–1377.

7 Wu, Y., Bose, S. (2005). Nanocrystalline hydroxyapatite: micelle templated synthesis and characterization. *Langmuir*, 21 (8), 3232–3234.

8 Zhang, S., Zhao, Y. (2012). Template synthesis of subnanometer gold clusters in interfacially cross-linked reverse micelles mediated by confined counterions. *Langmuir*, 28 (7), 3606–3613.

9 Petcharoen, K., Sirivat, A. (2012). Synthesis and characterization of magnetite nanoparticles via the chemical co-precipitation method. *Materials Science and Engineering: B*, 177 (5), 421–427.

10 Daou, T., Pourroy, G., Bégin-Colin, S., Greneche, J., Ulhaq-Bouillet, C., Legaré, P., Bernhardt, P., Leuvrey, C., Rogez, G. (2006). Hydrothermal synthesis of monodisperse magnetite nanoparticles. *Chemistry of Materials*, 18 (18), 4399–4404.

11 Sajanlal, P. R., Sreeprasad, T. S., Samal, A. K., Pradeep, T. (2011). Anisotropic nanomaterials: structure, growth, assembly, and functions. *Nano Reviews & Experiments*, 2 PMC3215190.

12 Tsuji, M., Hashimoto, M., Nishizawa, Y., Kubokawa, M., Tsuji, T. (2005). Microwave-Assisted Synthesis of Metallic Nanostructures in Solution. *Chemistry–A European Journal*, 11 (2), 440–452.

13 Duan, H., Wang, D., Li, Y. (2015). Green chemistry for nanoparticle synthesis. *Chemical Society Reviews*, 44 (16), 5778–5792.

14 Pang, X., Zhao, L., Han, W., Xin, X., Lin, Z. (2013). A general and robust strategy for the synthesis of nearly monodisperse colloidal nanocrystals. *Nature nanotechnology*, 8 (6), 426–431.

15 Mendoza-Garcia, A., Sun, S. (2016). Recent Advances in the High-Temperature Chemical Synthesis of Magnetic Nanoparticles. *Advanced Functional Materials*, 26 (22), 3809–3817.

16 Li, Q., Sun, S. (2016). Recent advances in the organic solution phase synthesis of metal nanoparticles and their electrocatalysis for energy conversion reactions. *Nano Energy*, 29, 178–197.

17 Shingubara, S. (2003). Fabrication of nanomaterials using porous alumina templates. *Journal of Nanoparticle Research*, 5 (1), 17–30.

18 Govindaraj, A., Satishkumar, B. C., Nath, M., Rao, C. N. R. (2000). Metal Nanowires and Intercalated Metal Layers in Single-Walled Carbon Nanotube Bundles. *Chemistry of Materials*, 12 (1), 202–205.

19 Niu, W., Zhang, L., Xu, G. (2013). Seed-mediated growth of noble metal nanocrystals: crystal growth and shape control. *Nanoscale*, 5 (8), 3172–3181.

20 Pascual, J. I., Méndez, J., Gómez-Herrero, J., Baró, A. M., Garcia, N., Landman, U., Luedtke, W. D., Bogachek, E. N., Cheng, H.-P. (1995). Properties of Metallic Nanowires: From Conductance Quantization to Localization. *Science*, 267 (5205), 1793–1795.

21 Teng, X., Han, W. Q., Ku, W., Hücker, M. (2008). Synthesis of ultrathin palladium and platinum nanowires and a study of their magnetic properties. *Angewandte Chemie*, 120 (11), 2085–2088.

22 Zhu, H., Zhang, S., Su, D., Jiang, G., Sun, S. (2015). Surface Profile Control of FeNiPt/Pt Core/Shell Nanowires for Oxygen Reduction Reaction. *Small*, 11(29), 3545–3549.

23 Koenigsmann, C., Santulli, A. C., Gong, K., Vukmirovic, M. B., Zhou, W.-P., Sutter, E., Wong, S. S., Adzic, R. R. (2011). Enhanced electrocatalytic performance of processed, ultrathin, supported Pd–Pt core–shell nanowire catalysts for the oxygen reduction reaction. *Journal of the American Chemical Society*, 133 (25), 9783–9795.

24 Hong, B. H., Bae, S. C., Lee, C.-W., Jeong, S., Kim, K. S. (2001). Ultrathin single-crystalline silver nanowire arrays formed in an ambient solution phase. *Science*, 294 (5541), 348–351.

25 Maurer, J. H. M., González-García, L., Reiser, B., Kanelidis, I., Kraus, T. (2016). Templated Self-Assembly of Ultrathin Gold Nanowires by Nanoimprinting for Transparent Flexible Electronics. *Nano Letters*, 16 (5), 2921–2925.

26 Xia, B. Y., Wu, H. B., Yan, Y., Lou, X. W., Wang, X. (2013). Ultrathin and Ultralong Single-Crystal Platinum Nanowire Assemblies with Highly Stable Electrocatalytic Activity. *Journal of the American Chemical Society*, 135 (25), 9480–9485.

27 Lal, S., Link, S., Halas, N. J. (2007). Nano-optics from sensing to waveguiding. *Nature photonics*, 1 (11), 641–648.

28 Song, J., Yang, X., Jacobson, O., Huang, P., Sun, X., Lin, L., Yan, X., Niu, G., Ma, Q., Chen, X. (2015). Ultrasmall gold nanorod vesicles with enhanced tumor accumulation and fast excretion from the body for cancer therapy. *Advanced Materials*, 27 (33), 4910–4917.

29 Cademartiri, L., Ozin, G. A. (2009). Ultrathin nanowires—a materials chemistry perspective. *Advanced Materials*, 21 (9), 1013–1020.

30 LaMer, V. K., Dinegar, R. H., Theory, (1950). Production and Mechanism of Formation of Monodispersed Hydrosols. *Journal of the American Chemical Society*, 72 (11), 4847–4854.

31 Jiang, Y. (2003). Forced hydrolysis and chemical co-precipitation. *Handbook of Nanophase and Nanostructured Materials*, pp. 55–71.

32 Watzky, M. A., Finke, R. G. (1997). Transition Metal Nanocluster Formation Kinetic and Mechanistic Studies. A New Mechanism When Hydrogen Is the Reductant: Slow, Continuous Nucleation and Fast Autocatalytic Surface Growth. *Journal of the American Chemical Society*, 119 (43), 10382–10400.

33 Gou, L., Murphy, C. J. (2005). Fine-Tuning the Shape of Gold Nanorods. *Chemistry of Materials*, 17 (14), 3668–3672.

34 Wang, C., Hou, Y., Kim, J., Sun, S. (2007). A general strategy for synthesizing FePt nanowires and nanorods. *Angewandte Chemie-International Edition*, 46 (33), 6333–6335.

35 Huang, X., Zheng, N. (2009). One-Pot, High-Yield Synthesis of 5-Fold Twinned Pd Nanowires and Nanorods. *Journal of the American Chemical Society*, 131 (13), 4602–4603.

36 Jun, Y. w., Choi, J. s., Cheon, J. (2006). Shape control of semiconductor and metal oxide nanocrystals through nonhydrolytic colloidal routes. *Angewandte Chemie International Edition*, 45 (21), 3414–3439.

37 Lim, B., Xia, Y. (2011). Metal nanocrystals with highly branched morphologies. *Angewandte Chemie International Edition*, 50 (1), 76–85.

38 Lu, X., Yavuz, M. S., Tuan, H.-Y., Korgel, B. A., Xia, Y. (2008). Ultrathin gold nanowires can be obtained by reducing polymeric strands of oleylamine – AuCl complexes formed via aurophilic interaction. *Journal of the American Chemical Society*, 130 (28), 8900–8901.

39 Zhu, W., Zhang, Y.-J., Zhang, H., Lv, H., Li, Q., Michalsky, R., Peterson, A. A., Sun, S. (2014). Active and Selective Conversion of CO2 to CO on Ultrathin Au Nanowires. *J. Am. Chem. Soc.*, 136 (46), 16132–16135.

40 Jana, N. R., Gearheart, L., Murphy, C. J. (2001). Wet Chemical Synthesis of High Aspect Ratio Cylindrical Gold Nanorods. *The Journal of Physical Chemistry B*, 105 (19), 4065–4067.

41 Sun, Y., Mayers, B., Herricks, T., Xia, Y. (2003). Polyol Synthesis of Uniform Silver Nanowires: A Plausible Growth Mechanism and the Supporting Evidence. *Nano Letters*, 3 (7), 955–960.

42 Chiu, C.-Y., Li, Y., Ruan, L., Ye, X., Murray, C. B., Huang, Y. (2011). Platinum nanocrystals selectively shaped using facet-specific peptide sequences. *Nature chemistry*, 3 (5), 393–399.

43 Chen, J., Herricks, T., Geissler, M., Xia, Y. (2004). Single-Crystal Nanowires of Platinum Can Be Synthesized by Controlling the Reaction Rate of a Polyol Process. *Journal of the American Chemical Society*, 126 (35), 10854–10855.

44 Wiley, B., Sun, Y., Xia, Y. (2005). Polyol Synthesis of Silver Nanostructures: Control of Product Morphology with Fe(II) or Fe(III) Species. *Langmuir*, 21 (18), 8077–8080.

45 Long, R., Zhou, S., Wiley, B. J., Xiong, Y. (2014). Oxidative etching for controlled synthesis of metal nanocrystals: atomic addition and subtraction. *Chemical Society Reviews*, 43 (17), 6288–6310.

46 Pratontep, S., Brinkmann, M., Nüesch, F., Zuppiroli, L. (2004). Correlated growth in ultrathin pentacene films on silicon oxide: Effect of deposition rate. *Physical Review B*, 69 (16), 165201.

47 Ottaviano, L., Parisse, P., Grossi, V., Passacantando, M. (2010). Nanowire directed diffusion limited aggregation growth of nanoparticles. *Journal of Non-Crystalline Solids*, 356 (37–40), 2076–2078.

48 Chang, J.-Y., Chang, J.-J., Lo, B., Tzing, S.-H., Ling, Y.-C. (2003). Silver nanoparticles spontaneous organize into nanowires and nanobanners in supercritical water. *Chemical Physics Letters*, 379 (3), 261–267.

49 Yu, Y. Y., Chang, S.-S., Lee, C.-L., Wang, C. R. C. (1997). Gold Nanorods: Electrochemical Synthesis and Optical Properties. *The Journal of Physical Chemistry B*, 101 (34), 6661–6664.

50 Krichevski, O., Tirosh, E., Markovich, G. (2006). Formation of Gold – Silver Nanowires in Thin Surfactant Solution Films. *Langmuir*, 22 (3), 867–870.

51 Jana, N. R., Gearheart, L., Murphy, C. J. (2001). Wet chemical synthesis of silver nanorods and nanowires of controllable aspect ratio. *Chemical Communications*, (7), 617–618.

52 Sun, Y., Yin, Y., Mayers, B. T., Herricks, T., Xia, Y. (2002). Uniform silver nanowires synthesis by reducing AgNO3 with ethylene glycol in the presence of seeds and poly (vinyl pyrrolidone). *Chemistry of Materials*, 14 (11), 4736–4745.

53 Sun, Y., Gates, B., Mayers, B., Xia, Y. (2002). Crystalline silver nanowires by soft solution processing. *Nano letters*, 2 (2), 165–168.

54 Gu, J., Zhang, Y.-W., Tao, F. F. (2012). Shape control of bimetallic nanocatalysts through well-designed colloidal chemistry approaches. *Chemical Society Reviews* 41 (24), 8050–8065.

55 Xia, Y., Yang, P., Sun, Y., Wu, Y., Mayers, B., Gates, B., Yin, Y., Kim, F., Yan, H. (2003). One-dimensional nanostructures: synthesis, characterization, and applications. *Advanced materials*, 15 (5), 353–389.

56 Zheng, H., Smith, R. K., Jun, Y.-W., Kisielowski, C., Dahmen, U., Alivisatos, A. P. (2009). Observation of Single Colloidal Platinum Nanocrystal Growth Trajectories. *Science*, 324 (5932), 1309–1312.

57 Guo, S., Li, D., Zhu, H., Zhang, S., Markovic, N. M., Stamenkovic, V. R., Sun, S. (2013). FePt and CoPt Nanowires as Efficient Catalysts for the Oxygen Reduction Reaction. *Angewandte Chemie-International Edition*, 52 (12), 3465–3468.

58 Liu, Q., Yan, Z., Henderson, N. L., Bauer, J. C., Goodman, D. W., Batteas, J. D., Schaak, R. E. (2009). Synthesis of CuPt nanorod catalysts with tunable lengths. *Journal of the American Chemical Society*, 131 (16), 5720–5721.

59 Yu, Y., Yang, W., Sun, X., Zhu, W., Li, X. Z., Sellmyer, D. J., Sun, S. (2014). Monodisperse MPt (M = Fe, Co, Ni, Cu, Zn) Nanoparticles Prepared from a Facile Oleylamine Reduction of Metal Salts. *Nano letters*, 14 (5), 2778–2782.

60 Zhu, H., Zhang, S., Guo, S., Su, D., Sun, S. (2013). Synthetic Control of FePtM Nanorods (M = Cu, Ni) To Enhance the Oxygen Reduction Reaction. *Journal of the American Chemical Society*, 135 (19), 7130–7133.

61 Yang, S., Hong, F., Wang, L., Guo, S., Song, X., Ding, B., Yang, Z. (2009). Ultrathin Pt-based alloy nanowire networks: synthesized by CTAB assistant two-phase water-chloroform micelles. *The Journal of Physical Chemistry C*, 114 (1), 203–207.

62 Maksimuk, S., Yang, S., Peng, Z., Yang, H. (2007). Synthesis and Characterization of Ordered Intermetallic PtPb Nanorods. *Journal of the American Chemical Society*, 129 (28), 8684–8685.

63 Li, Q., Wu, L., Wu, G., Su, D., Lv, H., Zhang, S., Zhu, W., Casimir, A., Zhu, H., Mendoza-Garcia, A., Sun, S. (2015). New approach to fully ordered fct-FePt nanoparticles for much enhanced electrocatalysis in acid. *Nano Lett*, 15 (4), 2468–73.

64 Zhu, C., Guo, S., Dong, S. (2012). PdM (M = Pt, Au) Bimetallic Alloy Nanowires with Enhanced Electrocatalytic Activity for Electro-oxidation of Small Molecules. *Advanced Materials*, 24 (17), 2326–2331.

65 Li, H.-H., Ma, S.-Y., Fu, Q.-Q., Liu, X.-J., Wu, L., Yu, S.-H. (2015). Scalable bromide-triggered synthesis of Pd@ Pt core–shell ultrathin nanowires with enhanced electrocatalytic performance toward oxygen reduction reaction. *Journal of the American Chemical Society*, 137 (24), 7862–7868.

66 Li, M., Zhao, Z., Cheng, T., Fortunelli, A., Chen, C.-Y., Yu, R., Zhang, Q., Gu, L., Merinov, B. V., Lin, Z. (2016). Ultrafine jagged platinum nanowires enable ultrahigh mass activity for the oxygen reduction reaction. *Science*, 354 (6318), 1414–1419.

67 Zhang, J., Fang, J. (2009). A General Strategy for Preparation of Pt 3d-Transition Metal (Co, Fe, Ni) Nanocubes. *Journal of the American Chemical Society*, 131 (51), 18543–18547.

68 Kang, Y., Ye, X., Murray, C. B. (2010). Size- and Shape-Selective Synthesis of Metal Nanocrystals and Nanowires Using CO as a Reducing Agent. *Angewandte Chemie International Edition*, 49 (35), 6156–6159.

69 Zhang, J., Mo, Y., Vukmirovic, M. B., Klie, R., Sasaki, K., Adzic, R. R. (2004). Platinum Monolayer Electrocatalysts for O2 Reduction: Pt Monolayer on Pd(111) and on Carbon-Supported Pd Nanoparticles. *The Journal of Physical Chemistry B*, 108 (30), 10955–10964.

70 Liu, R., Liu, J.-F., Zhang, Z.-M., Zhang, L.-Q., Sun, J.-F., Sun, M.-T., Jiang, G.-B. (2014). Submonolayer-Pt-Coated Ultrathin Au Nanowires and Their Self-Organized Nanoporous Film: SERS and Catalysis Active Substrates for Operando SERS Monitoring of Catalytic Reactions. *The journal of physical chemistry letters*, 5 (6), 969–975.

71 Liu, R., Liu, J.-F., Jiang, G.-B. (2010). Use of Triton X-114 as a weak capping agent for one-pot aqueous phase synthesis of ultrathin noble metal nanowires and a primary study of their electrocatalytic activity. *Chemical Communications*, 46 (37), 7010–7012.

72 Koenigsmann, C., Sutter, E., Adzic, R. R., Wong, S. S. (2012). Size-and Composition-Dependent Enhancement of Electrocatalytic Oxygen Reduction Performance in Ultrathin Palladium–Gold (Pd1–x Au x) Nanowires. *The Journal of Physical Chemistry C*, 116 (29), 15297–15306.

73 Koenigsmann, C., Sutter, E., Chiesa, T. A., Adzic, R. R., Wong, S. S. (2012). Highly Enhanced Electrocatalytic Oxygen Reduction Performance Observed in Bimetallic Palladium-Based Nanowires Prepared under Ambient, Surfactantless Conditions. *Nano Letters*, 12 (4), 2013–2020.

74 Yuan, Q., Wang, X. (2010). Aqueous-based route toward noble metal nanocrystals: morphology-controlled synthesis and their applications. *Nanoscale*, 2 (11), 2328–2335.

75 Yuan, Q., Zhou, Z., Zhuang, J., Wang, X. (2010). Seed displacement, epitaxial synthesis of Rh/Pt bimetallic ultrathin nanowires for highly selective oxidizing ethanol to CO2. *Chemistry of Materials*, 22 (7), 2395–2402.

76 Bin, D., Yang, B., Ren, F., Zhang, K., Yang, P., Du, Y. (2015). Facile synthesis of PdNi nanowire networks supported on reduced graphene oxide with enhanced catalytic performance for formic acid oxidation. *Journal of Materials Chemistry A*, 3 (26), 14001–14006.

77 Zhang, S., Zhang, X., Jiang, G., Zhu, H., Guo, S., Su, D., Lu, G., Sun, S. (2014). Tuning nanoparticle structure and surface strain for catalysis optimization. *Journal of the American Chemical Society*, 136 (21), 7734–7739.

78 Bu, L., Guo, S., Zhang, X., Shen, X., Su, D., Lu, G., Zhu, X., Yao, J., Guo, J., Huang, X. (2016). Surface engineering of hierarchical platinum-cobalt nanowires for efficient electrocatalysis. *Nature communications*, 7 pp. 1–10.

79 Bu, L., Ding, J., Guo, S., Zhang, X., Su, D., Zhu, X., Yao, J., Guo, J., Lu, G., Huang, X. (2015). A general method for multimetallic platinum alloy nanowires as highly active and stable oxygen reduction catalysts. *Advanced Materials*, 27 (44), 7204–7212.

80 Yuan, Q., Zhuang, J., Wang, X. (2009). Single-phase aqueous approach toward Pd sub-10 nm nanocubes and Pd–Pt heterostructured ultrathin nanowires. *Chemical Communications*, (43), 6613–6615.

81 Lu, Y., Chen, W. (2011). PdAg alloy nanowires: facile one-step synthesis and high electrocatalytic activity for formic acid oxidation. *ACS Catalysis*, 2 (1), 84–90.

82 Liao, H., Hou, Y. (2013). Liquid-Phase Templateless Synthesis of Pt-on-Pd0.85Bi0.15 Nanowires and PtPdBi Porous Nanoparticles with Superior Electrocatalytic Activity. *Chemistry of Materials*, 25 (3), 457–465.

83 Liao, H., Zhu, J., Hou, Y. (2014). Synthesis and electrocatalytic properties of PtBi nanoplatelets and PdBi nanowires. *Nanoscale*, 6 (2), 1049–1055.

84 Lu, Q., Rosen, J., Zhou, Y., Hutchings, G. S., Kimmel, Y. C., Chen, J. G., Jiao, F. (2014). A selective and efficient electrocatalyst for carbon dioxide reduction. *Nature communications*, 5 pp. 1–6.

85 Hong, X., Wang, D., Yu, R., Yan, H., Sun, Y., He, L., Niu, Z., Peng, Q., Li, Y., (2011). Ultrathin Au–Ag bimetallic nanowires with Coulomb blockade effects. *Chemical Communications*, 47 (18), 5160–5162.

86 Wang, D., Li, Y. (2010). One-Pot Protocol for Au-Based Hybrid Magnetic Nanostructures via a Noble-Metal-Induced Reduction Process. *Journal of the American Chemical Society*, 132 (18), 6280–6281.

87 Yang, Y., Wang, W., Li, X., Chen, W., Fan, N., Zou, C., Chen, X., Xu, X., Zhang, L., Huang, S. (2012). Controlled Growth of Ag/Au Bimetallic Nanorods through Kinetics Control. *Chemistry of Materials*, 25 (1), 34–41.

88 Velázquez-Salazar, J. J., Esparza, R., Mejía-Rosales, S. J., Estrada-Salas, R., Ponce, A., Deepak, F. L., Castro-Guerrero, C., José-Yacamán, M. (2011). Experimental Evidence of Icosahedral and Decahedral Packing in One-Dimensional Nanostructures. *ACS Nano*, 5 (8), 6272–6278.

89 Wang, Y., Wang, Q., Sun, H., Zhang, W., Chen, G., Wang, Y., Shen, X., Han, Y., Lu, X., Chen, H. (2011). Chiral Transformation: From Single Nanowire to Double Helix. *Journal of the American Chemical Society*, 133 (50), 20060–20063.

90 Guo, S., Zhang, S., Sun, X., Sun, S. (2011). Synthesis of Ultrathin FePtPd Nanowires and Their Use as Catalysts for Methanol Oxidation Reaction. *Journal of the American Chemical Society*, 133 (39), 15354–15357.

91 Guo, S., Zhang, S., Su, D., Sun, S. (2013). Seed-Mediated Synthesis of Core/Shell FePtM/FePt (M = Pd, Au) Nanowires and Their Electrocatalysis for Oxygen Reduction Reaction. *Journal of the American Chemical Society*, 135 (37), 13879–13884.

9

Bimetallic Nanoplates and Nanosheets

Bing Dong[1], Ziyu Yang[1], and Yanglong Hou[2]

[1] *Beijing Key Laboratory for Magnetoeletric Materials and Devices (BKL-MEMD), College of Engineering, Peking University, Beijing, China*
[2] *Beijing Key Laboratory for Magnetoeletric Materials and Devices (BKL-MEMD), and Beijing Innovation Center for Engineering Science and Advanced Technology (BIC-ESAT), College of Engineering, Peking University, Beijing, China*

9.1 Introduction

The compositions, crystal structures, and morphologies of nanomaterials have a great influence on their physical and chemical properties[1–3]. Researchers have made great efforts in nanostructured organization to design functional materials[4]. Due to their size and novel properties, nanostructures are interesting both for fundamental science and applications. So far, people have been able to synthesize nanostructures such as nanorods[5,6], nanobelts[7,8], nanowires[9,10], and nanotubes[11,12]. However, the precise fabrication of nanocrystals with unique shapes at a nanoscale level is significant for enhancing their performance in many applications, such as magnetic properties, catalysis, gas sensing, and so on. Such shape effects inherently result from the atomic arrangement on different exposed crystal planes[13].

Nanoplates and nanosheets with specific crystal planes and high aspect ratio—in particular, when their thickness is just one or a few atomic layers—exhibit special properties dissimilar to those of their bulk counterparts and other forms of nanostructures, which provides potential opportunities to meet the requirement of flexible and transparent nanodevices. These ultrathin nanoplates and nanosheets have epitomized the applications in microscopic superior optical, electronic, and magnetic nanodevices with the macroscopic flexibility and transparency. In particular, inspired by graphene, atomically inorganic two-dimensional (2D) nanocrystals are also receiving extraordinary interest because of their fascinating properties and enormous applicability in areas ranging from electronics to catalysis[17–20]. For example, polyvinylpyrrolidone (PVP)-supported single-layered rhodium nanosheets with thickness < 4 Å involve a δ-bonding framework, which can stabilize the single-layered structure, together with the PVP ligands[21]. The PVP-capped Rh nanosheets display greater superior catalytic activity and selectivity toward the target product than those of commercial Rh/C and PVP-capped Rh nanoparticles in hydrogenation of phenol and hydroformylation of 1-octene.

Bimetallic Nanostructures: Shape-Controlled Synthesis for Catalysis, Plasmonics, and Sensing Applications, First Edition. Edited by Ya-Wen Zhang.
© 2018 John Wiley & Sons Ltd. Published 2018 by John Wiley & Sons Ltd.

Bimetallic nanoplates and nanosheets, consisting of two distinct metals, such as magnetic metals and noble metals, are emerging as a new class of materials and have attracted much attention for their promising potentials in catalysis, magnetic sensors, electronics, optical detection, and biomedical applications[22–25] due to their synergetic effects between the two metals, which mainly include electronic effect,26 strain effect[27], geometric or ensemble effect[28], and other interfacial effects[29]. They are expected to display new properties or capabilities, not to be a combination of the properties associated with two distinct metals. Further, the relevant chemical, physical, or electrical performances of bimetallic nanoplates or nanosheets can be modified by changing their components. Take Pd nanosheets as an example. They usually show good catalytic performance as catalysts in heterogeneous reactions. However, Pd–Ag nanosheets with a Pd/Ag molar ratio of 1 have shown the highest catalytic activity among all the tested Pd–Ag nanosheets with different molar ratio, including Pd nanosheets[30]. This can be attributed to the fact that Pd is electronically promoted by Ag to give enhanced catalysis and the geometric effect generated from the Pd–Ag alloyed surface. Another, the Ni–Fe/NF (nickel foam) electrode, exhibits greater current density and more negative onset potential as compared with Ni/NF and Fe/NF catalysts[23]. It is evident that a rapid anodic current rise was observed for NiFe/NF with a small onset over potential of 232 mV, much less than that of Ni/NF (260 mV) and Fe/NF (265 mV).

In general, bimetallic nanoplates and nanosheets can be summarized as three types of structures: core–shell, heterostructure, or intermetallic and alloyed structures. Compared with monometallic nanoplates and nanosheets, it is harder to achieve effective control of the size, shape, architecture, and composition of functional bimetallic nanoplates and nanosheets because of the complexity and multiform of their structures[31].

Preparation of bimetallic nanoplates and nanosheets can be performed in the solid, gaseous, or solution phase. The solution phase is more powerful than both the solid phase method, which requires high-temperatures, long periods of time, and is difficult to obtain nanocrystals with high surface areas, and the gaseous phase method, which requires complicated apparatus and possessing low yields. However, it is very difficult to synchronously control the nucleation and growth of two distinct metals in the solution system due to their different intrinsic properties. In recent years, great efforts have been devoted to controllable preparation of bimetallic nanoplates and nanosheets. In this chapter, we first introduce several chemical routes for synthesis of bimetallic nanoplates or nanosheets. Then we will discuss some fascinating properties and corresponding applications, such as catalysis and optical and biomedical applications.

9.2 Synthesis of Bimetallic Nanoplates and Nanosheets

9.2.1 Seeded Epitaxial Growth Process

The seeded epitaxial growth process of bimetallic nanoplates and nanosheets usually consists of two steps: seed preparation and subsequent growth. This process is widely applied for the preparation of bimetallic nanoplates or nanosheets with core–shell structures, because it usually generates the products with relatively more narrow size and shape distributions and with higher yields. To avoid the galvanic reaction happening, the

reduction potential of the core metal (the seed) is usually higher than that of the shell metal. Based on this consideration, the Pd nanoplates were synthesized by reducing Na_2PdCl_4 precursor with PVP as a reducing agent, which then served as seeds for the nucleation of Pt atoms formed by reducing H_2PtCl_6 with citric acid. By this heterogeneous epitaxial growth, Pd@Pt core–shell nanoplates, with hexagonal and triangular shapes, were obtained[32]. Figure 9.1a and b reveal that a thin, uniform Pt shell was formed around the Pd nanoplate, and demonstrated the layer-by-layer epitaxial growth of Pt on Pd surface in this approach. A class of core–shell Pd@Ag nanostructures, integrating both tunable surface-plasmon-resonance (SPR) properties and photothermal stability, have also been studied[33]. In this synthesis, uniform hexagonal Pd nanoplates with 1.8 nm thick, are used as seeds to direct the epitaxial growth of Ag thereon. The thickness of the Ag layer can be chemically tuned by the amount of Ag supplied. Profiting from the uniformity and outstanding photothermal stability of the Pd seeds, the as-prepared core–shell Pd@Ag platelets are not only uniform in both size and shape (Figure 9.1c), but also display significantly enhanced photothermal stability compared with pure Ag nanostructures. Additionally, core–shell Pd@Au nanoplates were prepared (Figure 9.1d) as theranostic agents for in-vivo photoacoustic imaging, CT imaging, and

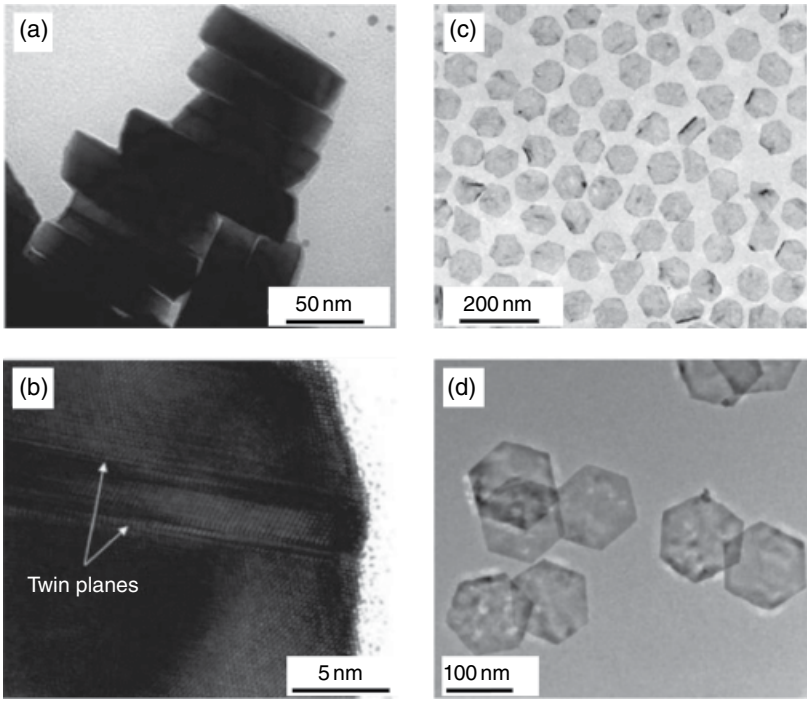

Figure 9.1 (a) Transmission electron microscopy (TEM) and (b) high-resolution transmission electron microscopy (HRTEM) images taken from the side faces of Pd–Pt nanoplates. Reproduced with permission from ref. [32]. Copyright (2008), American Chemical Society. (c) Representative large-area TEM image of Pd@Ag nanoplates. Reproduced with permission from ref. [33]. Copyright (2011), Wiley-VCH Verlag GmbH & Co. KGaA, Weinheim. (d) Representative TEM image Pd@Au nanoplates. Reproduced with permission from ref. [25]. Copyright (2014), Wiley-VCH Verlag GmbH & Co. KGaA, Weinheim.

photothermal therapy[25]. The synthesized core–shell Pd@Au nanoplates show strong near-IR (NIR) absorbance and excellent stability. By modifying their surface with thiol-polyethylene glycol (SH-PEG), the blood circulation of PEGylated Pd@Au nanoplates (Pd@Au-PEG) in vivo was prolonged. Through passive targeting, the accumulation of Pd@Au-PEG in the tumor site was higher than spherical Au nanoparticles with a similar hydrodynamic size.

Bimetallic nanoplates with Au core have also been successfully synthesized by using the seeded epitaxial growth method. Ultrathin face-centered-cubic (fcc) Au@Pt and Au@Pd core–shell nanoplates (Figure 9.2a and b) were obtained from hexagonal-close-packed (hcp) Au square sheets[34]. The Pt-layer growth results in a hcp-to-fcc phase transformation of the Au square sheets under ambient conditions. Interestingly, the obtained fcc Au@Pt rhombic nanoplates demonstrate a unique $(101)_f$ orientation with the same atomic arrangement extending from the Au core to the Pt shell. Importantly, this method can be extended to the epitaxial growth of Pd on hcp Au square sheets, resulting in the unprecedented formation of fcc Au@Pd rhombic nanoplates with $(101)_f$ orientation. In addition, Au@non-noble metal (Cu or Ni) core–shell nanoplates

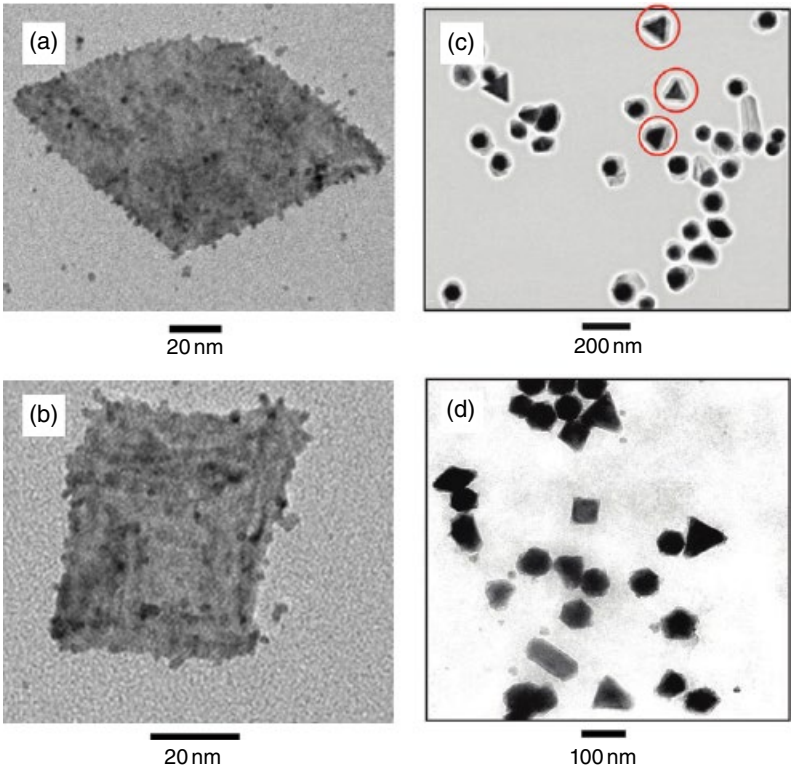

Figure 9.2 (a, b) Bright-field TEM image of a typical fcc Au@Pt rhombic nanoplate and a typical fcc Au@Pt square nanoplate. Reproduced with permission from ref. [34]. Copyright (2015), Wiley-VCH Verlag GmbH & Co. KGaA, Weinheim. (c, d) TEM images of Au@Cu and Au@Ni nanocrystals. Reproduced with permission from ref. [35,36]. Copyright (2011), American Chemical Society. Copyright 2010 American Chemical Society.

(Figure 9.2c and d) were prepared using a two-step reduction epitaxial growth method by Tsuji et al.[35,36]. First, mixtures of triangular and hexagonal plate like Au core seeds were prepared by reducing $HAuCl_4$ in ethylene glycol (EG) using microwave heating in the presence of PVP as a polymer surfactant. Then, Ni shells were overgrown on Au core seeds by reducing $Ni(NO_3)_2 \cdot 6H_2O$ in EG with NaOH and PVP using oil bath heating. Because a very large mismatch (13.6%) exists in lattice constants between Au (0.4079 nm) and Ni (0.3524 nm), the epitaxial growth of Ni shells over Au cores was expected to be difficult. Nevertheless, about 40 monolayers of Ni {111} shells were grown epitaxially on flat planes and sharp corners of Au {111} cores after heating reagent solution at 175 °C for 2 h. The selected area electron diffraction (SAED) patterns showed Ni layer parallel to Au layers.

In the case of Au@Cu with a smaller lattice mismatch of 11.4%, although the epitaxial growth of Cu {111} shells over Au core was observed, the growth rate on sharp corners was slower than that on flat {111} planes. In addition, by using a similar approach, 2D ultrathin Pd–Ag bimetallic nanosheets were used as model catalysts in selective dehydrogenation of formic acid for understanding the synergetic effects in bimetallic nanocatalysts.30 Because the nanosheets are utrathin, they can be used to probe the electronic and geometric structures using X-ray photoelectron spectroscopy and X-ray absorption spectroscopy. A series of highly active catalysts for hydrogen production from formic acid were successfully synthesized by controllably depositing Pd onto Ag nanoplates with different Ag nanoplanes, such as Ag {111}, Ag {100}, and the nanoplane on hexagonal close packing Ag crystal (Ag{hcp})[37].

9.2.2 Coreduction Process

The reduction of metal salts in a proper solvent is a common route to produce monometallic nanosheets. This simple strategy is also applied to preparing bimetallic nanosheets when two kinds of metal salts are put together. However, it is difficult to simultaneously control the reduction and nucleation process of the two metals because their redox potentials and chemical behaviors are different. According to the model of LaMer[38], highly monodispersed nanocrystals can only be prepared in a synthetic system, which can effectively separate nucleation and growth into two distinct steps. To avoid separate nucleation of two metals, proper reducing agent and reaction system should be selected. Recently, some groups have greatly developed this coreduction method and achieved the synthesis of bimetallic nanoplates or nanosheets, as well as controllable composition and structure by adopting proper reducing agent and reaction system. Peng et al. have developed a facile one-pot route for the synthesis of hexagonal and triangular Ni–Cu alloynanoplates, using oleylamine as a solvent and reducing agent, nickel (II) acetylacetonate and copper (II) chloridedihydrate as metal precursors, and trioctylphosphine as a capping agent[24]. Structural analyses (Figure 9.3a and b) indicate that the Ni–Cu nanoplates have an fcc crystalline structure and their side faces are bound by a mixture of {100} and {111} planes, while their top and bottom faces are bound by {111} planes. Noble bimetallic nanoplates, such as Ru–Pd, were synthesized via a facile polyol coreduction method, in which $Ru(acac)_3$ and $Pd(acac)_2$ were metal precursors and PVP act as the stabilizing agent[39]. It is suggested that the obtained nanoplates have alloyed structures over the full composition space and that they form through either monomer addition or coalescence mechanisms.

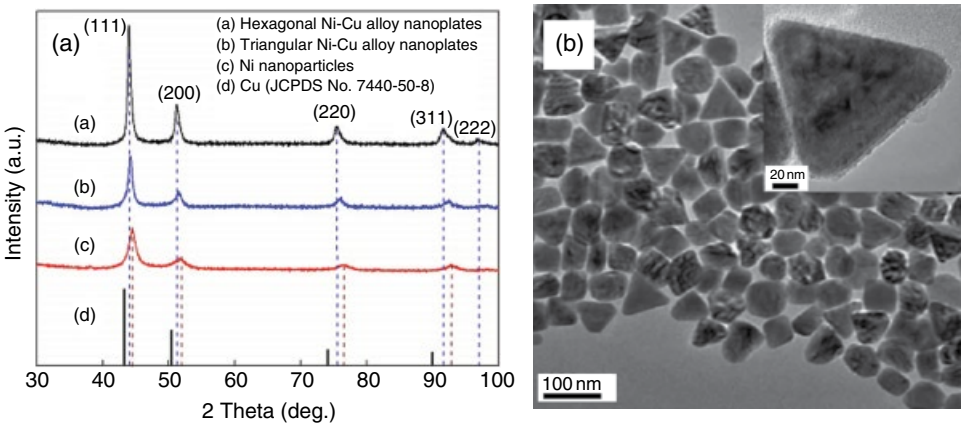

Figure 9.3 (a) X-ray diffraction (XRD) patterns and (b) TEM images of the Ni–Cu nanoplates when reaction temperature was 220 °C. Reproduced with permission from ref. [24]. Copyright (2012), Royal Society of Chemistry.

Recently, the synthesis of Pt–Bi nanomaterials has become a hot topic in catalysis due to their high catalytic activities and excellent stabilities[40–43]. Highly uniform and well-crystallized Bi–Rh nanoplates were obtained by low-temperature synthesis at 240 °C using the microwave-assisted polyol process[44]. In this reaction, the polyol acted as a solvent, reducing agent, and surfactant, while the microwave radiation led to fast and homogeneous nucleation and crystal growth. Electron microscopy analysis (Figure 9.4a and b) confirmed the presence of pseudohexagonal nanoplates with a primary particle diameter of 60 nm and high crystallinity. The above-mentioned Bi–Rh nanoplates exhibited an excellent selectivity toward ethylene of 88% at a conversion of 93% in the semihydrogenation of acetylene.

There are two problems in producing M–Bi nanostructures:

1) The bismuth precursor is easily hydrolyzed in water to form bismuth hydroxides or oxides.
2) In contrast with other metals, the melting point of bismuth is very low (271.3 °C), and overheating often leads to agglomeration of M–Bi nanocrystals.

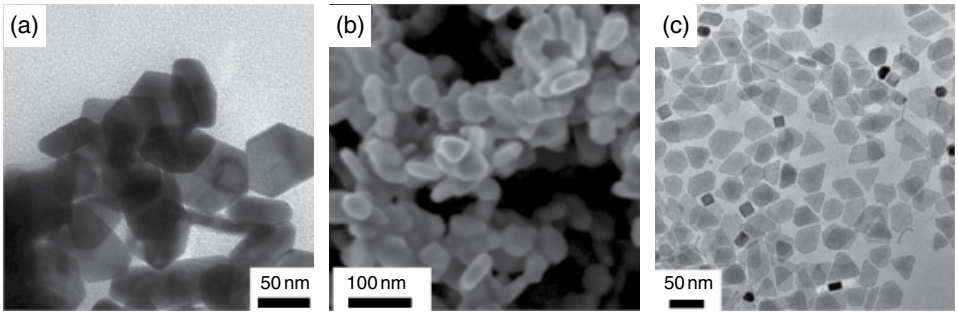

Figure 9.4 (a, b) TEM and SEM of BiRh nanoplates. Reproduced with permission from ref. [44]. Copyright 2012 American Chemical Society. (c) TEM image of lying Pt–Bi nanoplates. Reproduced with permission from ref. [45]. Copyright (2013), Royal Society of Chemistry.

In order to solve these problems, we designed a facile synthesis to prepare Pt–Bi nanoplatelets with controlled size and composition using a one-pot method (Figure 9.4c)[45]. The $Pt(acac)_2$ and $Bi(NE)_3$ were reduced simultaneously in the presence of OAm and NH_4Br. The as-prepared Pt–Bi nanoplatelets exhibit enhanced electrocatalytic activity toward formic acid and methanol oxidation with larger oxidation current density, higher tolerance to CO poisoning, and more negative onset potential in comparison with the commercial Pt/C catalyst. In addition, Lee et al. prepared BiPt nanoplates with a special atomic ratio, i.e., $Bi_{65}Pt_{35}$ bimetallic nanoplates, using oleylamine, 1-octadecene, 1,2-hexadecanediol as a reducer and $Pt(acac)_2$, and bismuth acetate as a metal precursor at a low temperature (100 °C) before the formation of $Bi_{21}Pt_{35}Pd_{44}$ porous nanoplates[46]. The $Bi_{65}Pt_{35}$ bimetallic nanoplates acted only as the sacrificial template.

9.2.3 Solvothermal Reaction

Hydrothermal and solvothermal methods are widely used in the synthesis of various nanomaterials due to their facile operation and simple setup[47]. However, compared to the other methods, these methods require relatively high energy consumption as a high temperature. Typically, the synthesis is conducted in a sealed autoclave at elevated temperature and pressure. Under such experimental conditions, water or nonaqueous solvents display variation in properties such as viscosity and dissociation constant.

Recently, solvothermal methods have been successfully employed in the synthesis of bimetallic nanosheets. For example, a solid–liquid interface mediated 2D growth method was used toward the synthesis of hierarchically coiled ultrathin bimetallic Ir–Rh nanosheets and Pt–Rh nanosheets (Figure 9.5a and b) using the benzyl alcohol solvothermal approach[48]. Interestingly, Ni–Co alloy nanosheets were obtained by Ghotbi et al. from reductive hydrothermal treatment of layered Ni–Co hydroxide carbonate, which was synthesized by the co-precipitation method using urea as precipitant agent[49]. This anionic layered Ni–Co hydroxide carbonate with hexagonal structure was constructed from nickel and cobalt ions within the layers and carbonate anions between the layers. Ni–Co alloys with pure cubic phase were obtained by a reductive hydrothermal-treatment of the layered precursor.

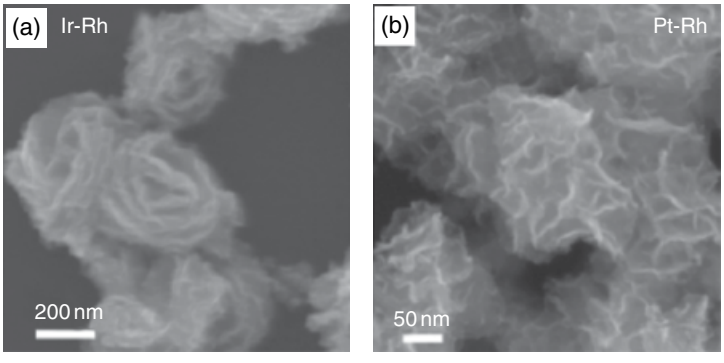

Figure 9.5 (a, b) SEM images of Ir–Rh and Pt–Rh nanosheets. Reproduced with permission from ref. [48]. Copyright (2016), Royal Society of Chemistry.

9.2.4 Galvanic Replacement Reaction

Since the heterogeneous nucleation and growth are mostly influenced by the difference in electronegativity between the two metals, it should be carefully considered when the galvanic replacement reaction is carried out. Unlike the seeded epitaxial growth, the metal with smaller electronegativity is more reactive and inert metal is usually selected as the seeds. In galvanic replacement reaction, an inactive metal is grown using an active metal as the template. Porous triangular Ag–Pd nanoplates of various bimetallic ratios were obtained by a galvanic displacement reaction, in which $Pd(OAc)_2$ reacted with Ag nanoplates[50–52]. The half-cell reactions and standard reduction potentials (E^{θ}) for this displacement reaction are as follows, and are a potential cause of the porous microstructure[50]:

$$\text{Anodic reaction}: Ag \rightarrow Ag^{+} + e^{-} \quad E^{\theta} = -0.7996V \tag{9.1}$$

$$\text{Cathodic reaction}: Pd^{2+} + 2e^{-} \rightarrow Pd \quad E^{\theta} = -0.951V \tag{9.2}$$

Hence, the net reaction potential is 0.1514 V. According to the formula $E = (RT/nF)\ln K$, the equilibrium constant K is calculated to be 3.83×104. It can be concluded that the displacement reaction using $Pd(OAc)_2$ easily proceeds and leads to the formation of triangular Ag/Pd nanoplates. Ag–Pt circular, hexagonal, and triangular nanoplates (Figure 9.6a, b, and c) were also prepared by the galvanic displacement reaction, in which added Pt^{2+} ions slowly reacted with the prepared Ag nanoplates templates, and used as electrocatalysts for hydrogen evolution reaction[53]. In addition, Luo et al. prepared the Ag–Au triangular nanoplates with tunable localized surface plasmon resonance and component via galvanic reaction[54]. The galvanic replacement between Ag nanoplates and $HAuCl_4$ is a face-selective etching process, and the free energies associated with the crystallographic planes of a fcc metal decrease in the order: $g(110) > g(100) > g(111)$[55]. Hence, the initial introduced $HAuCl_4$ would preferentially replace the Ag atoms around the edge (mainly on (110) and (100) planes) and form a ring-like structure. Owing to the close match of lattice spacing between Au and Ag, the ultrathin Au coating would form an alloyed structure, making a great contribution to stabilize the structure[56].

Actually, the procedure in galvanic replacement reaction is similar to the seeded-growth process, and usually involves a secondary metal ion and a pre-prepared metal in a reaction system. However, we should pay attention to an obvious difference between

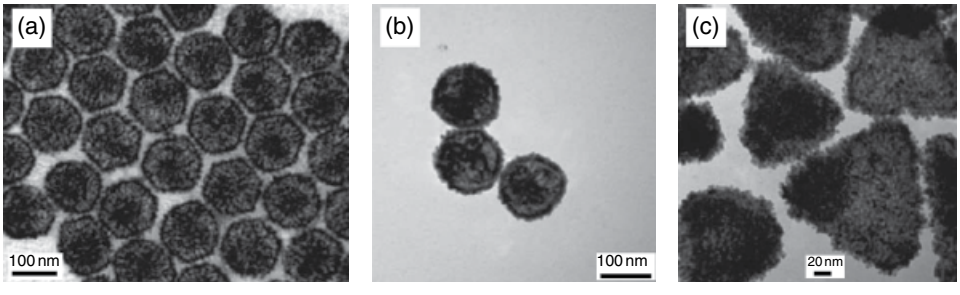

Figure 9.6 TEM images of Ag–Pt (a) hexagonal, (b) circular, and (c) triangular nanoplates. Reproduced with permission from ref. [53]. Copyright (2008), American Chemical Society.

the two processes. In the galvanic replacement process, the pre-prepared metal is used as a sacrificial template and will be partially consumed. In contrast, the pre-prepared metal is not destroyed but acts as a seed for the second metal growth in the seeded growth process.

Therefore, there are two key points to effectively synthesize bimetallic nanosheets by galvanic replacement reaction:

1) The amount of the secondary metal ion must be quantificationally controlled to avoid excessive consumption of pre-prepared metal template.
2) The replacement process must be effectively controlled to retain the morphology of the metal template.

The structure of final products strongly depends on the reaction conditions. If the conditions facilitate fast diffusion between the two metals during the galvanic reaction, alloys can be obtained. Otherwise, core–shell or yolk–shell bimetallic nanostructures will be produced[31].

9.2.5 Electrodeposition Process

The main driving force of electrodeposition process is the over potential, so the technology is flexible and the process is easy to carry out. The as-prepared products possess unique high density and low porosity. The influence of deposition variables, such as temperature, pH, and current density, is usually related to the morphology. Zhao et al. reported a hierarchically structured three-dimensional oxygen electrode prepared via a facile, one-step electrodeposition of amorphous, mesoporous nickel–iron hydroxide nanosheets onto nickel foam (NF) substrates[57]. The electrodeposition of nickel–iron hydroxide composites onto NF was undertaken in the electrolyte containing equal molar of nickel (II) and iron (III) nitrates. The deposition potential was controlled at −1.0 V versus Ag/AgCl to reduce NO_3- ions at the electrode surface, and then hydroxide ions were generated, increasing the pH value[58,59]. Ni^{2+} and Fe^{3+} ions reacted with local hydroxide ions to form bimetallic hydroxide, which deposited on the surface of electrodes. The reaction looks like this:

$$NO_3^- + 7H_2O + 8e^- \rightarrow NH_4 + 10OH^- \tag{9.3}$$

$$xNi^{2+} + yFe^{3+} + (2x+3y)OH^- \rightarrow Ni_xFe_yOH_{(2x+3y)} \tag{9.4}$$

The lateral extension of the nanosheet ranges from 50 nm to a few hundred nanometers, and the thickness is generally ~10 nm (Figure 9.7a). The rippled nanosheets are interconnected, forming mesoporous nickel–iron hydroxide nanosheets, with a pore size of ~50 nm. The nickel–iron hydroxide nanosheets scratched off from the NF substrate are highly transparent and show a rippled sheet structure with a dimension ~300 nm (Figure 9.7b). The three-dimensional (3D) interconnected macroscopic porous structure across the whole NF substrate offer a very high specific surface area, electrical conductivity, and integrity[60,61]. By the same method, Luo et al. fabricated a 3D electrode by a versatile and one-step electrodeposition of nickel–iron hydroxide nanosheets film on a Ni foam substrate, which showed high catalytic activity for both oxygen evolution reaction (OER) and hydrogen evolution reaction (HER) in basicmedia[23].

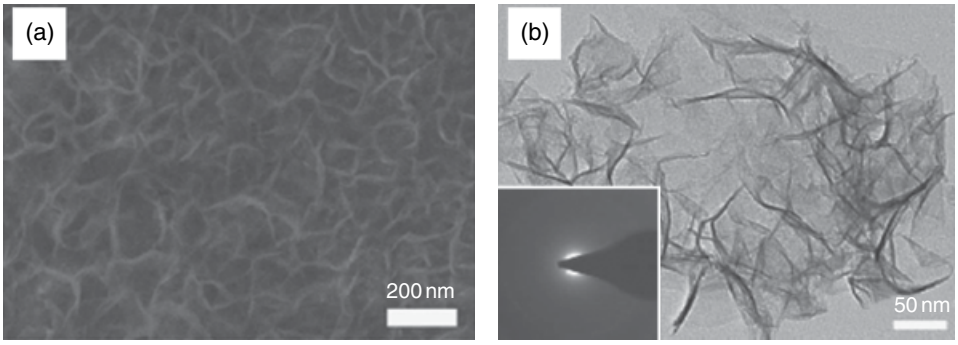

Figure 9.7 (a) High-resolution SEM image of the area squared in nickel–iron hydroxide nanosheets/NF electrode; (b) TEM image of Ni–Fe nanosheets scratched off from the nickel–iron hydroxide nanosheets/NF. Reproduced with permission from ref. [57]. Copyright (2015), Rights Managed by Nature Publishing Group.

9.2.6 Other Processes

Apart from the previous discussions, other methods are also reported for the preparation of bimetallic nanoplates or nanosheets. For example, Wang et al. have successfully synthesized free-standing ultrathin Pt–Cu alloy nanosheets of 4–6 atom thickness with diameters > 20 nm and tunable lateral size from 10 to 50 nm by a two-step method (Figure 9.8a), where gel-like materials were prepared in the first step and then they were used to confine the nucleation and subsequent growth process of the alloy nanosheets in the second step[62–64]. Subsequently, by slightly modifying, they prepared a most unusual Pt–Cu 2D alloy material that is 1–2 atoms thick (Figure 9.8b)[65]. In the reaction, ascorbic acid and potassium iodide play a crucial role. They control the thickness and size of the nanosheets. Sun and Lei reported an unusual method (i.e., chemical conversion of as-synthesized Ag nanoplates on GaAs substrates into Au–Ag alloy nanoplates)[66]. The success of compositional conversion is determined by the unique configuration of the Ag nanoplate/GaAs composite samples—that is, thin layers of oxide derived from the oxidation of GaAs cover the surfaces of the GaAs substrates. The schematic illustration is shown in Figure 9.8c.

Interestingly, to achieve uniform shape, Ahn et al. devised a tailored silica cage, in which particle synthesis generates a replica particle resembling a seed[67]. There is an advantage of this method that the shape of replicated nanoparticles can be varied through the initial shape of the seeds. With the optimization of the route, shape-persistent replica of Au–Ag bimetallic nanoplates can be synthesized in a tailored silica cage. A scheme for the replica synthesis is shown in Figure 9.9.

Sebastián and Jensen reported that a microfluidic synthesis in a micro-fabricated reactor (Figure 9.10) enables fast and facile synthesis of a wide library of metallic nanostructures, including bimetallic nanosheets and heterostructures[68]. In contrast to the traditional routes, the microfluidic continuous reacts at certain temperature and pressures produces nanocrystals on the time scales of seconds to minutes, which are realized by modification of precursor and reaction conditions, such as temperature, pressure, reactants, residence time, and flow conditions.

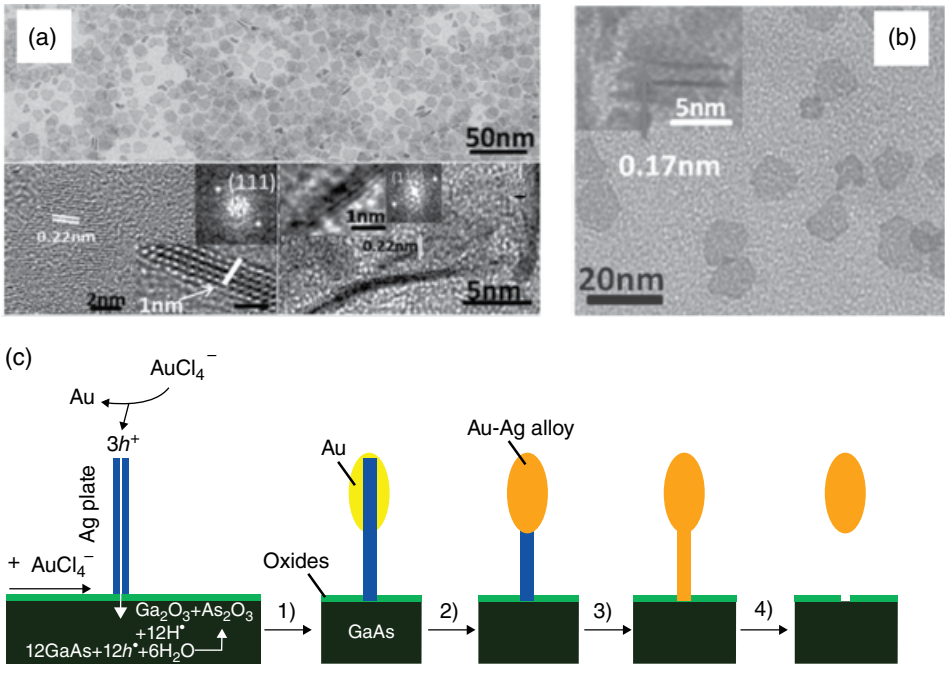

Figure 9.8 (a) TEM and HRTEM image of Pt–Cu nanosheets with a lateral average size of 10 nm. Reproduced with permission from ref. [64]. Copyright 2013 American Chemical Society. (b) TEM image of Pt–Cu nanosheets. Reproduced with permission from ref. [65]. Copyright (2015), Wiley-VCH Verlag GmbH & Co. KGaA, Weinheim. (c) Schematic illustration of the major steps involved in the conversion of Ag nanoplates into Au–Ag alloy nanoplates. Reproduced with permission from ref. [66]. Copyright (2009), Wiley-VCH Verlag GmbH & Co. KGaA, Weinheim.

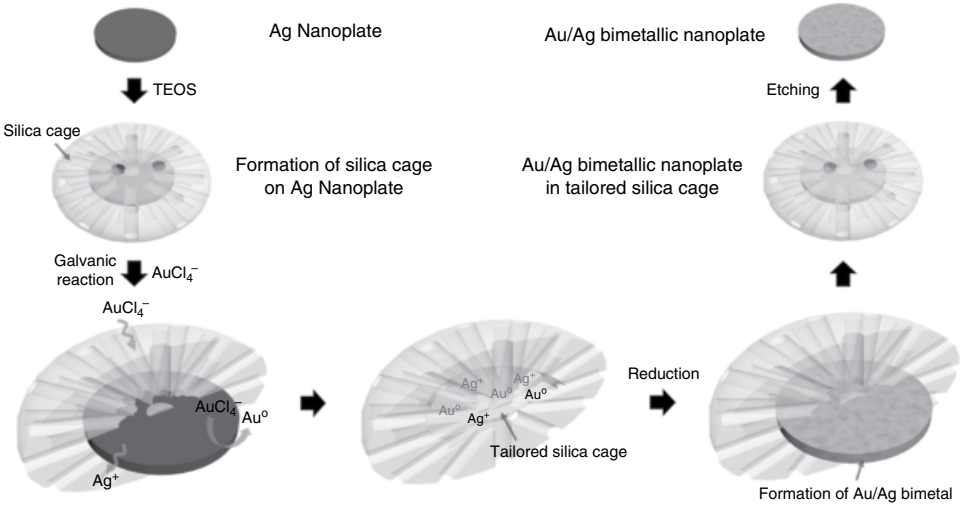

Figure 9.9 Scheme for the shape-persistent replica synthesis of the Au–Ag bimetallic nanoplate using a tailored silica cage. Reproduced with permission from ref. [67]. Copyright (2016), Wiley-VCH Verlag GmbH & Co. KGaA, Weinheim.

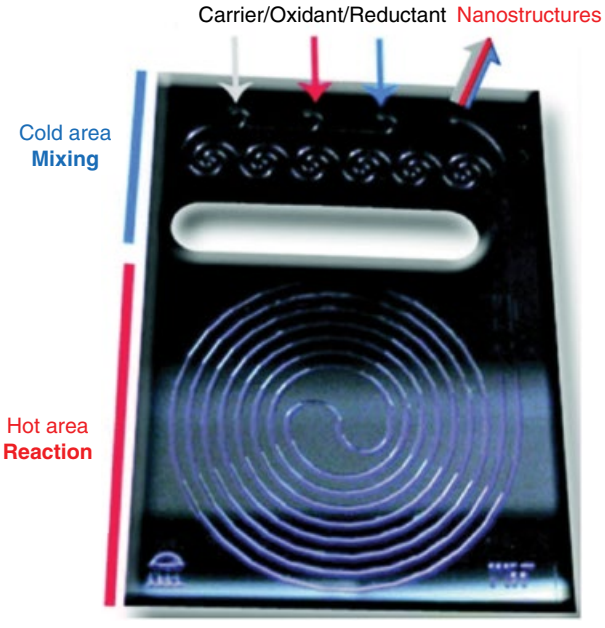

Figure 9.10 Silicon-Pyrex microfluidic reactor device used to synthesize the library of nanostructures. Reproduced with permission from ref. [68]. Published by The Royal Society of Chemistry.

9.3 Properties and Applications of Bimetallic Nanoplates and Nanosheets

9.3.1 Magnetic Properties

The bimetallic plates endow the materials with various changes in magnetic properties, such as coercivity, saturation magnetization, and magnetic anisotropy energy (MAE). For example, Osaka et al. described a three-element map indicating the coercivity and saturation magnetic flux density induced by alloying effects (Figure 9.11a and b)[69]. Anisotropy induced by shape distortions is theoretically predicted by Burkert et al., which shows an MAE even larger than that for Fe–Pt[70,71]. The Ni–Cu alloys nanoplates with face-centered cubic crystalline structure show extrinsic magnetic anisotropy resulted from the plate shape, which forms Ni–Cu with a higher divergence temperature in the field-cooled and zero-field-cooled curves[72]. The same shape anisotropy is also investigated in Fe–Co nanoplates prepared by surfactants-assisted ball milling[73].

In addition to the changes in magnetic properties, the bimetallic nanoplates are also fascinating in other magnetic related applications, such as microwave absorption. For example, the Fe–Co nanoplates exhibit excellent microwave absorption properties (the effective reflection loss values < -20 dB) in the frequency range of 3.7–10.5 GHz with the absorber thickness of 1.5–3.5 mm[74].

9.3.2 Catalytic Applications

Hydrogen has attracted enormous attention as a clean energy source due to its high gravimetric energy density and reputation as an environmentally friendly product. Splitting of water is one of the most efficient ways for producing H_2. However, water

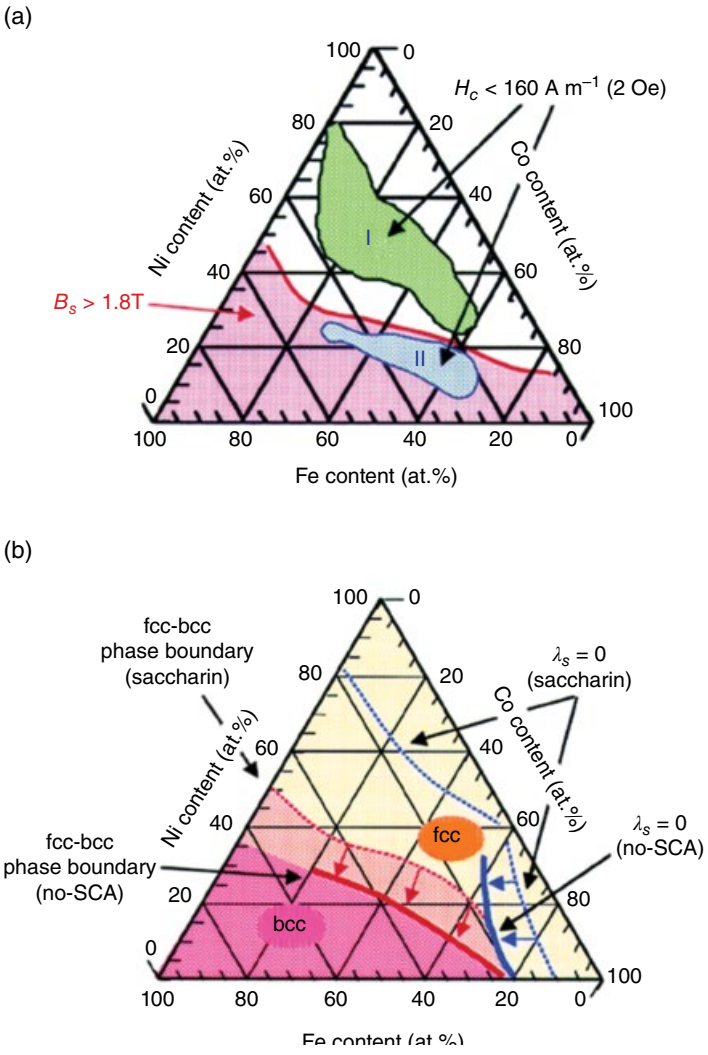

Figure 9.11 (a, b) Three-element maps showing compositions of electrochemical prepared CoNiFe films: (a) Map showing low-H_c regions (<160A m^{-1}) of two CoNiFe films produced by electroplating in baths with saccharin (region I) and with no sulphur-containing additives (SCA) (region II). Region I is located within the Bs = 1.0–1.7T region in the fcc single-phase area. Region II is located in the high-Bs (> 2.0T) region. (b) Map showing fcc–bcc phase boundaries and lines of zero λ_s. The fcc–bcc phase boundary in the film produced from the no-SCA bath is shifted to the left, towards the Ni-poor region. The λ_s = 0 line of the film produced from the no-SCA bath is also shifted to the left, toward the Fe-rich region. Reproduced with permission from ref. [69]. Copyright (1998), Rights Managed by Nature Publishing Group.

electrolysis still suffers from sluggish reaction kinetics, which requires onset potential higher than its thermodynamic value of 1.23 V. In order to improve the water splitting efficiency, high-performance electrocatalytic materials are being intensively investigated to facilitate the OER and HER. At present, typical electrocatalysts for water splitting reactions are mostly based on conventional noble metals, such as Pt for HER, and IrO_2 and RuO_2 for OER. However, the scarcity and the high cost of these catalysts make them

undesirable for widespread applications. The bimetallic nanosheets are emerging as effective catalysts for OER and HER. The enhanced activities of bimetallic nanosheets are mainly attributed to the synergetic effects from electronic effect, strain effect, geometric or ensemble effect, and other interfacial effects. Bimetallic nanosheets make it possible to reduce the overpotential for OER and HER even without the usage of conventional noble metals.

The Asiri group reported a facile one-step electrodeposition of Ni–Fe nanosheets film on Ni foam (Ni–Fe/NF) as a bifunctional catalytic material with high activity and stability for overall water splitting in basic electrolytes. The Ni–Fe/NF catalyst endows a current density of 10 mA/cm2 at a cell voltage of 1.64 V, which stimulates the development of bimetallic nanosheets as attractive bifunctional catalysts for electrochemical production of hydrogen fuels[23]. Besides, PD–Ag nanoplates have also been highly active catalysts for hydrogen production[37]. The high activity is attributed to the formation of PD–Ag alloy nanoplates, such as PD–Ag{111}, PD–Ag{100}, and PD–Ag{hcp}, with the activity order of nanoplates PD–Ag{hcp} > PD–Ag{111} > PD–Ag{100}. Particularly, the activity of PD–Ag {hcp} is up to an extremely high value. The plane on the hcp Ag crystal not only presents highly active catalysts for hydrogen generation but also may act as a potentially highly active nanomaterial for heterogeneous catalytic reactions.

The catalytic decomposition of formic acid to produce H_2 is also a big challenge, because efficient and selective catalysts are required to promote formic acid dehydrogenation ($HCOOH \rightarrow CO_2 + H_2$), rather than dehydration ($HCOOH \rightarrow CO + H_2O$)[30]. Pd–Ag bimetal nanosheets with different Ag/Pd ratios show high catalytic activity. The highest catalytic activity was achieved when the Ag/Pd molar ratio reached 1.

Ir–Rh nanosheets used as a catalyst for heterogeneous catalytic reactions have also been explored, as they show great activity in organic reactions. Free-standing Ir–Rh nanosheets exhibit high selectivities (86.1%) toward the selective reduction of nitrobenzene to azoxybenzene in ethanol[48]. Pt–Bi nanosheets exhibit enhanced electrocatalytic activity toward formic acid and methanol oxidation, higher tolerance to CO poisoning, and more negative onset potential in comparison with the commercial Pt–C catalyst. The outstanding catalytic property is due to the addition of the second metal, Bi. The bimetal nanosheets may offer promising potential applications in various catalysis fields, such as fuel cells and electrochemical and organic catalysis[44].

9.3.3 Optical and Biomedical Applications

Over the last decades, bimetallic nanostructures with SPR effects have been fully explored in broad applications, such as optical sensing of small molecules, spectra signal enhancement, photocatalysis, and photothermal therapy[75–79]. The SPR is capable in materials that possess a negative real and small positive imaginary dielectric constant, which originates from the coherent oscillation of the surface conduction electrons exited by electromagnetic radiation[80]. There is currently significant focus on understanding propagating and localized surface plasmons with the enhancement factors (EF) described as follows:

$$EF_{\mathrm{SERS}}(\omega_\upsilon) = \frac{\left|E_{\mathrm{out}}(\omega)^2\right|\left|E_{\mathrm{out}}(\omega-\omega_\upsilon)^2\right|}{E_0^4} = \frac{I_{\mathrm{SERS}}(\omega_\upsilon)/N_{\mathrm{surf}}}{I_{\mathrm{NRS}}(\omega_\upsilon)/N_{\mathrm{vol}}} \tag{9.5}$$

where $E_{out}(\omega)$ is the incident excitation, $E_{out}(\omega\text{-}\omega_\upsilon)$ is the resulting Stoke's shifted Raman, I_{SERS} (ω_υ) is SERS-enhanced Raman intensity, N_{surf} is the number of molecules bound to the enhancing metallic substrate, N_{surf} is the normal Raman intensity, and N_{vol} stand for the number of molecules in the excitation volume[80].

Usually, the Ag or Au nanoparticles and their anisotropic structures are used to tune the SPR over a wide spectra region, especially in the NIR region. Mirkin et al. reported the synthesis of Au_{core}–Ag_{shell} triangular bisfrustum nanocrystals by the reduction of Ag + ions onto Au triangular nanoprism seeds[81]. Via simulating the optical features based on atomic force microscope and scanning transmission electron microscopy experiments to simulate the optical features, it shows that the geometry of the structure is capable of tuning the SPR effects (Figure 9.12a). The Ag–Au triangular plates could also be fabricated through galvanic reaction[54]. Interestingly, the performed nanoplates exhibit tunable localized SPR and efficient two-photon luminescence under strong near-infrared laser and tough ion-contained environments, which is around double of that of Au nanorods of the two-photon absorption cross section. The Ag–Au shows much higher field strength than Ag from lighting rod effects (Figure 9.12b and c)[54].

Besides Au–Ag, the free-standing Pd sheets are also capable for SPR, though with the disadvantage that the sheets need to exhibit well-defined SPR absorption features[33]. In a previous study by Zheng et al., the ultrathin Pd sheets were coated with Ag at different thickness to integrate both tunable SPR properties and photothermal stability[33]. As reported by the authors, the resulting solution appears to be green when the Ag/Pd ratio is 1.8. As the Ag/Pd ratio is increased to 2.7, 3.6, 5.4, 7.3 and 11.0, the color of the products shifts from blue-green to blue, purple, to yellow, respectively (Figure 9.12d).

In addition to the SPR effects, bimetallic nanoplates are also well investigated in various biomedical applications. For example, Zheng et al. proposed a core–shell structured Pd@Au nanoplates as efficient theranostic agents. In order to achieve prolonged blood circulation time and to lower *in vivo* toxicity, polyethylene glycol is introduced to modify the Pd@Au surface. Figure 9.12e shows the photoacoustic imaging of the performed Pd@Au-PEG in tumor sites and the quantification photoacoustic signals at different time[25].

9.4 Conclusions and Perspectives

In summary, we briefly described recent developments related to solution synthesis of bimetallic nanoplates and nanosheets and their unique properties and corresponding applications in a few important fields. Some typical strategies for bimetallic nanoplates and nanosheets—including seeded epitaxial growth process, coreduction process, solvothermal methods, galvanic replacement reaction, and electrodeposition process—are introduced. The bimetallic nanoplates and nanosheets are promising candidates in a range of applications. However, some problems that obstruct the real applications of bimetallic nanoplates and nanosheets need to be addressed. On the one hand, there are few investigations for the general comprehension of nucleation and growth mechanism of bimetallic nanoplates and nanosheets due to the difficulty in detecting the movement and aggregation of metal atoms under experiment condition. On the other hand, large-scale economical production for bimetallic nanoplates and nanosheets is necessary for their widespread applications. Moreover, considering their application in catalytic reactions, the thicknesses of bimetallic nanoplates and nanosheets should be reduced to

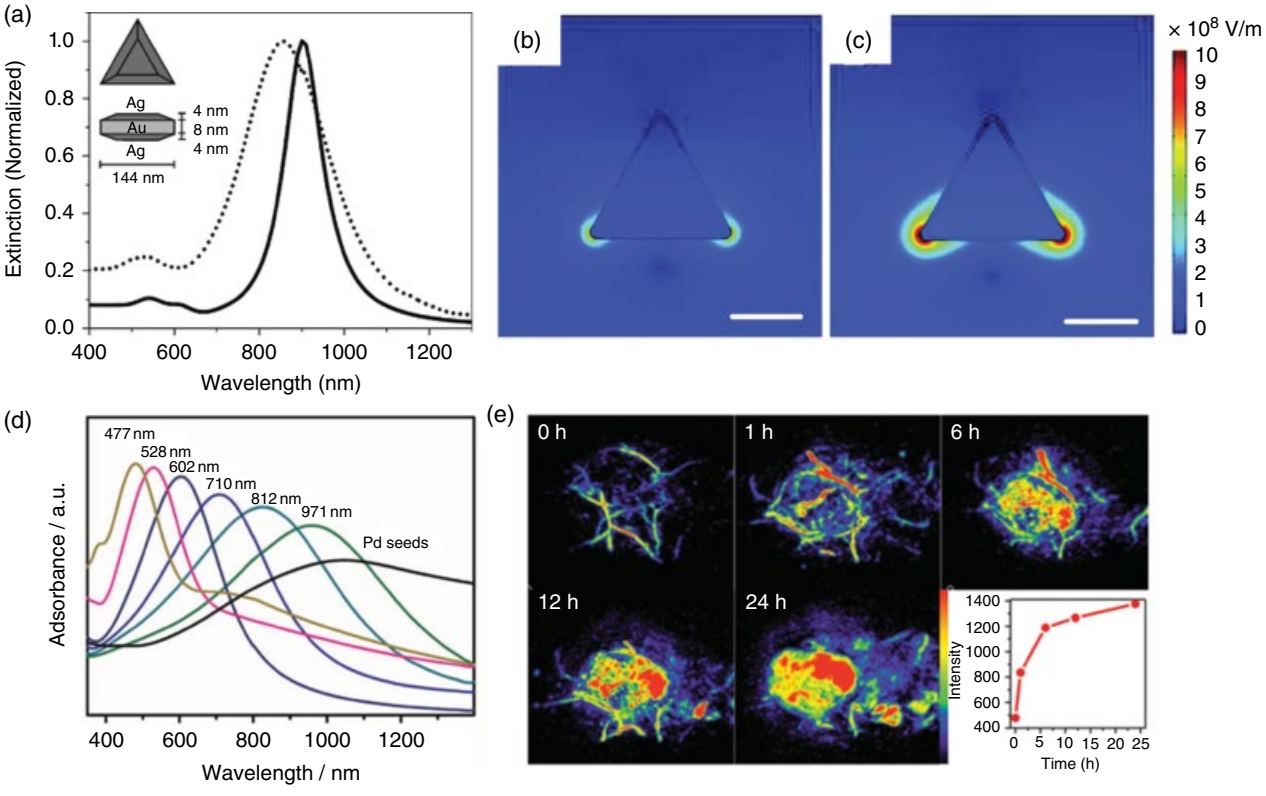

Figure 9.12 (a) Experimental (dotted line) and theoretical (DDA calculation, solid line) extinction spectra of Au_{core}-Ag_{shell} nanocrystals. Inset: structural model of Au_{core}-Ag_{shell} nanocrystal for the DDA calculation. Reproduced with permission from ref. [81]. Copyright (2009), American Chemical Society. (b, c) Electric field distributions of single. (b) Ag triangular nanoplates and (c) Ag–Au triangular nanoplates prepared with 1 ppm $HAuCl_4$ evaluated at $\lambda = 820$ nm. Water ($n = 1.33$) is assumed to be the surrounding media. Scale bar is 25 nm. Reproduced with permission from ref. [54]. Copyright (2014), Royal Society of Chemistry. (d) The precise tuning of the plasmon bands of the Pd@Ag core–shell bimetallic nanoplates by varying the $AgNO_3$/Pd nanoplates' molar ratio. From left to right, the samples were prepared using $AgNO_3$/Pd ratios of 1.8, 2.7, 3.6, 5.4, 7.3, and 11.0, respectively. Reproduced with permission from ref. [33]. Copyright (2011), Wiley-VCH Verlag GmbH & Co. KGaA, Weinheim. (e) Photoacoustic imaging of Pd@Au-PEG in tumor sites and quantification photoacoustic signals of tumor site at different time. Reproduced with permission from ref. [25]. Copyright (2014), Wiley-VCH Verlag GmbH & Co. KGaA, Weinheim.

enlarge their specific surface areas, which are critical factors for catalysis. The synthesis of single-atom layer bimetallic nanoplates and nanosheets has not yet been achieved. Therefore, there is still a long way to go to attain controlled synthesis of single-atom layer bimetallic nanoplates and nanosheets with desired sizes.

9.5 References

1 Pai, R. A., Humayun, R., Schulberg, M. T., Sengupta, A., Sun, J. N., and Watkins, J. J. (2004). Mesoporous silicates prepared using preorganized templates in supercritical fluids. *Science*, 303(5657), 507–510.

2 Yang, H. G., Sun, C. H., Qiao, S. Z., Zou, J., Liu, G., Smith, S. C., Cheng, H. M., and Lu, G. Q. (2008). Anatase TiO_2 single crystals with a large percentage of reactive facets. *Nature*, 453(7195), 638–641.

3 Yang, H. G., Liu, G., Qiao, S. Z., Sun, C. H., Jin, Y. G., Smith, S. C., Jin, Z., Cheng, H. M., and Lu, G. Q. (2009). Solvothermal synthesis and photoreactivity of anatase TiO_2 nanosheets with dominant {001} facets. *Journal of the American Chemical Society*, 131(11), 4078–4083.

4 Cölfen, H., and Mann, S. (2003). Higher-order organization by mesoscale self-assembly and transformation of hybrid nanostructures. *Angewandte Chemie International Edition*, 42(21), 2350–2365.

5 Wu, J. J., and Liu, S. C. (2002). Low-temperature growth of well-aligned ZnO nanorods by chemical vapor deposition. *Advanced materials*, 14(3), 215.

6 Han, W., Fan, S., Li, Q., and Hu, Y. (1997). Synthesis of gallium nitride nanorods through a carbon nanotube-confined reaction. *Science*, 277(5330), 1287–1289.

7 Pan, Z. W., Dai, Z. R., and Wang, Z. L. (2001). Nanobelts of semiconducting oxides. *Science*, 291(5510), 1947–1949.

8 Kolmakov, A., Klenov, D. O., Lilach, Y., Stemmer, S., and Moskovits, M. (2005). Enhanced gas sensing by individual SnO_2 nanowires and nanobelts functionalized with Pd catalyst particles. *Nano Letters*, 5(4), 667–673.

9 Duan, X., Huang, Y., Cui, Y., Wang, J., and Lieber, C. M. (2001). Indium phosphide nanowires as building blocks for nanoscale electronic and optoelectronic devices. *Nature*, 409(6816), 66–69.

10 Cui, Y., Lauhon, L. J., Gudiksen, M. S., Wang, J., and Lieber, C. M. (2001). Diameter-controlled synthesis of single-crystal silicon nanowires. *Applied Physics Letters*, 78(15), 2214–2216.

11 Ebbesen, T. W., and Ajayan, P. M. (1992). Large-scale synthesis of carbon. *Nature*, 358 p. 16.

12 Chopra, N. G., Luyken, R. J., Cherrey, K., and Crespi, V. H. (1995). Boron nitride nanotubes. *Science*, 269(5226) p. 966.

13 Ouyang, J., Pei, J., Kuang, Q., Xie, Z., and Zheng, L. (2014). Supersaturation-controlled shape evolution of α-Fe_2O_3 nanocrystals and their facet-dependent catalytic and sensing properties. *ACS Applied Materials & Interfaces*, 6(15), 12505–12514.

14 Teng, Y., Kusano, Y., Azuma, M., Haruta, M., and Shimakawa, Y. (2011). Morphology effects of Co_3O_4 nanocrystals catalyzing CO oxidation in a dry reactant gas stream. *Catalysis Science & Technology*, 1(6), 920–922.

15 Zeng, Y., Hao, R., Xing, B., Hou, Y., and Xu, Z. (2010). One-pot synthesis of Fe_3O_4 nanoprisms with controlled electrochemical properties. *Chemical Communications*, 46(22), 3920–3922.

16 Hou, Y., Kondoh, H., Shimojo, M., Kogure, T., and Ohta, T. (2005). High-yield preparation of uniform cobalt hydroxide and oxide nanoplatelets and their characterization. *The Journal of Physical Chemistry B*, 109(41), 19094–19098.

17 Sun, Y., Sun, Z., Gao, S., Cheng, H., Liu, Q., Piao, J., Yao, T., Wu, C., Hu, S., Wei, S., and Xie, Y. (2012). Fabrication of flexible and freestanding zinc chalcogenide single layers. *Nature Communications*, 3 p. 1057.

18 Zhu, Y., Murali, S., Stoller, M. D., Ganesh, K. J., Cai, W., Ferreira, P. J., Piekle, A., Wallace, R. M., Cychosz, K. A., Thommes, M., Su, D., Stach, E. A., and Ruoff, R. M. (2011). Carbon-based supercapacitors produced by activation of graphene. *Science*, 332(6037), 1537–1541.

19 Novoselov, K. S., Geim, A. K., Morozov, S. V., Jiang, D., Zhang, Y., Dubonos, S. V., Grigorieva, I. V., and Firsov, A. A. (2004). Electric field effect in atomically thin carbon films. *Science*, 306(5696), 666–669.

20 Zhang, Y., Tan, Y. W., Stormer, H. L., and Kim, P. (2005). Experimental observation of the quantum Hall effect and Berry's phase in graphene. *Nature*, 438(7065), 201–204.

21 Duan, H., Yan, N., Yu, R., Chang, C. R., Zhou, G., Hu, H. S., Rong, H., Niu, Z., Mao, J., Asakura, H., Tanaka, T., Dyson, P. J., Li, J., and Li, Y. (2014). Ultrathin rhodium nanosheets. *Nature Communications*, 5 pp. 3093–3101.

22 Huang, X., Zhao, Z., Fan, J., Tan, Y., and Zheng, N. (2011). Amine-assisted synthesis of concave polyhedral platinum nanocrystals having {411} high-index facets. *Journal of the American Chemical Society*, 133(13), 4718–4721.

23 Luo, Q., Peng, M., Sun, X., Luo, Y., and Asiri, A. M. (2016). Efficient electrochemical water splitting catalyzed by electrodeposited NiFe nanosheets film. *International Journal of Hydrogen Energy*, 41(21), 8785–8792.

24 Zhang, P., Sui, Y., Wang, C., Wang, Y., Cui, G., Wang, C., Liu, B., and Zou, B. (2014). A one-step green route to synthesize copper nanocrystals and their applications in catalysis and surface enhanced Raman scattering. *Nanoscale*, 6(10), 5343–5350.

25 Chen, M., Tang, S., Guo, Z., Wang, X., Mo, S., Huang, X., Liu, G., and Zheng, N. (2014). Core-shell Pd@Au nanoplates as theranostic agents for in-vivo photoacoustic imaging, CT imaging, and photothermal therapy. *Advanced Materials*, 26(48), 8210–8216.

26 Tedsree, K., Chan, C. W. A., Jones, S., Cuan, Q., Li, W. K., Gong, X. Q., and Tsang, S. C. E. (2011). 13C NMR guides rational design of nanocatalysts via chemisorption evaluation in liquid phase. *Science*, 332(6026), 224–228.

27 Zhang, S., Zhang, X., Jiang, G., Zhu, H., Guo, S., Su, D., Lu, G., and Sun, S. (2014). Tuning nanoparticle structure and surface strain for catalysis optimization. *Journal of the American Chemical Society*, 136(21), 7734–7739.

28 Maroun, F., Ozanam, F., Magnussen, O. M., and Behm, R. J. (2001). The role of atomic ensembles in the reactivity of bimetallic electrocatalysts. *Science*, 293(5536), 1811–1814.

29 Chen, G., Zhao, Y., Fu, G., Duchesne, P. N., Gu, L., Zheng, Y., Weng, X., Chen, M., Zhang, P., Pao, C. H., and Lee, J. F. (2014). Interfacial effects in iron–nickel hydroxide–platinum nanoparticles enhance catalytic oxidation. *Science*, 344(6183), 495–499.

30 Hu, C., Mu, X., Fan, J., Ma, H., Zhao, X., Chen, G., Zhou, Z., and Zheng, N. (2016). Interfacial effects in PdAg bimetallic nanosheets for selective dehydrogenation of formic acid. *ChemNanoMat*, 2(1), 28–32.

31 Wang, D., and Li, Y. (2011). Bimetallic nanocrystals: liquid-phase synthesis and catalytic applications. *Advanced Materials*, 23(9), 1044–1060.

32 Lim, B., Wang, J., Camargo, P. H., Jiang, M., Kim, M. J., and Xia, Y. (2008). Facile synthesis of bimetallic nanoplates consisting of Pd cores and Pt shells through seeded epitaxial growth. *Nano letters*, 8(8), 2535–2540.

33 Huang, X., Tang, S., Liu, B., Ren, B., and Zheng, N. (2011). Enhancing the photothermal stability of plasmonic metal Nanoplates by a core-shell architecture. *Advanced Materials*, 23(30), 3420–3425.

34 Fan, Z., Zhu, Y., Huang, X., Han, Y., Wang, Q., Liu, Q., Huang, Y., Gan, C. L., and Zhang, H. (2015). Synthesis of ultrathin face-centered-cubic Au@Pt and Au@Pd core-shell nanoplates from hexagonal-close-packed Au Square Sheets. *Angewandte Chemie International Edition*, 54(19), 5672–5676.

35 Tsuji, M., Yamaguchi, D., Matsunaga, M., and Ikedo, K. (2011). Epitaxial growth of Au@ Ni core-shell nanocrystals prepared using a two-step reduction method. *Crystal Growth & Design*, 11(5), 1995–2005.

36 Tsuji, M., Yamaguchi, D., Matsunaga, M., and Alam, M. J. (2010). Epitaxial growth of Au@Cu core shell nanocrystals prepared using the PVP-assisted polyol reduction method. *Crystal Growth & Design*, 10(12), 5129–5135.

37 Wang, W., He, T., Liu, X., He, W., Cong, H., Shen, Y., Yan, L., Zhang, X., Zhang, J., and Zhou, X. (2016). Highly active carbon supported Pd–Ag nanofacets catalysts for hydrogen production from HCOOH. *ACS Applied Materials & Interfaces*, 8(32), 20839–20848.

38 Redel, E., Walter, M., Thomann, R., Hussein, L., Krüger, M., and Janiak, C. (2010). Stop-and-go, stepwise and "ligand-free" nucleation, nanocrystal growth and formation of Au–NPs in ionic liquids (ILs). *Chemical Communications*, 46(7), 1159–1161.

39 Ma, X., Lin, R., Ofoli, R. Y., Mei, Z., and Jackson, J. E. (2016). Structural and morphological evaluation of Ru–Pd bimetallic nanocrystals. *Materials Chemistry and Physics*, 173 pp. 1–6.

40 Oana, M., Hoffmann, R., Abruña, H. D., and DiSalvo, F. J. (2005). Adsorption of CO on $PtBi_2$ and PtBi surfaces. *Surface science*, 574(1), 1–16.

41 Casado-Rivera, E., Gal, Z., Angelo, A. C. D., Lind, C., DiSalvo, F. J., and Abruña, H. D. (2003). Electrocatalytic oxidation of formic acid at an ordered intermetallic PtBi surface. *ChemPhysChem*, 4(2), 193–199.

42 Zhang, B. W., He, C. L., Jiang, Y. X., Chen, M. H., Li, Y. Y., Rao, L., and Sun, S. G. (2012). High activity of PtBi intermetallics supported on mesoporous carbon towards HCOOH electro-oxidation. *Electrochemistry Communications*, 25, 105–108.

43 Li, S. H., Zhao, Y., Chu, J., Li, W. W., Yu, H. Q., and Liu, G. (2013). Electrochemical degradation of methyl orange on Pt–Bi/C nanostructured electrode by a square-wave potential method. *Electrochimica Acta*, 92, 93–101.

44 Köhler, D., Heise, M., Baranov, A. I., Luo, Y., Geiger, D., Ruck, M., and Armbrüster, M. (2012). Synthesis of BiRh nanoplates with superior catalytic performance in the semihydrogenation of acetylene. *Chemistry of Materials*, 24(9), 1639–1644.

45 Liao, H., Zhu, J., and Hou, Y. (2014). Synthesis and electrocatalytic properties of PtBi nanoplatelets and PdBi nanowires. *Nanoscale*, 6(2), 1049–1055.

46 Lee, K. Y., Lee, Y. W., Kim, M., and Kim, T. H. (2014). Fabrication of $Bi_xPt_yPd_z$ alloy nanoporous plates with electro-catalytic activity. *Journal of Materials Chemistry A*, 2(8), 2735–2741.

47 Liu, B., and Zeng, H. C. (2003). Hydrothermal synthesis of ZnO nanorods in the diameter regime of 50 nm. *Journal of the American Chemical Society*, 125(15), 4430–4431.

48 Zhang, Z. P., Wang, X. Y., Yuan, K., Zhu, W., Zhang, T., Wang, Y. H., Ke, J., Zheng, X. Y., Yan, C. H., and Zhang, Y. W. (2016). Free-standing iridium and rhodium-based hierarchically-coiled ultrathin nanosheets for highly selective reduction of nitrobenzene to azoxybenzene under ambient conditions. *Nanoscale*, 8(34), 15744–15752.

49 Ghotbi, M. Y., Jolagah, A., and Afrasiabi, H. A. (2012). Nickel–cobalt alloy nanosheets obtained from reductive hydrothermal-treatment of nickel–cobalt hydroxide carbonate. *Materials Research Bulletin*, 47(3), 631–634.

50 Lee, C. L., Chiou, H. P., Syu, C. M., Liu, C. R., Yang, C. C., and Syu, C. C. (2011). Displacement triangular Ag/Pd nanoplate as methanol-tolerant electrocatalyst in oxygen reduction reaction. *International Journal of Hydrogen Energy*, 36(20), 12706–12714.

51 Lee, C. L., Tseng, C. M., Wu, R. B., Wu, C. C., and Syu, C. M. (2009). Porous Ag–Pd triangle nanoplates with tunable alloy ratio for catalyzing electroless copper deposition. *Colloids and Surfaces A: Physicochemical and Engineering Aspects*, 352(1), 84–87.

52 Lee, C. L., Tseng, C. M., and Wu, R. B. (2009). Triangular Ag/Pd nanoplates with sawtooth edges: Displacement synthesis and optical and catalytic properties. *Electrochemistry Communications*, 11(3), 627–630.

53 Lee, C. L., and Tseng, C. M. (2008). Ag–Pt nanoplates: galvanic displacement preparation and their applications as electrocatalysts. *The Journal of Physical Chemistry C*, 112(35), 13342–13345.

54 Sun, J., Wang, X., Liu, J., Wan, P., Liao, Q., Wang, F., Luo, L. and Sun, X. M. (2014). Highly stable Ag–Au nanoplates and nanoframes for two-photon luminescence. *RSC Advances*, 4(67), 35263–35267.

55 Zhang, C., Luo, L., Luo, J., Evans, D. G., and Sun, X. (2012). A process-analysis microsystem based on density gradient centrifugation and its application in the study of the galvanic replacement mechanism of Ag nanoplates with $HAuCl_4$. *Chemical Communications*, 48(58), 7241–7243.

56 Sun, Y., and Xia, Y. (2004). Mechanistic study on the replacement reaction between silver nanostructures and chloroauric acid in aqueous medium. *Journal of the American Chemical Society*, 126(12), 3892–3901.

57 Lu, X., and Zhao, C. (2015). Electrodeposition of hierarchically structured three-dimensional nickel–iron electrodes for efficient oxygen evolution at high current densities. *Nature communications*, 6, 6616–6622.

58 Zhao, D. D., Bao, S. J., Zhou, W. J., and Li, H. L. (2007). Preparation of hexagonal nanoporous nickel hydroxide film and its application for electrochemical capacitor. *Electrochemistry Communications*, 9(5), 869–874.

59 Yuan, C., Li, J., Hou, L., Zhang, X., Shen, L., and Lou, X. W. D. (2012). Ultrathin mesoporous $NiCo_2O_4$ nanosheets supported on Ni foam as advanced electrodes for supercapacitors. *Advanced Functional Materials*, 22(21), 4592–4597.

60 Chen, J., Sheng, K., Luo, P., Li, C., and Shi, G. (2012). Graphene hydrogels deposited in nickel foams for high-rate electrochemical capacitors. *Advanced Materials*, 24(33), 4569–4573.

61 Chang, Y. H., Lin, C. T., Chen, T. Y., Hsu, C. L., Lee, Y. H., Zhang, W., Wei, K. H., and Li, L. J. (2013). Highly efficient electrocatalytic hydrogen production by MoS_x grown on graphene-protected 3D Ni foams. *Advanced Materials*, 25(5), 756–760.

62 Xue, P., Lu, R., Huang, Y., Jin, M., Tan, C., Bao, C., Wang, Z., and Zhao, Y. (2004). Novel pearl-necklace porous CdS nanofiber templated by organogel. *Langmuir*, 20(15), 6470–6475.

63 Gao, P., Zhan, C., and Liu, M. (2006). Controlled synthesis of double-and multiwall silver nanotubes with template organogel from a bolaamphiphile. *Langmuir*, 22(2), 775–779.

64 Saleem, F., Zhang, Z., Xu, B., Xu, X., He, P., and Wang, X. (2013). Ultrathin Pt–Cu nanosheets and nanocones. *Journal of the American Chemical Society*, 135(49), 18304–18307.

65 Saleem, F., Xu, B., Ni, B., Liu, H., Nosheen, F., Li, H., and Wang, X. (2015). Atomically thick Pt–Cu nanosheets: self-assembled sandwich and nanoring-like structures. *Advanced Materials*, 27(12), 2013–2018.

66 Sun, Y., and Lei, C. (2009). Synthesis of Out-of-Substrate Au–Ag Nanoplates with Enhanced Stability for Catalysis. *Angewandte Chemie International Edition*, 48(37), pp. 6824–6827.

67 Roh, J., Back, S. H., and Ahn, D. J. (2016). Shape-persistent replica synthesis of gold/silver bimetallic nanoplates using tailored silica cages. *Small*, 12(10), 1322–1327.

68 Sebastián, V., and Jensen, K. F. (2016). Nanoengineering a library of metallic nanostructures using a single microfluidic reactor. *Nanoscale*, 8(33), 15288–15295.

69 Osaka, T., Takai, M., Hayashi, K., Ohashi, K., Saito, M., and Yamada, K. (1998). A soft magnetic CoNiFe film with high saturation magnetic flux density and low coercivity. *Nature*, 392(6678), 796–798.

70 Weller, D., Moser, A., Folks, L., Best, M. E., Lee, W., Toney, M. F., Schwichert, M., Thiele, J. U., and Doerner, M. F. (2000). High Kμ materials approach to 100 Gbits/in2. *IEEE Transactions on Magnetics*, 36(1), 10–15.

71 Burkert, T., Nordström, L., Eriksson, O., and Heinonen, O. (2004). Giant magnetic anisotropy in tetragonal FeCo alloys. *Physical Review Letters*, 93(2) p. 027203.

72 Guo, H., Chen, Y., Ping, H., Wang, L., and Peng, D. L. (2012). 'One-pot synthesis of hexagonal and triangular nickel–copper alloy nanoplates and their magnetic and catalytic properties. *Journal of Materials Chemistry*, 22(17), 8336–8344.

73 Poudyal, N., Rong, C. B., and Liu, J. P. (2011). Morphological and magnetic characterization of Fe, Co, and FeCo nanoplates and nanoparticles prepared by surfactants-assisted ball milling. *Journal of Applied Physics*, 109(7), 07B526.

74 Yang, Y., Xu, C., Xia, Y., Wang, T., and Li, F. (2010). Synthesis and microwave absorption properties of FeCo nanoplates. *Journal of Alloys and Compounds*, 493(1), 549–552.

75 Gordon, R., Sinton, D., Kavanagh, K. L., and Brolo, A. G. (2008). A new generation of sensors based on extraordinary optical transmission. *Accounts of Chemical Research*, 41(8), 1049–1057.

76 Langhammer, C., Yuan, Z., Zorić, I., and Kasemo, B. (2006). Plasmonic properties of supported Pt and Pd nanostructures. *Nano Letters*, 6(4), 833–838.

77 Larsson, E. M., Langhammer, C., Zorić, I., and Kasemo, B. (2009). Nanoplasmonic probes of catalytic reactions. *Science*, 326(5956), 1091–1094.

78 Lal, S., Clare, S. E., and Halas, N. J. (2008). Nanoshell-enabled photothermal cancer therapy: impending clinical impact. *Accounts of Chemical Research*, 41(12), 1842–1851.

79 Jain, P. K., Huang, X., El-Sayed, I. H., and El-Sayed, M. A. (2008). Noble metals on the nanoscale: optical and photothermal properties and some applications in imaging, sensing, biology, and medicine. *Accounts of Chemical Research*, 41(12), 1578–1586.

80 Willets, K. A. and Duyne, R. P. V. (2007). Localized surface pasmon resonance spectroscopy and sensing. *Annual Review of Physical Chemistry*., 58 pp. 267–297.

81 Yoo, H., Millstone, J. E., Li, S., Jang, J. W., Wei, W., Wu, J., Schatz, G. C., and Mirkin, C. A. (2009). Core-shell triangular bifrustums. *Nano Letters*, 9(8), 3038–3041.

Part III

Applications of Shape-Controlled Bimetallic Nanostructures

10

Electrocatalysis

Jiwhan Kim, Juhyuk Choi, Jinkyu Lim, and Hyunjoo Lee

Department of Chemical and Biomolecular Engineering, Korea Advanced Institute of Science and Technology, Daejeon, South Korea

10.1 Introduction

Bimetallic nanostructures have been developed to minimize the utilization of precious metals or to endow the secondary function to the primary metal surface. Pt-based alloy materials have been the most actively explored. The mixture of Pt with another precious metal of Pd or Ru has been investigated, in addition to the mixture of Pt with transition metals such as Ni, Co, or Fe. These mixtures would have the modified Pt electronic structure, the bifunctional effect from Pt and the secondary atom, and the modified surface structure without Pt ensemble sites. These features can affect the surface reaction with different activity, selectivity, and durability. Characterizing the features of the bimetallic nanostructures accurately can be quite challenging. Various techniques such as electron microscopy, X-ray diffraction, X-ray photoelectron spectroscopy (XPS), and X-ray absorption spectroscopy should be combined to evaluate the bimetallic structure properly. Recent advances such as scanning transmission electron microscopy mapping have especially enabled the direct observation of the bimetal distribution. The change in electronic structures can be observed by using XPS or X-ray absorption techniques of X-ray absorption near edge structure (XANES).

The bimetallic materials have been widely used for various surface reactions, and electrochemical reactions are the most important applications. As more environmentally friendly energy generation or energy usage becomes possible, fuel cells have become one of the most important alternatives for vehicles. The largest hurdle hindering the commercialization of the fuel cell is its high price, mainly due to the massive utilization of Pt catalysts. Pt-based alloy catalysts are the most realistic solution for minimizing Pt usage while retaining good activity and durability. The highest activity for the fuel cell cathode reaction, known as the oxygen reduction reaction, was reported for octahedral Pt–Ni alloy nanoparticles, which was predicted from a single crystalline model study. Their stability in acidic condition can be improved significantly by using Mo-doped Pt–Ni octahedra. Other types of electrochemical reactions from oxidizing

Bimetallic Nanostructures: Shape-Controlled Synthesis for Catalysis, Plasmonics, and Sensing Applications, First Edition. Edited by Ya-Wen Zhang.
© 2018 John Wiley & Sons Ltd. Published 2018 by John Wiley & Sons Ltd.

formic acid, methanol, and hydrogen, and oxygen evolution reaction can benefit from the bimetallic nanostructure as well.

In this review, we will cover the electronic, bifunctional, ensemble, and morphology effects of bimetallic structures. Many electrochemical reactions have been studied using various bimetallic structures, and their examples will be listed. Each reaction needs different features, so the best catalyst for respective electrochemical reactions is quite different. We hope that this short review will provide useful guidelines for developing even better bimetallic catalysts for the electrochemical reactions.

10.2 Effect of Bimetallic Nanostructures

Bimetallic nanocatalysts have been actively studied over the past few decades to improve their activity and durability for various electrocatalytic reactions. Unlike the monometallic catalysts, the bimetallic catalysts exhibit distinct properties resulting from modulations in the electronic structure, the bifunctional effect, the absence of surface ensemble sites, and the morphology effect. The details are explained in this chapter.

10.2.1 Electronic Effect

The surface electronic structure of the metallic catalyst can be modified by interactions with another metal. Density functional theory (DFT) calculations are often used as a tool to explain the electronic effect. Nørskov et al. reported on the modification of the surface Pt electronic structure by subsurface transition metals using DFT calculations[1, 2]. The d-orbitals of Pt can overlap more by interacting with subsurface transition metals, resulting in broadening the d-band. Then, the average value of d-band, which is often called the *d-band center*, decreases. This d-band center downshift causes dissociative adsorption energies of adsorbates such as H_2 and O_2 weaker than the bare Pt surface.

Figure 10.1 shows the relationship among the oxygen-binding energy, electronic structure, and catalytic activity for electrocatalytic oxygen reduction reaction (ORR). Figure 10.1a exhibits the oxygen binding energy of Pt–M (M = Ti, Fe, Co, Ni) bimetallic catalysts as a function of the surface Pt d-band center. All the Pt–M bimetallic catalysts show a decrease in oxygen binding energies followed by a d-band center downshift. Also, Figure 10.1b exhibits the relationship between the ORR activities of Pt–M bimetallic catalysts and d-band center downshift. Both the DFT calculation predictions and experimentally measured values display a volcano plot. This relationship clearly demonstrates the effect of the electronic effect on the catalytic activity. The modification in electronic structure by synthesizing bimetallic catalysts is an important tool for catalyst design.

10.2.2 Bifunctional Effect

Some electrocatalytic reactions need two different kinds of active sites. The catalysts containing active sites with different functions are called bifunctional catalysts. Each of the bifunctional metals has a different role in the reactions. Methanol oxidation reaction (MOR) is the important reaction for direct methanol fuel cells (DMFCs). Pt is

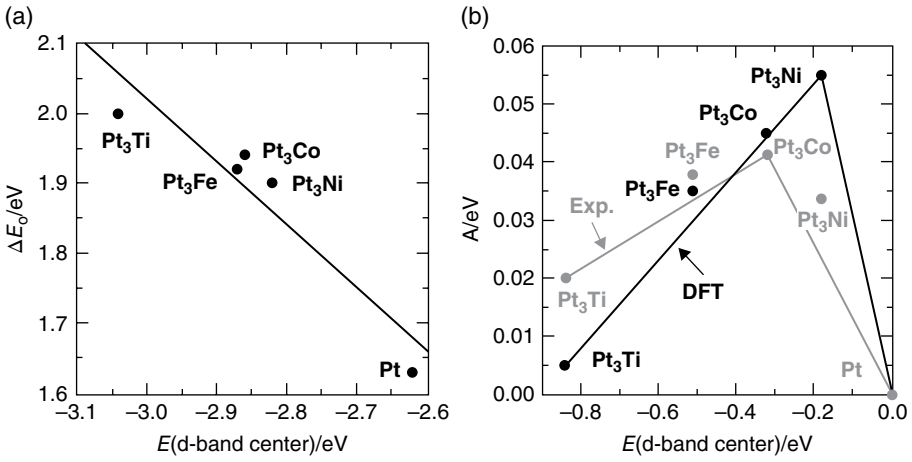

Figure 10.1 (a) The oxygen-binding energies as a function of d-band center. (b) ORR activities vs. the experimentally measured d-band center of Pt alloy relative to Pt. The calculated activities from DFT simulations are shown in the black line, and the measured activities from experiments are shown in the gray line. Reproduced from ref. [1] with permission.

generally used as catalysts for MOR. However, monometallic Pt catalysts are easily poisoned by CO molecules, which are produced as reaction intermediates during the methanol oxidation. PtRu bimetallic electrocatalysts with a bifunctional effect have been investigated with mitigated CO poisoning. Tong et al. suggested the bifunctional MOR mechanism on PtRu electrocatalysts[3].

$$\mathrm{Ru + H_2O \rightarrow Ru - OH + H^+ + e^-} \tag{10.1}$$

$$\mathrm{PtRu + CH_3OH \rightarrow PtRu - OCH_3 + H^+ + e^-} \tag{10.2}$$

$$\mathrm{PtRu - OCH_3 + Ru - OH \rightarrow PtRu = OOCH + Ru + 3H^+ + 3e^-} \tag{10.3}$$

$$\mathrm{PtRu = OOCH \rightarrow PtRu + CO_2 + H^+ + e^-} \tag{10.4}$$

As shown in Figure 10.2, first, CH_3OH is adsorbed on the Pt–Ru boundary to form a methoxy group ($-OCH_3$). Then, this methoxy group reacts with the adsorbed hydroxyl group (–OH) formed on the Ru atoms. The $-OCH_3$ and –OH group react to the formate (=OOCH). This formate is oxidized to the CO_2 at the Pt–Ru boundary. The coexistence of Pt and Ru sites hinders the indirect CO poisoning pathway, but promotes the direct pathway with enhanced activity and durability.

10.2.3 Ensemble Effect

Ensemble is defined by an assembly of surface-active atoms. Because the surface reaction is strongly affected by the atomic arrangement of the surface atoms, the ensembles also play an important role in enhancing the activity, selectivity, and durability. Some reactions necessitate the ensemble sites for the surface reaction, while the other

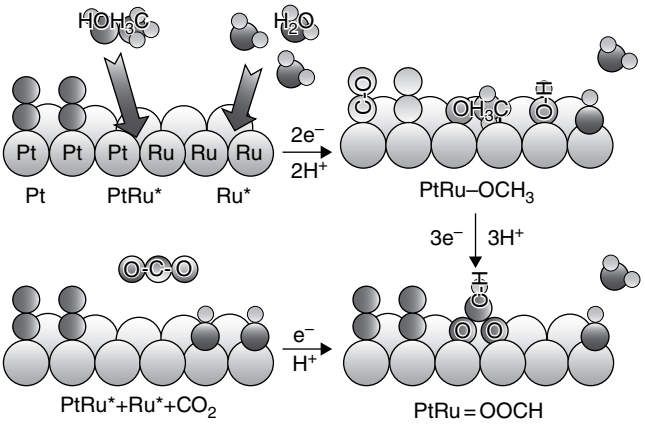

Figure 10.2 Scheme of the methanol oxidation reaction mechanism on the PtRu/C. Reproduced from ref. [3] with permission.

reactions need only a single atom site for the reaction. The effect of surface ensemble sites has been studied frequently. For example, Maroun et al. reported on the effect of surface ensembles in the bimetallic Pd–Au(111) surface on electrochemical CO or H_2 adsorption[4]. They prepared an atomically flat Pd–Au(111) surface using Pd electrodeposition on Au(111). Then, Pd atoms were selectively dissolved from the surface to prepare Pd ensembles with various surface compositions. They found that the critical ensemble for CO adsorption is a Pd monomer, whereas H adsorption is not possible on the Pd monomer, but requires Pd dimers or larger ensembles.

Rossmeisl et al. also reported the ensemble effect on Pt–Hg alloy nanoparticles for the selective H_2O_2 production[5]. The electrocatalytic oxygen reduction in acidic aqueous media toward H_2O_2 is presented by the following equations[6]:

$$O_2(g) + 2H^+ + 2e^- + * \rightarrow OOH^* + H^+ + e^- \tag{10.5}$$

$$OOH^* + H^+ + e^- \rightarrow H_2O_2(l) + * \tag{10.6}$$

While the two electron pathway induces the production of H_2O_2, the four electron pathway shown below generates H_2O instead[7]:

$$O_2(g) + 4H^+ + 4e^- \rightarrow OOH^* + 3H^+ + 3e^- \tag{10.7}$$

$$OOH^* + 3H^+ + 3e^- \rightarrow H_2O(l) + O^* + 2H^+ + 2e^- \tag{10.8}$$

$$H_2O(l) + O^* + 2H^+ + 2e^- \rightarrow H_2O(l) + OH^* + H^+ + e^- \tag{10.9}$$

$$H_2O(l) + OH^* + H^+ + e^- \rightarrow 2H_2O(l) \tag{10.10}$$

For a high selectivity toward H_2O_2 production, the dissociation of OOH* to O* (Figure 10.3) should be prohibited. Maintaining the O-O bond of OOH* is important

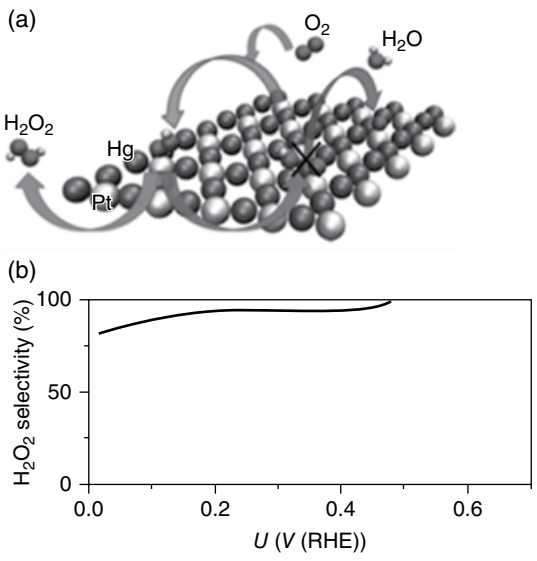

Figure 10.3 (a) Representation of the $PtHg_4$(110) surface. The oxygen reduction reaction to H_2O was prevented whereas the reduction to H_2O_2 was allowed. (b) H_2O_2 selectivity could be maximized by forming Pt monomers. Reproduced from ref. [5] with permission.

for the selective electrochemical reaction of oxygen to the H_2O_2. This O-O bond is easily broken on the Pt ensembles or Pt cluster. The $PtHg_4$ nanoparticles consisting of inactive Hg atoms and interstitially isolated Pt atoms were prepared (Figure 10.3a). The O-O bond could be preserved on the Pt monomers, resulting in a high selectivity toward the H_2O_2 production (Figure 10.3b).

10.2.4 Morphology Effect

Electrocatalytic performance can be enhanced by controlling the morphology of the nanoparticle catalysts[8]. Monometallic nanoparticles with different shapes exhibited morphology effect on electrochemical properties[9]. The morphology effect can be amplified by forming bimetallic nanostructure. As we mentioned previously, PtNi octahedral nanoparticle with (111) facets showed a record-high Pt mass activity for electrocatalytic oxygen reduction reaction (ORR). Although Pt(111) surface showed only slightly improved performance on ORR, its improvement was much more pronounced in Pt–Ni(111) [10]. This finding has led to intensive researches on the development of (111) faceted Pt–Ni nanoparticles[11]. The current state of art electrocatalyst for the ORR is Mo-doped octahedral Pt–Ni nanoparticles.

Some morphology that cannot be obtained in a monometallic system may be obtained by alloying the other metals. Our group reported the synthesis of shaped IrNi nanoparticles[12]. Although it is difficult to control the shape of Ir nanoparticles itself, it was possible to control the shape through alloying with other metals[13]. The shaped IrNi nanoparticles showed enhanced electrocatalytic oxygen evolution reaction (OER) performance[12]. Many Pt-based multimetallic hollow nanoframes or nanocages were reported as well[14–18]. Those shape-controlled nanoparticles exhibited high electrocatalytic performance toward ORR[14–16] or MOR[15, 17].

10.3 Characterization Techniques

Various analytical techniques have been used to study bimetallic nanostructures, such as electron microscopes, X-ray diffraction, X-ray photoelectron spectroscopy, X-ray absorption spectroscopy, and electrochemical measurement techniques. In this section, we will show how these techniques can contribute to elucidating the structures and properties of bimetallic catalysts by demonstrating several examples.

10.3.1 Electron Microscopy

Electron microscopy (EM) uses an accelerated electron beam as a source of illumination with a superior resolving power than a light microscope. The EM techniques are highly useful characterization methods for studying nanoparticles. Transmission electron microscopy (TEM) and high-resolution TEM (HR-TEM) use electron beams that pass through the sample. Both techniques require the samples to be dispersed on thin carbon-coated micro-grids. They confirm the morphology of nanostructures and produce a high contrast between the metal atoms and organic compounds. HR-TEM provides better resolution than TEM with information about not only the morphology of the nanoparticles, but also the atomic arrangement[19]. In previous studies, the morphology and atomic arrangement of bimetallic nanoparticles were shown by HR-TEM analysis, such as octahedral Pt_3Ni alloy[20], porous Pt_3Ni nanocrystals[21], $PtCu_3$ intermetallic core–shell[22], Pt_3Co nanowire assemblies[23], intermetallic Pt_3Ti and Pt_3V nanoparticles[24].

Scanning transmission electron microscope (STEM) is a mode of TEM equipped with additional scanning coils, which can produce images with atomic resolution. The different atoms can be identified due to the difference in contrast, which is proportional to the atomic number[25]. For example, the ordered intermetallic PtFe@Pt core–shell nanoparticles supported on carbon nanotubes have been characterized by STEM-based methods, as shown in Figure 10.4[26]. Figure 10.4a clearly shows the highly ordered atomic arrangement of Pt and Fe with different intensities and brightness. The intermetallic PtFe@Pt core–shell structure also can be confirmed by annular dark field (ADF)-STEM images. The elemental distribution and composition were analyzed by EDX mapping equipped in the STEM; Pt (Figure 10.4b) and Fe (Figure 10.4c) atoms

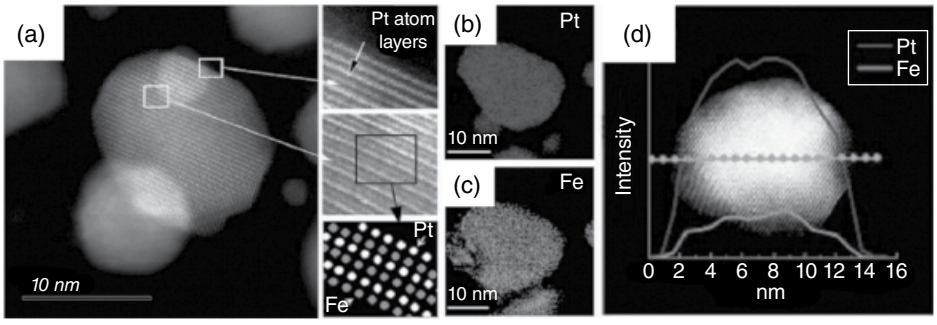

Figure 10.4 (a) ADF-STEM image, EDX elementary distribution maps for (b) Pt, (c) Fe, and EDX line scanning result for the PtFe@Pt/CNT electrocatalyst. Reproduced from ref. [26] with permission.

were found to be uniformly dispersed without segregation. Moreover, the EDX line scanning result showed the spatial distribution of each element inside the nanoparticle (Figure 10.4d).

Scanning electron microscope (SEM) can also show the morphology of the sample, even when a thin specimen cannot be prepared for TEM measurement. SEM collects low-energy secondary electrons ejected from the k-shell of the specimen atoms, so the image can be obtained even for a thick bulk phase. This SEM would be suitable for obtaining three-dimensional images of the bulk sample with information about microstructures[19]. Recently, fuel cell structures have been elucidated using focused-ion beam SEM tomography[27].

10.3.2 X-ray Diffraction Pattern (XRD)

XRD is a tool for identifying the atomic crystalline structure. XRD has been widely used to confirm the crystallinity, lattice spacing, size of crystal domain, extent of alloying, and the existence of an intermetallic phase. While the crystalline structure shows clear diffraction peaks, the amorphous peak shows only a broad shoulder. The exact location of the peak can provide information about lattice spacing. When the diffraction peak is sharp, it typically indicates that the crystalline domain is large. The nanoparticles usually show very broad peaks. The shift in the diffraction peaks is often a strong evidence of the formation of a bimetallic alloy. The intermetallic phase often shows additional diffraction peaks from the formation of a super-lattice. Figure 10.5a shows the diffraction peaks of Cu_xPt_{100-x} nanocubes with various compositions[28]. The peaks gradually shifted to higher 2θ values as the Cu content increased. The qualitative information about the chemical composition can be provided by XRD. As an another example, the crystalline structure of ordered intermetallic Pd_3Fe/C was confirmed by XRD, as shown in Figure 10.5b[29]. The pure Pd/C catalyst has only five XRD peaks of (111), (200), (220), (311), and (222) reflections originating from a face-centered cubic (fcc) Pd structure. The disordered Pd_3Fe/C also has five diffraction peaks, and the peaks

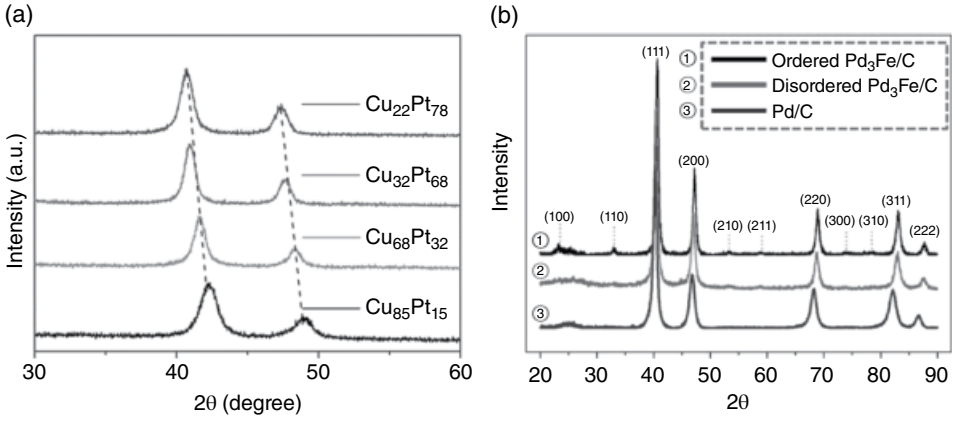

Figure 10.5 XRD patterns of (a) Cu_xPt_{100-x} nanocubes with different compositions; (b) ordered Pd_3Fe/C, disordered Pd_3Fe/C, and Pd/C. Drop lines correspond to Pd_3Fe (PDF Card 65-7280). Reproduced from ref. [28] for (a) and ref. [29] for (b) with permission.

shifted slightly to the higher angles. But the ordered Pd_3Fe/C has additional six peaks of (100), (110), (210), (211), (300), and (310) reflections resulting from the formation of a super-lattice, which are a strong evidence of the intermetallic crystalline structure.

10.3.3 X-ray Photoelectron Spectroscopy (XPS) and X-ray Absorption Spectroscopy (XAS)

X-ray photoelectron spectroscopy (XPS) is a surface-sensitive technique based on the photoelectric effect[19]. The elemental surface composition can be analyzed to the depth of 0–10 nm. The soft X-ray with a photon energy of 200–2000 eV is used to examine core-level electrons. The general X-ray source is either Al Kα (1486.6 eV) or Mg Kα (1253.6 eV) photons. The sample absorbs photons from the X-ray source, while the electrons in the core shell are ionized and emitted. The energy level of the emitted electrons is recorded. The XPS peaks appear at the specific binding energy region for each element. The peak shape and the specific peak position can provide information about the oxidation state and surface composition[30]. Figure 10.6a shows the XPS data for different compositions of Pt–Co nanowires[23]. The Pt 4f binding energy of Pt–Co bimetallic nanostructures were blue-shifted compared to Pt. The shift indicates that the electronic structure of Pt was modified by the interaction with Co atoms.

Valence-band XPS can also be used to measure the electronic structures of the surface atoms. The weak energy enables the examination of electrons in valence levels, providing more accurate information about the surface electronic structures[31]. The photons interact with the atoms located at the surface, ionizing the valence electrons. Figure 10.6b shows an example of valence band XPS data for the Pt_3M polycrystalline alloy, which clearly shows that the d-band density of states (DOS) is different for various kinds of secondary metals[32].

The X-ray absorption spectroscopy (XAS) provides information about average electronic structures for the bulk materials. This technique can provide information about the oxidation state, coordination numbers, and identification of the atoms surrounding the selected element[33]. The XAS is typically divided into two regimes: X-ray absorption near edge structure (XANES) and extended X-ray absorption fine structure (EXAFS). The XANES can provide information about the oxidation state and coordination chemistry (e.g., octahedral, tetrahedral coordination) through the edge position and white line intensity[34]. As the edge position is shifted positively more or the white line intensity is larger, the sample is oxidized more with vacant orbitals. Figure 10.6c shows an example of the urchin-like Pt_2Ni nanostructures. The electronic structure of the Pt L_3 edge was analyzed by XANES[35]. When the Pt precursors were treated at 240 °C for 15 min, they were reduced. The Pt_2Ni nanostructures have a lower white-line intensity than the commercial Pt/C catalysts, indicating that the Pt has more reduced states.

The EXAFS is used to estimate distances between atoms or coordination numbers, and identify neighboring atoms of the X-ray-absorbing atom. This method has a high sensitivity for a little distortion of the local structure and excellent spatial resolution. After the X-ray beam makes photoelectrons emit from the absorbing atom, the photoelectrons are backscattered by the surrounding atoms[19]. Then, oscillation occurs at the region of high energy. The analysis of the oscillation part can determine the

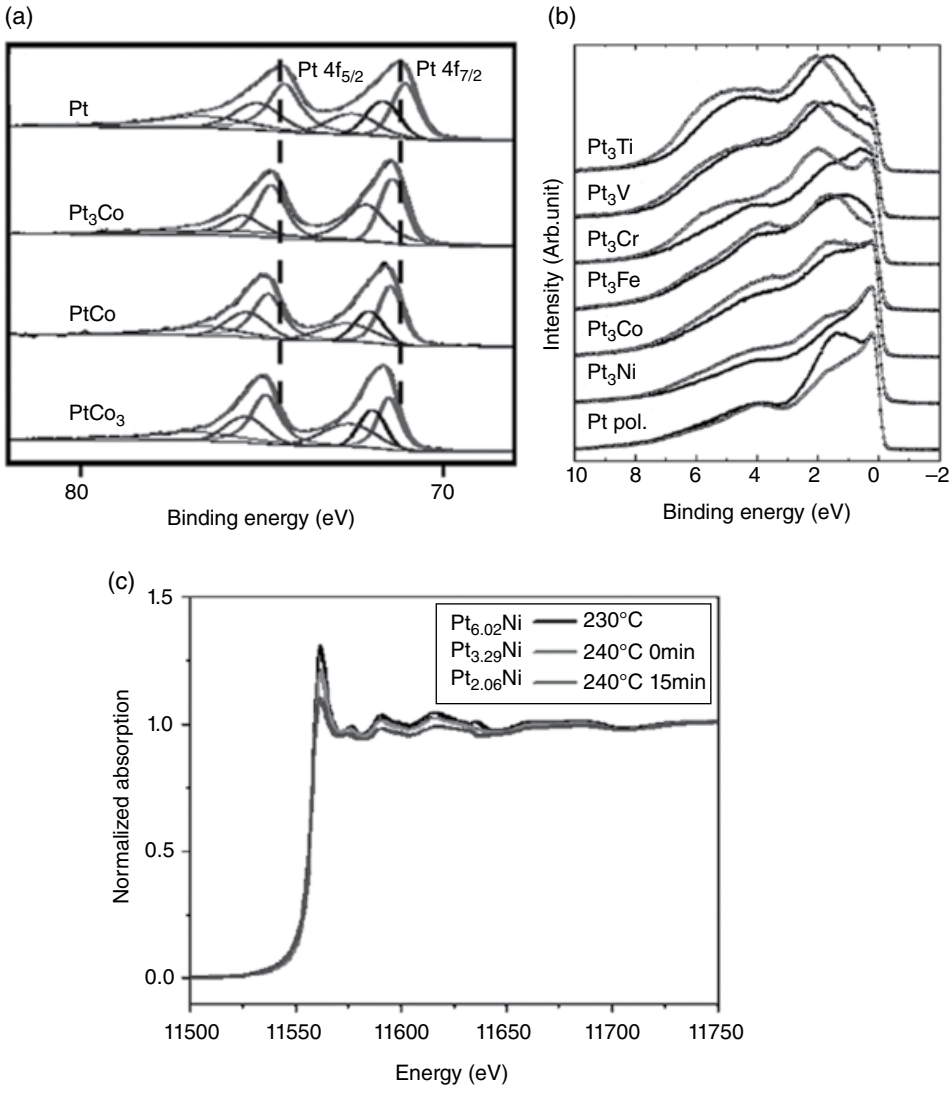

Figure 10.6 (a) XPS spectra of Pt–Co nanowires with various chemical compositions; (b) Valence-band XPS spectra of Pt_3M polycrystalline alloys after ion sputtering and thermal annealing; (c) Pt L_3 XANES spectra of Pt_2Ni nanostructures for various synthetic procedures. Reproduced from ref. [23] for (a), ref. [32] for (b), and ref. [35] for (c) with permission.

structural parameters such as coordination numbers, bond lengths, and extent of alloying in bimetallic nanoparticles[36]. Table 10.1 shows an example of EXAFS fitting results for PtFe/C material[37]. When the as-made PtFe/C, disordered (fcc)-PtFe/C, and ordered intermetallic (fct)-PtFe/C were compared, the ordered (fct)-PtFe nanoparticles had the shortest Pt–Pt distance and smallest Pt–Pt coordination number. The structure change in the Pt–Fe bimetallic materials were confirmed by the EXAFS technique.

Table 10.1 EXAFS fitting results for various Pt–Fe/C catalysts. Reproduced from ref. [37] with permission.

	Pt–Pt distance (Å)	Pt–Pt coordination number (N)	Pt–Fe distance (Å)	Pt–Fe coordination number (N)	Reduced Chi square value	R-factor
As-prepared PtFe/C	2.7480(8)	6.50(6)	2.6822(9)	0.93(1)	33.1	0.0081
Disordered fcc-PtFe/C	2.7371(9)	5.50(7)	2.6722(1)	2.44(9)	69.0	0.0043
Ordered fct-PtFe/C	2.7214(4)	4.26(5)	2.6730(2)	3.86(6)	13.9	0.0012

10.3.4 Electrochemical Measurements

There are many techniques to measure the electrocatalytic performances of bimetallic materials. Three-electrode cells can be used to test the performance of catalysts for various electrochemical reactions[38]. The three-electrode cell consists of a working electrode, a counter electrode, and a reference electrode. For the working electrode where the sample would be deposited, a glassy carbon electrode (GCE) or metal plate are generally used. To avoid the effect of mass transfer limitation, a rotating disk electrode (RDE) or rotating ring disk electrode (RRDE) are often used. The counter electrode carries currents to complete an electric circuit. A Pt wire or Pt mesh is generally used. The reference electrode guarantees a constant electrochemical potential in a broad range of the potentials, and it provides a standard point to measure the potential of the working electrode. Standard hydrogen electrode (SHE), saturated calomel electrode (SCE), or Ag–AgCl electrode are generally used.

The electrocatalysts often should be activated before the measurement[39]. Cyclic voltammetry (CV) or chronoampherometry (CA) can be used for the activation[40, 41]. The activation procedure can remove poisoned (or oxided) metal sites. However, the edges and corners of the metal nanoparticle can be easily rounded or aggregated. Especially, shape-controlled nanoparticles with distinct vertexes may be more vulnerable. In cases of bimetallic alloys, the secondary metals may dissolve during the activation. For example, the structure and shape of Cu_3Pt nanoparticles can be modulated by the dealloying process[40, 41]. The CV with different upper limit potentials, scan rates, number of cycles, and the CA with various holding potentials and time were conducted. After the dealloying process, the ordered intermetallic Cu_3Pt nanoparticles were changed into a Cu_3Pt core-Pt rich shell structure, porous structure, or cubic nanoparticles. Suitable activation conditions should be sought to maintain the structure and composition of the as-synthesized catalysts.

The catalytic performance can be evaluated by estimating mass activity and specific activity. It is relatively harder to obtain the accurate specific activity than the mass activity. To measure the specific activity, the electrochemically active surface area (ECSA) should be determined by measuring faradaic currents[42]. The measurement of reliable ECSA is essential to study the relationship between the specific activity and the structure of the catalysts[43]. The most popular approaches to assess the ECSA are

underpotential deposition (UPD) of hydrogen (H_{UPD}) or CO stripping. However, these methods can cause significant deviation in estimating ECSA for bimetallic nanoparticles. The studies showed that the estimated ECSA value for the bimetallic materials was quite different for H_{UPD}, CO stripping, and Cu_{UPD}[34, 42, 43]. The ECSA value estimated by Cu_{UPD} was the highest and the ECSA value estimated by H_{UPD} was the lowest[43]. This results from the different binding energies of Cu_{UPD}, CO_{ad}, and H_{UPD} on different surface metal atoms[34]. In the case of the $PtNi_3$ alloy, hydrogen was not well adsorbed at the surface due to the Ni oxide species[42].

10.4 Electrocatalytic Reactions Using Bimetallic Nanostructures

For energy and environmental issues, there has been much attention to electrochemical conversions combined with renewable energy[44]. Many recent advances in electrocatalysis have come from the development of bimetallic nanostructures[8]. Some important reactions and corresponding bimetallic nanostructured electrocatalysts are introduced in this section.

10.4.1 Oxygen Reduction Reaction (ORR)

The electrochemical oxygen reduction is an important reaction in proton exchange membrane fuel cells (PEMFCs). PEMFCs are an ideal and sustainable energy source because of their high efficiency and no emission. However, the high cost of PEMFCs is still a major obstacle for its commercialization in the market. This is mainly due to the heavy usage of expensive Pt metals in the PEMFCs cathode. The sluggish kinetics of the cathode reaction, ORR, typically requires using much Pt. Enhancing the ORR would contribute to minimizing Pt usage significantly and commercializing the PEMFCs.

10.4.1.1 ORR Using Pt–M Alloy Structures

Alloying Pt with the low-cost metals of Cu, Co, and Ni can reduce the catalyst cost, and the interaction between Pt and the metals can enhance the activity of Pt. The Pt–M bimetallic catalysts can be made by the colloidal synthesis method. First, Pt and the other metal precursors are dissolved in a solvent. Pt ions are reduced in advance because the reduction potential of Pt is usually higher than the other metals. The strong reducing agents such as $NaBH_4$ or hydrogen are necessary to form uniform bimetallic catalysts by preventing a prior Pt reduction[20, 45–47]. Additionally, the transition metals are easily leached out in an acid condition. The Pt-rich surface is usually formed by intentionally leaching the transition metals from the surface by thermal, electrochemical, or dealloying processes. The Pt shell can prevent additional leaching, with enhanced activity per unit surface Pt atom and improved durability[48–57]. For example, bimetallic $Pt_{25}Cu_{75}$ electrocatalysts can be prepared by conventional impregnation and thermal annealing[56]. Then, the Cu-rich surface is electrochemically dealloyed. This kind of procedure can make a Pt-rich surface and transition metal-rich core by thermodynamic rearrangement[57]. Underpotential deposition (UPD) is often used to form bimetallic catalysts. A metal monolayer can be deposited on the foreign metal substrate at the potential that is slightly more positive than the potential for bulk deposition[58].

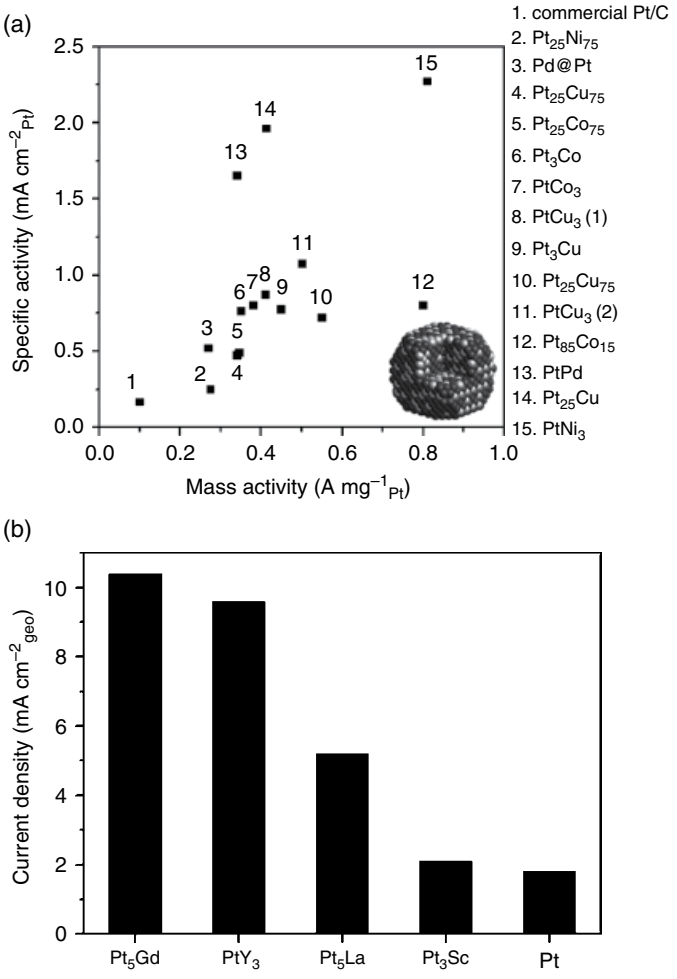

Figure 10.7 (a) The ORR mass activity versus specific activity for Pt–M (M: transition metals) alloys; (b) Kinetic current densities of Pt–M alloy for the ORR. Refs. in (a): 1 [48], 2 [48], 3 [63], 4 [48], 5 [48], 6 [50], 7 [49], 8 [49], 9 [51], 10 [56], 11 [54], 12 [53], 13 [63], 14 [52], 15 [64], Refs. in (b): Pt_5Gd [61], PtY_3 [60], Pt_5La [62], Pt_3Sc [60], Pt [60].

Adzic et al. reported Pd@Pt bimetallic catalysts with a Pt monolayer for the ORR[59]. Cu is first deposited on the Pd nanoparticles by the UPD technique. Then, the Pd@Cu is immersed into the K_2PtCl_4 solution, which allows for the irreversible replacement of Cu to Pt by galvanic replacement. The Pt surface of Pd@Pt nanoparticles can present a higher specific activity than Pt nanoparticles. Figure 10.7a displays mass activity versus specific activity for many Pt–M (M: transition metals) alloy catalysts. Among the various Pt–M materials, Pt_3Ni alloy presented the highest mass activity and specific activity.

Rare earth metals also formed bimetallic structures with Pt for the ORR. Figure 10.7b shows the ORR activity for Pt–M (M: rare earth metals) bimetallic catalysts. Nørskov et al. showed that Pt_3Y surface is located near the top of the volcano plot of oxygen-binding

energy versus ORR currents[60]. When the Pt_3Y catalyst was prepared and tested for the ORR, it showed approximately six times higher activity than the bare Pt. Chorkendorff et al. reported that Pt_5Gd has an ORR activity even higher than the Pt_3Y catalysts with exceptionally good durability[61]. Other Pt–rare earth metal bimetallic catalysts were also reported[62].

10.4.1.2 ORR Using Pt–M Intermetallic Structures

The ordered intermetallic structure has different properties from disordered alloys. The disordered alloy has a random local composition, atomic distribution, and nonuniform active sites[65]. However, the ordered intermetallic structure has a definite composition and uniform active sites with a well-defined structure[66, 67]. Therefore, the intermetallic structure can modify the d-band center[37, 68, 69] or geometric lattice strain[26, 70, 71] more precisely. Various Pt-based intermetallic nanoparticles have been studied such as Pt–Al[69], Pt–Bi[67, 68, 72, 73], Pt–Co[66], Pt–Co–Fe[74, 75], Pt–Co–Ni[25], Pt–Cr[74], Pt–Cu[22, 40, 41], Pt–Cu–Fe[76], Pt–Fe[26, 37, 77–79], Pt–Fe–Ni[74], Pt–Ni[80], Pt–Sb[81], Pt–Sn[82], Pt–Ti[24, 83], Pt–Pb[84–87], and Pt–V[24]. Additionally, intermetallic structures were also synthesized without Pt, such as Au–Cu[88, 89], Au–In[90], Ir–Ti[91], Pd–Fe[29], Pd–Bi[81], Pd–Sb[81], and Pd–Pb[92]. Generally, the intermetallic structure was prepared by annealing the alloy nanoparticles above 600 °C[22, 66, 72, 79, 93, 94]. For example, the change in the structure and composition upon thermal annealing was observed for Cu_3Pt nanoparticles using the in-situ HAADF STEM analysis[93]. The dynamic evolution of morphology, faceting, elemental segregation, phase transition, and changes in strain distribution were confirmed as a function of time and temperature. The fully ordered intermetallic nanoparticles were formed at 700 °C. Moreover, the DFT calculation showed that the energetic driving force for the disorder-to-order transition varies depending on the surface crystalline structure.

Preventing the aggregation of nanoparticles during thermal annealing is very important to form ordered intermetallic nanoparticles with high activity. Coating the nanoparticles with secondary materials can prevent the aggregation. For example, an N-doped carbon shell was formed during the thermal annealing on the surface of (fcc)-PtFe/C catalysts, and disordered (fcc)-PtFe nanoparticles were transformed into ordered (fct)-PtFe nanoparticles without significant aggregation upon the annealing[37]. MgO was coated on the PtFe nanoparticles to alleviate the aggregation[79]. However, these protecting methods may block the catalytic active sites at the nanoparticle surface with thick coating materials. The KCl matrix can also be used to endure a high annealing temperature while protecting the nanoparticles. The intermetallic Pt_3Ti[24], Pt_3V[24], Pd_3Fe[29], and Pt_3Fe[77] nanoparticles were synthesized using the KCl matrix methods. But the KCl matrix should be dissolved. Then, the resulting intermetallic nanoparticles cannot avoid agglomeration during the catalytic reaction. Recently, we have prepared Pt–Ti intermetallic nanoparticles by using TiO_2 layers formed at the surface of commercial Pt/C catalysts as the Ti source[95]. Thermal inter-diffusion at a high temperature allowed the formation of Pt–Ti intermetallic nanoparticles while the surface TiO_2 layer prevented aggregation.

Many Pt-based intermetallic nanoparticles have been tested for the ORR[29, 37, 66, 68, 79, 85]. Figure 10.8 shows the activity of commercial Pt/C and various Pt–M (M: transition metals) intermetallic catalysts for the ORR. There is a proportional

relationship between the mass activity and specific activity. The highest mass activity among the Pt–M intermetallic nanoparticles was reported for N-doped carbon coated (fct)-PtFe/C with 1.6 A/mg_{Pt}[37]. They showed not only high activity, but also high durability for the ORR. The N-doped carbon shell protected the nanoparticles from agglomerating during the annealing and the electrochemical reaction. According to in-situ XANES and EXAFS analyses, the high activity and durability resulted from electronic and geometric effects.

10.4.1.3 Model Surface

Stamenkovic et al. remarkably predicted that $Pt_3Ni(111)$ single crystalline would have approximately 90 times higher activity than Pt/C for the ORR[97]. They showed that the $Pt_3Ni(111)$ single crystalline surface has a Pt-rich top layer and Ni-rich second layer. DFT calculations showed that the d-band center of Pt_3Ni surfaces varies by the crystalline structure. Wang et al. reported on the ORR reaction energetics of Pt(100), Pt(111), PtNi(100), and PtNi(111) surfaces by DFT calculation. They suggested three types of ORR mechanisms[98]: oxygen dissociation mechanism, peroxyl mechanism, and peroxide mechanism.

1) Oxygen dissociation mechanism

$$O_2 + * \rightarrow O_2 * \tag{10.11}$$

$$O_2 * \rightarrow O * + O * \tag{10.12}$$

$$O * + H^+ + e^- \rightarrow OH * \tag{10.13}$$

$$OH * + H^+ + e^- \rightarrow H_2O(\mathrm{RDS}) \tag{10.14}$$

2) Peroxyl mechanism

$$O_2 + * \rightarrow O_2 * \tag{10.15}$$

$$O_2 * + H^+ + e^- \rightarrow OOH * \tag{10.16}$$

$$OOH * \rightarrow O * + OH * \tag{10.17}$$

$$O * + H^+ + e^- \rightarrow OH * (\mathrm{RDS}) \tag{10.18}$$

$$OH * + H^+ + e^- \rightarrow H_2O \tag{10.19}$$

3) Peroxide mechanism

$$O_2 + * \rightarrow O_2 * \tag{10.20}$$

$$O_2 * + H^+ + e^- \rightarrow OOH * (\mathrm{RDS}) \tag{10.21}$$

$$OOH * + H^+ + e^- \rightarrow HOOH * \tag{10.22}$$

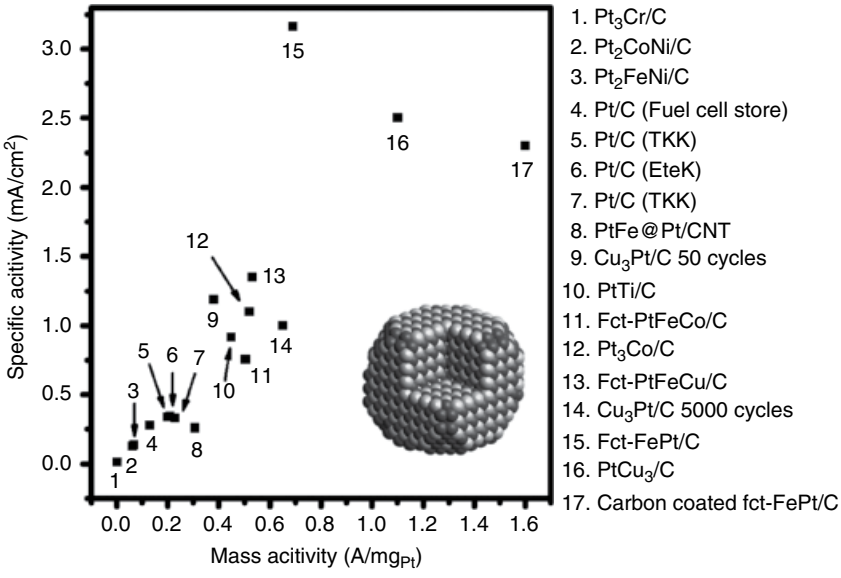

Figure 10.8 The ORR mass activity versus specific activity for commercial Pt/C and various Pt–M (M: transition metals) intermetallic catalysts. Refs. 1 [96], 2 [74], 3 [74], 4 [79], 5 [76], 6 [74], 7 [75], 8 [26], 9 [40], 10 [83], 11 [75], 12 [66], 13 [76], 14 [40], 15 [79], 16 [22], 17 [37].

$$HOOH^* \rightarrow OH^* + OH^* \tag{10.23}$$

$$OH^* + H^+ + e^- \rightarrow H_2O \tag{10.24}$$

Pt(100) and PtNi(100) surfaces would proceed by the oxygen dissociation mechanism, Pt(111) followed peroxyl mechanism, and PtNi(111) followed peroxide mechanism. Also, they estimated the activation energy for each step. On the Pt(100) surface, the activation energy of RDS is 0.80 eV, and the activation energy on Pt(111) or PtNi(100) is 0.79 eV. However, the activation energy of RDS on the PtNi(111) surface is 0.15 eV. Therefore, the PtNi(111) surface can expect a higher ORR activity. Figure 10.9 shows each ORR mechanism on the Pt(100), Pt(111), PtNi(100), and PtNi(111). Surely, this work predicted that the PtNi(111) surface would show high activity for the ORR.

10.4.1.4 Shape-Controlled Pt_3Ni Nanoparticles with (111) Facets

Since Stamenkovic's work reported in 2007, many efforts have been dedicated to synthesize Pt_3Ni nanoparticles with (111) facet. Figure 10.10 shows the enhancement of ORR activity for various shaped PtNi nanoparticles. Fang et al. reported the first synthesis of the octahedral Pt_3Ni nanoparticles and exhibited their ORR activity[99]. They used oleylamine, oleic acid, and tungsten hexacarbonyl ($W(CO)_6$). The oleylamine was used as a reducing agent and surface-stabilizer. The $W(CO)_6$ was the key for inducing the octahedral shape. Because of a lower reduction potential of W, the W makes the Pt precursor reduce rapidly in the early stages of the synthesis[100, 101]. Then, the high concentration of W cations would decelerate the Pt reduction under an equilibrium of $Pt^{2+} + W^0 \leftrightarrow W^{n+} + Pt^0$ at the later stage. This slow overgrowth promoted the formation

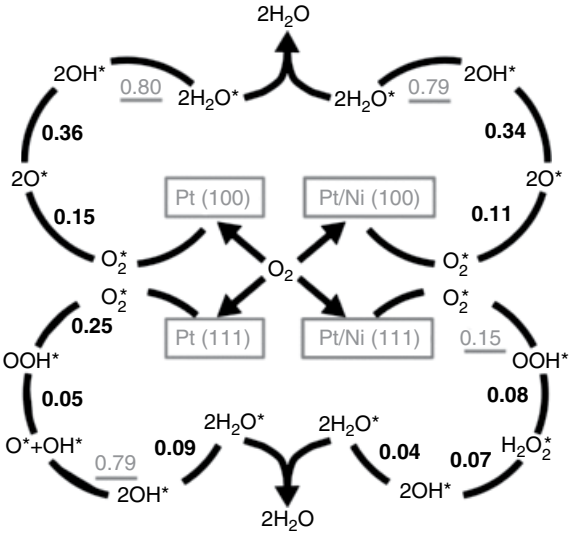

Figure 10.9 Scheme of ORR mechanism on Pt(100), Pt(111), PtNi(100), and PtNi(111). The numbers along the arrows indicate the activation energy for each step of the ORR. Reproduced from ref. [98] with permission.

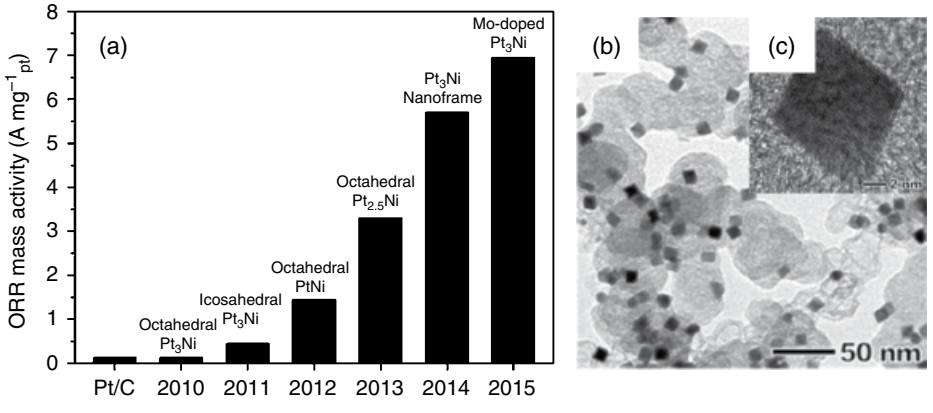

Figure 10.10 (a) Overview of mass activity enhancement using shape-controlled PtNi nanoparticles for the ORR. (b) Representative TEM images of octahedral Pt-Ni/C. Reproduced from ref. [105] with permission.

of $Pt_3Ni(111)$ facets. Although they successfully synthesized the octahedral Pt_3Ni, the nanoparticles exhibited only a comparable mass activity to the commercial Pt/C. Yang et al. reported on the octahedral Pt_3Ni catalyst with a significantly enhanced mass activity[102]. They also used oleylamine and oleic acid as a reducing agent and stabilizer, but they used the CO gas instead of metal carbonyl compounds. CO gas was strongly bounded to the metal surface and inhibited further metal reduction at the nanocrystal surface[103]. The octahedral Pt_3Ni catalyst exhibited an ORR mass activity of 0.44 A/mg_{Pt} at 0.9 V (vs. RHE), which reached approximately three times that of the

commercial Pt/C (0.14 A/mg_{Pt}). The same group later reported the synthesis of Pt_3Ni icosahedra made by the similar method using CO gas[104]. The Pt_3Ni icosahedra consisted of 30 edges and 20 (111) facets. These nanoparticles showed an even higher activity than the octahedral Pt_3Ni of 0.62 A/mg_{Pt} at 0.9 V (vs. RHE). Strasser et al. reported 9.5 nm-sized octahedral PtNi using dimethylformamide (DMF) as the only organic reagent[20]. DMF acted as a reducing agent and a solvent. A rapid heating rate (10 °C/min) was used for the fast reduction and high nucleation rate. This method resulted in a surfactant-free surface, with a high mass activity for the ORR. These octahedral PtNi nanoparticles showed the activity of 1.45 A/mg_{Pt} at 0.9 V (vs. RHE), which is approximately 10 times higher than the commercial Pt/C. Xia et al. reported the synthesis of 9 nm-sized $Pt_{2.5}Ni$ octahedral nanoparticles with a high mass activity of 3.3 A/mg_{Pt}[105]. They also used oleylamine, oleic acid, and $W(CO)_6$. Compared with Fang's group, however, they dissolved only small amounts of surfactants in a benzyl ether solvent. The additional treatment with acetic acid removed the remaining organic surfactant at the catalysts surface further, exhibiting high activity. Also, they found the role of CO during the synthesis. In the standard synthesis from Fang's group, Ar purging continued in the entire process. In Xia's group, however, Ar purging stopped immediately after $W(CO)_6$ was added to the solution. This method enabled them to make the $Pt_{2.5}Ni$ octahedra with well-defined (111) facets due to the presence of CO. When Ar gas flowed after the addition of $W(CO)_6$, the irregularly shaped $Pt_{2.5}Ni$ nanoparticles were synthesized. It clearly demonstrated the key role of CO for preparing well-defined (111) facets. Stamenkovic et al. introduced a new concept of hollow Pt_3Ni nanoframes using the structural evolution of bimetallic nanoparticles [14]. Starting from polyhedral $PtNi_3$ nanoparticles with a rhombic dodecahedral shape with more Pt at the edges, a hollow Pt_3Ni nanoframe structure was obtained by dissolving Ni atoms selectively. Thermal treatment at 370 ~ 400 °C in Ar atmosphere enabled a Pt skin surface. The nanoframes have a high ECSA, and reactants can access both internal and external surfaces easily due to the frame structure. These effects could lead to a high ORR mass activity of 5.7 A/mg_{Pt}. Huang et al. most recently reported transition metal-doped octahedral Pt_3Ni nanoparticles[11]. In their previous study, they synthesized octahedral PtNi nanoparticles using DMF and benzoic acid[106]. DMF was used as a reducing agent and solvent, and benzoic acid was used as a shaping agent. They further doped octahedral Pt_3Ni with various transition metals of V, Cr, Mn, Fe, Co, Mo, W, or Re. In particular, Mo-doped octahedral Pt_3Ni had a very high mass activity of 6.98 A/mg_{Pt}, which is 73 times higher than the commercial Pt/C. The Mo atoms were concentrated at the edge or vertex sites on the octahedral Pt_3Ni nanoparticles. They changed the oxygen binding energies at the facets to be weaker with higher ORR activity. Additionally, the doped Mo atoms at the vertexes increased the energy required to dissolve the Pt or Ni atoms nearby. Consequently, the doped Mo atoms inhibited the dissolution of Pt and Ni atoms from nanoparticles, thereby improving the stability of the nanoparticle catalysts.

10.4.1.5 Durability of the Bimetallic Nanoparticle Catalysts

Many studies using Pt alloys have shown high activity in ORR due to electronic effects between Pt and transition metals. However, the ORR activity typically decreases during the reaction in an acidic solution. Most transition metals are easily oxidized and dissolved. Although well-defined facets were prepared initially, the facets were degraded

eventually after being in the reaction for a long time. Furthermore, dissolved transition metals could be diffused and contaminate the membrane in the membrane electrode assembly (MEA)[107]. The contamination may have detrimental effects for the cell performance. Many attempts have been reported to prevent the dissolution of transition metals. Strasser et al. reported dealloyed structures for PtCu nanoparticles[56]. They synthesized Cu-rich Pt alloy ($Pt_{25}Cu_{75}$), and then electrochemical dealloying was performed to dissolve surface Cu atoms. The surface atomic composition was changed to $Pt_{93}Cu_7$. The Pt thick shell showed enhanced ORR mass activity, and was able to maintain the activity for 4,000 cycles of the accelerated durability test (ADT). Adzic et al. reported a unique structure with the Ni_4N core-Pt shell[108]. When the PtNi core–shell nanoparticles were treated with NH_3, Ni_4N formed in the core. The Ni_4N core modified the electronic structure of the surface Pt shell, and PtNiN core–shell nanoparticles have more surface contraction than pure Pt, which leads to the downshift of the d-band center and the weakening of the oxygen binding energy. Also, the N atoms enable the Pt atoms to diffuse from the core to the surface vacancy sites. These electronic and geometric effects led to the enhancement of activities and durability. After 35,000 cycles of ADT, the PtNiN core–shell nanoparticles showed no loss of ECSA and 11 mV negative shift of half-wave potential. Stamenkovic et al. introduced the multimetallic Ni-rich core, Au thin interlayer, and PtNi shell nanoparticles with enhanced durability for the ORR[109]. The subsurface Au layer could stabilize the surface PtNi shell without blocking surface active sites. The Ni@Au@PtNi catalysts presented an activity loss of 10% after 10,000 cycles. Adzic et al. reported that the existence of the Au cluster on Pt nanoparticles enhanced the durability significantly[110]. The deposition of Au clusters prevented the oxidation of Pt. Our group recently reported on Br-capped PtNi nanoparticles, (Figure 10.11), ref. [111]. Halide ions have often been used as capping agents to induce a specific shape[112, 113]. We post-treated octahedral PtNi nanoparticles with halide ions. DFT calculations predicted that the halide would be adsorbed more strongly with Ni atoms than Pt atoms. The Br-treated PtNi nanoparticles exhibited a superior stability for ORR in acid media. They presented a 7 mV negative shift of half-wave potential after 10,000 cycles, while the as-prepared PtNi and commercial Pt/C showed a shift of 34 mV and 57 mV, respectively. The Br treatment successfully prevented Ni leaching while preserving an octahedral shape.

10.4.2 Fuel Oxidation

Hydrogen is the most popular fuel for the anodic reaction of fuel cells. However, a high purity is required to avoid poisoning, and the difficulties with storing and transporting H_2 has made other fuels attractive. Direct fuel cells using small organics of methanol or formic acid have been tested for portable devices[81, 114]. Figure 10.12 shows the oxidation mechanisms of methanol and formic acid. There are two possible reaction pathways: an indirect CO poisoning path and direct path. When the reaction proceeds following the indirect pathway, the Pt catalyst is deactivated quickly because the Pt surface is poisoned by an intermediate CO_{ads} species[3, 115]. Pt-alloy catalysts have been used to lessen the poisoning [81]. Incorporating other metals can reduce the catalyst deactivation by modifying geometric or electronic structures. The Pt–Ru catalyst has been studied and utilized with alleviated surface poisoning[116–118]. Many other multimetallic catalysts have also been studied with some recent papers introduced here.

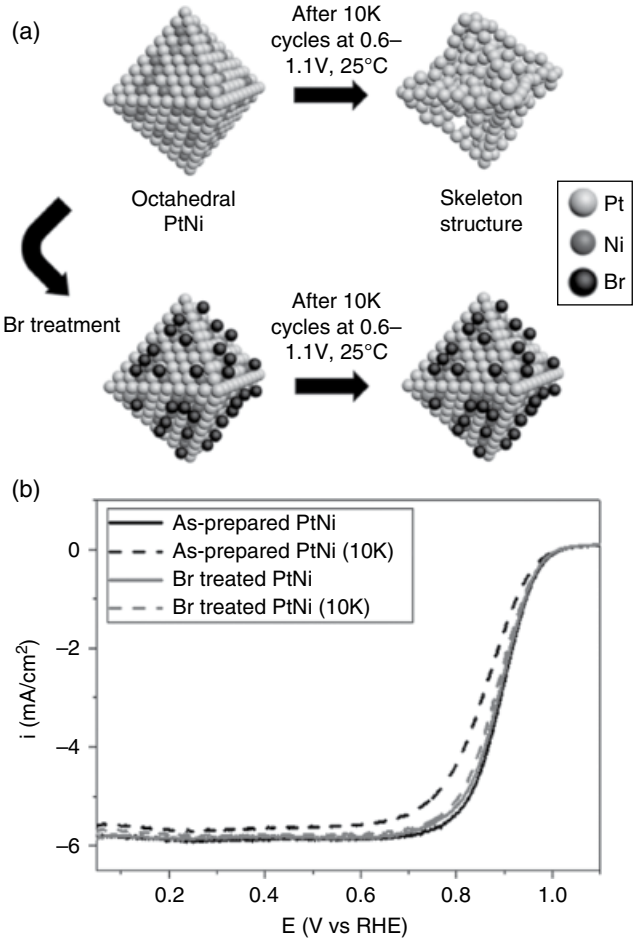

Figure 10.11 (a) A sketch of Br-treated Pt–Ni nanoparticles with enhanced durability; (b) Changes in the linear sweep voltammetry for the ORR after accelerated degradation test. Reproduced from ref. [111] with permission.

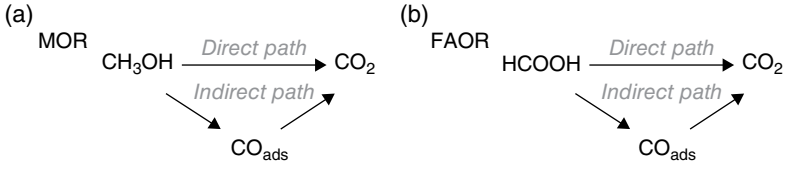

Figure 10.12 Reaction paths of (a) methanol oxidation reaction (MOR) and (b) formic acid oxidation reaction (FAOR). Both reactions have both direct path and indirect paths. CO_{ads} intermediates in the indirect path can cause catalyst poisoning.

10.4.2.1 Hydrogen Oxidation

Hydrogen is the most popular fuel for fuel cells. If the fuel is highly pure hydrogen, the commercial Pt/C catalysts show very good activity and durability at PEM conditions. The mechanism of hydrogen oxidation reaction (HOR) on Pt surface in acid media has been studied[44]. Despite its simplicity, there have been debates about hydrogen adsorption pathway on the Pt surface. Hydrogen can be adsorbed to the Pt surface

following Tafel step (Eq. 10.15) or Heyrovsky step (Eq. 10.16)[44, 119]. Then the adsorbed hydrogen is discharged following Volmer step (Eq. 10.17).[44, 119]

(Step 1-1) Tafel step: Langmuir-Hinshelwood mechanism

$$H_2 + 2\,Pt \rightarrow 2Pt - H \tag{10.25}$$

(Step 1-2) Heyrovsky step: Rideal-Eley mechanism

$$H_2 + Pt \rightarrow Pt - H + H^+ + e^- \tag{10.26}$$

(Step 2) Volmer step

$$Pt - H \rightarrow Pt + H^+ + e^- \tag{10.27}$$

However, even minimal amount of CO impurities can severely affect Pt activity[120, 121]. Hydrogen is mainly produced by steam reforming of hydrocarbon such as natural gas, which makes CO or CO_2 impurities inevitably in the final hydrogen product[120, 121]. Therefore, CO-tolerant Pt catalysts are desired for HOR. The Pt–Ru catalyst, which is known to have CO tolerance, was studied for the HOR[121, 122]. Pt–Sn [122, 123], Pt–Mo [124, 125], and Pt with 3d metals (Fe, Co, or Ni)[126] were also reported. Second metal M activates water and oxidizes CO adsorbed to the neighboring Pt surface[127, 128].

$$M + H_2O \rightarrow M - OH + H^+ + e^- \tag{10.28}$$

$$Pt - CO + M - OH \rightarrow Pt + M + CO_2 + H^+ + e^- \tag{10.29}$$

The moderate adsorption energy is important for the HOR, which can be tuned by incorporating other metals. Enhanced activity, as well as CO tolerance, can be expected with the alloy catalysts. In the case of alkaline full cell systems, there is a significant overpotential for the HOR that should be reduced by the appropriate HOR catalysts.

10.4.2.2 Methanol Oxidation

Methanol is used for direct methanol fuel cells (DMFC). The performance of DMFC is mainly controlled by the anodic reaction, which is methanol oxidation reaction (MOR), due to its high overpotential unlike H_2 oxidation[129]. The key issue of MOR catalysts is their tolerance to CO_{ads} poisoning, which is the intermediate of indirect pathway. Pt–Ru/C catalysts have been the most frequently used and have become the standard for MOR. The reason for the high performance had been firmly explained by the Watanabe-Motoo (W-M) mechanism for about 40 years[130]. The W-M mechanism insists that the hydroxyl group is adsorbed at the oxophilic Ru site and oxidizes the poisoning CO_{ads} formed at the Pt site, as shown below[3].

$$Pt - CO + HO - Ru \rightarrow Pt^* + Ru^* + CO_2 + H^+ + e^- \tag{10.30}$$

Very recently, however, Tong et al. reported the experimental results with a flow cell operation and isotope labeling, which refutes the W-M mechanism [3]. They explained the high performance of Pt–Ru/C with facilitation of the reaction toward the direct

path rather than the indirect path. The proposed mechanism is described in (2.01) ~ (2.04) and Figure 10.2. According to this mechanism, the MOR occurs at the Pt–Ru boundary site. When the Pt–Ru catalysts are used, the activation forming segregated Ru and Pt domains is always performed before the MOR, which leads the Pt–Ru boundary sites to be maximized[131]. However, the excessive activations can cause a decrease in activity due to Ru leaching[81, 116–118].

The Pt alloy with Pd has been actively studied. Pd can act like Ru in Pt–Ru catalysts and change the electronic structure of Pt[132]. In particular, the (100) facet of Pt–Pd alloy nanoparticles shows high activity and good stability[133]. Pt–Pd nanodendrites[134], Pt–Pd nanocages[135], and Pt–Pd dendritic shells with a hollow core[135] were reported for efficient MOR. Tertiary metals were also introduced such as Pt–Pd–Te nanowires[136] or Pt–Pd–Fe nanowires[137]. Tertiary metals can change the electronic structure and reduce the content of noble metals. Pt–Rh porous nanostructures were reported to have tolerance for surface poison and enhanced MOR activity[138]. The Rh activates water to provide surface oxygen species. Pt–Au bimetallic nanoparticles were also reported to have enhanced MOR activity[139–144]. The Pt provides sites for dehydrogenation and Au facilitates CO removal by forming Pt–CO_{ads} and Au-OH_{ads}[139–141]. Although Au itself has no activity, the CO adsorption energy at Pt sites can be controlled by forming alloys with Au[144]. Pt with some 3d metals such as Ni, Co, Cu, Ti, V, Zn, and Mn were also studied for the MOR. These 3d metals can change the electronic structures of Pt, resulting in the modulation of CO adsorption energy[145, 146]. The CO diffusion or oxidation can be accelerated. Many shape-controlled Pt–Ni bimetallic nanoparticles were reported for MOR: Pt–Ni multiarms[147], Pt–Ni flowers[147], porous Pt–Ni nanotubes[148, 149], Pt frame@Ni core–shell concave octahedra[150], and Pt–Ni nanoframes with Au islands[151]. Nanoporous Pt_1Co_{99} nanowires[23], Pt–Cu concave hexapods[152], Pt–Cu microwires[153], porous Pt–Cu nanocrystals[154], Pt–Cu nanoframes/nanocages[17, 18, 155], Pt–Cu york shell cubes[156], and Pt–Mn nanocubes[157] have also been reported. Intermetallic Pt_3Ti[24, 83], Pt_3V[24], and Pt_3Zn[158] were reported to have good performance. Pd-based bimetallic structures were also studied for methanol oxidation[159, 160]. Incorporating Ag to Pd can change the d-band center of the Pd, which changes the adsorption energy of the reactant and enhances the MOR activity[161–164]. Pd–Ag/CNTs [164] and Pd–Ag nanoframes[165] were also reported.

10.4.2.3 Formic Acid Oxidation

Pt–Pd bimetallic catalysts have been extensively studied for formic acid oxidation reaction (FAOR). The FAOR can follow either direct or indirect pathways, as shown in Figure 10.12. The indirect pathway typically generates surface-poisoning CO_{ads} species with poorer activity and durability. The modification in the electronic structure can induce the reaction to occur toward the direct path[8]. The coexistence of Pd and Pt at the surface presented good tolerance to poisoning[166]. Pt–Au nanostructures showed good activity for the FAOR as well as the MOR[140, 167]. Formic acid can be easily adsorbed at the Pt surface when the electronic structures of Pt are tuned by Au[168]. Several Pt–Au bimetallic nanostructures were reported such as Au@Pt dendrimer[169] and graphene decorated Pt–Au[170]. Recently, our group showed that as the size of Pt domain becomes very small up to an atomic level, the FAOR was promoted toward the direct pathway with a higher FAOR activity (Figure 10.13)[171]. When Pt was

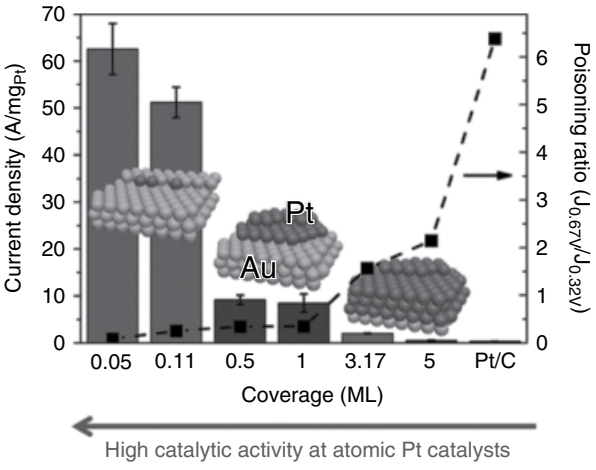

Figure 10.13 Schematic illustrations of three models with various coverages of Pt on Au nanooctahedra and their formic acid oxidation reaction data. As the Pt coverage decreases, the catalytic activity and tolerance to the poisoning increases. Reproduced from ref. [171] with permission.

atomically dispersed at the Au surface, the ensemble effect was suppressed and the bifunctional effect at the Pt–Au interface increased[171–173]. Transition metals were introduced for the FAOR. Various Pt–Cu bimetallic nanostructures were reported such as the Pt–Cu trigonal bipyramid nanoframes[174], Pt–Cu excavated rhombic dodecahedrons[175], Pt–Cu octahedra[176], and Pt–Ag–Cu@Pt–Cu core–shell concave octahedrons[177]. Non-Pt electrocatayst were reported for the FAOR such as Pd–Ir/CNTs[178], Pd–Au octapods[179], and hyperbranched Pd–Cu nanostructures[180].

10.4.2.4 Oxidation of Other Small Organics

Many other small organics have been studied and used as fuels for direct fuel cells. Due to the difficulties of C-C bond cracking, hydrocarbons intermediates can form and act as catalyst poisons. Furthermore, products other than CO_2 may be generated if the number of transferred electrons is lower than the required number to produce CO_2. As an example, when ethanol is oxidized, acetaldehyde can be obtained from the transfer of two electrons transfer, and acetic acid results from the transfer of four electrons transfer (in contrast to CO_2 produced from full oxidization with twelve electrons transfer)[181–183].

1) Two-electron transfer pathway:

$$C_2H_5OH + Pt \rightarrow Pt - CH_3CHO + 2H^+ + 2e^- \tag{10.31}$$

2) Four- (2 + 2) electron transfer pathway:

$$Pt + H_2O \rightarrow Pt - OH + H^+ + e^- \tag{10.32}$$

$$Pt - CH_3CHO + Pt - OH \rightarrow Pt - CH_3COOH + H^+ + e^- \tag{10.33}$$

3) Twelve-electron transfer pathway for full oxidation:

$$C_2H_5OH + 3H_2O \rightarrow 2CO_2 + 12H^+ + 12e^- \tag{10.34}$$

Ethanol is an eco-friendly fuel with large energy density and no toxicity, and it can be obtained from biomass [184]. Many bimetallic alloys (e.g., Pt–Au[143], Pt–Pd [184], Pt–Cu[185], and Pt–Sn[186]) were studied for electrocatalytic ethanol oxidation. Especially, Sn changes the d-band structure of Pt, which makes the adsorption energy of CO decrease[183, 187]. However, Pt–Sn usually tends to follow the two-electrons transfer pathway, producing acetaldehyde[188]. By incorporating tertiary metals, the reaction pathway can be tuned. Pt–Sn–Ce favors a four-electrons pathway, producing acetic acid[188]. Pt–Rh–SnO_2[189, 190], Pt–Ir–SnO_2[191], or Pt–Ni–Sn[192] can break the C-C bond and oxidize ethanol fully. Bimetallic non-Pt catalysts were also studied for ethanol oxidation. Ir–Sn core–shell[193], Pd–Co nanotubes[194], Pd–Ag alloy[162, 163], Pd–Au hexoctahedra[195], and Pd–Te alloy have been reported[196]. Many alloy electrocatalysts were studied for other small organics oxidation. Pt–Ru–Pd/C catalyst was reported for dimethyl ether oxidation[197], and Pt–Au for glucose oxidation [198]. Glycerol can also be oxidized electrocatalytically by Pt–Pd[199], Pt–Bi[200], or Pt–Pd–Bi catalysts[200].

10.4.3 Oxygen Evolution Reaction

Energy storage is important because the renewable energy resources are inherently intermittent[201]. The proton exchange membrane (PEM) water electrolyzers can store the renewable energy efficiently by converting electrical energy into chemical energy[202, 203]. Much attention has been focused on the water electrolysis, but a large overpotential at the OER hinders its applications[204]. The mechanism of the OER follows the four-electrons transfer pathway[205]:

$$M + H_2O \rightarrow M - OH + H^+ + e^- \tag{10.35}$$

$$M - OH \rightarrow M - O + H^+ + e^- \tag{10.36}$$

$$M - O + H_2O \rightarrow M - OOH + H^+ + e^- \tag{10.37}$$

$$M - OOH \rightarrow M + O_2 + H^+ + e^- \tag{10.38}$$

An inverse relationship between activity and stability has typically been observed for OER catalysts[204, 206, 207]. The activity and stability should be balanced, and Ir is the most widely used metal that satisfies this requirement. However, Ir is a very rare and expensive metal, so its minimization is highly needed. Forming an Ir alloy with transition metals can improve the OER activity and stability[208, 209].

10.4.3.1 Alloy with Another Precious Metals

Ir–Ru alloys have been most studied for OER[210–214]. They provide intermediate properties of Ir and Ru, and no synergic effect was observed. Ru provides good activity and a cheaper cost, and Ir provides good stability. The alloy can have reasonably good activity and stability. As Ru contents increase, the activity improves but the stability is degraded. The Tafel slope of the Ir–Ru alloy is similar to that of Ir, indicating that they follow the same OER mechanism[212]. Various Ir–Ru nanostructures were reported, such as Ir–Ru/ATO[210] or multimetallic Ir–Ru–Sn–Ta catalysts[211].

Recently, the Ir–Ru nanostructure with an Ir-protective skeleton was reported with enhanced stability and similar activity compared to commercial Ir–Ru catalysts[204]. Mo-doped Ir–Ru[215], Sn– or Nb– or F-doped Ir catalysts also showed enhanced OER activity[216, 217]. The Ir–Pt alloy has no synergy effect[218, 219]. The Ir–Pt alloy layer on Ti electrodes or Ir–Pt nanodendrites have been reported for the OER[220].

10.4.3.2 Alloy with 3d Metals

Many groups reported that OER activity and stability were enhanced by incorporating the 3d metals into Ir or Ru[208, 209, 221–223]. Although 3d metals might be dissolved in the highly corrosive condition of the PEM water electrolysis, the stability of Ir or Ru was often enhanced when they formed alloys with 3d metals[208, 209]. The d-orbital state of Ir or Ru can be tuned by incorporating the 3d metals, but it is controversial whether the enhanced catalytic performance results from the electronic structure change[221, 224, 225]. Strasser et al. reported that the Ir–Ni alloy nanoparticles had enhanced OER activity and stability in the acidic condition [208, 209]. They also studied the OER mechanism on Ir–Ni alloy films, finding a relationship between surface –OH groups and OER activity[221]. At the surface, the portion of divalent = O surface oxygen species, which is less reactive for the OER, decreases by forming more reactive –OH groups during Ni leaching (Figure 10.14).

Ni-, Co-, or Fe-doping can enhance the OER activity in Ru catalysts. Krtil et al. reported that Ru alloy with 3d metals improved OER activity significantly[223, 226–231]. When RuO_2 is modified with Ni or Co, the location of the intermediate –OH group is changed. The different location induces changes in the Gibbs free energy of intermediate reactions, resulting in enhanced activity[223]. Ir–Cu nanocages also showed improved activity and stability for the OER[224]. Cu-doping into IrO_2 can change the electronic structure of Ir 5d orbital by changing its octahedral geometry by the Jahn-Teller effect, as shown in Figure 10.15[225]. The formation of partial oxygen defects might be responsible for the OER activity enhancement.

10.5 Perspective

In recent years, impressive progress has been made in electrocatalysis by applying shape-controlled bimetallic nanoparticles. We now suggest several important issues that must be addressed for further developments. First, the electrocatalyst design should consider practical application. Although numerous materials have been reported as new electrocatalysts, only a few catalysts have been tested in full cell condition. Various conditions, such as mass transfer, water management, and mechanical properties, must be satisfied to make a real efficient device; however, those have been not considered in most material studies. Second, one should consider that the nanoparticle catalyst eventually should be used to fabricate membrane electrode assembly (MEA). Electrocatalysts are typically used with a proper electrolyte membrane, such as Nafion®. Bimetallic nanostructures usually suffer from leaching of secondary metal, and the leached metal ions may have a detrimental effect on the ionic conductivity of the membrane. Unfortunately, no shape-controlled bimetallic nanostructures has

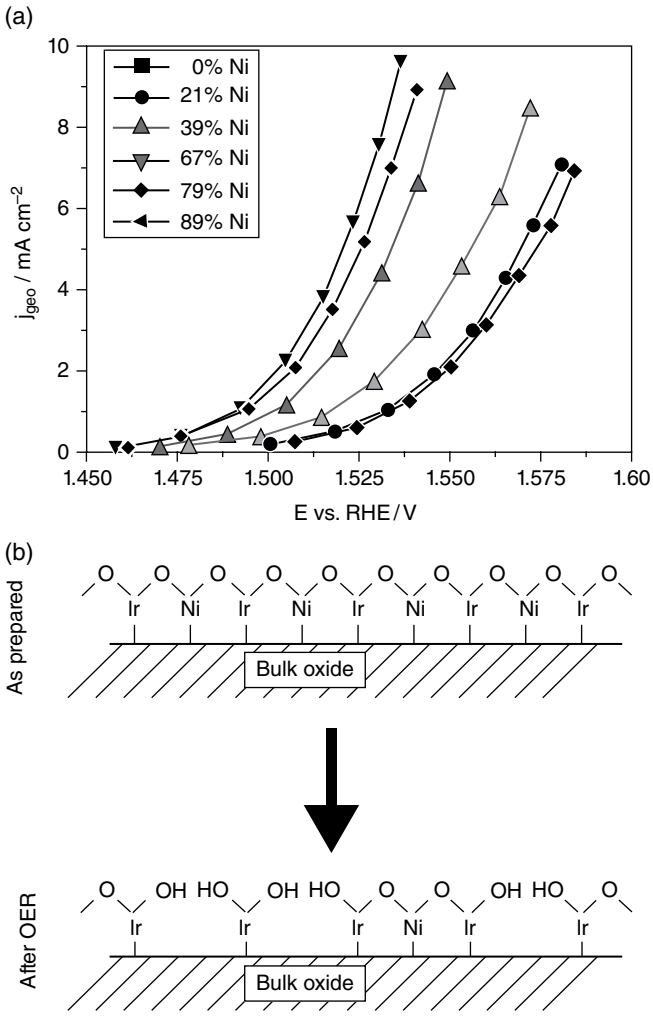

Figure 10.14 (a) OER polarization curves of Ir–Ni mixed oxide films with different Ir to Ni ratios. Alloying Ir and Ni has a beneficial effect on the electrocatalytic OER activity. (b) Model of Ni leaching from the surface of Ir–Ni mixed oxides. When Ni is leached, reactive surface hydroxyl groups are formed. Reproduced from ref. [221] with permission.

been reported for MEA due to this issue[232]. Third, in-depth understanding of electrochemical reactions at an atomic level is needed in order to help identify an ideal bimetallic nanostructure. For example, OER mechanism has not been elucidated yet, and it is hindering the development of the better OER catalyst. Fourth, the synthesis of shaped bimetallic nanostructures should be facile, clean, and easy to scale up for industrial applications. Most of the reported synthesis procedures for shaped bimetallic nanomaterials are quite tricky with a low production yield. We expect that the shape-controlled bimetallic nanostructures would make real impact in electrocatalysis by addressing these issues.

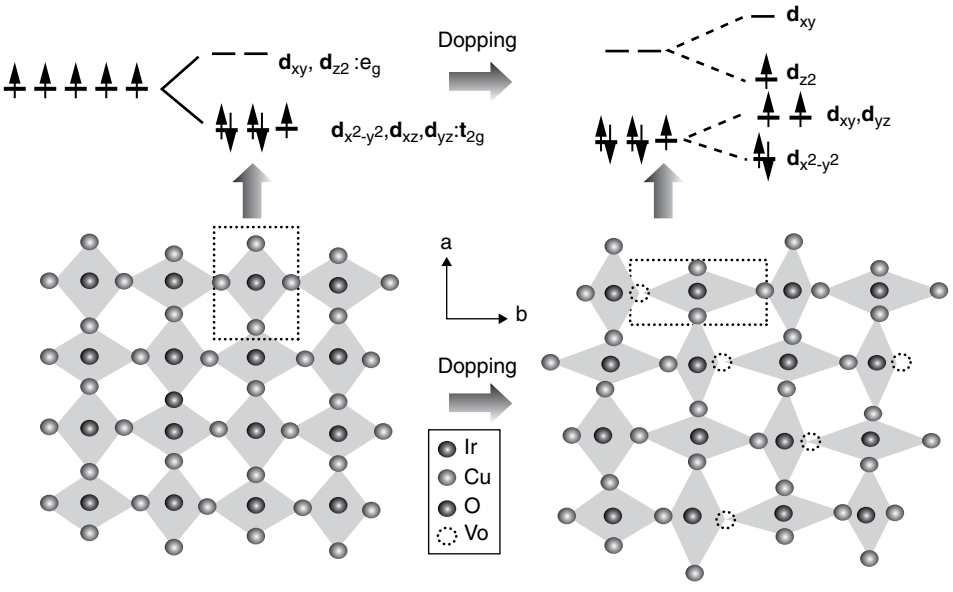

Figure 10.15 Schematic lattice diagram in the ab plane of IrO_2 (left) and substituted by Cu (right). The top row shows Ir-5d orbitals degeneracy of IrO_2 (left) and the lifted degeneracy and electron redistribution by doping with Cu. Reproduced from ref. [225] with permission.

10.6 Conclusion

Bimetallic nanostructures have been actively used as electrocatalysts for various electrochemical reactions of oxygen reduction reaction, the oxidation of methanol, formic acid, hydrogen, or other hydrocarbons, and oxygen evolution reaction. The bimetallic nature enables us to control the electronic structure of main metal atoms, change the surface geometric structure, and endow bifunctional properties. The bimetallic nanostructures have been elucidated using various techniques of electron microscopy, X-ray diffraction, X-ray absorption techniques, and electrochemical measurements. The Pt-based alloy and intermetallic structures have been developed to minimize the usage of expensive precious metals. The 3d transition metals of Ni, Co, and Fe have often been used to form the alloy or intermetallic structure. Pt–Ni alloy octahedral nanoparticles are the most interesting example showing how powerful controlling the shape and composition of nanoparticles can be to enhance the activity and durability for electrochemical reactions and to minimize the utilization of precious Pt. The Pt–Ni nano-octahedra presented 73 times higher activity than commercial Pt–C catalysts for oxygen reduction reaction. Their stability is a still important issue, but various techniques of doping and surface post-treatment show promising results enhancing both activity and durability. Exploring bimetallic nanostructures will continue to be the most active field for developing practical electrocatalysts.

10.7 Acknowledgments

This work was financially supported by the Global Frontier R&D Program at the Center for Multiscale Energy System (2011-0031575) and NRF-2015R1A2A2A01004467 through the National Research Foundation of Korea funded by the Ministry of Education, Science and Technology.

10.8 References

1 Stamenkovic, V., Mun, B. S., Mayrhofer, K. J. J., Ross, P. N., Markovic, N. M., Rossmeisl, J., Greeley, J., and Norskov, J. K. (2006). Changing the activity of electrocatalysts for oxygen reduction by tuning the surface electronic structure. *Angewandte Chemie International Edition*, 45 (18), 2897–2901.

2 Kitchin, J. R., Norskov, J. K., Barteau, M. A., and Chen, J. G. (2004). Modification of the surface electronic and chemical properties of Pt(111) by subsurface 3d transition metals. *Journal of Chemical Physics*, 120 (21), 10240–10246.

3 Chen, D. J., and Tong, Y. Y. J. (2015). Irrelevance of Carbon Monoxide Poisoning in the Methanol Oxidation Reaction on a PtRu Electrocatalyst. *Angewandte Chemie International Edition*, 54 (32), 9394–9398.

4 Maroun, F., Ozanam, F., Magnussen, O. M., and Behm, R. J. (2001). The role of atomic ensembles in the reactivity of bimetallic electrocatalysts. *Science*, 293 (5536), 1811–1814.

5 Siahrostami, S., Verdaguer-Casadevall, A., Karamad, M., Deiana, D., Malacrida, P., Wickman, B., Escudero-Escribano, M., Paoli, E. A., Frydendal, R., Hansen, T. W., Chorkendorff, I., Stephens, I. E. L., and Rossmeisl, J. (2013). Enabling direct H_2O_2 production through rational electrocatalyst design. *Nature Materials*, 12 (12), 1137–1143.

6 Viswanathan, V., Hansen, H. A., Rossmeisl, J., and Norskov, J. K. (2012). Unifying the $2e^-$ and $4e^-$ Reduction of oxygen on metal surfaces. *Journal of Physical Chemistry Letters*, 3 (20), 2948–2951.

7 Rossmeisl, J., Karlberg, G. S., Jaramillo, T., and Norskov, J. K. (2008). Steady state oxygen reduction and cyclic voltammetry. *Faraday Discussions*, 140 pp. 337–346.

8 Peng, Z. M., and Yang, H. (2009). Designer platinum nanoparticles: Control of shape, composition in alloy, nanostructure and electrocatalytic property. *Nano Today*, 4 (2), 143–164.

9 Yu, T., Kim, D. Y., Zhang, H., and Xia, Y. N. (2011). Platinum concave nanocubes with high-index facets and their enhanced activity for oxygen reduction reaction. *Angewandte Chemie International Edition*, 50 (12), 2773–2777.

10 Duan, Z. Y., and Wang, G. F. (2013). Comparison of reaction energetics for oxygen reduction reactions on Pt(100), Pt(111), Pt/Ni(100), and Pt/Ni(111) Surfaces: A first-principles study. *Journal of Physical Chemistry C*, 117 (12), 6284–6292.

11 Huang, X. Q., Zhao, Z. P., Cao, L., Chen, Y., Zhu, E. B., Lin, Z. Y., Li, M. F., Yan, A. M., Zettl, A., Wang, Y. M., Duan, X. F., Mueller, T., and Huang, Y. (2015). High-performance transition metal-doped Pt_3Ni octahedra for oxygen reduction reaction. *Science*, 348 (6240), 1230–1234.

12 Lim, J., Yang, S., Kim, C., Roh, C. W., Kwon, Y., Kim, Y. T., and Lee, H. (2016). Shaped Ir–Ni bimetallic nanoparticles for minimizing Ir utilization in oxygen evolution reaction. *Chemical Communications*, 52 (32), 5641–5644.

13 Xia, X. H., Figueroa-Cosme, L., Tao, J., Peng, H. C., Niu, G. D., Zhu, Y. M., and Xia, Y. N. (2014). Facile synthesis of iridium nanocrystals with well-controlled facets using seed-mediated growth. *Journal of the American Chemical Society*, 136 (31), 10878–10881.

14 Chen, C., Kang, Y. J., Huo, Z. Y., Zhu, Z. W., Huang, W. Y., Xin, H. L. L., Snyder, J. D., Li, D. G., Herron, J. A., Mavrikakis, M., Chi, M. F., More, K. L., Li, Y. D., Markovic, N. M., Somorjai, G. A., Yang, P. D., and Stamenkovic, V. R. (2014). Highly crystalline multimetallic nanoframes with three-dimensional electrocatalytic surfaces. *Science*, 343 (6177), 1339–1343.

15 Oh, A., Baik, H., Choi, D. S., Cheon, J. Y., Kim, B., Kim, H., Kwon, S. J., Joo, S. H., Jung, Y., and Lee, K. (2015). Skeletal octahedral nanoframe with cartesian coordinates via geometrically precise nanoscale phase segregation in a pt@ni core-shell nanocrystal. *ACS Nano*, 9 (3), 2856–2867.

16 Zhang, L., Roling, L. T., Wang, X., Vara, M., Chi, M. F., Liu, J. Y., Choi, S. I., Park, J., Herron, J. A., Xie, Z. X., Mavrikakis, M., and Xia, Y. N. (2015). Platinum-based nanocages with subnanometer-thick walls and well-defined, controllable facets. *Science*, 349 (6246), 412–416.

17 Ding, J. B., Zhu, X., Bu, L. Z., Yao, J. L., Guo, J., Guo, S. J., and Huang, X. Q. (2015). Highly open rhombic dodecahedral PtCu nanoframes. *Chemical Communications*, 51 (47), 9722–9725.

18 Xia, B. Y., Wu, H. B., Wang, X., and Lou, X. W. (2012). One-Pot Synthesis of Cubic $PtCu_3$ Nanocages with Enhanced Electrocatalytic Activity for the Methanol Oxidation Reaction. *Journal of the American Chemical Society*, 134 (34), 13934–13937.

19 Ferrando, R., Jellinek, J., and Johnston, R. L. (2008). Nanoalloys: From theory to applications of alloy clusters and nanoparticles. *Chemical Reviews*, 108 (3), 845–910.

20 Cui, C. H., Gan, L., Li, H. H., Yu, S. H., Heggen, M., and Strasser, P. (2012). Octahedral PtNi nanoparticle catalysts: exceptional oxygen reduction activity by tuning the alloy particle surface composition. *Nano Letters*, 12 (11), 5885–5889.

21 Huang, X. Q., Zhu, E. B., Chen, Y., Li, Y. J., Chiu, C. Y., Xu, Y. X., Lin, Z. Y., Duan, X. F., and Huang, Y. (2013). A facile strategy to pt_3ni nanocrystals with highly porous features as an enhanced oxygen reduction reaction catalyst. *Advanced Materials*, 25 (21), 2974–2979.

22 Bele, M., Jovanovic, P., Pavlisic, A., Jozinovic, B., Zorko, M., Recnik, A., Chernyshova, E., Hocevar, S., Hodnik, N., and Gaberscek, M. (2014). A highly active $PtCu_3$ intermetallic core-shell, multilayered Pt-skin, carbon embedded electrocatalyst produced by a scale-up sol-gel synthesis. *Chemical Communications*, 50 (86), 13124–13126.

23 Xia, B. Y., Wu, H. B., Li, N., Yan, Y., Lou, X. W., and Wang, X. (2015). One-Pot synthesis of Pt-Co alloy nanowire assemblies with tunable composition and enhanced electrocatalytic properties. *Angewandte Chemie International Edition*, 54 (12), 3797–3801.

24 Cui, Z. M., Chen, H., Zhao, M. T., Marshall, D., Yu, Y. C., Abruna, H., and DiSalvo, F. J. (2014). Synthesis of structurally ordered Pt_3Ti and Pt_3V nanoparticles as methanol oxidation catalysts. *Journal of the American Chemical Society*, 136 (29), 10206–10209.

25 Crewe, A. V., Wall, J., and Langmore, J. (1970). Visibility of single atoms. *Science*, 168 (3937), 1338–1340.

26 Liu, H. J., Dou, M. L., Wang, F., Liu, J. J., Ji, J., and Li, Z. L. (2015). Ordered intermetallic PtFe@Pt core-shell nanoparticles supported on carbon nanotubes with superior activity and durability as oxygen reduction reaction electrocatalysts. *RSC Advances*, 5 (81), 66471–66475.

27 Thiele, S., Furstenhaupt, T., Banham, D., Hutzenlaub, T., Birss, V., Ziegler, C., and Zengerle, R. (2013). Multiscale tomography of nanoporous carbon-supported noble metal catalyst layers. *Journal of Power Sources*, 228 pp. 185–192.

28 Zhao, X. Y., Luo, B. B., Long, R., Wang, C. M., and Xiong, Y. J. (2015). Composition-dependent activity of Cu–Pt alloy nanocubes for electrocatalytic CO_2 reduction. *Journal of Materials Chemistry A*, 3 (8), 4134–4138.

29 Cui, Z. M., Li, L. J., Manthiram, A., and Goodenough, J. B. (2015). Enhanced Cycling Stability of Hybrid Li-Air Batteries Enabled by ordered Pd_3Fe Intermetallic Electrocatalyst. *Journal of the American Chemical Society*, 137 (23), 7278–7281.

30 Koyasu, K., Mitsui, M., Nakajima, A., and Kaya, K. (2002). Photoelectron spectroscopy of palladium-doped gold cluster anions; Au_n,Pd^- ($n = 1–4$). *Chemical Physics Letters*, 358 (3–4), 224–230.

31 Mun, B. S., Lee, C., Stamenkovic, V., Markovic, N. M., and Ross, P. N. (2005). Electronic structure of Pd thin films on Re(0001) studied by high-resolution core-level and valence-band photoemission. *Physical Review B*, 71 (11) 115420

32 Mun, B. S., Watanabe, M., Rossi, M., Stamenkovic, V., Markovic, N. M., and Ross, P. N. (2005). A study of electronic structures of Pt_3M (M = Ti,V,Cr,Fe,Co,Ni) polycrystalline alloys with valence-band photoemission spectroscopy. *Journal of Chemical Physics*, 123 (20) 204717.

33 Russell, A. E., and Rose, A. (2004). X-ray absorption Spectroscopy of low temperature fuel cell catalysts. *Chemical Reviews*, 104 (10), 4613–4635.

34 Becknell, N., Kang, Y. J., Chen, C., Resasco, J., Kornienko, N., Guo, J. H., Markovic, N. M., Somorjai, G. A., Stamenkovic, V. R., and Yang, P. D. (2015). Atomic structure of Pt_3Ni nanoframe electrocatalysts by in situ X-ray absorption spectroscopy. *Journal of the American Chemical Society*, 137 (50), 15817–15824.

35 Choi, K. H., Jang, Y., Chung, D. Y., Seo, P., Jun, S. W., Lee, J. E., Oh, M. H., Shokouhimehr, M., Jung, N., Yoo, S. J., Sung, Y. E., and Hyeon, T. (2016). A simple synthesis of urchin-like Pt–Ni bimetallic nanostructures as enhanced electrocatalysts for the oxygen reduction reaction. *Chemical Communications*, 52 (3), 597–600.

36 Frenkel, A. I. (2012). Applications of extended X-ray absorption fine-structure spectroscopy to studies of bimetallic nanoparticle catalysts. *Chemical Society Reviews*, 41 (24), 8163–8178.

37 Chung, D. Y., Jun, S. W., Yoon, G., Kwon, S. G., Shin, D. Y., Seo, P., Yoo, J. M., Shin, H., Chung, Y. H., Kim, H., Mun, B. S., Lee, K. S., Lee, N. S., Yoo, S. J., Lim, D. H., Kang, K., Sung, Y. E., and Hyeon, T. (2015). Highly durable and active PtFe nanocatalyst for electrochemical oxygen reduction reaction. *Journal of the American Chemical Society*, 137 (49), 15478–15485.

38 Gasteiger, H. A., Kocha, S. S., Sompalli, B., and Wagner, F. T. (2005). Activity benchmarks and requirements for Pt, Pt-alloy, and non-Pt oxygen reduction catalysts for PEMFCs. *Applied Catalysis B:Environmental*, 56 (1–2), 9–35.

39 Ramaker, D. E., Korovina, A., Croze, V., Melke, J., and Roth, C. (2014). Following ORR intermediates adsorbed on a Pt cathode catalyst during break-in of a PEM fuel cell by in operando X-ray absorption spectroscopy. *Physical Chemistry Chemical Physics*, 16 (27), 13645–13653.

40 Wang, D. L., Yu, Y. C., Xin, H. L. L., Hovden, R., Ercius, P., Mundy, J. A., Chen, H., Richard, J. H., Muller, D. A., DiSalvo, F. J., and Abruna, H. D. (2012). *Tuning Oxygen Reduction Reaction Activity via Controllable Dealloying: A Nano Letters*, 12 (10), 5230–5238.

41 Wang, D. L., Yu, Y. C., Zhu, J., Liu, S. F., Muller, D. A., and Abruna, H. D. (2015). Morphology and Activity Tuning of Cu_3Pt/C Ordered Intermetallic Nanoparticles by Selective Electrochemical Dealloying. *Nano Letters*, 15 (2), 1343–1348.

42 Rudi, S., Cui, C. H., Gan, L., and Strasser, P. (2014). Comparative study of the electrocatalytically active surface areas (ECSAs) of Pt alloy nanoparticles evaluated by H-upd and CO-stripping voltammetry. *Electrocatalysis*, 5 (4), 408–418.

43 Shao, M. H., Odell, J. H., Choi, S. I., and Xia, Y. N. (2013). Electrochemical surface area measurements of platinum- and palladium-based nanoparticles. *Electrochemistry Communications*, 31 pp. 46–48.

44 Seh, Z. W., Kibsgaard, J., Dickens, C. F., Chorkendorff, I. B., Norskov, J. K., and Jaramillo, T. F. (2017). Combining theory and experiment in electrocatalysis: Insights into materials design. *Science*, 355 (6321).

45 Travitsky, N., Ripenbein, T., Golodnitsky, D., Rosenberg, Y., Burshtein, L., and Peled, E. (2006). Pt-, PtNi- and PtCo-supported catalysts for oxygen reduction in PEM fuel cells. *Journal of Power Sources*, 161 (2), 782–789.

46 Chen, Y. M., Yang, F., Dai, Y., Wang, W. Q., and Chen, S. L. (2008). Ni@Pt core-shell nanoparticles: Synthesis, structural and electrochemical properties. *Journal of Physical Chemistry C*, 112 (5), 1645–1649.

47 Tseng, C.-J., Lo, S.-T., Lo, S.-C., and Chu, P. P. (2006). Characterization of Pt–Cu binary catalysts for oxygen reduction for fuel cell applications. *Materials Chemistry and Physics*, 100 (2–3), 385–390.

48 Mani, P., Srivastava, R., and Strasser, P. (2011). Dealloyed binary PtM_3 (M = Cu, Co, Ni) and ternary $PtNi_3M$ (M = Cu, Co, Fe, Cr) electrocatalysts for the oxygen reduction reaction: Performance in polymer electrolyte membrane fuel cells. *Journal of Power Sources*, 196 (2), 666–673.

49 Oezaslan, M., and Strasser, P. (2011). Activity of dealloyed $PtCo_3$ and $PtCu_3$ nanoparticle electrocatalyst for oxygen reduction reaction in polymer electrolyte membrane fuel cell. *Journal of Power Sources*, 196 (12), 5240–5249.

50 Oezaslan, M., Hasché, F. d. r., and Strasser, P. (2012a). Oxygen electroreduction on $PtCo_3$, PtCo and Pt_3Co alloy nanoparticles for alkaline and acidic PEM fuel cells. *Journal of The Electrochemical Society*, 159 (4), B394–B405.

51 Oezaslan, M., Hasché, F. d. r., and Strasser, P. (2012b). $PtCu_3$, PtCu and Pt_3Cu alloy nanoparticle electrocatalysts for oxygen reduction reaction in alkaline and acidic media. *Journal of The Electrochemical Society*, 159 (4), B444–B454.

52 Mani, P., Srivastava, R., and Strasser, P. (2008). Dealloyed Pt–Cu core-shell nanoparticle electrocatalysts for use in PEM fuel cell cathodes. *Journal of Physical Chemistry C*, 112 (7), 2770–2778.

53 Kakade, B. A., Wang, H., Tamaki, T., Ohashi, H., and Yamaguchi, T. (2013). Enhanced oxygen reduction reaction by bimetallic CoPt and PdPt nanocrystals. *RSC Advances*, 3 (26), 10487–10496.

54 Sohn, Y., Park, J. H., Kim, P., and Joo, J. B. (2015). Dealloyed PtCu catalyst as an efficient electrocatalyst in oxygen reduction reaction. *Current Applied Physics*, 15 (9), 993–999.

55 Han, B. H., Carlton, C. E., Kongkanand, A., Kukreja, R. S., Theobald, B. R., Gan, L., O'Malley, R., Strasser, P., Wagner, F. T., and Shao-Horn, Y. (2015). Record activity and stability of dealloyed bimetallic catalysts for proton exchange membrane fuel cells. *Energy & Environmental Science*, 8 (1), 258–266.

56 Koh, S., and Strasser, P. (2007). Electrocatalysis on bimetallic surfaces: Modifying catalytic reactivity for oxygen reduction by voltammetric surface dealloying. *Journal of the American Chemical Society*, 129 (42), 12624–12625.

57 Strasser, P., Koha, S., and Greeley, J. (2008). Voltammetric surface dealloying of Pt bimetallic nanoparticles: an experimental and DFT computational analysis. *Physical Chemistry Chemical Physics*, 10 (25), 3670–3683.

58 Herrero, E., Buller, L. J., and Abruña, H. D. (2001). Underpotential deposition at single crystal surfaces of Au, Pt, Ag and other materials. *Chemical Reviews*, 101 (7), 1897–1930.

59 Wang, J. X., Inada, H., Wu, L. J., Zhu, Y. M., Choi, Y. M., Liu, P., Zhou, W. P., and Adzic, R. R. (2009). Oxygen reduction on well-defined core-shell nanocatalysts: particle size, facet, and Pt shell thickness effects. *Journal of the American Chemical Society*, 131 (47), 17298–17302.

60 Greeley, J., Stephens, I. E. L., Bondarenko, A. S., Johansson, T. P., Hansen, H. A., Jaramillo, T. F., Rossmeisl, J., Chorkendorff, I., and Norskov, J. K. (2009). Alloys of platinum and early transition metals as oxygen reduction electrocatalysts. *Nature Chemistry*, 1 (7), 552–556.

61 Escudero-Escribano, M., Verdaguer-Casadevall, A., Malacrida, P., Gronbjerg, U., Knudsen, B. P., Jepsen, A. K., Rossmeisl, J., Stephens, I. E., and Chorkendorff, I. (2012). Pt_5Gd as a highly active and stable catalyst for oxygen electroreduction. *Journal of the American Chemical Society*, 134 (40), 16476–16479.

62 Stephens, I. E. L., Bondarenko, A. S., Grønbjerg, U., Rossmeisl, J., and Chorkendorff, I. (2012). Understanding the electrocatalysis of oxygen reduction on platinum and its alloys. *Energy & Environmental Science*, 5 (5), 6744.

63 Liu, L., Samjeske, G., Nagamatsu, S.-i., Sekizawa, O., Nagasawa, K., Takao, S., Imaizumi, Y., Yamamoto, T., Uruga, T., and Iwasawa, Y. (2012). Enhanced oxygen reduction reaction activity and characterization of Pt–Pd/C bimetallic fuel cell catalysts with Pt-enriched surfaces in acid media. *The Journal of Physical Chemistry C*, 116 (44), 23453–23464.

64 Gan, L., Heggen, M., Rudi, S., and Strasser, P. (2012). Core-shell compositional fine structures of dealloyed Pt_xNi_{1-x} nanoparticles and their impact on oxygen reduction catalysis. *Nano Letters*, 12 (10), 5423–5430.

65 Bing, Y. H., Liu, H. S., Zhang, L., Ghosh, D., and Zhang, J. J. (2010). Nanostructured Pt-alloy electrocatalysts for PEM fuel cell oxygen reduction reaction. *Chemical Society Reviews*, 39 (6), 2184–2202.

66 Wang, D. L., Xin, H. L. L., Hovden, R., Wang, H. S., Yu, Y. C., Muller, D. A., DiSalvo, F. J., and Abruna, H. D. (2013). Structurally ordered intermetallic platinum-cobalt core-shell nanoparticles with enhanced activity and stability as oxygen reduction electrocatalysts. *Nature Materials*, 12 (1), 81–87.

67 Ji, X. L., Lee, K. T., Holden, R., Zhang, L., Zhang, J. J., Botton, G. A., Couillard, M., and Nazar, L. F. (2010). Nanocrystalline intermetallics on mesoporous carbon for direct formic acid fuel cell anodes. *Nature Chemistry*, 2 (4), 286–293.

68 Zhang, D. T., Wu, F. X., Peng, M. H., Wang, X. Y., Xia, D. G., and Guo, G. S. (2015). One-step, facile and ultrafast synthesis of phase- and size-controlled Pt-Bi intermetallic nanocatalysts through continuous-flow microfluidics. *Journal of the American Chemical Society*, 137 (19), 6263–6269.

69 Lang, X. Y., Han, G. F., Xiao, B. B., Gu, L., Yang, Z. Z., Wen, Z., Zhu, Y. F., Zhao, M., Li, J. C., and Jiang, Q. (2015). Mesostructured Intermetallic compounds of platinum and non-transition metals for enhanced electrocatalysis of oxygen reduction reaction. *Advanced Functional Materials*, 25 (2), 230–237.

70 Prabhudev, S., Bugnet, M., Bock, C., and Botton, G. A. (2013). Strained lattice with persistent atomic order in Pt_3Fe_2 intermetallic core-shell nanocatalysts. *ACS Nano*, 7 (7), 6103–6110.

71 Mukerjee, S., Srinivasan, S., Soriaga, M. P., and Mcbreen, J. (1995). Role of structural and electronic properties of Pt and Pt alloys on electrocatalysis of oxygen reduction—an *in situ* XANES and EXAFS investigation. *Journal of The Electrochemical Society*, 142 (5), 1409–1422.

72 Zhang, B. W., Jiang, Y. X., Ren, J., Qu, X. M., Xu, G. L., and Sun, S. G. (2015). PtBi intermetallic and PtBi intermetallic with the Bi-rich surface supported on porous graphitic carbon towards HCOOH electro-oxidation. *Electrochimica Acta*, 162 pp. 254–262.

73 Zhang, B. W., He, C. L., Jiang, Y. X., Chen, M. H., Li, Y. Y., Rao, L., and Sun, S. G. (2012). High activity of PtBi intermetallics supported on mesoporous carbon towards HCOOH electro-oxidation. *Electrochemistry Communications*, 25 pp. 105–108.

74 Nguyen, M. T., Wakabayashi, R. H., Yang, M. H., Abruna, H. D., and DiSalvo, F. J. (2015). Synthesis of carbon supported ordered tetragonal pseudo-ternary $Pt_2M'M''$ (M = Fe, Co, Ni) nanoparticles and their activity for oxygen reduction reaction. *Journal of Power Sources*, 280 pp. 459–466.

75 Arumugam, B., Kakade, B. A., Tamaki, T., Arao, M., Imai, H., and Yamaguchi, T. (2014). Enhanced activity and durability for the electroreduction of oxygen at a chemically ordered intermetallic PtFeCo catalyst. *RSC Advances*, 4 (52), 27510–27517.

76 Arumugam, B., Tamaki, T., and Yamaguchi, T. (2015). Beneficial role of copper in the enhancement of durability of ordered intermetallic PtFeCu catalyst for electrocatalytic oxygen reduction. *ACS Applied Materials & Interfaces*, 7 (30), 16311–16321.

77 Chen, H., Wang, D. L., Yu, Y. C., Newton, K. A., Muller, D. A., Abruna, H., and DiSalvo, F. J. (2012). A surfactant-free strategy for synthesizing, and processing intermetallic platinum-based nanoparticle catalysts. *Journal of the American Chemical Society*, 134 (44), 18453–18459.

78 Prabhudev, S., Bugnet, M., Zhu, G. Z., Bock, C., and Botton, G. A. (2015). Surface segregation of Fe in Pt-Fe alloy nanoparticles: its precedence and effect on the ordered-phase evolution during thermal annealing. *ChemCatChem*, 7 (22), 3655–3664.

79 Li, Q., Wu, L. H., Wu, G., Su, D., Lv, H. F., Zhang, S., Zhu, W. L., Casimir, A., Zhu, H. Y., Mendoza-Garcia, A., and Sun, S. H. (2015). New approach to fully ordered fct-FePt nanoparticles for much enhanced electrocatalysis in acid. *Nano Letters*, 15 (4), 2468–2473.

80 Leonard, B. M., Zhou, Q., Wu, D. N., and DiSalvo, F. J. (2011). Facile synthesis of PtNi intermetallic nanoparticles: influence of reducing agent and precursors on electrocatalytic activity. *Chemistry of Materials*, 23 (5), 1136–1146.

81 Casado-Rivera, E., Volpe, D. J., Alden, L., Lind, C., Downie, C., Vazquez-Alvarez, T., Angelo, A. C. D., DiSalvo, F. J., and Abruna, H. D. (2004). Electrocatalytic activity of

ordered intermetallic phases for fuel cell applications. *Journal of the American Chemical Society*, 126 (12), 4043–4049.

82 Sims, C. M., Ponce, A. A., Gaskell, K. J., and Eichhorn, B. W. (2015). CO tolerance of Pt and PtSn intermetallic electrocatalysts on synthetically modified reduced graphene oxide supports. *Dalton Transactions*, 44 (3), 977–987.

83 Abe, H., Matsumoto, F., Alden, L. R., Warren, S. C., Abruna, H. D., and DiSalvo, F. J. (2008). Electrocatalytic performance of fuel oxidation by Pt_3Ti nanoparticles. *Journal of the American Chemical Society*, 130 (16), 5452–5458.

84 Maksimuk, S., Yang, S. C., Peng, Z. M., and Yang, H. (2007). Synthesis and characterization of ordered intermetallic PtPb nanorods. *Journal of the American Chemical Society*, 129 (28), 8684–8685.

85 Ghosh, T., Vukmirovic, M. B., DiSalvo, F. J., and Adzic, R. R. (2010). Intermetallics as novel supports for Pt monolayer O_2 reduction electrocatalysts: potential for significantly improving properties. *Journal of the American Chemical Society*, 132 (3), 906–907.

86 Gunji, T., Sakai, K., Suzuki, Y., Kaneko, S., Tanabe, T., and Matsumoto, F. (2015). Enhanced oxygen reduction reaction on PtPb ordered intermetallic nanoparticle/TiO_2/carbon black in acidic aqueous solutions. *Catalysis Communications*, 61 pp. 1–5.

87 Youn, D. H., Han, S., Bae, G., and Lee, J. S. (2011). Carbon-supported PtPb intermetallic compounds for electrooxidation of methyl formate. *Electrochemistry Communications*, 13 (8), 806–809.

88 Sra, A. K., and Schaak, R. E. (2004). Synthesis of atomically ordered AuCu and $AuCu_3$ nanocrystals from bimetallic nanoparticle precursors. *Journal of the American Chemical Society*, 126 (21), 6667–6672.

89 Schaak, R. E., Sra, A. K., Leonard, B. M., Cable, R. E., Bauer, J. C., Han, Y. F., Means, J., Teizer, W., Vasquez, Y., and Funck, E. S. (2005). Metallurgy in a beaker: Nanoparticle toolkit for the rapid low-temperature solution synthesis of functional multimetallic solid-state materials. *Journal of the American Chemical Society*, 127 (10), 3506–3515.

90 Boyen, H. G., Ethirajan, A., Kastle, G., Weigl, F., Ziemann, P., Schmid, G., Garnier, M. G., Buttner, M., and Oelhafen, P. (2005). Alloy formation of supported gold nanoparticles at their transition from clusters to solids: Does size matter?. *Physical Review Letters*, 94 (1) 016804.

91 Terada, Y. (2008). Thermophysical Properties of L1(2) Intermetallic compounds of iridium thermal conductivity and thermal expansion of ir3x for ultra high-temperature applications. *Platinum Metals Review*, 52 (4), 208–214.

92 Furukawa, S., Yoshida, Y., and Komatsu, T. (2014). Chemoselective hydrogenation of nitrostyrene to aminostyrene over Pd- and Rh-Based intermetallic compounds. *ACS Catalysis*, 4 (5), 1441–1450.

93 Chi, M. F., Wang, C., Lei, Y. K., Wang, G. F., Li, D. G., More, K. L., Lupini, A., Allard, L. F., Markovic, N. M., and Stamenkovic, V. R. (2015). Surface faceting and elemental diffusion behaviour at atomic scale for alloy nanoparticles during in situ annealing. *Nature Communications*, 6.

94 Rong, C. B., Li, D. R., Nandwana, V., Poudyal, N., Ding, Y., Wang, Z. L., Zeng, H., and Liu, J. P. (2006). Size-dependent chemical and magnetic ordering in $L1_0$-FePt nanoparticles. *Advanced Materials*, 18 (22), 2984–2988.

95 Kim, J., Yang, S., and Lee, H. (2016). Platinum-titanium intermetallic nanoparticle catalysts for oxygen reduction reaction with enhanced activity and durability. *Electrochemistry Communications*, 66 pp. 66–70.

96 Zou, L. L., Li, J., Yuan, T., Zhou, Y., Li, X. M., and Yang, H. (2014). Structural transformation of carbon-supported Pt_3Cr nanoparticles from a disordered to an ordered phase as a durable oxygen reduction electrocatalyst. *Nanoscale*, 6 (18), 10686–10692.

97 Stamenkovic, V. R., Fowler, B., Mun, B. S., Wang, G. F., Ross, P. N., Lucas, C. A., and Markovic, N. M. (2007). Improved oxygen reduction activity on $Pt_3Ni(111)$ via increased surface site availability. *Science*, 315 (5811), 493–497.

98 Duan, Z., and Wang, G. (2013). Comparison of reaction energetics for oxygen reduction reactions on Pt(100), Pt(111), Pt/Ni(100), and Pt/Ni(111) Surfaces: A first-principles study. *The Journal of Physical Chemistry C*, 117 (12), 6284–6292.

99 Zhang, J., Yang, H. Z., Fang, J. Y., and Zou, S. Z. (2010). Synthesis and oxygen reduction activity of shape-controlled Pt_3Ni nanopolyhedra. *Nano Letters*, 10 (2), 638–644.

100 Chen, J., Herricks, T., Geissler, M., and Xia, Y. (2004). Single-crystal nanowires of platinum can be synthesized by controlling the reaction rate of a polyol process. *Journal of the American Chemical Society*, 126 (35), 10854–10855.

101 Gratzel, M. (2001). Photoelectrochemical cells. *Nature*, 414 (6861), 338–344.

102 Wu, J. B., Gross, A., and Yang, H. (2011). Shape and composition-controlled platinum alloy nanocrystals using carbon monoxide as reducing agent. *Nano Letters*, 11 (2), 798–802.

103 Xia, Y. N., Xiong, Y. J., Lim, B., and Skrabalak, S. E. (2009). Shape-controlled synthesis of metal nanocrystals: simple chemistry meets complex physics? *Angewandte Chemie International Edition*, 48 (1), 60–103.

104 Wu, J. B., Qi, L., You, H. J., Gross, A., Li, J., and Yang, H. (2012). Icosahedral platinum alloy nanocrystals with enhanced electrocatalytic activities. *Journal of the American Chemical Society*, 134 (29), 11880–11883.

105 Choi, S. I., Xie, S. F., Shao, M. H., Odell, J. H., Lu, N., Peng, H. C., Protsailo, L., Guerrero, S., Park, J. H., Xia, X. H., Wang, J. G., Kim, M. J., and Xia, Y. N. (2013). Synthesis and characterization of 9 nm Pt–Ni octahedra with a record high activity of 3.3 A/mg_{Pt} for the oxygen reduction reaction. *Nano Letters*, 13 (7), 3420–3425.

106 Huang, X. Q., Zhao, Z. P., Chen, Y., Zhu, E. B., Li, M. F., Duan, X. F., and Huang, Y. (2014). A rational design of carbon-supported dispersive Pt-based octahedra as efficient oxygen reduction reaction catalysts. *Energy & Environmental Science*, 7 (9), 2957–2962.

107 Colon-Mercado, H. R., and Popov, B. N. (2006). Stability of platinum based alloy cathode catalysts in PEM fuel cells. *Journal of Power Sources*, 155 (2), 253–263.

108 Kuttiyiel, K. A., Sasaki, K., Choi, Y. M., Su, D., Liu, P., and Adzic, R. R. (2012). Nitride stabilized PtNi core-shell nanocatalyst for high oxygen reduction activity. *Nano Letters*, 12 (12), 6266–6271.

109 Kang, Y. J., Snyder, J., Chi, M. F., Li, D. G., More, K. L., Markovic, N. M., and Stamenkovic, V. R. (2014). Multimetallic core/interlayer/shell nanostructures as advanced electrocatalysts. *Nano Letters*, 14 (11), 6361–6367.

110 Zhang, J., Sasaki, K., Sutter, E., and Adzic, R. R. (2007). Stabilization of platinum oxygen-reduction electrocatalysts using gold clusters. *Science*, 315 (5809), 220–222.

111 Choi, J., Lee, Y., Kim, J., and Lee, H. (2016). Enhancing stability of octahedral PtNi nanoparticles for oxygen reduction reaction by halide treatment. *Journal of Power Sources*, 307, 883–890.

112 Xiong, Y. J., Cai, H. G., Wiley, B. J., Wang, J. G., Kim, M. J., and Xia, Y. N. (2007). Synthesis and mechanistic study of palladium nanobars and nanorods. *Journal of the American Chemical Society*, 129 (12), 3665–3675.

113 Yuan, Q. A., Zhou, Z. Y., Zhuang, J., and Wang, X. (2010). Tunable aqueous phase synthesis and shape-dependent electrochemical properties of rhodium nanostructures. *Inorganic Chemistry*, 49 (12), 5515–5521.

114 Steele, B. C. H., and Heinzel, A. (2001). Materials for fuel-cell technologies. *Nature*, 414 (6861), 345–352.

115 Cuesta, A. (2006). At least three contiguous atoms are necessary for CO formation during methanol electrooxidation on platinum. *Journal of the American Chemical Society*, 128 (41), 13332–13333.

116 Schmidt, T. J., Gasteiger, H. A., and Behm, R. J. (1999). Rotating disk electrode measurements on the CO tolerance of a high-surface area Pt/Vulcan carbon fuel cell catalyst. *Journal of The Electrochemical Society*, 146 (4), 1296–1304.

117 Ren, X. M., Zelenay, P., Thomas, S., Davey, J., and Gottesfeld, S. (2000). Recent advances in direct methanol fuel cells at Los Alamos National Laboratory. *Journal of Power Sources*, 86 (1–2), 111–116.

118 Costamagna, P., and Srinivasan, S. (2001). Quantum jumps in the PEMFC science and technology from the 1960s to the year 2000 Part I. Fundamental scientific aspects. *Journal of Power Sources*, 102 (1–2), 242–252.

119 Innocente, A. F., and Angelo, A. C. D. (2006). Electrocatalysis of oxidation of hydrogen on platinum ordered intermetallic phases: Kinetic and mechanistic studies. *Journal of Power Sources*, 162 (1), 151–159.

120 Hassan, A., Paganin, V. A., and Ticianelli, E. A. (2015). Pt modified tungsten carbide as anode electrocatalyst for hydrogen oxidation in proton exchange membrane fuel cell: CO tolerance and stability. *Applied Catalysis B: Environmental*, 165, 611–619.

121 Pedersen, C. M., Escudero-Escribano, M., Velazquez-Palenzuela, A., Christensen, L. H., Chorkendorff, I., and Stephens, I. E. L. (2015). Benchmarking Pt-based electrocatalysts for low temperature fuel cell reactions with the rotating disk electrode: oxygen reduction and hydrogen oxidation in the presence of CO (review article). *Electrochimica Acta*, 179, 647–657.

122 Liu, P., Logadottir, A., and Norskov, J. K. (2003). Modeling the electro-oxidation of CO and H_2/CO on Pt, Ru, PtRu and Pt_3Sn. *Electrochimica Acta*, 48 (25–26), 3731–3742.

123 Arenz, M., Stamenkovic, V., Blizanac, B. B., Mayrhofer, K. J. J., Markovic, N. M., and Ross, P. N. (2005). Carbon-supported Pt–Sn electrocatalysts for the anodic oxidation of H_2, CO, and H_2/CO mixtures. Part II: The structure-activity relationship. *Journal of Catalysis*, 232 (2), 402–410.

124 Grgur, B. N., Markovic, N. M., and Ross, P. N. (1998). Electrooxidation of H_2, CO, and H_2/CO mixtures on a well-characterized $Pt_{70}Mo_{30}$ bulk alloy electrode. *Journal of Physical Chemistry B*, 102 (14), 2494–2501.

125 Grgur, B. N., Markovic, N. M., and Ross, P. N. (1999). The electro-oxidation of H_2 and H_2/CO mixtures on carbon-supported Pt_xMo_y alloy catalysts. *Journal of the Electrochemical Society*, 146 (5), 1613–1619.

126 Igarashi, H., Fujino, T., Zhu, Y. M., Uchida, H., and Watanabe, M. (2001). CO Tolerance of Pt alloy electrocatalysts for polymer electrolyte fuel cells and the detoxification mechanism. *Physical Chemistry Chemical Physics*, 3 (3), 306–314.

127 Giorgi, L., Pozio, A., Bracchini, C., Giorgi, R., and Turtu, S. (2001). H_2 and H_2/CO oxidation mechanism on Pt/C, Ru/C and Pt–Ru/C electrocatalysts. *Journal of Applied Electrochemistry*, 31 pp. 325–334.

128 Velazquez, A., Centellas, F., Garrido, J. A., Arias, C., Rodriguez, R. M., Brillas, E., and Cabot, P. L. (2010). Structure of carbon-supported Pt–Ru nanoparticles and their electrocatalytic behavior for hydrogen oxidation reaction. *Journal of Power Sources*, 195 (3), 710–719.

129 Petrii, O. A. (2008). Pt–Ru electrocatalysts for fuel cells: a representative review. *Journal of Solid State Electrochemistry*, 12 (5), 609–642.

130 Watanabe, M., and Motoo, S. (1975). Electrocatalysis by ad-atoms: Part III. enhancement of the oxidation of carbon monoxide on platinum by ruthenium ad-atoms. *Electroanalytical Chemistry and lnterfacial Electrochemistry*, 60 (3), 275–283.

131 Chen, D. J., Sun, S. G., and Tong, Y. Y. J. (2014). On the chemistry of activation of a commercial carbon-supported PtRu electrocatalyst for the methanol oxidation reaction. *Chemical Communications*, 50 (85), 12963–12965.

132 Liu, Y., Chi, M. F., Mazumder, V., More, K. L., Soled, S., Henao, J. D., and Sun, S. H. (2011). Composition-controlled synthesis of bimetallic pdpt nanoparticles and their electro-oxidation of methanol. *Chemistry of Materials*, 23 (18), 4199–4203.

133 Yin, A. X., Min, X. Q., Zhang, Y. W., and Yan, C. H. (2011). Shape-selective synthesis and facet-dependent enhanced electrocatalytic activity and durability of monodisperse sub-10 nm Pt-Pd tetrahedrons and cubes. *Journal of the American Chemical Society*, 133 (11), 3816–3819.

134 Wang, L., Nemoto, Y., and Yamauchi, Y. (2011). Direct synthesis of spatially-controlled Pt-on-Pd bimetallic nanodendrites with superior electrocatalytic activity. *Journal of the American Chemical Society*, 133 (25), 9674–9677.

135 Wang, L., and Yamauchi, Y. (2013). Metallic nanocages: Synthesis of bimetallic Pt–Pd hollow nanoparticles with dendritic shells by selective chemical etching. *Journal of the American Chemical Society*, 135 (45), 16762–16765.

136 Li, H. H., Zhao, S., Gong, M., Cui, C. H., He, D., Liang, H. W., Wu, L., and Yu, S. H. (2013). Ultrathin PtPdTe nanowires as superior catalysts for methanol electrooxidation. *Angewandte Chemie International Edition*, 52 (29), 7472–7476.

137 Guo, S. J., Zhang, S., Sun, X. L., and Sun, S. H. (2011). Synthesis of Ultrathin FePtPd nanowires and their use as catalysts for methanol oxidation reaction. *Journal of the American Chemical Society*, 133 (39), 15354–15357.

138 Zhang, Y., Janyasupab, M., Liu, C. W., Li, X. X., Xu, J. Q., and Liu, C. C. (2012). Three dimensional PtRh alloy porous nanostructures: tuning the atomic composition and controlling the morphology for the application of direct methanol fuel cells. *Advanced Functional Materials*, 22 (17), 3570–3575.

139 Zhou, S. H., Jackson, G. S., and Eichhorn, B. (2007). AuPt alloy nanoparticles for CO–tolerant hydrogen activation: Architectural effects in Au–Pt bimetallic nanocatalysts. *Advanced Functional Materials*, 17 (16), 3099–3104.

140 Zhang, Z. H., Wang, Y., and Wang, X. G. (2011). Nanoporous bimetallic Pt–Au alloy nanocomposites with superior catalytic activity towards electro-oxidation of methanol and formic acid. *Nanoscale*, 3 (4), 1663–1674.

141 Luo, J., Maye, M. M., Kariuki, N. N., Wang, L. Y., Njoki, P., Lin, Y., Schadt, M., Naslund, H. R., and Zhong, C. J. (2005). Electrocatalytic oxidation of methanol:

carbon-supported gold-platinum nanoparticle catalysts prepared by two-phase protocol. *Catalysis Today*, 99 (3–4), 291–297.

142 Lou, Y. B., Maye, M. M., Han, L., Luo, J., and Zhong, C. J. (2001). Gold-platinum alloy nanoparticle assembly as catalyst for methanol electrooxidation. *Chemical Communications* (5), 473–474.

143 Anderson, J., Karakoti, A., Diaz, D. J., and Seal, S. (2010). Nanoceria-modified platinum-gold composite electrodes for the electrochemical oxidation of methanol and ethanol in acidic media. *Journal of Physical Chemistry C*, 114 (10), 4595–4602.

144 Suntivich, J., Xu, Z. C., Carlton, C. E., Kim, J., Han, B. H., Lee, S. W., Bonnet, N., Marzari, N., Allard, L. F., Gasteiger, H. A., Hamad-Schifferli, K., and Shao-Horn, Y. (2013). Surface composition tuning of Au–Pt bimetallic nanoparticles for enhanced carbon monoxide and methanol electro-oxidation. *Journal of the American Chemical Society*, 135 (21), 7985–7991.

145 Park, K. W., Choi, J. H., Kwon, B. K., Lee, S. A., Sung, Y. E., Ha, H. Y., Hong, S. A., Kim, H., and Wieckowski, A. (2002). Chemical and electronic effects of Ni in Pt/Ni and Pt/Ru/Ni alloy nanoparticles in methanol electrooxidation. *Journal of Physical Chemistry B*, 106 (8), 1869–1877.

146 Antolini, E., Salgado, J. R. C., and Gonzalez, E. R. (2006). The methanol oxidation reaction on platinum alloys with the first row transition metals: The case of Pt–Co and –Ni alloy electrocatalysts for DMFCs: A short review. *Applied Catalysis B: Environmental*, 63 (1–2), 137–149.

147 Liu, X. J., Cui, C. H., Gong, M., Li, H. H., Xue, Y., Fan, F. J., and Yu, S. H. (2013). Pt–Ni alloyed nanocrystals with controlled architectures for enhanced methanol oxidation. *Chemical Communications*, 49 (77), 8704–8706.

148 Cui, C. H., Li, H. H., and Yu, S. H. (2011). Large-scale restructuring of porous Pt–Ni nanoparticle tubes for methanol oxidation: A highly reactive, stable, and restorable fuel cell catalyst. *Chemical Science*, 2 (8), 1611–1614.

149 Ye, S. H., Feng, J. X., Wang, A. L., Xu, H., and Li, G. R. (2015). Multi-layered Pt/Ni nanotube arrays with enhanced catalytic performance for methanol electrooxidation. *Journal of Materials Chemistry A*, 3 (46), 23201–23206.

150 Wang, S., Yang, G., and Yang, S. C. (2015). Pt-Frame@Ni quasi core-shell concave octahedral $ptni_3$ bimetallic nanocrystals for electrocatalytic methanol oxidation and hydrogen evolution. *Journal of Physical Chemistry C*, 119 (50), 27938–27945.

151 Wu, Y. E., Wang, D. S., Zhou, G., Yu, R., Chen, C., and Li, Y. D. (2014). Sophisticated construction of Au islands on Pt–Ni: An ideal trimetallic nanoframe catalyst. *Journal of the American Chemical Society*, 136 (33), 11594–11597.

152 Liu, X. W., Wang, W. Y., Li, H., Li, L. S., Zhou, G. B., Yu, R., Wang, D. S., and Li, Y. D. (2013). One-pot protocol for bimetallic Pt/Cu hexapod concave nanocrystals with enhanced electrocatalytic activity. *Scientific Reports*, 3: 1404.

153 Qiu, H. J., Shen, X., Wang, J. Q., Hirata, A., Fujita, T., Wang, Y., and Chen, M. W. (2015). Aligned nanoporous Pt–Cu bimetallic microwires with high catalytic activity toward methanol electrooxidation. *ACS Catalysis*, 5 (6), 3779–3785.

154 Eid, K., Wang, H. J., He, P., Wang, K. M., Ahamad, T., Alshehri, S. M., Yamauchi, Y., and Wang, L. (2015). One-step synthesis of porous bimetallic PtCu nanocrystals with high electrocatalytic activity for methanol oxidation reaction. *Nanoscale*, 7 (40), 16860–16866.

155 Han, L., Liu, H., Cui, P. L., Peng, Z. J., Zhang, S. J., and Yang, J. (2014). Alloy Cu_3Pt nanoframes through the structure evolution in Cu–Pt nanoparticles with a core-shell construction. *Scientific Reports*, 4: 6414.

156 Ye, S. H., He, X. J., Ding, L. X., Pan, Z. W., Tong, Y. X., Wu, M. M., and Li, G. R. (2014). Cu_2O template synthesis of high-performance PtCu alloy yolk-shell cube catalysts for direct methanol fuel cells. *Chemical Communications*, 50 (82), 12337–12340.

157 Kang, Y. J., and Murray, C. B. (2010). Synthesis and Electrocatalytic Properties of Cubic Mn–Pt Nanocrystals (Nanocubes). *Journal of the American Chemical Society*, 132 (22), 7568–7569.

158 Kang, Y. J., Pyo, J. B., Ye, X. C., Gordon, T. R., and Murray, C. B. (2012). Synthesis, shape control, and methanol electro-oxidation properties of Pt–Zn alloy and Pt_3Zn intermetallic nanocrystals. *ACS Nano*, 6 (6), 5642–5647.

159 Ye, J. Q., Liu, H. P., Xu, C. W., Jiang, S. P., and Tong, Y. X. (2007). Electrooxidation of 2-propanol on Pt, Pd, and Au in alkaline medium. *Electrochemistry Communications*, 9 (12), 2760–2763.

160 Gasteiger, H. A., Markovic, N., Ross, P. N., and Cairns, E. J. (1993). Methanol Electrooxidation on Well-Characterized Pt–Ru Alloys. *Journal of Physical Chemistry*, 97 (46), 12020–12029.

161 Hammer, B., and Norskov, J. K. (2000). Theoretical surface science and catalysis—Calculations and concepts. *Advances in Catalysis, Vol* 45, 45 pp. 71–129.

162 Safavi, A., Kazemi, H., Momeni, S., Tohidi, M., and Mehrin, P. K. (2013). Facile electrocatalytic oxidation of ethanol using Ag/Pd nanoalloys modified carbon ionic liquid electrode. *International Journal of Hydrogen Energy*, 38 (8), 3380–3386.

163 Nguyen, S. T., Law, H. M., Nguyen, H. T., Kristian, N., Wang, S. Y., Chan, S. H., and Wang, X. (2009). Enhancement effect of Ag for Pd/C towards the ethanol electro-oxidation in alkaline media. *Applied Catalysis B: Environmental*, 91 (1–2), 507–515.

164 Wang, Y., Sheng, Z. M., Yang, H. B., Jiang, S. P., and Li, C. M. (2010). Electrocatalysis of carbon black- or activated carbon nanotubes-supported Pd–Ag towards methanol oxidation in alkaline media. *International Journal of Hydrogen Energy*, 35 (19), 10087–10093.

165 Xu, L., Luo, Z. M., Fan, Z. X., Yu, S. J., Chen, J. Z., Liao, Y. S., and Xue, C. (2015). Controllable Galvanic Synthesis of Triangular Ag–Pd Alloy Nanoframes for Efficient Electrocatalytic Methanol Oxidation. *Chemistry—A European Journal*, 21 (24), 8691–8695.

166 Lee, H. J., Habas, S. E., Somorjai, G. A., and Yang, P. D. (2008). Localized Pd overgrowth on cubic Pt nanocrystals for enhanced electrocatalytic oxidation of formic acid. *Journal of the American Chemical Society*, 130 (16), 5406–5407.

167 Yu, X. W., and Pickup, P. G. (2011). Screening of PdM and PtM catalysts in a multi-anode direct formic acid fuel cell. *Journal of Applied Electrochemistry*, 41 (5), 589–597.

168 Park, I. S., Lee, K. S., Choi, J. H., Park, H. Y., and Sung, Y. E. (2007). Surface structure of Pt-modified Au nanoparticles and electrocatalytic activity in formic acid electro-oxidation. *Journal of Physical Chemistry C*, 111 (51), 19126–19133.

169 Iyyamperumal, R., Zhang, L., Henkelman, G., and Crooks, R. M. (2013). Efficient electrocatalytic oxidation of formic acid using Au@Pt dendrimer-encapsulated nanoparticles. *Journal of the American Chemical Society*, 135 (15), 5521–5524.

170 Zhang, S., Shao, Y. Y., Liao, H. G., Liu, J., Aksay, I. A., Yin, G. P., and Lin, Y. H. (2011). Graphene decorated with PtAu alloy nanoparticles: facile synthesis and promising application for formic acid oxidation. *Chemistry of Materials*, 23 (5), 1079–1081.

171 Yang, S., and Lee, H. (2013). Atomically dispersed platinum on gold nano-octahedra with high catalytic activity on formic acid oxidation. *ACS Catalysis*, 3 (3), 437–443.

172 Kristian, N., Yan, Y. S., and Wang, X. (2008). Highly efficient submonolayer Pt-decorated Au nano-catalysts for formic acid oxidation. *Chemical Communications* (3), 353–355.

173 Zhang, G. R., Zhao, D., Feng, Y. Y., Zhang, B. S., Su, D. S., Liu, G., and Xu, B. Q. (2012). Catalytic Pt-on-Au nanostructures: Why Pt becomes more active on smaller Au particles. *ACS Nano*, 6 (3), 2226–2236.

174 Chen, S., Su, H. Y., Wang, Y. C., Wu, W. L., and Zeng, J. (2015). Size-Controlled Synthesis of platinum-copper hierarchical trigonal bipyramid nanoframes. *Angewandte Chemie International Edition*, 54 (1), 108–113.

175 Jia, Y. Y., Jiang, Y. Q., Zhang, J. W., Zhang, L., Chen, Q. L., Xie, Z. X., and Zheng, L. S. (2014). Unique excavated rhombic dodecahedral $PtCu_3$ alloy nanocrystals constructed with ultrathin nanosheets of high-energy {110} facets. *Journal of the American Chemical Society*, 136 (10), 3748–3751.

176 Zhang, J., Yang, H. Z., Martens, B., Luo, Z. P., Xu, D., Wang, Y. X., Zou, S. Z., and Fang, J. Y. (2012). Pt–Cu nanoctahedra: synthesis and comparative study with nanocubes on their electrochemical catalytic performance. *Chemical Science*, 3 (11), 3302–3306.

177 Fu, G. T., Xia, B. Y., Ma, R. G., Chen, Y., Tang, Y. W., and Lee, J. M. (2015). Trimetallic PtAgCu@PtCu core@shell concave nanooctahedrons with enhanced activity for formic acid oxidation reaction. *Nano Energy*, 12 pp. 824–832.

178 Chen, J. W., Li, Y. J., Liu, S. R., Wang, G., Tian, J., Jiang, C. P., Zhu, S. F., and Wang, R. L. (2013). Remarkable activity of PdIr nanoparticles supported on the surface of carbon nanotubes pretreated via a sonochemical process for formic acid electro-oxidation. *Applied Surface Science*, 287 pp. 457–460.

179 Wang, L. B., Wang, Y. C., Guo, H. Y., Huang, J. L., Zhao, Y. L., Liu, Q. Y., Wu, X., and Zeng, J. (2015). Au–Pd alloy octapods with high electrocatalytic activity for the oxidation of formic acid. *Particle & Particle Systems Characterization*, 32 (3), 295–300.

180 Jiang, B., Li, C., Malgras, V., Bando, Y., and Yamauchi, Y. (2016). Three-dimensional hyperbranched PdCu nanostructures with high electrocatalytic activity. *Chemical Communications*, 52 pp. 1186–1189.

181 Antolini, E., and Gonzalez, E. R. (2010). Alkaline direct alcohol fuel cells. *Journal of Power Sources*, 195 (11), 3431–3450.

182 Kowal, A., Li, M., Shao, M., Sasaki, K., Vukmirovic, M. B., Zhang, J., Marinkovic, N. S., Liu, P., Frenkel, A. I., and Adzic, R. R. (2009). Ternary $Pt/Rh/SnO_2$ electrocatalysts for oxidizing ethanol to CO_2. *Nature Materials*, 8 (4), 325–330.

183 Vigier, F., Coutanceau, C., Hahn, F., Belgsir, E. M., and Lamy, C. (2004). On the mechanism of ethanol electro-oxidation on Pt and PtSn catalysts: electrochemical and in situ IR reflectance spectroscopy studies. *Journal of Electroanalytical Chemistry*, 563 (1), 81–89.

184 Yang, X., Yang, Q. D., Xu, J., and Lee, C. S. (2012). Bimetallic PtPd nanoparticles on Nafion-graphene film as catalyst for ethanol electro-oxidation. *Journal of Materials Chemistry*, 22 (16), 8057–8062.

185 Saleem, F., Zhang, Z. C., Xu, B., Xu, X. B., He, P. L., and Wang, X. (2013). Ultrathin Pt–Cu nanosheets and nanocones. *Journal of the American Chemical Society*, 135 (49), 18304–18307.

186 Jiang, L., Colmenares, L., Jusys, Z., Sun, G. Q., and Behm, R. J. (2007). Ethanol electrooxidation on novel carbon supported $Pt/SnO_x/C$ catalysts with varied Pt: Sn ratio. *Electrochimica Acta*, 53 (2), 377–389.

187 Silva, J. C. M., Parreira, L. S., De Souza, R. F. B., Calegaro, M. L., Spinace, E. V., Neto, A. O., and Santos, M. C. (2011). PtSn/C alloyed and non-alloyed materials: Differences in the ethanol electro-oxidation reaction pathways. *Applied Catalysis B: Environmental*, 110 pp. 141–147.

188 De Souza, R. F. B., Parreira, L. S., Silva, J. C. M., Simoes, F. C., Calegaro, M. L., Giz, M. J., Camara, G. A., Neto, A. O., and Santos, M. C. (2011). PtSnCe/C electrocatalysts for ethanol oxidation: DEFC and FTIR "in-situ" studies. *International Journal of Hydrogen Energy*, 36 (18), 11519–11527.

189 Du, W. X., Wang, Q., LaScala, C. A., Zhang, L. H., Su, D., Frenkel, A. I., Mathur, V. K., and Teng, X. W. (2011). Ternary PtSnRh–SnO_2 nanoclusters: synthesis and electroactivity for ethanol oxidation fuel cell reaction. *Journal of Materials Chemistry*, 21 (24), 8887–8892.

190 Li, M., Kowal, A., Sasaki, K., Marinkovic, N., Su, D., Korach, E., Liu, P., and Adzic, R. R. (2010). Ethanol oxidation on the ternary Pt–Rh–SnO_2/C electrocatalysts with varied Pt:Rh:Sn ratios. *Electrochimica Acta*, 55 (14), 4331–4338.

191 Li, M., Cullen, D. A., Sasaki, K., Marinkovic, N. S., More, K., and Adzic, R. R. (2013). Ternary electrocatalysts for oxidizing ethanol to carbon dioxide: making Ir capable of splitting C-C bond. *Journal of the American Chemical Society*, 135 (1), 132–141.

192 Beyhan, S., Leger, J. M., and Kadirgan, F. (2013). Pronounced synergetic effect of the nano-sized PtSnNi/C catalyst for ethanol oxidation in direct ethanol fuel cell. *Applied Catalysis B: Environmental*, 130 pp. 305–313.

193 Du, W. X., Wang, Q., Saxner, D., Deskins, N. A., Su, D., Krzanowski, J. E., Frenkel, A. I., and Teng, X. W. (2011). Highly active iridium/iridium–tin/tin oxide heterogeneous nanoparticles as alternative electrocatalysts for the ethanol oxidation reaction. *Journal of the American Chemical Society*, 133 (38), 15172–15183.

194 Wang, A. L., He, X. J., Lu, X. F., Xu, H., Tong, Y. X., and Li, G. R. (2015). Palladium–cobalt nanotube arrays supported on carbon fiber cloth as high-performance flexible electrocatalysts for ethanol oxidation. *Angewandte Chemie International Edition*, 54 (12), 3669–3673.

195 Lee, Y. W., Kim, D., Hong, J. W., Kang, S. W., Lee, S. B., and Han, S. W. (2013). Kinetically controlled growth of polyhedral bimetallic alloy nanocrystals exclusively bound by high-index facets: AuPd hexoctahedra. *Small*, 9 (5), 660–665.

196 Cai, J. D., Huang, Y. Y., and Guo, Y. L. (2014). $PdTe_x$/C nanocatalysts with high catalytic activity for ethanol electro-oxidation in alkaline medium. *Applied Catalysis B: Environmental*, 150 pp. 230–237.

197 Li, Q., Wen, X. D., Wu, G., Chung, H. T., Gao, R., and Zelenay, P. (2015). High-activity PtRuPd/C catalyst for direct dimethyl ether fuel cells. *Angewandte Chemie International Edition*, 54 (26), 7524–7528.

198 Basu, D., and Basu, S. (2011). Synthesis and characterization of Pt–Au/C catalyst for glucose electro-oxidation for the application in direct glucose fuel cell. *International Journal of Hydrogen Energy*, 36 (22), 14923–14929.

199 Grace, A. N., and Pandian, K. (2006). Pt, Pt–Pd and Pt–Pd/Ru nanoparticles entrapped polyaniline electrodes—A potent electrocatalyst towards the oxidation of glycerol. *Electrochemistry Communications*, 8 (8), 1340–1348.

200 Simoes, M., Baranton, S., and Coutanceau, C. (2011). Enhancement of catalytic properties for glycerol electrooxidation on Pt and Pd nanoparticles induced by Bi surface modification. *Applied Catalysis B: Environmental*, 110 pp. 40–49.

201 Yang, Z. G., Zhang, J. L., Kintner-Meyer, M. C. W., Lu, X. C., Choi, D. W., Lemmon, J. P., and Liu, J. (2011). Electrochemical energy storage for green grid. *Chemical Reviews*, 111 (5), 3577–3613.

202 Reier, T., Oezaslan, M., and Strasser, P. (2012). Electrocatalytic oxygen evolution reaction (OER) on Ru, Ir, and Pt catalysts: A comparative study of nanoparticles and bulk materials. *ACS Catalysis*, 2 (8), 1765–1772.

203 Antolini, E. (2014). Iridium as catalyst and cocatalyst for oxygen evolution/reduction in acidic polymer electrolyte membrane electrolyzers and fuel cells. *ACS Catalysis*, 4 (5), 1426–1440.

204 Danilovic, N., Subbaraman, R., Chang, K. C., Chang, S. H., Kang, Y. J., Snyder, J., Paulikas, A. P., Strmcnik, D., Kim, Y. T., Myers, D., Stamenkovic, V. R., and Markovic, N. M. (2014a). Using surface segregation to design stable Ru–Ir oxides for the oxygen evolution reaction in acidic environments. *Angewandte Chemie International Edition*, 53 (51), 14016–14021.

205 Rossmeisl, J., Qu, Z. W., Zhu, H., Kroes, G. J., and Norskov, J. K. (2007). Electrolysis of water on oxide surfaces. *Journal of Electroanalytical Chemistry*, 607 (1–2), 83–89.

206 Danilovic, N., Subbaraman, R., Chang, K. C., Chang, S. H., Kang, Y. J. J., Snyder, J., Paulikas, A. P., Strmcnik, D., Kim, Y. T., Myers, D., Stamenkovic, V. R., and Markovic, N. M. (2014b). Activity-stability trends for the oxygen evolution reaction on monometallic oxides in acidic environments. *Journal of Physical Chemistry Letters*, 5 (14), 2474–2478.

207 Chang, S. H., Danilovic, N., Chang, K. C., Subbaraman, R., Paulikas, A. P., Fong, D. D., Highland, M. J., Baldo, P. M., Stamenkovic, V. R., Freeland, J. W., Eastman, J. A., and Markovic, N. M. (2014). Functional links between stability and reactivity of strontium ruthenate single crystals during oxygen evolution. *Nature Communications*, 5.

208 Nong, H. N., Gan, L., Willinger, E., Teschner, D., and Strasser, P. (2014). IrO_x core-shell nanocatalysts for cost- and energy-efficient electrochemical water splitting. *Chemical Science*, 5 (8), 2955–2963.

209 Nong, H. N., Oh, H. S., Reier, T., Willinger, E., Willinger, M. G., Petkov, V., Teschner, D., and Strasser, P. (2015). Oxide-supported $IrNiO_x$ core-shell particles as efficient, cost-effective, and stable catalysts for electrochemical water splitting. *Angewandte Chemie International Edition*, 54 (10), 2975–2979.

210 Marshall, A. T., and Haverkamp, R. G. (2010). Electrocatalytic activity of IrO_2–RuO_2 supported on Sb-doped SnO2 nanoparticles. *Electrochimica Acta*, 55 (6), 1978–1984.

211 Marshall, A., Borresen, B., Hagen, G., Tsypkin, M., and Tunold, R. (2007). Hydrogen production by advanced proton exchange membrane (PEM) water electrolysers—Reduced energy consumption by improved electrocatalysis. *Energy*, 32 (4), 431–436.

212 Siracusano, S., Van Dijk, N., Payne-Johnson, E., Baglio, V., and Arico, A. S. (2015). Nanosized IrO_x and $IrRuO_x$ electrocatalysts for the O_2 evolution reaction in PEM water electrolysers. *Applied Catalysis B: Environmental*, 164 pp. 488–495.

213 Cheng, J. B., Zhang, H. M., Chen, G. B., and Zhang, Y. N. (2009). Study of $Ir_xRu_{1-x}O_2$ oxides as anodic electrocatalysts for solid polymer electrolyte water electrolysis. *Electrochimica Acta*, 54 (26), 6250–6256.

214 Li, G. F., Yu, H. M., Song, W., Wang, X. Y., Li, Y. K., Shao, Z. G., and Yi, B. L. (2012). Zeolite-templated $Ir_xRu_{1-x}O_2$ electrocatalysts for oxygen evolution reaction in solid polymer electrolyte water electrolyzers. *International Journal of Hydrogen Energy*, 37 (22), 16786–16794.

215 Cheng, J. B., Zhang, H. M., Ma, H. P., Zhong, H. X., and Zou, Y. (2009). Preparation of $Ir_{0.4}Ru_{0.6}Mo_xO_y$ for oxygen evolution by modified Adams' fusion method. *International Journal of Hydrogen Energy*, 34 (16), 6609–6624.

216 Kadakia, K., Datta, M. K., Jampani, P. H., Park, S. K., and Kumta, P. N. (2013). Novel F-doped IrO_2 oxygen evolution electrocatalyst for PEM based water electrolysis. *Journal of Power Sources*, 222 pp. 313–317.

217 Kadakia, K., Datta, M. K., Velikokhatnyi, O. I., Jampani, P. H., and Kumta, P. N. (2014). Fluorine doped (Ir,Sn,Nb)O_2 anode electro-catalyst for oxygen evolution via PEM based water electrolysis. *International Journal of Hydrogen Energy*, 39 (2), 664–674.

218 Papazisi, K. M., Siokou, A., Balomenou, S., and Tsiplakides, D. (2012). Preparation and characterization of $Ir_xPt_{1-x}O_2$ anode electrocatalysts for the oxygen evolution reaction. *International Journal of Hydrogen Energy*, 37 (21), 16642–16648.

219 DaSilva, L. A., Alves, V. A., Trasatti, S., and Boodts, J. F. C. (1997). Surface and electrocatalytic properties of ternary oxides $Ir_{0.3}Ti_{(0.7-x)}Pt_xO_2$. Oxygen evolution from acidic solution. *Journal of Electroanalytical Chemistry*, 427 (1–2), 97–104.

220 Zhang, G., Shao, Z. G., Lu, W. T., Li, G. F., Liu, F. Q., and Yi, B. L. (2012). One-pot synthesis of Ir@Pt nanodendrites as highly active bifunctional electrocatalysts for oxygen reduction and oxygen evolution in acidic medium. *Electrochemistry Communications*, 22 pp. 145–148.

221 Reier, T., Pawolek, Z., Cherevko, S., Bruns, M., Jones, T., Teschner, D., Selve, S., Bergmann, A., Nong, H. N., Schlogl, R., Mayrhofer, K. J. J., and Strasser, P. (2015). Molecular insight in structure and activity of highly efficient, low-Ir Ir–Ni oxide catalysts for electrochemical water splitting (OER). *Journal of the American Chemical Society*, 137 (40), 13031–13040.

222 Moghaddam, R. B., Wang, C., Sorge, J. B., Brett, M. J., and Bergens, S. H. (2015). Easily prepared, high activity Ir–Ni oxide catalysts for water oxidation. *Electrochemistry Communications*, 60 pp. 109–112.

223 Halck, N. B., Petrykin, V., Krtil, P., and Rossmeisl, J. (2014). Beyond the volcano limitations in electrocatalysis-oxygen evolution reaction. *Physical Chemistry Chemical Physics*, 16 (27), 13682–13688.

224 Wang, C., Sui, Y. M., Xiao, G. J., Yang, X. Y., Wei, Y. J., Zou, G. T., and Zou, B. (2015). Synthesis of Cu–Ir nanocages with enhanced electrocatalytic activity for the oxygen evolution reaction. *Journal of Materials Chemistry A*, 3 (39), 19669–19673.

225 Sun, W., Song, Y., Gong, X. Q., Cao, L. M., and Yang, J. (2015). An efficiently tuned d-orbital occupation of IrO_2 by doping with Cu for enhancing the oxygen evolution reaction activity. *Chemical Science*, 6 (8), 4993–4999.

226 Petrykin, V., Bastl, Z., Franc, J., Macounova, K., Makarova, M., Mukerjee, S., Ramaswamy, N., Spirovova, I., and Krtil, P. (2009). Local structure of nanocrystalline $Ru_{1-x}Ni_xO_{2-}\delta$ dioxide and its implications for electrocatalytic behavior—An XPS and XAS study. *Journal of Physical Chemistry C*, 113 (52), 21657–21666.

227 Makarova, M. V., Jirkovsky, J., Klementova, M., Jirka, I., Macounova, K., and Krtil, P. (2008). The electrocatalytic behavior of $Ru_{0.8}Co_{0.2}O_{2-x}$-the effect of particle shape and surface composition. *Electrochimica Acta*, 53 (5), 2656–2664.

228 Macounova, K., Makarova, M., Jirkovsky, J., Franc, J., and Krtil, P. (2008). Parallel oxygen and chlorine evolution on $Ru_{1-x}Ni_xO_{2-y}$ nanostructured electrodes. *Electrochimica Acta*, 53 (21), 6126–6134.

229 Macounova, K., Makarova, M., Franc, J., Jirkovsky, J., and Krtil, P. (2008). Influence of oxygen on reactivity of $Ru_{1-x}Fe_xO_{2-y}$-doped materials. *Electrochemical and Solid State Letters*, 11 (12), F27–F29.

230 Macounova, K., Jirkovsky, J., Makarova, M. V., Franc, J., and Krtil, P. (2009). Oxygen evolution on $Ru_{1-x}Ni_xO_{2-y}$ nanocrystalline electrodes. *Journal of Solid State Electrochemistry*, 13 (6), 959–965.

231 Jirkovsky, J., Makarova, M., and Krtil, P. (2006). Particle size dependence of oxygen evolution reaction on nanocrystalline RuO_2 and $Ru_{0.8}Co_{0.2}O_{2-x}$. *Electrochemistry Communications*, 8 (9), 1417–1422.

232 Kongkanand, A., and Mathias, M. F. (2016). The priority and challenge of high-power performance of low-platinum proton-exchange membrane fuel cells. *Journal of Physical Chemistry Letters*, 7 (7), 1127–1137.

11

Heterogeneous Catalysis

Yuchen Pei[1] *and Wenyu Huang*[1,2]

[1] *Department of Chemistry, Iowa State University, Ames, IA, USA*
[2] *Ames Laboratory, U.S. Department of Energy, Ames, IA, USA*

11.1 Introduction

Heterogeneous catalysts have been widely used in the industry in the production of important chemicals, the manufacture of pharmaceuticals, energy conversion, and environmental remediation. The major tasks in developing heterogeneous catalysts are fulfilling the rapid conversion of catalyzed reactions and ensuring high selectivity to desired products[1]. Precious metals have served as heterogeneous catalysts in many reactions, including hydrogenation, oxidation, condensation, and coupling reactions[2]. The catalytic capability of precious metals is likely originated from their low *d*-band centers, dispersive orbitals, more outer electrons, versatile coordination capabilities, and stable chemical properties. Many bimetallic catalysts have also been developed with modified electronic and geometric structures that provide more control to tune reaction pathways[3, 4].

Bimetallic catalysts containing inexpensive secondary metals can reduce the usage of precious metals. Many heterogeneous catalysts employ metallic nanoparticles (NPs) because of their increased surface area-to-volume ratio. Metallic NPs also expose very active undercoordinated active sites (e.g., corners, edges, kinks, steps, and twin boundaries)[5]. Extensive studies have been conducted to elucidate the effect of surface structure on the catalytic properties of bimetallic NPs, which have opened immense possibilities to rationally design the structure of bimetallic NPs for heterogeneous catalysis.

The catalytic properties of bimetallic NPs are highly dependent on their composition, size, and shape. Bimetallic NPs with optimized compositions can lead to enhanced catalytic properties arising from synergistic effects between different metal elements, where the metal-to-metal interaction can modify their electronic property, create lattice strain, and alternate reaction pathway[6, 7]. The size effect on catalysis has been discovered on both monometallic and bimetallic NPs due to the change in the atom distribution at the face, edge, and corner sites[8]. The shape-dependent catalytic property of bimetallic NPs is a fast-growing research area because of the development of advanced synthetic strategies[9–11]. Bimetallic NPs of various morphologies have been

Bimetallic Nanostructures: Shape-Controlled Synthesis for Catalysis, Plasmonics, and Sensing Applications, First Edition. Edited by Ya-Wen Zhang.
© 2018 John Wiley & Sons Ltd. Published 2018 by John Wiley & Sons Ltd.

synthesized, such as cubes, polyhedron, hollow box/cages, dumbbell-type NPs, dendrite NPs and their related assemblies[12, 13]. Increasing the surface with more defect sites is one advantage of bimetallic NPs with complicated structures, such as dumbbell-type, dendrite, and porous NPs. Another structural benefit of shape-controlled bimetallic NPs is to expose ordered and predictable crystal facets, which provides an ideal platform to explore the catalytic properties of well-defined bimetallic surfaces.

The surface structure of heterogeneous catalysts determines their catalytic properties. However, an atomic level understanding of the structure-property relationship has not been established. Three critical factors restrict the clear illustration of bimetallic surfaces. First, the surface of bimetallic NPs has many defect sites and lattice strains, which are beneficial for catalysis but hard for characterization[14]. Second, the capping agents used to stabilize bimetallic NPs could also induce more surface uncertainties[15]. Third, the chemical environment during catalytic reactions could cause structural changes of the bimetallic surface, which further complicates the understanding of the atomic structures responsible for their catalytic properties[16]. For these reasons, shape-controlled bimetallic NPs, with well-defined facets, are highly desirable to elucidate the effect of bimetallic surfaces in heterogeneous catalysis.

Since the composition, size, and shape of bimetallic NPs are closely correlated parameters during their synthesis; we will summarize the recent progress in composition-, size-, and shape-dependent catalytic properties of various shaped bimetallic NPs. To illustrate the structure-properties relationship of shape-controlled bimetallic NPs, we will discuss four categories of reactions, including oxidation, hydrogenation, hydrogen evolution, and coupling reactions. These state-of-the-art investigations on catalysis can guide the architecture design of bimetallic NPs in the understanding of the structure-property relationship of bimetallic surfaces.

11.2 Oxidation

11.2.1 CO Oxidation

CO oxidation has been used as a model reaction to probe the structure of metallic surfaces. Following the most-accepted Langmuir-Hinshelwood mechanism, the adsorbed O_2 molecule dissociates into O atoms (O_{ad}) that react with adsorbed CO_{ad} to form CO_2[17]. Several intermediate steps in the Langmuir-Hinshelwood mechanism have been proposed as possible rate-determining steps under different CO/O_2 pressures. Since CO adsorbs strongly on precious metal surface, the desorption of CO is the rate determining step at high CO/O_2 ratios (>2), where CO is the dominant molecule on precious metal surface[18–20]. However, at low CO/O_2 ratios, the reaction mechanism becomes more complicated, because several steps could be the rate-determining step, such as O_2 dissociation, competitive adsorption of CO_{ad}/O_{ad}, and association of CO_{ad}/O_{ad}[21]. Catalytic behaviors of these adsorbed species can be dramatically altered when adsorbed on different metallic facets. CO oxidation is valuable in studying the relationship between surface structure and catalytic property. Another important feature of CO oxidation is that CO and O_2 can reconstruct metal surface[22, 23].

11.2.1.1 Monometallic NPs

CO oxidation has been studied extensively in the monometallic system. The Murray group prepared well-defined and monodisperse Pt nanocubes with (100) facets and Pt octahedra with (111) facets[24]. CO oxidation was used to probe their differences in surface structure. CO oxidation is structurally insensitive when the ratio of CO to O_2 is larger than 40. Similar activation energies were observed on both Pt facets, confirming that CO desorption was the rate-determining step when both facets exhibited the high CO coverage. However, these facets tended to be structurally sensitive for CO oxidation at decreased CO/O_2 ratios (<1). Different activation energies were observed on these facets, and the (111) surface displayed a faster reaction rate than the (100) surface (Figure 11.1a). The similar CO reaction order (–0.65) but different O_2 reaction order, 0.97 on (111) and 0.68 on (100) further implied that CO oxidation is structurally sensitive in an O_2-rich environment (Figure 11.1b).

11.2.1.2 Compositional and Structural Effect in Bimetallic NPs

For the bimetallic system, the reaction pathway of CO oxidation can be challenging to illustrate, because CO oxidation is highly dependent on the composition and structure of bimetallic catalysts. The composition and structure of bimetallic surfaces can be readily reconstructed to deviate from their original structures when exposed to different gas environments. Some pioneering work has demonstrated how chemical reactions can induce the surface reconstruction that alters the catalytic mechanism, especially at the nanoscale[14, 16, 25]. Two control factors are usually studied in the bimetallic system that lead to surface reconstruction and different catalytic properties. One is the modulation of the bimetallic surface composition between metals and metal oxides of different surface energies. The second factor is how the defective surface (i.e., step, terrace, kick, and twin boundary) can induce surface heterogeneity and vary the adsorption of the dominant surface species in catalysis.

For the variance of surface composition, the Somorjai group performed *in situ* studies on the surface segregation of $Rh_{0.5}Pd_{0.5}$ and $Pt_{0.5}Pd_{0.5}$ NPs under oxidizing (NO, O_2), catalytic (CO, NO), and reducing (CO, H_2) atmospheres using ambient pressure X-ray photoelectron spectroscopy (AP-XPS)[23]. The major driving force for the surface reconstruction is to minimize the surface energy of NPs during these treatments. In an oxidative environment, the dominant surface species on bimetallic NPs are either the metal with a lower surface energy or a stable metal oxide. Since metallic Pd has a lower surface energy than metallic Rh, and Pd oxide is less stable than Rh oxides[26, 27], metallic Pd and oxidized Rh should be the favorable species on the surface. The AP-XPS results on $Rh_{0.5}Pd_{0.5}$ agree with this prediction. The initial $Rh_{0.5}Pd_{0.5}$ NPs had a Pd core and a Rh shell. Upon exposure to oxidizing atmospheres (NO, O_2), the surface of Rh–Pd NPs became rich in Rh oxides. After switching to a reducing atmosphere (H_2), Rh–Pd oxides were reduced to metallic Rh–Pd, forming a Rh core/Pd shell structure when Rh migrated into the inner core. The catalytic atmosphere (CO + NO) induced a similar surface reconstruction as the H_2 because CO could serve as a reducing agent. In the case of $Pt_{0.5}Pd_{0.5}$ NPs (Pt core/Pd shell), Pt is not as prone to oxidation as Pd, and the surface energy of Pt is higher than Pd[26, 27]. Thus, the Pd shell in $Pt_{0.5}Pd_{0.5}$ NPs was oxidized to form PdO_x shell when exposed to NO. Under a reducing atmosphere, the PdO_x shell was reduced to form a Pd-rich shell. This study emphasizes that bimetallic surface composition can be modulated by the chemical property of surrounding gas

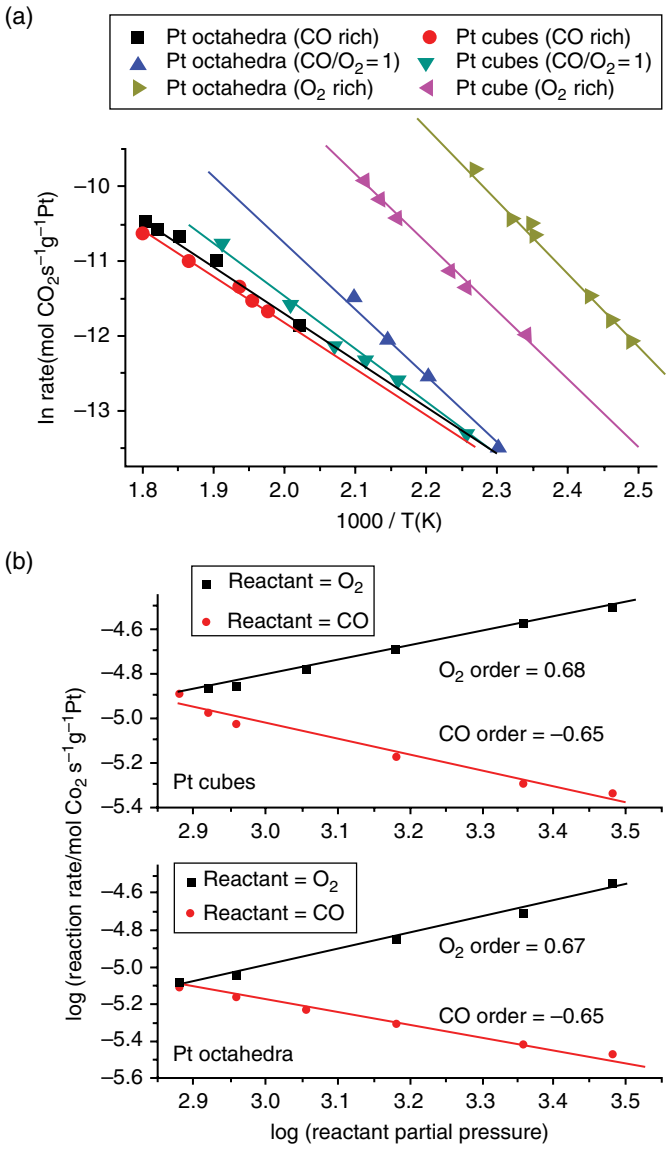

Figure 11.1 (a) The Arrhenius plot for CO oxidation on Pt nanocubes and octahedra with different CO/O_2 ratios; (b) the reaction orders of O_2 and CO for Pt nanocubes and octahedra. Reprinted (adapted) with permission from ref. [24]. Copyright (2013), American Chemical Society.

environment and the reconstruction is mainly driven by minimizing the surface energy of the bimetallic NPs.

Another study conducted by the Tao group addressed how surface structures affect the dispersion of metal sites on the surface of shape-controlled Pt–Cu NPs[28]. This study utilized different pretreatment conditions to vary the surface composition and structure of bimetallic Pt–Cu NPs, which correspondingly changed their catalytic performance in CO oxidation. The authors believed that this strategy functioned as a

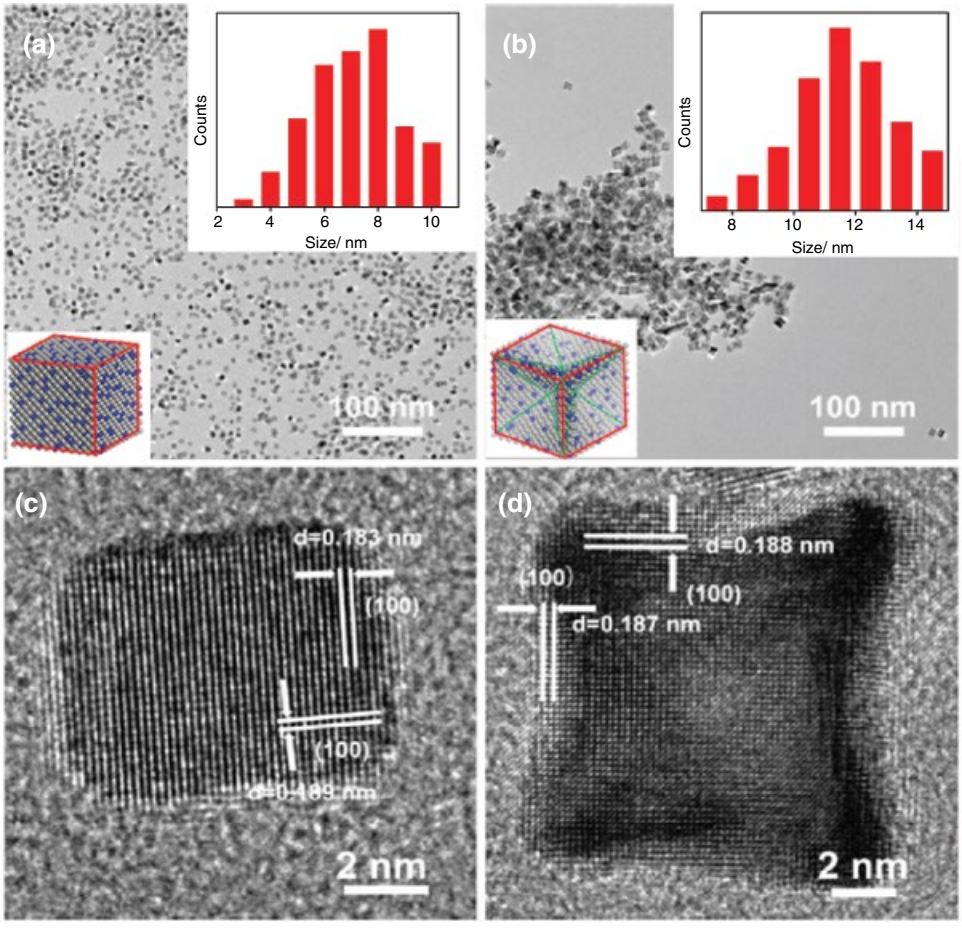

Figure 11.2 Transmission electron microscopy (TEM) images of (a, c) Pt–Cu RNCs and (b, d) Pt–Cu CNCs. Reprinted (adapted) with permission from ref. [28]. Copyright (2017), American Chemical Society.

post-synthesis reaction in the gas phase, creating "new" catalysts from the original NPs. Two types of bimetallic Pt–Cu NPs with different morphologies were synthesized in regular cubes (RNCs) and concave cubes (CNCs), as shown in Figure 11.2. The CNCs exposed more step sites with low coordination numbers compared to the RNCs, which rendered CNCs an excellent platform to study whether these stepped surfaces could induce surface reconstruction that impacts catalysis. Both Pt–Cu NPs were synthesized under similar conditions by co–reducing Pt and Cu precursors in the presence of poly(vinylpyrrolidone) (PVP), Cl^-, and Br^-. Br^- can induce the cubic morphology of Pt–Cu RNCs, whereas the Pt–Cu CNCs were obtained by increasing the concentration of Cl^-. Pt–Cu RNCs and CNCs exhibited similar sizes, capping agents, and bulk compositions. Three pretreatment conditions were conducted to modulate the surface of Pt–Cu NPs: (1) untreated control directly from the synthesis, (2) H_2 reduction, and (3) H_2 reduction and then CO treatment. CO oxidation was chosen to evaluate Pt–Cu RNCs and Pt–Cu CNCs under each of the three pretreatment conditions. Pt–Cu RNCs

and CNCs exhibited dramatically different catalytic results after the various pretreatment procedures (Table 11.1). Pt–Cu CNCs showed improved catalytic activities after either H_2 reduction or H_2/CO treatment in comparison to the untreated CNCs. Pt–Cu RNCs showed higher activity and lower activation energy only after H_2 reduction, greatly surpassing the untreated RNCs. On the contrary, the H_2/CO treatment decreased the activity of RNCs. To investigate the surface structure, the authors conducted extensive characterization on Pt–Cu CNCs and Pt–Cu RNCs, including AP-XPS, elemental mapping, energy dispersive X-ray spectroscopy (EDS) line scan, and extended X-ray absorption fine structure (EXAFS). AP-XPS and elemental mapping revealed a similar compositional transition for both Pt–Cu CNCs and RNCs during the three pretreatment conditions: a Pt-rich surface in the untreated sample, a Pt dominant surface after H_2 reduction, and a Pt–Cu mixture surface after H_2/CO treatment.

This similar trend in surface composition determined by AP-XPS and elemental mappings cannot explain the dramatically varied catalytic results of Pt–Cu RNCs and CNCs. EXAFS coupled with AP-XPS and EDS line scans of these NPs provide a clearer picture on the difference of the Pt and Cu dispersion on these two catalysts (Figure 11.3 and 11.4). For Pt–Cu RNCs, the H_2 reduction can induce a significant increase in Pt surface concentration, and the surface Cu concentration decreases from 19% to 1%. Meanwhile, EDS line scans confirm that Cu stays within the sublayers to form a Pt-skin/Cu subsurface structure. The activation energy of Pt–Cu RNCs after H_2 reduction is lower than that of the pure Pt nanocubes after similar H_2 reduction, which indicates that the Cu subsurface affects the catalytic property of the surface Pt layer. The H_2/CO treatment of Pt–Cu RNCs induced a well-distributed Pt–Cu alloy surface that has a low activity. Their observed activation energy is closed to the reported Pt–Cu alloy, likely confirming the formation of alloy Pt–Cu surface. Pt–Cu CNCs have different structural evolution compared to Pt–Cu RNCs. The migration of Pt was also observed on the surface of Pt–Cu CNCs after H_2 reduction. However, there is more Cu remnant (4%) on the surface of Pt–Cu CNCs compared to that of Pt–Cu RNCs, explaining why Pt–Cu CNCs show improved activity after H_2 reduction to untreated CNCs, but still lower than that of Pt–Cu RNCs. Considering the H_2/CO treatment, a significant amount of Cu remained on the surface of both Pt–Cu CNCs and RNCs. Regarding activity, Pt–Cu

Table 11.1 The summary of activation energies of Pt RNCs, PtCu RNCs and Pt–Cu CNCs treated in various gas atmospheres for CO oxidation. Reprinted (adapted) with permission from ref. [28]. Copyright (2017), American Chemical Society.

Entry	Catalysts	Postsynthesis treatments	Activation energy (kJ/mol)
1	pure Pt RNC-H_2	H_2, 200 °C	92 ± 5
2	Pt–Cu RNC-as synthesized	N/A	128 ± 7
3	Pt–Cu RNC-H_2	H_2, 200 °C	39 ± 4
4	Pt–Cu RNC-H_2-CO	H_2 at 200 °C, CO at 350 °C	173 ± 11
5	Pt–Cu CNC-as synthesized	N/A	109 ± 10
6	Pt–Cu CNC-H_2	H_2, 200 °C	72 ± 6
7	Pt–Cu CNC-H_2-CO	H_2 at 200 °C, CO at 200 °C	80 ± 8

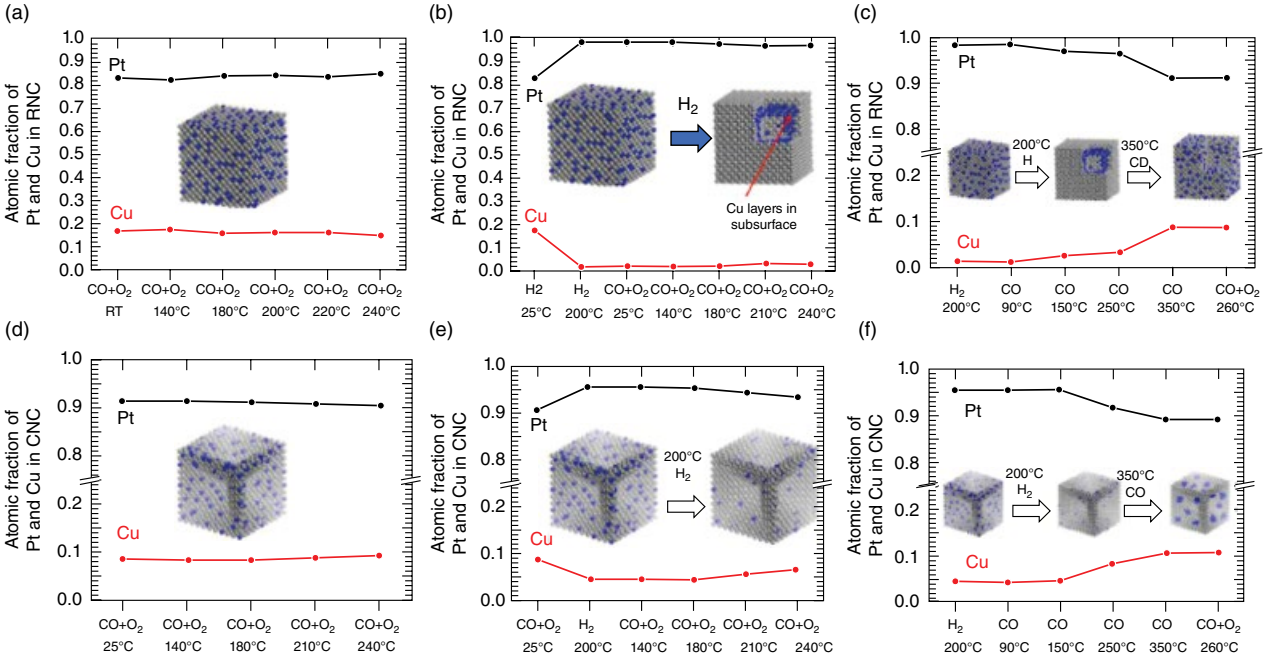

Figure 11.3 The surface evolution of Pt–Cu RNCs and Pt–Cu CNCs regarding the composition and dispersion of Pt and Cu fractions after post-synthesis and then in the CO oxidation reaction: (a–c) Pt–Cu RNCs of (a) untreated, (b) treated in H_2, (c) treated in H_2 and then in CO; (d–f) Pt–Cu CNCs of (d) untreated, (e) treated in H_2, and (f) treated in H_2 and then in CO. The inserted structure models depict the surface evolution under these gas atmospheres. Reprinted (adapted) with permission from ref. [28]. Copyright (2017), American Chemical Society.

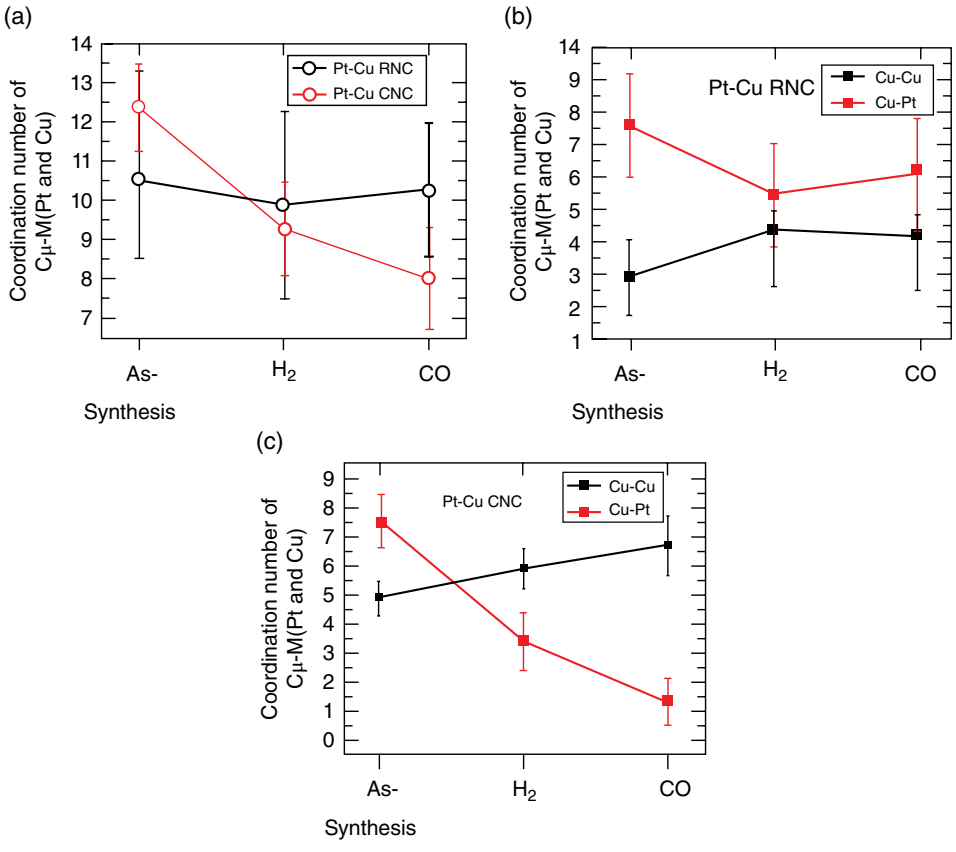

Figure 11.4 The evolution of coordination numbers under different treatment conditions: (a) overall coordination number of Cu–M, CN(Cu–Cu) + CN(Cu–Pt), in Pt–Cu RNCs and Pt–Cu CNCs, (b) the coordination number of Cu–Cu and Cu–Pt in Pt–Cu RNCs, and (c) the coordination number of Cu–Cu and Cu–Pt in Pt–Cu CNCs. Reprinted (adapted) with permission from ref. [28]. Copyright (2017), American Chemical Society.

CNCs did not show any activity drop, while PtCu RNCs did. Therefore, Pt–Cu CNCs and RNCs must have different surface Cu dispersion after H_2/CO treatment. Unlike the alloyed Pt–Cu surface observed in Pt–Cu RNCs after H_2/CO treatment, the surface Cu on Pt–Cu CNCs can instead segregate into Cu clusters. EXAFS results confirmed this phase segregation, where the coordination number of Cu–Pt in Pt–Cu CNCs decreased after H_2/CO treatment.

Knowing the structure difference on the surface of Pt–Cu CNCs and RNCs, it is intriguing to correlate these surface reconstructions with the specific morphologies of the regular and concave cubes. Density functional theory (DFT) calculations on Pt–Cu (310) suggest that both the migration of inner Cu to the top of Pt(310) and the segregation of Cu to the edge site of PtCu(310) are thermodynamically favorable when CO is adsorbed on this surface, an indication that Cu can concentrate on a high index facet. The concave structure of Pt–Cu CNCs shows more step surfaces, facilitating the replacement of Cu to the step-edged Pt, which is consistent with the observation that the Cu segregates on the

surface Pt–Cu CNCs, but Pt–Cu alloy was observed on Pt–Cu RNCs after H_2/CO treatment. This study demonstrates the shape effect of bimetallic NCs on CO oxidation due to the surface reconstruction triggered by different chemical pretreatments.

Chemically triggered phase segregation has been further utilized in the preparation of metal-metal oxide dumbbell structures using bimetallic alloys. For example, the Schaak group has achieved various dumbbell NPs such as Au/Cu_2S and Au/CuO_x NPs from Au–Cu alloys treated with sulfur or oxygen[29, 30]. The Sun group has prepared Au/Pt/AuAg-Fe_3O_4 dumbbell NPs by exposing the corresponding Au/Pt/AuAg-Fe NPs to air[31]. Fe_3O_4 oxides were observed to grow epitaxially on precious metal NPs. The as-synthesized dumbbell Au/FeO_x and Pt/FeO_x exhibit 25–50 °C lower switch-off temperatures in CO oxidation than commercial Au/FeO_x and Pt/FeO_x catalysts.

11.2.2 Preferential CO Oxidation in H_2-Rich Feeds (PROX)

The purpose of preferential CO oxidation in H_2-rich gas (PROX) is to remove CO impurity in H_2 feed gas produced by coal/steam reforming[32, 33]. High-quality H_2 is essential to fulfilling the increasing demand for proton-exchange membrane fuel cells (PEMFCs), where a small fraction of CO can poison the Pt-based expensive but widely used electrocatalysts[34, 35]. Two benchmarks are important in PROX to evaluate the performance of catalysts: (1) high preference for CO oxidation rather than undesirable H_2 oxidation, and (2) low-temperature activity[36]. Due to the higher energy barrier required for CO oxidation in comparison to that required for H_2 oxidation on many precious metals, only a few monometallic catalysts have been developed towards improving selectivity to CO oxidation. However, the monometallic catalysts suffer from many drawbacks. Supported Au catalysts have high CO oxidation activity at low temperatures[37, 38], but the poor stability and the lack of resistance to CO_2 and moisture restrict their applications. Supported Pt catalysts are more resistant to CO_2 and moisture, but they have low activity at low temperatures due to the strong CO adsorption on Pt[39]. The decrease in selectivity is also problematic for supported Pt catalysts at higher reaction temperature. To address these drawbacks of monometallic systems, endeavors to tune the electronic structures of the metallic surface have been reported, such as using an FeO_x support[40] and downsizing the Pt ensembles[41]. Another strategy that enables the electronic modulation is to use bimetallic alloys. We herein discuss both the composition and structural factors in tuning the activity and selectivity of shape-controlled bimetallic NPs in PROX.

11.2.2.1 Spherical Core–Shell NPs

The Mavrikakis and Eichhorn groups have performed pioneering work to develop several spherical metallic core/Pt shell catalysts (i.e., Ru–Pt, Rh–Pt, Ir–Pt, Au–Pt, and Pd–Pt) and studied their PROX catalytic pathways[42–44]. For 0.1% CO in H_2 feeds, the PROX activity decreased in the order of Ru@Pt > Rh@Pt > Ir@Pt > Pd@Pt > Pt > Au@Pt. H_2 oxidation and CO oxidation occur simultaneously in all of these compositions. Due to the higher energy barrier of H_2 oxidation compared to CO oxidation, the temperature threshold to initiate CO oxidation is relatively lower than the side pathway of H_2 oxidation. However, the temperature ranges for both reactions at high conversion have significant overlaps. Thus, the desirable catalysts for PROX should show a high

activity for CO oxidation at low temperatures. The high selectivity can be achieved by controlling the reaction temperature to reach complete conversion in CO oxidation. Meanwhile, this temperature is still below the temperature required to light off H_2 oxidation. Among the aforementioned metal–Pt combinations, the highest activity was obtained with Ru@Pt catalysts. To demonstrate the structural benefits of Ru–Pt catalysts, five samples have been run in PROX including Ru@Pt, annealed Ru@Pt, alloyed RuPt, a physical mixture of Pt and Ru, and pure Pt NPs. Among these catalysts, Ru@Pt NPs show nearly complete CO oxidation at 20 °C with 0.1% CO in H_2 feeds. Since the onset (light off) temperature of H_2 oxidation for Ru@Pt is 22 °C (Figure 11.5), this core–shell Ru@Pt catalyst shows an excellent selectivity in PROX. Even with 1% CO in H_2 feeds, Rh@Pt can still achieve a 70% conversion and 80% selectivity. To elucidate the origin of the high activity/selectivity of Ru@Pt, DFT calculations were employed to show the binding energy of key species (i.e., O*, CO, H, and O_2) on Pt-covered Ru(0001), as shown in Table 11.2. From the most-accepted PROX mechanism, weakening CO adsorption and promoting reactivity of O_2 are two key steps to enhance CO oxidation at low temperatures. The calculated binding energies of CO and O* are lower on Pt–Ru(0001) in comparison to that of Pt(111). Besides, Ru sublayer can downshift the *d*-band center of Pt top layer, and thereby weaken the adsorption strength of various adsorbed species. These results verify that Pt–Ru(0001) can facilitate CO oxidation. Interestingly, the authors found that Ru@Pt catalysts were less active without the aid of H_2. DFT calculations demonstrate that an increasing energy barrier for O_2 dissociation over Ru–Pt(0001) in the absence of H_2, and the formation process of $O^* + H^* = OH^*$ is more favorable on Ru–Pt(0001) than on Pt(111) in the presence of CO. These energy barrier calculations reflect that the reactive O* is more favorable on Ru–Pt(0001) with the aid of H_2, indicating a novel H-assisted O_2 dissociation mechanism on Ru–Pt(0001). This mechanism can explain the activity of core–shell Ru@Pt in PROX at low temperatures.

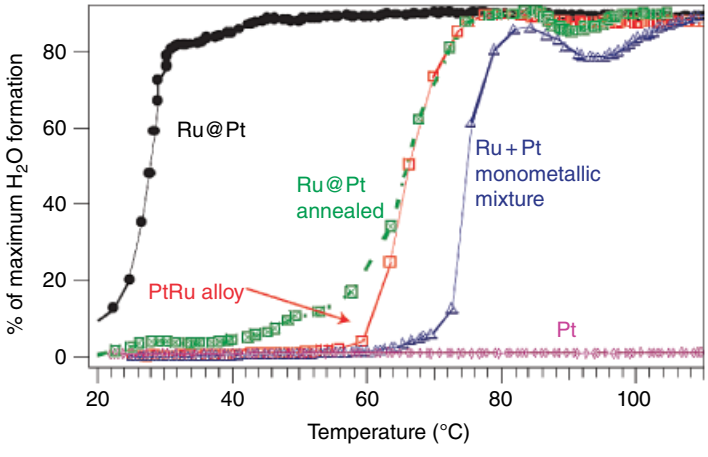

Figure 11.5 Temperature-programmed reduction (TPR) results of different Ru–Pt NP illustrating the formation of H_2O vs. temperature with 0.1 vol.% CO contaminated H_2 feed. Ru@Pt shows the lowest temperature to light off H_2 oxidation (22 °C). Source from ref. [42]. Copyright (2008), Nature Publishing Group.

Table 11.2 Calculated Perdew-Wang binding energies of adsorbed species at Pt(111) and Pt*/Ru(0001). Source from ref. [42]. Copyright (2008), Nature Publishing Group.

PART I	**Pt(111)**	**Pt*/Ru(0001)**	**PART II**	**Pt(111)**	**Pt*/Ru(0001)**
d-band center of surface Pt atoms, ε_d (eV)	−2.53	−2.98		−2.53	−2.98
Species	Binding energy (eV)	Binding energy (eV)	Elementary reactions	E_a (eV)	E_a (eV)
O_2	−0.65	−0.26	$H_2 + 2^* = 2H^*$	0	0.16
O	−3.87	−3.11	$O_2 + 2^* = 2O^*$	0.77	1.05
H	−2.72	−2.42	$O_2 + H = O_2H$	0.33	0.25
O_2H	−1.09	−0.95	$O_2H^{**} = O^* + OH^*$	0.16	0.42
OH	−2.09	−1.91	$O^* + H^* = OH^* + ^*$	0.85	0.58
CO	−1.82	−1.25	$OH^* + H^* = H_2O^* + ^*$	0.10	0.15
H_2O	−0.27	−0.20	$CO^* + O^* = CO_2^*$	0.79	0.41

11.2.2.2 Hollow Cubic NPs

Besides spherical shaped NPs, the Xia group has studied cubic nanocages of Pd–Pt alloys for PROX [45]. In the presence of Br^-, $PtCl_4^{2-}$, and citric acid, cubic Pd NPs can be transformed into concave nanocages of Pt–Pd alloys (Figure 11.6). Galvanic replacement etches Pd from the inner surface to introduce a hollow interior, whereas citric acid can co-reduce Pt and Pd forming nanocage frameworks. The Br^- selectively adsorbed on Pd(100) can enhance the rate of galvanic replacement on cubic faces, leading to a concave structure. The authors employed cubic Pd NPs of 8, 12, and 20 nm in diameter to prepare PdPt nanocages. These nanocages were studied under PROX condition with 0.1% CO and 0.5% O_2 in H_2 gas (Figure 11.7). The PROX activity increases in the order of downsizing the size of Pt–Pd nanocages, indicating that the higher surface area and thinner wall thickness can promote activity. However, the selectivity drops more dramatically for smaller NPs (Figure 11.6), which suggests that the larger hollow interiors in PtPd NPs might enhance the selectivity to CO oxidation by suppressing the undesirable H_2 oxidation.

11.2.3 Selective Oxidation of Alcohols and Amines

The selective oxidation of alcohols to aldehydes and organic acids is of great importance in petrochemical, pharmaceutical, and biorefinery industries[46, 47]. Recent studies have demonstrated that the size[48], shape[49], and composition[50] of metal-based catalysts dramatically affect their catalytic properties. Since the discovery of Au-catalyzed oxidation reactions by M. Haruta[51, 52], Au-based catalysts have been extensively utilized for alcohol oxidations. Corma and García[53] and Tsukuda[54] have explored the metal-support interaction and size effect of supported Au catalysts in the aerobic oxidation of primary and secondary alcohols. CeO_2[53], TiO_2[55], and hydroapatite[56] were reported as effective supports to maximize the strong metal-support interactions

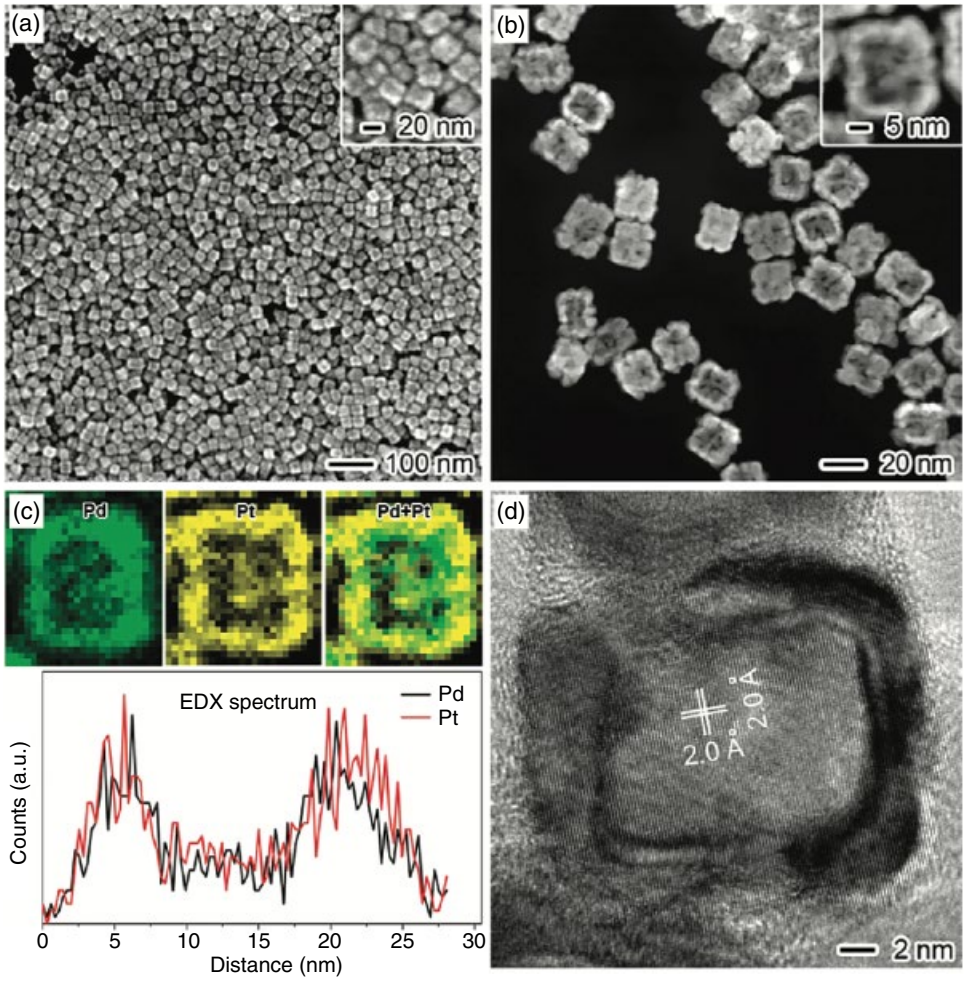

Figure 11.6 (a, b) Scanning electron microscope (SEM) and TEM images of Pd-Pt nanocages. (c, d) Elemental mappings and a high-resolution TEM image of Pd-Pt nanocages, where both Pt and Pd were observed in the framework of nanocages. Reprinted (adapted) with permission from ref. [45]. Copyright (2011), American Chemical Society.

(SMSI) on Au-oxide interfaces. The Tsukuda group has found a volcano-shaped curve correlating the activity to the size of Au clusters (<2 nm), which demonstrated that an optimal Au cluster (Au_{39}) is crucial to obtain proper electronic structures for benzyl alcohol oxidation[54].

Well-defined Au–Pd NPs with synergistic effect have been reported to be active and selective for alcohol oxidation reactions[58]. The Tilly group has prepared a series of Pd-coated Au icosahedral NPs[57]. The thickness of Pd shells can be tunable under a gradual reduction by H_2, and their icosahedral morphology was well maintained (Figure 11.8). The cubic icosahedral structure consists of 20 (111) facet-terminated, apex-sharing tetrahedral building blocks. There are 30 twin boundaries and 20 (111) facets in this structure. The atoms at twin boundaries and edges have low coordination

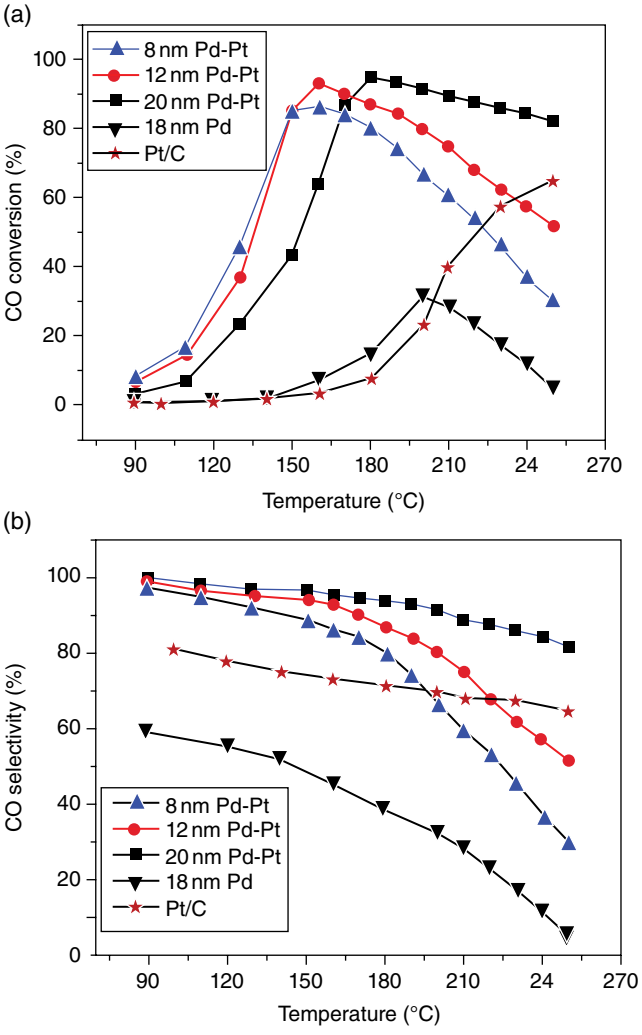

Figure 11.7 (a) Activity and (b) selectivity as a function of temperature for Pd-Pt nanocages of various sizes in PROX. Reprinted (adapted) with permission from ref. [45]. Copyright (2011), American Chemical Society.

numbers that can lead to high catalytic activities. The shape effect was evidenced by the enhanced activity of icosahedral NPs in comparison to spherical NPs. The composition effect was evaluated in benzyl alcohol oxidation catalyzed by Au–Pd icosahedral NPs of various Pd shell thicknesses. The thickness of Pd shells varies from 0.4, 0.8, 1.5, 2.2, to 3.2 nm, synthesized by quenching the Pd coating process at different reduction times. As shown in Figure 11.9, a volcano-shaped curve of activity vs. Pd shell thickness was observed, demonstrating that the 2.2 nm is the optimal Pd shell thickness. These catalytic results suggest a strong synergistic effect between Pd and Au that maximizes their oxidation activity. The selectivity of icosahedral Au–Pd NPs was also evaluated with

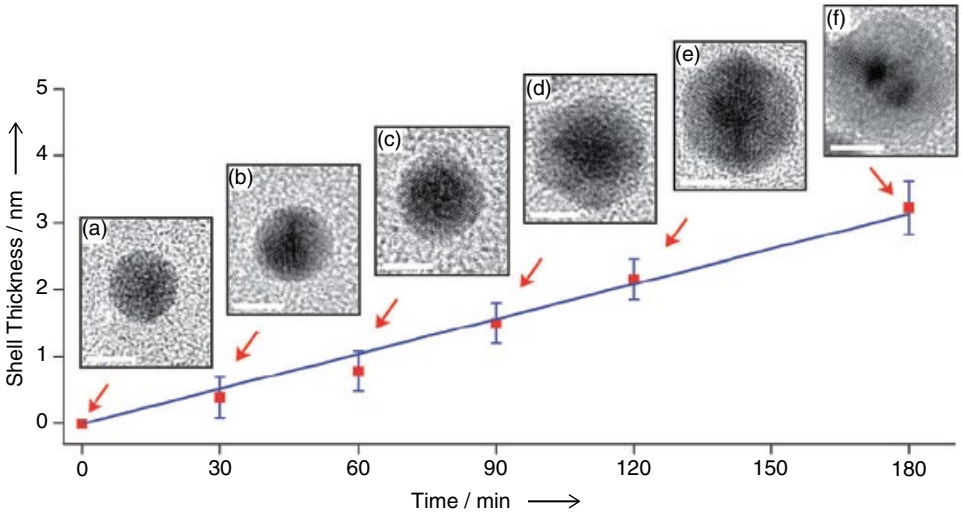

Figure 11.8 The plot of Pd shell thickness (nm) vs. time (min) for the seeded growth of icosahedral Au–Pd core–shell NPs. Source from ref. [57]. Copyright (2012), John Wiley and Sons.

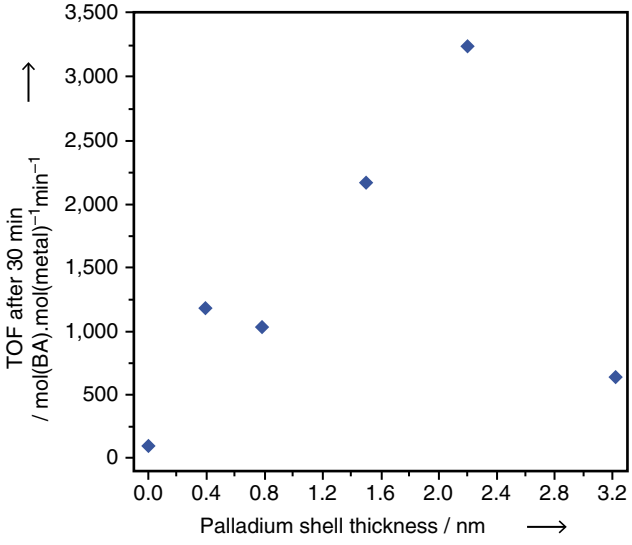

Figure 11.9 The turnover frequency (TOF) in benzyl alcohol oxidation vs. Pd shell thickness. The TOF increases and then decreases as the Pd shells become thicker. The highest TOF occurs on Au–Pd NPs with a 2.2 nm Pd shell. Source from ref. [57]. Copyright (2012), John Wiley and Sons.

benzaldehyde as the desired product, and the Pd shell thickness did not largely impact the selectivity. However, the Au–Pd NPs with 2.2 nm Pd shells still showed the highest selectivity to benzaldehyde.

Icosahedral Au–Pd NPs also showed structural benefits compared to multifaceted NPs in the selective oxidations of glycerol to glyceric acid and 1,2-propanediol to lactic acid [59]. Four catalysts were prepared for the selective oxidation of alcohols, including

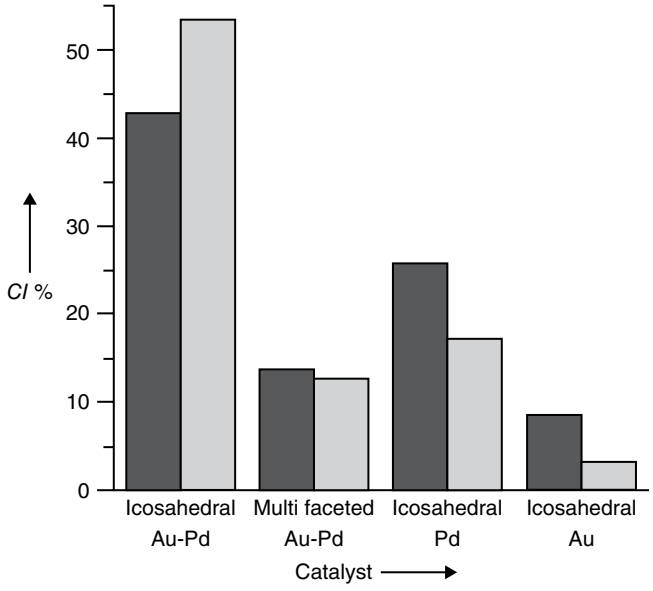

Figure 11.10 Conversion for the oxidation of glycerol (black) and 1,2-propanediol (grey) catalyzed by icosahedral Au–Pd, multifaceted Au–Pd, icosahedral Pd and icosahedral Au NPs. Source from ref. [59]. Copyright (2013), John Wiley and Sons.

icosahedral Au–Pd, multifaceted Au–Pd, icosahedral Au, and icosahedral Pd NPs. Glycerol is a byproduct of biodiesel synthesis, and 1,2-propanediol can be produced from glycerol[60–62]. Icosahedral Au–Pd NPs showed the best activity for both reactions among the four catalysts, indicating a similar synergistic effect between Au and Pd (Figure 11.10). Multifaceted Au–Pd NPs are slightly less active than pure icosahedral Pd NPs, which suggests that icosahedral monometallic Pd NPs (exposing more active sites) can compensate for the activity in comparison to the bimetallic multifaceted Au–Pd NPs with synergistic promotions.

The oxidation of o-phenylenediamine (OPDA) to 2,3-diamino-phenazine (DAP) is an important model reaction for the oxidation of amines. The product DAP has a strong ultraviolet–visible (UV–Vis) absorption at 420 nm [63], while the reactant OPDA does not. Therefore, UV–Vis spectroscopy is well suited for monitoring this reaction. The Yang group has synthesized Pd-Rh NPs of four structures: core–shell nanocubes, nanoboxes, core–frame nanocubes, and nanoframes as shown in Figure 11.11[64]. A two-step approach was developed to synthesize the Pd–Rh core–frame nanocubes and nanoframes. The addition of formaldehyde led to the selective deposition of Rh on the edges of Pd cubic seeds and the formation of Pd–Rh core–frame NPs. The subsequent HNO_3 treatment removed the inner Pd cores forming the hollow Pd-Rh nanoframes (Figure 11.12). The catalytic activity of these Pd–Rh NPs in OPDA oxidation follows an increasing order as nanoboxes > nanoframes >> core–frame nanocubes > core–shell nanocubes (Figure 11.13). The two hollow structures displayed higher activity with more accessible active sites. The high Rh contents in these hollow structures can also contribute to their high activity because pure Rh is more active than pure Pd in the OPDA oxidation.

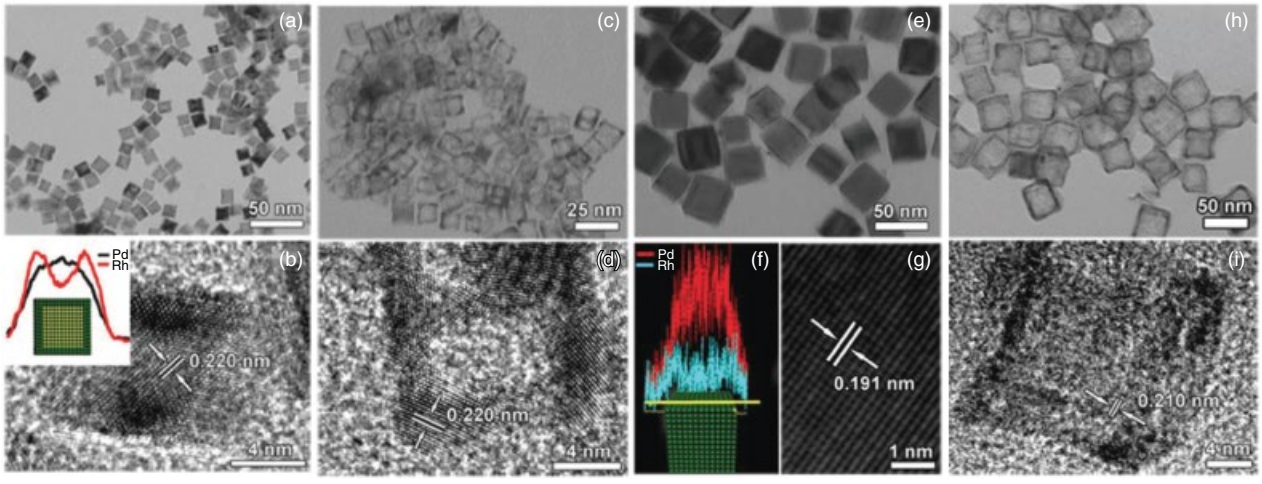

Figure 11.11 TEM images of Pd–Rh (a, b) core–frame nanocubes, (c, d) nanoframes obtained by the HNO_3 etching of Pd–Rh core–frame nanocubes, (e, g) core–shell nanocubes, and (h, i) nanoboxes obtained by the HNO_3 etching of Pd–Rh core–shell nanocubes. The inserted figures in (b) and (f) are acquired by EDS line scans. Reproduced from ref. [64] with permission from The Royal Society of Chemistry.

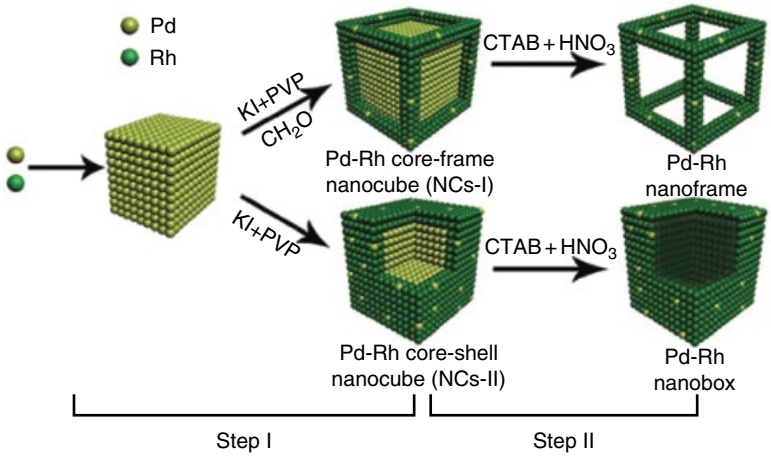

Figure 11.12 The synthesis scheme of Pd–Rh catalysts including Pd–Rh core–frame nanocubes, Pd–Rh nanoframes, Pd–Rh core–shell nanocubes, and Pd–Rh nanoboxes. NCs in the figure denotes as nanocrystals. Reproduced from ref. [64] with permission from The Royal Society of Chemistry.

11.3 Hydrogenation/Dehydrogenation

11.3.1 Selective Hydrogenation of Nitroarenes

Functionalized anilines are important chemicals widely used as pharmaceuticals, herbicides, and pigments[65]. The selective hydrogenation of nitroarenes is a general approach to synthesize these functionalized anilines. Among them, the ideal model reaction is the hydrogenation of nitrobenzene. Nitrobenzene has only one functional group (nitro group), but the hydrogenated products can vary between fully hydrogenated aniline, incompletely hydrogenated hydroxylamine/nitrosobenzene, coupled aromatic azo- and azoxy-compounds, and cyclohexylamine/dicyclohexylamine[66]. The range of possible products complicates the selectivity of this model reaction, and the catalytic pathways have not been fully understood. There are emerging interests to discover more efficient catalysts to produce functionalized anilines from the direct hydrogenation of corresponding nitroarenes. The key requirement of this reaction is to achieve high selectivity to the reduction of nitro groups in the presence of many reducible/leaving groups of nitroarenes, such as alkene, alkyne, aldehyde, halides, methoxyl, and ester groups. Conventional synthesis of functionalized anilines uses Zn/NH_3 and $Na_2S_2O_4$ as reducing agents[67]. However, this strategy generates a significant amount of waste, and these reducing agents are not sustainable[68]. Supported monometallic catalysts[69–71] and alloys[72–74] are two major categories of heterogeneous catalysts that target chemoselective hydrogenation of nitroarenes. For achieving high selectivity in the hydrogenation of the nitro group, catalysts mostly need to have a preferential adsorption of the nitro group compared to other functional groups[74–76]. The Corma group has demonstrated a metal-support interaction over Au/TiO_2 catalysts that showed high selectivity in the reduction of nitro groups[77]. The Komatsu group has discovered many selective alloy catalysts for this reaction, suggesting that secondary metals can be used to tune the geometric and/or electronic properties of the primary

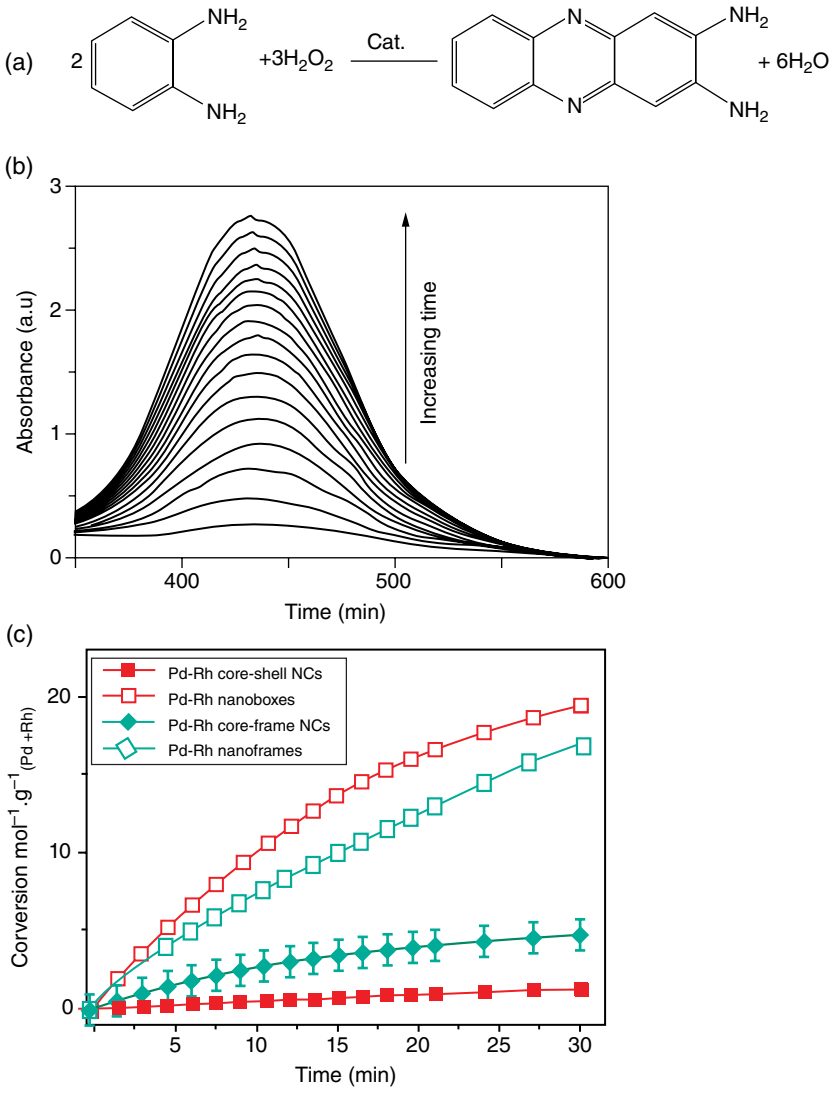

Figure 11.13 UV-Vis spectra of OPDA oxidation to DAP in the presence of four Pd-Rh catalysts. The peak growth at 420 nm indicates the formation of DAP. NCs in the figure denotes as nanocrystals. Reproduced from ref. [64] with permission from The Royal Society of Chemistry.

metal component and their catalytic properties[74, 78, 79]. Herein, we focus our discussion on the composition and shape effects of bimetallic NPs in the selective hydrogenation of nitroarenes.

11.3.1.1 Spherical and Random-Shaped NPs

Many reports discussed the synergistic effect of bimetallic NPs in enhancing the hydrogenation activity and selectivity of nitroarenes[72, 73, 78, 79]. Precious metals (Pd, Pt, and Rh) are excellent hydrogenation catalysts[80], which often lead to

over-hydrogenated products. Various bimetallic catalysts have been studied to improve the selectivity of these precious metals, such as PdPb[74], AuPt[73, 75], and RhNi[81]. The composition effect of spherical and randomly shaped NPs has been discussed to elucidate the bimetallic synergistic effect in the selective hydrogenation of nitroarenes. An early study by the Yu group has demonstrated that the addition of $RuCl_3$ into homogenous $PdCl_2$ catalysts in the presence of NaOAc can dramatically improve the selectivity of *p*-chloronitrobenezene hydrogenation by retarding the undesirable C-Cl oxidative addition on Pd centers[82]. The Toshima group has studied ~2 nm spherical Ni–Pd NPs in the hydrogenation of nitrobenzene under 1 atm H_2 at 30 °C and concluded that a 0.6:1 between Pd to Ni is the optimal ratio for the highest activity[83]. Rh–Ni NPs of random shapes have also been demonstrated as efficient, selective, and robust catalysts for the hydrogenation of 4-nitrobenzylaldehyde[81]. The best activity and selectivity occurs on Rh_3Ni NPs (Rh to Ni ratio = 3:1). Rh_3Ni NPs showed high selectivity for the hydrogenation of the nitro group for a broad substrate scope, including halides, methyl-, formyl-, methyl ester, methoxy- and hydroxymethyl- groups. The Patra group has reported on the size effect of Au@Ag core/shell NPs in the 4-nitrophenol hydrogenation[84]. The sizes of inner Au cores can be controlled at 10, 20, 40, 60, 80, and 100 nm, while the thickness of outer Ag shells is fixed at 10 nm. Enhanced activity was observed with the increase of the Au core sizes, as summarized in Table 11.3 (the inserted TEM images show the corresponding Au@Ag core–shell NPs). The Au@Ag NPs with larger

Table 11.3 The catalytic results of 4-nitrophenol reduction by Au@Ag bimetallic core–shell NPs. Reprinted (adapted) with permission from ref. [84]. Copyright (2014), American Chemical Society.

System		Reaction efficiency (%)	Rate constant (min^{-1})
10 nm core Au@Ag	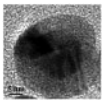	41.8	0.054
20 nm core Au@Ag	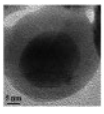	49.5	0.084
40 nm core Au@Ag	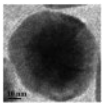	61.4	0.113
60 nm core Au@Ag	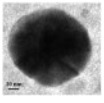	73.2	0.138
80 nm core Au@Ag	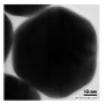	81.7	0.166
100 nm core Au@Ag	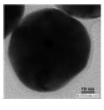	96.5	0.212

Au cores showed higher activity than those with smaller Au cores, which was explained by the greater electron donation from larger Au cores to the outer Ag shells, promoting their hydrogenation activity.

Beside the synergistic effect and compositional tunability of bimetallic NPs in the hydrogenation of nitroarenes, the effect of capping agents on these NPs are also important in tuning their catalytic properties. Due to the high thermal stability from the mesoporous silica ($mSiO_2$) encapsulated NPs, the Huang group has synthesized a series of spherical Pt–Pd@$mSiO_2$ catalysts with tunable Pt/Pd ratios. The high-temperature calcination can endow the Pt–Pd@$mSiO_2$ NPs with clean surfaces and no aggregation[85]. These thermally stable Pt–Pd@$mSiO_2$ NPs are ideal platforms for studying the role of capping agents in catalysis. In comparison to oleylamine capped Pt–Pd NPs with comparable sizes, the Pt–Pd@$mSiO_2$ NPs with clean surfaces can dramatically improve both activity and selectivity in the hydrogenation of nitrobenzene, strongly indicating that capping molecules can impact catalytic behaviors of NPs. When comparing the catalysis of NPs with different shapes, compositions, and structures, the effects of capping agents need to be carefully considered to obtain valid conclusions.

11.3.1.2 Dendrite NPs

In general, bimetallic NPs are synthesized by either a coreduction of metal precursors or a seeded growth method that ensures the morphological control[13]. The seeded growth method can synthesize bimetallic NPs with different morphologies, such as spheres, solid polyhedra, hollow structures, and even assemblies of several NPs[12]. Coreduction of metal precursors usually results in NPs with spherical morphologies. However, when the reduction of different precursors is carefully controlled, NPs with dendrite-like morphology can be obtained. The dendrite NPs have a more open and branched structure through the assembly of small clusters. This unique structure renders dendrite NPs with higher surface areas and more under-coordinated sites, which often results in high catalytic activities.

The Li group has prepared Pt–Ni nanodendrite NPs with a highly branched morphology using $Ni(acac)_2$, $Pt(acac)_2$, octadecene and didodecyldimethylammonium bromide co-mixed in oleylamine/oleic acid (OAm/OA) solution[86]. The branched Pt–Ni nanostructures were formed by heating the solution at 250 °C. As formed Pt–Ni dendrite NPs are Pt-rich (ca. 90%), but both Pt and Ni are evenly dispersed through the whole NP as confirmed by the EDS mapping of the NPs. The growth mechanism was explored by a time-dependent study (Figure 11.14), which suggested a rapid growth of small Pt–Ni seeds and the subsequent assembly to form the final branched structure. The hydrogenation of nitrobenzene was used to probe the advantages of these Pt–Ni dendrite NPs. Solid Pt–Ni NPs with irregular shapes were synthesized under similar conditions as a control catalyst to the branched Pt–Ni NPs. The Pt–Ni dendrite NPs show significantly higher activity in comparison to the irregularly shaped Pt–Ni NPs, and as well as the reported concave/corroded Pt–Ni nanocubes (discussed in Section 11.2.1.3). The enhanced activity of the Pt–Ni dendrite NPs was ascribed to the high surface area and more exposed active sites.

Another benefit of bimetallic dendrite NPs is their compositional modulation. The Song group has prepared a series of Au–Pd alloyed dendrites by the coreduction of $HAuCl_4$ and H_2PdCl_4 in the presence of OAm, OA, Triton X-100, Pluronic-P123/F-127,

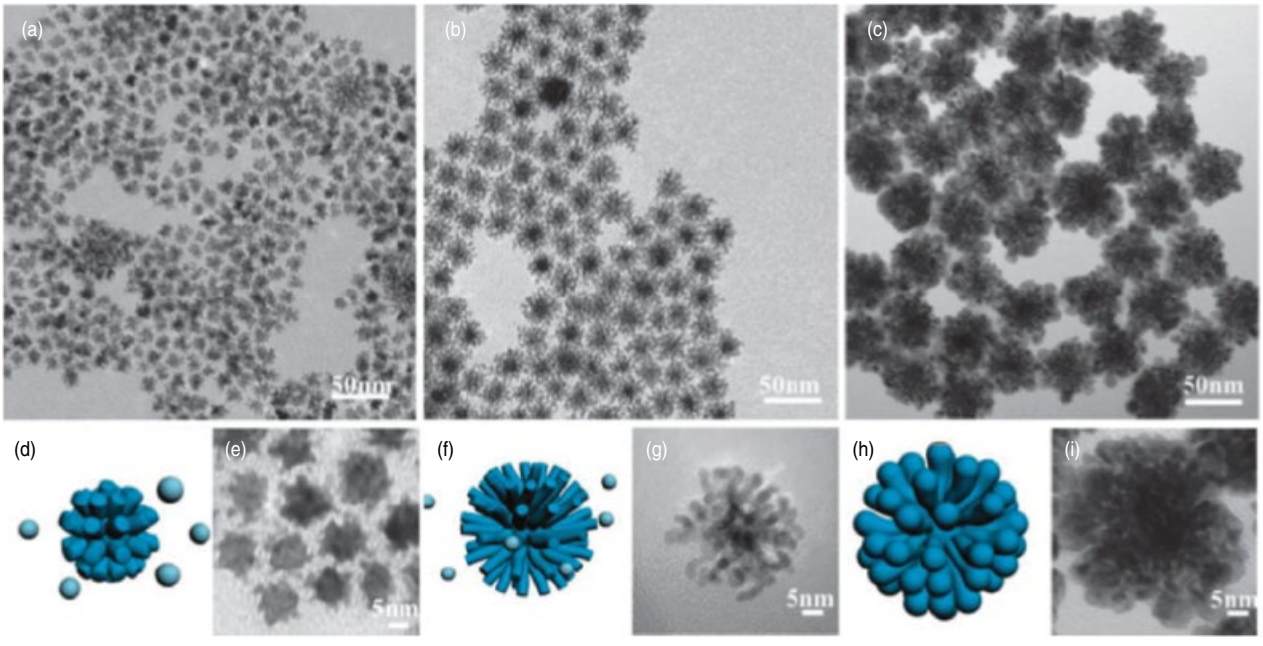

Figure 11.14 TEM images of Pt–Ni samples collected at (a, e) 100 minutes, (b, g) 120 minutes, (c, i) 480 minutes. The inserted figures (d, f, h) illustrate a model of Pt–Ni samples collected at these different times. Reproduced from ref. [86] with permission from The Royal Society of Chemistry.

and ascorbic acid/HCOOH/$NaBH_4$[87]. By varying capping agents, reducing agents, reduction time, and temperature, they could adjust the degree of branching and the size of Au–Pd dendrite NPs. The EDS mapping of Au and Pd indicates the well-distributed Pd and Au, and the major diffraction peaks in powder X-ray diffraction (PXRD) patterns of Au–Pd dendrites confirm the formation of alloy phases. The growth mechanism of Au–Pd dendrites is very close to that of previously discussed Pt–Ni nanodendrites, where a homogeneous nucleation occurs first followed by aggregation to form the dendrite structure. Au–Pd dendrites showed enhanced activity in comparison to pure Au and pure Pd in the hydrogenation of 2-nitrophenol. A compositional dependence was also observed and Pd_1Au_1 showed the maximum activity when compared to Au-rich Au_3Pd_1 and Pd-rich Au_1Pd_3 samples.

11.3.1.3 Cubic/Octahedral NPs

The shape effect of Pt–Pd alloys has been demonstrated in the hydrogenation of nitrobenzene by the Huang group[88]. Two shaped Pt–Pd nanocrystals were prepared by the coreduction of Pt and Pd precursors in dimethyl formamide as shown in Figure 11.15. The minimum lattice mismatch of Pt and Pd facilitates the formation of Pt–Pd alloys. I^- and Cl^- were used as the morphology-directing agents leading to the respective (100)-terminated Pt–Pd nanocubes and (111)-terminated Pt–Pd octahedra. The molar ratios of Pt/Pd were tuned for both cubic and octahedral NPs by adjusting the Pt/Pd precursor ratios. Nitrobenzene hydrogenation was chosen to evaluate these

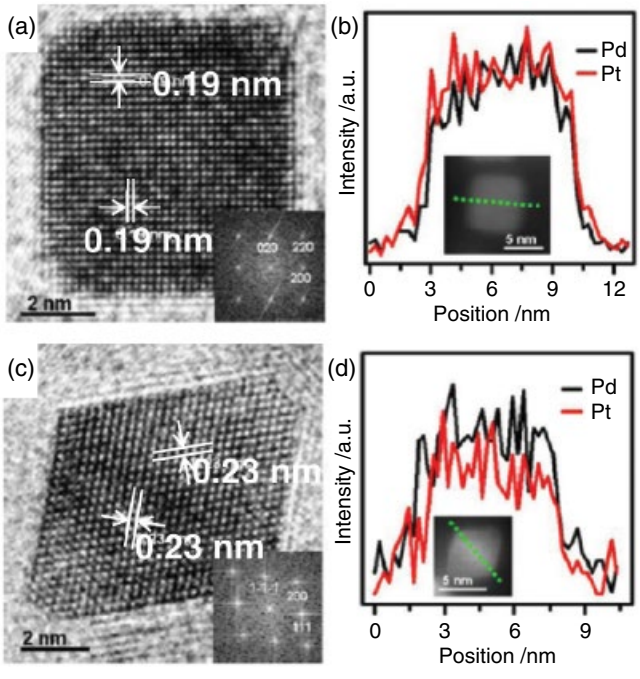

Figure 11.15 High-resolution TEM (HRTEM) images of Pt–Pd (a) nanocubes and (c) octahedra. EDS line scans of Pt–Pd (b) nanocubes and (d) octahedra. Reprinted (adapted) with permission from ref. [88]. Copyright (2012), American Chemical Society.

two Pt–Pd NP morphologies of three different compositions (Table 11.4). For both nanocubes and octahedra, an optimal Pt/Pd ratio (1:1) led to the maximum reaction activity, indicating a compositional dependence of Pt–Pd alloy NPs in nitrobenzene hydrogenation. On the other hand, at similar Pt/Pd ratios, (111)-terminated Pt–Pd octahedra were consistently more active than (100)-terminated Pt–Pd nanocubes in all the tested Pt/Pd ratios. These results suggest that the exposed facets of Pt–Pd alloy NPs can strongly alter their activity, and the (111) facets of Pt–Pd NPs are more active than their (100) counterparts in the hydrogenation of nitrobenzene.

Pd@Pt core–shell octahedral NPs have also been reported as active and selective catalysts for the hydrogenation of *p*-chloronitrobenzene[89]. Octahedral Pd@Pt NPs of 6–8 nm in diameter were prepared by a seed-mediated growth strategy using Pd seeds, $(NH_4)_2PtCl_6$, and ethylene glycol. The thickness of Pt shells is tunable (1, 2, or 3–4 atomic layers) by varying the Pt/Pd ratios (0.25, 0.5, or 1). The Pt–Pd NPs prepared with an even lower Pt/Pd ratio (0.125) show incomplete coverage of Pt shells on Pd seeds as illustrated in Figure 11.16. CO-diffuse reflectance infrared Fourier transform (DRIFT) studies demonstrate the intensity of the 1870 cm^{-1} peak, attributed to CO adsorption on Pd sites, decreases as the molar ratio of Pt/Pd increase (Figure 11.17). The catalytic activities of a physical mixture of (Pt + Pd) and Pt/Pd = 0.125 NPs with incomplete Pt

Table 11.4 Catalytic summary of PdPd nanocubes and Pt–Pd octahedra in the hydrogenation of nitrobenzene.[a] Reprinted (adapted) with permission from ref. [88]. Copyright (2012), American Chemical Society.

Pt–Pd nanocrystals	Conversion (%)	Mole of surface atoms	TOF (s^{-1})
(111)-terminated $Pt_{33}Pd_{67}$	43.1	3.30×10^{-8}	3.63
(111)-terminated $Pt_{52}Pd_{48}$	84.1	3.30×10^{-8}	7.08
(111)-terminated $Pt_{65}Pd_{35}$	64.3	3.24×10^{-8}	5.51
cubic $Pt_{34}Pd_{66}$	65.0	1.66×10^{-8}	10.88
cubic $Pt_{51}Pd_{49}$	99.4	1.64×10^{-8}	16.84
cubic $Pt_{67}Pd_{33}$	79.9	1.66×10^{-8}	13.37

[a] Reaction conditions: 2.0 mmol nitrobenezene, 1.0 mL ethanol containing 0.1 mM Pt–Pd nanocrystals, 9.0 mL ethanol, 1 atm H_2, 120 min, room temperature.

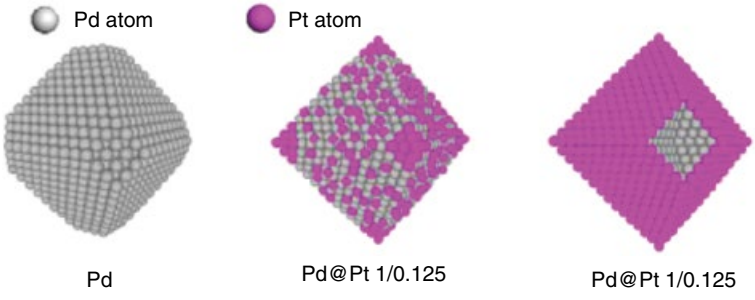

Figure 11.16 Schematic illustration of Pd, Pd@Pt (1/0.125) and Pd@Pt (1/0.25) NPs. Reprinted (adapted) with permission from ref. [89]. Copyright (2015), American Chemical Society.

coverage fall in between those of pure Pt and pure Pd. However, Pd@Pt core–shell octahedral NPs with increased Pt/Pd ratios (0.25 and 0.5) show enhanced activity/selectivity (Table 11.5). Increasing the Pt/Pd ratio further to 1.0 (3–4 atomic layers) leads to a slight activity decrease. These results suggest that a proper thickness of Pt shell on Pd core can

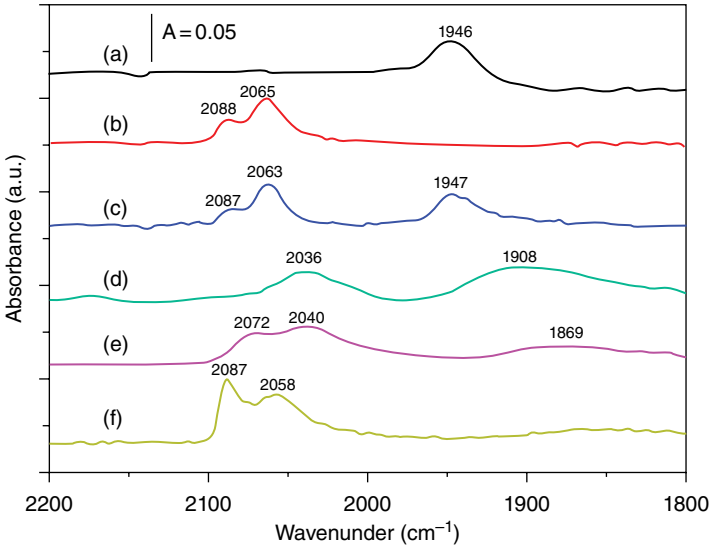

Figure 11.17 CO-DRIFT spectra (CO as the probe molecule) of (a) Pd/Al_2O_3, (b) Pt/Al_2O_3, (c) the physical mixture of Pd/Al_2O_3 and Pt/Al_2O_3 (with a Pt:Pd ratio of 1:1), (d) Pd@Pt-1/0.125/Al_2O_3, (e) Pd@Pt-1/0.25/Al_2O_3, and (f) Pd@Pt-1/1/Al_2O_3. Reprinted (adapted) with permission from ref. [89]. Copyright (2015), American Chemical Society.

Table 11.5 Catalytic performance for the hydrogenation of *p*-chloronitrobenzene over supported Pt, Pd, and Pd@Pt core–shell NPs.[a] Reprinted (adapted) with permission from ref. [89]. Copyright (2015), American Chemical Society.

		Selectivity (%)			
Catalyst	**Conversion (%)**	**p-CAN**	**AN**	**4-AP**	**Other**
Pt/Al_2O_3	79.5	81.5	12.4	2.4	3.7
Pd/Al_2O_3	61.7	45.8	43.0	9.3	1.9
(Pd + Pt)-1/0.25/Al_2O_3	74.3	60.9	29.2	5.2	4.7
Pd@Pt-1/0.125/Al_2O_3	70.7	69.8	14.7	11.4	4.1
Pd@Pt-1/0.25/Al_2O_3	98.5	82.1	10.4	7.1	0.4
Pd@Pt-1/0.5/Al_2O_3	97.4	87.9	9.5	2.6	0.0
Pd@Pt-1/0.75/Al_2O_3	91.2	86.3	11.4	2.3	0.0
Pd@Pt-1/1/Al_2O_3	88.0	86.9	11.0	2.1	0.0

[a] Reaction conditions: 2.0 g *p*-chloronitrobenzene, 0.100 g supported catalysts, 50 mL ethanol, 0.10 MPa H_2, 45 °C, 3 h. *p*-CAN denotes *p*-chloroaniline, AN denotes aniline, and 4-AP denotes 4-amino-phenol.

maximize the synergistic effect of Pd@Pt in the hydrogenation of *p*-chloronitrobenzene. Moreover, the Pt–Pd NPs with one layer of Pt is a chemically stable state under the reaction conditions. The monolayer Pt shell can be transformed into a Pt–Pd alloyed surface under a H_2 treatment. The *p*-chloronitrobenzene hydrogenation reaction can drive the alloyed Pt–Pd shell back to the original structure of a monolayer Pt shell on the Pd core. This surface reconstruction indicates that the reactant or product (*p*-chloronitrobenzene or *p*-chloroaniline) can stabilize the Pt monolayer on Pd, which is supported by DFT calculations that these two molecules have more negative binding energies on Pt(111) than on Pd(111).

Similarly, the Li group has synthesized Pt–Ni alloy NPs of different morphologies, i.e., octahedra, truncated octahedra, and cubes, by varying the inhibition agents during the particle growth [90]. These Pt–Ni NPs showed a synergistic effect in nitrobenzene hydrogenation, where Pt–Ni NPs displayed higher activity than either pure Pt or Ni NPs. These Pt–Ni NPs can be further transformed into Pt–Ni concave/corroded octahedra derived by dimethylglyoxime etching of the solid Pt–Ni octahedral NPs [91]. Dimethylglyoxime acts as an etching agent to remove Ni through a chelation process. A time-dependent etching study revealed that the etching started from the corner/edge sites along the (100) direction, which could shape the sharp edges/corners of octahedra into an intermediate round morphology (Figure 11.18). Further etching occurs along (110) and (111) directions and finally leads to the excavated facets of the corroded octahedra. This preferential etching is due to the higher surface energy of the edge/corner atoms that are more susceptible to be removed than those atoms on the more stable (111) facet. The corroded Pt–Ni_3 NPs have high Brunauer–Emmett–Teller (BET)

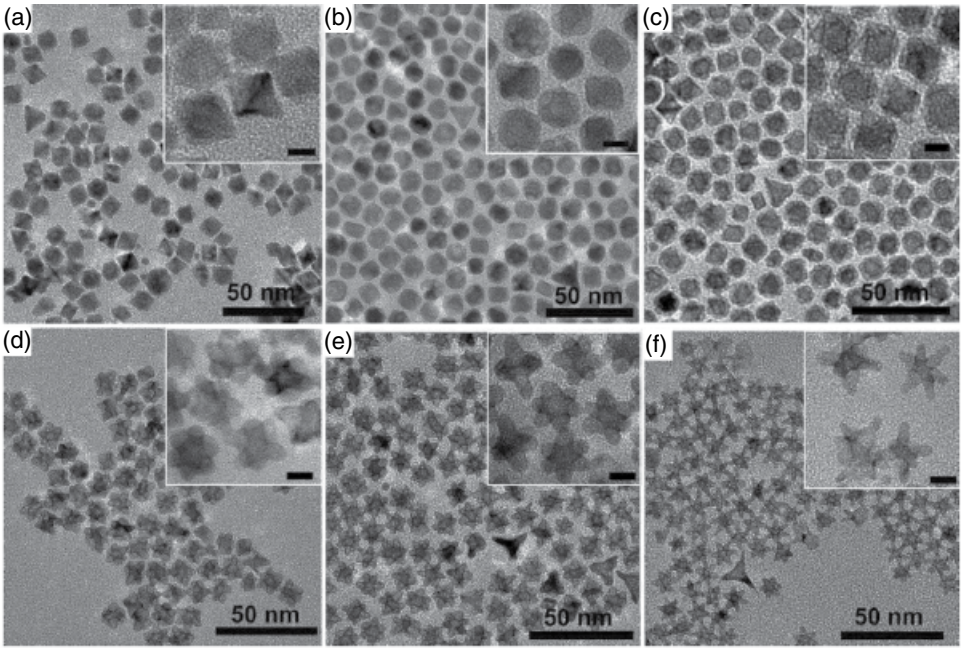

Figure 11.18 TEM and HRTEM images of Pt–Ni_{10} NPs etched for different times: (a) 15 min, (b) 30 min, (c) 1 h, (d) 3 h, (e) 6 h, (f) 12 h. Source from ref. [91]. Copyright (2012), John Wiley and Sons.

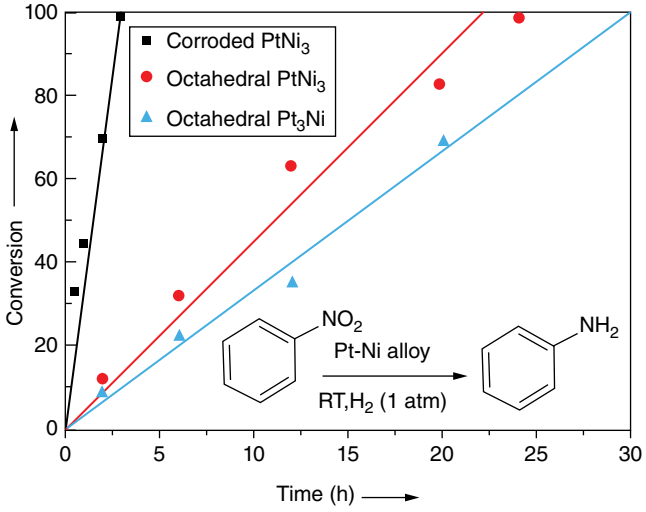

Figure 11.19 Conversion of nitrobenzene hydrogenation as a function of time over corroded Pt–Ni_3, octahedral Pt–Ni_3, and octahedral Pt_3Ni NPs. The composition effect was observed as the reaction rate on Pt–Ni_3 was faster than on Pt_3Ni NPs. The corroded Pt–Ni_3 NPs has the highest activity, evidencing the shape effect of concave structures in promoting the activity. Source from ref. [91]. Copyright (2012), John Wiley and Sons.

surface areas (64 m^2/g) than their parent Pt–Ni_3 octahedra (38 m^2/g). The corroded Pt–Ni_3 NPs have 7.9 and 10.5 times higher TOFs than those of solid octahedral Pt–Ni_3 and octahedral Pt_3Ni, respectively (Figure 11.19). The high activity of corroded Pt–Ni_3 is likely originated from the increased surface area and more exposed edge/corner atoms with low coordination numbers formed during the etching process.

Au–Ag core–shell NPs have also been prepared in a spectrum of morphologies, including nanocubes, truncated cubes, cuboctahedra, truncated octahedra, and octahedra [92]. The synthesis of these NPs utilizes a seeded-growth strategy starting from the well-defined rhombic dodecahedral Au seeds, followed by the growth of Ag shells. Adjusting the amount of ascorbic acid (reducing agent) and NaOH controls the growth rate of Au–Ag core–shell NPs and leads to different shapes. The octahedral and cubic Au@Ag NPs were used to demonstrate the shape effect in the reduction of 2-amino-5-nitrophenol by $NaBH_4$. Octahedral NPs are more active than the cubic ones. Cubic and octahedral NPs expose (100) and (111) facets with surface atomic densities of 12.0 and 13.8 Ag atoms/nm^2, respectively. The high atomic density on (111) facets was used to explain the high activity of the octahedral NPs. However, the difference in molecule binding energies on different facets could also induce different activities. Other Au–Ag core–shell structures also show shape-dependent catalytic properties, such as concave Au–Ag core–shell nanocubes[93] and Au–Ag core–shell nanopyramids[94].

11.3.1.4 Hollow NPs

The shape effect in nanodendrites and concave nanocubes demonstrates that a higher surface area of NPs is beneficial to catalysis. Similarly, the hollow structures also have higher surface area than their solid counterparts, which could lead to enhanced catalytic activities[95]. In this section, we will first discuss a porous Au–Ag hollow structure

serving as an example to show the catalytic enhancement of void interiors[96]. The nanocage effect in hollow structures will be further discussed, where reactants are encapsulated inside the cage[97].

The Jin group has demonstrated the benefit of the high surface area endowed by Ag–Au bimetallic hollow and porous nanoshells (HPNSs) for the reduction of *p*-nitrophenol using $NaBH_4$ [96]. The hollow nanoshells were synthesized via a one-pot reduction of Au precursors on Ag NPs of 50–60 nm with the aid of hydroxylamine (NH_2OH). The hollow structure formed *in situ* via a colloid seed-engaged replacement reaction and a colloid-mediated deposition reaction. A subsequent H_2O_2 treatment etches away the extra Ag and leads to the formation of porous Au–Ag hollow shell structures. The thickness of nanoshells is proportional to the amount of the Au precursor used. Four samples with different Au shell thicknesses were prepared and denoted as samples I-IV. Sample I has the thickest shell, and sample IV has the thinnest shell. The reaction rate of sample I falls in between those of pure Au and Ag NPs, while sample IV, with the thinnest nanoshell, displays the highest activity exceeding Au and Ag NPs (Figure 11.20). The degree of porosity was also evaluated on sample IV by varying the amount of H_2O_2 etchant, denoted as samples IV_0, IV_1, IV_2, and IV_3 with 0, 10, 20, and 30 μL H_2O_2 added, respectively (Figure 11.21). Sample IV_0 has an intact nanoshell presenting the lowest activity, and the activity increases by adding more H_2O_2 that created more porous hollow structures.

The nanocage effect is another interesting phenomenon extensively observed in hollow structures[98–102], where the hollow cavities can confine and concentrate the reactants, hence often promoting the activity. To justify the high catalytic efficiency endowed by the confinement effect, it is crucial to prove that the reaction occurs more on the internal than on the external surface of the nanocages. To validate this hypothesis, the El-Sayed group has prepared bimetallic Pd/Pt nanocages by galvanic replacement of Ag by Pd–Pt in Ag nanocubes[97]. The addition order of Pt or Pd precursors can induce different Pt–Pd shell structures with either Pt or Pd at the inner surface. For example, if Pt was added first followed by the addition of Pd, the formed nanocage will have Pd at the inner surface and Pt at the outer surface. Pt–Pd alloy NPs, pure Pt NPs,

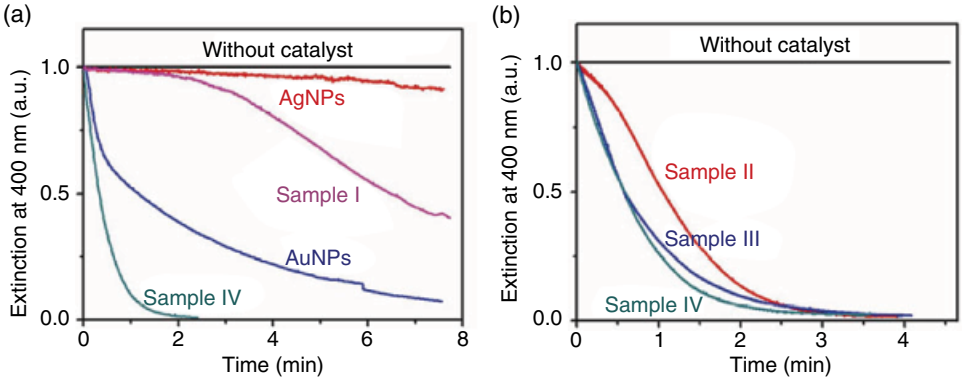

Figure 11.20 Extinction of *p*-nitrophenol (400 nm) vs. time. (a) Ag, Au NPs, samples I and IV were used as catalysts, and sample IV with the thinnest nanoshells shows the highest reaction rate. (b) Samples II–IV were used as catalysts, and the reaction rates decrease as the thickness of nanoshells increase. Source from ref. [96]. Copyright (2012), Springer.

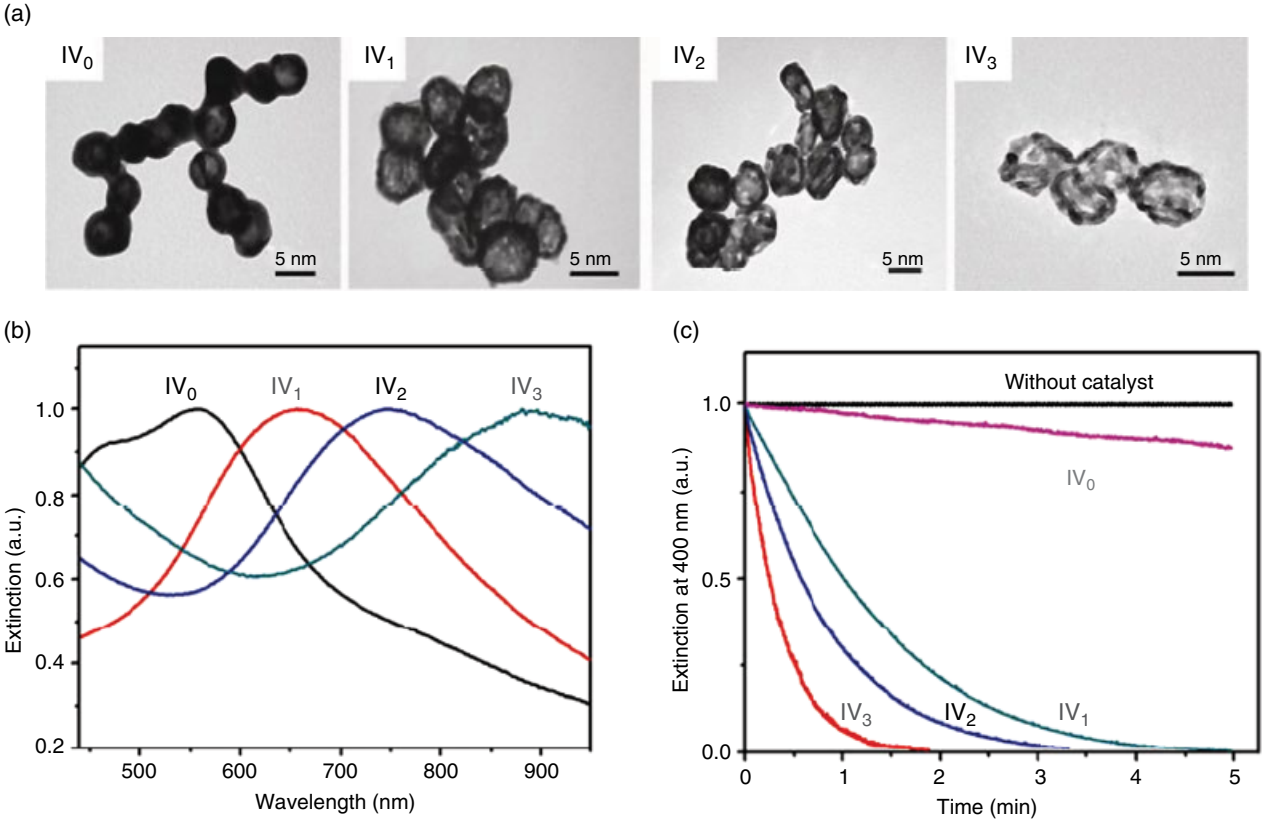

Figure 11.21 (a) TEM images and (b) extinction spectra of the HPNSs (sample IV) after the bimetallic Ag–Au hollow shells had been treated with different volumes of H_2O_2: (IV_0) 0, (IV_1) 10, (IV_2) 20, and (IV_3) 30 µL. (c) Extinction for *p*-nitrophenol (400 nm) vs. time with samples $IV_{0\text{-}3}$ used as catalysts. Source from ref. [96]. Copyright (2012), Springer.

and pure Pd NPs were also prepared as control catalysts. In the reduction of 4-nitrophenol, the activation energies of these five samples fall into two categories, as shown in Figure 11.22 and Table 11.6. Pure Pd is much more active than pure Pt. Pd–Pt nanocages with Pt at the inner surface behaves like the pure Pt NPs with a higher activation energy. On the other hand, the Pt–Pd nanocages with Pd at the inner surfaces behave like pure Pd and alloyed Pt–Pd NPs. These results suggest that the reaction readily occurs at the inner surface of the nanocages with reactant molecules trapped inside the void interiors of the nanocages.

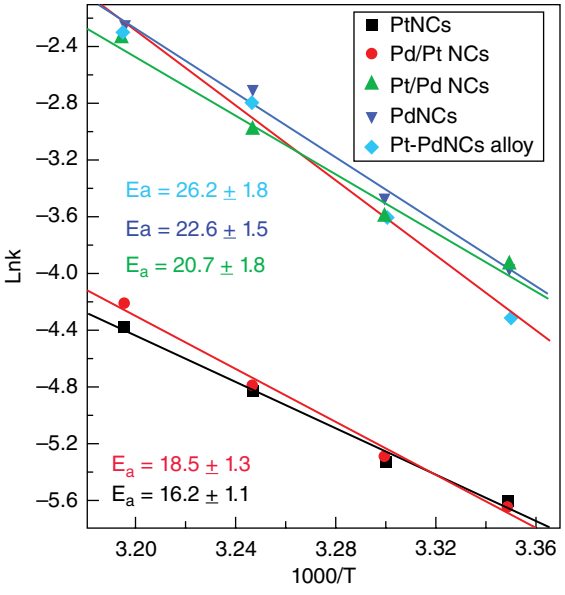

Figure 11.22 Arrhenius plots for the reduction of 4-nitrophenol over Pt, Pd/Pt nanoshells, Pt/Pd nanoshells, Pt–Pd alloy, and Pd NPs. NCs in the figure denotes as nanocrystals. Reprinted (adapted) with permission from ref. [97]. Copyright (2010), American Chemical Society.

Table 11.6 Catalytic results for the reduction of 4-nitrophenol over Pt NPs, Pd/Pt nanoshells, Pt/Pd nanoshells, Pt–Pd alloy NPs and Pd NPs. NCs in the table denotes as nanocrystals. Reprinted (adapted) with permission from ref. [97]. Copyright (2010), American Chemical Society.

Nanocatalyst	Cavity size (nm)	Rate constant (25 °C, min^{-1})	Activation energy (kcal/mol)	Entropy of activation (cal/mol.K)	Frequency factor (min^{-1})
Pt-Pd alloy NCs	47	$-0.0133 \pm 1.1 \times 10^{-4}$	26.2 ± 1.8	79.4 ± 6.0	1.76×10^{17}
Pd NCs	57	$-0.019 \pm 8.7 \times 10^{-4}$	22.6 ± 1.5	67.8 ± 5.0	5.10×10^{14}
Pt/Pd NCs	51	$-0.019 \pm 2.0 \times 10^{-4}$	18.5 ± 1.3	50.4 ± 4.2	8.80×10^{9}
Pd/Pt NCs	53	$-0.0035 \pm 1.3 \times 10^{-4}$	20.7 ± 1.8	61.4 ± 6.0	2.13×10^{13}
Pt NCs	52	$-0.0036 \pm 2.0 \times 10^{-4}$	16.2 ± 1.1	43.2 ± 3.6	2.31×10^{9}

11.3.2 Hydrogenation of Alkenes and Alkynes

The hydrogenation of alkenes, such as ethylene[103, 104], propene[105, 106], and benzene[107, 108], is an ideal set of model reactions to study the structure-property relationship of catalysts. For example, benzene hydrogenation is a structure-sensitive reaction[108], while ethylene hydrogenation on Pt surface is structure-insensitive[109]. The selective hydrogenation of alkynes is another well-studied hydrogenation reaction. The objective of transforming alkynes selectively to alkenes can be used to remove the trace amount of alkynes from alkenes[110–113]. For example, a trace amount of acetylene impurity decreases the efficiency of catalysts utilized in the polymerization of ethylene[114], one of the most produced chemicals globally. Meanwhile, the hydrogenation of acetylene or ethylene to ethane decreases the atomic efficiency of the product because ethane cannot be used in the polymerization process. Therefore, the selective hydrogenation of acetylene to ethylene has a great value for the chemical industry. In this section, we will first discuss the shape effect of Pt NPs in benzene hydrogenation[108], and continue the discussion on the shape effect from the monometallic surface to bimetallic systems for various alkene hydrogenations[115]. Finally, we will focus on bimetallic NPs for the more complicated alkyne hydrogenation.

11.3.2.1 The Alkene Hydrogenation on Pt NPs

The Somorjai and Yang groups have obtained significant insight into the structure-property relationships over cubic and cuboctahedral Pt NPs (12 nm), capped with tetradecyltrimethylammonium bromide[108]. The cubic and cuboctahedral Pt NPs are dominated by (100) and (111) facets. Benzene hydrogenation is a structure-sensitive reaction based on surface science studies on Pt single crystals[116]. The Pt(100) facet solely facilitates the formation of cyclohexane, while both cyclohexane and cyclohexene form on Pt(111). Similar behavior was observed on the shape-controlled Pt NPs as shown in Table 11.7. For cubic Pt NPs, cyclohexane was the only hydrogenation product observed. Cuboctahedral Pt NPs produced both cyclohexane and cyclohexene. These Pt NPs have a lower activation energy and higher TOFs than bulk Pt, which can be attributed to the higher specific density of corner/edge Pt sites on Pt NPs with low coordination numbers. The fact that the low coordinated Pt sites display high activity is widely seen in nanomaterials when the size of NPs decreases to the nanometer regime. Several other

Table 11.7 Apparent activation energy and turnover frequency for benzene hydrogenation over Pt NPs and Pt single crystals. Reprinted (adapted) with permission from ref. [108]. Copyright (2007), American Chemical Society.

		TTAB-stabilized Pt NPs		Pt Single crystals	
Property	Reaction product	cubic	cuboctahedral	Pt(100)	Pt(111)
apparent activation energy[a]	cyclohexane	10.9 ± 0.4	8.3 ± 0.2	15.7 ± 0.1	9.8 ± 0.1
(kcal/mol)	cyclohexene	NA	12.2 ± 0.4	NA	18.3 ± 0.8
maximum turnover rate[b]	cyclohexane	0.93 ± 0.06	0.90 ± 0.12	0.27 ± 0.01	0.30 ± 0.01
(molecules/Pt sites/s)	cyclohexene	NA	0.8 ± 0.01	NA	0.015 ± 0.02

[a] Measured in the temperature range of 310–400 K.
[b] Measured at 380 K for Pt NPs and 420 K for Pt single crystals.

studies also used Pt NPs with defined shapes to probe size and shape effects on catalysis[24, 109, 117]. In contrast, 5–7 nm Pt NPs of cubic and polyhedral shapes were studied for ethylene hydrogenation, and no size/shape effect was observed, which confirms that ethylene hydrogenation is insensitive to structure. The hydrogenation of other molecules has also been studied over various Pt NPs, such as pyrrole[109], ethylene[118], and cinchonidine[119].

11.3.2.2 Alkene Hydrogenation on Shaped Bimetallic NPs

In comparison to monometallic NPs, bimetallic catalysts permit more compositional, electronic and structural tunability[13], For example, a secondary metal can modify the electron density of precious metals and also dilute the active precious metal centers[81]. The addition of 3d transition metals into precious metals is the most used strategy to reduce the usage of precious metals. However, the surface composition of bimetallic catalysts is usually different from their bulk phases, complicating the study of their catalytic properties. Alkene hydrogenation serves as an excellent model reaction to probe the activity of bimetallic NPs, similar to the studies above on Pt NPs. We will show research endeavors to address this question from both theoretical calculations and experimental studies.

DFT calculation is a powerful tool to explore reaction mechanisms. In DFT calculation, an ideal surface is typically constructed without considering experimental uncertainties. The adsorption/desorption energies and favored reaction pathways are calculated to explain or even predict the realistic reaction environment[120], especially for the reactions catalyzed by the shaped bimetallic NPs with well-defined facets. For example, the deposition of a 3d metal on single crystal Pt(111) at room temperature forms a surface monolayer of the 3d metal (denoted as 3d-Pt-Pt). At elevated temperatures, the Pt sublayer segregates to the surface to form a Pt top-layer-3d metal sublayer structure (Pt-3d-Pt)[121–124]. This structural evolution was explained by a lower surface energy of Pt in comparison to 3d transition metals[125, 126]. The release of elastic strain could also drive the heavier Pt atoms to the surface and form an atomic layer[127]. Under realistic catalytic conditions, surface reconstruction could happen on the bimetallic surface due to the interaction of reaction molecules with surface atoms. Accepting that this reconstruction is universal, many studies have shown how the reconstructed bimetallic surface can alter the catalytic pathways[16, 23, 25]. The Chen group has performed systematic DFT calculations in correlating hydrogenation activity with the specific bimetallic surfaces [115], such as Co, Ni, Fe, and Cu deposited on Pt(111). The authors studied the catalytic properties of 3d-Pt-Pt(111) and Pt-3d-Pt(111) in cyclohexene hydrogenation and dehydrogenation reactions by evaluating the hydrogen binding energy (HBE) and the cyclohexene binding energy (CBE). The DFT calculations of the CBE/HBE on two structural models (Pt-3d-Pt/3d-Pt-Pt) agree well with the desorption temperatures for H_2 and cyclohexene in temperature-programmed desorption (TPD) as shown in Figure 11.23. These DFT calculation results indicate a dramatic change in electronic structures of Pt-3d transition metal systems. However, the realistic hydrogenation/dehydrogenation activity is more complicated and cannot be attributed solely to either CBE or HBE. It has long been realized that for optimal catalytic properties, a proper balance between the adsorption strength of reactants and products is required. The composition and structure of catalyst surface can strongly affect the adsorption energy of molecules, which can lead to a composition-dependent volcano curve of activity (Figure 11.24). In this study, Pt–Ni–Pt surface shows the highest activity in

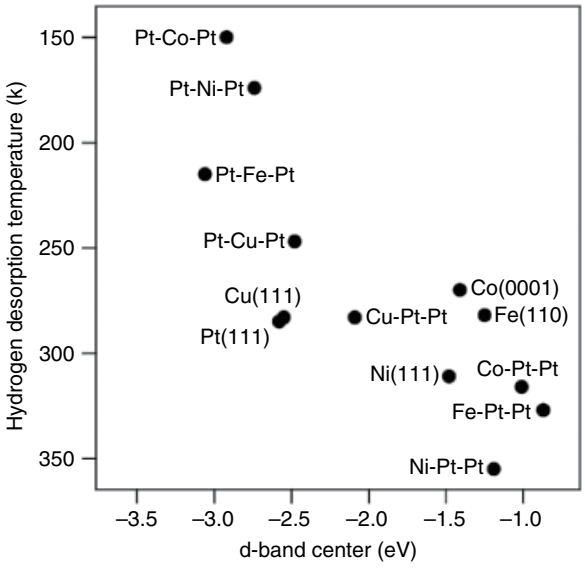

Figure 11.23 Hydrogen desorption peak temperature as a function of *d*-band center. Reprinted from ref. [115]. Copyright (2008), with permission from Elsevier.

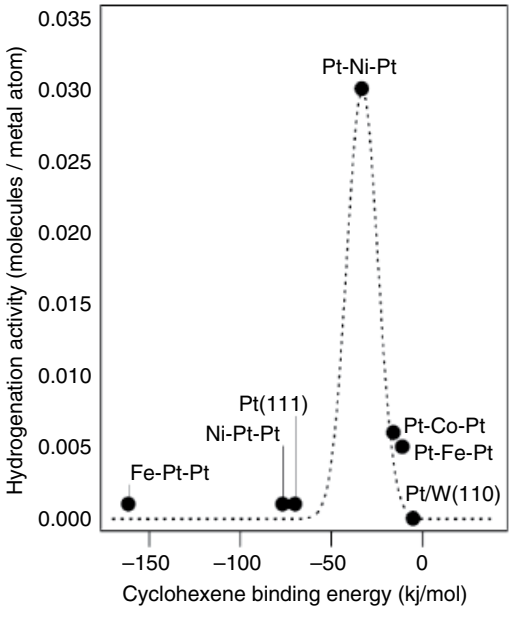

Figure 11.24 Correlation between hydrogenation activity as a function of theoretically calculated CBE. Reprinted from ref. [115]. Copyright (2008), with permission from Elsevier.

cyclohexene hydrogenation, in comparison to other Pt-3d-Pt and 3d-Pt-Pt model surfaces with Fe or Co as the secondary metal.

Several experimental studies on shaped Pt–Ni NPs have demonstrated the shape and composition effect on alkene hydrogenation reactions. The Li group has synthesized alloy Pt–Ni NPs with well-defined octahedral, truncated octahedral and cubic shapes [90]. These NPs were synthesized by the coreduction of $Ni(acac)_2$ and $Pt(acac)_2$ in benzyl alcohol with PVP as the capping agent. The authors used benzoic acid, aniline, and CO/KBr as the growth inhibition agents that could respectively lead to octahedral, truncated octahedral, and cubic Pt–Ni NPs. Among these three shaped Pt–Ni NPs, Pt and Ni bulk ratios can be easily controlled, which is advantageous for studying the synergistic and compositional effect in catalysis. Specifically, octahedral and cubic NPs expose (111) and (100) facets, respectively. Truncated octahedral NPs expose both (111) and (100) facets. Additionally, these NPs dissolve in either polar or nonpolar solvents, depending on using benzyl alcohol/PVP or oleylamine as the capping agents. Due to the advantages already mentioned, these shaped Pt–Ni NPs are optimal experimental platforms to study the structure-property relationship between bimetallic crystal facets and their catalysis. In section 11.2.1.3, we mentioned the synergistic effect between Pt–Ni in nitrobenzene hydrogenation. Here, the authors used styrene hydrogenation and benzalacetone hydrogenation to study the compositional effect of octahedral Pt–Ni NPs with Pt/Ni ratios of 0, 1/3, 1, 2, 3, 10, and pure Pt. A volcano shaped curve of activity vs. Ni% was observed in the order of $Pt–Ni_2 > Pt–Ni \approx Pt–Ni_3 > Pt_3Ni > Pt–Ni_{10} > Pt > Ni$, reflecting the synergistic effect in the composition-activity relationship. However, when the Pt–Ni NPs contain too much Ni, the inert Ni layer would be the dominant coverage on the Pt–Ni surface, leading to the decreased reaction rate. Albeit the electronic modulations of Ni to Pt, Pt segregation could also explain the higher activity of alloy Pt–Ni NPs in comparison to their pure metals. Pt was observed to be concentrated on corner/edge sites of these Pt–Ni NPs, especially for truncated octahedral ones, where the low-coordination Pt sites show high activity. Unlike Pt, Ni was observed to distribute more evenly across the whole NPs, which could explain the formation of a surface Ni thin layer responsible for the low activity at high Ni concentrations. A similar effect has also been observed on Ni–Pt–Pd polyhedral NPs in 1-octene hydrogenation [128]. The as-prepared Ni–Pt–Pd NP shows an interesting assembled structure with Pd–Ni core–shell encaged by a Pt frame, which forms due to the segregation of Pt to the edge/corner sites of the polyhedral NP. The activity of the freshly prepared Ni–Pd–Pt NPs is very low, which can be ascribed to the strong binding of oleylamine capping molecules as well as the high Ni coverage. After an acid-etching step, these Ni–Pt–Pd NPs show comparable activity to pure Pt NPs, even containing less Pt. The highly tunable composition and shape of bimetallic NPs bring great opportunities to demonstrate the structure-property relationship in catalysis.

11.3.2.3 Semi-Hydrogenation of Alkynes on Shaped Bimetallic NPs

Alkene and alkyne hydrogenation have been employed as model reactions to elucidate the catalysis of bimetallic NPs with morphology controls. In the selective hydrogenation of alkynes, researchers aim for two primary targets: promoting the hydrogenation of alkynes to desirable alkenes and suppressing the subsequent over-hydrogenation of alkenes[110, 112]. On pure precious metals, such as Pt and Pd, alkenes are kinetically stable intermediates that have been observed in the early hydrogenation stage[129,

130]. However, alkenes are not thermodynamically stable products, which will eventually evolve into over-hydrogenated alkanes. In most cases, the hydrogenation of alkenes is observed to be almost instantaneous but slightly slower than the initial semi-hydrogenation of alkynes[131–133]. Bimetallic NPs can suppress the over-hydrogenation pathway of alkenes to undesirable alkanes, due to a weaker adsorption energy of alkenes on the modulated bimetallic surfaces with unique geometric and electronic structures[134, 135].

The Skrabalak group has studied the synergistic effect of Au@Pd octahedral NPs with various thicknesses of Pd shells (i.e., 1–2 nm, 5–6 nm, and 7–8 nm), targeting the selective hydrogenation of 2-hexyne[136]. As-prepared Au@Pd NPs resemble the octahedral morphology of Au seeds. Core–shell structures can tune the electronic properties of shell metals due to the electron donation from core metals. These core–shell NPs provided an ideal platform to validate the Hammer-Nøskov model [137], in which the binding strength of an adsorbent is correlated to the *d*-band center of the metal surface. The binding strength of adsorbents on bimetallic metal surfaces can be enhanced due to the electron donation from core to shell metals that pushes the *d*-band center of shell metals closer to the Fermi level, which increases their catalytic activity. Of note, the assembly of core–shell structures relies on the minimal lattice mismatch between the core and shell metal, but the strain induced by the lattice mismatch in core–shell NPs is beneficial to their electronic, optical, and catalytic properties[138–140]. In Au@Pd octahedral NPs, increasing the Pd shell thickness decreases their activity in the selective hydrogenation of 2-hexyne, as shown in Table 11.8. Au@Pd NPs of the thinnest Pd shell (1–2 nm) are the most active catalyst in comparison to pure Pd and Au@Pd NPs of thicker shells (5–6 nm and 7–8 nm). Au@Pd NPs with a 5–6 nm shell have similar activity as pure Pd, but those with a 7–8 nm Pd shell are less active than pure Pd. XPS results show that thicker Pd shells lead to a lower binding energy of Pd (Figure 11.25). As the thickness of the Pd shell increases to 7–8 nm, the binding energy of surface Pd shifts back to the position of bulk Pd. This XPS trend suggests that increasing the Pd shell thickness (from 1–2 nm to 5–6 nm) results in the Au core donating more electrons to the shell, but this donation becomes weaker when Pd shells are 7–8 nm. According to the Hammer-Nøskov model, the decrease and increase in Pd binding energies with the increase of Pd shell thickness suggests that a volcano-shaped activity-Pd shell thickness curve should be observed, where a 5–6 nm Pd shell was supposed to be optimal in regards to the strongest electron donation of Au. The most electron donation should theoretically lead to the strongest binding between 2-hexyne and Pd, and consequently

Table 11.8 Catalytic results of Pd and Au@Pd octahedra in the hydrogenation of 2-hexyne and their respective geometric parameters. Reproduced from ref. [136] with permission from The Royal Society of Chemistry.

	Edge length (nm)	Shell thickness (nm)	Selectivity (%)	TOF(s^{-1})
Pd octahedra	37	–	86.5 (±1.2)	5.9 (± 0.4)
Au@Pd octahedra	37	1–2	94.5 (± 0.8)	14.0 (± 0.6)
	40	5–6	88.2 (± 1.8)	5.0 (± 0.3)
	42	7–9	91.3 (± 0.7)	3.5 (± 0.2)

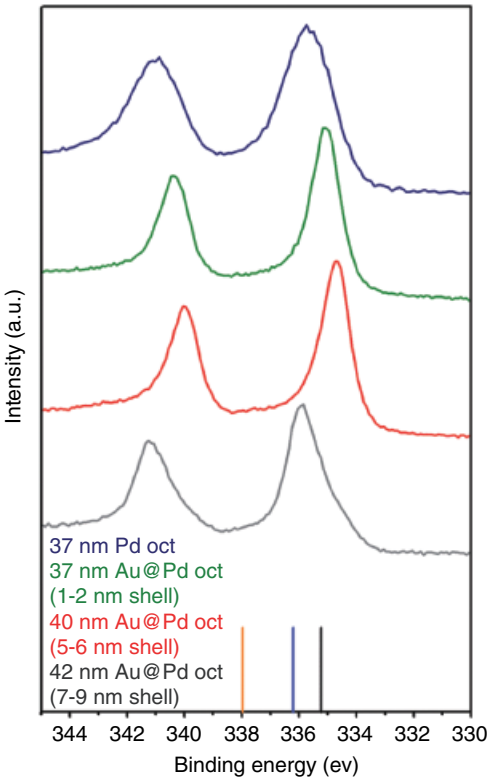

Figure 11.25 XPS spectra (Pd 3d) of 37 nm Pd, 37 nm Au@Pd, 40 nm Au@Pd and 42 nm Au@Pd octahedra. The three lines corresponds to the respective standard Pd(0), Pd(I) and Pd(II) binding energy. Reproduced from ref. [136] with permission from The Royal Society of Chemistry.

highest conversion to hexene. However, a consistent decrease in activity was observed as the Pd shell became thicker and the optimal activity occurs at the thinnest Pd shells. The authors attributed this controversy to the diminishing of (111) facets replaced by (100) facets as the Pd shell grows, since Pd(111) has been reported to be more active in the hydrogenation of 2-hexyne compared to Pd(100). However, it cannot be ruled out that the too strong bindings of 2-hexyne on 5–6 nm Pd shell can be adverse to activity. All Au@Pd NPs show high selectivity to cis-2-hexene. Only a slight increase of the over hydrogenated hexane is observed at the full conversion of hexyne, which could be explained by the kinetically stable nature of 2-hexene in these reactions.

The Sàfràn group has synthesized Au@Pd NPs with even thinner Pd shell[141], which showed different trends in activity and selectivity in comparison with those of the thicker Pd shells discussed in the previous paragraph. These Au@Pd core–shell NPs have 5–6 nm Au cores and 0.12 nm (a monolayer) to 1.5 nm Pd shells based on calculation. The semi-hydrogenation of acetylene in propene stream was studied to probe the activity and selectivity of these small Au@Pd NPs. As the thickness of Pd shell increases, the activity for the semi-hydrogenation of acetylene increases and then drops, exhibiting the highest activity at the Pd/Au ratios of 0.3/1. The activity-Pd shell thickness relationship is consistent with the Hammer-Nøskov model (the Pd shell thickness: 0–1.5 nm

in this study). The synergistic effect between Au and Pd is due to the electron transfer from the Au core to outer Pd shells, but this electronic modification becomes weaker when a thicker Pd shells were deposited. Reduction treatment can convert core/shell Au@Pd NPs into alloy Au–Pd NPs, which showed decreased activity with the increase of the reduction temperature. However, the over hydrogenation of acetylene can be readily suppressed and the selectivity to ethylene is improved on alloy Au–Pd NPs.

These two studies support a complicated correlation between activity and selectivity of bimetallic NPs. However, there are still great opportunities to explore these shape-, structure-, size-, and composition-dependent catalytic properties on these bimetallic NPs. More studies on the structure-property relationship of bimetallic NPs are highly desirable to achieve the nanoscale understandings.

Given bimetallic NPs (e.g., Pt–Sn, Pt–Ga, and Pd–Zn) can enhance the selectivity of alkenes in the semi-hydrogenation of alkynes[135], another interesting question is the control of cis- and trans-conformation of as-formed alkenes. The shape effects of bimetallic NPs in tuning cis-/trans-configuration of alkenes have not been well studied. However, this conformation control is highly important in the total synthesis and the pharmaceutical industry[142]. We shall briefly mention this progress in metallic NP systems. Cis-alkene is kinetically favored during the hydrogenation of alkynes but will transform into trans-alkenes due to the thermodynamically more favored trans-configuration. There are two major strategies to achieve the configuration controls on metallic systems. One strategy is to modulate the transformation rate of alkynes to cis- vs. trans-alkenes. The Zaera group has discovered that Pt surfaces of higher Miller indices could facilitate the formation of cis-alkenes because cis-alkenes are more kinetically stable when adsorbed on such facets in comparison to their trans- counterparts due to a steric hindrance during the cis- to trans- transformation[143]. Considering the thermodynamical preference of trans-species, the Komatsu group has reported the intermetallic RhSb catalysts with high selectivity to trans-alkenes during the hydrogenation of alkynes where the intermetallic surface can prevent the over-hydrogenation to alkanes[135, 144]. Besides the pure bimetallic NPs, the encapsulation of porous materials of bimetallic NPs is another strategy to induce the cis-/trans-selectivity. Flower-like RhNi NPs encapsulated by metal-organic framework-74 (MOF-74) structure was reported with high cis-selectivity in alkyne semi-hydrogenation, which is attributed to the small cage of MOF-74[145].

11.3.3 Selective Hydrogenation of α,β-Unsaturated Aldehydes

α,β-unsaturated aldehydes are one category of organic molecules containing conjugated C = C and C = O groups. Acroleins, crotonaldehyde, and cinnamaldehyde are typical *α,β*-unsaturated aldehydes. These *α,β*-unsaturated aldehydes serve as precursors to producing many valuable unsaturated alcohols through the selective hydrogenation of the more polar C = O groups in the presence of C = C groups[146–148]. The saturated aldehyde (selective hydrogenation of C = C) and the saturated alcohols (hydrogenation of both C = C and C = O) are not desirable products. However, the hydrogenation of C = C bond is more thermodynamically favored in comparison with that of C = O bond. Therefore, C = C bond is usually hydrogenated first on precious metal catalysts. The addition of Fe[149], Co[150], and Sn[151] to precious metal-based catalysts is an effective approach to promoting the selectivity to C = O hydrogenation of *α,β*-unsaturated aldehydes.

These bimetallic NPs, with shape, composition, and/or size control are well studied to tune their catalytic selectivity in the hydrogenation of α,β-unsaturated aldehydes[147, 152–155]. Moreover, since capping agents are widely used in synthesizing bimetallic NPs, the catalytic effect of the capping agent is also worth considering[156, 157]. We shall discuss the selective hydrogenation of α,β-unsaturated aldehydes on bimetallic catalysts from two perspectives: the synergistic effect of bimetallic combinations, and the effect of capping agents.

11.3.3.1 The Synergy of Bimetallic Combinations

Using bimetallic NPs to tune selectivity in the hydrogenation of unsaturated aldehydes usually involves structural, compositional and size effects. Using Pt–Co NPs with Co decorated on Pt, the Bishop group has studied the compositional and size effect[157]. Pt NPs of 2.8–14.4 nm were prepared first and then decorated with Co. The Co atoms were deposited preferentially on the low coordination sites of Pt NPs as shown in Figure 11.26. Cinnamaldehyde (CAL) hydrogenation was used to probe the active sites of Pt and Pt–Co NPs. The hydrogenation products vary between desirable cinnamyl alcohol (COL), and undesired hydrocinnamaldehyde (HCAL)/hydrocinnamyl alcohol (HCOL). It is well known that the low coordination Pt sites have a strong binding to C = C bonds, so the suppression of the low coordination sites is advantageous to reduce the C = C hydrogenation leading to a high selectivity to COL. The size effect of Pt was studied first, and the small Pt NPs did show poor selectivity to COL due to the presence of more low coordination sites on small sized Pt. The presence of Pt low coordination sites is confirmed by CO-attenuated total reflection (ATR)-FTIR, in which the bridged-CO adsorption peak (suggesting low-coordination Pt sites) is more intense on small Pt NPs. Large Pt NPs, containing relatively less low coordination sites, show higher selectivity in C = O hydrogenation. For bimetallic Pt–Co NPs, several phenomenal effects were observed. First, the authors want to study the compositional effect by changing the amount of Co deposition on 4.8 nm Pt NPs. Remarkably, the EDS compositional analysis of all Pt–Co NPs demonstrates that the actual Co-loading remains the same regardless of varying the amount of added Co precursors (Table 11.9). The constant Co-loading strongly validates that Co atoms can only be deposited on the low coordination Pt sites. The authors then varied the size of Pt–Co NPs. The catalytic results of these Pt–Co NPs in the CAL hydrogenation are listed in Table 11.10. The smaller Pt–Co NPs give higher selectivity to COL in comparison to larger Pt–Co NPs, which is opposite to the

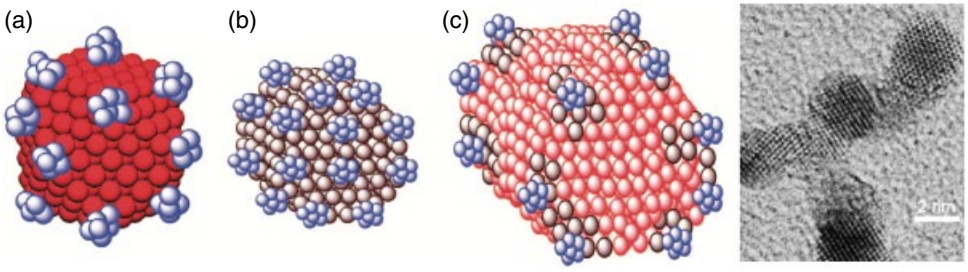

Figure 11.26 Schematic illustration of Co-decorated Pt NPs where Co atoms were preferentially deposited on the corner sites of Pt NPs and the inserted TEM image is a typical 3.3 nm Pt NPs. Reprinted (adapted) with permission from ref. [157]. Copyright (2008), American Chemical Society.

Table 11.9 The EDS compositional analysis of Co decorated Pt with different amounts of added Co precursors and their catalysis toward the CAL hydrogenation. Reprinted (adapted) with permission from ref. [157]. Copyright (2008), American Chemical Society.

Molar ratios Co/Pt recipe (EDS Co/Pt ratio of solid product)	% CAL conversion	% selectivity to cinnamyl alcohol (COL)
0 (0)	18.82	41.4
0.24 (0.17)	58.38	61.2
0.49 (0.18)	81.77	73.6
0.98 (0.18)	91.06	99.6
1.47 (0.18)	90.83	99.1
3.91 (n.d.)	76.40	98.1

Table 11.10 The wavenumber of linear CO adsorption and the selectivity to COL over Co decorated Pt with different sizes. Reprinted (adapted) with permission from ref. [157]. Copyright (2008), American Chemical Society.

Co decorated Pt nanocrystal size (nm)	% selectivity toward unsaturated alcohol (COL)	Linear peak position (cm^{-1})
4.0	99.7	2047
6.1	99.4	2052
14.6	96.8	2061
17.4	89.4	2063
24.8 (Pt only)	85.3	2060

selectivity trend observed on pure Pt NPs of different sizes. To understand the selectivity trend in PtCo NPs, the authors used CO-ATR-FTIR to study the surface structure of Pt–Co NPs with various sizes (Table 11.10). With the size increase of Pt–Co NPs, the vibration absorption atop CO shifts to a larger wavenumber. The CO adsorbed on atop sites of 17.4 nm Pt–Co NPs displays almost similar peak position as that on pure Pt NPs (24.8 nm). The atop CO vibration shifts to larger wavenumbers on large NPs suggesting that the electron donation of Co (δ^+) to Pt (δ^-) is stronger on the small-sized Pt–Co NPs. The Co (δ^+) can attract the carbonyl group (C = O) in CAL in a more head-on geometry. Meanwhile, the Pt (δ^-) can destabilize C = C bindings. These two effects in bimetallic Pt–Co NPs can enhance the selectivity to desirable COL in the selective hydrogenation of CAL, which is more prominent on small Pt–Co NPs than large ones.

Considering the shape effect of bimetallic NPs on C = O/C = C selectivity, the Li group has studied the selective hydrogenation of benzalacetone over octahedral Pt–Ni NPs with (111) facets, truncated octahedral with a mixture of (111) and (100) facets, and cubic with (100) facets[90]. The activity is decreasing in the order of octahedral > truncated octahedral > cubic, which agrees with the reduced amount of (111) facets. Therefore, the (111) facet of Pt–Ni NPs is more active in the hydrogenation of benzalacetone in comparison to (100) facet, evidencing the shape effect in bimetallic Pt–Ni NPs.

11.3.3.2 Capping Agent Effect

The colloidal synthesis of bimetallic NPs uses capping agents, which could affect the selectivity of these particles in the hydrogenation of α,β-unsaturated aldehydes. The adsorption of capping agents can prevent the aggregation of NPs by decreasing their surface energies[158]. However, strong binding of capping molecules could poison the surface active sites[85]. On the contrary, some capping molecules can align on the surface of metal NPs to form self-assembled structures, which can lead to higher selectivity[158–160]. The Fu and Zheng group have studied the capping agent effect of Pt_3Co NPs capped with oleylamine (OAm) for the selective hydrogenation of CAL[161]. As-prepared Pt_3Co NPs have a well-defined truncated octahedral shape with uniform facets for the ordered adsorption of OAm (Figure 11.27). DFT calculations suggest that OAm molecules rigidly pack on the surface of Pt_3Co NPs. This rigid geometry of OAm confines the CAL molecule standing on the Pt_3Co surface, and only the C = O end group interacts with the particle surface, leading to the high selectivity to COL as illustrated by Figure 11.28. This prediction by DFT calculation was confirmed by the high selectivity of COL observed on OAm-capped Pt_3Co NPs. Furthermore, a series of OAm analog amines with different carbon chain lengths from C_4NH_2 to $C_{18}NH_2$ have been studied for the hydrogenation of CAL (Figure 11.29). The amine molecules with shorter carbon chains can diffuse more easily on the Pt_3Co surfaces or are more liable to dissolve in the solvent, leading to a less-ordered assembly and decreased selectivity to COL. On the other hand, this higher mobility of capping amines can enhance the diffusion of CAL and lead to high activities. This study demonstrated a molecular level engineering of capping agents on the

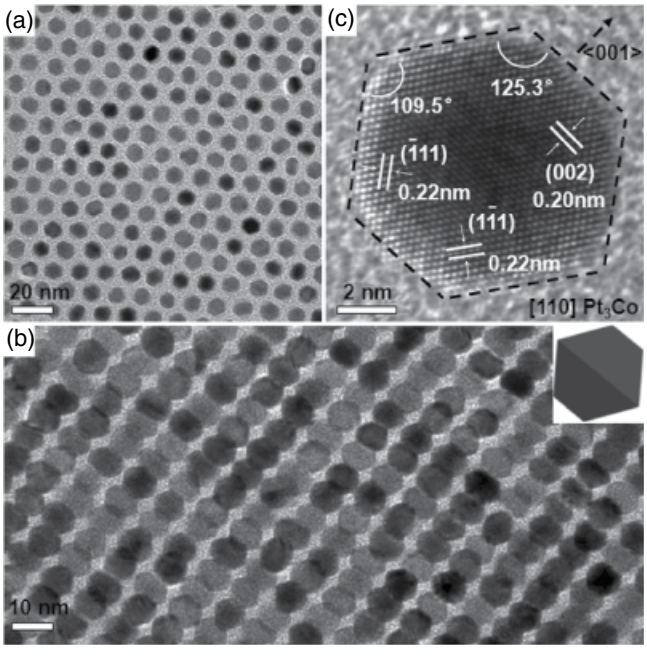

Figure 11.27 TEM images of (a, b) 8.2 nm Pt_3Co NPs. (c) HRTEM image of single Pt_3Co NPs along the [110] axis. Source from ref. [161]. Copyright (2012), John Wiley and Sons.

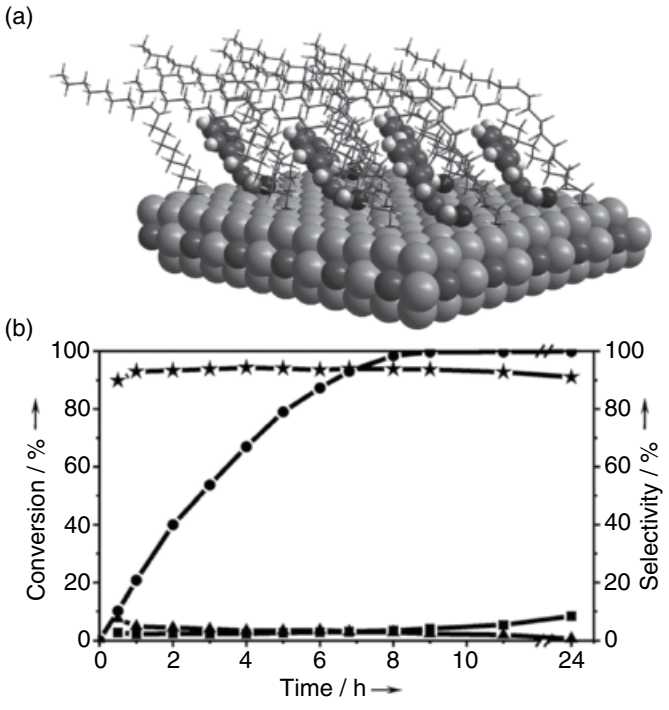

Figure 11.28 (a) DFT calculation suggested CAL adsorption (ball-stick model) assembly on $Pt_3Co(100)$ facet capped by OAm (line model). (b) Conversion of CAL and selectivity to COL (solid star), HCAL (solid triangle) and HCOL (solid square) as a function of time over OAm-capped Pt_3Co NPs. Source from ref. [161]. Copyright (2012), John Wiley and Sons.

bimetallic surface in tuning their catalytic properties. The Rodionov group has also reported similar observation on the capping effect of bimetallic Pt–Fe NPs in CAL hydrogenation[156].

11.4 H_2 Evolution Reaction

Catalytic and photocatalytic H_2 production/evolution from H_2-storage chemicals is a typical model reaction to evaluate the hydrogenation/dehydrogenation capabilities of bimetallic NPs[162–167]. H_2 evolution reactions have a relatively clear mechanism and fewer by-products, which can be used to generate clean H_2 feeds[168]. The common H_2-storage materials are small molecules, such as ammonia borane (BH_3NH_3)[169], $NaBH_4$[170], hydrazine[164], formic acid[167], and low carbon alcohols[171]. Pt-, Rh-, Fe-, and Ni-based bimetallic catalysts are widely used in this reaction, because these metals are active hydrogenation catalysts[172, 173]. High surface areas of heterogeneous catalysts associated with the facet- or size-control have been realized as important factors to efficiently catalyze dehydrogenation reactions [117, 174–177].

The Sun group has prepared hexagonal NiCo nanoplates and icosahedral NiCo NPs by the hydrothermal treatment of nickel acetate and cobalt acetate in a mixture of ethyl

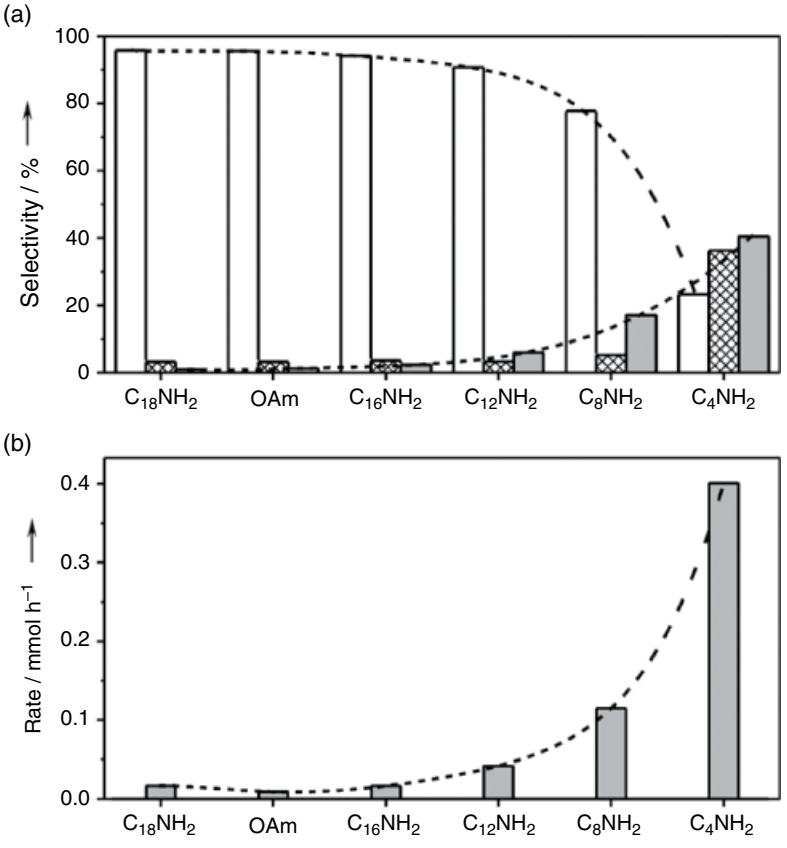

Figure 11.29 (a) Selectivity to COL (white bar), HCAL (cross-hatch bar) and HCOL (grey bar) on Pt_3Co NPs capped with amines of different carbon chain lengths. (b) The reaction rate of CAL as a function of amine-capped Pt_3Co NPs with different carbon chains. Source from ref. [161]. Copyright (2012), John Wiley and Sons.

alcohol, water, propylene glycol, and methanol, where methanol could control the growth of NPs[178]. The absence of methanol resulted in an icosahedral NiCo morphology rather than the nanoplates (Figure 11.30). After depositing a submonolayer of Pt on these Ni–Co NPs by galvanic replacement, the Ni–Co–Pt NPs were used as catalysts for the decomposition of BH_3NH_3 and KBH_4. The Ni–Co–Pt hexagonal nanoplates were more active in generating H_2 than their icosahedral counterparts. This morphology advantage was observed in both Ni–Co and Ni–Co–Pt catalysts for both BH_3NH_3 and KBH_4 decomposition. The Ni–Co–Pt catalysts are even more active than pure Pt in BH_3NH_3 decomposition, evidencing the significant synergistic effect between Ni, Co, and Pt by tuning the Pt *d*-band centers and the surface strain. Additionally, the icosahedral NPs also expose a large area of active crystal planes ($28.21 \times 10^6\,m^2$ for nanoplates and $6.81 \times 10^6\,m^2$ for icosahedral NPs per m^3). Similar Ni–Cu nanocubes/polyhedrons were also explored as active catalysts for the decomposition of $NaBH_4$ [179]. The optimal compositional effect was demonstrated with 50–60 mol.% Cu to be the most active catalysts with the highest H_2 formation rate.

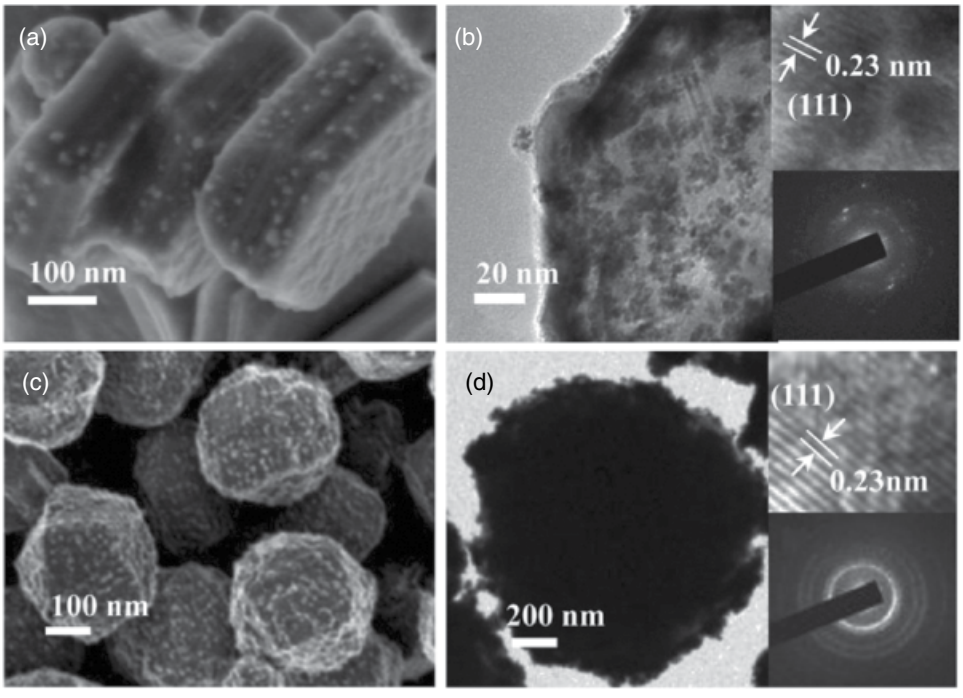

Figure 11.30 (a) SEM and (b) TEM images of Ni-Co-Pt hexagonal nanoplates. (c) SEM and (d) TEM images of Ni–Co–Pt icosahedral NPs. The inserted images in (b) and (d) are respective HRTEM images and selected area electron diffraction patterns. Reprinted from ref. [178]. Copyright (2012), with permission from Elsevier.

Nanoframes are interesting catalysts because of their high surface areas and high density of low coordination sites. The Zhang group has prepared Rh–Cu nano-octahedral frames (NOHFs) on carbons derived from the Rh–Cu nano-octahedrons (NOHs) by a two-step acid etching process[180]. The first acetic acid treatment removes surface capping agents and gently etches surface Cu. The later HCl/O_2 etching removes more Cu and generates the hollow Rh–Cu NOHFs. The NOHFs have a more Rh-rich surface with more edge and stepped sites, albeit the remnant Cu content is still high (ca. 30 molar percent to Rh), as shown in Figure 11.31d. The decomposition of hydrazine was used to evaluate the activity of NOHs and NOHFs (Figure 11.32). After normalizing to the Rh content, the TOFs follow in the order of Rh–Cu NOHFs/C ($33.7\,h^{-1}$) > Rh/C ($21.8\,h^{-1}$) > Rh–Cu NOHs ($11.1\,h^{-1}$). The lower activity of solid NOHs to pure Rh is due to the addition of the inactive Cu. Interestingly, the TOF of Rh–Cu NOHFs is enhanced by three times over that of the NOHs. The high activity of Rh–Cu NOHFs is attributed to the surface segregation of Rh on edge and stepped sites, the open framework of NOHFs holding larger specific surface areas, and the high density of low coordination Rh sites.

Other hybrid nanomaterials involving bimetallic structures have also been studied for H_2 evolution reaction. The Bar-Sadan group has reported a tip-rod structure with bimetallic Au–Pd NPs as tips on semiconductor CdS/CdSe rods[181]. This hybrid tip-rod structure employs the CdS/CdSe as the electron photoexcitation carrier and the

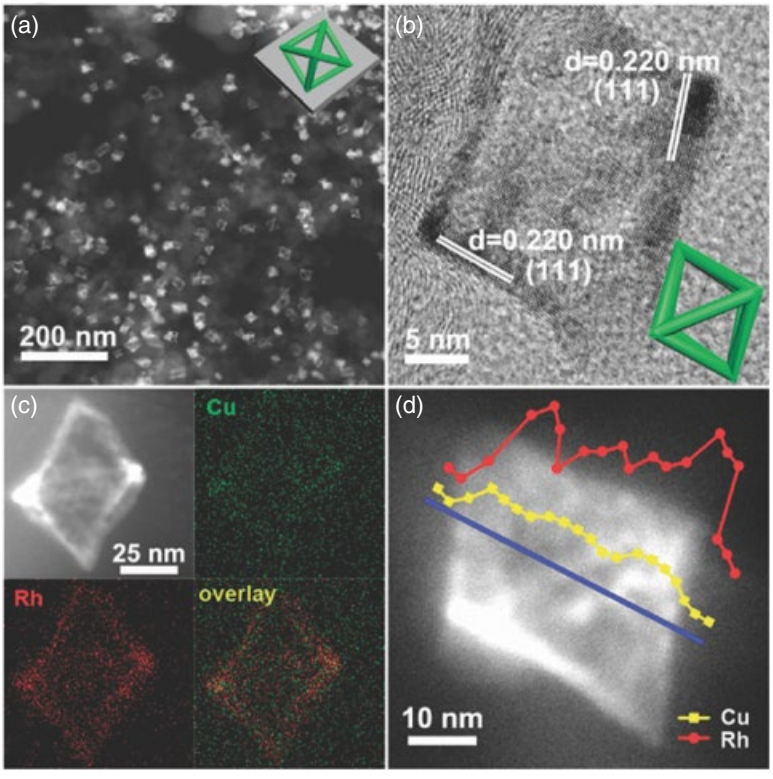

Figure 11.31 (a) High-angle annular dark-filed-scanning transmission electron microscopy (HAADF-STEM), (b) HRTEM image, (c) EDS elemental mappings, and (d) EDS line scan of Rh–Cu NOHFs/C. Reproduced from ref. [180] with permission from The Royal Society of Chemistry.

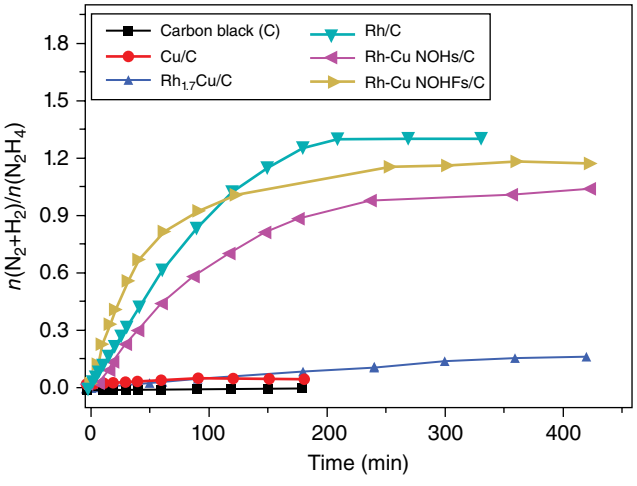

Figure 11.32 The decomposition of hydrous hydrazine (mole fraction of $(N_2 + H_2)/N_2H_4$) vs. time over carbon black, Cu/C, $Rh_{1.7}Cu/C$, Rh/C, Rh–Cu NOHs/C and Rh–Cu NOHFs/C. Reproduced from ref. [180] with permission from The Royal Society of Chemistry.

bimetallic NPs as the active center for catalytic reactions. The CdS/CdSe rods with Au–Pd tips show the highest activity for the photocatalytic decomposition of 2-propanol than those with pure Au, Pd, and Au@Pd core/shell tips.

11.5 Coupling Reactions

Carbon–carbon (C-C) coupling reactions are of great importance in organic methodology to synthesize new molecules for both fundamental research and practical applications [182–185]. There are several different coupling reactions, e.g., Suzuki-Miyaura[186–188], Negishi[189, 190], Stille[191, 192], Heck[193, 194], Sonogashira[195, 196], and Ullmann [197] reactions. These coupling reactions are based on the oxidative addition/reductive elimination mechanism around metal centers reacting between the organohalides and different active hydrocarbons[198–200]. For example, Suzuki-Miyaura reaction utilizes organoboronic acid and organohalides to construct C–C bonds[188]. Stille and Negishi reaction uses the respective stannanes/organozinc compounds reacting with organohalides to induce C–C coupling[191, 199]. Heck reaction occurs on aryl/vinyl halides reacting with activated alkenes. Sonogashira reaction is similar to Heck reaction where aryl/vinyl halides react with terminal alkynes[193, 196]. Ullmann reaction is the self-coupling of aryl halides catalyzed by Cu[197]. Homogenous Pd-based organometallic compounds are efficient catalysts for these reactions, but they suffer from poor recyclability. Extensive endeavors have been conducted to transfer these coupling reactions to heterogeneous catalytic systems based on Pd NPs. However, there are debates as to whether the active sites are truly heterogeneous and whether the leached metal species is responsible for the activity[200]. Many monometallic heterogeneous catalysts are very active with good recyclability[201–203]. Researchers further discovered bimetallic NPs with enhanced activity and selectivity compared with the monometallic Pd[204–208]. These bimetallic NPs are advantageous due to their tunable electronic and structural properties. Moreover, the addition of inexpensive secondary metals can reduce the usage of precious metals. In this section, we will focus specifically on the shape effect of bimetallic NPs on these coupling reactions.

11.5.1 Spherical NPs

We will discuss spherical NPs as the foundation for other bimetallic NPs with more sophisticated morphology[154]. Spherical NPs lack the defined facet control. Therefore, most thermodynamically stable facets are presumed to be the dominant surface that has the lowest surface energy. The Hyeon group has prepared Ni@Pd core/shell NPs in oleylamine with trioctylphosphine as the capping agent[204]. The Ni–Pd core–shell NPs maximize the usage of Pd, and the inner Ni can modulate the electronic structures of the Pd shell. The Ni–Pd NPs showed enhanced activity in the Sonogashira reaction of phenylacetylene and aryl halides in comparison to pure Pd NPs. Pd–Ni alloy NPs were also reported by the Li group as active catalysts for Suzuki-Miyaura coupling[209]. In this study, octadecylamine functions as both the solvent and the capping agent, and tetra-n-octylammonium bromide acts as both the phase-transfer solvent and the co-capping agent. The authors tuned the composition of Pd–Ni NPs from 5 to 50 mol.%,

and observed increased activity corresponding to the increase of Ni. These alloyed Pd–Ni NPs did not catalyze the self-coupling reaction between aryl halides, evidencing the high selectivity in Suzuki-Miyaura reaction. The increased activity was attributed to the higher electronegativity of Ni in Pd–Ni alloyed NPs, albeit further catalytic studies on catalysts with Ni fraction over 50 mol.% were not performed. The two studies demonstrate the synergistic benefits of bimetallic NPs in improving the activity of coupling reactions. Especially, these bimetallic NPs are recyclable and resistant to deactivation. These NPs are further validated as heterogeneous catalysts because the coupling reaction ceased in the filtrated reaction solution after removing any solid catalysts. The leached Pd was negligible detected by elemental analysis.

11.5.2 Polyhedral NPs

Polyhedral NPs have more structural advantages in comparison to the aforementioned spherical NPs because they could afford high index facets. High index facets usually have higher surface energies than those low index facets on spherical NPs. The high index facets also expose more undercoordinated atoms at kinks, edges, and corners with high activity in heterogeneous catalysis[210, 211]. Another catalytic benefit of the shape-controlled polyhedral NPs is using their well-controlled facets to study facet-dependent catalytic properties.

11.5.2.1 Promotion of Activity Arising from High Index Facets and Larger Surface Area

The Yan group has synthesized two high-index faceted Au@Pd core–shell NPs to address the catalytic promotion effect from the high index facets[212]. The heteroepitaxial growth of 3 nm Pd on Au tetrahexahedral (THH) and octahedral seeds (50–60 nm) generates respective Pd THH and trisoctahedral (TOH) shells. Both Pd TOH and THH nanoshells are covered with high index facets as shown in Figure 11.33. There are 24 (730) facets on THH nanocrystals and 24 (221) facets on TOH nanocrystals. HAADF-STEM images demonstrate the presence of (730) facet on Pd THH nanoshells and the (221) facets on Pd TOH nanoshells. These high index (730) and (221) facets have, respectively, 3/7 and 1/3 of the overall Pd surface atoms at the step sites, which could be more active for catalysis. As a comparison, Pd cubic NPs were also prepared with only (100) facets exposed. Pd THH, TOH nanoshells, and cubic NPs were evaluated using the Suzuki-Miyaura reaction between iodobenzene and phenylboronic acid (Table 11.11). Pd THH and TOH nanoshells showed nearly two times higher conversion/TON in comparison to Pd cubic NPs. This enhancement can be attributed to more low coordinated Pd atoms on the high index facets of THH and TOH NPs than those on cubic NPs.

The Han group has further synthesized the Au–Pd TOH alloy NPs enclosed by (441) facets[213]. The (441) facet can be imagined as the replica of (110) and (111) facets, representing steps and terraces on the surface of these TOH NPs. Differing from the Yan group using Au as seeds, these Au–Pd TOH NPs were synthesized by the coreduction of Au and Pd precursors. Pd and Au in these Au–Pd TOH NPs with (441) facets are evenly distributed through the particles characterized by elemental mappings. Suzuki-Miyaura reaction was used to evaluate the synergistic and shape effects of Au–Pd TOH alloy, TOH core/shell, and octahedral alloy NPs. After normalizing the activity to the mass of Pd, the TOH alloy NPs have the highest activity, indicating that the most significant synergistic effect exists between Au and Pd in these alloy NPs with high index

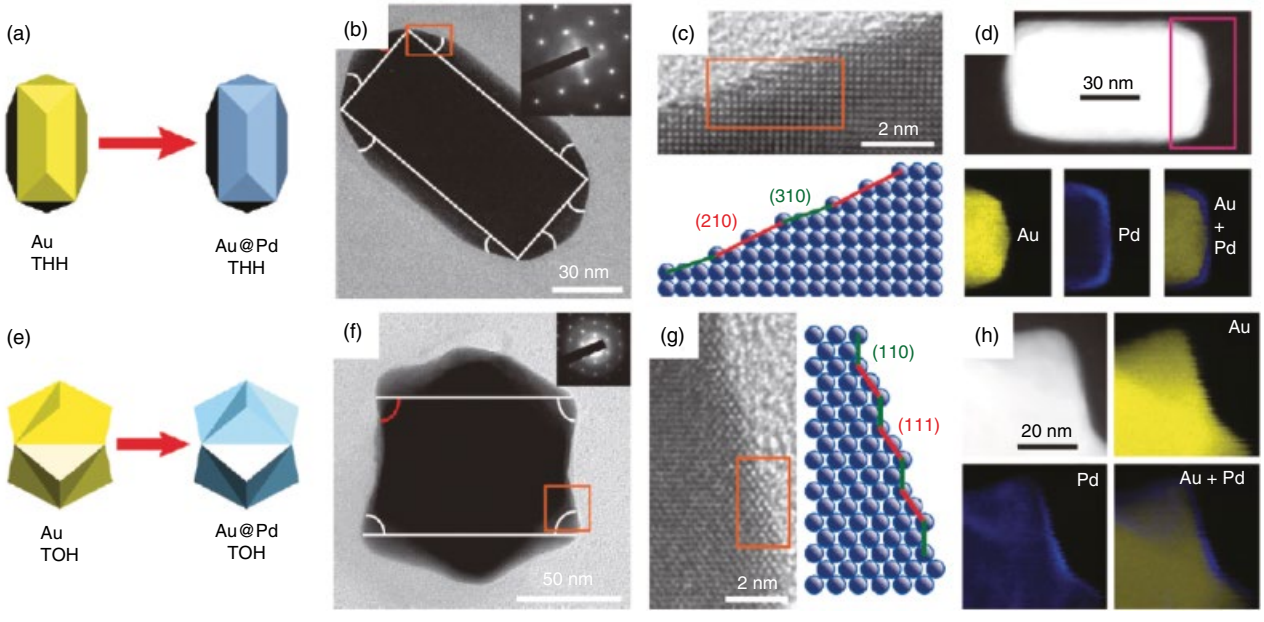

Figure 11.33 Synthesis schemes and HRTEM images of Au@Pd (a–c) THH and (e–g) TOH NPs. Elemental mappings of Au@Pd (d) THH and (h) TOH NPs to show the core/shell structure. The inserted pictures in (c) and (g) represent the construction of (730) and (221) facets. Reprinted (adapted) with permission from ref. [212]. Copyright (2011) American Chemical Society.

Table 11.11 Reaction yields and TONs (normalized to surface Pd) for Pd THH, TOH, and control catalysts for the Suzuki-Miyaura reaction of iodobenzene and phenylboronic acid. Reprinted (adapted) with permission from ref. [212]. Copyright (2011) American Chemical Society.

Catalyst	Yield (%)	Number of surface Pd atoms	TON (s^{-1})
THH Pd nanoshells	94 ± 1	4.38×10^{15}	10.8 ± 0.1
recycled THH Pd nanoshells	86	4.38×10^{15}	9.9
TOH Pd nanoshells	96 ± 5	4.03×10^{15}	11.9 ± 0.5
recycled TON Pd nanoshells	86	4.03×10^{15}	10.7
Pd nanocubes	57 ± 7	6.92×10^{15}	4.2 ± 0.3
Au-Pd core–shell nanocubes	56 ± 10	1.77×10^{15}	1.6 ± 0.2

facets. These structure-property studies have endorsed that high index facets are beneficial to the catalytic activity of bimetallic Au–Pd alloy NPs.

Another strategy to generate high index facets with more defects and unsaturated sites is to chemically evolve the as-formed bimetallic NPs. The Huang group has prepared similar Au@Pd NPs, and they noticed that the concentration decrease of octahedral Au seeds evolved the Au@Pd NPs from octahedral to truncated octahedral, cuboctahedral, truncated cubic, and concave cubic structures[214]. Specifically, the concave cubic NPs expose the combination of (410), (510), (610), (720), and (830) facets, while the cubic NPs theoretically only expose (100) facet. The exposition of high index facets endows the concave cubic NPs with three times higher TOFs than cubic NPs in the Suzuki-Miyaura coupling between iodobenzene and phenylboronic acid. The Li group has also introduced a trimetallic system, Pt–Ni@Au NPs, for Suzuki-Miyaura reactions[215]. The Pt–Ni_3 octahedral NPs can be evolved into concave octahedra of Pt_3Ni NPs by the chemical etching of Ni in dimethylglyoxime as illustrated in Figure 11.34. The concave nature can expose more unsaturated step and corner sites. Interestingly, the third metals such as Rh, Au, Ag, and Cu could selectively fill the concave area until the perfect (111) facets of octahedral NPs was recovered. Therefore, the authors prepared unique Pt_3Ni@Au trimetallic concave octahedral NPs, where the surface concentration of Au is tunable. The shapes of trimetallic Pt_3Ni@Au NPs can vary from concave $Pt_3Ni@Au_{0.5}$ with the lowest Au surface concentration, concave $Pt_3Ni@Au_2$ with partially filled void spaces (medium Au surface concentration), and the almost octahedral shaped $Pt_3Ni@Au_8$ NPs (high Au surface concentration). The catalytic properties of these three NPs were studied as summarized in Figure 11.35. Only $Pt_3Ni@Au_{0.5}$ NPs with the lowest Au surface concentration showed a higher activity than Pt_3Ni concave NPs and further increasing surface Au retarded the reactivity. Since Pt is the active species for Suzuki-Miyaura coupling, and the Au(0) is inactive for C-X bond (X = halides) activation[216], increasing surface Au will block the accessibility of active Pt sites, leading to a lower catalytic activity of $Pt_3Ni@Au_2$ and $Pt_3Ni@Au_8$. On the other hand, Pt_3Ni@Au with a low surface concentration of Au can indeed promote the activity. The enhanced activity was attributed to the presence of Au that facilitates the reduction of Pt (II) to Pt (0) because the oxidation state of Pt increases from 0 to 2+ during the oxidative addition and falls back to 0 during the subsequent reductive elimination in Suzuki-Miyaura coupling reaction.

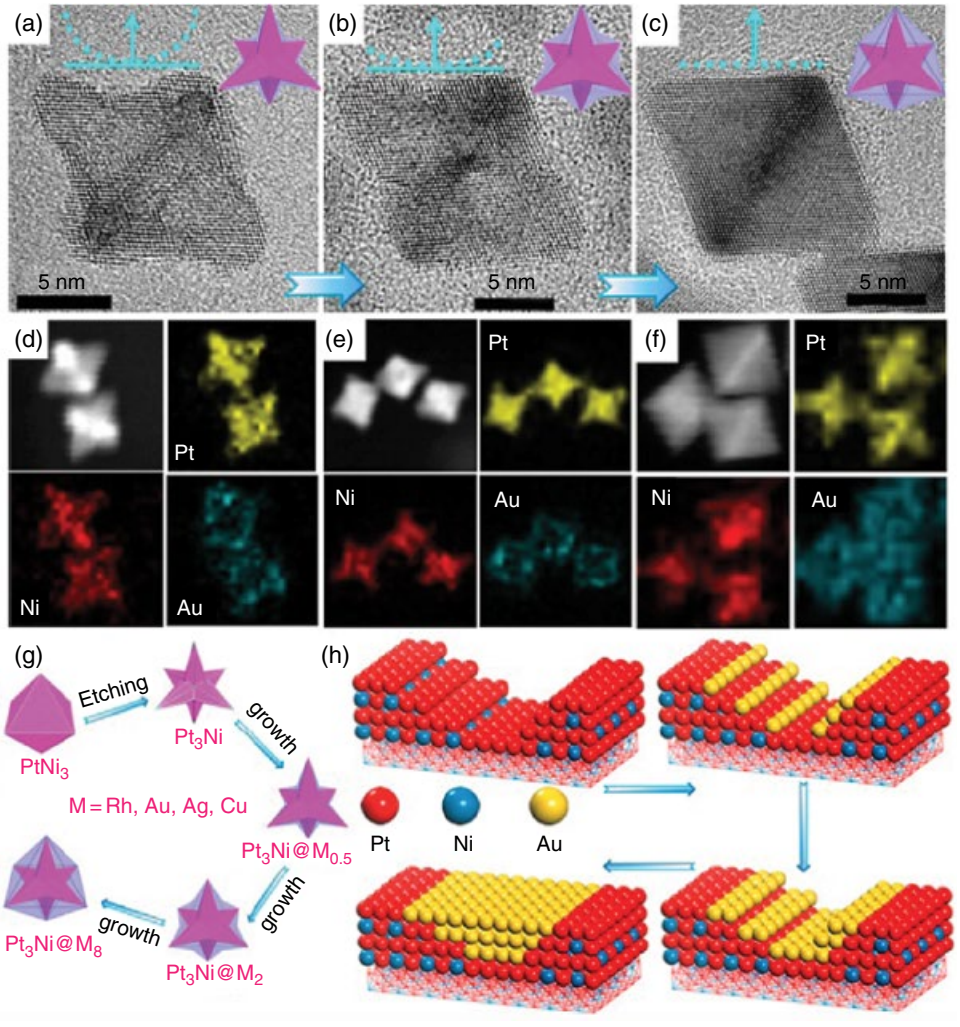

Figure 11.34 Spherical aberration (SA)-corrected HRTEM images of (a) $Pt_3Ni@Au_{0.5}$, (b) $Pt_3Ni@Au_2$, (c) $Pt_3Ni@Au_8$, and (d–f) their corresponding elemental mapping results. (g) Scheme to show the evolution of Pt_3Ni to $Pt_3Ni@M$ (M = Rh, Au, Ag, and Cu), and (h) the growth of Au to filled the concaved structures. Reprinted (adapted) with permission from ref. [215]. Copyright (2013), American Chemical Society.

Besides the concave morphology of cubic NPs, nanoflower structures were also synthesized with increased surface areas and concentration of surface defect sites. The Huang group has prepared branched Pd nanoflowers using hexadecylpyridinium chloride (HDPC) as the shape-directing agent[217]. The flower-like Pd NPs have a high surface area ($61.2\,m^2/g$) with small Pd clusters and open frameworks, which show enhanced activities in Suzuki-Miyaura coupling and the hydrogenation of nitrobenzene/styrene in comparison to solid Pd NPs and a Pd/C control catalyst. The flower-like structures of Au@Pd bimetallic NPs have also been reported by the Wiley group, although the activity promotion is not significant in the Suzuki coupling reaction between iodobenzene and phenylboronic acid[218].

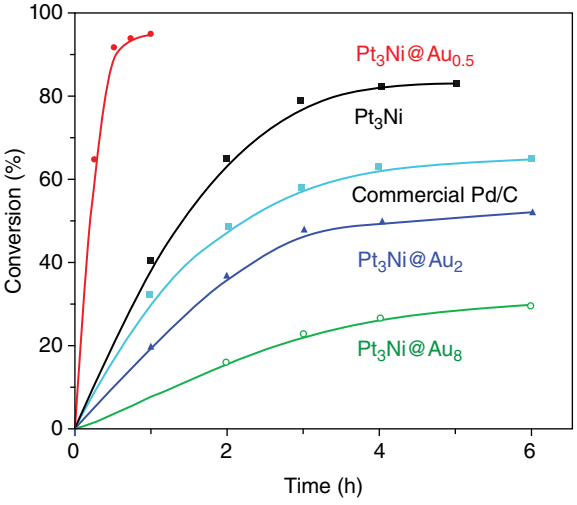

Figure 11.35 Conversion vs. reaction time in Suzuki-Miyraura reaction over $Pt_3Ni@Au_{0.5}$, $Pt_3Ni@Au_2$, $Pt_3Ni@Au_8$, Pt_3Ni, and commercial Pd/C catalysts. Reprinted (adapted) with permission from ref. [215]. Copyright (2013), American Chemical Society.

11.5.2.2 The Facet-Activity Relationship

To elucidate the facet-activity relationship in shape-controlled NPs, the Zhang group has studied the catalysis of cubic Pd–Rh hollow nanocubes (h-NCs), truncated octahedral nanocrystals (NTOs), solid cubic nanocubes (NCs), and icosahedral nanocrystals (NIs) in Suzuki-Miyaura coupling reaction (Figure 11.36)[219]. These nanocrystals were prepared by a one-pot hydrothermal reduction of Pd and Rh precursors using PVP as the capping agent, and Br^-/I^- as the shape control agents. The cubic Pd–Rh NCs form first and then evolve into hollow nanocrystals in the presence of I^-. Without I^-, Pd–Rh nanocrystals stay as solid NCs. The increase of Br^- inhibits the growth of nanocrystals and leads to NTOs, solid NCs, and NIs. The catalytic activities of these Rh–Pd nanocrystals follow a decreasing order of Pd–Rh h-NCs> > Pd–Rh NCs > Pd NCs > Pd–Rh NTOs > ~Pd–Rh NIs (Figure 11.37). The mechanism of Suzuki-Miyaura coupling reactions involves oxidative addition and reductive elimination steps. The hollow interiors of Pd–Rh h-NCs can provide more Pd on edge and corners that are more easily to be oxidized. These hollow structures could also facilitate the diffusion of reactants through the thin shells. Both the better mass transfer through the thin shells and more accessible active sites could render the hollow particles with enhanced catalytic activity. Moreover, when comparing the solid NCs, NTOs, and NIs, the facet-activity relationship is more significant. The solid NCs hold solely (100) facets, NTOs have eight (111) and six (100) facets, and NIs expose only (111) facets. According to the activity order of NCs > > NTOs > ~ NIs, the (100) facet is more active when compared to the (111) facet in Suzuki-Miyaura couplings, likely due to the better adsorption of reactants and higher efficiency in activating C–X bonds on (100) facets. It is noticeable that the decrease in activity is not proportional to the decrease in (100) facets, likely due to the presence of twin planes in NIs that hold more defects with high activities compensating the activity drop of the (100) facets. The compositional effect was also studied over Pd–Rh h-NCs, but no obvious correlation was observed, indicating that Suzuki-Miyaura

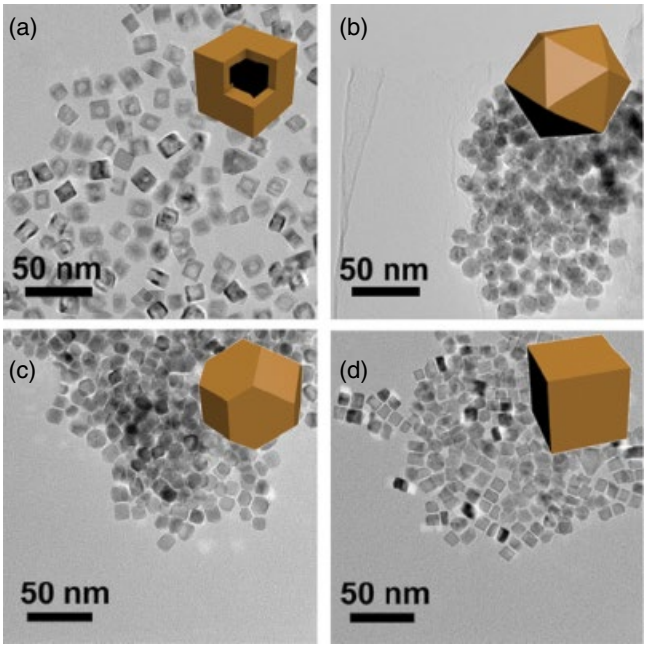

Figure 11.36 TEM images of (a) Pd–Rh h-NCs, (b) Pd–Rh NIs, (c) Pd–Rh NTOs, and (d) solid Pd–Rh NCs. Reprinted (adapted) with permission from ref. [219]. Copyright (2014), American Chemical Society.

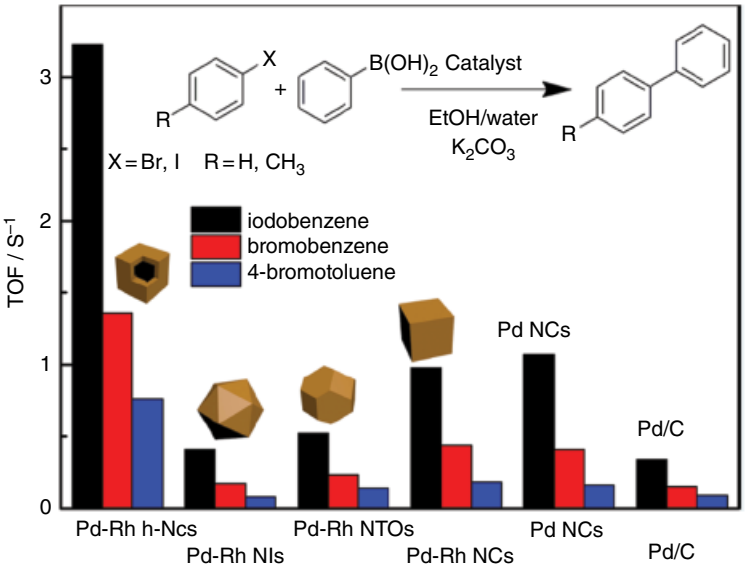

Figure 11.37 TOF comparison of Pd–Rh h-NCs, NIs, NTOs, solid NCs, Pd NCs and Pd/C in the Suzuki-Miyaura reactions of benzylboronic acid and various phenyl halides. Reprinted (adapted) with permission from ref. [219]. Copyright (2014), American Chemical Society.

coupling is insensitive to the compositions of Pd–Rh h-NCs in this study. The Zhou group has also reported the structural advantages of hollow Pd–Fe nanospheres[220]. The Pd–Fe hollow spheres were synthesized by a vesicle-assisted method that showed higher activity in Suzuki-Miyaura, Sonogashira, and Ullmann coupling reactions in comparison to their solid counterparts.

11.6 Conclusion

The ultimate purpose in heterogeneous catalysis is to tailor the structure and composition of catalysts to obtain high activity, selectivity, and stability on targeted reactions. The deepened mechanism insights, newly developed synthesis methodologies, and more advanced computational capabilities already showed significant advancement in the development of heterogeneous catalysts. In this chapter, we outlined the catalytic applications of shape-controlled bimetallic NPs in four most reported reactions including oxidation, hydrogenation, hydrogen evolution and coupling reactions. We focused on the shape-, size-, and composition-dependent catalytic properties of bimetallic NPs.

Bimetallic NPs of many unique shapes and structures have been synthesized to study the structure-property relationship. The fast development of characterization techniques with atomic resolution enables us to obtain atomic-level information of bimetallic surfaces. However, it is still challenging to reach a definitive conclusion on the detailed catalytic mechanism of bimetallic NPs. This is partially because the bimetallic surface is complicated with compositional, electronic, and geometric changes. Additionally, the chemically induced surface reconstruction further increases the structural uncertainty of bimetallic surfaces. Another limitation is the lack of *in situ* techniques to trace the surface changes under reaction conditions, especially at high temperature and pressure.

Although a unified overview of heterogeneous catalysis on bimetallic surface has not been established, there are enormous opportunities to engineer bimetallic NPs of different shapes and structures to garner valuable understandings on how bimetallic structures influence their catalytic properties.

11.7 Acknowledgments

This work was supported by funding from Iowa State University. Acknowledgment is also made to the donors of the American Chemical Society Petroleum Research Fund, for partial support of this research. We greatly thank Heather MacMurdo, Raghu V. Maligal-Ganesh, and Zhiyuan Qi for their valuable suggestions.

11.8 References

1 An, K., Somorjai, G.A. (2015). Nanocatalysis I: synthesis of metal and bimetallic nanoparticles and porous oxides and their catalytic reaction studies. *Catalysis Letters*, 145 (1), 233–248.

2 Zhang, H., Jin, M.S., Xia, Y.N. (2012). Enhancing the catalytic and electrocatalytic properties of Pt-based catalysts by forming bimetallic nanocrystals with Pd. *Chemical Society Reviews*, 41 (24), 8035–8049.

3 Greeley, J., Mavrikakis, M. (2004). Alloy catalysts designed from first principles. *Nature Materials*, 3 (11), 810–815.

4 Yu, W.T., Porosoff, M.D., Chen, J.G.G. (2012). Review of Pt-based bimetallic catalysis: from model surfaces to supported catalysts. *Chemical Reviews*, 112 (11), 5780–5817.

5 Narayanan, R., El-Sayed, M.A. (2005). Catalysis with transition metal nanoparticles in colloidal solution: nanoparticle shape dependence and stability. *Journal of Physical Chemistry B*, 109 (26), 12663–12676.

6 Francesco, I.N., Fontaine-Vive, F., Antoniotti, S. (2014). Synergy in the catalytic activity of bimetallic nanoparticles and new synthetic methods for the preparation of fine chemicals. *ChemCatChem*, 6 (10), 2784–2791.

7 Singh, A.K., Xu, Q. (2013). Synergistic catalysis over bimetallic alloy nanoparticles. *ChemCatChem*, 5 (3), 652–676.

8 Cao, S.W., Tao, F., Tang, Y., Li, Y.T., Yu, J.G. (2016). Size- and shape-dependent catalytic performances of oxidation and reduction reactions on nanocatalysts. *Chemical Society Reviews*, 45 (17), 4747–4765.

9 Wang, D.S., Li, Y.D. (2011). Bimetallic nanocrystals: liquid–phase synthesis and catalytic applications. *Advanced Materials*, 23 (9), 1044–1060.

10 Xia, Y.N., Xiong, Y.J., Lim, B., Skrabalak, S.E. (2009). Shape-controlled synthesis of metal nanocrystals: simple chemistry meets complex physics? *Angewandte Chemie-International Edition*, 48 (1), 60–103.

11 An, K., Somorjai, G.A. (2012). Size and Shape Control of Metal Nanoparticles for Reaction Selectivity in Catalysis. *ChemCatChem*, 4 (10), 1512–1524.

12 Gu, J., Zhang, Y.W., Tao, F. (2012). Shape control of bimetallic nanocatalysts through well-designed colloidal chemistry approaches. *Chemical Society Reviews*, 41 (24), 8050–8065.

13 Gilroy, K.D., Ruditskiy, A., Peng, H.C., Qin, D., Xia, Y.N. (2016). Bimetallic nanocrystals: syntheses, properties, and applications. *Chemical Reviews*, 116 (18), 10414–10472.

14 Wu, J.B., Li, P.P., Pan, Y.T., Warren, S., Yin, X., Yang, H. (2012). Surface lattice-engineered bimetallic nanoparticles and their catalytic properties. *Chemical Society Reviews*, 41 (24), 8066–8074.

15 Niu, Z.Q., Li, Y.D. (2014). Removal and utilization of capping agents in nanocatalysis. *Chemistry of Materials*, 26 (1), 72–83.

16 Tanaka, K. (1996). Chemical reconstruction and catalysis of metal and bimetallic surfaces. *Surface Science*, 357 (1–3), 721–728.

17 Campbell, C.T., Ertl, G., Kuipers, H., Segner, J. (1980). A molecular-beam study of the catalytic-oxidation of Co on a Pt(111) surface. *Journal of Chemical Physics*, 73 (11), 5862–5873.

18 Gland, J.L., Kollin, E.B. (1983). Carbon-monoxide oxidation on the Pt(111) surface—temperature programmed reaction of coadsorbed atomic oxygen and carbon-monoxide. *Journal of Chemical Physics*, 78 (2), 963–974.

19 Berlowitz, P.J., Peden, C.H.F., Goodman, D.W. (1988). Kinetics of CO oxidation on single-crystal Pd, Pt, and Ir. *Journal of Physical Chemistry*, 92 (18), 5213–5221.

20 Su, X.C., Cremer, P.S., Shen, Y.R., Somorjai, G.A. (1997). High-pressure CO oxidation on Pt(111) Monitored with infrared-visible sum frequency generation (SFG). *Journal of the American Chemical Society*, 119 (17), 3994–4000.

21 Chen, M.S., Cal, Y., Yan, Z., Gath, K.K., Axnanda, S., Goodman, D.W. (2007). Highly active surfaces for CO oxidation on Rh, Pd, and Pt. *Surface Science*, 601 (23), 5326–5331.

22 Park, J.Y., Zhang, Y., Grass, M., Zhang, T., Somorjai, G.A. (2008). Tuning of catalytic CO oxidation by changing composition of Rh – Pt bimetallic nanoparticles. *Nano Letters*, 8 (2), 673–677.

23 Tao, F., Grass, M.E., Zhang, Y., Butcher, D.R., Renza, J.R., Liu, Z., Chung, J.Y., Mun, B.S., Salmeron, M., Somorjai, G.A. (2008). Reaction-driven restructuring of Rh–Pd and Pt–Pd core–shell nanoparticles. *Science*, 322 (5903), 932–934.

24 Kang, Y., Li, M., Cai, Y., Cargnello, M., Daiz, R.E., Gordon, T.R., Wieder, N.L., Adzic, R.R., Gorte, R.J., Stach, E.A., Murray, C.B. (2014). Heterogeneous catalysts need not be so "heterogeneous": monodisperse pt nanocrystals by combining shape-controlled synthesis and purification by colloidal recrystallization. *Journal of the American Chemical Society*, 135 (7), 2741–2747.

25 Rodriguez-Lopez, J.L., Montejano-Carrizales, J.M., Pal, U., Sanchez-Ramirez, J.F., Troiani, H.E., Garcia, D., Miki-Yoshida, M., Jose-Yacaman, M. (2004). Surface reconstruction and decahedral structure of bimetallic nanoparticles. *Physical Review Letters*, 92 (19), 192101–192104.

26 Skriver, H.L., Rosengaard, N.M. (1992). Surface-energy and work function of elemental metals. *Physical Review B*, 46 (11), 7157–7168.

27 Salmeron, M., Brewer, L., Somorjai, G.A. (1981). The structure and stability of surface platinum oxide and of oxides of other noble-metals. *Surface Science*, 112 (3), 207–228.

28 Shan, J., Zhang, S., Choksi, T., Nguyen, L., Bonifacio, C., Li, Y., Zhu, W., Tang, Y., Yang, J.C., Greeley, J., Frenkel, A.I., Tao, F. (2017). Tuning catalytic performance through a single or sequential post-synthesis reaction(s) in a gas phase. *ACS Catalysis*, 7 (1), 191–204.

29 Motl, N.E., Bondi, J.F., Schaak, R.E. (2012). Synthesis of colloidal Au–Cu_2S heterodimers via chemically triggered phase segregation of AuCu nanoparticles. *Chemistry of Materials*, 24 (9), 1552–1554.

30 Buck, M.R., Bondi, J.F., Schaak, R.E. (2012). A total-synthesis framework for the construction of high-order colloidal hybrid nanoparticles. *Nature Chemistry*, 4 (1), 37–44.

31 Wang, C., Yin, H., Dai, S., Sun, S. (2010). A general approach to noble metal-metal oxide dumbbell nanoparticles and their catalytic application for CO oxidation. *Chemistry of Materials*, 22 (19), 3277–3282.

32 Korotkikh, O., Farrauto, R. (2000). Selective catalytic oxidation of CO in H_2: fuel cell applications. *Catalysis Today*, 62 (2–3), 249–254.

33 Trimm, D.L. (2005). Minimisation of carbon monoxide in a hydrogen stream for fuel cell application. *Applied Catalysis A-General*, 296 (1), 1–11.

34 Goltsov, V.A., Veziroglu, T.N. (2001). From hydrogen economy to hydrogen civilization. *International Journal of Hydrogen Energy*, 26 (9), 909–915.

35 Jimenez, S., Soler, J., Valenzuela, R.X., Daza, L. (2005). Assessment of the performance of A PEMFC in the presence of CO. *Journal of Power Sources*, 151, 69–73.

36 Lin, J., Qiao, B.T., Liu, J.Y., Huang, Y.Q., Wang, A.Q., Li, L., Zhang, W.S., Allard, L.F., Wang, X.D., Zhang, T. (2012). Design of a highly active Ir/Fe(OH)$_x$ catalyst: versatile application of Pt-group metals for the preferential oxidation of carbon monoxide. *Angewandte Chemie-International Edition*, 51 (12), 2920–2924.

37 Lakshmanan, P., Park, J.E., Park, E.D. (2014). Recent advances in preferential oxidation of CO in H_2 over gold catalysts. *Catalysis Surveys from Asia*, 18 (2), 75–88.

38 Haruta, M., Yamada, N., Kobayashi, T., Iijima, S. (1989). Gold catalysts prepared by coprecipitation for low-temperature oxidation of hydrogen and of carbon-monoxide. *Journal of Catalysis*, 115 (2), 301–309.

39 Oh, S.H., Sinkevitch, R.M. (1993). Carbon-monoxide removal from hydrogen-rich fuel-cell feedstreams by selective catalytic-oxidation. *Journal of Catalysis*, 142 (1), 254–262.

40 Feng, X., Wang, A., Qiao, B., Li, J., Liu, J., Zhang, T. (2013). Single-atom catalysts: a new frontier in heterogeneous catalysis. *Accounts of Chemical Research*, 46 (8), 1740–1748.

41 Wei, H., Liu, X., Wang, A., Zhang, L., Qiao, B., Yang, X., Huang, Y., Miao, S., Liu, J., Zhang, T. (2014). FeO_x-supported platinum single-atom and pseudo-single-atom catalysts for chemoselective hydrogenation of functionalized nitroarenes. *Nature Communications*, 5, 5634–5642.

42 Alayoglu, S., Nilekar, A.U., Mavrikakis, M., Eichhorn, B. (2008). Ru–Pt core–shell nanoparticles for preferential oxidation of carbon monoxide in hydrogen. *Nature Materials*, 7 (4), 333–338.

43 Nilekar, A.U., Alayoglu, S., Eichhorn, B., Mavrikakis, M. (2010). Preferiential CO oxidation in hydrogen: reactivity of core–shell nanoparticles. *Journal of the American Chemical Society*, 132 (21), 7418–7428.

44 Alayoglu, S., Eichhorn, B. (2008). Rh–Pt bimetallic catalysts: synthesis, characterizaiton and catalysis of core–shell, alloy, and monometallic nanoparticles. *Journal of the American Chemical Society*, 130 (51), 17479–17486.

45 Zhang, H., Jin, M., Liu, H., Wang, J., Kim, M.J., Yang, D., Xie, Z., Liu, J., Xia, Y. (2011). Facile synthesis of Pd–Pt alloy nanocages and their enhanced performance for preferential oxidation of CO in excess hydrogen. *ACS Nano*, 5 (10), 8212–8222.

46 Mallat, T., Baiker, A. (2000). Preface—catalytic oxidation for the synthesis of specialty and fine chemicals. *Catalysis Today*, 57 (1–2), 1–2.

47 Sheldon, R.A., Arends, I.W.C.E., Ten Brink, G.J., Dijksman, A. (2002). Green, catalytic oxidations of alcohols. *Accounts of Chemical Research*, 35 (9), 774–781.

48 Tsunoyama, H., Sakurai, H., Negishi, Y., Tsukuda, T. (2005). Size-specific catalytic activity of polymer-stabilized gold nanoclusters for aerobic alcohol oxidation in water. *Journal of the American Chemical Society*, 127 (26), 9374–9375.

49 Liu, J., Yang, H.Q., Kleitz, F., Chen, Z.G., Yang, T.Y., Strounina, E., Lu, G.Q., Qiao, S.Z. (2012). Yolk–shell hybrid materials with a periodic mesoporous organosilica shell: ideal nanoreactors for selective alcohol oxidation. *Advanced Functional Materials*, 22 (3), 591–599.

50 Villa, A., Janjic, N., Spontoni, P., Wang, D., Su, D.S., Prati, L. (2009). Au–Pd/AC as catalysts for alcohol oxidation: effect of reaction parameters on catalytic activity and selectivity. *Applied Catalysis A-General*, 364 (1–2), 221–228.

51 Xie, X.W., Li, Y., Liu, Z.Q., Haruta, M., Shen, W.J. (2009). Low-temperature oxidation of CO catalysed by Co_3O_4 nanorods. *Nature*, 458 (7239), 746–749.

52 Haruta, M., Tsubota, S., Kobayashi, T., Kageyama, H., Genet, M.J., Delmon, B. (1993). Low-temperature oxidation of Co over gold supported on TiO_2, Alpha-Fe_2O_3, and Co_3O_4. *Journal of Catalysis*, 144 (1), 175–192.

53 Abad, A., Concepcion, P., Corma, A., Garcia, H. (2005). A collaborative effect between gold and a support induces the selective oxidation of alcohols. *Angewandte Chemie–International Edition*, 44 (26), 4066–4069.

54 Liu, Y., Tsunoyama, H., Akita, T., Xie, S., Tsukuda, T. (2011). Aerobic oxidation of cyclohexane catalyzed by size-controlled Au clusters on hydroxyapatite: size effect in the sub-2 nm regime. *ACS Catalysis*, 1 (1), 2–6.

55 Enache, D.I., Edwards, J.K., Landon, P., Solsona-Espriu, B., Carley, A.F., Herzing, A.A., Watanabe, M., Kiely, C.J., Knight, D.W., Hutchings, G.J. (2006). Solvent-free oxidation of primary alcohols to aldehydes using Au–Pd/TiO_2 catalysts. *Science*, 311 (5759), 362–365.

56 Mori, K., Hara, T., Mizugaki, T., Ebitani, K., Kaneda, K. (2004). Hydroxyapatite-supported palladium nanoclusters: a highly active heterogeneous catalyst for selective oxidation of alcohols by use of molecular oxygen. *Journal of the American Chemical Society*, 126 (34), 10657–10666.

57 Henning, A.M., Watt, J., Miedziak, P., Cheong, S., Santonastaso, M., Song, M., Takeda, Y., Kirkland, A.I., Taylor, S.H., Tilley, R.D. (2013). Gold-palladium core–shell nanocrystals with size and shape control optimized for catalytic performance. *Angewandte Chemie–International Edition*, 125, 1517–1520.

58 Lee, A.F., Hackett, S.F.J., Hutchings, G.J., Lizzit, S., Naughton, J., Wilson, K. (2009). In situ X-ray studies of crotyl alchohol selective oxidation over Au/Pd(111) surface alloys. *Catalysis Today*, 145, 251–257.

59 Cheong, S., Graham, L., Brett, G.L., Henning, A.M., Watt, J., Miedziak, P.J., Song, M., Takeda, Y., Taylor, S.H., Tilley, R.D. (2013). Au–Pd core–shell nanoparticles as alcohol oxidation catalysts: effect of shape and composition. *ChemSusChem*, 6 (10), 1858–1862.

60 Painter, R.M., Pearson, D.M., Waymouth, R.M. (2010). Selective catalytic oxidation of glycerol to dihydroxyacetone. *Angewandte Chemie–International Edition*, 49 (49), 9456–9459.

61 Pagliaro, M., Ciriminna, R., Kimura, H., Rossi, M., Della Pina, C. (2007). Von Glycerin zu höherwertigen Produkten. *Angewandte Chemie*, 119 (24), 4516–4522.

62 Behr, A., Eilting, J., Irawadi, K., Leschinski, J., Lindner, F. (2008). Improved utilisation of renewable resources: new important derivatives of glycerol. *Green Chemistry*, 10 (1), 13–30.

63 Ye, W., Guo, X., Xie, F., Zhu, R., Zhao, Q., Yang, J. (2014). Kinetics-controlled growth of bimetallic RhAg on Au nanorods and their catalytic properties. *Nanoscale*, 6 (8), 4258–4263.

64 Ye, W., Kou, S., Guo, X., Xie, F., Sun, H., Lu, H., Yang, J. (2015). Controlled synthesis of bimetallic Pd–Rh nanoframes and nanoboxes with high catalytic peformances. *Nanoscale*, 7 (21), 9558–9562.

65 Burawoy, A., Critchley, J.P. (1959). Electronic spectra of organic molecules and their interpretation. *Tetrahedron*, 5 (4), 340–351.

66 Corma, A., Concepción, P., Serna, P. (2007). A different reaction pathway for the reduction of aromatic nitro compounds on gold catalysts. *Angewandte Chemie*, 119 (38), 7404–7407.

67 Sheldon, R.A., Van Bekkum, H. (2008). *Fine Chemicals through Heterogeneous Catalysis*. Hoboken: John Wiley & Sons.

68 Downig, R.S., Kunkeler, P.J., van Bekkum, H. (1997). Catalytic synthesis of aromatic amines. *Catalysis Today*, 37 (2), 121–136.

69 Mitsudome, T., Mikami, Y., Matoba, M., Mizugaki, T., Jitsukawa, K., Kaneda, K. (2012). Design of a silver–cerium dioxide core–shell nanocomposite catalyst for chemoselective reduction reactions. *Angewandte Chemie–International Edition*, 51 (1), 136–139.

70 Cardenas-Lizana, F., Gomez-Quero, S., Keane, M.A. (2008). Exclusive production of chloroaniline from chloronitrobenzene over Au/TiO_2 and Au/Al_2O_3. *ChemSusChem*, 1 (3), 215–221.

71 Shimizu, K., Miyamoto, Y., Kawasaki, T., Tanji, T., Tai, Y., Satsuma, A. (2009). Chemoselective hydrogenation of nitroaromatics by supported gold catalysts: mechanistic reasons of size- and support-dependent activity and selectivity. *Journal of Physical Chemistry C*, 113 (41), 17803–17810.

72 Wang, A.Q., Liu, X.Y., Mou, C.Y., Zhang, T. (2013). Understanding the synergistic effects of gold bimetallic catalysts. *Journal of Catalysis*, 308, 258–271.

73 Serna, P., Concepción, P., Corma, A. (2009). Design of highly active and chemoselective bimetallic gold–platinum hydrogenation catalysts through kinetic and isotopic studies. *Journal of Catalysis*, 265 (1), 19–25.

74 Furukawa, S., Yoshida, Y., Komatsu, T. (2014). Chemoselective hydrogenation of nitrostyrene to aminostyrene over Pd- and Rh-based intermetallic compounds. *ACS Catalysis*, 4 (5), 1441–1450.

75 Serna, P., Boronat, M., Corma, A. (2011). Tuning the behavior of Au and Pt catalysts for the chemoselective hydrogenation of nitroaromatic compounds. *Topics in Catalysis*, 54 (5–7), 439–446.

76 Boronat, M., Corma, A. (2010). Origin of the different activity and selectivity toward hydrogenation of single metal Au and Pt on TiO_2 and bimetallic $Au–Pt/TiO_2$ Catalysts. *Langmuir*, 26 (21), 16607–16614.

77 Corma, A., Serna, P. (2006). Chemoselective hydrogenation of nitro compounds with supported gold catalysts. *Science*, 313, 332–334.

78 Furukawa, S., Takahashi, K., Komatsu, T. (2016). Well-structured bimetallic surface capable of molecular recognition for chemoselective nitroarene hydrogenation. *Chemical Science*, 7 (7), 4476–4484.

79 Iihama, S., Furukawa, S., Komatsu, T. (2016). Efficient catalytic system for chemoselective hydrogenation of halonitrobenzene to haloaniline using PtZn intermetallic compound. *ACS Catalysis*, 6 (2), 742–746.

80 Bullock, R.M. (2013). Abundant metals give precious hydrogenation performance. *Science*, 342 (6162), 1054–1055.

81 Cai, S., Duan, H., Rong, H., Wang, D., Li, L., He, W., Li, Y. (2013). Highly active and selective catalysis of bimetallic Rh_3Ni_1 nanoparticles in the hydrogenation of nitroarenes. *ACS Catalysis*, 3, 608–612.

82 Yu, Z., Liao, S., Xu, Y., Yang, B., Yu, D. (1995). A remarkable synergic effect of polymer-anchored bimetallic palladium-ruthenium catalysts in the selective hydrogenation of p-chloronitrobenzene. *Journal of the Chemical Society, Chemical Communications*, (11), 1155–1156.

83 Lu, P., Teranishi, T., Asakura, K., Miyake, M., Toshima, N. (1999). Polymer-protected Ni/Pd bimetallic nano-clusters: preparation, characterization and catalysis for hydrogenation of nitrobenzene. *Journal of Physical Chemistry B*, 103 (44), 9673–9682.

84 Haldar, K.K., Kundu, S., Patra, A. (2014). Core-size-dependent catalytic properties of bimetallic Au/Ag core–shell nanoparticles. *ACS Applied Materials & Interfaces*, 6 (24), 21946–21953.

85 Pei, Y., Maligal-Ganesh, R.V., Xiao, C., Goh, T.W., Brashler, K., Gustafson, J.A., Huang, W. (2015). An inorganic capping strategy for the seeded growth of versatile bimetallic nanostructures. *Nanoscale*, 7 (40), 16721–16728.

86 Wang, W., Wang, D., Liu, X., Peng, Q., Li, Y. (2013). Pt–Ni nanodendrites with high hydrogenation activity. *Chemical Communications*, 49 (28), 2903–2905.

87 Shi, L., Wang, A., Zhang, T., Zhang, B., Su, D., Li, H., Song, Y. (2014). One-step synthesis of Au–Pd alloy nanodendrites and their catalytic activity. *Journal of Physical Chemistry C*, 117 (24), 12526–12536.

88 Huang, X., Li, Y., Li, Y., Zhou, H., Duan, X., Huang, Y. (2012). Synthesis of Pt–Pd bimetal nanocrystals with controllable shape, composition, and their tunable catalytic properties. *Nano Letters*, 12 (8), 4265–4270.

89 Zhang, P., Hu, Y., Li, B., Zhang, Q., Zhou, C., Yu, H., Zhang, X., Chen, L., Eichhorn, B., Zhou, S. (2015). Kinetically stabilized Pd@Pt core–shell octahedral nanoparticles with thin Pt layers for enhanced catalytic hydrogenation performance. *ACS Catalysis*, 5 (2), 1335–1343.

90 Wu, Y., Cai, S., Wang, D., He, W., Li, Y. (2012). Syntheses of water-soluble octahedral, truncated octahedral, and cubic Pt–Ni nanocrystals and their structure—activity study in model hydrogenation reactions. *Journal of the American Chemical Society*, 134 (21), 8975–8981.

91 Wu, Y., Wang, D., Niu, Z., Chen, P., Zhou, G., Li, Y. (2012). A strategy for designing a concave Pt–Ni alloy through controllable chemical etching. *Angewandte Chemie–International Edition*, 51 (50), 12524–12528.

92 Tsao, Y.-C., Rej, S., Chiu, C.-Y., Huang, M.H. (2014). Aqueous phase synthesis of Au–Ag core–shell nanocrystals with tunable shapes and their optical and catalytic properties. *Journal of the American Chemical Society*, 136 (1), 396–404.

93 Li, H., Wu, H., Zhai, Y., Xu, X., Jin, Y. (2013). Synthesis of monodisperse plasmonic Au core–Pt shell concave nanocubes with superior catalytic and electrocatalytic activity. *ACS Catalysis*, 3 (9), 2045–2051.

94 Zarick, H.F., Erwin, W.R., Aufrecht, J., Coppola, A., Rogers, B.R., Pint, C.L., Bardhan, R. (2014). Morphological modulation of bimetallic nanostructures for accelerated catalysis. *Journal of Materials Chemistry A*, 2 (19), 7088–7098.

95 Prieto, G., Tuysuz, H., Duyckaerts, N., Knossalla, J., Wang, G.H., Schuth, F. (2016). Hollow nano- and microstructures as catalysts. *Chemical Reviews*, 116 (22), 14056–14119.

96 Wu, H., Wang, P., He, H., Jin, Y. (2012). Controlled synthesis of porous Ag/Au bimetallic hollow nanoshells with tunable plasmonic and catalytic properties. *Nano Research*, 5 (2), 135–144.

97 Mahmoud, M.A., Saira, F., El-Sayed, M.A. (2010). Experimental evidence for the nanocage effect in catalysis with hollow nanoparticles. *Nano Letters*, 10 (9), 3764–3769.

98 Wang, L., Yamauchi, Y. (2013). Metallic nanocages: synthesis of bimetallic Pt–Pd hollow nanoparticles with dendritic shells by selective chemical etching. *Journal of the American Chemical Society*, 135 (45), 16762–16765.

99 Xia, B.Y., Wu, H.B., Wang, X., Lou, X.W. (2012). One-pot synthesis of cubic $PtCu_3$ nanocages with enhanced electrocatalytic activity for the methanol oxidation reaction. *Journal of the American Chemical Society*, 134 (34), 13934–13937.

100 Mahmoud, M.A., El-Sayed, M.A. (2011). Time dependence and signs of the shift of the surface plasmon resonance frequency in nanocages elucidate the nanocatalysis mechanism in hollow nanoparticles. *Nano Letters*, 11 (3), 946–953.

101 Chen, J.Y., McLellan, J.M., Siekkinen, A., Xiong, Y.J., Li, Z.Y., Xia, Y.N. (2006). Facile synthesis of gold–silver nanocages with controllable pores on the surface. *Journal of the American Chemical Society*, 128 (46), 14776–14777.

102 Zhang, L., Roling, L.T., Wang, X., Vara, M., Chi, M.F., Liu, J.Y., Choi, S.I., Park, J., Herron, J.A., Xie, Z.X., Mavrikakis, M., Xia, Y.N. (2015). Platinum-based nanocages with subnanometer-thick walls and well-defined, controllable facets. *Science*, 349 (6246), 412–416.

103 Cremer, P.S., Su, X.C., Shen, Y.R., Somorjai, G.A. (1996). Ethylene hydrogenation on Pt(111) monitored in situ at high pressures using sum frequency generation. *Journal of the American Chemical Society*, 118 (12), 2942–2949.

104 Anderson, A.B., Choe, S.J. (1989). Ethylene hydrogenation mechanism on the Pt(111) surface—theoretical determination. *Journal of Physical Chemistry*, 93 (16), 6145–6149.

105 Yoo, J.W., Hathcock, D.J., El-Sayed, M.A. (2003). Propene hydrogenation over truncated octahedral Pt nanoparticles supported on alumina. *Journal of Catalysis*, 214 (1), 1–7.

106 Galvagno, S., Staiti, P., Antonucci, P., Donato, A., Pietropaolo, R. (1983). Kinetics of propene hydrogenation over platinum and platinum tin catalysts supported on polyamide. *Journal of the Chemical Society—Faraday Transactions I*, 79 (11), 2605–2612.

107 Mu, X.D., Meng, J.Q., Li, Z.C., Kou, Y. (2005). Rhodium nanoparticles stabilized by ionic copolymers in ionic liquids: long lifetime nanocluster catalysts for benzene hydrogenation. *Journal of the American Chemical Society*, 127 (27), 9694–9695.

108 Bratlie, K.M., Lee, H., Komvopoulos, K., Yang, P., Somorjai, G.A. (2007). Platinum nanoparticle shape effects on benzene hydrogenation selectivity. *Nano Letters*, 7 (10), 3097–3101.

109 Tsung, C.K., Kuhn, J.N., Huang, W., Aliaga, C., Hung, L.-I., Somorjai, G.A., Yang, P. (2009). Sub-10 nm platinum nanocrystals with size and shape control: catalytic study for ethylene and pyrrole hydrogenation. *Journal of the American Chemical Society*, 131 (16), 5816–5822.

110 Lopez, N., Vargas-Fuentes, C. (2012). Promoters in the hydrogenation of alkynes in mixtures: insights from density functional theory. *Chemical Communications*, 48 (10), 1379–1391.

111 Molnar, A., Smith, G.V., Bartok, M. (1986). Selective hydrogenation of alkynes over metallic glasses. *Journal of Catalysis*, 101 (1), 67–72.

112 Rajaram, J., Narula, A.P.S., Chawla, H.P.S., Dev, S. (1983). Semihydrogenation of acetylenes—modified lindlar catalyst. *Tetrahedron*, 39 (13), 2315–2322.

113 Panja, C., Saliba, N.A., Koel, B.E. (2001). Acetylene chemisorption on Sn/Pt(100) alloys. *Journal of Physical Chemistry B*, 105 (18), 3786–3796.

114 Chen, B., Dingerdissen, U., Krauter, J.G.E., Rotgerink, H.G.J.L., Mobus, K., Ostgard, D.J., Panster, P., Riermeier, T.H., Seebald, S., Tacke, T., Trauthwein, H. (2005). New developments in hydrogenation catalysis particularly in synthesis of fine and intermediate chemicals. *Applied Catalysis A—General*, 280 (1), 17–46.

115 Humbert, P.M., Chen, J.G. (2008). Correlating hydrogenation activity with binding energies of hydrogen and cyclohexene on M/Pt(111) (M = Fe, Co, Ni, Cu) Bimetallic Surfaces. *Journal of Catalysis*, 257 (2), 297–306.

116 Bratlie, K.M., Kliewer, C.J., Somorjai, G.A. (2006). Structure effects of benzene hydrogenation studied with sum frequency generation vibrational spectroscopy and kinetics on Pt(111) and Pt(100) single-crystal surfaces. *Journal of Physical Chemistry B*, 110 (36), 17925–17930.

117 Zhu, J., Yang, M.L., Yu, Y.D., Zhu, Y.A., Sui, Z.J., Zhou, X.G., Holmen, A., Chen, D. (2015). Size-dependent reaction mechanism and kinetics for propane dehydrogenation over Pt catalysts. *ACS Catalysis*, 5 (11), 6310–6319.

118 Grass, M.E., Yue, Y., Habas, S.E., Rioux, R.M., Teall, C.I., Yang, P., Somorjai, G.A. (2008). Silver ion mediated shape control of platinum nanoparticles: removal of silver by selective etching leads to increased catalytic activity. *Journal of Physical Chemistry C*, 112 (13), 4797–4804.

119 Schmidt, E., Vargas, A., Mallat, T., Baiker, A. (2009). Shape-selective enantioselective hydrogenation on Pt nanoparticles. *Journal of the American Chemical Society*, 131 (34), 12358–12367.

120 Hansgen, D.A., Vlachos, D.G., Chen, J.G.G. (2010). Using first principles to predict bimetallic catalysts for the ammonia decomposition reaction. *Nature Chemistry*, 2 (6), 484–489.

121 Massardier, J., Bertolini, J.C. (1984). $Pt_{0.5}Ni_{0.5}$(111) Single-crystal alloy—activity and selectivity for hydrogenation of 1,3-butadiene as compared to pure Pt(111). *Journal of Catalysis*, 90 (2), 358–361.

122 Lee, T.Y., Sarbach, S., Kuhnke, K., Kern, K. (2006). Growth and Surface Alloying of Fe on Pt(997). *Surface Science*, 600 (16), 3266–3273.

123 Barrett, N.T., Belkhou, R., Thiele, J., Guillot, C. (1995). A Core-Level Photoemission Spectroscopy Study of the Formation of Surface Alloy Cu/Pt(111) – Comparison with Pt/Cu(111). *Surface Science*, 331, 776–781.

124 Tsay, J.S., Shern, C.S. (1996). Diffusion and alloy formation of Co ultrathin films on Pt(111). *Journal of Applied Physics*, 80 (7), 3777–3781.

125 Kitchin, J.R., Khan, N.A., Barteau, M.A., Chen, J.G., Yakshinksiy, B., Madey, T.E. (2003). Elucidation of the active surface and origin of the weak metal-hydrogen bond on Ni/Pt(111) bimetallic surfaces: a surface science and density functional theory study. *Surface Science*, 544 (2–3), 295–308.

126 Menning, C.A., Hwu, H.H., Chen, J.G.G. (2006). Experimental and theoretical investigation of the stability of Pt-3d-Pt(111) bimetallic surfaces under oxygen environment. *Journal of Physical Chemistry B*, 110 (31), 15471–15477.

127 Creemers, C., Deurinck, P. (1997). Platinum segregation to the (111) surface of ordered $Pt_{80}Fe_{20}$: LEIS results and model simulations. *Surface and Interface Analysis*, 25 (3), 177–190.

128 Jeyadevan, B., Cuya, J.L., Inoue, Y., Shinoda, K., Ito, T., Mott, D., Higashimine, K., Maenosono, S., Matsumoto, T., Miyamura, H. (2014). Novel nickel–palladium catalysts encased in a platinum nanocage. *RSC Advances*, 4 (51), 26667–26672.

129 Wilhite, B.A., McCready, M.J., Varma, A. (2002). Kinetics of phenylacetylene hydrogenation over Pt/gamma-Al_2O_3 catalyst. *Industrial & Engineering Chemistry Research*, 41 (14), 3345–3350.

130 Delangel, G., Benitez, J.L. (1993). Selective hydrogenation of phenylacetylene on Pd/Al_2O_3—effect of the addition of Pt and particle-size. *Reaction Kinetics and Catalysis Letters*, 51 (2), 547–553.

131 Carturan, G., Cocco, G., Facchin, G., Navazio, G. (1984). Phenylacetylene hydrogenation with Pd, Pt and Pd–Pt alloy catalysts dispersed on amorphous supports—effect of Pt/Pd ratio on catalytic activity and selectivity. *Journal of Molecular Catalysis*, 26 (3), 375–384.

132 Crespo-Quesada, M., Dykeman, R.R., Laurenczy, G., Dyson, P.J., Kiwi-Minsker, L. (2011). Supported nitrogen-modified Pd nanoparticles for the selective hydrogenation of 1-hexyne. *Journal of Catalysis*, 279 (1), 66–74.

133 Dobrovolna, Z., Kacer, P., Cerveny, L. (1998). Competitive hydrogenation in alkene-alkyne-diene systems with palladium and platinum catalysts. *Journal of Molecular Catalysis A-Chemical*, 130 (3), 279–284.

134 Mitsudome, T., Urayama, T., Yamazaki, K., Maehara, Y., Yamasaki, J., Gohara, K., Maeno, Z., Mizugaki, T., Jitsukawa, K., Kaneda, K. (2016). Design of core-Pd/shell-Ag nanocomposite catalyst for selective semihydrogenation of alkynes. *ACS Catalysis*, 6 (2), 666–670.

135 Furukawa, S., Komatsu, T. (2016). Selective hydrogenation of functionalized alkynes to (E)-alkenes, using ordered alloys as catalysts. *ACS Catalysis*, 6 (3), 2121–2125.

136 Laska, M., Skrabalak, S.E. (2016). A balancing act: manipulating reactivity of shape-controlled metal nanocatalysts through bimetallic architecture. *J. Mater. Chem. A*, 4 (18), 6911–6918.

137 Hammer, B., Norskov, J.K. (2000). Theoretical surface science and catalysis—calculations and concepts. *Advances in Catalysis*, 45 (2000), 71–129.

138 Strasser, P., Koh, S., Anniyev, T., Greeley, J., More, K., Yu, C.F., Liu, Z.C., Kaya, S., Nordlund, D., Ogasawara, H., Toney, M.F., Nilsson, A. (2010). Lattice-strain control of the activity in dealloyed core–shell fuel cell catalysts. *Nature Chemistry*, 2 (6), 454–460.

139 Giri, G., Verploegen, E., Mannsfeld, S.C.B., Atahan-Evernk, S., Aspuru-Guzik, A., Toney, M.F., Bao, Z.N. (2012). Tuning charge transport in solution sheared organic semiconductors using lattice strain. *Nature*, 480 (7378), 504–508.

140 Kasatkin, I., Kurr, P., Kniep, B., Trunschke, A., Schlogl, R. (2007). Role of lattice strain and defects in copper particles on the activity of Cu/ZnO/Al_2O_3 catalysts for methanol synthesis. *Angewandte Chemie–International Edition*, 46 (38), 7324–7327.

141 Sárkány, A., Geszti, O., Sáfrán, G. (2008). Preparation of Pd shell–Au core/SiO_2 catalyst and catalytic activity for acetylene hydrogenation. *Applied Catalysis A-General*, 350 (2), 157–163.

142 Dugave, C., Demange, L. (2003). Cis-trans isomerization of organic molecules and biomolecules: implications and applications. *Chemical Reviews*, 103 (7), 2475–2532.

143 Lee, I., Delbecq, F., Morales, R., Albiter, M.A., Zaera, F. (2009). Tuning selectivity in catalysis by controlling particle shape. *Nature Materials*, 8 (2), 132–138.

144 Furukawa, S., Ochi, K., Luo, H., Miyazaki, M., Komatsu, T. (2015). Selective stereochemical catalysis controlled by specific atomic arrangement of ordered alloys. *ChemCatChem*, 7 (21), 3472–3479.

145 Chen, L., Li, H., Zhan, W., Cao, Z., Chen, J., Jiang, Q., Jiang, Y., Xie, Z., Kuang, Q., Zheng, L. (2016). Controlled encapsulation of flower-like Rh–Ni alloys with MOFs via tunable template dealloying for enhanced selective hydrogenation of alkyne. *ACS Applied Materials & Interfaces*, 8 (45), 31059–31066.

146 Gallezot, P., Richard, D. (1998). Selective hydrogenation of α,β-unsaturated aldehydes. *Catalysis Reviews*, 40 (1–2), 81–126.

147 Claus, P. (1998). Selective hydrogenation of alpha, beta-unsaturated aldehydes and other C = O and C = C bonds containing compounds. *Topics in Catalysis*, 5 (1–4), 51–62.

148 Blackmond, D.G., Oukaci, R., Blanc, B., Gallezot, P. (1991). Geometric and electronic effects in the selective hydrogenation of alpha,beta-unsaturated aldehydes over zeolite-supported metals. *Journal of Catalysis*, 131 (2), 401–411.

149 Wu, J.C.S., Cheng, T.S., Lai, C.L. (2006). Boron nitride supported PtFe catalysts for selective hydrogenation of crotonaldehyde. *Applied Catalysis A-General*, 314 (2), 233–239.

150 Li, Y., Zhu, P.F., Zhou, R.X. (2008). Selective hydrogenation of cinnamaldehyde to cinnamyl alcohol with carbon nanotubes supported Pt–Co catalysts. *Applied Surface Science*, 254 (9), 2609–2614.

151 Poltarzewski, Z., Galvagno, S., Pietropaolo, R., Staiti, P. (1986). Hydrogenation of alpha, beta-unsaturated aldehydes over Pt–Sn/nylon. *Journal of Catalysis*, 102 (1), 190–198.

152 Yuan, Y., Yao, S., Wang, M., Lou, S., Yan, N. (2013). Recent progress in chemoselective hydrogenation of α, β-unsaturated aldehyde to unsaturated alcohol over nanomaterials. *Current Organic Chemistry*, 17 (4), 400–413.

153 Astruc, D. (2008). *Nanoparticles and Catalysis* Hoboken, NJ: John Wiley & Sons.

154 Song, S., Liu, R., Zhang, Y., Feng, J., Liu, D., Xing, Y., Zhao, F., Zhang, H. (2010). Colloidal noble-metal and bimetallic alloy nanocrystals: a general synthetic method and their catalytic hydrogenation properties. *Chemistry*, 16 (21), 6251–6256.

155 Zheng, J.W., Lin, H.Q., Wang, Y.N., Zheng, X.L., Duan, X.P., Yuan, Y.Z. (2013). Efficient low-temperature selective hydrogenation of esters on bimetallic Au–Ag/SBA-15 catalyst. *Journal of Catalysis*, 297, 110–118.

156 Vu, K.B., Bukhryakov, K.V., Anjum, D.H., Rodionov, V.O. (2015). surface-bound ligands modulate chemoselectivity and activity of a bimetallic nanoparticle catalyst. *ACS Catalysis*, 5 (4), 2529–2533.

157 Tsang, S.C., Cailuo, N., Oduro, W., Kong, A.T.S., Clifton, L., Yu, K.M.K., Thiebaut, B., Cookson, J., Bishop, P. (2008). Engineering preformed cobalt-doped platinum nanocatalysts for ultraselective hydrogenation. *ACS Nano*, 2 (12), 2547–2553.

158 Sadeghmoghaddam, E., Gu, H., Shon, Y.-S. (2012). Pd nanoparticle-catalyzed isomerization vs hydrogenation of allyl alcohol: solvent-dependent regioselectivity. *ACS Catalysis*, 2 (9), 1838–1845.

159 Xian, J., Hua, Q., Jiang, Z., Ma, Y., Huang, W. (2012). Size-dependent interaction of the poly(N-vinyl-2-pyrrolidone) capping ligand with Pd nanocrystals. *Langmuir*, 28 (17), 6736–6741.

160 Kwon, S.G., Krylova, G., Sumer, A., Schwartz, M.M., Bunel, E.E., Marshall, C.L., Chattopadhyay, S., Lee, B., Jellinek, J., Shevchenko, E.V. (2012). Capping ligands as selectivity switchers in hydrogenation reactions. *Nano Letters*, 12 (10), 5382–5388.

161 Wu, B., Huang, H., Yang, J., Zheng, N., Fu, G. (2012). Selective hydrogenation of alpha, beta-unsaturated aldehydes catalyzed by amine-capped platinum-cobalt nanocrystals. *Angewandte Chemie-International Edition*, 51 (14), 3440–3443.

162 Alhumaidan, F., Cresswell, D., Garforth, A. (2011). Hydrogen storage in liquid organic hydride: producing hydrogen catalytically from methylcyclohexane. *Energy & Fuels*, 25 (10), 4217–4234.

163 Au, M., Meziani, M.J., Sun, Y.P., Pinkerton, F.E. (2011). Synthesis and performance evaluation of bimetallic lithium borohydrides as hydrogen storage media. *Journal of Physical Chemistry C*, 115 (42), 20765–20773.

164 Singh, S.K., Singh, A.K., Aranishi, K., Xu, Q. (2011). Noble-metal-free bimetallic nanoparticle-catalyzed selective hydrogen generation from hydrous hydrazine for chemical hydrogen storage. *Journal of the American Chemical Society*, 133 (49), 19638–19641.

165 Singh, S.K., Xu, Q.A. (2010). Bimetallic Ni–Pt nanocatalysts for selective decomposition of hydrazine in aqueous solution to hydrogen at room temperature for chemical hydrogen storage. *Inorganic Chemistry*, 49 (13), 6148–6152.

166 Chambers, M.B., Kurtz, D.A., Pitman, C.L., Brennaman, M.K., Miller, A.J.M. (2016). Efficient photochemical dihydrogen generation initiated by a bimetallic self-quenching mechanism. *Journal of the American Chemical Society*, 138 (41), 13509–13512.

167 Yu, W.Y., Mullen, G.M., Flaherty, D.W., Mullins, C.B. (2014). Selective hydrogen production from formic acid decomposition on Pd–Au bimetallic surfaces. *Journal of the American Chemical Society*, 136 (31), 11070–11078.

168 Graetz, J. (2009). New approaches to hydrogen storage. *Chemical Society Reviews*, 38 (1), 73–82.

169 Jiang, H.L., Umegaki, T., Akita, T., Zhang, X.B., Haruta, M., Xu, Q. (2010). Bimetallic Au–Ni nanoparticles embedded in SiO_2 nanospheres: synergetic catalysis in hydrolytic dehydrogenation of ammonia borane. *Chemistry–A European Journal*, 16 (10), 3132–3137.

170 Tsai, C.W., Chen, H.M., Liu, R.S., Lee, J.F., Chang, S.M., Weng, B.J. (2012). Magnetically recyclable Fe@Co core–shell catalysts for dehydrogenation of sodium borohydride in fuel cells. *International Journal of Hydrogen Energy*, 37 (4), 3338–3343.

171 Rioux, R.M., Vannice, M.A. (2005). Hydrogenation/dehydrogenation reactions: isopropanol dehydrogenation over copper catalysts. *Journal of Catalysis*, 234 (1), 247–247.

172 Esswein, A.J., Nocera, D.G. (2007). Hydrogen production by molecular photocatalysis. *Chemical Reviews*, 107 (10), 4022–4047.

173 Belkova, N.V., Epstein, L.M., Filippov, O.A., Shubina, E.S. (2016). Hydrogen and dihydrogen bonds in the reactions of metal hydrides. *Chemical Reviews*, 116 (15), 8545–8587.

174 Zhan, W.W., Zhu, Q.L., Xu, Q. (2016). Dehydrogenation of ammonia borane by metal nanoparticle catalysts. *ACS Catalysis*, 6 (10), 6892–6905.

175 Jiang, X., Yan, X.X., Ren, W.Y., Jia, Y.F., Chen, J.N., Sun, D.M., Xu, L., Tang, Y.W. (2016). Porous AgPt@Pt nanooctahedra as an efficient catalyst toward formic acid oxidation with predominant dehydrogenation pathway. *ACS Applied Materials & Interfaces*, 8 (45), 31076–31082.

176 Du, P., Wu, P., Cai, C.X. (2015). Mechanistic insight into the facet-dependent adsorption of methanol on a Pt_3Ni nanocatalyst. *Journal of Physical Chemistry C*, 119 (32), 18352–18363.

177 Suh, M.P., Park, H.J., Prasad, T.K., Lim, D.W. (2012). Hydrogen storage in metal-organic frameworks. *Chemical Reviews*, 112 (2), 782–835.

178 Wen, M., Zhou, S., Wu, Q., Zhang, J., Wu, Q., Wang, C., Sun, Y. (2013). Construction of NiCo–Pt nanopolyhedron inlay-structures and their highly efficient catalysis hydrolytic dehydrogenation toward ammonia borane. *Journal of Power Sources*, 232, 86–93.

179 Zhang, Y., Huang, W., Habas, S.E., Kuhn, J.N., Grass, M.E., Yamada, Y., Yang, P., Somorjai, G.A. (2008). Near-monodisperse Ni–Cu bimetallic nanocrystals of variable composition: controlled synthesis and catalytic activity for H_2 generation. *Journal of Physical Chemistry C*, 112 (32), 12092–12095.

180 Zhang, Z.P., Zhu, W., Yan, C.H., Zhang, Y.W. (2015). Selective synthesis of rhodium-based nanoframe catalysts by chemical etching of 3d metals. *Chemical Communications*, 51 (19), 3997–4000.

181 Aronovitch, E., Kalisman, P., Mangel, S., Houben, L., Amirav, L., Bar-Sadan, M. (2015). Designing bimetallic co-catalysts: a party of two. *The Journal of Physical Chemistry Letters*, 6 (18), 3760–3764.

182 Schmidt, N.G., Eger, E., Kroutil, W. (2016). Building bridges: biocatalytic C–C-bond formation toward multifunctional products. *ACS Catalysis*, 6 (7), 4286–4311.

183 Ren, T. (2008). Peripheral covalent modification of inorganic and organometallic compounds through C–C bond formation reactions. *Chemical Reviews*, 108 (10), 4185–4207.

184 Partyka, D.V. (2011). Transmetalation of unsaturated carbon nucleophiles from boron-containing species to the mid to late d-block metals of relevance to catalytic C–X coupling reactions (X = C, F, N, O, Pb, S, Se, Te). *Chemical Reviews*, 111 (3), 1529–1595.

185 Magano, J., Dunetz, J.R. (2015). Large-scale applications of transition metal-catalyzed couplings for the synthesis of pharmaceuticals. *Chemical Reviews*, 111 (3), 2177–2250.

186 Miyaura, N., Yamada, K., Suzuki, A. (1979). New stereospecific cross-coupling by the palladium-catalyzed reaction of 1-alkenylboranes with 1-alkenyl or 1-alkynyl halides. *Tetrahedron Letters*, 20 (36), 3437–3440.

187 Wolfe, J.P., Buchwald, S.L. (1999). A highly active catalyst for the room-temperature amination and Suzuki coupling of aryl chlorides. *Angewandte Chemie-International Edition*, 38 (16), 2413–2416.

188 Miyaura, N., Suzuki, A. (1995). Palladium-catalyzed cross-coupling reactions of organoboron compounds. *Chemical Reviews*, 95 (7), 2457–2483.

189 Negishi, E.I., King, A.O., Klima, W.L., Patterson, W., Silveira, A. (1980). Conversion of methyl ketones into terminal acetylenes and (E)-trisubstituted olefins of terpenoid origin. *Journal of Organic Chemistry*, 45 (12), 2526–2528.

190 Negishi, E., Matsushita, H., Okukado, N. (1981). Selective carbon–carbon bond formation via transition-metal catalysis. 20. Highly selective synthesis of allylated arenes and diarylmethanes via palladium-catalyzed cross coupling involving benzylic derivatives. *Tetrahedron Letters*, 22 (29), 2715–2718.

191 Stille, J.K. (1986). The palladium-catalyzed cross-coupling reactions of organotin reagents with organic electrophiles. *Angewandte Chemie-International Edition*, 25 (6), 508–523.

192 Scott, W.J., Stille, J.K. (1986). Palladium-catalyzed coupling of vinyl triflates with organostannanes—synthetic and mechanistic studies. *Journal of the American Chemical Society*, 108 (11), 3033–3040.

193 Dieck, H.A., Heck, F.R. (1975). Palladium catalyzed synthesis of aryl, heterocyclic and vinylic acetylene derivatives. *Journal of Organometallic Chemistry*, 93 (2), 259–263.

194 Fischetti, W., Mak, K.T., Stakem, F.G., Kim, J.I., Rheingold, A.L., Heck, R.F. (1983). Palladium-catalyzed syntheses of conjugated polyenes. *Journal of Organic Chemistry*, 48 (7), 948–955.

195 Takahashi, S., Kuroyama, Y., Sonogashira, K., Hagihara, N. (1980). A convenient synthesis of ethynylarenes and diethynylarenes. *Synthesis-Stuttgart*, (8), 627–630.

196 Sonogashira, K. (2002). Development of Pd–Cu catalyzed cross-coupling of terminal acetylenes with sp(2)-carbon halides. *Journal of Organometallic Chemistry*, 653 (1–2), 46–49.

197 Fanta, P.E. (1946). The ullmann synthesis of biaryls. *Chemical Reviews*, 38 (1), 139–196.

198 Souillart, L., Cramer, N. (2015). Catalytic C–C bond activations via oxidative addition to transition metals. *Chemical Reviews*, 115 (17), 9410–9464.

199 Negishi, E., Anastasia, L. (2003). Palladium-catalyzed alkynylation. *Chemical Reviews*, 103 (5), 1979–2017.

200 Phan, N.T.S., Van Der Sluys, M., Jones, C.W. (2006). On the nature of the active species in palladium catalyzed Mizoroki-Heck and Suzuki-Miyaura couplings—homogeneous or heterogeneous catalysis, a critical review. *Advanced Synthesis & Catalysis*, 348 (6), 609–679.

201 Andrews, S.P., Stepan, A.F., Tanaka, H., Ley, S.V., Smith, M.D. (2005). Heterogeneous or homogeneous? A case study involving palladium-containing perovskites in the Suzuki reaction. *Advanced Synthesis & Catalysis*, 347 (5), 647–654.

202 Calo, V., Nacci, A., Monopoli, A., Montingelli, F. (2005). Pd nanoparticles as efficient catalysts for Suzuki and Stille coupling reactions of aryl halides in ionic liquids. *Journal of Organic Chemistry*, 70 (15), 6040–6044.

203 Balanta, A., Godard, C., Claver, C. (2011). Pd nanoparticles for C–C coupling reactions. *Chemical Society Reviews*, 40 (10), 4973–4985.

204 Son, S.U., Jang, Y., Park, J., Na, H.B., Park, H.M., Yun, H.J., Lee, J., Hyeon, T. (2004). Designed synthesis of atom-economical Pd/Ni bimetallic nanoparticle-based catalysts for sonogashira coupling reactions. *Journal of the American Chemical Society*, 126 (16), 5026–5027.

205 Reetz, M.T., Breinbauer, R., Wanninger, K. (1996). Suzuki and Heck reactions catalyzed by preformed palladium clusters and palladium/nickel bimetallic clusters. *Tetrahedron Letters*, 37 (26), 4499–4502.

206 Lipshutz, B.H., Nihan, D.M., Vinogradova, E., Taft, B.R., Bogkovic, Z.V. (2008). Copper plus nickel-in-charcoal (Cu–Ni/C): a bimetallic, heterogeneous catalyst for cross-couplings. *Organic Letters*, 10 (19), 4279–4282.

207 Felpin, F.X., Fouquet, E. (2008). Heterogeneous multifunctional catalysts for tandem processes: an approach toward sustainability. *ChemSusChem*, 1 (8–9), 718–724.

208 Rai, R.K., Gupta, K., Behrens, S., Li, J., Xu, Q., Singh, S.K. (2015). Highly active bimetallic nickel–palladium alloy nanoparticle catalyzed Suzuki-Miyaura reactions. *ChemCatChem*, 7 (12), 1806–1812.

209 Wu, Y., Wang, D., Zhao, P., Niu, Z., Peng, Q., Li, Y. (2011). Monodispersed Pd–Ni nanoparticles: composition control synthesis and catalytic properties in the Miyaura-Suzuki reaction. *Inorganic Chemistry*, 50 (6), 2046–2048.

210 Somorjai, G.A., Blakely, D.W. (1975). Mechanism of catalysis of hydrocarbon reactions by platinum surfaces. *Nature*, 258 (5536), 580–583.

211 Tian, N., Zhou, Z.Y., Sun, S.G., Ding, Y., Wang, Z.L. (2007). Synthesis of tetrahexahedral platinum nanocrystals with high-index facets and high electro-oxidation activity. *Science*, 316 (5825), 732–735.

212 Wang, F., Li, C., Sun, L.D., Wu, H., Ming, T., Wang, J., Yu, J.C., Yan, C.H. (2011). Heteroepitaxial growth of high-index-faceted palladium nanoshells and their catalytic performance. *Journal of the American Chemical Society*, 133 (4), 1106–1111.

213 Hong, J.W., Kim, M., Kim, Y., Han, S.W. (2012). Trisoctahedral Au–Pd alloy nanocrystals with high-index facets and their excellent catalytic performance. *Chemistry*, 18 (52), 16626–16630.

214 Yang, C.W., Chanda, K., Lin, P.H., Wang, Y.N., Liao, C.W., Huang, M.H. (2011). Fabrication of Au–Pd core–shell heterostructures with systematic shape evolution using octahedral nanocrystal cores and their catalytic activity. *Journal of the American Chemical Society*, 133 (49), 19993–20000.

215 Wu, Y., Wang, D., Chen, X., Zhou, G., Yu, R., Li, Y. (2013). Defect-dominated shape recovery of nanocrystals: a new strategy for trimetallic catalysts. *Journal of the American Chemical Society*, 135 (33), 12220–12223.

216 Wegner, H.A., Auzias, M. (2011). Gold for C–C coupling reactions: a Swiss-army-knife catalyst? *Angewandte Chemie-International Edition*, 50 (36), 8236–8247.

217 Huang, X., Li, Y., Chen, Y., Zhou, E., Xu, Y., Zhou, H., Duan, X., Huang, Y. (2013). Palladium-based nanostructures with highly porous features and perpendicular pore channels as enhanced organic catalysts. *Angewandte Chemie-International Edition*, 52 (9), 2520–2524.

218 Xu, J., Wilson, A.R., Rathmell, A.R., Howe, J., Chi, M., Wiley, B.J. (2011). Synthesis and catalytic properties of Au–Pd nanoflowers. *ACS Nano*, 5 (8), 6119–6127.

219 Wang, S.-B., Zhu, W., Ke, J., Lin, M., Zhang, Y.-W. (2014). Pd–Rh nanocrystals with tunable morphologies and compositions as efficient catalysts toward Suzuki cross-coupling reactions. *ACS Catalysis*, 4 (7), 2298–2306.

220 Li, H., Zhu, Z., Li, H., Li, P., Zhou, X. (2010). Recyclable hollow Pd–Fe nanospheric catalyst for Sonogashira-, Heck-, and Ullmann-type coupling reactions of aryl halide in aqueous media. *Journal of Colloid and Interface Science*, 349 (2), 613–619.

12

Plasmonics

Liang Zhou, Tian Zhao, Xiao-Yong Wang, Ling-Dong Sun, and Chun-Hua Yan

College of Chemistry and Molecular Engineering, Peking University, Beijing, China

In the past few decades, the nanostructures of noble metals, such as gold, silver, palladium, with unique surface plasmon resonance (SPR) phenomena and applications in optics, electronics, catalysis, photochemistry and magnetism, have attracted wide research attention[1–8]. More researchers are engaged in regulating the SPR frequency of this monodisperse nanoparticles to meet the requirements for application. The local electric field generated by the surface plasmon can enhance the fluorescence and Raman signal of the nearby dye molecules, which has great potential for use in detection and medical imaging.

12.1 Introduction to Plasmonics

In 1875, Dr. Michael Faraday first reported the bright red color of gold sol, which could be adjusted between the ruby and the amethyst color[9]. Faraday listed a number of factors that may affect the color of the gold nanoparticles, and demonstrated that small changes in particle size would change the color of the sol. This comprehensive paper is the foundation of modern colloidal science. Faraday's report also trigged the experimental and theoretical studies on metal particles. The color of the metal solution was further studied with scattering and classical electromagnetic theory. After years of research, it was found that the unique optical properties of the noble metal nanostructures, especially the local SPR properties, are due to the interaction of the incident electromagnetic field with the free electrons of the noble metal nanostructures.

Plasmon is the collective oscillation of free electrons[10] with respect to positive nuclei of a metal atom. When interacting with a light filed, the electric field of an electromagnetic wave makes the electron moves away from its balance site, but the positive nuclei enforce it to move back. This makes the free electrons oscillate under light. If the light frequency is lower than the plasma frequency, it will be reflected. On the contrary, it will

Bimetallic Nanostructures: Shape-Controlled Synthesis for Catalysis, Plasmonics, and Sensing Applications, First Edition. Edited by Ya-Wen Zhang.
© 2018 John Wiley & Sons Ltd. Published 2018 by John Wiley & Sons Ltd.

transmit into metal, although decay exponentially with penetration depth. As for the plasma frequency, ω_p, can be expressed as:

$$\omega_{p=\sqrt{ne^2/m\varepsilon_0}}$$

where n is the electron density, e is the electron charge, m is the electron mass, and ε_0 is the permittivity of the free space, respectively. As n is large enough for a metal, its plasma frequency is generally located in the UV region. In this case, the visible light is reflected, which makes metal glitter in the visible range. Plasma is one of the most important properties of metals (Figure 12.1a).

For a metal nanoparticle, the plasmon is confined at the surface, taking the form of surface plasmon, as localized surface plasmon (Figure 12.1b). It strongly interacts with light, resulting in polaritons at the vacuum interface. As the plasmon is excited, light will be coupled with the plasmons, and electric part of light wave will oscillate resonantly. This is one of the most important phenomenon of metal nanoparticles, surface

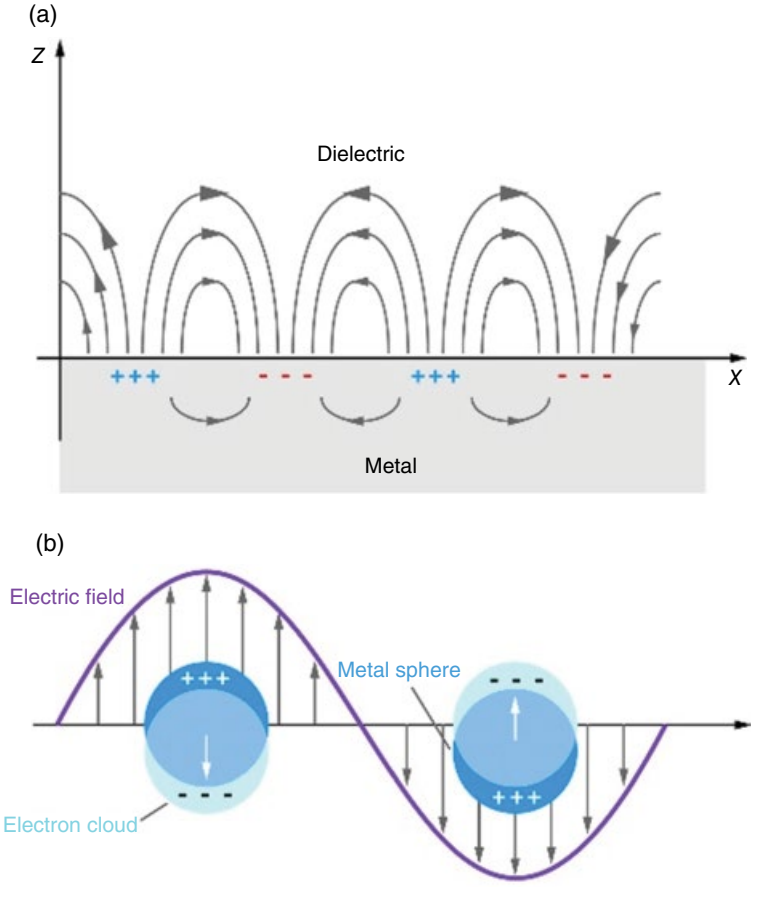

Figure 12.1 Schematic illustration of (a) surface plasmon and (b) a localized surface plasmon. Reprinted with permission from ref. [10]. Copyright (2007), Annual Reviews.

plasmon resonance, SPR. The SPR frequency of gold is located in the visible; it absorbs green light and red is transmitted, which make the colloidal solution appears gemstone red, as Faraday reported. It will red-shift with increasing particle size, but the color is still red. If the shape changes into an anisotropic one, such as rod-like, two-resonance mode will arise. Besides the radial one at green region, a longitudinal one comes from electron resonance along the axial, located in the longer wavelength, also appears. And two absorption bands can be noticed from the absorption spectra. This changes the color of the sol.

The resonance of this free electrons leads to strong optical extinction including scattering and absorption. The SPR frequency of the noble metal nanostructures is determined by a number of influencing factors, such as the size[11], shape, agglomeration state[10], composition[12], surface charge and dielectric surroundings[13, 14], etc. When the shape or size of a nanoparticle changes, its surface geometry changes will lead to changes in the frequency of free electrons, and accordingly, the light absorption and scattering will also change.

Taking the gold nanorod as an example, simply changing the aspect ratio can change its longitudinal SPR from the visible to the near infrared region (Figure 12.2). On the other hand, changing the dielectric constant of the nanostructured solution environment will affect the charge density on the surface of the nanoparticles, and also lead to changes in the vibration frequency of free electrons in the noble metal nanoparticles. As the surface plasmon is located within the visible range, the aqueous solution of the noble metal nanostructure exhibits a bright color, which is not available for its bulk

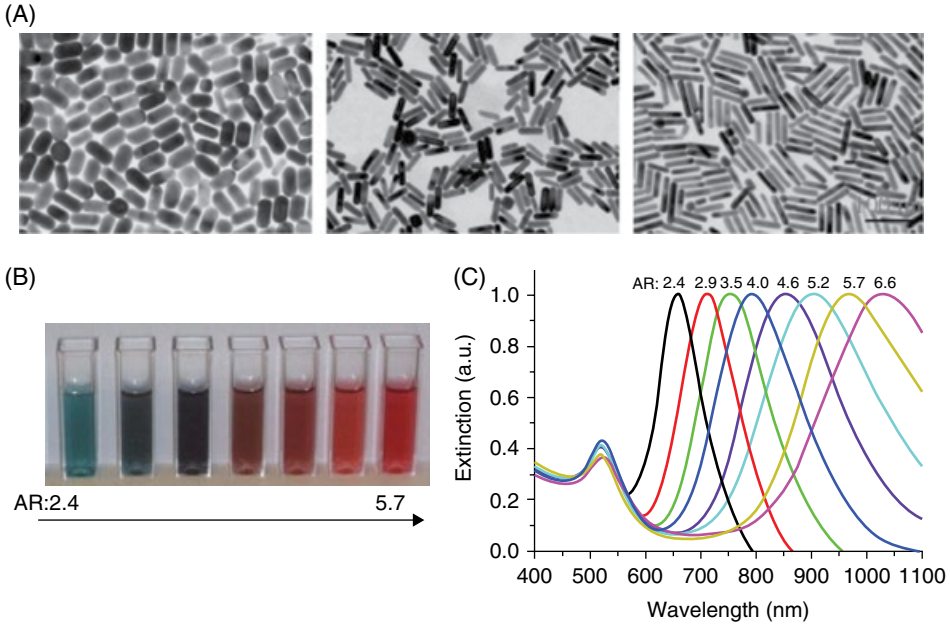

Figure 12.2 Tunable optical properties of gold nanorods by changing the aspect ratios. Gold nanorods of different aspect ratios exhibit different dimensions as seen by TEM (A), in different color (B) and different SPR wavelength (C). Reprinted with permission from ref. [11]. Copyright (2010), Elsevier Ltd.

counterpart. In addition to the solution environment, molecules that chemically bond to the surface of the nanoparticles will also change the charge density on their surface, resulting in the movement of the SPR band. This method can be used to detect the presence of molecules that are linked to noble metal nanoparticles[15]. Based on its local SPR, noble metal nanostructures can be used for chemical detection, modulation, and amplification of multiple optical signals[16, 17].

Due to the concern of the plasma resonance properties of the noble metal surface, a series of theoretical studies have been carried out on the SPR of gold nanoparticles. Mie et al. initially calculated SPR by solving the Maxwell equation of gold nanospheres interacting with the electromagnetic field. Later, Gans et al. extended this theory to the calculation of short cylinder rods with the consideration of dipole oscillations. Discrete dipole approximation (DDA), a powerful numerical method to calculate optical properties of gold with arbitrary geometry and composition, was developed to simulate the SPR band. Similarly, time domain finite difference method (FDTD) is also used to calculate and simulate the SPR of noble metal nanostructures with arbitrary geometries[8].

The nonspherical noble metal nanoparticles typically have two or more SPR modes compared to spherical nanoparticles, which having only one SPR mode. The adjustable amplitude of the SPR of the nonspherical noble metal nanoparticles is also larger than that of the spherical ones. Therefore, the nonspherical nanoparticles have more important application prospects in many fields. The gold nanorods have both radial and axial SPR modes, which correspond to the vertical and parallel to the electrons in the axial direction of the nanorods. The radial SPR wavelength near 520 nm is consistent with that of the spherical particles and does not change with the aspect ratio. The axial SPR wavelength is linearly dependent with the aspect ratio, so the deviation of particle shape from sphere will cause a significant change in the color of the solution[2, 16, 18].

Moreover, the noble metal nanorods with quasi-one-dimensional structures have a curvature greater at the end than the same volume of nanospheres. Since the local electric field enhancement is correlated with the increasing particle curvature[19], the nanorod tip will have a stronger local electric field, resulting in a stronger surface-enhanced Raman scattering (SERS)[20]. Recently, the control of the shape of the noble metal nanostructures has received extensive attention. And noble metal nanoparticles with various shapes and structures have been successfully synthesized as shown in Figure 12.3, including nanorods[21, 22], nanowires[23], nanocubes[24], nancages[25], nanopalte[26], and nanopolyhedra[27].

12.2 Preparation of Gold Nanoparticles

The first synthesis of gold nanoparticles can be traced back to the fifth or fourth century BC and products containing gold nanoparticles have been found in China and Egypt. Since then, gold nanoproducts had been widely used in art products and drugs. One of the most famous arts is the *Lycurgus Cup*, which is preserved in the British Museum of London. It was made in Rome in the fourth century. It appears green in reflect light, but red in transmittance. Barber proved that the reason for this phenomenon was that the glass produced in the *Lycurgus Cup* contained about 70 nm gold-silver alloy particles[28].

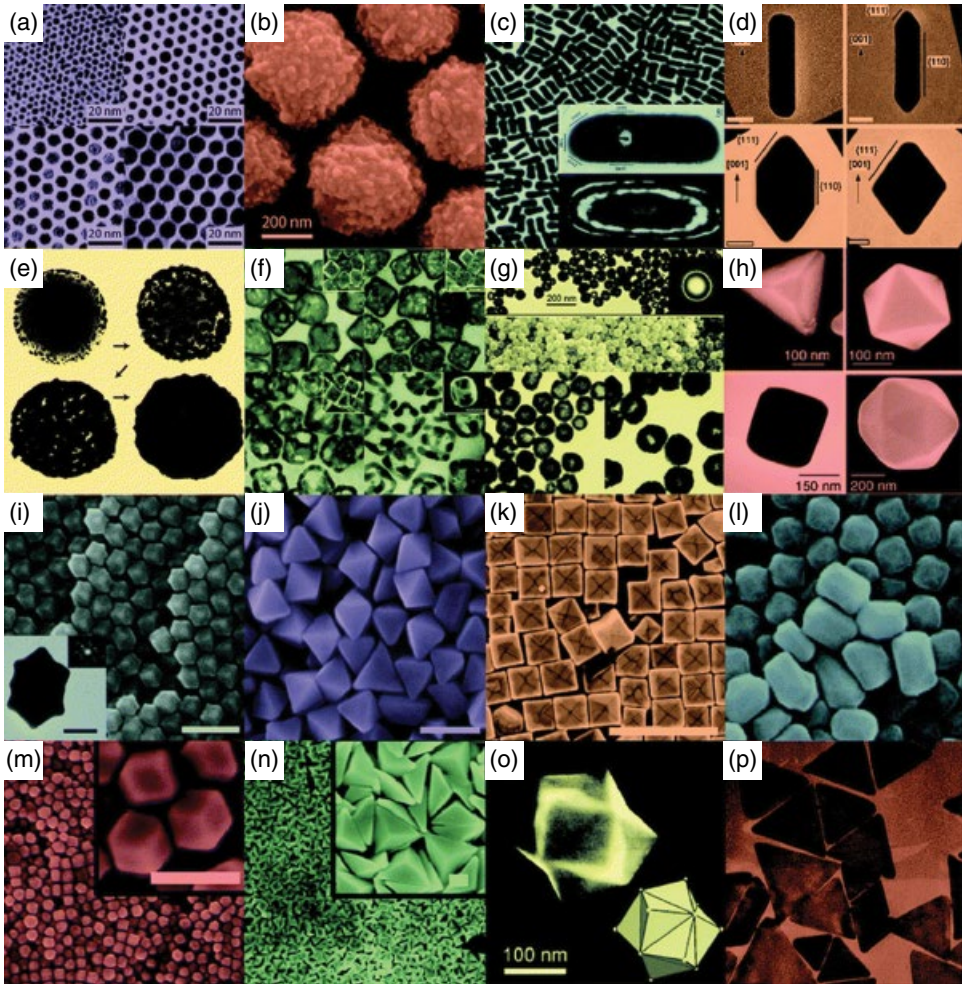

Figure 12.3 Gold nanoparticles of various size and shape. (a) Small and (b) large nanospheres (c) end- obtuse nanorods (d) end-sharpened nanorods (e) nanoshells (f) nanocages (g) hollow nanospheres (h) tetrahedron, octahedron, cube, icosahedron nanopolyhedra (i) rhombic dodecahedra (j) octahedra (k) concave nanocubes (l) tetrahexahedra (m) rhombic dodecahedra (n) obtuse triangular bipyramids (o) trisoctahedra, and (p) nanoplates. Reprint with permission from ref. [27]. Copyright (2012), Royal Society of Chemistry.

The fine particles reported by Michael Faraday were formed from the reduction of gold chloride by phosphorus. Until recently, most of colloidal synthetic methods for gold nanoparticles followed a similar way, as dissolved gold salt is reduced. In the presence of surface-capping ligands, the nanoparticles can now be separated by electrostatic repulsion. Sodium borohydride is used as the reductant, and thiol group and halide containing surfactants are generally used to protect the nanoparticles from aggregation.

In recent decades, attempts have been made to develop and improve various methods for synthesizing a variety of noble metal nanostructures, including photolithography, electron beam lithography, electrochemical deposition with templates[29, 30]

photochemical synthesis, acoustic chemistry, thermal decomposition techniques, and seed-induced chemical reduction techniques[22, 24]. Among them, triangular nanoparticles were prepared by photochemical methods[26], arrays of triangular nanoparticles were prepared by nanosphere template lithography[31].

There are a number of wet chemistry methods to prepare of gold nanostructures. Gold nanorods were prepared with the alumina template using electrochemical deposition[32, 33]. Cetyltrimethylammonium chloride (CTAC 25–30 wt%) was used as a soft template[32], and the morphology of the particles evolved from sphere into wormlike one. Schönenberger et al.[34] reported a method of preparing gold nanowires using etched polycarbonate membranes as templates. Yu et al.[33] developed an electrochemical reduction method to get gold nanorods in the presence of cationic surfactants. The yield of the gold nanorods was much higher than that of the porous alumina template. Photochemical methods were used to synthesis single crystal gold nanorods with a high yield[35]. Additional progress in the synthesis is seed-mediated growth of good-quality gold nanorods, obtained by Murphy et al. [22–24].

At present, the seed-mediated growth and overgrowth method is one of the most effective wet chemical techniques for the synthesis of gold nanoparticles[36]. The process is schematic described in Figure 12.4. The origin of this method can be traced back to the 1920s[2] and it has been extensively studied for preparation of monodisperse metal nanoparticles. Nearly monodispersed Au nanorods with a very high yields and uniformity was obtained with this method, with two steps of seed preparation and nanoparticle growth with seed. In a typical synthesis, gold seeds, ~1.5 nm small Au nanoparticles, are first prepared by reducing chloroauric acid with sodium borohydride in an aqueous CTAB solution. A certain amount of the seed solution is then added into gold precursors solution, which is obtained by reducing chloroauric acid to Au(I) complex ions with ascorbic acid in an aqueous CTAB solution. The added seeds thereafter catalyze the further reduction of Au(I) to form Au nanorods. In addition to gold nanorods, the seed-mediated method has been used for the growth of spherical gold

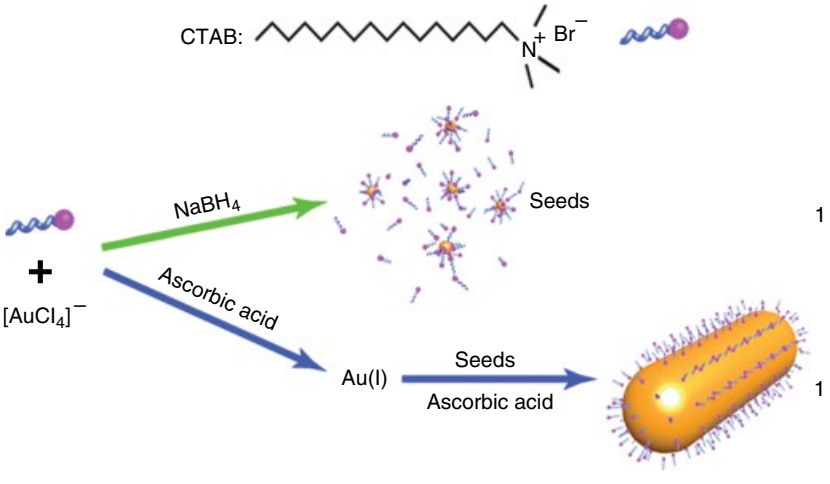

Figure 12.4 Schematic illustration of the seed-mediated growth method for Au nanorods. Reprint with permission from ref. [36]. Copyright (2013), Royal Society of Chemistry.

nanoparticles, and the growth behavior was investigated with a mild and broad range of reductant. The aspect ratio of gold nanoparticles can be controlled by changing the ratio of seeds to gold precursors. Most importantly, the growth of gold nanorods could be controlled in a quantitative manner with the aid of silver nitrate[37, 38], which makes it an effective and feasible way to yield uniform gold nanorods. Ag(I) ions bond selectively to {110} facets of Au nanocrystals and slow down their growth rate, leading to the longitudinal growth of the nanorods.

12.3 Assembly of Gold Nanoparticles

With progress in synthesis, the size and morphology of noble metal nanoparticles can be well controlled[2]. Another challenge remaining is to assemble these nanoparticles into different scale ranges with predetermined functionality and properties. Studies have shown that electromagnetic energy can be transferred via the coupling between the resonance of surface plasmons, and it can be propagated along the chain of gold nanoparticles[39, 40]. At present, this waveguide material mainly relies on electron beam lithography method, which has limitations for the subwavelength optical and electrical materials integration.

It has been pointed out that the frequency of LSPR could be affected by the interaction of electrons nearby the nanoparticles. This induced an enhanced localized electric field on the surface of the nanoparticles, which attenuates with distance. The localized electric field interacts with adjacent nanoparticles, and could be affected by the assemblies. This phenomenon is called SPR coupling[41] and usually causes a red-shift of the SPR band. The spectral shift increases with the size of the assembly and the decreased spacing between particles[42]. The LSPR band red-shifts or blue-shifts as the incident light is parallel or perpendicular to the axial direction of the two coupling particles[43], and it is polarization dependent. A large number of studies have shown that the assembly or agglomeration of gold nanoparticles in a tight manner will cause redshifts of the SPR frequency[42, 44, 45]. Moreover, the assembly of the gold nanorods end to end and side by side will cause red- and blue-shift of the longitudinal SPR, respectively[46–48].

12.3.1 Assembly of Gold Nanoparticles

The assembly of gold nanorods in CTAB solution was initially studied by El-Sayed et al.[49]. With the increased nanoparticle concentration and ionic strength of the solution, gold nanorods can be assembled into one-dimensional and three-dimensional structures. Murphy et al. have conducted similar studies using longer nanorods, and they found that surfactants can interact with gold nanorods, resulting in densely packed liquid crystalline assemblies[50]. The research on nanoparticle assemblies extends to not only the intrinsic driving force of the assembly but also the packing architecture or pattern from nanoparticles with different shape and anisotropy[51]. Yang et al. used the Langmuir-Blodgett technique to study the behavior of rod-like nanoparticles in the formation of one-dimensional structures[40], and monolayer with partial nematic arrangement and multilayer with nematic configuration were obtained with pressure.

The assembly of gold nanorods can also be achieved by surface modification and chemical bond formation. Dujardin et al. reported the incorporation of gold nanorods

into anisotropic three-dimensional aggregates via DNA hybridization[52]. Murphy et al. reported that gold nanorods assembled end-to-end benefited from biorecognition, such as specific recognition of biotin and avidin, antigens, and antibodies[53]. As the recognition of biomolecules is specific, the nanoparticles can be assembled efficiently.

Chemical bonds are robust in forming assembly of gold nanorods. Thomas et al. achieved ordered end-to-end assembly of gold nanorods by using mercaptopropionic acid, cysteine or glycine in acetonitrile-water mixed solution. Intermolecular hydrogen bonds formed with carboxyl groups and mercapto groups on the surface of gold nanorods were confirmed for assembly[48, 53]. With the addition of the carboxylic acid derivative, the longitudual SPR gradually moves toward the longer wavelength direction. The reason for this spectral change is attributed to the mutual coupling of the SPR. However, if a certain amount of acetonitrile was introduced in aqueous dispersion of nanoparticles, irregular agglomeration of the nanoparticles formed, resulting in instability of the entire system.

A hybridization diagram has been developed to understand the plasmon coupling modes. Under the excitation of light polarized along the length of Au nanorods, linearly end-to-end assembles can support a red-shifted coupled plasmon mode, while side-by-side assembles support a slightly blue-shifted coupled plasmon mode[54, 55]. The plasmon coupling can be well understood by the hybridization model, similar to the molecular orbital theory (Figure 12.5)[46]. The charge redistribution on the Au nanorod assembly exhibits an attractive manner for the end-to-end plasmon mode and a repulsive manner for the side-by-side mode, respectively. The transverse plasmon coupling modes carried by Au nanorods is usually very weak.

12.3.2 Reversible Assembly of Gold Nanoparticles

Gold nanoparticles show strong light absorption and scattering ability in the SPR regions, which is several orders higher than that of fluorescent dyes[56], and are attractive in optoelectronics applications[25]. They have great potential in regulating the optical behavior of nanostructures when LSPR overlap with the excitation of the luminescent molecules[57]. This will be a simple way to avoid the consideration of complex factors for preparation and modification. Although a lot of concern has been devoted to getting gold nanoparticles with various shapes and sizes, once these nanoparticles are synthesized, their SPR are determined and are difficult to change feasibly. When these nanoparticles are assembled, the SPR band red-shifts for the coupling between nanoparticles. It is expected that the assembly of such gold nanoparticles can be worked in a simple and controllable manner to adjust the SPR bands for applications.

At present, functional polymers[58], carbohydrates[59–61], biomolecules such as DNA[62–66], proteins[67, 68], polypeptides[69, 70], and other functional groups[71] are used in reversible assembly of inorganic nanoparticles, which can be controlled by external stimuli, such as pH, cations, and temperature. The SPR band shift reversibly via the assembly and disassembly of gold nanoparticles has been reported. It is obvious that the larger shift of the SPR is favorable to meet the needs for detection and sensing. However, most of the reports only achieve shifts of tens of nanometers[64, 65] other than shift of more than 100 nm. And the reversibility of the assembly is not stable for further application.

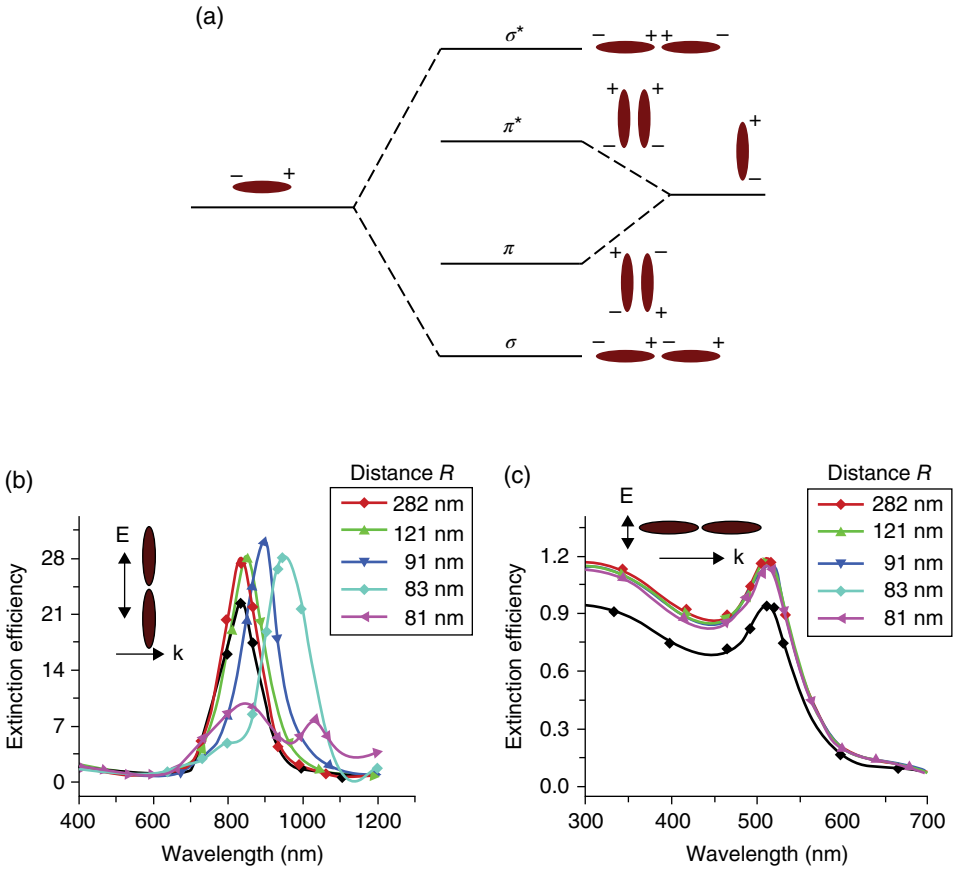

Figure 12.5 Schematic of the coupled longitudinal plasmon excitation in nanorod dimers and simulated extinction spectra of gold nanorods ($a \approx 80$ nm, $b \approx 20$ nm) assembled in an end-to-end orientation. (a) Longitudinal plasmon excitation and (b) transverse plasmon excitation of a pair of nanorods as a function of the inter-nanorod center-to-center distance. Reprinted with permission from ref. [55]. Copyright (2006), American Chemical Society.

12.3.3 Assembly of Gold Nanoparticles on Substrate

To assembly inorganic nanoparticles chemically lead to functional materials with tunable structures and properties. To couple nanoparticles on nanotubes, nanowires or nanofibers, both electric and size, shape-dependent optical properties will be enriched. At present, most of the matrix used for this one-dimensional assembly is focused on carbon nanotubes, and the nanoparticles could be selected as metal and semiconductor nanoparticles, gold[72–81], platinum[82], and cadmium selenide[83, 84]. Other inorganic or organic nanotubes, nanowires, and nanofibers could also be good candidates to extend physical and chemical properties related with composition and morphology.

SPR-related absorption and scattering of gold and silver nanoparticles can be extended from the visible to the infrared region. Noble metal nanoparticles have potential applications not only in optics, catalysis, but also in biotechnology[85, 86]. They can generate strong local electric field near the surface, as the electrons are resonantly excited.

In particular, when the distance between the noble metal nanoparticles is small, SPR coupling between the particles leads to a *hotspot*, with a strong local electric field localized between the nanoparticles. The hot spot has been used to amplify fluorescence[87–89], Raman scattering[90–93], and second harmonic generation[94]. The amplified fluorescence and Raman will improve the detection sensitivity for medical imaging and diagnosis applications[95, 96].

Another form of precious metal-containing assemblies is noble metal core–shell structure, which consists of a dielectric core and a very thin noble metal shell. The SPR band can be adjusted over a wide range by changing the ratio of its inner and outer diameters[97–99], to cover a range of visible to infrared, which is of great value in optical and biotechnology application. This kind of nanoshell has been used to suppress the photo-oxidation of luminescent polymer films[100], and wavelength-sensitive, remote light-control microfluidic devices[101]. Gold nanoshells also have many attractive properties, such as high biocompatibility, good light stability, and convenient binding capacity; they are expected to be used for biomedical diagnosis and treatment, such as immunoassay[102], light-stimulated drug delivery[103], and cell imaging and photothermal therapy[104].

12.4 Plasmonics of Bimetallic Nanocrystals

Surface Plasmon Resonance (SPR) is one of the most important properties of noble metals, which holds great promise for bio-imagining, molecular detecting, and solar cells[105]. One can precisely modulate nanocrystals' SPR properties by controlling its size, shape, electron density, as well as dielectric constant of surroundings. For example, by changing the aspect ratio of gold nanocrystals, the resonant wavelength can be tuned among the visible region. However, there are still some challenges. For example, Ag has excellent SPR properties but poor stability, Pt, Pd has poor SPR properties but outstanding catalytic properties, and their SPR peaks are among UV region. The establishment of seed-mediated bimetallic nanocrystals paves the way to solve these problems. Because of the synergistic effect, bimetallic nanocrystals not only have properties of single component but also some extraordinary properties[106]. Development of bimetallic nanocrystals has greatly enriched library of plasmonic materials.

Bimetallic nanocrystals have received increasing attention in the past ten years. Their synthesis method and SPR properties have been widely investigated[107]. Among them, Au–Ag and Au–Pd are the most studied ones. In the following parts, we will briefly introduce (i) Au–Ag bimetallic nanostructure; (ii) Au–Pd nanostructure; and (iii) other nanostructures.

12.4.1 Au–Ag Nanostructure

Gold and silver are receiving intensive interest because their SPR peaks can be modulated easily from visible region to NIR. Ag nanoparticles have been heavily used for Surface Enhanced Raman Scatting (SERS) due to their extraordinary optical properties. Compared with other noble metals, silver has less optical loss and is considered as the best one for plasmonic nanostructures[108]. However, its relatively high chemical activity hinders its development. Gold is another hot material for plasmonic nanocrystals. By changing reaction conditions, we can obtain Au nanocrystals with different shape,

size, and colors. Au nanocrystals have better stability and can be kept even for couples of years. Au and Ag have similar physical and chemical properties, so it is easy to synthesize Au–Ag bimetallic nanocrystals using the seed-mediated epitaxial method. Up to now, various Au–Ag nanocrystals have been synthesized. Accordingly, most of them have more SPR modes and better tunability because of synergistic effect. Au–Ag alloy nanoparticles can be synthesized by gradually annealing. Compared with mono-component nanocrystals, it has better SPR property and stability[108]. Au-Ag core–shell nanostructure is another common architecture. Because of its high degree of crystallinity and aspect ratio, we can obtain different types of multipolar plasmonic peaks. It is of vital importance for the study of SPR properties.

Au–Ag bimetallic nanocrystals are mostly synthesized by seed-mediated epitaxial growth. Although Au and Ag have almost the same lattice constant, it is impossible to get monodispersed Au–Ag bimetallic nanocrystals through one-pot synthesis. Both thermodynamic and kinetic factors should be considered. In a typical synthesis process, Au nanocrystals are always used as seeds, and Ag is deposited on it through slow reduction of silver salts. As a result, morphology of Au seed, temperature, and coordinated ligands have great influence on the final bimetallic nanocrystals[109].

Different morphology of Au nanocrystals exposes different facets, so they have different energy, which will influence subsequent Ag deposition. As shown in Figure 12.6,

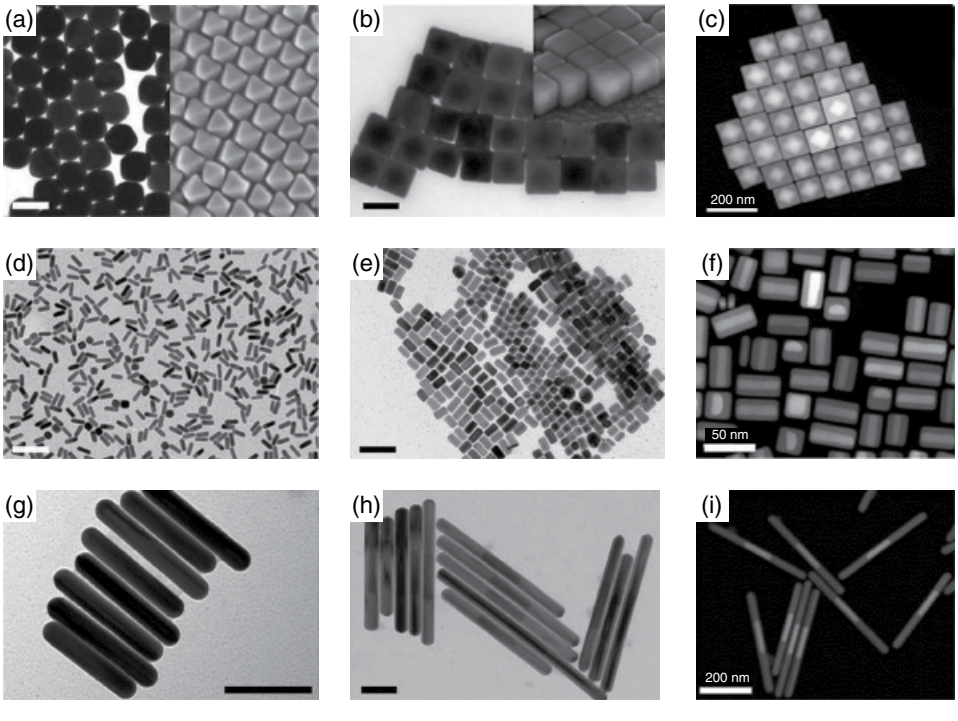

Figure 12.6 Representative TEM and SEM images of the different gold nanoparticles used as seeds (left column, scale bars: 100 nm) and the corresponding Au@Ag counterparts after silver growth (middle column, scale bars: 100 nm). The right column displays HAADF-STEM images of the same core–shell particles, where the silver shells can be easily discerned from the gold cores. Reprinted with permission from ref. [109]. Copyright (2013), American Chemical Society.

Sergio et al.[110] obtained different Au–Ag bimetallic nanocrystals using different Au seeds. For octahedral Au seeds, the overgrowth of Ag resulted in Au@Ag nanocubes, while rectangular primes were obtained using single crystalline Au nanorods as seeds. Both of them were exposed Ag (100) facets because of its low surface energy. However, for octahedral seeds, there are six (111) facets with the same energy, so growth rate of Ag on different facets is the same. Thus, they got isotropy nanocubes. As for single crystalline nanorod with tip and side (100) facets and lateral (520) facets, Ag preferentially grew on the (100) facet, which resulted in anisotropy growth. Interestingly, when they used pentatwinned nanorods as seeds, Au@Ag nanorods with large aspect ratio were got. It was because of their different exposed facets. Similarly, ligands could be adsorbed on the seeds' surface to change their energy, so the growth process would be different. In order to synthesize monodispersed Au@Ag bimetallic nanocrystals, the reduction rate of Ag should be slow to amplify difference of different facets. Even so, it is difficult to obtain long Au@Ag nanorods with a large aspect ratio. Because of lattice mismatch between Au and Ag, lattice strain becomes larger with Ag growth, which will result in flocculation and subsequent sedimentation. Thus, overgrowth will terminate. Wang et al. used an air-bath shaker to solve this problem. By this method, they got Au@Ag nanorods with length up to several micrometers, which had excellent multipolar plasmon resonance.

Owing to forming bimetallic nanocrystals, not only are Au–Ag SPR properties greatly improved but also a larger peak shift is obtained more easily. For alloy nanoparticles, the SPR peak shift can be simply ascribed to the change of dielectric constant. Joseph et al.[110] synthesized Au–Ag alloy through the annealing of Au@Ag nanoparticles. These alloy nanoparticles showed only one SPR peak. Peak position blue-shifted linearly with increasing content of Ag, while red-shift occurred with Au increasing. They found that experiment and theory agreed well by extracting the dielectric constant from the ellipsometric data.

For Au–Ag core–shell nanostructures, the SPR peaks are more complicated. In a typical core–shell structure, we can obtain SPR peaks from both single component and SPR coupling. Generally, optical properties of bimetallic nanocrystals are dominated by shell component. Huang et al.[112] synthesized cubic, truncated cubic, cuboctahedral, truncated octahedral, and octahedral Au@Ag core–shell nanocrystals using Au rhombic dodecahedra as seeds. They found a thin Ag shell resulted in blue-shift of SPR peaks owing to SPR coupling between Au and Ag. By increasing the thickness of Ag shell, the SPR peaks red-shifted as a result of particle sizes. Xia et al.[111] observed the same phenomenon in Au@Ag nanocubes. They found that the intense resonance of Ag shell dominated the SPR properties with increasing Ag component. Observation of a complete resonance of Au core required only 3 nm Ag shell thickness.

In noble-metal nanocrystal, more than one SPR peak can be obtained because of various ways the nanocrystals can be polarized. For typical nanorods, we will get two SPR peaks on account of longitudinal mode resonant at longer wavelength and transverse mode resonant at shorter wavelength, as described in Figure 12.7. Both of them can be easily adjusted by changing nanorods' length or thickness. Liz-Marzsn et al.[113] synthesized Ag–Au–Ag segmented nanorods using penta-twinned Au nanorods as seeds. Ag was reduced at both ends of each nanorod. They found that the length of bimetallic nanorods could be precisely controlled from several hundred nanometers to micrometers while their thickness stayed the same. It is reasonable that the transverse mode stayed almost the same while the longitudinal mode greatly red-shifted with length increasing.

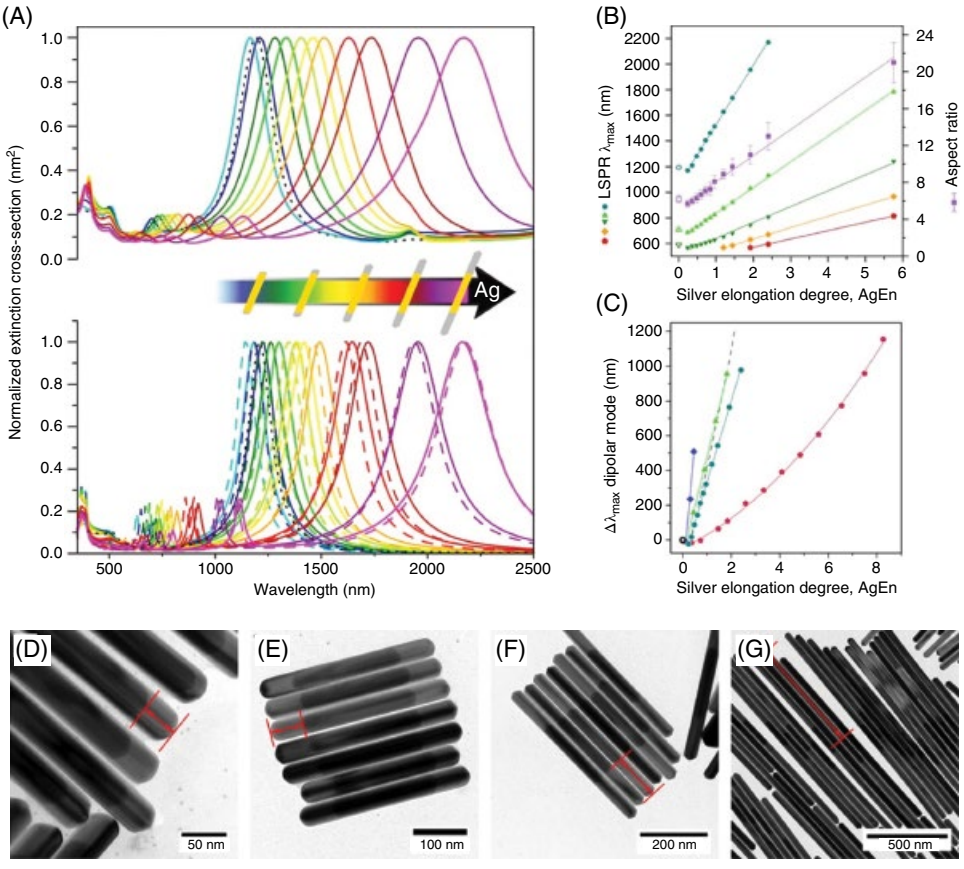

Figure 12.7 (A) Upper panel: Vis-NIR spectra recorded during silver growth. The PT–Au NR core is displayed as a black-dotted curve; Lower panel: calculated (BEM) extinction spectra of AgAuAg (solid curves) and pure Ag (dashed curves) NWs with dimensions corresponding to the experimental ones (same color code). (B) Resonance wavelengths for the dipolar and second through fifth order multipolar modes vs *AgEn*. The aspect ratio is also plotted for reference. Solid lines are linear fits to the data. The positions of the corresponding modes for the PT Au NR cores are plotted as open symbols. (C) Wavelength shift of the dipolar plasmon mode for growth with a faster addition rate, and for the standard rate on PT–Au NRs with different dimensions (180 × 34 nm; 180 × 32 nm; 210 × 32 nm). The dashed gray line represents a theoretical estimate, using the silver-to-gold volume ratio in one nanowire as *AgEn*. The open black circle is the common origin. D-G: Representative TEM images at four different values of *AgEn* = 0.72, 1.2, 2.4, 11.52, corresponding to silver elongations per tip of 33 ± 6 nm, 61 ± 9 nm, 130 ± 20 nm, and 660 ± 90 nm, and longitudinal dipolar plasmon resonances at 1405, 1630, and 2170 nm, respectively. The dipolar plasmon for G lies beyond the measurement spectral window. Reprinted with permission from ref. [113]. Copyright (2015), American Chemical Society

As shown in Figure 12.8, SPR peaks could be changed from ~1100 nm up to 2250 nm by controlling the Ag–Au–Ag nanorods' length. They also found that when nanorods grew to a certain length, Au seeds did not dominate the SPR peak position. That is, Ag shell will shield the influence of Au seeds. Wang et al.[114] obtained similar Ag–Au–Ag nanorods using penta-twinned Au nanobipyramids as seeds. Through air-bath shaker method, they got high-quality nanocrystals, which had several multipolar plasmon resonances. As shown in Figure 12.8, Ag–Au–Ag nanorods had two prominent peaks

coming from the longitudinal dipolar plasmon mode and transverse plasmon mode. The shoulder peak at 350 nm was due to plasmon resonance of bulk silver. There were multiple peaks between two strong SPR peaks that originated from multipolar plasmon modes of different orders. From FDTD calculations, they confirmed that these two peaks were from longitude quadrupolar and octupolar plasmon modes. It is because of the high aspect ratio, high quality, and excellent monodispersity that can we observe those multipolar plasmon mode.

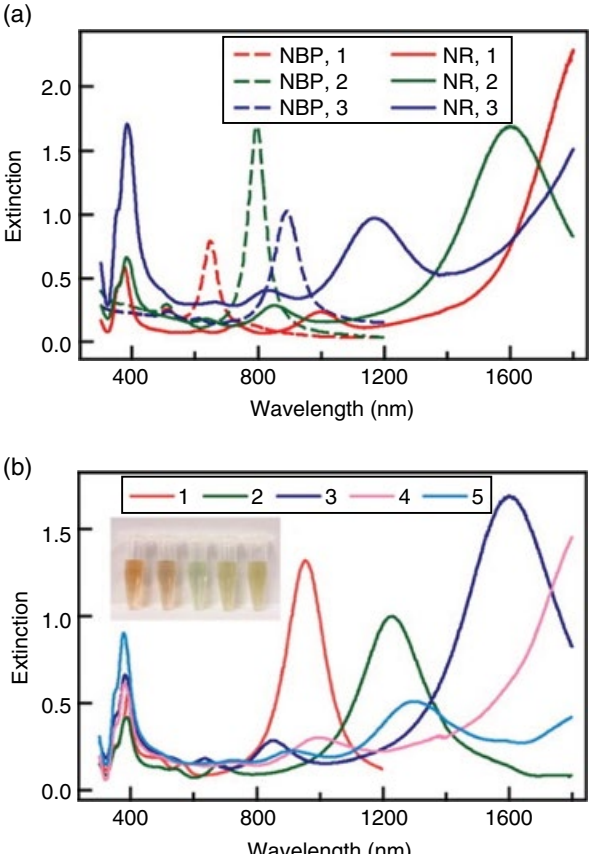

Figure 12.8 Extinction spectra and FDTD simulations of the Au NBP-directed Ag nanorods. (a) Experimental extinction spectra of the Au NBP samples and the corresponding Ag nanorod samples with different diameters. (b) Experimental extinction spectra of the Ag nanorods with different lengths. The inset shows a photograph of samples 1 to 5 from left to right. The spectra beyond the wavelength of 1300 nm were measured with D_2O. (c) Simulated extinction cross-section spectra of the Au–NBP-cored Ag nanorods and the pure Ag nanorods, together with the measured extinction spectrum. (d) Charge distribution contours of the Au–NBP-cored Ag nanorod (left) and the pure Ag nanorod (right). From top to bottom, the wavelengths of the considered peaks are 1231, 680, 551, and 380 nm for the Au–NBP-cored Ag nanorod and 1227, 677, 522, and 372 nm for the pure Ag nanorod, respectively. For $n = 1$ and $n = 3$ peaks, the excitation light is incident perpendicularly to and polarized along the rod length axis. For the transverse plasmon peak, the excitation light is polarized perpendicularly to the length axis. For the $n = 2$ peak, the excitation light is incident at an angle of 45° relative to the length axis and polarized in the plane determined jointly by the incident light wavevector and the rod length axis. Reprinted with permission from ref. [114]. Copyright (2015), American Chemical Society.

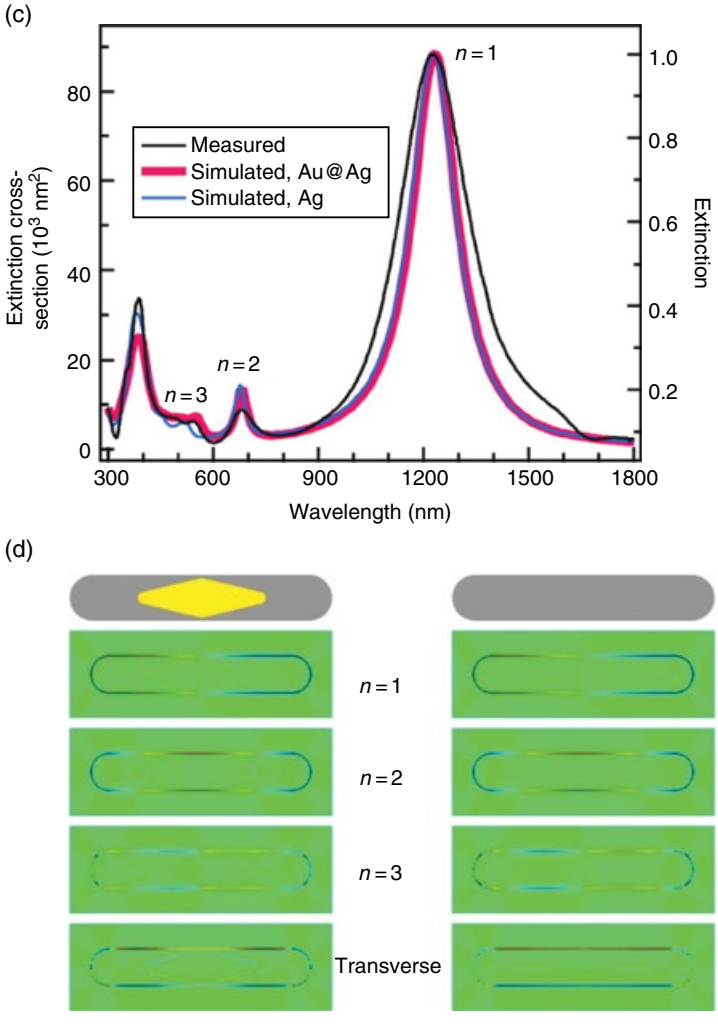

Figure 12.8 (Continued)

12.4.2 Au–Pd Nanostructure

Palladium has a unique electron structure that endows it with excellent catalytic properties for Suzuki and Sonogashira coupling, hydrogenation, and formic acid oxidation reactions[115]. However, Pd has poor SPR properties. Its resonant peaks are in UV region, which holds their development in optical applications. Recently, bimetallic nanocrystals based on Pd have attracted numerous attention, especially for Au–Pd nanocrystals. In virtue of synergistic effect, Au–Pd nanocrystals have an easy modulation of SPR peaks and outstanding catalytic properties. With different length and thickness, their resonant peak can be changed from UV to NIR regions. Many references have reported that ultimate light-induced SPR effects enhance catalytic performance of nanocrystals. For example, for Suzuki coupling reactions catalyzed by Pd tipped Au nanoparticles, laser illumination will result in a two-time yield of the normal one[116]. Those SPR induced catalytic enhancements open a new door for catalysis.

Epitaxial growth is the common method to synthesize Au–Ag bimetallic nanocrystals, but it does not work efficiently for Au–Pd system. Au and Pd both have the face-centered cubic structure with lattice constant of 0.404 and 0.389 nm. The lattice mismatch makes it difficult to epitaxially grow Pd on Au nanoparticles.[117] Moreover, the different electrochemical reduction potentials also add the difficulties. Like Au–Ag system, growth of Au–Pd nanostructure is severely influenced by seeds' morphology and coordinated ligands. Sara et al.[118] used Au–Pd coreduction method to obtain multibranched nanocrystals. They used octahedral, cubic, and rhombic dodecahedral single crystalline Au nanocrystals as seeds but got the same Au@AuPd nanostructure. They all had eight branches with O_h symmetry. They found that because of the faster reduction of Au than Pd, all the three samples would form cubic Au intermediate and grow into the same products. However, if the seeds were changed to Pd octahedral, they got 24-branched O_h nanostructures. Huang et al. increased temperature to 50 °C to get Au@Pd bimetallic nanocrystals. Using octahedral Au as seeds, they obtained cubic, truncated cubic, cuboctahedral, truncated octahedral, and octahedral nanostructures by changing dosage of precursor, surfactant, and Au seeds. Core–multishell Au–Pd nanostructures were first synthesized by Wang et al.[117]. Using Au nanooctahedron/Pd nanocube as seeds, they got Au@Pd@Au@Pd/ Pd@Au@Pd@Au core–multishell structure. They found that the shape of the products relied on the outer-shell component. For the Au outer shell, they got sphere-like crystals while cubic nanostructure was obtained by a Pd outer shell. Galvanic reduction is an effective way to synthesize bimetallic nanocrystals. Ma et al.[119] synthesized Au@Ag nanorods as seeds, and later Galvanic reduction of H_2PdCl_6 resulted in Pd tipped Au bipyramid nanostructure, which had excellent SPR properties. They found that a Galvanic reaction was most likely to happen on the side facet and that ascorbic acid could accelerate Pd reduction.

For Au-Pd bimetallic nanocrystals, Pd played a negative role in their SPR properties. In Pd tipped Au bipyramids, SPR property would be damped by Pd component, which resulted in a weaker scatting intensity and broadened peaks. As shown in Figure 12.9, for Au–Pd core–shell nanostructures, SPR properties were dominated by exterior shell. SPR properties are suppressed with Pd-shell-terminated nanocrystals while Au-terminated ones have recovered resonant properties and stronger intensity with thicker shell[117].

As shown in Figure 12.10, Au seeds showed resonant peak at 500 nm. After growth of the Pd shell, their peaks gradually vanished because of Pd poor SPR properties in visible region. The following growth of Au made nanocrystals regain their excellent SPR property. In addition, morphology and shell thickness play an important role in SPR of Au–Pd core–shell nanostructure. Also shown in Figure 12.10, different Au–Pd nanocrystals have unique resonant positions[117]. With increased Pd thickness, peak position at UV region red-shifted owing to Pd SPR. However, the peak at about 500 nm belonging to Au seeds was damped with increasing Pd thickness. The critical thickness for observing an obvious Au resonance was no more than 5.5 nm. It was obvious that different morphology of nanocrystals had different peak position.

Owing to their unique SPR properties of Au–Pd bimetallic nanocrystals, they have been applied in many emerging fields. Pd metal is sensitive to hydrogen and can adsorb H_2 to form PdH. In a core–shell Au@Pd nanostructure, formation of PdH will increase the local external dielectric environment of Au core, which results in a red- shift of Au SPR peak position[16]. The peak shift can be described by the quasistatic approximation:

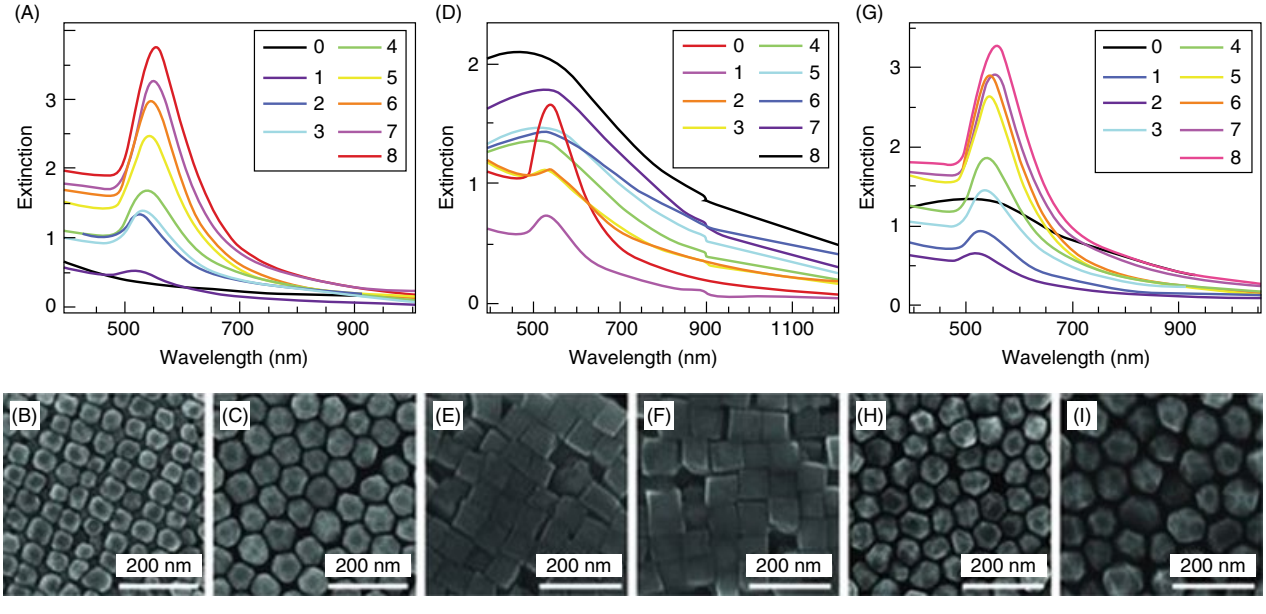

Figure 12.9 Shell-thickness-dependent evolution of the extinction spectra with the Pd nanocubes as the cores. (A–C) Pd@Au nanocrystals; (A) extinction spectra of the products obtained from the growth with the volume of $HAuCl_4$ increasing from 0 (curve 0) to 0.200 mL (curve 8); (B, C) SEM images of the products corresponding to the curves 2 and 6, respectively. (D–F) Pd@Au@Pd nanocrystals; (D) extinction spectra of the products obtained from the growth with the volume of H_2PdCl_4 increasing from 0 (curve 0) to 0.160 mL (curve 8); (E, F) SEM images of the products corresponding to the curves 4 and 8, respectively; (G–I) Pd@Au@Pd@Au nanocrystals; (G) extinction spectra of the products obtained from the growth with the volume of $HAuCl_4$ increasing from 0 (curve 0) to 0.200 mL (curve 8); and (H, I) SEM images of the products corresponding to the curves 4 and 8, respectively. Reprinted with permission from ref. [117]. Copyright (2010), Wiley-VCH Verlag GmbH &Co. KGaA, Weinheim.

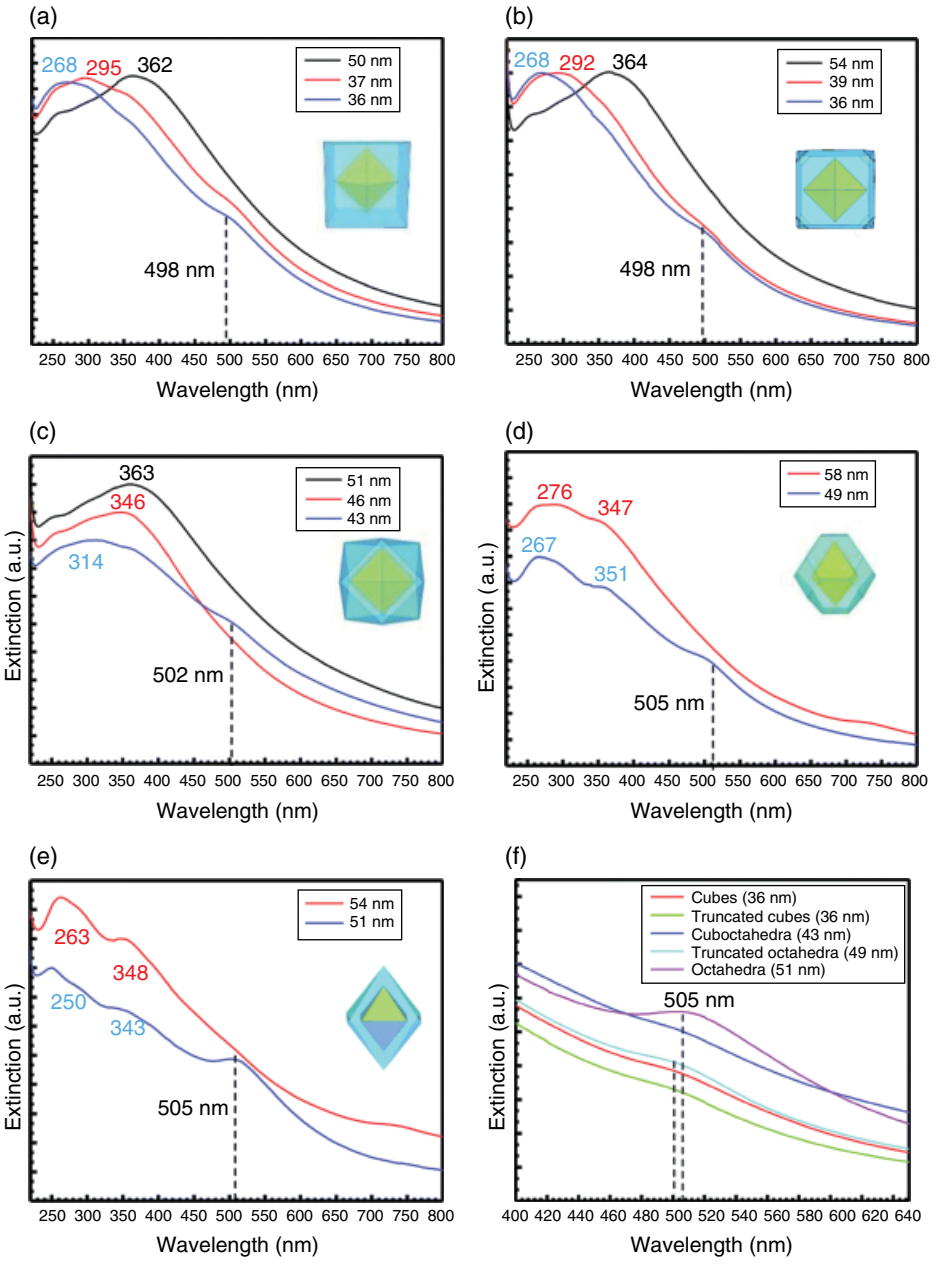

Figure 12.10 UV-vis absorption spectra of the Au–Pd core–shell: (a) cubes; (b) truncated cubes; (c) cuboctahedra; (d) truncated octahedra; and (e) octahedra with different sizes. The Au core size is 35 nm. (f) Combined UV-vis absorption spectra of Au–Pd nanocrystals with thinnest shell thicknesses. Reprinted with permission from ref. [115]. Copyright (2014), Royal Society of Chemistry.

$$\frac{\Delta\lambda}{\Delta n} = \frac{2\varepsilon_r}{n}\left(\frac{\partial\varepsilon_r}{\partial\lambda}\,|\,\lambda_0\right)^{-1}$$

The λ, n, ε_r, and λ_0 are the wavelength of incident light, medium refractive index, real part of dielectric function, and SPR maximum band position. Thus, Au@Pd nanostructure can be served as a refractive index (RI)-based hydrogen sensor. Its sensitivity is related to the nanostructure. Pd is also an excellent catalyst for many important reactions. Ma et al.[119] synthesized Pd tipped Au bipyramids, which showed high catalytic property for reduction of 4-nitrophenal. Xia et al.[120] synthesized Au@AuPd nanocrystals with high index facet, and it had a 27.3 times greater activity than a commercial Pd/C catalyst.

Amazingly, Wang et al.[116] synthesized Pd-tipped Au nanorods. When irradiated with laser at their SPR wavelength, twice the yield of Suzuki coupling was obtained. They found that Au nanorods core was served as plasmonic component while Pd nanoparticles acted as catalyst. Under illustration of laser, hot electron was generated in Au nanorods. Those hot electrons could migrate from Au to Pd nanoparticles, which would inject into organic reagent later and thus could enhance catalytic activity. Additionally, heat would also generate at the same time, and increased temperatures could accelerate coupling rates. Thus, both plasmonic photocatalysis and photothermal heating contributed to the activity.

12.4.3 Other Bimetallic Plasmonic Nanostructures

Apart from Au, Ag, and Pd, there are many other metal elements with SPR properties. Copper and platinum are among the most studied ones. Rao et al.[121] synthesized Au–Cu alloy films at liquid–liquid interface. The Au and Cu precursors were dissolved in an organic layer while the reducing agents were in an aqueous layer. By increasing the Cu content, the resonant peak red-shifted and broadened, which might be related to its unique electron structure and poor SPR property. Kedia et al.[122] used the coreduction method to obtain Au–Cu nano-dumpling alloys. With the help of PVP, the composition could be precisely controlled by changing dosage of precursors. They also found that doping of Cu would make peak position damped and red-shifted.

Similar to Pd, Pt has SPR peak in UV regions and has excellent catalytic properties. Combining Pt with other metals with good optical properties is an efficient way to synthesize dual-functional nanoparticles. Park et al.[123] obtained Au–Pt core–shell nanostructures by a seed-mediated method. They found that growth of Pt could be controlled in specific sites of Au nanoplates. As shown in Figure 12.11, uniform growth would happen if Au nanodisks were used as seeds. If Au@Ag nanodisks were used as seeds, Pt would preferentially grow at the edge of Au nanodisks induced by Galvanic reduction. Finally, they got Au@Pt(rim) nanodisks. For both samples, introducing of Pt would damp Au SPR properties. With increasing Pt contents, SPR peaks broadened and red-shifted because of their change in aspect ratio. Due to outstanding Pt, those bimetallic nanocrystals had amazing stabilities and retained their original shape without aggregation even after two months.

Chen et al.[124] synthesized Pt–Ag nanocages with reduction of Ag nanocubes. Introducing Pt elements impeded SPR of Ag nanoparticles, but also endowed them

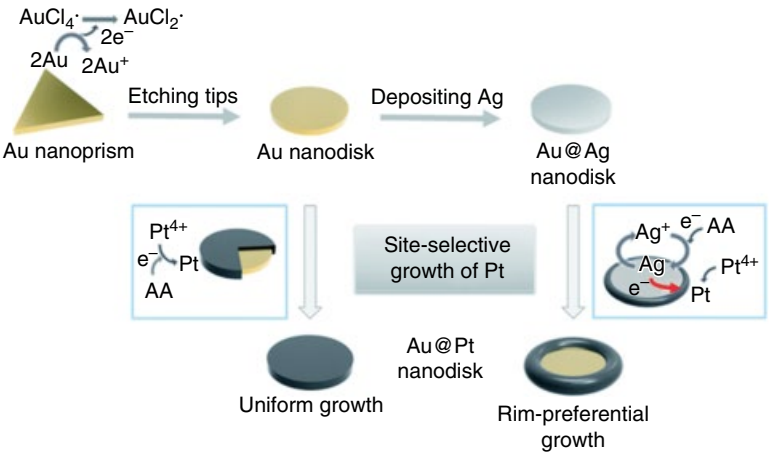

Figure 12.11 Schematic illustration of the experimental procedures regarding rim-preferential growth and uniform growth of Pt on Au nanoplates. Reprinted with permission from ref. [123]. Copyright (2014), Royal Society of Chemistry.

with good catalytic properties. Under light illumination, it could catalyze water to form hydrogen peroxide. Using a rotating ring disk electrode and XANES, they studied the process of hydrogen peroxide formation *in situ*. They found that hot electrons would generate in Ag nanoparticles under light irradiation and transfer to Pt sites later. O_2 adsorbed at Pt surface would be activated and react with water. They concluded that plasmon-induced hot-electron transfer governed the reaction.

In the past few years, a giant improvement of bimetallic nanocrystals has been realized. Various methods have been used to synthesize those unique structures. Compared with single component nanocrystals, bimetallic ones have better SPR properties, stability, and catalytic activity. Those make them ideal materials for use in biodetecting and photocatalysis in the near future.

12.5 Application of Plasmonic Nanostructures

Due to the strong SPR of noble nanoparticles, they have been used to form a variety of composite materials—for example, with hydrogels[125, 126], polymers[127, 188], silica[129] and bacteria[130]. Moreover, recent advances in the synthesis and assembly of gold nanoparticles with good biocompatibility which is convenient for conjugation with a variety of biological ligands, antibodies[131], have led to the increasing research interest in optics and photonics[40], especially in the field of biological detection, drug diagnosis and treatment[92, 132–134].

Recently, gold nanoparticles show application potentials in optical coherence tomography contrast agents[134, 135], chemical and biological detection[134, 137], two-photon fluorescence angiography[138, 139], gene delivery vector[140], and cancer-induced hyperthermia[141], and is expected to replace the traditional luminescent and fluorophore. The optical properties of nanoparticles play an important role as biomechanical and therapeutic agents. For example, its higher scattering cross-section makes it convenient in imaging based on scattering; on the other hand, its higher absorption

cross-section makes it possible to produce efficient photoheating with minimal laser excitation. In practical in situ biological detection, imaging, and photothermal therapy applications, it is ideal that the SPR band be at 650–900 nm, which have a larger penetration depth[142]. The following section will list a few application examples of gold or silver nanoparticles.

12.5.1 Bio-Imaging Application

With good scattering and absorption ability, gold nanostructures can be used as contrast agents in cell imaging[143–146]. The surface plasmon scattering produced by the gold nanostructures is sufficient to achieve sensitive imaging using conventional spectroscopy techniques under dark field irradiation[147]. When a gold nanostructure is excited by a white light source, only the light whose frequency matches its SPR is strongly scattered to give a color image on a black background[148] The diagnostic sensitivity can be improved with targeted labeling of gold nanoparticles. Combined with spectroscopic character, cell imaging can provide more information for cancer or other disease diagnoses.

Conventional biomedical imaging contrast agents are light absorbers and fluorescent dyes[149]. Quantum dots have been reported for biological and cellular imaging because of their unique size-dependent fluorescence properties[150, 151]. However, the potential toxicity and cytotoxicity are two major limiting factors for its application *in vitro* and *in vivo*. Colloidal gold nanoparticles are becoming important for imaging for its unique properties in immune studies[131], such as good biocompatibility, no photobleaching, and good chemical and thermal stability[151]. Gold nanoparticles bound to antibodies have also been widely used as biomarkers and contrast in electron microscopy studies[152].

Sokolov et al. used gold nanoparticles for cancer cell imaging with laser confocal microscopy[153]. El-Sayed et al. have shown that dark field imaging has a great potential in cancer detection[154]. Gold nanoparticles, combined with an antibody that specifically recognizes the epidermal growth factor receptor protein overexpressed in cancer cells, was used to target cancer cells to differentiate them from the healthy ones. The intense surface plasmon scattering makes the labeled cells clearly visible in the dark field microscopy, and there is no interference from healthy ones without specific binding. SPR-enhanced scattering allows gold nanoparticles to be successfully applied to specific biomolecular imaging and cancer cell detection, which can be extended to other diseases with appropriate biomarkers.

12.5.2 Photothermal Application

The SPR absorption of noble metal nanostructures can be efficiently converted into heat energy in the order of picoseconds[155]. This rapid photothermal conversion can be used to heat the local surroundings of nanoparticles, where the SPR frequency can be tuned to match that of light irradiation for efficient photothermal conversion. In these applications, it is necessary to optimize the size and morphology of the nanoparticles to have a high absorption cross section and a low scattering cross section, thereby maximizing the photothermal effect with minimal laser irradiation dose. Therefore, gold nanostructures can be used not only for cancer cell imaging and diagnosis but also for the overheating and killing of cancer cells based on photothermal therapy[153–157].

In clinical application, near-infrared light located in the 650–900 nm region shows great expectation for photothermal therapy of tumors that are deeply embedded within tissues, for the longer wavelength light has a larger penetration depth.[152] In this case, the SPR band of the nanoparticles must be located in near-infrared region. The SPR band of spherical gold nanoparticles is visible and is difficult to adjust to meet photothermal therapy applications. The SPR of gold nanorods and SiO_2–Au core–shell nanostructures can be adjusted from visible to the near infrared, making them superior for photothermal therapy application. For example, Hirsch et al. succeeded in destroying human breast cancer cells with SiO_2–Au core–shell nanoparticles via photothermal treatment[153]. Recently, Loo et al. reported anti-Her2 antibodies labeled SiO_2–Au core–shell nanoparticles could be used for simultaneous imaging and photothermal therapy of breast cancer cells[104]. Spherical gold nanoparticles are also used to target and selectively destroy cancer cells with argon ion laser irradiation[155, 156]. And typically, gold nanorods are also used to bind to anti-EGFR antibodies for cell imaging *in vitro* and photothermal therapy[157].

12.5.3 Biodetection Based on SPR

Studies have shown that the SPR of noble metal nanostructures are closely dependent on the interaction between adjacent particles. When the particles are brought into close contact, the interaction between the particles will result in the coupling of the SPR with a red-shift. Jain et al. explain the dependence of spectra shift of SPR band on distance and assembly direction of the noble metal nanoparticles.[46] Assembly of gold nanoparticles via interaction of surfactants, DNA, etc., into end-to-end and shoulder-to-shoulder mode have been achieved[42–48].

Assembly-induced red-shift of SPR band also has great potential for bioassay.[44, 66] Mirkin et al. used the DNA recognition to induce the aggregation of gold nanoparticles. In this process, single-stranded DNAs previously combined with gold nanoparticles were mixed with a free single-strand DNA, both ends of which could bind to the two single-strand DNAs, respectively. By the interaction between DNAs, one end of free single-strand DNA binds to gold nanoparticles via complimentary recognition and the other end binds to another gold nanoparticle similarly. This brought the nanoparticles close and assembled. Assembly will cause the SPR band to red-shift in the spectrum and to change the color of the nanoparticle solution, which provides a means for detecting the presence or absence of a particular DNA strand[45, 158]. This technique has now been popularized by the use of various interactions between molecules to achieve the assembly of nanoparticles to detect metal ions, proteins, and even biomarkers for diagnosis.

As already mentioned, the SPR frequency of the noble metal nanostructures is closely dependent on the dielectric properties of solvent, adsorbed species[159–161]. When the refraction coefficient of the surroundings increases, the SPR frequency of the noble metal nanostructures will red-shift. And it is sensitive to the ambient refractive index, which makes it possible to detect chemical and biological matter with SPR band[162, 163]. In the case of extremely low concentrations of analytes, such as the detection of contaminants and biological agents, noble metal nanostructures with high refractive index sensitivity show great promise. The detection of the low concentration of material

requires that the SPR wavelength be able to produce a larger shift corresponding to a small change of the ambient permittivity. The shape of the nanoparticles also has an important role on the sensitivity of SPR band[164, 165]. Particles with higher curvature in shape are usually more sensitive to changes in environmental permittivity. Thus, changing the shape of the nanostructures is an effective and direct way to enhance sensitivity. For example, the longitudinal SPR band of the gold nanorods is more sensitive to the environment than that of the nanospheres. And the greater the aspect ratio of the nanorods, the greater the sensitivity[102]. In addition to the response sensitivity, the practical application also requires a narrower bandwidth of the SPR band to ensure the accuracy of the movement.

Gold and silver nanoparticles with different shapes and sizes have been studied for detection and analysis[132, 159, 160, 166–172]. Van Duyne used silver nanoparticle arrays, obtained from photolithography, to detect proteins[159, 162], antibodies[132] and Alzheimer's disease biomarkers[167, 168]. The SPR band of the silver nanoprism and the nanocomposite will gradually red-shift with the increase of the surface-coated thiol compound. And it red-shifts about 4.4 nm with the increasing length of the alkane chain by adding each carbon atom[169–172]. Härtling et al. pointed out that gold nanoparticles can be used to detect nanoscale ferroelectric domains[173], residual mercury in the order of one hundred thousandths of drink water[174], and to monitor the interaction of biomolecules[175].

12.6 Concluding Remarks

The past few decades have witnessed great efforts made in studying plasmonic properties of noble metal nanoparticles. Multifarious synthesized methods of noble nanoparticles and their applications have been developed. In this chapter, we briefly introduced fundamental knowledge about plasmonics, plasmonic gold nanoparticles and their assembly, plasmonic bimetallic nanoparticles and their applications mainly in biology and medicine. Since SPR properties of metal nanoparticles are size and shape dependent, a lot of work focused on the controlled synthesis of noble metal nanoparticles, especially for Au. Seed-mediated growth method had been developed as a general method to obtain Au nanorods, nanoprims, nanoplates, whose LSPR wavelength span from visible to IR region. Those effective methods made it accessible for us to design and synthesize metal nanoparticles with expected SPR properties. In order to expand the library of plasmonic behavior, bimetallic nanomaterials have been designed. Benefiting from the synergistic effect of the bimetallics, excellent LSPR properties and catalytic activity have been combined to make them ideal candidate materials for photocatalysis studies.

As a result of LSPR, electric field near the metal nanoparticle surface would be significantly enhanced, and thus the luminescence and Raman signal of nearby particles or molecules would be greatly magnified. This phenomenon had been used in biodetection and imaging. In addition, as gold nanoparticles are excited, hot electrons would generate local heat and are used as photothermal therapy for cancer. In conclusion, bimetallic nanoparticles with unique plasmonic properties will have potential applications in the fields such as biology and catalysis.

12.7 References

1 El-Sayed, M. A. (2001). Some interesting properties of metals confined in time and nanometer space of different shapes. *Accounts of Chemistry Research*, 34(4), 257–264.
2 Pérez-Juste, J., Pastoriza-Santos, I., Liz-Marzán, L. M., Mulvaney, P. (2005). Gold nanorods: Synthesis, characterization and applications. *Coordination Chemical Reviews*, 249(17), 1870–1901.
3 Burda, C., Chen, X., Narayanan, R., and El-Sayed, M. A. (2005). Chemistry and properties of nanocrystals of different shapes. *Chemical Reviews*, 105(4), 1025–1102.
4 Link, S., El-Sayed, M. A. (1999). Spectral properties and relaxation dynamics of surface plasmon electronic oscillations in gold and silver nanodots and nanorods. *The Journal of Physical Chemistry B*, 103(40), 8410–8426.
5 Link, S., El-Sayed, M. A. (2003). Optical properties and ultrafasr dynamics of metallic nanocrystals. *Annual Review of Physics Chemistry*, 54(1), 331–366.
6 Kamat, P. V. (2002). Photophysical, photochemical and photocatalytic aspects of metal nanoparticles. *The Journal of Physical Chemistry B*, 106(32), 7729–7744.
7 Sun, S., Murray, C. B., Weller, D., Folks, L., Moser, A. (2000). Monodisperse FePt nanoparticles and ferromagnetic FePt nanocrystal superlattices. *Science*, 287(5460), 1989–1992.
8 Puntes, V. F., Krishnan, K. M., Alivisatos, A. P. (2001). Colloidal nanocrystal shape and size control: the case of cobalt. *Science*, 291(5511), 2115–2117.
9 Faraday, M. (1857). Experimental relations of gold (and other metals) to light. *Philosophical Transactions of the Royal Society*, 147, 145–181.
10 Willets, K. A., Van Duyne R. P. (2007). Localized surface plasmon resonance spectroscopy and sensing. *Annual Review of Physics Chemistry*, 58(1), 267–297.
11 Huang, X., and El-Sayed M. A. (2010). Gold nanoparticles: Optical properties and implementations in cancer diagnosis and photothermal therapy. *Journal of Advanced Research*, 1(1), 13–28.
12 Murphy, C. J., Sau, T. K., Gole, A. M., Orendorff, C. J., Gao, J., Gou, L. F., Hunyadi, S. E., Li, T. (2005). Anisotropic metal nanoparticles: synthesis, assembly, and optical applications. *The Journal of Physical Chemistry B*, 109(29), 13857–13870.
13 Jackson, J. B., Halas, N. J. (2001). Silver nanoshells: variations in morphologies and optical properties. *The Journal of Physical Chemistry B*, 105(14), 2743–2746.
14 Bohren, C. F., Huffman, D. R. (1983). Absorption and scattering of light by small particles. New York: John Wiley & Sons.
15 Ni, W. H., Chen, H. J., Su, J., Sun, Z. H., Wang, J. F., Wu, H. K. (2010). Effects of dyes, gold nanocrystals, pH, and metal ions on the plasmonic and molecular resonance coupling. *Journal of the American Chemical Society*, 132(13), 4806–4814.
16 Eustis, S., El-Sayed, M. A. (2006). Why gold nanoparticles are more precious than pretty gold: noble metal surface plasmon resonance and its enhancement of the radiative and nonradiative properties of nanocrystals of different shapes. *Chemical Society Reviews*, 35(3), 209–217.
17 Chen, H. J., Ming, T., Zhao, L., Wang, F., Sun, L. D., Wang, J. F., Yan, C.-H. (2010). Plasmon-molecule interactions. *Nano Today*, 5(5), 494–505.
18 Kelly, K. L., Coronado, E., Zhao, L., Schatz, G. C. (2003). The optical properties of metal nanoparticles. *The Journal of Physical Chemistry B*, 107(3), 668–677.

19 Murphy, C. J., Sau, T. K., Gole, A., Orendorff, C. J. (2005). Surfactant-directed synthesis and optical properties of one-dimensional plasmonic metallic nanostructures. *MRS Bulletin*, 30(5), 349–355.

20 Yan, B., Yang, Y., Wang, Y. (2003). Comment on "Simulation of the Optical Absorption Spectra of Gold Nanorods as a Function of Their Aspect Ratio and the Effect of the Medium Dielectric Constant." *The Journal of Physical Chemistry B*, 107(34), 9159–9159.

21 Alexei, K. (2007). Chemical dynamics in condensed phases: relaxation, transfer and reactions in condensed molecular systems. *ChemPhysChem*, 8(8), 1250–1252.

22 Jana, N. R., Gearheart, L., Murphy, C. J. (2001). Wet chemical synthesis of high aspect ratio cylindrical gold nanorods. *The Journal of Physical Chemistry B*, 105(19), 4065–4067.

23 Murphy, C. J., Jana, N. R. (2001). Seed-mediated growth approach for shape-controlled synthesis of spheroidal and rod-like gold nanoparticles using a surfactant template. *Advanced Materials*, 13(18), 1389–1393.

24 Sau, T. K., Murphy, C. J. (2004). Room temperature, high-yield synthesis of multiple shapes of gold nanoparticles in aqueous solution. *Journal of the American Chemical Society*, 126(28), 8648–8649.

25 Sun, Y., Xia, Y. (2002). Shape-controlled synthesis of gold and silver nanoparticles. *Science*, 298(5601), 2176–2179.

26 Jin, R., Cao, Y., Mirkin, C. A., Kelly, K. L., Schatz, G. C., Zheng, J. (2001). Photoinduced conversion of silver nanospheres to nanoprisms. *Science*, 294(5548), 1901–1903.

27 Dreaden, E. C., Alkilany, A. M., Huang, X., Murphy, C. J., El-Sayed, M. A. (2012). The golden age: gold nanoparticles for biomedicine. *Chemical Society Reviews*, 41(7), 2740–2779.

28 Mulvaney, P. (2001). Not all that's gold does glitter. *MRS Bulletin*, 26(12), 1009–1013.

29 Foss., C. A. Jr., Hornyak, G. L., Stockert, J. A., Martin, C. R. (1992). Optical properties of composite membranes containing arrays of nanoscopic gold cylinders. *The Journal of Physical Chemistry*, 96(19), 7497–7499.

30 Martin, C. R. (1994). Nanomaterials: A membrane-based synthetic approach. *Science*, 266(5193), 1961–1966.

31 Hulteen, J. C., Van Duyne, R. R., Nanosphere lithography: a materials general fabrication process for periodic particle array surfaces (1995). *Journal of Vacuum Science and Technology A*, 13(3), 1553–1558.

32 Esumi, K., Matshuhisa, K., Torigoe, K. (1995). Preparation of rodlike gold particles by UV irradiation using cationic micelles as a template. *Langmuir*, 11(9), 3285–3289.

33 Schönenberger, C., Van der Zande, B. M. I. E., Fokkink, L. G. J., Henny M., Schmid, C., Krüger, M., Bachtold, A., Huber, R., Birk, H., Staufer, U. (1997). Template Synthesis of Nanowires in Porous Polycarbonate Membranes: Electrochemistry and Morphology. *The Journal of Physical Chemistry B*, 101(28), 5497–5505.

34 Yu, Y., Chang, S. S., Lee, C. L., Wang, C. R. C. (1997). Gold nanorods: electrochemical synthesis and optical properties. *The Journal of Physical Chemistry B*, 101(34), 6661–6664.

35 Kim, F., Song, J. H., Yang, P. (2002). Photochemical Synthesis of Gold Nanorods. *Journal of the American Chemical Society*, 124(28), 14316–14317.

36 Chen, H., Shao, L., Li, Q., Wang, J. (2013). Gold nanorods and their plasmonic properties. *Chemical Society Reviews*, 42(7), 2679–2724.

37 Kim, S., Jin, J., Kim, Y.-J., Park, I.-Y., Kim, Y., Kim, S.-W. (2008). High-harmonic generation by resonant plasmon field enhancement. *Nature*, 453(7196), 757–760.

38 Savasta, S., Saija, R., Ridolfo, A., Di Stefano, O., Denti, P., Borghese, F. (2010). Nanopolaritons: vacuum rabi splitting with a single quantum dot in the center of a dimer nanoantenna. *ACS Nano*, 4(11), 6369–6376.

39 Jana, N. R. (2004). Shape effect in nanoparticle self-assembly. *Angewandte Chemie International Edition*, 43(12), 1536–1540.

40 Kim, F., Kwan, S., Akana, J., Yang, P. (2001). Langmuir – Blodgett nanorod assembly. *Journal of the American Chemical Society*, 123(18), 4360–4361.

41 Sonnichsen, C., Reinhard, B. M., Liphardt, J., Alivisatos, A. P. (2005). A molecular ruler based on plasmon coupling of single gold and silver nanoparticles. *Nature Biotechnology*, 23(6), 741–745.

42 Storhoff, J. J., Lazarides, A. A., Mucic, R. C., Mirkin, C. A., Letsinger, R. L., Schatz, G. C. (2000). What controls the optical properties of DNA-linked gold nanoparticle assemblies? *Journal of the American Chemical Society*, 122(19), 4640–4650.

43 Rechberger, W., Hohenau, A., Leitner, A., Krenn, J. R., Lamprecht, B., Aussenegg, F. R. (2003). Optical properties of two interacting gold nanoparticles. *Optics Communications*, 220(1), 137–141.

44 Elghanian, R., Storhoff, J. J., Mucic, R. C., Letsinger, R. L., Mirkin, C. A. (1997). Selective colorimetric detection of polynucleotides based on the distance-dependent optical properties of gold nanoparticles. *Science*, 277(5329), 1078–1081.

45 Storhoff, J. J., Elghanian, R., Mucic, R. C., Mirkin, C. A., Letsinger, R. L. (1998). One-pot colorimetric differentiation of polynucleotides with single base imperfections using gold nanoparticle probes. *Journal of the American Chemical Society*, 120(9), 1959–1964.

46 Jain, P. K., Eustis, S., El-Sayed, M. A. (2006). Plasmon coupling in nanorod assemblies: optical absorption, discrete dipole approximation simulation, and exciton-coupling model. *The Journal of Physical Chemistry B*, 110(37), 18243–18253.

47 Gluodenis, M., Foss, C. A. (2002). The effect of mutual orientation on the spectra of metal nanoparticle rod – rod and rod – sphere pairs. *The Journal of Physical Chemistry B*, 106(37), 9484–9489.

48 Thomas, K. G., Barazzouk, S., Ipe, B. I., Joseph, S. T. S., Kamat, P. V. (2004). Uniaxial plasmon coupling through longitudinal self-assembly of gold nanorods. *The Journal of Physical Chemistry B*, 108(35), 13066–13068.

49 Nikoobakht, B., Wang, Z. L., El-Sayed, M. A. (2000). Self-assembly of gold nanorods. *The Journal of Physical Chemistry B*, 104(36), 8635–8640.

50 Jana, N. R., Gearheart, L. A., Obare, S. O., Johnson, C. J., Edler, K. J., Mann, S., Murphy, C. J. (2002). Liquid crystalline assemblies of ordered gold nanorods. *Journal of Materials Chemistry*, 12(10), 2909–2912.

51 Y. H. Lee, W. X. Shi, H. K. Lee, R. B. Jiang, I. Y. Phang, Y. Cui, L. Isa, Y. J. Yang, J. F. Wang, S. Z. Li, X. Y. Ling (2015). Nanoscale surface chemistry directs the tunable assembly of silver octahedra into three two-dimensional plasmonic superlattices. *Nature Communications*, 6, 6990.

52 Dujardin, E., Hsin, L.-B., Wang, C. R. C., Mann, S. (2001). DNA-driven self-assembly of gold nanorods. *Chemical Communications*, 14(14), 1264–1265.

53 Caswell, K. K., Wilson, J. N., Bunz, U. H. F., Murphy, C. J. (2003). Preferential end-to-end assembly of gold nanorods by Biotin – Streptavidin Connectors. *Journal of the American Chemical Society*, 125(46), 13914–13915.

54 Halas, N. J., Lal, S., Chang, W.-S., Link, S., Nordlander, P. (2011). Plasmons in strongly coupled metallic nanostructures. *Chemical Reviews*, 111(6), 3913–3961.

55 Wang, Y., DePrince, A. E., Gray, S. K., Lin, X.-M., Pelton, M. (2010). Solvent-mediated end-to-end assembly of gold nanorods. *The Journal of Physical Chemistry Letters*, 1(18), 2692–2698.

56 Liu, X., Dai, Q., Austin, L., Coutts, J., Knowles, G., Zou, J., Chen, H., Huo, Q. (2008). A one-step homogeneous immunoassay for cancer biomarker detection using gold nanoparticle probes coupled with dynamic light scattering. *Journal of the American Chemical Society*, 130(9), 2780–2782.

57 Chen, Y., Munechika, K., Ginger, D. S. (2007). Dependence of fluorescence intensity on the spectral overlap between fluorophores and plasmon resonant single silver nanoparticles. *Nano Letters*, 7(3), 690–696.

58 Walker, C. H., St. John, J. V., Wisian-Neilson, P. (2001). Synthesis and size control of gold nanoparticles stabilized by poly(methylphenylphosphazene). *Journal of the American Chemical Society*, 123(16), 3846–3847.

59 de la Fuente, J. M., Barrientos, A. G., Rojas, T. C., Rojo, J., Cañada, J., Fernández, A., Penadés, S. (2001). Gold glyconanoparticles as water-soluble polyvalent models to study carbohydrate interactions. *Angewandte Chemie International Edition*, 40(12), 2257–2261.

60 Otsuka, H., Akiyama, Y., Nagasaki, Y., Kataoka, K. (2001). Quantitative and reversible lectin-induced association of gold nanoparticles modified with α-Lactosyl-ω-mercapto-poly(ethylene glycol). *Journal of the American Chemical Society*, 123(34), 8226–8230.

61 Hernáiz, M. J., de la Fuente, J. M., Barrientos, Á. G., Penadés, S. (2002). A model system mimicking glycosphingolipid clusters to quantify carbohydrate self-interactions by surface plasmon resonance. *Angewandte Chemie International Edition*, 114(9), 1554–1557.

62 Alivisatos, A. P., Johnsson, K. P., Peng, X., Wilson, T. E., Loweth, C. J., Bruchez, M. P., Schultz, P. G. (1996). Organization of 'nanocrystal molecules' using DNA. *Nature*, 382(6592), 609–611.

63 Lee, J.-S., Lytton-Jean, A. K. R., Hurst, S. J., Mirkin, C. A. (2007). Silver nanoparticle oligonucleotide conjugates based on DNA with triple cyclic disulfide moieties. *Nano Letters*, 7(7), 2112–2115.

64 Jung, Y. H., Lee, K.-B., Kim, Y.-G., Choi, I. S. (2006). Proton-fueled, reversible assembly of gold nanoparticles by controlled triplex formation. *Angewandte Chemie International Edition*, 45(36), 5960–5963.

65 Sharma, J., Chhabra, R., Yan, H., Liu, Y. (2007). pH-driven conformational switch of "i-motif" DNA for the reversible assembly of gold nanoparticles. *Chemical Communications*, 5(5), 477–479.

66 Mirkin, C. A., Letsinger, R. L., Mucic, R. C., Storhoff, J. J. (1996). A DNA-based method for rationally assembling nanoparticles into macroscopic materials. *Nature*, 382(6592), 607–609.

67 Niemeyer, C. M. (2001). Nanoparticles, proteins, and nucleic acids: biotechnology meets materials science. *Angewandte Chemie International Edition*, 40(22), 4128–4158.

68 Gole, A., Murphy, C. J. (2005). Biotin – Streptavidin-induced aggregation of gold nanorods: tuning rod – rod orientation. *Langmuir*, 21(23), 10756–10762.

69 Xu, L., Guo, Y., Xie, R., Zhuang, J., Yang, W., Li, T. (2002). Three-dimensional assembly of Au nanoparticles using dipeptides. *Nanotechnology*, 13(6), 725–728.

70 Slocik, J. M., Tam, F., Halas, N. J., Naik, R. R. (2007). Peptide-assembled optically responsive nanoparticle complexes. *Nano Letters*, 7(4), 1054–1058.

71 Li, J., Wang, J., Gavalas, V. G., Atwood, D. A., Bachas, L. G. (2003). Alumina – Pepsin Hybrid Nanoparticles with Orientation-Specific Enzyme Coupling. *Nano Letters*, 3(1), 55–58.

72 Fullam, S., Cottell, D., Rensmo, H., Fitzmaurice, D. (2000). Carbon nanotube templated self-assembly and thermal processing of gold nanowires. *Advanced Materials*, 12(19), 1430–1432.

73 Jiang, K., Eitan, A., Schadler, L. S., Ajayan, P. M., Siegel, R. W., Grobert, N., Mayne, M., Reyes-Reyes, M., Terrones, H., Terrones, M. (2003). Selective attachment of gold nanoparticles to nitrogen-doped carbon nanotubes. *Nano Letters*, 3(3), 275–277.

74 Ellis, A. V., Vijayamohanan, K., Goswami, R., Chakrapani, N., Ramanathan, L. S., Ajayan, P. M., Ramanath, G. (2003). Hydrophobic anchoring of monolayer-protected gold nanoclusters to carbon nanotubes. *Nano Letters*, 3(3), 279–282.

75 Correa-Duarte, M. A., Sobal, N., Liz-Marzán, L. M., Giersig, M. (2004). Linear assemblies of silica-coated gold nanoparticles using carbon nanotubes as templates. *Advanced Materials*, 16(23–24), 2179–2184.

76 Moghaddam, M. J., Taylor, S., Gao, M., Huang, S., Dai, L., McCall, M. J. (2004). Highly efficient binding of DNA on the sidewalls and tips of carbon nanotubes using photochemistry. *Nano Letters*, 4(1), 89–93.

77 Correa-Duarte, M. A., Pérez-Juste, J., Sánchez-Iglesias, A., Giersig, M., Liz-Marzán, L. M. (2005). Aligning Au nanorods by using carbon nanotubes as templates. *Angewandte Chemie International Edition*, 44(28), 4375–4378.

78 Zanella, R., Basiuk, E. V., Santiago, P., Basiuk, V. A., Mireles, E., Puente-Lee, I., Saniger, J. M. (2005). Deposition of gold nanoparticles onto thiol-functionalized multiwalled carbon nanotubes. *The Journal of Physical Chemistry B*, 109(34), 16290–16295.

79 Rahman, G. M. A., Guldi, D. M., Zambon, E., Pasquato, L., Tagmatarchis, N., Prato, M. (2005). Dispersable carbon nanotube/gold nanohybrids: evidence for strong electronic interactions. *Small*, 1(5), 527–530.

80 Ou, Y.-Y., Huang, M. H. (2006). High-density assembly of gold nanoparticles on multiwalled carbon nanotubes using 1-pyrenemethylamine as interlinker. *The Journal of Physical Chemistry B*, 110(5), 2031–2036.

81 Huang, W., Chen, H., Zuo, J.-M. (2006). One-Dimensional Self-Assembly of Metallic Nanostructures on Single-Walled Carbon-Nanotube Bundles. *Small*, 2(12), 1418–1421.

82 Choi, H. C., Shim, M., Bangsaruntip, S., Dai, H. (2002). Spontaneous Reduction of Metal Ions on the Sidewalls of Carbon Nanotubes. *Journal of the American Chemical Society*, 124(31), 9058–9059.

83 Banerjee, S., Wong, S. S. (2002). Synthesis and Characterization of Carbon Nanotube – Nanocrystal Heterostructures. *Nano Letters*, 2(3), 195–200.

84 Haremza, J. M., Hahn, M. A., Krauss, T. D., Chen, S., Calcines, J. (2002). Attachment of Single CdSe Nanocrystals to Individual Single-Walled Carbon Nanotubes. *Nano Letters*, 2(11), 1253–1258.

85 Schmid, G., Corain, B. (2003). Nanoparticulated Gold: Syntheses, Structures, Electronics, and Reactivities. *European Journal of Inorganic Chemistry*, 2003(17), 3081–3098.

86 Daniel, M.-C., Astruc, D. (2004). Gold Nanoparticles: Assembly, Supramolecular Chemistry, Quantum-Size-Related Properties, and Applications toward Biology, Catalysis, and Nanotechnology. *Chemical Reviews*, 104(1), 293–346.

87 Aslan, K., Leonenko, Z., Lakowicz, J. R., Geddes, C. D. (2005). Fast and Slow Deposition of Silver Nanorods on Planar Surfaces: Application to Metal-Enhanced Fluorescence. *The Journal of Physical Chemistry B*, 109(8), 3157–3162.

88 Aslan, K., Lakowicz, J. R., Geddes, C. D. (2005). Rapid Deposition of Triangular Silver Nanoplates on Planar Surfaces: Application to Metal-Enhanced Fluorescence. *The Journal of Physical Chemistry B*, 109(13), 6247–6251.

89 Zhang, J., Matveeva, E., Gryczynski, I., Leonenko, Z., Lakowicz, J. R. (2005). Metal-Enhanced Fluoroimmunoassay on a Silver Film by Vapor Deposition. *The Journal of Physical Chemistry B*, 109(16), 7969–7975.

90 Freeman, R. G., Grabar, K. C., Allison, K. J., Bright, R. M., Davis, J. A., Guthrie, A. P., Hommer, M. B., Jackson, M. A., Smith, P. C., Walter, D. G., Natan, M. J. (1995). Self-Assembled Metal Colloid Monolayers: An Approach to SERS Substrates. *Science*, 267(5204), 1629–1632.

91 Nikoobakht, B., El-Sayed, M. A. (2003). Surface-Enhanced Raman Scattering Studies on Aggregated Gold Nanorods, *The Journal of Physical Chemistry A*, 107(18), 3372–3378.

92 Tao, A., Kim, F., Hess, C., Goldberger, J., He, R., Sun, Y., Xia, Y., Yang, P. (2003). Langmuir – Blodgett Silver Nanowire Monolayers for Molecular Sensing Using Surface-Enhanced Raman Spectroscopy. *Nano Letters*, 3(9), 1229–1233.

93 Orendorff, C. J., Gole, A., Sau, T. K., Murphy, C. J. (2005). Surface-Enhanced Raman Spectroscopy of Self-Assembled Monolayers: Sandwich Architecture and Nanoparticle Shape Dependence. *Analytical Chemistry*, 77(10), 3261–3266.

94 Hayakawa, T., Usui, Y., Bharathi, S., Nogami, M. (2004). Second Harmonic Generation from Coupled Surface-Plasmon Resonances in Self-Assembled Gold-Nanoparticle Monolayers Coated with an Aminosilane. *Advanced Materials*, 16(16), 1408–1412.

95 Shafer-Peltier, K. E., Haynes, C. L., Glucksberg, M. R., Van Duyne, R. P. (2003). Toward a Glucose Biosensor Based on Surface-Enhanced Raman Scattering. *Journal of the American Chemical Society*, 125(2), 588–593.

96 Zhang, X., Young, M. A., Lyandres, O., Van Duyne, R. P. (2005). Rapid Detection of an Anthrax Biomarker by Surface-Enhanced Raman Spectroscopy. *Journal of the American Chemical Society*, 127(12), 4484–4489.

97 Oldenburg, S. J., Averitt, R. D., Westcott, S. L., Halas, N. J. (1998). Nanoengineering of optical resonances. *Chemical Physics Letters*, 288(2–4), 243–247.

98 Prodan, E., Nordlander, P. (2003). Structural tunability of the plasmon resonances in metallic nanoshells. *Nano Letters*, 3(4), 543–547.

99 Prodan, E., Radloff, C., Halas, N. J., Nordlander, P. (2003). A hybridization model for the plasmon response of complex nanostructures. *Science*, 302(5644), 419–422.

100 Hale, G. D., Jackson, J. B., Shmakova, O. E., Lee, T. R., Halas, N. J. (2001). Enhancing the active lifetime of luminescent semiconducting polymers via doping with metal nanoshells. *Applied Physics Letters*, 78(11), 1502–1504.

101 Sershen, S. R., Mensing, G. A., Ng, M., Halas, N. J., Beebe, D. J., West, J. L. (2005). Independent optical control of microfluidic valves formed from optomechanically responsive nanocomposite hydrogels. *Advanced Materials*, 17(11), 1366–1368.

102 Hirsch, L. R., Jackson, J. B., Lee, A., Halas, N. J., West, J. L. (2003). A whole blood immunoassay using gold nanoshells. *Analytical Chemistry*, 75(10), 2377–2381.

103 Sershen, S. R., Westcott, S. L., Halas, N. J., West, J. L. (2000). Temperature-sensitive polymer-nanoshell composites for photothermally modulated drug delivery. *Journal of Biomedical Materials Research Part A*, 51(3), 293–298.

104 Loo, C., Lowery, A., Halas, N., West, J., Drezek, R. (2005). Immunotargeted nanoshells for integrated cancer imaging and therapy. *Nano Letters*, 5(4), 709–711.

105 Gilroy, K. D., Ruditskiy, A., Peng, H. C., Qin, D., Xia, Y. (2016). Bimetallic Nanocrystals: Syntheses, Properties, and Applications. *Chemical Reviews*, 116(18), 10414–10472.

106 Zhang, C., Chen, B.-Q., Li, Z.-Y., Xia, Y., Chen, Y.-G. (2015). Surface Plasmon Resonance in Bimetallic Core–Shell Nanoparticles. *The Journal of Physical Chemistry C*, 119(29), 16836–16845.

107 Lee, S., Jang, H. J., Jang, H. Y., Kim, S. K., Park, S. (2016). Component conversion from pure Au nanorods to multiblock Ag-Au-Ag nanorods assisted by Pt nanoframe templates. *Nanoscale*, 8(26), 12874–12878.

108 Han, Q., Zhang, C., Gao, W., Han, Z., Liu, T., Li, C., Wang, Z., He, E., Zheng, H. (2016). Ag-Au alloy nanoparticles: Synthesis and in situ monitoring SERS of plasmonic catalysis. *Sensors and Actuators B: Chemical*, 231, 609–614.

109 Gómez-Graña, S., Goris, B., Altantzis, T., Fernández-López, C., Carbó-Argibay, E., Guerrero-Martínez, A., Almora-Barrios, N., López, N., Pastoriza-Santos, I., Pérez-Juste, J., Bals, S., Van Tendeloo, G., Liz-Marzán, L. M. (2013). Au@Ag Nanoparticles: Halides Stabilize {100} Facets. *The Journal of Physical Chemistry Letters*, 4(13), 2209–2216.

110 Shore, M. S., Wang, J., Johnston-Peck, A. C., Oldenburg, A. L., Tracy, J. B. (2011). Synthesis of Au(Core)/Ag(Shell) nanoparticles and their conversion to AuAg alloy nanoparticles. *Small*, 7(2), 230–234.

111 Ma, Y., Li, W., Cho, E. C., Li, Z., Yu, T., Xia, Y. (2010). Au@Ag core–shell nanocubes with finely tuned and well-controlled sizes, shell thicknesses, and optical properties. *ACS Nano*, 4(11), 6725–6734.

112 Tsao, Y. C.; Rej, S.; Chiu, C. Y.; Huang, M. H. (2014). Aqueous Phase Synthesis of Au-Ag Core–shell Nanocrystals with Tunable Shapes and Their Optical and Catalytic Properties. *Journal of the American Chemical Society*, 136(1), 396–404.

113 Mayer, M., Scarabelli, L., March, K., Altantzis, T., Tebbe, M., Kociak, M., Liz-Marzán, L. M. (2015). Controlled living nanowire growth: precise control over the morphology and optical properties of AgAuAg bimetallic nanowires. *Nano Letters*, 15(8), 5427–5437.

114 Zhuo, X., Zhu, X., Li, Q., Yang, Z., Wang, J. (2015). Gold nanobipyramid-directed growth of length-variable silver nanorods with multipolar plasmon resonances. *ACS Nano*, 9(7), 7523–7535.

115 Chiu, C. Y., Yang, M. Y., Lin, F. C., Huang, J. S., Huang, M. H. (2014). Facile synthesis of Au-Pd core–shell nanocrystals with systematic shape evolution and tunable size for plasmonic property examination. *Nanoscale*, 6(13), 7656–7665.

116 Wang, F., Li, C., Chen, H., Jiang, R., Sun, L. D., Li, Q., Wang, J., Yu, J. C., Yan, C. H. (2013). Plasmonic harvesting of light energy for Suzuki coupling reactions. *Journal of The American Chemical Society*, 135(15), 5588–5601.

117 Wang, F., Sun, L. D., Feng, W., Chen, H., Yeung, M. H., Wang, J., Yan, C. H. (2010). Heteroepitaxial growth of core–shell and core-multishell nanocrystals composed of palladium and gold. *Small*, 6(22), 2566–2575.

118 Weiner, R. G., DeSantis, C. J., Cardoso, M. B., Skrabalak, S. E. (2014). Diffusion and Seed Shape: Intertwined Parameters in the Synthesis of Branched Metal Nanostructures. *ACS Nano*, 8(8), 8625–8635.

119 Zhou, L., Liu, Z., Zhang, H., Cheng, S., Fan, L. J., Ma, W. (2014). Site-specific growth of AgPd nanodendrites on highly purified Au bipyramids with remarkable catalytic performance. *Nanoscale*, 6(21), 12971–12980.

120 Bi, C., Feng, C., Miao, T., Song, Y., Wang, D., Xia, H. (2015). Understanding the effect of ultrathin AuPd alloy shells of irregularly shaped Au@AuPd nanoparticles with high-index facets on enhanced performance of ethanol oxidation. *Nanoscale*, 7(47), 20105–20116.

121 Agrawal, V., Mahalakshmi, P., Kulkarni, G., Rao, C. (2006). Nanocrystalline Films of Au–Ag, Au–Cu and Au–Ag–Cu Alloys Formed at the Organic-Aqueous Interface. *Langmuir*, 22(4), 1846–1851.

122 Verma, M., Kedia, A., Kumar, P. S. (2016, May). Gold-Copper alloy "nano-dumplings" with tunable compositions and plasmonic properties. In AIP Conference Proceedings (Vol. 1728, No. 1, p. 020325). AIP Publishing.

123 Jang, H. J., Hong, S., Ham, S., Shuford, K. L., Park, S. (2014). Site-specific growth of a Pt shell on Au nanoplates: tailoring their surface plasmonic behavior, *Nanoscale*, 6(13), 7339–7345.

124 Lin, S. C., Hsu, C. S., Chiu, S. Y., Liao, T. Y., Chen, H. M. (2017). Edgeless Ag-Pt Bimetallic Nanocages: In Situ Monitor Plasmon-Induced Suppression of Hydrogen Peroxide Formation. *Journal of the American Chemical Society*, 139(6), 2224–2233.

125 Gorelikov, I., Field, L. M., Kumacheva, E. (2004). Hybrid microgels photoresponsive in the near-infrared spectral range. *Journal of the American Chemical Society*, 126(49), 15938–15939.

126 Karg, M., Pastoriza-Santos, I., Pérez-Juste, J., Hellweg, T., Liz-Marzán, L. M. (2007). Nanorod-Coated PNIPAM Microgels: Thermoresponsive Optical Properties. *Small*, 3(7), 1222–1229.

127 Pérez-Juste, J., Rodríguez-González, B., Mulvaney, P., & Liz-Marzán, L. M. (2005) Optical Control and Patterning of Gold-Nanorod-Poly (vinyl alcohol) Nanocomposite Films. *Advanced Functional Materials*, 15(7), 1065–1071.

128 Murphy, C. J., Orendorff, C. J. (2005). Alignment of gold nanorods in polymer composites and on polymer surfaces. *Advanced Materials*, 17(18), 2173–2177.

129 Chon, J. W., Bullen, C., Zijlstra, P., Gu, M. (2007). Spectral encoding on Gold Nanorods Doped in a Silica Sol-Gel Matrix and Its Application to High-Density Optical Data Storage. *Advanced Functional Materials*, 17(6), 875–880.

130 Berry, V., Gole, A., Kundu, S., Murphy, C. J., Saraf, R. F. (2005). Deposition of CTAB-terminated nanorods on bacteria to form highly conducting hybrid systems. *Journal of the American Chemical Society*, 127(50), 17600–17601.

131 Katz, E., Willner, I. (2004). Integrated nanoparticle–biomolecule hybrid systems: synthesis, properties, and applications. *Angewandte Chemie International Edition*, 43(45), 6042–6108.

132 J. C. Riboh, A. J. Haes, A. D. McFarland, C. Ranjit, R. P. Van Duyne (2003). A Nanoscale Optical Biosensor: Real-Time Immunoassay in Physiological Buffer Enabled by Improved Nanoparticle Adhesion. *Journal of Physical Chemistry B*, 2003, 107(8), 1772–1780.

133 Rosi, N. L., Mirkin, C. A. (2005). Nanostructures in biodiagnostics. *Chemical Reviews*, 105(4), 1547–1562.

134 Chen, J., Wiley, B., Li, Z. Y., Campbell, D., Saeki, F., Cang, H., Xia, Y. (2005). Gold nanocages: engineering their structure for biomedical applications. *Advanced Materials*, 17(18), 2255–2261.

135 Chen, J., Saeki, F., Wiley, B. J., Cang, H., Cobb, M. J., Li, Z. Y., Xia, Y. (2005). Gold nanocages: bioconjugation and their potential use as optical imaging contrast agents. *Nano Letters*, 5(3), 473–477.

136 Liao, H., Hafner, J. H. (2005). Gold nanorod bioconjugates. *Chemistry of Materials*, 17(18), 4636–4641.

137 Chen-Zhong Li, Keith B. Male, Sabahudin Hrapovic John H. T. (2005). Luong fluorescence properties of gold nanorods and their application for DNA biosensing. *Chemical Communications* (31), 3924–3926.

138 Wang, H., Huff, T. B., Zweifel, D. A., He, W., Low, P. S., Wei, A., Cheng, J. X. (2005). In vitro and in vivo two-photon luminescence imaging of single gold nanorods. *Proceedings of the National Academy of Sciences of the United States of America*, 102(44), 15752–15756.

139 K. Imura, T. Nagahara, H. Okamoto, Near-Field Two-Photon-Induced Photoluminescence from single gold nanorods and imaging of plasmon modes. *The Journal of Physical Chemistry B* 2005, 109(27), 13214–13220.

140 Takahashi, H., Niidome, Y., Yamada, S. (2005). Controlled release of plasmid DNA from gold nanorods induced by pulsed near-infrared light. *Chemical Communications*, 17(17), 2247–2249.

141 Hirsch, L. R., Stafford, R. J., Bankson, J. A., Sershen, S. R., Rivera, B., Price, R. E., West, J. L. (2003). Nanoshell-mediated near-infrared thermal therapy of tumors under magnetic resonance guidance. *Proceedings of the National Academy of Sciences*, 100(23), 13549–13554.

142 Weissleder, R. (2001). A clearer vision for in vivo imaging. *Nature Biotechnology*, 19(4), 316–316.

143 Yelin, D., Oron, D., Thiberge, S., Moses, E., Silberberg, Y. (2003). Multiphoton plasmon-resonance microscopy. *Optics Express*, 11(12), 1385–1391.

144 Wang, Y., Xie, X., Wang, X., Ku, G., Gill, K. L., O'Neal, D. P., Wang, L. V. (2004). Photoacoustic tomography of a nanoshell contrast agent in the in vivo rat brain. *Nano Letters*, 4(9), 1689–1692.

145 Sokolov, K., Follen, M., Aaron, J., Pavlova, I., Malpica, A., Lotan, R., Richards-Kortum, R. (2003). Real-time vital optical imaging of precancer using anti-epidermal growth factor receptor antibodies conjugated to gold nanoparticles. *Cancer Research*, 63(9), 1999–2004.

146 El-Sayed, I. H., Huang, X., El-Sayed, M. A. (2005). Surface plasmon resonance scattering and absorption of anti-EGFR antibody conjugated gold nanoparticles in cancer diagnostics: applications in oral cancer. *Nano Letters*, 5(5), 829–834.

147 Jain, P. K., Huang, X., El-Sayed, I. H., El-Sayed, M. A. (2007). Review of some interesting surface plasmon resonance-enhanced properties of noble metal nanoparticles and their applications to biosystems. *Plasmonics*, 2(3), 107–118.

148 Bugaj, J. E., Achilefu, S., Dorshow, R. B., Rajagopalan, R. (2001). Novel fluorescent contrast agents for optical imaging of in vivo tumors based on a receptor-targeted dye-peptide conjugate platform. *Journal of Biomedical Optics*, 6(2), 122–133.

149 Bruchez, M., Moronne, M., Gin, P., Weiss, S., Alivisatos, A. P. (1998). Semiconductor nanocrystals as fluorescent biological labels. *Science*, 281(5385), 2013–2016.

150 Chan, W. C., Nie, S. (1998). Quantum dot bioconjugates for ultrasensitive nonisotopic detection. *Science*, 281(5385), 2016–2018.

151 Landsman, M. L., Kwant, G., Mook, G. A., Zijlstra, W. G (1976). Light-absorbing properties, stability, and spectral stabilization of indocyanine green. *Journal of Applied Physiology*, 40(4), 575–583.

152 Boyde, A. (1991). Colloidal gold. principles, methods and application. *Journal of Anatomy*, 176, 215.

153 Link, S., El-Sayed, M. A. (2000). Shape and size dependence of radiative, non-radiative and photothermal properties of gold nanocrystals. *International Reviews in Physical Chemistry*, 19(3), 409–453.

154 Hirsch, L. R., Stafford, R. J., Bankson, J. A., Sershen, S. R., Rivera, B., Price, R. E., West, J. L. (2003). Nanoshell-mediated near-infrared thermal therapy of tumors under magnetic resonance guidance. *Proceedings of the National Academy of Sciences*, 100(23), 13549–13554.

155 El-Sayed, I. H., Huang, X., El-Sayed, M. A. (2006). Selective laser photo-thermal therapy of epithelial carcinoma using anti-EGFR antibody conjugated gold nanoparticles. *Cancer Letters*, 239(1), 129–135.

156 Huang, X., Jain, P. K., El-Sayed, I. H., El-Sayed, M. A. (2006). Determination of the minimum temperature required for selective photothermal destruction of cancer cells with the use of immunotargeted gold nanoparticles. *Photochemistry and Photobiology*, 82(2), 412–417.

157 Huang, X., El-Sayed, I. H., Qian, W., El-Sayed, M. A. (2006). Cancer cell imaging and photothermal therapy in the near-infrared region by using gold nanorods. *Journal of the American Chemical Society*, 128(6), 2115–2120.

158 Chowdury, M. H., Coates, C. C., Julian, A. M., Coté, G. L. (2004). Detection of differences in oligonucleotide-influenced aggregation of colloidal gold nanoparticles using absorption spectroscopy. *Journal of Biomedical Optics*, 9(6), 1347–1358.

159 Haes, A. J., Van Duyne, R. P. (2002). A nanoscale optical biosensor: sensitivity and selectivity of an approach based on the localized surface plasmon resonance spectroscopy of triangular silver nanoparticles. *Journal of the American Chemical Society*, 124(35), 10596–10604.

160 Malinsky, M. D., Kelly, K. L., Schatz, G. C., Van Duyne, R. P. (2001). Chain length dependence and sensing capabilities of the localized surface plasmon resonance of silver nanoparticles chemically modified with alkanethiol self-assembled monolayers. *Journal of the American Chemical Society*, 123(7), 1471–1482.

161 Jain P. K., Qian W., El-Sayed M. A. (2006). Ultrafast cooling of photoexcited electrons in gold nanoparticle – thiolated DNA conjugates involves the dissociation of the gold—thiol bond. *Journal of the American Chemical Society*, 128(7), 2426–2433.

162 Yonzon C. R., Stuar D. A., Zhang X., McFarland A. D., Haynes C. L., Van Duyne R. P. (2005). Towards advanced chemical and biological nanosensors—an overview. *Talanta*, 67(3), 438–448.

163 K. A. Willets, R. P. Van Duyne (2007). Localized surface plasmon resonance spectroscopy and sensing. *Annual Review of Physical Chemistry*, 58(1), 267–297.

164 McFarland A. D., Van Duyne R. P. (2003). Single silver nanoparticles as real-time optical sensors with zeptomole sensitivity. *Nano Letters*, 3(8), 1057–1062.

165 Raschke G., Brogl S., Susha A. S., Rogach A. L., Klar T. A., Feldmann J., Fieres B., N Petkov., Bein T., Nichtl A., Kurzinger K. (2004). Gold nanoshells improve single nanoparticle molecular sensors. *Nano Letters*, 4(10), 1853–1857.

166 Yonzon C. R., Jeoung E., Zou S. L., Schatz G. C., Mrksich M., Van Duyne R. P. (2004). Comparative analysis of localized and propagating surface plasmon resonance sensors: the binding of concanavalin A to a monosaccharide functionalized self-assembled monolayer. *Journal of the American Chemical Society*, 126(39), 12669–12672.

167 Haes A. J., Hall W. P., Chang L., Klein W. L., Van Duyne R. P. (2004). A localized surface plasmon resonance biosensor: First steps toward an assay for Alzheimer's disease. *Nano Letters*, 4(6), 1029–1034.

168 Haes A. J., Chang L., Klein W. L., Van Duyne R. P. (2005). Detection of a biomarker for Alzheimer's disease from synthetic and clinical samples using a nanoscale optical biosensor. *Journal of the American Chemical Society*, 127(7), 2264–2271.

169 Haes A. J., Zou S., Schatz G. C., Van Duyne R. P. (2004). A nanoscale optical biosensor: the long range distance dependence of the localized surface plasmon resonance of noble metal nanoparticles. *The Journal of Physical Chemistry B*, 108(1), 109–116.

170 Whitney A. V., Elam J. W., Zou S., Zinovev A. V., Stair P. C., Schatz G. C., Van Duyne R. P. (2005). Localized surface plasmon resonance nanosensor: a high-resolution distance-dependence study using atomic layer deposition. *The Journal of Physical Chemistry B*, 109(43), 20522–20528.

171 Sherry L. J., Chang S.-H., Schatz G. C., Van Duyne R. P., Wiley B. J., Xia Y. (2005). Localized surface plasmon resonance spectroscopy of single silver nanocubes. *Nano Letters*, 5(10), 2034–2038.

172 Sherry L. J., Jin R. C., Mirkin C. A., Schatz G. C., Van Duyne R. P. (2006). Localized surface plasmon resonance spectroscopy of single silver triangular nanoprisms. *Nano Letters*, 6(9), 2060–2065.

173 Härtling T., Eng L. M. (2005), Gold-particle-mediated detection of ferroelectric domains on the nanometer scale. *Applied Physics Letters*, 87(14), 142902.

174 Rex M., Hernandez F. E., Campiglia A. D. (2006). Pushing the limits of mercury sensors with gold nanorods. *Analytic Chemistry*, 78(2), 445–451.

175 Raschke G., Kowarik S., Franzl T., Sönnichsen C., Klar T. A., Feldmann J., Nichtl A., Kürzinger K. (2003). Biomolecular recognition based on single gold nanoparticle light scattering. *Nano Letters*, 3(7), 935–938.

13

Sensing

Haijuan Li and Yongdong Jin

State Key Laboratory of Electroanalytical Chemistry, Changchun Institute of Applied Chemistry, Chinese Academy of Sciences

A sensor can selectively recognize (bind with) the target analyte in a complex matrix and produce a measurable signal. The device can give real-time quantitative information about the chemical composition of the environment where it is placed. It is ideal that the sensor can respond quickly and continuously while produce negligible disturbance to its surroundings. Generally, a sensor is composed of at least two parts: a recognition part that can selectively bind (detect) the target analyte in a complex matrix and signal transducer part that can generate measurable signals. A catalyst is often necessary to produce a secondary analyte that can generate a measurable signal[1].

Compared with bulk metals, metal particles in nanometer size often exhibit unique optical, electronic, and catalytic properties attributed to their quantum-scale dimensions[2–4]. For platinum group metals (including Pt, Pd, Rh, Ru, and Ir), when reduced to nanometer size, their specific surface areas and the proportion of low-coordination atoms would be drastically increased. As a result, the catalytic property would be greatly increased. For plasmonic metals (such as Au and Ag), when transferred into nanocrystals would absorb visible light attributed to localized surface plasmon resonance (LSPR). When the sizes of noble-metal nanoparticles (Au, Ag, and Pt) are under 2 nm, they exhibit fluorescence properties. These nanoparticles can produce signals when stimulated by incident light or other irritations. Thanks to the nanoengineering technique, the surface of the nanoparticles can be precisely functioned by recognition groups, which can interact with target analytes. When interacted with target analytes, the signal outputs change quantitatively or qualitatively. The metal nanomaterials are endowed with unique properties that make them good candidates for constructing sensors. Moreover, bimetallic nanoparticles often provide scientists more ways to optimize their chemical and physical properties than their monometallic counterpart. Therefore, sensors based on bimetallic nanoparticles often have better sensitivity and selectivity and have attracted great concern because of their potential applications in both research and practical uses.

In this chapter, we will introduce the state of art of the bimetallic sensors and the mechanisms of the sensing.

Bimetallic Nanostructures: Shape-Controlled Synthesis for Catalysis, Plasmonics, and Sensing Applications, First Edition. Edited by Ya-Wen Zhang.
© 2018 John Wiley & Sons Ltd. Published 2018 by John Wiley & Sons Ltd.

13.1 Plasmonic Sensors

Plasmons are phenomenons of noble metals that represent collective oscillation of the conduction electrons[5–8]. We may understand the plasmon oscillation of the metal as oscillations of electron gas around the fixed ionic cores when excited by external electric field. At the interface of a metal and its dielectric surroundings, the plasmons are called surface plasmons or surface plasmon polaritons. By a grating or a defect in the metal surface, surface plasmons can be stimulated by incident light and the light can be coupled into upright or propagating of surface plasmon modes. Surface plasmon resonance (SPR) applies to a collective oscillation of free electrons in the conduction band when excited by the incident light. Since the collective oscillation of the free electrons is confined to the surface of the nanoparticles, it is called the localized surface plasmon resonance (LSPR). This is an attractive nanoscale phenomenon of noble metals that has aroused intense attention in recent years. The resonances bring about spectral absorption and scattering, as well as electromagnetic enhancements in near-field. The spectral peak is very sensitive to dielectric environment and is the foundation for constructing plasmonic sensors. The strong electromagnetic near-field enhancement (FE), spatially localized at the nanometer scale, can reach several orders of magnitude, is the basis for surface-enhanced resonance scattering (SERS) detection.

13.1.1 Bimetallic SPR Sensors

SPR sensors based on metallic nanoparticles are very powerful tools for sensitive detecting low molecular weight analytes with extremely dilute concentrations[5–8]. The mechanism of the SPR sensor is based on the monitoring of the refractive-index variations of the medium on the surface of the sensor. It is well known that the refractive-index of a plasmon reporter is exceptionally sensitive to its local environment. In these techniques, changes in the refractive index of the surrounding medium of a flat or periodically structured noble-metal film would result SPR resonance shift, which can be measured by angular interrogation, wavelength interrogation, or intensity measurements. This technique is widely used in monitoring surface binding events typically for those biomolecules. Silver nanoparticles (Ag NPs) showed a stronger and sharper plasmon resonance than gold nanoparticles (Au NPs) and plasmonic sensors based on Ag NPs exhibited a higher sensitivity than those based on Au NPs. However, their instability has severely limited their widespread use. The structures of Ag NPs are very sensitive to moisture, acids, oxidation, heat, and light. Therefore, Ag NPs alone are rarely used as sensors. The introduction of another metal element to Ag nanostructures can improve their stability and maintain their excellent plasmonic properties. Song et al.[9] constructed an Au/Ag bimetallic alloy-amplified SPR immunoassay system. The Au/Ag alloy nanocomposites exhibited excellent stability and high sensitivity. The bimetallic Au/Ag hybrid nanostructures was prepared with the same method to prepared citrate-stabilized Au NPs with exception that the precursors was Au and Ag with a molar ratio (0.27 : 0.73). Then Au/Ag hybrid nanostructures were immobilized on the surface of gold substrate modified with sulfhydryl groups. X-ray photoelectron spectroscopy (XPS) technique was used to test the immobilization of Au/Ag hybrid nanostructures. Here, the model target analyte was human IgG. Rabbit anti-human IgG was immobilized on the surface of Au/Ag bimetallic nanostructures modified Au film. Samples

containing human IgG solutions were injected to the sensing system. A custom-built wavelength modulation SPR biosensor was employed to monitor the protein-binding interaction. The Au/Ag bimetallic alloy exhibited a detection range of 0.15–40.00 mg mL^{-1} to the response of IgG, which was broader than those obtained by Au NPs with the same particle size and those without nanoparticle-amplification.

Yin et al. have prepared highly stable Ag@Au nanoplates with very thin layer of Au atoms[10]. Since the Au layer was very thin, the plasmonic property of the Ag nanostructures was reserved and the galvanic replacement was minimized. The Au outside layer is facile for further chemical modifications for SPR biosensing. Galvanic replacement would not only destructively etch the original Ag nanostructures, leading enormous change of the optical property, but also cause nonuniformity of Au deposition since the reaction is initiated only locally at certain high-energy sites[11, 12]. The authors minimized the galvanic replacement by first lowering the reduction potential of the Au salt by complexation with I^-, and second by adding polyvinylpyrrolidone (PVP) to stabilize the silver nanostructure against the corrosion by gold ions. As shown in their TEM images, most of the original triangular/hexagonal shapes were retained. A layer of Au atoms as thin as 0.5 nm was deposited on the surface of the Ag plate, as confirmed by both STEM image and EDS line scan. The thin coating ensures that the plasmonic property of the Ag structure is maintained and avoids the corrosion of the Ag nanostructure by external environment. Protected by the Au layer, the Ag@Au nanoplates were very stable in the presence of PBS, NaCl, or H_2O_2. The Au layer enables the application of the Ag@Au nanoplates for many bioanalytical analyses. In the study, streptavidin was chosen as a model protein. The SPR sensor for streptavidin was conducted in a flow channel with Kretchmann configuration in which a thin gold film is deposited on a glass substrate and then attached to a prism. A laser beam irradiates the gold substrate, the SPR angle corresponding to the variations of the refractive index on the thin gold film upon the binding of analytes is monitored and used to quantify analytes absorbed on the sensing surface. In a typical measurement, the gold film was first decorated with 11-mercaptoundecanoic acid (MUA), then biotin was coupled with the carboxy group of MUA by amidation. These films could absorb streptavidin specifically through the biotin–streptavidin interaction. Finally, biotin-labled Ag@Au nanoplates were added to increase the SPR signal. The SPR angle was monitored throughout the process to obtain quantitative data. This method is generally applicable to many other systems, containing nucleic acid, peptides, and carbohydrates, by modification the sensors with corresponding recognition element.

13.1.2 Sensors Based on LSPR Peak Shift

13.1.2.1 LSPR Shift Induced by Binding of the Analytes with the Sensor

The LSPRs of metal nanoparticles are very sensitive to their local dielectric environment. As a result, the peak position and outline of the LSPR will greatly change when other substances are brought into their proximity. Based on this concept, lots of LSPR sensors have been developed.

Plasmonic hydrogen sensor is a very good example. Since H_2 can ignite explosively when their concentrations exceed 4%, hydrogen sensing is essential at each step of its production, storage, and utilization. Metal palladium nanocrystals can absorb H_2 reversibly by incorporating hydrogen atoms into their lattice[13]. The absorption and

release of H_2 lead to the change of the dielectric properties and make optical sensing possible. Since the interband transitions of Pd NPs spread all over the visible region, their LSPRs occupied very broad spectral resonance profiles, which hinder the direct use of Pd NPs in optical H_2 sensing.

In 2011, Liu et al. fabricated a model system consist of a triangular gold nanoplate in the proximity of Pd NPs by electron beam lithography[14]. Since gold nanoparticles have very strong plasmon near-fields, they can sensitively detect the change in the dielectric function of the proximal palladium nanoparticle when it absorbs or releases hydrogen. Dark-field microscopy with attached spectrometer was applied to study the optical change of the system upon the absorption of H_2 at single particle level (Figure 13.1a). Therefore, the inhomogeneous broadening that often occurred on nanoparticle ensembles was prevented. As shown in Figure 13.1a, when the distance between gold triangle and the Pd NPs was about 10 nm, as the H_2 pressure was increased from 0 to 1% pressure, a 5 nm red-shift of the scattering spectroscopy was observed and the resonance intensity was dramatic decreased. The detection sensitivity was highly dependent on the distance between Au NP and Pd NP because the local field enhancement decreased dramatically as the distance increased. Meantime, as the near field enhancement is mostly located at the corners, gold triangle with sharp tips provide a more sensitive detection response than gold nanorods. As shown in the control experiment, single Pd NP was not able to fulfill the sensing job (Figure 13.1b). Later, they studied the adsorption/desorption behavior of H_2 on single Au/Pd core–shell NPs with different shapes and Pd shell thickness (Figure 13.1c)[15]. The LSPR of the Au core was very sensitive to the absorption and desorption of H_2 on the surface of the Pd shell, which enable fast detection of H_2 at low concentrations. In this study, they found that the H_2 uptake trajectory was depend on the shape of the nanocrystal. This work has motivated the synthesis of core–shell plasmonic H_2 sensors with a plasmonic core and an H_2-sensitive Pd shell. Chiu et al. synthesized a series of shapes of Au@Pd core–shell nanostructures containing tetrahexahedra, octahedral and cubes[16]. Nearly reversible spectral responses were obtained by these Au@Pd nanocrystals and selectivity studies showed that O_2 and CO have negligible influence on the detection of H_2. Jiang et al. compared plasmonic response to hydrogen of Au nanorod core with continuous and discontinuous Pd shells[17]. Extinction spectra of Au@Pd ensembles deposited on glass slides was used to test the absorption and release of H_2. The absorption of H_2 on the Au/Pd nanocrystal could cause the red-shift of extinction spectra, and the Au/Pd nanocrystals with continuous Pd shell exhibited a larger plasmon shift than those with discontinuous Pd shell. A plasmon shift as high as 56 nm was achieved for Au/Pd nanostructures with continuous Pd shell when exposed to H_2 concentration below the explosion limit, and a limit of detection as low as 0.2% was achieved that showed application potential for H_2 sensing.

13.1.2.2 LSPR Sensors Based on Selective Etching of a Metallic Component from the Preformed Bimetallic Nanoparticles

Jin's group has innovatively constructed a sensitive enzyme-responsive Ag/Au plasmonic biosensor for glucose detection[18]. Here, the GOx enzyme was immobilized on the surface of Ag/Au bimetallic hollow nanoshells. In the presence of oxygen, enzymatic oxidation of glucose would produce H_2O_2 (Equation 13.1), which can selectively dissolute Ag from the preformed Ag/Au bimetallic nanoshells (Figure 13.2a). As the etching proceeds, the surface plasmon peak of the resultant porous nanoshells red-shift in

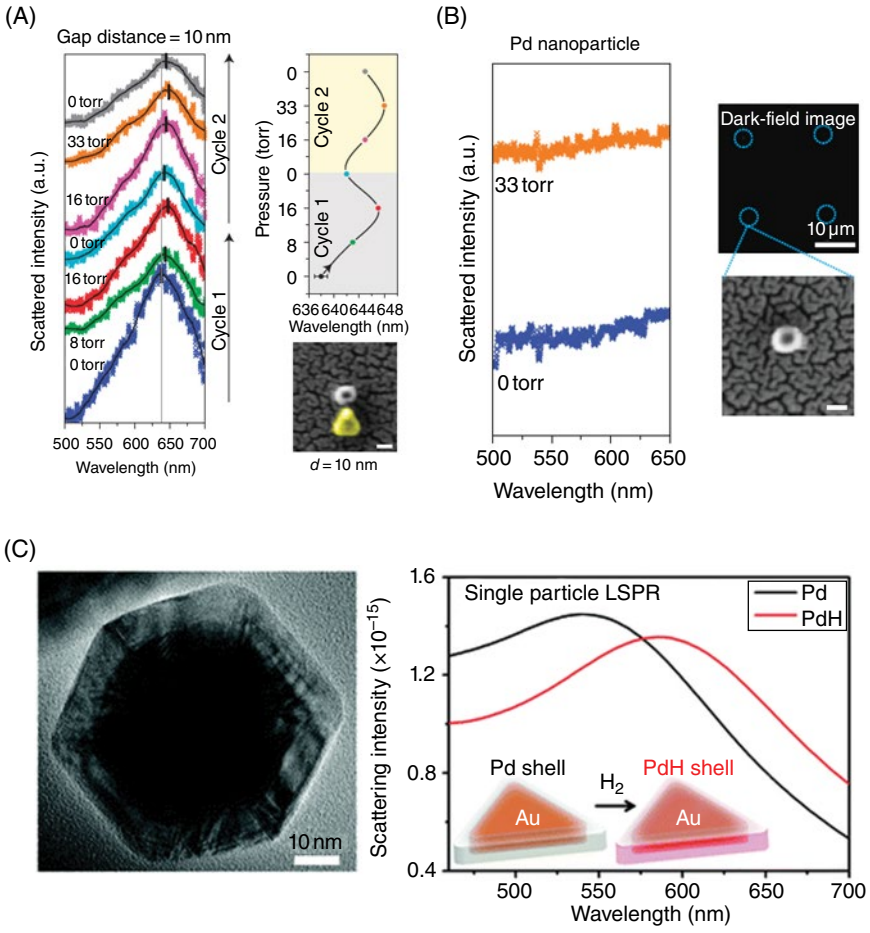

Figure 13.1 (A) Scattering spectra of individual Au NP with controlled H_2 pressure in two cycles. The distance between the Au triangle and the Pd NP is 10 nm. 33 torr approximately matches with a 4% H_2 concentration. Upper right shows the resonance peak shift in response to H_2 in two cycles. (B) Control experiment, scattering measurements of individual Pd NP with controlled H_2 pressure. The right chart is dark-field image of the Pd NPs and SEM image of individual Pd NP; scale bar 50 nm. (C) HRTEM image of Au@Pd icosahedron square and scattering measurement of Au@Pd octahedra before and after exposure to H_2. Inset: scheme of the reversible transformation from Au@Pd to Au@PdH upon exposure to H_2. Figure (A) and (B) were reprinted with permission from ref 14. © from 2011 Macmillan Publishers Ltd. Figure (C) adapted with permission from ref 15. © 2013 American Chemical Society.

response to the concentration change of H_2O_2, and accordingly is a measurement of the concentration change of the glucose in the system. This optical sensor can detect glucose with concentrations in the range of ~ 1–2 orders of magnitude and down to $\sim 0.5 \times 10^{-6}$ M, and the sensor was used to detect glucose concentration in serum.

$$\mathrm{D-glucose} + \mathrm{O_2} + \mathrm{H_2O} \rightarrow \mathrm{D-gluconic} + \mathrm{H_2O_2} \tag{13.1}$$

The colloidal plasmonic Ag/Au nanoshells coated with glucose oxidase (GOx) were then used as self-sensing nanoprobes for *in situ* optical probing of surface-confined

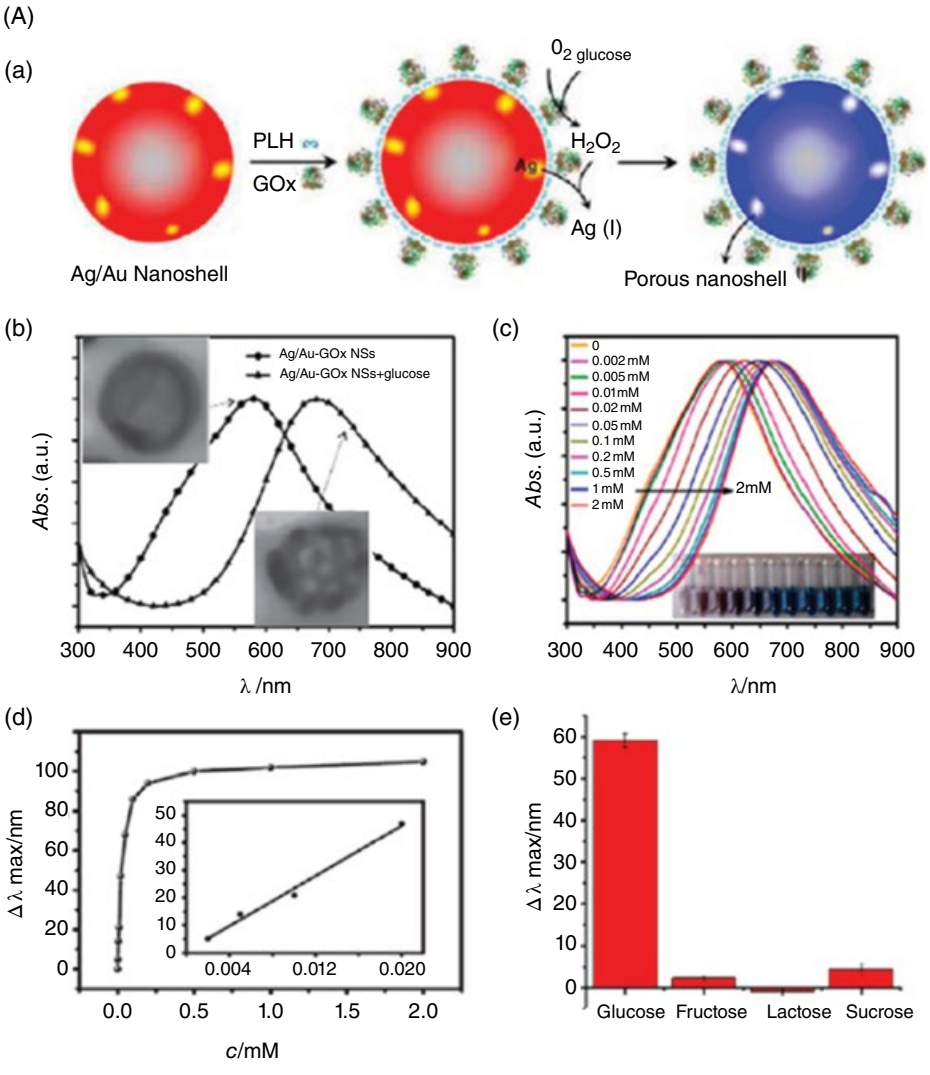

Figure 13.2 (A) Schematic illustration of the preparation of hybrid Ag/Au-GOx NSs (a) and their application in glucose sensing (b–e). (b) The normalized UV-vis extinction spectra of the Ag/Au-GOx NSs before and after the incubation with glucose, insets are the corresponding TEM images. (c) The normalized UV-vis extinction spectra of the Ag/Au-GOx NSs after 30 min incubation with different concentrations of glucose. Inset: photographs of the corresponding reaction solutions. (d) The relationship of SPR peak shift ($\Delta\lambda_{max}$) versus glucose concentration. Inset shows the linear dependence of $\Delta\lambda_{max}$ on glucose concentration. (e) Selectivity study with fructose, lactose, and sucrose. Reprinted with permission from ref. 18. Copyright 2012 Wiley-VCH. (B) In vitro dark-field microscopy-based visual identification of cancer cells. Reprinted with permission from ref. 21. Copyright 2015 American Chemical Society.

enzymatic activity, which is at least 1 – 2 orders of magnitude more sensitive than standard colorimetric assays for detecting GOx activity[19, 20]. They found that enzymatic activity of monolayer-confined GOx on colloidal Ag/Au NPs was significantly enhanced as compared with free GOx, with a low apparent Michaelis – Menten constant Km of ~ 0.115 mM and high turnover kcat/Km of ~ 8394 $M^{-1} \cdot s^{-1}$; compared with the

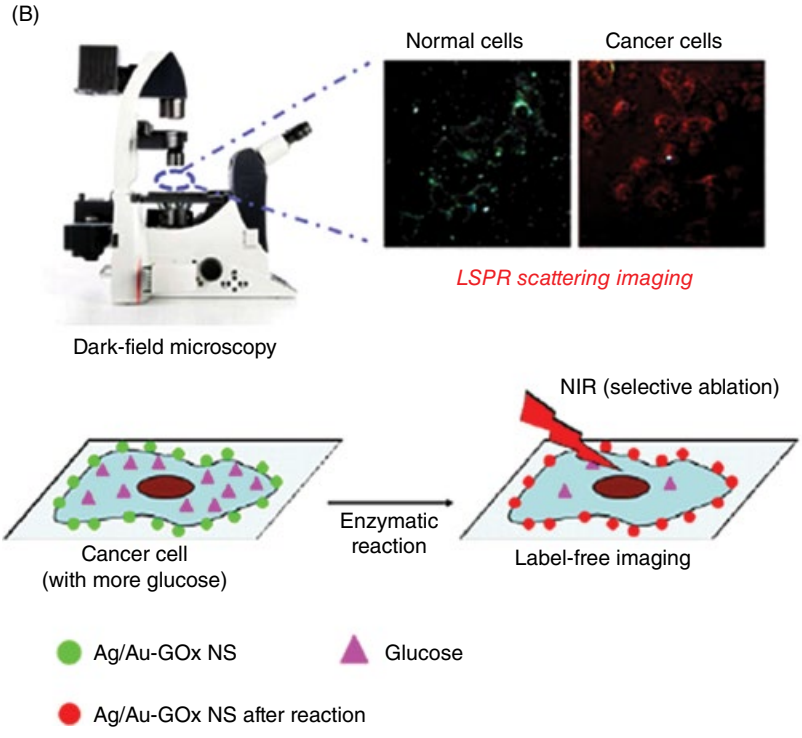

Figure 13.2 (Continued)

"anchored-type" suspending GOx, the outmost polyelectrolyte monolayer-protected "sandwiched-type" GOx exhibits significantly improved enzymatic activities toward higher temperatures and wider pH range.

The LSPR peak shift of the bimetallic nanoshells is related to the rate of enzymatic reaction of GOx. Furthermore, the glucose sensitive plasmnonic sensor was applied to in vitro visual discriminate and photothermal ablate of cancer cells (Figure 13.2b). Compared with normal cells, cancer cells usually have a higher glucose uptake level. After incubating with the Ag/Au nanoprobes, despite the coverage of the nanoprobes on cell surfaces are very similar, dark-field scattering images are quite different, as normal cells are yellow-green colored and tumor cells are orange/red-colored[21].

Besides, Au/Ag bimetallic nanostructures are often used as colorimetric probes to detect cyanide[22, 23]. In the existence of oxygen, cyanide could dissolve gold and silver and form metal–cyanide complex (Figure 13.3a). The mechanism is based on the following two reactions (Eqs. 13.1 and 13.2). Based on this concept, researchers have developed many colorimetric cyanide sensors. Zeng et al. have prepared Au@Ag core/shell NPs via gold NPs assisted Tollens method. The optical property of the Au@Ag NPs is very sensitive to their core–shell ratio; a tiny change could cause an obvious spectral and/or color variation (Figure 13.3b). Interference study showed that 18 anions like halogen had no effect on the detection. A limit of detection of 0.4 μM was achieved, which is much lower than the maximum limit regulated by the WHO (1.9 μM) in drinking water. The Au@Ag NPs were immobilized into agarose gels and cyanide detection in natural water samples was achieved without any pretreatment. Similarly, Ag@Au

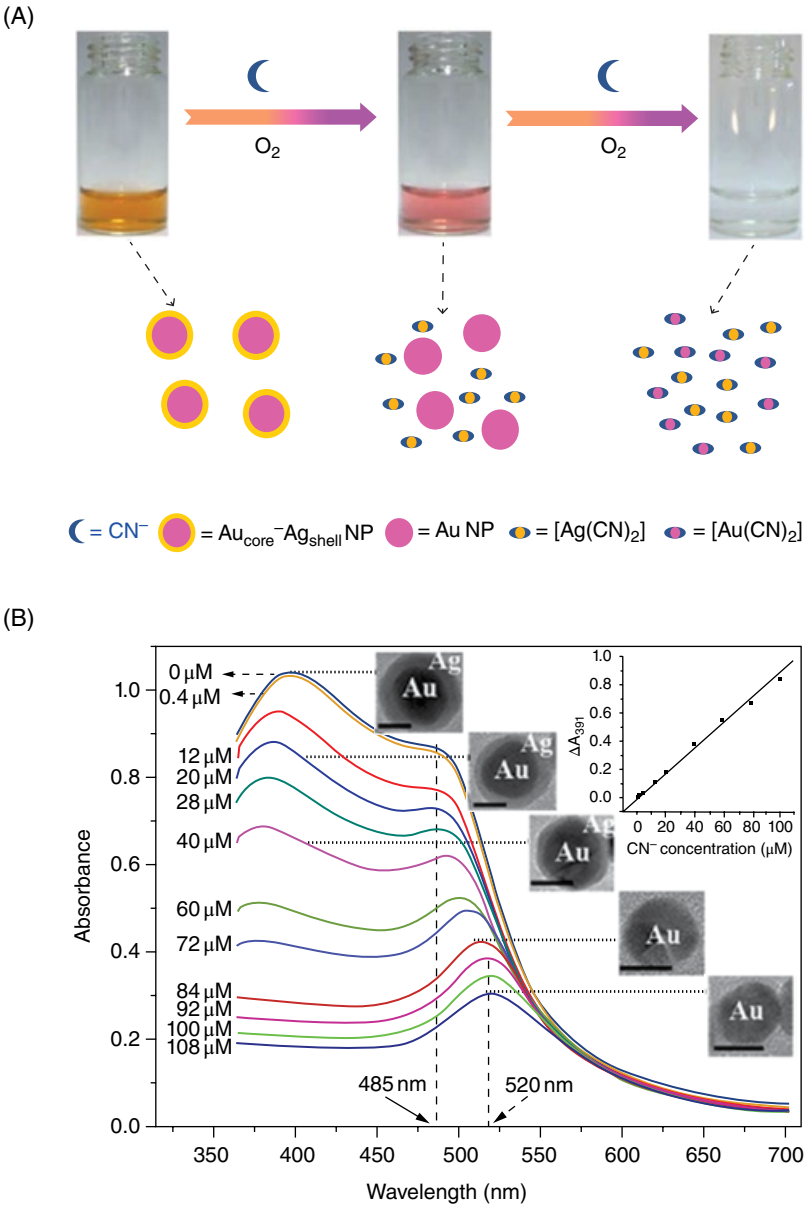

Figure 13.3 (A) Schematic diagram of the Au@Ag core/shell NPs for the colorimetric detection of cyanide. (B) Representative TEM images of the Au@Ag core/shell NPs treated with different amounts of cyanide; the black scale bar represents the length of 10 nm and upper right corner is the linear plot of ΔA_{394} versus the cyanide concentration. Reprinted with permission from ref 22. © 2014 The royal society of chemistry.

core–shell NPs have been applied to detect cyanide, and a detection limit of 0.16 μM was achieved[23].

$$4Ag + 8CN^- + 2H_2O + O_2 \rightarrow 4\left[Ag(CN)_2\right]^- + 4OH^- \quad (13.2)$$

$$4Au + 8CN^- + 2H_2O + O_2 \rightarrow 4\left[Au(CN)_2\right]^- + 4OH^- \quad (13.3)$$

13.1.2.3 LSPR Sensors Based on Enzyme-Guided Metallic Crystal Growth

When a plasmonic nanosensor interacts with a second metallic nanostructure at short distance, the LSPR peak would shift greatly. In 2012, Liz-Marzán et al. developed the concept that by tailing the LSPR of gold nanosensors by formation of Ag nanostructures in situ[24]. The sensing mechanism was based on the growth of Ag controlled by the enzyme GOx. The enzymatic reaction of GOx produces H_2O_2, which can reduce silver ions. When the concentration of GOx is low, epitaxial growth of Ag on Au nanostars would occur, resulting a large blue-shift of the LSPR of the nanostars. When the concentration of GOx is high, nucleation of Ag in solution is favored; thus, less Ag was deposited on the Au nanostars, generating a small LSPR shift. The novelty of this method is that the LSPR shift is oppositely proportional to the analyte concentration, indicating at the lowest concentration of the analyte, the signal output is the highest, which enables this method to develop highly sensitive sensors. The GOx can link to a variety of antibodies and act as the label in enzyme-linked immunoassay. Here, a cancer biomarker prostate-specific antigen in whole serum was detected by this method and a detection limit as low as 10^{-18} g mL^{-1} was achieved.

Recently, Wang et al. have developed antioxidants (vitamin C (Vc) sensor based on seed-mediated growth of Ag on the surfaces of Au nanocages[25]. In the present of Vc, Ag^+ would be reduced on the surface of Au nanocages instead of self-nucleation. Consequently, the LSPR of the Au nanocages would blue shift as the component and morphology were both changed. A linear relationship between LSPR peak shift of the sensor and the Vc concentration within 0.05–7.5 μM was obtained. Interference experiments showed that many amino acid and mineral salts that often coexist with Vc would not affect the detection, and Vc in pharmaceutical products was detected by this sensor.

Recently, with the invention of dark-field microscopy, analysis on the basis of the localized resonance scattering of individual plasmonic nanoparticles (PNP) has become more and more popular attributed to its big promise in analytical and biological field[26–28]. Yeung et al. developed a novel strategy for highly sensitive mapping of sulfide in living cells based on the localized resonance scattering of individual Au NR@Ag nanostructures[29]. In the presence of oxygen, Ag atom can be quickly oxidized to Ag_2S, leading the spectrum of the probe shift to the longer wavelength. The spectral shift of the nanoprobe is specific to sulfide, and a linear logarithmic relationship between spectral shift and sulfide concentrations in the range of 0.01 nM to 10 mM has been obtained. Therefore, sulfide concentration and its variation in living cell could be calculated in real time by dynamic measurements of the spectral shifts of the nanoprobes. This concept has been proved both experimentally and theoretically. Thus, intracellular monitoring of local H_2S variation can be achieved with single PNPs as optical probes. Later, they improve the throughput measurement of H_2S by employing RGB colorimetric analysis using Au@Ag spherical NPs as molecular probes (Figure 13.5)[30].

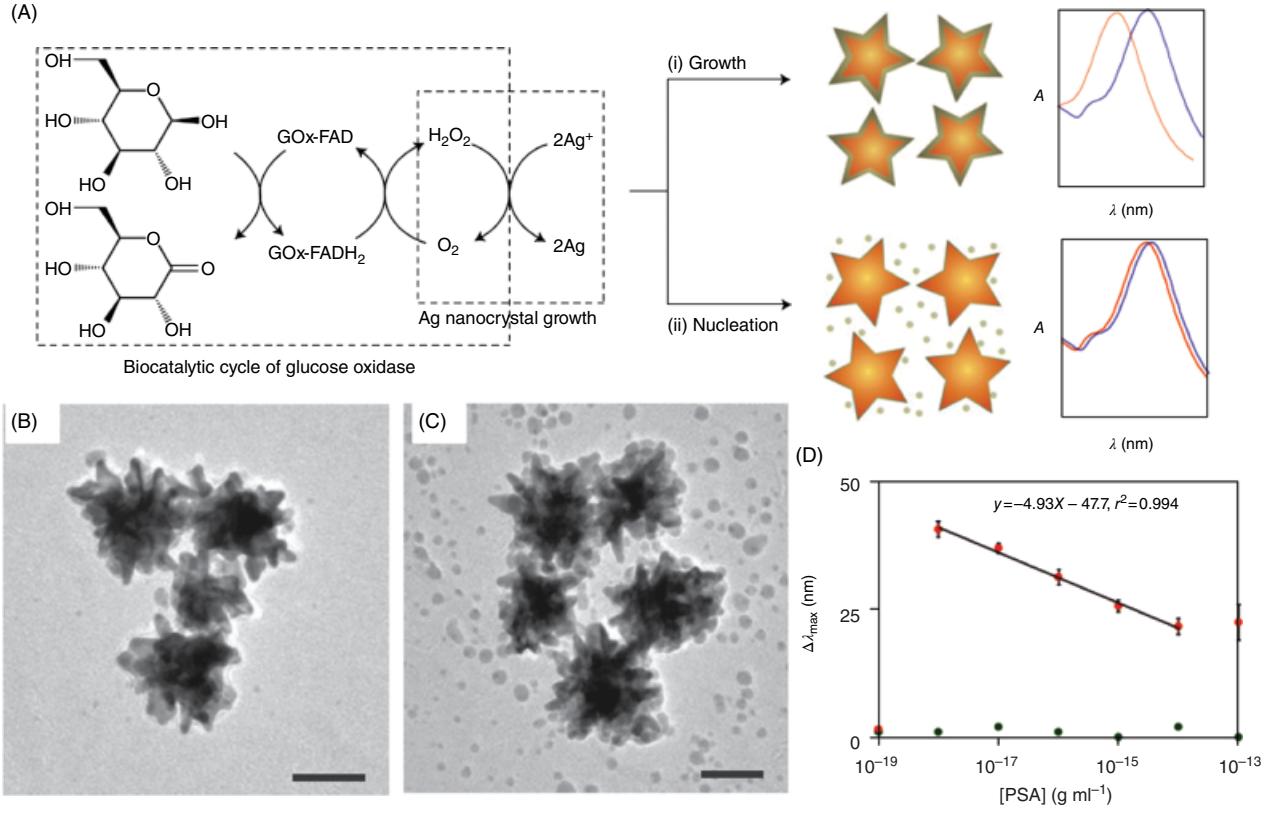

Figure 13.4 (A) GOx-controlled deposition/nucleation of Ag, leading to the LSPR shift of Au nanostars. (B), (C) TEM images after the signal-generation step when gold nanostars were modified with 10^{-20} g ml-1 GOx (B) and 10^{-14} g ml^{-1} GOx (C); scale bars, 50 nm. (D) Dose–response curve showing inverse sensitivity, with LSPR spectral shift reducing with increasing PSA concentration in serum. Adapted with permission from ref 24. © 2012 Nature Publishing Group.

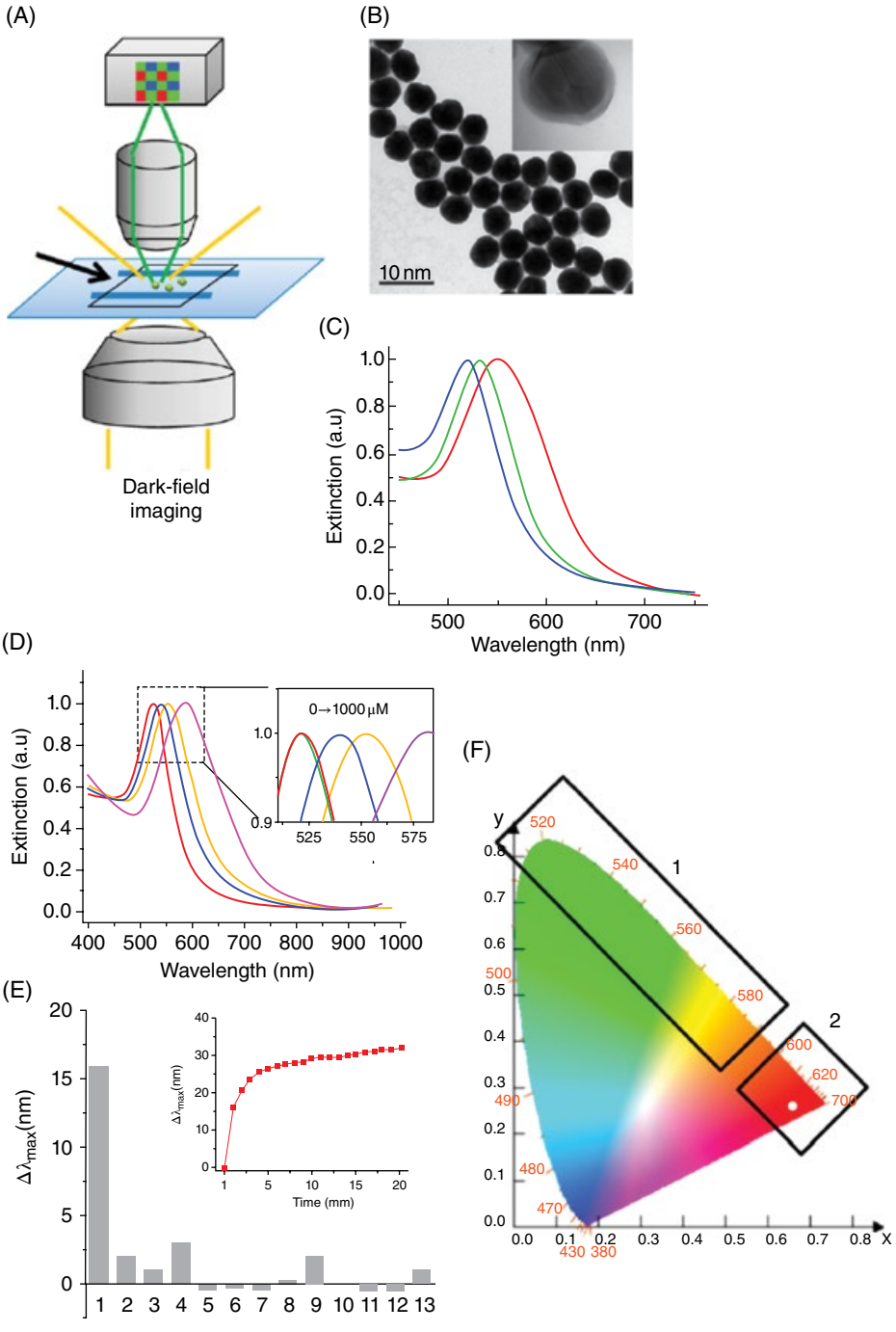

Figure 13.5 (A) Scheme of sensing with dark-field microscopy and colorimetric analysis at single particle level. (B) TEM images of Au–Ag PNPs. (C) Normalized UV–vis spectra of Au NPs, Au–Ag core–shell PNPs, and Au–Ag_2S core–shell PNPs. (D) Normalized UV–vis spectra of Au–Ag core–shell PNPs solution with the addition of different concentrations of NaHS. (E) Specific studies in the presence of cysteine, glutathione, and other common anions. Legend: (1) HS– (10 μM), (2) cysteine, (3) glutathione, (4) $S_2O_3^{2-}$, (5) SO_3^{2-}, (6) SCN^-, (7) NO_3^-, (8) NO_2^-, (9) Cl^-, (10) Br^-, (11) I^-, (12) CH_3COO^-, and (13) CO_3^{2-}. Inset is the time-dependent increase of $\Delta\lambda_{max}$ after addition of 100 μM NaHS. (F) The color response regions of the spherical Au–Ag PNPs, 1, and the rod-shaped AuNR–Ag PNPs, 2, in the CIE 1931 colorimetric diagram. Adapted with permission from ref 30. © 2014 American chemical society.

The spectral of the Au@Ag nanospheres with diameter of 51 nm turned to be most matching with the color-sensitive domain of the CCD camera. High sensitive and high-throughput hydrogen sulfide detection has been achieved by quantifying the color change of the individual PNPs due to the oxidation. With rapid color RGB analysis, a high density of individual PNPs can be monitored simultaneously, enabling high-throughput H_2S sensing. Since the sensing is based on calculation of the color change of a high density of Au@Ag nanoprobes, spectrometer, grating and the entrance slit restriction on the detection area is nonessential.

13.2 Bimetallic Sensors Based on Surface-Enhanced Raman Spectroscopy

Surface-enhanced Raman spectroscopy / scattering (SERS) is a phenomenon in which Raman scattering is enhanced when molecules of interest are excited in the proximity or on the surface of roughened metal substrate. The enhancement factor can be up to 12 orders of magnitude, which implies that even a single molecule can be detected by this technique. SERS was first discovered in the 1970s[31, 32], now it has gradually become an important tool in analytical science[33, 34]. The basic enhancement mechanism has been argued for several decades. We now recognize that the enhancement is principally based on three distinct resonances: namely, the SPR of the substrate metal, the charge transfer resonance among the metal substrate and molecule, and the molecular resonance[35–37]. Compared with standard Raman scattering, SERS requires metal nanostructures as substrate. Gold and silver are the most widely used metals as SERS substrate. Attributed to the excellent plasmonic efficiency and ideal electromagnetic enhancement in the visible range, silver is very popular in SERS[38–41], and Ag nanostructures often possess higher SERS enhancement. Gold is attractive in the area of biological applications owing to its good biocompatibility, high stability, and ease to be modified[42]. The Au–Ag bimetallic nanostructures combine the advantage of both metals, and are widely used in the detection of DNA, protein, and many other small molecules. Cao et al. have developed high sensitive and selective SERS probes for multiplex detection of oligonucleotides[44] and proteins[45]. Take the protein detection as an example, as shown in Figure 13.6a and b. Two kinds of Raman dye-functionalized nanoparticle probes with specific protein-binding affinities have been designed for examining the interactions of protein and small molecules (type I) and interactions of protein and protein (type II). Type I probes are composed of Au NPs modified by oligonucleotides (A_{10}). The oligonucleotide was modified with a Raman dye at one end and contained recognition groups for small molecules. Thus, the probe can selectively recognize the target molecule in a complex environment by their recognition element and exhibit the typical Raman signatures of the Raman dye. For type II probe, the Au NPs were modified with antibody as recognition element for specific antigens and Raman-dye-modified alkylthiol-capped oligonucleotides for characteristic Raman signatures. Bovine serum albumin (BSA) was used to further passivate the metal surface. In a typical test, the detection was finished in a protein array format with aldehyde-functionalized glass slides (Figure 13.7c). First, the protein sample was spotted onto the glass sides. Then, the protein chip was exposed to a Raman

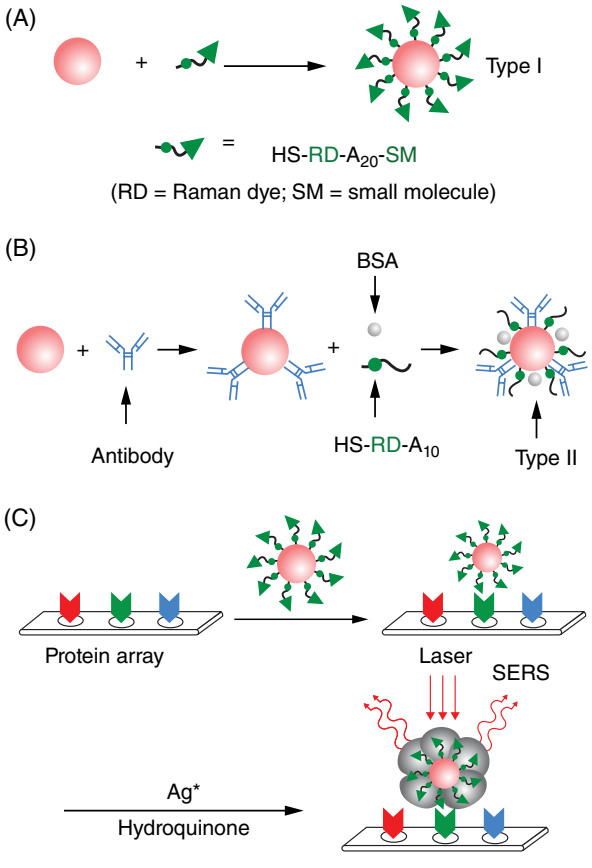

Figure 13.6 (A) Scheme of NPs with Raman spectroscopic fingerprints for DNA and RNA detection. Flatbed scanner images of Ag-enhanced microarrays (B) and corresponding Raman spectra (C) Each color correlated to a specific Raman dye and corresponded to a different DNA sequence. No false-positives or false-negatives were observed. Two nanoparticle probes (A: type I, B: type II) for protein detection. (C) SERS detection of type I probe after immobilization on a chip and silver staining. Figures are adapted with permission from ref. 45. Copyright 2003 American chemical society.

probe suspension for about 2 h. After washing, silver reinforcement was conducted with the reduction of Ag^+ by hydroquinone to increase SERS signal, and corresponding SERS spectrum of the dye can be obtained with Raman spectrometer coupled to a fiberoptic probe. The effectiveness and selectivity of type I and type II probes was tested in a series of screening experiments using different target molecules.

"Hotspots" are essential to enhance the sensitivity of the SERS analysis. The Raman scattering of the target molecules can be highly enhanced by the"hotspots" of the NPs where the electromagnetic field is extraordinarily intense[46]. Researchers have endeavored to build such hotspots, like various kinds of Au–Ag nanostructures with inter-or intra-particle nanogaps[47–52], roughened surface[53, 54], and sharp corners[55, 56]. Recently, Liu et al. reported a dealloying method to construct porous

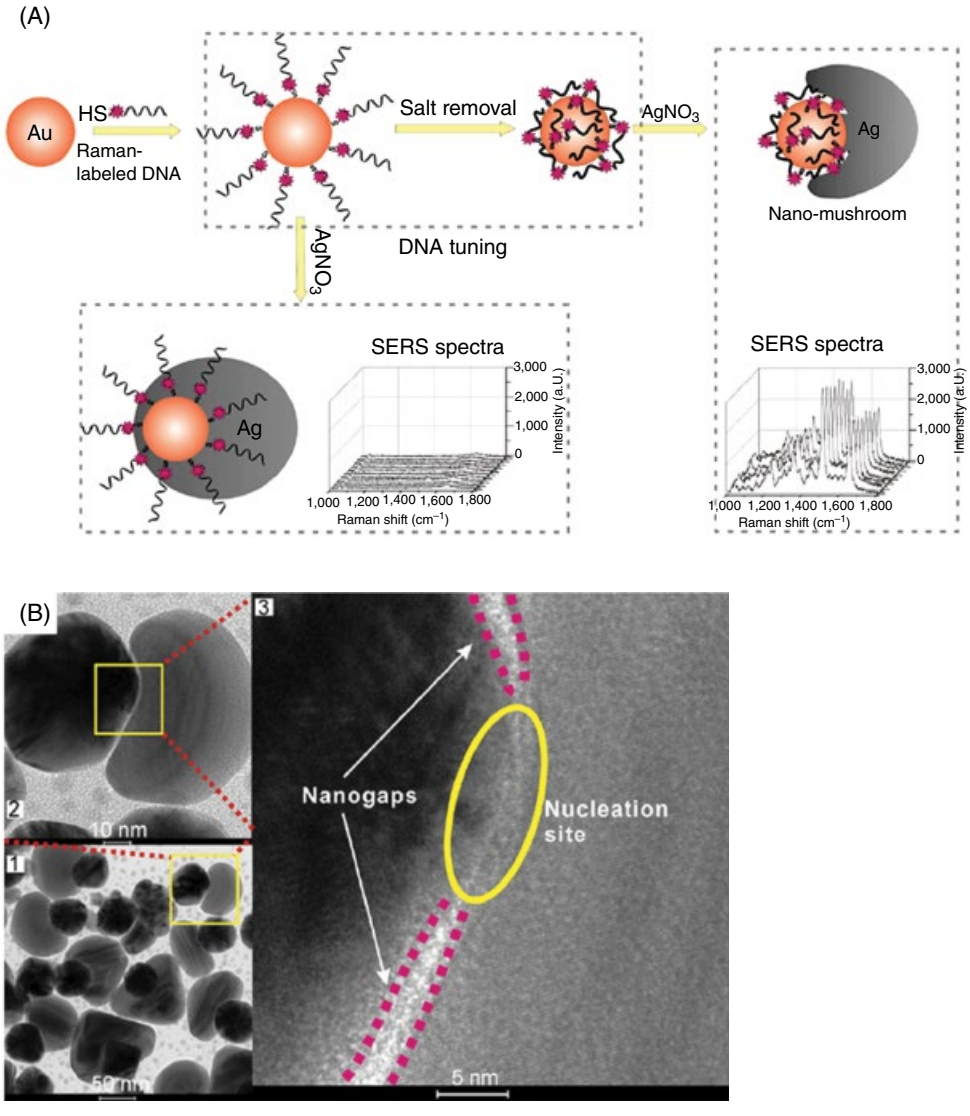

Figure 13.7 (A) Scheme of the synthesis process of nano-mushrooms and the detection of DNA. Gold NPs functionalized with Raman-labeled DNA were used to oriented growth of silver on their surfaces. Mushroom-like nanostructures with interior nanogaps produced much stronger SERS signals than those without nanogaps (B) TEM image of nano-mushrooms with different magnifications. Adapted with permission from ref 52. © 2015 Springer Nature.

Au/Ag alloy NPs with lots of inherent hotspots[51]. The Au–Ag alloy NPs were enclosed in ultrathin hollow silica shells instead of capping ligands for stabilization. The clean and porous NPs effectively coupled with the LSPR and provided abundant inherent hotspots. These hotspots were readily accessible for target molecules since the surface of the NPs was very clean. Both of these characters enabled the material as a highly sensitive SERS sensor.

Nanometer gap junction of inter-or intra-particles can effectively couple LSPR and produce hot spots for SERS analysis[46–51]. Extensive efforts have been extended to engineer these gaps. Shen et al. developed a DNA oriented method for preparing Au/Ag nano-mushrooms with interior nanogaps (Figure 13.7)[52]. The sensitivity of the mushrooms sensor is associated with the nanogap area between the Au head and the Ag cap. The area of the nanogap can be controlled by surface density of 6-carboxy-X-rhodamine modified oligonucleotide on Au NPs. SERS enhancement factor of $\sim 1.0 \times 10^9$ was obtained, which was much higher than that for Au–Ag nanostructures without nanogaps.

The discriminating power of SERS enabled it widely used in areas like arts and archeology, forensics, and the detection of pharmaceuticals[46, 57]. Moreover, the plasmonic metals were frequently integrated with catalytic metals to construct bifunctional complex to monitor the catalytic process. By rationally design, hybrid metal nanostructures with both high plasmonic/SERS activity and a large surface area of the catalytically active metal can be synthesized. Up to now, raspberry-shaped Au–Pt–Au core–shell NPs[58], Pt-tipped-Au NRs[59], Pd-tipped-Au NRs[60], Au@Pd[61], and so on have been developed to study the catalytic process of Pt or Pd by SERS.

13.3 Electrochemical Sensors Based on Bimetallic Nanoparticles

Attributed to their advantage of simplicity, low energy demand and ease to be minimized, electrochemical sensors are very suitable to develop portable sensing device[1]. The mechanism of the electrochemical sensors is based on charge transport on the electrode and electrochemically active species, which can be oxidized or reduced on the surface of the electrode. Compared to the plasmonic sensors, where signals are generated by interactions of sensors and target analytes, electrochemical sensors employ electrocatalyst to facility electron transfer between reactants and the electrode. The electrocatalyst can accelerate the reaction rate while it is not consumed. Due to synergistic and electronic effect, electrochemical sensors based on bimetallic metals often provide higher sensitivity and selectivity than their monometallic counterparts. Since the biosensors incorporated with enzymes often encounter long-term stability problems and difficulties in accessing its active site, researchers are endeavoring to develop nonenzymatic sensors. So here we will mainly focus on bimetallic nonenzymatic sensors. This section was grouped by target analytes.

13.3.1 Detection of Heavy Metal Ions

Most of the heavy metals are poisonous and can cause serious environmental problems, and relevant lows are gradually tightening up. Researchers are endeavoring to develop sensors to detect heavy metals in the environment. Owing to its fast electron transfer kinetics, nanomaterials like nanocarbons and metal nanoparticles are popularly used in electrochemical sensors to detect heavy metal ions, and biomolecules like enzymes and DNA aptamers are often used as recognition element.

In 2010, Gong and co-workers developed a high sensitive and high selective Hg^{2+} sensor based on Au–Pt bimetallic nanoparticles/organic nanofibers modified glassy carbon electrode[62]. Here Au–Pt bimetallic nanoparticles were uniformly distributed

in the interlaced organic nanofibers matrix and acted as microelectrode ensembles. A low detection limit of 0.008 ppb (S/N = 3) was achieved, which is much lower than the guideline value from the World Health Organization (WHO). Interference experiments showed that the detection was not affected by other metal ions associated with merry detection and merry in practical water samples was detected and the results were comparable with those obtained by ICPMS.

The narrow-band gap p-type semiconductor Te nanostructures have proven to be very promising in a wide application such as piezoelectronic devices and photoconductive detectors. Moreover, due to the high anisotropic properties, Te atom usually form helical chain structure and often used as sacrificed templates to synthesize many novel nanostructures[63, 64]. In 2013, Wang et al. developed an Au-decorated tripod-shaped Te hybrid based electrochemical sensor to selective detect arsenic ions (Figure 13.8)[65]. The Au–Te hybrids were synthesized in two steps: hydrothermal syntheses of tripod shaped Te planar microstructure and galvanic replacement process of $HAuCl_4$ with Te template. As (III) and Cu (II) were simultaneously detected by square wave anodic using stripping voltammetry with Au–Te hybrid electrode. The limit of detection of As (III)

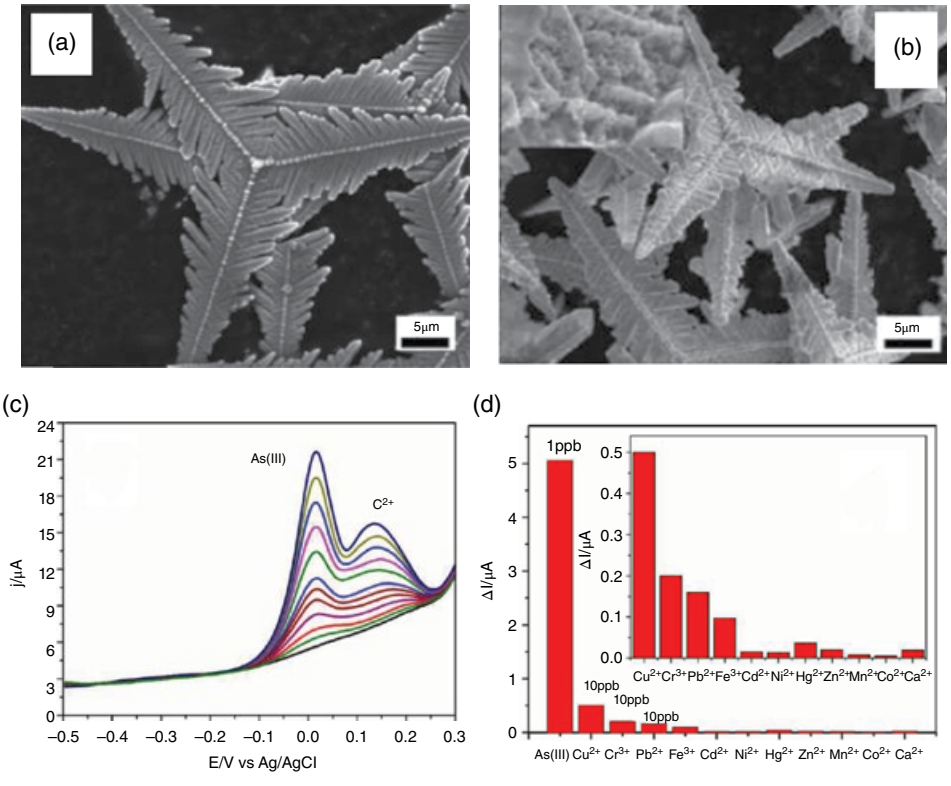

Figure 13.8 (a) and (b) High-magnification SEM of Te and Au/Te product. (c) Square wave anodic stripping of As (III) and Cu (II) mixtures on Au/Te modified GC electrode. (d) Interference experiment of other metal ions on the detection of As (III). The concentration of As (III) is 1 ppb, while the concentration of all other ions tested here is 10 ppb. Adapted with permission from ref 65. © 2013 American Chemical Society.

was as low as 0.0026 ppb, which was more than two orders lower than that obtained by bare Au electrode. The excellent achievement was attributed to its unique 3D morphology that rich in ledges and kicks for catalytic reactions.

DNAzymes are a kind of specific DNAs that with the help of special metal ions can cleave specific substrates. The DNAzymes showed high metal-binding affinity and specificity and are often used to detect metal ions. Up to now, many kinds of metal ions have been detected in the assistance of DNAzymes, such as Pb^{2+} and Hg^{2+} ions. In 2014, Chen et al. developed a Pb^{2+} sensor based on a three-dimensionally ordered macroporous Au/Pd bimetallic electrode and with the assistance of DNAzymes as the recognition element. The limit of detection as low as 1×10^{-19} M was archived partly attributed to the good electronic conductivity and the large active surface area of three dimensionally ordered macroporous Au/Pd bimetallic electrode[66].

13.3.2 Detection of Uric Acid

Uric acid (UA; 2,6,8-trihydroxypurine) is the final product of purine nucleotide catabolism. The typical concentration of UA in blood is in the range of 200–430 μM for male and 140–360 μM for female. A higher level of UA in the blood may be a sign of gout, renal failure, leukemia, or other pathological conditions[67]. Clinical detection of UA is generally relied on enzymatic biosensors[68]. UA is an electrochemically active compound and can be oxidized easily by common electrode. Electrochemical methods such as square wave voltammetry, cyclic voltammetry, chronoamperometry, and differential pulse voltammetry can be used to detect UA in the solution. For the detection of UA, ascorbic acid is a common disrupter since it often coexists in the biofluid of humans and the oxidation peaks of ascorbic acid and UA are very close and often overlapped. Modified electrodes are often used to selectively detect UA in solution. For example, Zn_3Ni alloy-modified graphite was used to detect UA in human urine and blood[69], and sensors to simultaneously detect multi-analyte have been developed. In 2007, Yogeswaran et al. developed an electrochemical sensor based on Pt/Au bimetallic nanoparticles deposited multiwall CNTs to simultaneously detect AA, epinephrine and UA[70]. Due to the high electrocatalytic activity of the nanocomposite, well-separated oxidation peaks of AA, epinephrine and UA were obtained with separations of 0.222 and 0.131 V. In 2013, Yan et al. developed a one-step reduction method to anchor Pd–Pt bimetallic nanoparticles on reduced graphene oxide[71]. The nanocomposites modified electrode was fabricated and used to detect AA, dopamine, and UA in a mixture.

13.3.3 Nonenzymatic Detection of Hydrogen Peroxide

Hydrogen peroxide (H_2O_2) sensing is becoming more and more important in analytical science since it is an important molecule in the areas ranging from industrial, medical and health care, food processing, to international public safety[72]. In the industrial area, H_2O_2 sensing is widely used in paper bleaching, every sterile package, cleaning supplies, textile industry, and minerals. Beyond its industrial significance, H_2O_2 is a very important molecule in biological and medical field. It is related to many biological processes and is an outgrowth of lots of oxidases like glucose oxidase, urate oxidase, cholesterol oxidase, and so on. Hence, it is of great practical significance to develop

a rapid, low-cost, and accurate H_2O_2 sensor. Since H_2O_2 shows no UV or fluorescence signals, electrochemical sensors are good choices.

It is important to eliminate the influence of other electroactive substance coexists in the system. Ascorbic acid, dopamine, and urine acid are common disruptors in biological fluid that may lead to a faulty measurement for H_2O_2 sensing. In Weng's work, they found that even at a low potential of 0.2 V (vs. Ag/AgCl), ascorbic acid (0.57–5.68 mM) could be detected with sensitivities of 178 and 169 A $cm^{-2}mM^{-1}$ for Pt and Ni foil electrodes, respectively[72]. Therefore, improving the selectivity is an important component to construct a practical H_2O_2 sensor.

Many excellent reviews on H_2O_2 sensing have been published[73]. Here we will focus on the bimetallic nanoparticle sensors solely. Compared with their monometallic counterparts, bimetallic nanoparticles often possess higher electrocatalytic activities, better selectivity, and longer stabilities[74, 75]. In H_2O_2 sensors, various kinds of carbons have been used as bimetallic nanoparticles' support to get better dispersity, increase the specific surface area of the electrode, and improve the electronic conductivity.

Due to their high catalytic activity, enormous platinum-based bimetallic nanoparticles Pt–M (M = Au, Pd, Ru, Ir, Cu, Ni, Rh, etc.) have been developed for H_2O_2 sensing. Janyasupab et al. examined the selectivity and sensitivity of several Pt-based bimetallic electrocatalysts containing PtNi, PtCu, PtPd and PtRh toward H_2O_2 detection[76]. The performance of these electrocatalysts was investigated in the presence of a high content of UA (85 mg/L) and AA (15 mg/L), which are at the highest concentration limit normally found in human body. Among these bimetallic electrocatalysts, Pt–Rh showed a remarkable sensitivity of 839.9 A mM^{-1} cm^{-2} ($R^2 = 0.998$) with 0.86% decrease in current in existence of the AA and UA. Table 13.1 compares the performances of the bimetallic catalysts in this study. In Cui's work, Pt–Au bimetallic nanoclusters were *in situ* electrodeposited on the surface of reduced graphene oxides (rGO) / GC[77]. The electrochemical sensor based on Pt–Au NCs-RGO displayed a favorable electrocatalytic activity toward the reduction of H_2O_2, with the limit of detection as low as 8 nM. In 2015, Li et al. synthesized Au@Pt@Au triple layers bimetallic nanoparticles on the support of GO, with both Au and Pt exposed in the outer layer. These nanocomposites possess peroxide like activity and can be used for electrocatalytic reduction and oxidation of H_2O_2. The bimetallic sensor was applied to detect H_2O_2 released from living cell

Table 13.1 Sensitivity and selectivity performance of Pt based bimetallic catalysts. Adapted with permission from ref 76. © 2013 Elevier B.V.

	Pure H_2O_2		Mixture of (H_2O_2 + AA + UA)				
Metal	Sensitivity ($\mu A\ mM^{-1}$)	R^2	Sensitivity (μAmM^{-1})	R^2	LOD (μM) (n = 9)	Linear range (upper limit, mM)	Degree of interference (%)
PtCu	13.61	0.992	3.61	0.996	12.2	4.0	−73.48
PtNi	40.91	0.995	37.89	0.989	31.5	2.0	−7.38
PtPd	47.05	0.990	54.29	0.991	114	3.0	+15.39
PtRh	161.68	0.998	160.29	0.991	34.8	2.0	−0.86

and demonstrated potential use in bioapplications[78]. For traditional core–shell nanostructures with only the shell component exposed to the environment, the catalytic activity of the core component may be weakened. In this study, protuberances Au was deposited on the Pt shell of Au@Pt structure, and a raspberry-like Au@Pt@Au structure was formed. The synthesized nanocomposites possess bidirectional electrocatalytic activity toward the reduction and oxidation of H_2O_2.

In 2015, Shang et al. synthesized AuPd hollow nanoparticles on the support of nitrogen-doped graphene[79]. Co NPs were used as a sacrificial template to reduce $HAuCl_4$ and Na_2PdCl_4 simultaneously. Attributed to the high specific area of hollow structures of AuPd nanostructures and synergistic effect between the nitrogen-doped graphene and AuPd nanoparticles, the hybrid films showed high electrocatalytic activities toward H_2O_2 reduction and a sensitivity of 5059.5 $\mu A\, mM^{-1}\, cm^{-2}$ was obtained.

Besides the Pt-based bimetallic sensors, Au based bimetallic catalysts like Au–Ag are often used to construct H_2O_2 sensors. Li et al. constructed Au–Ag bimetallic nanosensors with a series of component proportions[80]. $Ag_{67.3}Au_{32.7}$ bimetallic nanoparticles showed a remarkable enhanced performance for H_2O_2 detection. At an applied potential of –0.5 V (vs Ag/AgCl), fast responsible time (less than 5 seconds), higher sensitivity of 600 $mA\, mM^{-1}\, cm^{-2}$ and a linear range from 0.01 to 68 mM ($R^2 = 0.998$) were obtained (Figure 13.9 a and b), and the addition of common interferences AA, UA, and glucose did not vary the current signal at the applied potential (Figure 13.9c).

13.3.4 Detection of Glucose

As of 2015, about 415 million people suffer from diabetes around the world, which is responsible for about 1 to 5 million deaths every year[81–83]. Therefore, the development of an inexpensive and disposable glucose sensor is of great practical significance. Wang and Chen published comprehensive and special reviews on electrochemical glucose sensors in 2008 and 2013, respectively[84, 85]. Here we will focus on bimetallic sensors. Despite the unique selectivity found in enzyme-based biosensors, their construction is often more complex and long-term stability is problematic[86, 87]. The integrity of the enzymes structures is easily destroyed during the sensor construction and the active enzyme is often hidden in the central of the protein. The nonenzymatic sensors obviate these problems since the inherent enzymatic activity of the bimetallic sensor relies on the direct electro-oxidation of glucose on the electrode. Many enzyme-free glucose sensors based on bimetallic nanostructures have been developed.

In Wang's work, 3D nanoporous PtPb nanostructures with various ratio of Pt–Pb have been synthesized on the substrate of Ti by a one-step hydrothermal method[88]. The as-prepared Pt–Pb 3D network showed sensitive amperometric response toward glucose at a negative potential of -80 mV (vs. Ag/AgCl). At this potential, interference from AA, UA, and 4-acetamidophenol is effectively avoided.

In addition to the cyclic voltammograms and chronoamperometry, chronoimpedance method has been developed to detect glucose. Mayorga-Martinez et al. have constructed Au–Pt bimetallic nanowires for nonenzymatic impedancimetric determination of glucose[89]. In their study, a screen-printed electrode was used as a working electrode and the chronoimpedance technique was used to detect glucose. A thin layer of iridium oxide was electrodeposited on the electrode to decrease the electrode–electrolyte interface impedance and glutaraldehyde was used as a cross-linking

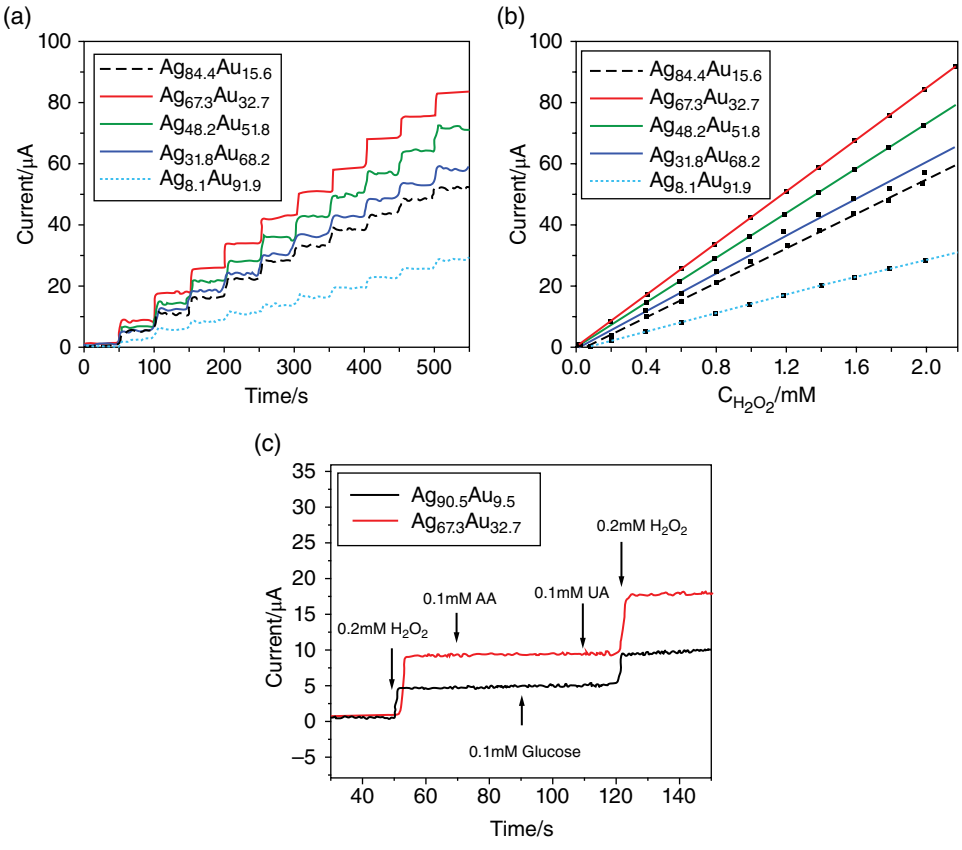

Figure 13.9 (a) Amperometric responses of different proportions of bimetal modified GC electrodes upon the successive addition of 0.2 mM H_2O_2 into the stirring 0.1M PBS solution (applied potential: - 0.5 V). (b) Linear relationships of different proportions of bimetal modified GC electrodes between the response current and the concentration of H_2O_2. (c) I–t curves of $Ag_{90.5}Au_{9.5}$ and $Ag_{67.3}Au_{32.7}$ NPs modified GC electrodes in stirring 0.1 M PBS solution with addition of H_2O_2, AA, UA, and glucose solution. Adapted with permission from ref 80. © 2013 The royal society of chemistry.

agent to immobilize Au–Pt nanowires. Au–Pt nanowires were *in situ* electrodeposited on the surface of the electrode. When a series concentration of glucose in the range of 20 μM to 140 μM was added, the impedancimetric response increased consequently. The low detection range may be suitable for detecting glucose in saliva, urine and sweat, or diluted blood. The proposed mechanism (shown in Figure 13.11a) is attributed to the charge transfer during the oxidation of glucose to glucuronic acid and H_2O_2 on an Au surface and the reduction of H_2O_2 on the Pt surface. UA and AA showed no interference due to the low dc potential (100 mV) coupled with chronoimpedance (Figure 13.11 b).

13.3.5 Electrochemical Immunosensors

Due to the high electrocatalytic activity, bimetallic nanoparticles have been used to construct electrochemical immunosensors. Yang et al. designed a sandwich electrochemical

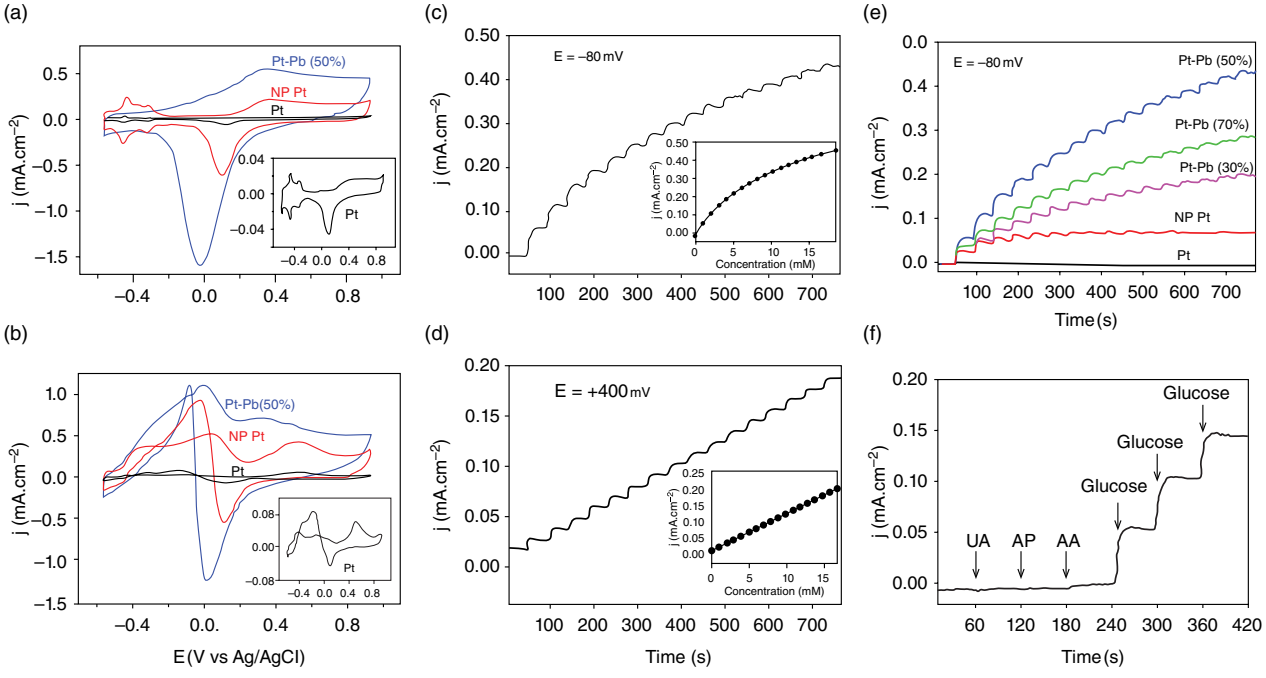

Figure 13.10 Cyclic voltammograms (CVs) of different electrodes in the absence (a) and presence (b) of 10 mM glucose at a scan rate of 10 mV s^{-1}. Insets are the magnified CVs of the corresponding Pt wire electrode. Chronoamperometry curves of Pt-Pb (50%) electrode with successive addition of 1 mM glucose (1-16 mM), (c) -80 mV and (d) 400 mV. Insets are relationship of currents with glucose concentrations. (e) Chronoamperometry curves of the different electrodes with the successive addition of 1 mM glucose (1-16 mM) at -80 mV. (f) Specific study. Adapted with permission from ref 88. © 2013American Chemical Society.

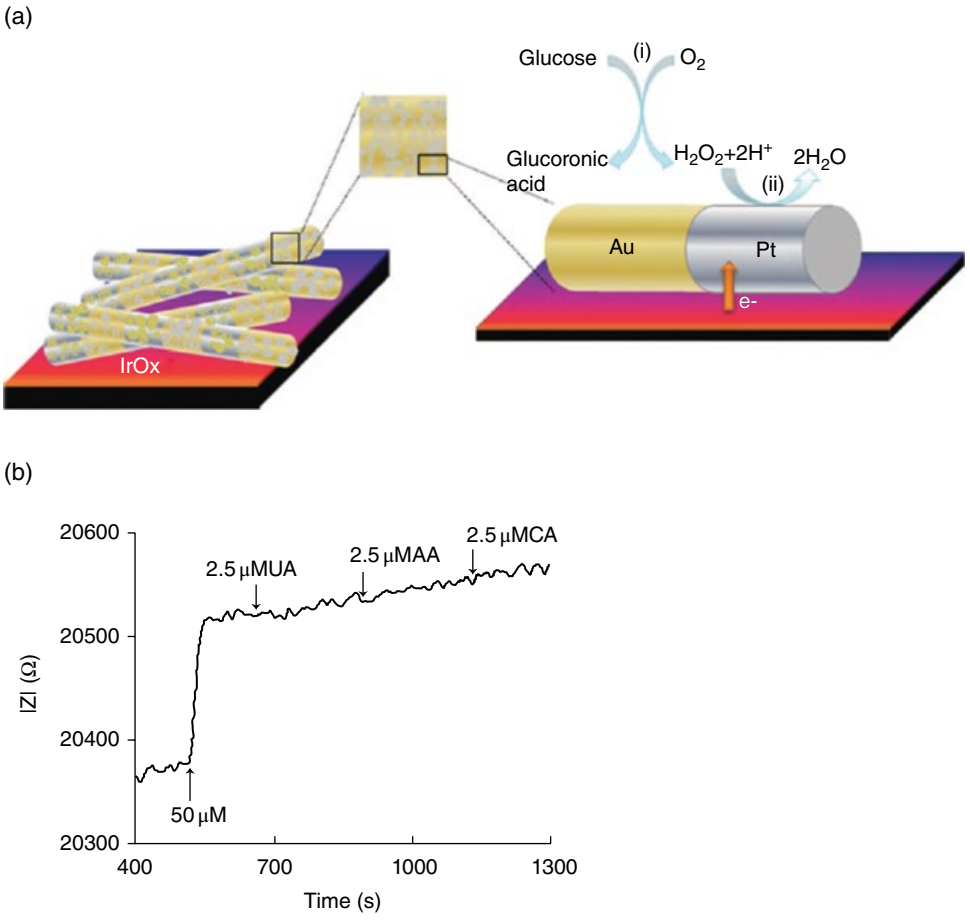

Figure 13.11 (a) Proposed mechanism for the glucose electrocatalytic detection using Au–Pt NW. (i) Glucose is transported by convection to the gold surface, where it is oxidized to glucuronic acid by reducing O_2 to H_2O_2, (ii) H_2O_2 decomposes into H_2O on the platinum surface. (b) Evaluation of interfering species. Adapted with permission from ref 89. © 2013 The royal society of chemistry.

immunosensor with Au functionalized porous graphene nanoparticles (Au-PGO) as sensing platform and Au@Pd core–shell bimetallic functionalized graphene nanocomposites (Au@Pd-Gra) as signal enhancers (Figure 13.12)[90]. Attributed to its large surface area, Au@Pd-Gra was used to immobilize redox probe-thionine (Thi), horseradish peroxidase (HRP), and secondary antibodies (Ab2). With the high electrocatalytic activity, at the presence of H_2O_2, carbohydrate antigen 19-9 (CA19-9) was sensitively detected with a low detection limit of 0.006 U mL^{-1}. Similarly, Au–Pt bimetallic nanochains, Pd/Pt nanostructures deposited on graphene have been prepared to immobilize Ab2 and enhance the electrochemical signal to detect carcinoembryonic antigen and human tissue polypeptide antigen respectively[91, 92]. The method is also applicable to other antigens. The electrochemical immunosensor combines the high specificity of the immunoassay and the high sensitivity of the electrochemical method and has potential application values.

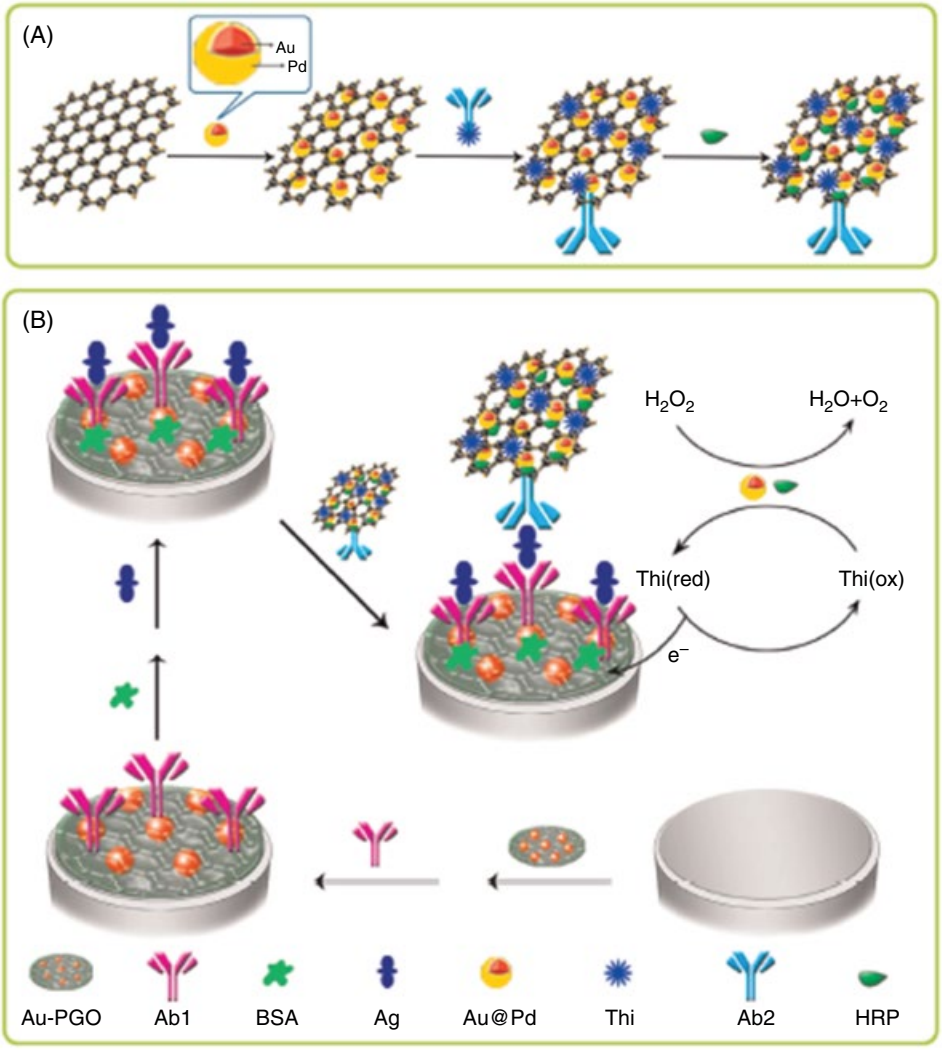

Figure 13.12 (A) The procedure to prepare Ab2 bioconjugate (Au@Pd-Gra/Thi-Ab2/HRP). (B) Fabrication of sandwich immunosensor and the signal amplification mechanism. Adapted with permission from ref 90. © 2015 Elevier B.V.

13.3.6 Detection of other Electroactive Molecules

In addition to the above small molecules, electrochemical bimetallic sensors have been designed to detect biological molecules such as dopamine, glutamate, long noncoding RNA, cholesterol, and so on[93–97]. Dopamine and glutamate are two important neurotransmitters in the central nervous system, and accurately monitoring their concentrations is important to study neurological disorders. Huang et al. fabricated a dopamine sensor by decorating Ag–Pt bimetallic nanoparticles on electrospun nanoporous carbon nanofibers. A limit of detection of 0.11 μM was achieved[93], and selectivity study showed that common interferences like uric acid and ascorbic acid would not

interfere with the detection. Yu et al. developed a glutamate sensor by incorporating a hydroxyl functionalized ionic liquid with electrodeposited bimetallic Au–Pt NPs and nafion to construct a $[C_3(OH)_2mim][BF_4]$-Au/Pt-Nafion composite, then glutamate oxidase was immobilized on it. Glutamate was detected at –200 mV sensitively and reproducibly[94]. Long noncoding RNA is related to upregulated hepatocellular carcinoma (HCC), Liu et al. deposited Pt–Pd bimetallic nanodendrites/nanoflower-like clusters on graphene oxide/Au/horseradish peroxidase to increase the sensor's sensitivity for the detection of HCC[95]. High cholesterol is considered as a key risk factor for cardiovascular disease. One electrochemical method to detect cholesterol is to construct cholesterol oxidase biosensors. Pt–Pd and Au–Pt bimetallic NPs were used to catalyze the oxidation and reduction of H_2O_2 and eliminate interference and overvoltage problems[96, 97].

13.4 Sensors Based on the Enzyme-Mimicking Properties of Bimetallic NPs

Attributed to their high specificity, high efficiency, and mild reaction conditions, natural enzymes are widely used in biosensors and other analytical processes[98, 99]. Enzymes are essentially proteins, but they are quite costly and their activities are very sensitive to the environment—denaturation and digestion can influence their long-term stability. To overcome these problems, artificial enzymes have been actively researched for their potential as convenient and highly stable substitutes to natural enzymes[100, 101]. Many nanomaterials, containing nanocarbons, noble metal nanomaterials, and metal oxides materials have been proved to possess enzyme-mimicking properties. Bimetallic nanomaterials possess enhanced catalytic property attributed to the synergistic effect and the electronic effect. Sensors based on the enzyme mimics properties of bimetallic NPs, and this trait has been widely used in the detection of H_2O_2[103], glucose[104], metal ions[105, 106], thrombin[107], biothiols[108], cancer cells[109, 110], and more.

It is well known that the catalytic properties of the nanomaterials are greatly dependent on the size, shape and composition. Attributed to their high surface area, dendritic and porous structures often exhibit higher catalytic activities[111]. Ge et al. prepared porous Pd@Au NPs as mimicking natural peroxidases and developed a colorimetric method to detect human chronic myelogenous leukemia cell lines (K-562), in which 3,3.5,5'-tetramethylbenzidine (TMB) was used as substrate (Figure 13.13)[110]. At the presence of the catalyst, peroxidase TMB could be oxidized by H_2O_2 and produce a blue color. UV-vis spectral was used to study the catalytic activity (Figure 13.13b). The absorption peak at 652 nm is attributed to the oxidation of TMB (oxTMB). As shown in Figure 13.13b, Pd@Au NPs and H_2O_2 were both required for the oxidation of TMB, demonstrating that the porous Pd@Au NPs possess an intrinsic peroxidase-like activity. Compared with the natural enzyme HRP (Figure 13.13c), the oxidation of TMB by H_2O_2 with Pd@Au was fast and completed. Based on the peroxidase-like activity of the Pd@Au NPs, the authors developed a colorimetric method to detect cancer cell. By click chemistry, azide-functionalized folic acid was conjugated to terminal alkyne-functionalized Pd@Au NPs in aqueous solutions. The folic acid functionalized Pd@Au NPs could strongly conjugate on the cell surface by folate receptor (FR), which is a represent

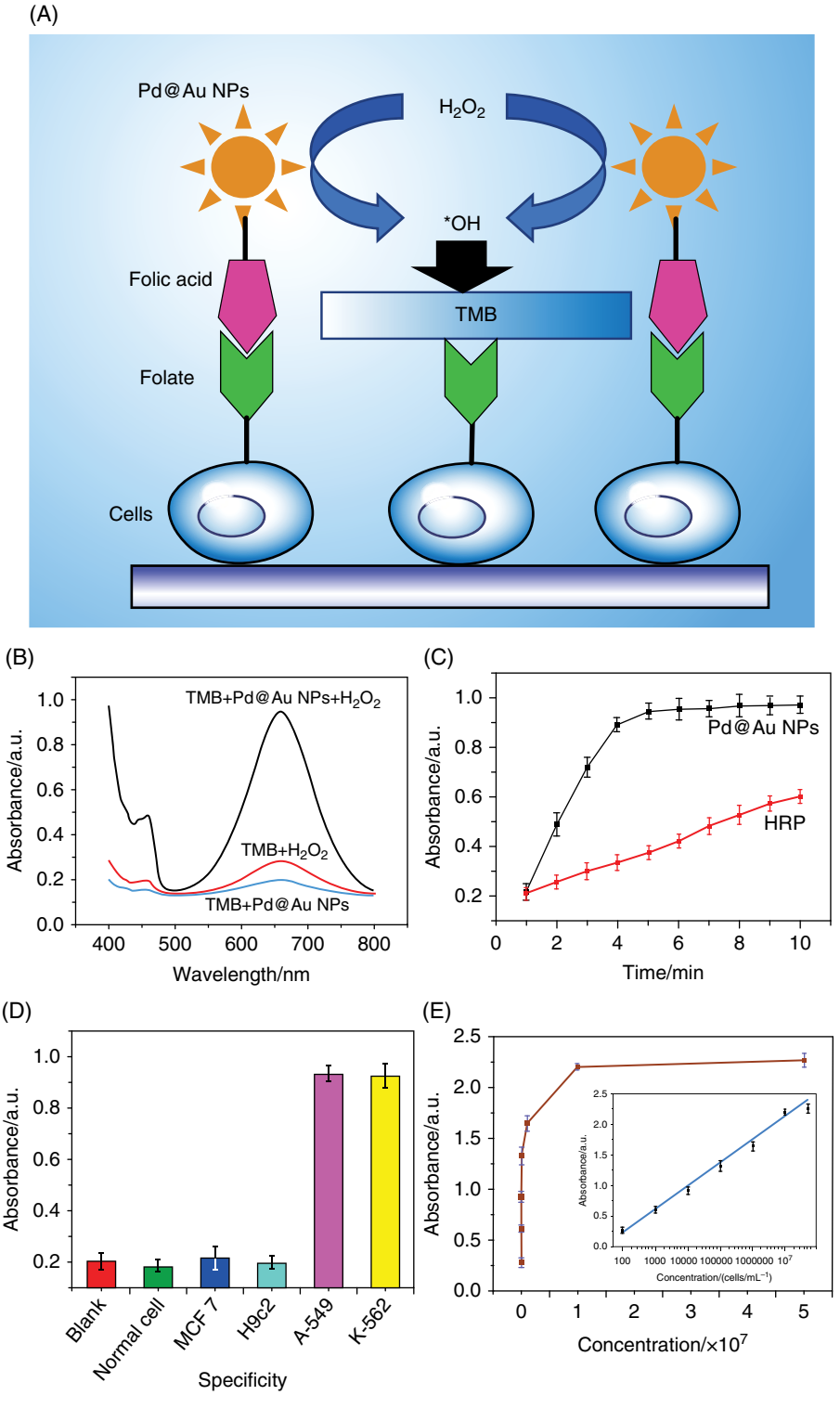

Figure 13.13 (A) The upper panel is scheme of the proposed mechanism for cell detection. (B) UV-vis spectra recorded under different conditions, (C) absorbance changes of TMB with Pd@Au NP and HRP catalyst. (D) Specificity of porous Pd@Au NP-based toward folate-positive cells; (E) relationship of absorbance intensity at 652 nm with the concentration of cells, inset is the linear calibration plot for cells. The error bars was calculated from five parallel measurements. Adapted with permission from ref 110. © 2014 The royal society of chemistry.

biomarker for some cancer cell[112]. In some kind of cancer cells, FR would overexpress, while for normal cells, it would not overexpress. Therefore, based on the specific and strong recognition of folic acid functionalized Pd@Au NPs with cancer cells, a selective and effective sensor for cancer cells can be constructed and K-562 cells were detected. The folic acid-conjugated Pd@Au NPs provided both recognition functionality for cancer cells and catalytic functionality for the oxidation of TMB by H_2O_2, which provided the color change. The specificity experiments showed that the strong signals were observed for K-562 and A-549 cells, which overexpressed the folate receptor. Other cells, including breast carcinoma cell line (MCF-7), cardiac myocytes (H9c2), and normal cells that did not overexpress the folate receptor produced no signal change. These results proved that the colorimetric assay based on the folic acid-conjugated Pd@Au NPs exhibited excellent selectivity for the folate-overexpressing cells.

13.5 Sensors Based on Luminescent Bimetallic Nanoclusters

In recent years, ultrasmall bimetallic nanoclusters have attracted enormous attentions attributed to their quantum-scale dimensions (about 2 nm), interesting molecular-like properties, controllable compositions, bimetallic synergistic effect, and rich surface chemistry[113–115]. The development in synthesis technique also promoted their wide applications in catalysis, sensors, and biomedicine. Their high fluorescence intensity, low toxicity, and rich surface chemistry have endowed them good candidates for sensors. Here, we will mainly introduce their application in sensors.

13.5.1 Detection of Heavy Metal Ions

The introduction of Ag element into the Au nanoclusters (NCs) often lead to significant changes in gold catalysis and luminescence performance[116–123], which was called *silver effect*. Zhou et al. prepared mercaptosuccinic acid stabilized Ag–Au alloy nanoclusters (MSA – AgAu NCs) by a three-step method (Figure 13.14a)[120]. Firstly, citrate-stabilized silver cores with diameters about 6–30 nm were synthesized by the reduction of $NaBH_4$. Second, Ag NPs were etched by MSA to a small size about 1.8 nm. Third, $HAuCl_4$ solution was added to the as-prepared MSA – Ag NCs to obtain MSA – AgAu NCs. The as-prepared MSA – AgAu NCs displayed a symmetric emission spectrum at 637 nm, and the maximum excitation wavelength was 390 nm (Figure 13.14b). The color of MSA – AgAu NCs solution was light yellow, and when it was under UV light at 365 nm it emitted a bright red color (inset of Figure 13.14b). The quantum yield of MSA – AgAu NCs was 1.6%, using lysozyme-stabilized Ag NCs as the standard[124]. In order to improve their biocompatibility and longer stability in high concentration salts, m-PEG-NH_2 was covalently attached to MSA – AgAu NCs by EDC chemistry. As in the presence of Al^{3+}, the fluorescence intensity of PEGylated MSA – AgAu NCs was much enhanced, the bimetallic NCs used as a turn-on fluorescence sensor for Al^{3+} (Figure 13.14c). The enhancement was possibly due to the formation of AuAl alloy as revealed by XPS, DLS, and ζ-potential data[125, 126]. The fluorescence intensity of the bimetallic NCs was gradually increased with increasing Al^{3+} concentration in the range between 2.0 to 2000 μM (Figure 13.14d). The detection

limit was 0.8 μM and this sensitivity could satisfy the demand of the World Health Organization on drinking water with the maximum level (7.4 μM) of Al^{3+}. The selectivity of the probe was studied in the presence of lots of metal ions common coexist in drinking water. It turned out that Pb^{2+} would slightly enhance the fluorescence of the probe, while Fe^{3+}, Fe^{2+}, Cu^{2+}, and Hg^{2+} would quench the intensity. The authors chose two chelating agent PDCA (for Cu^{2+} and Pb^{2+}) and MSA (for Fe^{3+}, Fe^{2+}, and Hg^{2+}) to mask their inference. By addition of two chelating agents, the interfering ions were effectively masked (Figure 13.14e). With similar means, bimetallic nanoclusters have been widely used in the detection of metal ions including Hg^{2+}[121, 127–130], Cu^{2+}[121, 131], Pb^{2+}[132], Cd^{2+}[133], Fe^{3+}[134] ions and so on.

13.5.2 Detection of Sulfide Anion

Sulfide anion is toxic and harmful to living organisms. It is often exist in the industrial waste. In recent years, bimetallic nanoclusters have been developed to fluorimetric analysis of sulfide anion owing to their high sensitivity and convenience[135, 136]. In Chen's work, DNA-templated Au/Ag nanoclusters (DNA-Au/Ag NCs) were synthesized by a one-step method that Au^{3+} and Ag^{+} were reduced by $NaBH_4$ in the presence of DNA (5'-CCCTTAATCCCC-3')[135]. Since S^{2-} could quench the fluorescence of DNA-Au/Ag NCs via the interaction between S^{2-} and Au, Ag atoms, S^{2-} ions could be sensitively detected through the changes in fluorescence intensity. A detection limit as low as 0.83 nM was achieved. Interfere study showed that I^{-} would disturb the sensing of S^{2-} due to the formation of insoluble AuI and AgI[136]. The interference was eliminated by the addition of $S_2O_8^{2-}$, since $S_2O_8^{2-}$ and I^{-} generate SO_4^{2-} and I_2[137]. S^{2-} ions in natural water samples was detected by these probes, indicating that it was suitable to complicated samples.

13.5.3 Detection of Other Small Molecules

Guan et al. have developed a sensitive method to detect H_2O_2 and herbicide propazine by red-shift and fluorescence enhancement of bovine serum albumin (BSA)-protected AgAu-BSA NCs[139]. AuAg NCs were prepared by incorporating Ag^{+} in the synthesis of BSA-protected Au NCs. With the increase of the Ag^{+} concentration in the synthesis solution, the as-prepared AuAg NCs show a large blue-shift in fluorescence compared to Au NCs. When the concentration of the Ag ion was 10 mM ($Ag^{+}/Au^{3+} = 2/1$), the obtained AuAg NCs were denoted as AuAg-10NCs. The blue-shift is attributed to the incorporation of Ag into Au NCs[140]. It is interesting that upon the addition of H_2O_2, the fluorescence peak of the AuAg NCs with higher level of Ag content would shift to the long wavelength direction (Figure 13.15A). For NCs with no or a lower content of Ag, the red-shift of the fluorescence peak would not happen. When H_2O_2 concentration is in the range of 0 to 200 mM, a linear relationship between fluorescence peak wavelength and H_2O_2 concentration was obtained. As reported[141], H_2O_2 would quench the fluorescence of Au NCs due to the decomposition of Au NCs, indicating that AuAg-10NCs may be decomposed first, and as H_2O_2 was consumed with reaction time, new Au NCs are formed once again. This conception was confirmed by XPS spectrum. After reaction with H_2O_2 for 10 h, the final solution was dialyzed for 48 h to remove free metal ions. Then characteristic XPS spectrum and mass spectrum showed that the final products

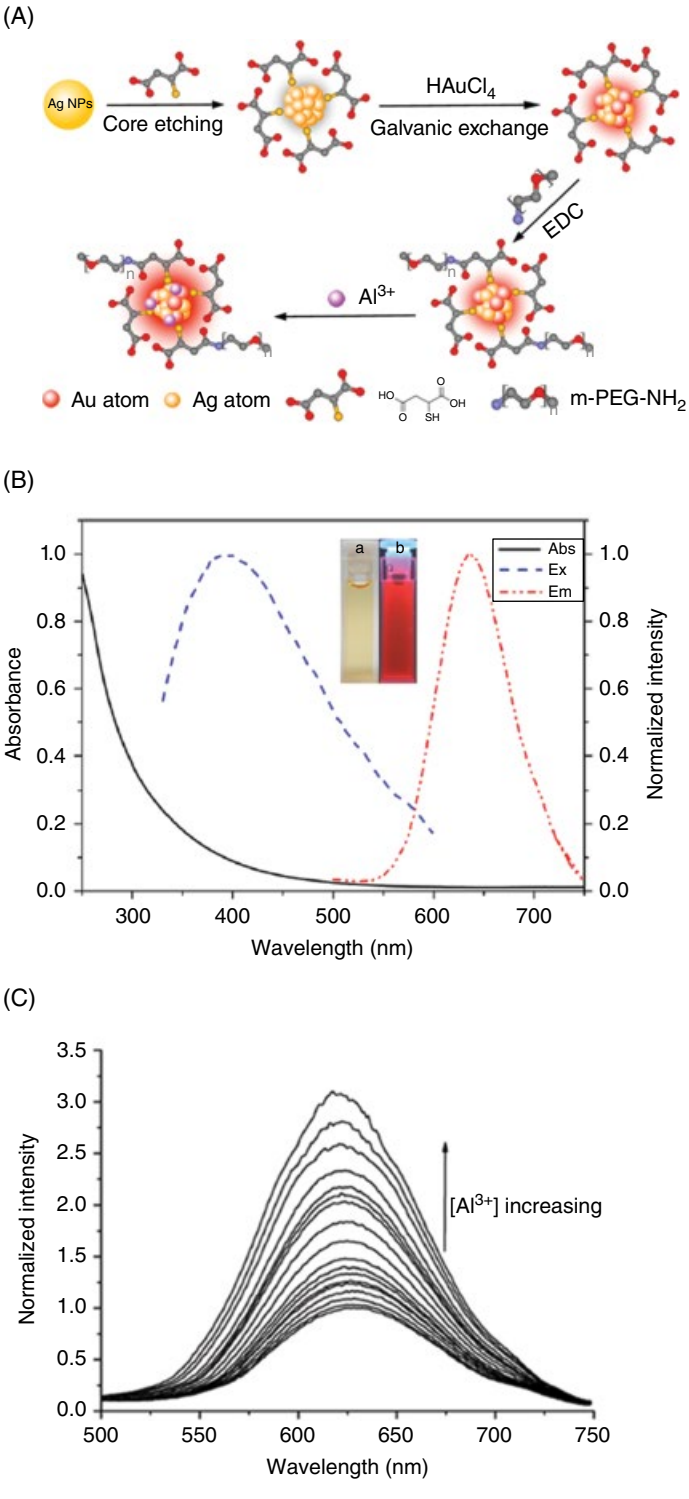

Figure 13.14 (A) Scheme of the synthesis process for MSA–AgAu NCs and the detection of Al^{3+} ions. (B) Optical properties of the as-prepared MSA–AgAu NCs. Inset are photographs of MSA–AgAu NCs under visible light (a) and UV light at 365 nm (b). (C) Emission intensity of PEGylated MSA–AgAu NCs increased with the increasing of Al^{3+} concentration. (D) Relationship between relative fluorescence intensity and Al^{3+} concentration. The inset shows the linear range from 2 to 30 μM of Al^{3+}. (E) Selectivity of PEGylated MSA–AgAu NCs toward Al^{3+}. Adapted with permission from ref 120. © 2013 American Chemical Society.

(D)

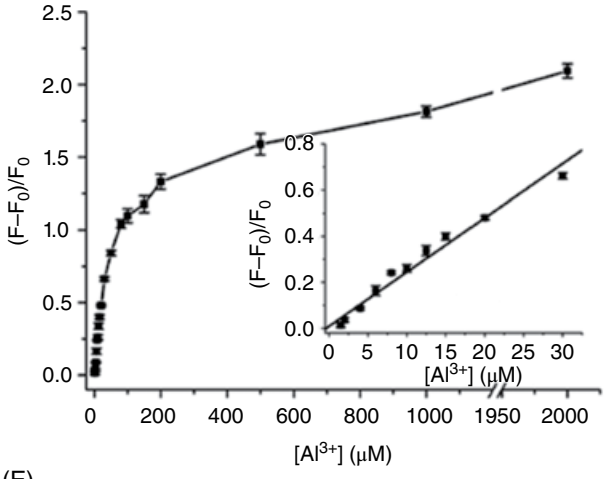

(E)

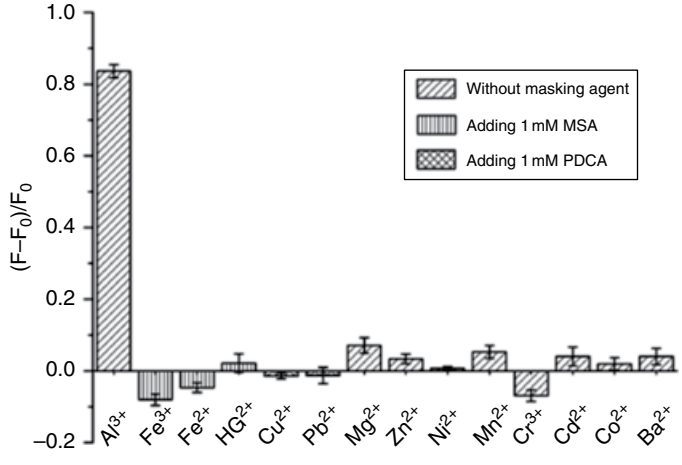

Figure 13.14 (Continued)

were Au_{11}-BSA and Au_{25}-BSA NCs and there was no Ag element in the final product, which confirmed that AuAg-10 NCs were decomposed and new Au NCs were formed after the addition of H_2O_2. The detection of H_2O_2 takes a long time (about 10 h), which may restrict their wide applications. Furthermore, AuAg-10 NCs was used to detect herbicides propazine. After the addition of 1 mM propazine, a large fluorescence enhancement of AuAg-10 NCs (about 8.5 times) was achieved. In the control experiment, only a small change in fluorescence was obtained for Au NCs after propazine additions, illustrating that Ag element actually takes effect for the enhancement of the fluorescence. Based on DFT simulations, the high binding energy of propazine to Ag^+ ions on the surface of AuAg-10 NCs causes the fluorescence enhancement. The detection can be finished in 30 min. The fluorescence of AuAg-10 NCs was very sensitive to the addition of propazine, so it can be detected even at a concentration as low as 0.1 nM.

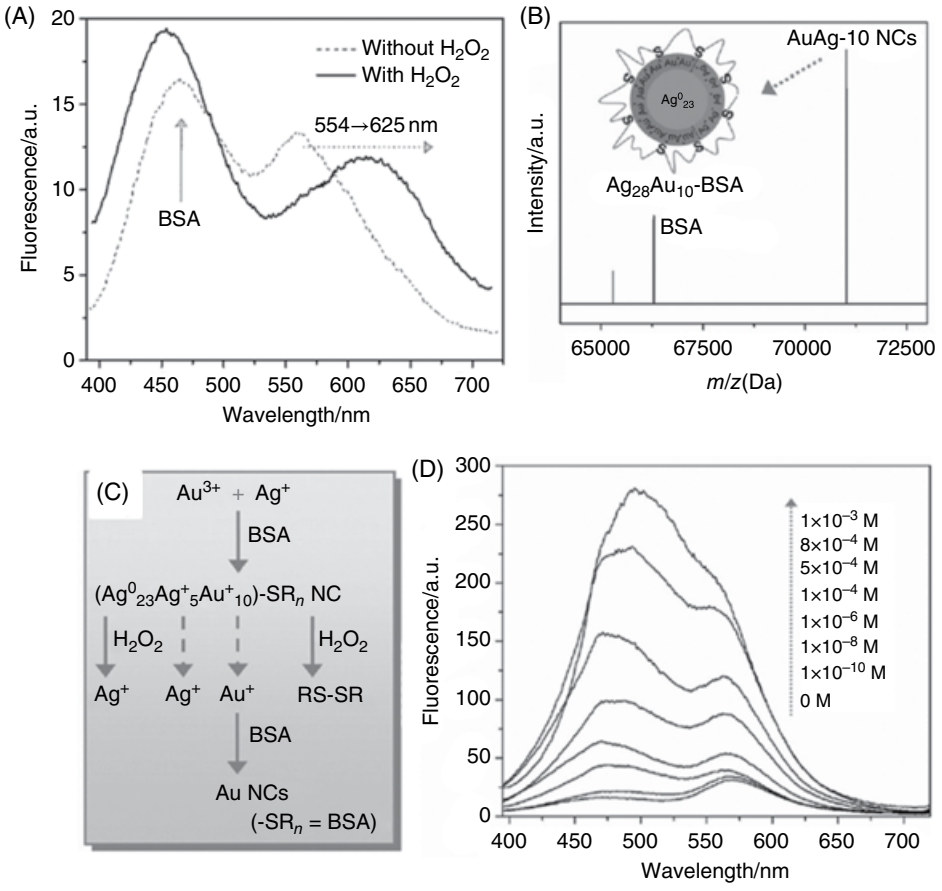

Figure 13.15 (A) Fluorescence spectra of AuAg-10 NCs before and after H_2O_2 incubation for 10 h (the peak at 450 nm is from BSA molecules). (B) MALDI-TOF mass spectrum of AuAg-10 NCs. The molecular mass of BSA molecules and BSA protected AuAg-10 NCs was 66000 Da and 71000 Da, so the mass of AuAg-10 NCs was about 5000 Da, and the XPS spectra have showed that the Ag/Au atomic ratio for AuAg-10 NCs is 28:10, so it can be calculated that structure of AuAg-10 NCs are $Ag_{28}Au_{10}$-BSA. (C) Interaction of $Ag_{28}Au_{10}$ NCs with H_2O_2. (D) Fluorescence spectra of AuAg-10 NCs with different concentrations of propazine after incubation for 30 min. Adapted with permission from ref 139. © 2016 Wiley-VCH.

The detection limit is far below its health value in drinking water (10 mg/mL, 40 nM) established by the EPA[142], and thus, it is desirable to develop further the sensitive and selective detection of propazine based on the fluorescence enhancement of AuAg-10 NCs.

Some thiol-containing biomolecules like cysteine (Cys)[129, 143, 144] and homocysteine (hCys)[130] have been detected by fluorometric method with bimetallic nanoclusters. The detections of thiol-containing biomolecules were based on enhancing or quenching of fluorescence intensity caused by ligand exchange with the stabilizing agent of the NCs. However, the photoluminescence responses for thiol-containing biomolecules were very similar, and it was unable to eliminate mutual interference with each other[130, 143]. The detection often gave a total amount of them.

13.6 Conclusions

Bimetallic sensors take advantage of both their component and exhibit-improved properties, such as tunable optical properties, enhanced local electromagnetic field, and strong catalytic activity, which has attracted wide attention in areas ranging from environmental monitoring, food safety, to medical applications. Here, we outlined the current research status of bimetallic sensors in five categories including plasmonic sensors, SERS sensors, electrochemical sensors, sensors based on the enzyme-mimicking properties of bimetallic NPs, and luminescent nanoclusters sensors. It is impossible for us to cover all of the bimetallic sensors, so we have focused on the detection mechanism on the examples just outlined.

The final destination of a sensor is to provide in situ quantitative information about the target analytes in a complex environment. Walking from laboratories to application is the common goal of all kinds of sensors. Specificity may be the primary question that needs to be resolved before commercialization. Capping ligands or surface functionalization may provide effective protection for NPs sensors from hostile environments. The interface between NPs core and the environment is a domain area that needs to be designed carefully to optimize NPs sensor's performance[2].

13.7 Acknowledgments

This work was financially supported by the National Natural Science Foundation of China (Grant Nos. 21475125) and the Hundred Talents Program of the Chinese Academy of Sciences.

13.8 References

1 Rick, J., Tsai, M.-C., and Hwang, B. J. (2016). Biosensors incorporating bimetallic nanoparticles. *Nanomaterials*, 6(5), 5–35.
2 Howes, P. D., Chandrawati, R., and Steven, M. M. (2014). Colloidal nanoparticles as advanced biological censors. *Science*, 346 (6205), 1247390
3 Gilroy, K. D., Ruditskiy, A., Peng, H. C., Qin, D., and Xia, Y. N. (2016). Bimetallic nanocrystals: syntheses, properties, and applications. *Chemical Reviews*, 116 (18), 10414–10472.
4 Gu, J., Zhang, Y. W., and Tao, F. (2012). Shape control of bimetallic nanocatalysts through well-designed colloidal chemistry approaches. *Chemical Society Reviews*, 24 (41), 8050–8065.
5 Mayer, K. M., and Hafner, J. H. (2011). Localized surface plasmon resonance sensors. *Chemical Reviews*, 111 (6), 3828–3857.
6 Zeng, S. W., Baillargeat, D., Ho H. P., and Yong, K. T. (2014). Nanomaterials enhanced surface plasmon resonance for biological and chemical sensing applications. *Chemical Society Reviews*, 43 (10), 3426–3452.
7 Puiu, M., and Bala, C. (2016). SPR and SPR imaging: recent trends in developing nanodevices for detection and real-time monitoring of biomolecular events. *Sensors*, 16 (6), 870–885.

8 Stewart, M. E., Anderton, C. R., Thompson, L. B., Maria, J., Gray, S. K., Rogers, J. A., and Nuzzo. R. G. (2008). Nanostructured plasmonic sensors. *Chemical Reviews*, 108 (2), 494–521.

9 Wang, J., Song, D. Q., Wang, L. Y., Zhang, H., Zhang, H. Q., and Sun, Y. (2011). Design and performances of immunoassay based on SPR biosensor with Au/Ag alloy nanocomposites. *Sensors and Actuators B-Chemical*, 157 (2), 547–553.

10 Gao, C. B., Lu, Z.D., Liu, Y., Zhang, Q., Chi, M. F., Cheng, Q., and Yin, Y. D. (2012). Highly stable silver nanoplates for surface plasmon resonance biosensing. *Angewandte Chemie International Edition*, 51 (23), 5629–5633.

11 Metraux, G. S., Cao, Y. C., Jin, R. C., and Mirkin, C. A. (2003). Triangular nanoframes made of gold and silver. *Nano Letters*, 3 (4), 519–522.

12 Sun, Y. G., and Wang, Y. X. (2011). Monitoring of galvanic replacement reaction between silver nanowires and $HAuCl_4$ by in situ transmission X–ray microscopy. *Nano Letters*, 11 (10), 4386–4392.

13 Baldi, A., Narayan, T. C., Koh, A. L., and Dionne, J. A. (2014). In situ detection of hydrogen-induced phase transitions in individual palladium nanocrystals. *Nature Materials*, 13 (12), 1143–1148.

14 Liu, N., Tang, M. L., Hentschel, M., Giessen, H., and Alivisatos, A. P. (2011). Nanoantenna-enhanced gas sensing in a single tailored nanofocus. *Nature Materials*, 10 (8), 631–636.

15 Tang, M. L., Liu, N., Dionne, J. A., and Alivisatos, A. P. (2011). Observations of shape-dependent hydrogen uptake trajectories from single nanocrystals. *Journal of the American Chemical Society*, 133 (34), 13220–13223.

16 Chiu, C. Y., and Huang, M. H. (2013). Polyhedral Au–Pd Core–shell nanocrystals as highly spectrally responsive and reusable hydrogen sensors in aqueous solution. *Angewandte Chemie Intrenational Edition*, 52 (48), 12709–12713.

17 Jiang, R. B., Qin, F., Ruan, Q. F., Wang, J. F., and Jin, C. G. (2014). Ultrasensitive plasmonic response of bimetallic Au/Pd nanostructures to hydrogen. *Advanced Functtional Materials*, 24 (46), 7328–7337.

18 He, H. L., Xu, X. L., Wu, H. X., and Jin, Y. D. (2012). Enzymatic plasmonic engineering of Ag/Au bimetallic nanoshells and their use for sensitive optical glucose sensing. *Advanced Materials*, 24 (13), 1736–1740.

19 He, H. L., Xu, X. L., Wu, H. X., Zhai, Y. J., and Jin, Y. D. (2013). In situ nanoplasmonic probing of enzymatic activity of monolayer-confined glucose oxidase on colloidal nanoparticles. *Analytical Chemistry*, 85 (9), 4546–4553.

20 Jin, Y. D. (2014). Multifunctional compact hybrid Au nanoshells: a new generation of nanoplasmonic probes for biosensing, imaging, and controlled release. *Accounts of Chemical Research*, 47 (1), 138–148.

21 Chen, L. M., Li, H. J., He, H. L., Wu, H. X., and Jin, Y. D. (2015). Smart plasmonic glucose nanosensors as generic theranostic agents for targeting-free cancer cell screening and killing. *Analytical Chemistry*, 87 (13), 6868–6874.

22 Zeng, J. B., Cao, Y. Y., Chen, J. J., Wang, X. D., Yu, J. F., Yu, B. B., Yan, Z. F., and Chen, X. (2014). Au@Ag core/shell nanoparticles as colorimetric probes for cyanide sensing. *Nanoscale*, 6 (17), 9939–9943.

23 Li, Y. R., Wang, Q. R., Zhou, X. M., Wen, C. Y., Yu, J. F., Han, X. G., Li, X. Y., Yan, Z. F., and Zeng, J. B. (2016). A convenient colorimetric method for sensitive and specific detection of cyanide using Ag@Au core–shell nanoparticles. *Sensors and Actuators B Chemical*, 228 (2), 366–372.

24 Rodriguez-Lorenzo, L., de la Rica, R., Alvarez-Puebla, R. A., Liz-Marzan, L. M., and Stevens, M. M. (2012). Plasmonic nanosensors with inverse sensitivity by means of enzyme-guided crystal growth. *Nature Materials*, 11 (7), 604–607.

25 Howes, P. D., Rana, S., and Stevens, M. M. (2014). Plasmonic nanomaterials for biodiagnostics. *Chemical Society Reviews*, 43 (11), 3835–3853.

26 Wang, Y., Zhang, P., Mao, X. X., Fu, W. S., and Liu, C. (2016). Seed-mediated growth of bimetallic nanoparticles as an effective strategy for sensitive detection of vitamin c. *Sensors and Actuators B: Chemical*, 231 (1), 95–101.

27 Stewart, M. E., Anderton, C. R., Thompson, L. B., Maria, J., Gray, S. K., Rogers, J. A., and Nuzzo, R. G. (2008). Nanostructured plasmonic sensors. *Chemical Reviews*, 108 (2), 494–521.

28 Saha, K., Agasti, S. S., Kim, C., Li, X. N., and Rotello, V. M. (2012). Gold nanoparticles in chemical and biological sensing. *Chemical Reviews*, 112 (5), 2739–2779.

29 Xiong, B., Zhou, R., Hao, J. R., Jia, Y. H., He, Y., and Yeung, E. S. (2013). Highly sensitive sulphide mapping in live cells by kinetic spectral analysis of single Au–Ag core–shell nanoparticles. *Nature Communications*, 4 pp. 1708 – 1716.

30 Hao, J. R., Xiong, B., Chen, X. D., He, Y., and Yeung, E. S. (2014). High-throughput sulfide sensing with colorimetric analysis of single Au–Ag core–shell nanoparticles. *Analytical Chemistry*, 86 (10), 4663–4667.

31 Hu, P. P., Zheng, L. L., Zhan, L., Li, J. Y., Zhen, S. J., Liu, H., Luo, L. F., Xiao, G. F., and Huang, C. Z. (2013). Metal-enhanced fluorescence of nano-core–shell structure used for sensitive detection of prion protein with a dual-aptamer strategy. *Analytica Chimica Acta*, 787 (17), 239–245.

32 Shahjamali, M. M., Bosman, M., Cao, S., Huang, X., Saadat, S., Martinsson, E., Aili, D., Tay, Y. Y., Liedberg, B., Loo, S. C. J., Zhang, H., Boey, F., and Xue, C. (2012). Gold coating of silver nanoprisms. *Advanced Functional Materials*, 22 (4), 849–854.

33 Lee, B. H., Hsu, M. S., Hsu, Y. C., Lo, C. W., and Huang, C. L. (2010). A facile method to obtain highly stable silver nanoplate colloids with desired surface plasmon resonance wavelengths. *The Journal of Physical Chemistry C*, 114 (14), 6222–6227.

34 Fleischmann, M., Hendra, P. J., and McQuillan, A. J. (1974). Raman spectra of pyridine adsorbed at a silver electrode. *Chemical Physics Letters*, 26 (2), 163–166.

35 Jeanmaire, D. L., and Van Duyne, R. P. (1977). Surface Raman spectroelectrochemistry: Part I. Heterocyclic, aromatic, and aliphatic amines adsorbed on the anodized silver electrode. *Journal of Electroanalytical Chemistry and Interfacial Electrochemistry*, 84 (1), 1–20.

36 Schluecker, S. (2014). Surface-enhanced Raman spectroscopy: concepts and chemical applications. *Angewandte Chemie International Edition*, 53 (19), 4756–4795.

37 Muehlethaler, C.; Leona, M., and Lombardi, J. R. (2016). Review of surface enhanced Raman scattering applications in forensic science. *Analytical Chemistry*, 88 (1), 152–169.

38 Lombardi, J. R., and Birke, R. L. (2008). A unified approach to surface-enhanced Raman spectroscopy. *The Journal of Physical Chemistry C*, 112 (14), 5605–5617.

39 Londero, P. S., Leona, M., and Lombardi, J. R. (2013). Definitive evidence for linked resonances in surface-enhanced Raman scattering: excitation profile of Cu phthalocyanine. *Applied Physics Letters*, 102 (11) 111101.

40 Kreibig, U., and Vollmer, M. Optical properties of metal clusters; Springer Series in Materials Science 25; Springer-Verlag: New York, 1995.

41 Jiang, R. B., Chen, H. J., Shao, L., Li, Q., and Wang, J. F. (2012). Unraveling the evolution and nature of the plasmons in (Au Core)-(Ag Shell) nanorods. *Advanced Materials*, 24 (35), OP200–OP207.

42 Samal, A. K., Polavarapu, L., Rodal-Cedeira, S., Liz-Marzán, L. M., Pérez-Juste, J., and Pastoriza-Santos, I. (2013). Size tunable Au@Ag core–shell nanoparticles: synthesis and surface-enhanced Raman scattering properties. *Langmuir*, 48 (29), 15076–15082.

43 Dreaden, E. C., Alkilany, A. M., Huang, X., Murphy, C. J., and El-Sayed, M. A. (2012). The golden age: gold nanoparticles for biomedicine. *Chemical Society Reviews*, 41 (7), 2740–2779.

44 Cao, Y. W. C., Jin, R. C., and Mirkin, C. A. (2002). Nanoparticles with Raman spectroscopic fingerprints for DNA and RNA detection. *Science*, 297 (5586), 1536–1540.

45 Cao, Y. C., Jin, R. C., Nam, J. M., Thaxton, C. S., and Mirkin, C. A. (2003). Raman dye-labeled nanoparticle probes for proteins. *Journal of the American Chemical Society*, 125 (48), 14676–14677.

46 Jahn, M., Patze, S., Hidi, I. J., Knipper, R., Radu, A. I., Mühlig, A., Yüksel, S., Peksa, V., Weber, K., Mayerhöfer, T., Cialla-May, D., and Popp, J. (2016). Plasmonic nanostructures for surface enhanced spectroscopic methods. *Analyst*, 141, 756–793.

47 Wustholz, K. L., Henry, A. I., McMahon, J. M., Freeman, R. G., Valley, N., Piotti, M. E., Natan, M. J., Schatz, G. C., and Van Duyne, R. P. (2010). Structure – activity relationships in gold nanoparticle dimers and trimers for surface-enhanced Raman spectroscopy. *Journal of the American Chemical Society*, 132 (31), 10903–10910.

48 Li, W., Camargo, P. H. C., Au, L., Zhang, Q., Rycenga, M., and Xia, Y. N. (2010). Etching and Dimerization: A simple and versatile route to dimers of silver nanospheres with a range of sizes. *Angewandte Chemie International Edition*, 49 (1), 164–168.

49 Lim, D. K., Jeon, K. S., Hwang, J. H., Kim, H., Kwon, S., Suh, Y. D., and Nam, J. M. (2011). Highly uniform and reproducible surface-enhanced Raman Scattering from DNA-tailorable nanoparticles with 1-nm interior gap. *Nature Nanotechnology*, 6 (7), 452–460.

50 Zhang, L., Liu, T. Z., Liu, K., Han, L., Yin, Y. D., and Gao, C. B. (2015). Gold nanoframes by nonepitaxial growth of Au on AgI nanocrystals for surface-enhanced Raman spectroscopy. *Nano Letters*, 15 (7), 4448–4454.

51 Liu, K., Bai, Y. C., Zhang, L., Yang, Z. B., Fan, Q. K., Zheng, H. Q., Yin, Y. D., and Gao, C. B. (2016). Porous Au–Ag nanospheres with high-density and highly accessible hotspots for SERS analysis. *Nano Letters*, 16 (6), 3675–3681.

52 Shen, J. L., Su, J., Yan, J., Zhao, B., Wang, D. F., Wang, S. Y., Li, K., Liu, M. M., He, Y., Mathur, S., Fan, C. H., and Song, S. P. (2015). Bimetallic nano-mushrooms with DNA-mediated interior nanogaps for high-efficiency SERS signal amplification. *Nano Research*, 8 (3), 731–742.

53 You, H. J., Ji, Y. T., Wang, L., Yang, S. C., Yang, Z. M., Fang, J. X., Song, X. P., and Ding, B. J. (2012) Interface synthesis of gold mesocrystals with highly roughened surfaces for surface-enhanced Raman spectroscopy. *Journal of Materials Chemistry*, 22 (5), 1998–2006.

54 Camargo, P. H. C., Rycenga, M., Au, L., and Xia, Y. N. (2009). Isolating and probing the hot spot formed between two silver nanocubes. *Angewandte Chemie International Edition*, 48 (12), 2180–2184.

55 Fang, J. X., Du, S. Y., Lebedkin, S., Li, Z. Y., Kruk, R., Kappes, M., and Hahn, H. (2010). Gold mesostructures with tailored surface topography and their self-assembly arrays for surface-enhanced Raman spectroscopy. *Nano Letters*, 10 (12), 5006–5013.

56 Liu, Z., Yang, Z. B., Peng, B., Cao, C., Zhang, C., You, H. J., Xiong, Q. H., Li, Z. Y., and Fang, J. X. (2014). Highly sensitive, uniform, and reproducible surface enhanced Raman spectroscopy from hollow Au–Ag alloy nanourchins. *Advanced Materials*, 26 (15), 2431–2439.

57 Muehlethaler, C., Leona, M., and Lombardi, J. R. (2016). Review of surface enhanced Raman scattering applications in forensic science. *Analytical Biochemistry*, 88 (1), 152 – 169.

58 Xie, W., Herrmann, C., Kçmpe, K., Haase, M., and Schlcker, S. (2011). Synthesis of bifunctional Au/Pt/Au core/shell nanoraspberries for in situ SERS monitoring of platinum-catalyzed reactions. *Journal of the American Chemical Society*, 133 (48), 19302–19305.

59 Zheng, Z. K., Tachikawa, T., and Majima, T. (2014). Single-particle study of Pt-modified Au nanorods for plasmon-enhanced hydrogen generation in visible to near-infrared region. *Journal of the American Chemical Society*, 136 (19), 6870 – 6873.

60 Zheng, Z. K., Tachikawa, T., and Majima, T. (2015). Plasmon-enhanced formic acid dehydrogenation using anisotropic Pd–Au nanorods studied at the single-particle level. *Journal of the American Chemical Society*, 137 (2), 948–957.

61 Wang, F., Li, C. H., Chen, H. J., Jiang, R. B., Sun, L.-D., Li, Q., Wang, J. F., Yu, J. C., and Yan, C.-H. (2013). Plasmonic harvesting of light energy for Suzuki coupling reactions. *Journal of the American Chemical Society*, 135 (15), 5588–5601.

62 Gong, J., Zhou, T., Song, D., Zhang, L., and Hu, X. (2010). Stripping Voltammetric Detection of mercury (II) based on a bimetallic Au – Pt inorganic – organic hybrid nanocomposite modified glassy carbon electrode. *Analytical Chemistry*, 82 (2), 567–573.

63 Siciliano, T., Filippo, E., Genga, A., Micocci, G., Siciliano, M., and Tepore, A. (2009). Single-crystalline Te microtubes: synthesis and NO_2 gas sensor application. *Sensors and Actuators B: Chemical*, 142 (1), 185–190.

64 Zhao, A. W., Ye, C. H., Meng, G. W., Zhang, L. D., and Ajayan, P. M. (2003). Tellurium nanowire arrays synthesized by electrochemical and electrophoretic deposition. *Journal of Materials Research*, 18 (10), 2318–2322.

65 Wang, D. M., Zhao, Y. W., Jin, H. L., Zhuang, J. X., Zhang, W. M., Wang, S., and Wang, J. C. (2013). Synthesis of Au-decorated tripod-shaped Te hybrids for applications in the ultrasensitive detection of arsenic. *ACS Applied Materials & Interfaces*, 5 (12), 5733–5740.

66 Chen, X. J., Tian, R., Zhang, Q., and Yao, C. (2014). Target-induced electronic switch for ultrasensitive detection of Pb2+ based on three dimensionally ordered macroporous Au–Pd bimetallic electrode. *Biosensors and Bioelectronics*, 53 (1), 90–98.

67 Ndamanisha, J. C., and Guo, L. P. (2008). Electrochemical determination of uric acid at ordered mesoporous carbon functionalized with ferrocenecarboxylic acid-modified electrode. *Biosensors and Bioelectronics*, 23(11), 1680–1685.

68 Erden, P. E., and Kilic, E. (2013). A review of enzymatic uric acid biosensors based on amperometric detection. *Talanta*, 107 pp. 312–323.

69 Tehrani, R. M. A., and Ab Ghani, S. (2010). Voltammetric analysis of uric acid by zinc-nickel nanoalloy coated composite graphite. *Sensors and Actuators B: Chemical*, 145 (1), 20–24.

70 Yogeswaran, U., Thiagarajan, S., and Chen, S. M. (2007). Nanocomposite of functional multiwall carbon nanotubes with nafion, nano platinum, and nano biosensing film for simultaneous determination of ascorbic acid, epinephrine, and uric acid. *Analytical Biochemistry*, 365 (1), 122–131.

71 Yan, J., Liu, S., Zhang, Z. Q., He, G. W., Zhou, P., Liang, H. Y., Tian, L. L., Zhou, X. M., and Jiang, H. J. (2013). Simultaneous electrochemical detection of ascorbic acid, dopamine and uric acid based on graphene anchored with Pd–Pt nanoparticles. *Colloids and Surfaces B-Biointerfaces*, 111 pp. 392–397.

72 Weng, Y.-C., and Hsiao, Y.-L. (2011). Comparison of Pt and Ni foil electrodes for amperometric sensing of ascorbic acid. *Journal of Electroanalytical Chemistry* 651 (2), 160–165.

73 Chen, S. H.; Yuan, R.; Chai, Y. Q.; Hu, F. X. (2013). Electrochemical sensing of hydrogen peroxide using metal nanoparticles: a review. *Microchimica Acta*, 180 (1–2), 15–32.

74 Che, X., Yuan, R., Chai, Y. Q., Ma, L. P., Li, W. J., and Li, J. J. (2009). Hydrogen peroxide sensor based on horseradish peroxidase immobilized on an electrode modified with DNA-L-cysteine-gold-platinum nanoparticles in polypyrrole film. *Microchimica Acta*, 167 (3–4), 159–165.

75 Manivannan, S., and Ramaraj, R. (2009). Core–shell Au/Ag nanoparticles embedded in silicate sol-gel network for sensor application towards hydrogen peroxide. *Journal of Chemical Sciences*, 121 (5), 735–743.

76 Janyasupab, M., Liu, C. W., Zhang, Y., Wang, K. W., and Liu, C. C. (2013). Bimetallic Pt–M (M = Cu, Ni, Pd, and Rh) nanoporous for H_2O_2 based amperometric biosensors. *Sensors and Actuators B: Chemical*, 179 pp. 209–214.

77 Cui, X., Wu, S. N., Li, Y. X., and Wan, G. (2015). Sensing hydrogen peroxide using a glassy carbon electrode modified with in-situ electrodeposited platinum-gold bimetallic nanoclusters on a graphene surface. *Microchimica Acta*, 182 (1–2), 265–272.

78 Li, X.-R., Xu, M.-C., Chen, H.-Y., and Xu, J.-J. (2015). Bimetallic Au@Pt@Au core–shell nanoparticles on graphene oxide nanosheets for high-performance H_2O_2 bi-directional sensing. *Journal of Materials Chemistry B*, 3 (21), 4355–4362.

79 Shang, L., Zeng, B. Z., and Zhao, F. Q. (2015). Fabrication of novel nitrogen-doped graphene–hollow AuPd nanoparticle hybrid films for the highly efficient electrocatalytic reduction of H_2O_2. *ACS Applied Materials & Interfaces*, 7 (1), 122–128.

80 Li, W. Z., Kuai, L., Qin, Q., and Geng, B. Y. (2013). Ag–Au bimetallic nanostructures: co-reduction synthesis and their component-dependent performance for enzyme-free H_2O_2 sensing. *Journal of Materials Chemistry A*, 1 (24), 7111–7117.

81 Diabetes mellitus. From Wikipedia. https://en.wikipedia.org/wiki/Diabetes_mellitus

82 The top 10 causes of death Fact sheet N°310″. World Health Organization. Oct 2013.

83 Update 2015″. IDF. International Diabetes Federation. p. 13. Retrieved 21 Mar 2016.

84 Wang, J. (2008). Electrochemical glucose biosensors. *Chemical Reviews*, 108 (2), 814–825.

85 Chen, C., Xie, Q. J., Yang, D. W., Xiao, H. L., Fu, Y., Tan, Y., and Yao, S. (2013). Recent advances in electrochemical glucose biosensors: a review. *RSC Advances*, 3 (14), 4473–4491.

86 Chen, K. J., Lee, C. F., Rick, J., Wang, S. H., Liu, C. C., and Hwang, B. J. (2012). Fabrication and application of amperometric glucose biosensor based on a novel PtPd bimetallic nanoparticle decorated multi-walled carbon nanotube catalyst. *Biosensors and Bioelectronics*, 33 (1), 75–81.

87 Yang, J., Deng, S. Y., Lei, J. P., Ju, H. X., and Gunasekaran, S. (2011). Electrochemical synthesis of reduced graphene sheet–AuPd alloy nanoparticle composites for enzymatic biosensing. *Biosensors and Bioelectronics*, 29 (1), 159–166.

88 Wang, J. P.; Thomas, D. F.; Chen, A. C. (2008). Nonenzymatic electrochemical glucose sensor based on nanoporous PtPb networks. *Analytical Chemistry*, 4 (80), 997–1004.

89 Mayorga-Martinez, C. C., Guix, M., Madrid, R. E., and Merkoci, A. (2012). Bimetallic nanowires as electrocatalysts for nonenzymatic real-time impedancimetric detection of glucose. *Chemical Communications*, 48 (11), 1686–1688.

90 Yang, F., Yang, Z., Zhuo, Y., Chai, Y., and Yuan, R. (2015). Ultrasensitive electrochemical immunosensor for carbohydrate antigen 19-9 using Au/porous graphene nanocomposites as platform and Au@Pd core/shell bimetallic functionalized graphene nanocomposites as signal enhancers. *Biosensors and Bioelectronics*, 66, 356–362.

91 Cao, X., Wang, N., Jia, S., Guo, L., and Li, K. (2013). Bimetallic AuPt nanochains: synthesis and their application in electrochemical immunosensor for the detection of carcinoembryonic antigen. *Biosensors and Bioelectronics*, 39, 226–230.

92 Wang, Y. G., Wei, Q., Zhang, Y., Wu, D., Ma, H. M., Guo, A. P., and Du, B. (2014). A sandwich-type immunosensor using Pd–Pt nanocrystals as labels for sensitive detection of human tissue polypeptide antigen. *Nanotechnology*, 25 (5) 055102.

93 Huang, Y. P., Miao, Y. E., Ji, S. S., Tjiu, W. W., and Liu, T. X. (2014). Electrospun carbon nanofibers decorated with Ag–Pt bimetallic nanoparticles for selective detection of dopamine. *ACS Applied Material & Interfaces*, 6 (15), 12449–12456.

94 Yu, Y. Y., Liu, X. Q., Jiang, D. W., Sun, Q. A., Zhou, T. S., Zhu, M., Jin, L. T., and Shi, G.Y. (2011). $[C_3(OH)_2mim][BF_4]$–Au/Pt biosensor for glutamate sensing in vivo integrated with on-line microdialysis system. *Biosensors and Bioelectronics*, 26, 3227–3232.

95 Liu, F., Xiang, G., Jiang, D., Zhang, L., Chen, X., Liu, L., Luo, F., Li, Y., Liu, C., and Pu, X. (2015). Ultrasensitive strategy based on PtPd nanodendrite/nano-flower-like@GO signal amplification for the detection of long non-coding RNA. *Biosensors and Bioelectronics*, 74, 214–221.

96 Safavi, A., and Farjami, F. (2011). Electrodeposition of gold–platinum alloy nanoparticles on ionic liquid-chitosan composite film and its application in fabricating an amperometric cholesterol biosensor. *Biosensors and Bioelectronics*, 26, 2547–2552.

97 Cao, S., Zhang, L., Chai, Y., and Yuan, R. (2013). Electrochemistry of cholesterol biosensor based on a novel Pt–Pd bimetallic nanoparticle decorated graphene catalyst. *Talanta*, 109, 167–172.

98 Wolfenden, R., Snider, M. J. (2001). The depth of chemical time and the power of enzymes as catalysts. *Accounts of Chemical Research*, 12 (34), 938–945.

99 Lin, Y. H., Ren, J. S., and Qu, X. G. (2014). Catalytically active nanomaterials: a promising candidate for artificial enzymes. *Accounts of Chemical Research*, 47 (4), 1097–1105.

100 Wei, H., and Wang, E. K. (2013). Nanomaterials with enzyme-like characteristics (nanozymes): next-generation artificial enzymes. *Chemical Society Reviews*, 42 (14), 6060–6093.

101 Kotov, N. A. (2010). Inorganic nanoparticles as protein mimics. *Science*, 330 (6001), 188–189.

102 Murakami, Y., Kikuchi, J-I., Hisaeda, Y., and Hayashida, O. (1996). Artificial Enzymes. *Chemical Reviews*, 96 (2), 721–758.

103 He, W. W, Wu, X. C., Liu, J. B., Hu, X. N., Zhang, K., Hou, S., Zhou, W. Y., and Xie, S. S. (2010). Design of AgM bimetallic alloy nanostructures (M = Au, Pd, Pt) with tunable morphology and peroxidase-like activity. *Chemistry of Materials*, 22 (9), 2988–2994.

104 Han, L., Li, C. C., Zhang, T., Lang, Q. L., and Liu, A. H. (2015). Au@Ag Heterogeneous nanorods as nanozyme interfaces with peroxidase-like activity and their application for one-pot analysis of glucose at nearly neutral pH. *ACS Applied Materials & Interfaces*, 7 (26), 14463–14470.

105 Tseng, C. W., Chang, H. Y., Chang, J. Y., and Huang, C. C. (2012). Detection of mercury ions based on mercury-induced switching of enzyme-like activity of platinum/gold nanoparticles. *Nanoscale*, 4 (21), 6823–6830.

106 Zhang, K., Hu, X., Liu, J., Yin, J.-J., Hou, S., Wen, T., He, W., Ji, Y., Guo, Y., Wang, Q., and Wu, X. (2011). Formation of PdPt alloy nanodots on gold nanorods: tuning oxidase-like activities via composition. *Langmuir*, 27 (6), 2796–2803.

107 Zheng, C., Zheng, A. X., Liu, B., Zhang, X. L., He, Y., Li, J., Yang, H. H., and Chen, G. N. (2014). One-pot synthesized DNA-templated Ag/Pt bimetallic nanoclusters as peroxidase mimics for colorimetric detection of thrombin. *Chemical Communications*, 50 (86), 13103–13106.

108 Sun, Y. H., Wang, J., Li, W., Zhang, J. L., Zhang, Y. D., and Fu, Y. (2015). DNA-stabilized bimetallic nanozyme and its application on colorimetric assay of biothiols. *Biosensors and Bioelectronics*, 74, 1038–1046.

109 Ye, X. S., Shi, H., He, X. X., Wang, K. M., He, D. G., Yan, L. A., Xu, F. Z., Lei, Y. L., Tang, J. L., and Yu, Y. R. (2015). Iodide-responsive Cu–Au nanoparticle-based colorimetric platform for ultrasensitive detection of target cancer cells. *Analytical Chemistry*, 87 (14), 7141–7147.

110 Ge, S. G, Liu, F., Liu, W. Y., Yan, M., Song, X. R., and Yu, J. H. (2014). Colorimetric assay of K-562 cells based on folic acid-conjugated porous bimetallic Pd@Au nanoparticles for point-of-care testing. *Chemical Communications*, 50 (4), 475–477.

111 Huang, X. Q., Li, Y. J., Chen, Y., Zhou, E. B., Xu, Y. X., Zhou, H. L., Duan, X. F., and Huang, Y. (2013). Palladium-based nanostructures with highly porous features and perpendicular pore channels as enhanced organic catalysts. *Angewandte Chemie International Edition*, 52 (9), 2520–2524.

112 Liu, J.-M., Chen, J.-T., and Yan, X.-P. (2013). Near infrared fluorescent trypsin stabilized gold nanoclusters as surface plasmon enhanced energy transfer biosensor and in vivo cancer imaging bioprobe. *Analytical Chemistry*, 85 (6), 3238–3245.

113 Yuan, X., Dou, X. Y., Zheng, K. Y., and Xie, J. P. (2015). Recent advances in the synthesis and applications of ultrasmall bimetallic nanoclusters. *Particle & Particle Systems Characterization*, 32 (6), 613–629.

114 Shang, L., Dong, S. J., and Nienhaus, G. U. (2011). Ultra-small fluorescent metal nanoclusters: synthesis and biological applications. *Nano Today*, 6 (4), 401–418.

115 Ganguly, M., Jana, J., Pal, A., and Pal, T. (2016). Synergism of gold and silver invites enhanced fluorescence for practical applications. *RSC Advances*, 6 (21), 17683–17703.

116 Petersen, J. L., and Shi, X. (2012). "Silver effect" in gold (I) catalysis: an overlooked important factor. *Journal of the American Chemical Society*, 134 (21), 9012–9019.

117 Wang, S. X., Meng, X. M., Das, A., Li, T., Song, Y. B., Cao, T. T., Zhu, X. Y., Zhu, M. Z., and Jin, R. C. (2014). A 200-fold quantum yield boost in the photoluminescence of silverdoped Ag_xAu_{25-x} nanoclusters: The 13th silver atom matters. *Angewandte Chemie International Edition*, 53 (9), 2376–2380.

118 Le G. X., Trouillet, V., Spies, C., Li, K., Laaksonen, T., Auerbach, D., Jung, G., and Schneider, M. (2012). High photostability and enhanced fluorescence of gold nanoclusters by silver doping. *Nanoscale*, 4 (24), 7624–7631.

119 Negishi, Y., Iwai, T., and Ide, M. (2010). Continuous modulation of electronic structure of stable thiolate-protected Au_{25} cluster by Ag doping. *Chemical Communications*, 46 (26), 4713–4715.

120 Zhou, T. Y., Lin, L. P., Rong, M. C., Jiang, Y. Q., and Chen, X. (2013). Silver-gold alloy nanoclusters as a fluorescence-enhanced probe for aluminum ion sensing. *Analytical Chemistry*, 85 (20), 9839–9844.

121 Xie, J., Zheng, Y., and Ying, J. Y. (2010). Highly selective and ultrasensitive detection of Hg^{2+} based on fluorescence quenching of Au nanoclusters by Hg^{2+}-Au^{+} interactions. *Chemical Communications*, 46 (6), 961–963.

122 Sun, J., Wu, H. X., and Jin, Y. D. (2014). Synthesis of thiolated Ag/Au bimetallic nanoclusters exhibiting an anti-galvanic reduction mechanism and composition-dependent fluorescence. *Nanoscale*, 6 (10), 5449–5457.

123 Zhang, N., Si, Y. M., Sun, Z. Z., Chen, L. J., Li, R., Qiao, Y. C., and Wang, H. (2014). Rapid, selective, and ultrasensitive fluorimetric analysis of mercury and copper levels in blood using bimetallic gold-silver nanoclusters with "silver effect"-enhanced red fluorescence. *Analytical Chemistry*, 86 (23), 11714–11721.

124 Zhou, T. Y., Huang, Y. H., Li, W. B., Cai, Z. M., Luo, F., Yang, C. Y. J., and Chen, X. (2012). Facile synthesis of red-emitting lysozyme-stabilized Ag nanoclusters. *Nanoscale*, 4 (17), 5312–5315.

125 Murray, J., Okamoto, H., and Massalski, T. Bull. (1987) *Alloy Phase Diagrams*, 8, 20–30.

126 Lee, J. J., Bae, I. T., Scherson, D. A., Miller, B., and Wheeler, K. A. (2000). Underpotential deposition of aluminum and alloy formation on polycrystalline gold electrodes from $AlCl_3$/EMIC room-temperature molten salts. *Journal of the Electrochemical Society*, 147 (2), 562–566.

127 Ganguly, M., Mondal, C., Pal, J., Pal, A., Negishi, Y., and Pal, T. (2014). Fluorescent Au(i)@Ag_2/Ag_3 giant cluster for selective sensing of mercury (ii) ion. *Dalton Transactions*, 43 (30), 11557–11565.

128 Chen, T. H., Lu, C. Y., and Tseng, W. L. (2013). One-pot synthesis of two-sized clusters for ratiometric sensing of Hg^{2+}. *Talanta*, 117 pp. 258–262.

129 Ding, S. N., and Guo, Y. X. (2015). One-pot synthesis of dual-emitting BSA-Pt-Au bimetallic nanoclusters for fluorescence ratiometric detection of mercury ions and cysteine. *Analytical Methods*, 7 (14), 5787–5793.

130 Zhang, J., Yuan, Y., Wang, Y., Sun, F., Liang, G., Jiang, Z., and Yu, S.-H. (2015). Microwave-assisted synthesis of photoluminescent glutathione-capped Au/Ag nanoclusters: A unique sensor-on-a-nanoparticle for metal ions, anions, and small molecules. *Nano Research*, 8 (7), 2329–2339.

131 Liu, H. Y., Zhang, X., Wu, X. M., Jiang, L. P., Burda, C., and Zhu, J. J. (2011). Rapid sonochemical synthesis of highly luminescent non-toxic AuNCs and Au@AgNCs and Cu (ii) sensing. *Chemical Communications*, 47 (14), 4237–4239.

132 Ganguly, M., Mondal, C., Jana, J., Pal, A., and Pal, T. (2014). Photoproduced fluorescent Au(I)@(Ag_2/Ag_3)-thiolate giant cluster: an intriguing sensing platform for DMSO and Pb(II). *Langmuir*, 30 (1), 348–357.

133 Wang, Z. X., Guo, Y. X., and Ding, S. N. (2015). Fluorometric determination of cadmium(II) and mercury(II) using nanoclusters consisting of a gold-nickel alloy. *Microchimica Acta*, 182 (13), 2223–2231.

134 Huang, H., Li, H., Feng, J. J., and Wang, A. J. (2016). One-step green synthesis of fluorescent bimetallic Au/Ag nanoclusters for temperature sensing and in vitro detection of Fe^{3+}. *Sensors and Actuators B: Chemical*, 223 pp. 550–556.

135 Wang, Z. X., Zheng, C. L., and Ding, S. N. (2014). Label-free detection of sulfide ions based on fluorescence quenching of unmodified core–shell Au@Ag nanoclusters. *RSC Advances*, 4 (19), 9825–9829.

136 Chen, W. Y., Lan, G. Y., and Chang, H. T. (2011). Use of fluorescent DNA-templated gold/silver nanoclusters for the detection of sulfide ions. *Analytical Chemistry*, 83 (24), 9450–9455.

137 Whitten, K. W., Davis, R. E., Peck, M. L., and Stanley, G. G. (2009) Chemistry (9th ed.). Belmont: Brooks/Cole-Thompson Learning.

138 Harris, D. C. (2005) Exploring Chemical Analysis, 3rd ed. New York: W. H. Freeman and Company.

139 Guan, G. J., Cai, Y. Q., Liu, S. H., Yu, H. D., Bai, S. Q., Cheng, Y., Tang, T., Bharathi, M. S., Zhang, Y. W., and Han, M. Y. (2016). High-level incorporation of silver in gold nanoclusters: fluorescence redshift upon interaction with hydrogen peroxide and fluorescence enhancement with herbicide. *Chemistry-a European Journal*, 22 (5), 1675–1681.

140 Huang, C. C., Liao, H. Y., Shiang, Y. C., Lin, Z. H., Yang, Z., and Chang, H. T. (2009). Synthesis of wavelength-tunable luminescent gold and gold/silver nanodots. *Journal of Materials Chemistry*, 19 (6), 755–759.

141 Guan, G. J., Liu, S. H., Cai, Y. Q., Low, M., Bharathi, M. S., Zhang, S. Y., Bai, S. Q., Zhang, Y. W., and Han, M. Y. (2014). Destabilization of gold clusters for controlled nanosynthesis: from clusters to polyhedra. *Advanced Materials*, 26 (21), 3427–3432.

142 Guan, G. J., Yang, L., Mei, Q. S., Zhang, K., Zhang, Z. P., and Han, M.-Y. (2012). Chemiluminescence switching on peroxidase-like Fe_3O_4 nanoparticles for selective detection and simultaneous determination of various pesticides. *Analytical Chemistry*, 84 (21), 9492–9497.

143 Gui, R. J., Wang, Y. F., and Sun, J. (2014). Protein-stabilized fluorescent nanocrystals consisting of a gold core and a silver shell for detecting the total amount of cysteine and homocysteine. *Microchimica Acta*, 181 (11), 1231–1238.

144 Sun, J., Yang, F., Zhao, D., Chen, C. X., and Yang, X. R. (2015). Integrated logic gate for fluorescence turn-on detection of histidine and cysteine based on Ag/Au bimetallic nanoclusters–Cu^{2+} ensemble. *ACS Applied Materials & Interfaces*, 7 (12), 6860–6866.

Index

a

accelerated durability test (ADT) 334
adsorption energy 119
advanced light source (ALS) 85
Ag concave NCs 154
Ag convex NCs 154
aggregation-based growth 249
aggregation–directed growth 275
Ag–Pd nanodendrites 261
alloyed structure 10
ambient pressure X-ray photoelectron spectroscopy (AP-XPS) 362
ammonia synthesis 3
anisotropic overgrowth 12
anode reaction 261
anodic aluminium oxide (AAO) 180
ascorbic acid (AA) 109
assembly 173
assembly of gold nanoparticles 431
atomic migration 173
atomic radius 12
atom types 99
Au–Ag nanostructure 434
Au nanorods 430
Au–Pd nanocrystals 124
Au–Pd nanostructure 439

b

basin-hopping (BH) algorithm 33
BEP relations 45
bifunctional effect 7
bimetallic alloy nanowires 277
bimetallic concave 134
bimetallic convex 133
bimetallic core–shell nanowires 277
bimetallic dendritic nanostructures 247
bimetallic heterogeneous catalysts 44
bimetallic nanocrystals 91
bimetallic nanoframes 172
bimetallic nanoparticle catalysts 333
bimetallic nanoparticles 6
bimetallic nanoplates 294
bimetallic nanopolyhedrons 99
bimetallic nanoporous structures 181
bimetallic nanosheets 297
bimetallic nanospheres 100
bimetallic nanostructure-dependent performance 12
bimetallic nanostructures 10
bimetallic noble metals 155
bimetallic NPs 390
bimetallic plasmonic nanostructures 443
bimetallic SPR sensors 460
bimetallic systems 23
bimetallic tortuous nanowires 277
biodetection based on SPR 446
bio-imaging application 445
biomedical applications 306
biomedical diagnosis and treatment 434
biomolecules 432
biosynthesis 222
bond energy 12

Bimetallic Nanostructures: Shape-Controlled Synthesis for Catalysis, Plasmonics, and Sensing Applications, First Edition. Edited by Ya-Wen Zhang.
© 2018 John Wiley & Sons Ltd. Published 2018 by John Wiley & Sons Ltd.

bottom-up approach 176
bottom-up strategy 173
bovine serum albumin (BSA) 485
Brunauer–Emmett–Teller (BET) 384
building blocks 218

c

capping agent effect 398
capping agents 104
capping ligand 140
carbon–carbon (C-C) coupling reactions 403
catalytic applications 304
cathode reaction 261
cetyltrimethylammonium bromide (CTAB) 108
cetyltrimethylammonium chloride (CTAC) 146
charge transfer 12
chemical adsorption 41
chemical environment 361
chemically catalytic behaviors 161
chemical synthesis 273
chronoampherometry (CA) 326
cinnamaldehyde (CAL) 396
cinnamyl alcohol (COL) 396
cluster expansion formalism 32
CO adsorption 73
coercivity 304
colloidal synthesis 108
computational design 44
concave cubes (CNCs) 364
concave tetrahedra (CTH) 163
continuity equation 177
continuous growth 17
controlled synthesis 17
coordination ligand 248
CO oxidation 163
CO poisoning 13
coreduction 113
core–shell 10
core–shell nanocrystals 102
CO stripping 327
Coulomb interaction 25
counter electrode 326
coupling reactions 403
crossover (or mating) 35
crystal facets 149
crystallites coalescence 17, 134
cubic NPs 392
cyclic voltammetry (CV) 326
cyclohexene binding energy (CBE) 390

d

d-band center 7, 318
d-band model 41
d-band theory 120
dehydroascorbic acid (DHA) 256
dehydrogenation 376
dendrite NPs 379
density-functional theory (DFT) 24
didodecyldimethylammonium bromide (DDAB) 146
diffuse reflectance infrared fourier transform spectroscopy (DRIFTS) 72
dimethylformamide (DMF) 333
directional aggregation 282
direct methanol fuel cells (DMFC) 336
dislocation 249
distribution-property correlation 13
DNAzymes 475
dopamine 481

e

electroactive molecules 481
electrocatalytic performance 156
electrochemical dealloying 173, 210
electrochemical immunosensors 478
electrochemically active surface area (ECSA) 326
electrochemical measurements 326
electrochemical reactions 317
electrochemical sensors 473
electrodeposition 257
electron density 25
electron energy loss spectroscopy (EELS) 63
electronic effect 7
electronic structure 318
electron microscopy 61
elemental composition 13
embedded atom model (EAM) 30
empirical inter-atomic potentials 29

emulsion-Induced hollow micelle (EIHM) 185
energy dispersive spectroscopy (EDS) 61
enhancement factors (EF) 306
ensemble effect 7
environmental TEM (ETEM) 62
enzyme-guided metallic crystal growth 467
enzyme-mimicking properties 482
epitaxial growth 11
equilibrium shape 103
ethanol oxidation reaction (EOR) 265
ethylenediaminetetraacetate (EDTA) 197
exchange-correlation functional 26
extended X-ray absorption fine structure (EXAFS) 79

f

F127 186
face-centered-cubic (fcc) 296
facet-activity relationship 408
facet-specific capping agents 111
facet type 119
fermi level 120
ferromagnetism 272
Finke-Watzky two–step mechanism 274
first Brillouin zone 104
first-principles approaches 24
formic acid oxidation reaction (FAOR) 337
formic acid oxidation reaction (FOR) 158
Fourier transform infrared spectroscopy (FTIR) 72
fuel cells 317
fuel oxidation 334

g

galvanic replacement reaction 117
gaseous phase method 294
gaseous-state method 17
generalized gradient approximation (GGA) 27
genetic algorithm (GA) 35
geometric effects 248
geometric structure-property correlation 15
Gibbs-Thomson equation 106
Gibbs-Wulff theorem 103
glassy carbon electrode (GCE) 326
global minimum (GM) structure 33
global optimization methods 23
glucose oxidase (GOx) 463
glucose sensor 477
glutamate 481
gold nanoparticles 428
grandcanonical MC simulation (GMC) 38
growth principle 107

h

Hammer-Nøskov model 393
hard template 178
Hartree-Fock approximation 24
H_2/CO treatment 365
heavy metal ions 473
heterogeneous catalysts 360
heterogeneous catalytic reactions 118
heterogeneous nucleation 104
heterostructure 10
hexagonal-close-packed (hcp) 11
hexoctahedral (HOH) 147
Heyrovsky step 336
highest occupied molecular orbital (HOMO) 4
high-index facets 16, 404
high-resolution TEM (HRTEM) 62
high-throughput screening 49
Hohenberg-Kohn (HK) theorems 25
hollow cubic NCs 370
hollow nanocubes (h-NCs) 408
hollow nanostructures 202
hollow NPs 385
homogeneous nucleation 104
hotspot 434
hydrogenation 161
hydrogenation catalysts 377
hydrogenation of alkenes 389
hydrogenation of alkynes 389
hydrogenation of nitrobenzene 376
hydrogen binding energy (HBE) 390
hydrogen-evolving reactions (HERs) 156
hydrogen oxidation reaction (HOR) 335

hydrogen peroxide 475
hydrothermal and solvothermal methods 299

i
icosahedral nanocrystals (NIs) 408
incipient wetness impregnation 71
infrared (IR) spectroscopy 61
initialization 35
in situ characterization techniques 62
integrated tempering sampling (ITS) 37
inter-atomic potentials 23
intermetallic compound 100
intermetallic structure 10
island growth 12
iteration 35

k
K-edges 81
kinetically controlled growth 275
kinetic driving forces 174
kinetic energy 24
kinetic equation 177
kinetic processes 24
Kirkendall effect 173
Kohn-Sham equation 25

l
LaMer model 104
Langmuir-Hinshelwood mechanism 336
lattice mismatch 110
lattice models 31
lattice strain 8
lattice stress 7
ligand-directed branching 249
ligand effect 44
liquid-phase methods 248
local density approximation (LDA) 26
localized surface plasmon resonance (LSPR) 5
local minimum (LM) structure 39
long-chain alkylamines 275
long-range order (LRO) 62
low-angle annular dark-field scanning TEM (LAADF-STEM) 68
lowest unoccupied molecular orbital (LUMO) 4
LSPR peak shift 461
luminescent bimetallic nanoclusters 484
lyotropic liquid crystals (LLCs) 182

m
magnetic anisotropy energy (MAE) 304
magnetic properties 304
magnetron sputtering 71
mass activity 263
mass conservation equation 177
membrane electrode assembly (MEA) 334
meta-GGA (mGGA) 27
metallic nanoparticles 3
metal nanocrystals 99
metal nanomaterials 247
metal-organic framework (MOF) 197
metal precursor 248
methanol oxidation reaction (MOR) 9
Methfessel and Paxton (MP) 28
micelle-mediated growth 274
micro-fabricated reactor 302
microwave absorption 304
model surface 330
molecular dynamics (MD) 34
molecular dynamics simulation 36
monolayer bimetallic surfaces (MBS) 43
monometallic nanodendrites 247
monometallic NCs 362
Monte Carlo (MC) simulation 38
morphology effect 321
multi-stage galvanic replacement reaction (MGRR) 251
multiwall carbon nanotubes (MWCNTs) 255
mutation 35

n
nanoboxes 202
nanocage effect 386
nanocages 202
nanocube 6
nanodendrites 249
nano-octahedral frames (NOHFs) 401
nanooctahedron 6

nano-octahedrons (NOHs) 401
nanoplates 293
nanoporous materials 172
nanoscale phase segregation 219
nanosheets 293
nanostructured particles 3
nanotetrahedron 6
nanowires 271
national synchrotron light source (NSLS) 79
natural selection 35
near-infrared light 446
near-IR (NIR) 296
4-nitrophenol reduction 163
noble metal 133
nonenzymatic detection 475
NO oxidation 73
nucleation mechanism 104

o
octahedral NPs 381
octahedron 105
oleylamine (OAm) 398
oleylamine-mediated synthesis 278
optical applications 247
oriented attachment mechanism 215
Ostwald ripening 173
oxidation mechanisms 334
oxidation of o-phenylenediamine (OPDA) 374
oxidative etching 173
oxygen dissociation mechanism 330
oxygen evolution reaction (OER) 265
oxygen reduction reaction (ORR) 7

p
pair potentials 29
peroxide mechanism 330
peroxyl mechanism 330
phase structure-property correlation 16
photothermal application 445
plasmon 425
plasmonic hydrogen sensor 461
plasmonic metals 9
plasmonics 258
plasmonic sensors 460
platinum group metals 459
polyhedral NPs 404
polyol approach 140
polyvinylpyrrolidone (PVP) 108
post-synthesis modification 257
potential energy surface (PES) 23
preferential CO oxidation in H_2-rich feeds (PROX) 368
primary battery 251
projected density of states (PDOS) 42
proton-exchange membrane fuel cells (PEMFCs) 133
proton exchange membrane (PEM) water electrolyzers 339
Pt–Cu nanostructures 158
Pt–M alloy structures 327
Pt–M intermetallic structures 329
Pt–Ni nanocrystals 123
Pt_3Ni nanoparticles 331
Pt NPs 389
Pt–Pd concave NCs 160
Pt–Pd nanocrystals 123
Pt–Pd nanodendrites 253

q
quantum dots 445
quantum size effect 3

r
Raman spectroscopy 61
rare earth metals 328
redox potentials 108
reductant 249
reduction rate 108
reference electrode 326
regular cubes (RNCs) 364
reversible assembly 432
rhodamine 6G (R6G) 259
rhombohedral tetrapod (RTP) 163
Rideal-Eley mechanism 336
rotating disk electrode (RDE) 326
rotating ring disk electrode (RRDE) 326

s
Sabatier principle 47
sacrifice metal 251
sacrificial template 188

saturated calomel electrode (SCE) 326
saturation magnetization 304
scanning electron microscope (SEM) 61
scanning transmission electron microscopy (STEM) 62
Schrödinger equation 24
second-moment approximation to the tight-binding model (SMTB) 30
seeded epitaxial growth process 294
seeded-growth 17
seed-mediated growth 116
selected area electron diffraction (SAED) 62
selective etching 135
selective hydrogenation of nitroarenes 376
selective hydrogenation of α,β-unsaturated aldehydes 395
selective oxidation of alcohols 370
self-consistent-field (SCF) 24
semi-grandcanonical Monte Carlo (SGMC) 39
semi-hydrogenation of alkynes 392
sensing 459
sensor 459
shape-dependent catalytic properties 361
shape-dependent catalytic reactions 123
shape evolution 103
short-range order (SRO) 62
site-specific etching 142
size distribution 106
size-induced metal-insulator transition 4
size–property correlation 14
small molecules 485
soft template 181
sol-gel approach 177
solid–liquid–solid (SLS) 66
solid phase method 294
solid solution 100
solid-state method 17
solution-state method 17
solvothermal reaction 299
specific activity 263
spherical core–shell NCs 368
spherical NPs 403
spherical-shaped NPs 377
square-wave-potential (SWP) 147
standard hydrogen electrode (SHE) 326
standard reduction potential 108
statistical approaches 24
strain effect 43
strong metal-support interactions (SMSI) 370
structure-property relationship 18
sulfide anion 485
superposition approach 39
supersaturation 273
supraspheres 177
surface effect 3
surface energy 12
surface enhanced Raman spectra (SERS) 16
surface plasmon resonance (SPR) 13
surface reactions 317
surface structure 361
Suzuki coupling reaction 124
Suzuki-Miyaura reaction 403
synchrotron radiation source (SRS) 79
synergetic effects 7
synthetic fundamentals 273

t

Tafel step 336
template-assisted method 178
templating 173
tetrahedron 105
tetrahexahedra (THH) 148, 404
3,3,5,5'-tetramethylbenzidine (TMB) 482
theoretical simulation 23
thermal decomposition 114
thermodynamic driving force 174
thermodynamic properties 39
3d metals 340
three-dimensional networks 177
three-electrode cells 326
TB Ising model (TBIM) 31
top-down approach 174
top-down strategy 173
total energy (free energy) 105
transition metal (TM) 41
transition state and adsorption energy–scaling relations 45

transmission electron microscope (TEM) 61
trapezohedron (TPH) 149
trisoctahedra (TOH) 146, 404
truncated octahedral nanocrystals (NTOs) 408
turnover frequency (TOF) 161
twin defect 249
two-dimensional structures 15

u

ultrathin nanowires 271
underpotential deposition (UPD) 102
underpotential deposition (UPD) of hydrogen 327
uric acid 475

v

vapor deposition 71
volcano plot 47
Volmer step 336

w

Watanabe-Motoo (W-M) mechanism 336
wave-function theory (WFT) 24
wet chemical methods 71
working electrode 326
Wulff polyhedron 103

x

X-ray absorption fine structure (XAFS) 61
X-ray absorption near edge spectroscopy (XANES) 79
X-ray absorption spectroscopy (XAS) 61
X-ray diffraction (XRD) 61
X-ray photoelectron spectroscopy (XPS) 61

z

zero-dimensional nanoparticles 15